N69-18059-071

NASA TM X- 53793

NASA TECHNICAL
MEMORANDUM

CASE FILE
COPY

NASA TM X-53793

RESEARCH ACHIEVEMENTS REVIEWS

VOLUME II

Series 1 through 12

RESEARCH AND DEVELOPMENT OPERATIONS
GEORGE C. MARSHALL SPACE FLIGHT CENTER
MARSHALL SPACE FLIGHT CENTER, ALABAMA

GEORGE C. MARSHALL SPACE FLIGHT CENTER

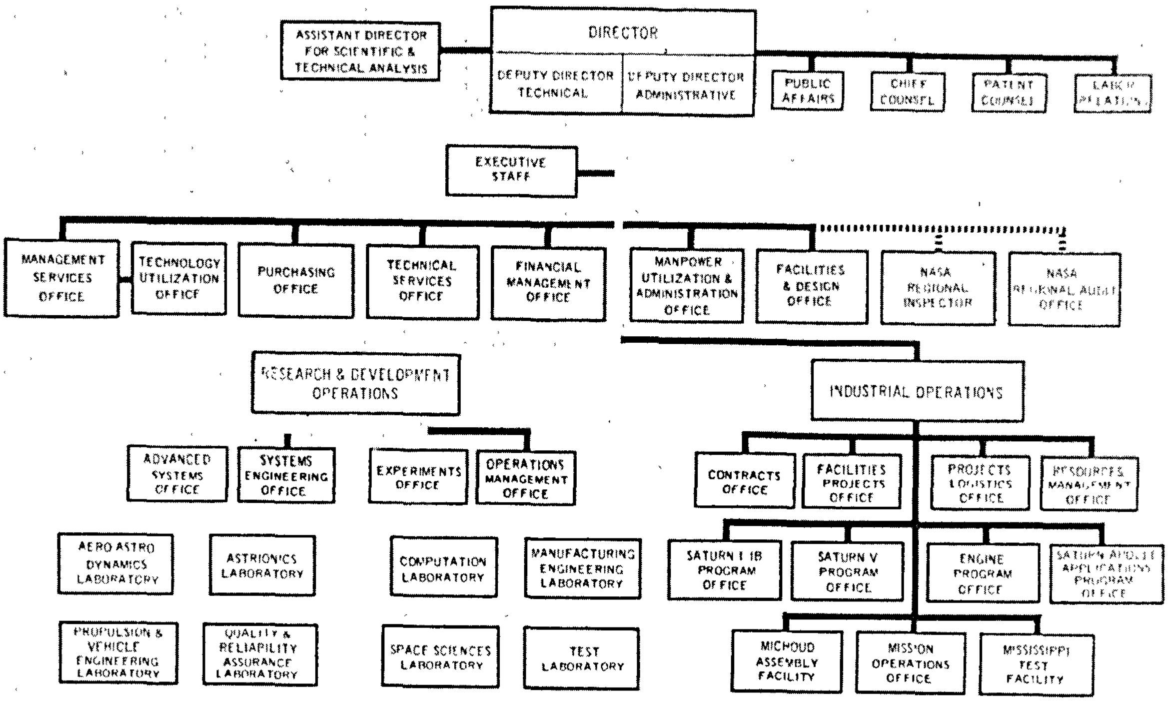

RESEARCH ACHIEVEMENTS REVIEWS COVER THE FOLLOWING FIELDS OF RESEARCH

- Radiation Physics
- Thermophysics
- Chemical Propulsion
- Cryogenic Technology
- Electronics
- Control Systems
- Materials
- Manufacturing
- Ground Testing
- Quality Assurance and Checkout
- Terrestrial and Space Environment
- Aerodynamics
- Instrumentation
- Power Systems
- Guidance Concepts
- Astrodynamics
- Advanced Tracking Systems
- Communication Systems
- Structures
- Mathematics and Computation
- Advanced Propulsion
- Lunar and Meteoroid Physics

1968

NASA TM X-53793

RESEARCH ACHIEVEMENTS REVIEWS
Volume II

Research Program Office
Experiments Office
Research and Development Operations
George C. Marshall Space Flight Center
Marshall Space Flight Center, Alabama

For information concerning the Research Achievements Reviews, contact: Chief, Research Program Office, R-EO-R, Marshall Space Flight Center, Huntsville, Alabama.

PREFACE

In 1955, the team that has since become the Marshall Space Flight Center (MSFC) began to organize the research program within its various laboratories and offices. The purpose of that program was twofold: to support existing development projects by research studies, and to prepare future development projects by advancing the state of the art of rockets and space flights. The effort during the first year was modest and covered relatively few tasks. Communication of results was comparatively easy.

However, as the research program expanded, communication of results threatened to become a serious problem. In February 1965, Dr. Ernst Stuhlinger, Director, Research Projects Laboratory (now Space Sciences Laboratory) initiated a series of Research Achievements Reviews through which the results of research accomplished by the laboratories of the Marshall Space Flight Center were published. Each review covered one or two fields of research in a form readily usable by specialists, systems engineers, and program managers. The review of February 24, 1966, completed the first series. Each review of that first series was documented in the "Research Achievements Review Series," and later compiled and published in a single volume.

In March 1966, a second series of Research Achievements Reviews was started. That second series emphasized research areas of greatest concentration of effort, of most rapid progress, or of most pertinent interest and was published as "Research Achievements Review Reports, Volume II." Volume II covered reviews from March 1966, through February 1968.

This volume is a compilation of that second series of Research Achievements Reviews, each of which is a complete reprint of the review as separately printed — except No. 8 which is a summary rather than a detailed treatment. Review No. 8 dealt with applications of third generation computers and was primarily of interest only to MSFC personnel.

The yearly effort of Marshall Center's research program today represents several millions of dollars and hundreds of tasks, but the twofold purpose of the research program remains unchanged. And, because effective communication of research results continues to be of major importance, the Research Achievements Reviews are now in a third series. Each of the reviews is being documented separately, as was done for the first and second series. The third series will extend from March 1968, through February 1970. When completed, the third series also will be compiled and published in a single volume.

William G. Johnson
Director, Experiments Office

TABLE OF CONTENTS

RADIATION PHYSICS RESEARCH AT MSFC

March 31, 1966

By

Russell D. Shelton

TABLE OF CONTENTS

RADIATION RESEARCH AT MARSHALL SPACE FLIGHT CENTER

by Russell D. Shelton

Page

LIST OF ILLUSTRATIONS

LIST OF ILLUSTRATIONS (Continued)

LIST OF TABLES

RADIATION RESEARCH AT MARSHALL SPACE FLIGHT CENTER

By

Russell D. Shelton

SUMMARY

The status and scope of the Radiation Research Program at Marshall Space Flight Center are described in this report. The application of radiation to engineering problems and the effects of nuclear and space radiation on materials and components are discussed. Much of the progress made in the last year consists of the continued accumulation of engineering data. The Propulsion and Vehicle Engineering Laboratory has continued its testing of materials under reactor space radiation environments. The Astrionics Laboratory is concerned with the effects of radiation on electronic components and the development and calibration of instrumentation for the measurement of the radiation environment. The Research Projects Laboratory has been primarily concerned with the transport of radiation through shields and the aspects of radiation from the physical viewpoint. Appropriate contracts and publications in the field of radiation physics are referenced. Several applications of radiation for the solution of engineering problems are discussed briefly to indicate their feasibility and to provide contract and document references.

INTRODUCTION

Radiation research at the Marshall Space Flight Center (MSFC) is applied in nature and is distributed among organizational elements according to their missions and responsibilities. The effects of radiation on materials is studied by the Materials Division of the Propulsion and Vehicle Engineering Laboratory; the effects of radiation on electronic components is the concern of the Astrionics Laboratory, which is largely electrical engineering in composition. Radiation research is incorporated into existing studies and in laboratories as an integral part of a project or program. For example, a complete description of the dielectric properties must include a knowledge of whether these properties are moisture-, radiation-, or temperature-dependent. From the environmental viewpoint, radiation in the form of X-rays, gammas, neutrons, protons and electrons is just another environmental factor which must be considered by the engineer in his effort to produce equipment which will perform properly.

An effort is also being made to understand the basic transport of radiations through matter and of charged particles through electromagnetic fields. These studies are essential for an understanding and evaluation of problems in technical areas such as advanced propulsion concepts, nuclear power supplies for space applications, spaceship design, nuclear test facility planning, interaction of charged particles with space vehicles, space experiment planning and integration, thermonuclear power, Civil Defense and calibration requirements for radiation measuring instruments.

The presence of high energy charged particle radiation in space is of immediate concern for manned space missions and relative to hazards as a function of time, position and the amount and kind of shielding. These hazards extend to the spacecraft's components and materials exposed to space radiation. A recent example of such a problem was that of charge storage in dielectrics and subsequent Lichtenberg discharges which could produce electrical interference with spacecraft systems. Space experiments, whether or not they are concerned with radiation measurements, must be examined from the viewpoint of their sensitivity to radiations which are not of direct interest, but which may be naturally present in space or present because of radioisotopes in the spacecraft.

The interpretation of many space measurements requires an understanding of how the measured signal interacts with its environment on the way to the detector. The techniques of radiation transport are universally applicable to photons, whether they arise as thermal radiation from hot bodies, as gamma rays emitted from reactors, or as X-rays produced by solar proton bombardment of the lunar surface. The concepts of collisions and cross sections are useful not only on the microscopic scale but also on the planetary scale in the discussion of meteoroid populations.

Electrons, protons, neutrons and photons are the primary concern of this report. Energetic electrons and protons exist naturally in the space environment in the form of trapped radiation, solar flare ejections and cosmic rays. Neutrons and photons, the latter of which may be called X-rays, gammas or bremsstrahlung, depending on their origin, arise because of electron and proton interactions with spacecraft, the atmosphere of the earth, and the lunar surface, and may also arise from radioisotope and nuclear power supplies. Electrons and protons, being charged particles, interact with both matter and electromagnetic fields, whereas neutrons and photons are neutral particles and, for most purposes, interact only with matter.

This report is concerned with radiation research at MSFC and associated contractors. References to published work and NASA contract numbers are included as a guide for those whose interest extends to specific areas.

FACILITIES, PRESENT AND PLANNED

Facilities are usually justified and built because of highly specific program demands. Whether or not they have application to other situations depends on a number of factors such as the versatility of the facility and the associated personnel. As a rule, research facilities and personnel are expected to be more basic and general in orientation, although immediate program requirements may regiment and closely define the work for extended periods of time. The radiation facilities at MSFC are built around some type of radiation source, e.g., a Van de Graaff accelerator, a Co^{60} array, or an X-ray machine. With each radiation facility there must be enough equipment to guarantee safety and to permit measurement, definition, and calibration of the radiation environment produced in the facility. Personnel associated with the facility must have the specialized knowledge and training to use it efficiently and safely.

The location of a facility within an organizational segment does not preclude its use by outside personnel in an entirely different application. For example, Dr. Charlotte Lee of Alabama A & M College was permitted to use the Van de Graaff in the Materials Division for radiological studies.

THE VAN DE GRAAFF FACILITY

The Van de Graaff charged particle accelerator, located in the Materials Division of the Propulsion and Vehicle Engineering Laboratory, is a particularly versatile device for producing various kinds of radiation in energy ranges of interest in space application. The MSFC Van de Graaff Facility (Figs. 1 and 2) was designed for the multiple capability of simultaneously irradiating materials with ions, ultraviolet, infrared and possibly electrons in a vacuum environment. It can also be used to generate large quantities of X-rays by accelerating electrons into high-Z target material and neutrons by accelerating deuterons into a deuterium or tritium target.

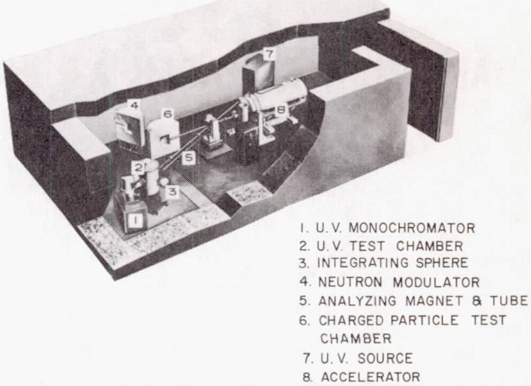

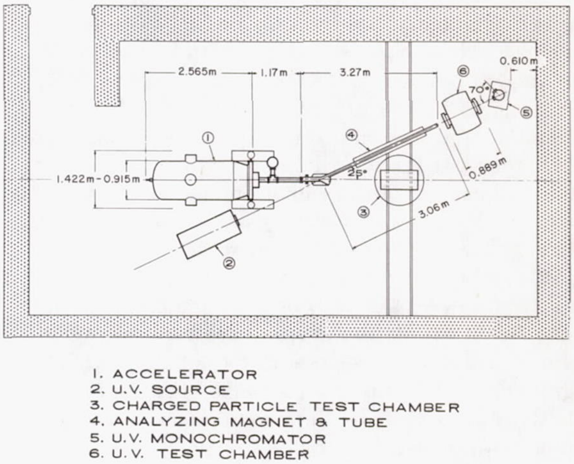

FIGURE 2. SCHEMATIC OF VAN DE GRAAFF FACILITY

ASTRIONICS RADIATION FACILITY

The radiation facility, located in the Instrumentation and Communication Division of the Astrionics Laboratory, is geared toward the testing of electronic components and the development and testing of various kinds of radiation instrumentation. The facility shown in Figures 3 and 4 will house in Hot Cell "B" a 20,000-curie Co^{60} source for gamma irradiations at the dose rate up to 4×10^6 roentgens per hour. Remote manipulators in both hot cells will permit assembly and arrangement of intense radioisotope sources needed for radiation effects testing and instrument calibration.

This basic radiation facility is supported by a large electronics organization with complete capability in all aspects of circuit design, digital techniques, flight instrumentation and environmental testing. The supporting equipment associated with this facility includes a 400-channel pulse height analyzer (RIDL Model 34-12B), a 2π proportional counter system (NMC Model PCC-10A) for radioactivity measurements, and a vacuum pumping system.

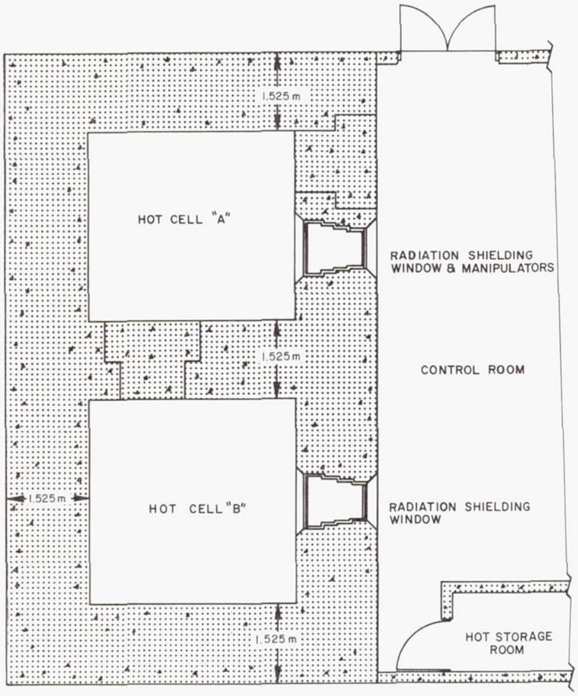

FIGURE 3. SCHEMATIC OF ASTRIONICS LABORATORY'S HOT CELL RADIATION FACILITY

Hot Cell "A" is presently occupied by a neutron generator (Texas Nuclear Model 9900). The device accelerates deuterons into a deuteron or tritium target, thereby producing in excess of 10^{11} neutrons per second from deuteron-deuteron and deuteron-tritium nuclear reactions. This device can also produce energetic protons from the deuteron-tritium reaction, and gamma rays from neutron capture and inelastic collisions.

Also available at this facility is an X-ray generator (Norelco Model MG-100) capable of operating up to 100 kiloelectron volts and producing 2.5×10^6 roentgens per hour at 10 centimeters and a collection of encapsulated sources, including a polonium-beryllium source delivering 1.9×10^6 neutrons per second.

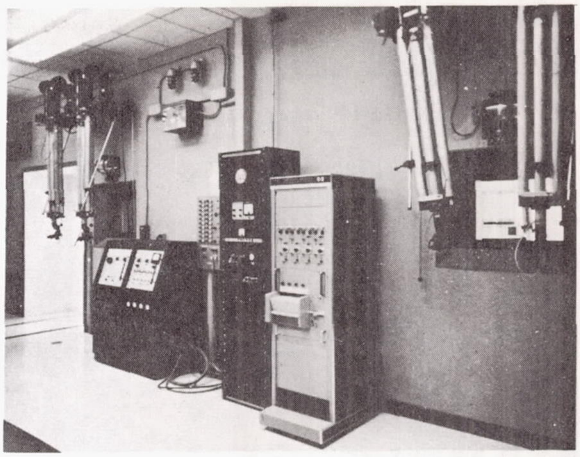

FIGURE 4. ASTRIONICS LABORATORY'S HOT CELL RADIATION FACILITY

OTHER RADIATION FACILITIES

A number of low-level radiation facilities are associated with special radioisotope applications such as shield evaluation, leak detection, instrument calibration, gas pressure and density measurements, and tracer applications. Table I enumerates a number of radioisotope users and their interests. Table II lists a number of radioisotope applications of interest to various R & D people who may or may not have radioisotopes with which to experiment. As a rule, each radioisotope on the premises has some storage facility associated with it and the necessary safety and application appurtenances such as film badges, radiation survey meters, radiation detectors and specialized electronics equipment.

RADIATION EFFECTS ON MATERIALS

The space environment contains several types of radiation which may change the bulk or surface properties of materials. The low-energy protons and alpha particles ejected by solar flares can change surface properties such as emissivity and absorptivity. The high-energy electrons and protons, produced by solar flares or present in the captured radiation belts or cosmic rays, can change the optical properties of lenses and windows and damage solar cells and photographic film. The ultraviolet radiation can promote chemical reactions and outgassing in organics. Neutron and gamma radiation arising from reactors used in nuclear stages for primary propulsion can present a serious materials problem, especially in the immediate vicinity of the reactor. For several years, the Materials Division of the

TABLE I. RADIOISOTOPE USERS AT MSFC

USER	No. of Sources	Purpose
A. M. Payne, R-TEST-IDT	16	Gas density measurements
H. D. Burke, R-ASTR-IMT	5	Instrument calibration and research
B. Corder, R-QUAL-AVR	3	Leak testing
A. Hafner, R-ASTR-IMP	2	Density measurements
R. Potter, R-RP-N	8	Electron density measurements
H. Hilker, R-QUAL	1	Leak testing
T. Knowling, R-P&VE-MEE	4	Instrument calibration
W. White, R-TEST	50	Density measurements in cryogenic fluids
C. Jacks, Emergency Planning	1	Civil Defense
E. Parrish, R-AERO	4	Gas density measurements
E. Donald, R-TEST	6	Gas density measurements
W. L. Kimmons, R-ASTR	1	Ionization pump

TABLE II. USES OF RADIATION SOURCES

- Design and calibration of radiation detectors
- Leak detection
- Velocity indication
- Damage studies
    - Materials
    - Components
- Radiation effects
    - Materials
    - Electronic components
- Radiation research
    - Shielding
    - Activation
- Density measurement
    - Vacuum chamber
    - Cryogenic fluids
- Random number generators
- Tracer techniques
    - Wear, Ablation, Flow rates,
    - Chemical and Biological processes
- Solid-state research
- X-ray techniques
    - Proton shield evaluation
    - Gas density measurements
    - Saturn V test stand checkout
    - Inspection of components
    - Liquid level indicators
    - Disconnect signals
- Civil defense planning
- Ionization pump

Propulsion and Vehicle Engineering Laboratory has been studying the effects of various kinds of radiation on materials important to space vehicles. These radiation effects are measured and described in the manner common to materials testing, i. e., as an integral part of a complete materials testing and development program which considers all possible environmental aspects, including radiation. Radiation testing of materials has followed two main lines: (1) that of evaluating materials in a nuclear rocket radiation environment, and (2) that of evaluating materials in a space radiation environment. In some cases, radiation damage in one situation can be related to that in another, but as a rule the change in components, materials, exposure times and environments involved does not permit easy and reliable extrapolation from one situation to another.

The combined effects of space environmental parameters on space vehicle materials has been studied under both inhouse and contractor effort [1] with emphasis on solving the problems of making appropriate in situ measurements of samples during simultaneous exposure to several environmental factors such as low temperature, vacuum, ultraviolet radiation, electrons and protons.

The combined effects of nuclear radiation, cryogenic temperature, and vacuum on the electrical properties of engineering materials has been studied in considerable depth and detail by Gause and McKannan [2, 3, 4]. The measurement of material properties during reactor irradiation is made difficult and expensive by the fact that the test equipment is damaged and activated, and by the requirement of remote operation and instrumentation. Consequently, most material tests have been made before and after irradiation. Materials recently tested [5] under combined nuclear radiation, cryogenic and vacuum environments are shown in Table III [6]. For testing details and lists of other materials tested, a contractor's report is recommended [7].

TABLE III. MATERIALS TESTED UNDER COMBINED NUCLEAR RADIATION, CRYOGENIC, AND VACUUM ENVIRONMENTS

AEROBOND 430, EPOXY PHENOLIC ADHESIVE
LEXAN, POLYCARBONATE / GLASS LAMINATE
KYNAR, VINYLIDENE FLUORIDE PLASTIC
SILASTIC 1410, SILICONE ELASTOMER
MYLAR C, POLYESTER FILM
SYLGARD 182, SILICONE POTTING COMPOUND
Q94-002 FLUOROSILICONE SEALANT
PRP-2277 NEOPRENE ELASTOMERIC SEAL
PRP-19007 FLUOROCARBON ELASTOMERIC SEAL
PRP-737 ACRYLONITRIDE ELASTOMERIC SEAL
CRP-20-2 POLYURETHANE FOAM (CO_2 BLOWING AGENT)
CRP-20-2X POLYURETHANE FOAM (FREON BLOWING AGENT)
CRP-20-2X EPOXY FOAM (FREON BLOWING AGENT)

RADIATION EFFECTS ON ELECTRONIC COMPONENTS AND SYSTEMS

The effects of nuclear radiation on electronic components has been of design importance since the advent of nuclear fission power and was investigated with considerable resources during the development of the nuclear powered airplane. In the space environment, the familiar problems associated with the neutrons and gammas from nuclear power reactors are augmented by the presence of energetic electrons and protons and other high-energy charged particle radiations.

THE EFFECTS OF REACTOR RADIATION ON ELECTRONIC COMPONENTS

Interest in propulsion by nuclear heat exchanger rockets has resulted in studies [8] of the effects of reactor radiation on electronic components in environments such as that shown in Figure 5 [9].

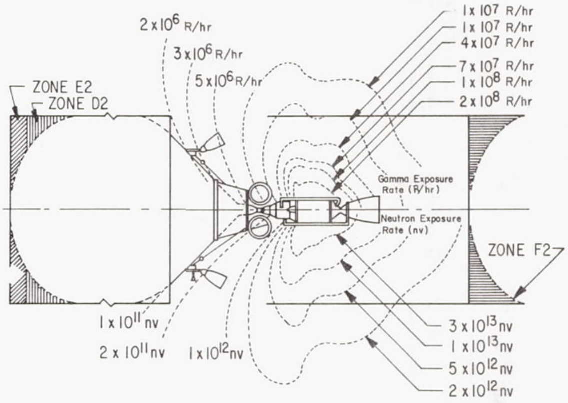

	NEUTRONS (n)		GAMMA (γ)	
ZONE	TOTAL EXPOSURE n/cm^2	PEAK RATE n/cm^2-sec	TOTAL EXPOSURE R	PEAK RATE R/hr
D-2	1.7×10^9	4×10^8	9.2×10^3	1.6×10^5
E-2	3.3×10^9	6.2×10^8	1.3×10^4	2.2×10^5
F-2	1×10^{12}	1×10^{11}	2.8×10^2	2.8×10^5

FIGURE 5. RADIATION FLUX FIELDS OF A NUCLEAR HEAT-EXCHANGER ROCKET

Emphasis has been placed on the study of the more susceptible semiconductor devices, the less sensitive electronic components such as resistors, capacitors, inductors and electron tubes, and the design of circuits "hardened" to radiation.

An example of the hardening process is shown in Figures 6 - 8. In Figure 6, an unhardened power supply showed severe degradation at 10^4 roentgens exposure. With some attention to component selection based on radiation testing histories and some circuit redesign, power supplies can be hardened sufficiently to survive a 3 x 10^5 roentgens exposure, as shown in Figure 7 [10]. With a special effort at design for radiation survival and some sacrifices in what might be an optimum design without the radiation problem, it is possible to push the useful operation [11] of the system beyond an exposure of 5 x 10^6 roentgens or 10^{14} nvt (neutrons per square centimeter) as shown in Figure 8.

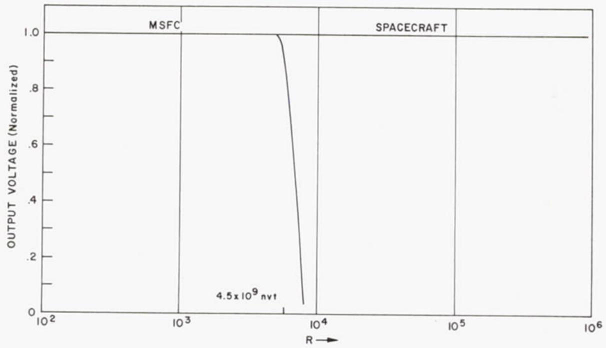

FIGURE 6. PERFORMANCE OF IRRADIATED UNHARDENED POWER SUPPLY

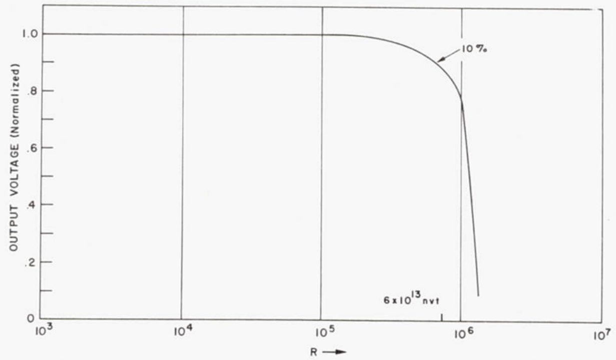

FIGURE 7. PERFORMANCE OF IRRADIATED HIGH-VOLTAGE POWER SUPPLY MODIFIED FOR RADIATION ENVIRONMENT

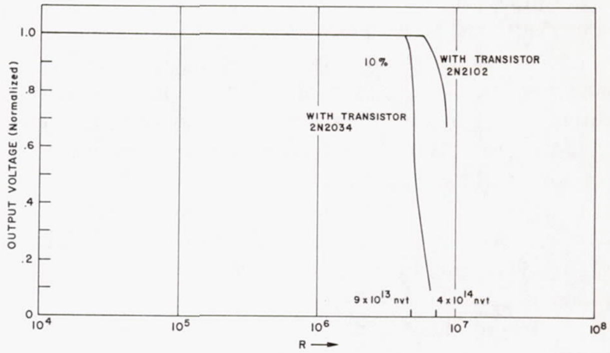

FIGURE 8. PERFORMANCE OF IRRADIATED SERVOAMPLIFIERS WITH SPECIAL DESIGN FOR RADIATION ENVIRONMENT

The study of problems existing for Saturn measurement components used in conjunction with a RIFT stage has proceeded with preliminary testing at the Georgia Nuclear Laboratories of Lockheed. Twenty-five out of twenty-eight units withstood ten times the levels expected in the reactor inflight test (RIFT) instrument unit [12]. A summary of the categories of devices tested is given in Table IV. Other items listed [13] included a large number of solid-state devices, capacitors, differential amplifiers, transistors, resistors, cables, batteries and exploding bridge wire parts. In future tests, emphasis will be placed on microelectronics and new devices which show promise of useful application.

TABLE IV. SATURN MEASUREMENT DEVICES IN A REACTOR RADIATION ENVIRONMENT

Temperature Gauge	AC Amplifier
Temperature Transducer	Microphone
Pressure Transducer	Emitter Follower
DC Amplifier	Accelerometer
Carrier Amplifier	Rate Gyro
Power Supply	Ion Chamber System
Leak Detector	Semiconductor Radiation Detectors

In a radiation environment some electronic elements such as transistors fail long before other transistors, supposedly identical, suffer significant radiation damage, resulting in failure of random components. Apparently there were deviations in materials or transistor production techniques which were not discernible in the initial tests but which later became important in the radiation environment. It would be desirable to separate these potential maverick elements from the group before they are used in components to be exposed to radiation.

In order to select transistors which are uniformly resistant to radiation, a study [14] of the relevance of various design and manufacturing features to radiation survival is under way. Particular attention is being paid to possible surface effects and auxiliary materials because failures have occurred long before the basic semiconductor properties should have changed under irradiation.

Another approach to improving radiation resistance is to go to new semiconductor materials. Silicon carbide amplifiers now being developed [15] are expected to survive an irradiation of 10^{14} to 10^{15} nvt at temperatures of 573° to 673° K.

THE EFFECTS OF CHARGED PARTICLE RADIATION ON ELECTRONIC COMPONENTS

Because of the low radiation doses associated with components afforded even a minimum of shielding by spacecraft shells and normal packaging envelopes, damage by the electrons and protons present in space has not been viewed as a serious problem for the average electronic circuit. However, some components such as solar cells and electrical cables are directly exposed to the radiation environment and some protection must be provided.

The damaging effect of charged particle radiation on solar cells has been studied both experimentally [16a] and theoretically [16b], and is presently guarded against by specially designed covers which incorporate good optical properties but probably more shielding than is necessary. If large solar arrays are used for propulsion power, more attention must be given to establishing minimum weight shields [17].

The storage of charge in dielectrics exposed to radiation has been studied for many years. In space, charge accumulation because of exposure to electrons and protons can easily cause spurious currents in the picoampere range. In addition, the charge storage distorts the local electric field, and if the field becomes intense enough, dielectric breakdown and spurious signal production can occur. Distortions of the local electric field by charge accumulation in dielectric paints used to achieve a proper heat balance can affect sensitive measurements of the space plasma. A large number of small Lichtenberg discharges in such paints might produce electrical noise which would interfere with satellite electrical systems.

SHIELDING AND TRANSPORT STUDIES

The study of the propagation of radiation through matter and force fields is of paramount interest in the fields of physics and astronomy, and is often designated by such names as radiation shielding or radiation transport. Radiation shielding research at MSFC is directed toward answering a number of operational and design questions: How much shielding should be applied to a solar cell which must operate for one year in a 1000-kilometer equatorial earth orbit? How long can an astronaut safely remain in stationary earth orbit without a solar flare storm cellar? How much shielding and what kind of material should be used to protect photographic film in a manned space vehicle designed for a three-week stay on the moon? What should be the amount, composition, and disposition of shielding for a manned Mars landing vehicle using nuclear rocket and nuclear electric propulsion? How do radioisotope power supplies interfere with radiation experiments? To answer such questions, one must know what kind of radiation is involved; how it is distributed with respect to time, energy and position; how it interacts with matter; and how much radiation exposure can be tolerated. These are not simple questions and can be attacked only by dedicated, competent and specialized study.

The uncertainties in shielding calculations can be associated with a lack of knowledge in the radiation environment, errors and omissions in computing the interaction of radiation with matter and fields, and errors in estimating the tolerance to radiation of the item to be shielded. Shielding interests at MSFC have been concerned primarily with transport problems, but have had to consider the other aspects to provide answers to questions of practical interest. In general, environmental data were obtained from compilations by specialists under joint NASA and DOD contract to accumulate, extrapolate, and refine radiation data available from U. S. and U. S. S. R. satellite measurements.

PROTON SHIELDING

The big uncertainties have been removed from the transport part of proton shielding, and the major concern is with computing refinements to economically handle the complex geometries normally associated with men and spacecraft. Machine costs can be reduced considerably by devising simplified analytical functions to represent the mass of physical data associated with proton energy spectra and penetration formulations [18]. Most of the interest in space shielding has been associated with high-energy protons [19] because of their great penetrating power and their capability of producing secondary radiations.

As the problems of proton shielding have become better understood and more stabilized, and as the capability to use specialized machine codes have become more widespread, demands for simplified, accurate and convenient compilation of computer input data have increased. Figure 9, taken from a recent study [20], shows the relative error incurred when a relatively simple and analytical expression is substituted for more accurate but highly cumbersome Bethe-Bloch formulation. Table V gives the eye and abdomen radiation doses [21] for an eight-man spacecraft using 2.54 and 19.3 centimeters of polyethylene shielding during a large solar flare. In these calculations, the emphasis is on a complicated geometry with simplified radiation data input. The effect of considering equipment and other new members in the calculation is in dramatic evidence.

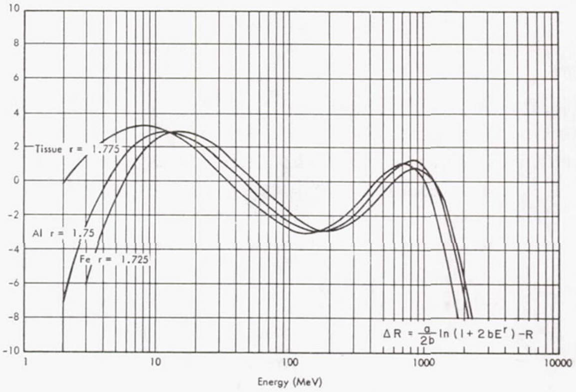

FIGURE 9. PROTON RANGE ERROR CURVE

TABLE V. EYE AND ABDOMEN RADIATION DOSES FOR AN EIGHT-MAN SPACECRAFT DURING A SOLAR FLARE

$$\frac{d\phi}{dp} = 5.675 \times 10^8 \exp(-p/80) \quad \frac{\text{Protons}}{\text{cm}^2 - \text{MV}}$$

Detectors	1E	1A	2E	2A	3E	3A	4E	5E	5A	6E
19.3 cm Polyethylene										
Shield Only	2.87	2.87	1.49	2.07	3.00	2.51	2.36	1.59	2.08	1.62
Shield + Equipment	1.82	1.92	1.36	1.80	2.18	2.10	1.66	1.43	1.80	1.44
Shield + Crew + Equipment	1.17	0.29	0.78	0.20	1.24	0.30	1.28	0.82	0.20	0.84
2.54 cm Polyethylene										
Shield Only	203.	194.	98.0	122.	198.	165.	176.	107.	124.	105.
Shield + Equipment	83.5	95.5	91.6	96.5	116.	115.	88.6	98.1	97.4	89.5
Shield + Crew + Equipment	30.4	1.87	47.6	1.16	42.1	2.12	54.4	48.9	1.23	49.7

E = detector in eye
A = detector in abdomen
1 = middle crew member at instrument console
2 = crew member in top bunk, head under instrument console
3 = crew member in hatchway
4 = right crew member at instrument console
5 = crew member in top bunk, feet under instrument console
6 = crew member in bottom bunk, head under instrument console

The proton environment varies greatly with time [22], and many studies are concerned with the worst probable situations. Figure 10, taken from a recent calculation by M. O. Burrell, shows the proton dose for the three largest solar flares in the last solar cycle. Here again, simplified representations of the solar flare spectra and the proton range formulations were used.

ELECTRON AND BREMSSTRAHLUNG PENETRATIONS

The Monte Carlo work of Martin Berger [23] of the National Bureau of Standards has been reduced to a few simple equations which can be incorporated into

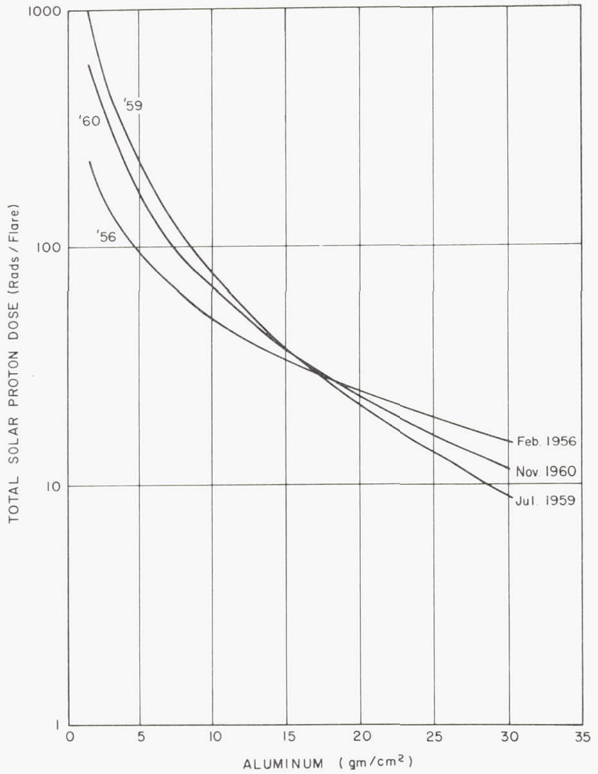

FIGURE 10. ACCUMULATIVE DOSE THROUGH VARIED THICKNESSES OF ALUMINUM FROM SOLAR PROTONS AND COSMIC RAYS

a computer code to calculate number, energy and dose penetrations for both normal and isotropically incident electrons. More sophisticated analytical codes have been written to calculate in a reasonable fashion the bremsstrahlung production and penetration in various materials. These codes are quite useful in obtaining realistic estimates of electron and bremsstrahlung doses in satellite orbits [24]. Results based on their application will be presented later in this report.

ELECTRON INTERACTIONS

The interactions of electrons with matter are extremely complicated and are of current concern to the studies of quantum electrodynamics and quantum field theory. Recently, M. E. Rose suggested that the picture might be further complicated by the facts that the electron sees a multipole nuclear field [25] and that bremsstrahlung emission can occur from both the electron and the nucleus. Because of its intrinsic difficulty, both theoretically and experimentally, the work on electron interactions has been characterized by intense interest and close cooperation by a highly select and specialized group of people. Experimental work has progressed at General Atomic [26] and Ling-Temco-Vought [27] and theoretical work has been done at General Atomics [26], National Bureau of Standards [28], and Union Carbide Corporation [29].

The agreement between theory and experiment has advanced satisfactorily as shown in Figures 11-13, [26, 27]. The experimental work has required painstaking effort to avoid background problems [30]. The theoretical effort has become quite involved in the truncation of series [31] for greatest accuracy, the sophistication of Monte Carlo techniques [32], and the evaluation of integrals which resist conventional approaches [33].

The interactions of electrons with matter are of basic importance for shielding of personnel and equipment on space vehicles from electrons in space. The present investigations were prompted by inadequacies in existing experimental data and theoretical methods.

An effort was undertaken to provide the shield designer with a straightforward, sufficiently accurate formula for establishing bremsstrahlung dose

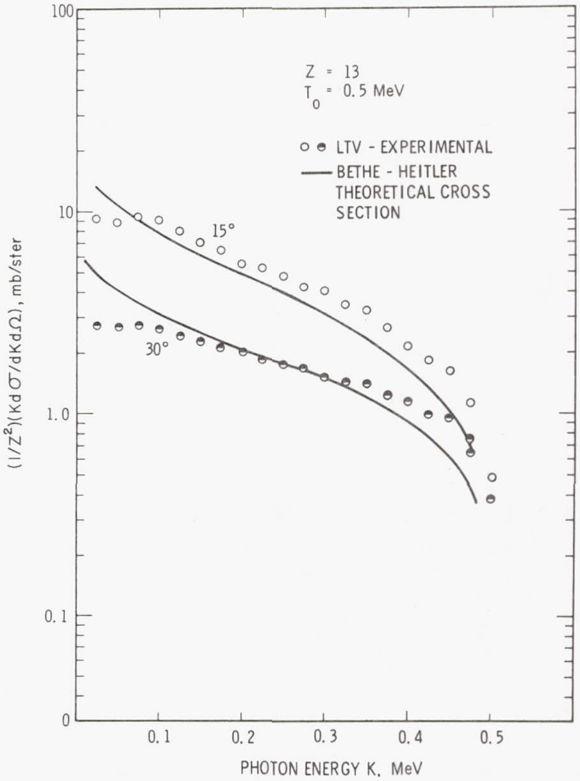

FIGURE 11. THIN TARGET DIFFERENTIAL CROSS SECTIONS

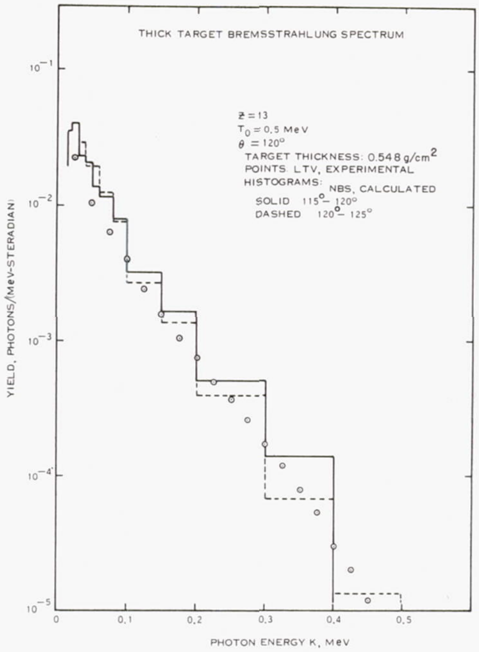

FIGURE 12. THICK TARGET BREMSSTRAHLUNG SPECTRUM

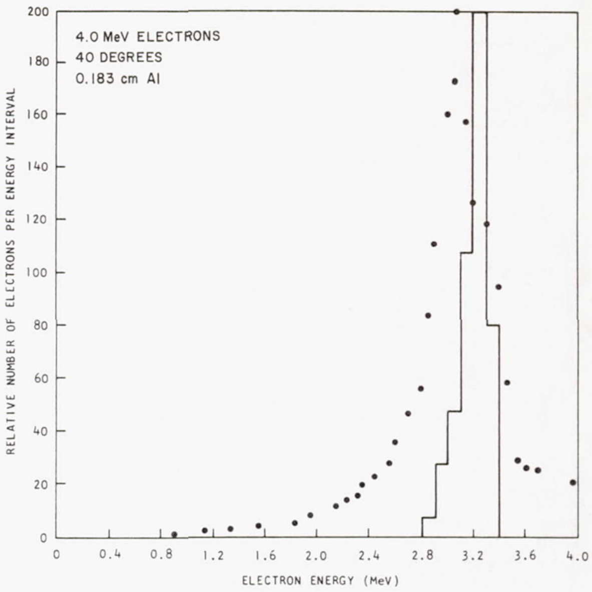

FIGURE 13. ELECTRON ENERGY SPECTRUM AT FORTY DEGREES FOR A 0.183-cm THICK ALUMINUM SLAB TARGET

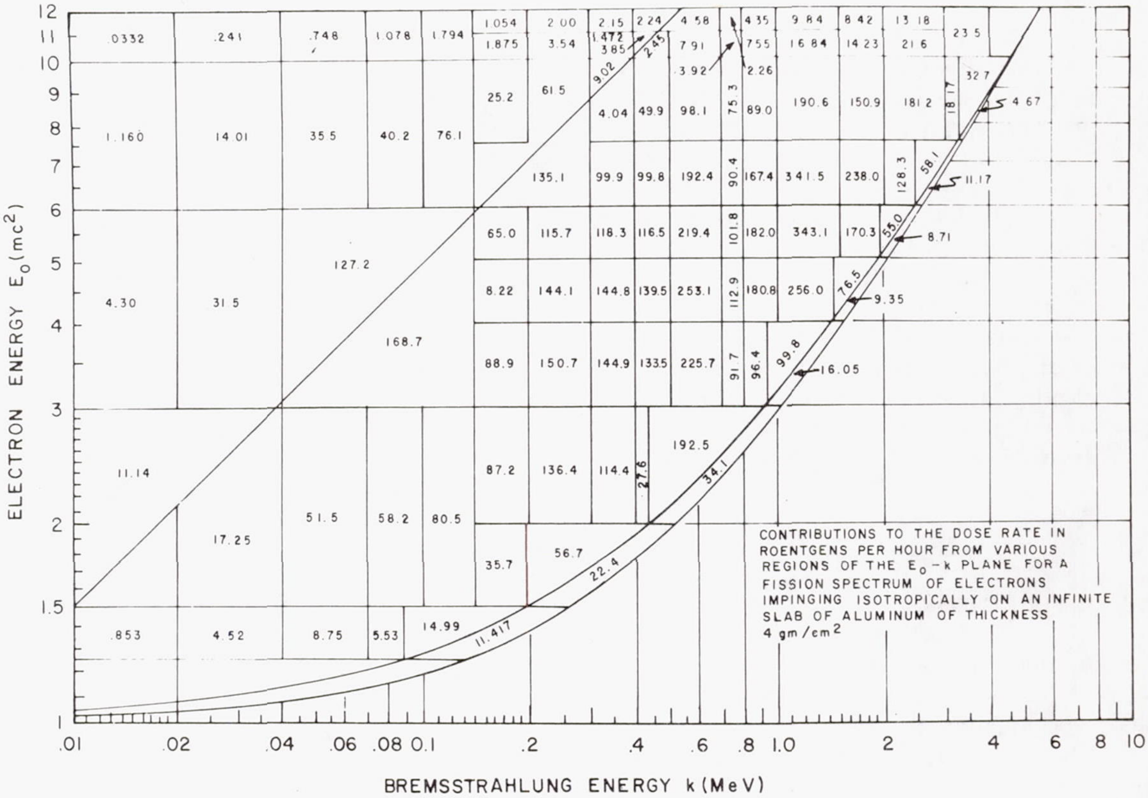

FIGURE 14. ERRORS IN BREMSSTRAHLUNG DOSE CALCULATION DUE TO INACCURACIES IN INPUT CROSS SECTION DATA

as a function of incident electron spectrum and shield parameters [34-35]. One of the essential problems was to estimate the errors incurred in the calculated result due to inaccuracies in the input bremsstrahlung production cross section data. Some of the results of this effort are shown in Figure 14 [35]. The detailed explanation of this work is in the process of being published. An interesting calculation associated with the above work was performed by M. O. Burrell and is shown in Figure 15. Here, the integrated proton flux at the end of each orbit is plotted and compared to an accumulative average. The high points are associated with passages through the South Atlantic anomaly.

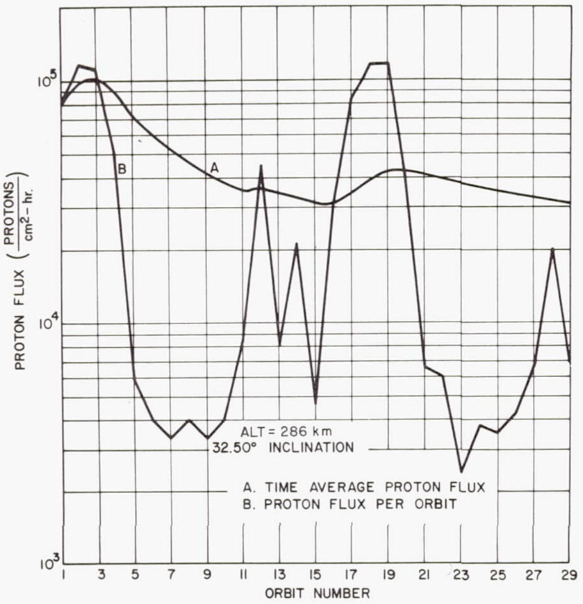

FIGURE 15. PROTON FLUX CURVES FOR EARTH ORBITS

REACTOR RADIATION SHIELDING

Comparison, Evaluation, and Shield Calculation Methods

Work was undertaken [37] to effect a comparison and evaluation of various shield calculation methods as applied to typical reactor systems for nuclear rocket propulsion. To this end, two simplified reactor-shield configurations were chosen, and insofar as possible, the same cross section input data were used in all calculations.

Three classes of calculation methods were employed: point kernel, discrete ordinates or angular segmentation, and stochastic or Monte Carlo. Two or more existing operational programs of each type were considered.

Criteria adopted for code evaluation include the following:

(a) Type and detail of data obtainable

(b) Flexibility for treatment of system configuration, radiation sources and types of radiation interactions

(c) Computer running time and time required for problem preparation

(d) Relative difficulty of operation

(e) Comparative accuracy of output.

Results of the study are presented in Lockheed-Georgia Report ER-8236, Evaluation of Methods for Computing Nuclear Rocket Radiation Fields.

Two figures relating to this work [38] are shown below. Figure 16 gives an outline of the two shield models which were used in the calculations. Figure 17 shows a dose rate traverse computed for configuration A, using five different calculational methods.

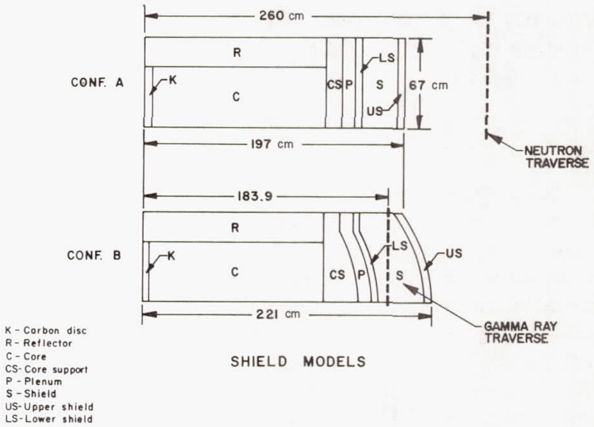

FIGURE 16. RADIATION SHIELD MODELS USED IN COMPUTING NUCLEAR ROCKET RADIATION FIELDS

A follow-on study is planned that will choose one or perhaps two of the most promising methods, convert these to Fortran IV, check them on MSFC computing equipment and train personnel in their operation.

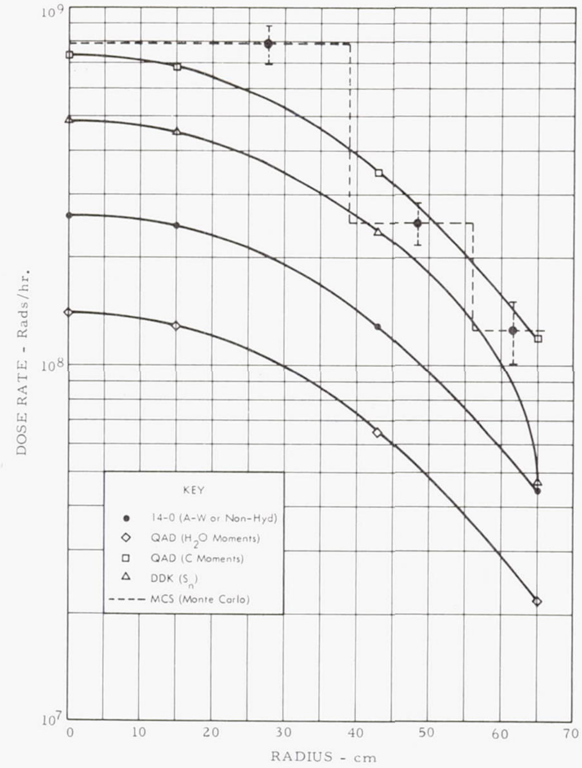

FIGURE 17. NEUTRON DOSE RATE TRAVERSE USING DIFFERENT CALCULATION METHODS

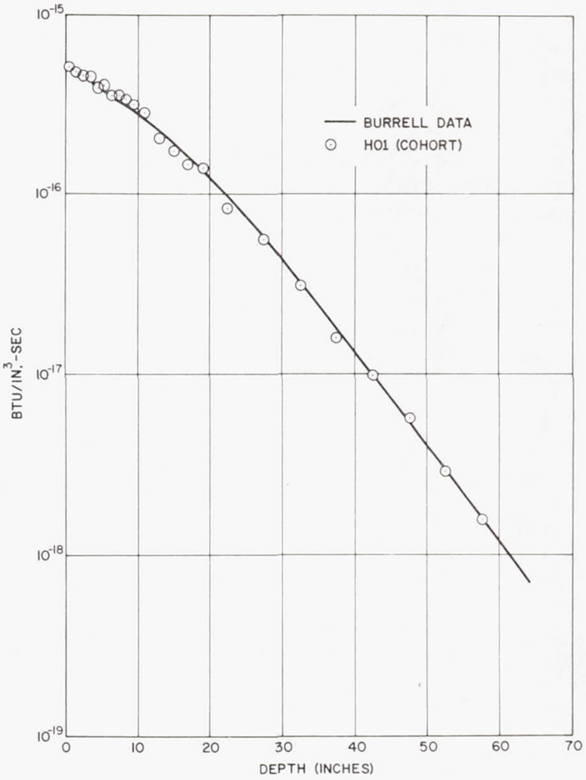

FIGURE 18. HEAT DEPOSITION VERSUS DEPTH FOR 7 MeV NEUTRONS IN A LIQUID HYDROGEN SLAB

Development of Machine Codes for Calculating Radiation Fields in Nuclear Rockets

The development of a Monte Carlo calculation program to predict the dose and heating inside and outside typical nuclear rocket reactor shield systems and in the hydrogen fuel tank has been in progress for several years. A current contract [39] with Radiation Research Associates, Fort Worth, should result in a completely checked-out Fortran IV version of the program (called COHORT) and in the training of MSFC personnel to operate the program on the MSFC computing equipment. Essentially all of the component routines have now been checked out, and some sample test problems have been run. One simple geometry problem is that of determining heat deposition in a semi-infinite slab of hydrogen. Results of this calculation for a normally-incident plane beam of 7-megaelectron-volt neutrons are shown in Figure 18 [40], together with results determined previously by Burrell [41] using his special purpose hydrogen heat deposition code.

Radiation Research is also planning to use COHORT on one of the sample configurations employed by Lockheed-Georgia in their shield evaluation study to obtain a direct comparison against other calculation methods.

ELECTROMAGNETIC SHIELDING

The research program on active or electromagnetic shielding has continued in two main areas: analysis of the motions of charged particles in magnetic fields, and advancement in the development of superconducting magnets that will be required for such shields.

Two types of active shields have been shown to be competitive with passive or bulk shielding from the standpoint of system mass: (1) The magnetic shield which employs purely magnetic forces to deflect charged particles away from a spacecraft, and (2) the plasma shield which repels positively charged particles electrostatically while being held in position around the spacecraft by a magnetic field. Magnetic shields have earlier been shown [42, 43] to be feasible and competitive provided the shielded volumes are large enough and allowable primary dose rates for extended missions are set low enough. Plasma shields, because they require much smaller magnetic fields and therefore lighter magnetic structures, could be considerably lighter than either passive or purely magnetic shields for all shielded volumes and dose rate requirements. However, the rather early state of research on the plasma shield concept and the fact that it has not yet been demonstrated that a successful plasma shield concept can be built prevents any firm predictions of the competitive positions of magnetic and plasma shields.

Charged Particle Motion

Several aspects of the theory of charged particle motion in axially symmetric magnetic fields were extended during the past year. A theoretical treatment of the problem of specifying the shielding capabilities of general axial field configurations, and application to some particular fields was published [44]. Figure 19 shows a number of limiting cases for charged particle exclusion from the vicinity of a pair of coaxial current loops whose symmetry axis is the vertical axis. This general work was also extended [45] to a case of geomagnetic interest - a dipole plus coaxial quadrupole. Related work was also carried out under the laboratory support contract. This work resulted in an annotated bibliography [46] of the literature on charged particle motion and magnetic shielding. More recent studies under this task [47] are considering the permissible particle fluxes in the vicinity of a dipole field (plus various equatorial current ring configurations) and of the fields of solenoids.

Development of Superconducting Magnets

Work to advance the physics and technology of large, high field superconducting coils was actively pursued over the past year with five contracts [48-52] covering a number of areas of investigation.

The chief topic of concern was the attempt to understand in detail supercurrent instabilities in

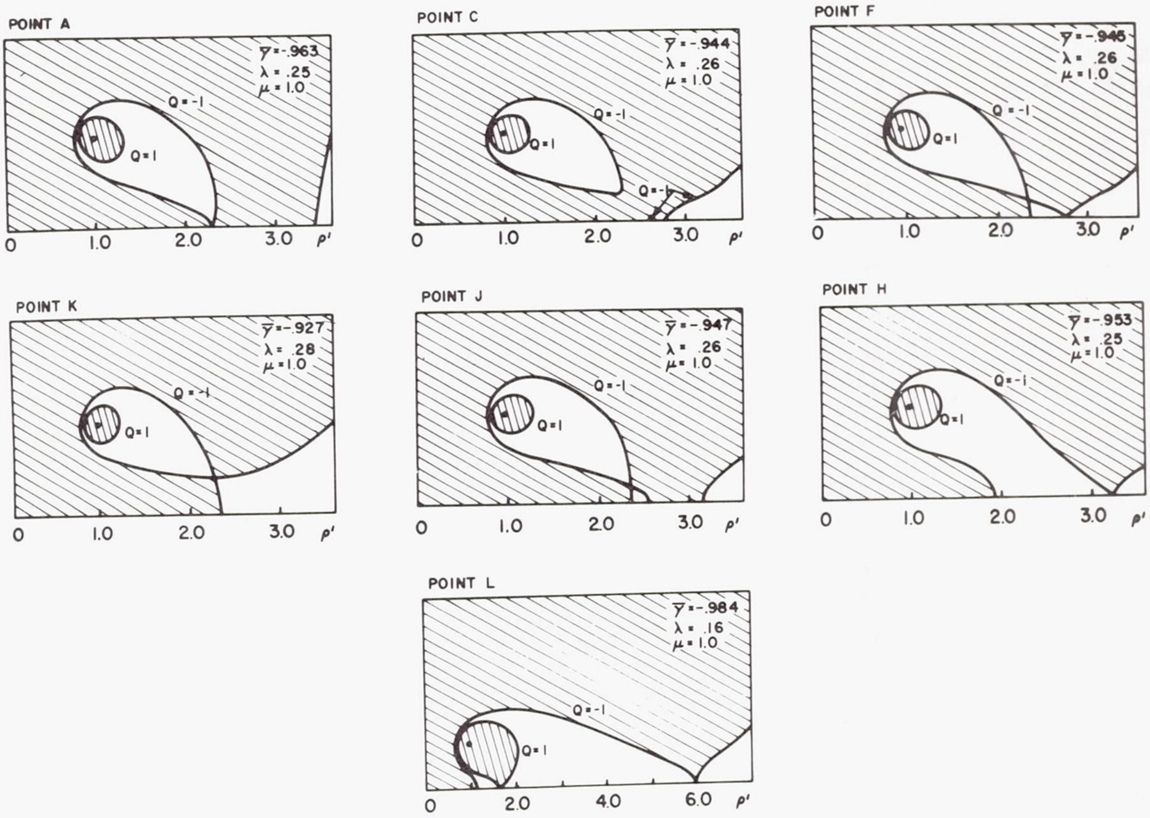

FIGURE 19. CRITICAL POINTS IN THE (ρ , θ) PLANE OF A DOUBLE-PARALLEL LOOP SYSTEM

superconductors. These instabilities, due to nonuniform flux motion through the magnetic windings as the field is changed, prevent the attainment of theoretically possible fields without the use of involved and expensive metallurgical and manufacturing methods. The effects on these instabilities due to metallurgical structure and history, conductor shape and winding configurations, and magnetic and thermal environment were the subject of considerable research effort [53-64]. Other work covered the changes in superconductive properties due to nuclear irradiation [55], microprobe techniques for mapping field and current distributions within coil windings [62, 63], flux pumping techniques for energizing high current windings by means of low current power sources [64], and use of the superfluid properties of Helium II to improve the cooling within tightly wound magnets without separate cooling passages [64].

Work performed under this program and by other organizations continues to advance the magnetic field strength and working volume of superconducting magnets as illustrated in Figure 20. The devices indicated by X are the more important of those tested or under construction during the past year. Shown also are the field-volume combinations which will be required for magnetic and for plasma shields. As magnet sizes and field strengths increase, problems of providing an environment of liquid helium for refrigeration, of providing structural strength to withstand the high magnetic forces, and of providing access to the useful high field region become correspondingly more serious, and costs rise accordingly - hence the small number of new devices.

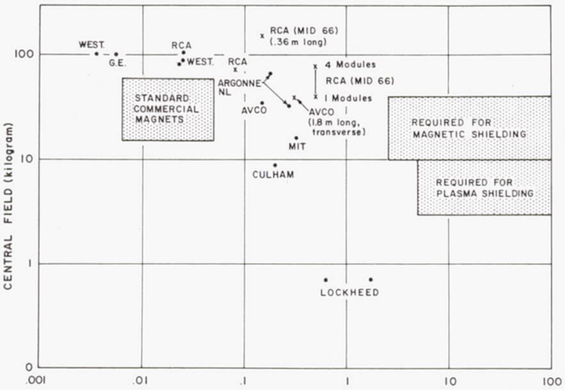

FIGURE 20. SUPERCONDUCTING MAGNETS, JANUARY 1966

The Plasma Shield Concept

The recent plasma shield work at Avco [65] has been characterized by active theoretical work and the construction of new experimental apparatus. Several lines of important collateral research seem to be developing along with the plasma shield. The plasma shield concept [66] shown in Figure 21 is as follows: By means of a strong magnetic field supplied by superconducting magnets, electrons are removed and excluded from the space vehicle, which assumes a positive charge. The electric field provided by the charge separation protects the spacecraft from energetic positively charged particles.

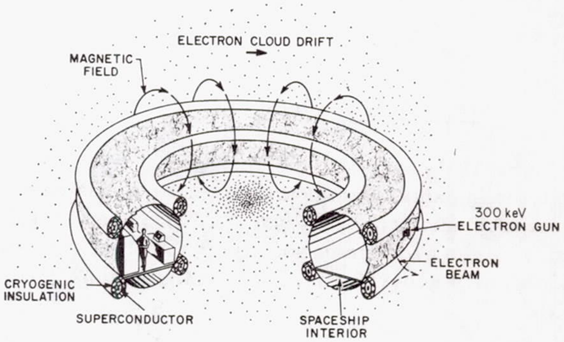

FIGURE 21. SCHEMATIC DIAGRAM OF A SPACE VEHICLE USING A PLASMA RADIATION SHIELD

The interesting feature of the plasma shield is that it establishes an electric potential hill on the inside of a magnetic field about which a cloud of electrons migrates. The electrons can move across the field to the positively charged region only by collisions with each other or with neutral gas atoms and ions. By measuring the rate of electron migration, it is speculated that gas pressures as low as 2.67 x 10^{-16} newtons per square meter can be measured.

By inverting the configuration so that electrons are on the inside of the magnetic field, there is created a potential well into which positive ions can be injected and contained at very high energies. This means that the plasma shield concept could evolve into a high-energy reaction chamber [67] useful for studying collision and nuclear processes. It is also possible to think of the device as a high voltage generator. The voltages which the developers think will be feasible are shown in Figure 22 [66].

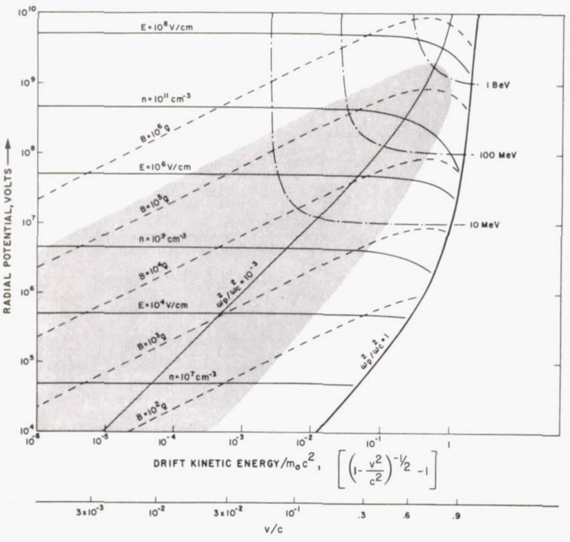

FIGURE 22. MAP OF ONE-METER ELECTRON PLASMA CONTAINMENT DEVICE

Another possibility consists of using the device as an oscillator at microwave frequencies [68] with the ability to radiate over a widely adjustable frequency range without wave guides and antennae.

PARTICLE POPULATIONS AND METEOROID DISTRIBUTIONS

The behavior of particle swarms has been studied (1) for the purpose of providing the physical framework for understanding measured distributions of meteoroids and dust particles and (2) for computing the relative hazards associated with dispersions by explosions in orbit and on the lunar surface. The relation of the distribution functions to such parameters as satellite motion, distance from the earth, meteoroid velocity and direction of injection has been discussed in a series of published papers [69-73]. Present work is concerned with the distribution of debris on the lunar surface by active seismic shots [74].

A recent study of bound orbits [75] published by Hale and Wright in the JGR, resulted in data such as that shown in Figure 23, which shows what happens to particles injected isotropically at various altitudes as a function of injection velocity. The most interesting feature of this study is the fact that the flux maximum for such distributions always occurs at less than 1.5 earth radii away from the center of the earth. The fraction of particles in surviving orbits to total particles injected isotropically at r_0 is shown in Figure 24 [75].

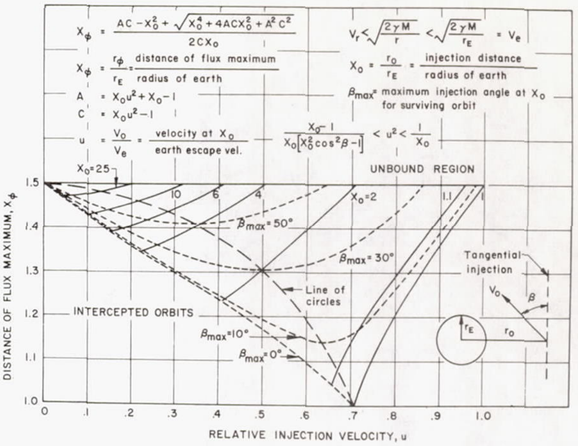

FIGURE 23. RADIAL DISTANCE OF FLUX MAXIMUM FOR BOUNDED PARTICLES

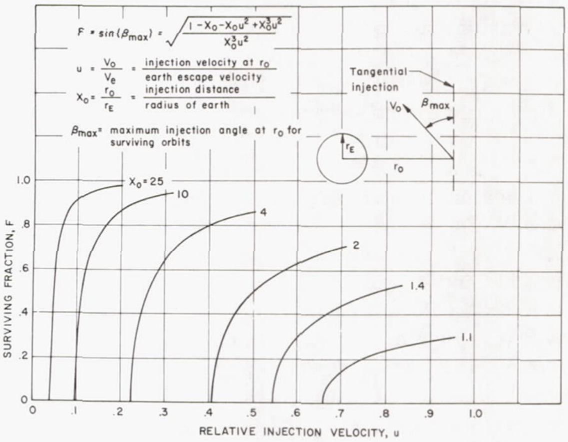

FIGURE 24. FRACTION OF PARTICLES IN SURVIVING ORBITS TO TOTAL PARTICLES INJECTED ISOTROPICALLY AT r_0

ELECTRONIC CHARGE STORAGE PHENOMENA

In order to learn more about the phenomena resulting from electronic charge storage in dielectrics in general and the observable effects in particular to be expected when Pegasus panels are subjected to the electron bombardment in the charged particle belts around the earth, a small experimental program was undertaken under contract with Lockheed-Georgia Nuclear Laboratories. To this purpose, a specially designed strontium-yttrium beta ray source was fabricated by the Isotope Division of the Oak Ridge National Laboratory. The source (Fig. 25) comprises

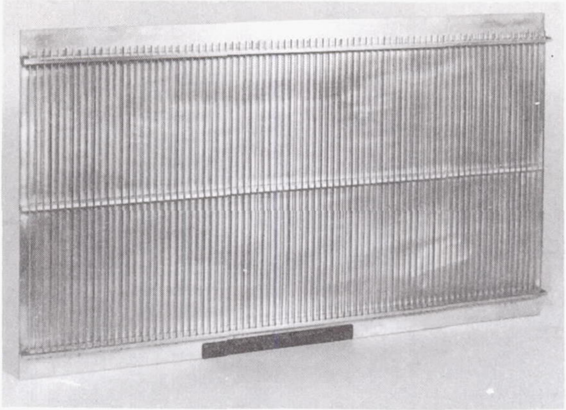

FIGURE 25. STRONTIUM-YTTRIUM BETA RAY SOURCE

80 tubes with an active length of about 20 inches (51 centimeters) and a total source strength of approximately 800 curies. Assembled in a rectangular array, the source provides an essentially uniform irradiation flux of about 5×10^8 electrons per square centimeter per second over an area of about 20 inches by 40 inches (51 centimeters by 102 centimeters) at distances a few centimeters from the tube surfaces.

The contractor, using this source, an environmental chamber constructed previously under an unrelated NASA contract, and one of the large hot cells available at the Dawsonville Nuclear Laboratories, assembled and instrumented an experimental arrangement to test a Pegasus panel under electric bombardment in a cryogenic and vacuum environment. A vacuum of 6.66×10^{-4} newtons per square meter was obtained, with temperature down to 208° K. Principal instrumentation consisted of an oscilloscope and camera to record pulse size and shape and a timing circuit. Typical circuit arrangements are shown in Figure 26.

For the experimental configuration employed, a multitude of pulses have been observed. The largest pulse seen was 2.4 volts; all others were below 2 volts, with the majority in the 50- to 200-millivolt range. Pulses of both polarities result, apparently independent of the impressed voltage. At 208° K a discharge rate of 1/2 pulse to 1 pulse per minute was observed. As the temperature is increased, the pulse rate decreases until at about 258° K no pulses are observed. The size of the pulses seems to indicate that the capacitor is breaking down only locally.

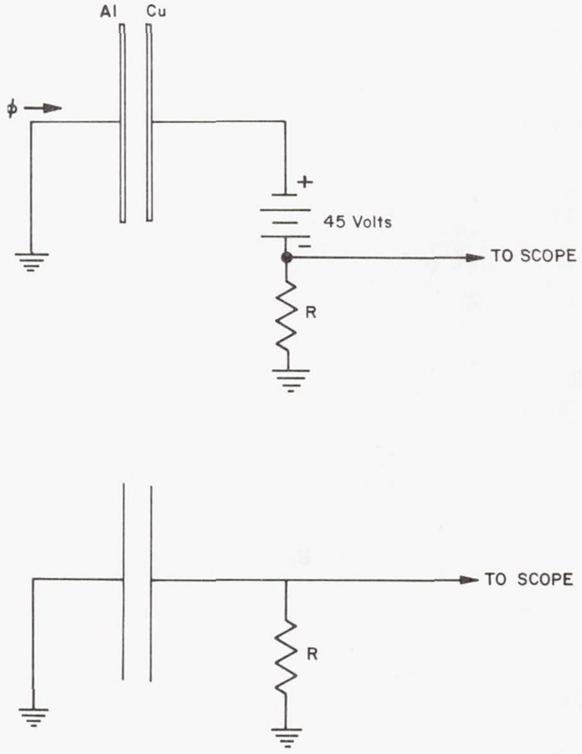

FIGURE 26. PEGASUS OSCILLOSCOPE CIRCUITS

Hopefully a follow-on study can be conducted in which an environment more nearly like that encountered by Pegasus satellites can be simulated. In particular, plans are being made to vary the temperature through a cycle of 233° to 313° K, try to cycle the radiation intensity, use a filtering network such as that used in flight and perhaps test a "hit microplane" in the radiation environment. Additional measurements will help materially to understand the basic discharge mechanism, and successively smaller rings will be etched in one of the panels to effectively produce capacitors of different areas. Plans also specify the use of different panel thicknesses, different type capacitors, and to test more carefully for effects of temperature on pulse size and frequency.

PROJECT SUPPORT

ORBITAL AND TRAJECTORY CODES FOR RADIATION DOSE CALCULATIONS

The objective of this work was to develop computer codes that provide the integrated electrons and proton flares and energy spectra encountered by a spacecraft orbiting or traversing the trapped radiations surrounding the earth. First, the coordinates of the satellite as a function of time were computed from the six orbital elements defining the particular mission. These coordinates were then converted into the B-L coordinates of McIlwain's [76] using a

48-term expansion [77] for the magnetic field of the earth. Using the data compilation of Vette's [78], the magnetic coordinates were used to find energy spectra and fluxes for each coordinate point. A time integral of the radiation exposure was then made and penetrations were calculated.

Among the various project-oriented tasks undertaken by using the orbital and trajectory codes during the past year was the evaluation of the space radiation hazard in the SIV-B hydrogen tank, the radiation hazard and shielding requirements in a synchronous orbit, and the radiation dose analysis of six trajectories to the moon. The latter work was performed for NASA Headquarters after help in evaluating conflicting results obtained by two industrial contractors. Figure 27 represents a summary of the SIV-B workshop radiation hazard analysis. Figure 28 is a typical curve of the electron and bremsstrahlung hazard in a synchronous orbit, and Table VI gives the shelter weight requirements for a synchronous orbit where the radiation is about 40-rads skin dose and about 25 rads at the bone marrow. Figure 29 shows the radiation doses from electrons and bremsstrahlung for three different trajectories to the moon starting at a parking altitude of 200 kilometers above the earth. The important point of this graph is the extreme variations in radiation dose along different escape orbits through the trapped radiation belts.

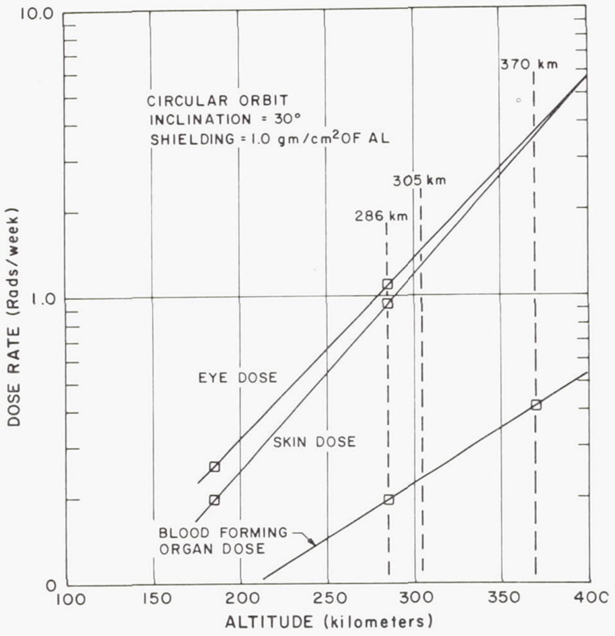

FIGURE 27. SPACE RADIATION DOSE FOR ONE WEEK EXPOSURE IN THE S-IVB HYDROGEN TANK

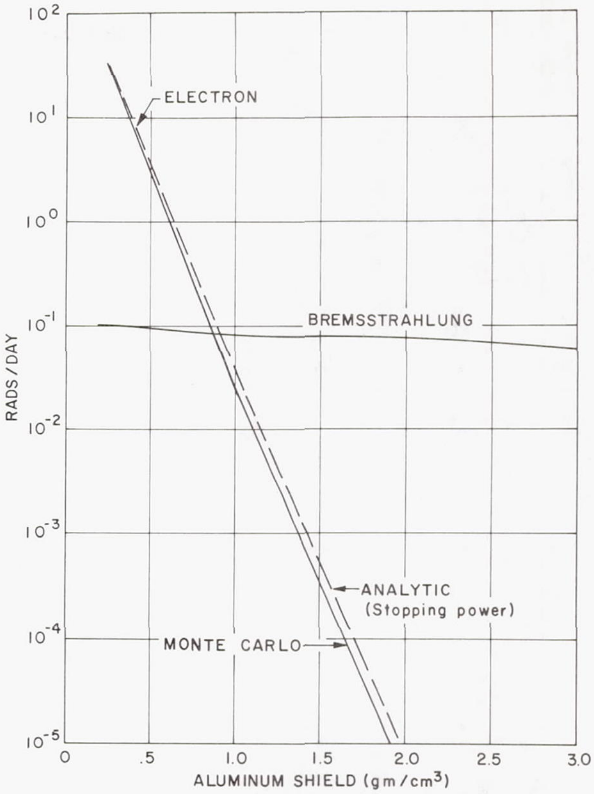

FIGURE 28. SYNCHRONOUS ORBIT ELECTRON DOSE

TABLE VI. SHELTER WEIGHT REQUIREMENTS FOR A SYNCHRONOUS ORBIT DUE TO ELECTRON AND BREMSSTRAHLUNG HAZARD

	$(CH_2)_n$	AL
INSIDE CM		
THICKNESS	10 cm	5.3 cm
MASS	1313 kg (2890 lbm)	1810 kg (3980 lbm)
OUTSIDE CM		
THICKNESS	15 cm	7.5 cm
MASS	2080 kg (4420 lbm)	2750 kg (6050 lbm)

NUCLEAR GROUND TEST MODULE

There were no specifically identified radiation studies associated with this effort, although the air scattering capabilities of the COHORT machine code were designed with possibilities such as ground testing of nuclear rockets in mind.

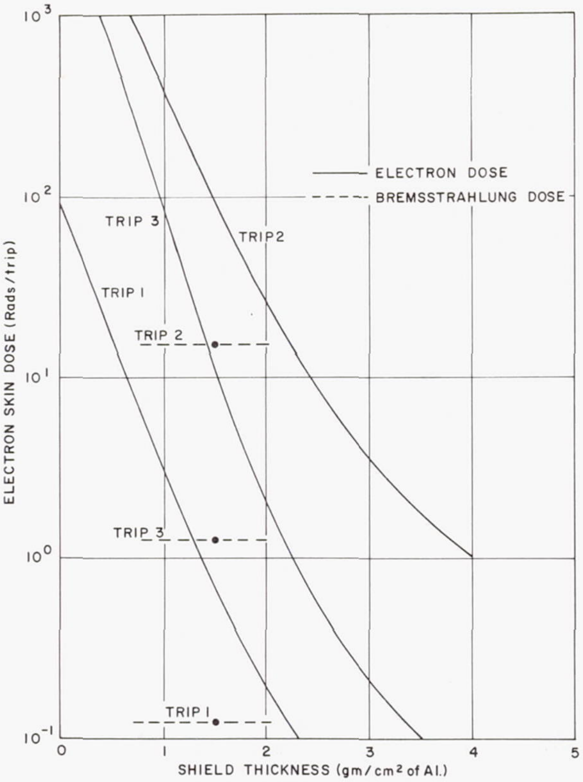

FIGURE 29. ELECTRON AND BREMSSTRAHLUNG DOSE CURVES

EXPERIMENT INTEGRATION

Experiments will be exposed to the radiation naturally present in space and to radiation associated with space power supplies using radioisotopes or reactors. In addition, the experiments may depend on other components such as solar cells or external cables that are also sensitive to radiation. Table VII lists other areas which will receive considerable attention in such experiments. It is probable that the interpretation of certain radiation measurements will require extensive analysis from the radiation transport viewpoint. For example, a measurement of neutron albedo from low orbit must be concerned with such factors as neutron production in the atmosphere by high energy protons, propagation of neutrons through the atmosphere and production of neutrons within the spacecraft itself. From the experiment viewpoint, the particular interest in radiation will depend on what is being measured, the degree of radiation exposure and whether or not the effects of radiation on other parts of the spacecraft are harmful to the particular experiment. No enlightening formula for predicting the importance of radiation to experiments can be given, but a number of specific examples are now past history. If radiation affects the temperature central surfaces, the experiment will suffer. If the solar cells are insufficiently shielded, they may be overexposed by radiation. If external points are good insulators, they may store charges and produce electric fields intense enough to interfere with interpretations of plasma measurements that are already difficult enough to interpret. If charged particle radiation is stored in dielectrics to the extent that catastrophic breakdown occurs, the electric signals produced could feed into the spacecraft logic system and cause spurious counts. Radiation-induced conductivity and spurious currents can also occur. These and other problems are associated with radiation in space, and there will undoubtedly be new experiments and new problems with even worse radiation environments.

TABLE VII. RADIATION AND EXPERIMENT INTEGRATION

SOLAR CELL DAMAGE
CHANGE IN TEMPERATURE CONTROL SURFACES
RADIATION PRODUCED IN SPACECRAFT
RADIOISOTOPE POWER SUPPLIES
RADIOISOTOPE APPLICATIONS
CHARGE STORAGE AND ELECTRICAL DISCHARGES
SPURIOUS CURRENTS
INDUCED CONDUCTIVITY
FILM DARKENING
ASTRONAUT EXPOSURE

PEGASUS DATA

Before the Pegasus satellites were launched, there was concern that the electrons in the Van Allen belts would be stored in the dielectrics of connecting cables and capacitors and that subsequent electrical discharges would be counted as meteoroid hits. The problem was circumvented by using the lowest possible orbits and designing the electronic circuitry to discriminate against pulses of the wrong size, shape, or polarity.

To confirm that electron fluxes were low enough to prevent spurious discharges, a simple two-threshold electron spectrometer (Fig. 30) was carried on each spacecraft. Much valuable data have been collected on the distribution of electron fluxes in the South Atlantic anomaly region of the radiation belts. A typical plot in B-L coordinates of Pegasus I data is shown in Figure 31, together with predicted fluxes for the same time period.

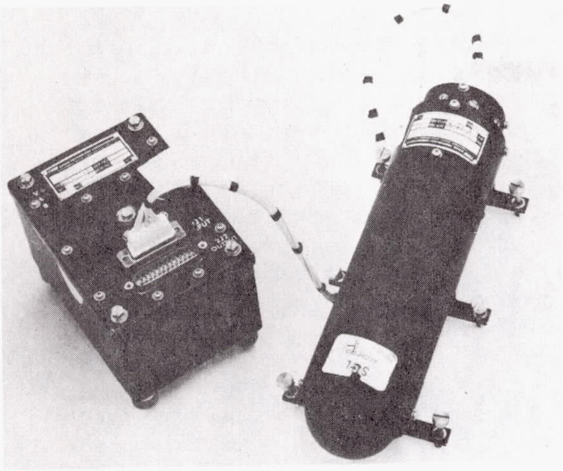

FIGURE 30. PEGASUS ELECTRON SPECTROMETER

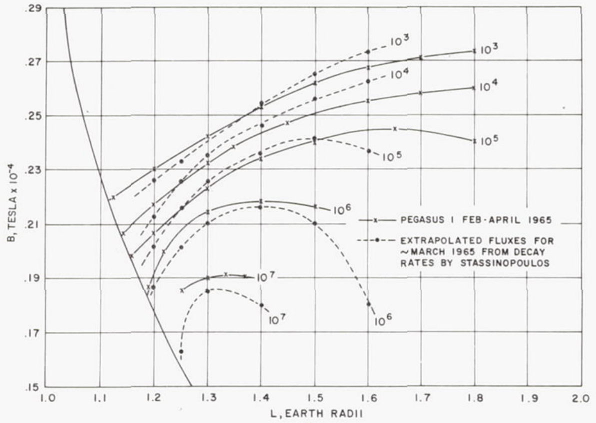

FIGURE 31. PEGASUS ISOFLUX CONTOURS FOR ELECTRONS

ADVANCED PROPULSION

Almost every advanced propulsion system for manned exploration envisions the use of nuclear power in some form and is motivated by the desire for longer voyages in space. An artist's concept of one such system is shown in Figure 32. The neutron and gamma radiation from the reactors must be shielded, and since greater distances are to be covered, man is exposed to space radiations for longer periods of time. In a recent paper [79], the radiation problems associated with a nuclear, nuclear-electric spacecraft were studied for a manned Mars expedition. Radiation sources considered were Van Allen belts, solar flares, cosmic rays, a nuclear heat exchanger reactor and a nuclear electric power supply. Because the flight was planned to occur during a period of relatively quiet sun, the dominant radiation dose came from the reactor systems. A typical reactor shield design is shown in Figure 33. Tungsten is employed primarily as an efficient gamma-ray shield; lithium is used primarily to attenuate neutrons. The shield is heavily contoured to reduce the weight of the system and is left unshielded in directions in which the radiation will neither strike personnel or equipment nor scatter off structural members of the spacecraft. Because of the shield shaping, personnel activities about the spacecraft would have to be carefully controlled. Specifications for the shield system are given in Table VIII.

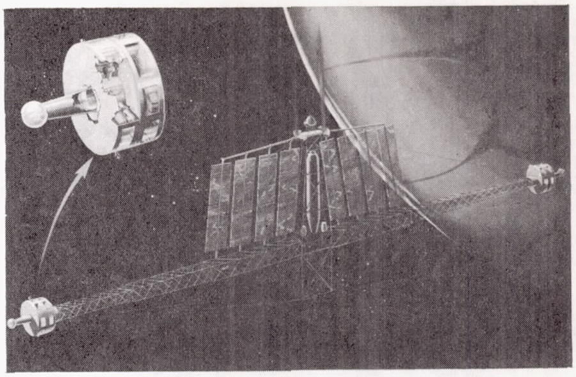

FIGURE 32. ELECTRIC SPACESHIP FOR MANNED MARS FLIGHT

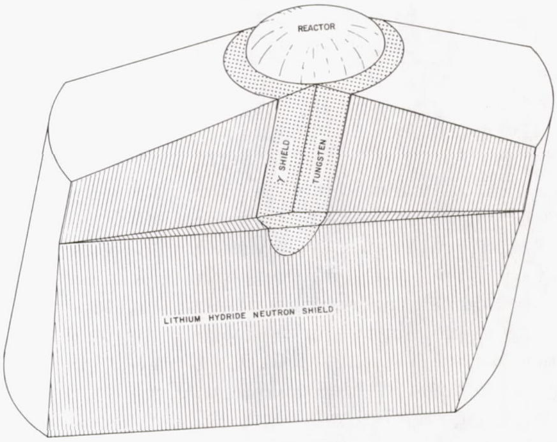

FIGURE 33. REACTOR SHIELD FOR ELECTRIC SPACESHIP

TABLE VIII. REACTOR SHIELD SPECIFICATIONS FOR THE NUCLEAR ELECTRIC SPACESHIP

REACTOR POWER (THERMAL)	134 MW
ELECTRIC POWER	20 MW
URANIUM LOADING (U^{233})	4.5×10^3 kg
REACTOR MASS	1.2×10^4 kg
LiH MASS	1.7×10^4 kg
TUNGSTEN MASS	3.3×10^4 kg
TOTAL REACTOR AND SHIELD MASS	6.2×10^4 kg

RADIOISOTOPE APPLICATIONS AND INSTRUMENTATION

The interposition of matter between a radiation source and a radiation detector reduces the signal received by the detector. Since the days of Roentgen, this phenomenon has had wide application for determining the distribution of matter in inaccessible places. The use of gamma rays to evaluate proton and electron shields is essentially the classical X-ray technique with emphasis on Compton scattering, which is sensitive to electron areal density, the determining factor in proton shielding. The diagnosis of scattered as well as transmitted radiation is also of importance in many applications. The value of radioisotope tracers was demonstrated extensively shortly after the fission process was brought under control and radioisotopes became easily available. The Mossbauer effect made possible the use of radiation sources to determine relative motion between a source and detector and introduced a new kind of velocity meter and accelerometer.

RADIOISOTOPE FUEL GAUGE

The determination of the amount of propellant in a tank under zero gravity conditions is not a straightforward matter. One way to do it is to "X-ray" the propellant mass by means of several radioisotope sources and radiation detectors and to compute the mass from the measured radiation attenuations [80]. How well this technique works has not been demonstrated under space conditions, but is expected to be tested on the LEM descent module in MSFC Experiment No. 3.

VAPOR QUALITY METER

To insure proper pressure regulation in a tank containing liquid hydrogen, it is necessary to vent the vapor boiling off because of heat leakage into the system. However, it is important to prevent the ejection of liquid along with the vapor as the liquid sloshes or undergoes redistribution because of vehicle motion or surface tension forces in a zero gravity environment. The purpose of the vapor quality meter is to measure the density of hydrogen in the hydrogen vent line and thereby determine if liquid is escaping. The vapor quality or Q-meter was developed for use with the LH_2 experiment on Vehicle 203, and may also be flown on Vehicles 501-503.

There are several designs of vapor quality meters. In one design [81] useful for large pipes, gamma radiation is scattered by the volume of interest according to the mass of hydrogen there. The scattered photons are reduced in energy and may be analyzed selectively to yield a signal proportional to the mass of hydrogen viewed jointly by the radioisotope source and radiation detector. In another design [82] useful for smaller pipes, the reduction of beta transmission from source to detector is analyzed to determine the quantity of liquid present in the vent line.

The extent to which radioisotope quality meters will be applied is not determined at this time, although their use appears certain. The addition of one Curie of Americium 241 in the meter using the gamma-scattering technique presents problems from the safety and interference viewpoints, and it may happen that the degree of application will depend on the development of a design which uses a very small beta source.

LEAK DETECTION

The use of radioisotopes for leak detection [83] is based on the assumption that a radioactive gas under pressure will enter a leaky component which has been previously outgassing in a vacuum. The leak rate is determined by how radioactive the component becomes and how fast it decays. So far the process seems to be well understood, but there is a problem of correlating the radioisotope method with mass spectrometer techniques.

RADIOISOTOPE STAGE SEPARATION INDICATOR

The use of radioisotopes to measure distance depends on the fact that the radiation intensity obeys the inverse square law, i.e., the intensity of radiation falling on a detector varies inversely as the square of the distance between source and detector. In one proposed system [84] the relative position between two planes (the interface between two stages) is to be determined by using three sources in one plane and six detectors in the other.

NEUTRON SPECTROMETER

A satisfactory method for measuring neutron spectra has not yet been developed although this problem has been attacked vigorously since nuclear fission was achieved. The RIFT program introduced the requirement of measuring neutron fluxes and energy spectra in a large nuclear stage filled with hydrogen and powered by a reactor operating in the gigawatt levels. In almost all cases the neutron spectrometer must operate in a gamma-ray background to which it must be relatively insensitive. Also, it must be designed so that it does not saturate in relatively high-level neutron and gamma fluxes or be too sensitive to spurious signals in a low-level radiation environment.

The neutron spectrometer under development [85] by IITRI uses the exoergic reaction ${}_0N^1 + {}_2He^3 \rightarrow {}_1P^1 + {}_1H^3 + 800$ kiloelectron volts in a small chamber filled with He^3 gas. To discriminate against noise, the chamber is divided into two parts (acting as proportional counters); a solid state detector is then placed on each end of the chamber. By adding the four pulse contributions and incorporating the proper coincidence requirements, a neutron spectrometer capable of operating in rather intense fields has been obtained. In a recent test [86] this device shows a count rate of 5×10^3 counts per minute in a gamma field of 10^6 roentgens per hour, or roughly 10^{11} photons per square centimeter per second. A neutron flux of 10^8 neutrons per square centimeter per second would produce roughly ten times this count rate. This reasonably good gamma discrimination will be necessary in the RIFT (or a similar) nuclear stage because liquid hydrogen is a poor gamma and good neutron shield, which means that neutrons will be counted in a strong gamma field.

CONCLUSIONS

The technology of radiation is common enough to provide a broad base in space engineering. The increased use of radioisotope power supplies and nuclear stations for space exploration could produce a greatly increased emphasis on the aspects of radiation interactions with materials and components, and the interference of radiation sources with scientific and engineering experiments. In addition, radiation would impose operational constraints on manned missions in space, more from the biological viewpoint than from the consideration of damage to equipment. It is possible that operational aspects of nuclear systems will require considerable additional attention because of the many interesting cosmological experiments concerned with the measurements of radiations that are very similar to those arising from radioisotopes used on spacecraft and from reactors used for propulsion and power supplies.

REFERENCES

1. Investigation of the Combined Effects of Space Environmental Parameters on Space Vehicle Materials. Contract NAS8-20210, Hughes Aircraft Company, July 1, 1965 to July 1, 1966.

2. McKannan, E. C.; and Gause, R. L.: Effects of Nuclear Radiation and Cryogenic Temperatures on Non-Metallic Engineering Materials. Reprinted from J. Spacecraft Rockets by AIAA, Vol. 2, No. 4, Oct. 19, 1964, p. 558.

3. McKannan, E. C.; and Gause, R. L.: Effects of Nuclear Radiation and Cryogenic Temperatures on Engineering Materials. NASA TM X-53152, Oct. 22, 1964.

4. Gause, R. L.; and McKannan, E. C.: Effects of Nuclear Radiation, Cryogenic Temperature, and Vacuum on the Electrical Properties of Dielectric Materials. NASA TM X-53152, March 30, 1965.

5. Investigation of the Combined Effects of Nuclear Radiation, Cryogenic Temperatures, and Vacuum on Engineering Materials. Contract NAS8-2450, General Dynamics Corporation, Nov. 9, 1961 to April 9, 1966.

6. Lucas, W. R.: Materials Research Advisory Committee Member Report. Report No. 14, Sept. 15, 1965, p. 78.

7. Investigation of the Combined Effects of Space Environmental Parameters on Space Vehicle Materials. Final Report, NAS8-2450, General Dynamics Corporation, April 1966.

8. Design Guidelines for Circuitry in a Nuclear Reactor-Propelled Spacecraft.Contract NAS8-11755, Lockheed Missiles and Space Company, Huntsville.

9. Design Guidelines for Circuitry in a Nuclear Reactor-Propelled Spacecraft.Contract NAS8-11755, Lockheed Missiles and Space Company/ Lockheed Aircraft Corporation, Report No. LMSC/HRECA 712479, Oct. 1965.

10. Irradiation of Transformer Feedback Amplifiers and Polarized Capacitors. Contract NAS8-5332, Lockheed-Georgia Company/Lockheed Aircraft Corporation, Report No. 7346.

11. Irradiation of Transformer Feedback Amplifiers and Polarized Capacitors. Contract NAS8-5332, Lockheed-Georgia Company/Lockheed Aircraft Corporation, Report No. 7681, Dec. 5, 1964.

12. Burke, H.; and Ponder, T., et al.: Nuclear Radiation Effects of Typical MSFC-Astrionics Measurement Components. MSFC-R-ASTR-IN-65-1, Jan. 29, 1965.

13. Irradiation of Transformer Feedback Amplifiers and Polarized Capacitors. Contract NAS8-5332, Georgia Nuclear Laboratories/Lockheed Aircraft Corporation, Dec. 5, 1964.

14. Study to Investigate the Effects of Ionization Radiation on Transistor Surfaces. Contract NAS8-20135, Bendix Corporation.

15. Design Development and Fabrication of Prototype Silicon Carbide Amplifiers. Contract NAS8-11861, Westinghouse Corporation.

16a. Keller, J. W.; Shelton, R. D.; Potter, R. A.; and Lacy, L.: A Study of the Effect of Geomagnetically Trapped Radiation on Bare Solar Cells. Proceedings of the IRE, Nov. 1962.

16b. A Study of Radiation Effects on Composite Structures. Contract NAS8-20206, Lockheed-Georgia Company, June 25, 1965 to May 25, 1966.

REFERENCES (Continued)

17. Twenty Watt/Pound Solar Array Feasibility Study. Jet Propulsion Laboratory Contract 951132; Boeing Company, Final Review, Jan. 19, 1966.

18. Burrell, M. O.: The Calculation of Proton Penetration and Dose Rates. NASA TM X-53063, Aug. 17, 1964.

19. Second Symposium on Protection Against Radiation in Space. NASA SP-71, 1965.

20. Data Compilation and Evaluation of Space Shielding Problems. Contract NAS8-11164; ER-7777, Vol. 1, 1965.

21. Data Compilation and Evaluation of Space Shielding Problems. Contract NAS8-11164; ER-7777, Vol. 2, 1965.

22. Webber, W. R.: An Evaluation of the Radiation Hazard Due to Solar-Particle Events. Boeing Company, Report No. D2-90469, Dec. 1963.

23. Berger, M. J.; and Seltzer, S. M.: Tables of Energy Losses and Ranges of Electrons and Positrons. NASA SP-3012, National Bureau of Standards, 1964.

24. Burrell, M. O.; and Wright, J. J.: Orbital Calculations and Trapped Radiation Mapping. NASA TM X-53406, March 8, 1966.

25. Rose, M. E.: Invited Lecture at the University of Alabama, Huntsville, March 21, 1966.

26. Electron Shield Studies. Contract NAS8-11304, General Dynamics Corporation, June 29, 1964 to May 29, 1966.

27. Investigation of Electron Interaction with Matter. Contract NASw-948, Ling-Temco-Vought, May 11, 1964 to May 11, 1966.

28. Studies of the Penetration of High Energy Radiation Through Matter. Contract R-80, U. S. National Bureau of Standards, Dec. 31, 1963 to Dec. 31, 1966.

29. Theoretical Calculations of Bremsstrahlung Cross Section. Contract NASw-1235, Union Carbide Corporation, May 30, 1964 to May 30, 1966.

30. Jupiter, C. P.; Merkel, G.; and Parez, J.: Measurement of Energy Straggling of 8-MeV Electrons in Aluminum. Bull. Am. Phys. Soc., Vol. 10, No. 6, 1965, p. 725.

31. Pomraning, G. C.: A Method for Computing $\int_{-1}^{1} dx\, P_k^j(x)\, P_n^m(x)$. J. Am. Nuc. Soc., Vol. 23, No. 4, Dec. 1965, p. 395.

32. Berger, M. J.: Monte Carlo Calculation of the Penetration and Diffusion of Fast Charged Particles. Methods in Computational Physics, Academic Press, New York, N.Y., Vol. 1, 1963, p. 135.

33. Zerby, C. D., et al.: Bremsstrahlungen Cross Sections. NASw-1235, Union Carbide Corporation (UCRI-370), Quarterly Progress Report.

34. Investigation of Bremsstrahlung Production in a Shielding Material. Final Report, NAS8-11083, Advanced Research Corporation, May 1965.

REFERENCES (Continued)

35. Bremsstrahlung Production Cross Sections for Shielding Against Electrons in Space. Final Report, NAS8-11083, Advanced Research Corporation, May 1965.

36. Investigation of Electron Interaction with Matter. Final Report, NASw-948, Ling-Temco-Vought, Report No. 0-71000/5R-13, May 1965.

37. Evaluation of Theoretical Calculation Methods for Determining Radiation Fields in Nuclear Rocket Systems. Modification No. 5, NAS8-9500. Lockheed Missiles and Space Company/ Lockheed-Georgia Company, June 18, 1964 to Dec. 18, 1965.

38. Evaluation of Methods for Computing Nuclear Rocket Radiation Fields. Modification No. 5, NAS8-9500, Lockheed-Georgia Company, Report No. ER-8236, Dec. 1965, pp. 39 and 75.

39. Study of COHORT Shielding. Contract NAS8-20195, Radiation Research Associates, Inc., June 17, 1965 to June 17, 1966.

40. Wells, M. B.; and Collins, D. G.: Monthly Progress Report No. 7, Radiation Associates, Inc., Jan. 1 - Jan. 31, 1966.

41. Burrell, M. O.: Nuclear Radiation Transfer and Heat Deposition Rates in Liquid Hydrogen. MSFC Report MTP-RP-62-1, Feb. 15, 1962.

42. Bernert, R. E.; and Stekly, Z. J. J.: Systems Analysis of Superconducting Magnets for Space Radiation Shielding. Contract NAS8-5278, Avco-Everett Research Laboratory, Everett, Massachusetts, March 1964.

43. Bernert, R. E.: Design of a Mars Class Radiation Shield Using a Superconducting Magnet. Contract NAS8-5278, Avco-Everett Research Laboratory, Everett, Massachusetts, Sept. 1964.

44. Urban, E. W.: Critical Störmer Conditions in Quadrupole and Double Ring Current Fields. J. Math. Phys., 6, 1966, Dec. 1965.

45. Urban, E. W.; and Lacy, L. L.: The Störmer Problem for the Second Order Field of the Earth. Southeastern Section Meeting of the American Physical Society, University of Virginia, Nov. 1965.

46. McDonald, P. F.: An Annotated Bibliography on Motion of Charged Particles in Magnetic Fields and Magnetic Shielding Against Space Radiation. Contract NAS8-20166, Brown Engineering Company, Huntsville, Alabama, Oct. 1965.

47. Theoretical Investigation of the Motion of Charged Particles in Electromagnetic Fields. Contract NAS8-20166, Technical Directive 2820-001, Brown Engineering Co., Huntsville, Alabama, July 1965 to July 1966.

48. Experimental Investigation of Advanced Superconducting Magnets. Contract NAS8-5279, Avco-Everett Research Laboratory, Everett, Massachusetts, May 1963 to Feb. 1966.

49. Study of Properties of Superconductors at Elevated Temperatures. Contract NAS8-11272, Radio Corporation of America, Camden, N. J., June 1964 to June 1966

50. Investigation of Current Degradation Phenomenon in Superconducting Solenoids. Contract NAS8-5356, Atomics International, Canoga Park, California, May 1963 to Jan. 1966.

REFERENCES (Continued)

51. Investigation of the Mechanisms of Superconductivity by Nuclear Irradiation. Contract NAS8-11098, Westinghouse Research Laboratory, Pittsburgh, Pennsylvania, Sept. 1963 to Dec. 1965.

52. Anon: Experimental Simulation of Large High-Field Superconducting Magnet Operation. Government Order H-76798, Oak Ridge National Laboratory, Oak Ridge, Tennessee, April 1964 to Feb. 1966.

53. Hoag, E. D.: Magnet Optical Observations of the Current Density Distribution in Strip Superconductors. Third International Conference on Nonlinear Magnetics (INTERMAG), April 21-23, 1965.

54. Hoag, E. D.: Elimination of Critical Current Degradation in Wide Samples of Strip Superconductors. 11th. Annual Conference on Magnetism and Magnetic Materials, Nov. 16-19, 1965.

55. Keller, E. L., et al.: Investigation of the Mechanisms of Superconductivity by Nuclear Irradiation, Final Report, NAS8-11098, Westinghouse Research Laboratories, Pittsburgh, Pennsylvania, Dec. 15, 1965.

56. Salter, L. C.; and Raymond, J. W.: Effect of Annealing Time and Temperature on the Critical Current and Resistive Upper Critical Field of Nb-Ti Wire. American Physical Society Meeting, Washington, D. C., April 26-29, 1965.

57. Raymond, J. W.; and Salter, L. C.: The Effect of Thermal History on the Superconducting Properties of Ti-22% Nb Alloy. American Physical Society Meeting, Washington, D. C., April 26-29, 1965.

58. Anon: Investigation of Current Degradation Phenomenon in Superconducting Solenoids AI-66-21, Summary Report, NAS8-5356, Atomics International, Canoga Park, California, Jan. 14, 1966.

59. Anon: Study of Properties of High-Field Superconductors at Elevated Temperatures. Technical Summary Report, NAS8-11272, Radio Corporation of America, Camden, New Jersey, July 26, 1965.

60. Gauster, W. F.; and Coffey, D. L.: Experimental Simulation of Large High-Field Superconducting Magnet Operation. Government Order H-76798, Oak Ridge National Laboratory, Oak Ridge, Tennessee, ORNL-TM-1083, March 23, 1965.

61. Gauster, W. F., et al.: Experimental Simulation of Large High-Field Superconducting Magnet Operation. Government Order H-76798, Oak Ridge National Laboratory, Oak Ridge, Tennessee, ORNL-TM-1173, June 23, 1965.

62. Gauster, W. F., et al.: Experimental Simulation of Large High-Field Superconducting Magnet Operation. Government Order H-76798, Oak Ridge National Laboratory, Oak Ridge, Tennessee, ORNL-TM-1266, Sept. 7, 1965.

63. Gauster, W. F., et al.: Experimental Simulation of Large High-Field Superconducting Magnet Operation. Government Order H-76798, Oak Ridge National Laboratory, Oak Ridge, Tennessee, ORNL-TM-1398, Jan 26, 1966.

64. Hoag, E.: Experimental Investigation of Advanced Superconducting Magnets. Annual Report, NAS8-5279, Avco-Everett Research Laboratory, Everett, Massachusetts, July 1965.

65. Study of Plasma Radiation Shielding. Contract NASw-1101, Avco-Everett Research Laboratory, Nov. 30, 1965 to Nov. 30, 1966.

66. Levy, R. H.; and Janes, S.: Plasma Radiation Shielding, NASw-1101 and AF49(638)-1553, Avco Corporation, Report No. 179, Dec. 1965.

REFERENCES (Continued)

67. Janes, G. S.; Levy, R. H.; Bethe, H. A; and Feld, B. T.: On a New Type of Accelerator for Heavy Ions. AF49(638)-1553, Avco Corporation, Research Report 235, Dec. 1965.

68. Advances in "Plasma Radiation Shielding" Research. Memorandum from A. Reetz, NASA Headquarters to R. N. Seitz, May 27, 1965.

69. Shelton, R. D.; Stern, H.; and Hale, D. P.: Some Aspects of the Distribution of Meteoric Flux About an Attractive Center. Presented at COSPAR Fourth International Space Symposium, Warsaw, Poland, June 1963.

70. Hale, D. P.; and Wright, J. J.: Meteoric Flux and Density Fields About an Infinitesimal Attractive Center Generated by a Stream Monoenergetic and Monodirectional at Infinity. Published in J. Geophys. Res., Vol. 69, No. 17, Sept. 1, 1964, p. 3709.

71. Hale, D. P.; and Wright, J. J.: Meteoric Flux and Density Fields About a Finite Attractive Center Generated by a Stream Monoenergetic and Monodirectional at Infinity. Published in J. Geophys. Res., Vol. 69, No. 17, Sept. 1, 1964, p. 3719.

72. Shelton, R. D.; Stern, H.; and Wright, J. J.: The Synthesis of Meteoroid Distributions from Monoenergetic Monodirectional Kernels. Astron. J., Vol. 70, No. 2, March 1965, p. 166.

73. Shelton, R. D.; Stern, H.; Hale, D. P.; and Wright, J. J.: On the Calculation of Meteoroid Flux Patterns Relative to a Moving Detector Given on Unbound Pattern About an Attractive Center. Astron. J., Vol. 70, No. 4, May 1965, p. 275.

74. Computation of Debris Problem Caused by Active Seismic Shots on the Lunar Surface. Contract NAS8-20166, Brown Engineering Company, Oct. 18, 1965 to May 1, 1966.

75. Hale, D. P.; and Wright, J. J.: On the Flux-Density Patterns of Gravitationally Bound Particles About a Finite Attractive Center. J. Geophys. Res., Vol. 70, No. 13, July 1, 1965.

76. McIlwain, C. E.: Coordinates for Mapping the Distribution of Magnetically Trapped Particles. J. Geophys. Res., 66:3681-4078, 1963.

77. Jensen, D. C.; and Cain, J. C.: An Interim Geomagnetic Field. J. Geophys. Res., 67, 3568, 1962.

78. Vette, J. I.: Models of the Trapped Radiation Environment. NASA SP-3024, Aerospace Corporation, 1966.

79. Stuhlinger, E.; King, J. C.; Shelton, R. D.; and Woodcock, G. R.: Study of a Nerva-Electric Manned Mars Vehicle. Published in the proceedings of the AIAA/AAS Stepping Stones to Mars Meeting, Baltimore, Maryland, March 20-30, 1966, p. 288.

80. Determination of the Propellant Mass in a Large Storage Tank by Nucleonic Radiation Techniques. Contract NAS8-11311, Giannini Controls Corporation, June 1964 to May 1965.

81. Preliminary Design of LH_2 Quality Meter. Industrial Nucleonics, July 1, 1964 to July 1, 1965.

82. Hermetic Seal Evaluation. Contract NAS8-5394, Nuclear Engineering Department, Mississippi State University, May 15, 1963 to Feb. 15, 1965.

83. Hermetic Seal Evaluation of Electronic Components. Contract NAS8-20109, Nuclear Engineering Department, Mississippi State University, April 1, 1965 to Oct. 1, 1966.

REFERENCES (Concluded)

84. Special Device for Measuring the Separation of Two Stages of a Space Vehicle. Contract NAS8-11995, General Dynamics, Fort Worth, July 1965 to July 1966.

85. Design and Development of a Fast Neutron Spectrometer. Contract NAS8-11885, Illinois Institute of Technology Research, June 1965 to June 1966.

86. Design and Development of a Fast Neutron Spectrometer. NAS8-11885, Monthly Progress Report, IITRI-A-6135-9, Feb. 10, 1966.

Page
Intentionally
Left Blank

2

THERMOPHYSICS RESEARCH AT MSFC

March 31, 1966

By

Gary M. Arnett
Harlan D. Burke
Gerhard B. Heller
Billy P. Jones
Edgar R. Miller
William C. Snoddy

Page
Intentionally
Left Blank

Page
Intentionally
Left Blank

Page

INTRODUCTION TO RESEARCH ACHIEVEMENTS REVIEW ON THERMOPHYSICS RESEARCH AT MSFC

LIST OF ILLUSTRATIONS

EXPERIMENTAL RESULTS IN THERMAL SIMILITUDE

by Billy P. Jones

Page

LIST OF ILLUSTRATIONS

EMISSIVITY PHYSICS

by Edgar R. Miller

LIST OF TABLES

LIST OF ILLUSTRATIONS

ULTRAVIOLET INTERACTIONS WITH SOLID MATERIALS

by Gary M. Arnett

LIST OF TABLES

LIST OF ILLUSTRATIONS

CONTENTS (Continued) . . .

PEGASUS THERMAL EXPERIMENTAL RESULTS

by William C. Snoddy

LIST OF ILLUSTRATIONS

CONTENTS (Continued). . .

RESEARCH IN INSTRUMENTATION FOR RADIOMETRY AND SPECTROMETRY

by Harlan D. Burke

LIST OF TABLES

LIST OF ILLUSTRATIONS

CONTENTS (Concluded). . .

INTRODUCTION TO RESEARCH ACHIEVEMENTS REVIEW ON THERMOPHYSICS RESEARCH AT MSFC

By

Gerhard B. Heller

Research on thermal problems is conducted by various laboratories at MSFC. The Research Achievements Review given a year ago covered an over-all summary of thermophysics research and achievements in 1964 or before [1]. In this research review, several of these subjects are presented in more detail and include the achievements of the past year. Emphasis is placed on thermophysics as it pertains to space flight, especially with regard to radiation exchange with the environment. Research on thermal problems of launch vehicles is also mentioned. Aero-Astrodynamics Laboratory and Propulsion and Vehicle Engineering Laboratory are studying rocket base heating due to the effects of rocket engine jets and plumes. Aero-Astrodynamics Laboratory is studying the flow fields generated by interaction of multiple rocket jets and the interaction with the surrounding air flow. Theories are being developed for radiative transfer from the rocket exhaust gases and from carbon particles in the S-IB and S-IC rocket engine plumes. Thermal engineering problems are involved in cryogenic research in connection with liquid hydrogen. This includes studies of zero-gravity heat transfer of liquid hydrogen. Research in these two areas by Aero-Astrodynamics and Propulsion and Vehicle Engineering Laboratories was included in earlier research review reports by members of these laboratories [2, 3]. Materials research on thermal control coatings by P& VE Laboratory was covered in the Research Achievements Review Series No. 7 [4].

Astrionics Laboratory is concerned with temperature measuring devices for flight on Saturn vehicles. A thermal environmental effects sensor developed for Research Projects Laboratory (RPL) has been described in Research Achievements Review Series No. 5 [5]. Results of the sensor measurements are presented in this series.

Research Projects Laboratory is presently concerned with thermophysics research of the thermal space environment and thermal control of space vehicles.

This review consists of five papers on the following subjects: thermal similitude by B. P. Jones, emissivity physics research by E. Miller, ultraviolet radiation effects on thermal control coatings by G. Arnett, evaluation of Pegasus thermal experiments by W. C. Snoddy (all of Research Projects Laboratory), and thermophysical instruments by H. Burke (of Astrionics Laboratory). The achievements covered in these papers are indicative of thermophysics research at Marshall, but are not a complete representation. A few examples follow.

Klaus Schocken of RPL has conducted research on the modes of heat transfer of underdense dielectric materials. Figure 1 shows that heat transfer as a function of bulk density has a distinct minimum. This is because radiative transfer decreases with increasing density; however, the transfer by interface conductance between the powder particles increases. Research is conducted theoretically and experimentally to determine the modes of heat transfer. Results of this work are also applicable to the conductance of lunar surface materials.

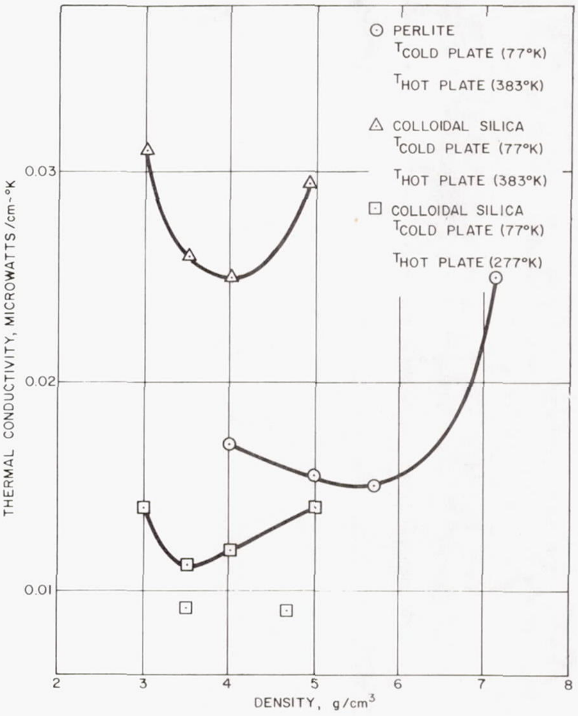

FIGURE 1. EFFECT OF CHANGE IN DENSITY ON THERMAL CONDUCTIVITY OF EVACUATED POWDERS

In the area of research on thermal control, Tommy Bannister of RPL has studied a space radiator using fusible materials. Figure 2 shows a laboratory model being studied by Northrop personnel under an MSFC contract. The fusible material is enclosed between two shells. Aluminum honeycomb is used to increase the heat conductivity between the upper and lower plate. In the experimental model a heater is mounted on the upper shell and the lower shell radiates to the liquid nitrogen-cooled walls of a vacuum chamber.

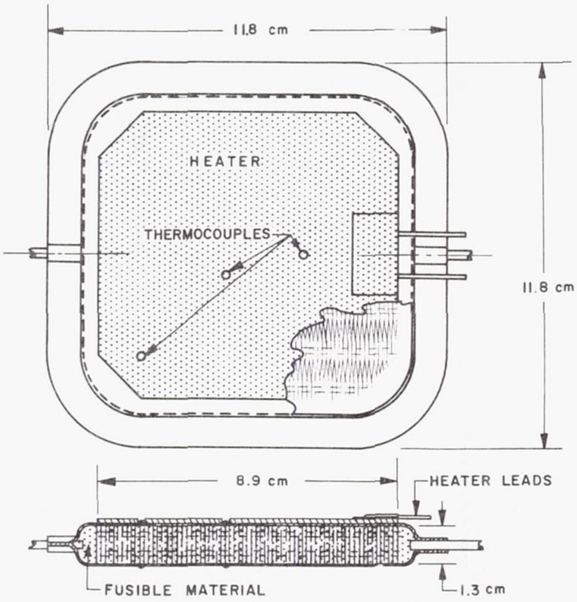

FIGURE 2. HEAT OF FUSION RADIATOR (ADIABATIC TEST MODEL)

A reversible heat storage device can be used to solve many problems resulting from the thermal environment of space. For example, a space thermal radiator, which would normally be sized for the extreme temperatures caused by the cyclic solar heating and cooling of a satellite eclipsed by the earth, could be designed for an average temperature by using a fusible material radiator. On Mars, where diurnal thermal variations are very severe, solar energy can be stored during the day to maintain moderate temperatures during the Martian night.

Laboratory studies are presently concentrated on improving the low thermal diffusivity of the liquid layer and reducing the expansion and contraction of fusible material between the liquid and solid state. A packaging technique has been developed that increases the thermal diffusivity while maintaining the fusible material in thermal contact with the heat source during all phases of operation.

REFERENCES

1. Thermophysics Research at MSFC. Research Achievements Review Series No. 2, NASA TM X-53490, 1965.
2. Cryogenics Research at MSFC. Research Achievements Review Series No. 3, NASA TM X-53515, 1965.
3. Terrestrial and Space Environment Research at MSFC. Research Achievements Review Series No. 11, NASA TM X-53507, 1965.
4. Materials Research at MSFC. Research Achievements Review Series No. 7, NASA TM X-53383, 1965.
5. Electronics Research at MSFC. Research Achievements Review Series No. 5, NASA TM X-53364, 1965.

Page
Intentionally
Left Blank

EXPERIMENTAL RESULTS IN THERMAL SIMILITUDE

By

Billy P. Jones

SUMMARY

Earlier analytical work in thermal similitude is reviewed briefly to indicate the background and preparation for scale model experiments. Recent experimental results in thermal similarity are then presented. Results are included from experiments done by research contract with the Lockheed Missiles and Space Company and the ARO, Inc. Model design for the ARO, Inc., experiments was done inhouse.

Experimental confirmation was obtained for the derived modeling criteria for the transient mode. Geometric distortion in minor dimensions was found to be a useful technique, as predicted by the analysis.

The direction that future experimental and theoretical work should take is indicated.

INTRODUCTION

This presentation is primarily a summary of recent experimental results in thermal similitude. It is appropriate to briefly review the analytical work that preceded these experiments [1-5]. A large part of this analysis was done inhouse.

Earlier analytical work was concerned with the derivation of criteria for obtaining thermal similarity (the basis for thermal modeling). The considerations involved have well established analogies in wind tunnel testing to obtain information for aircraft design, model experiments to obtain data on the design of marine harbor and port facilities, and scale modeling of ships to obtain design information or to study their behavior under various conditions. Thermal modeling in space-related problems is a fairly recent activity.

SIMILITUDE RESULTS

DERIVATION OF CRITERIA

There are two established approaches to deriving the criteria for physical similarity. If descriptive differential equations can be written for the problem, the criteria can be derived from them. This approach has been used, and some of the experimental results discussed are for the purpose of verifying the derived modeling laws [2, 3, 5].

The other approach may be used when adequate descriptive equations are not available or when the equations are so complicated as to be difficult to treat. The method is based essentially on the so-called "π-Theorem." A recent reformulation of this principle was cast in the form of matrix algebra that can be programmed on a digital computer so that all possible sets of modeling criteria will be derived [1, 4]. In a relatively simple example for the temperature distribution with time in two opposed parallel disks connected by a rod, there resulted 57 sets of independent ratios, each set containing 5 ratios. Only one set is chosen for model design, but having all ratios exhibited allows the proper choice to be made. These two seemingly different approaches have connection through the group theory of abstract algebra that will be mentioned later.

EXPERIMENTAL VERIFICATION

The experimental results presented were obtained by research contract with the Lockheed Missiles and Space Company at Palo Alto, California, and the ARO, Inc., at Tullahoma under a Project SUPER arrangement with Arnold Engineering Development Center. Model design for the Tullahoma experiments was done inhouse. It was desirable to test our analysis by experiments to verify the derived thermal modeling laws. It was also necessary to learn some of the practical difficulties and techniques for designing, building, and testing models. All experiments used both a full-scale prototype and one or more scaled-down models, each tested under thermally similar conditions so that data could be compared for direct verification of the modeling. In addition, the analysis indicated that geometric distortion in the minor dimensions would be a useful technique in satisfying the modeling rules. This technique was used in the design of models when appropriate.

None of the experiments used actual flight hardware. However, the geometries, construction, materials, and thermal properties of the objects modeled did resemble simplified versions of situations that would be expected in actual hardware. The experiments proceeded from the simpler to the more complicated cases. All results presented are for transient conditions. Work at Marshall has concentrated on thermal problems that have time as a variable, thus time enters into the modeling criteria that must be satisfied. For this reason, the transient criteria are more difficult to satisfy than the corresponding criteria for the steady state.

EXPERIMENTAL APPARATUS AND DATA

Figure 1 shows the test installation for a cylinder, sphere and inclined plane exchanging energy by radiation only. The objects are asymmetrically located with respect to one another and there is mutual infrared shadowing. Solar insolation was simulated by resistance heaters in the plates, and internal generation was simulated by heaters in the cylinders. Tests on both a full-scale prototype and a one-half-scale model were run so that measurements could be compared [6].

Temperature-time curves are shown in Figure 2 for both model and prototype for each of the three objects. The heater in the plate was cycled with a period of about 4 hours, and the heater in the cylinder remained energized throughout the experiment. These figures show only one thermocouple location on each object, but they are fairly representative for the plate and cylinder. The curve shown for the sphere is representative of about one-half of all the measurements made on it.

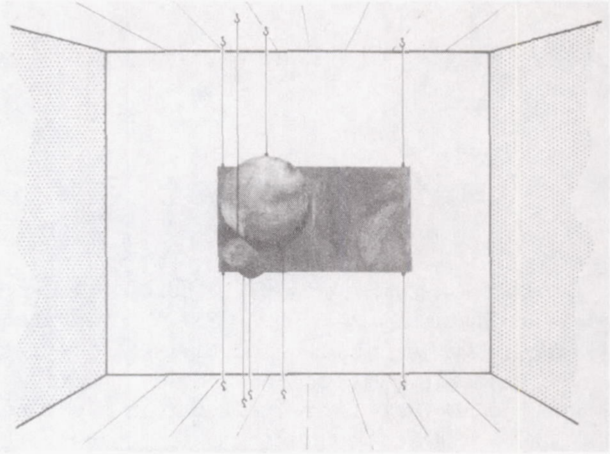

FIGURE 1. MODELS INSTALLED IN VACUUM CHAMBER

The remainder of the experimental work discussed was done under a research contract by Robert E. Rolling at the Lockheed Missiles and Space Company, Palo Alto, California.

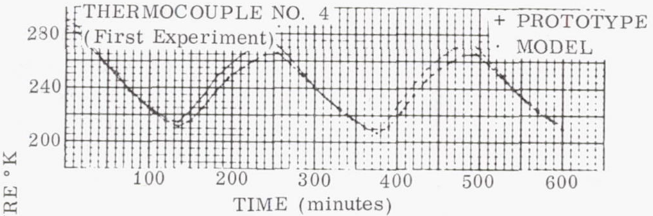

PROTOTYPE AND MODEL SPHERE

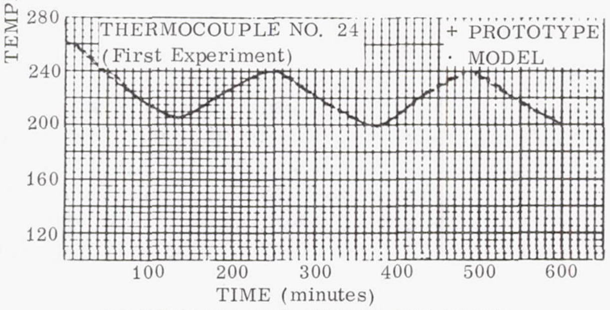

PROTOTYPE AND MODEL CYLINDER

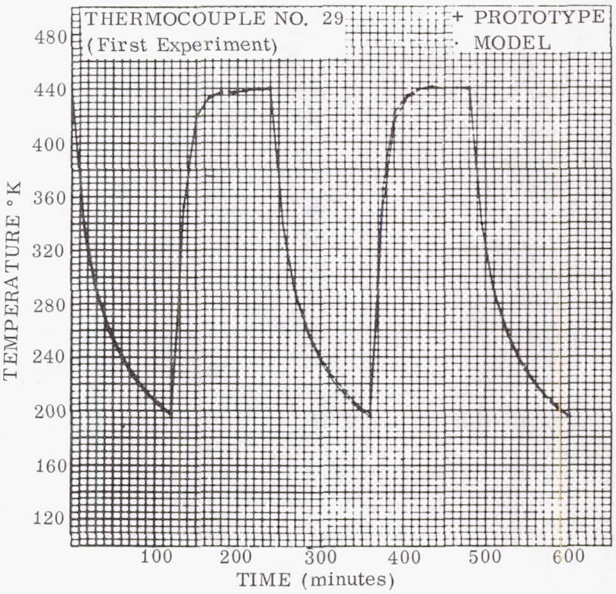

PROTOTYPE AND MODEL PLATE

FIGURE 2. THERMAL SIMILITUDE - TULLAHOMA EXPERIMENTS

Figure 3 shows a prototype and two models, one model is $\frac{1}{2}$ scale, the other $\frac{1}{4}$ scale. They each consisted of two opposed disks with four connecting tubular members. An electric resistance heater was installed in the box attached to one of the disks. This was intended to simulate internal dissipation of equipment. The white surfaces were illuminated by an array of tungsten filament lamps with reflectors to simulate solar insolation. The internal heater was cycled with a period of 20 minutes. The external lamps were cycled with a period of 87 minutes.

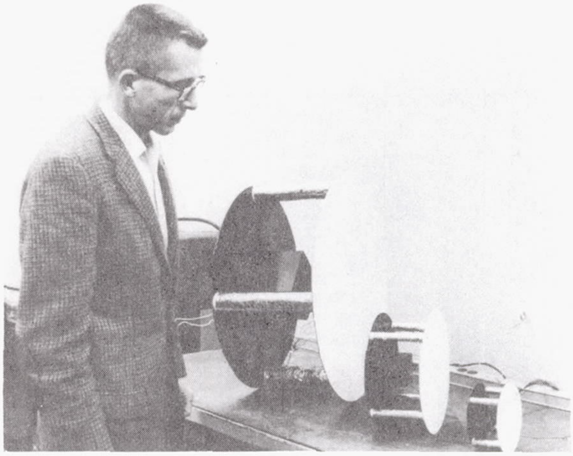

FIGURE 3. PROTOTYPE, $\frac{1}{2}$-SCALE AND $\frac{1}{4}$-SCALE MODELS

Figures 4 and 5 are examples of the results which showed differences at the maximum, minimum, and average temperatures up to 9°K.

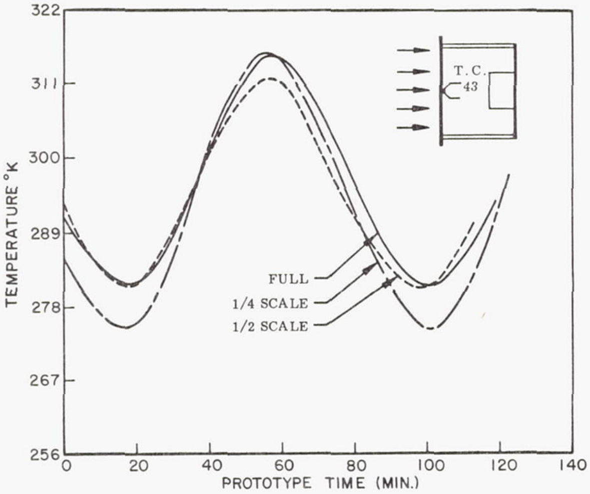

FIGURE 4. FRONT PLATE TEMPERATURE

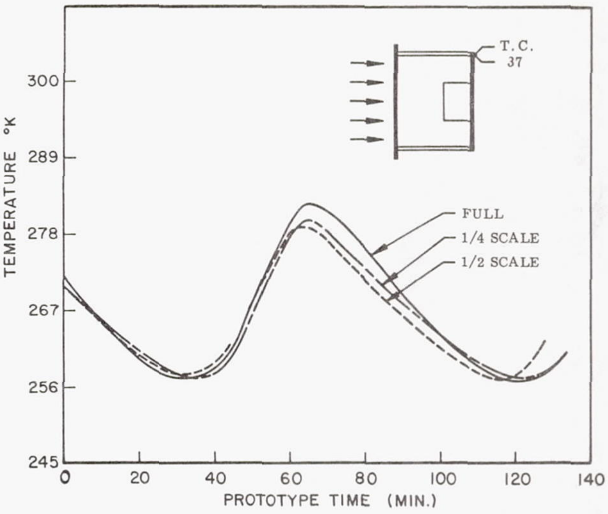

FIGURE 5. BACK PLATE EDGE TEMPERATURE

In the next series of experiments, a truncated cone-shaped object was used (Fig. 6). The full-scale cone height was 0.9144 meters (36 inches) and the base was 0.9144 meters (36 inches).

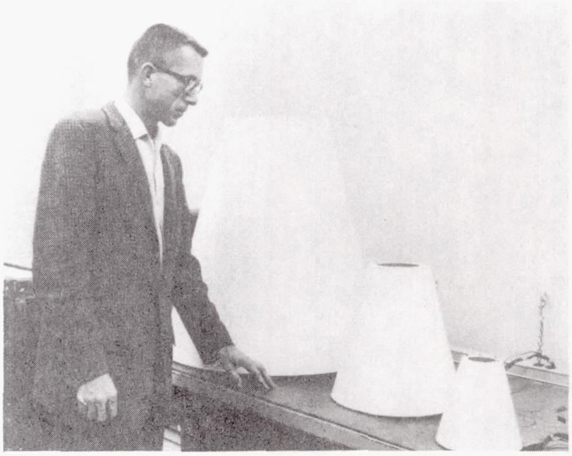

FIGURE 6. $\frac{1}{1}$-, $\frac{1}{2}$-, $\frac{1}{4}$-SCALE CONE MODELS

Four rods were mounted internally and ran the length of the cone (Fig. 7). Between two of the rods is a bare tungsten filament, and between the other two is a box with a heater inside. Again, $\frac{1}{2}$- and $\frac{1}{4}$-scale models were used.

An array of tungsten filament lamps with reflectors was again used to simulate solar insolation. In one set of experiments the base ends of the cones were

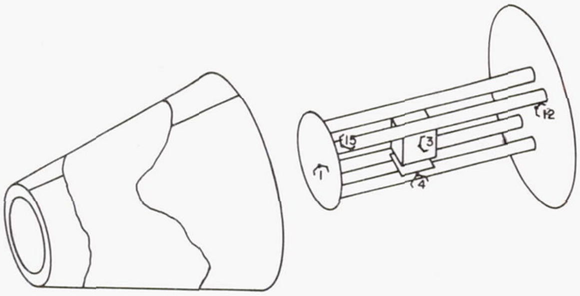

FIGURE 7. INTERNAL ARRANGEMENT

irradiated; in another set, the truncated ends were irradiated. Figure 8 shows the device used to rotate the cones for the two different sets of tests. They were rotated without disturbing the vacuum and low-temperature chamber wall conditions. Only some results of the set of tests where the bases were irradiated are given because the other results are of the same modeling quality.

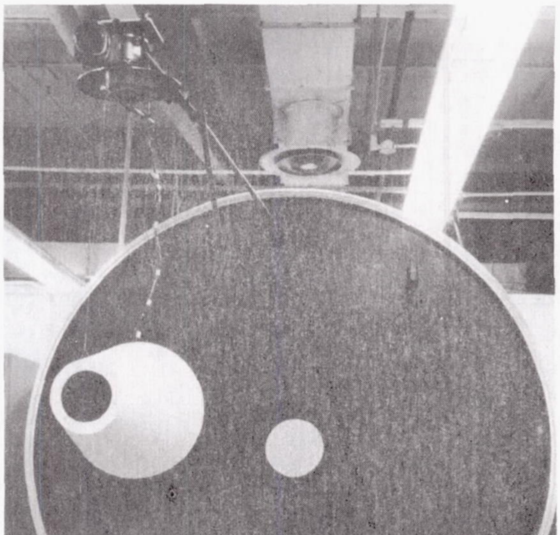

FIGURE 8. CONE INSTALLATION

Figure 9 shows the temperature-time curves for the prototype and both models for a measurement on the skin of the internal heater box enclosure. Figure 10 shows the results for a measurement which was on the inside of the base at its geometric center. All results were within 8°K for both sets of tests between model and prototype.

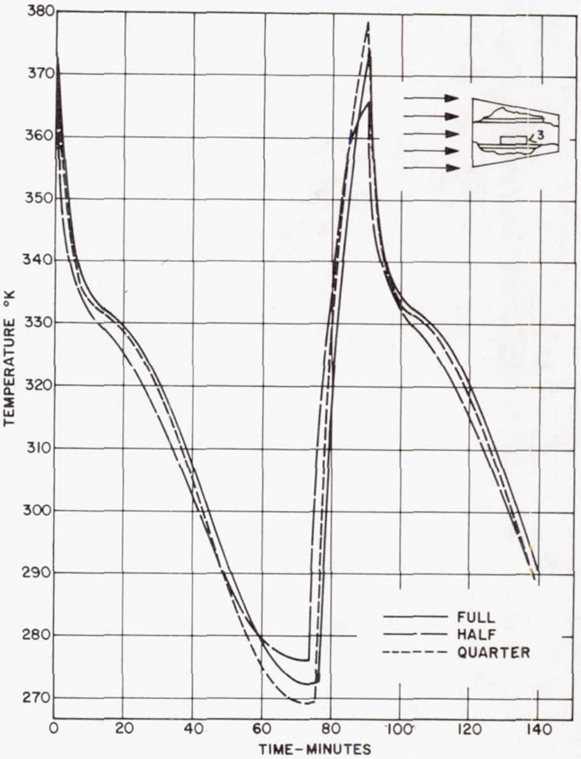

FIGURE 9. CONFIGURATION C - TRANSIENT THERMAL RESPONSE (T. C. No 3)

CONCLUSION

Experimental confirmation was obtained for the derived thermal modeling criteria for the transient case for several situations that represent simplified versions in the thermal aspects of flight hardware. Geometric distortion in minor dimensions was found to be a useful technique in satisfying the criteria, and the work has identified some useful techniques for model design. Progress made in these experiments indicates that thermal similitude can be a useful addition to our methods of solving thermal problems during the design phase.

FUTURE RESEARCH

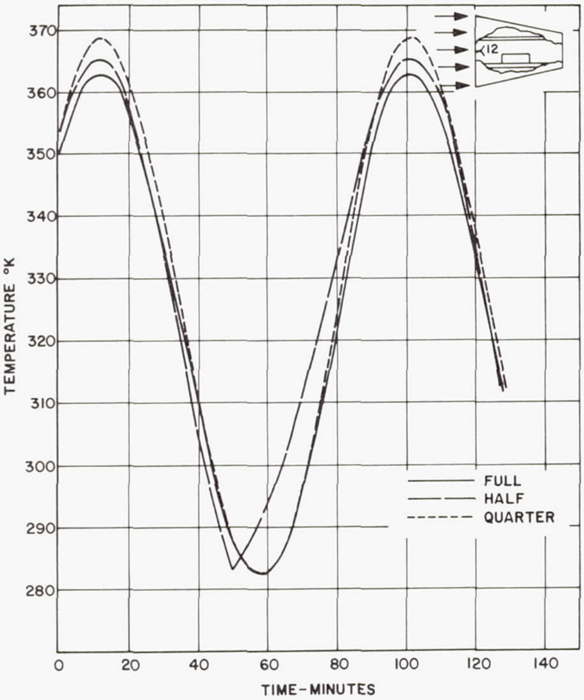

FIGURE 10. CONFIGURATION C - TRANSIENT THERMAL RESPONSE (T. C. No 12)

Future work should take two directions. First, more complicated configurations should be used in the scale modeling experiments. Second, further study should be made of the theoretical aspects. A skeleton for a unifying theory seems to exist through the concept of abstract groups. For example, Laszlo [8] has recently shown that a set of independent "π"-ratios for any particular physical problem forms the basis for a finite abelian group. Birkhoff [9] has already pointed out that the group theoretical concept underlies both the purely algebraic approach (e. g., the computer program discussed earlier) and the differential equations approach to the derivation of modeling criteria. In fact, such considerations have far-reaching implications in that they sometimes lead to a means for solving boundary value problems [10]. This can be important because many of the engineering and physics problems are stated in the form of partial differential equations together with certain boundary value conditions. There seems to be a fairly wide gap between the more abstract theory and everyday practices of modeling. It would be appropriate to do more research in this direction with the hope that results may be used to strengthen the applications side. Two research contracts that are slanted toward further research into the theory were recently initiated. One of them is with the University of Michigan, the other with Georgia Institute of Technology. Thus, future research in thermal similitude at Marshall takes both a theoretical and experimental direction.

REFERENCES

1. Watkins, J. R.: Thermal Similitude Using Brand's Theorem. Proceedings of Conference on Thermal Scale Modeling, NASA/OART, February 1964.

2. Jones, B. P.: Similitude Research in Space Vehicle Thermal Problems. Proceedings of Conference on Thermal Scale Modeling, NASA/OART, February 1964.

3. Jones, B. P.: Thermal Similitude Studies. Journal of Spacecraft and Rockets, Vol. 1, No. 4, July-August 1964.

4. Watkins, J. R.: Sets of Similarity Ratios for Thermal Modeling. NASA TND-3452, May 1966.

5. Rolling, R. E.: Results of Transient Thermal Modeling in a Simulated Space Environment. AIAA Thermophysics Specialist Conference, Paper No. 65-659, September 1965.

6. Jones, B. P.; and Harrison, J. K.: A Set of Experiments in Thermal Similitude. NASA TMX-53346, October 1965.

7. Rolling, R. E.: Thermal Modeling of a Truncated Cone in a Simulated Space Environment. AIAA Space Simulation Conference, September 1966.

8. Laszlo, A.: Systematization of Dimensionless Quantities by Group Theory. Int. J. Heat Mass Transfer, Vol. 7, 1964.

9. Birkhoff, G.: Hydrodynamics (A Study in Logic, Fact, and Similitude). Princeton University Press, 2nd ed., 1960.

10. Hansen, A.: Similarity Analysis of Boundary Value Problems in Engineering. Prentice Hall, Inc., 1964.

EMISSIVITY PHYSICS

By

Edgar R. Miller

SUMMARY

The activities of Research Projects Laboratory in emissivity physics have been primarily concerned with theoretical and experimental studies of optical and thermal control surface properties in the space environments. Various studies are presented to show some of the important problems in the area of thermal control coatings. The results of Research Projects Laboratory's theoretical and experimental work in many facets of emissivity physics are briefly discussed and appropriate references included.

INTRODUCTION

All space vehicle heat exchanges with its environment are radiative. The final average temperature of the space vehicle is a function of its absorption of these electromagnetic radiations and its ability to emit energy at these temperatures.

The sources of electromagnetic radiation are: 1) direct solar, 2) planetary reflection of solar energy, and 3) infrared radiations from planetary bodies and atmospheres.

Nearly all the thermal energy of solar radiation, either direct or indirect, is within the wavelengths of 0.2 to 3.0 micrometers, whereas the energy from planetary bodies and atmospheres is mainly contained in the 3.0- to about 50-micrometer region of the electromagnetic spectrum. This 3.0- to 50-micrometer region is also where most space vehicles must emit thermal energy.

The passive control of a space vehicle's temperature within desired limits depends on (1) how well the optical properties of the vehicle's thermal control surfaces are known and (2) the ability to understand and predict the effects of the space environments on the optical properties of these surfaces.

Much of our work in the area of emissivity physics has been centered upon the space environmental effects on the emissivity and optical absorption of thermal control surfaces and the associated problems of laboratory simulation and measurements.

These environments include: (1) low-energy charged particles of the solar wind, (2) solar electromagnetic radiation, and (3) micrometeoroids.

EFFECTS OF SOLAR WIND

The solar wind consists primarily of low-energy charged particles summarized in the following table.

TABLE I

FLUX, VELOCITY, AND ENERGY OF PRINCIPAL SOLAR WIND CONSTITUENTS

Particle	Constituents at One Astronomical Unit		
	Flux ($cm^{-2}sec^{-1}$)	Velocity (km/sec)	Energy (keV)
Proton (solar wind)	2×10^8	600	1.85
Proton (solar wind)	2×10^9	1000	5.0
α particle (solar wind)	3×10^7	600	7.4
α particle (solar wind)	3×10^8	1000	20

Figure 1 shows the optical degrading effects (in terms of change in solar absorptance) on the IIT Research Institute S-13 coating that consists of ZnO pigmented methyl silicone; this coating was used on the Pegasus satellites. The samples were bombarded

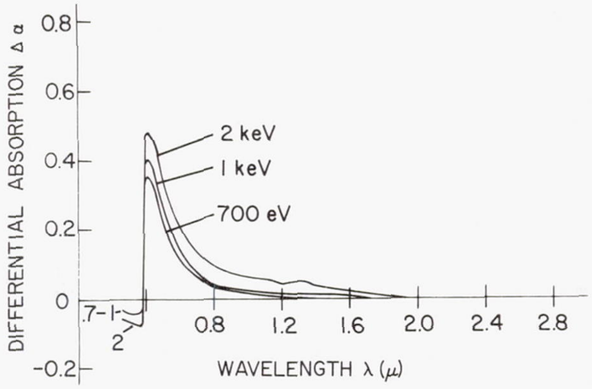

FIGURE 1. OPTICAL DEGRADING EFFECTS OF HYDROGEN ION BOMBARDMENT ON S-13

with ionic hydrogen gas (primarily H_2^+) in a duoplasmatron system. The hemispheric reflectance was measured in air before and after bombardment. Differential spectral absorptance was calculated from the reflectance data.

Figure 1 also shows the effect is increased with higher particle energy for the same integrated flux; this relation may not be true for higher energy regions where the penetration power is so great that the bulk rather than the optical surface is damaged.

Figure 2 shows the effect of helium (primarily He^+) bombardment on S-13 and Z-93 (ZnO pigmented K_2SiO_3) coatings. The Z-93 coating is to be used on the Apollo radiator. This figure points out two interesting phenomena. First, it is apparent that considerable damage is caused by the physical rather than chemical interaction of the particle, and physical rather than chemical interaction of the particle and the material. Second, the Z-93 is seen to be damaged considerably in the infrared region while the short wavelength absorption band is much narrower. This infrared damage is seen in ZnO powders and S-13 from in situ measurements after ultraviolet irradiation while almost no effect is seen in Z-93 in this spectral region after ultraviolet irradiation and with in situ measurements. This will be discussed more fully under electromagnetic effects.

Finally, in Figure 3, the effects of particle mass are shown (velocity is kept constant). Because of less surface penetration power the heavier particle, with the exception of helium and hydrogen, is less effective in producing the degradation. This was also indicated by the data showing the effects of energy, the more energetic particles having a greater penetration depth and producing more damage. The samples shown in Figures 2 and 3 were bombarded in an r-f plasma chamber. The bombarding system and the work are fully described in [1, 2].

This work was done in conjunction with Dr. Wehner and Gordon Jorgenson at Litton Systems, Incorporated. Work was also performed on the theoretical aspects of optical absorption [3].

EFFECTS OF ELECTROMAGNETIC IRRADIATION

In situ measurements have only recently been performed on thermal control surfaces in connection with simulated space environments. It was discovered that severe degradation of solar reflectance is present on the S-13 coating system.

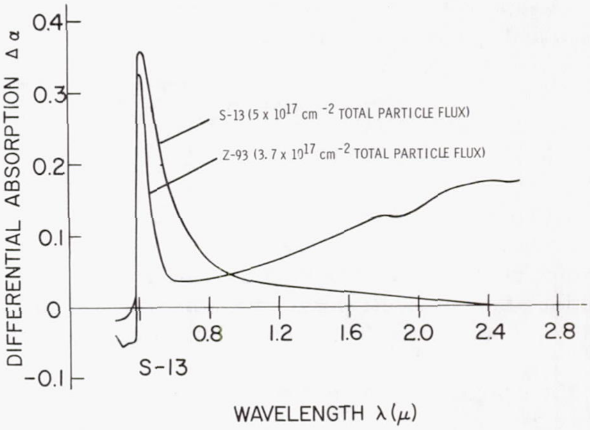

FIGURE 2. OPTICAL DEGRADING EFFECTS OF HELIUM ION BOMBARDMENT ON S-13 AND Z-93

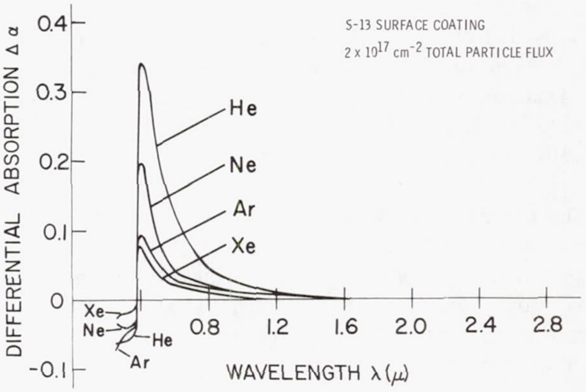

FIGURE 3. EFFECTS OF BOMBARDING PARTICLE MASS ON SURFACE CONTROL COATINGS

Figure 4 shows in situ bidirectional reflectance of S-13 before, during and after exposure to ultraviolet irradiation. It is seen that damage occurs very quickly in the infrared region and subsequent irradiation produces very little further damage. When air is readmitted to the chamber, full recovery is seen to occur and the sample regains its original reflective properties. The total integrated solar absorptance is calculated to change by about 40 percent, while if measured in the normal manner, i. e., taken out of the chamber and measured in air, almost no change would have been seen.

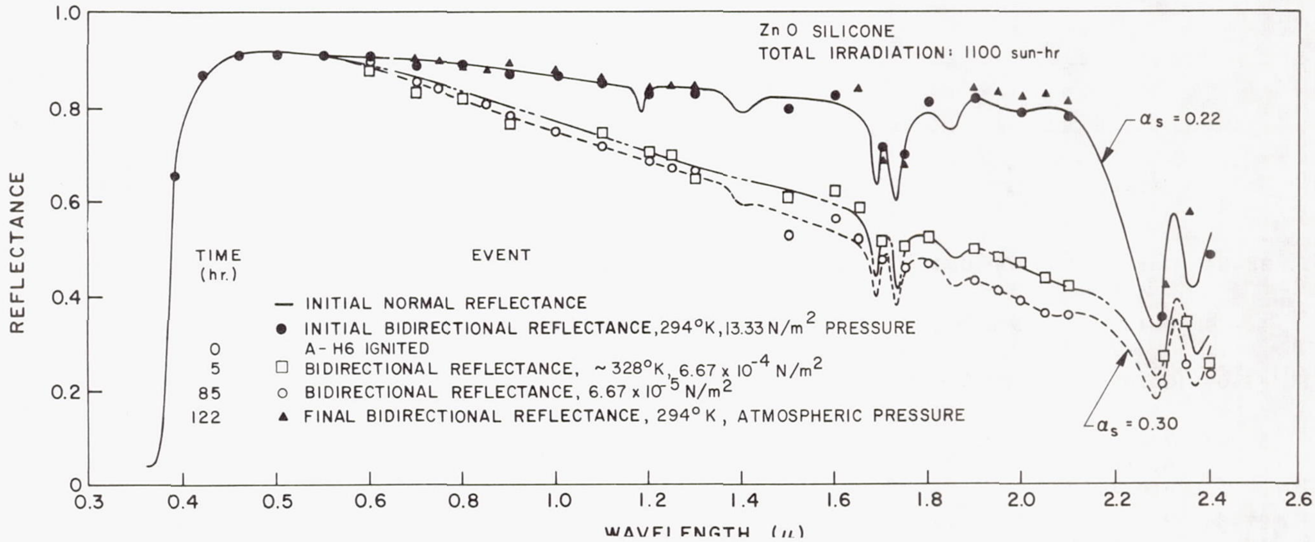

FIGURE 4. IN SITU SPECTRAL REFLECTANCE MEASUREMENTS ON ULTRAVIOLET IRRADIATED S-13

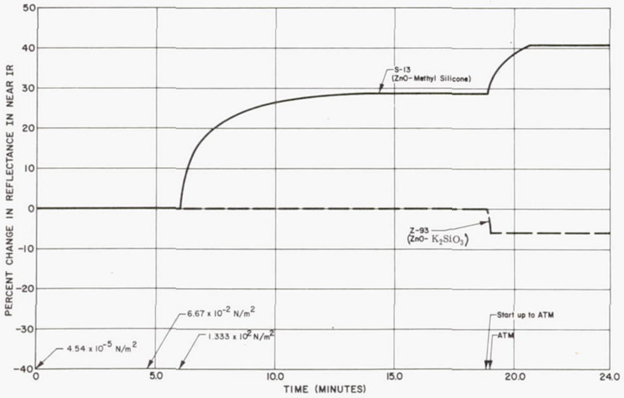

FIGURE 5. EFFECT OF ATMOSPHERIC EXPOSURE ON UV DEGRADED S-13 AND Z-93 COATINGS

Figure 5 shows the results of work performed inhouse in which the speed of the bleaching effect can be seen. The relative reflectance is monitored with a radiometer with a peak sensitivity at about 0.5 to 2.0 microns and air is admitted to the chamber to a pressure level of 130 newtons per square meter. In less than two minutes the samples have bleached more than 20 percent. Subsequent bleaching occurs when ambient pressure is admitted to the chamber.

The effect is not seen in the Z-93 coating system. In fact, there is a very slight increase in the in situ reflectance due to loss of water of hydration and consequent decreased water band absorption in this wavelength region. However, the damage to Z-93 by α particle simulation appears very similar to the damage seen in S-13 from in situ measurements, indicating that possibly some of the damage to Z-93 may have been masked since the measurements were taken in air before and after bombardment. Also indicated is the possible severe degradation by the combined environments of electromagnetic and solar wind irradiations.

The effect in ZnO and S-13 is thought to be photodesorption and adsorption of oxygen from the ZnO.

Additional work will be required in determining the effects of combined particulate and electromagnetic irradiations and performing in situ measurements of optical properties [2].

Much of this work was done under contract to Lockheed Missiles and Space Company [4] and is also being studied at IITRI [5].

MICROMETEOROID EFFECTS

Micrometeoroid erosion has demonstrated a significant effect on the optical properties of certain thermal control surfaces such as metallic coatings. Figure 6 shows increases in emittance from almost 0 to 100 percent, and solar absorptance increase up to 30 percent. These data are representative of the damage that might occur in a year at one astronomical unit.

TOTAL DIRECTIONAL EMITTANCE (θ = 15°) OF THE TEST SAMPLES

	DESCRIPTION			EMITTANCE			SOLAR ABSORPTANCE		
	Materials	Impacts	% Coverage	Initial ϵ	After ϵ	Increase $\Delta\epsilon$	Initial α	After α	Increase $\Delta\alpha$
38-64	Gold	100,000	9.1	$.02_0$	$.02_1$	$.00_1$	$.23_7$	$.27_3$	$.03_6$
47-64	Gold	200,000	15.1	$.02_2$	$.02_8$	$.00_6$	$.23_2$	$.27_1$	$.03_9$
47-64	Gold	400,000	~30	$.02_0$	$.04_4$	$.02_4$	$.24_0$	$.29_3$	$.05_3$
51-64	304 Stainless Steel	300,000	~ 8	$.09_6$	$.11_4$	$.01_8$	$.45_4$	$.46_3$	$.00_9$
97-64	304 Stainless Steel	600,000	~16	$.10_3$	$.12_8$	$.02_5$	$.45_4$	$.48_3$	$.02_9$
40-64	Vacuum Deposited Aluminum	300,000	-	$.02_3$	$.04_0$	$.01_7$	$.11_0$	$.13_0$	$.02_0$
105-64	Vacuum Deposited Aluminum	600,000	-	$.03_0$	$.06_0$	$.03_0$	$.12_0$	$.15_8$	$.03_8$

FIGURE 6. EFFECT OF SIMULATED MICROMETEORITE BOMBARDMENT UPON INTEGRATED DIRECTIONAL REFLECTANCE

Perhaps an even more significant effect of meteoroid bombardment on optical properties is the introduction of a diffuse component on reflected radiation. Figure 7 gives the ratio of specular reflectance before and after bombardment. The performance of remote sensing and other optical components such as mirrors, lenses and windows will be significantly affected by such degradation.

Analytical models of the scattered light from meteoroid degraded surfaces are needed to more fully understand and predict the effects on systems performance. Thompson Ramo-Woolridge performed this work under contract from MSFC [6].

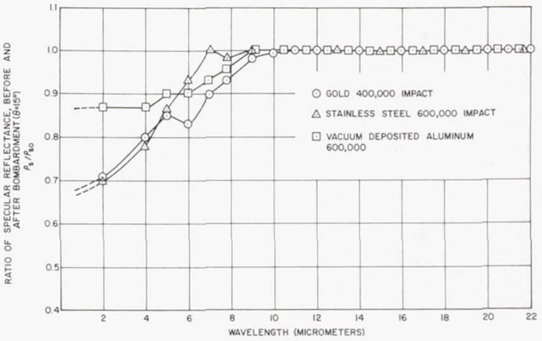

FIGURE 7. EFFECT OF MICROMETEOROID BOMBARDMENT UPON THE SPECULAR REFLECTANCE

THERMAL CONTROL SURFACES FLIGHT EXPERIMENT ON PEGASUS III

Figure 8 shows the mounting location of two of the eight coupons containing a total of 352 individual thermal control surface samples which were attached to the wing surfaces of Pegasus III in the hope that one day an astronaut could make in situ measurements and return the samples to earth for further laboratory studies. In situ measurements are

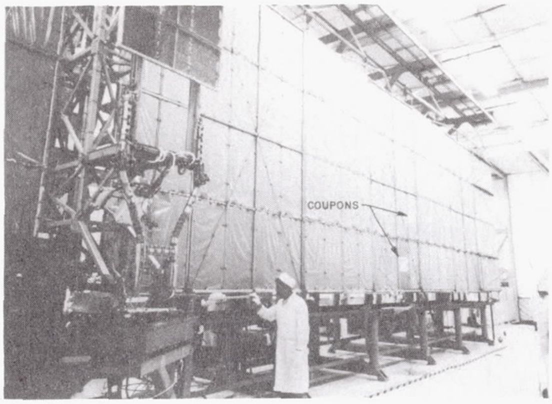

FIGURE 8. LOCATION OF THERMAL CONTROL SURFACE COUPONS ON PEGASUS III

necessary due to the anomalous infrared degradation exhibited by some thermal control surfaces upon ultraviolet irradiation which has been discussed previously. These samples represent the work of four NASA Centers, six private industries and industrial firms, one Army Ordnance Missile Laboratory and one foreign country.

The coatings on board have been flown or will be flown on Pegasus, Saturn, Apollo, Mariner, Lunar Orbiter and many others. Figure 9 shows a close-up of one of the coupons and the attached thermal control coating samples. Research Projects Laboratory collected the samples from the various contributors, catalogued, performed measurements, and mounted the samples to the coupons on very short notice.

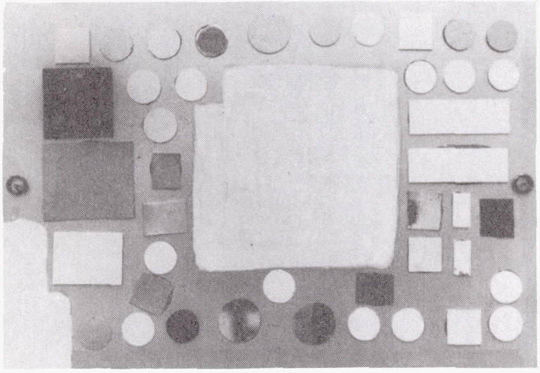

FIGURE 9. CLOSE-UP OF THERMAL CONTROL SURFACE COUPONS ON PEGASUS III

Although no definite plans have been made to recover these coupons, much valuable data will be obtained when such recovery is made.

Research Projects Laboratory is working on space-stable coatings of various types in conjunction with the Air Force (WADC) under Project SUPER [7]. Also, RPL is studying the theoretical directional back-scattering of oriented dielectric cylinders for possible use in thermal control [8].

Dr. Schocken of Research Projects Laboratory has studied the basic theory of emissivity and has found that the value of emissivity of metals under equilibrium conditions differs in the presence or absence of other electromagnetic fields [9].

Measurements and Standards. Research Projects Laboratory has been working toward obtaining better optical property measurements such as obtaining better radiometric sources and receiver standards, participating in industry and NASA sponsored "round robins" on measurements, and obtaining specialized equipment such as a bidirectional spectroreflectometer and an in situ environmental effects chamber.

Research Projects Laboratory also participated in a series of tests carried out by the Propulsion & Vehicle Engineering Laboratory to obtain the effects of solid deposits from solids, rockets, or thermal control surfaces.

Research Projects Laboratory's portable integrating sphere spectroreflectometer (Fig. 10) was taken to the Tullahoma test site to obtain immediate measurements of optical degradation on these surfaces due to rocket plume impingement.

CONCLUSION

Research Projects Laboratory's activities in the emissivity physics areas have elucidated problems over a broad range from the theoretical and experimental research to Saturn and Saturn payload activities.

Additional experimentation in the area of thermal control surfaces (including the need for combined environmental studies and in situ measurements), is necessary to obtain a better understanding of the effects of synergism and bleaching.

In situ measurements and recovery of the Pegasus III thermal control samples would provide many answers on long-term stability in the low-earth orbit space environment of almost all important coating systems.

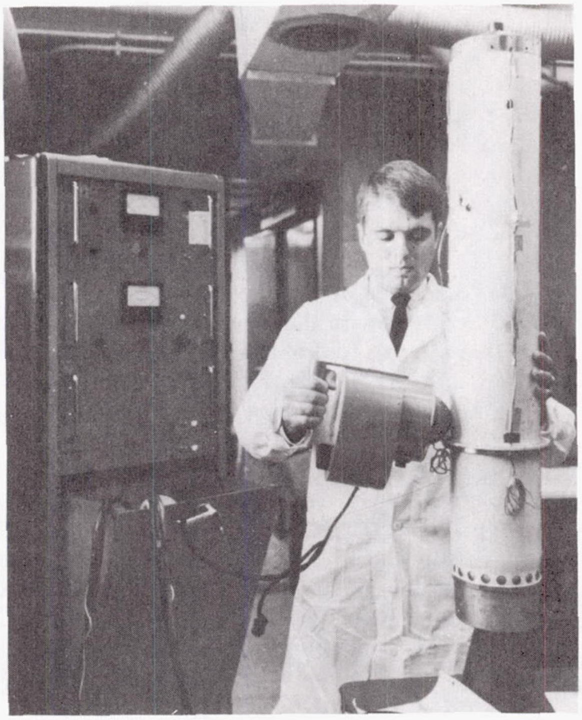

FIGURE 10. PORTABLE INTEGRATING SPHERE SPECTROREFLECTOMETER

Research Projects Laboratory is continuing many contractual and inhouse experimental efforts including the optical properties of solids (emissivity, absorptivity, transmissivity, scattering, and optical constants) and laboratory instrumentation and measurements.

REFERENCES

1. Solar Wind Damage to Spacecraft Thermal Control Surfaces. Contract No. NAS8-11269, Litton Systems, Inc., July 1965.

2. Miller, E. R.: Effect of Solar Wind Bombardment on Thermal Control Surfaces. NASA TMX-53426, April 15, 1966.

3. Calculations of the Optical Absorption of an F-Center in ZnO by Simpson's Method. Contract No. NAS8-20166, Brown Engineering TN R-172, December 1965.

4. Solar Radiation Induced Damage to Optical Properties of ZnO-type Pigments. Contract NAS8-11266, Technical Summary Report, Lockheed Missiles and Space Company, Palo Alto, Calif., June 1965.

5. Development of Space-Stable Thermal Control Coatings. Contract NAS8-5379, Report No. IITRI-U 6002-36 (Triannual Report), IIT Research Institute, Chicago, Illinois.

6. Study of Micrometeoroid Damage to Thermal Control Materials. Final Technical Report, Contract NAS8-11149, TRW No. 4146-6009-SV-000, February 1965.

7. Thermal Control Surfaces. First Annual Progress Report, Project SUPER PR-No. H-71465, July 1965.

8. Directionally Reflective Coating Study. Technical Summary Report, Contract No. NAS8-11273, Ling-Temco-Vought No. 00.603, May 1965.

9. Theoretical Study of the Radiative Emissivity of Materials. Contract NAS8-5210, PEC Corporation, Boulder, Colorado.

Page
Intentionally
Left Blank

ULTRAVIOLET INTERACTIONS WITH SOLID MATERIALS

By

Gary M. Arnett

SUMMARY

Studies elucidating some of the major problems connected with spacecraft coating instability when exposed to solar ultraviolet irradiation are presented. The studies are concentrated on ZnO-type pigmented thermal control coatings which are among the most stable white coatings available at the present time. Basic experimental and theoretical research efforts in this area, both inhouse and on contract, are presented along with preliminary conclusions of various aspects of the program.

INTRODUCTION

Successful operation of space vehicles demands that components be maintained within their designed temperature limits. Control of temperature on an operational spacecraft is based on the exchange of radiant energy with the vehicle's environment, and therefore depends upon the optical properties of the exterior surfaces. Design requirements often dictate the use of a surface with a low ratio of solar absorptance, α_s, to the emittance, ϵ_{IR}. These surfaces are generally susceptible to damage by natural or induced radiation in space, resulting in an increase in solar absorption. The emittance is generally unaffected.

Of all sources of radiation encountered in space, both natural and induced, the ultraviolet portion, that is the 2000 to 4000 angstrom region of the solar spectrum, is the most important source of damage to surfaces with a low ratio of solar absorption to thermal emittance. For most low α_s/ϵ_{IR} surfaces, ultraviolet induced damage is at least as great as that due to other forms of radiation. In addition, all space vehicles are exposed to high fluxes of solar radiation. In contrast, not all vehicles experience high doses of Van Allen, nuclear, or other forms of high-energy radiation. Since 96.9 percent of solar radiation is between the wavelengths of 0.2 microns and 2.6 microns, the solar absorption of a material is essentially determined by its optical properties in this wavelength range.

Over the past five years a large body of data on the effects of simulated solar ultraviolet radiation in vacuum on low α_s/ϵ_{IR} thermal control surfaces has been generated by various agencies concerned with spacecraft temperature control. In the past, time requirements forced efforts to be limited to accumulating relatively crude engineering design data. Available information on solar-radiation-induced damage to thermal control surfaces is almost entirely empirical. Since complete environmental simulation is never achieved in the laboratory, precise prediction of behavior in space from existing laboratory testing data is not possible. This has been illustrated by comparison of laboratory and spacecraft data [1].

The type of low α_s/ϵ_{IR} surface generally applied on spacecraft is a white coating made up of a pigment dispersed in a binder. A definitive understanding of the changes in the spectra of such systems is impossible unless the individual behavior of each component is first understood. Therefore a detailed study has been undertaken to better understand the behavior of the pigment itself. If this study is to produce positive results, it must concentrate on one pigmenting material. The ideal pigment would possess the following attributes:

(1) Simple, well-defined chemical and electronic structure

(2) Data available on the optical, electrical and related physical properties

(3) Representative of a class of stable white pigments

(4) In use in promising thermal control coatings.

Zinc oxide possesses each of the above characteristics to a greater degree than any other single material. ZnO, when used as a pigment with a methyl silicone or potassium silicate binder, is one of the most ultraviolet-stable thermal control coatings available. Furthermore, its properties are similar to those of titanium dioxide, zinc sulfide and stannic oxide, which are used as pigments in promising white thermal control surfaces. From this information it was decided that the study of ZnO would provide a logical starting point for investigation of the mechanisms involved in solar-radiation-induced damage to low α_s/ϵ_{IR} surfaces.

Research Projects Laboratory has approached this theoretical and experimental research problem with both inhouse investigations and on contract with Lockheed Missiles and Space Company's Research Laboratories. The studies have been directed toward identifying the primary mechanisms involved in solar-radiation-induced damage to the optical properties of ZnO-type semiconductor pigments, as exemplified by ZnO itself. Knowledge of the damage mechanism will greatly simplify the problem by providing a rational basis both for the design of environmental tests and for interpretation of the resulting data. Ultimately, it is hoped that such knowledge will guide material specialists in the development of optimum materials for thermal control purposes.

The work reported under the contractual portion of this paper was conducted at Lockheed Missiles and Space Company's Research Laboratories, Palo Alto, California, under the direction of Mr. L. A. McKellar and Dr. S. A. Greenberg (Contract NAS8-11266). The inhouse portion was conducted in the laboratories of Research Projects Laboratory, Marshall Space Flight Center.

CONTRACTUAL EFFORTS

The work conducted on the previously mentioned contract can be summarized by the following studies: (1) optical transmission and reflectance studies, (2) in situ bidirectional studies, (3) photoconductivity measurements, and (4) theoretical band structure studies. Discussed below will be typical results obtained under each of the four major areas of effort.

Figure 1 shows a typical radiation test of the spectral reflectance of particulate ZnO before and after ultraviolet irradiation in vacuum. One of the most interesting features of this type of study is the comparison of the optical properties exhibited by samples that had identical irradiation times of 860 sun-hours. One was measured within one hour after irradiation and the other was exposed to atmospheric conditions for 120 hours before measurements were performed. The 120-hour time-lapse measurement demonstrates considerable bleaching throughout the spectrum. The sample irradiated for 950 sun-hours (nearly 100 sun-hours longer than the other cases) and measured just under two hours after exposure to atmospheric conditions, appeared to have less damage than the sample irradiated for 860 sun-hours that was measured within one hour after exposure to the atmosphere. Here one sun-hour is defined as the

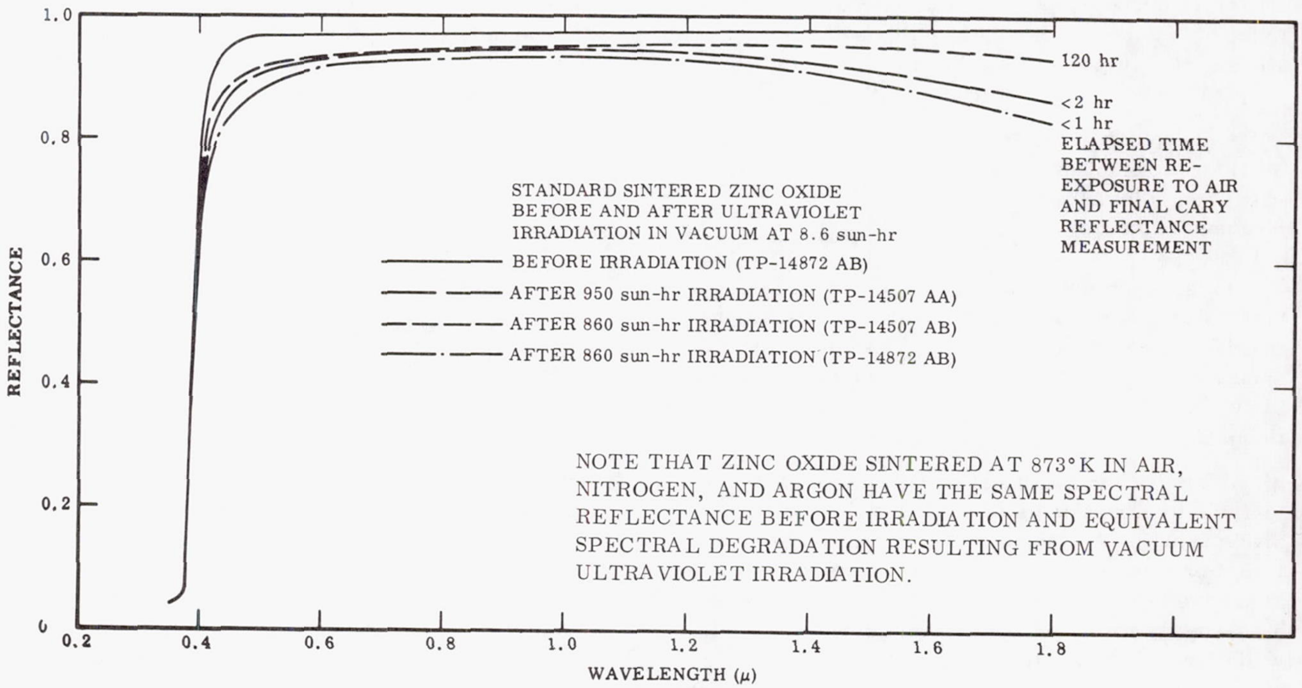

FIGURE 1. SPECTRAL REFLECTANCE OF PARTICULATE ZnO BEFORE AND AFTER UV IRRADIATION IN VACUUM

amount of irradiation incident upon a sample in outer space at one astronomical unit from the sun in the region of 2000 to 4000 angstroms. It should also be noted in this figure that little, if any, shift in the band edge can be detected for samples measured in this manner. Results such as these indicate that at least some of the induced damage is not permanent but is subject to bleaching. For true measurements of the induced damage, such as that encountered in outer space, samples must be measured while still in their irradiation environment. This study led to the development of what Lockheed calls their "in situ bidirectional reflectance device." Spectral results received from this device are normalized around 6000 angstroms measurement as obtained from their integrating sphere. Thus the instrument has proven to be a good and accurate device for making in situ reflectance or transmission measurements. Figure 2 demonstrates results obtained from this instrument. The before-irradiation curve is not shown in this figure, but would be identical to the unirradiated curve in Figure 1. In Figure 2 the edge of the absorption band has moved out into the visible region after only 52 hours of irradiation. Sometime after terminating the irradiation and before allowing the pressure to rise within the vacuum chamber, the edge of the absorption band is recovered. It should be noted in Figure 2 that the initial bidirectional measurement was taken 20 minutes before termination of irradiation and the next measurement was taken 5 $\frac{1}{2}$ hours before allowing the pressure to rise 10.68 newtons per square meter (80 microns). It has been demonstrated that if the pressure is allowed to come to a somewhat higher value of 66.7 to 133.3 newtons per square meter (500 to 1000 microns), the recovery is instantaneous, especially in the infrared region, but as can be seen, is not happening at a pressure of 10.68 newtons per square meter (80 microns).

Figure 3 shows the spectral dependence of optical absorption and photoconductivity. These studies have been performed to obtain information on the recombination and trapping states that bear directly on the degradation mechanism, and also to lay the groundwork for the use of the photoconductivity technique in investigating defects produced in degraded single crystals. The first point to note on the optical absorption data is the apparent shift of ~ 0.04 electron volts of the fundamental absorption edge to low energy with the Li addition (Li doping reduces the number of electron charge carriers). This shift is either the result of a high density of shallow acceptor states or a deformation of the lattice itself caused by the high impurity concentration. The absorption data do not go to high enough values of the absorption coefficient to resolve this point.

The measurements of the spectral dependence of the photoconductivity were carried out at room temperature in air on the Li-doped crystal. Radiation from a Xenon compact arc source was passed through

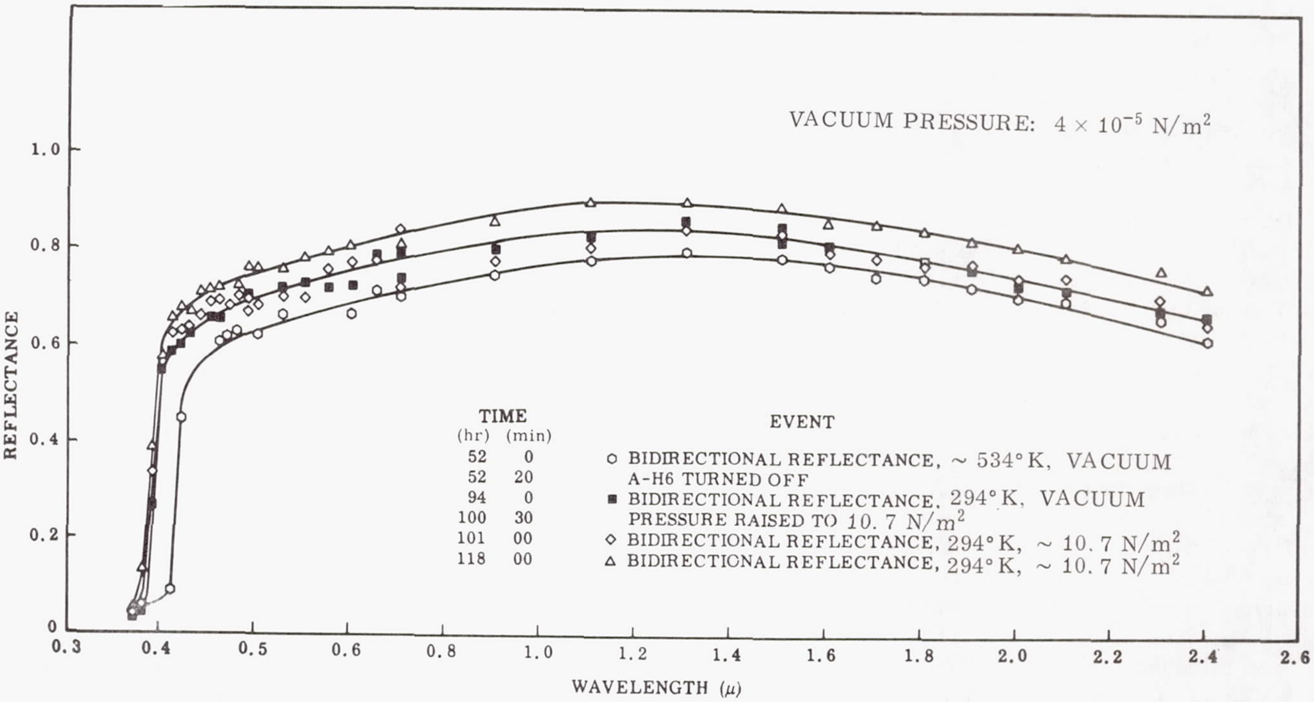

FIGURE 2. RECOVERY OF UNPRESSED, UNSINTERED ZnO AT 294°K

a Perkin-Elmer 112 monochromator and then brought to focus on the sample. The chopping frequency of 1 kilocycle was chosen to insure that only the fast photoconductive process was being observed. Figure 3 compares the photoconductive response and the absorption edge data on the Li-doped sample. The essential feature is that the photoconductivity observed is a bulk as opposed to a surface phenomenon, which is supported by the following arguments. The photoconductive signal decreases as the absorption coefficient increases sharply because of the band-to-band absorption that is the fundamental band edge. The sample surface was purposely not etched, thus providing a surface with a high recombination rate. Therefore in these experiments, radiation which is absorbed very close to the surface (that results from a high absorption coefficient) does not give rise to a photoconductive signal. The next feature to note is that the signal peaks at the wavelength for which the absorption coefficient corresponds approximately (order of magnitude) to the reciprocal of the sample thickness or ~ 0.04 centimeters. At longer wavelengths an increasing amount of the incident energy is transmitted through the sample because of the decreasing absorption coefficient. The photoconductive responses decrease proportionately.

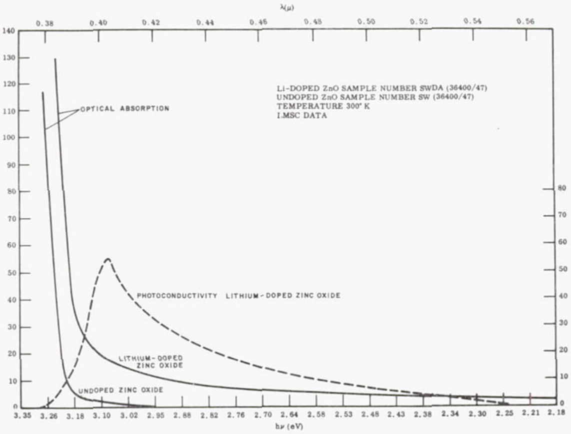

FIGURE 3. SPECTRAL DEPENDENCE OF OPTICAL ABSORPTION AND PHOTOCONDUCTIVITY

The results of the photoconductivity studies lend strength to the bulk impurity state model used in the theoretical studies. Figure 4 shows this impurity model with the band-gap energy at 3.2 electron volts, which corresponds to 0.38 microns.

To round out the theoretical portion of the first phase of this program, it was felt that a thorough understanding of the electronic energy band structure of a crystal was a necessary prerequisite for the detailed interpretation of many important transport and optical properties. Therefore, theoretical band structure studies of ZnO were initiated to complement the experimental program. To the best of our knowledge, no serious attempt has previously been made to elucidate the electronic band structure of ZnO. Therefore, our efforts in this area should be both useful and unique.

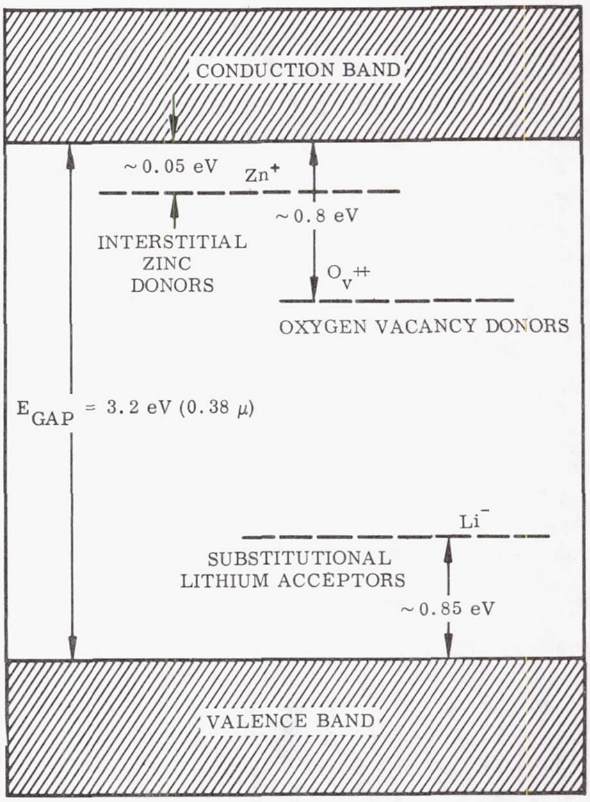

FIGURE 4. BULK IMPURITY STATES

After detailed consideration of the chemical, electronic, and physical structure of ZnS and ZnO, it was determined that the band structure calculations could best be accomplished by utilizing the "method of corresponding states," with ZnS calculations being the basis for work carried out on ZnO. Thus the reliability of the ZnO results cannot be any better than the ZnS calculations that were carried out by Herman and Skillman using the orthogonalized-plane-wave method. An energy band model was derived for ZnO from these calculations, which are too detailed and complex to discuss in this paper (for further information on these calculations, see contract report mentioned in acknowledgements). The plausibility of the desired model was then tested by the method of weak binding (the nearly free electron model) and by the method of tight binding. These tests indicated that the derived band structure for ZnO was probably a good first estimate [2]. Further work in this area may prove to be quite valuable because of the crucial role that the energy band structure can play in estimating the energy levels of both surface states and bulk impurity states.

INHOUSE EFFORTS

The Space Thermodynamics Branch of Research Projects Laboratory at Marshall Space Flight Center is conducting inhouse experimental and theoretical studies on the interaction of electromagnetic radiation with solid state matter. The major parts of the inhouse efforts can be outlined as follows: (1) ultraviolet irradiation parameter studies, (2) electrical conductivity studies, (2) optical absorption studies, (4) magnetic susceptibility studies, and (5) electron paramagnetic resonance studies. Figure 5 shows the main ultraviolet irradiation facility. Early in the program the use of a diffusion-pumped vacuum system was discontinued because oil contaminated the ZnO-type materials; therefore, a sorption-rough and ion-fine pumping system is now used to keep contamination to a minimum. A residual gas analyzer was placed within the system as a permanent fixture (not shown in figure). This will allow the experimenter to study the partial pressure of the gases evolving from the sample material during ultraviolet irradiation. After conducting studies of the intensity versus time of the high-pressure mercury arc lamps used as the ultraviolet irradiation source, it became evident that some type of intensity control was needed to compensate for the erratic behavior of the lamp. The control on the left and the housing on top of the irradiation chamber provide (through a series of servomechanisms) a constant intensity of irradiation upon the sample. The system allows the experimenter to readily choose the intensity, or during irradiation, change the intensity of irradiation upon the sample, with continuous recording of intensity and irradiation time. The intensity-monitoring device is an Eppley thermopile which can be filtered with a selection of eight different filters located on a filter wheel, with the position of interest selected on the control console.

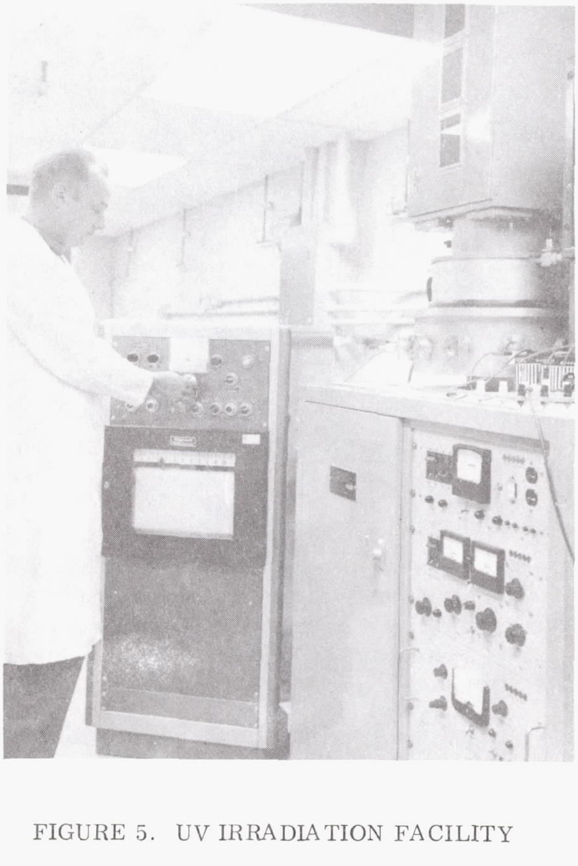

FIGURE 5. UV IRRADIATION FACILITY

The specific study being conducted using the apparatus shown in Figure 5 is the effect of ultraviolet irradiation on the electrical conductivity of ZnO single crystals [3]. The irradiation was filtered using a Corning CS7-37 filter so that the principal illuminating wavelengths were concentrated about 3650 angstroms, which is equal to or greater than the band gap energy in ZnO. The sample was irradiated for 50 hours at 0.013 watt per square centimeter and Table I shows the results obtained. The observed increase in conductivity after 50 hours of irradiation may result from

TABLE I. RESULTS OF ELECTRICAL RESISTIVITY STUDIES

	Time (min) after Potential is Applied			
Electrical conductivity in $\text{ohm}^{-1}\text{cm}^{-1}$	0	4	8	10
Before irradiation in air	$5{\cdot}50\times10^{-3}$			$4{\cdot}685\times10^{-3}$
After irradiation in vacuum	$7{\cdot}127\times10^{-3}$	$9{\cdot}528\times10^{-3}$	$1{\cdot}003\times10^{-2}$	$1{\cdot}003\times10^{-2}$
After irradiation and letting air in vacuum chamber	$4{\cdot}685\times10^{-3}$	$4{\cdot}78\times10^{-3}$	$4{\cdot}499\times10^{-3}$	$4{\cdot}499\times10^{-3}$

the loss of oxygen from the sample, while the excess zinc atoms become ionized and diffuse into interstitial positions in the lattice, which accommodates them. The oxygen evolved has little chance of being reabsorbed by the crystal because of the vacuum environment of approximately 5.34×10^{-5} newtons per square meter (4×10^{-7} torr). Electrons which make possible the electric conduction are removed from the zinc and compared in a similar way with thermal excitation, as reported by Scharowsky. The increase in the conductivity of the crystal implies that the zinc atoms are not electrically neutral. However, lowering the conductivity by allowing air to enter the vacuum chamber is an indication that current strength is decreased by oxygen presssure and the chemisorption of oxygen. It seems probable that the effect of heating may be comparable with the effect of ultraviolet irradiation, but no definite conclusion can yet be drawn. It is hoped that the bleaching of the resistivity noticed in these data can be correlated with the optical bleaching data which were obtained under similiar circumstances.

Figure 6 shows data received from inhouse optical absorption studies.* The ZnO crystal disc used here was subjected to similar irradiation parameters as mentioned in the previous study. The absorption measurements were not made in situ, but the measurements made are a good indication of the permanent bulk damage induced by the ultraviolet irradiation. Of special interest is the recovery of the sample in the infrared such that the absorption coefficient is less after irradiation and bleaching than before irradiation. This phenomenon cannot be adequately explained at this time.

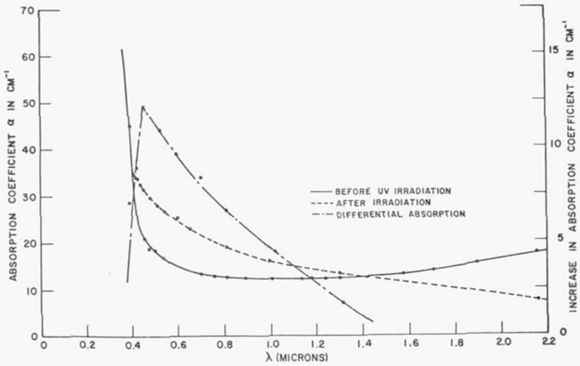

FIGURE 6. OPTICAL ABSORPTION IN ZnO SINGLE CRYSTAL OF THICKNESS 0.21539 mm AT 300°K

ZnO displays basically diamagnetic properties; the susceptibility of ZnO becomes less and less diamagnetic with ultraviolet irradiation, which demonstrates the paramagnetic nature of the induced damage sites.

Figure 7 shows a portion of the magnetic susceptibility equipment being utilized to study magnetic properties of ZnO before, after, and during ultraviolet exposure. The microbalance shown at the top of Figure 7 is operated along with the electromagnet at a distance of six feet or greater to reduce disturbances when making precise measurements. Measurements are taken at the same distance with the help of a lamp and scale arrangement and a counterbalancing coil mounted on the center of the beam arm which is supported by a small quartz fiber.

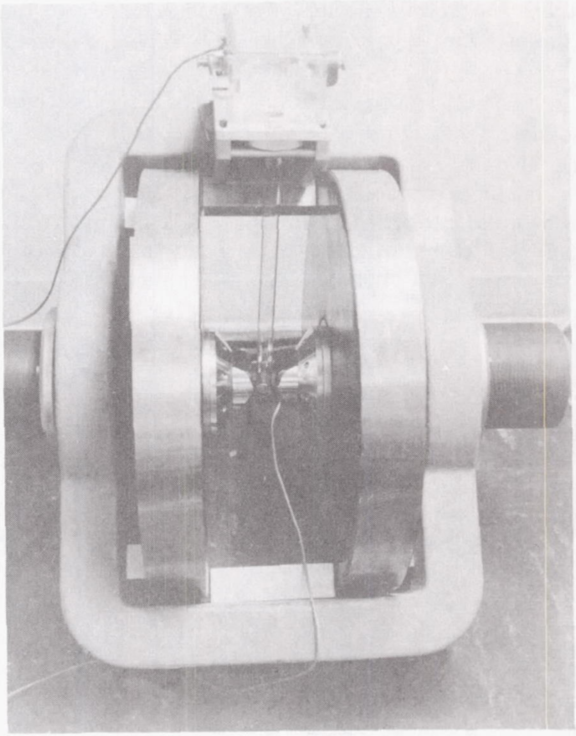

FIGURE 7. ELECTROMAGNET WITH MICROBALANCE

---

* Lal, R. B.; and Miller, E. R.: "Effect of Ultraviolet Irradiation on Fundamental Optical Absorption in ZnO Single Crystals" (to be published later).

Inhouse studies are also being conducted on the absolute spin concentration, g-value measurements, and the spin-spin and spin-lattice relaxation time using an electron paramagnetic resonance apparatus shown in Figure 8. In this figure, the ultraviolet radiation source, used in irradiating the ZnO particulate or single crystal samples, is being placed between the pole-tips of the magnet. ZnO displays no resonance absorption before irradiation. Because of the bleaching phenomenon observed, the irradiation must be conducted while measurements are being taken. When the density of the unpaired electrons, or paramagnetic centers, increase into the sensitivity range of the instrument, resonance absorption is recorded. The instrument has the dual sample cavity capability so that resonance spectra can be directly compared to a calibrated sample. Thus far, observations have been made of the resonance spectra and the instantaneous bleaching when irradiation is terminated. Precise g-value or Landau factor measurements are presently being conducted along with detailed studies of the relaxation phenomena.

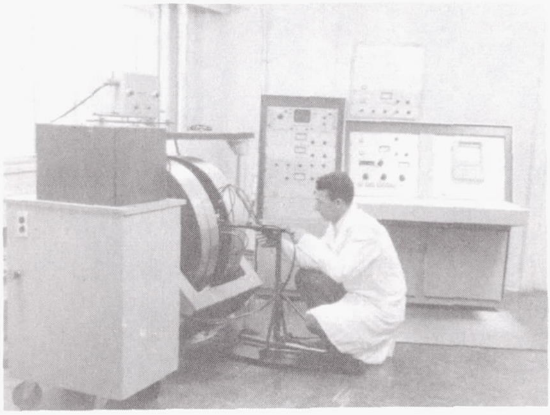

FIGURE 8. INSTRUMENT FOR MEASURING ELECTRON PARAMAGNETIC RESONANCE ABSORPTION

Figure 9 shows the X-ray spectrometer used in making detailed impurity concentration measurements on all samples of ZnO before basic magnetic or optical absorption studies are conducted.

CONCLUSION

The program has proceeded to the point where a preliminary model of the ultraviolet-induced damage mechanism can be formulated, although there are many unanswered questions. Throughout the course of the experimental studies, one unifying trend in the data has been apparent - many of the changes in the optical properties of zinc oxide appear in part to be connected with the photoadsorption and desorption of oxygen by the crystal.

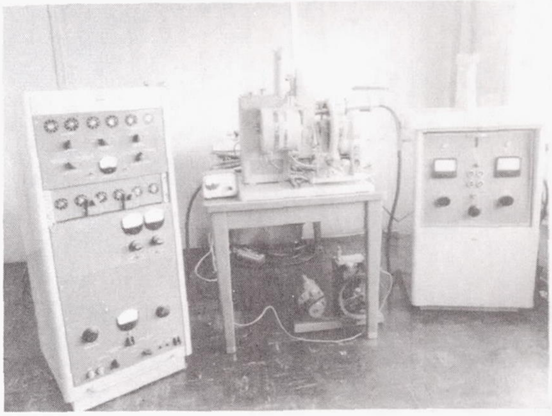

FIGURE 9. X-RAY SPECTROMETER

REFERENCES

1. Neel, C. B.: Research on the Stability of Thermal-Control Coatings for Spacecraft. NASA TMX-51196, October 1963.
2. Lockheed Missiles and Space Company, Technical Summary Report, Contract No. NAS8-11266, June 27, 1964 - June 27, 1965.
3. Lal, R. B.; and Arnett, G. M.: Nature, 208, 1305.

PEGASUS THERMAL EXPERIMENTAL RESULTS

By

William C. Snoddy

SUMMARY

Results thus far obtained from the analysis of Pegasus orbital thermal data indicate that the temperature of the on-board electronics for all three Pegasus spacecraft is being maintained within the desired range in spite of an overheating of the S-IV stage and the service module adapter. The S-IV stage and the service module adapter were designed to act as heat sinks for the electronics. At this time it is believed that the overheating was caused by a degradation of the optical characteristics of the paint applied to these areas. This degradation is presumed to have resulted from damage caused by plume impingement from the retrorockets on the booster during stage separation and from the rocket used to jettison the Apollo escape tower. The successful operation of the thermal louvers attached to the electronics canister is credited with maintaining the proper thermal environment even though these difficulties were encountered.

Results from an "environmental effect sensor package" indicate a space-environment-induced degradation of several thermal control coatings. Some of these supposedly "space-stable" coatings have had a 100 percent increase in their solar absorptance to infrared emittance ratio. Results from these sensors are also used to study the earth's albedo. The albedo has been found to vary greatly and results are now being correlated to weather photographs.

INTRODUCTION

The first Pegasus spacecraft was placed in orbit on February 16, 1965 followed by a second one on May 25, 1965 and the final one on July 30, 1965. The primary objective of this series of satellites is the further definition of the meteoroid hazard to manned space flights. In addition to telemetering data regarding the meteoroid environment, each of the spacecraft has transmitted many millions of bits of thermal information. These thermal data are being evaluated inhouse at Marshall Space Flight Center; a discussion of some of the results obtained thus far follows.

EVALUATION OF THERMAL DESIGN OF LARGE AREAS

Two sections of the Pegasus spacecraft represent the largest, inflexible surface of any satellite ever placed in orbit having a lifetime of more than a year. These are the meteoroid detector panels with 200 square meters of surface and the S-IV stage together with the service module adapter having a total of about 300 square meters of exterior surface (Fig. 1).

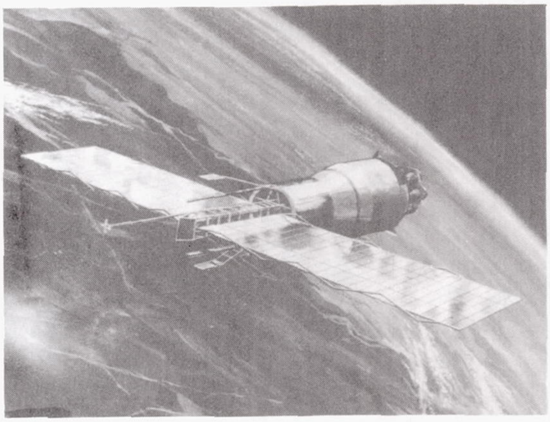

FIGURE 1. PEGASUS SATELLITE

In the case of the detector panels, the initial question to be answered by thermal data analysis was whether the temperature of the panels with their coating of MTL-3 Alodine remained within the design range of 165° to 395°K. Some typical data from Pegasus I are shown in Figure 2 and indicate a maximum temperature of about 350°K with a minimum of 225°K. The top curve in Figure 2 represents the temperature of the side of the detector panels facing the sun; the bottom curve represents the temperature for the side away from the sun. The large variations are caused by passage of the satellite through the earth's shadow. Continuous monitoring of these temperature probes indicates that these values represent near extremes. Therefore, the temperatures of the detector panels on Pegasus I as well as the other Pegasus

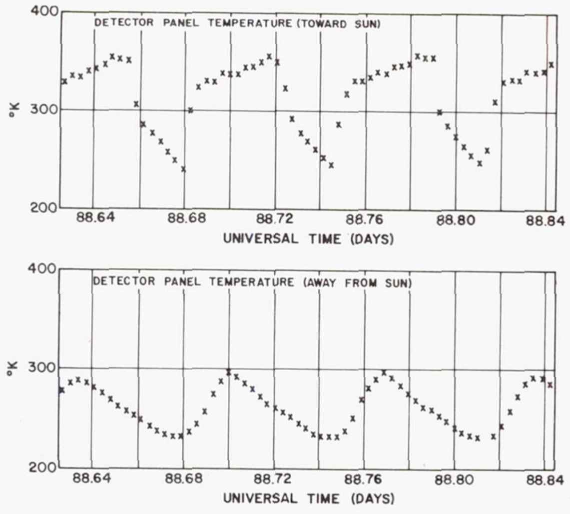

FIGURE 2. PEGASUS I DETECTOR PANEL TEMPERATURE VARIATION

satellites have thus far remained well within the design range.

The temperature of the service module adapter at the top of the S-IV stage has been 20° to 30°K warmer than expected throughout the lifetime of all three Pegasus satellites. Since this area, together with the S-IV stage, is used as a radiative heat sink by the Pegasus electronics, such an increase in temperature has a direct bearing on their temperatures. The cause of these warmer temperatures is apparently the result of a higher than expected ratio of solar absorptance (α_s) to infrared emittance (ϵ_t) of the exterior surface. The surface in this case was a zinc-oxide pigmented methyl silicone paint (designated S-13). The expected α_s/ϵ_t value for this paint was 0.22 and this was the value measured by personnel from the R-RP-T laboratory on the pad a few days before launch. However, detailed analysis of the telemetered thermal data indicates an orbital value of α_s/ϵ_t of about 0.5, an increase factor of two or more (Fig. 3). Part of this increase can be explained by the unexpected degradation by ultraviolet radiation of S-13 discussed earlier in this review by E. Miller and G. Arnett. The rest of the increase seems most likely to have been caused by contamination of the paint by plume impingement from the retrorockets during booster separation and subsequent solar ultraviolet degradation. It is well known that S-13 is stable to ultraviolet radiation only so long as it is exceptionally clean. Thus, all of the degradation that might have taken years, if ever, to occur took place apparently during the first few days or perhaps even hours in orbit. The gap in the data for the first 20 days (Fig. 3) was caused by difficulties in analysis resulting from complex altitude variations.

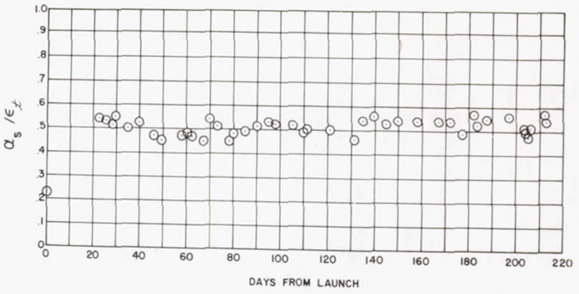

FIGURE 3. S-13 COATING DEGRADATION ON THE PEGASUS I SMA

ELECTRONIC CANISTER TEMPERATURES AND LOUVER OPERATION

The electronics of the Pegasus spacecraft are located mainly in a canister inside the payload adapter (service module adapter) at the bottom of the center section structure (Figs. 4 and 5). During flight the top and side of this canister are covered with superinsulation to prevent heat losses. A louver assembly attached to the bottom of the canister (Figs. 5 and 6) is designed to furnish automatic radiative coupling with the service module adapter and the S-IV stage which act as heat sinks. Each louver blade is driven by a bimetallic strip such that the louvers normally remain closed. However, a rise in canister temperature will cause the louvers to open allowing the excess heat to be lost by radiation. The main point of concern with the operation of the louvers was the requirement for long lifetime (18 months) reliability. By indirect methods utilizing telemetered temperature and spacecraft orientation data, the apparent average opening angle of the louver blades was determined for several times during the first eight months in orbit for Pegasus I (Fig. 7). The points shown in Figure 7 are representative of a great number of similarly generated data points. This analysis has shown that the louvers appear to be performing successfully. The higher than expected temperature of the service module adapter (SMA) and the S-IV stage is apparent by the fact that the louvers never appeared

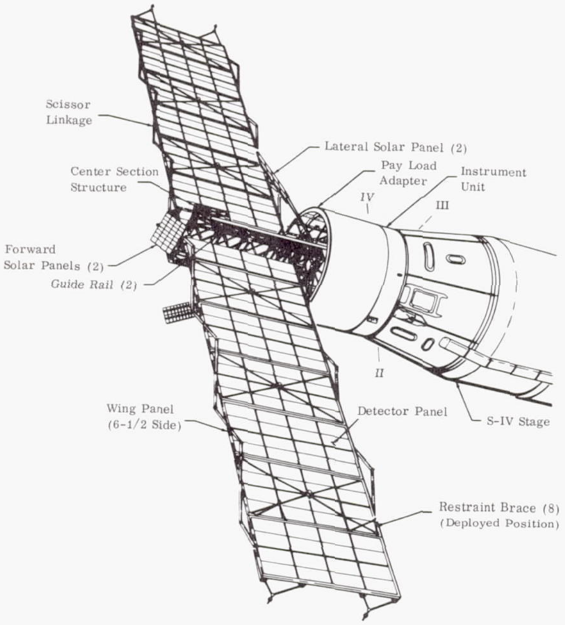

FIGURE 4. MICROMETEOROID MEASURING CAPSULE

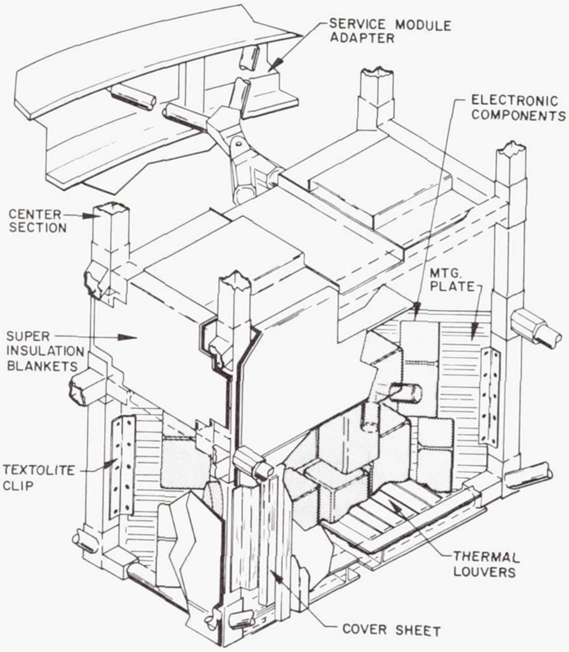

FIGURE 5. ELECTRONICS CANISTER

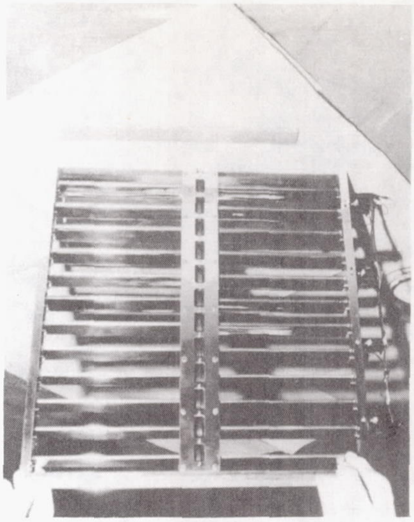

FIGURE 6. LOUVER ASSEMBLY

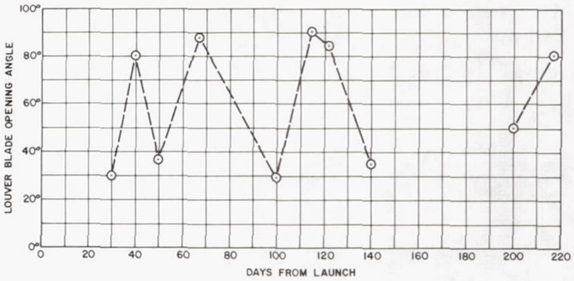

FIGURE 7. LOUVER ACTIVITY, PEGASUS I

to be fully closed even though the original design was such that they were to remain closed almost 90 percent of the time. Thus, without an active system such as the louvers, serious thermal problems could have resulted from these higher sink temperatures.

How well the louvers have compensated for external thermal variations is apparent by the behavior of a representative canister temperature such as an internal battery temperature (Fig. 8). During the first 290 days of Pegasus I's lifetime this temperature reached a maximum of 305° K and a minimum of 293° K. After this time there was approximately a 10° K rise in temperature which has been traced to a failure in an external zener-diode package.

ENVIRONMENTAL EFFECT SENSORS

Also flown on each of the Pegasus spacecraft was a small sensor package composed of four thermally

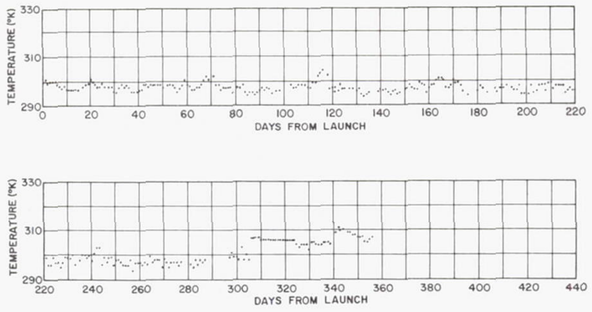

FIGURE 8. INTERNAL BATTERY TEMPERATURE, PEGASUS I

isolated discs (Figs. 9 and 10). The discs are mounted such that they have a two-pi steradian view of space and the temperature of each is stored and telemetered upon command. A different thermal control coating is applied to each disc, and by knowing their temperatures and the satellite's altitude the radiometric characteristics of these coatings as a function of time in space can be determined. Such a determination for the sensor on Pegasus I gave the results shown in Figure 11. The initial sharp rise in α_s/ϵ_t for both the S-13 and rutile paints is apparently the same increase recently measured in the lab and discussed earlier in this review. It should be pointed out that this sensor as well as the entire Pegasus spacecraft was covered by a dummy Apollo spacecraft during ascent, and thus was not exposed to the retrorocket plume discussed previously in connection with the degradation of the S-13 on the

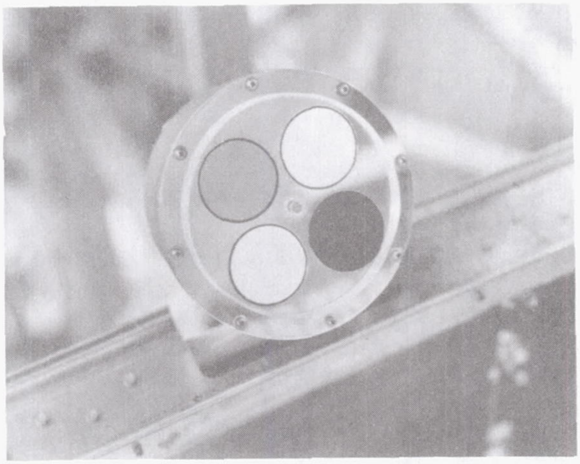

FIGURE 9. SENSOR PACKAGE WITH FOUR DISCS

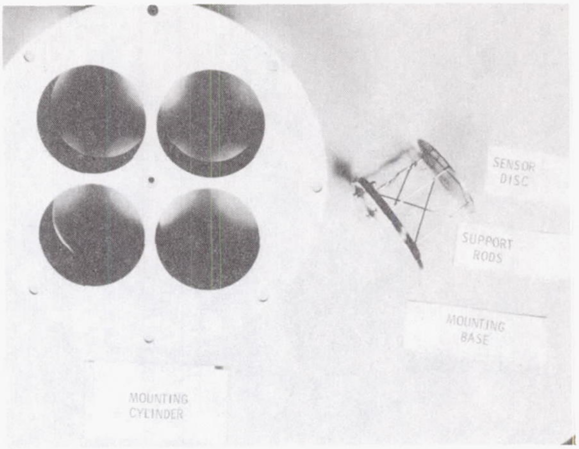

FIGURE 10. COMPONENTS OF SENSOR PACKAGE

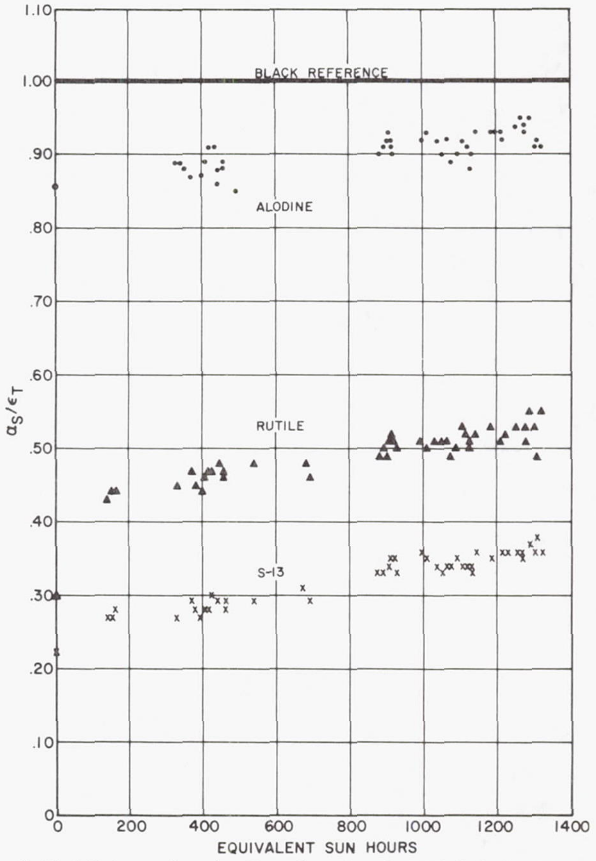

(Initial Values of α_s/ϵ_t Based on Pre Launch Lab Measurements)

FIGURE 11. PEGASUS I ENVIRONMENTAL EFFECT SENSOR DATA

S-IV stage. Still the amount of degradation shown by this protected "space-stable" S-13 paint on the environment effect sensor indicates the nature of the problem faced by the thermal engineer in the selection of thermal control coatings. In many applications a degradation in this amount is sufficient to cause a 30° to 40°K rise in temperature which could lead to a catastrophic failure.

Once the radiometric characteristics of the disc have been ascertained, it is possible to measure the earth albedo flux during the times the sensor faces the earth. Preliminary efforts have given the results shown in Figure 12, where the effective earth albedo is plotted as a function of position in orbit. The "effective earth albedo" is the same as the Bond* albedo assuming a diffuse earth with homogeneous reflectance characteristics. However, it should be noted that the measurements themselves indicate the inhomogeneous characteristic of the earth's surface. Thus, the determination of a "Bond albedo" is useful for comparison purposes only. These data are now being analyzed with the aid of Tiros and Essa photographs in an attempt to correlate cloud cover and terrain conditions with the measured results.

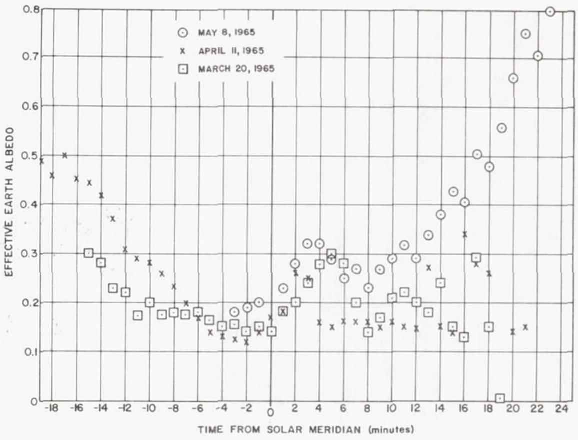

FIGURE 12. PEGASUS I ALBEDO MEASUREMENTS

CONCLUSION

In conclusion, it is noted that the analysis of Pegasus thermal data has, thus far, resulted in extremely worthwhile results. It is anticipated that these results will be further amplified as these studies continue. Such studies will include a comparison of results between Pegasus I, II, and III; a correlation of albedo measurements with cloud cover and theoretically predicted Rayleigh scattering; and the continuation of thermal coating degradation analysis.

---

* Bond albedo is the ratio of the total light energy reflected from a planet to the total light energy incident.

Page
Intentionally
Left Blank

RESEARCH IN INSTRUMENTATION FOR RADIOMETRY AND SPECTROMETRY

By

Harlan D. Burke

SUMMARY

Infrared measuring systems typical of those flown on the Saturn vehicles are discussed. These systems are used to detect fires in the vehicle and to determine spectral characteristics of the exhaust plume, heat flux to the heat shield from the hot gases in the exhaust, and heat flux to other vehicle structures from aerodynamic forces during ascent. The principle of operation and typical parameters of each type of instrument are discussed.

INTRODUCTION

Infrared measurements on the Saturn vehicles are concerned with determining the spectral characteristics of the plume and the convective, radiative, and total heat fluxes incident to the heat shield from the hot gases in the engine exhausts, and the heat flux to other vehicle structures as a result of the aerodynamic forces encountered during ascent. Extensive wind tunnel tests on scale models and captive test firings have permitted the thermal design of systems to theoretically approximate the heating rates obtained during flight. Actual flight data are used to correlate the effectiveness of the test programs leading to the thermal design of the vehicle parameters. The complexity of the problems of heat flux analysis has required the research and development of highly specialized radiometer and spectrometer instrumentation systems for flight measurements.

The infrared and heating rate measuring devices and systems used in the Saturn program have changed with technology and as confidence in the techniques was established. The instruments used by MSFC are the integrated and direct reading radiometers, color wheel radiometers, infrared spectrometers, and special systems such as those used in fire detectors. No one instrument will provide all the data required for complete thermal analysis of heating rates obtained during flight. This discussion will briefly describe the features of each system and illustrate design techniques.

INTEGRATING RADIOMETERS

These instruments are ideally suited for measurement of total heat flux over a period of time. Rapidly fluctuating heating rates are not recorded and time-of-flight data are obtained only through time-consuming analysis of the radiometer data and the environmental conditions. Many types of radiometers are used in space vehicle instrumentation programs. The slope calorimeter has been most frequently used by MSFC. Its principle of operation is that given any thermally isolated mass of known dimensions and thermal properties, it is possible to solve for the heating rate to which it has been exposed by knowing its temperature versus time history. Thermal isolation of the mass minimizes conduction losses to the mounting wall. While it is possible to reduce these losses, there are conduction losses inherent to each design. These losses can be determined accurately and individual calibration curves can be established.

The radiometer as shown in Figure 1 (a) measures the total convective and radiant energy incident to its surface. Radiant energy only is measured by the radiometer shown in Figure 1 (b). The convective component is prevented from reaching the radiometer sensing surface by a lens system. The lens material in this instrument can be selected to permit transmission in spectral ranges of particular interest. Sapphire and quartz have been the primary filter materials used by MSFC because the radiation to be measured is almost entirely within the 0.2- to 5-micron region.

Figure 1 (c) shows a typical equation used to obtain the heating rate data to the sensor. When the total energy absorbed by the radiometer is desired, the equation

$$\int_{t=t_o}^{t} q\,dt$$

would be applicable. Theoretical analysis of the flight data is accomplished by comparing the temperature as a function of time curves, shown in Figure 2 (a), with the heat flux as a function of rate of change of temperature with time curves, shown in

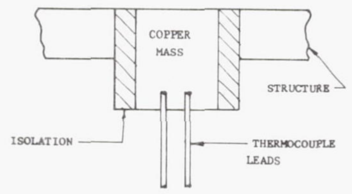

(a) TOTAL

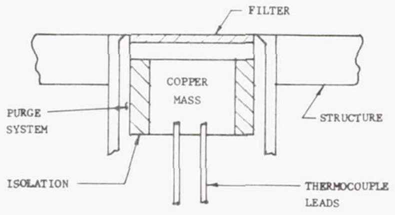

(b) RADIANT

(c) HEAT FLUX EQUATION

$$\dot{q} = \rho C_p L \frac{dT}{dt} + K(T - T_o) + \epsilon\sigma T^4$$

Where:

$\dot{q}$ = Absorbed Heat Flux
ρ = Mass Density of Slug
C_p = Specific Heat of Slug
L = Slug Thickness
T = Slug Temperature
T_o = Initial Slug Temperature
ϵ = Emissivity
t = Time
K = Loss Constant
σ = Stephan-Boltzmann Constant

FIGURE 1. TYPICAL SLOPE RADIOMETER

Figure 2 (b). Experimental analysis of the integrated flight data is accomplished by programming a heat flux into a simulated flight radiometer installation to exactly reproduce the flight data. This programmed heat flux is then observed with a standard heating rate radiometer. The theoretical and experimental analyses reduce the integrated flight data (shown in Figure 2 d as integrated flight data) as a function of temperature and time, to incident heat flux as a function of time as shown in Figure 2 (d).

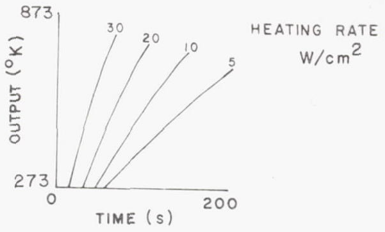

(a) EXPOSURE TIME VS SLUG TEMPERATURE

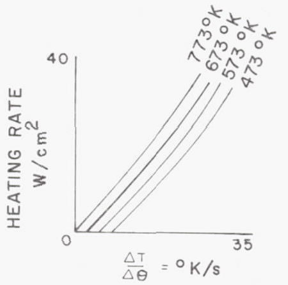

(b) CALIBRATION CURVE

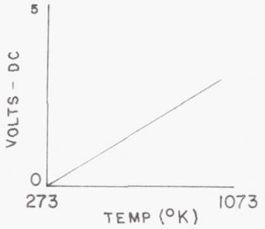

(c) AMPLIFIER CALIBRATION

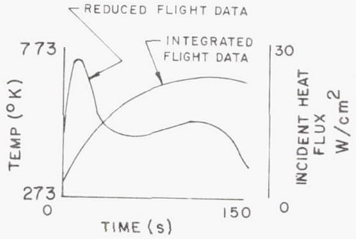

(d) RAW FLIGHT DATA VS REDUCED FLIGHT DATA

FIGURE 2. CALIBRATION AND DATA CURVES FOR SLOPE RADIOMETER

DIRECT READING RADIOMETER

The outputs of direct reading radiometers are directly proportional to the incident heating rates. Fast response and recovery times can be designed into the detector system to permit measurement of transient heating rates. These features minimize the time required for calibration and data reduction. The asymptotic or membrane calorimeter is the most advanced instrument for flight measurements. This type of heating rate sensor is different from the slope or integrated radiometer in that its output is proportional to the temperature gradient between the center of a thin constantan disc and its periphery. This temperature gradient is directly proportional to the heating rate. Figure 3 illustrates the basic design of the sensor and the equation that expresses the relationship between the heating rate and output signal. This dependence of $\dot{Q}$ on ΔT could indicate a nonlinearity if the thermal EMF curve of the temperature sensor is not linear. In practice, the conductivity K changes with temperature in the opposite direction by approximately the same ratio. Figure 4 shows typical calibration curves and flight data.

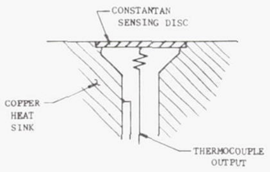

(a) TOTAL

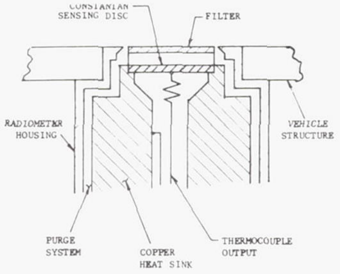

(b) RADIANT

(c) HEATING RATE EQUATION

$$\dot{Q} = 4.52 \frac{SK}{R^2} \Delta T$$

Where:

$\dot{Q}$ = Heating Rate in Watts/cm^2

S = Sensor Thickness

K = Sensor Thermal Conductivity

R = Radius of Active Sensor

ΔT = Temperature Differential

FIGURE 3. TYPICAL DIRECT OUTPUT RADIOMETER

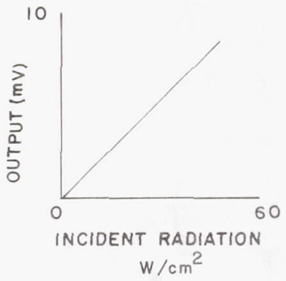

(a) CALIBRATION CURVE

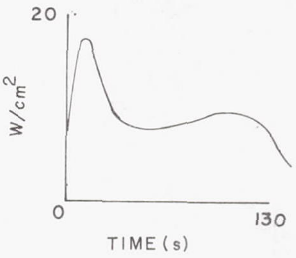

(b) FLIGHT DATA

FIGURE 4. CALIBRATION AND DATA CURVES FOR DIRECT OUTPUT RADIOMETER

COLOR WHEEL RADIOMETER

The color wheel radiometer was developed for MSFC by Minneapolis Honeywell under contract NAS8-5099. It is a rapid scan spectral radiometer operating in the infrared spectrum from 2 to 5 microns with ten separate spectral bands. The system is normally used to measure the spectral distribution of rocket plumes but can be modified to measure any selected bands for which filters are available. The radiometer has been flight qualified to the Saturn IB environmental requirements. The block diagram of the radiometer is shown in Figure 5. The design features (1) an 11.4-centimeter (4.5-inch)-diameter Dall-Kirkham optical system with a clear aperture of 77.4 square centimeters (12 square inches) and a field of view at 50 percent transmission of 3.2 milliradians in the Z axis and 4.6 milliradians in the Y axis, (2) a germanium window that allows the passage of infrared radiation, but seals the radiometer against the entrance of dust, (3) a rotating filter wheel turning at approximately three revolutions per second containing ten spectral filters, (4) a radiation chopper wheel that modulates the incoming radiation at a frequency of 1066 cycles per second, (5) a lead selenide detector and a cooling cryostat for maintaining the detector at the temperature of liquid nitrogen, (6) a tuned amplifier with a bandpass of 320 cycles per

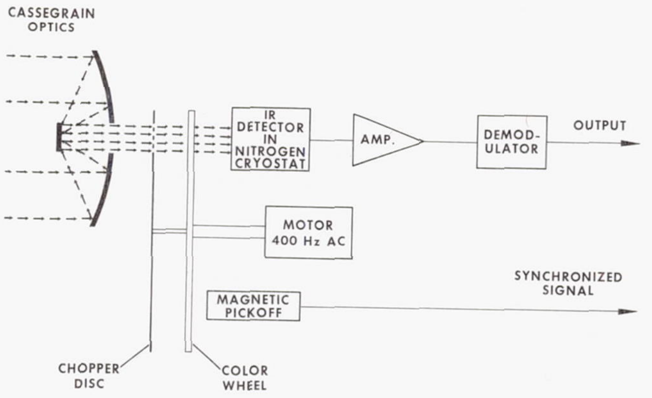

FIGURE 5. BLOCK DIAGRAM OF COLOR WHEEL RADIOMETER

second centered at 1066 cycles per second for amplifying the detector signal, (7) a half-wave rectifier and filter for converting the ac signal to dc signal, and (8) a power supply to provide both detector and amplifier bias voltages.

Figure 6 shows the spectral coverage of the filters used in the filter wheel as a function of percent transmission. These filters are mounted in the wheel and the radiometer as shown in Figure 7. The output of the radiometer for a 1000° K black body is shown in Figure 8. Figure 9 illustrates an actual output of a burning paper sheet and an infrared lamp. The instrument is calibrated with a series of black body cavities, and data reduction is accomplished by comparing the flight data with the calibration curves for each channel. The typical D* for the PbS detector is 2.5×10^{11} centimeters × (cycles per second)$^{\frac{1}{2}}$ per watt.

SCANNING GRATING SPECTROMETER

A two-channel scanning grating spectrometer was developed for MSFC and the Air Force Cambridge Research Laboratory (AFCRL) by Block Engineering Company under purchase order H-92160. The AFCRL and MSFC performed a joint measurement on the S-IB-203 vehicle to determine the signature characteristics of the S-IB engines and the spectral distribution

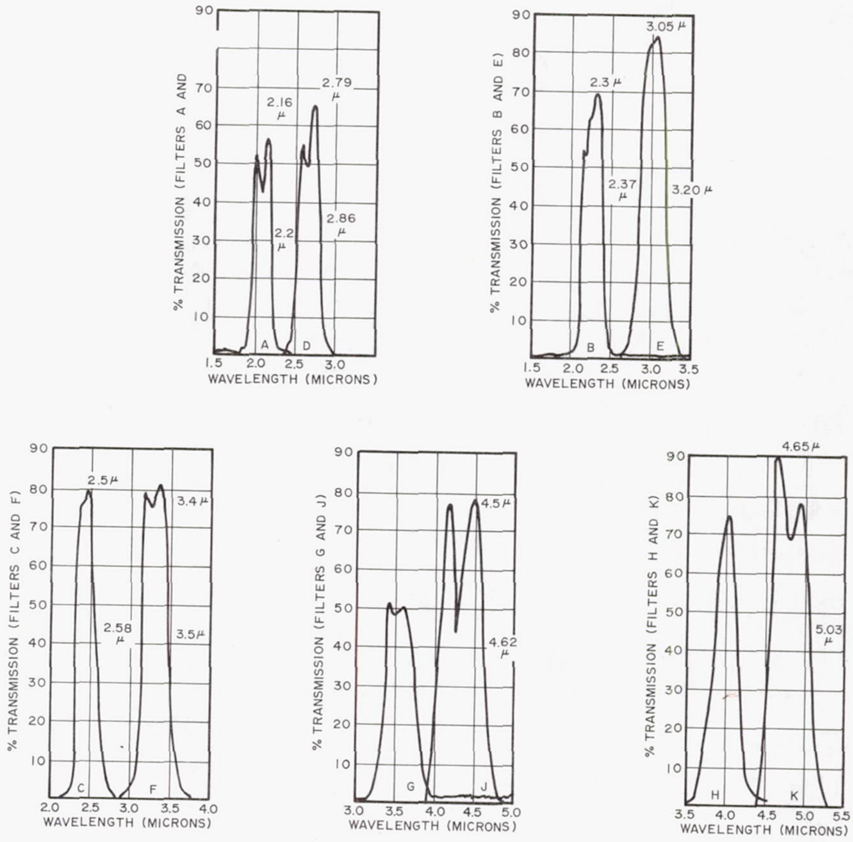

FIGURE 6. COLOR WHEEL SPECTRAL COVERAGE

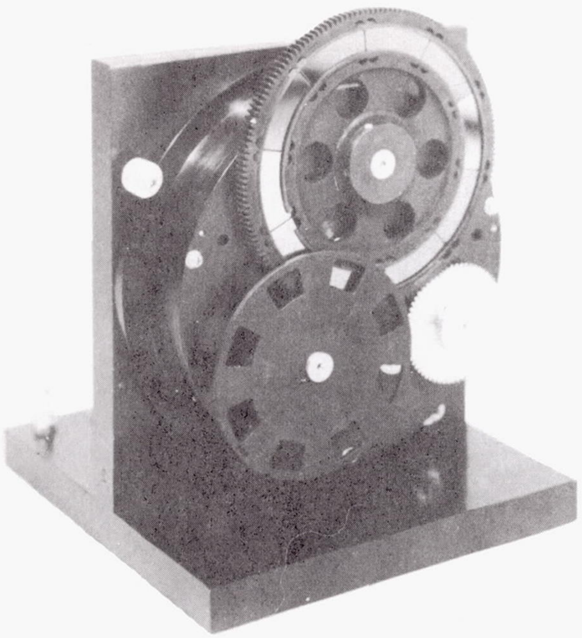

FIGURE 7. FILTER COLOR WHEEL AND RADIOMETER

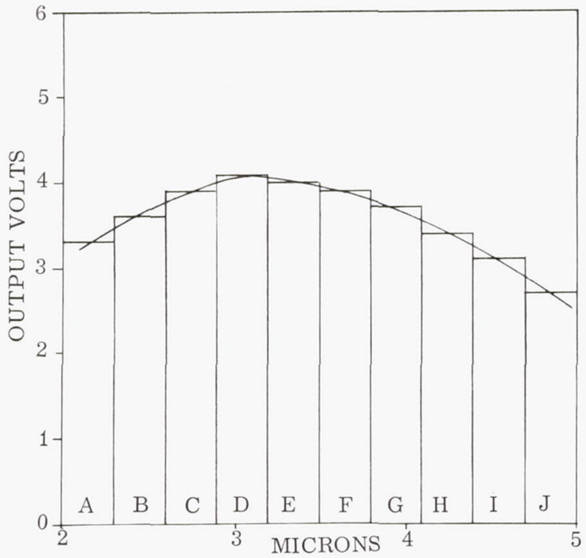

FIGURE 8. TYPICAL RADIOMETER CALIBRATION CURVE FOR 1000°K BLACK BODY

of the radiating components in the hot gases of the plume. One channel scanned the near infrared in the 1.5- to 2.3-micron spectral range. The other channel scanned the intermediate infrared in the 2.3- to 4.6-micron spectral range. The instrument was flight qualified to the Saturn IB heat shield environment.

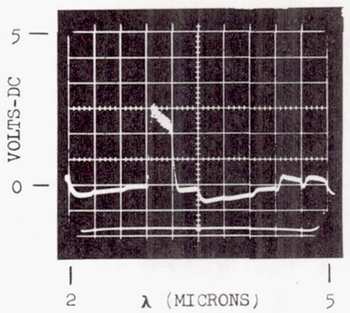

(a) BURNING PAPER

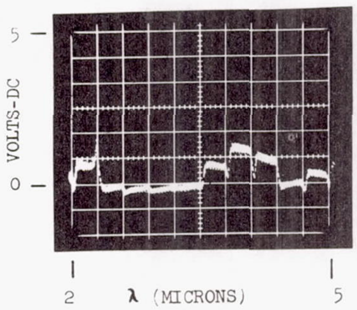

(b) INFRARED LAMP

FIGURE 9. COLOR WHEEL RADIOMETER OUTPUT FOR BURNING PAPER AND INFRARED LAMP

Figure 10 is a block diagram of the spectrometer. The near infrared and intermediate infrared are functionally similar. Incident radiation entering the system is chopped and passed through a curved entrance slit to a 45 degree mirror and onto a spherical collimating mirror. The radiation is reflected from the collimating mirror to the dispersing grating and

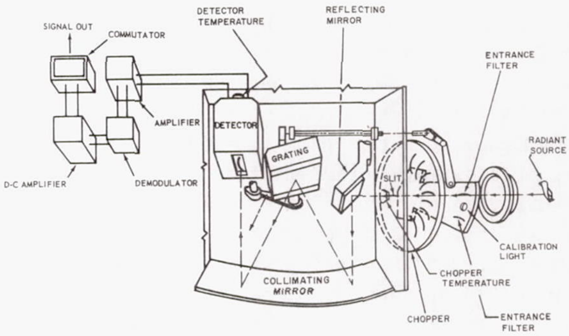

FIGURE 10. BLOCK DIAGRAM OF TWO-CHANNEL SCANNING SPECTROMETER

then back to the collimating mirror to be focused on the detector. The detector in each channel is geometrically shaped to act as an exit slit. The near IR channel uses a PbS detector and the intermediate IR channel uses a PbSe detector.

The output from each detector is preamplified and sent to a logarithmic amplifier designed to permit acceptance of inputs with a dynamic range of 5000:1. The summing circuits in the logarithmic amplifier are synchronized with the chopper by a reference light received by a solar cell through the chopper blades. Calibration lights for each channel are provided for continuous inflight reference. A typical output wave train for the system is shown in Figure 11.

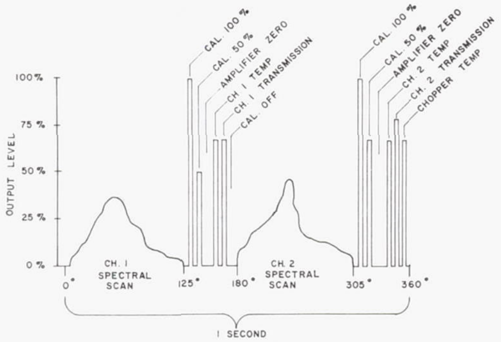

FIGURE 11. OUTPUT WAVE TRAIN FOR TWO-CHANNEL SCANNING GRATING SPECTROMETER

A summary of the system requirements is shown in Table I. The system is to scan in three angular positions of 5 degrees, 0 degrees, and -5 degrees around a reference center line. This is accomplished by mechanically stepping the spherical mirror. In each spatial position, the scanning grating is rocked through the angles necessary to scan the required 1.15- to 2.3, and 2.3- to 4.6-micron spectral ranges. The scanning rate can be adjusted, but is nominally set for one second per scan. The spectral range is scanned by the grating design and the rocking angle.

The intended application of this instrument does not require the detectors to be cooled. A nitrogen purge is provided to prevent contamination of the optical system. Figure 12 shows the instrument installed on the flight heat shield.

TABLE I. SYSTEM REQUIREMENTS FOR SCANNING GRATING SPECTROMETER

Spatial Scan	3 positions of 15 degrees (+5 degrees, 0 degrees, and -5 degrees)
Field of View	-2 degrees by 2 degrees
Spatial Scan Rate	One per second
Spectral Scans	1.1 to 2.2 microns and 2.3 to 4.6 microns
Resolution	0.1 micron
Wavelength Repeatability	+ 0.02 micron
Wavelength Accuracy	+ 0.04 micron
Dynamic Range	10^3 log
Spectral Scan Rate	Each wavelength once per second
Signal Output	0 to 5 Vdc with output impedance less than 5000 ohms
Nitrogen Purge	.0037 m/s (8 SCFM) STP, 5.2×10^6 N/m^2 (750 psi) required
Power	2 amperes ± 20%@ 28 ± 3 Vdc
Outline Dimensions	16.5 cm × 19.5 cm × 24.9 cm
Mass	11.4 kg maximum
D* PbS	1.47×10^{10} cm Hz$^{\frac{1}{2}}$/W
D* PbSe	1.8×10^7 cm Hz$^{\frac{1}{2}}$/W

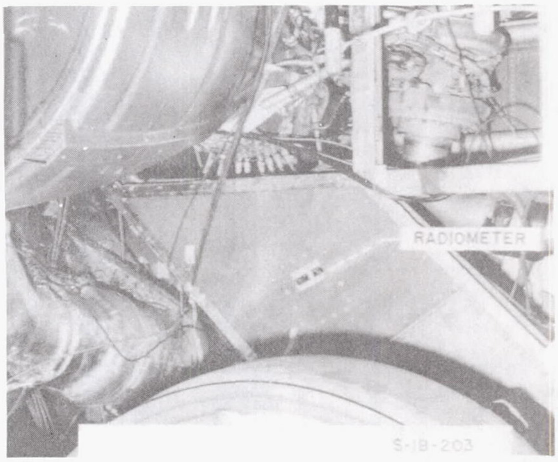

FIGURE 12. SCANNING GRATING SPECTROMETER INSTALLATION

SPECIAL SYSTEMS

A number of systems have been designed for functions that are based upon the spectral distribution of emitting sources. Marshall Space Flight Center and Rocketdyne, under NAS8-11656, have conducted a study to obtain data on the radiative characteristics of hydrogen fires and to apply these data to the design and development of a fire detection system for the upper stages of the Saturn vehicle. The system requirements were that it must discriminate against false signals from sunlight and from the rocket engine exhaust plume radiation, while subjected to the physical environments of a Saturn V vehicle.

This effort not only studied the spectral characteristics of the J-2 rocket engine exhaust radiation, but also included the following experimental investigations: (1) the effect of ambient pressure and oxygen enrichment on the likelihood of hydrogen fires and explosions, (2) possible ignition sources in the Saturn vehicle and evaluation of the hydrogen air flammability limits using such sources, (3) spectra of hydrogen air diffusion flames containing samples of materials found in Saturn vehicle compartments, (4) transmission of ultraviolet radiation through fog, smoke, and contaminants over distances typical of Saturn vehicle compartments, and (5) flicker frequency measurements of J-2 rocket engine exhaust radiation.

The hydrogen fire detection system in Figure 13 will respond only to time-varying radiation of appropriate wavelengths and of sufficient intensity to exceed threshold detectivity. The system will discriminate between hydrogen air fires and time-varying or steady-state sunlight.

The detection system consists of (1) the radiometer, in which time-varying ultraviolet and visible radiation is photoelectrically detected, and (2) the control unit in which the produced electronic signals are processed.

A proportional, time-varying electrical signal is generated by the radiometer when it views a source of radiation whose intensity changes with time and the emitted radiation is in the selected spectral region. A two-lens optical system, with an 8.5-degree field of view, directs radiation onto an ultraviolet-sensitive photodiode detector. Two optical filters are used to limit the detector's response to the 2600 to 3200 angstrom region characteristic of the OH molecule emission. The first filter is nickel sulfate hexahydrate and is positioned in front of the ultraviolet detector. The second filter is made of Corning glass, Type 7-54, and is positioned between the lenses. This second filter is also a partially reflecting mirror to reflect light onto a visible photodiode detector. Electrical signals from the detectors are amplified by preamplifiers contained in the radiometer. A cross-sectional drawing of the radiometer is shown in Figure 14.

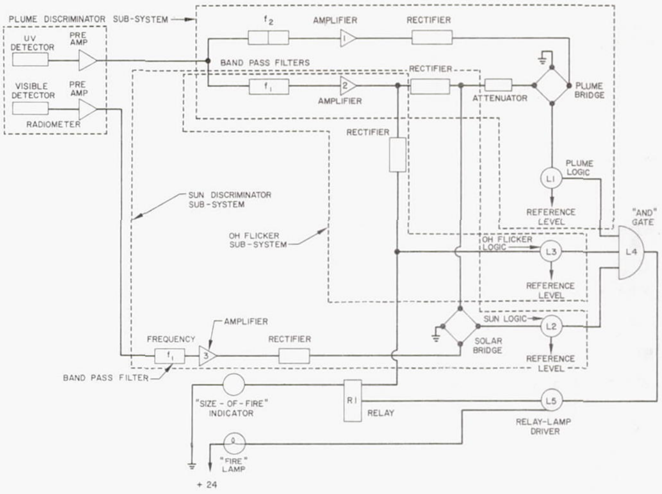

FIGURE 13. BLOCK DIAGRAM OF HYDROGEN FIRE DETECTION SYSTEM

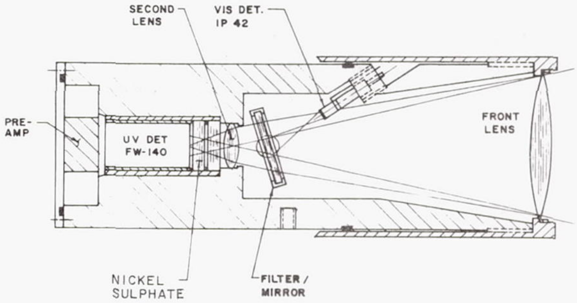

FIGURE 14. FIRE DETECTION RADIOMETER

The control unit processes the electrical signals from the radiometer. The signal processing system is composed of the sun discriminator, plume discriminator, and OH flicker.

Since the system responds only to time-varying radiation, the sun is a possible false signal source only when the sunlight is modulated by a vibrating vehicle member or by the atmosphere. Sunlight discrimination is accomplished by the two-color method which is basically the detection of the amplitude versus wavelength envelope by a two point wavelength approximation. The amplified signals from the visible detector and the ultraviolet detector are applied to separate legs of a bridge network. The other two legs of the bridge are resistances whose ratio is equal to the ratio of extraterrestrial solar radiation in the spectral bandpasses of the radiometer filters. The operation of the bridge is such that a false signal indication will be sent to the logic system for as long as the bridge sees the ratio of ultraviolet to visible radiation as that in sunlight at sea level or space vacuum. If the ultraviolet to visible radiation ratio is different, as when a hydrogen fire is observed, the output of the bridge to the logic system is a positive signal indication.

The electrical output of the two filters in the ultraviolet detector signal system are compared in a null bridge network similar to the solar bridge. When the signal source is the rocket exhaust plume, the output to the logic system indicates a false signal. If the radiation is other than the plume, the indication is positive.

In the OH flicker system, a positive indication is applied to the logic system when the time-varying ultraviolet radiation detected is of sufficient intensity. When the signal applied to the logic module is less than this value, the signal to the logic system indicates a false signal.

The hydrogen fire detection provides an indication only if the signals from the solar discriminator, plume discriminator, and OH flicker are positive. Figure 15 shows the first breadboard system. The output indication of a fire in this unit is only a meter and light, but capability exists for providing additional logic circuits for emergency detection systems.

CONCLUSION

The systems discussed have been typical of the instruments flown so far on Saturn vehicles. Proposed inflight MSFC experiments and future Apollo scientific payloads will require even more complex radiation detection and analyzing systems. Special applications of these techniques will include systems such as those required in the lunar and terrestrial mapping and surveying programs, guidance systems, horizon seekers, weather mapping, tracking of targets, surface absorptivity, emittance analysis, and surface reflectance measurements.

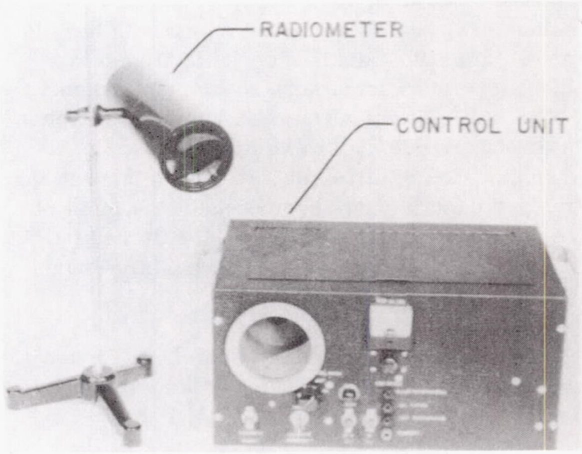

FIGURE 15. BREADBOARD HYDROGEN FIRE DETECTION SYSTEM

Page
Intentionally
Left Blank

ELECTRONICS RESEARCH AT MSFC

May 26, 1966

By

Dorrance L. Anderson
George A. Bailey
James F. Blanche
James L. Hayes
Robert L. Kurtz
T. C. Lawson
Owen Rowe

Page
Intentionally
Left Blank

Page
Intentionally
Left Blank

TABLE OF CONTENTS

OPTICAL ANGULAR DEVIATIONS OF 6328Å RADIATION CAUSED BY REFRACTIVE AND TURBULENT EFFECTS OF THE ATMOSPHERE

by Robert L. Kurtz and James L. Hayes

LIST OF TABLES

LIST OF ILLUSTRATIONS

TABLE OF CONTENTS

NONDESTRUCTIVE TESTING TECHNIQUES FOR MULTILAYER PRINTED WIRING BOARDS

by James F. Blanche

LIST OF TABLES

LIST OF ILLUSTRATIONS

TABLE OF CONTENTS

OPTICAL MEMORY WITH FERRIMAGNETIC STORAGE ELEMENT

by George A. Bailey

LIST OF ILLUSTRATIONS

TABLE OF CONTENTS

LARGE AREA METAL-OXIDE-SEMICONDUCTOR DEVICES

by Dorrance L. Anderson

TABLE OF CONTENTS (Concluded)

LIST OF ILLUSTRATIONS

TABLE OF CONTENTS

MICROELECTRONICS FOR THE GYRO STABILIZED PLATFORM

by Owen Rowe

LIST OF ILLUSTRATIONS

LIST OF ILLUSTRATIONS (Concluded)

TABLE OF CONTENTS

INTEGRATED CIRCUITS IN TELEMETRY SYSTEMS

by T. C. Lawson

LIST OF ILLUSTRATIONS

LIST OF ILLUSTRATIONS (Concluded)

OPTICAL ANGULAR DEVIATIONS OF 6328Å RADIATION CAUSED BY REFRACTIVE AND TURBULENT EFFECTS OF THE ATMOSPHERE

By

Robert L. Kurtz

and

James L. Hayes

SUMMARY

Atmospheric turbulence causes the image of a stationary optical source to fluctuate in intensity and position. Amplitude and frequency measurements of this random position fluctuation of the image have been made. Data were recorded over a period of approximately six months and over two different path lengths. The system and site are described. Statistical evaluation of a selected range of these data, 0 to 15 Hz, needed to determine the limitation of an experimental optical tracking system is presented and discussed.

LIST OF SYMBOLS

H = Horizontal

R = Receive

T = Transmit

V = Vertical

$\bar{\sigma}$ = Sample mean

$\sigma comp$ = Composite standard deviation of the combined sets

σ_i = Rms for 0 to 15 Hertz

μ = Mean of composite amplitude density

μ_i = Mean of individual amplitude density

n = Number of observations

s = Sample standard deviation

INTRODUCTION

Turbulence between the optical transmitting point and the receiving system causes the image of that point to blur and fluctuate, both in position and intensity. This random position fluctuation of the image causes a stationary source to appear to move over a finite area with varying amplitude and frequency. The accuracy of locating this source in space is limited by the varying amplitude of the laser beam fluctuations. Measurements of these fluctuations were taken over two path lengths: case I path length of 3,200 meters and case II path length of 165 meters. The elevation angle of both paths was approximately 4 degrees with the receiving telescope approximately 2 meters above the ground level. Both paths were over varying types of terrain and ground cover. The transmission path of case I lay in a northeasterly direction, and that of case II in a westerly direction.

The magnitudes of the apparent angular deviation of the source vary with the frequency of the atmospheric fluctuations. For case I, the highest magnitudes of fluctuations occur for the frequency range 0 to 50 Hz; for case II, 0 to 10 Hz. The magnitudes of the angular fluctuations of the laser beam are reduced by a factor of at least 2, typically after 50 Hz for case I and after 10 Hz for case II. For case I, the composite rms for the 0 to 150 Hz range is approximately twice the composite rms for the range 0 to 15 Hz. For case II, the composite rms of 0 to 150 Hz is approximately 1.5 times that of 0 to 15 Hz. For a factor of 20 difference in path length of the two cases, their mean amplitude of fluctuation varied by a factor of 1.7.

Measurements of the amplitude and frequency of these apparent angular deviations of the source were recorded over a period of approximately six months under varying atmospheric conditions. The purpose of this paper is to present the results of a statistical evaluation of a selected range of these data, 0 to 15 Hz, needed to determine the system limitation of the precision optical tracking system for advanced launch vehicles (POTSALV) being developed by this agency.

DESCRIPTION OF SIGNAL DETECTION SYSTEM AND METHOD OF SIGNAL PROCESSING

TRANSFER CURVE

An electromagnetic field around the neck of the star tracker tube of the signal detection equipment sweeps the sensitive area of the star tracker tube over the cathode in a cruciform pattern. No angular deviation (error signal) and consequently no output voltage is present when the focused laser beam is in the center of the scan pattern. As the laser beam target moves off center of the scan pattern because of increasing angular deviation, a larger output voltage is developed. This output voltage is proportional to the angle of deviation, as shown by the transfer curve in Figure 1, and is determined in the following manner. The transmitting and receiving systems were placed a known distance apart. The transmitter was displaced a small distance Δd left and right of and perpendicular to the direction of transmission. This movement produces an error signal and an output voltage which is proportional to an angle α with respect to the optical axis of the system.

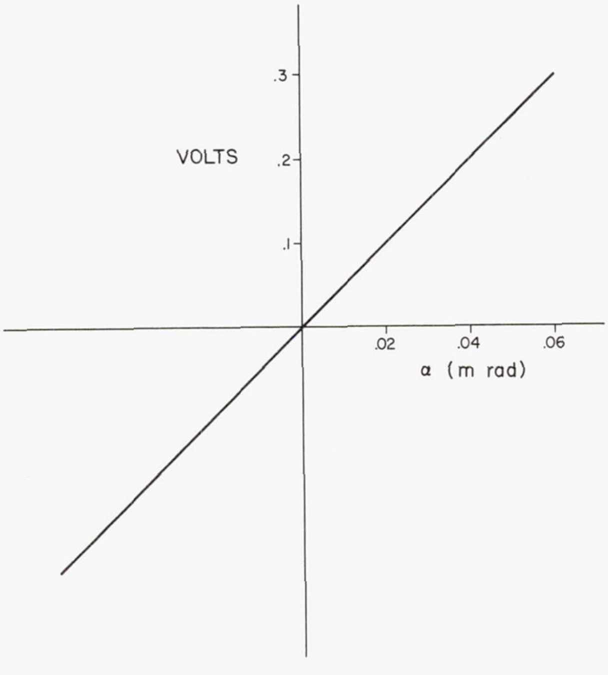

FIGURE 1. TRANSFER CURVE

SYSTEM OPERATION

A block diagram (Fig. 2) shows a remotely located laser source transmitting a 6328 angstrom beam. The laser beam with the angular deviations imposed on it is accepted by the Questar telescope. Energy from the laser beam is sharply focused onto the cathode of the star tracker tube that is electrostatically focused. An internal aperture defines a small area of sensitivity on the tube's cathode. This area is swept over a wider area of the cathode in a cruciform pattern by a quadrature magnetic field imposed by a coil around the neck of the tube. The magnitude and frequency of the apparent angular deviations of an optical source are detected as a result of the displacement of the source's image from the center of this cruciform pattern. The position of the focused spot off center of this cruciform scan pattern produces a signal which is then applied to a squaring amplifier and automatic gain control (AGC) network. On applying this output to the digital phase discriminator, the signal is phase compared to a square wave

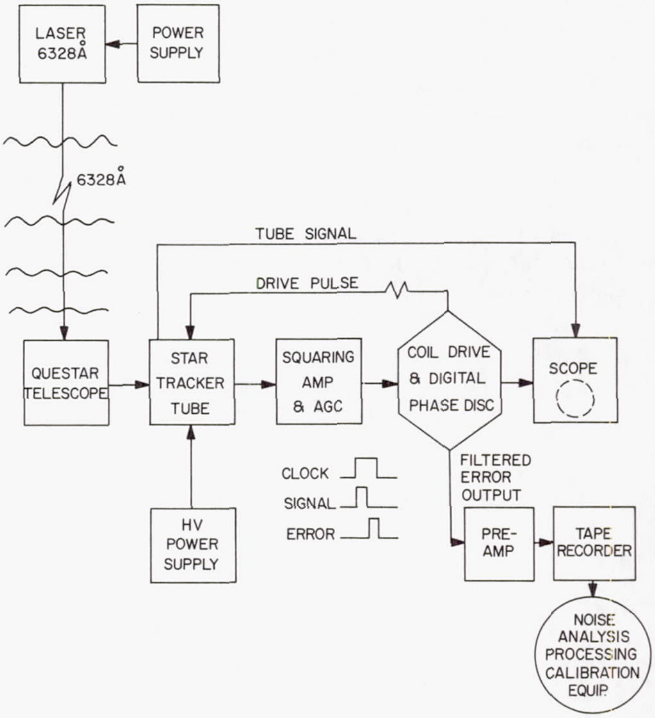

FIGURE 2. BLOCK DIAGRAM OF SIGNAL DETECTION SYSTEM

clock pulse and an output voltage is developed. The outputs are voltages in two channels proportional to an angle taken with respect to the system's optical axis. The two channels represent angular deflections in the horizontal and vertical axes. This fluctuating output voltage is low-pass filtered from 0 to 150 Hz and recorded on magnetic tape.

SIGNAL PROCESSING

The data, recorded on magnetic tape at 19 centimeters per second (7.5 inches per second) was processed by the Noise Analysis Section of Astrionics Laboratory.* A frequency spectrum analysis was performed, giving the amplitude (V_{rms}) versus frequency range of the fluctuating output voltage on the magnetic tape (2 to 150 Hz) with an effective analyzer filter bandwidth of approximately 1 Hz. The amplitude density curves are found through additional processing of the initial raw data, using the probability density analyzer.

PRESENTATION OF DATA

PROCEDURE

The apparent position fluctuation of the 6328 angstrom laser source was recorded as a fluctuating voltage on magnetic tape. Angular deviations were measured for two cases; case I has a transmission path length approximately 20 times longer than case II. The amplitude (V_{rms}) versus frequency plot of this information shows the magnitude of angular variations with frequencies of fluctuations. Amplitudes of frequencies of fluctuation up to 150 Hz were measured. The frequency region of primary interest was 0 to 15 Hz, since vehicle vibration frequencies greater than 15 Hz have negligible amplitude considering the tracking system's operation. Only this 0 to 15 Hz frequency region of primary interest is analyzed statistically. The analysis produced (1) the distribution of individual rms (σ_i) values about their mean, affording a probability prediction about the limit of rms value, and (2) the composite amplitude density distribution from individual amplitude density distributions, affording a probability prediction of limit of peak value.

DATA ANALYSIS

Case I. Data from the selected region of interest, 0 to 15 Hz, were analyzed. In this 15 Hz region, three successive 5 Hz intervals (W) were considered, producing three values of amplitude (A). These three amplitude values were used to calculate the individual rms (σ_i) of the corresponding amplitude densities.

Using

$$\sigma_i = \text{rms} = \left[\sum_i (A_i)^2 \ (W_i) \right]^{\frac{1}{2}} \qquad (1)$$

where

A_i = amplitude

W = interval width

σ_i = rms for 0 to 15 Hz

the individual σ_i's (rms) were calculated for all 55 runs and tabulated in order of increasing magnitude in Table I.

TABLE I. RMS VALUES FOR 0 TO 15 Hz FOR CASE I

Curve	0 to 15 Hz rms μrad	Curve	0 to 15 Hz rms μrad
BH6	8.4	BV14	15.5
BH11	9.1	BH2	15.6
BV5	9.2	DV2	15.7
BH7	10.1	DH1	15.8
BH9	10.3	DH6	16.1
BV3	11.9	AH2	16.2
BV9	12.0	EH2	16.4
BH4	12.5	CH2	16.8
AH4	12.6	EV1	16.8
BH12	12.7	AH1	17.0
CH3	13.0	BV8	17.1
AH5	13.2	CV3	17.1
BV13	13.2	DH2	17.1
BV11	13.3	EV3	17.3
BV4	13.4	EH1	17.7
BH5	13.4	EV2	18.4
BH8	13.6	DH7	19.0
BH3	13.8	CV1	19.4
AV1	14.2	DH4	19.6
BV2	14.4	CV4	19.9
BH10	14.4	DH5	20.9
BV6	14.8	CV2	21.0
DV1	14.8	DV3	21.0
BV10	15.0	CH1	21.9
BV1	15.2	DH3	21.9
BV7	15.2	DV4	21.9
BV12	15.5	CH4	22.0
		CV5	22.0

Explanation of curve notation: A, B, C, D, and E resulted from an attempt to group the curves by their shape. H and V are horizontal or vertical observations. For detailed information, refer to Reference 1.

---

* Acknowledgment is given to Messrs Heinrich Hahn, K. D. Rudolph, and Paul Martin for their work in processing this volume of data.

From the σ_i's (rms) values of Table I a frequency histogram was prepared (Fig. 3) to present the combined data from the horizontal and vertical measurements. Each measurement, horizontal and vertical, is considered an independent observation. The 55 observations constitute one sample. The sample mean and sample standard deviation of this distribution were computed as follows:

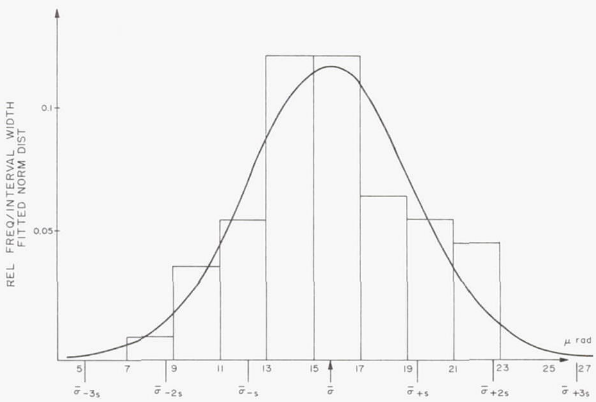

FIGURE 3. FITTED NORMAL DISTRIBUTIONS - CASE I

$$\text{Sample mean } \bar{\sigma} = \sum_{i=1}^{n} \frac{\sigma_i}{n} = 15.74 \text{ microradians} \qquad (2)$$

where

n = total number of samples

σ_i = rms values (Table I).

The sample standard deviation is given by:

$$s = \left[\frac{\sum_{i=1}^{n}(\sigma_i - \bar{\sigma})^2}{n-1}\right]^{\frac{1}{2}}$$

$$= \left[\frac{\sum_{i=1}^{n}\sigma_i^2 - \frac{\left(\sum_{i=1}^{n}\sigma_i\right)^2}{n}}{n-1}\right]^{\frac{1}{2}} \qquad (3)$$

and

$s = 3.51$ microradians.

Normal distribution is characterized by a skewness of 0 and a Kurtosis of 3 where

$$\text{Skewness} = \alpha = \frac{\mu_3}{s^3} = \frac{\frac{1}{n}\sum_{i=1}^{n}(\sigma_i - \bar{\sigma})^3}{s^3} \qquad (4)$$

$$\text{Kurtosis} = \alpha_4 = \frac{\mu_4}{s^4} = \frac{1}{s^4}\,\frac{1}{n}\sum_{i=1}^{n}(\sigma_i - \bar{\sigma})^4 \qquad (5)$$

where μ_3 and μ_4 are the 3d and 4th moment about the mean.

The distribution of combined horizontal and vertical data has

$\alpha_3 = 0.15$

and

$\alpha_4 = 3.12$

and therefore closely approximates normal or Gaussian distribution. A normal distribution curve was fitted to the observed data after a method by Hald [2] (Fig. 3).

Since the sample mean and sample standard deviation are not the true mean and true standard deviation, a confidence level must be placed on the rms limit. Using the tables of Bowker's and Lieberman's [3] and data of Figure 3, the probability is 0.97 that for any random sample at least 99 percent of the rms values in the sample are less than or equal to 26 microradians.

A probability prediction of the limit of peak value is afforded by the composite amplitude density distribution found in the following manner. The raw data, when processed by the probability density analyzer, produce the individual amplitude density plots for each individual observation.

From the fact that mean $\mu_i = 0$, treating each individual run as a set and using the standard deviations from Table I, a composite amplitude density distribution is found using a method by Kenny [4].

The equation for combining n sets into a single set is

$$N\,\sigma^2\text{comp} = \sum_{i=1}^{n} k_i\,\sigma_i^2 + \sum_{i=1}^{n} k_i\,d_i^2 \qquad (6)$$

where

$$N = \sum_{i=1}^{n} k_i$$

$$d_i = \mu_i - \mu$$

and

μ_i = mean of individual amplitude density

μ = mean of composite amplitude density

For application here

$d_i = 0$ since $\mu_i = \mu = 0$,

and $k_i = k = 1$ since we treat each run as a set of equal weight, i.e., each run represents an equal amount of sampling.

$$N = \sum_{i=1}^{n} k_i = nk = n = \text{number of individual sets or runs.}$$

Equation (6) becomes

$$\sigma\,\text{comp} = \left[\frac{1}{n} \sum_{i=1}^{n} \sigma_i^{\,2}\right]^{\frac{1}{2}} \qquad (7)$$

where σ_i is found from Table I and σ comp is the composite standard deviation or the combined sets.

Using eq. (7) and summing over the entire range of n sets yields the composite standard deviation

σcomp = 16.1 microradians.

This composite sigma provides the composite amplitude density distribution (Fig. 4). From this we can state that for any random sample at least 99 percent of the total time the peak amplitude of the angular deviation will be less than or equal to 48.3 microradians. In other words, for any random instant, chances are 1 in 100 for the occurrence of a peak amplitude greater than 48.3 microradians.

Case II. Raw data processed in the same manner as case I produces amplitude (V rms) versus frequency of fluctuation curves, normalized to a 1 Hz bandwidth. The measured horizontal and vertical deviations were considered independent observations and analyzed collectively in the selected region of 0 to 15 Hz.

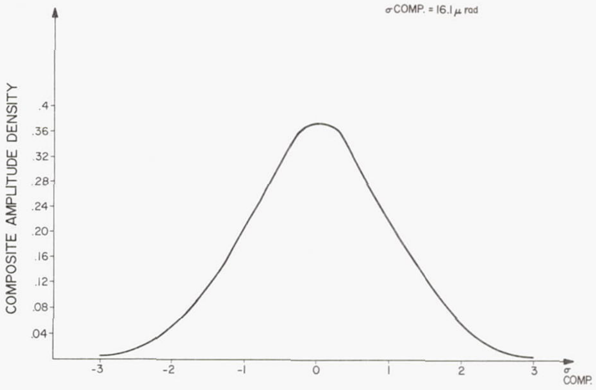

FIGURE 4. COMPOSITE AMPLITUDE DENSITY - CASE I

The individual σ (rms) for 0 to 15 Hz for each of the 52 runs is tabulated in order of increasing magnitude (Table II). From the σ (rms) values of Table II a frequency histogram was prepared showing the distribution of combined horizontal and vertical measurements (Fig. 5). The 52 observations constitute one sample. The sample mean and sample standard deviation of this distribution were calculated using eq. (2, 3).

TABLE II. RMS VALUES FOR 0 TO 15 Hz FOR CASE II

Curve	0 to 15 Hz rms μrad	Curve	0 to 15 Hz rms μrad
V5	5.2	V26	8.8
H16	5.4	V18	8.9
H18	5.5	H10	9.4
H8	5.9	H21	9.5
H22	6.0	V21	9.8
H5	6.1	H25	10.0
H24	6.1	H1	10.1
V15	6.4	H3	10.1
H17	6.4	V25	10.2
H20	6.4	H23	10.4
V24	6.4	V10	10.8
H9	6.5	V13	10.8
V16	6.5	V14	10.8
V20	6.6	V3	11.0
V22	7.2	H7	11.2
H26	7.5	V19	11.5
V9	7.7	V1	11.8
H15	7.9	V4	11.8
H14	8.1	H13	12.0
V6	8.2	V17	12.0
H6	8.3	V8	12.6
H19	8.3	H11	13.2
V23	8.3	V12	13.6
H2	8.4	H12	14.0
V2	8.4	V7	14.2
H4	8.4	V11	14.6

Explanation of curve notation: A, B, C, D, and E resulted from an attempt to group the curves by their shape. H and V are horizontal or vertical observations. For detailed information, refer to Reference 1.

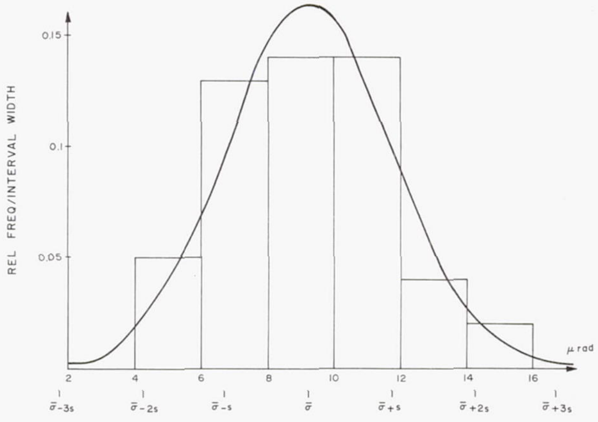

FIGURE 5. FITTED NORMAL DISTRIBUTIONS - CASE II

Sample mean $= \sigma = \sum_{i=1}^{n} \frac{\sigma_i}{n} = 9.19$ microradians.

Sample standard deviation $= s = \left[\frac{\sum_{i=1}^{n} \sigma_i^2 - \frac{\left(\sum_{i=1}^{n} \sigma_i\right)^2}{n}}{n-1} \right]^{\frac{1}{2}}$

= 2.50 microradians.

Skewness and Kurtosis for this distribution were respectively

$\alpha_3 = .35$

$\alpha_4 = 2.01.$

Therefore, the distribution of case II is not as Gaussian as that for case I. The atmospheric process controlling optical angular deviations is known to be Gaussian. The departure of case II distribution from Gaussian is felt to be caused by the operation of heavy construction equipment in proximity to the experimental site. Evidence of this was exhibited in the data by large-amplitude low-frequency spikes, which were not present in case I data. A normal distribution curve was fitted to the observed data after a method by Hald [1] (Fig. 5).

From the data of Figure 5 and again using the tables of Bowker's and Lieberman's [2], the probability is 0.97 that for any random sample at least 99 percent of the rms values in the sample are less than or equal to 17 microradians.

A probability prediction of the limit of peak value is afforded by the composite amplitude density distribution of case II, found in the following manner. As in case I, the processed data produces the individual amplitude densities.

The processing method shows the mean $\mu_i = 0$ for individual amplitude density distribution. Using the standard deviation values of Table II and eq. (7) the composite standard deviation of the combined sets is

$$\sigma \text{ comp} = \left[\frac{1}{n} \sum_{i=1}^{n} \sigma_i^2 \right]^{\frac{1}{2}} = 9.52 \text{ microradians.}$$

This composite sigma provides the composite amplitude density plot (Fig. 6). For any random sample 99 percent of the total time the peak amplitude of the angular deviation will be less than or equal to 28.5 microradians. Thus at any random instant, chances are 1 in 100 for the occurrence of a peak amplitude greater than 28 microradians.

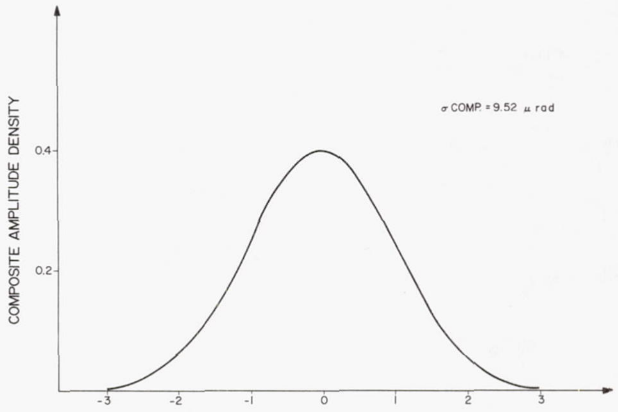

FIGURE 6. COMPOSITE AMPLITUDE DENSITY - CASE II

CONCLUSIONS

Data on atmospheric angular deviations were recorded for approximately six months and over two different path lengths. Data from each case were analyzed for the selected frequency range 0 to 15 Hz. Basic results* of the two path length measurements are tabulated as follows:

	Case I	Case II
Path length	3,200 m	165 m
Rms mean 0 to 15 Hz	15.74 μrad	9.19 μrad
Limiting rms 0 to 15 Hz	26 μrad	17 μrad
Limiting peak 0 to 15 Hz	48.3 μrad	28.6 μrad
$\frac{\text{rms 0 to 150 Hz}}{\text{rms 0 to 15 Hz}}$	2	1.5

---

* For detailed information on the method of signal processing and the volume of measured data, the reader is referred to Reference 1.

REFERENCES

1. Kurtz, Robert L.; and Hayes, James L.: Optical Angular Deviations of 6328A Radiation Caused by Refractive and Turbulent Effects of the Atmosphere. NASA TN D-3439, May 1966.

2. Hald, A.: Statistical Theory with Engineering Applications. John Wiley and Sons, Inc., New York, 1960.

3. Bowker, Albert H.; and Lieberman, Gerald J.: Engineering Statistics. Prentice-Hall, Inc., New Jersey, 1961.

4. Kinney, John F.: Mathematics of Statistics. D. Van Nostrand Co. Inc., 1948.

Page
Intentionally
Left Blank

NONDESTRUCTIVE TESTING TECHNIQUES FOR MULTILAYER PRINTED WIRING BOARDS

By

James F. Blanche

SUMMARY

A number of nondestructive testing techniques were examined as potential inspection methods for multilayer printed wiring boards. The techniques of axial transverse laminography and mutual coupling appeared most promising, and their capabilities were theoretically and experimentally verified. Axial transverse laminography is a radiographic technique that allows inspection of a thin section of a thick sample without physically sectioning the sample. It allows inspection of a conductor plane that is separated vertically from other conductor planes by as little as 0.10 mm (0.004 in.) and will detect flaws smaller than 0.02 mm (0.0007 in.). Laminography is rapid and readily lends itself to mass inspection of multilayer boards. Mutual coupling is an eddy current nondestructive testing technique that will detect a defect smaller than 0.003 mm (0.0001 in.) in the through-connection. Mutual coupling has more limitations for mass inspection than laminography because it requires probing each hole to be inspected. Application of the mutual coupling technique is envisioned as an adjunct to laminography in inspecting multilayer boards.

INTRODUCTION

One of the basic needs in the electronics field is for a high density interconnection technique that is compact, is reliable, and will eliminate the possibility of human error in wiring. Point-to-point wiring of electronic assemblies introduces the possibility for human error with every wire connected and the assembly often becomes a maze of wires. Conventional single and double sided printed circuit cards will not allow compact interconnection of microelectronic circuits. One obvious solution to this problem of high density interconnections is the multilayer printed circuit board. It allows very high interconnection density and the interconnections are identical in all assemblies using any particular circuit, so much of the possibility of human error is eliminated. However, the reliability of this system is questionable. Multilayer printed circuit boards are generally fabricated in such a way that the internal joints formed cannot be inspected. In the most widely used multilayer system a number of copper clad sheets bonded to an insulating material are etched with the appropriate circuit pattern. The layers are laminated together and holes are drilled through the laminated assembly at the points where interlayer connections are to be made, thus exposing the edge of the copper conductors at the appropriate level. The layers are then electrically connected by plating copper onto the wall of the hole or by fusing an eyelet, tubelet, or post into the hole. Optimum interconnection is achieved when 100 percent of the surface of the hole is covered with the conducting material to a prescribed minimum thickness; and when the cylinder, thus formed, is interconnected with 100 percent of the intersecting area of the printed conductor at each layer. The problem of reliability arises in the inspection of the joints formed at the interface of the exposed edge of the printed conductors and the plated wall.

In the past, inspection has been made in several ways. One method has been to pass a high current through the joints on the theory that any poor joints will be burned out. The problem is that this stress testing may create new marginal joints. Another technique has been to check continuity of the circuitry. This method will detect opens and shorts but will tell little about the quality of the joints. Some manufacturers X-ray their multilayer circuit boards to determine how closely the layers are aligned with one another. However, an internal layer tends to be masked by the layers above it, particularly on boards with dense circuitry.

A program was initiated with the Illinois Institute of Technology Research Institute (IITRI) under contract NAS8-11288 to develop a technique to nondestructively inspect multilayer printed circuit boards. If possible, the technique was to be rapid and accurate and lend itself to mass testing. A number of techniques were examined for relative promise in fulfilling program requirements. Some of the techniques were as follows.

Techniques Involving Heat

1. Thermographic powder is applied to the surface of the board. Under ultraviolet light the

fluoresence of this powder decreases with increasing temperature and will therefore detect hot spots in the board.

2. Detection of infrared or electromagnetic radiation in the millimeter range would also detect hot spots in the board.

These techniques lose both sensitivity and resolution as the number of layers increases.

Eddy Current Techniques

Passing an ac current through a coil placed in a plated-through or eyelet hole will cause eddy current to flow in the metal on the sides of the hole. The fields of these eddy currents will in turn affect the electrical properties of the coil. By varying the frequency of the ac current and detecting the changes in the coil caused by the behavior of the eddy currents, it is possible to determine the characteristics of the joints. One of the detection systems used with the eddy current techniques was selected for more detailed study.

Intermodulation Technique

Currents of two different frequencies are passed through the printed wiring. Currents at intermodulation frequencies are then produced by any electrical nonlinearity. These intermodulation currents can easily be filtered out to detect even small nonlinearities. Attempts to detect a defect using an intermodulation technique were successful but difficulties were encountered in reproducing test results and in pinpointing the defective connection.

E-Field Sensors

Faults in printed wiring boards and plated-through holes may be found by the irregularities they cause in the equipotential surfaces of the currents flowing through the wiring. Several probing techniques to detect the irregularities were examined. These techniques are theoretically workable but there are a number of practical difficulties that would limit the usefulness of these methods.

Radiography

Neutron radiography was investigated but resolution and contrast were of insufficient quality. Autoradiography might be used if the hole plating material could be doped but the film would have to be inserted into the hole to be inspected. Electron microscopy is primarily limited to descriptions of surface characteristics. X-ray basically is limited by the masking effect of circuit layers above the layer being inspected. The most important result of these radiographic investigations was the discovery of a technique known as axial transverse laminography which was chosen for detailed examination since it appeared to meet most of our nondestructive test requirements.

AXIAL TRANSVERSE LAMINOGRAPHY

Axial transverse laminography is a radiographic technique which allows a view of a thin section of a thick sample without physically sectioning the sample.* The technique depends on the smearing of all unwanted images over a large area while the image of interest remains sharp throughout the exposure. This result is achieved by synchronously rotating the sample and the film during exposure. The system is shown schematically in Figure 1. It consists of a point X-ray source, a rotating test table which holds the sample to be inspected, and a rotating film table. The plane that will be inspected is geometrically defined by the system. This plane is located at the intersection of the main axis and rotary axis one and will be parallel to the film plane.

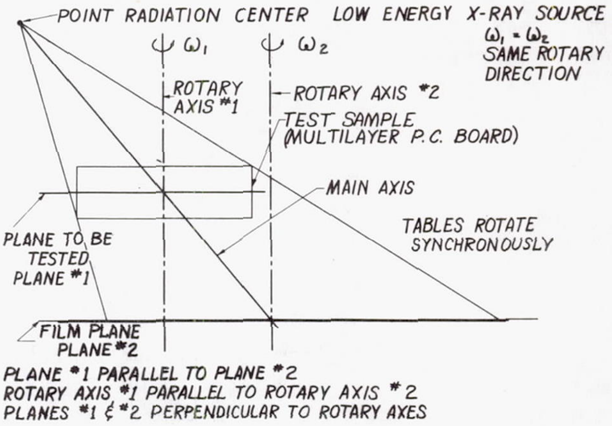

FIGURE 1. AXIAL TRANSVERSE LAMINOGRAPHY

The laboratory setup is shown in Figure 2. The low energy X-ray tube (25 keV silver K X-ray) is shown in the upper right corner. The source diameter is approximately 0.03810 mm (0.0015 in.). The grid pattern shown on the film table is for vacuum hold-down of the film. The two tables are rim driven by a single motor through rubber drive rings. Changing the compression of the rubber ring causes a variation in the driving ratio allowing precise synchronism to be achieved. The operation of the

---

*This technique was suggested and is being perfected by Dr. Robert Moler of IITRI. It was adapted from the systems of tomography and solidography which are used in the medical field.

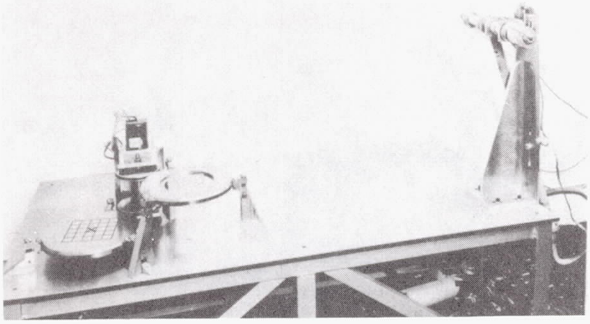

FIGURE 2. PLATE I EXPERIMENTAL LAMINOGRAPH

system is described in Figure 3. Consider line C-B to be a through-connection in a multilayer sample at the initial point of exposure to X-ray. C-B will project $\bar{C}$ - $\bar{B}$ onto the film. Now consider the same line C-B after it has rotated 180 degrees about rotary axis 1. The line is now defined as C' - B'. While C-B was rotating one half revolution the initial image $\bar{C}$-$\bar{B}$ was also rotating one half revolution about rotary axis 2 to position $\bar{C}'$ - $\bar{B}'$. C' - B' now projects a new image C'' - B'' onto the film. It will be noted that the only point where the initial ($\bar{C}'$ - $\bar{B}'$) and the new (C'' - B'') image coincide or reinforce is at point C where the sample through-connection touches the geometric plane of inspection. This example considers only two positions of the line C-B. It must be recognized that C - B is in reality projecting an image onto the film continuously throughout at least one complete revolution of the sample and film tables. Thus, it will be seen that the projected image of any point in the sample plane A-A' will reinforce itself continuously as long as the sample and film tables are rotating synchronously, while any point outside this plane will smear out or average over a larger area. For any given vertical displacement of an object of fixed size from the plane of inspection in the sample, the area over which the object will smear is determined by the angle which the main axis makes with the horizontal plane. The angle used in the laboratory model was 20 degrees; however, a geometric analysis was performed to determine the layering sensitivity for various angles and various vertical displacements from the plane of inspection in the sample. The results of this analysis are shown in Figure 4. The curves assume a 76.2 cm (30 in.) horizontal displacement of the center of rotation of the sample from the X-ray source. Y is the vertical displacement above or below the plane of inspection of a spot 0.36 mm (0.014 in.) in diameter. The curve shows the ratio of the common area of projection of this spot to the projection of the same spot in the sample plane. It will be noted that for a vertical displacement of 0.10 mm (0.004 in.) and an angle of 20 degrees only 5 percent of the projected area of the spot is continuously reinforced or not smeared out.

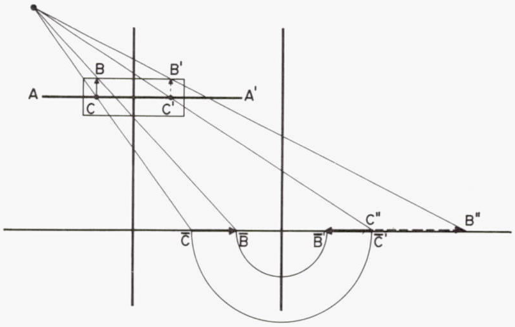

FIGURE 3. OPERATION OF THE SYSTEM

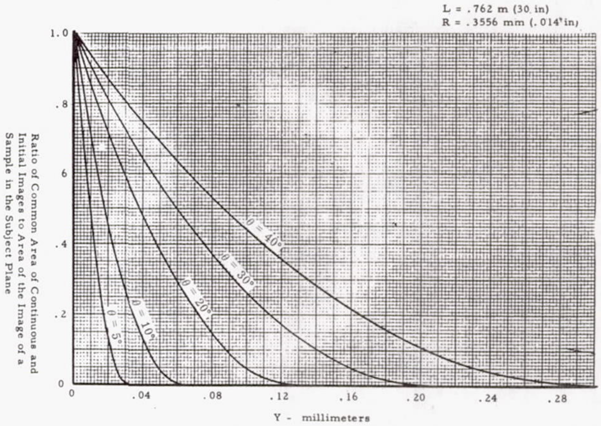

FIGURE 4. EFFECT OF ANGULAR VARIATION OF MAIN AXIS

One of the sample multilayer boards used in this program is shown in Figure 5. It is a 7 layer board with four circuit patterns. Each pattern is a hole matrix with defects built into the circuit. The patterns range from widely spaced holes to dense spacing. The most dense matrix has 100 holes or 700 joints per 6.54 cm^2 (1 $in.^2$). The optimum interconnection has been defined as that where the plated cylinder makes contact with 360 degrees of the exposed conductor surface to which it is joined. Some geometric deviations were introduced into the board such as intentionally misregistering the land areas for one

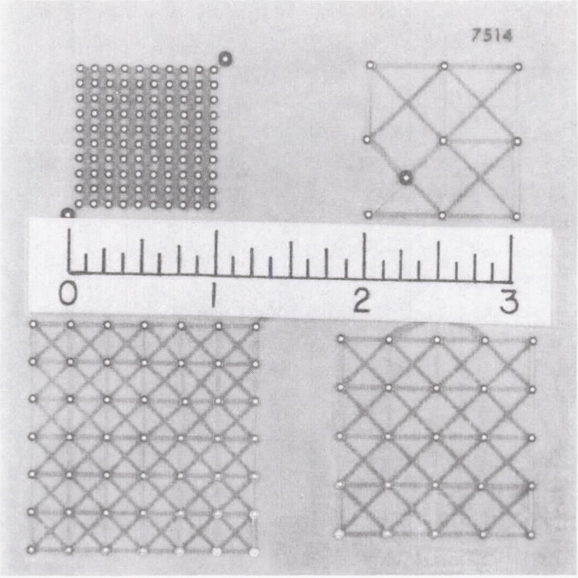

FIGURE 5. MULTILAYER TEST SAMPLE

hole in each matrix and creating open circuits by hairline fractures. The through-connections are made by plating the holes with approximately 0.004 cm (0.0015 in.) of copper. Figures 6 and 7 are laminographs of layers 3 and 4, respectively. The

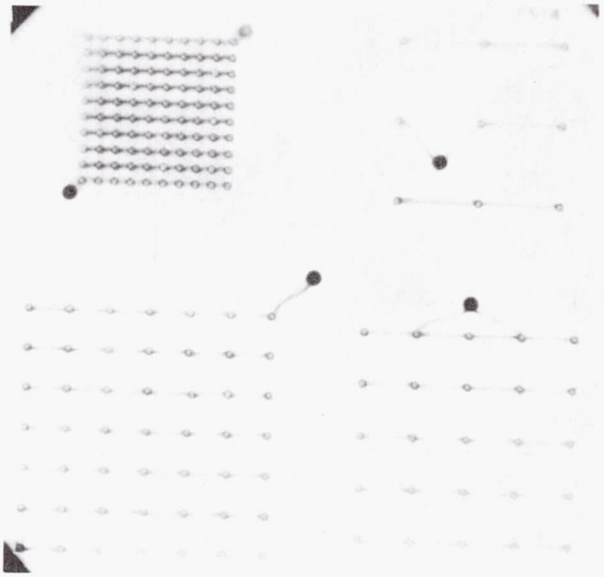

FIGURE 6. LAYER 3 OF MULTILAYER TEST SAMPLE

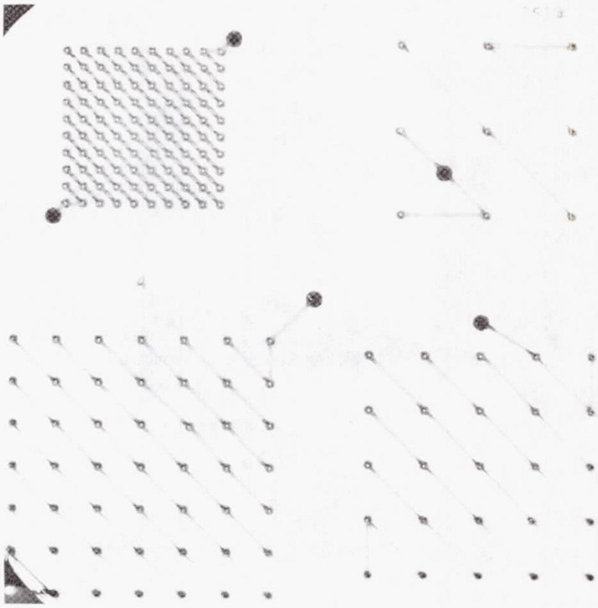

FIGURE 7. LAYER 4 OF MULTILAYER TEST SAMPLE

The two layers are separated by 0.01 cm (0.004 in.). The cuts on the diagonal line in the upper right hand pattern of layer 4 range from 37 to 88 microns wide. These laminographs have proven that the concept of axial transverse laminography is a sound one. It can separate layers at least as close together as 0.01 cm (0.004 in.) and can easily detect flaws as small as 0.02 mm (0.0007 in.).

A practical limitation is presented by the use of film. Having to take a picture of each layer and then develop and examine the film is a time consuming process. If the internal layers of the sample are not plane, several pictures of each layer may be required for complete inspection. To alleviate this problem a different approach is being taken in the laminograph now being developed by IITRI (contract NAS8-20640). Figure 8 shows the schematic. The film plate has been replaced with a fluorescent screen. The visual image from the screen is focused through a lens onto a de-rotation prism rotating at one-half the screen speed and in the opposite direction. The stationary image from the prism is projected into a closed circuit television system. The fluorescent screen will have the capability for vertical movement to change the plane of inspection in the sample. This design allows the operator to be at a remote station thus permitting safe use of higher energy, higher intensity X-ray for better resolution. The conversion to an immediate visual image of the sample produces a continuous scanning device. The operator can scan through the

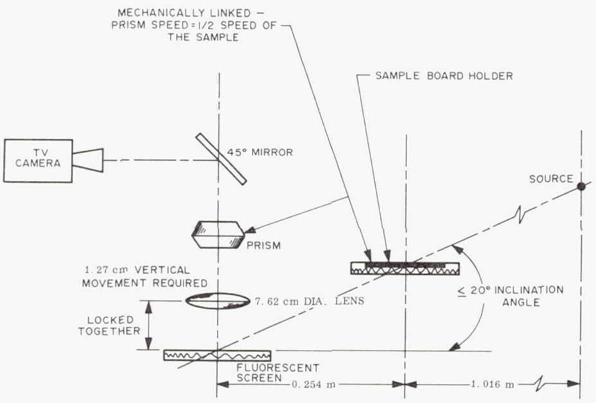

FIGURE 8. LAMINOGRAPH SCHEMATIC

complete board. A zoom attachment on the camera allows a questionable area of the sample to be magnified for more detailed inspection. Photographs of the image may be made at any time for a permanent record.

MUTUAL COUPLING

Although laminography will provide the capability to rapidly inspect multilayer printed circuit boards, the expected detail resolution of approximately 0.03 mm (0.0007 in.) may not show one serious type of defect which is an order of magnitude smaller than this. This defect is epoxy smear over the exposed surface of the internal conductors caused by improper drilling. The epoxy thus masks the internal conductors during the hole plating process and results in either an open circuit or a joint which may have far less than the desired 360 degrees of interconnection. To inspect for this condition the technique of mutual coupling has been developed. This technique uses the presence of the gap or high resistance area of the connection to develop an output signal.

The application of this technique is shown in Figure 9. Two coils wound in the form of a figure "8" are magnetically shielded from each other and formed into a single probe which is inserted into the through-hole. A signal generator is connected to one of the coils, called the excitation coil. The second coil, called the pickup coil, is shielded from the direct field of the exciting coil. When there is no gap between the plated hole and the pad, the currents that are induced in the pad circulate in the region of the pad near the exciting coil and hence induce little voltage in the pickup coil. When the probe is brought near a gap between the plated hole and the printed conductor, the magnetic field from the excitation coil induces a current in the loop formed by the edge of the gap. The magnetic field from this current which circulates around the gap induces a voltage in the pickup coil. This coil is connected to a tuned voltmeter which indicates the presence of the induced voltage.

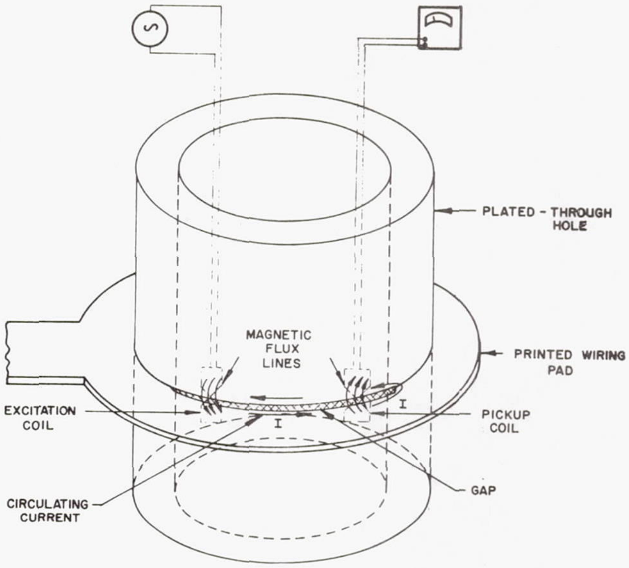

FIGURE 9. PRINCIPLE OF OPERATION OF MUTUAL COUPLING PROBE

Initially a large 1.36 cm (0.85 in.) diameter probe was constructed to verify the concept (Fig. 10).

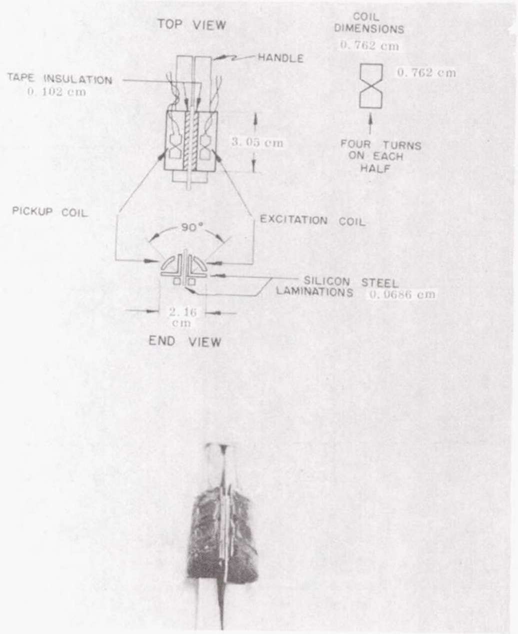

FIGURE 10. LARGE MUTUAL COUPLING PROBE

A second probe 1/10 the diameter of the initial probe was then constructed to determine the effect of miniaturization on the experimental results. When this proved successful a further reduction of 4:1 was made to produce a probe with a diameter of 0. 51 mm (0. 020 in.). The comparative sizes of the probes are shown in Figure 11. The results of the test run are tabulated in Table 1. In one test a bare copper wire was wrapped around a conducting cylinder. By varying the tension on the wire a connection having low resistance but mechanically unstable characteristics was formed. The mutual coupling probe could adequately detect this type of connection.

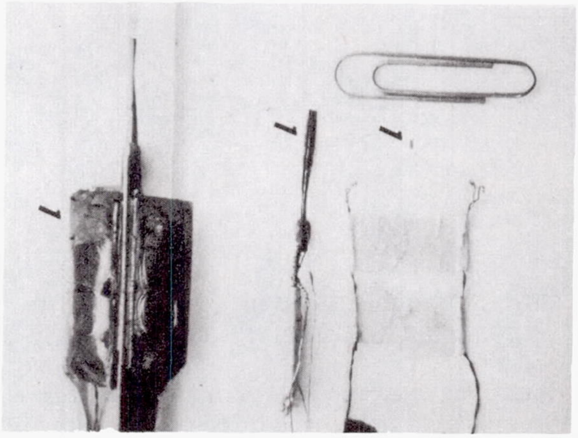

FIGURE 11. COMPARATIVE SIZES OF MUTUAL COUPLING PROBES

Tests were also conducted to determine the minimum practical gap angle that could be detected. It was found that for a reasonable ratio of peak gap voltage to cylinder wall voltage of 5:1, the minimum gap angle is approximately 60 degrees. This involves rotational as well as axial motion of the probe. The probe as designed for laboratory verification of the testing technique was very delicate and is unsatisfactory for practical application. A development program on the probe is presently underway. The probe will be a single piece of electrical steel with flats on it. A layer of electrical insulation is grown on the probe and single turn figure "8" coils will be deposited on the flats. A number of coils will be deposited upon a single probe so that rotation within the hole will not be required for a complete profile. The same control tapes used in the automatic tape control drill to make the board could be used to program the probing of the plated-through holes.

TABLE I. PICKUP COIL VOLTAGES FOR THREE MUTUAL COUPLING PROBES

(Excitation Current - 100 mA)

Probe Parameters	Cylinder Wall Thickness Millimeters (Inches)	Gap Width Millimeters (Inches)	Cylinder Wall Voltage, V_{cw} Microvolts	Soldered Connection Voltage, V_{sc} Microvolts	Gap Voltage, V_g Microvolts	Ratio $\frac{V_g}{V_{sc}}$
Probe Dia. = 21. 59 mm (. 85) freq. = 50 kHz cyl mat'l = brass	. 686 (. 027)	. 038 (. 0015)	. 39	. 57	15. 6	27. 4
Probe Dia. 2. 03 mm (. 080) freq. = 500 kHz cyl mat'l = copper	. 102 (. 004)	varied	. 41	. 78	4. 6	5. 9
Probe Dia. . 51 mm (. 0015) freq. = 2 MHz cyl mat'l = copper	. 038 (. 0015)	< . 0025 (< . 0001)	. 12	--	1. 0	8. 34*

* $\frac{V_g}{V_{cw}}$

CONCLUSIONS AND RECOMMENDATIONS

Laboratory experiments have verified the feasibility of both axial transverse laminography and mutual coupling as nondestructive testing techniques for the inspection of multilayer printed circuit boards. Laminography is well suited for mass inspection of multilayer boards. It will detect flaws as small as 0.02 mm (0.0007 in.) and can distinguish conductor layers separated from adjacent layers by 0.10 mm (0.004 in.); thus it can be used for screening the boards. Work is presently underway to transform the laboratory model into a piece of practical hardware. The new system will use optical and closed circuit television techniques in conjunction with a fluorescent screen to produce a continuous scanning laminograph with the capability to make permanent records.

The application of laminography is not limited to the inspection of multilayer printed wiring boards. It should become a powerful nondestructive testing tool for detailed examination of the interior of solid homogeneous or non-homogeneous bodies.

Mutual coupling can be used as an adjunct to laminography in the detection of extremely small gaps in the through-connections, but it is more limited in application because it requires probing each through-connection to be inspected. The laboratory model of the 0.51 mm (0.020 in.) diameter probe was difficult to fabricate and was too fragile to be practical. Work is being done to deposit 4 to 6 coils on a single probe to simplify the probing operation, to improve the geometry of the probe, and to reduce the minimum gap angle that can be detected. While these two complementary techniques will not answer all the questions concerning the quality of multilayer wiring boards, they will go a long way toward answering the question of reliability of the interconnections.

Page
Intentionally
Left Blank

OPTICAL MEMORY WITH FERRIMAGNETIC STORAGE ELEMENT

By

George A. Bailey

SUMMARY

A fifteen month effort to fabricate a magneto-optic memory is summarized. The scope of work included efforts to produce a material that would operate at room temperature without compensation. The material was evaluated to determine its magnetic, optical, and thermal properties such that the design of the memory might be optimized. To demonstrate the results of the experimentation, a feasibility model was designed and fabricated.

The storage element chosen was gadolinium iron garnet doped with aluminum. Information is written into the memory by simultaneously applying heat and a magnetic field to a spot. Since the coercivity of the material is temperature dependent, only the heated portion of the garnet is affected by the field. The readout signal is derived from the Faraday rotation of a polarized beam of light by the element. The state of magnetization of a region is determined by observing the direction of Faraday rotation.

INTRODUCTION

It is generally recognized that for large random access systems (greater than 10^6 words) the most debilitating influence on the system comes not from the memory element, but from the peripheral interconnections and equipment. The optimum system would require the highest degree of reliability.

One technique to eliminate the large numbers of accession interconnections is to use optics. With proper techniques a beam of light may be steered randomly to any point within a memory matrix. This eliminates the large logic decoding trees with the attendant drive lines. Optical accession memories have been devised using the Kerr effect, but the writing functions must still be line driven. Memories have been proposed using holographic and photochromic devices; however, they have not progressed much past the conceptual stage of development. On the other hand, the ferrimagnetic memory is both written and read optically; thus, it has greater potential for mass memory application.

COMPENSATION POINT MEMORY

The storage element used is a gadolinium iron garnet, which exhibits the necessary ferrimagnetic properties; that is, the magnetic moments of gadolinium and iron align in opposition, and the magnitude of the moments is temperature dependent. The resultant magnetic moment of the element is the difference between these two sublattice moments. At a particular temperature the magnetic moments of gadolinium and iron are equal and opposite, thereby cancelling each other. This temperature is called the compensation temperature or compensation point.

At the compensation point there is no net magnetic moment; therefore, the element is unaffected by external magnetic fields. Since the magnetic moments of gadolinium and iron exactly cancel, no further reduction in energy would be accomplished by the application of a field. This point is illustrated in Figure 1. The memory described below operates around this compensation point.

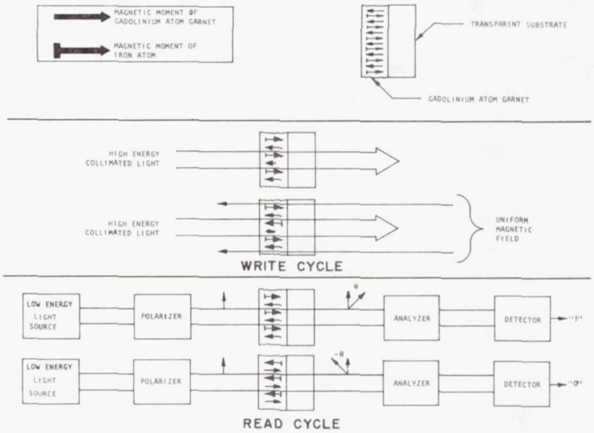

FIGURE 1. WRITE AND READ CYCLES FOR INFORMATION STORAGE AND RETRIEVAL

The construction of the compensation point memory is shown in Figure 2. The memory element is a thin slab of ferrimagnetic material which is held at its compensation temperature. The magnetic

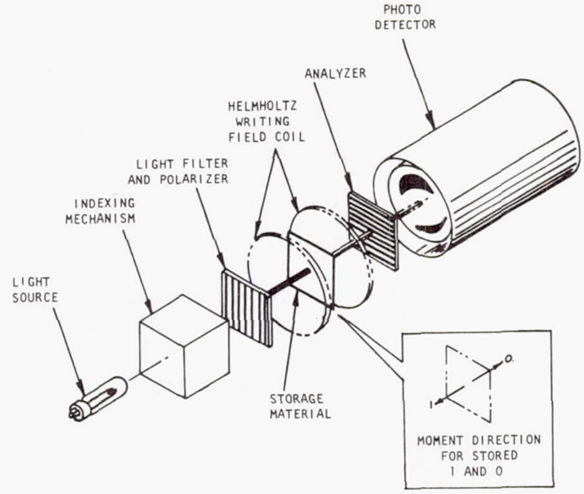

FIGURE 2. COMPENSATION-POINT MEMORY CONSTRUCTION

easy axis is normal to the slab. Writing is accomplished by heating a local area to reduce the coercivity and then applying a magnetic write field to set the memory. The write field is applied by a single Helmholtz coil. The magnitude of the field is much lower than the coercivity at the compensation temperature, but is greater than the coercivity in the heated area. Consequently, only the magnetic moment in the heated area is oriented in the direction of the applied field. Reading is accomplished by applying a beam of polarized light to the spot to be read. The transmitted light is passed through an analyzer and detected by a phototube. Because of the Faraday effect, the plane of polarization of the incident light is rotated as it passes through the magnetic medium. The rotation of the plane of polarization is clockwise or counterclockwise depending upon whether the magnetization is parallel or anti-parallel to the beam of light. One direction is defined as binary 1, the other as binary 0. Consequently, a stored 1 can be distinguished from a stored 0 by observing the amplitude of the transmitted light. The readout is, obviously, nondestructive.

The write cycle time depends on the thermal relaxation time of the memory element, the temperature change required to take the element from a non-disturb to write state, and the magnitude of the write field. The variation of coercivity with temperature about a compensation point is shown in Figure 3. To write into the memory, the temperature of the selected bit must be raised to at least T_r, such that a write field of H_W may operate on the spot, and then reduced to $T_C + T_A$ before the write field can be removed. Thus, the write cycle consists of selecting a spot, raising, and then lowering its temperature in the presence of a field. The cycle time depends upon how fast these operations can be performed. The writing time can be reduced by increasing the power of the heating pulse. The time required to lower the temperature will depend upon the thermal relaxation time constant of the material.

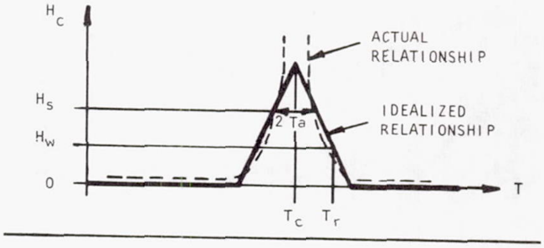

FIGURE 3. IDEALIZED POINT OF COERCIVITY VERSUS TEMPERATURE VARIATION

The material required for a fast-write-cycle memory should have an H_C versus T relationship with the general shape of that shown in Figure 3. The effective sheet coercivity, H_S, should be as high as possible for the specified variation in ambient temperature, T_C, and the slope of the curve should be as steep as possible. The material should have a large thermal conduction coefficient; or preferably, it should be prepared on a transparent substrate with a large thermal conduction and large specific heat. Since the element is heated by a beam of light, the storage element should be sufficiently opaque to absorb energy and sufficiently transparent to be heated internally.

The read operation is based on the use of polarized light and the Faraday effect. A large rotation of the plane of polarization of the read light beam is desired to improve the discrimination between 1 and 0 outputs and to relieve the requirements on the analyzer. Since the magnitude of the rotation is proportional to the thickness, thick elements are seemingly preferred. However, absorption of the light implies that thin samples are desirable. A figure of merit is the ratio of the rotation power to the absorption coefficient. Thickness considerations impose practical limitations on the choices for light sources and detectors. The read cycle time is determined primarily by the indexing time and the detector speed.

Since no switching is involved in the read operation, the time delay in the storage medium is negligible.

ELEMENT PREPARATION

Three primary methods of preparing the gadolinium iron garnet were investigated: thin films, polycrystalline samples and single crystals. The results of the thin films were disappointing. Polycrystalline materials were obtained and found to be quite comparable in optical absorption and Faraday rotation to the single crystal material. However, polycrystalline samples could not be made as thin as the single crystal material and the polycrystalline material did not exhibit magnetic anisotropy. Therefore, the direction perpendicular to the plane of the element could not be made into an easy direction. Single crystal material was prepared by the molten flux method.

TEMPERATURE COMPENSATION

In the gadolinium iron garnet, $Gd_3Fe_5O_{12}$, the iron ions occupy two different sites. Three of the atoms in the unit cell occupy tetrahedral sites, and the other two occupy octahedral sites. The iron atoms in the octahedral and tetrahedral sites are coupled antiferromagnetically. The resultant magnetization of the iron atoms is coincident with the iron atoms in the tetrahedral sites.

The gadolinium ions are coupled antiferromagnetically to the net moment of the iron ions. The coupling is much weaker than that between the iron ions. As a consequence the magnetization of the gadolinium ions drops very quickly with increasing temperature approximately as 1/T. Therefore, at temperatures near the curie point, the magnetization of the iron ions is dominant. However, since the gadolinium has a saturation moment larger than the resultant magnetization of the iron ions, the moment of the gadolinium ions is predominant at low temperatures. The temperature at which the gadolinium and iron magnetic moments are equal is called the compensation point.

Figure 4 shows a plot of the magnetization of the iron ions and the gadolinium ions as a function of temperature. The total magnetization is also shown. At the temperature marked, Tc, the magnetization of the gadolinium and iron ions cancels.

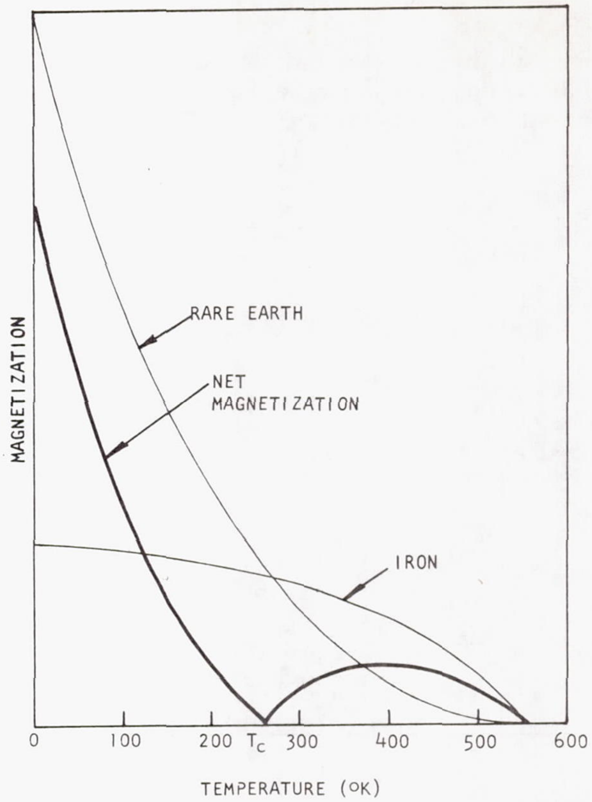

FIGURE 4. MAGNETIZATION OF A TYPICAL RARE EARTH (GARNET)

The compensation temperature of gadolinium iron garnet is 288°K. The substitution of aluminum for the iron reduces the moment of the iron lattice. The aluminum preferentially occupies the tetrahedral sites because the aluminum atom is smaller than the iron atom and also the tetrahedral sites are smaller than the octahedral sites. A reduction in the net magnetization of the iron lattice raises the temperature at which the iron lattice is compensated by the gadolinium lattice. This program dictated a memory which could operate at room temperature without compensation. It was found that four percent by volume of aluminum substituted for the iron resulted in crystals with a compensation temperature very close to room temperature.

BASIC MEASUREMENTS

To design a memory based on gadolinium aluminum iron garnet, measurements of certain magnetic and optical properties of the material are essential. Both the compensation temperature and the coercivity were determined with the aid of a vibrating magnetometer; a sample is vibrated in a dc magnetic field, and the magnetization is sensed with a pick-up coil. Figure 5 illustrates plots of magnetization versus temperature of three different samples. The temperature at which the magnetization is minimum is the compensation point. Reversing the dc field and noting the reversal of magnetization gives the value of the coercive force. A typical plot is shown in Figure 6.

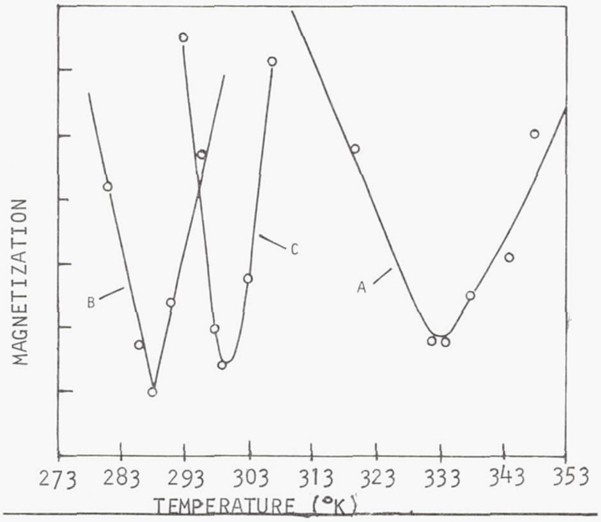

FIGURE 5. MAGNETIZATION VERSUS TEMPERATURE OF THREE GADOLINIUM IRON GARNET SAMPLES WITH DIFFERENT ALUMINUM DOPING

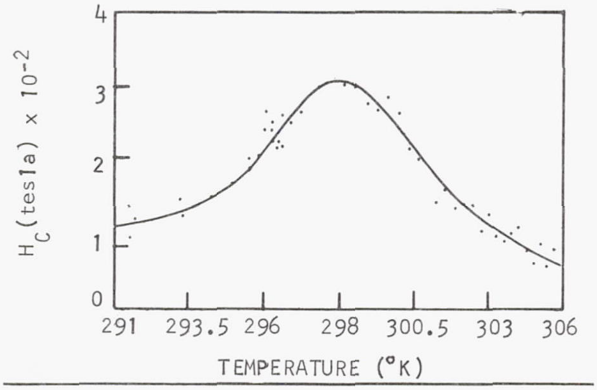

FIGURE 6. COERCIVE FORCE OF GADOLINIUM IRON GARNET

These results indicate the temperature stability of the memory. For example, to write into the memory by heating a bit 6°K above the compensation temperature, a field of 7843 amperes per meter (100 oersteds) would be needed to switch the heated area. This field would not affect the unheated portion of the platelet as long as the temperature is maintained within 6°K of the compensation temperature. The sharper the peak, the easier the writing; however, a sharp peak requires better temperature stability.

The optical absorption measurements were obtained with a spectrophotometer. A typical run is shown in Figure 7. The optimum wavelength is one that has the largest rotation of polarization per loss by absorption. These results indicate that, if the Faraday rotation is not significantly reduced, the longer wavelengths are more desirable.

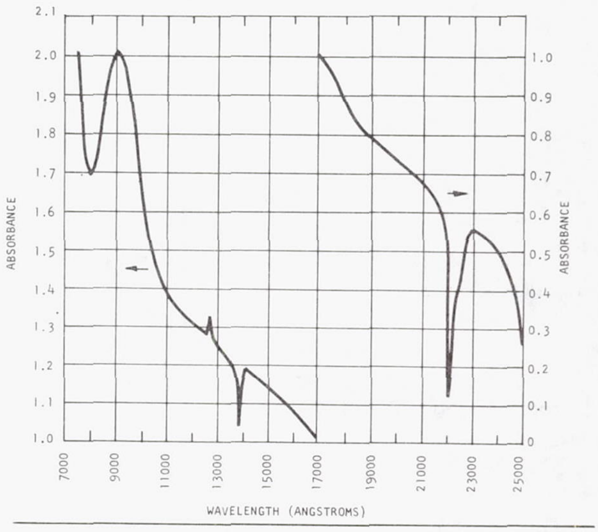

FIGURE 7. OPTICAL ABSORPTION OF GADOLINIUM IRON GARNET

Faraday rotation measurements were obtained with the aid of the arrangement shown in Figure 8. The laser beam was modulated at 90 Hz, passed through a polarizer, the sample, and an analyzer, and then detected by a photomultiplier. The laser beam was also detected by a phototransistor and this signal in the differential amplifier. The results of a typical set of measurements are shown in Figure 9.

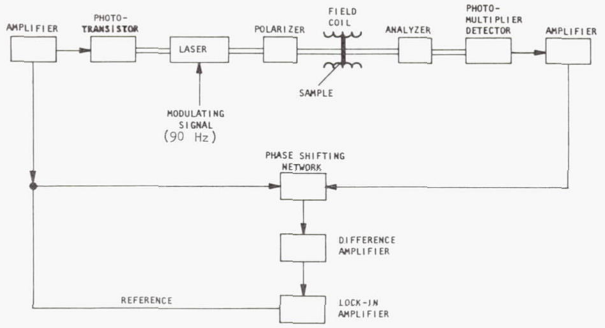

FIGURE 8. FARADAY ROTATION MEASUREMENT EQUIPMENT

From these curves it is evident that the temperature stability depends upon the magnetic field used for writing. With a field of 784 amperes per meter (10 oersteds), no rotation occurs over a range of above 6°K. For a 1500 amperes per meter (20 oersted) field, the temperature range over which no rotation occurred was reduced to about 3°K.

CONCLUSIONS

Based on the experimental information, a feasibility model of the concept has been designed and fabricated. A block diagram of the system is illustrated in Figure 10. The memory elements are on 25 micron (1 mil) centers that probably can be reduced to 2.5 micron (0.1 mil) centers. With an argon laser, Faraday rotations of 9 degrees are obtained, therefore detection is no problem. The small memory elements have greatly enhanced the cycle times of the memory. Since the beam from the laser could not be reduced to this micron range, a special diffraction-limited focusing lens had to be used. The present major difficulty is securing some type of nonmechanical laser scanning apparatus. Various techniques have been proposed; for example, modulating

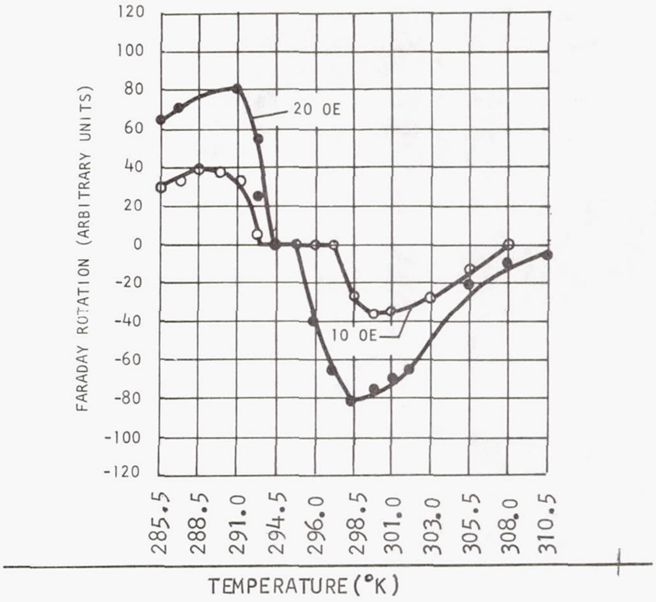

FIGURE 9. FARADAY ROTATION VERSUS TEMPERATURE FOR TWO DRIVE FIELDS

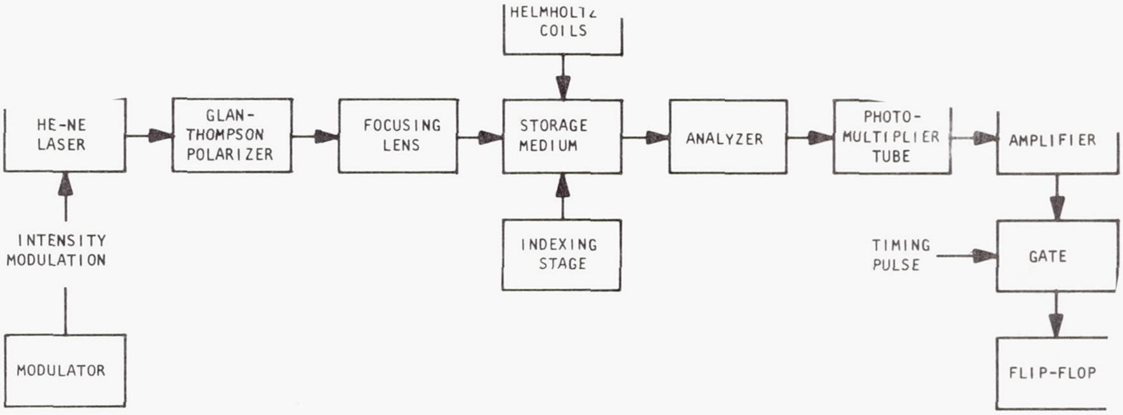

FIGURE 10. BLOCK DIAGRAM OF PROPOSED SYSTEM

the index of refraction of crystals, employing standing waves in crystals, and revolving mirrors on the end of a turbine dentist's drill. All of these ideas are basically mechanical operations and are, therefore, limited in speed. The technique offering the most promise is the combination of potassium dihydrogen phosphate and calcite arrangement that can be driven by digital signals. Overall, this system promises a 10^8 bit memory on a 6.5 square centimeter (one square inch) substrate which can be randomly accessed without hard line interconnections.

LARGE AREA METAL-OXIDE-SEMICONDUCTOR DEVICES

By

Dorrance L. Anderson

SUMMARY

The Solid State Devices Section at MSFC has followed the development of metal-oxide-semiconductor (MOS) devices for several years. Interest in this field stems from its importance in several electronic applications. A large area MOS transistor is being developed for incorporation in an integrated circuit and for studying certain problems in fabricating MOS devices.

This paper describes the design and development of a "P" channel MOS transistor with a channel width of 1.8 centimeters. Calculations are made on drain to source current, input capacity, and transconductance.

Areas for research in MOS structures are discussed with particular interest being placed on materials and techniques that promise improvements attainable in the near future. Semiconductors, dielectrics, and metal systems are discussed separately with possible direction for fruitful research in each.

INTRODUCTION

Rapid advances are now being made in metal-oxide-semiconductor (MOS) technology as a result of increased development efforts and funds being expended. Some advantages offered by MOS devices and circuits are small size, low power consumption, simple construction, high yield, and high input impedance with an output characteristic similar to that of a pentode vacuum tube.

Although there will be some uses for individual MOS devices, the greatest use will be in large scale integration of many functions into a single chip. Because of high yields and small size, very complex arrays are possible.

A program to develop an MOS device having a large area was to have resulted in an MOS technology capability and a transistor for use in a special circuit. Because of the large size and channel width, fabrication of the transistor proved to be difficult. The design and fabrication of the device are described below.

LARGE AREA MOS DEVICE

A "P" channel enhancement mode transistor with a current capacity of approximately one-fourth ampere was desired. Silicon was used as the semiconductor material, thermally grown silicon dioxide formed the gate dielectric, and aluminum served as the metal contacts. Since current rating and transconductance depend on channel width, an interdigitated structure was designed for greater channel width per given surface area. A small experimental MOS device with a 15 micron channel length and a 25 micron channel width is shown in Figure 1. The solid aluminum

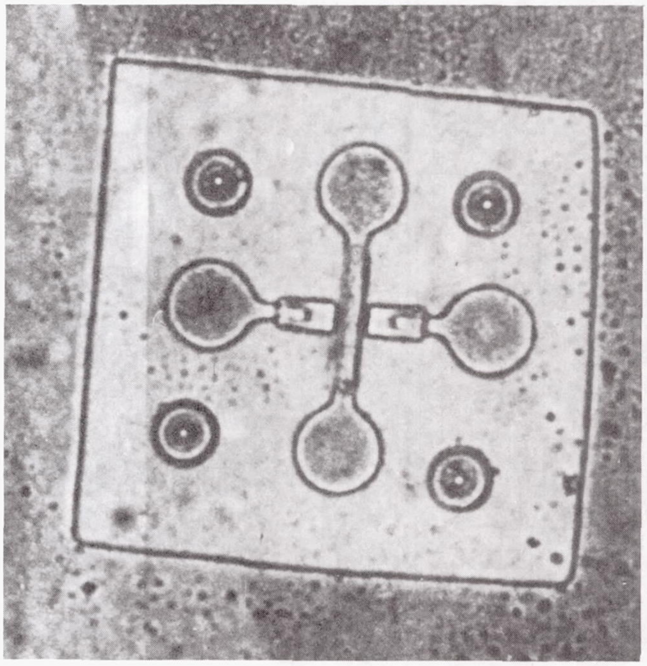

FIGURE 1. TOP VIEW OF SMALL MOS DEVICE PRIOR TO WIRE BONDING

stripe with a pad on each end is the gate metallization over the channel. Figure 2 shows the large area device with the same channel length of 15 microns but with a channel width of approximately 1.8 centimeters. Figure 3 shows the wafer just before diffusion of source and drain; the light areas are the openings in the oxide with the silicon exposed. Figure 4 was taken just before the aluminum pattern was applied; the light areas are the exposed silicon in the source and drain regions, the dark areas are silicon dioxide, and the medium zigzag stripe is the thinner oxide over the channel.

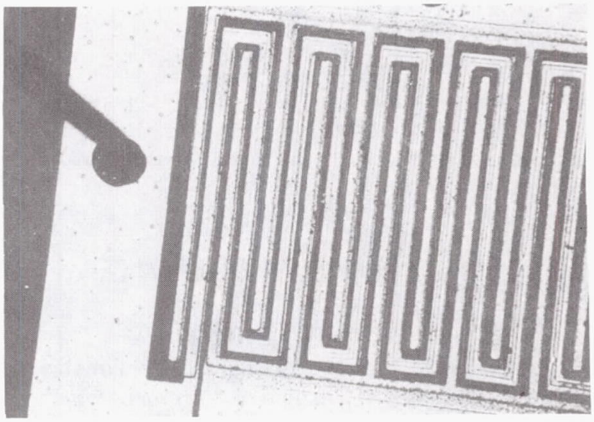

FIGURE 2. COMPLETED LARGE AREA MOS DEVICE

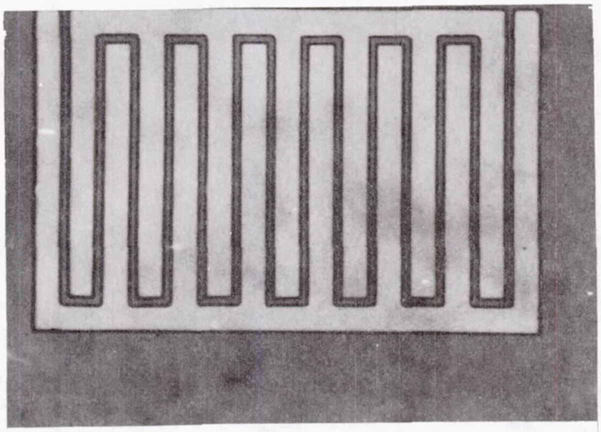

FIGURE 3. EXPERIMENTAL LARGE AREA MOS DEVICE READY FOR DIFFUSION

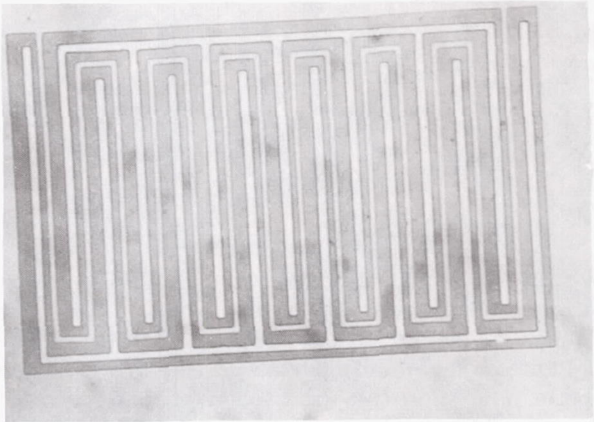

FIGURE 4. LARGE AREA EXPERIMENTAL MOS SHOWING WAFER PRIOR TO METALLIZATION

FABRICATION

A detailed step-by-step breakdown of the fabrication process is shown in Figure 5. The following is a description of these steps:

1. An N-type wafer of 6 to 7 ohm centimeters was chosen. The wafer had previously been lapped and chemically etched. The wafer was cleaned in ethyl alcohol and dried under a sun lamp for 15 minutes.

2. An oxide of 4500 angstroms was thermally grown in an open tube furnace at a temperature of 1373° K. The first 15 minutes of growth was in dry oxygen. This was followed by one hour in steam and finished with 15 minutes in dry nitrogen.

3. After oxidation, the wafer is placed on a spinner and photoresist is applied. The photoresist is air dried for 15 seconds and spun at 10 000 rpm for 30 seconds, resulting in a uniform coating. It is then placed in an oven and baked 40 minutes at 333° K.

4. The photoresist is exposed by aligning a previously prepared photographic mask over the wafer and exposing it to ultraviolet light for one minute. The wafer is then placed in an oven at 453° K for 30 minutes to cure the photoresist before oxide etch.

5. The exposed oxide is etched down to the silicon with a buffered solution of hydrofluoric acid containing acetic acid, ammonium fluoride and deionized water.

6. The polymerized resist is removed with boiling j100-strip solution.

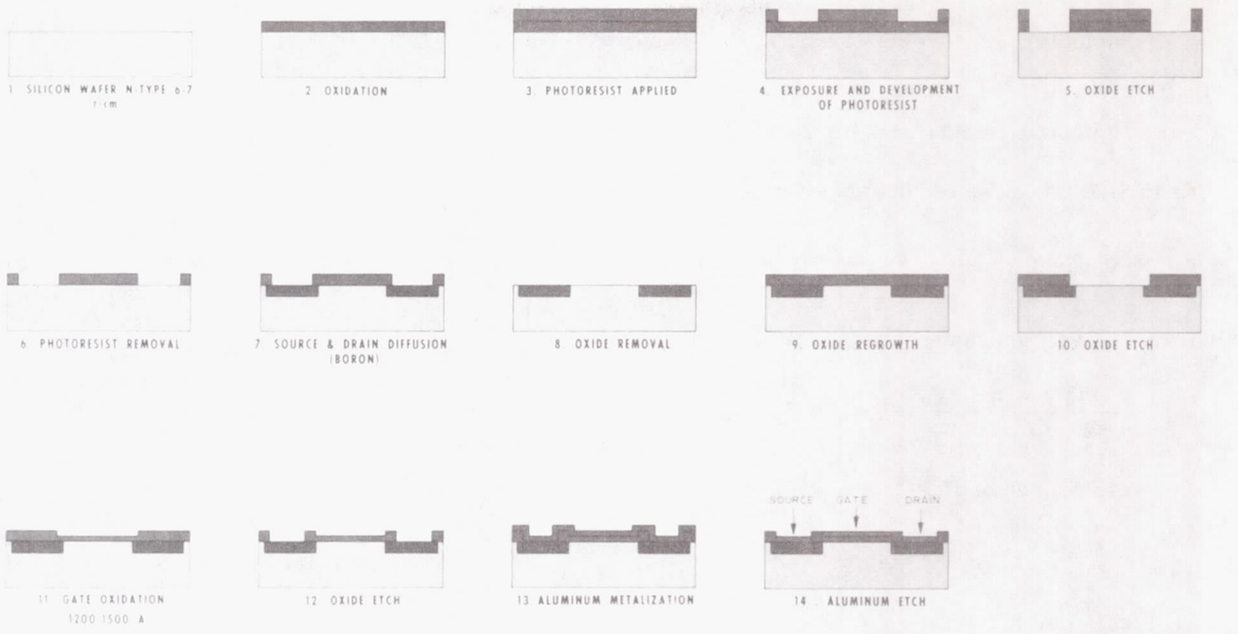

FIGURE 5. PROCESS STEPS FOR MAKING "P" CHANNEL MOS TRANSISTOR

7. Source and drain diffusion are made in an open tube furnace at 1473° K. A gas system is used with diborane as the dopant and argon as the carrier. Diffusion time is approximately 40 minutes and depth of diffusion 4 microns.

8. Because of doping impurities in the oxide, it is stripped from the entire wafer with the buffered etch solution used in step 5.

9. A new oxide is regrown by the same process used in step 2.

10. To obtain a thin layer of oxide over the channel between source and drain, the oxide is etched down to the silicon.

11. An oxide 2000 angstroms thick is grown over the channel in dry oxygen at 1373° K for 45 minutes. It is easier to grow a 2000 angstrom oxide than to etch back from a thicker one.

12. Oxide is removed from source and drain areas for metallization contacts. The etch is the same used in step 5.

13. The entire surface of the wafer is coated with aluminum by vapor deposition. This is accomplished in a vacuum system at 1.3×10^{-4} newtons per square meter (10^{-6} torr).

14. Aluminum is removed from the entire wafer except over the gate region, source and drain contact areas, and contact pads. This is accomplished by using photo-engraving techniques previously described and a buffered solution of phosphoric acid, nitric acid, and deionized water.

The wafer is now ready for dicing and mounting of the individual chips on headers.

DESIGN

To determine the current capacity per centimeter of channel width, the following formula was used:

$$I_{ds} = \frac{\mu_0 C_i V_g}{2\ell}$$

where

μ_0 = 250 = hole mobility

C_i = capacity/cm^2

V_g = gate voltage

ℓ = channel length in cm

$C_i = 0.08842 \text{ K} \frac{A}{d} \; \mu\mu\text{F}$

where

K = dielectric const. = 3.8 for SiO_2

A = area in cm^2

d = dielectric thickness in cm .

With an SiO_2 thickness of 2000 angstroms

$$C_i = 0.08842\ (3.8)\ \frac{1}{2 \times 10^{-5}} = 0.0168\ \mu F/cm^2.$$

With V_g = 1 volt and channel length of 15 microns

$$I_{ds} = \frac{250\ (.0168 \times 10^{-6})}{2\ (15 \times 10^{-4})} = 1.4\ mA/cm\ .$$

With a gate voltage of 10

$$I_{ds} = 10^2 \times 1.40 = 140\ mA$$

for a 0.25 A device

250/140 = 1.8 cm channel width required.

Tranconductance per cm of channel width at V_g = 1V

$$gm = \frac{\mu_0 C_i V_g}{\ell}$$

$$= \frac{250\ (.0168)1}{15 \times 10^{-4}} = 2800\ \mu\ mho/cm$$

or 1.8 × 2800 = 5000 μ mho for the device

at V_g = 10 volts, gm = 50,000 μ mho .

Although the values measured on completed devices were not as high as the theoretical values, the results were satisfactory for the application. Development is continuing on MOS devices with special emphasis on oxide growing. Oxides will be grown at temperatures around 1273° K under various conditions of gas flow to minimize immobile charge density. This should reduce threshold voltages, which were excessively high in the devices fabricated to date.

RESEARCH AREAS

Because of the vast amount of existing knowledge in bipolar planar technology, the development of MOS devices has largely used the same materials and techniques. The MOS transistor, however, operates on an entirely different principle and a new look should be taken at promising semiconductor materials. Gallium arsenide, for instance, has higher mobility and offers the promise of higher speed devices. A study to compare various semiconductor materials for specific use in MOS devices could prove very beneficial.

Although thermally grown SiO_2 has spawned the planar technology and consequently the integrated circuit industry, it still is not the ideal masking and insulating agent. Neither is it the ideal dielectric for the gate of an MOS transistor. Silicon nitride is denser, has a higher dielectric constant, and has shown signs of making devices more stable under temperature and radiation environments. Silicon nitride is more difficult to etch than silicon dioxide, and efforts are now concentrated on window cutting techniques to use silicon nitride in mass production.

Another interesting approach to field effect devices is replacing the dielectric with ferroelectric materials. Then by applying a potential to the gate, a channel can be enhanced or depleted by voltage pulses. This has the requirements of a memory cell.

The possibilities for research in gate insulating materials are almost unlimited. This is probably the most fruitful area in MOS research.

In general the surface has only been scratched in MOS technology. The field is wide open for research in semiconductors, dielectrics, and metals as applied to field effect devices.

MICROELECTRONICS FOR THE GYRO STABILIZED PLATFORM

By

Owen Rowe

SUMMARY

The microminiaturization of the gas bearing gyro servoloop electronics and associated circuitry for the platform are discussed. Emphasis is placed on the redesign of the electronics to achieve maximum monolithic integration. A number of circuits are presented to demonstrate the achievements. Evidence is shown that linear-analog circuits can be miniaturized with corresponding benefits.

INTRODUCTION

For several reasons, the stabilized-platform electronics were built with large elements. The circuits were the linear-analog type and were designed to handle large dynamic signal levels and high power output. Long time constants are involved in operating the gyro, and precise specifications must be met; therefore, the circuits could not easily be miniaturized. Also, the semiconductor industry waited to develop the required circuitry because of their concentration on digital circuits.

Approximately two years ago, a serious effort was started to miniaturize the platform electronics. With increased reliability as the main objective, an appraisal of miniaturization techniques was made. The decision was to design for maximum use of the monolithic integrated chips. Some forms of hybrid circuitry using the deposited films and discrete components were more advanced, but they did not show as high a reliability potential. The hybrid approaches involved too many interconnections of dissimilar materials. The design approach using the monolithic integrated chips depended upon further development of standard as well as custom integrated circuits.

DESIGN PHILOSOPHY

It was evident that extensive circuit redesign was required for microminiaturization. First the large elements such as transformers, reactors and large capacitors had to be eliminated. These elements comprised approximately two-thirds of the volume and weight. Secondly, the power dissipation in the circuits had to be reduced to avoid the massive heat sinks. The circuits also had to be designed for long time constants, freedom from ground loops, immunity to noise and cross-talk, good linearity, and low-null drift or good dc stability. To obtain these goals with integrated circuits required new concepts in circuit design philosophy. Previously, with discrete elements, a minimum number of transistors were used along with the large elements to obtain a given circuit function. In monolithic chips, transistors are a real bargain, and many transistors should be used to the exclusion of large elements.

INERTIAL STABILIZED PLATFORM SYSTEM

Figure 1 shows the four major assemblies that make up the platform system. The system functions are (1) accelerometer sensing and reference, (2) vehicle attitude and programing, and (3) guidance reference coordinates. The stable platform assembly contains the inertial sensors and the associated gimbals. The ac power supply is a static inverter for converting battery power to 3 phase 400 Hz to drive the gyro wheels and to supply other reference voltages. The servoamplifier box contains six sets

FIGURE 1. INERTIAL STABILIZED PLATFORM SYSTEM SATURN V & IB

of servoelectronics and miscellaneous control circuitry. The accelerometer signal conditioner contains the wave shaping amplifiers for the output signals of the accelerometers. With developments to date, it is possible to eliminate the servoamplifier and accelerometer boxes and place the microelectronics aboard the platform.

Figure 2 shows one-half of the sliding contacts at a gimbal point. Servo signals from the platform pass through the contacts to the amplifier box and back onto the platform to the torquers. Placing the electronics aboard the platform would greatly reduce the required number of sliding contacts and hence improve reliability. In addition, a tremendous amount of wiring, cabling, and interconnecting plugs would be eliminated.

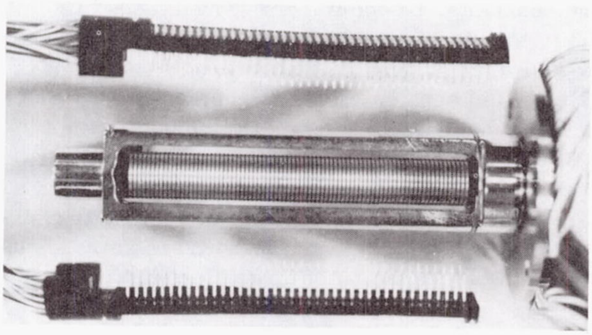

FIGURE 2. GIMBAL PIVOT SLIP RING

MINIATURIZATION OF SPECIFIC CIRCUITS

The top row of modules in Figure 3 is the discrete component version of servoelectronics in use at present. The second row down is a hybrid version consisting of some integrated circuits complemented by discrete components. This was a step in developing the near totally integrated version as shown in the bottom row. A servoamplifier now occupies a volume of approximately 920 cubic centimeters (56 cubic inches). The integrated version can be packaged in approximately 16. 4 cubic centimeters (one cubic inch). One package configuration being considered is a 6. 03 centimeter (2 3/8 inch)-diameter disc 0. 95 centimeter (3/8 inch) thick.

Figure 4 outlines the three major functional blocks of a servoamplifier.

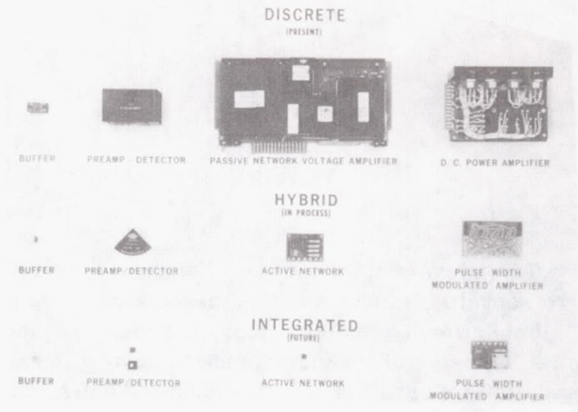

FIGURE 3. PLATFORM SERVO ELECTRONICS

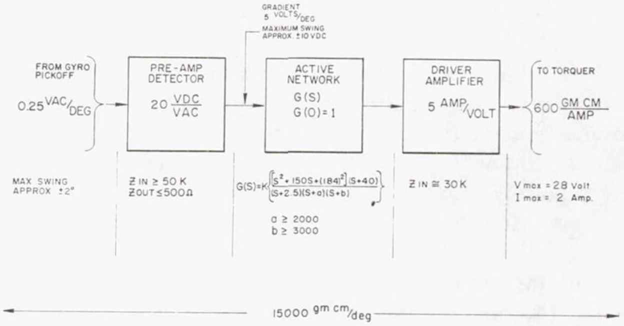

FIGURE 4. FUNCTIONAL BLOCK DIAGRAM

The preamplifier/demodulator, as shown in Figure 5, amplifies the gyro pickoff signal, demodulates with a full wave phase sensitive demodulator, and filters out the carrier ripple. This unit can easily be packaged in one-quarter of the 6. 03 centimeter (2 3/8 inch)-disc configuration.

Figure 6 shows a phase and gain curve plot of a near complete integrated version of a network that will occupy even less than one-quarter of the 6. 03 centimeter (2 3/8 inch) disc.

The power amplifier section can logically be divided into a modulator section and a power amplifier section as shown in Figure 7. This portion of the servoelectronics represents the greatest advancement. Both sections can be mounted in a quarter of the 6. 03 centimeter (2 3/8 inch) disc. The power section is a complete bridge circuit made up of four

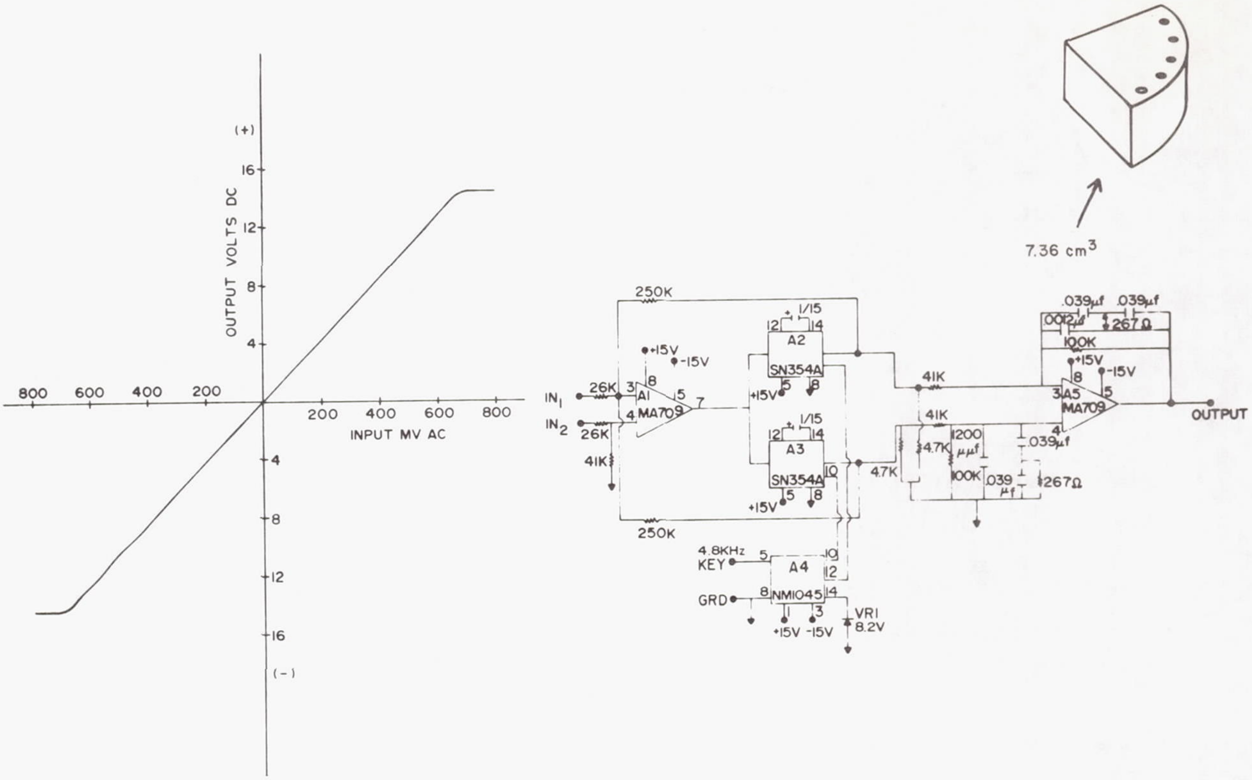

FIGURE 5. AC PREAMPLIFIER, PHASE SENSITIVE DEMODULATOR, AND LOW PASS FILTER

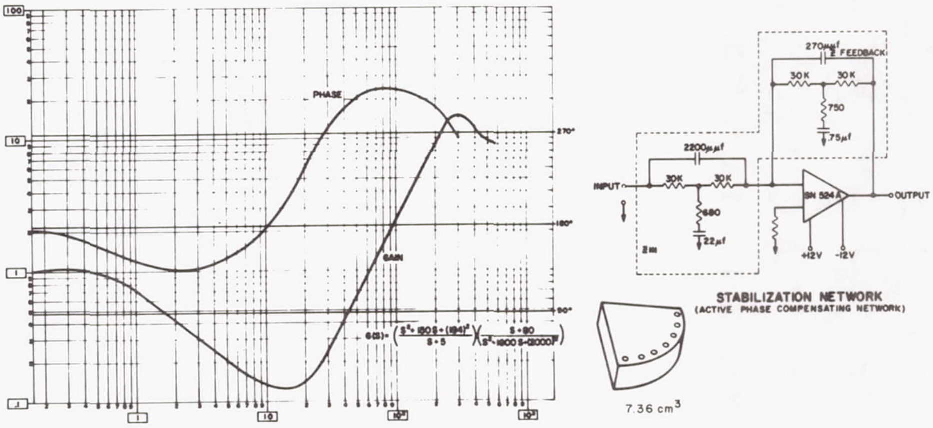

FIGURE 6. PHASE AND GAIN CURVE PLOT FOR THE STABILIZATION NETWORK

integrated chips mounted in one power transistor case. It can drive a 70-watt gimbal torquer with plenty of margin in power capability.

Figure 8 depicts a simplified concept of the pulse width modulator. In effect, the modulator sums the error signal with a fixed triangular wave and gives an output of pulses, with the width proportional to the error signal level.

Figure 9 helps in explaining the operation of the power bridge. For the no-signal condition, the upper switches are closed and the bottom switches are open. For one direction of pulse, an upper switch opens and the one below it closes. Current flows as shown. At the end of the pulse, the switches return to their original condition and current flows around the upper loop.

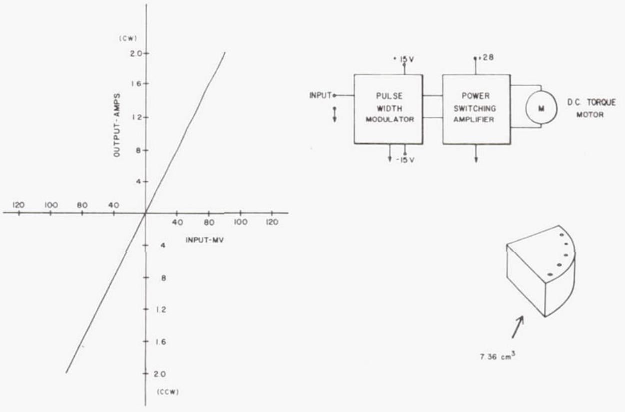

FIGURE 7. POWER AMPLIFIER SECTION

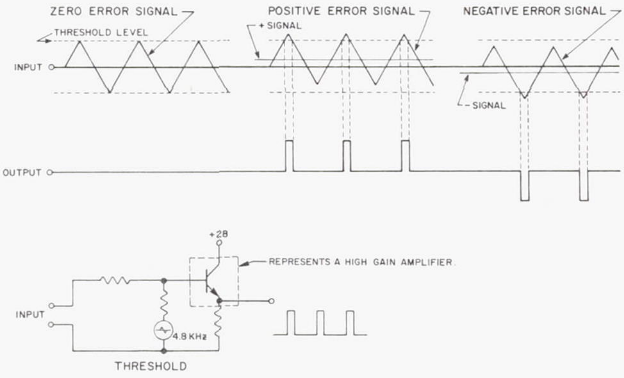

FIGURE 8. PULSE WIDTH MODULATION

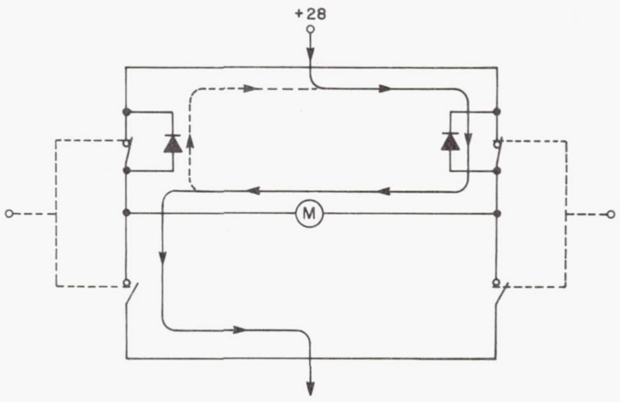

FIGURE 9. POWER BRIDGE

A number of applications, other than the servo-amplifier, can use this modulator and power switch. Some of these are the pulse width modulated power control, the dc to dc converter, and the output stage of a static inverter.

Some electronics, other than that of the platform servos, have been miniaturized. Figure 10 shows the block diagram and performance curve of a single chip monolithic integrated amplifier. In this case an isolation transformer is required to prevent ground loops between the vehicle and GSE batteries. Figure 11 shows the packaging with at least a 5 to 1 reduction in size.

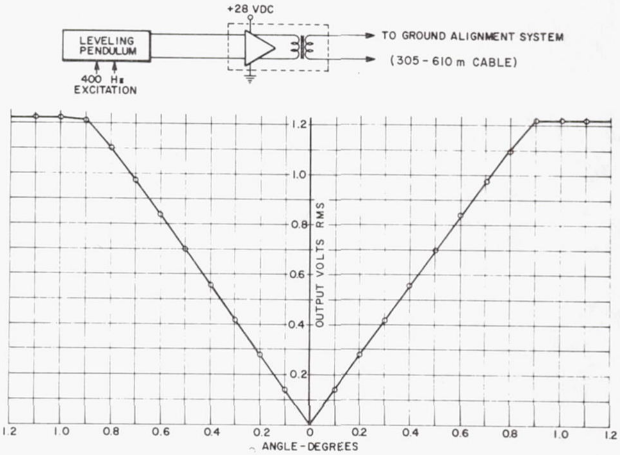

FIGURE 10. INTEGRATED PENDULUM PREAMPLIFIER

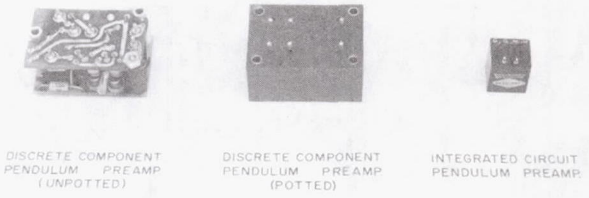
DISCRETE COMPONENT PENDULUM PREAMP (UNPOTTED)

DISCRETE COMPONENT PENDULUM PREAMP (POTTED)

INTEGRATED CIRCUIT PENDULUM PREAMP.

FIGURE 11. PLATFORM SERVO ELECTRONICS (POTTED & UNPOTTED)

Another area of achievement is the electronics for the PIGA encoder output. Figure 12 shows in block form one signal channel of which there are four on each accelerometer. As shown earlier, the wave shaping amplifiers were in the accelerometer-signal-conditioner box. As shown in Figure 13, all the electronics for the four encoder channels can be placed on the accelerometer.

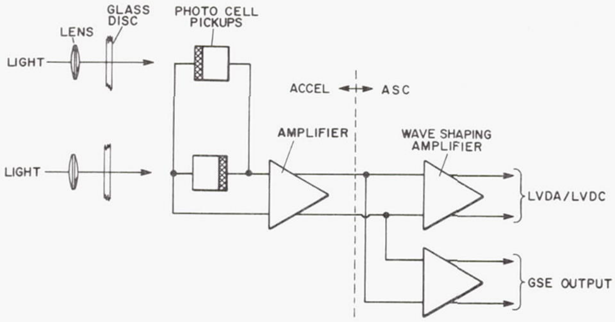

FIGURE 12. ACCELEROMETER OUTPUT CHANNEL

CONCLUSION

Microminiaturization of the platform electronics produces (1) increased reliability because of a 10/1 reduction in fixed interconnections (solder and weld), a 3/1 reduction in pressure interconnections (plugs and slip rings), and a 10/1 reduction in the number of elements; (2) electrically equal or better performance by better element matching and thermal tracking, and less noise and cross-talk on shorter leads and cables; (3) overall 100/1 size and weight reductions; (4) up to 10/1 cost reduction; (5) feasibility of redundancy; and (6) results of the program that are directly applicable to other inertial systems, applicable to GSE as new designs are required, and innovations directly applicable in industry.

FIGURE 13. PLATFORM SERVO ELECTRONIC ACCELERATOR

Page
Intentionally
Left Blank

INTEGRATED CIRCUITS IN TELEMETRY SYSTEMS

By

T. C. Lawson

SUMMARY

Operation of the Saturn V vehicle's instrumentation system requires a highly reliable and flexible telemetry system that can also be easily adaptable to future programs such as the Apollo Applications Program (AAP).

The development work now being conducted to achieve such a system is presented. New equipment for greater system flexibility, such as a telemetry data compressor, is discussed. Improvements in existing equipment by using integrated circuits for superior reliability are also presented to include modernization of multiplexers and pulse code modulation equipment.

INTRODUCTION

Today's critical and rapidly changing instrumentation requirements place severe demands upon the telemetry system. The Telemetry Branch at Marshall Space Flight Center is presently engaged in the design and development of a highly reliable, flexible telemetry system that will meet the instrumentation requirements of the Saturn V vehicle and be easily adaptable to future programs such as the Apollo Applications Program (AAP). Existing designs are being made more reliable by using integrated circuitry that will be phased into the Saturn V and other programs. Also, new equipment is being designed for greater telemetry system flexibility.

PRESENT SYSTEM

The present telemetry system consists of approximately twelve pieces of equipment that can be interconnected in various ways to provide the instrumentation for processing both analog and digital measuring signals. Figure 1 shows a typical system used on the S-IB stage for vehicles SA-201 through SA-204. None of this equipment contains integrated circuits.

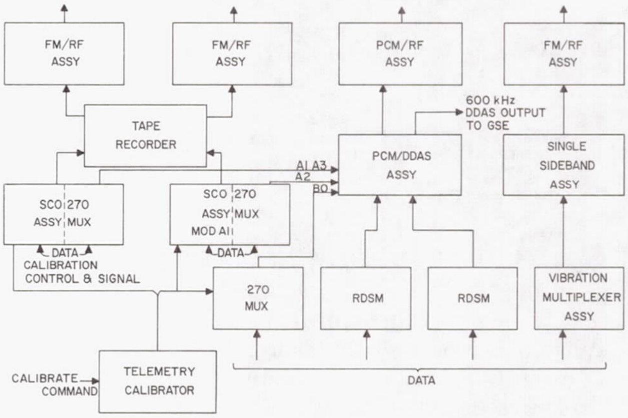

FIGURE 1. TYPICAL TELEMETRY SYSTEM

NEW DEVELOPMENTS

The pulse code modulation/digital data acquisition system (PCM/DDAS) (Fig. 1) must process many channels of information for transmission. Some of the information is rapidly changing and must be sampled often; while some remains fairly constant and only has to be monitored. To transmit the data that are not changing is an inefficient use of the RF spectrum.

A unit is being developed that will remove the redundant or repetitious data and thereby conserve bandwidth. This system will be inserted between the PCM/DDAS assembly and the output. Figure 2 is a flow diagram of this system.

When a new measurement is received by this system, the previous value for that particular measurement is recalled from memory along with a predetermined tolerance. The new and previous values are then compared. If the new value is equal to the previously transmitted value within the tolerance established for that particular measurement, the previously transmitted value is restored to memory and the system sequences to the next channel. No data are transmitted.

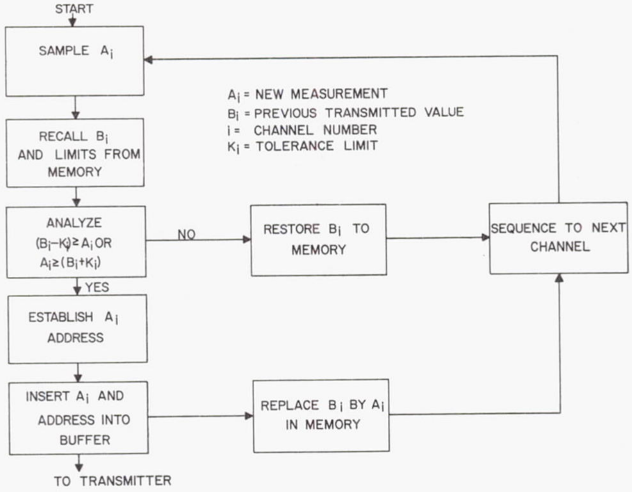

FIGURE 2. DATA COMPRESSOR

If the new value does not fall within the tolerance range of the previously transmitted value, an address is established for the new value. The address and value are inserted into a buffer and transmitted and stored in the memory in place of the previously transmitted value and its address. This design will result in either a reduction in bandwidth and the associated improved signal-to-noise ratio or will increase the amount of useful data that can be handled.

A prototype and two units capable of passing flight requirements have been constructed. Figure 3 shows the mechanical design and the complexity of the unit. Without integrated circuits, this equipment would not be feasible for flight use.

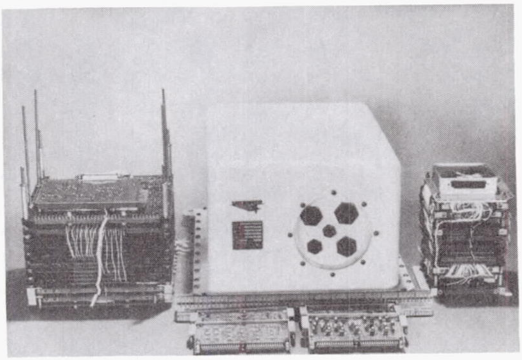

FIGURE 3. DATA COMPRESSOR

As shown in Figure 1, the 270 multiplexer requires many data input lines (up to 234). These inputs may be from remote parts of a stage on the vehicle. Integrated circuits result in improved reliability and reduction in weight of the electronic equipment, but some consideration must be given to the large amount of cabling mass with its many connections.

Figure 4 shows a new system under development that will group measurements in various locations of the vehicle stage. A central control unit will transmit a channel address on a single address line to remotely placed measuring sources or multiplexers. The source containing the data of the transmitted address will then return the measurement to the central unit. The various measurements will time-share a single address line and a single data line.

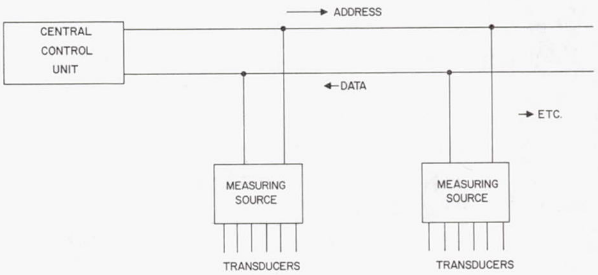

FIGURE 4. ADDRESSABLE TIME DIVISION DATA SYSTEM

Figure 5 shows the address system for the addressable time division data system. The central control unit generates the program in non return to zero (NRZ) form and converts it to a return to zero

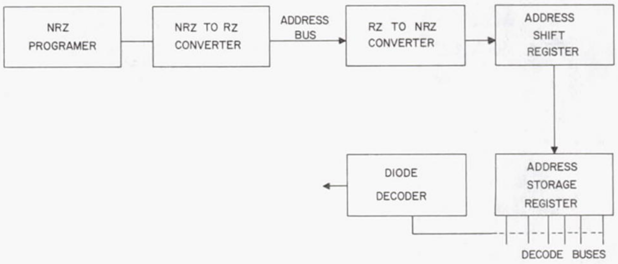

FIGURE 5. ADDRESS SYSTEM FOR THE ADDRESSABLE TIME DIVISION DATA SYSTEM

(RZ) form for transmission. In the measuring source the RZ address is used to obtain a clock signal and is converted back to NRZ and transferred into an address shift register and then to a storage register. A diode network decodes the address information in the shift register and closes the addressed data gate. Transmission to the measuring source in the RZ form eliminates the need for a separate clock or oscillator in each multiplexer.

A feasibility breadboard using integrated circuits has been constructed and tested. Additional work is now being done on the address recognition circuit and the complete design is being assembled in flight configuration for final testing.

Use of this system will greatly reduce the number of cable connections and cable mass for sensors on remote parts of a stage.

In Figure 1 all the data processed in the PCM/DDAS system are shown being transmitted either on the 600 kHz voltage controlled oscillator (VCO) line or by the PCM/RF transmitter. These data are sometimes required for use aboard the vehicle. A computer interface unit (CIU) is used to extract any desired data from the PCM/DDAS assembly, store it, condition it, and then present it to an onboard computer or other device when requested. This unit now exists in discrete form and is used in the Instrument Unit on the Saturn vehicle. Figure 6 is a block diagram of the system. Synchronization is provided by the PCM/DDAS assembly. An address is presented to the CIU by the computer, causing any previously stored information to clear. A data request signal is then applied. When the same address appears in the PCM/DDAS system as determined by the address comparators, the information for that address is transferred from the PCM/DDAS system into holding registers in the CIU and a data ready signal is transmitted to the computer. As long as the data request signal is present, the system will update itself every time the data are available. When the data request signal is removed, the last requested value will be stored and will be available to the computer until the address is changed.

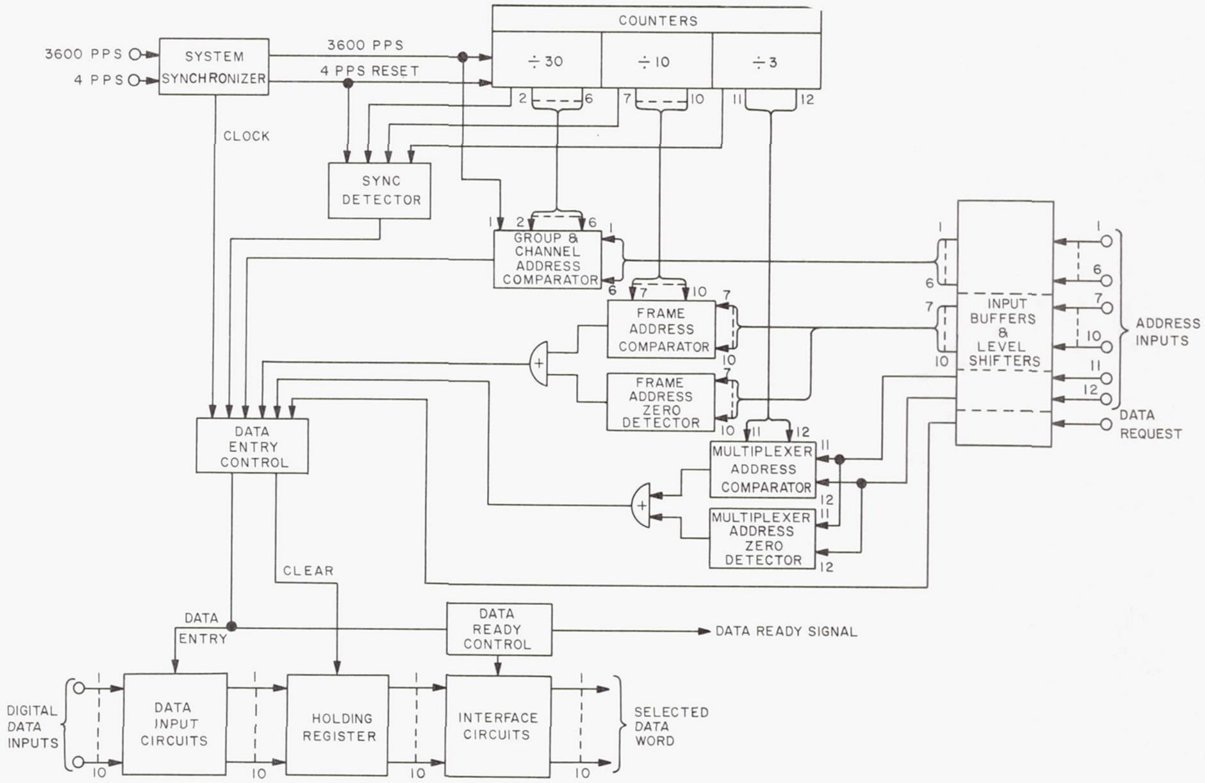

FIGURE 6. COMPUTER INTERFACE UNIT

An integrated circuit version is being developed that will improve the reliability and also permit more flexibility. The frequency of operation will be doubled to allow more data to be handled; pulse widths are being changed for use with equipment other than the onboard computer, such as an onboard data storage unit now being designed.

The new version will consist of monolithic integrated circuits except for the output stage and the power supply. The high voltage required at the output prohibits the use of present day integrated circuits.

Isolation between the PCM/DDAS system and the internal circuitry of the CIU will be accomplished by optics. This method will provide perfect isolation and yet will not involve transformers. The device to be used is an experimental Texas Instruments SNX1304 (Fig. 7) that consists of a gallium arsenide light emitter optically coupled to an integrated silicon photodetector feed-back-amplifier circuit. Common-mode rejection should also be very good.

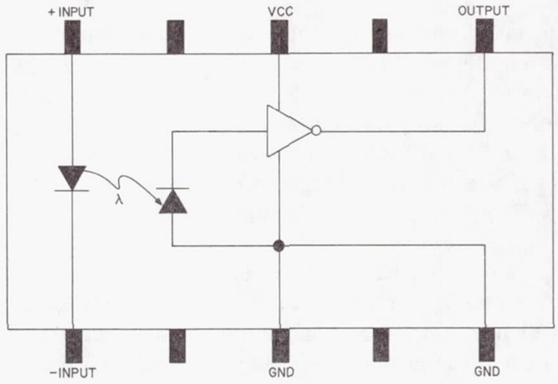

FIGURE 7. TEXAS INSTRUMENTS SNX1304 OPTOELECTRONIC PULSE AMPLIFIER

One of the subsystems shown in Figure 1, the PCM/DDAS subsystem, processes data from a very large number of sources. Its reliability is important in achieving overall reliability of the other subsystems that supply data to it. An integrated circuit version of this system has been designed that has essentially the same functional design as its discrete forerunner. Figure 8 is a block diagram of the system. The frequency of the clock will be doubled and the necessary

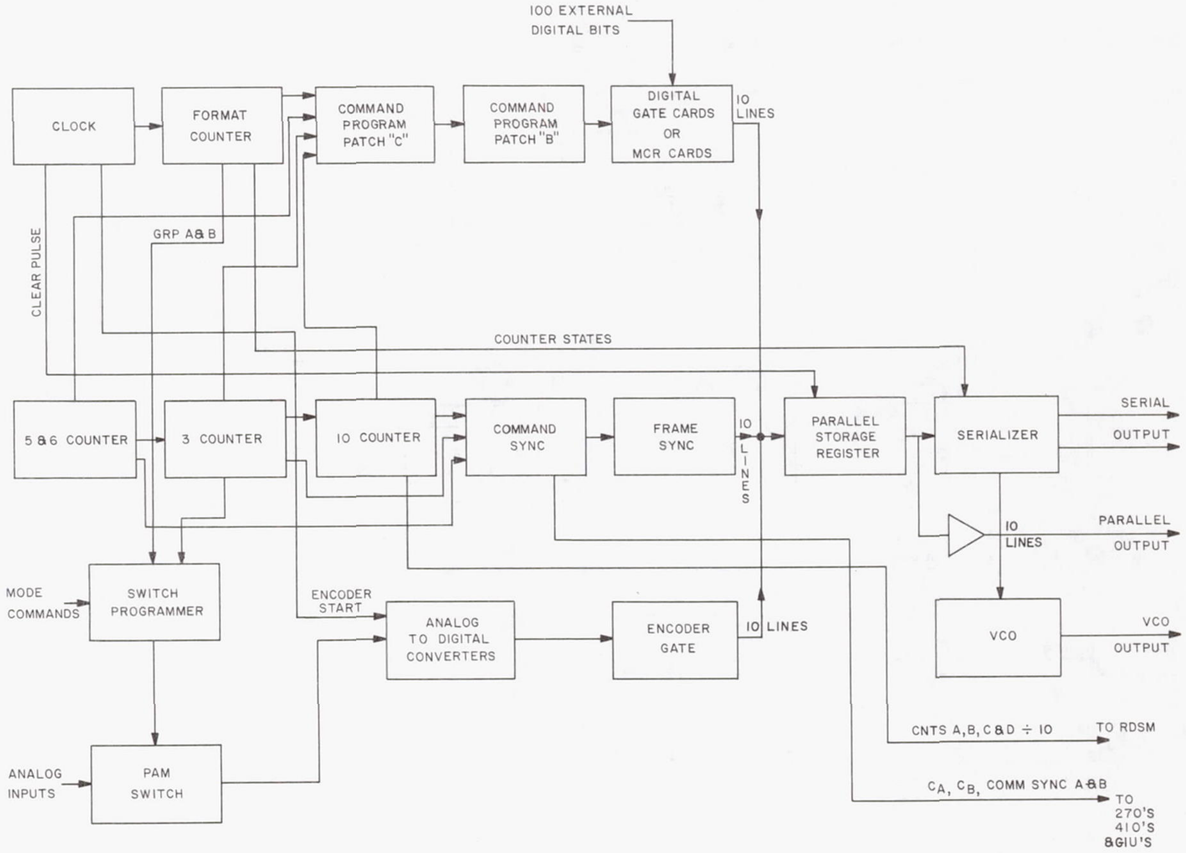

FIGURE 8. PCM/DDAS MODEL 302

circuitry will be added to permit doubling the amount of data that can be handled. The analog-to-digital (AD) converter will be left in its present discrete form because of the accuracy required; however, a program has been started to develop an integrated circuit AD converter.

Buffer amplifiers will be added to the parallel outputs in the integrated circuit version to provide better isolation between the serial and parallel outputs. In the present system, difficulty has been experienced when other equipment on the parallel outputs inserted spurious signals back into the serializer.

A new approach will be taken on some of the printed circuit boards in this development. The concentration of integrated circuits on a single layer or double-side printed circuit board is limited by the interconnecting lines rather than the components. Yet, many techniques used on multilayer boards are considered unreliable. Figure 9 is a cross section view of a board that should overcome most of the unreliable characteristics of multilayer boards. Manufacture of this board starts with a single layer board which is etched. The conductor is either copper or a weldable material, such as Kovar. Feed-through points are then etched through the epoxy insulator. The board is masked and the etched holes are filled by copper plating. The second layer circuit is next plated on, with masking, followed by an insulating layer. Feed-through points to the third layer are then etched, and so on for the remaining layers. The last insulating layer may be backed by a heat conducting material.

This type of fabrication yields a homogeneous mass for feed-through points that can be drilled for terminal posts. Interconnections of interlayers do not use up valuable components mounting space on the top layer. This process will be used on the main interconnection board, or motherboard, and a few of the component boards.

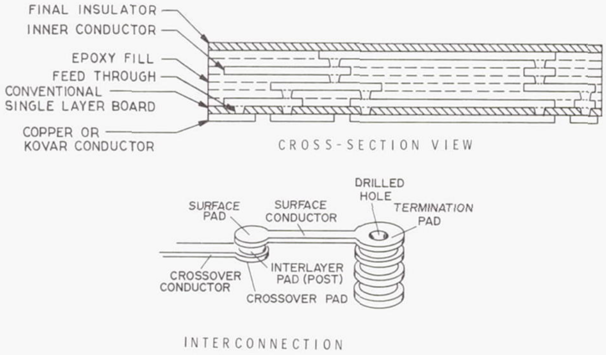

FIGURE 9. INTELLUX MULTILAYER BOARD

This development is an interim approach since the AD converter requirements push integrated circuitry capabilities at this time. The existing unit is shown in Figure 10. The redesign will be packaged entirely in the lower portion with the upper part removed. Even with this hybrid approach, the component count is reduced approximately 13:1, which should represent a considerable improvement in reliability.

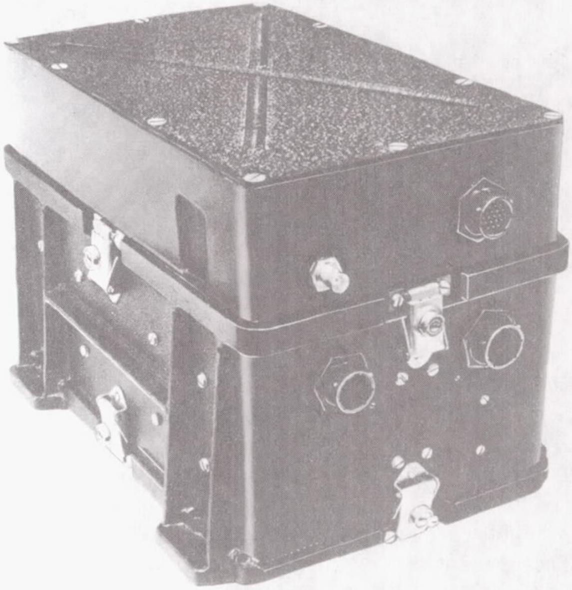

FIGURE 10. PCM/DDAS ASSEMBLY

The electrical design work is complete and a breadboard has been constructed and tested. Mechanical design is approximately 50 percent complete.

The 270 multiplexer requires a transformer to operate each data input channel. Transformers are considered one of the least reliable components of this system. In the present system, ten gates with their transformers are mounted on a printed circuit board. The buffer amplifier for the output of the gates and the transformer drivers are mounted on other boards. A new design using integrated circuits has been completed which will replace the transformers, the gates, the transformer drivers, and buffer amplifier. Figure 11 shows a comparison of the two versions. Gate drivers compatible with the

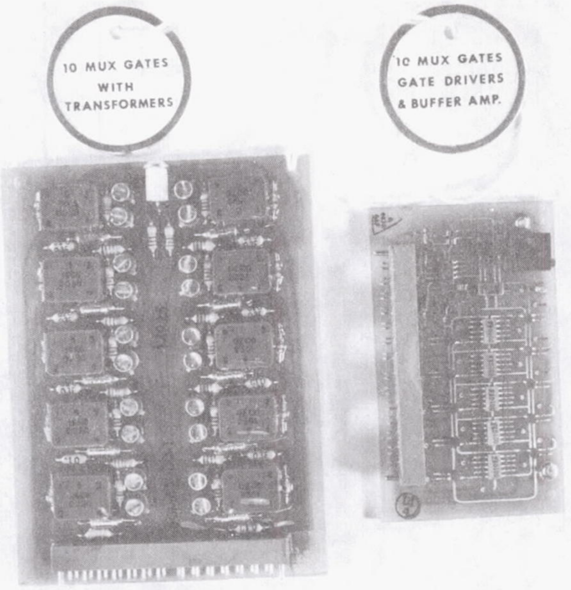

FIGURE 11. MULTIPLEXER GATES

Texas Instruments "51 series" were developed and are capable of driving either metallic oxide semiconductors (MOS) or conventional field-effect gates. The present circuit employs conventional field-effect transistors (FET's). This new circuit has an error of approximately 0.06 percent of full scale over the temperature range of 253° K to 358° K, of which the major portion is in the buffer amplifier. This compares with the discrete version.

Now that a suitable gate is developed, the entire 270 multiplexer is being redesigned. Electrical design and breadboarding have been completed. Mechanical packaging has begun and will serve as a test for new packaging concepts.

Integrated circuit designs are resulting in up to a 20:1 reduction in the number of components, one of the main contributors to improved reliability. Fewer components require fewer connectors; therefore, a different mechanical approach must be taken in packaging integrated circuit telemetry systems. The next figures show the result of a packaging study which seems to offer an improvement in reliability from a mechanical viewpoint.

The integrated circuits will be mounted on small boards up to 5 centimeters (2 inches) square (Fig. 12). These boards will be grouped according to their function and interconnected by welding with flexible cable. The boards will have a damping material on each side edge and will be stacked together, with the damping material providing the separation. Figure 13 shows the accessibility of the boards after interconnection.

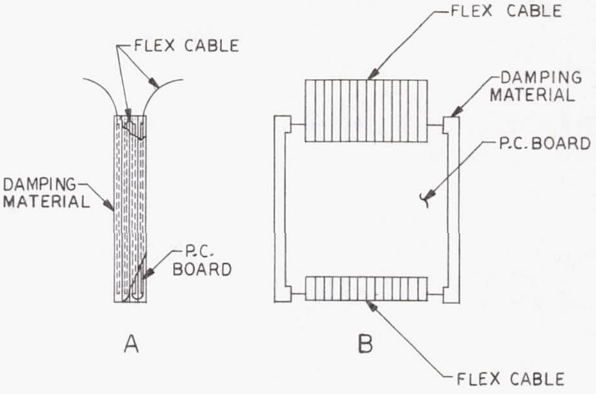

FIGURE 12. PRINTED CIRCUIT BOARD ASSEMBLY

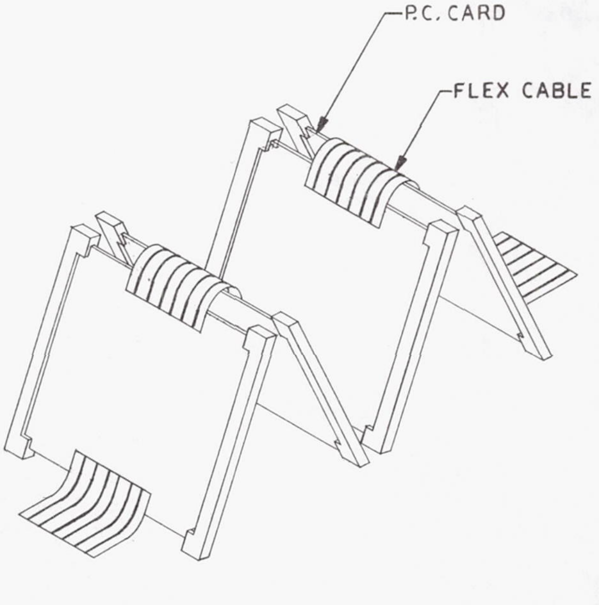

FIGURE 13. INTERCONNECTED PRINTED CIRCUIT BOARDS

Each group of boards will then fit tightly into a cavity as shown in Figure 14, and the groups will be interconnected by means of flex cable and a multilayer motherboard as shown in Figure 15. Holes in the motherboard over each cavity will allow a group to be extracted for troubleshooting. Full electrical checkout can also be accomplished before final assembly (Fig. 16) in the outer casting.

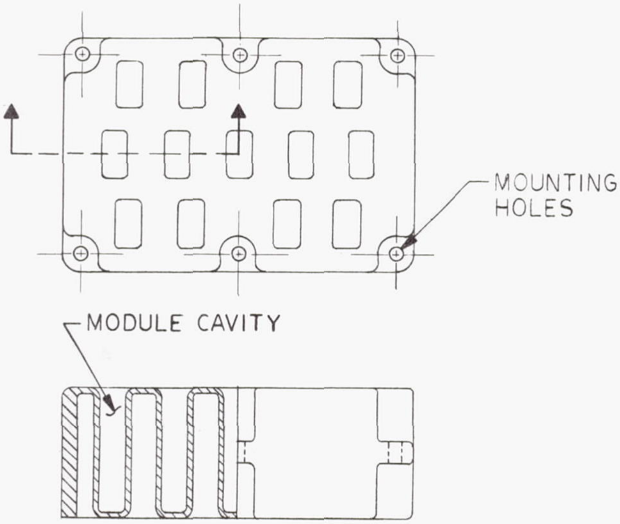

FIGURE 14. ELECTRONICS CHASSIS

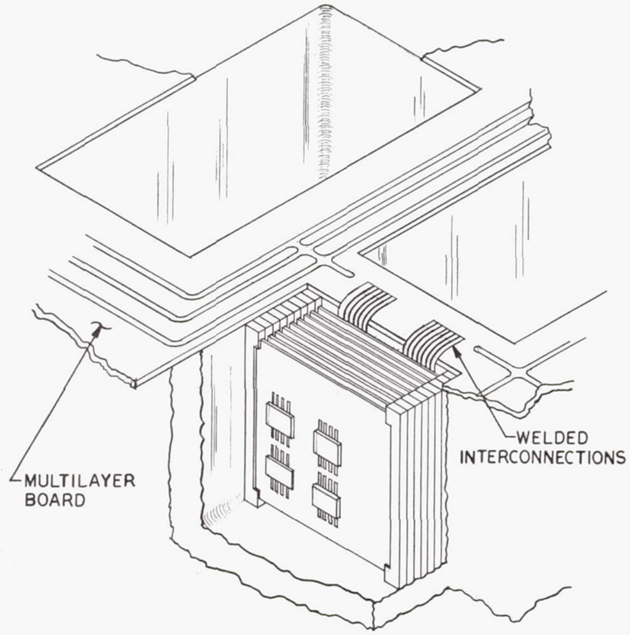

FIGURE 15. ELECTRONICS CHASSIS ASSEMBLY TECHNIQUE

This mechanical design should provide a reliable packaging technique and yet be easily accessible for electrical checkout.

Often it is desirable to prove out a logic design before incorporating it into a system. An integrated circuit patch board is being built for this purpose.

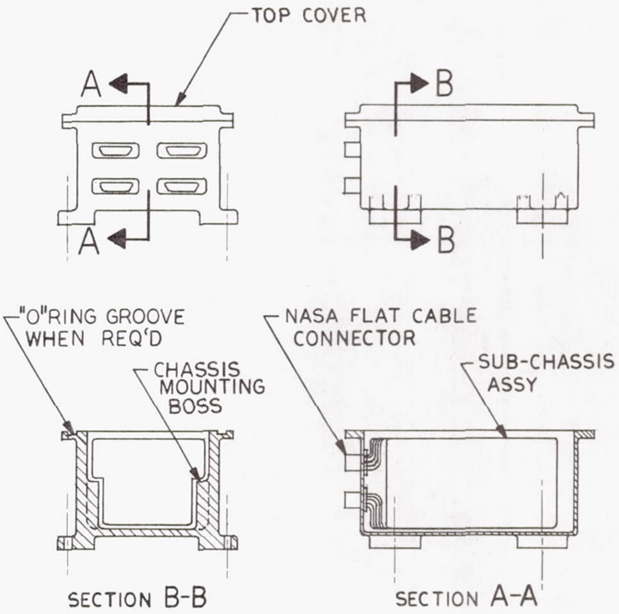

FIGURE 16. FINAL ASSEMBLY

Integrated circuits that will perform almost any logic function are being wired into a rack and the signal inputs and outputs are connected to patch sockets on a panel (Fig. 17). Figure 18 is a front view of the

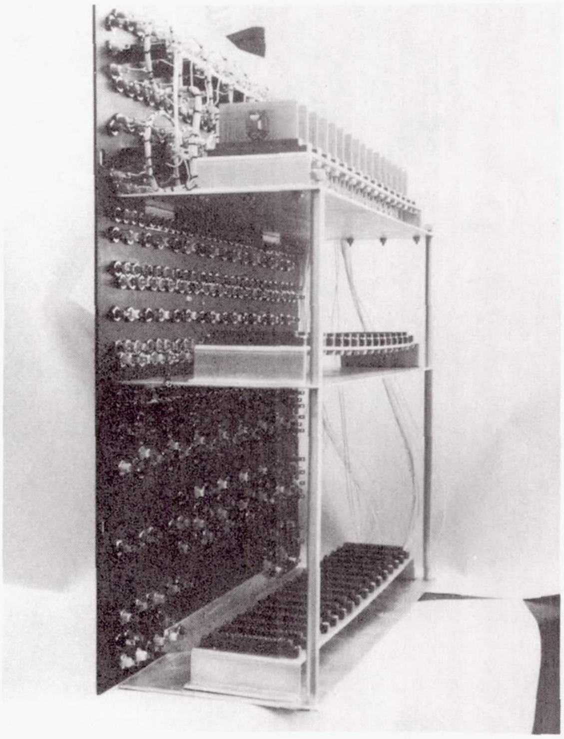

FIGURE 17. INTEGRATED CIRCUIT PATCH PANEL (REAR VIEW)

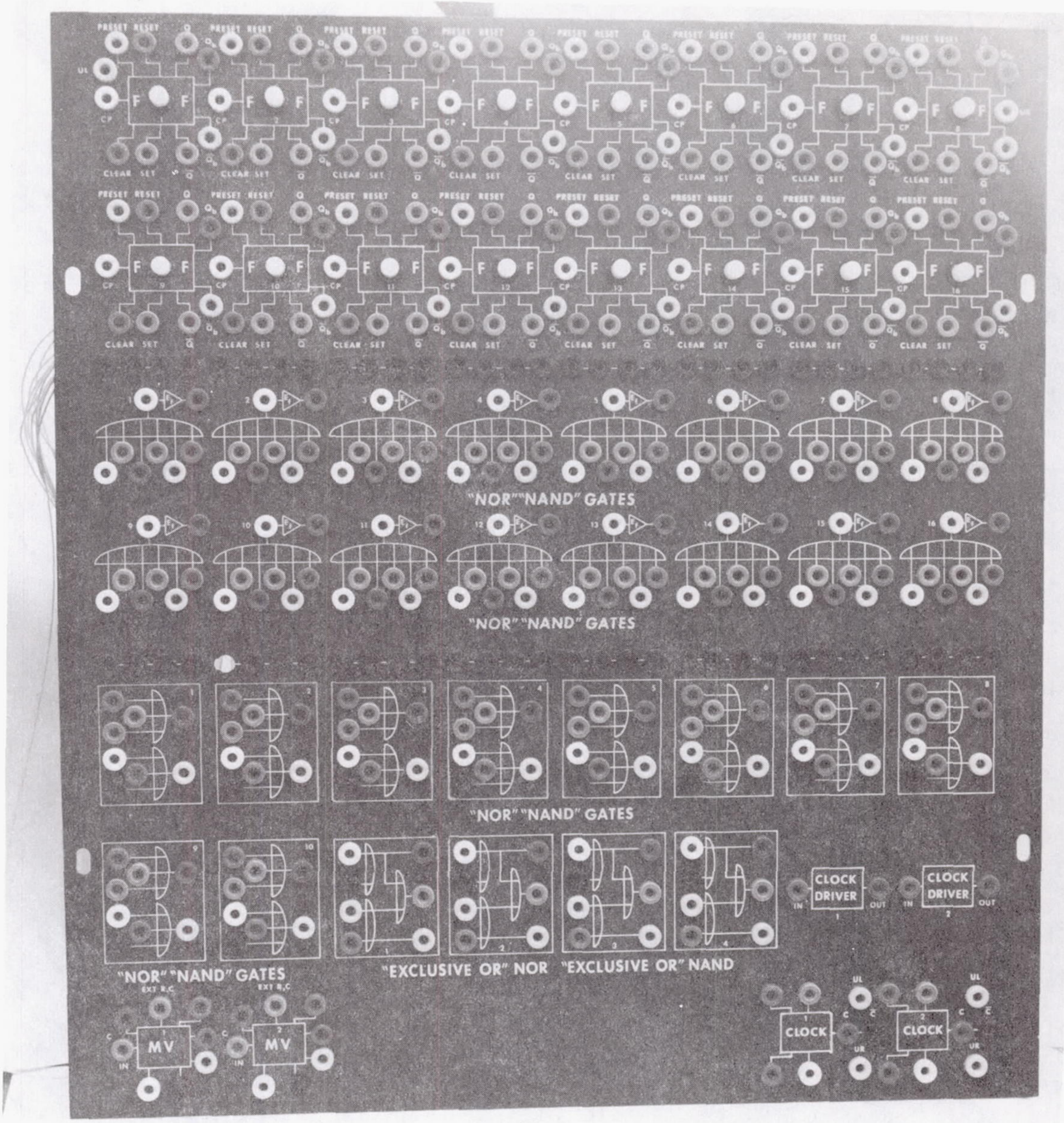

FIGURE 18. INTEGRATED CIRCUIT PATCH PANEL (FRONT VIEW)

panel. Transistorized indicator lights are connected to each flipflop to indicate its state. With the use of patch cords, a simple logic circuit can be checked in a very short time.

4

MATERIALS RESEARCH AT MSFC

July 28, 1966

By

Charles E. Cataldo
James E. Curry
Raymond L. Gause
James E. Kingsbury
Eugene C. McKannan

Page
Intentionally
Left Blank

Page
Intentionally
Left Blank

CONTENTS...

LIST OF TABLES

LIST OF ILLUSTRATIONS

CONTENTS (Continued)...

Page

STRESS CORROSION

by Charles E. Cataldo

LIST OF TABLES

LIST OF ILLUSTRATIONS

Page

EVALUATION OF MATERIALS BY NON-DESTRUCTIVE MEANS

by Raymond L. Gause

LIST OF TABLES

LIST OF ILLUSTRATIONS

MATERIAL DESIGNS FOR ELECTRONIC APPLICATIONS

by Eugene C. McKannan and James E. Curry

Page

LIST OF TABLES

LIST OF ILLUSTRATIONS

Page

NON-METALLIC MATERIALS

by James E. Curry

LIST OF TABLES

LIST OF ILLUSTRATIONS

CONTENTS (Concluded) . . .

INTRODUCTION TO MATERIALS RESEARCH AT MSFC

By

James E. Kingsbury

The overall mission of the Materials Division is to support the Saturn Program. In addition, progress continues on actively pursuing the development of inflight experiments necessary to support the Apollo-Saturn Program and the Apollo Applications Program. Included in this effort is the responsibility to anticipate future needs of the space exploration effort. This work permits the investigation of a variety of potential materials developments, and some results of this effort will be discussed. The complexities involved in a successful materials development program are not always apparent. Materials that take months or years to develop are quickly accepted. The technology and experimentation required to develop a reliable adhesive will first require considerable design time and learning the proper adhesive application process. Likewise, materials with induced stresses and in corrosive environments present a challenge to the Materials Division to develop new materials and applications to prevent stress-corrosion failures. Thus, the elimination of stress-corrosion failures depends partially on decreasing the stress produced by forming, joining, and material assembly operations to include isolating the materials from a corrosive environment. For the present, efforts must be concentrated on eliminating these failures by first understanding the fundamental mechanisms that contribute to the stress-corrosion failures. The Materials Division also has the advantage of being able to capitalize on the available industrial research potential to achieve these goals.

Page
Intentionally
Left Blank

DIFFUSION BONDING OF DISSIMILAR METALS

By

Charles E. Cataldo

SUMMARY

A study of metal joining methods led to the diffusion bonding process using diffusion bonding aids. The diffusion bonding process and construction of diffusion bonded dissimilar metal joints are briefly described. Construction of four tank assemblies by the diffusion bonding process was followed by cycling and burst tests to determine the strength of the bonded joints. Test results on the four tanks are discussed and related to the general use of diffisuion bonded alloy combinations.

INTRODUCTION

To provide a potential means of reducing the weight and realizing certain other advantages in propellant ducting components in the Saturn V vehicle, a reliable method for joining aluminum alloy 2219 to type 321 stainless steel in cylindrical form was needed. To meet this objective, an experimental program was conducted by The Boeing Company, Seattle, Washington, under the technical direction of the Materials Division of the Propulsion and Vehicle Engineering Laboratory. The program was to provide a joint that could be bonded as a unit and then welded into the duct system without the use of mechanical joints, as shown in Figure 1.

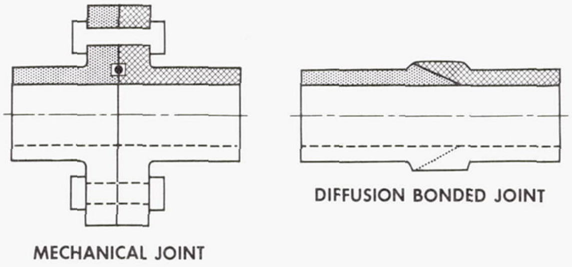

FIGURE 1. SCHEMATIC OF MECHANICAL AND DIFFUSION BONDED JOINTS

DIFFUSION BONDING

JOINING METHODS

A number of potential joining methods and the problems associated with each of these methods were studied. The most promising methods, including brazing, fusion welding, and diffusion bonding were selected for limited evaluation by metallographic examination, mechanical property tests, and corrosion tests. The two most promising methods, fusion welding and diffusion bonding, were then further evaluated by assembling and testing sub-scale 20.8-cm (8-in.) diameter burst test cylinders. The most promising method selected from this phase was diffusion bonding. This method was then used to fabricate 50.8-cm (20-in.) diameter tank assemblies under production conditions. Thermal shock, pressure cycling, leak tests, and burst tests were conducted at room temperature and at 77.5°K (-320°F) on the 50.8-cm (20-in.) diameter tank assemblies.

Although use of the brazing or fusion welding process was considered technically feasible for making tubular joints, these processes were found to have limitations because embrittling layers were formed at the joint interfaces. Widely different physical properties, such as the coefficient of thermal expansion and melting, would be expected to present metallurgical and processing difficulties, particularly when large diameter tank assemblies are required. The diffusion bonding process offered the most potential for making the desired joints.

DIFFUSION AIDS

Since high deformation would be required when bonding materials in their natural state, the use of diffusion aids was evaluated in an attempt to obtain good bonds without excessive deformation of the aluminum alloy member. Copper and silver plating diffusion aids were evaluated. Silver plating, in conjunction with conventional pretreatments designed to insure proper plating adherence, provided optimum joint characteristics. Tests demonstrated that this plating has excellent resistance to oxidation and a high resistance to contamination.

DIFFUSION PROCESS

Preproduction development work was conducted on flat specimens to establish basic processing parameters. The significant processing parameters that provided the best strength and ductility were as follows: (1) The 321 stainless steel and 2219 aluminum alloy components were electroplated with 0.00127-cm (0.0005-in.) thick silver. (2) Just prior to bonding, the electroplated surfaces were abraded lightly with 240-grit sandpaper and then cleaned with acetone. (3) Using an air atmosphere furnace, specimens were held at 533°K - 589°K (500°F - 600°F) for two to four hours under pressure sufficient to cause compressive yielding that was obtained using a pressure of $1.38\text{-}1.72 \times 10^8$ N/m^2 (20-25 ksi). Deformation occurs in the aluminum thickness and no significant deformation occurs in the stainless steel. Single and double lap shear specimens were tested at room temperature, at 77.5°K and at 20.4°K (-320° F and -423° F). Test results are shown in Table I. Typically, shear strength at room temperature exceeds 1.033×10^8 N/m^2 (15 000 psi), with 20 to 30% increases, respectively, at 77.5°K and at 20.4°K (-320°F and -423°F).

TABLE I. SUMMARY OF MECHANICAL TEST RESULTS

Type Specimen	Stress, N/m$^2 \times 10^8$ (psi)		
	298°K (77°F)	77.5°K (-320°F)	20.4°K (-423°F)
Double Lap	1.000 (14 500)	1.085 (15 750)	1.410 (20 450)
	1.092 (15 880)	1.279 (18 550)	1.420 (20 600)
	0.984 (14 280)	1.441 (20 900)	1.655 (24 000)
Single Lap	1.219 (17 690)	1.310 (19 000)	1.371 (19 900)
	1.131 (16 410)	1.263 (18 310)	1.442 (20 930)
	1.090 (15 800)	1.603 (23 250)	1.120 (16 250)

TANK CONSTRUCTION AND TESTING

The processing parameters established during the preproduction development were applied in making 50.8-cm (20-in.) diameter tank assemblies. Pressure was controlled by using a differential thermal expansion apparatus. Figure 2 is a simplified schematic tooling arrangement. The inner mandrel of the 321 stainless steel has a linear thermal expansion between room temperature and 755° K (900°F), approximately 50% greater than that of the T-1 steel outer mandrel. Calculations revealed that the 50.8-cm (20-in.) inner stainless steel ring has a free diametric expansion approximately 0.762 cm (0.30 in.) greater than the low alloy steel restraining ring at 589°K (600°F). However, during actual bonding, the compressive pressure from the restraining ring would prevent this total expansion from occurring; likewise, the bonding pressure places the external alloy steel ring in hoop tension and results in expanding to a greater diameter than would occur on its free expansion at 589°K (600°F). Calculations showed that to create an internal bonding pressure which approximates the compressive yield strength of the 2219-T62 alloy, the outer restraining ring must be installed using a shrink-fit. This interference fit is required to provide the preload to supplement the pressure from the differential expansion of the tooling.

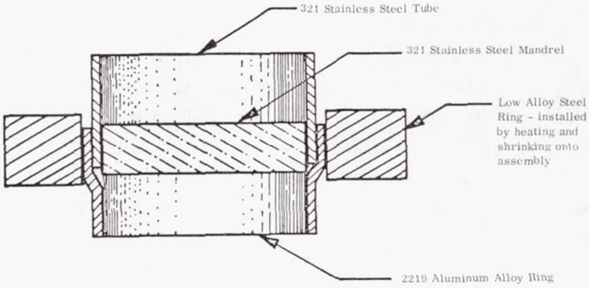

FIGURE 2. DIFFERENTIAL THERMAL EXPANSION TOOLING ARRANGEMENT FOR TUBULAR JOINTS

Figure 3 shows a typical 50.8-cm (20-in.) diameter transition joint. Four transition joints were prepared and tested by helium leak checking and thermal shocking between room temperature and 77.5°K (-320°F). Each unit successfully passed the thermal shock test which consisted of ten cycles between room temperature and 77.5°K (-320°F). Each transition joint was welded into a tank as shown in Figure 4, and a helium leak check was made.

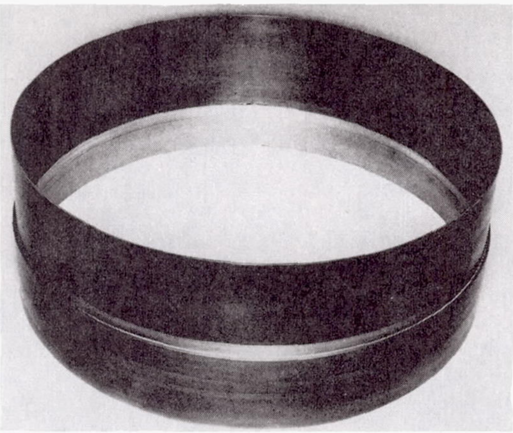

FIGURE 3. 50.8-cm (20-in.) DIAMETER 2219-321 TRANSITION JOINT

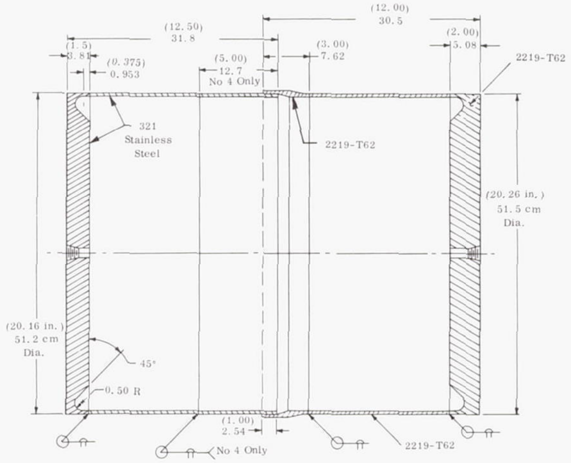

FIGURE 4. CROSS SECTION OF TEST TANK

The tanks were leak tight except for tank assembly number 2, which exhibited a leak in the joint. This leak was attributed to insufficient pressure during the bonding cycle because of shrinkage of the inner mandrel during processing. This situation was corrected on the third and fourth assemblies.

The tanks were pressure cycled at room temperature and 77.5°K (-320°F) followed by burst testing. The chart in Table II summarizes the test results. The first tank successfully passed pressure cycling of two-hundred cycles at 2.41×10^6 N/m^2 (350 psig). The tank failed at 3.24×10^6 N/m^2 (470 psig) in the room temperature burst test. The second assembly was pressurized with liquid nitrogen and failed during the 82nd pressure cycle at 2.41×10^6 N/m^2 (350 psig).

TABLE II. SUMMARY OF 50.8-cm (20-in.) DIAMETER TANK TESTS

Tank No.	Test Method	Cycle Pressure N/m$^2 \times 10^6$ (psig)	Number Cycles	Burst Pressure N/m$^2 \times 10^6$ (psig)	$\frac{Pr}{t}$ [1] N/m$^2 \times 10^8$ (psi)
1	Water at Room Temperature	2.41 (350)	200	3.24 (470)	2.590 (37 600)
2	LN$_2$ (-320°F) 77.5°K	2.41 (350)	85 (Failed)	-	1.930 (28 000)
3	LN$_2$ (-320°F) 77.5°K	2.41 (350)	92 [2]	3.48 (505)	2.785 (40,400)
4	LN$_2$ (-320°F) 77.5°K	2.135 (310) 1.655 (240)	60 140	4.62 (670)	3.695 (53 600)

[1] Based on 0.318-cm (0.125-in.) Aluminum Wall Thickness

[2] Cycling Pump Failed on 92nd Cycle

This tank had only compressively yielded 0.0025-0.0050 cm (0.001-0.002 in.) because of insufficient pressure during bonding. This was attributed to shrinkage of the inner mandrel during the processing of assemblies numbers 1 and 2 as discussed previously. Earlier work had indicated that at least 0.010 cm (0.004 in.) compressive yielding of the aluminum was required for sound joints.

The third tank passed the pressure cycling test using liquid nitrogen as the pressurizing medium. The tank had been subjected to 92 cycles at 2.41×10^6 N/m^2 (350 psig) when the cycling pumps failed. The cycling test was terminated at that point, and the burst test was conducted. The tank failed at 3.48×10^6 N/m^2 (505 psig) at 77.5°K (-320°F).

The fourth and final tank assembly was fabricated using the experience gained from the first three assemblies, and hence provided the best results. This assembly successfully passed a two-step cycling test of 60 cycles at 2.135×10^6 N/m^2 (310 psig) and 140 cycles at 1.655×10^6 N/m^2 (240 psig) using liquid nitrogen as the pressurizing medium. The tank ruptured at 4.62×10^6 N/m^2 (670 psig) during the burst test. This pressure corresponds to a hoop stress of 3.695×10^8 N/m^2 (53 600 psig).

Peel loading caused by deformation of the aluminum alloy contributed to failure initiation in all cases. Redesign of the joints to provide a slight increase in wall thickness of the aluminum alloy member should significantly decrease the peel loading and result in higher burst pressures. By proper joint design, the joint can be made to be as strong as the base metal.

Additional diffusion bonding studies are being conducted on other alloy combinations. The influence of the primary diffusion parameters of time, temperature and pressure will be studied along with examining the process variables such as surface preparation, atmosphere and intermediate materials. Both solid state joining and press and roll bonding are being studied for the six combinations in Table III.

CONCLUSION

Based on studies that have been completed to date, all alloy combinations listed in Table III can be bonded without surface coatings or intermediates; however, better joint strength and metallurgical characteristics can be obtained by using diffusion aids. Designers should take advantage of this previously unfeasible process of joining dissimilar metals (Table IV). Experience gained to date has indicated that there are only few limits on the alloy combinations that can be joined by diffusion bonding.

TABLE III. DISSIMILAR ALLOY COMBINATIONS

(1) 2219 Aluminum Alloy to 5 Al - 2.5 Sn Titanium Alloy

(2) 2219 Aluminum Alloy to 321 Stainless Steel

(3) 7106 Aluminum Alloy to 321 Stainless Steel

(4) Inconel 718 Alloy to 321 Stainless Steel

(5) 8 Al - 1 Mo - 1V Titanium Alloy to 321 Stainless Steel

(6) Inconel 600 Alloy to 8 Al - 1 Mo - 1Y Titanium Alloy

TABLE IV. ADVANTAGES AND DISADVANTAGES OF DIFFUSION BONDED DISSIMILAR JOINTS

Advantages

- Weight Saving
- No Seal Problem
- No Distortion during Fabrication
- Heat Treated or Cold Worked Temper can be Retained
- Control over Formation of Brittle Intermediate Phases
- Compact Design

Disadvantages

- Close Control over Processing Parameters Required
- Corrosion Possible if Joint not Protected

STRESS CORROSION

By

Charles E. Cataldo

SUMMARY

This article recounts briefly some of the more critical stress-corrosion failures that have been experienced at Marshall Space Flight Center and the corrective action taken. Some of the recent stress-corrosion studies are described and preliminary results tabulated. Specific problems described are the H-1 Engine LOX dome, the pneumatic line fitting sleeve problems and the more recent problem with wave springs used on MF-flared tube fittings. The use of nitric oxide in preventing stress-corrosion failures in titanium tanks is also discussed.

SATURN VEHICLE STRESS-CORROSION FAILURES AT MSFC

Stress-corrosion failures of high-strength metal aerospace components have occurred on the H-1 engine. The LOX dome is the forward closure on the H-1 engine combustion chamber through which liquid oxygen enters the injector (Fig. 1, 2). The dome was fabricated initially from a 7079-T6 aluminum die forging. In 1960 a dome was found cracked on the Saturn I, and later other domes cracked. Figure 3 shows a typical crack in one of these domes, and for a comparison, Figure 4 shows a dome exposed to salt spray for 24 days. The intergranular stress-corrosion cracking that is typical of most high strength aluminum alloys is shown in Figure 5.

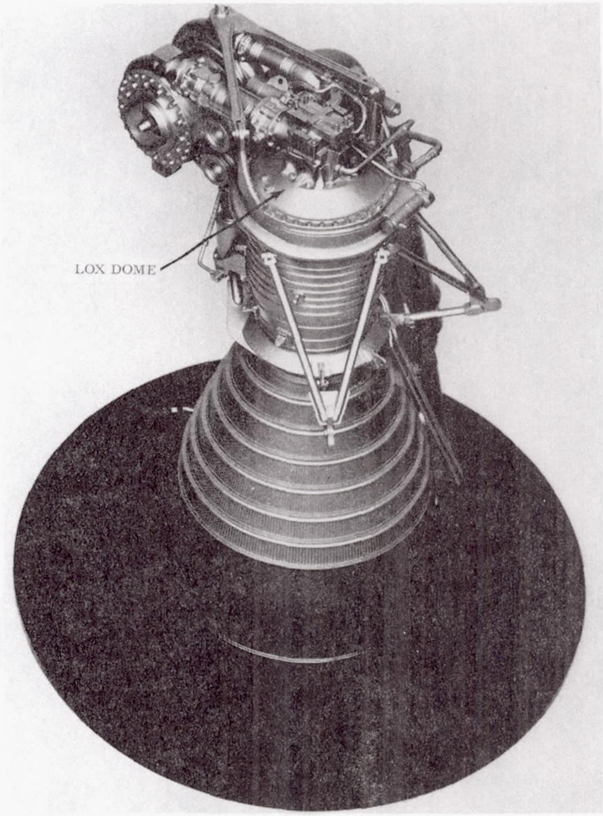

FIGURE 1. LOX DOME ON H-1 ENGINE

Other than having a susceptible material to begin with, three conditions are necessary for stress-corrosion failures to occur. These are tensile stresses on the surface, a corrosive medium and time for the failure to develop. A check of the manufacturing sequence of this LOX dome indicated that the material was forged, heat treated and machined. After being heat treated, this type of forging is in a highly stressed condition because of its forged shape and the quench operation. Generally, such a forged part contains high residual compressive stresses on the surface and high tensile stresses within. This results from rapid cooling of the surface in the quench process and differential cooling of the center of the cross section. The center of the forging cools last, and contraction tends to pull the surface and produce compressive stresses. Subsequent machining removes the compressively stressed material and exposes material under high tensile stresses. These factors, coupled with sufficient time and exposure to atmospheric conditions that constitute the corrosive medium, are likely to result in stress-corrosion failure.

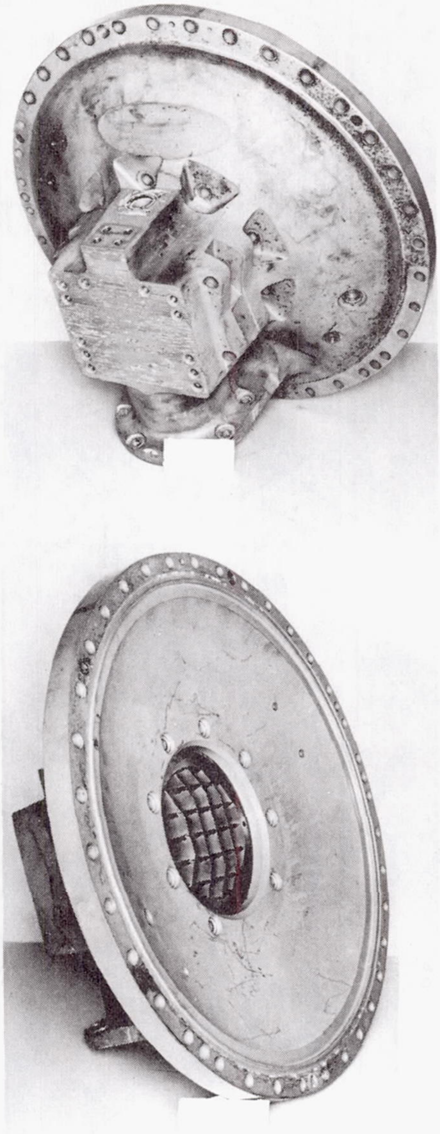

FIGURE 2. TWO VIEWS OF H-1 ENGINE LOX DOME

The LOX domes were reworked following the initial failures. The modification consisted of (1) stripping the anodized coating, (2) reheat-treating to T6 condition, (3) finish machining to correct any out-of-tolerance condition resulting from heat treatment, (4) shot peening surfaces and pressure rolling inside of bolt holes, (5) honing the sealing surfaces, and (6) re-anodizing and painting.

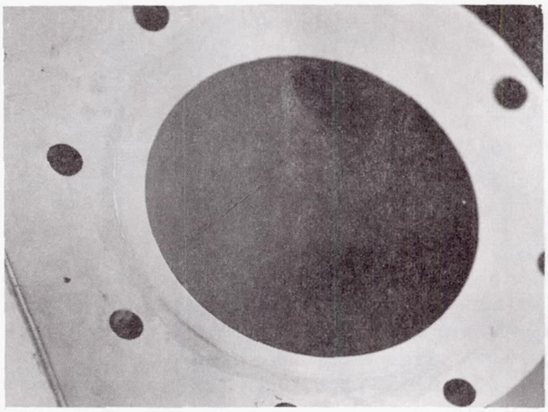

FIGURE 3. CRACK IN LOX INLET OF DOME (SERVICE FAILURE)

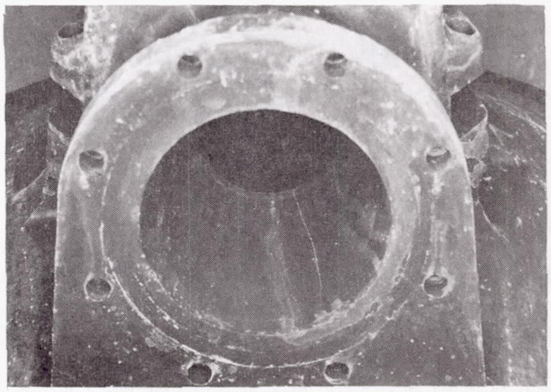

FIGURE 4. CRACK IN LOX INLET OF LOX DOME (SALT SPRAY EXPOSURE)

FIGURE 5. MICROSTRUCTURE OF CRACK IN DOME FROM ENGINE (MAG. 200X)

Since the 7079-T6 alloy was known to be highly susceptible to stress-corrosion cracking, steps were taken to initiate fabrication of the domes from 7075-T73 aluminum alloy that is practically immune to stress-corrosion cracking. Reworking the 7079-T6 LOX domes prevented failure until one of these modified domes failed on the Saturn I vehicle SA-7 (1964). By this time the domes being fabricated from 7075-T73 were ready for use. These new domes were immediately installed and have been satisfactory to date.

The stress-corrosion failures of the sleeves used on flared pneumatic tube fittings and on the wave springs used on MF type fittings were similar, because in both cases the failures were caused by stresses applied by torquing the fittings rather than by the residual stresses caused by the heat-treating operation.

The tubing sleeves (Fig. 6) were fabricated from AM-355 stainless steel. Sleeves of this design have been made from a variety of materials for several years and problems with cracking have been attributed to various reasons such as poor machining techniques, improper fit, inclusions in the material and poor flaring techniques. In this case, however, the problem was attributed to stress-corrosion cracking.

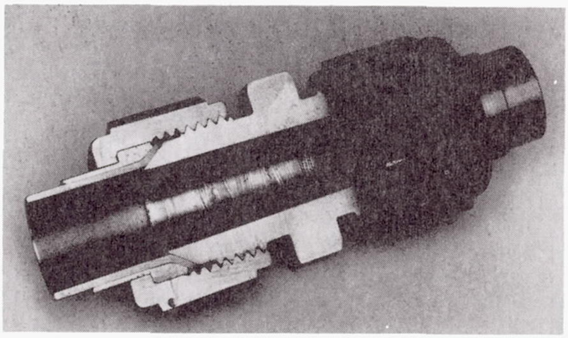

FIGURE 6. CROSS SECTION OF FLARED TUBE FITTING

The typical failure mode of the tubing sleeves is shown in Figure 7. AM 355 stainless steel is a precipitation hardening alloy, and under certain conditions is quite susceptible to stress-corrosion cracking. The heat treatment used is the most important factor in controlling this phenomenon. An intensive stress-corrosion study of the sleeve material revealed that the alloy was susceptible to stress-corrosion cracking in the particular heat treatment that was being used (SCT 1000), and was almost immune to stress-corrosion cracking in the fully hardened (FH) SCT 1000 heat treatment that involved an additional step in the heat treatment and minimized the formation of carbide particles in the grain boundaries of the material.

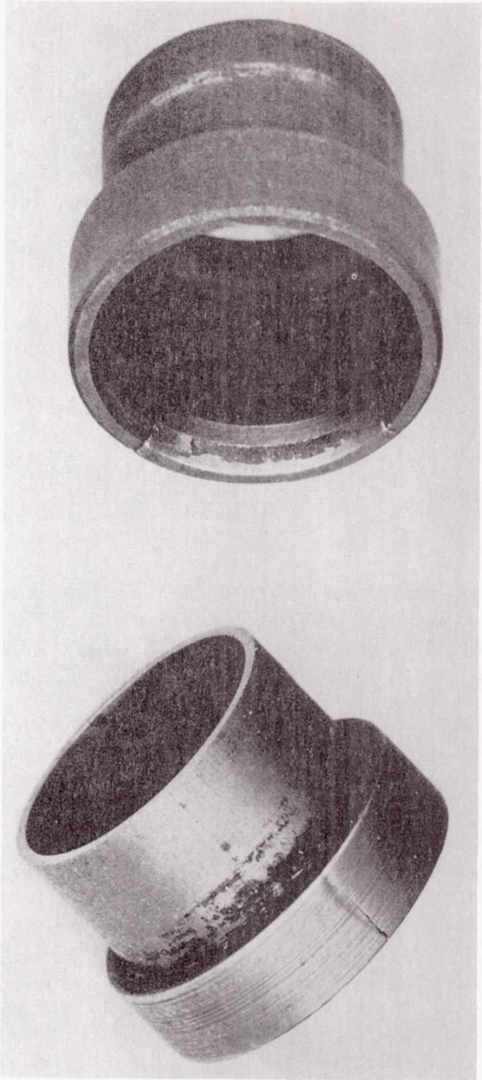

FIGURE 7. CRACKS IN SLEEVES REMOVED FROM SERVICE

A comparison of the microstructure of SCT-1000 and FH SCT-1000 is shown in Figure 8. The results

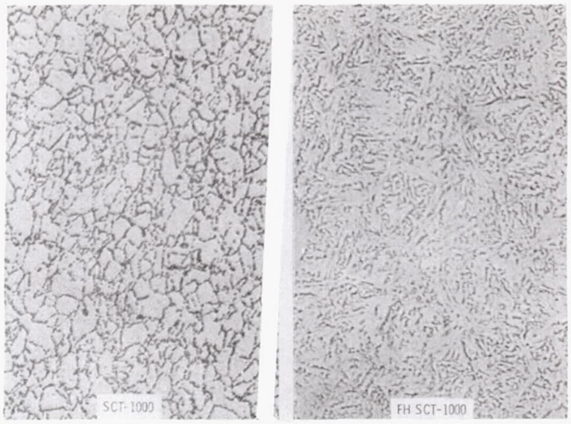

FIGURE 8. MICROSTRUCTURES OF HEAT TREATED AM 355 (MAG. 500X)

of a study on various heat-treated conditions under different exposure environments are given in Table I. All existing sleeves for the Saturn vehicle were reheat-treated to the fully hardened (FH) SCT-1000 heat treatment with very good results.

TABLE I. STRESS CORROSION EVALUATION OF AM-355 STAINLESS STEEL

Heat Treatment	Stress % Y. S.	Failure / Tests	Days to Failure Range
SCT 850	25-100	12/12	2-114
SCT 1000	25-100	14/24	30-156
FH SCT 850	25	0/6	NF (180)
	50-100	7/18	151-152
FH SCT 900	25-50	0/6	NF (180)
	75-100	3/6	97-156
FH SCT 950	25-100	0/12	NF (180)
FH SCT 1000	25-100	0/24	NF (180)

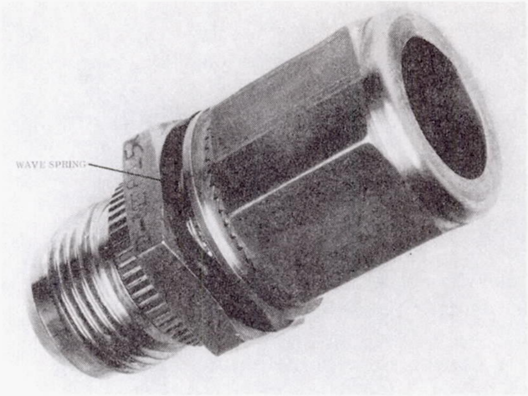

FIGURE 9. USE OF WAVE SPRING IN MF FITTING

Figure 9 shows the use of a wave spring in an MF type fitting. The spring is used to force a retainer with ratchet teeth against the fitting nut to maintain a preset torque. The wave spring problem was similar to the sleeve problem in that tensile stresses were introduced into the part by torquing the flared tube fitting. A precipitation-hardening alloy (17-7pH) was involved. Although tests indicated that the stress-corrosion susceptibility of this alloy could be greatly improved by a different heat treatment, the treatment used reduced the strength to a point where it could not be used for this application. The problem was solved by changing to Inconel-718 alloy that was not susceptible to stress-corrosion cracking.

STRESS CORROSION FAILURE STUDIES

The Materials Division has applied maximum effort in the study of the stress-corrosion susceptibility of the alloys presently being used in the Saturn V vehicles and other newer alloys being developed. Contractors were requested to report the use of all alloys susceptible to stress-corrosion cracking. Drawings of these parts have been studied and changes have been recommended where necessary.

In the past year many aerospace organizations have increased their work in stress-corrosion studies. Although few conclusive facts have been established regarding the true mechanism of this phenomenon, the fact that more people have become aware of the problem has had a major effect in reducing failures. Thus stress corrosion can be prevented by careful attention to the choice of alloys and tempers and especially by strict adherence to good design and assembly practices.

The four primary conditions that contribute to stress-corrosion failures were used as guidelines to formulate the matrix of the stress-corrosion evaluation program within the Materials Division.

These conditions are (1) susceptible material, (2) tensile stresses, (3) environment, and (4) time. The combination of these conditions will result in stress-corrosion failures, providing the relative weight of just the right combination is sufficient. For most of our space vehicle applications the variables of corrosive environment and time cannot be regulated. Therefore, considerable emphasis has been placed on controlling the materials and the tensile stresses involved.

As was indicated in the examples of the stress-corrosion problems that have occurred in the Saturn S-I and S-IC stages, these particular problems were solved by either changing the alloy or the heat treatment. Many potential stress-corrosion problems have been prevented by the appropriate use of coatings, plating, and other surface treatments. This is the simplest form of protection where susceptible alloys must be used because of other considerations. The commonly used treatments include shot peening, galvanic type coatings, organic paints, anodic type coatings and combinations of these processes.

In a recent study, 15 protective systems were selected for evaluation in preventing or reducing the susceptibility of stress corrosion of aluminum alloys. Specimens of alloys known to be highly susceptible to stress corrosion (2014-T651, 7079-T651, 2024-T351 and 7178-T651) were coated with various protective systems, stressed and exposed to four environments, i.e., alternate immersion in a salt solution, an industrial site and two seacoast environments. The overall results are shown in Table II.

TABLE II. SUMMARY COMPARISON OF THE EFFECTIVENESS OF COATINGS

Coating System:

<u>Recommended Systems</u> (0 to 5 Percent Failures)

- Shot Peen + Epoxy
- 7072 Metallized + Epoxy
- 7072 Metallized

<u>Restricted Applications</u> (35 to 45 Percent Failures)

- Zinc Electroplate
- Shot Peened
- Primer + Epoxy
- Primer + Polyurethane
- Primer + Al Pigmented Epoxy + Epoxy

<u>Not Recommended</u> (50 to 97 Percent Failures)

- Zinc Rich Paint
- Epoxy
- Polyurethane
- Zinc Chromate Primer
- Sulphuric Acid Anodize
- Hard Anodize

The best protection appears to be the use of a combination of shot peening or metallizing in addition to a top coat of epoxy-polyamide. Of the galvanic type coatings, 7072 metallizing and zinc electroplate, the 7072 metallized aluminum is the preferred coating, but galvanic coatings have many manufacturing disadvantages. Shot peening is capable of providing good protection, provided that all the tension surfaces that are or may be exposed are adequately peened, and severe surface corrosion is not encountered. If surface corrosion is expected, additional protection against general corrosion must be provided to prevent penetration of the compressive layer produced by peening. Shot peening appears most effective when performed after the sustained tension has been introduced. Good protection is also possible from the use of chromate primers plus organic coatings such as epoxy-polyamide or polyurethane paint, providing the paint envelope remains intact and is not broken by inadvertent mechanical damage. The epoxy is the better of the two coatings. Anodic films such as sulphuric acid anodizing are not effective methods of preventing stress-corrosion cracking.

TESTING FOR STRESS CORROSION FAILURE SUSCEPTIBILITY

With respect to determining the resistance of a material to stress-corrosion cracking, the development of aluminum alloys and tempers with a high order of resistance such as 2219-T851 and -T87, and 7075-T73, has generated a need for a rapid test that can be used to screen alloys. Current specifications for such alloys require a 30-day stress-corrosion test by alternate immersion in a 3.5 percent sodium chloride (NaCl) solution. A typical alternate immersion test apparatus is shown in Figure 10. Rapid test procedures are desired and successful methods have been found for testing the 7075-T73 alloy. This method involves conductivity and potential measurement techniques.

The above techniques have not been adequate for 2219 aluminum alloy. Many electrolytes are being investigated in an effort to obtain a corrodent more aggressive than sodium chloride solutions for 2219 alloy. At the present time, a solution containing 3.5 percent NaCl + 0.7 percent chromic acid and 1.0 percent potassium dichromate appears very promising.

Although no major stress-corrosion failures have occurred in welded joints, the change in metallurgy as a result of heating could change the stress-corrosion susceptibility. Localized stresses

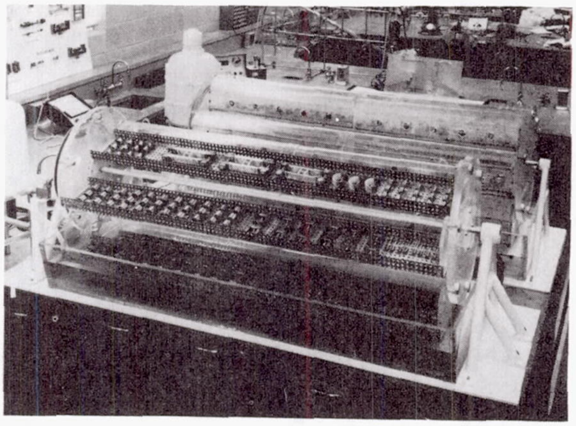

FIGURE 10. ALTERNATE IMMERSION TESTER

are also present in weldments. Considerable work in this area is presently being conducted on aluminum alloys 2219-T87, 2014-T6, and four relatively new high strength weldable alloys, i.e., X7002, X7106, X7039, and X7139. Results of these stress-corrosion tests indicate very good resistance of weldments of all six alloys when stressed to 75 percent of the weld yield strength. While post-weld aging increases the weld strength and decreases the localized corrosion at the heat-affected zone, the resistance to stress corrosion is markedly decreased.

TABLE III. APPROXIMATE THRESHOLD STRESS OF ALUMINUM ALLOYS

Alloy	Grain Direction	Threshold Stress $N/m^2 \times 10^8$ (ksi)
7001-T75	Short Transverse	3.45 (50)
7075-T73		3.10 (45)
2219-T8		2.96 (43)
2024-T8		1.72-2.07 (25-30)
2024-T3 & -T4		<1.38 (<20)
2014-T6		<1.03 (<15)
2017-T4		<1.03 (<15)
7039-T61 & -T64		<1.03 (<15)
7106-T6351		<0.69 (<10)
7139-T6351		<0.69 (<10)

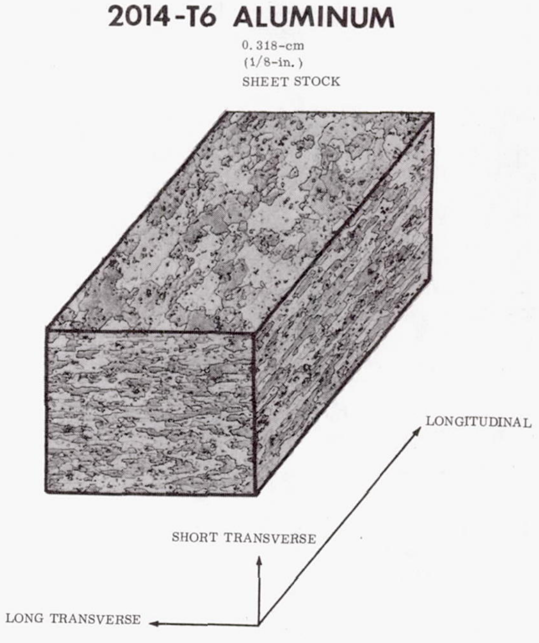

FIGURE 11. GRAIN ORIENTATION IN ALUMINUM SHEET

Some additional work has been done in the Materials Division to determine threshold stresses below which stress-corrosion failure of a metal will not occur. There is no specific method, such as calculated rate of corrosion based on weight loss, for classifying materials as to stress-corrosion cracking susceptibility. Some investigators tend to place too much emphasis on relating time to failure in classifying alloys. A representative failure time, i.e., true average, mean failure, median failure, geometric mean failure, is very difficult to obtain and the method of loading has a pronounced effect on failure time. The threshold stress (stress level below which failure is not encountered) appears to be one of the most meaningful methods of comparing materials. Table III gives preliminary test data from a series of tests wherein test specimens were exposed to alternate immersion to 3.5 percent NaCl testing at various short transverse stress levels for nominal periods of 90 days. The indicated threshold stress level gives a relative merit of susceptibility of the material and provides an indication of safe design values. The term "short transverse" has been mentioned in describing several evaluations. Figure 11 illustrates a typical cross section of 2014-T6 aluminum sheet with the indicated grain directions and corresponding microstructures. Most stress-corrosion evaluations consider primarily the short-transverse grain direction because this is the most susceptible direction for stress-corrosion cracking to occur.

Table IV lists a number of structural alloys with respect to their overall stress-corrosion cracking characteristics. Note that some of the alloys have no temper designations and are considered susceptible or resistant in all tempers, while others are listed with specific temper designations. This particular listing is representative of some of the major alloys used in the Saturn V system, and the materials listed have been evaluated by exposure to alternate immersion testing in 3.5 percent sodium chloride solution.

TABLE IV. STRESS CORROSION SUSCEPTIBLE AND RESISTANT ALLOYS

SUSCEPTIBLE ALLOYS		RESISTANT ALLOYS	
Aluminum	Steel	Aluminum	Steel
● 2014 ● 2219-T3 & -T4 ● 2024-T3 & -T4 ● 7001-T6 ● 7106 & 7039 ● 7075-T6 ● 7178 ● 7079 ● 195 Casting ● 220 Casting	● 17-4 PH & 17-7 PH ● AM-350 & AM-355 ● 410 ● Low Alloy Steel at High Strength Levels ● Maraging Steel	● 3000, 5000, & 6000 Series ● 2219-T6 & -T8 ● 2024-T6 & -T8 ● 7001-T75 ● 7075-T73 ● Most Castings	● 300 Series ● AM-355, FH SCT 1000 ● A-286 Nickel Alloys ● Inconel 718 ● Waspaloy

So far, major emphasis has been placed on aluminum and stainless steel stress-corrosion problems, but another case involving titanium occurred recently. In July 1965, a 6Al-4V titanium tank used for storage of nitrogen tetroxide (N_2O_4) failed while undergoing a pressure test. An extensive study of N_2O_4 revealed that N_2O_4 of previous manufacture that had been stored for several years would generally not cause cracking of the titanium, whereas N_2O_4 of recent manufacture would cause stressed titanium specimens to fail in a matter of hours. Chemical analysis revealed that the old N_2O_4 contained oxides of nitrogen, predominately nitric oxide (NO). In order to determine whether the nitric oxide was actually inhibiting the cracking, a considerable amount of the old N_2O_4 was purified by passing pure oxygen through the liquid and then vacuum distilling. The purified material was alternately frozen and distilled under reduced pressure several times to remove any highly volatile products. Stressed specimens of titanium exposed to this highly purified material failed in a matter of hours. These studies indicated that nitric oxide present in amounts of 0.25 percent or more will act as an inhibitor in preventing the cracking. The procurement specification for N_2O_4 was changed to incorporate sufficient NO in N_2O_4. The addition of NO has no apparent effect on the characteristics of N_2O_4 as a rocket engine propellant. This solution did not involve a change of alloy or temper of the alloy, but rather the use of an inhibitor for stress-corrosion cracking.

CONCLUSION

Although great strides have been made in combating stress corrosion, stress-corrosion failures are still possible. The phenomena of stress-corrosion cracking have been found to be very unpredictable. Carefully machined specimens of a susceptible alloy taken from the same piece of plate, exposed to the same environment and stressed to the same level, may have very random failure times or may not fail. Being able to determine the condition of a component with regard to stress corrosion during its service lifetime would be of great value. Therefore a number of studies have been initiated to develop nondestructive methods to determine the stress-corrosion susceptibility of a material or component. Several programs have also been awarded for studying the basic mechanisms and other aspects of stress corrosion. In these studies, such nondestructive techniques as internal friction, electrical conductivity, ultrasonic surface attenuation and acoustic emission techniques are being used.

EVALUATION OF MATERIALS BY NON-DESTRUCTIVE MEANS

By

Raymond L. Gause

SUMMARY

The factors that result in a failure caused by stress corrosion are discussed and the various methods used to detect stress corrosion are mentioned. The role of non-destructive testing in solving the stress corrosion problem is outlined. Experimental techniques that may be capable of detecting and measuring stress corrosion and residual stress are discussed. In addition, equations are given for the ultrasonic wave propagation in an anisotropic medium.

LIST OF SYMBOLS

English Symbols

c_{ij}	the first order elastic constants.
c_{ijkl}	the second order elastic constants.
D_{ij}	the coefficients of the wave equations for an anisotropic body.
$\hat{e}$	the strain tensor.
e_{kl}	the components of the strain tensor.
F	the fraction of the crystallites in an aggregate which are oriented in the most preferential way.
h	the thickness of the elastic medium parallel to the direction of propagation.
K	the ratio of the angular frequency to the wave velocity.
l_1 l_2 l_3	the direction cosines of the normal to the wave front.
$\hat{T}$	the strain tensor.
T_{ij}	the components of the strain tensor.
t	time.
t_1	the specimen transit time for a distortional wave polarized along the X_1 axis.
t_2	the specimen transit time for a distortional wave polarized along the X_2 axis.
U_j	the components of the displacement.
U_{jo}	the components of the displacement amplitude of a plane harmonic wave.
V	the velocity of a distortional wave in an isotropic medium.
V_1	the velocity of a distortional wave in a medium of oriented crystallites when the particle motion is parallel to the X_1 axis.
V_2	the velocity of a distortional wave in a medium of oriented crystallites when the particle motion is parallel to the X_2 axis.
$\frac{\Delta V}{V}$	the fractional velocity change associated with the double refraction of a distortional wave propagating in an anisotropic body.
v	the general velocity of a plane wave in an anisotropic body.
X_1	the distortional wave velocity when the axis of polarization is parallel to the X_1 axis.
X_2	the distortional wave velocity when the axis of polarization is parallel to the X_2 axis.

Greek Symbols

ζ	the elastic displacement in the X_3 direction.
η	the elastic displacement in the X_2 direction.
ν	the angle between the plane of vibration of a plane polarized wave and the X axis.

ξ	the elastic displacement in the X_1 direction.
ρ	the density of an undeformed elastic medium.
ψ	the phase angle.
ω	the angular frequency.

INTRODUCTION

Figure 1 is a logic diagram that shows the various paths that can be taken to insure that no stress-corrosion failures occur. The four factors required for the initiation of stress corrosion are (1) a susceptible material, (2) a tensile stress, (3) a corrosive environment, and (4) time. Since factors of time and environment are always present during prelaunch checkout, any solution of the stress-corrosion problem must involve the elimination of the susceptible material or the tensile stress. Means have been devised by which certain susceptible alloys can be made resistant to stress corrosion by processes such as coatings and shot peening the surface to produce a compressive residual stress. This approach provides answers for specific alloys but does not constitute a solution of the problem. A real solution will be obtained only when the stress-corrosion mechanism is fully understood. Presently, a visually detected crack is the first evidence of stress corrosion. Research efforts are thus limited because the initiation and process for the occurrence of a microscopic crack cannot be determined. Nondestructive testing techniques must be developed to specify the events that result in a stress-corrosion failure. Stress corrosion may be prevented by reducing or eliminating existing residual tensile stresses that are produced by fabrication or assembly processes. However, this requires a method of measuring these residual stresses.

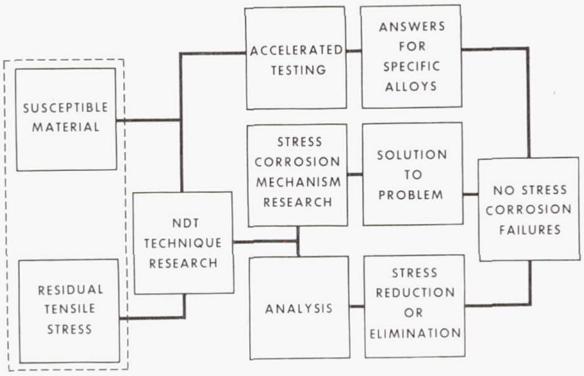

FIGURE 1. APPROACH TO STRESS-CORROSION PROBLEM

EXPERIMENTAL METHODS FOR DETECTING STRESS CORROSION

Several studies are being conducted to develop methods for detecting the presence of stress corrosion. (1) Internal friction measurements have been made on alloy 7079-T6 to determine whether the internal friction changes when the material is exposed to stress and a corrosive environment. It was found that the energy losses increased with time and also varied with the grain direction. When the stress was removed, the internal friction did not change, and the corrosive environment acting alone had little effect on the damping capacity. Thus the internal friction does change as the stress-corrosion process progresses. (2) Laboratory tests have revealed that the attenuation of ultrasonic surface waves is sensitive to stress-corrosion damage. (3) Acoustic emissions have been detected when aluminum specimens were exposed to stress and a corrosive environment. The emissions were different when only stress was applied, indicating that emissions were produced by changes in the microstructure caused by the stress-corrosion process. (4) The electrical conductivity changes when stressed aluminum specimens are exposed to a corrosive environment, whereas stress or early stages of corrosion alone have little effect on electrical conductivity. Higher frequencies caused greater sensitivity to changes. No changes were observed from applying compressive stresses. These four areas of investigation are concerned with the detection of stress corrosion.

Efforts to date for the analysis of residual stress have primarily been devoted to studying the effect of stress on ultrasonic surface and shear wave velocities. Table I gives the acoustic velocity data obtained for surface and shear waves in 2024-T351, 6061-T651, and 7075-T651 aluminum alloys. There is a considerable difference in delay or transit time (which is directly proportional to velocity) when the materials are subjected to stresses of 7×10^6 N/m^2 (1000 psi) and the yield stress.

TABLE I. ACOUSTIC VELOCITY DATA*

Characteristic	Alloy			
	2024	6061	7075	
Temper	T351	T651-T6	T651	
Modulus N/m^2 (lb/in^2)	7.3×10^{10} (10.6×10^6)	7.0×10^{10} (10^7)	7.2×10^{10} (10.4×10^6)	
Yield N/m^2 (lb/in^2)	3.3×10^8 (47×10^3)	2.8×10^8 (40×10^3)	5.0×10^8 (73×10^3)	
Delay Time for 2.54 cm (1 in.) Path Length at 7×10^6 N/m^2 (10^3 psi), Strain Corrected	1.93 nsec 1.04	3.32 nsec 0.556	3.61 nsec 0.239	(Shear Wave) (Surface Wave)
Delay Time at Yield for 2.54 cm (1 in.) Path Length (nsec)	90.8 48.8	133 22.2	263 17.5	(Shear Wave) (Surface Wave)
Absolute Velocity Shear Wave (m/sec)	3300	3045	3480	
Absolute Velocity Surface Wave (m/sec)	3030	2905	3030	

* Measurements were made at 7 MHz with the exception of Surface Wave Data for 7075 which were made at 5 MHz.

STRESS ANALYSIS

Perhaps the most promising technique being investigated for the analysis of stress is that based on the birefringence of ultrasonic shear waves. Figure 2 is a schematic representation showing the result of a shear wave propagating through an anisotropic material (in this case the anisotropy is caused by the applied stress). If the wave is polarized parallel to the direction of the applied stress (that is, if the particle motion is parallel to the stress direction), the wave will propagate through the material with one velocity, whereas, if it is polarized perpendicular to the stress it will have a different velocity. For any other polarization, birefringence will occur and the wave will be resolved into two components, one traveling parallel and the other perpendicular to the stress direction, with the resultant particle motion as shown. The phase difference between the two components can be used to determine the degree of anisotropy of the material, which in this case is assumed to be caused by stress. Figure 3 is a graph of data that were obtained for 6061-T6 aluminum that had been cold rolled by various amounts. Birefringence is given in terms of the fractional velocity difference $\Delta V/V$ which is merely the difference between the velocities of the two wave components divided by the average velocity in an isotropic medium. The cold rolling did not change the slope of the stress-birefringence curve but only affected the initial value of the birefringence. The data presented are in agreement with the theory of stress-induced birefringence based on non-linear elasticity theory. One of the complications of this method of stress analysis is that the anisotropy which causes the birefringence can be caused by sources other than stress. In cold rolled material, the other principal source of anisotropy is preferred grain or crystallite orientation. Figure 4 illustrates crystallite preferred orientation. Shown are crystallites randomly oriented, and some that have a particular crystallographic direction aligned parallel to the rolling direction and a specific plane aligned parallel to the rolling plane. Figure 5 illustrates a shear wave propagating through a specimen having preferred grain orientation. One wave component is propagating through the material with a velocity $\dot{X}_1$ parallel to the rolling direction and the other wave component traveling parallel to the long transverse direction

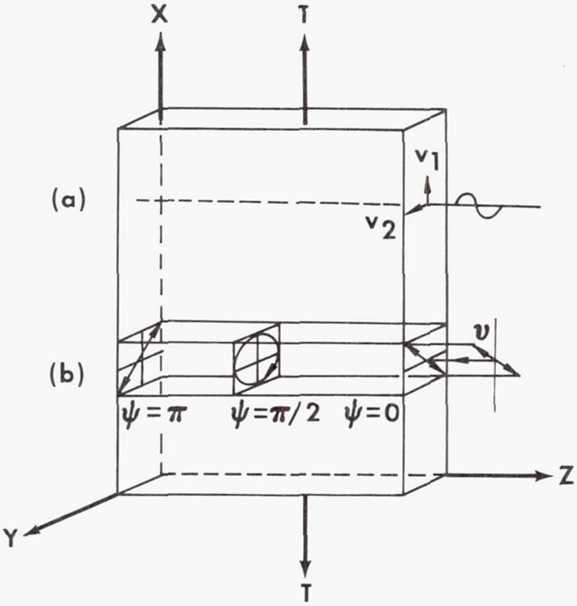

FIGURE 2. (a) DISTORTIONAL WAVE PROPAGATION IN AN ANISOTROPIC MEDIUM AND (b) THE RESULTING PARTICLE MOTION

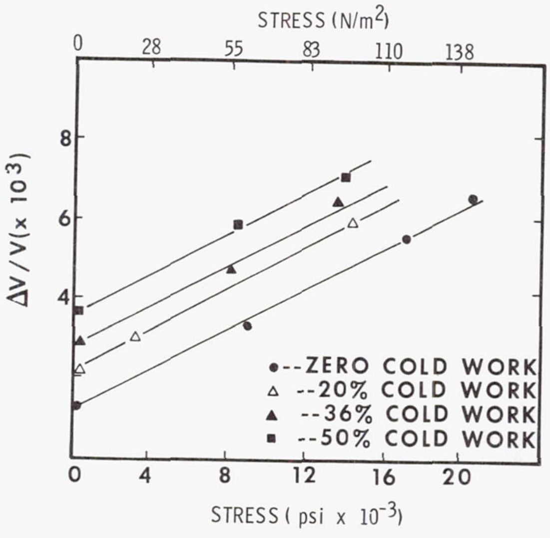

FIGURE 3. STRESS-INDUCED BIREFRINGENCE IN COLD-WORKED 6061-T6 ALUMINUM

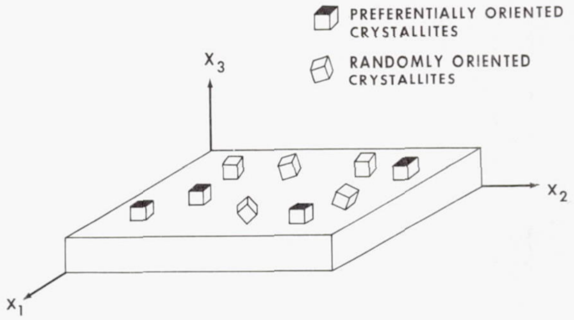

FIGURE 4. CRYSTALLITE PREFERRED ORIENTATION IN A SHEET OF ROLLED METAL

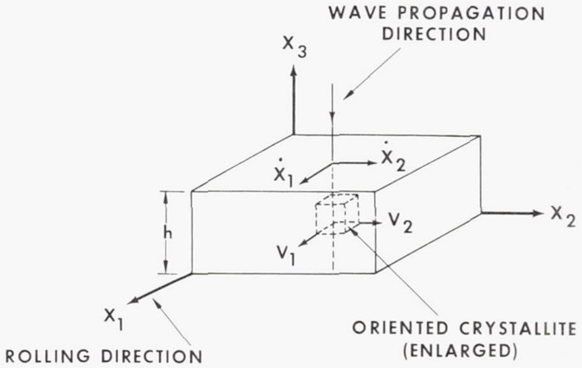

FIGURE 5. WAVE BIREFRINGENCE CAUSED BY PREFERRED ORIENTATION IN ROLLED METAL SHEET

with a velocity $\dot{X}_2$. When the waves reach the oriented crystallite, the velocities of propagation (V_1 and V_2) will depend on the particular orientation possessed by the crystallite. If it is assumed that the path length in the oriented crystallites is proportional to the number of oriented crystallites, the shear wave transit times are

$$t_1 = h(1 - F)/V + hF/V_1$$

and

$$t_2 = h(1 - F)/V + hF/V_2$$

whose difference is

$$t_1 - t_2 = hF(V_2 - V_1)/V_1 V_2 .$$

The above relationship in terms of velocity is

$$(h/X_1 - h/X_2) = \frac{hF\,(V_2 - V_1)}{V_1\,V_2}$$

and

$$\frac{X_2 - X_1}{X_1\;X_2} = \frac{F\,(V_2 - V_1)}{V_1\;V_2}\;.$$

If

$$X_2 - X_1 = \Delta V \text{ and } X_1\,X_2 \cong V^2\,,$$

then

$$\Delta V/V\,(\rho) = VF\,(V_2 - V_1)/V_1\,V_2\;.$$

The results of this analysis show that, theoretically, the birefringence is a function of the fraction of the crystallites possessing a preferred orientation and the velocities V_1 and V_2 of the waves in the oriented crystallites. To determine the magnitude of this effect, specimens of aluminum were cold rolled to various degrees and the birefringence was measured. X-ray diffraction pole figures were then obtained from which the degree and type of orientation could be obtained. Figure 6 illustrates the pole figure that was obtained for 6061-T6 aluminum cold rolled 50%. The type of orientation indicated by this pole figure is illustrated in Figure 7. Thus, the orientation is known but the wave velocities for an aluminum crystallite with this orientation have to be known in order to calculate the birefringence resulting from the preferred orientation. Figure 8 shows the general state of stress for a crystal. By using this general stress condition, the following list of equations of motion for wave propagation in anisotropic media can be obtained.

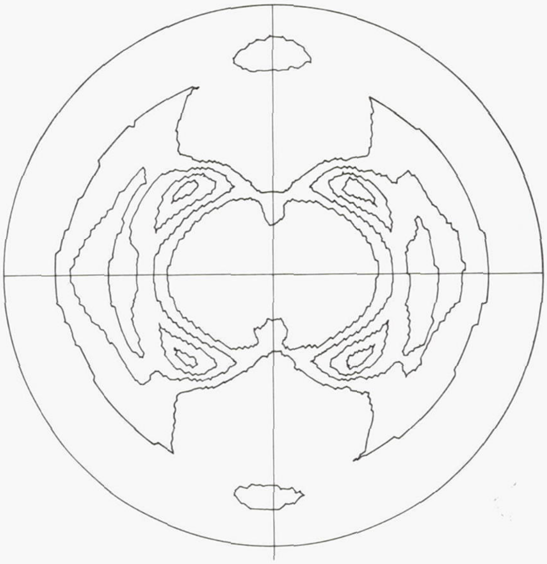

FIGURE 6. ALUMINUM (111) POLE FIGURE

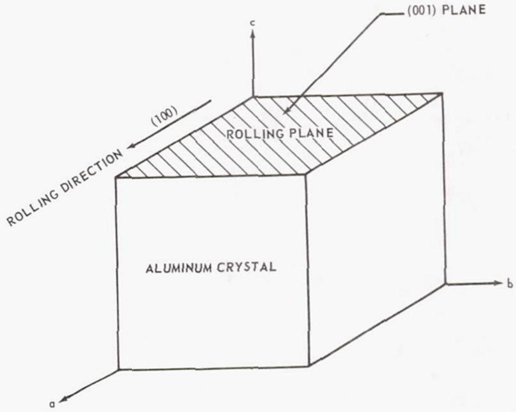

FIGURE 7. BASIC ORIENTATION PRODUCED IN COLD-ROLLED 6061-T6 ALUMINUM

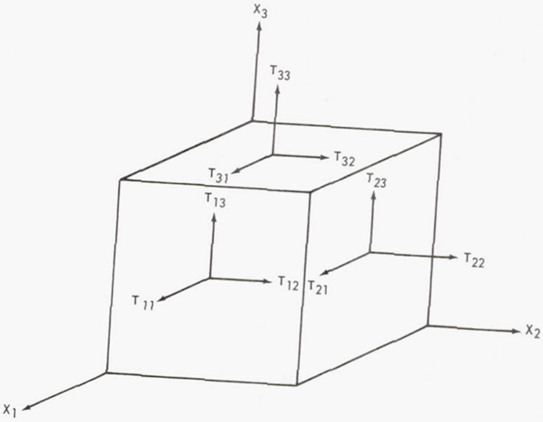

FIGURE 8. THE COMPONENTS OF STRESS FOR A RECTANGULAR CARTESIAN COORDINATE SYSTEM

$$\rho\ddot{\xi} = \frac{\partial T_{11}}{\partial X_1} + \frac{\partial T_{21}}{\partial X_2} + \frac{\partial T_{31}}{\partial X_3} ,$$

$$\rho\ddot{\eta} = \frac{\partial T_{12}}{\partial X_1} + \frac{\partial T_{22}}{\partial X_2} + \frac{\partial T_{32}}{\partial X_3} ,$$

$$\rho\ddot{\zeta} = \frac{\partial T_{13}}{\partial X_1} + \frac{\partial T_{23}}{\partial X_2} + \frac{\partial T_{33}}{\partial X_3} .$$

Tensor representation of the above equations is

$$\rho\ddot{U}_j = \frac{\partial T_{ij}}{\partial X_i};\ i,\ j = 1,\ 2,\ 3.$$

Generalized Hooke's Law in tensor form is

$$T_{ij} = c_{ijkl}\, e_{kl} .$$

Strain - displacement relationship in tensor form is

$$e_{kl} = 1/2 \left[\frac{\partial U_k}{\partial X_l} + \frac{\partial U_l}{\partial X_k} \right]$$

and assume the case of a plane harmonic wave propagating through the medium is given by

$$U_j = U_{jo} \exp\left[i\left(\omega t - K l_n X_n\right)\right];\ j,\ n = 1,\ 2,\ 3$$

where $K = \frac{\omega}{v}$ and l_n are the direction cosines of the normal to the wavefront.

By applying the generalized relationship for Hooke's law and the strain-displacement relationship and assuming the case of a plane wave, the following three equations involving the wave velocity can be obtained from the previous list of equations for wave propagation.

$$\rho v^2 U_1 = D_{11} U_1 + D_{12} U_2 + D_{13} U_3$$

$$\rho v^2 U_2 = D_{12} U_1 + D_{22} U_2 + D_{23} U_3$$

$$\rho v^2 U_3 = D_{13} U_1 + D_{23} U_2 + D_{33} U_3$$

where

$$D_{11} = c_{11} l_1^2 + c_{66} l_2^2 + c_{55} l_3^2 + 2 c_{16} l_1 l_2 + 2 c_{56} l_2 l_3 + 2 c_{15} l_1 l_2 .$$

$$D_{12} = c_{16} l_1^2 + c_{26} l_2^2 + c_{45} l_3^2 + (c_{12} + c_{66}) l_1 l_2 + (c_{25} + c_{46}) l_2 l_3 + (c_{14} + c_{56}) l_1 l_3 .$$

$$D_{13} = c_{15} l_1^2 + c_{46} l_2^2 + c_{35} l_3^2 + (c_{14} + c_{56}) l_1 l_2 + (c_{36} + c_{45}) l_2 l_3 + (c_{13} + c_{55}) l_1 l_3 .$$

$$D_{22} = c_{66} l_1^2 + c_{22} l_2^2 + c_{44} l_3^2 + 2 c_{26} l_1 l_2 + 2 c_{24} l_2 l_3 + 2 c_{46} l_1 l_3 .$$

$$D_{33} = c_{55} l_1^2 + c_{44} l_2^2 + c_{33} l_3^2 + 2 c_{45} l_1 l_2 + 2 c_{34} l_2 l_3 + 2 c_{35} l_1 l_3 .$$

$$D_{23} = c_{56} l_1^2 + c_{24} l_2^2 + c_{34} l_3^2 + (c_{25} + c_{46}) l_1 l_2 + (c_{23} + c_{44}) l_2 l_3 + (c_{36} + c_{45}) l_1 l_3 .$$

The D_{ij} coefficients are functions of the direction cosines of the normal to the wavefront and the elastic constants of the material. The condition that these three homogeneous equations have a non-vanishing solution is that the following determinant be zero.

$$\begin{vmatrix} (D_{11} - \rho v^2) & D_{12} & D_{13} \\ D_{12} & (D_{22} - \rho v^2) & D_{23} \\ D_{13} & D_{23} & (D_{33} - \rho v^2) \end{vmatrix} = 0.$$

Since aluminum has only three non-zero independent elastic constants (C_{11}, C_{12}, and C_{44}), the D_{ij} coefficients for the specific case of aluminum become

$$D_{11} = c_{11} l_1^2,\quad D_{12} = c_{12} l_1 l_2,\quad D_{13} = 0 .$$

$$D_{22} = c_{44} l_3^2,\quad D_{23} = c_{44} l_2 l_3,\quad D_{33} = c_{44} l_2^2 .$$

Thus, the determinant simplifies to

$$\begin{vmatrix} (D_{11} - \rho v^2) & D_{12} & 0 \\ D_{12} & (D_{22} - \rho v^2) & D_{23} \\ 0 & D_{23} & (D_{33} - \rho v^2) \end{vmatrix} = 0 .$$

If the D_{ij} coefficients are calculated for the specific orientation shown previously, the two velocities are the same. Thus the birefringence is zero, theoretically. The result indicates that the experimentally determined birefringence is caused entirely by stress.

CONCLUSION

Research is progressing toward a solution for the non-destructive measurement and analysis of stress corrosion and residual stress. Experimental methods to detect stress corrosion are by (1) internal friction, (2) electrical conductivity, (3) surface wave attenuation, and (4) acoustic emission. Experimental methods to analyze residual stress are by (1) surface wave velocity changes, (2) shear wave velocity changes, and (3) shear wave birefringence. Any successful technique will be of tremendous value in eliminating stress-corrosion failures.

Page
Intentionally
Left Blank

MATERIAL DESIGNS FOR ELECTRONIC APPLICATIONS

By

Eugene C. McKannan and James E. Curry

SUMMARY

1. Motor Brushes. The development of new materials for fabrication of dc motor brushes is discussed. The need for brush materials having good electrical and lubricating properties while operating in a vacuum environment required evaluation of numerous materials. A discussion follows of the wear process as affected by velocity, current density, material fabrication and initial operation. The evaluation of complete motor assemblies emphasizes high contact efficiency, high temperature resistance, and low noise level.

2. Dielectrics for Wire Coatings. A comparison is made of the use of a thin polyimide coating versus a teflon coating for insulating wires in cryogenic environments. The mechanical and electrical properties of both wire insulation materials are presented.

3. Electrical Properties of Cryogenic Fluids. The breakdown voltage (strength) of several liquid cryogens was determined. The gaseous and liquid breakdown strengths of three cryogens are compared. A theory for the breakdown strengths of the liquid cryogens was formulated and contributes an important link in the basic theory of electrical discharge.

4. Potting Compounds. The protection of electronic circuitry by potting compounds and coating resins is discussed. The adhesion, thermal expansion and dielectric properties as affected by chemical stability of the materials are mentioned. The necessity for careful preparation of the protective potting compounds and coatings is explained. The complex materials evolving from experiments in developing potting and coating compounds are provided by combining desirable molecular structures from different polymers and by providing new curing systems.

DC MOTOR BRUSHES

The development of improved electrical brushes was needed to realize the benefits of simple direct current (dc) rotating equipment in the space environment. Some typical applications for dc motors are (1) the drive motor for the pumps on the hydraulic system, the cooling system, or the life-support system, (2) the deployment and positioning of solar panels and wings, (3) attitude control when using angular momentum in flywheels and torque motors as in the Apollo Telescope Mount, and (4) the high-powered driving and lifting motors in moon-based equipment. Dc motors provide the least complex solution to the problem of converting electrical energy to mechanical energy in space. All the power generating devices produce direct current, and the use of direct rather than alternating current precludes the additional weight and complexity of inverters. Direct current motors also offer the advantages of sensitive control and high torque at low speeds.

Brush motors are simpler than motors in which the field is switched with external high-powered transistors or other electronic commutation methods. However, a materials development was required because standard graphite brushes wore very rapidly in a vacuum environment. The lubricity of graphite depends upon the water vapor or oxygen in the atmosphere rather than upon its own inherent structure. The problem of the rapid wear of graphite brushes in high altitude aircraft was solved by adding metallic halides to the brushes. However, this correction does not work at the very low pressures of orbital altitudes.

A search was initiated for a new material that would be suitable for motor brushes used in space vehicles. Based on the Materials Division's experience with dry film lubricants, crystal structure, and other solid state properties, the following list of materials was selected for testing: disulfides, diselenides, and ditellurides of molybdenum, tungsten, niobium, tantalum, and titanium in combination with the additives of silver, silver sulfide, copper or iron. Table I gives the service life of commercially available graphite and high altitude brushes compared with molybdenum disulfide (MoS_2) and silver (Ag) brushes that have operated so well in vacuum. The best experience to date has been obtained with $NbSe_2$ and MoS_2 mixtures.

In addition to being dependent upon solid state properties, the brush characteristics also depend

TABLE I. MOTOR BRUSHES AT 2000 rpm IN VACUUM ENVIRONMENT OF 1.33 × 10^{-6} N/m^2, 300° K (10^{-8} mm Hg, 80° F)

% Composition	Service Life, Hours	Wear Rate cm/hr (in./hr)	Current Density A/cm^2 (A/$in.^2$)
Graphite	6	2.54 (1.0)	0.775 (5)
High Altitude	28	2.54 × 10^{-2} (10^{-2})	0.775 (5)
90 MoS_2 - 10 Ag	2080	2.54 × 10^{-5} (10^{-5})	1.55 (10)
86 MoS_2 - 14 Ag	5600	2.54 × 10^{-5} (10^{-5})	1.55 (10)
73 MoS_2 - 27 Ag	5580	2.54 × 10^{-6} (10^{-6})	2.64 (17)
60 MoS_2 - 40 Ag	32	2.54 × 10^{-3} (10^{-3})	1.86 (12)
100% $NbSe_2$	2480+	2.54 × 10^{-4} (10^{-4})	3.10 (20)
80 $NbSe_2$ - 20 MoS_2	1200+	2.54 × 10^{-4} (10^{-4})	3.10 (20)

upon preparation conditions because they are formed by compaction of powder. Powder with the smallest attainable particle size (2.5 μ) is mixed in measured ratios and placed in a graphite mold. Mold pressure is applied to about 2.41 × 10^7 N/m^2 (3500 psi). The temperature is then increased to 1200° K for purposes of sintering. These conditions are held for a few minutes, the pressure is released and the temperature is reduced. A solid piece is produced from which several brushes may then be cut. Anisotropy, or directionality in properties, is introduced because the material compacts with a preferred grain orientation. Therefore, the brushes must be cut so that the laminations in the contact face are perpendicular to the direction of pressing and are parallel to the axis of the commutator shaft. Good brushes must have high conductivity, or conversely, low resistivity, with minimum friction, wear, and noise. Figure 1 illustrates electrical properties of several brush materials. Pure silver is shown for purposes of comparison. $NbSe_2$ is a good conductor and a moderately good lubricant in vacuum. MoS_2 is a semiconductor whose resistivity curve would be far off the top of Figure 1 and have an opposite slope to the curves shown. However, its resistivity decreases with the addition of increasing amounts of silver.

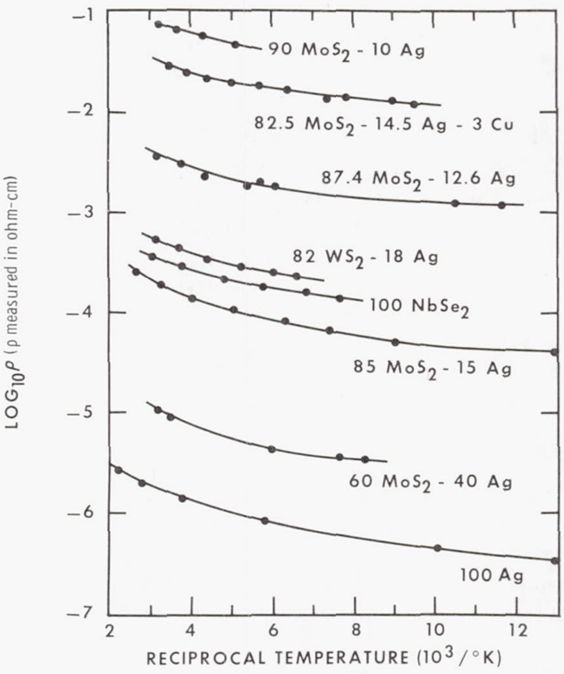

FIGURE 1. RESISTIVITY VS. TEMPERATURE OF BRUSH MATERIALS

The conduction process appears to be a combination of the continuous metallic conduction over very small cross sectional paths, coincident with the conduction of a highly degenerate semiconductor (the host material). The host lattice contains added metallic atoms in sufficient concentration that they interact with each other. When this interaction is sufficiently strong, these atoms form an electronic structure of their own, independent of the host lattice.

The wear process begins with an unstable, transient condition. A film of the brush material must be transferred to the commutator, and the oxide coating on the commutator must be removed in order for stable electrical conduction to proceed. The film formation on the commutator begins immediately but requires several hours to become stable. Figure 2 is a plot of wear rate, contact resistance, and noise level for the run-in or initial instability of a typical brush material. The run-in time is required to establish contact spots on the commutator surface by

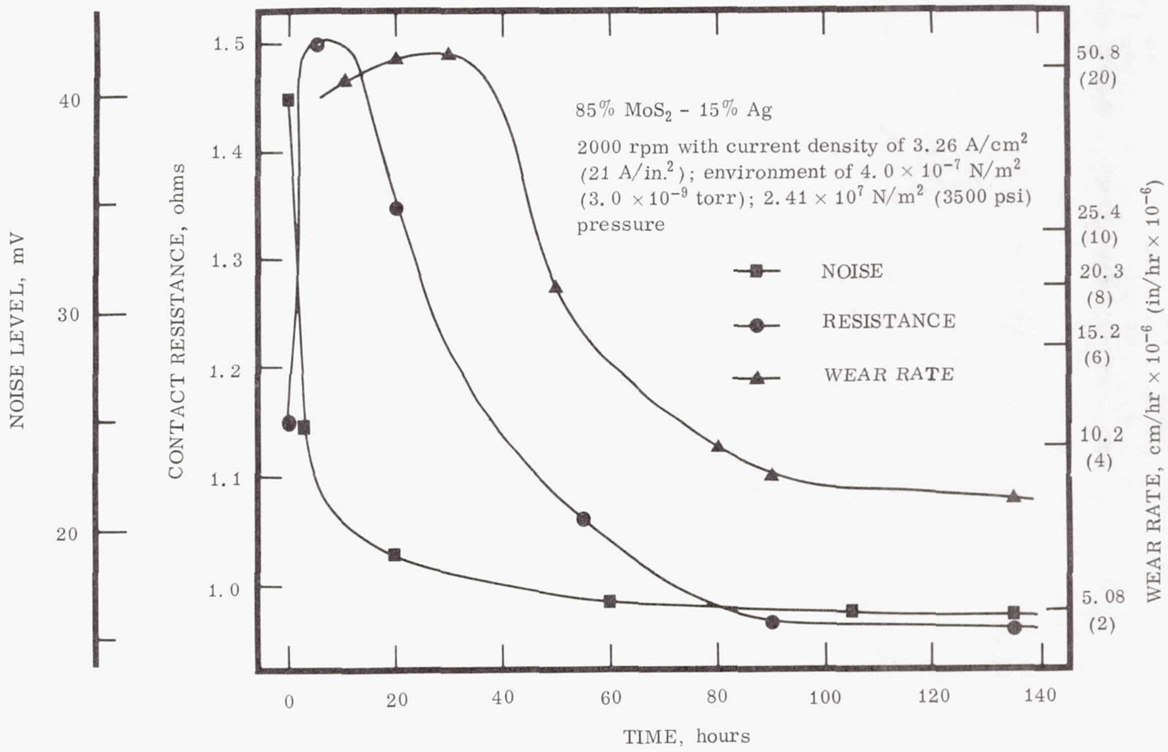

FIGURE 2. RUN-IN PARAMETERS

the process of fretting the oxide coating. The fretting action is required to breakdown and penetrate the copper-oxide layer. The wear rate is dependent upon the surface temperature created during this fretting action.

When examining the effects of wear rate caused by the variation in motor speed (rpm), as the speed is increased the wear rate rises sharply and then stabilizes to a relatively uniform, low value. The contact resistance also increases and then reduces to a steady value over the same period of time. Individual contact points are established on the brush face for each particular speed of rotation, and if the speed is increased, the contact areas are effectively reduced. Additional work or fretting the copper oxide is required to establish a larger contact area, and until this occurs, surface temperature increases with a resulting increase in the brush wear rate. Figure 3 shows the dependence of rotational speed on the stable wear rate. Material pressed at 2.41 × 10^7 N/m^2 (3 500 psi) is harder than that pressed at 2.1 × 10^7 N/m^2 (3 000 psi) and thus produces the more stable wear characteristics. Results on materials pressed at even higher pressures indicated no further improvement. These results indicate that the lubricating film is very stable for long periods of time in vacuum once the initial run-in is accomplished.

Wear rate also is dependent on the current density through the brush (Fig. 4). The wear rate decreases rapidly as the film is transferred to the commutator in the same manner as the wear rate depended on the rotational speed. When the current density is increased, the wear rate increases because of the heating effect and reduced contact surface. At the higher current density the wear rate will stabilize at a greatly reduced value after the initial run-in. At some value in current density the temperature in the interface appears to be high enough to soften the destructive particles and the wear rate decreases.

Apparently when arcing occurred, caused by brush bounce from discontinuities in film transfer, the metallic element such as silver agglomerates near the contact interface and separates from the host material (MoS_2) because of differential thermal expansion. Although useful for long periods of time, the MoS_2-metallic brushes were troublesome once high temperature arcing was initiated. The arcing problem with silver (Ag) led to increased emphasis on the highly conductive niobium diselenide.

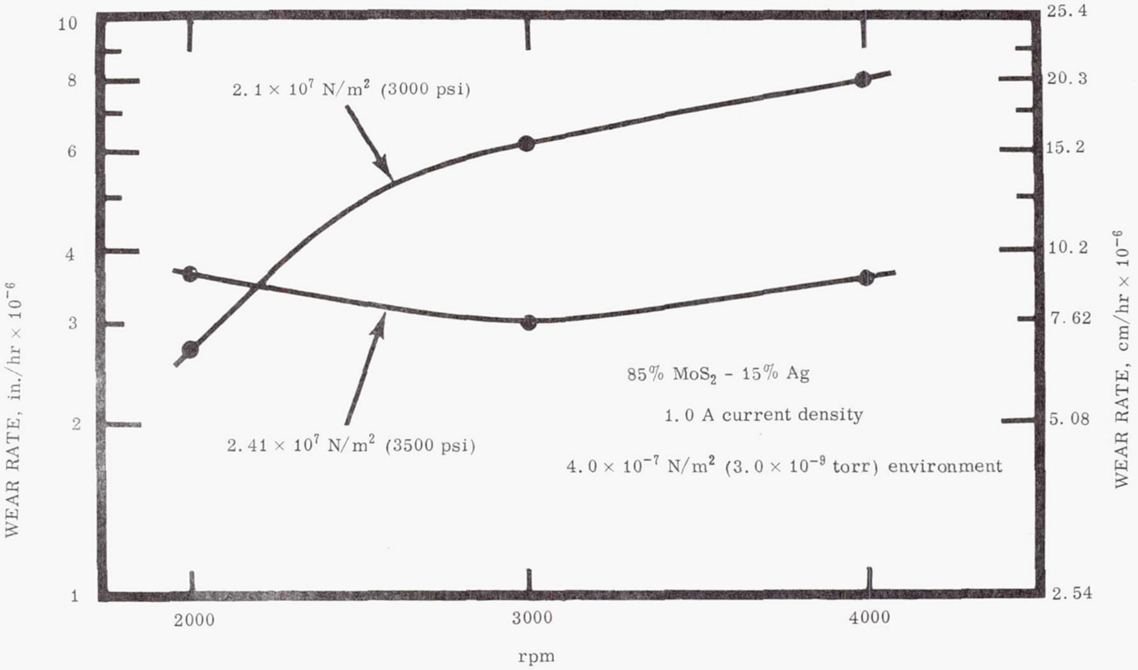

FIGURE 3. WEAR RATE VS. VELOCITY

Noise measurements were made to provide additional information about the run-in process. Figure 5 shows two oscilloscope traces. In each case the lower curve is a trigger-wave form derived from the driving magnets. A high noise level and the purely random nature of noise during run-in are evident in the trace that was obtained during the first hour of running. This is a characteristic of the fretting process. The rms value of the noise is greater than 60 mV. Except for the periodic spike as the brush trailing edge leaves each segment of the commutator

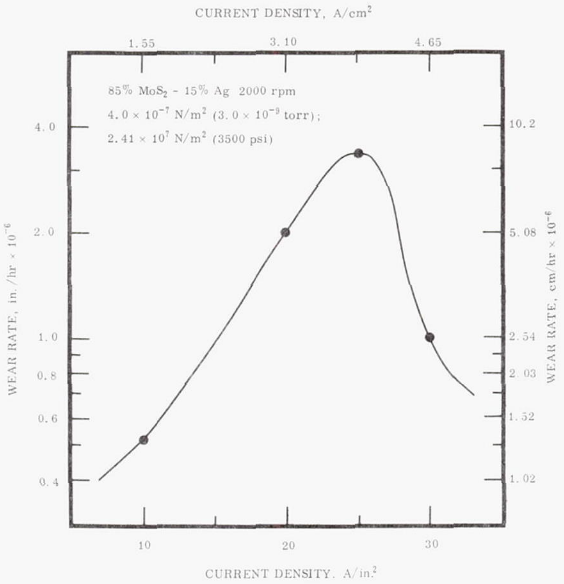

FIGURE 4. WEAR RATE VS. CURRENT

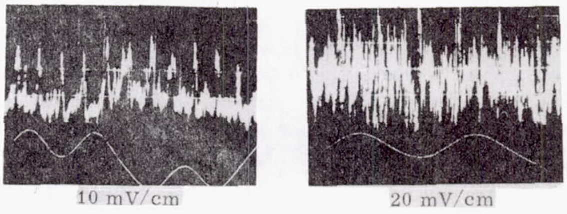

AFTER RUN-IN

DURING RUN-IN

FIGURE 5. BRUSH NOISE

and collapses its magnetic field, the low random noise is shown after run-in. The periodic spike is approximately 25 mV and the general noise level is less than 10 mV. These traces indicate that the developed brushes are less noisy in vacuum than are typical carbon brushes when operating in air.

The final proof for the brush or other motor material has been the evaluation of complete motors. Table II lists the results from many successful motor-generator tests. Over 1500 hours of intermittent operations have been accumulated on one motor-generator set. This set has been operated at ambient conditions from 77°K (-196°C) to over 503°K (+230°C) in an environment at 1.33×10^{-4} N/m^2 (10^{-6} mm Hg). The most recent tests have involved brushes of MoS_2 and $NbSe_2$. These brushes have provided high contact efficiency, high temperature resistance, and low noise. Concurrent programs on bearings and on electrical insulation for use in motors and in other applications in space have provided the other critical elements of the successful motors. However, the most critical component of the dc motor operating in vacuum is the brush.

TABLE II. DC MOTOR GENERATOR EVALUATIONS IN ENVIRONMENT OF 1.33×10^{-4} N/m^2 (10^{-6} mm Hg)

Ambient Temperature, °K	97	294	423	503
Shaft Temperature, °K	288	433	471	508
Input Power, W	85	190	183	220
Motor Efficiency, %	52	49	49	49
Velocity, rpm	700	600	580	615
Torque, N-m (in.-lbs)	1.02 (9)	1.36 (12)	1.58 (14)	1.58 (14)
Brush	MoS_2/Ag		$NbSe_2/MoS_2$	

The experience of the Materials Division indicates that all of the materials are available to design, build, and operate motors in the space environment for long periods of time at reasonably high loads.

DIELECTRICS FOR WIRE COATING

Teflon (TFE) is almost universally used throughout the Saturn vehicle and in other space applications. It is an extremely satisfactory wire coating except for its lack of flexibility in the cryogenic environment. Cabling is routed through a liquid hydrogen tank to provide voltage to liquid level sensors, to thermocouple temperature sensors, or to electrodes for electro-phoretic control of the liquid hydrogen surface in zero gravity. When equipment is operated on the moon's surface, the same cold temperature conditions will prevail during the lunar night. Hence, several probable insulation schemes were evaluated to provide a flexible wire coating for a cryogenic environment. Most of the polymeric materials available for such wire coatings have a glassy transition temperature which makes them extremely stiff and brittle at cold temperatures. But one of the means by which a cold temperature flexible coating may be obtained is to use a material which has very little change in its elastic properties with temperature. High temperature resistant insulations provide a first clue. A very thin coating will serve as a cold temperature flexible material if the thin coating will provide the mechanical toughness and the electrical insulation required. A thin coating undergoes much less stress in bending than a thicker coating.

The following list of materials was considered for wire coatings for cryogenic service: (1) enamels - polyvinyl formal, polyester, polyamide, aluminum phosphate, polyimide; (2) extrusions - polyvinyl chloride, polytetrafluoroethylene; (3) fibers - glass, asbestos, polyester. The polyimide coating provided the greatest mechanical protection in addition to completely adequate insulation in a very thin film 38 μ (1.5 mils) thick as compared to the typical Teflon insulation of 280 μ thickness (11 mils). In addition, the thin-film polyimide insulation is LOX compatible and could reduce the mass of each Saturn V stage by 136 kg (300 lbs) considering the 45 700 m (150 000 ft) of insulated conductors in each stage. Table III gives some mechanical properties of the polyimide thin coating as compared to the thicker coating of Teflon used in the standard wire construction. The relative flexibility is indicated by the size of the mandrel around which a wire can be bent at any given temperature. While these wires are equally flexible at room temperature, the Teflon wire requires 10 times the diameter at cryogenic temperatures to avoid cracking. This is a standard flexibility

TABLE III. MECHANICAL WIRE COATING PROPERTIES

	Polyimide	TFE
• Coating Thickness, μ (mils)		
	35.6 (1.4)	280 (11.0)
• Flexibility, Minimum Diameter Bend, cm (in.)		
296°K	0.163 (0.064)	0.163 (0.064)
213°K	0.318 (0.125)	0.318 (0.125)
77°K	0.318 (0.125)	3.18 (1.250)
4°K	0.318 (0.125)	3.18 (1.250)
• Compression Cut-through, Breakdown (kV)		
After 48 Hours Under 98 N force (22 lbf)		
77°K	9.0	25.0
296°K	13.9	15.0
393°K	14.0	Short
523°K	11.5	Short

TABLE IV. ELECTRICAL WIRE COATING PROPERTIES

	Polyimide	TFE
• Dielectric Constant	3.0	2.0
• Dissipation Factor	0.0009	0.0003
• Resistivity, ohms		
After 15 Days at 353°K and 95% RH		
Surface	2×10^{13}	2×10^{13}
Volume	7×10^{12}	2×10^{13}
• Breakdown Voltage, (kV)		
296°K Air	13	19
213°K Air	12	19
77°K LN_2	9	19
20°K LH_2	9	17
4°K LHe	8	17
523°K Air	8	16
After 120 Days at 393°K		
in Air	13	17
in Vacuum	16	19
After 15 Days at 353°K and 95% RH		
	12	18

test used throughout the wire and cable industry. In addition, scraping, tearing, or cutting when pressed against a sharp edge or point is an important mechanical property. The data show that when these wires are given a standard cut-through test, the Teflon relaxes and allows the conductor to be shorted, whereas the tougher polyimide coating continues to provide protection.

The dielectric constant of the polyimide material is slightly greater than that of Teflon (Table IV), and the increase in the capacitance between wires will increase the cross talk. This property is controlled by spacing and twisting the wire. The dissipation factor is slightly higher for the polyimide material, but is entirely acceptable in most signal wire applications. The surface and volume resistivities are quite similar for both coatings in vacuum or in liquid cryogens.

One of the most common tests used to compare wire insulations after any given environmental exposure is the dielectric breakdown or high voltage sparkover. Table IV compares 280 μ thickness (11 mils) of Teflon to 35.6 μ thickness ($1\frac{1}{2}$ mils) of polyimide, with breakdown voltages in kilovolts. Since a breakdown strength of 8 kV is satisfactory for most space vehicle applications, the safety factor for either material is large. The thickness of the Teflon insulation is generally not required for breakdown strength or any other electrical properties, but rather to provide a large safety factor for the mechanical properties such as cut-through or scrape resistance. With such a tough insulation as the polyimide material, the extra safety factor in thickness is not required.

ELECTRICAL PROPERTIES OF CRYOGENIC FLUIDS

When any wire coating mechanically splits or cracks during a breakdown test, it will not necessarily breakdown electrically unless enough moisture and dirt are present for a discharge path. When the cracking occurs in air the discharge path is always present, but when the cracking occurs in LN_2 or LH_2 or LHe, the fluid is a sufficiently clean dielectric to help insulate the conductor. The fluid does not provide mechanical separation, however. A literature search indicated that no data were available on the breakdown strength of liquid hydrogen. Previously, researchers in this field used hydrocarbons like transformer oils rather than liquid hydrogen. The breakdown strength of liquid hydrogen was needed because of its importance in and around wire coatings (in filling cracks and in permeating into the insulation), and in electrophoretic control of LH_2 in zero gravity.

Figure 6 graphs the breakdown voltage versus spacing of 1.27-cm diameter ($\frac{1}{2}$-in. diameter) spheres in 3 cryogens: liquid hydrogen, liquid nitrogen, and liquid helium. Past experience with gasses had not indicated that liquid hydrogen had such a high breakdown strength. Figure 7 indicates the breakdown strength of gaseous nitrogen, gaseous hydrogen, and gaseous helium. These data correlate with the Townsend discharge process for gases, which is dependent on the kinetic mean free path. In the liquid, however, the positions of the hydrogen and nitrogen were reversed. This was difficult to explain until it was realized that a different process would prevail in the liquid. Breakdown theory is well described for gases by Townsend and for regular solids by energy band theory, but a good theory for the breakdown strength of liquids did not exist. These experimental data suggested that the inter-atomic spacing of the atoms in the liquid might be a controlling factor, and as shown in Figure 8, the liquid hydrogen breakdown strength can be explained in this manner. Physically, the covalent radius in a liquid has much the same effect on ionization as the mean free path in a gas. Therefore, the covalent radius

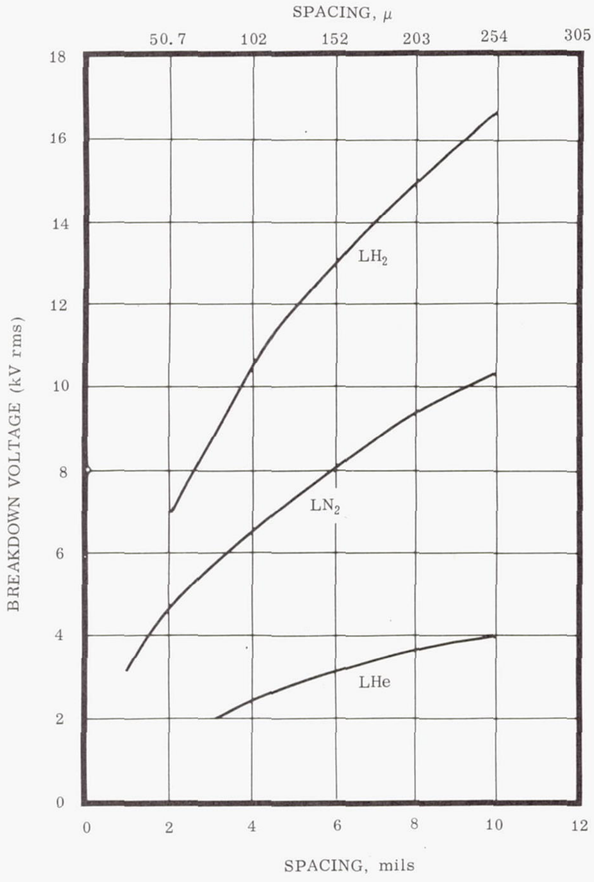

FIGURE 6. 60 Hz BREAKDOWN IN CRYOGENS

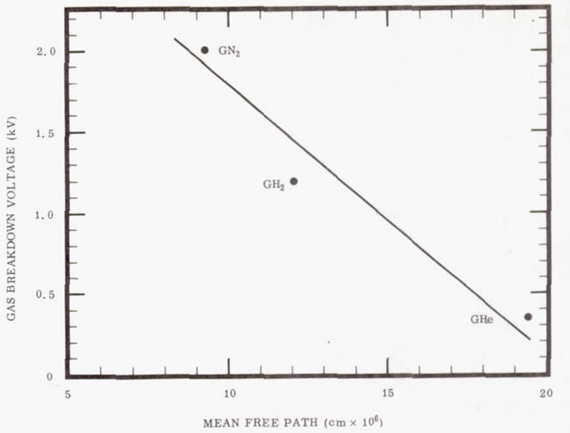

FIGURE 7. GASEOUS BREAKDOWN

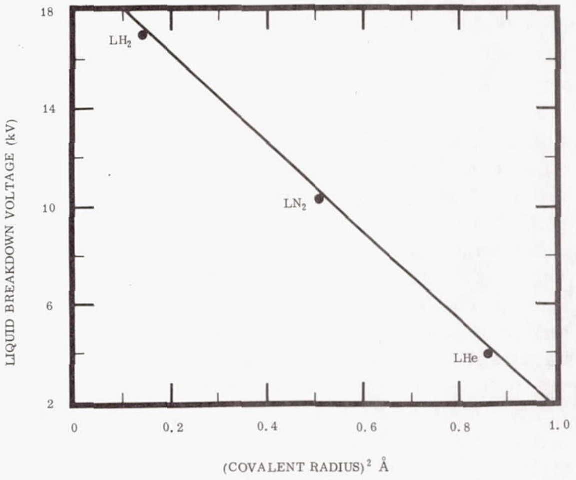

FIGURE 8. LIQUID BREAKDOWN

gives an indication of the theoretical mechanism of breakdown strength in liquids and provides a modification to Townsend's theory to make it applicable to liquids. The results of this work make an important contribution to the basic theory of electrical discharge.

One problem arose when it was determined that a bubble was formed with each discharge. If the bubble occurred first, it would initiate a typical gas discharge. However, all observations led to the conclusion that the bubble was the result of energy dissipation after the discharge because a test was made well below the boiling point where no nucleate boiling bubbles were present and because the observed bubbles never spanned the entire distance between electrodes. At least some liquid was always involved in the discharge.

The knowledge of the breakdown strength of liquid hydrogen makes the electrophoretic control of liquid hydrogen surfaces in zero gravity much more feasible than in other cryogenic liquids. From the safety point of view, an electrostatic discharge which might by chance occur in liquid hydrogen is not as dangerous as it previously might have been considered.

POTTING COMPOUNDS

The requirements for casting and coating resins for the protective encapsulation of electronic circuitry fall into two categories depending upon the nature of the electronics. For cordwood modules where the circuit elements are stacked in a three dimensional array (Fig. 9), a potting compound or filled resin that can be poured around the components is normally used. This resin cures or hardens under conditions that must not be detrimental to the components. It serves to mechanically ruggedize the assembly and provides the dielectric environment for the circuitry. The other category (Fig. 10) is a conformal coating which is normally applied to printed circuit boards for some of the same reasons. A conformal coating must cure to an elastomeric or rubbery solid, while potting compounds cure to a more rigid solid. A sampling of the most critical requirements that must be met by each type of material is listed in Table V.

There are no known commercial products in either category which satisfy all of these requirements. Some of the requirements are quite contradictory; for example, good polymer dielectrics are not generally good adhesives. Yet, good adhesion to a variety of substrates is an obvious requirement of both potting compounds and conformal coatings. It is essential that the potting compound's linear coefficient of thermal expansion approach that of the circuitry materials. So far, this has been impossible without the addition of inorganic powders or fillers to the resins. Organic polymers

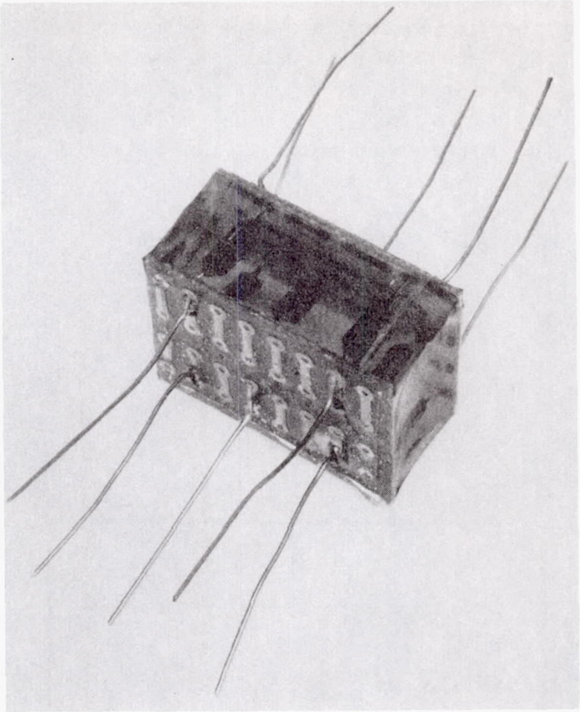

FIGURE 9. CORDWOOD MODULE IN POTTING COMPOUND

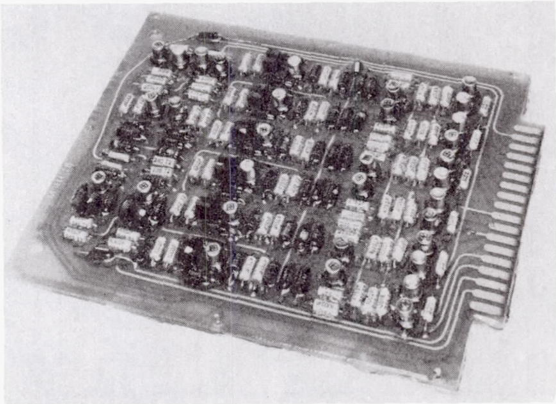

FIGURE 10. PRINTED CIRCUIT BOARD WITH CONFORMAL COATING

TABLE V. REQUIRED PROPERTIES FOR POTTING COMPOUNDS AND CONFORMAL COATINGS

Property	Potting Material	Conformal Coating
Coefficient of linear thermal expansion	$10\text{-}20 \times 10^{-6}$ in/in – °C maximum	--
Dielectric constant (1 kHz)	3. 0 maximum	3. 0 maximum
Dissipation factor (1 kHz)	0. 01 maximum	0. 01 maximum
Volume resistivity	10^{14} ohm-cm minimum	10^{14} ohm-cm minimum
Outgassing potential	100 micromoles max./100 gms. resin after 500 hours/150° C/ 1.33×10^{-3} N/m^2 (10^{-5} torr)	Same
Water absorption	0. 5% maximum	0. 5% maximum
Adhesion, N/m^2 (psi)	0.35×10^7 (500)	0.35×10^7 (500)
Sterilization tolerance		
(1) Dry heat	withstand 135° C for 24 hours	Same
(2) Ethylene oxide	withstand Et0 environment of 500 ± 50 mg/liter atmosphere for 24 hours @ 24° C and 35% RH	Same

inherently have much higher coefficients of thermal expansion than are desired for electronic uses.

Prolonged chemical and thermal stability is essential for several reasons in addition to the requirement for sterilization. Degradation of the polymer can adversely affect its dielectric properties. The outgassing products evolved during thermal degradation can contaminate life support systems and optical surfaces.

The Materials Division is working to develop improved potting and conformal coating resins. The generic classes of resins, e. g. , silicones, epoxies, or polyurethanes, contain certain individual combinations having the necessary properties. Through molecular architecture the linkages and substituents that confer desirable properties on individual polymer classes can be incorporated into a single molecular chain.

A curing agent or catalyst (Fig. 11) must be added to the base resin to harden it into a useful encapsulant. Amines, which are organic derivatives of ammonia, are popular curing agents for epoxies. Limited experimentation with novel amine curing agents indicates that they can bring commercial epoxies closer in line with present requirements. Some epoxies cured with n-methylaniline-formaldehyde adducts developed under this program have dielectric constants that vary less than 0. 1 unit over the temperature range from 25 to 150° C. Simultaneous optimization of curing agent, base resin and other additives are required for a good epoxy resin.

As for the base resin problem, epoxies and silicones individually have complementary desirable traits and some individual disadvantages. Figure 12 shows a polymer structure prepared during our program that structurally incorporates certain linkages common to both epoxies and silicones, which are identified in the formula. This polymer is a result of both polymer systems and combines some properties of each. The properties tabulated in Figure 12 show the success in meeting some of the requirements.

The examination of any highly complex material of this type is always subject to our ability to prepare it. In this case, virtually none of the starting intermediates were available commercially and some had never been reported in chemical literature. To complicate matters, a polymer of the above structure cannot be formed by conventional processes of epoxy chemistry, and more than ten individual synthetic steps are needed for its preparation by the process now used. Other approaches are being investigated to improve this situation.

Similar logic has led to studying urethane-silazane polymers shown in Figure 13. This polymer should have a lower dielectric constant and improved thermal stability. There may be a hydrolytic stability problem with the silazane linkage, but the magnitude of this effect cannot be evaluated quantitatively until the actual polymer is evaluated. The synthesis program has progressed to a point that urethane-silazane structures can be prepared.

The basic approach to potting compounds has been solved. Combining the functionality

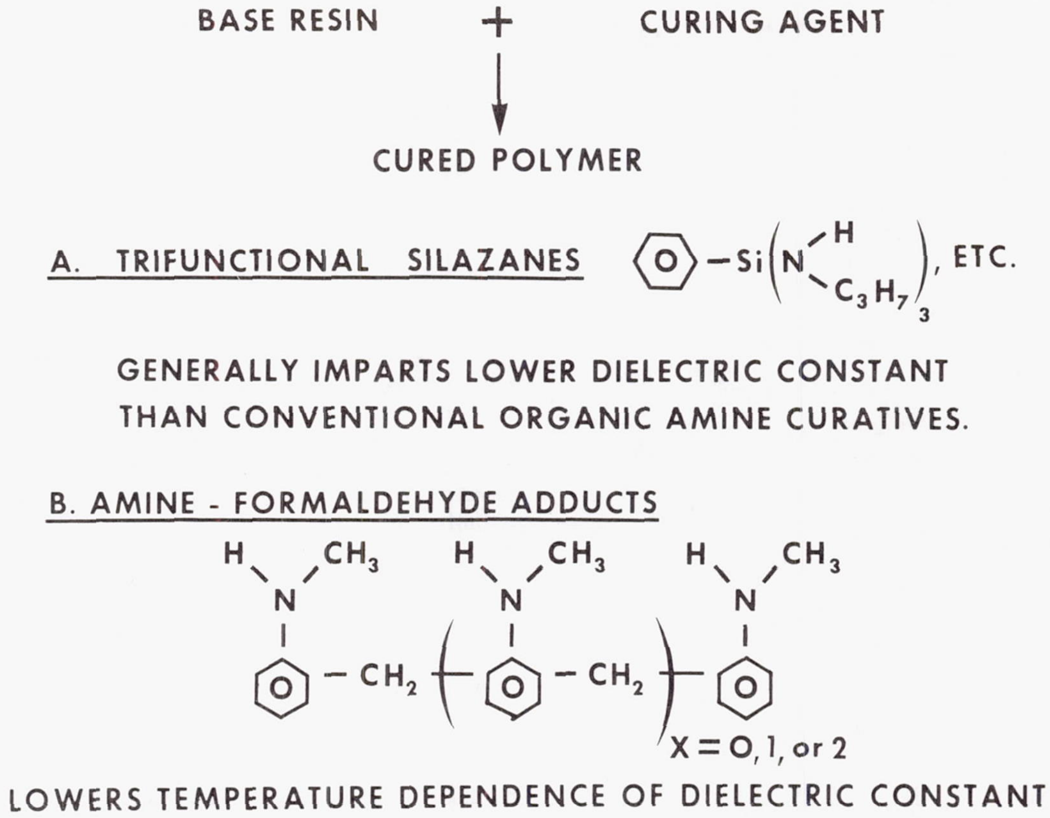

GENERALLY IMPARTS LOWER DIELECTRIC CONSTANT THAN CONVENTIONAL ORGANIC AMINE CURATIVES.

LOWERS TEMPERATURE DEPENDENCE OF DIELECTRIC CONSTANT

FIGURE 11. NOVEL CURING AGENTS FOR CONVENTIONAL EPOXIES

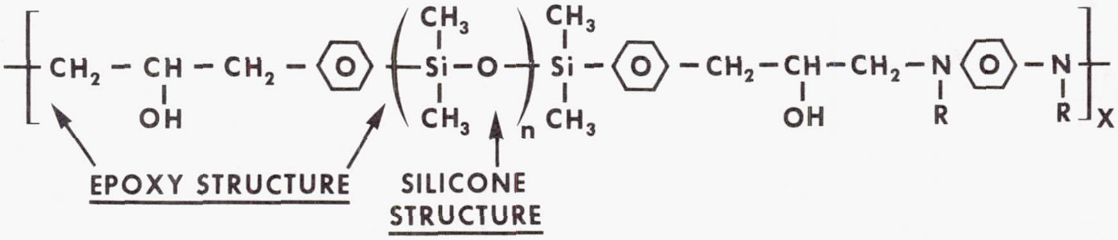

PHYSICAL FORM RANGES FROM ELASTOMERIC TO RIGID SOLID DEPENDING UPON VALUE OF n

KEY PROPERTIES	EPOXY - SILICONE	TARGET VALUES
DIELECTRIC CONSTANT AT 1 kC	2.4 AT 25°C 2.8 AT 150°C	3.0 MAXIMUM
DISSIPATION FACTOR AT 1 kC AND 25°C	0.008	0.01 MAXIMUM
VOLUME RESISTIVITY ohm-cm	7 X 10^{13}	10^{14} AT 25°C 10^{10} AT 100°C MINIMUM
ETHYLENE OXIDE ABSORPTION	0.15% BY WEIGHT	NO DELETERIOUS EFFECTS

FIGURE 12. EPOXY-SILICONE POLYMERS

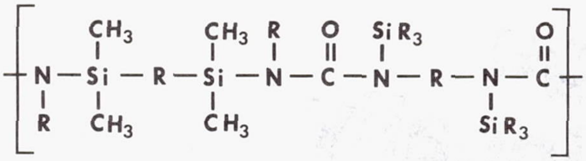

$$\left[-\underset{\mathrm{R}}{\underset{|}{\mathrm{N}}}-\overset{\mathrm{CH_3}}{\overset{|}{\underset{\mathrm{CH_3}}{\underset{|}{\mathrm{Si}}}}}-\mathrm{R}-\overset{\mathrm{CH_3}}{\overset{|}{\underset{\mathrm{CH_3}}{\underset{|}{\mathrm{Si}}}}}-\overset{\mathrm{R}}{\overset{|}{\mathrm{N}}}-\overset{\mathrm{O}}{\overset{\|}{\mathrm{C}}}-\overset{\mathrm{SiR_3}}{\overset{|}{\mathrm{N}}}-\mathrm{R}-\underset{\mathrm{SiR_3}}{\underset{|}{\mathrm{N}}}-\overset{\mathrm{O}}{\overset{\|}{\mathrm{C}}}-\right]$$

PRESUMED ADVANTAGES

BETTER ETHYLENE OXIDE TOLERANCE AND BETTER DIELECTRIC PROPERTIES THAN CONVENTIONAL POLYURETHANES

FIGURE 13. URETHANE-SILAZANE POLYMERS

characteristic of several known polymer systems into a single composite polymer can amplify or nullify traits of the individual systems. Although this approach is largely empirical, it has yielded significantly improved materials. Developing more efficient means to manufacture these materials will permit a more detailed evaluation and provide potting and coating resins with properties much closer to those which are required.

Page
Intentionally
Left Blank

NON-METALLIC MATERIALS

By

James E. Curry

SUMMARY

Cryogenic Insulation. The development of a novel cryogenic multilayer insulation system with micrometeoroid protection capabilities is described. The insulation consists of alternating plastic foam spacer layers and aluminized Mylar reflective layers. Each aluminized Mylar layer is applied under controlled tension by a tape wrapping process and the exterior of the insulation is covered by a resin-impregnated glass fabric which protects the insulation from mechanical damage and serves as the primary micrometeoroid bumper. Large calorimeter test data for several versions of this insulation indicate attractive thermal performance and ease of purging and evacuation. Hypervelocity impact studies have demonstrated that the insulations will provide a measure of protection against micrometeoroid damage to the tank.

Adhesives Research. The total adhesives research effort is summarized with reference to supporting research contracts which supplement parallel inhouse studies now underway on critical aspects of adhesive technology. The goal of this program is to provide new or modified adhesive materials and to identify the optimum conditions for their application, curing and use. As an example of the total effort, a single program on polyurethane adhesives is discussed in detail. Significant data have been obtained on the response of these materials to various aging environments. The aging response of the adhesive applied to aluminum adherends is affected by the presence of primers. The role of various primers is an integral part of this study.

Membrane Diffusion Theory. The permeation of gases and vapors through polymeric seals and films is a subject of wide interest in the space program. This phenomenon frequently occurs under conditions which involve concentration and/or time dependent diffusion coefficients. Some recent theoretical developments are reviewed which indicate that purely concentration-dependent effects can now be treated by an extension of the time lag theory. In ideal cases where time dependent effects are secondary, the nature of the concentration dependence of the diffusion coefficient can be inferred by simple time lag experiments.

CRYOGENIC INSULATION DEVELOPMENT

The micrometeoroid problem will be of increasing concern for space missions of extended duration. The best efforts so far to simulate the micrometeoroid hazard have indicated that many of the micrometeoroid bumper materials are identical or similar to components of several cryogenic insulation systems now in use or under development. In view of this fact, a program is underway in collaboration with Goodyear Aerospace Corporation to combine the insulation and micrometeoroid protective functions into a single composite material.

The initial goals of this effort are summarized in Table I. Certainly, insulations of even higher performance are needed, and these goals are visualized purely as evolutionary steps in that direction. The physical nature of the insulation was not specified. The first materials evaluated were a variety of low density [32 kg/m^3 (2 lb/ft^3)] polyurethane foams. Although no plastic foams are known which provide the required thermal performance, it was suspected that a foam would be used in some fashion in the final insulation configuration. This preliminary work with foams also served to check the calorimetric devices and techniques that were used later in the program.

TABLE I. INITIAL INSULATION GOALS

1. Maximum vacuum heat leak = 0.789 W/m^2 (0.25 Btu/ft^2-hr)
2. Maximum weight = 2.44 kg/m^2 (0.5 lbs/ft^2)
3. Prevent penetration by hypervelocity particles at 9144 m/s (30 000 fps) in the 10^{-5} to 10^{-1} g mass range.
4. No internal air or moisture condensation
5. Ability to withstand 506° K (450° F) outer skin ascent conditions
6. Provide insulation under both prelaunch and launch conditions.

The work on foams demonstrated that they are partially transparent in the infrared range. Although this is not surprising, the magnitude of the effect in the low density foams studied in this program was somewhat alarming. A variety of mineral opacifiers were added to various foam pre-mixes to minimize this effect. These additives were not effective at levels that would avoid prohibitive conduction losses.

The best thermal performance obtained from foams was through the use of metallic additives to simulate multilayer characteristics. Conductivity values below $0.00144 \frac{\text{J}}{\text{m} \cdot {}^\circ\text{K} \cdot \text{sec}} \left(0.01 \frac{\text{Btu-in}}{\text{ft}^2\text{-}{}^\circ\text{F-hr}}\right)$ were obtained with some of these systems in the 32 kg/m^3 (2 lb/ft^3) range. This is near the attainable limit of known foam systems of practical density and strength. The possibility of further improvement hinges upon some spectacular developments in plastic foam technology. At the present time it is not evident what form these developments would take.

The most obvious remaining route to higher performance insulation is the reflective multilayer approach. Two well known systems of this type are shown in Figure 1. The supremacy of this type of insulation under vacuum conditions when compared with other passive systems now available is unquestioned, but purging or evacuation is required to provide reasonable thermal efficiency under prelaunch conditions. The physical form of the insulation makes it difficult to evacuate and the insulation is difficult to attach to the exterior of complex tanks without losing some of its thermal efficiency.

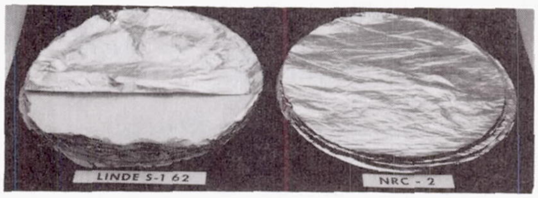

FIGURE 1. REFLECTIVE MULTILAYER INSULATION MATERIALS

This program has resulted in a method of applying multilayer insulation that promises to minimize these problems. At present, a tape-wrapping process is used to apply aluminized mylar reflective layers over resilient foam spacers. The 6.35 μ thick (1/4 mil) aluminized Mylar tape is 1.27-cm (1/2-inch) wide and is wrapped over the foam spacers in a polar pattern. A modified filament winding machine keeps the tape under controlled tension (Fig. 2). Foam spacer layers are applied by lightly cinch-wrapping them around the tank (Fig. 3). The precut gore segments of each spacer layer are bonded lightly over the ends with a contact adhesive.

Some typical calorimeter data for tape-wrapped insulations with various foam spacers are shown in Figures 4-6. They are compared to the Linde S-I 62 insulation under variable compressive loading. Apparent conductivities (Fig. 4) are somewhat higher than the Linde insulation. The conductivity-density product (Fig. 5) is lower in most cases for the tape-wrapped insulations. The heat leak-insulation density product (Fig. 6) seems to suggest a significant advantage for the tape-wrapped insulations. On the strength of these data, tape-wrapped insulations were then applied to the large cylindrical tank shown pictorially in Figure 2 and schematically in Figure 7.

The central 0.762-m (2 1/2-ft) diameter by 1.22-m (4-ft) long measuring section was protected by end guards and separate fill and drain connections were provided for all three sections. This tank was designed to fit in a large vacuum system at Goodyear's Wingfoot Lake Test facility.

Two insulation systems have been tested on this tank with liquid hydrogen as the cryogen. These insulations are shown in Figure 8. Both insulations have identical outer sections, consisting of 37 layers each of foam spacer and tape-wrapped reflector beneath a polyurethane impregnated glass fabric. The ground hold section of one insulation consisted of eleven multilayer combinations which were enclosed in a MAAM (Mylar-aluminum-aluminum-Mylar) vacuum bag. The ground hold section of the other insulation was a sealed Mylar honeycomb layer, comparable to the inner section of the dual seal insulation.

Typical performance data for both insulations are shown in Table II. Vacuum performance of the full multilayer version was outstanding, but after five fill and drain cycles under simulated atmospheric conditions the ground hold performance was very poor. Leakage through the vacuum bag into the ground hold section had occurred. This problem has been encountered in other local and contracted insulation projects. The other insulation with a sealed cell ground hold section proved more reliable

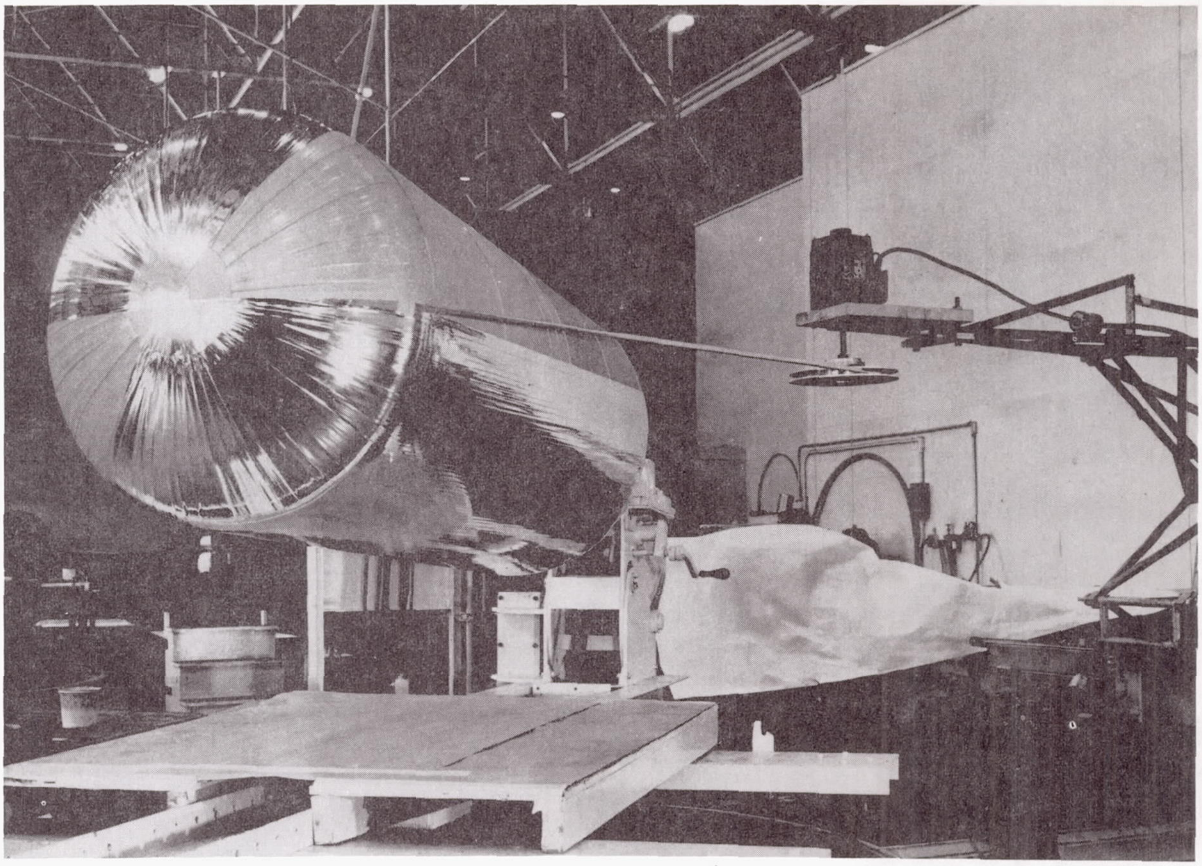

FIGURE 2. INSULATION APPLICATION PROCESS

FIGURE 3. FOAM SPACERS SEPARATING INSULATION LAYERS

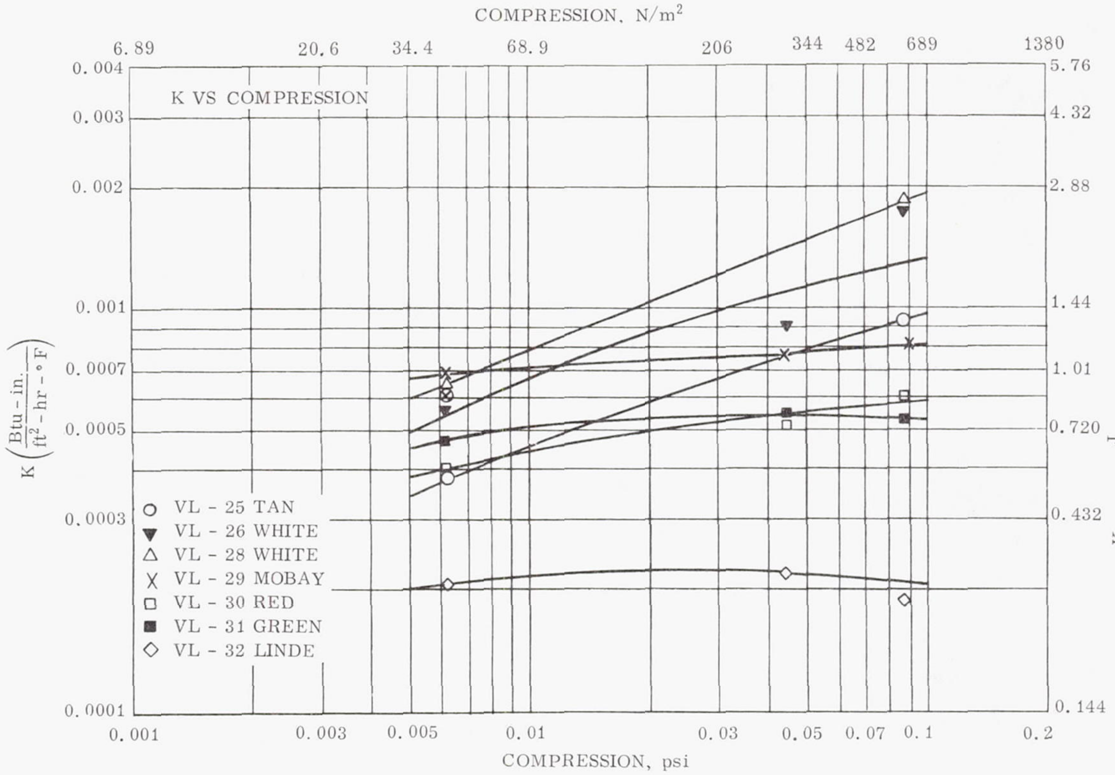

FIGURE 4. EFFECT OF EXTERNAL COMPRESSION ON APPARENT K FOR MULTILAYER INSULATIONS

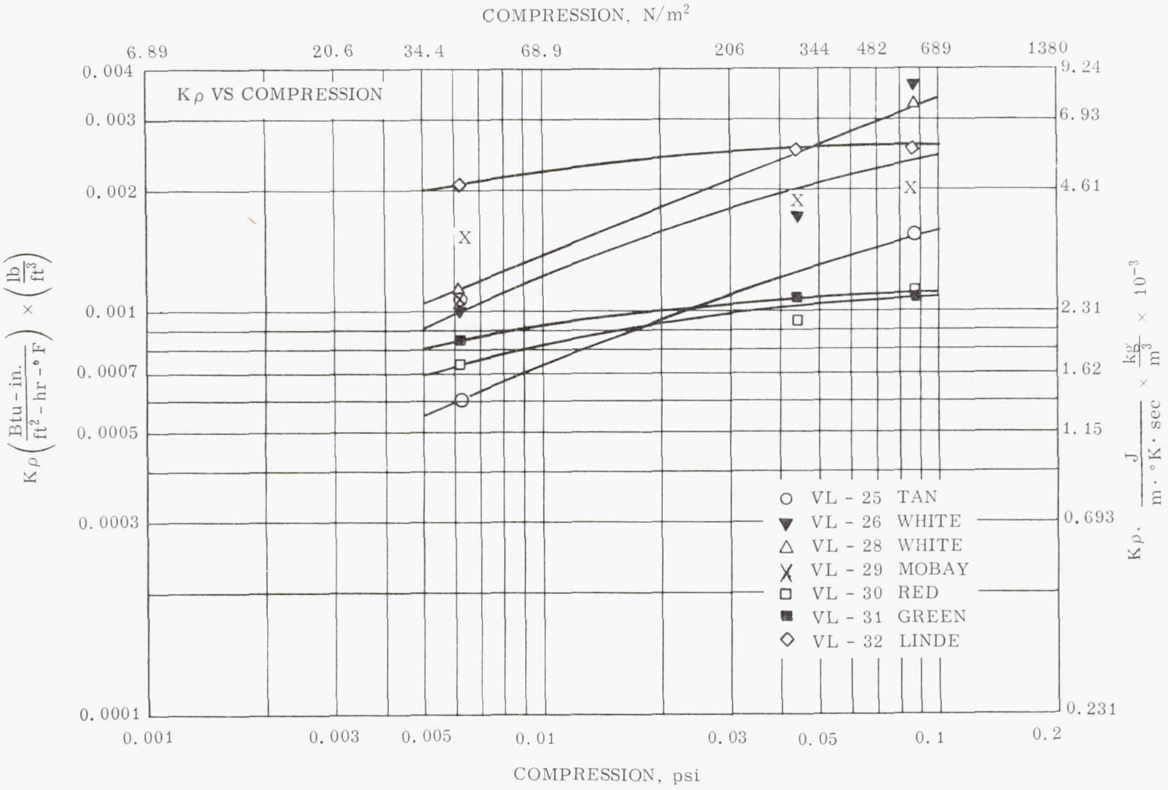

FIGURE 5. EFFECT OF EXTERNAL COMPRESSION ON Kρ FOR MULTILAYER INSULATIONS

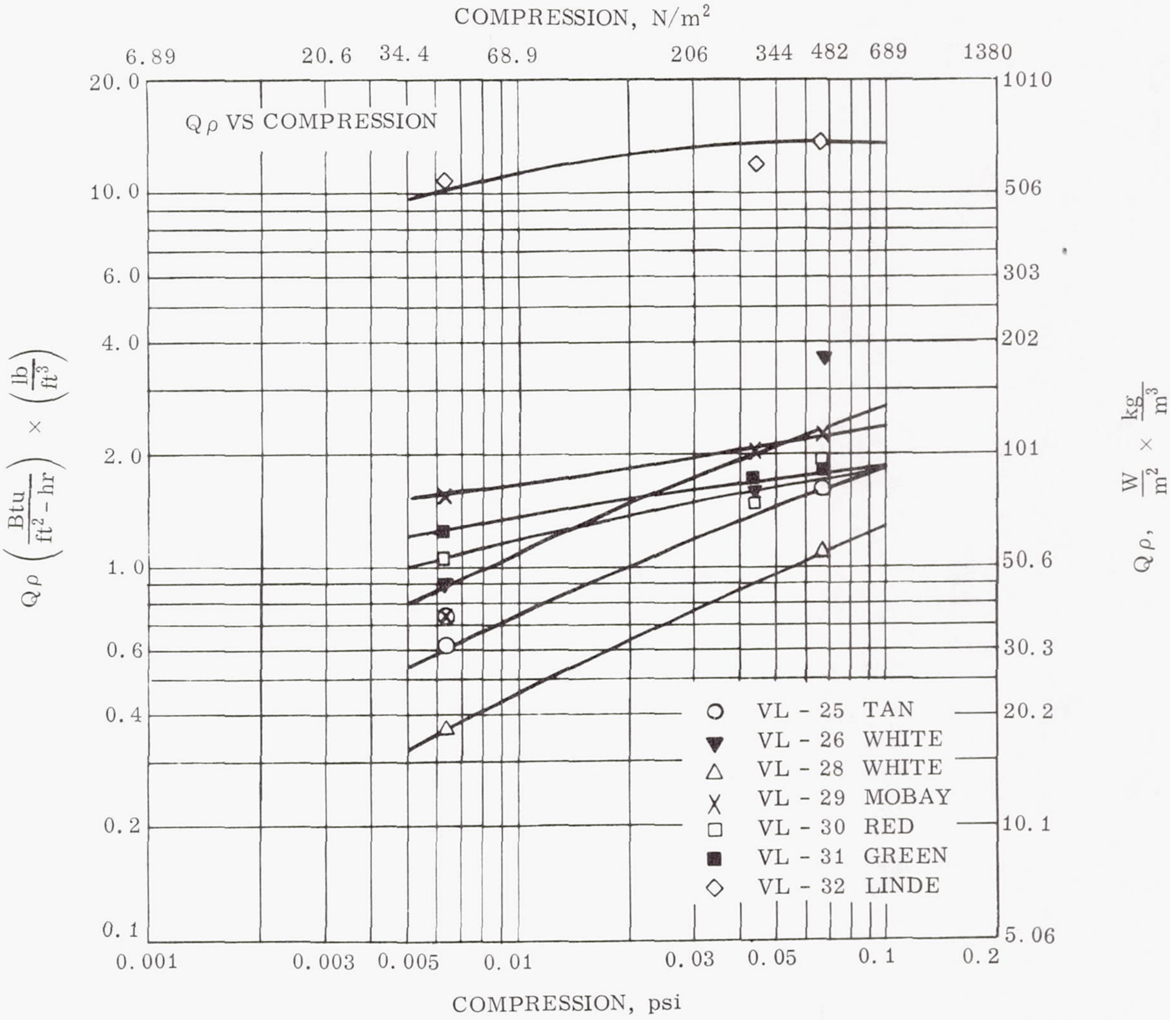

FIGURE 6. EFFECT OF EXTERNAL COMPRESSION ON $Q\rho$ FOR MULTILAYER INSULATIONS

in these tests even though its insulation performance is not as good as the ideal performance of the full multilayer version. Until a damage-resistant vacuum bag material is developed, the ideal ground hold performance of the full multilayer insulation cannot be achieved in this fashion.

Since it may be impractical to machine-wrap some tanks, attempts are being made to fabricate this insulation in panels, which will permit its piecewise attachment to the tank by a cinch-wrap contact adhesive combination. Our present contract calls for Goodyear to apply a mutually selected version of this insulation to a large test tank at least 1.78 m (70 in.) in diameter. This tank should be available for testing at this center next May or June. If the insulation continues to show promise for that size tank, an inflight experiment will be proposed.

Micrometeoroid test work is being done by IIT Research Institute under subcontract to Goodyear. A one week mission for a vehicle 10.7 m (35 ft) in diameter by 30.5 m (100 ft) in length was assumed and calculations based upon generally accepted mass-flux relationships indicated that particles in the 10^{-4} to 10^{-2} gram mass range would be the most probable sources of damage. Every variant of these insulations considered so far has been tested in IIT Research Institute's light gas gun facility with 17 and 70 mg Pyrex projectiles. No damage to the simulated tank structure has been detected when these particles

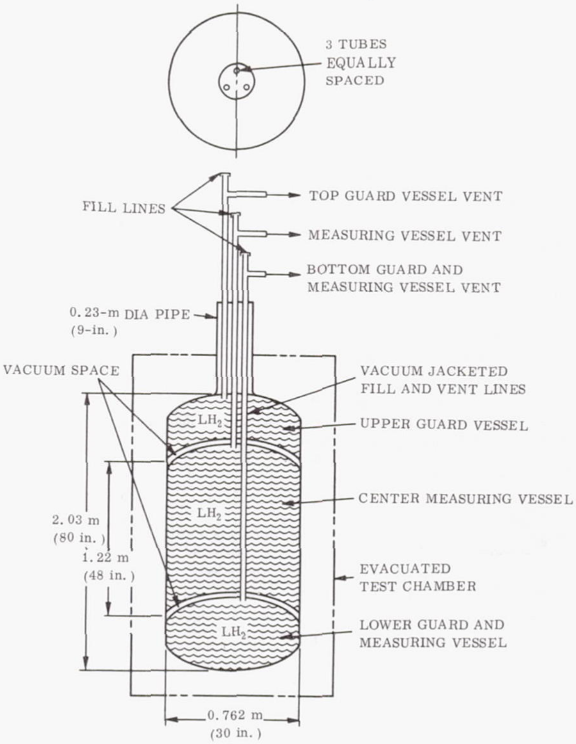

FIGURE 7. CYLINDRICAL CALORIMETER

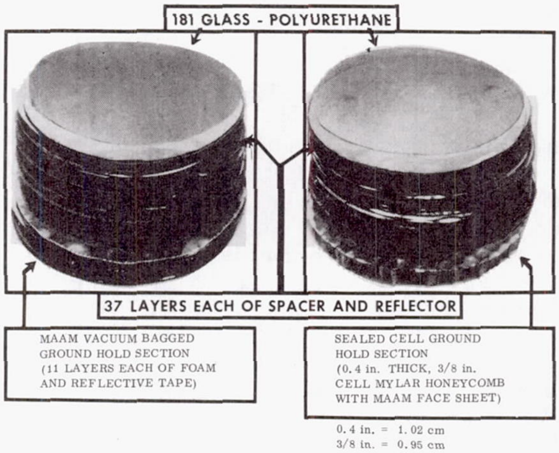

FIGURE 8. TAPE WRAPPED MULTILAYER INSULATIONS

TABLE II. PERFORMANCE OF MULTILAYER INSULATIONS

Test Condition	Vacuum-Bagged Ground Hold Section K	Q	Sealed Cell Ground Hold Section K	Q
	$\frac{J}{m \cdot {}^\circ K \cdot sec}$	$\frac{W}{m^2}$		
	$K\left(\frac{Btu\text{-}in.}{ft^2\text{-}{}^\circ F\text{-}hr}\right)$	$Q\left(\frac{Btu}{hr\text{-}ft^2}\right)$		
Vacuum	5.48×10^{-5} (3.8×10^{-4})	0.284 (0.09)	8.65×10^{-5} (6×10^{-4})	0.473 (0.15)
Ground Hold	0.0677-0.0750 (0.47-0.52)	284-316 (90-100)	0.0432-0.0621 (0.30-0.38)	189-236 (60-75)

were impacted on the insulation at velocities ranging from 6710-7930 m/s (22 000-26 000 fps). Despite a limited ability to approximate the true environment, it is believed that these insulations will certainly furnish some protection from micrometeoroids.

Finally, it is recognized that deriving the maximum benefit from superinsulations will require new concepts in tankage support and other hardware to minimize the heat leak from these sources. This problem is being studied in other programs.

In conclusion, this particular system of insulation design and attachment appears to be a realistic means of achieving the desired thermal performance of multilayer insulations while minimizing the practical problems of attachment, installation, purging, and evacuation. This insulation can be purged and evacuated as a single bulk material characterized by a high apparent permeability, and this alone has been a problem with multilayer insulations.

ADHESIVES RESEARCH

Table III is a current listing of major adhesives research and development efforts now being pursued by the Materials Division. A parallel inhouse experimental effort is being conducted on each contract goal. A brief outline follows the approach being followed on each program.

A selective examination of parameters governing performance of polyurethane adhesive systems has been attempted under the first program. These have included variations in the catalyst/resin ratio, variations in cure cycle, effect of humidity level

TABLE III. ADHESIVES RESEARCH

Contract	Title
NAS 8-11958	Optimization of the Performance of a Polyurethane Adhesive System over the Temperature Range of -253° to +93° C (-423° to +200° F)
NAS 8-11068	Development of Structural Adhesives Suitable for Use with Liquid Oxygen
NAS 8-20406	Development of Improved Structural Adhesives for Use over a Wide Temperature Range of -253° to +150° C (-423° to +302° F)
NAS 8-11371	Development of Improved Semi-Organic Structural Adhesives for Elevated Temperature Applications

during the bonding process, effect of bond line thickness, effect of catalyst/resin mix technique, effect of different primers for the adherends, and variations observed between operators. Data were obtained using aluminum lap shear and T-peel specimens.

Liquid oxygen compatible adhesives being sought under the second project require development of fluorocarbon or Teflon-like polymers with adhesive properties. During the past year an internal synthesis program for highly fluorinated polymers was initiated; accomplishments to date have included the synthesis of several fluorinated monomers previously unreported in chemical literature. Polymerization reactions of these monomers are being studied.

A broader spectrum of materials is being studied during the next effort. Improved adhesives without any restrictions on their chemical composition are being developed. These adhesives must be useful at both cryogenic and moderately elevated temperatures. Blends of urethane and epoxy prepolymers with variations in curing systems have comprised the major part of the inhouse effort in this area.

The final program on semi-organic structural adhesives is based upon chelate structures, or organic polymers which contain metal atoms anchored by a particularly stable form of chemical bonding. It was hoped that this same type of bonding could be activated at the adhesive-metal adherend interface, but this has not yet been confirmed.

This discussion of the overall program covered the major identifiable problem areas in adhesives technology that are under investigation. However, the development of the adhesive is only the beginning. The response of the adhesive system to a variety of environments, both during the bonding process and during the service life of the bonded assembly, must be determined.

Some existing adhesives have undesirable traits and weaknesses that must be examined experimentally. A commercially available polyurethane adhesive in widespread use in our programs is being studied exhaustively in this context because of its inherent temperamentality. A major part of this work was concentrated upon the response of this adhesive to aging environments and the evaluation of new primer systems that are now available for this adhesive.

Accelerated aging of polyurethane bonded aluminum lap shear specimens has been accomplished under experimental conditions more severe than normal ambient surroundings. Figure 9 shows data obtained when lap shear specimens bonded with Narmco 7343/7139 adhesive system were stored at 311° K (100° F) at a humidity of 100%. Three series of adherends were used: (a) primed with 3M Company's XC-3901, a silane derivative; (b) primed with Goodyear's G-207 primer; (c) unprimed. These lap shear values were obtained at room temperature. Over a period of 35 days, progressive bond deterioration is evident in all three series. Initial strengths,

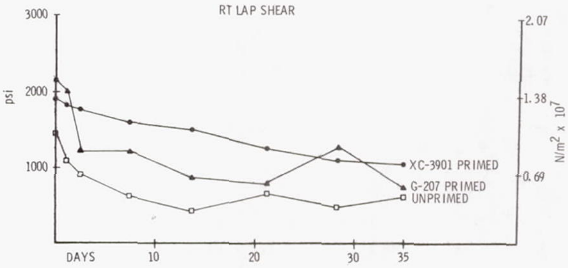

FIGURE 9. LAP SHEAR SPECIMENS (NARMCO 7343/7139) AGED AT 311° K (100° F); 100% HUMIDITY

and, therefore, final strengths for primed specimens were better than for unprimed.

The same relationship holds for specimens tested at 356°K (180° F) (Fig. 10). Bond strengths are again weakened over a 35 day period. The silane derivative, XC-3901, is patently superior to G-207 as a primer at this temperature.

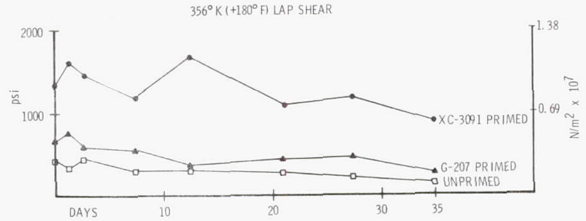

FIGURE 10. LAP SHEAR SPECIMENS (NARMCO 7343/7139) AGED AT 311°K (100° F); 100% HUMIDITY

Specimens tested at 88.6°K (-300° F) (Fig. 11) do not clearly reflect adverse aging effects for primed samples. XC-3901 primed adherends also yield bonds with higher strengths at this temperature than do the G-207 treated adherends.

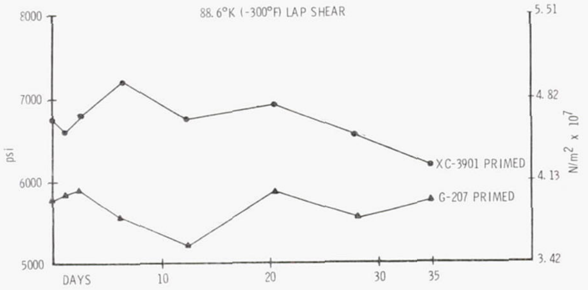

FIGURE 11. LAP SHEAR SPECIMENS (NARMCO 7343/7139) AGED AT 311°K (100° F); 100% HUMIDITY

Since these data were plotted, additional points were obtained in each series at each of three test temperatures. No further bond deterioration was observed after this extended period of aging under this relatively severe experiment.

A similar experiment with milder aging conditions, 294°K (70° F) at 100% humidity, extended over a period of eight weeks with specimens being tested at room temperature and at 77.6°K (-320° F). Results are summarized in Figure 12 for the 77.6°K (-320° F) lap shear tests. The effect of the 294°K (70° F) aging exposure is less severe than the 311°K (100° F) exposure, as would be expected. In these studies another silane primer system, Dow Corning's Z-6020 product, was evaluated and over the full temperature spectrum gave better results than the unprimed specimens or the G-207 primer. Under these conditions, there is no significant deterioration from initial values in the case of the primed samples. This same trend was evident in tests at other temperatures.

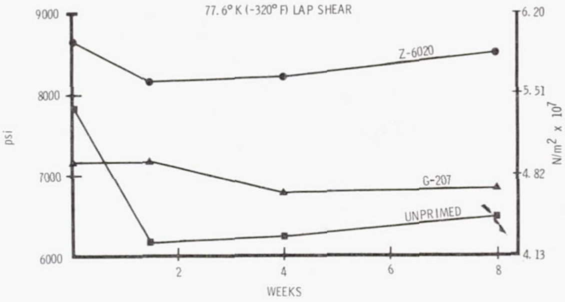

FIGURE 12. LAP SHEAR SPECIMENS (NARMCO 7343/7139) AGED AT 294°K (70° F); 100% HUMIDITY

A long term aging study under ambient, outdoor conditions is also in progress. Aluminum lap shear adherends, bonded with the 7343/7139 adhesive system, are stored outside in a ventilated metal cabinet, protected only from direct precipitation. Figure 13 shows room temperature test results obtained during the first six months on the same three sample types. There is no firmly significant change in the strength values obtained at other test temperatures.

Additional interesting data have demonstrated the beneficial effects of silane-type primers on aluminum lap shear specimens bonded with the 7343/7139 polyurethane adhesive systems. Figure 14 summarizes the results of room temperature tests. Although the values obtained for unprimed specimens were quite good, averaging 1.46×10^7 N/m^2 (2121 psi), the strength of specimens primed with

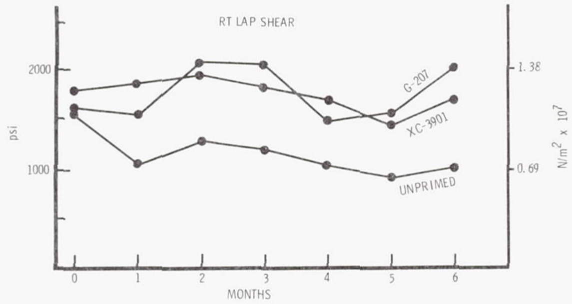

FIGURE 13. LAP SHEAR SPECIMENS (NARMCO 7343/7139) AGED IN AMBIENT OUTDOOR ENVIRONMENT

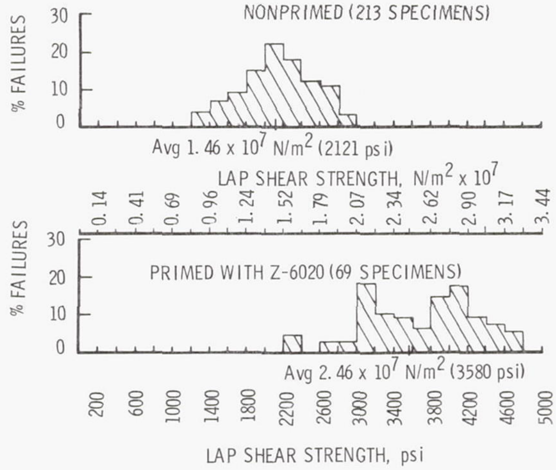

FIGURE 14. DISTRIBUTION OF ROOM TEMPERATURE STRENGTHS (NARMCO 7343/7139)

Dow Corning Z-6020 was considerably improved, yielding an average of 2.46 × 10^7 N/m^2 (3580 psi), and more important, a higher minimum value for the series (1.38 vs 0.826 N/m^2 × 10^7) (2000 vs 1200 psi). Similar benefits are evident when samples are tested at other temperatures. Figure 15 shows strength distribution obtained at a test temperature of 339°K (+150°F).

This briefly and partially defines the scope of activities needed to acquire a sound working level of familiarity with one model adhesive system. The most striking observations evident from this work are the regulatory and beneficial effects of some of the new primers now becoming available. They promote the formation and maintenance of higher bond strengths and apparently can also serve to inhibit strength degradation by the dual effects of temperature and humidity. Finally, it is clear that the effect of an aging environment on an adhesive bond is a function of the service conditions to which the bond will ultimately be exposed.

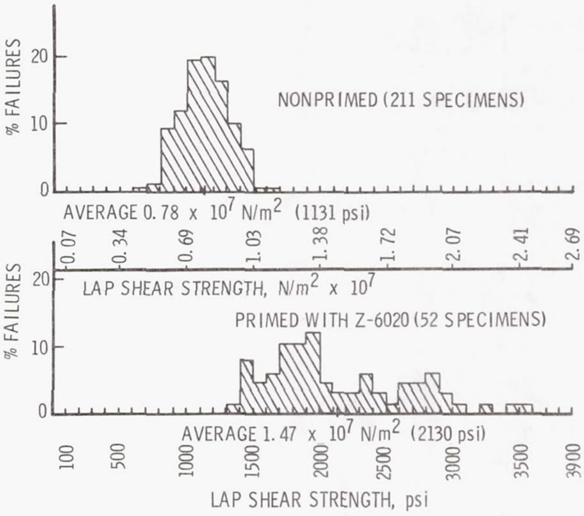

FIGURE 15. DISTRIBUTION OF 339°K (150°F) LAP SHEAR STRENGTHS (NARMCO 7343/7139)

MEMBRANE DIFFUSION THEORY

Permeation is a recurring environmental problem in using plastic films, bladders and other shapes. Generally polymers or plastics are characterized by permeation rates much higher than metallic components of equivalent geometry. A great amount of work has been and is being done by others in this field. The effort discussed here is an attempt to combine some isolated theoretical developments which promise to greatly simplify the study, analysis and prediction of permeation and diffusion effects.

The overall permeation process through membranes is usually considered to take place in three steps [1]: (1) The penetrant dissolves at the membrane face bordering the zone of highest concentration or pressure, (2) Penetrant molecules then move by activated diffusion through "holes" created in the polymer matrix by the random thermally induced motion of polymer chain segments, (3) At the downstream or lower concentration face, the penetrant is desorbed.

The diffusion step is usually the rate-controlling phase of the overall process and it is the step most sensitive to variations in polymer and penetrant structure. Thus, it is desirable to study only the diffusional aspect of the overall process.

It is intuitively evident from the preceding argument that steady state permeation measurements do not readily permit separate analysis of solubility and diffusional effects. This can be done easily by transient state permeation measurements if the diffusion coefficient (D) is not a function of penetrant concentration and is not altered by other time dependent processes. This so called time lag approach was developed by Daynes [2] and has been used by numerous other authors [3, 4]. The diffusion coefficient (D) is defined in Fick's Laws of Diffusion (Fig. 16) for unidirectional diffusion in the x direction where J = the mass flux of penetrant per unit membrane area in the direction of the concentration gradient that is the driving force, C = concentration, and t = time.

To briefly outline the time lag theory, consider a semi-infinite membrane of thickness l which is suddenly exposed on one face to a penetrant concentration C_2 while the downstream face is maintained at zero concentration. There will be a transient period preceding the development of steady state conditions. The boundary and initial conditions are given in Figure 16.

Mathematically the total concentration at any point within the membrane can be considered the sum of two separate concentrations as specified in Figure 17. In effect, C_a is assumed to be position dependent only while C_b incorporates all of the time dependency of this transient state. The boundary and initial conditions for C_b are identical to those for

$$J = -D\frac{\partial C}{\partial x}$$

Fick's Laws

$$\frac{\partial C}{\partial t} = -D\frac{\partial^2 C}{\partial x^2}$$

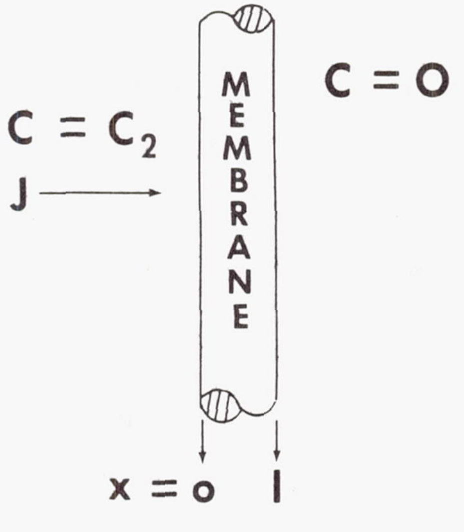

boundary and initial conditions

$C = 0$ at $t = 0$ at $0 < x < l$

$C = 0$ at $X = l$

$C = C_2$ at $X = 0$

FIGURE 16. DIFFUSION THROUGH MEMBRANES

$$\text{if } C = C_a + C_b$$

$C_a = 0 \text{ at } x = l$	$C_b = \dfrac{-C_2(l-x)}{l} \text{ at } t = 0$
$C_a = C_2 \text{ at } x = 0$	$C_b = 0 \text{ at } t = \infty$
$C_a = \dfrac{C_2(l-x)}{l} \text{ for } 0 < x < l$	$C_b = 0 \text{ at } x = 0$
	$C_b = 0 \text{ at } x = l$

$$C_{x,t} = C_2 \left[\frac{l-x}{l} - \frac{2}{\pi} \sum_{n=1}^{\infty} \frac{1}{n} \sin \frac{n\pi x}{l} \exp\left(\frac{-Dn^2\pi^2 t}{l^2} \right) \right]$$

FOURIER SOLUTION

at large t (steady state):

$$C_{s(x)} = \frac{C_2(l-x)}{l}$$

FIGURE 17. FOURIER MASS TRANSFER SOLUTION

temperature in the analogous heat transfer problem where a semi-infinite slab initially at a uniform temperature is plunged into a "zero" temperature environment [5]. The equation ultimately obtained for the concentration as a function of both time and position is the Fourier Solution (Fig. 17). The contribution of the summation term decreases with time and the steady state concentration distribution ($C_{s(x)}$) is obtained.

Now, assume that the total mass flux issuing from the downstream x = l membrane area (A) accumulates in a hypothetical volume (V) until penetrant concentration C_g is attained at a time t (Fig. 18). The rate of penetrant concentration (C_g) increase in a hypothetical downstream volume (V) can be related to Fick's first law as shown in Figure 18. The concentration gradient is obtained by differentiation of the solution for $C_{x,t}$ in Figure 17 and evaluating dC/dx at x = l. This permits the estimation of C_g at large values of time (t), which would be well within the steady state permeation realm.

Note that it is possible to solve this equation for t. If steady state conditions had existed from the beginning of the experiment (t = 0), some shorter time designated t* would have been required to develop the same concentration C_g that was developed in the longer experiment spanning the transient state. Equating these expressions for C_g permits the calculation of the time lag L that is defined as t - t*.

In principle, the time lag approach permits calculation of a constant diffusion coefficient from the membrane thickness and observed time lag in spite of the simultaneously-occurring solubility effects. The graphical interpretation of the time lag is shown in Figure 19. Deviations from this relationship have been observed in many cases of practical interest. These instances have been rather indiscriminately labled "non-Fickian diffusion" by some investigators.

If time dependent relaxation effects in the membrane material are relegated to a minor role, one

$$V\int_0^t \frac{dC_g}{dt} = \left[J_t\right]_{x=l} A = -AD\left(\frac{dC}{dx}\right)_{x=l}$$

$$C_g = \frac{DC_2A}{Vl}\left[t + 2\frac{l^2}{D\pi^2}\sum_{n=1}^{\infty}\frac{(-1)^n}{n^2}\exp\left(\frac{-Dn^2\pi^2 t}{l^2}\right)\right]$$

$$\text{or } C_g = \frac{DC_2A}{Vl}\left[t - \frac{l^2}{6D}\right] \text{ at large } t$$

$$\frac{C_gV}{t^\star} = \frac{DC_2A}{l} \; ; \quad C_g = \frac{DC_2t^\star A}{Vl}$$

Equating Values For C_g:

$$t - t^\star = L = \frac{l^2}{6D} \; ; \quad D = \frac{l^2}{6L}$$

FIGURE 18. TIME LAG APPROACH

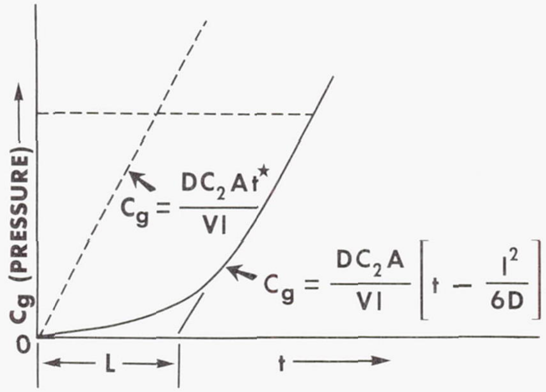

FIGURE 19. GRAPHICAL SIGNIFICANCE OF TIME LAG

$$\frac{\partial C}{\partial t} = \frac{\partial}{\partial x}\left(D_c \frac{\partial C}{\partial x}\right)$$

$$\begin{aligned} \text{where } D_c &= f\,(D_o, C) \\ D_c &= D_o\,(1 + aC) \\ \text{or } D_c &= D_o \exp\,(bc)\text{, etc.} \end{aligned}$$

FIGURE 20. FICK'S SECOND LAW FOR CONCENTRATION-DEPENDENT DIFFUSION COEFFICIENT (D)

possible explanation for these deviations would be that there exists a variation of the diffusion coefficient with penetrant concentration (Fig. 20). D_c is a variable diffusion coefficient, and D_o is a hypothetical "zero concentration" diffusion coefficient (Fig. 20). Although a steady state permeation rate is attained in concentration dependent systems, the experimentally observed time lag is not as straightforwardly related to the diffusion coefficient as it was in the earlier case.

One notable contribution in dealing with concentration dependent situations has been made by Holstein [6] who pointed out that the Fourier solution to Fick's first law equation can be subjected to the series transformation in Figure 21 [7]. Substituting in J_t for y and Z, another version of the flux equation is obtained in which the time parameter (t) is in the denominator of the negative exponent. Rearranging and taking the logarithm of both sides permits the conclusion stated in Figure 21.

$$\left|J_t\right|_{x=l} = \frac{DC_2}{l}\left[1 + 2\sum_{1}^{\infty} \cos n\pi \exp\left(-\frac{Dn^2\pi^2 t}{l^2}\right)\right]$$

$$\downarrow$$

apply $\sum_{-\infty}^{\infty} \exp\left(-\frac{\pi n^2}{z}\right) \exp 2\pi i n y = \sqrt{z}\sum_{-\infty}^{\infty} \exp\left[-\pi(n+y)^2 z\right]$

by setting $y = \frac{1}{2}$ and $z = \frac{l^2}{\pi D t}$

$$\downarrow$$

$$\left|J_t\right|_{x=l} = 2C_2\sqrt{\frac{D}{\pi t}}\exp\left(-\frac{l^2}{4Dt}\right) = \frac{V}{A}\,\frac{dC_g}{dt}$$

conclusion: $\frac{1}{t}$ versus $\ln\left(\frac{dC_g}{dt}\sqrt{t}\right)$ plot has slope $\left(\frac{-l^2}{4D}\right)$

FIGURE 21. HOLSTEIN TRANSFORMATION VALID FOR SHORT TIME MEASUREMENTS

Thus, if the diffusion coefficient is constant, a plot of $\ln \frac{dC_g}{dt}\sqrt{t}$ versus 1/t should be a straight line of slope $\left(\frac{-l^2}{4D}\right)$. More importantly, if the diffusion coefficient is concentration dependent, the plot can be extrapolated to t = 0 and the slope at that point may be used to calculate D_o, the zero concentration diffusion coefficient. This is one of the parameters needed to define the variability of the true diffusion coefficient with concentration.

A second contribution has been made by Frisch [8] who has defined the significance of the time lag in concentration dependent systems. The two key equations that result from his treatment are shown in Figure 22. D_c is some inferred or assumed function of D_o and C, while $C_{s(x)}$ is the position-dependent steady state concentration. In principle, the first equation is used to obtain C_s as a function

$$\int_{C_{s}(x)}^{C_2} D_c\, dC = \frac{x}{l}\int_{0}^{C_2} D_c\, dC$$

$$L = \frac{\int_0^l x\, C_{s(x)}\, dx}{\int_0^{C_2} D_c\, dC}$$

where $D_c = D_o(1 + ac)$

or $D_o \exp(bc)$ etc.

FIGURE 22. FRISCH TIME LAG EQUATIONS FOR D VARYING WITH C

of x and that result is used to calculate a time lag which is then compared with experimental observations. The functional form of D_c is known for some membrane-penetrant systems; in many cases the data are represented by equations like those in Figure 22.

Theoretically, the picture is now complete. From a single transient state permeation experiment, the value of D_o can be calculated using the short-time transform of the Fourier flux equation. Using the time lag measured later in the same experiment, a constant in one of these equations can be adjusted to obtain all of the information necessary to describe the diffusional process in terms of the concentration dependent differential diffusion coefficient. In spite of the potentially great saving in time and experimental effort offered by this approach, it has been only partially tested in some work reported recently by Meares [9]. Experimental work is being planned to establish if this approach will clarify practical permeation problems. If this line of reasoning can be extended to systems that are complicated by time dependent relaxation effects in the membrane material, an interesting experimental probe would then be available for studying segmental motion in the polymer solid state. Some of the problems discussed previously arise directly from our lack of understanding of the nature, frequency and extent of this segmental motion.

REFERENCES

1. Lebovits, A.: Modern Plastics. Vol. 43, No. 7, 1966, p. 139.
2. Daynes, H. A.: Proceedings of the Royal Society of London (Series A). Vol. 97, 1920, p. 286.
3. Barrer, R. M.: Diffusion In and Through Solids. Cambridge University Press, New York, 1941, p. 18 ff.
4. Jost, W.: Diffusion in Solids, Liquids and Gases. Academic Press, Inc., New York, 1966.
5. Carslaw, H. S.; and Jaeger, J. C.: Conduction of Heat in Solids. Oxford University Press, New York, 1959, p. 92 ff.
6. Holstein, T.: Research Report 60-94411-9-D. Westinghouse Electric Company, December 20, 1951.
7. Courant, R.; and Hilbert, D.: Methods of Mathematical Physics. Second Edition.
8. Frisch, H. L.: Journal of Physical Chemistry. Vol. 61, 1957, p. 93, and Vol. 62, 1958, p. 401.
9. Meares, P.: Journal of Applied Polymer Science. Vol. 9, 1965, p. 917.

Page
Intentionally
Left Blank

5

QUALITY AND RELIABILITY ASSURANCE RESEARCH AT MSFC

September 29, 1966

By

James B. Beal
Robert L. Brown
Leon C. Hamiter, Jr.
Frederic E. Wells

Page
Intentionally
Left Blank

Page
Intentionally
Left Blank

FAST SCAN INFRARED MICROSCOPE FOR IMPROVING MICROELECTRONIC DEVICE RELIABILITY

by Leon C. Hamiter, Jr.

LIST OF ILLUSTRATIONS

CONTENTS (Continued)

USE OF SLURRIES FOR HYDROSTATIC TESTING

by Frederic E. Wells

AUTOMATED ULTRASONIC SCANNING BY TRIANGULATION METHODS - THE DICKINSON SYSTEM

by Robert L. Brown

LIST OF ILLUSTRATIONS

ULTRASONIC EMISSION DETECTOR EVALUATION OF THE STRENGTH OF BONDED MATERIALS

by James B. Beal

LIST OF TABLES

LIST OF ILLUSTRATIONS

FAST SCAN INFRARED MICROSCOPE FOR IMPROVING MICROELECTRONIC DEVICE RELIABILITY

By

Leon C. Hamiter, Jr.

SUMMARY

The emission of infrared radiation by semiconductor chips led to a method for testing microminiature circuits with an infrared microscope. A description of infrared radiation is presented and is related to the electrical power dissipation of an electronic part. A description of the composition and operation of the infrared microscope is presented. The feasibility of inspection of the elements and circuit junctions of microelectronic chips is demonstrated. Thermal maps of circuits are examined for defects and design problems. The possibility of using the infrared microscope for testing transistors is discussed.

INTRODUCTION

Technological progress is a two-step function. First, a new device is created, and second, means to manufacture it in a better and more consistent way are sought. The world of microelectronics is now in the second phase, with progress being made towards better manufacturing methods and processes.

Infrared testing is being developed to yield large amounts of information on thermal and electromechanical parameters affecting the reliability of microelectronic devices. Conventional test equipment and methods cannot measure these factors because of the minute size and inaccessibility of the elements.

Semiconductor chips have an area approximately 1 mm^2, and within this chip some integrated circuits contain dozens of transistors, diodes and resistors. The electrical interconnections are often only a few microns in width, which makes physical contact with them for test purposes not only difficult but also dangerous to their mechanical and electrical integrity. On a practical basis, probe measurements can only be made prior to dicing and encapsulation.

Ordinarily, only input and output measurements can be obtained through the use of conventional test equipment. In the case of complex integrated circuitry this is inadequate because it does not give information about the performance of the individual elements of the network. Marginal performance of an element could go undetected because of the compensating effect of another element. Furthermore, several design or manufacturing defects that may eventually cause a failure cannot be detected by conventional testing. Figure 1 shows some of the failure mechanisms and defective conditions in this class.

SEMICONDUCTOR BULK MATERIAL	RESISTIVITY IRREGULARITIES DISLOCATIONS LATTICE ANOMALIES SECONDARY BREAKDOWN
DESIGN	JUNCTION PROXIMITY THERMAL INTERACTION
SURFACE	PINHOLES CONTAMINATION ION MIGRATION CHANNELING
MECHANICAL	UNEVEN METAL DEPOSITION POOR BONDING OF DEPOSITED ELEMENTS POOR BONDING OF LEAD WIRES POOR DIE BONDING CRACKS, VOIDS, AND SCRATCHES

FIGURE 1. LIST OF SEMICONDUCTOR DEFECTS

INFRARED RADIATION

Infrared radiation, or "invisible light," is an electromagnetic oscillation of the same type as the electromagnetic waves that are called "visible light." The electromagnetic radiation band extends from the very low frequencies of the typical house current oscillations to the extremely high frequencies of the gamma rays and cosmic rays produced by variations in energy of subatomic particles. All of these radiations are of the same nature, travel at the same speed (the speed of light), and transport energy.

The infrared radiation is contained in the band between the visible light and the radio waves. The infrared radiation is generated by the vibrational and rotational movements of the atoms and the molecules of which physical matter is composed. Consequently, the spectrum of the infrared radiation emitted by physical matter is extremely broad and peaks at a frequency that varies with temperature.

A physical body containing atomic and subatomic particles of all possible sizes would emit at all infrared frequencies, on an uninterrupted spectral band. Such a physical body is called a "blackbody," and although it does not exist in nature, very close approximations to it can be made, and infrared radiation laws are formulated upon it. The shape of this component's radiation band will depend upon its temperature and surface condition, or "emissivity."

Besides the infrared radiation emitted by physical matter because of thermal agitation, infrared radiation is also being emitted by semiconductors independently from the thermal status. This infrared radiation is called recombination radiation and results from the energy liberated by the current carriers when they step down from the higher energy level of the carrier band to the lower energy level of the valence band (the electron hole pairs recombine). This recombination radiation is directly proportional to the amount of current flowing through the semiconductor and its variations of the current flow. Detection and measurement of the recombination radiation should allow the modulated operation and even pulse operation of semiconductors to be analyzed without any time delay. The recombination radiation takes place in a different wavelength than the radiation caused by thermal effects, and with the use of adequate filters, each radiation can be read independently.

Wherever electrical current flows, a fraction of it turns into heat. This is generally called "power dissipation" and results in a temperature rise of the element through which the current flows. This thermal rise increases the power of the infrared radiation emitted by the surface of the element, and in turn this variation can be measured by an adequate infrared detector.

A direct correlation can be established between the electrical power dissipation of an electronic part of a given design, and the infrared radiation emitted by it. This correlation is the key to the infrared evaluation of electrically energized microelectronic circuits.

Passive elements can be evaluated by plotting their temperature variation when subjected to a thermal gradient. This is done by mapping the infrared radiation emitted by each surface point of the target. Then the physical anomalies such as material discontinuities, lack of proper bonding, cross-section variations, etc., can be detected and evaluated.

When the target is a semiconductor chip, the infrared test equipment requirements are set by its physical size, the temperature gradients to be observed and the speed at which thermal flooding of the target takes place.

INFRARED MICROSCOPE

Figure 2 is a photograph of the fast scan infrared microscope developed by Raytheon Company under contract for MSFC. On the left is the pedestal for mounting the device under examination. The microscope is for alignment and visual observation of the sample. The upper right area contains the drive mechanism for the helix and polygon scanning system. Figure 3 is a functional block diagram of the instrument. Basically the unit can be divided into five major sections: optics, scanning system, detector with cryogenic cooling, signal processing and display system.

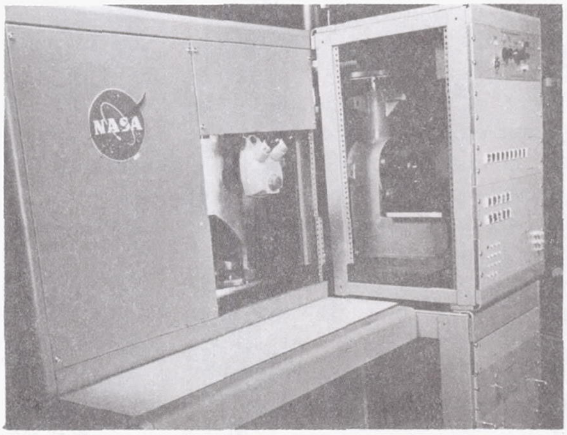

FIGURE 2. FAST SCAN INFRARED MICROSCOPE

OPTICS

Larger than normal optics with several unique properties were deliberately chosen for the infrared microscope. The detector aperture requirements were satisfied by using a 7.6 to 1 magnifying system.

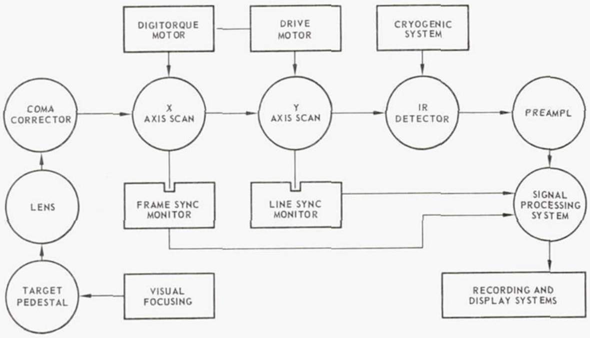

FIGURE 3. BLOCK DIAGRAM OF FAST SCAN INFRARED MICROSCOPE

A diameter of 20.3 centimeters (8 inches) was chosen for the primary lens, and the focal ratio was set at F 1.1. This long focal length enables the object to be away from the primary optics in a space of its own. It further permits the use of an off-axis system; the only aberrations from this system occur because the field is spherical rather than flat. However, under the conditions in which this device will be used, these aberrations are not a major factor. Optical resolution of a diffraction-limited characteristic is achieved in a lens system having a concentric, spherically round, germanium corrector and a spherical primary lens.

SCANNING SYSTEM

The high-speed, infrared microscope requred a unique scanning system. This requirement was met by development of a polygon helix scanner in which a polygon, having 64 internal facets and 64 spaces, is rotated for the aperture mask of the detector at a speed of 1000 lines per second. This scanned beam is relayed to a pair of flat annuli oriented to fold the beam 180 degrees. Only a small segment of each annuli is used. The main effect is to provide the system with a corner reflector. This would be the effect if the annuli were perfect doughnut-shaped flat surfaces of glass; however, they are split with one end raised 0.381 centimeter (0.15 inch) to form a helix. When rotated together, these helixes transversely move the optical image as far as necessary to permit scanning a 1 1/2 millimeter surface at 10 Hz linear speed and 90 percent efficiency.

DETECTOR WITH CRYOGENIC COOLING

The detector and the cooling system were chosen to be compatible with the rest of the microscope. The detector has a 0.000762-centimeter (0.0003-inch) diameter aperture with an aperture limiting mask of 13 degrees in one axis and 6 degrees in the other axis. This aperture will permit the detector to see all areas in the target plane. The detector is mercury-doped germanium with a normal operating temperature of 30°K. Cooling is provided by a Malaker Mark 7 closed-cycle cryogenic cooler. The closed-cycle system offered significant advantages over the manually-filled helium system which was the alternate system.

SIGNAL PROCESSING

Signal processing for the infrared microscope was made as simple as possible. The detector amplifier and log post-amplifier have variable gains and a variable bandwidth. To provide x and y drives for the cathode-ray oscilloscope or magnetic tape, synchronizing pulses come from both the polygon wheel and the helix wheels. The net result is an ability to provide a single frame image of the target to be scanned, as well as radiation amplitude versus time data on a continuous basis.

DISPLAY SYSTEM

The instrument's output is an analog signal having a maximum frequency of 100 Hz and the indexing of a video signal. Because of these characteristics, the output can best be connected to a conventional video tape recorder. Information from the video tape recorder can then be reproduced sequentially as video images on an oscilloscope, and line scans can be recorded directly on a strip chart recorder. In addition, information from the video recorder can be used as the input to an analog to digital converter, whose output proceeds into a buffer unit for storage and future computer processing.

The smallest elements of an integrated circuit are the junctions which can be only a few microns wide. Consequently, the area resolution of an adequate infrared system should be able to view them. Possibly an even finer resolution capability would be useful, but the wavelength of the radiation emitted by the target is the limiting factor. Therefore, the instrument was designed to have the following capabilities:

Area Resolution	20 microns
Temperature Resolution	1°K at 298°K ambient
Frame Composition	100 lines/frame
Scan Speed	1000 lines/second
Optical Magnification	7.6
Depth of Field	± 20 microns
System Efficiency	40%
IR Wavelength	6 - 12 microns

Once a microelectronic-device prototype has been built and is operating, a thermal map of it will enable the design engineer to verify that the thermoelectric stress is as calculated at every point of the unit. Electrical overstress, resulting in excessive power dissipation and thermal interaction thus causing unwanted heating of sensitive elements, will be apparent. Once these conditions have been pinpointed, design changes can be implemented and their effects verified on a modified prototype.

Thermal maps of production units can be compared with standards established for each basic device, and any significant variations during the production process will be apparent. From this information, suitable process changes can be made to correct the defects or anomalous devices can be discarded.

Figure 4 shows the circuit diagram and physical layout of a diode transistor logic dual 3 input gate that was evaluated for its thermal design characteristics. The location of every fifth line of scan of the fifty made is shown by the dotted lines. The size of this chip is 0.127 centimeter on each side (50 mil by 50 mil).

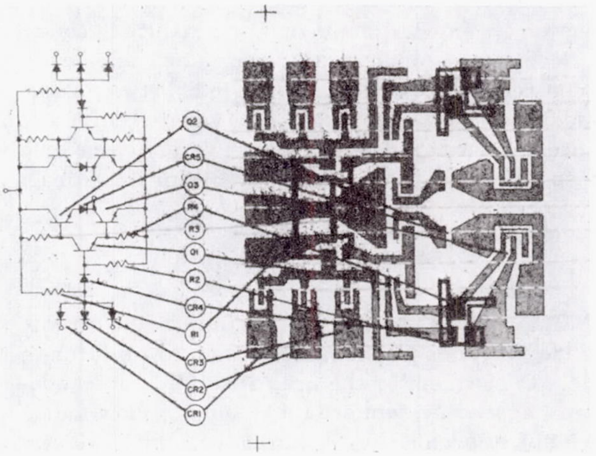

FIGURE 4. SCHEMATIC DIAGRAM AND PHYSICAL LAYOUT OF DUAL GATE

Figure 5 is a collection of the scope displays of each scan line of the fifty scans that were made.

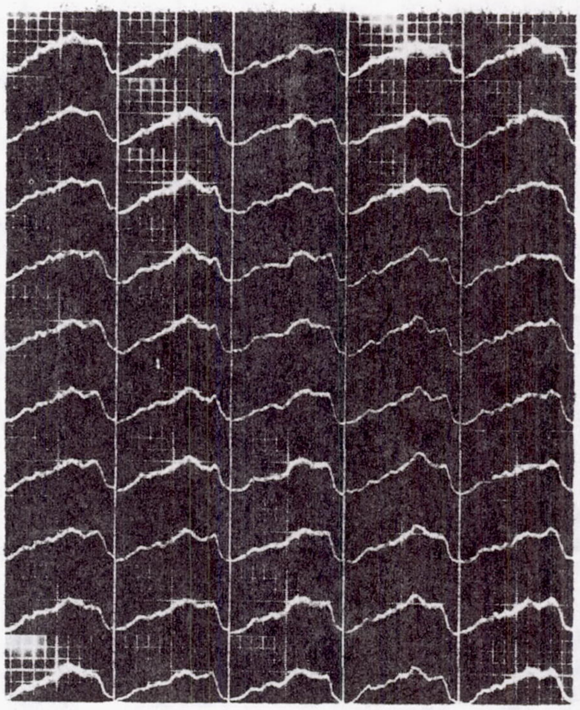

FIGURE 5. FIFTY INFRARED SCAN LINES OF MICROCIRCUIT

A cutout was made of each of the lines of scan and assembled into an IR profile of the circuit, as shown in Figure 6. By correlating Figures 4 and 6 you can relate the peak infrared emission to resistors and transistors within the chip. This analysis shows a maximum temperature rise in the circuit of 393°K with no major concentrations of heat. The evaluation indicates this circuit design has a relative uniform thermal gradient. Figure 7 shows a single line of scan superimposed over a layout of the circuit. The infrared radiation profile shows the location and temperature of the diode and transistor junctions and buried resistors in the chip.

Figure 8 shows a single line scan of a good circuit and a circuit with poor bond that was measured at 1, 6, 16, and 46 seconds during warmup. Warmup is rather slow in the good unit, so that at the end of 46 seconds the temperature has reached approximately 363°K. The temperature in the bad unit at the end of the same time has reached approximately 388°K. Under the infrared scan is an X-ray of the units that shows the void causing the elevated temperature. No voids are seen under the good circuit.

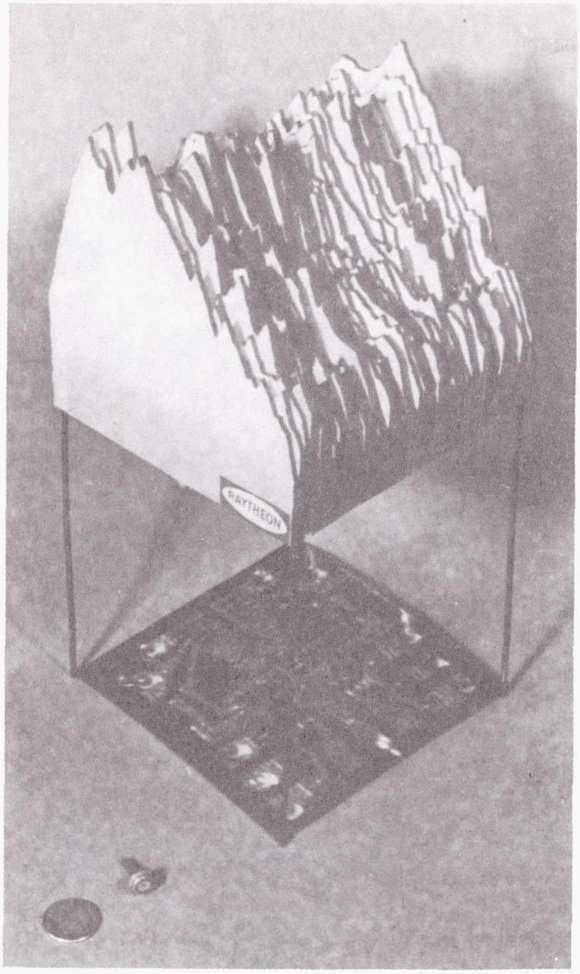

FIGURE 6. INFRARED PROFILE AND PHOTOGRAPH OF MICROCIRCUIT

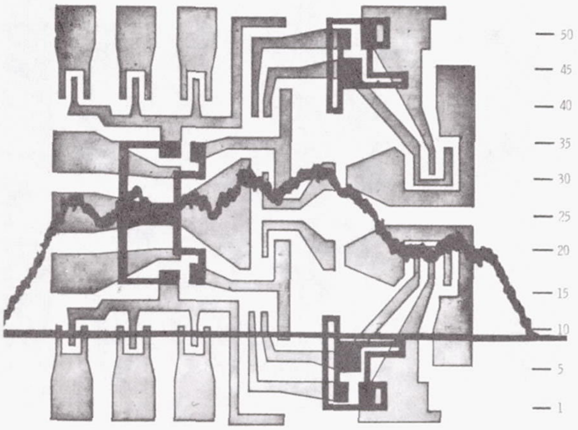

FIGURE 7. SINGLE SCAN IR SUPERIMPOSED ON CIRCUIT SCHEMATIC

Figure 9 depicts the scans made of a circuit containing a crack in the silicon. The scan line labeled initial warmup was made about 10 seconds after power was applied. This scan line shows a large drop in IR in the area of the crack.

The scan line made after thermal stabilization shows the same condition, but less pronounced. The defect is readily detected when initial power is applied, but not as easily detected after thermal equilibrium is reached. This is a good example of the need for an instrument to scan at a fast speed and have a fast response detector.

A study is in progress to determine the possibility of using infrared to predict transistors likely to fail because of second breakdown, and to pinpoint the area where the breakdown will occur. The 2N1722 power transistor used for this study is shown in Figure 10. The chip of this transistor is 0.635 centimeter (250 mils) square. The infrared profile of the transistor was measured just prior to driving it into breakdown and was found to be uniform and normal throughout the chip. The device was then driven into second breakdown and measured with the infrared microscope. The infrared spike shown in Figure 11 was found at the point of second breakdown. The breakdown occurred at a small point within the 0.127 centimeter (50 mils) square as shown in Figure 12, and there was deterioration around this point. This IR peak represents a spot temperature of more than 1073°K.

FUTURE PLANS

The following investigations, using the infrared microscope, are being planned over the next 12 months.

1. Conduct detail studies of devices containing thermal related failure mechanisms to establish an explicit relationship between the infrared emission of these units and good units. From this information detailed test procedures and acceptance criteria can be developed for microcircuits.

2. Establish standards for the thermal and infrared design of microcircuits and detailed procedures for IR evaluation of circuits as a part of qualification and lot acceptance tests.

3. Locate the instrument in a microcircuit manufacturer's plant for approximately three months of testing to establish the relationship between effectiveness and efficiency of infrared testing of microcircuits in accomplishing the above functions.

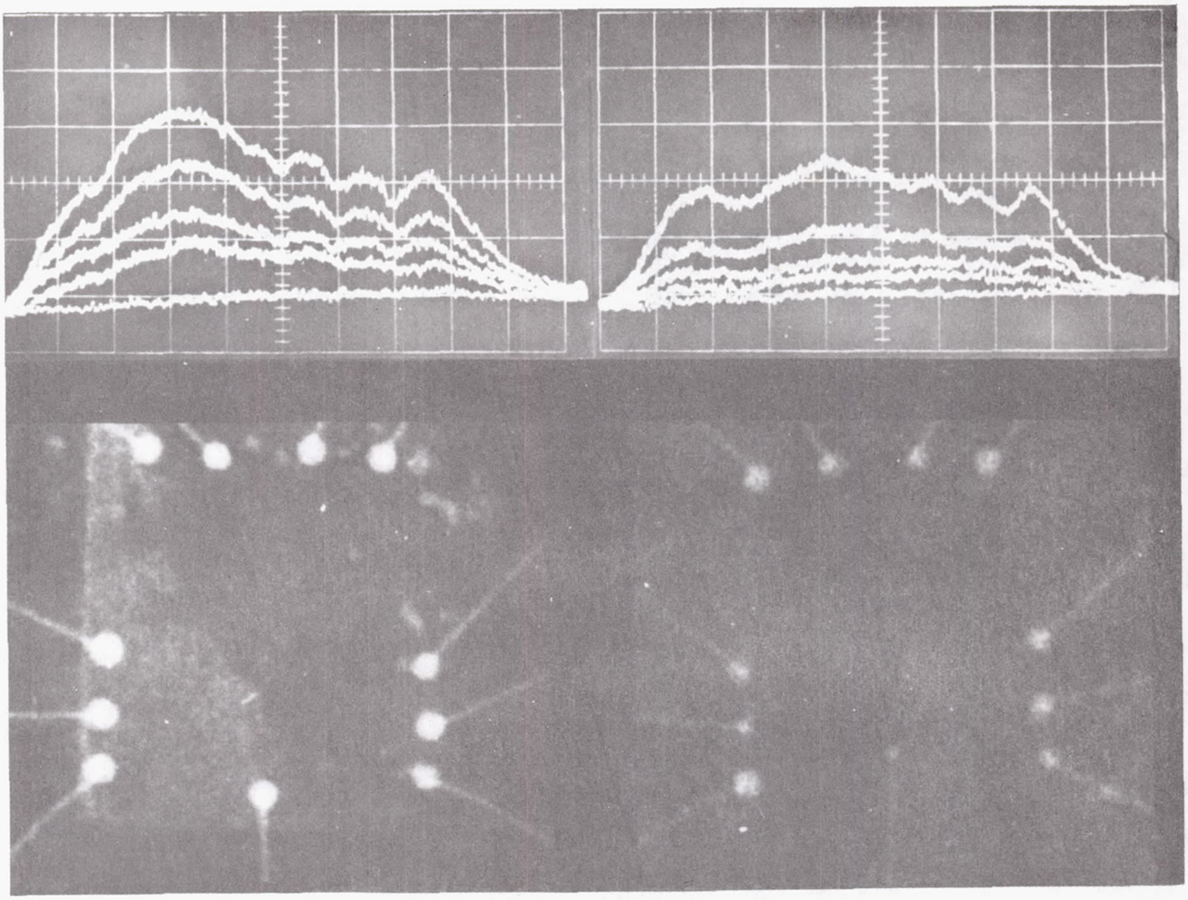

FIGURE 8. IR SCAN OF CIRCUIT AT 0, 1, 6, 16, 46 SECONDS DURING WARMUP AS RELATED TO X-RAY OF UNIT

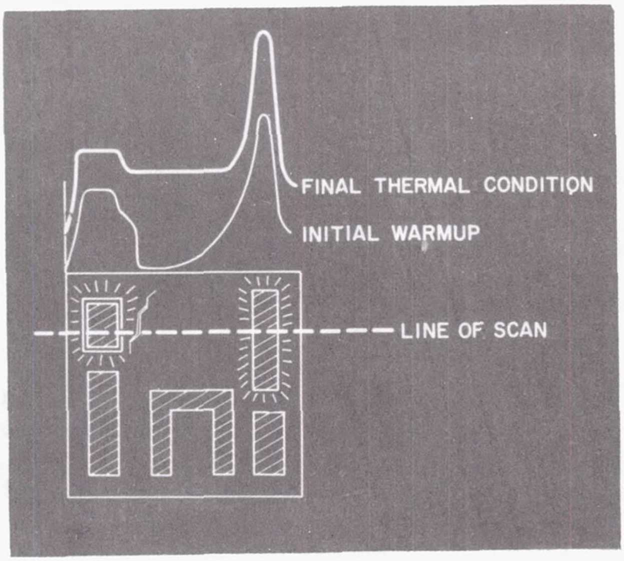

FIGURE 9. IR SCAN OF CIRCUIT WITH A CRACK IN THE SILICON

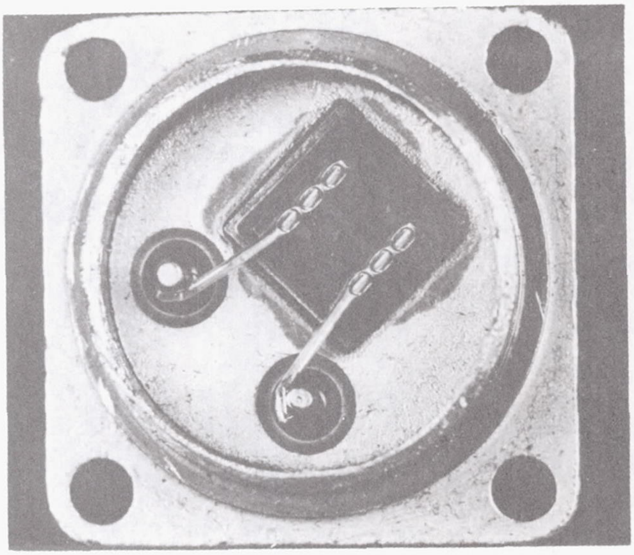

FIGURE 10. POWER TRANSISTOR USED FOR SECOND BREAKDOWN STUDY

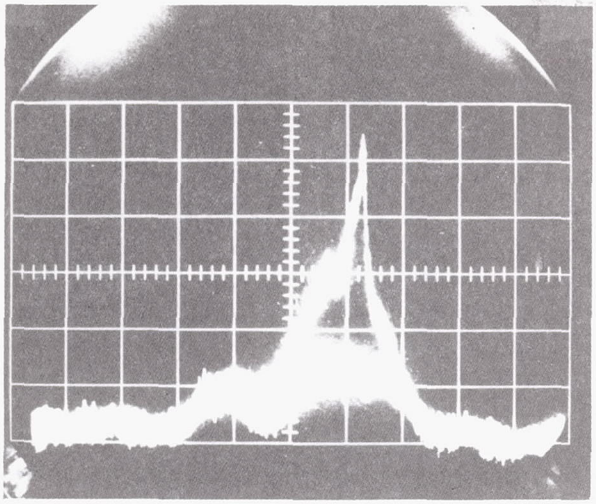

FIGURE 11. NORMAL AND SECOND BREAKDOWN INFRARED EMISSION

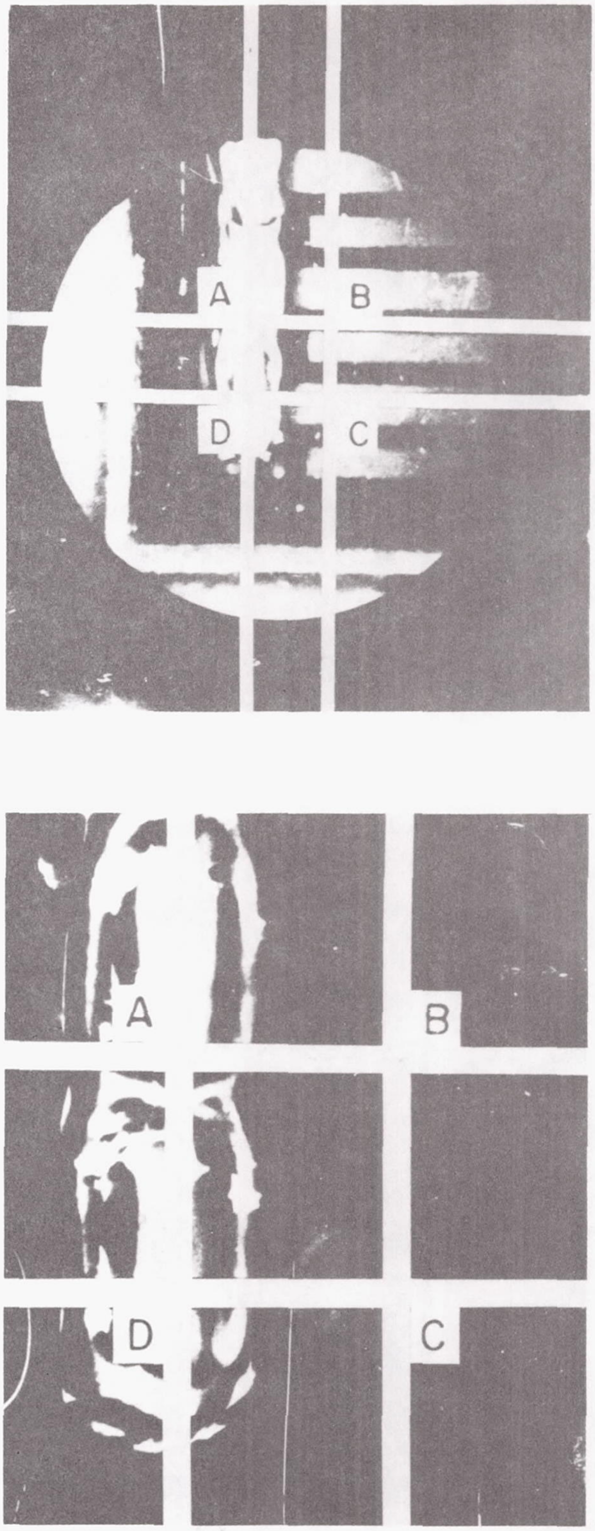

FIGURE 12. AREA WHERE SECOND BREAKDOWN OCCURRED

Page
Intentionally
Left Blank

USE OF SLURRIES FOR HYDROSTATIC TESTING

By

Frederic E. Wells

SUMMARY

The hydrostatic proof testing of tanks to their full flight loads by the use of slurries is discussed. Guidelines for necessary slurry characteristics are established. Slurries to meet these NASA criteria were developed and evaluated by the Georgia Institute of Technology. Tests were conducted for slurry viscosity under shear stresses, for exposure to sunlight, for compatibility with two cryogenic liquids, and for corrosion on various tank surface materials. The economics of producing slurries with the required specific gravity is mentioned. The usefulness of further experimentation by using a pilot plant is explained.

INTRODUCTION

Proof testing of propellant tanks to full load is necessary because of the very narrow margins imposed on vehicle designs by weight considerations. These designs have resulted in tanks with yield to design load ratios of 1.1 to 1.0. Any defects in raw material or fabrication can result in a disastrous failure during static firing or in flight. In-process inspection will detect most defects; however, only a full load proof test can give the assurance required for a major vehicle, especially if it is manned.

Heavy propellant in a boost situation causes a much steeper pressure gradient than that of a proof test using water in a 1 g static environment. As an example, lox in a 4 g boost causes a gradient of 4.18 N/cm^2 per meter of tank height (1.99 psi per foot of tank height). This is four and a half times the gradient that can be produced with water in a static proof test. This means that a lox tank 19.7 meters (60 feet) in length would have a pressure gradient between forward and aft bulkheads of 82 N/cm^2 (119 psi) in a 4 g boost, while the pressure gradient that could be produced by a water static proof test would only be 17.9 N/cm^2 (26 psi).

It is apparent that a lox or RP-1 tank cannot be tested to actual flight loads with water without causing a serious overload on the upper bulkhead and upper portions of the tank. The result is an untested tank or a tank overdesigned (with a resulting weight penalty) to meet the requirements of hydrostatic proof testing. This is not a problem on the older designs with constant wall thickness; however, increased tank size has made the tapered wall thickness designs look very attractive for weight reduction.

The desirability of carrying the tapered wall design to the ultimate, combined with the necessity of a 100-percent proof test, has led to considerable work to develop methods of achieving pressure gradients to match anticipated flight loads. One solution was the zone gradient method that was developed at MSFC and reported in document IN-R-QUAL-64-43. This method is feasible within the following limitations: (1) it cannot be used on a tank other than a basic cylinder, and (2) a given set of fixtures can only be used on one diameter tank. A change in tank diameter requires a complete new set of fixtures.

A concept that would not require fixtures for the tank and would be adaptable to any tank configuration was still needed. An obvious solution would be the use of a fluid for the test media that would be dense enough to produce a pressure gradient matching the flight loads. A true liquid that possesses the characteristics for this type of proof testing does not exist; however, the concept of slurries was believed to be worth investigating in detail, and a contract was awarded to Georgia Institute of Technology to investigate this approach.

CRITERIA FOR SLURRIES

To meet the requirements for proof testing, a slurry must be capable of being produced with a specific gravity range from 2.0 to 6.0; be chemically stable; be nonsettling for extended periods of time; be inert to liquid oxygen, liquid nitrogen and hydrocarbon fuels; transmit hydraulic pressure as does a true incompressible fluid; be compatible with stage component materials; be readily prepared and pumped with conventional processing equipment; and be easily removed from tanks and piping by water flushing.

To be economically feasible, finished slurry formulations must be reasonably priced and composed of such readily available materials that purchases of large quantities would not seriously disturb existing markets.

GEORGIA INSTITUTE OF TECHNOLOGY STUDY

This study was to develop high density slurries with specific gravities from 2.0 to about 6.0 to be used as the pressure transmitting media in the hydrostatic testing of stage propellant tanks. Slurries meeting specific gravity requirements were to be thoroughly tested and characterized, and recommendations were to be made for suitable types of equipment for the preparation, pumping, and storage of the slurries.

An extensive survey of the chemical and physical properties of a large number of dense, granular solids revealed several solids that possessed many of the properties desired for the purpose of this study. Water was selected for use as the continuous medium in the slurry formulations, principally because it is relatively inert, cheap, and plentiful.

Water-based slurries were formulated from a large number of materials, and it was conclusively shown that specific gravities from 2.0 to 6.0 could be achieved with conventional chemical processing equipment. Lead oxide was the most suitable of the solids tested for producing stable slurries with a wide range of specific gravities. Barium sulfate slurries also demonstrated very favorable characteristics for the lower densities. The necessary particle size distribution, the optimum type and amount of dispersing agent, and a suitable preparation procedure were developed for producing these slurries.

Different types and amounts of dispersing agents were used to determine the optimum. The type and amount of primary dispersing agent used determines the polarity of the slurry and, to some extent, the viscosity.

Several thickening and gelling agents were also evaluated. The goal was to select an agent that would completely disperse the solid particles and then select a second material to establish a weak gel structure in the slurry. A weak gel structure established under static conditions will greatly impede solids settling and result in a soft, readily redispersible sludge when significant settling has occurred after long-term storage. A slurry thus formulated will be rather viscous yet flow readily when shear is applied.

Since slurries are inherently non-Newtonian in character, apparent viscosities at various shear rates are often necessary to specify their flow properties. Measurements of this type are also frequently needed to define time-dependent flow properties such as thixotropic or rheopectic behavior wherein shear-stress varies with time when a constant shear rate is applied to the slurry. Controlled thixotropy is a very desirable characteristic for maintaining stability against particle settling under static conditions and yet permitting reasonable viscosities when a shear gradient is applied to the slurry. These are reversible phenomena; that is, it reverts to its original gel-like structure when shear stresses are removed.

Since apparent viscosity is a primary factor determining stirring and pumping costs and apparent viscosity varies with the rate of shear, the apparent viscosity of each slurry was determined at the same rate of shear to give a basis for comparison in determining the optimum amounts of the dispersing and gelling agent.

Several different types of agitation systems were evaluated. These included propellers, paddles, turbine impellers, and high-shear twin blade homogenizers. A turbine-type impeller located very near the bottom of the mixing container gave the best combination of fluid shear and circulation needed for dispersing large quantities of solids. The use of hot water improved the rate of solids wetting and also resulted in lower power requirements for mixing because of decreased slurry viscosities at elevated temperatures.

PERFORMANCE TESTS ON LEAD OXIDE AND BARIUM SULFATE SLURRIES

Direct exposure of lead oxide slurries to sunlight caused a series of color changes from bright yellow to a dull red-brown. In some instances, the color further changed to black upon prolonged exposure to sunlight. These color changes occurred only within a very thin layer at the surfaces of the sample containers. These darker films were somewhat more difficult to remove by water rinsing than the usual film, but otherwise presented no difficulties. No measurable density alterations were noticed after these changes occurred. Examination of a Pourbaix diagram for lead and water reveals that litharge is the most stable state for lead at these pH levels, so very little overall change in oxidation states would be predicted.

Tests conducted with liquid nitrogen and liquid oxygen indicate that deposited slurry films are completely compatible with these liquids.

Hydrostatic pressure testing at local barometric pressure and at elevated pressures demonstrated that the slurries possessed the required fluid characteristics to transmit hydraulic pressure.

Wet slurry films were easily removed from aluminum and glass surfaces by rinsing with cold water. However, if the lead oxide films were allowed to dry, removal was considerably more difficult and some abrasive action was often required.

In the corrosion tests, stainless steel and aluminum alloy samples were partially and totally immersed in the slurries for extended time periods, i. e., 12 to 21 days. The stainless steel samples showed no reaction to this immersion. The untreated aluminum sampled did show some reaction after extended immersion. This reaction consisted essentially of a reduction of the lead oxide in contact with the aluminum surface to yield a surface film of lead and lead oxides. The most obvious way to minimize this type of reaction is to adjust the slurry pH to neutral. Anodized aluminum samples showed no significant reaction.

ECONOMIC CONSIDERATIONS

A preliminary economic analysis indicated that barium sulfate slurries are desirable for specific gravities to about 3. 0. Lead oxide slurries are recommended for specific gravities above 3. 0. The economics of purchasing the required quantities of the slurries from commercial suppliers were compared with those of building an onsite processing plant for producing the slurries. This preliminary analysis favors the construction of an onsite facility.

FUTURE PLANS

The Georgia Institute of Technology has clearly demonstrated the feasibility of producing slurries that can be used for hydrostatic proof testing of flight tankage to full flight loads. Small-scale model testing of these slurries is needed. These tests would be conducted under conditions dynamically similar to actual operating conditions. The high density slurries developed in this study should also be examined periodically for possible destabilization or stratification with formation of a density gradient. The unfavorable tendency of high pH slurry solids to decompose when in contact with aluminum alloys remains a possible disadvantage to their use as proof testing media. Additional corrosion studies are needed to solve the above problems and to determine the construction materials to use in slurry production facilities. Pilot plant studies should also be performed to determine the type of materials, equipment, and processing procedures that would be most feasible for producing large quantities of slurry in an onsite facility.

Page
Intentionally
Left Blank

AUTOMATED ULTRASONIC SCANNING BY TRIANGULATION METHODS - THE DICKINSON SYSTEM

By

Robert L. Brown

SUMMARY

The advantages of ultrasonic testing compared with previous nondestructive test methods are discussed. The capabilities of an "acoustic spectrometer" are demonstrated in a practical test on a section of S-IC fuel tank. Operation of the acoustic spectrometer by servos rotating the transducers that supply the computer with position information is explained. The location of the transducers and the computer's method of locating flaws in welds through scattered ultrasonic energy is discussed. An accurate method for examining welds and verifying the existence of detected flaws is presented.* The system's accuracy and automated operation by remote control are mentioned as ideal qualities for repetitive examination of a ship's hull or a nuclear reactor where severe service conditions exist.

INTRODUCTION

Perhaps the oldest nondestructive test, other than visual examination, is sonic testing. It still remains a valuable and valid test for quality in noncritical applications. The test lacks sensitivity because of a fundamental reason. If a flaw is to be detected by its influence on frequency and resonance, it must be large in relationship to a wavelength of the frequency generated. Middle "C," which is in the mid-range of frequencies where our ears are most sensitive, has a wavelength greater than 2.3 meters (7 feet) in the common engineering metals. Since rejection limits for flaws in critical applications are normally specified in microns (thousandths of an inch) in cross section, detection by sonic testing using audible frequencies is not possible.

The solution to detecting flaws can be provided by ultrasonic testing. Equipment capable of generating and detecting sonic frequencies in megahertz (millions of cycles per second) is standard, and within these frequencies, wavelengths in microns (thousandths of an inch) allow any reasonable limitation on flaw size to be met. It is common practice to operate ultrasonic testers at a level of sensitivity that allows flaws smaller than the rejectable size to be identified. This capability has made ultrasonic testing a recognized nondestructive testing method.

The major handicap in ultrasonic testing is scanning speed. The pulse rate must be slow enough to be clearly differentiated by electronic means from shot-type noise, and travel speed must be slow enough to allow interrogation of each flaw by at least three pulses. To be consistently free of phantom indications requires an almost ideal system.

The high degree of acceptance of conventional ultrasonic testing methods may lead to a tendency to disregard unconventional testing possibilities. Recently, a West Coast company was developing an ultrasonic testing system unique in many important concepts. These concepts, while new to ultrasonic inspection devices, were well established in other applications and would hasten the inspection of many of the welds in the Saturn V system. This potential led the laboratory to contract for a system specifically engineered for space vehicle applications. This system, the acoustic spectrometer, is now being evaluated inhouse to further determine the capabilities and limitations of the system.

ACOUSTIC SPECTROMETER

Figure 1 shows the acoustic spectrometer set up in the evaluation laboratory. A panel that has a configuration duplicating a section of the 10.8-meter (33-foot) diameter S-IC fuel tank is shown. The required tooling is being attached to the test panel. This tooling was designed for use in the production application referred to earlier. A horizontal weld may be seen extending across the top third of the test panel and a vertical weld at the center. These welds contain flaws which have been preciseiy

---

* Evaluation of this equipment is continuing.

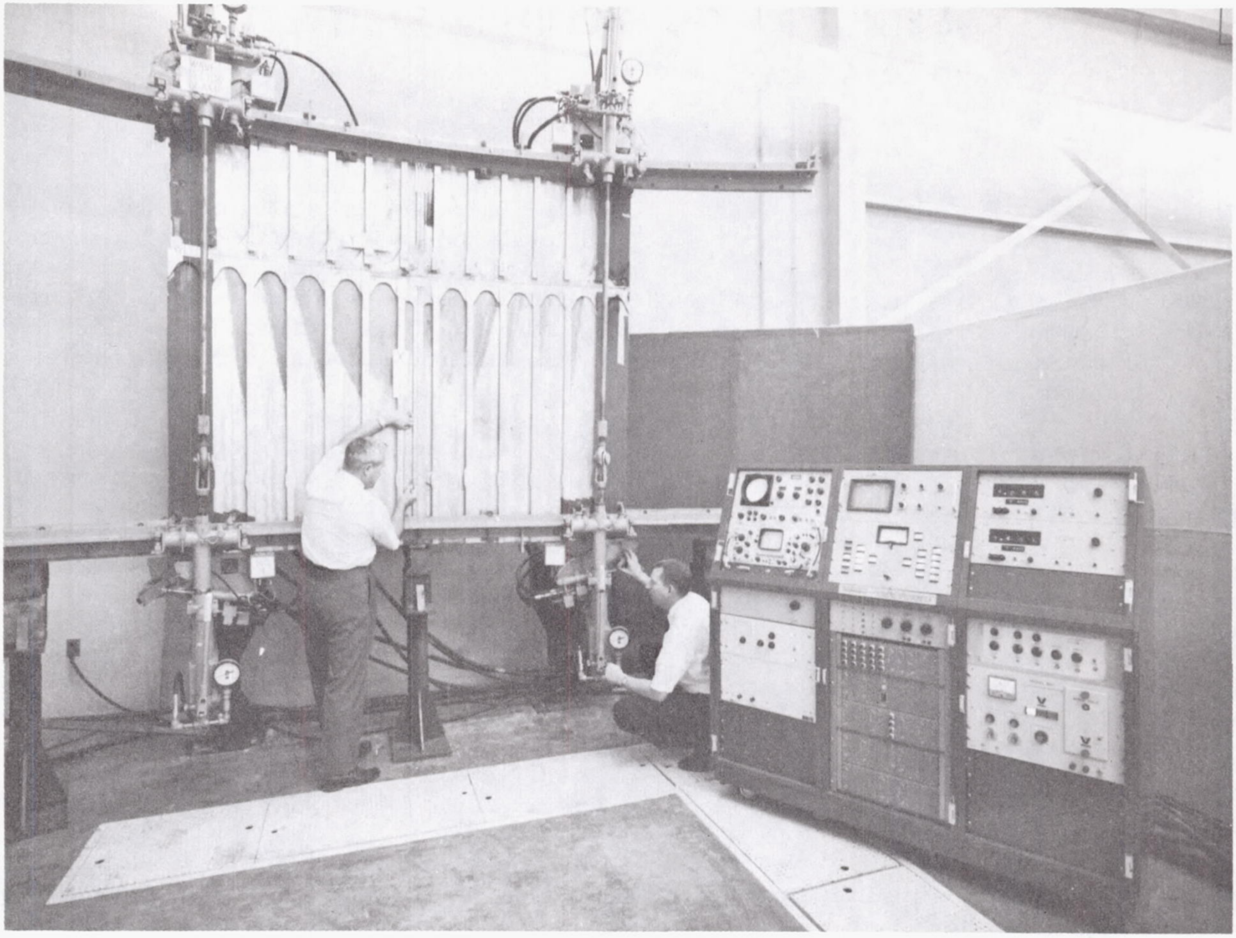

FIGURE 1. ACOUSTIC SPECTROMETER INSPECTION OF S-IC FUEL TANK SECTION

located and evaluated by X-ray and conventional ultrasonic methods. This simulates a test that would normally be performed on the cylindrical tank section. Prior to welding to the bulkhead assemblies, all welds in the vertical and circumferential directions would be inspected, repaired if necessary, and accepted, without moving the ultrasonic transducers from their locations.

The acoustic spectrometer differs from the conventional ultrasonic tester in that it is much more complex, as a necessary consequence of the new approach taken with respect to data acquisition and analysis. This increased complexity is reflected in the console shown to the right in Figure 1. The acoustic spectrometer is classified as a pulse system in which one transducer acts as a transmitter, and one or more receive information in the form of ultrasonic energy scattered from flaws.

All transducers (this system has provision for five) are identical and can be programmed to act interchangeably as transmitters or as receivers. The system does not use the "single crystal" mode of operation in which one transducer acts as both transmitter and receiver.

Instead of shock excitation by single pulses, the transducers are driven by widely spaced pulse bursts which are variable in amplitude, duration, and spacing. The burst frequency is independent of pulse spacing. The duty cycle is low, always under one percent, which permits 1500 volt excitation without harm to the titanate transducers. The resultant, highly damped wave train of ultrasonics is at the frequency of the burst and can be tuned over a wide range. This ultrasonic energy is fed into a system of acoustical lenses and directors where it is narrowed into a highly collimated beam inside an acoustic waveguide. This unit is coupled to a wave director so that it may be rotated around a quadrant of a circle by a hydraulic servo. The unit will transmit a very narrow beam of sound into an attached plate, acting as a rotational, highly directional acoustic antenna, which has the same directional pattern in receive or transmit modes. As an aid to visualization, use of the terms "transmitted" and "received" beams is a convenience found helpful in working with this equipment.

Figure 2 is a sketch of a typical setup using four transducers. The sonic ray traces are sketched in to illustrate the triangular pattern of distances and angles that the computer solves in locating flaws. Positioning of the transducers is important because the basis of the computer's calculations for location of flaws is the accuracy of the base distances from which the locations of the intersections of the transmitted beam and the received beams are computed.

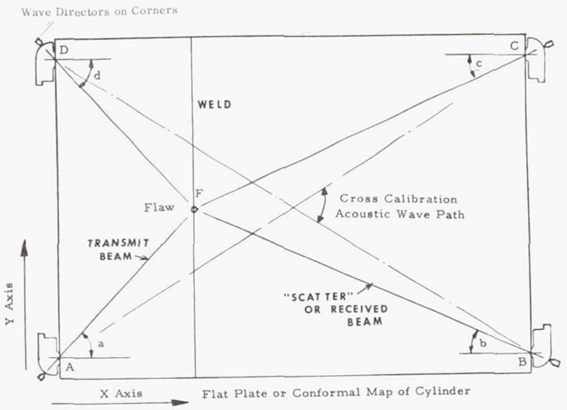

FIGURE 2. LOCATION OF FLAWS BY MULTIPLE WAVE DIRECTORS

Oscilloscopic studies indicate that the shell is shock excited into compression waves, resonant in the thickness mode - symmetrical Lamb waves - and the conversion is highly efficient if the input ultrasonic excitation frequency approximates the resonant frequency of the plate thickness. The particular shell panel which is presently set up in the acoustic spectrometer was found to respond to the following: burst frequency, 2.32 megahertz; burst width, 150 microseconds; 150 bursts per second, and 1,000 volt peak excitation to the transducers.

The wave directors are coupled into the shell by soft metal shims under high compression which so effectively bridge the gap between plate edge and wave guide that the acoustic impedance is negligible. This coupling transfers perhaps 10 times the sonic energy as a fluid. Tests have shown no benefit from fluid in this joint. The clamping force is obtained from hydraulic actuators which are preset to exert the correct pressure.

Figure 3 is a block diagram of the acoustic spectrometer system. A transducer and its functional parts are shown to the right of the blocks which indicate the control and display functions. The computer is the heart of the system. This is a small analogue three-channel computer, each channel identical in its circuitry. The transducer-to-transducer distances are manually set into the computer's input in the form of voltages taken from precision potentiometers. The transducer angle positions that are required to calculate the X and Y coordinates of the intersect point of the transmit and receive beam are controlled by voltage feedback from tangent potentiometers attached to the pivots of the wave directors.

The computer continuously solves the equations of position for all transducers and feeds this angular information into the servos on each transducer separately. Each servo rotates its transducer to an angle that gives an output voltage on the waveguide tangent potentiometer that, fed into the computer, satisfies the equation of position that the computer is continuously solving. Since all active transducers are positioned by their independent computers, all transmitted and received beams remain pointed at the calculated intersect point. The computer's calculated coordinates of this point are read out as X and Y distances by a pair of digital voltmeters in inches and decimals of an inch. This intersect point is where the "scatter" that carries useful information originates. A toggle switch, which has four independently closed positions, switches driving voltages to the appropriate circuit to move the intersect in the direction indicated by the position of the handle; plus or minus X, or plus or minus Y. The motion is constrained by the computer to move in X or Y directions only. No combination of these motions is possible, but combinations of sequences of X and Y motion allow all areas to be covered to any degree of thoroughness required. This constraint is a great advantage when welds, such as the S-IC circumferential welds, lie completely in the X or Y direction. The beam is steered by sequential moves in the X and Y direction to the correct starting point as shown by the coordinates displayed by the digital position indicators. The computer will then steer the intersect along the weld until the limit of the scan is reached. This directing system is quite accurate; the preliminary data indicate that an error in angle is less than one degree.

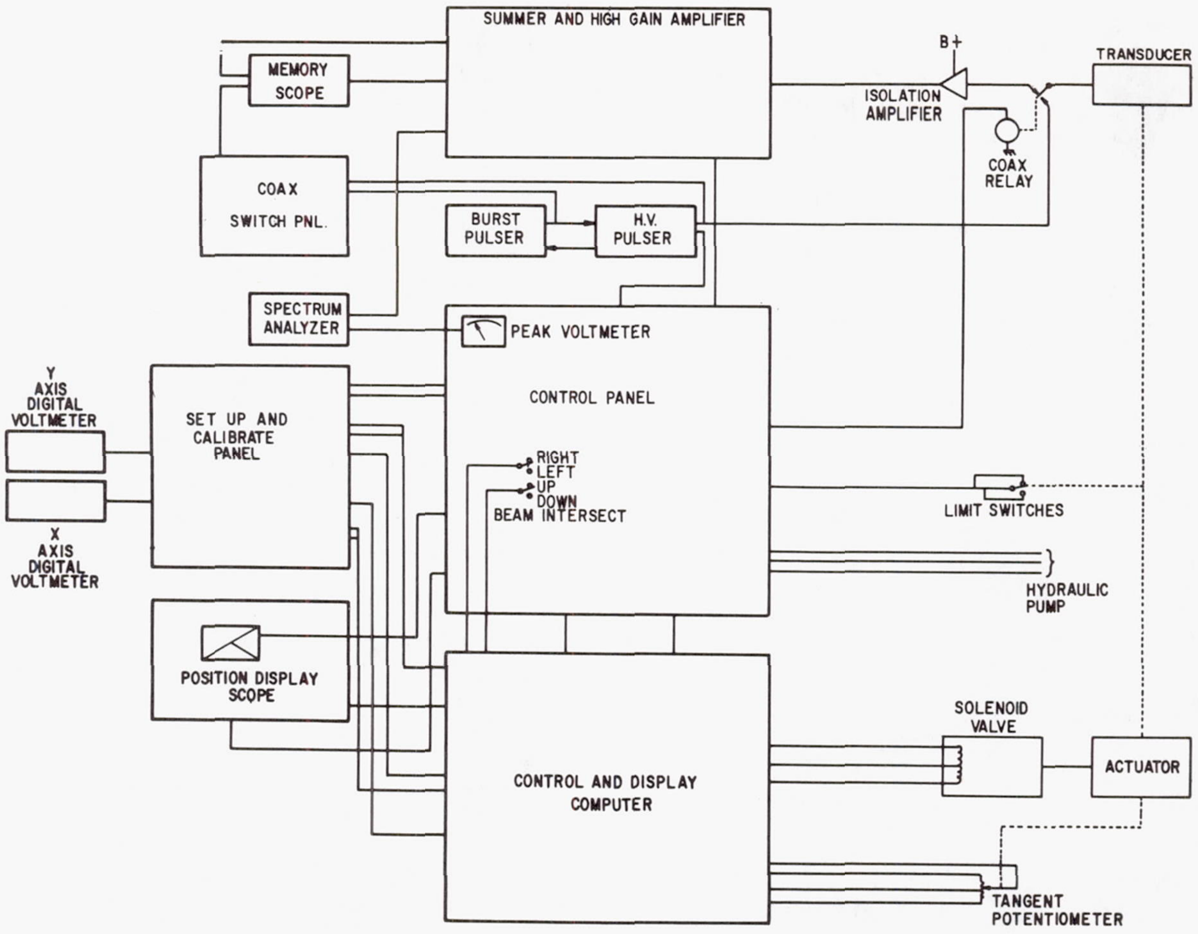

FIGURE 3. BLOCK DIAGRAM OF ACOUSTIC SPECTROMETER SYSTEM

A second position indicator in the form of a cathode ray oscilloscope is provided at the top of the center panel. This oscilloscope displays the ray paths followed by the ultrasonic beams in the structure as generated by those transducers active at the time of display, allowing visualization of directions, travel, and position, all of which are difficult to handle without such an aid. A coordinate grid on this readout giving distances in feet was used during the evaluation. Since the display was for all practical purposes a "real time" readout, this display was the preferred means of monitoring the ultrasonic system while the operator is "steering" by the four-way switch.

While "intersect point" is mentioned frequently, the word "point" is a convenience and is not intended to imply that a point can be resolved. A flaw such as a small round pore can be located within a small circular area which is the "limit of resolution" for the system. This circle may be approximately 2.5-centimeters (1-inch) in diameter at 3.3-meters (10-feet) distance from the transducers. When the acoustic spectrometer is used to evaluate welds, which may contain only an occasional rejectable flaw, this circle is a small enough limit. To verify the exact location of the flaw, a conventional portable ultrasonic tester will pinpoint the exact position.

An important feature of the system is a time-dependent gate that can be set to receive "scatter" from the intersect point, and which can block "scatter" from other parts of the plate. This suppresses the background noise in the system, thus increasing the strength of the flaw signal.

Flaw analysis is an integral part of flaw detection. The acoustic spectrometer is equipped with several devices which aid in this important function. Since the system is intended for highly automated operation, primary reliance in flaw detection is on a spectrum analyzer which reduces the flaw return information to a voltage that is fed into a peak-reading voltmeter. The peak voltage from the flaw signal return is then compared to a preset reject level set at the smallest rejectable flaw size. The system will give an indication at each detected flaw having a cross section larger than the preset limit. The operator analyzes each flaw by confirming the automatic flaw signal indication on a cathode ray oscilloscope. This oscilloscope presents the conventional time base versus amplitude, with the exception that the time gate only allows the "first reflection" or "scatter" signal to be displayed. The time gate is opened enough to allow the conditions along the weld to be shown on the oscilloscope, and analysis is a function of the operator's skill and experience in interpreting the changes in the pattern as the intersect point travels through flaws. This analysis is then applied to evaluate the reject circuitry and to evaluate the system as a whole.

Equipment closely related to the acoustic spectrometer can perform such tasks as routine ultrasonic examination of plates in the rolling mill. With tape input and recorder outputs, ultrasonic devices could be used to search for hull damage on ships and to monitor reactors where severe or dangerous operating conditions exist. A highly automated ultrasonic system could perform a nondestructive testing task on a routine, repetitive basis in situations where conventional ultrasonic testers cannot be used.

ULTRASONIC EMISSION DETECTOR EVALUATION OF THE STRENGTH OF BONDED MATERIALS

By

James B. Beal

SUMMARY

A program to measure adhesive bond strength was conducted. A study into the causes for weak adhesive bonds was made to determine the best methods of nondestructive testing of the adhesives. The discontinuities in the bond layer are discussed and related to ultrasonic signals. Bond stress methods and possible test techniques are listed. The measurement of bond strength by producing consistent weak bonds and the causes for the weak bonds are discussed. Fabrication of test samples are presented.* The operation and capabilities of the ultrasonic emission detection equipment are explained, and the advantages and disadvantages of the equipment are listed.

INTRODUCTION

Aerospace industry requirements have rapidly accelerated the use of adhesive bonding in structural applications. Composite structures, particularly those using honeycomb, are to a large extent adhesive bonded today. The major problem posed by the use of composite structures has been the variability of bond strength obtained and the lack of suitable nondestructive equipment for determination of bond strength. The exact causes of these strength variations are difficult to establish because the causes can be related to every phase of bonding, i.e., material properties, material and adhesive handling, and processing techniques (Table I). The soundness of an adhesive bonded assembly must be assured by two methods. One is the verification of every phase of bonding, commonly called process control, and the other is end-item evaluation (final inspection).

Contract NAS8-11456, "Nondestructive Testing For Evaluation of Strength of Bonded Material," was initiated June 29, 1964, with General American Transportation Corporation [1]. This contract was to develop a nondestructive method or system for evaluating adhesion bond strengths in composite adhesive bonded structures. Acceptable methods for detecting bondline voids, debonding, bondline variations, and porosity were available at that time, but no nondestructive techniques were available that would measure adhesion bond strengths in all adhesives specified for this program, i.e., FM-1000, HT-424, Narmco 7343/7139 and Metlbond 329. These adhesives were used to make specimens of aluminum bonded to aluminum; aluminum face sheets to aluminum honeycomb core, and aluminum facesheets to phenolic core.

TABLE I. REDUCTION OF BONDING PROBLEMS BY USING NONDESTRUCTIVE TESTING

Causes of Bonding Problem	% Without NDT	% Using NDT
1. Design Deficiencies	30	25
2. Corrosion	7	5
3. Machining Errors	10	0
4. Improper Processing	9	0
5. Misuse or Handling	10	5
6. Fabrication Error	12	0
7. Material Defects	22	0
	100%	35%

The literature survey phase of nondestructive testing revealed that the number of papers published on the subject of bond strength evaluation, for the adhesion strength of the bondline, were relatively few. Available papers were concerned with particular equipment for detection of voids, delaminations, porosity, bondline variations, and the cohesive strength of some adhesive systems, but the equipment was inadequate for detecting weak bonds in adhesion. The need existed for a bond strength

---

* The Ultrasonic Emission Detector and the methods of equating the noise signal level of a stressed bonded structure to an indication of bond strength were developed by testing these samples.

evaluation system and a method of producing consistently poor adhesion bonds of predictable values in order to adequately evaluate equipment bond strength indications.

ADHESIVE BONDING

Adhesive manufacturers and users agree that strict controls are necessary over all adhesive bonding processes and the numerous associated fabrication variables. Considerations for a good bond include the formation of a strong wetable oxide surface on the metal to be bonded, proper wetting of the surface with the adhesive, elimination of contaminants, and control of the fitting, temperature, and pressure of the bond.

The majority of present nondestructive test instruments fall within two categories: (1) vibration inputs to structures by means of resonant, sonic, and ultrasonic frequencies, and (2) structural proof stress tests consisting of internal pressurization, external tension stress induction, and limited destructive shear. A study was conducted into the nature of bonding to determine what properties affect adhesive bond strength and to determine the nondestructive test technique best suited for the measurement of strength properties. The apparent failure of an adhesive bond was attributed to causes such as surface contaminants of a low cohesive force, or of chemical compositions that weaken the layer of adhesive near the surface. The cause of weak bonds did not appear to be the weakening of the basic bond forces, but rather the failure to form the bond in the first place. Thus, the strength of the surface layer of the adhesive was more important than the nature of its bonding forces. Any contamination affecting the strength of the first layer of adhesive was very important. Small areas of contamination can cause stress risers that propagate cracks parallel with and close to the bondline.

If the contamination and discontinuities in the bond layer cause stress risers and contribute to the failure of a bond, it is possible to have complete adhesion over the greater portion of an area and still have a weak bond not detectable by other nondestructive means. It was assumed that detectable sonic and ultrasonic signals would result from stress concentrations in contaminated areas of the samples before the stressed bondline reached the point of failure. Noise emission from stressed areas would result as the weak bonds failed selectively in the areas of highest stress.

EVALUATION OF ADHESIVE BOND STRENGTH

The possibility of small contaminated areas being able to affect the total bond strength indicated that some method of stressing the bondline to fail the weak areas would be necessary. Because the small contaminated areas will be exposed to very high stresses when the bondline is loaded, the areas will emit sonic and ultrasonic signals that can be detected by sensitive listening devices long before the complete bondline reaches its ultimate strength. This phenomenon will provide additional data during proof tests of edge-sealed sandwich structures containing perforated honeycomb core, and during static load tests of adhesive bonded brackets.

Theoretical and bond stress methods considered for this program were: (1) rapid decompression of samples containing perforated honeycomb core, (2) high pressure external to a vacuum cup on a bonded structure containing a perforated honeycomb core placed in a pressure chamber, (3) electrical bond stress methods from forces produced by stationary charges, magnetic fields, and eddy currents, (4) force pulses by vibration and energy transfer to the bondline (forces produced by ultrasonics and shock wave stressing), and (5) mechanical methods by static or dynamic loading of bonded brackets or the structure.

Test techniques to be investigated for this program were: (1) sonic and ultrasonic emission detection of signals from failing bonds, (2) ultrasonic attenuation with applied stress, (3) brittle coatings, stresscoat or equivalents, and (4) birefringent photoelastic plastic coatings.

In any nondestructive test system, an important consideration is the production of sample flaws. This is particularly difficult in the testing of bond strength because the flaw mechanism relationships are not clearly known. In practice, poor bonds can be caused by a failure in the cohesive strength of the bulk of the adhesive or in an adhesion failure to the faying surface. These failures occur because of material and structural variations. If the structural materials and adhesives have suitable material properties, the unsatisfactory bonds which cause failures and which must be detected by the inspection system seem to result from: (1) improper cleaning and etching as a result of contaminated cleaning and etching baths or inadequate process controls, (2) a weak interface in the bondline may be present from contamination such as moisture or surface oxides caused by long-time surface exposures before priming or applying the adhesive, (3) degradation of the adhesive material's cohesive strength. This may occur adjacent to the bondline because of contamination of the adhesive with moisture or other chemicals, or poor cure and fit-up practices, and (4) small contaminations that act as stress risers can cause the failure to progress along the bondline. The various contaminants are introduced at every stage of fabrication until the structure is complete.

The above conditions must be simulated as closely as possible to produce suitable imperfections affecting bond strength. Attempts to simulate understrength bonds produced a successful method, designated photomicroflaw, which was used for controlling bondline strength of test specimens.

Other methods of bond contamination that were investigated and found unsuitable because of lack of predictability were: (1) exposure of face sheets to water solutions, (2) exposure of face sheets to oils and greases, (3) variation of face sheet cleaning methods, (4) exposure of cleaned, protected face sheets to long time storage conditions, and (5) partial cure or aging of the adhesives.

The photomicroflaw technique involves coating the surfaces of specimens to be bonded with a photosensitive emulsion and exposing the surface to an intense light source through a grid (Fig. 1). The emulsion is washed away by the developer at the areas where light is stopped by the grid. Photographer's screen-tints, the size and density controlled dots on a polyester film base, are used for the grid. This satisfies the need for simulating poor bond strengths through controlled surface contamination.

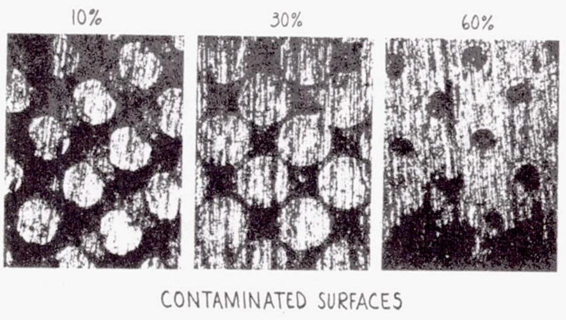

FIGURE 1. PHOTOMICROFLAW TECHNIQUES

The importance of proper process control during bonding operations is shown in Figure 2. This graphically illustrates the effects of bondline contamination on bond strength. Adhesive bond strength drops of twenty-five to thirty-eight percent occur when a surface to be bonded is degraded uniformly by ten percent contamination. This indicates that the higher the bondline stress, the more effect a small defect, debond, or weak bond can have as a stress riser. This significantly illustrates the need for contamination control in the process of fabrication. Assembly of components should be performed as soon as possible after the cleaning operation has been completed.

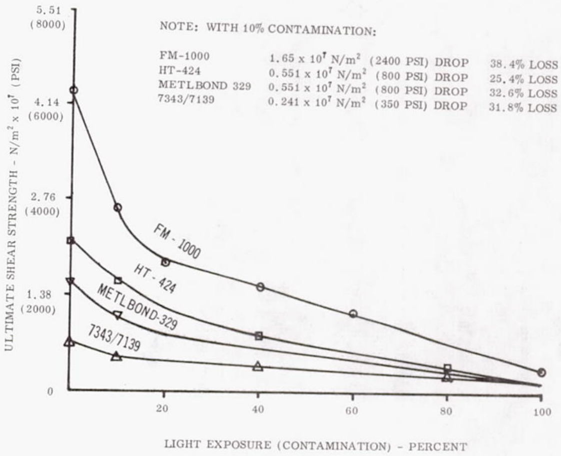

FIGURE 2. PHOTOMICROFLAW CONTROL OF BOND STRENGTH WITH LAP SHEAR SAMPLES

During this program it was noted that thirty to forty percent bond strength reduction occurred for cleaned face sheets which were protected against surface contamination and stored for one month prior to test sample preparation with FM-1000 adhesive. These results also gave emphasis to the rigid holding time and handling requirements for cleaned parts prior to adhesive application, assembly, and cure.

Specimens with bonds of known strength are required for suitable evaluation of nondestructive test equipment developed for this program. The development of confidence in production of specimens with controlled bond strengths requires destructive tests in accordance with established specifications. All specimens for this program, lap shear, drum peel, flatwise ring tension for metal-to-metal tests, and other specimens required, were prepared in accordance with military specifications for bonded structures [2,3]. In the flatwise ring tension tests (Fig. 3), specimens were made from three inch diameter cylindrical aluminum blocks. Two blocks were required for each test specimen with one block containing a central machined recess. These specimens were prepared in order to represent metal-to-metal bonded laminate construction and bonded brackets.

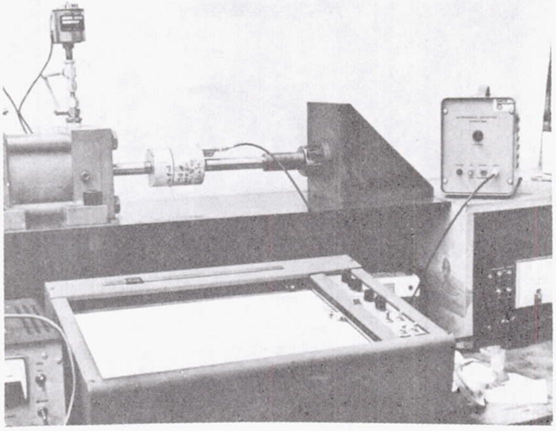

FIGURE 3. FLATWISE RING TENSION TEST APPARATUS

No problems were encountered in the preparation of test samples with the exception of the Narmco 7343/7139. This is a two component adhesive which requires mixing before use, and many problems were encountered in producing samples. The material is very sensitive to ambient environmental conditions. The variability of this adhesive is well known, however, it is the best cryogenic adhesive available. Because of the difficulty in preparing samples, this adhesive was not used in the equipment evaluation tests. The adhesive's room temperature elasticity precluded testing by the ultrasonic emission detector. It may be possible that further tests, conducted at the cryogenic operating temperatures normally associated with this adhesive, would produce useful data.

Adhesion bond strength degradation was attempted by environmental exposures of samples to high temperature of 533°K (500°F) for two hours, low temperature of 84.2°K (-308°F) for two hours, and vacuum exposure to 1.07×10^{-4} N/m^2 (8.0×10^{-7} torr). No degradation of bond strength was discernable by either nondestructive or destructive test.

To evaluate metal-to-metal adhesive bonds, test samples were fabricated using cylindrical aluminum blocks with annular recesses for ring tension flatwise tests. The transducer was attached to the cylindrical block by a threaded stud. The first few samples were broken so the operator, while listening with the headphones, could become familiar with the sounds preceding bond breakage. The bond force on the remaining samples was increased to the point just prior to bond breakage, as judged by the operator. A ten percent increase of this maximum force applied to the bond was considered the predicted bond failure point.

The application of ultrasonic emission detection for sandwich bond strength evaluation required another means of stressing the bondline. To achieve large bond stresses, a suction cup was fabricated with a springmounted ultrasonic transducer in its center, for use in a pressure chamber. With the inside of the vacuum cup vented to atmosphere, the force on the bond is equivalent to the pressure in the chamber. The transducer, installed within the vacuum cup, transmits the ultrasonic bond stress noise emissions to the equipment. The signals are monitored and the predicted bond failure point is judged by the operator. This type of testing is impractical for large sandwich structure evaluations. The same results may be obtained by edge-sealing of the structure and installation of removable pressure valves.

ULTRASONIC EMISSION DETECTOR

The ultrasonic emission detection equipment constructed for this program may be applied as shown in Figure 4. A transducer or microphone capable of detecting or measuring ultrasonic vibrations is mounted on the metal surface of the test specimen in the vicinity of the bond. For a large complex structure, several transducers may be required. The transducer output is amplified and selectivity filtered so that only vibrations in a particular frequency band are passed on to the data translation system, which converts these signals to frequencies in the audio spectrum, permitting the signals from the specimen to be heard via a set

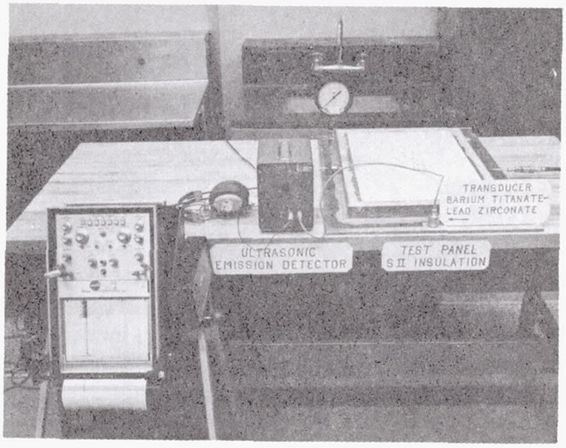

FIGURE 4. ULTRASONIC EMISSION DETECTOR APPARATUS

of earphones or a loudspeaker. The data can be suitably processed for display on an oscilloscope or a recorder through the accessory equipment outlet on the back of the chassis.

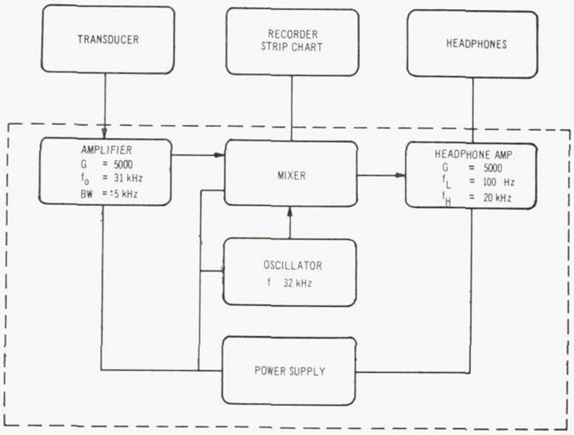

FIGURE 5. BLOCK DIAGRAM OF ULTRASONIC EMISSION DETECTOR

Figure 5 is a block diagram of this unit. The output of the transducer is amplified with a gain of 5000 and a restricted usable bandwidth of 5 kHz on either side of a 31 kHz center frequency. This allows energy in a frequency band of 26 kHz through 36 kHz to be amplified and processed. The input of this amplifier can handle large signals below 26 kHz without distortion so that the noise pulses, either from the test fixture or a shop environment, which are below 26 kHz, are attenuated and do not disturb the system. The amplifier output and a signal from a 32 kHz oscillator are fed to a mixer. The mixer produces the sum and difference frequencies of the two inputs, although only the difference frequencies are used. These difference frequencies are in the audible range (approximately 0-6 kHz); therefore, one output of the mixer is connected to a set of headphones for use by the operator in monitoring the noise generated by the adhesive under stress. The other output of the mixer is used to drive a recorder, or other accessory; thus the data from this equipment can be interpreted while the sample or structure is being stressed.

Acoustical energy in the sonic and ultrasonic region is generated when stresses are applied to materials. This effect is presently being used by Delcon Corporation and Western Inspection Service to detect evidences of plastic deformation in metal structures, and by the Metals & Ceramics Division of Wright-Patterson in Dayton to determine how boron filaments break up.

Results indicate that adhesive ultrasonic emission above 16 kHz can be used to predict when a bond will fail. Acoustic emission also occurs at lower frequencies, however, considerable noise is generated below 16 kHz by the test fixture, as shown in Figure 6. For each of the adhesives tested, i.e., FM-1000, HT-424, and Metlbond 329, there is a large increase in noise above 16 kHz as the ultimate strength of the bond is approached. Thus, if a method of stressing a bond is available, this technique provides a means of determining bond strength.

The acoustical energy generated from sandwich or metal-to-mêtal bonded specimens under stress can easily be distinguished from the sounds of the test stand or environment. The adhesive produces many very short duration bursts of energy that sound like a high-pitched crackling noise. The amplitude of the emitted signals becomes significantly stronger as the yield stress is approached, and can be used to predict the yield point and ultimate strength without damage to the structure.

The test results presented in Table II for metal-to-metal bonds are for Metlbond 329 and HT-424 adhesives only. Strength limitations of the test

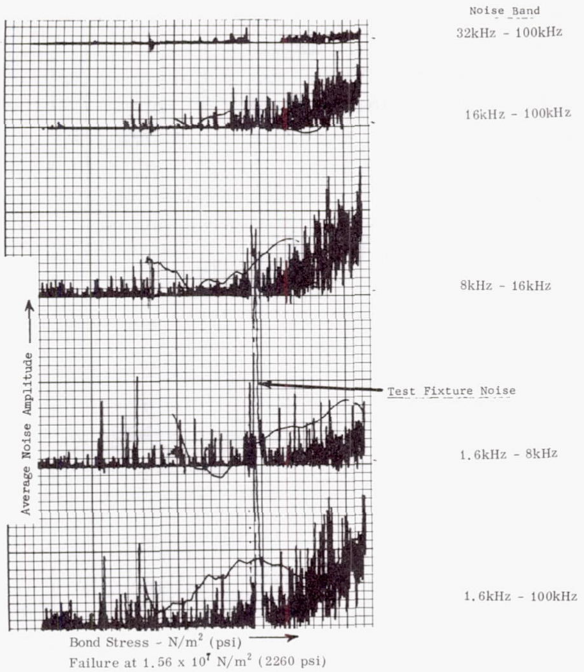

FIGURE 6. STRESS NOISE EMISSION SPECTRUM FOR HT-424 ADHESIVE IN FLATWISE TENSION AND 40% BONDLINE CONTAMINATION

fixture prevented evaluation of FM-1000. Other investigations of FM-1000 verify that it has similar acoustic emission response characteristics.

The prediction errors ranged from three to thirty percent, i.e., deviation of predicted breaking point from actual failure. This range is influenced by the evaluation of the ultrasonic emission method and the ultrasonic attenuation method at the same time on the same specimen. The predicted value of the breaking point was determined initially by stressing the sample at a constantly increasing rate to the maximum bond pressure determined by the operator. From this point upward to the actual failure point, the specimens were subjected to alternate tension - compression cycling from the dynamics required for the ultrasonic attenuation test. This varying stress rate influenced the point at which the actual breaking point occurred and thereby produced the large errors. The incorporation of an electronic gating circuit at the output of the detector would decrease the possibility of operator judgment error. The electronic gating circuit can be set to energize a warning lamp or buzzer when the amplitude of the average peak-to-peak noise level, as determined from previous destructive tests, reaches the point where ultimate strength may be predicted.

Methods employing internal pressure to stress the face sheets of sandwich panels having a perforated honeycomb core must consider the porosity of the adhesive if the integrity of the bond between the adhesive and the face sheet is to be verified. The thickness of the face sheet determines what portion of the force is absorbed in the face sheet and what portion of the force stresses the bond. With a thicker face sheet, the samples failed at a substantially higher value.

Testing sandwich panels with phenolic honeycomb core revealed that the phenolic core generates more ultrasonic energy than the adhesive. The phenolic core was not perforated to relieve internal pressure as was the aluminum honeycomb core, therefore, the high pressure vacuum cup and other internal stress induction methods could not be used. External compression or tension can be used to determine when core failure begins for unperforated phenolic core sandwich panels. Further evaluation of perforated non-metallic core sandwich structures is advised, based upon cryogenic insulation used on the S-II stage of the Saturn V vehicle.

Noise emission spectrum graphs supplied by the contractor were essentially the same for both perforated core or laminated types of bonded structures. Well bonded samples emitted little or no noise below ninety percent ultimate strength, while poorly bonded samples started emitting noise at lower levels, depending on the adhesive used. Further inhouse work on equipment applications will expand the prediction results based on structures and adhesive systems used in Saturn and subsequent programs.

The Ultrasonic Emission Detector is applicable, nondestructively, to metal bonded to metal, and metal bonded to non-metal in laminate and sandwich core structures. It is limited to some extent by configuration, materials, and stress induction methods. Some of the merits of this equipment are as follows: (1) Low bond strength can be detected. When concentrated stresses sufficient to cause limited failure occur in defective areas, the noise emission is large enough, in most adhesives, for determination of the ultimate bond strength or bond quality. The weaker the bond the more noise emitted for a given stress, as tiny areas fail in the weak bond locations. The total amount of noise emitted, may, therefore, be equated to an indication of bond quality. Some examples of the multitude of material and structural variations which affect bond strength and produce noise are voids and porosities, inadequate cleaning, debonded areas, residual stresses, and inadequate cure. (2) The equipment is

TABLE II. BOND STRENGTH PREDICTION RESULTS

ADHESIVE	CONTAMINATION	ESTIMATED 90% ULTIMATE STRENGTH $N/m^2 \times 10^7$ (psi)	PREDICTED ULTIMATE STRENGTH $N/m^2 \times 10^7$ (psi)	ACTUAL ULTIMATE STRENGTH $N/m^2 \times 10^7$ (psi)	PERCENT DEVIATION OF PREDICTED BREAKING POINT FROM ACTUAL BREAKING POINT
MB-329	NONE	1.72 (2500)	1.90 (2750)	2.58 (3750)	-27%
	20%	1.45 (2100)	1.60 (2310)	1.74 (2520)	- 8%
	20%	1.45 (2100)	1.60 (2310)	1.50 (2180*)	+ 6%
	30%	1.10 (1600)	1.21 (1760)	1.31 (1900*)	- 7%
	40%	0.965 (1400)	1.06 (1540)	1.03 (1500)	+ 3%
	40%	0.689 (1000)	0.758 (1100)	0.792 (1150)	- 4%
HT-424	NONE	4.00 (5800)	4.40 (6380)	3.72 (5400*)	+18%
	20%	2.45 (3550)	2.69 (3900)	2.20 (3200*)	+22%
	20%	1.50 (2180)	1.65 (2400)	1.43 (2075)	+16%
	40%	1.63 (2360)	1.79 (2600)	1.84 (2670*)	- 3%
	40%	2.55 (3700)	2.81 (4070)	2.15 (3120*)	+30%

* ± 5% accuracy; all others ± 1%

NOTES:

1. TESTS PERFORMED IN FLATWISE RING TENSION BETWEEN CYLINDRICAL BLOCKS. ONE BLOCK RECESSED TO FORM OUTER ANNULUS OF 32.2 cm^2 (5 $in.^2$) BOND AREA.
2. FIXTURE STRENGTH LIMITS PREVENTED FM-1000 TEST.
3. THE POINT FROM WHICH, BASED ON HEARING JUDGMENT, A 10% INCREASE WOULD FAIL THE TEST SAMPLE.
4. IN ALTERNATE TENSION-COMPRESSION CYCLING.

portable. (3) It is independent of configuration. The sound is transmitted along the face sheet material to the stationary transducer. Configuration size may influence sound level, but has not been evaluated as yet. (4) No liquid couplants are required. (5) The equipment is inexpensive at approximately one thousand dollars per unit, exclusive of accessory recording equipment which is in standard lab supply. (6) Large areas can be evaluated in one operation. Noise emitted by highly stressed areas is radiated in all directions through the face sheet to the stationary transducer or transducers. Maximum area of coverage by one transducer has not been determined. (7) Nominal skill is required to operate the equipment. (8) It can readily be adapted for automatic test evaluation. With attachment of an electronic gating circuit to the equipment output, a go-no-go system can be devised based on the level of noise emission detected. Location of noise emitting areas can be established by three or more transducers and the use of triangulation techniques. Scanning of the structure is not required since the transducer or transducers are stationary. The bonded structures that are rejected can be tested with other types of equipment to determine the cause of excessive noise emission. (9) This equipment may be used on metal and non-metal composites if the transducer can be mounted on the bonded metal surface.

The limitations of the Ultrasonic Emission Detector equipment are as follows: (1) Surface contact is required. The transducer must be securely attached to the structure. (2) Structural bondline stressing is required. (3) Density, material, and thickness combination affect the readout, as on all nondestructive test methods. The noise level emitted by stressed structures will decrease with increased face sheet thickness and core density, for a given stress. Variation in metals will affect the readout because of their different densities. (4) The equipment does not define defects. Only noise signal levels, as emitted from areas of high stress concentration, are discerned and interpreted from noise level standards. (5) The basic equipment does not locate defects. An instrument with three channel capability and three transducers could be used with triangulation techniques and a real-time computer to locate defect areas. (6) Structural test specimen evaluation is required prior to equipment production applications. Noise level standards must be determined. Values must be established for panel reject/accept conditions based on noise emission ranges from satisfactory panels. (7) The transducer must be applied to a metal surface. Nonmetallic surfaces rapidly attenuate the noise signals from distant areas. Further application studies will be made to determine exact distance limitations in all types of bonded structures and their component materials. (8) The basic equipment requires operator interpretation of audio signal intensity. The operator's sense of hearing may vary at times and produce inconsistent results. Minimum backup equipment for optimum evaluation would be an electronic gating circuit and a strip chart recorder. (9) Access to both sides of the test surface for transducer attachment may be required for a bonded honeycomb sandwich structure. No evaluations were performed on a sandwich structure to determine if the opposite side stress noise emission level was high enough to use only one transducer.

Specific areas where further development of this equipment is recommended for adhesion bond strength analysis are as follows: (1) Equipment may be used to obtain data on the dual-seal and the 4.06-centimeter (1.6-inch) foam and plastic laminate panels during proof-pressure tests of panel integrity on the S-II cryogenic insulation. (2) A check on each individual edge-sealed section of the instrument unit structure by pressurization may be performed. (3) Nondestructive and destructive test data may be obtained during the strength tests to be performed inhouse on the 3.05- and 6.60-meter (120- and 260-inch) diameter metal honeycomb sandwich shrouds. A check of each individual edge-sealed section by pressurization would be required. (4) Data may be obtained where the common bulkheads of the S-II and S-IV stages can be internally pressurized or externally stressed. It may also be possible to monitor bulkhead bondline noise emissions over periods of storage or installation time where built-in residual stresses may cause gradual debonding. (5) Payload shrouds and nosecones may be evaluated by proof pressure or static loading. (6) Data may be obtained from structural destructive tests of any bonded structure bonded with the adhesives, or equivalent, evaluated by this program. Information from these tests indicates when the adhesive bonds start to yield, and gives the bondline stress noise emission characteristics from stress induction until complete structural failure. Yield point and allowable noise levels may then be established for the particular structure and used on future nondestructive test evaluations. (7) Structural static or dynamic load tests of bonded brackets or other bonded structural attachments will give information on the bond integrity. The possibility exists that a static test would start a bond failure, but failure would not occur in creep before completion of the test period. Noise emission from the bondline during static stress would indicate the quality of the bond.

In order to extend applications of the Ultrasonic Emission Detector, test programs are under way to establish the maximum evaluation range of the transducer and the effect of other adhesives, metals, and nonmetals that are used in bonded structures. Evaluation of defective bonds and associated noise emission characteristics will be undertaken.

CONCLUSION

The contract with General American Transportation Corporation was completed on September 8, 1965, with a demonstration of ultrasonic emission detection equipment for adhesion bond strength determinations in stressed composite structures. For bondline strength control, the photomicroflaw method satisfied the need for simulation of poor bond strengths through controlled surface contamination.

Rigid cleaning, holding time limits, and handling requirements for cleaned parts prior to bonding, as contained in all satisfactory specifications and as required by military specification MIL-A-9067C, "Process and Inspection Requirements for Adhesive Bonding," were verified by this program [4].

The ultrasonic signal emissions from a stressed bondline, modulated for acoustic monitoring, were found to be a reliable indication of bond strength. Noise signal level increases with the amount of stress applied to the bondline. Weak bonds and delaminated areas produced noise above established standard levels, thus indicating rejection of the defective panel. The Ultrasonic Emission Detector may be used to evaluate destructive tests on specimens and structures. Data obtained will indicate when the adhesive bond starts to yield and give the bondline stress noise emission characteristics from stress induction until complete structural failure, so that allowable noise level standards may be established for nondestructive evaluation. Nondestructive evaluation may be made on structures containing perforated cores that can be edge-sealed and internally pressurized, and on structures where stresses can be induced externally by mechanical fasteners or fixtures. Brackets and associated attachments, bonded to structures, may also be evaluated and are one of the most immediate applications for this equipment.

REFERENCES

1. Schmitz, Gerald; and Frank, Louis: Nondestructive Testing for Evaluation of Strength of Bonded Material. Contract NAS8-11456, General American Research Division, General American Transportation Corporation, Niles, Illinois, September 1966.

2. Military Specification MIL-A-005090E (Wep), Adhesives, Heat Resistant, Airframe Structural, Metal to Metal. April 22, 1963.

3. Military Specification MIL-A-25463 (ASG), Adhesive Metallic Structural Sandwich Construction. January 14, 1958.

4. Military Specification MIL-A-9067C, Adhesive Bonding, Process and Inspection Requirements for.

BIBLIOGRAPHY

1. Braddock, P. H.: New Method for NDT Uses Ultrasonic Waves from Loads. Metalworking News, October 5, 1964.

2. Judge, John F.: Nondestructive Testing Fundamental to Advanced Materials Development. Missiles and Rockets Publication, February 22, 1965, pages 27-32.

3. New NDT Method Probe: The Look, Sound, and Smell of Quality. Steel, The Metalworking Weekly, February 14, 1966.

4. Schmitz, G. L.: Nondestructive Testing of Adhesive Bonds. Design News Publication, September 15, 1966, page 182-185.

5. Simpkins, Alan B.: Silent Sounds of Industry. Design News Publication, March 16, 1966, pages 50-53.

Page
Intentionally
Left Blank

CHEMICAL PROPULSION RESEARCH AT MSFC

6

January 26, 1967

By

Keith B. Chandler
Peter G. Haas
Robert R. Head
James R. Thompson, Jr.
Ralph G. Weitenbeck

Page
Intentionally
Left Blank

CONTENTS. . .

IMPROVED FLUID CONNECTORS

by Peter G. Haas

LIST OF TABLES

LIST OF ILLUSTRATIONS

MAIN SEAL TECHNOLOGY FOR VENT VALVES

by Ralph G. Weitenbeck

CONTENTS (Continued). . .

LIST OF TABLES

LIST OF ILLUSTRATIONS

FLUID MECHANICS

by Robert R. Head

CONTENTS (Continued). . .

LIST OF ILLUSTRATIONS

LARGE ENGINE TECHNOLOGY

by Keith B. Chandler

LIST OF TABLES

LIST OF ILLUSTRATIONS

CONTENTS (Continued). . .

J-2 EXPERIMENTAL ENGINEERING PROGRAM (J-2X)

by James R. Thompson, Jr.

LIST OF ILLUSTRATIONS

CONTENTS (Concluded). . .

IMPROVED FLUID CONNECTORS

By

Peter G. Haas

SUMMARY

The requirement for reduced leakage and mass in space vehicles, and improved reliability and handling of fluid connectors called for advances in current technology. A major portion of Contract NAS8-11523, the feasibility study of a new semi-permanent connector, has demonstrated a successful fluid connector design concept which could lead to replacing most of the separable connectors in future space vehicles with the semi-permanent connectors. The design features, tooling concept, and development steps are discussed, and test data are given in this report. While the last task of the technology contract (combined environmental tests) is being concluded, a new contract (NAS8-20572) proceeds to develop all sizes of the new connector design and perform a formal qualification test.

INTRODUCTION

Statistical review of Launch vehicle fluid connections indicates a marked trend toward separable connectors (flanged or threaded joints) instead of the usual brazed or welded permanent connections (Fig. 1). This trend is caused by the many advantages of separable connection such as ready access to subassemblies for test or checkout purposes, easy quality control, consistent performance, and high experience level.

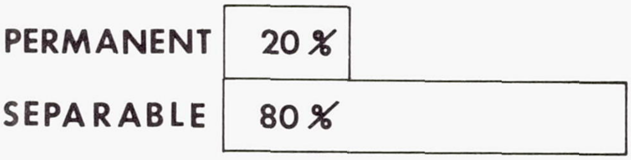

FIGURE 1. PRESENT FLUID CONNECTORS

Since there are more than 9000 joints in some vehicles, the extent of the 4 to 1 ratio in Figure 1 should be examined, especially for an operational vehicle.

A closer look at statistics on the sizes of the separable connectors reveals that the majority of the connectors are in the "tube range," below 0.038 m (1 1/2 in.) outside diameter (Fig. 2). One-sixth of the connectors are constructed from aluminum alloys, the rest are stainless steel.

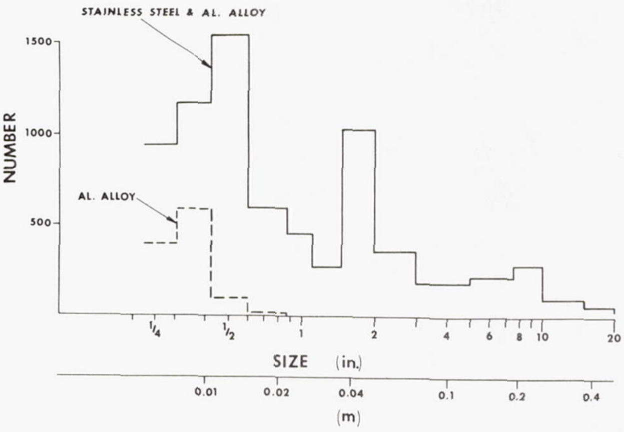

FIGURE 2. PRESENT FLUID CONNECTORS

Semi-permanent Connectors. Most of these tube connectors do not need to be reassembled for an unlimited number of times, yet their operation does exceed the restrictions of a permanent assembly. Combining the features of a permanent joint -- extremely low leakage, minimum relaxation of sealing members -- with the option of a limited number of reassemblies -- three to four times before major rework--resulted in establishing the semi-permanent connector concept (Fig. 3).

The preferred concept of a semi-permanent connector is certainly mechanical because (1) inherently easier quality control enhances reliability, (2) clean reassembly prevents contamination of the system, and (3) minimum mass of the complete system is assured since the tube maintains its strength at the connector interface.

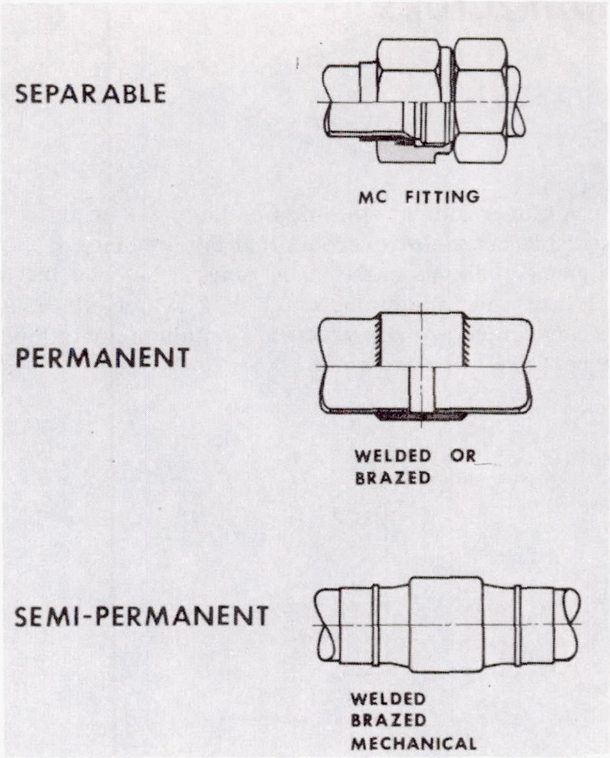

FIGURE 3. TUBE CONNECTIONS

FEASIBILITY STUDY ON THE X-CONNECTOR

A connector (the X-connector) is being developed by the Parker Aircraft Company* to meet the required characteristics (Fig. 4). In terms of the design, the operational requirements are (1) The material shall be Stainless Steel, (2) The primary size range is 0.0063 through 0.0317 m (1/4 through 1 1/4 in.), (3) The temperature range is 19° K (-425° F) to 645° K (700° F), (4) The operating pressure is 3.1×10^7 N/m^2 (4500 psi) for high pressure systems, and 0.69×10^7 N/m^2 (1000 psi) for low pressure systems, (5) Field assembly and reassembly of the connectors is practical, and (6) Leakage is below 10^{-12} m^3/s (10^{-6} cc/s) of Helium at standard conditions. Futhermore, essential design objectives must be verified such as (1) consistent assembly performance, (2) positive quality assurance, (3) minimum connector mass, (4) no restriction on tubing material condition, (5) possible standardization of parts for any configuration, (6) concept adaptable to duct sizes [0.038 m (1 1/2 in.) and up], (7) practical production and easy handling, and (8) low cost.

The present effort is to develop the connector for the 0.0127 m (1/2 in.) tube size only, to demonstrate the feasibility of the concept. The

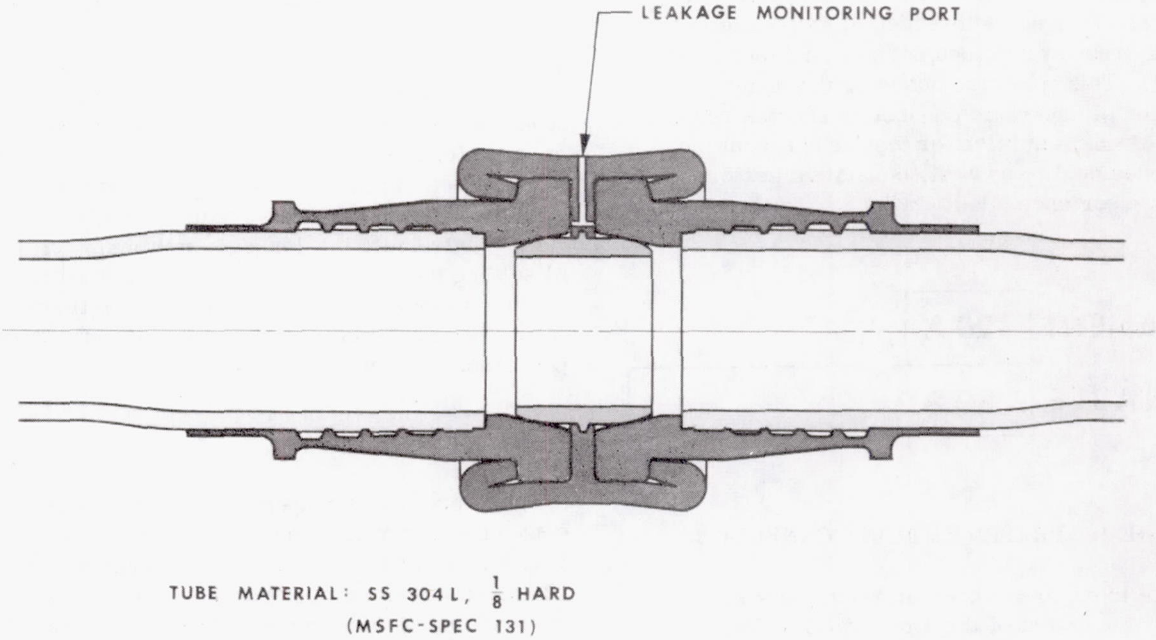

FIGURE 4. X-CONNECTOR

---

* Subcontractor in Contract NAS8-11523 with General Electric (Table I) and contractor in NAS8-20572.

TABLE I. CONTRACT NAS8-11523

Zero-Leakage Design of Tube and Duct Connectors for Deep Space Travel

General Electric Co.

Begin: June 29, 1963
End: April 1, 1967 (Projected)

Parker Aircraft: Subcontractor for Feasibility Study on the X-Connector

Subcontract:

Phase I: Configuration
- Seal Concept
- Structural Members
- Tooling
- Performance Test and Evaluation
- Design Optimization

Phase II: Feasibility Demonstration
- Sample Production
- Verification Tests
  - Proof & Burst Pressure
  - Leakage
  - Tension Load
- Combined Environmental Tests
  - Leakage
  - Temperature Extremes
  - Vibration

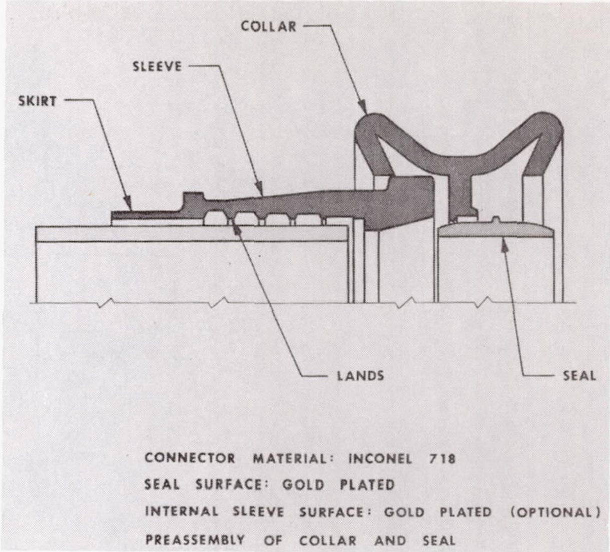

CONNECTOR MATERIAL: INCONEL 718
SEAL SURFACE: GOLD PLATED
INTERNAL SLEEVE SURFACE: GOLD PLATED (OPTIONAL)
PREASSEMBLY OF COLLAR AND SEAL

FIGURE 5. X-CONNECTOR

configuration of the X-connector has been set and includes the parts in Figure 5. The material for all connector parts is Nickelbase alloy 718 because of its high strength and excellent performance at extreme environments, and for good formability.

A locating ledge on the sleeve assures proper positioning of the tube. To transfer shear loads, the contacting rings, or lands, provide high-stress contacts with the mating tube. Also, the lands provide redundant seals. The reduced section in the skirt or fantail minimizes stress concentration in the transition region between connector and full tube, and can dampen during vibration. The sealing surface on the conical part of the sleeve is recessed and thus safe from damage. The collar links the two connector halves, and consists of two lips and stops for the sleeves. The seal engages the conical sealing surfaces of the sleeve with a high preload. Gold plating of the seal prevents galling at installation and fills any surface irregularities.

Two shop operations are needed to preassemble the connector. The first is swaging the sleeve to the tube end. The radial expansion tool (Fig. 6) seats the tube in the sleeve and expands the sleeve a predetermined amount. Springback of the sleeve exerts adequate residual forces. By embedding the contact rings into the tube surface, the sleeve is keyed to the tube and gives local, heavy deformation to penetrate surface imperfections. Optional gold plating of the internal sleeve surface eliminates existing tubing irregularities.

By stretching the sleeve-tube assembly beyond yield stress, the effect of their radial tolerances is nullified for swaging results.

The second shop operation is a collar-seal attachment process. This preassembly -- swaging of the seal to the collar -- is part of the production process of the components. In the original connector concept, collar and seal were one piece; however, for ease of fabrication a separate machining operation and preassembly was chosen. The permanent subassembly of both parts prevents installation of the connector without a seal and properly locates the seal at assembly.

Connector Assembly. With subassemblies made, the final in-place installation and collar connection is completed by another swaging operation (Fig. 7). The collar swaging tool, powered by hydraulic pressure, consists of the scissors assembly power pack and a splittable wedge assembly (detail A).

The sleeve flanges are engaged in the collar, and the swage tool is closed around the unformed

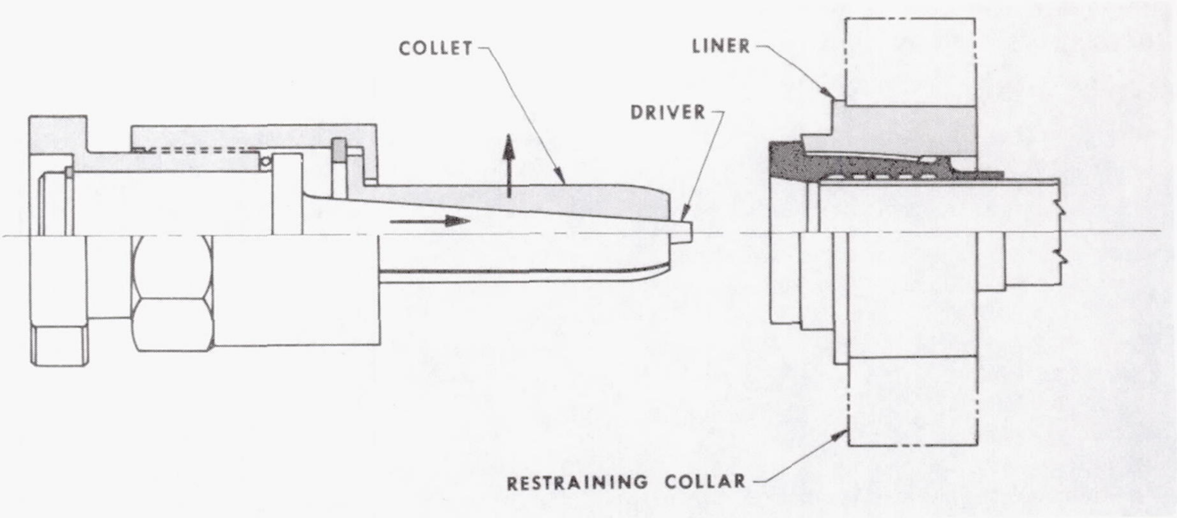

FIGURE 6. TUBE-SLEEVE SWAGING

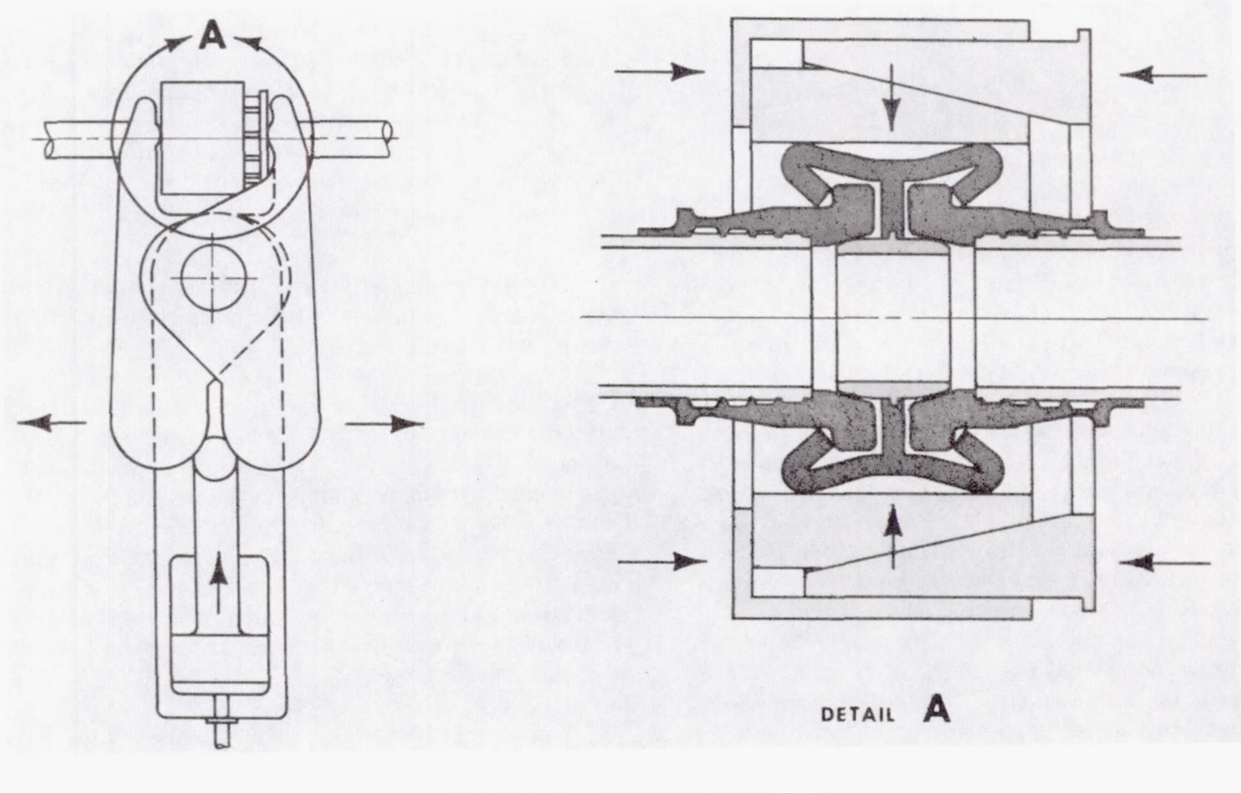

FIGURE 7. COLLAR SWAGING

connector. Closing the tool assures proper engagement and alignment of the parts for adequate collar forming. The tool is then tightened axially to keep the parts in close engagement. Next, hydraulic pressure is applied. The power causes a ring of radially-moving wedges to form the x-shaped collar into a cylinder. During this operation, the collar lips move in radially to engage the sleeve flanges and finally to drive the sleeves into the solid stop of the collar, closing the high spring rate circuit of forces.

The toggle action of the collar drives the seals into their seats with a yielding action. This eliminates the effects of dimensional tolerances between seal and sleeve seat, and maintains ample seating stress for leaktight operation. The gold plate on the sealing surface shears into the asperities of the mating surface as a caulking compound.

The seating stresses at the edges of the collar top are high enough to make a secondary seal at the flange. Any leak from the primary seal area is collected at the monitoring port (Fig. 4).

Connector Separation. Separation and reassembly, vital to the semi-permanent connector concept, is achieved readily: to separate the connector, the collar lips are simply cut off to release the sleeve shoulders. Another mode is unswaging the collar.

A tool package -- similar to the wedge assembly of Figure 7 but with an inverse mechanism -- inserted in the swage power pack provides the means for unswaging and separation. After separation and disposal of the collar and seal, the tube ends are ready for reassembly with a new collar.

Significant features of the design concept of the mechanical, semi-permanent X-connector are that (1) The seal is not a main structural member. This basic design principle is demonstrated by the closed load loop consisting of the sleeve flange, collar stop, collar lips and sleeve shoulder. Large variations of forces on the coupling cause no motion of the flanges relative to the stops, and therefore do not endanger seal integrity, (2) For a leaktight seal, local stress of one seal member should be well above yield strength. The seal spring makes and sustains a high preload to yield the gold plate on the seal interface, (3) The mechanical, plastic deformation of mating connector parts (used extensively) has several advantages: yielding into place avoids critical tolerances and thus lowers production costs; better reproducibility of assembly operation requires fewer dimensional checks; permanent location of mating parts prevents disengagement and leakage; and work hardening gives greater effective strength of materials, (4) Optimum transfer of loads from the connector to the free tube by the reduced cross-section of the fantail area, and (5) Effective leakage monitoring of all four possible leak-paths: seal leakage monitoring at the central collar location, and tapping the sleeve between two lands for checkout of tube-sleeve swage leakage.

CONNECTOR DEVELOPMENT STATUS

Development of a 0.0127 m (1/2 in.) tube size connector started with three basic design-element investigations: swaged connection of tube and sleeve, collar forming, and seal performance. After a series of iterations -- redesign, test and evaluation of likely candidates -- integration of the most effective basic components into a connector was achieved.

The iterative development effort on the element level included:

1. Tube-sleeve swage:	variation of tube wall thickness and material strength, variation of the number of sleeve lands, variation of sleeve yielding.
2. Collar forming:	variation of material, forming tool study, collar cross-section as a parameter, forming motion study.
3. Seal performance:	variation of materials, gold plating study, seal penetration study.

Testing of final configurations demonstrated adequate performance under tensile load, in vibratory fatigue with and without heat load, and under impulse and burst pressures. Mass spectrometer leak measuring was done during or after tests to verify that leakage was below 10^{-6} scc/s of Helium.

Subsequently, complete 0.0127 m (1/2 in.) connectors were designed, fabricated, and tested. In Figure 8 leakage test results are listed for eight connectors. The tests were made to assess quality and reliable fabrication of tube-sleeve swages of connector assemblies by measuring leakage across singular lands. Indicated leak-rates occurred at proof pressure level of 6.21×10^7 N/m^2 (9000 psi); there was no excessive leakage at the rated pressure of 3.10×10^7 N/m^2 (4500 psi). "Leakage of full connector" denotes leakage monitoring across all lands (no monitoring holes) using long-duration-pressure application to avoid the effect of leakage-flow delay caused by the series of voids between the sleeve lands. The vibration tests were performed for 10^6 cycles at stress levels up to 2.42×10^8 N/m^2 (35 ksi). Stress levels were defined as the maximum fiber stress on the tube adjacent to the connector.

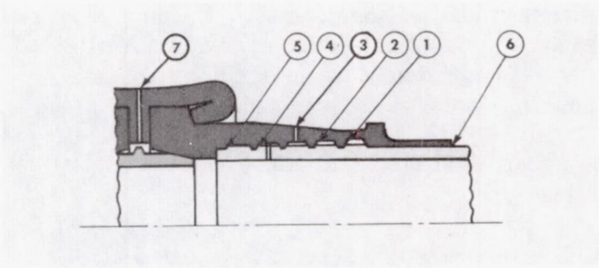

LEAKAGE MEASUREMENT: He MASS SPECTROMETER
SENSITIVITY 2×10^{-14} m^3/s (2×10^{-8} scc/s)

TEST PRESSURE: 6.21×10^7 N/m^2 (9000 psi) (PROOF PRESSURE)

LEAKAGE OF SINGULAR LANDS (① TO ⑤)
12 ASSEMBLIES: 3 EVENTS BEFORE } VIBRATION
0 EVENTS AFTER

LEAKAGE OF FULL CONNECTOR (⑥, ⑦)
4 ASSEMBLIES: NONE

FIGURE 8. LEAKAGE TESTS

Test results of connector assemblies under impulse, tensile, and burst tests are indicated in Figure 9.

IMPULSE TESTS

Peak Pressure = 1.5 Operating Pressure
10,000 Cycles
No Leakage
No Damage

TENSILE TESTS

Tensile Load = 4 x End Load Caused by Operating Pressure.
No Connector Failure

BURST TESTS

Burst Pressure = 4 x Operating Pressure
No Connector Failure

FIGURE 9. CONNECTOR ASSEMBLY TEST RESULTS

Comparative fatigue test results are shown in Figure 10. Reduction of fatigue strength caused by the stress discontinuity induced by the connector appears as the slope change in the logarithmic fatigue chart. Unfortunately, no comparative values from other connector types are yet available.

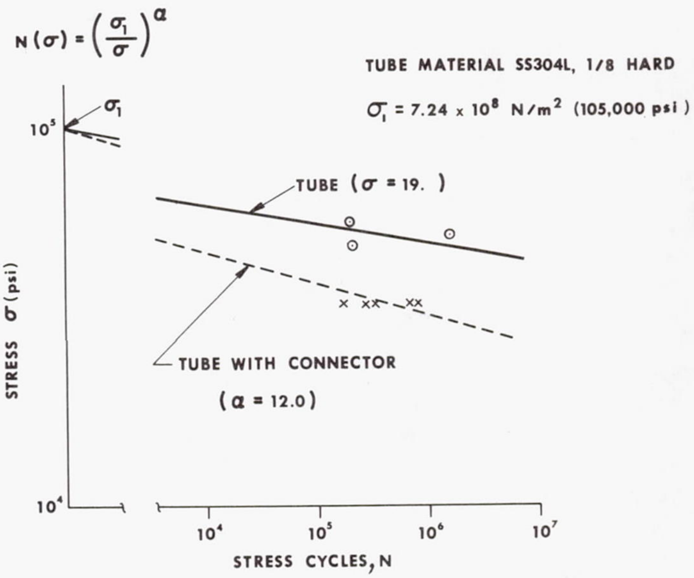

FIGURE 10. FATIGUE TESTS

After completion of the test series the final attempt at feasibility demonstration of the X-connector concept is underway in a series of combined environmental tests. The test program with 26 connector samples includes (1) leakage and proof pressure for hardware checkout, (2) low temperature (LN_2) at operating pressure, with mass spectrometer leakage monitoring, (3) high temperature [645°K (700°F)] at operating pressure, with leakage measurement, (4) high temperature at operating pressure, under vibration, with leakage measurement, and (5) long-duration measurement of leakage of several connectors (sleeves without leakage monitoring capability). All other assemblies have monitoring holes tapping the first sleeve void (between land 3 and 4 of Fig. 8).

FUTURE EFFORT

Presently, the X-connector design and development in Contract NAS8-20572 are attempted for the standard tube sizes 0.0063, 0.0095, 0.0127, 0.0191, 0.0254, 0.0317 m (1/4, 3/8, 1/2, 3/4, 1, 1 1/4 in.) and associated tooling (Table II). This effort includes two operating pressure levels: the previously defined 3.1×10^7 N/m^2 (4500 psi), and 0.69×10^7 N/m^2 (1000 psi) for low-pressure applications. The definition of low-pressure tubing will result in extensive system mass reduction, particularly in the larger tube sizes.

The development program will be continued in a production phase to form connector samples and tooling, and a test phase for flight qualification of the X-connector. Immediate application of the connectors on flight vehicles is then planned.

TABLE II. CONTRACT NAS8-20572

Development and Qualification of Improved
Fluid Connectors
Parker Aircraft Co
Begin: June 29, 66
End: June 29, 68 (Proj.)

Phase I:	Design and Evaluation -Develop all Standard Tube Sizes -Develop Tooling
Phase II:	Production -Qualification Samples -Tooling
Phase III:	Qualification
Phase IV:	Documentation

Page
Intentionally
Left Blank

MAIN SEAL TECHNOLOGY FOR VENT VALVES

By

Ralph G. Weitenbeck

SUMMARY

A program was implemented to improve the effectiveness of large-diameter vent valves for use in the LOX, fuel, and helium systems of space vehicles. At the time the development contract was signed, the norm for leakage of the valve under consideration was 67 scc/s. Areas of work on the vent valve included the bellows, actuators, shaft and main seals. Of main importance was the work done on the main seal. Leakage test results were in the order of 1.0 scc/s at 505°K (450°F), 1.0 scc/s at 295°K (70°F), and 11.0 scc/s at 77.5°K (-320°F).

INTRODUCTION

The main seal evaluation phase of the program consisted of the study, testing, and development of a valve seal of a flapper and seat arrangement. The operational requirements were as follows: (1) size, 25.4 cm (10 in.) internal diameter, (2) pressure, 0 to 344 000 N/m^2 (0 to 50 psig), (3) temperature, 77.5°K to 505°K (-320°F to +450°F), (4) leakage, 13.7 scc/s nitrogen, and (5) life, 2000 cycles.

DESIGN APPROACH

The initial design approach was to use a moving member (flexible flapper) to seat against a thin land on a fixed seat. For rigidity of the flapper when working close to the seat, a stiff backup member supported the flapper as it rose off the seat. Seating load was maintained by the pressure force acting over the area of the flapper. Relatively little change in design concept occurred during development.

Choice of flapper material was based on (1) high tensile strength at elevated temperatures, and (2) good impact strength at cryogenic temperatures. The materials considered and their significant mechanical properties are in Table I. Of these materials, Inconel 718 had the highest tensile strength at a high temperature of 589°K (+600°F) and also demonstrated acceptable impact strength at a cryogenic temperature of 77.5°K (-320°F). This material gives the lightest possible flapper.

TABLE I. SIGNIFICANT MECHANICAL PROPERTIES OF MATERIALS CONSIDERED FOR 25.4 cm (10 IN.) FLAPPER

Mechanical Properties in $N/m^2 \times 10^5$ (psi $\times 10^3$)	A-286	Inconel-X	Inconel-718
Tensile Strength at Room Temperature	9.64 (140)	13.4 (195)	13.8 (200)
Tensile Strength at 589°K (600°F)	8.26 (120)	9.64 (140)	12.7 (185)
Yield Strength at Room Temperature	6.20 (90)	9.64 (140)	11.7 (170)
Yield Strength at 589°K (+600°F)	5.16 (75)	8.26 (120)	10.7 (155)
Impact Strength Charpy V-Notch at 77.5°K (-320°F)	3.44-4.13 (50 - 60)	2.06-2.76 (30 - 40)	1.24 (18)

In the development work five (5) flapper and seat configurations were designed and tested, each new configuration evolving from test information of the preceding configurations. The nominal seal, configuration No. 1, came from these considerations: (1) The flapper must be flexible enough to conform to waviness in the seat caused by thermal and pressure stresses, (2) Since the flapper is flexible, a rigid backup support must be incorporated to prevent flutter and buzz, and (3) The seat and flapper materials must be of sufficient hardness to prevent galling and wear.

The most significant problem inherent in configurations 1 through 4 was an high-impact unit loading caused by the fast closure speed. The closure time of 40 msec was increased to 175 msec before testing configuration No. 5.

Also, after further study of the seal configuration, a configuration of Inconel 718 flapper material and seat material of A-286 was tested again. The reasons for this change were (1) The softer material in a flapper and seat combination will be deformed during use, (2) The narrower member in a seat and flapper combination should be constructed of the softer material. This will, in effect, deform the entire surface of the narrow member and allow the wide member (flapper) to shift slightly from cycle to cycle without impairing sealing quality, (3) A-286 is a relatively softer material than Inconel 718 and so was the logical choice for the narrower member (the seat), and (4) The stronger (harder) material should be used for the flapper to allow building a lighter weight part.

Configuration No. 5 (Fig. 1 and 2) was subjected to 7900 endurance cycles. The leakage at 344 000 N/m^2 (50 psig) at room temperature did not exceed 1.4 scc/s nitrogen. After the 7900 endurance cycles the seat and flapper were disassembled, inspected, and reinstalled in the test fixture.

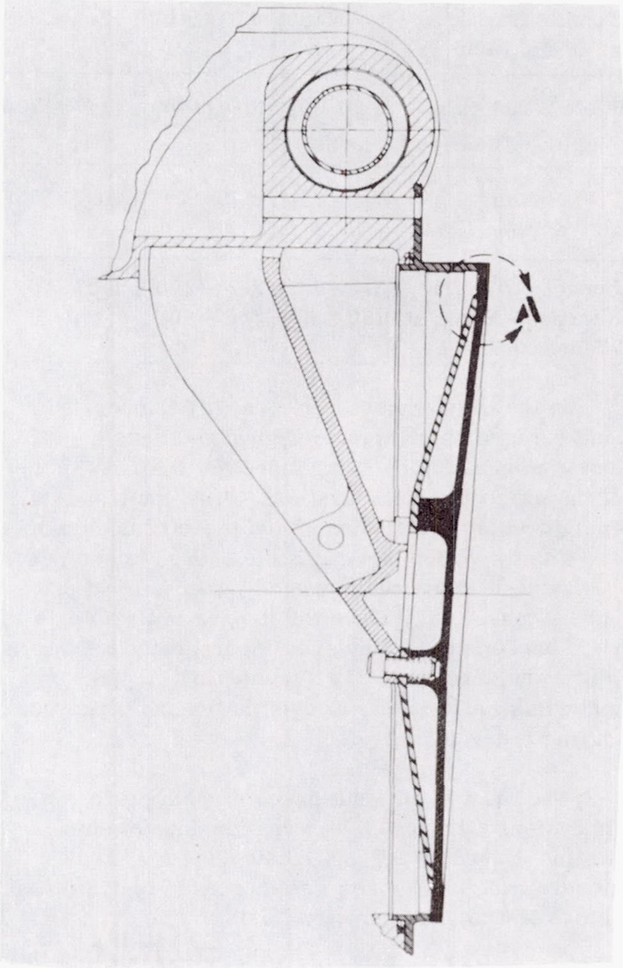

FIGURE 1. FLAPPER AND SEAT ARRANGEMENT

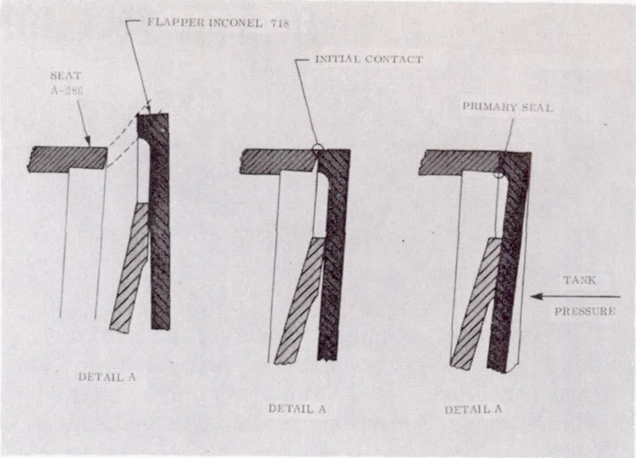

FIGURE 2. FLAPPER AND SEAT ARRANGEMENT DETAIL "A"

Leakage tests at 505°K (+450° F), room ambient and 77.5°K (-320° F) were performed with N_2 and He gas. The results of this test are in Table II. This highly successful test verified the acceptability of the final design.

TABLE II. LEAKAGE RESULTS AFTER 7900 CYCLES

Temp °K	Pressure $N/m^2 \times 10^5$ (psig)	Medium	Leakage scc/s
505 (450° F)	3.44 (50)	GN_2	<1.0
505 (450° F)	1.72 (25)	GN_2	<1.0
505 (450° F)	3.44 (50)	He	<1.0
505 (450° F)	1.72 (25)	He	<1.0
Room	3.44 (50)	GN_2	1.0
Room	1.72 (25)	GN_2	1.0
Room	3.44 (50)	He	1.3
Room	1.72 (25)	He	1.2
77.5 (-320° F)	3.44 (50)	GN_2	10.9
77.5 (-320° F)	1.72 (25)	GN_2	6.3*
77.5 (-320° F)	3.44 (50)	He	26.0
77.5 -320° F	1.72 (25)	He	17.5**

* Present Norm = 67 scc/s
** Present Norm = 133 scc/s

The test fixture (Fig. 3) consisted of a simple pneumatic actuator operated at 5.16×10^6 N/m^2 (750 psi), 2 bar linkage arrangements, and the seal configuration.

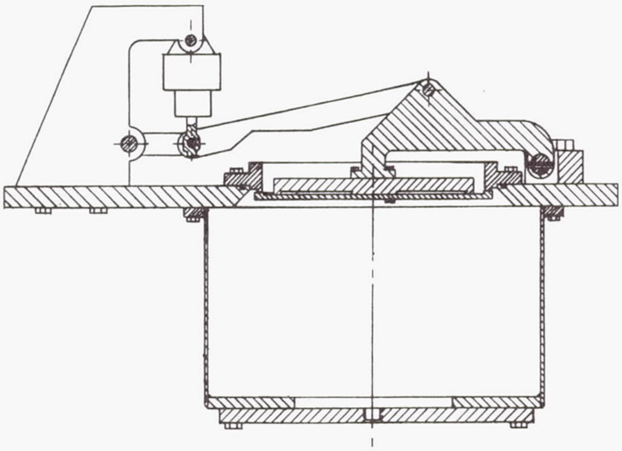

FIGURE 3. ASSEMBLY OF TEST FIXTURE AND SEAT CONFIGURATION

CONCLUSION

Evaluation of the results of the development tests verified the success of the program and confirmed that it was possible to produce a metal-to-metal seal to reliably meet low-leakage requirements. The results of this development were further confirmed by successful completion of a 25.4 cm (10 in.) LOX Vent and Relief Valve Program in which this seal was used. Overall excellent valve performance was demonstrated in meeting the 13.7 scc/s leakage requirement through a temperature band of 505°K to 77.5°K (+450°F to -320°F) (Figs. 4 and 5).

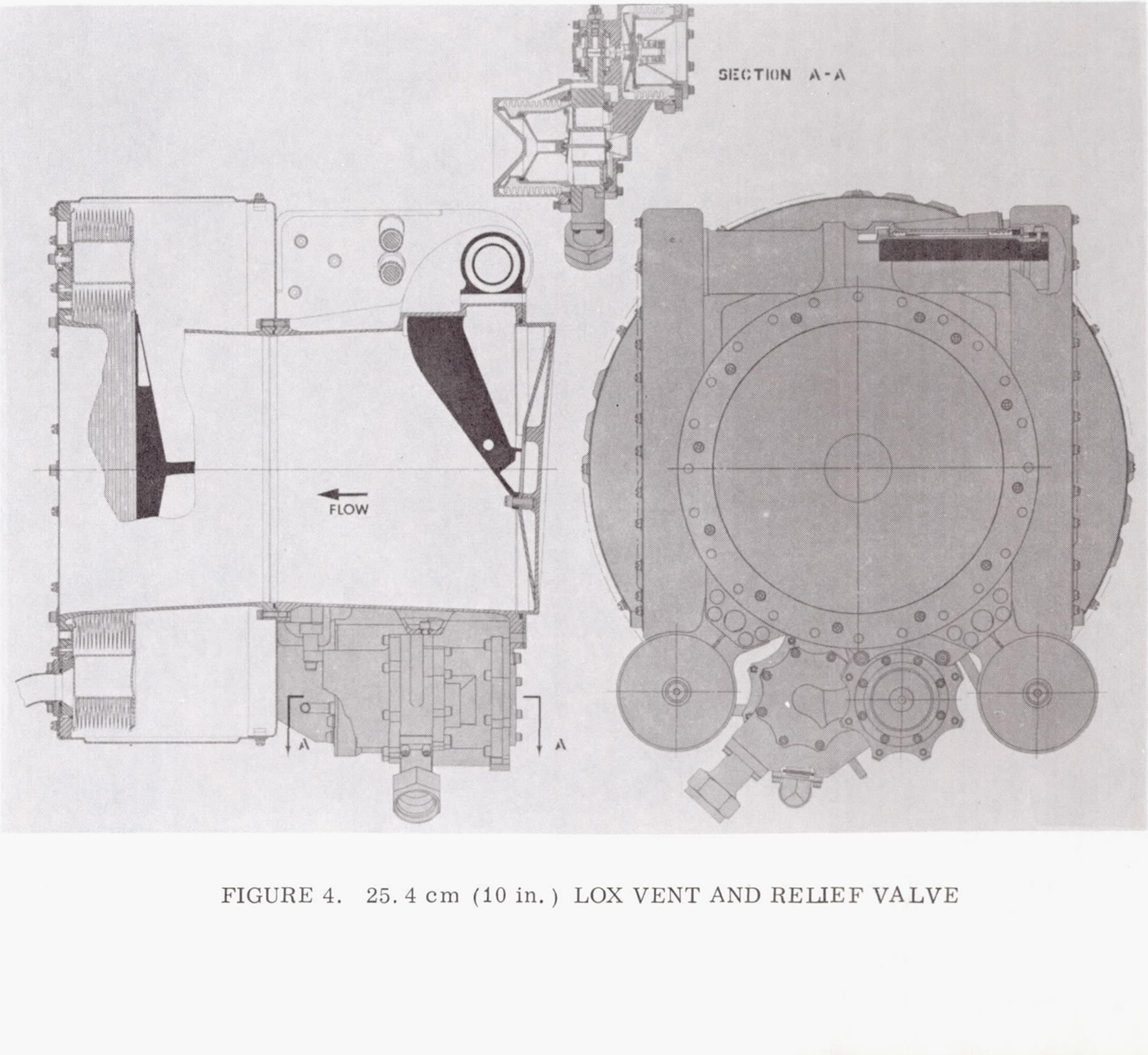

FIGURE 4. 25.4 cm (10 in.) LOX VENT AND RELIEF VALVE

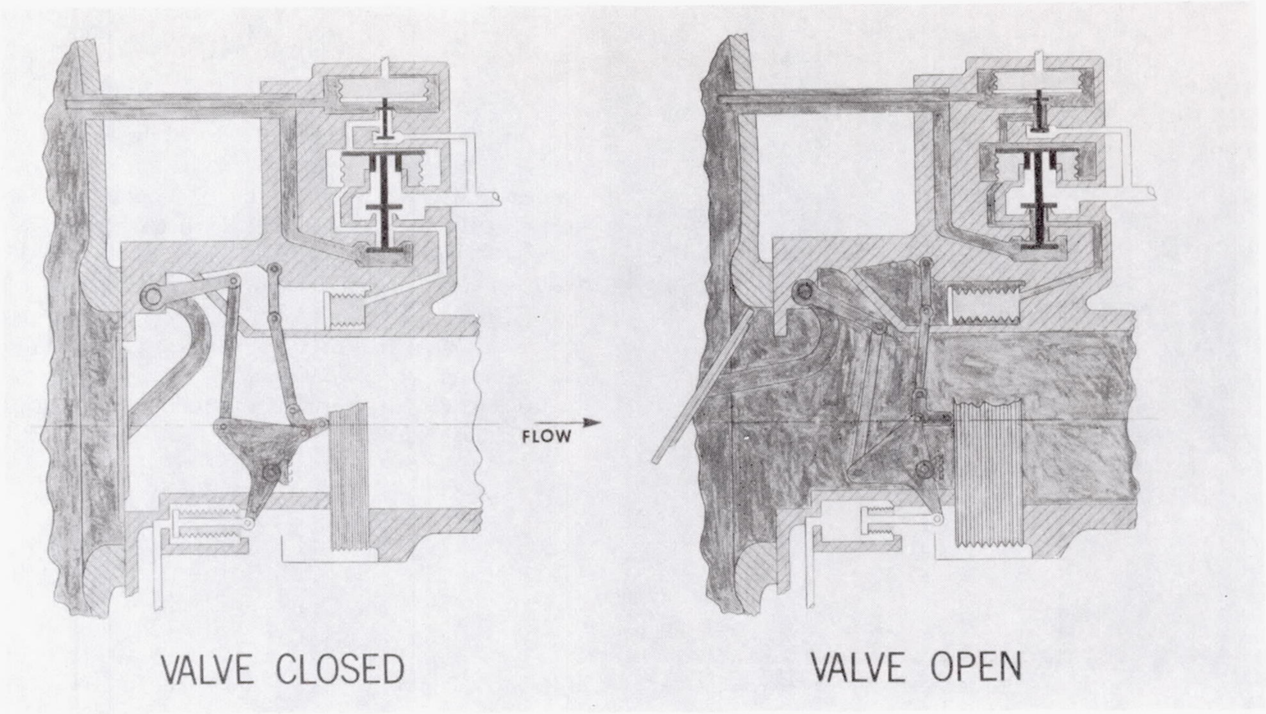

FIGURE 5. 25.4 cm (10 in.) LOX VENT AND RELIEF VALVE SCHEMATIC

FLUID MECHANICS

By

Robert R. Head

SUMMARY

Three areas of inhouse research in fluid mechanics are discussed: bubble dynamics, two-phase flow and flow measurement by laser Doppler shift.

Bubble Dynamics. Terminal velocities were determined for an inert gas injected as a single bubble into an LN_2 column. A dimensionless parameter was found, which together with the classical dimensionless parameters permits experimental simulation of low g (gravity) effects at one g.

Liquid columns of water and methanol were longitudinally vibrated within the frequency range experienced on launch vehicles, and the bubbles and bubble clusters were studied. Mathematical expressions were obtained that define the condition for inception.

Two-Phase Flow. Two-phase flow in cryogenic systems was experimentally investigated and compared with the theoretical models for frozen equilibrium and shifting equilibrium. Analysis of two-phase flow as a single component was found by the frozen equilibrium model to be accurate for qualities above thirty-five percent.

Flow Measurement by Laser Doppler Shift. A laser velocimeter operating from the principle of the Doppler shift was used to investigate point velocities in a turbulent fluid flowing in a pipe. There was no protuberance of the flow stream. The velocity distribution was determined at each point and for each rate of bulk flow stream. The frequency response of the base instrument and electronics is sufficient to measure all frequencies of turbulence investigated.

The data were verified by comparing the mean velocity profile calculated from the probability distribution function with profiles determined by other methods of mean velocity measurement. The variance of the distribution function was verified by comparison with data on turbulent diffusion. The velocity distribution function as derived from statistical reasoning was found to properly describe the measured axial velocity components. The change in the variance of the velocity distribution function is derived and is compared with the measured variance.

DYNAMICS OF HELIUM BUBBLES IN LN_2

INTRODUCTION

The voids in liquids, called bubbles, consist of vapor from the parent liquid, dissolved or captured gases, inert gases in the liquid or combinations of these. Gas bubbling has been advantageously employed in our missiles and space vehicles. On the Jupiter vehicle, gaseous nitrogen was injected into the fuel line to prevent freezing in the line and stratification in the fuel tank. The same is employed in the first stage of the Saturn I and Saturn V vehicles. The principal objective is mass transfer. In the suction lines of the cryogenic propellants for most stages of the Saturn I and V vehicles, gaseous helium is injected for the primary purpose of cooling the propellants, although some mass transfer is present. In the case of cryogenic propellants the vapor pressure is relatively high and cooling occurs from the liquid flashing into the voids created by the helium bubbles.

Disadvantages from bubbles are those such as flow restrictions caused by cavitation, noise and vibration resulting from rapid bubble collapse and flashing caused from static pressure drop. Also there are bubbles produced by vibrating surfaces. In one case it was found that bubbles produced on a vibrating liquid level sensor caused erroneous readings.

In an attempt to have a better understanding of the phenomena and mechanics of bubbles, inhouse and contracted research studies have been initiated. In recent years extensive studies have been made relating to bubble motion, mechanism, and nucleations, both because of their technological implications and because it is a fascinating scientific problem encompassing many studies.

In nearly all papers on the motion of bubbles in liquids, the authors have recognized the following factors as pertinent: bubble velocity, V, gravity, g, gravitational constant, g_c, liquid density, ρ_l, gas density, ρ_g, viscosity, μ, surface tension, σ, pressure, P, and bubble radius, R.

Although this list does not complete the set of quantities needed to specify the system, the effects of other factors are believed to be negligible.

It is possible to group these factors into five dimensionless parameters in terms of which the nine physical quantities can be described.

Reynolds Number, $\pi_{Re} = \frac{\bar{V}\rho R}{\mu} = \frac{\text{inertial force}}{\text{viscous force}}$, and relates dynamic similarity.

Froude Number, $\pi_{FR} = \frac{\bar{V}^2}{g R}$, $\frac{\text{inertial force}}{\text{gravitational force}}$, and relates to wave and surface behavior.

Weber Number, $\pi_{We} = \frac{\bar{V}^2 \rho R}{g_c \sigma} = \frac{\text{inertial force}}{\text{surface tension}}$, and relates to bubble formation.

Drag Coefficient, $\pi_D = \frac{(\rho_l - \rho_g) R g}{\rho \bar{V}^2} = \frac{\text{gravitational force}}{\text{inertial force}}$, and relates to free settling velocity.

Bond Number, $\pi_{Bo} = \frac{(\rho_l - \rho_g) R^2 g}{g_c \sigma} = \frac{\text{gravitational force}}{\text{surface tension}}$, and relates to breakup of bubble.

$G_1 = \frac{g \mu^4}{\rho \sigma^3} = \frac{N^3_{We} \, N_{FR}}{N^4_{Re}}$ and relates to pressure gradient.

Therefore, reasonable correlation is provided between bubbles rising in different fluids when plotted in terms of the above dimensionless parameters.

The first aspect of bubble dynamics studies involved high speed photographic observation of single bubbles and clusters of bubbles injected into a cryogenic liquid column.

EXPERIMENTATION

The experimental study covered gas bubble dynamics for terminal velocity, bubble collapse and natural bubble frequency. The experimental facility was designed to obtain the maximum information and still provide flexibility, to verify dimensionless parameters, and to study bubble collapse and bubble natural frequency for various gases in a cryogenic fluid.

One of the most difficult problems was to produce only a single bubble in a cryogen. Liquid nitrogen was used as the non-volatile liquid component in all cases. The gases injected were helium and nitrogen.

The diagram for gas flow, pressure control, and instrumentation is shown schematically in Figure 1.

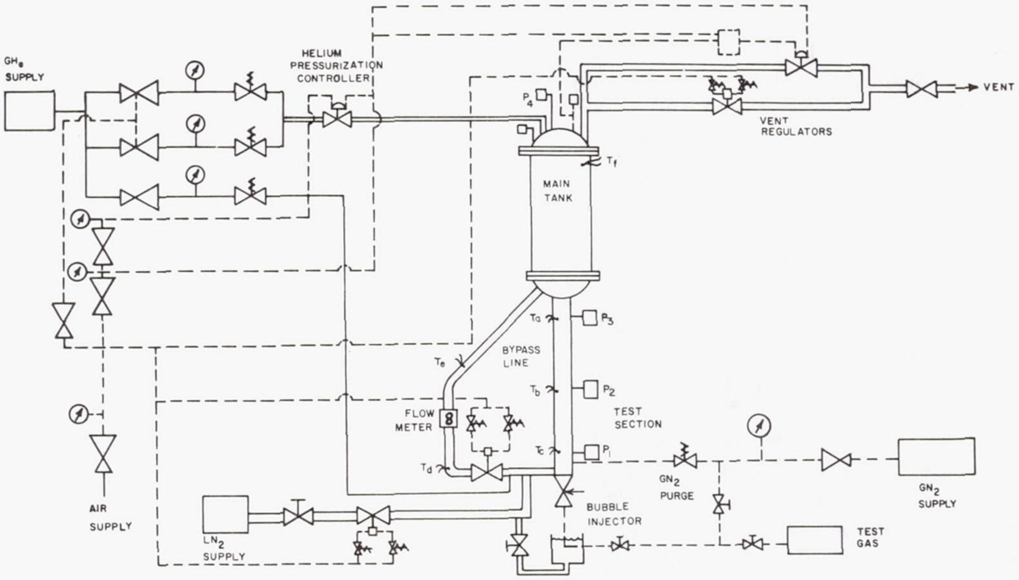

FIGURE 1. SCHEMATIC DIAGRAM FOR GAS FLOW, PRESSURE CONTROL AND INSTRUMENTATION

The test gas used in the experiment was passed from the cylinder equipped with pressure regulator through a chill bath of liquid nitrogen before entering the bubble injector. A needle valve with a micrometer attachment was used to adjust the rate of gas for bubble injection.

The tank pressure can be adjusted between atmospheric pressure and 0.34×10^6 N/m^2 (50 psig) by injecting helium above the liquid in the tank. The rate of pressurization can be controlled. The vent regulator, which was situated on the top of the tank, was set for a maximum pressure of 0.34×10^6 N/m^2 (50 psig). The tank pressure was measured by Wiancko transducers, monitored by strip chart recorder and recorded on an oscillograph. Pressure is read to $\pm 0.34 \times 10^4$ N/m^2 (± 0.5 psi) with an accuracy of 2%.

The general view of the experimental facility in Figure 1, from left to right, shows the storage tanks above the test section, the liquid nitrogen trailer and fill lines, and the portable gas tanks of helium and nitrogen. A close-up of the test section in Figure 2 shows the arrangement of the test section by-pass line, chill line, and a camera in position along with various pressure gages.

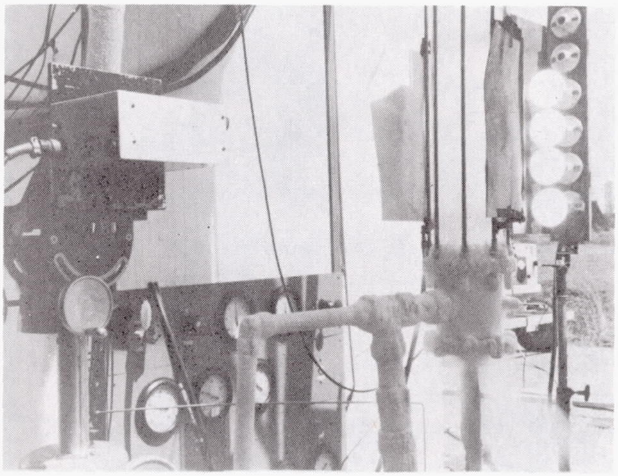

FIGURE 2. BUBBLE DYNAMICS - EXPERIMENTAL SETUP

Because of the extent of arithmetic manipulation needed for the reduction of data, a computer program was employed. The computer program contains three main parts: reduction of experimental data, calculation of the analytical solution for the particular conditions of the experiment on an analog computer, and plotting of both theoretical and experimental data.

RESULTS

Since bubbles of different sizes will assume different shapes, the characteristic length used was one-half the average horizontal length of a bubble. Figure 3 shows the terminal velocity of helium bubbles in liquid nitrogen at 75°K (-324°F) as a function of the characteristic length (the radius of the bubble).

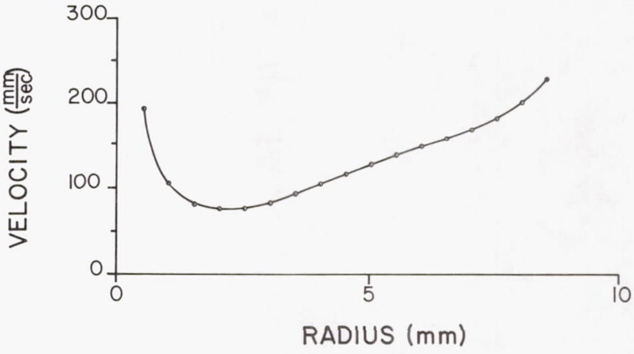

FIGURE 3. VELOCITY VS. BUBBLE RADIUS

A more generally employed presentation shows the drag coefficient as a function of Reynolds Number with a third parameter, G_1, as defined earlier, kept constant (Fig. 4).

Other experimenters have shown that up to a Reynolds Number of 70 a bubble behaves like a rigid sphere. For a Reynolds Number of 70 to 600, the hydrodynamic and surface tension forces are both important in determining the shape and consequently the drag coefficient of the bubble. As the bubble size increases, the shape of the bubble becomes flatter with a consequent rise in the value of the drag coefficient. For a Reynolds Number greater than 5000, surface tension plays a relatively minor role in determining the shape of the bubble; hydrodynamic forces acting on the bubble result in a mushroom shape bubble.

Since the inhouse experiments were all conducted in liquid nitrogen at one temperature with only the bubble size being varied independently, no information concerning the effect of the parameter G_1 can be derived from these data. This G_1 parameter was chosen so as to be independent of the variables in the experiments. It may be varied independently of the Reynolds number by changing either the pressure gradient or the properties of the liquid. A few

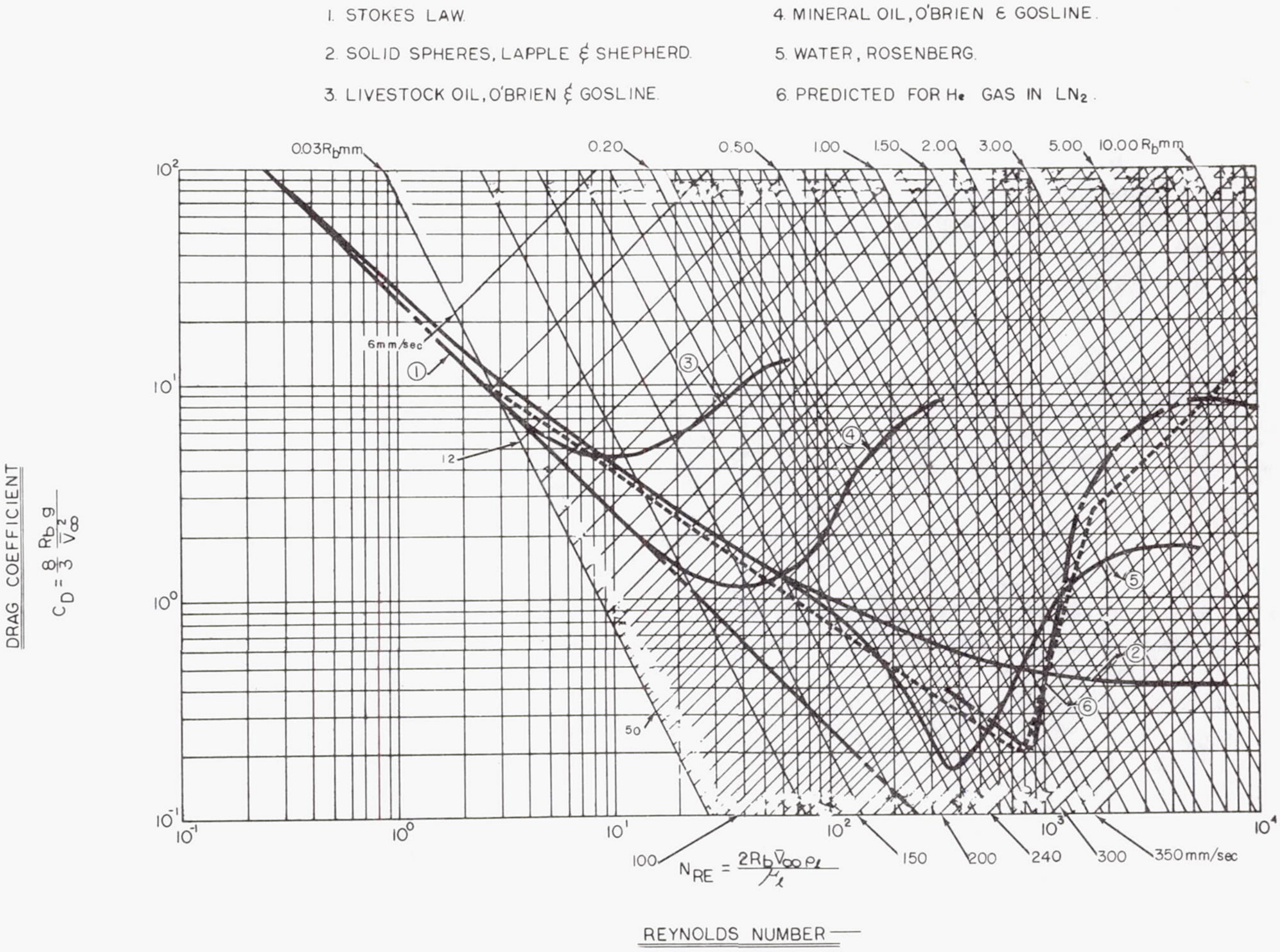

FIGURE 4. DRAG COEFFICIENT VS. REYNOLDS NUMBER

generalizations appear justified, both from the expected influences of the variables incorporated in the parameter G_1 and other authors' data.

From other authors' data it appears that for very low Reynolds Numbers, the bubble behavior is almost independent of the value of the parameter G_1, the bubbles acting as rigid spheres. A puzzling aspect of the problem is the existence of a critical value of the Reynolds Number beyond which the drag coefficient of the bubble departs from that of a rigid sphere, yet the bubbles are still spherical. The available data are not sufficient to indicate definitely whether the Reynolds Number at which this break takes place is a function only of G_1 or whether the phenomenon depends upon some property of the fluids not considered in this analysis. A tentative observation is that the greater the value of G_1, the lower is the critical Reynolds Number.

Most hydrodynamics problems are concerned solely with the variation of drag coefficient with Reynolds Number for a single fluid. The form of G_1 indicates that for a specific liquid at a given temperature, changing the pressure gradient is equivalent to varying G_1. Therefore in using different liquids the same sort of information is being obtained as if the pressure gradient were varied, provided our assumption concerning the relevant physical variables is correct.

The Bond Number indicates the ability of the bubbles to remain as an entirety. As the Bond Number increases, the bubble becomes less stable. At a Bond Number of 275 (approximately 8 mm radius) the bubble was noted to break up into two or more smaller bubbles. Since the Bond Number is the force ratio of gravity to surface tension, and surface tension force decreases as the bubble radius increases, the Bond Number should increase as the bubble radius increases. At this Bond Number, the gravitational force is much larger.

CONCLUSIONS

The motion of a gaseous bubble in a liquid can best be characterized by the use of four dimensionless numbers: The drag coefficient, Reynolds Number, Bond Number, and the fourth parameter, G_1, which for a specific liquid is proportional to the pressure gradient. The effect of G_1 on the relation between the drag coefficient and Reynolds Number is uncertain since only incomplete data are available. The Bond Number indicates the upper limit for any particular gas bubble in a liquid.

BUBBLE DYNAMICS IN VIBRATED LIQUID COLUMNS

INTRODUCTION

The experimental work in bubble dynamics was extended to the production and coalescence of bubbles by longitudinal vibrations of a liquid column filled with water and methanol.

Some parametric experimental results along with a review of the literature indicate very definite trends: higher ullage pressures require larger energy input for inception; the lower the liquid height, the higher the natural frequency of the liquid and container; and wall thickness and length/diameter ratio have a significant effect on the inception of bubble coalescence.

Several variables that must be examined closely to determine their effect are the gas content in the liquid, other properties of the liquid, properties of the container, and time dependency of inception.

Thus far, the research project is exploratory in nature and parametric tests are being run to determine general trends and to select parameters to be used for future investigations.

One of the most difficult problems encountered is the development of a non-visual method of detecting the presence of the bubble clusters. Encouraging results have been obtained during sinusoidal vibration; as the bubble clusters form they distort the sinusoidal vibration of the container by causing high frequency perturbations in the displacement of the shaker. With random vibration these high frequency perturbations are already present even without the formation of bubble clusters, and therefore a capacitance type quality meter will probably be required to detect the clusters if they cannot be visually detected.

EXPERIMENTATION

The test program presently is investigating the effects of various variables in the formation and coalescence of bubbles in longitudinally vibrating liquid-filled elastic containers.

Initial tests were conducted using a 15.24 cm (6 in.) ID × 1.27 cm (1/2 in.) wall × 91.5 cm (36 in.) long plexiglas container with a flat bottom and an open top. This container filled with methanol was mounted on a 22 200 N force (5000 lbf) vibration exciter. A schematic is given in Figure 5.

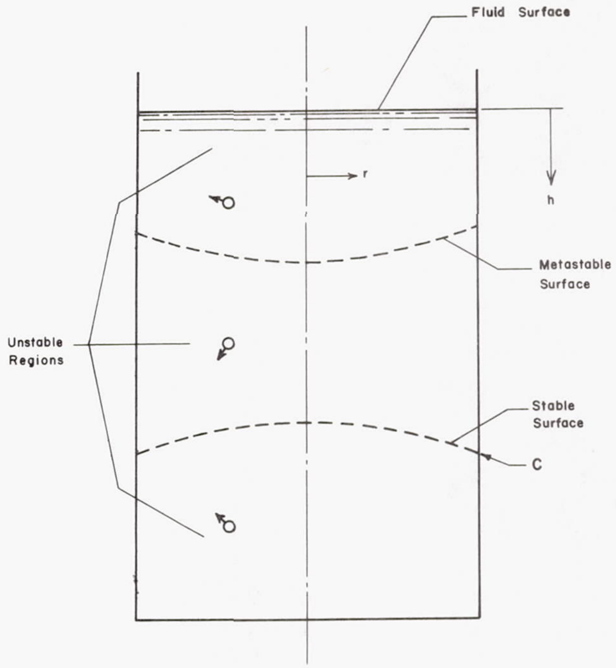

FIGURE 5. BUBBLE BEHAVIOR IN ELASTIC TANKS

The bubbles were formed in two distinct ways. The first was a surface effect where liquid droplets sloshed free of the surface; the droplets fell back through the surface and formed gas bubbles under the surface (Figs. 6 and 7). In the second method bubbles were formed at higher frequencies by the separation of dissolved gas out of the liquid, creating a very unstable condition (Figs. 7 and 8).

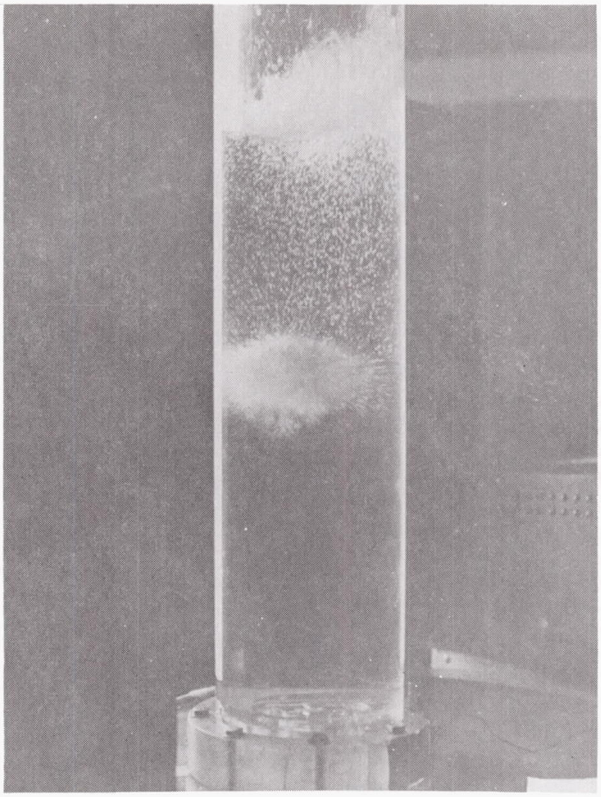

FIGURE 6. LONGITUDINAL VIBRATION - LOW FREQUENCY (100 Hz), 10-15 g's

At sufficiently large vibration amplitudes, these bubbles migrated to the lower region of the column where they formed a large aggregate of bubbles. This phenomenon has been named CILIVIC (coalescence in liquids in a vibrating column). When the bubble aggregate has become sufficiently large, it rises to the surface where it remains, causing an area of foam under a severly disturbed surface.

Under random vibration (20-2000 Hz) that closely simulates the vibration that occurs during firing of large rocket engines, CILIVIC may occur in the tanks, suction lines, at the inlet to or in the propellant pumps, and even in the LOX domes.

To initiate bubble formation in a vibrating liquid, the local pressure level must be reduced to a sufficiently low value during a portion of the vibration cycle. For purposes of simplicity, it is assumed that bubbles will form at a particular location if the minimum instantaneous pressure falls below some threshold pressure value, P_T.

For pure liquids it might be expected that P_T would be close to the saturation pressure at the liquid temperature. This idea represents a considerable over-simplification. In reality the situation is far more complicated because the threshold pressure required to produce bubbles is dependent upon frequency, surface tension, dissolved gas properties, and a number of other factors.

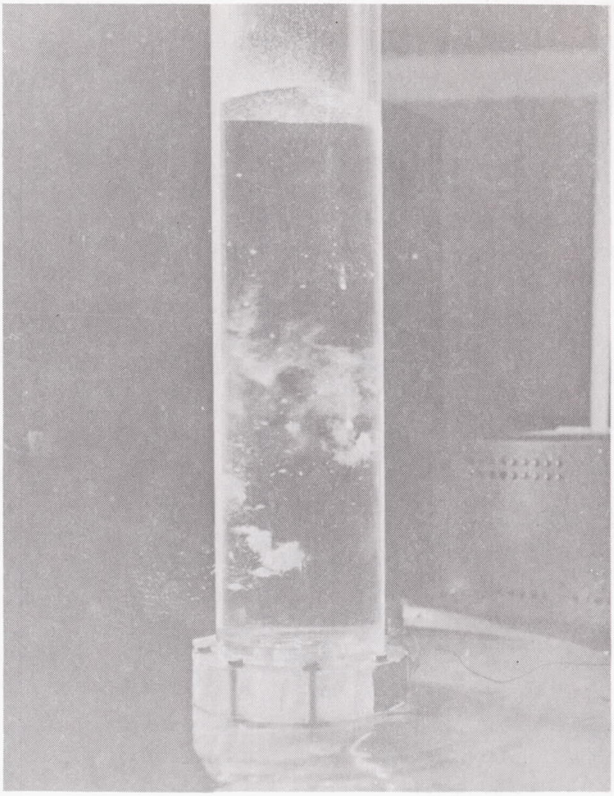

FIGURE 7. LONGITUDINAL VIBRATION - INTERMEDIATE FREQUENCY (290 Hz), 20 g's

The condition for inception of bubble formation in the system is obtained in the following equations:

$$G_T = \left[1 + \left(\frac{P_u}{pgL}\right)\left(1 - \frac{P_T}{P_u}\right)\right]\left(\frac{\Omega}{\tan\Omega}\right) \qquad (1)$$

and

$$G_T \approx \left[\frac{\pi}{2} + \left(\frac{P_u}{pgL}\right)\left(1 - \frac{P_T}{P_u}\right)\Omega\right] |\cos\Omega|. \qquad (2)$$

Where,

G_T	threshold acceleration level required to produce bubbles
P_u	ullage pressure

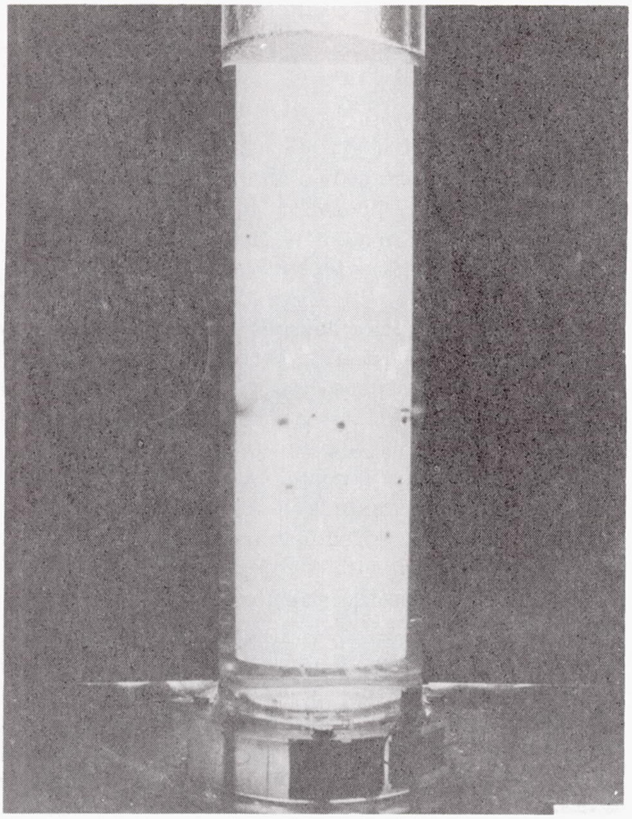

FIGURE 8. LONGITUDINAL VIBRATION - HIGH FREQUENCY (450 Hz), 30 g's

P_T	threshold pressure required to produce bubbles
ρ	fluid density
g	acceleration of gravity
L	length of the liquid column
Ω	dimensionless angular frequency, $\frac{\omega L}{c}$.

G_T represents the threshold acceleration level required to produce bubble formation. Equation (1) gives the acceleration level required to produce bubble formation at the bottom of the cylinder for $G_T > 1$ when $\Omega < \frac{\pi}{2}$, while equation (2) gives the level required to produce bubbles close to $\frac{X}{L} = \frac{\pi}{2\Omega}$ when $\Omega > \frac{\pi}{2}$ (provided that $\frac{G_T}{|\cos \Omega|} >> 1$).

RESULTS

Longitudinally vibrated liquid columns exhibit a variety of characteristics; however, these can be broken down into two distinct phenomena. The first is a surface effect where gas is entrapped in the fluid and small bubbles coalesce into a much larger pulsating aggregate at the bottom of the tank. The aggregate periodically disintegrates or plodes causing a severe surface disturbance (Fig. 6). The second effect is a separation of the gas in the liquid at discrete layers located at what appears as pressure nodes of the wave fields (Figs. 7 and 8).

At random vibration such as that developed during firing of large rocket engines, coalescence in a liquid vibrating column (CILIVIC) can occur at the inlet to the propellant pumps or in the pumps themselves and in the LOX domes, and in the long suction lines or elbows. At times CILIVICS may even be helpful.

A parametric test program is presently being initiated to investigate the effects of some of the variables in the formation and coalescence of bubbles in longitudinally vibrating liquid filled elastic containers.

The initial tests were conducted using a 15.24 cm (6 in.) ID × 1.27 cm (1/2 in.) wall × 91.5 cm (36 in.) long plexiglas container with a flat bottom and an open top. This container was mounted on a 22 200 N force (5000 lbf) vibration exciter and filled with methyl alcohol to a height of 50.8 cm (20 in.) above the tank bottom. When the container was vibrated at low frequencies (40 to 150 Hz), the surface would begin to slosh. As the acceleration was increased, the surface slosh became violent, and droplets of the fluid were thrown free of the surface. When these droplets fell back through the fluid surface, they formed gas bubbles under the surface. Buoyancy then caused these bubbles to return to the surface. As the acceleration level was increased further, however, the bubbles would migrate to the bottom of the container instead of floating upward. As the number of bubbles within the liquid increased, the migration of the bubbles from the surface increased until a large aggregate of bubbles formed within the fluid. Although a quasi-steady state was reached, this aggregate would continue to grow very slowly and with this growth it would finally reach the surface. The migration of small bubbles would again start and form another cluster within the fluid.

When the container was vibrated at the higher frequencies, the large sloshing motion of the free surface was absent. As the acceleration level was increased, only standing waves were visible on the surface until, with a sharp cracking noise, bubble clusters formed at discrete layers in the tank. These clusters moved rapidly and violently around in the container, and as some went to the surface, new clusters formed. The clusters rotated at a rather high speed. When a cluster neared the free surface, the spinning motion made a surface spray above the bubble.

The parametric studies to some degree have determined the effect of the ullage pressure, the liquid height, and the time of imposed vibration on the formation of the bubble clusters. The ullage pressure in these containers was varied. The time in which bubbles form depends on the acceleration level. For example, as is shown in Figure 9, an imposed vibration of 12 g's at 110 Hz will cause a bubble cluster to form after 120 seconds. The size of the bubble and bubble clusters is related inversely to the frequency of vibration (Fig. 10).

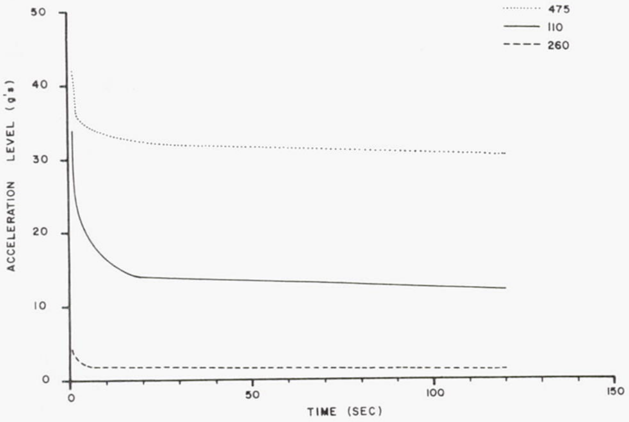

FIGURE 9. VARIATION OF BUBBLE FORMATION WITH DWELL TIME

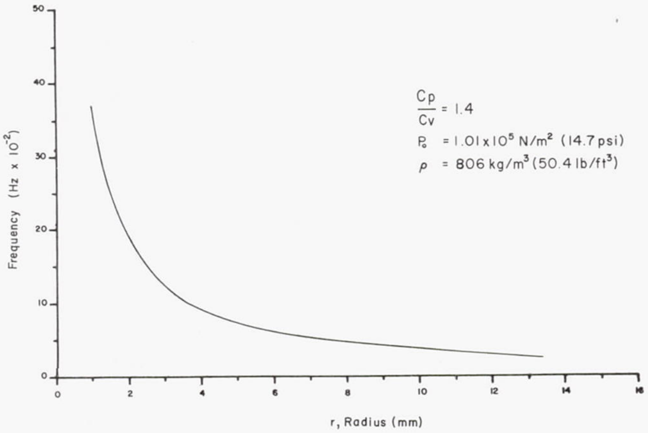

FIGURE 10. BUBBLE RADIUS VS. FREQUENCY

TWO-PHASE FLOW

INTRODUCTION

The investigation of two-phase fluid flow phenomena is important in answering questions on the venting of cryogenic propellant tanks while in space, chilling of transfer and engine propellant lines, and generally advancing the technology in launch vehicle design.

During the past two decades an exponential increase in efforts has been expended to describe the various phenomena associated with two-phase (gas-liquid) flow. Much of this effort has been directed toward application for nuclear reactor design. Consequently, most experimental data have been gathered using steam-water mixtures. Recently, the development of vehicles required data on the behavior of two-phase fluid flow with cryogenic systems. This work covers inhouse investigations with cryogenic fluids.

Two-phase fluid flow exhibits a critical flow phenomenon analagous to that of a compressible fluid. When a compressible fluid flows through a restriction, such as a converging nozzle, the fluid velocity is increased by decreasing the downstream pressure until a limiting or critical velocity is attained in the throat of the restriction. This limiting velocity is coincident with the speed of sound in the fluid, and the downstream pressure producing the critical velocity is the critical pressure.

In the divergent section of the nozzle the velocity may then become supersonic for some distance until a shock wave reduces the velocity to a subsonic value, or the velocity may start decreasing as soon as the fluid undergoes its maximum velocity at the minimum cross-sectional area of the restriction. The governing equations may be derived from the equations of fluid motion, the energy equation and the equation of continuity.

Two-phase critical flow is not as readily analyzed as is compressible fluid flow because of thermodynamic metastability and flow pattern considerations. Analyses based on a homogeneous fluid in thermodynamic equilibrium and the various two-phase patterns yield good results in long tubes where no large amount of thermodynamic metastability exists. Analyses assuming no exchange of mass from one phase to the other are also used to predict the critical two-phase flow rate.

EXPERIMENTATION

Experiments were conducted to determine the critical flow rate of two-phase nitrogen. All data were collected using a stagnation pressure of 0.172×10^6 N/m^2 (25 psia). To assure critical flow, the downstream pressure was decreased until further decreases in downstream pressure produced no change in flow rate. This pressure was then used as the critical receiver pressure and experiments were conducted using a downstream pressure substantially below this apparent critical pressure. The fluid was not observed visually within the experimental apparatus.

The experimental apparatus (Fig. 11) consisted of a 4.75 cm (1.87 in.) inside diameter × 86.4 cm (34 in.) long horizontal cylindrical plenum chamber. The two-phase fluid enters the plenum through a 1.07 cm (0.42 in.) diameter square-edge orifice and exits through a 2.87 cm (1.13 in.) diameter square edge orifice into a vacuum chamber. All results presented are for the 1.07 cm (0.42 in.) diameter orifice. Two-phase fluid flow was generated upstream of the plenum by mixing liquid and gaseous nitrogen.

RESULTS

Thirty-six experiments were conducted that covered the entire quality range. Experimental mass flow rates, ζc, are plotted versus stagnation quality in Figure 12, and are compared to the predicted flow rates.

On comparing the experimental data to the various predictions, the experimental data were most closely approximated by the Frozen Equilibrium Model. This is indicative of a large amount of thermodynamic metastability while flowing through the orifice. Many references on critical two-phase fluid flow indicate that the assumption of thermodynamic equilibrium should not be invoked in restrictions with length-to-diameter ratios of less than ten, and the experimental data confirm this assumption.

Most analytical predictions overpredict the critical mass flow rate for low quality fluids. This phenomenon was noted on comparing the experimental data to predictions. Stratified flow probably existed in the experimental apparatus, and this digression from the proposed models may explain the difference between this experimental data and other predictions.

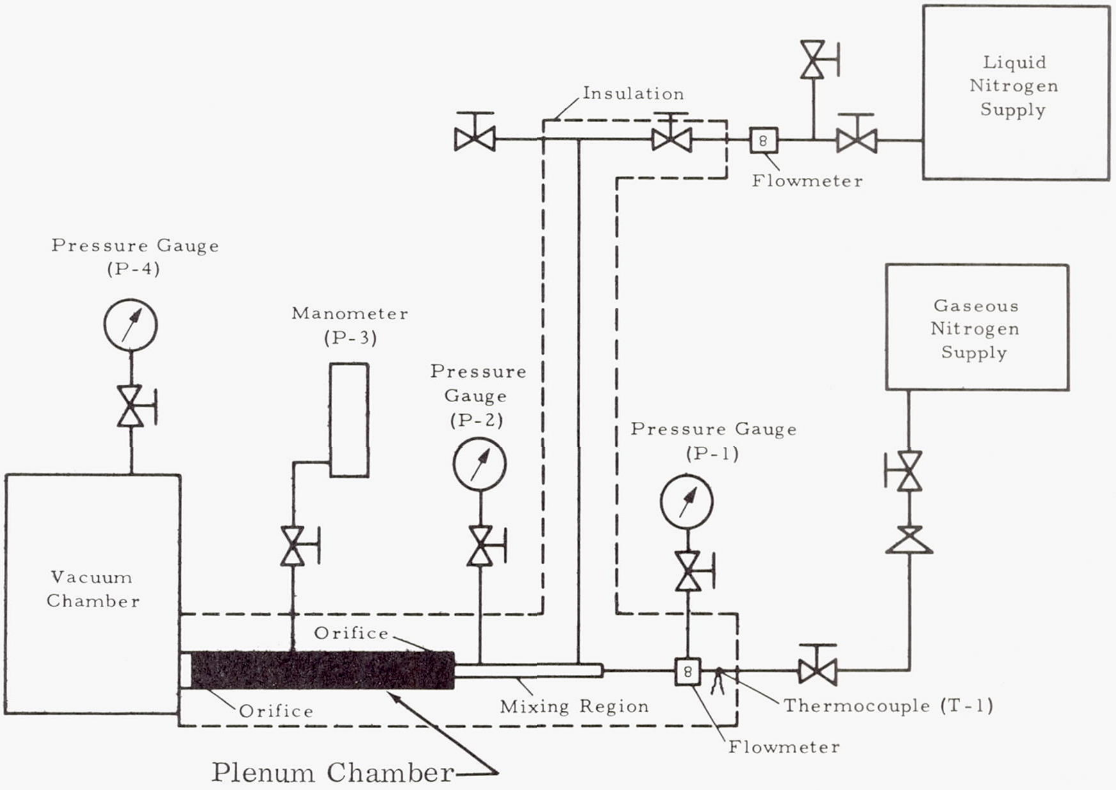

FIGURE 11. SCHEMATIC OF TWO-PHASE FLOW

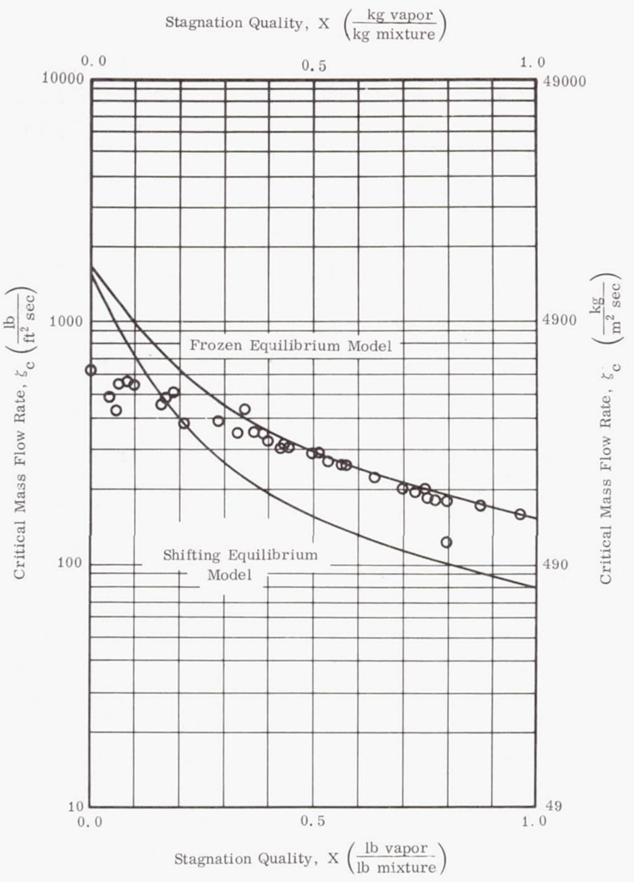

FIGURE 12. CRITICAL MASS FLOW RATE VS. STAGNATION QUALITY

VARIATION OF STATISTICAL THEORY OF TURBULENCE

INTRODUCTION

The various techniques used to measure the velocity of liquids in turbulent flow have traditionally involved the use of some device protruding into the flow stream. Most devices of this type have insufficient response, hence turbulent fluid flow measurements were difficult. In this investigation a beam of light measures the velocity of the fluid by application of the Doppler effect. Furthermore, an electronic system was developed to measure the velocity distribution at a point, and to have a frequency response believed to be well above that required.

The purpose of this investigation is to define the velocity distributions for liquids in turbulent flow for various Reynolds Numbers and at several radial positions in the pipe. The velocity distributions were measured and from them the mean and the variance were established. In addition, the distributions obtained are illustrated and reveal the skewness as affected by the radial position in the pipe. The results obtained provide new information on turbulent liquid flow.

Previous investigators have used eddy diffusion data to determine inferences concerning the velocity distribution. Foreman, Lewis and George in an earlier report described the technique for using the laser for Doppler measurement in fluids.

APPARATUS

The velocimeter system is composed of three separate elements (Fig. 13). A liquid flow loop provides a constant bulk flow through a glass tube of 2.2 cm inside diameter. The driving force for flow is obtained from a pump or from an elevated tank. The flow system is standard and thus is not described. A gas laser is used with associated optical equipment and is referred to as the optical system. The third part of the system is the electronics that convert the optical measurement into a useable electronic signal.

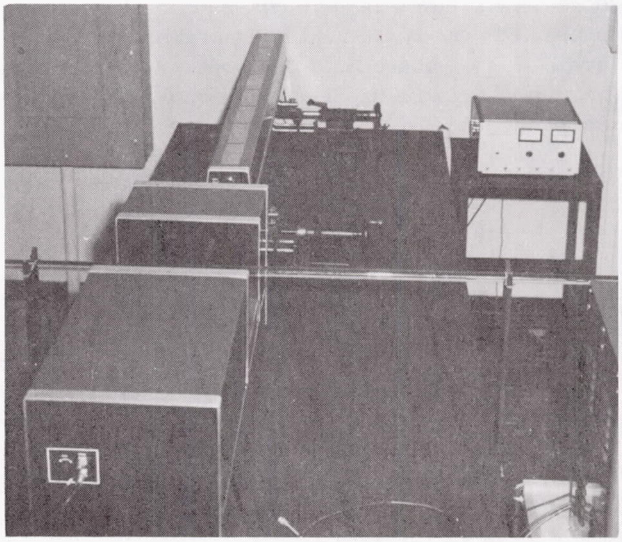

FIGURE 13. VELOCIMETER SYSTEM

The Optical System schematic is shown in Figure 14. A He - Ne gas laser was used to provide a beam of coherent light that was directed through the glass tube as shown in Figure 15. The focal point was located at six different positions throughout the course of the investigation. Light is scattered from the focal point by small particles in the water. A lens arranged at a known angle was aimed to receive the light scattered at that angle. This light differs in frequency from the parent beam because of the Doppler effect produced by the motion of the solids in the water. These two light beams when recombined on the cathode of a photomultiplier tube produce a heterodyne signal. For the studies described in this paper, the heterodyne frequency was less than 500 kHz. The optical system was mounted on a moveable platform separate from the glass tube. This feature permits traversing the fluid within the pipe. The optical arrangement measured the longitudinal component of the velocity at the focal point. Concisely, the optical system provides a heterodyne signal that is directly proportional to the longitudinal component of the fluid velocity at the focal point.

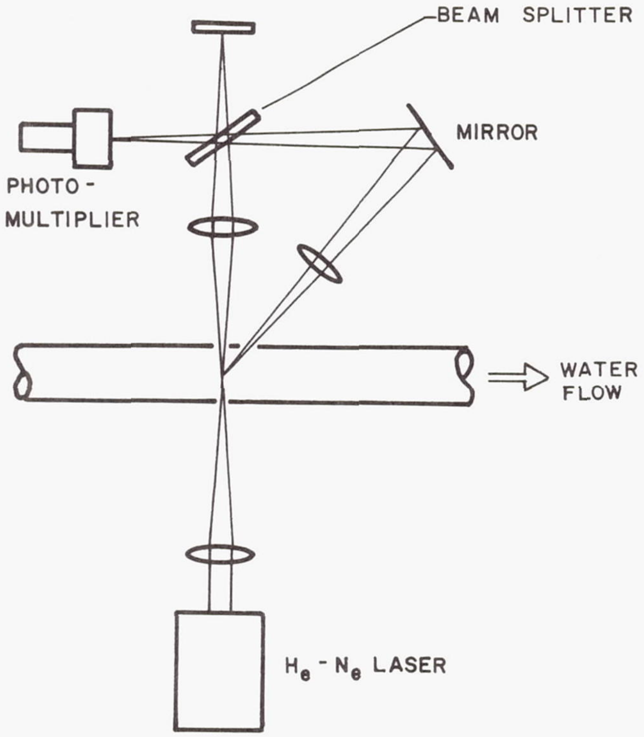

FIGURE 14. OPTICAL SYSTEM SCHEMATIC

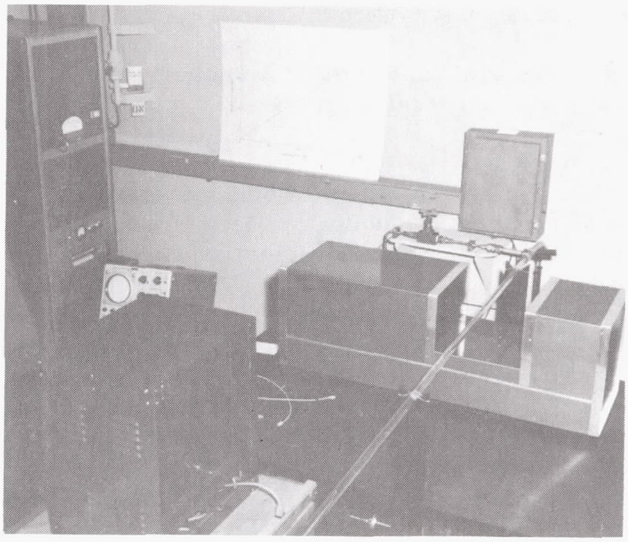

FIGURE 15. VELOCIMETER SYSTEM

RESULTS

Velocity distributions were obtained at the center line of the tube for four Reynolds Numbers, and velocity profile measurements were made at five radii. Figures 16 and 17 show typical point velocity distributions obtained at Reynolds Numbers of 4605 and 9310. The same general shapes result at other Reynolds Numbers with a shift in velocity and variance. Since the velocity is directly proportional to the heterodyne frequency, the velocity distribution functions are derived directly from the heterodyne frequency distributions.

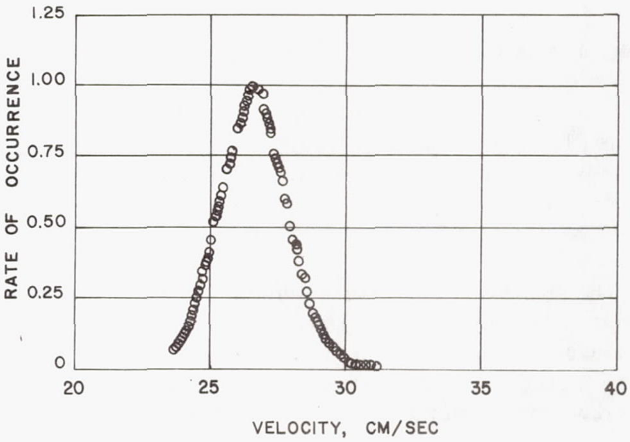

FIGURE 16. POINT VELOCITY DISTRIBUTION, $N_{Re} = 4605$

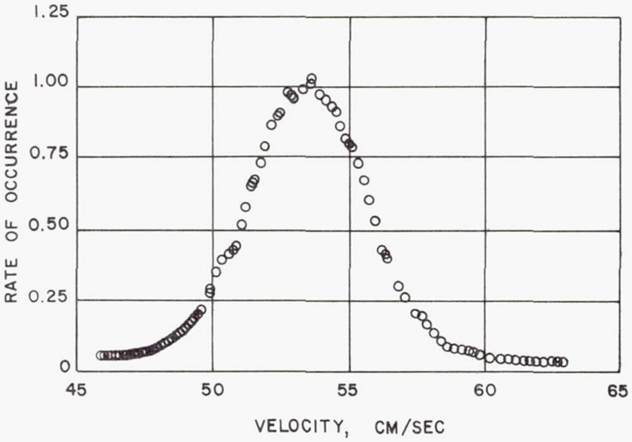

FIGURE 17. POINT VELOCITY DISTRIBUTION, $N_{Re} = 9310$

Figure 18 shows a velocity profile obtained by plotting the mean velocities measured at several radii within the pipe. The continuous curve represents Nikuradse's data and in general there is very close agreement. Measurements closer to the wall are possible but were inconvenient because of the changes required; hence, they were not attempted during this investigation.

CONCLUSIONS

The measured velocity distribution function is verified for both its mean value and the variance. The mean velocities were verified with existing data by Nikuradse and a profile in radius of the mean values is shown in Figure 18.

The shape of the measured distribution function agreed with concentration gradients measured near the source. The measured variances were verified by calculating the corresponding eddy diffusivities and comparing with the measured eddy diffusivities.

The general velocity distribution function was established with data and a statistical derivation.

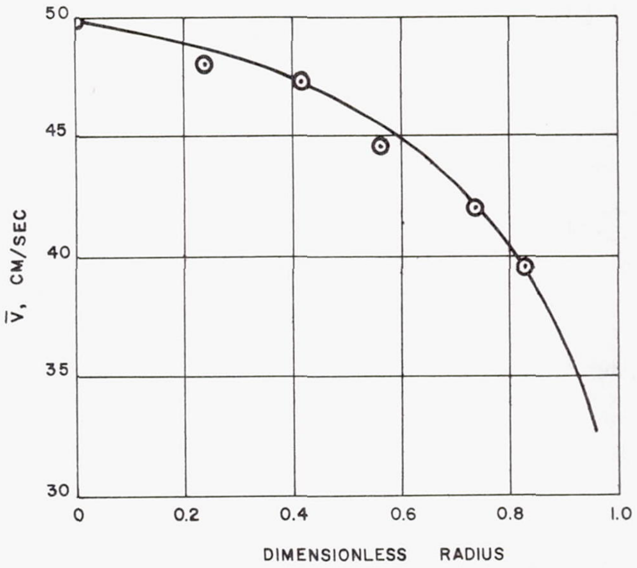

FIGURE 18. MEAN VELOCITY PROFILE, $N_{Re} = 8510$

The general velocity distribution function accounts for the increase in skewness in the distribution function that appears when the position of measurement approaches the radius of the pipe wall. Sufficient velocity data are not yet available near the wall to completely confirm the general velocity distribution function; however, the existing data show good agreement. Further, the velocity distribution as measured near the center of the pipe is a normal distribution which is in agreement with the derived general velocity distribution function.

It was established that the distribution function and the variation in radius agreed with statistical concepts.

Using statistical concepts of fluid mechanics as shown by papers in the bibliography, it is possible to derive the function describing the variation of the variance as a function of the radius. This function is verified by the data obtained.

BIBLIOGRAPHY

1. Blount, D. H.; Fritz, C.; and Ponder, C. A.: Bubble Coalescence in a Longitudinally Vibrated Liquid Column. Part I - NASA TMX-53180, 1964.

2. Campbell, H. M., Jr.; and Overcamp, T. J.: Critical Flow Rate of Two-Phase Nitrogen. Proceedings of the Southeastern Symposium on Missiles and Space Vehicles Sciences Sponsored by the American Astronautical Society, Dec. 5, 6, 7, 1966, pp 46-1 to 46-11.

3. Campbell, H. M., Jr.; and Head, R. R.: Analysis of Fluid Conditions in the Discharge Line of a Cryogenic Container Undergoing Self-Pressurized Draining. Proceedings of the Southeastern Symposium on Missiles and Space Vehicles Sciences, Sponsored by the American Astronautical Society, Dec. 5, 6, 7, 1966, pp 47-1 to 47-12.

4. Campbell, H. M., Jr.: Fluid Quality in a Self-Pressurized Container Discharge Line. NASA TMX-53330, 1965.

5. Fritz, C.: Study of Gas Bubble Dynamics. Part I - IN-R-P& VE-P-64-5, 1964.

6. Fritz, C.: Study of Gas Bubble Dynamics. Part II - IN-R-P& VE-P-65-13, 1965.

7. Overcamp, T. S.; and Schoenhals, R. J.: Pressure Distribution and Bubble Formation Induced by Longitudinal Vibration of a Flexible Liquid-Filled Cylinder. NASA TMX-53353, 1965.

8. Tomme, W. J.; and Welch, N. E.: Study of Turbulence with Data Obtained with a Laser Velocimeter. A.I.A.A. Bulletin, Vol. 2, No. 11, Jan. 1967.

9. Tomme, W. J.; and Welch, N. E.: Study of Turbulence with Data Obtained with a Laser Velocimeter. A.I.A.A. Conference, New York, Jan. 22-26, 1967.

10. Tomme, W. J.; and Welch, N. E.: Correlation of Velocity Distribution in Functions for Turbulent Pipe Flow. ASME-AICh. E Conference, August 1967.

Page
Intentionally
Left Blank

LARGE ENGINE TECHNOLOGY

By

Keith B. Chandler

SUMMARY

The Nation's present launch vehicles should suffice for space exploration objectives for the next 10 to 15 years. A sound technological base is being prepared now for future missions that will require additional performance.

To find an improved engine for upper stages, two primary paths are being pursued. One is an extension of the capability of the Bell-nozzle engine (by increased chamber pressure); the other is the use of unconventional geometry (e.g., annular combustion chamber and aerospike nozzle). Design studies and certain discrete component and sub-assembly tasks offer the required technology base, using guidelines from systematic studies of advanced vehicles and missions.

Though the requirement for a new launch vehicle larger than present ones is not urgent, a limited effort consisting of two major and one minor concepts is being considered. One concept is the plug multichamber, a cluster of modular engines mounted on the periphery of the base of the vehicle and surrounding a truncated plug. Another concept is a toroidal chamber around the periphery of the base of the vehicle and exhausting onto a truncated plug (aerodynamic spike). The other possibility is a group of modular toroidal engines clustered in the conventional manner. Analytical and limited experimental investigations are being conducted for future propulsion systems.

INTRODUCTION

The Nation's present launch vehicles possess a massive capability to launch large payloads into earth orbit and lunar trajectories. Extensive use of this huge capability is planned by having larger payloads and more ambitions missions than originally conceived. Thus the immediate objective is to further develop spacecraft and payloads for greater benefits. The need for new launch vehicles is not so urgent, but is certainly included in plans for the future. The Nation's present stable of launch vehicles (SATURNS, ATLASES, THORS, and TITANS) should accomplish the space objectives for the next 10 to 15 years. This does not exclude a need for change. Specific missions will dictate modification of available hardware, and eventually there will be missions requiring additional performance.

To find an improved engine for upper stages, we now pursue two primary paths in our engine technology efforts: one is an extension of capability in the bell-nozzle engine (by increased chamber pressure) for higher thrust and higher specific impulse in the current dimensional envelope; the other is the use of unconventional geometry (e.g., annular combustion chamber and aerospike nozzle). The actual performance (specific impulse) of these two configurations is still to be demonstrated; but of even greater importance than performance are the vehicle/engine interface considerations such as simplicity, commonality (usefulness in more than one stage or application), throttleability and service life. Based on the technology conducted on these configurations to date, the data available are insufficient to make a selection between the two at this time.

Since there are no firm mission requirements for an advanced engine, a development program is unwarranted. There is, however, a need for establishing a technological base from which a development program could be undertaken. Certain discrete component and sub-assembly tasks offer this technology base, and systematic studies of advanced vehicles have provided guidelines for an advanced engine. The values in Table I are being used for the component investigations.

ADVANCED ENGINE, BELL

The basic effort in the high-pressure-bell configuration is the Advanced Engine Design Study (Bell)[1]. This is a comprehensive program aiming for a specific definition of an advanced bell-engine in the 1.56 MN thrust (350,000 lb thrust) class. Special attention in this program is on the requirements identified in the studies of uprated

TABLE I. ADVANCED ENGINE GUIDELINES

Thrust	1.40 to 2.22 MN (315,000 to 500,000 lb, in vacuum)
Thrust Range	Main Stage and Idle Mode
Specific Impulse, sec	450+
Mixture Ratio, o/f	5 to 7
Dia (Max)	2.03 to 3.56 m (80 to 140 in.)
Length (Max)	3.38 to 3.86 m (133 to 290 in.)
NPSH Fuel	0 to 79.3 m (0 to 260 ft)
NPSH Oxidizer	0 to 21.3 m (0 to 70 ft)

future launch vehicles and the Reusable Orbital Transport. The objectives are selection of an engine cycle and integration of specific components for the best over-all balance of performance, operational characteristics, dependability, and installation flexibility. For use in vehicle studies, parametric engine performance data and an estimate of development cost and time are being prepared, and critical engine components or advanced concepts that should be verified experimentally are being identified. One of the objectives of the Advanced Engine, Bell (AEB) design is an engine suitable for several installations. This objective implies that the design must avoid concepts that would (1) burden the vehicle with operation-restricting features to compensate for limited thrust response, (2) require additional systems for engine preconditioning, or (3) impose restrictions on vehicle-command sequencing.

The cycle selected is one known as the "preburner" cycle (Fig. 1). Most of the hydrogen and some of the oxygen is burned in the preburner. The resulting low-temperature gas approximately 922° K (1200° F) drives the two turbopumps and then flows into the main chamber, where the hot, hydrogen-rich gases are mixed with the balance of the oxygen and hydrogen to complete combustion. The chamber pressure of the preburner is approximately 3.44×10^7 N/m^2 (5000 psi); the pressure in the main chamber is approximately 2.06×10^7 N/m^2 (3000 psi).

The concept illustrated includes an extendible nozzle cooled by hydrogen flowing through a tube bundle and "dumped" (exhausted) through tiny nozzles at the exit of the main nozzle. The specific performance of this warm hydrogen is almost equal to that of the gases from the main chamber. A full-scale mock-up is pictured in the right side of Figure 2, with the nozzle in the retracted position. In Figure 3 the nozzle is in the extended position. In application, the nozzle is stored in the retracted position to reduce interstage length. In a sea-level-launch application, the nozzle would be in the retracted position at launch, and extended at the appropriate altitude to gain higher performance from the higher expansion ratio (Fig. 4). When used in an upper stage, the nozzle would be extended after the stages are separated and before ignition of the engine.

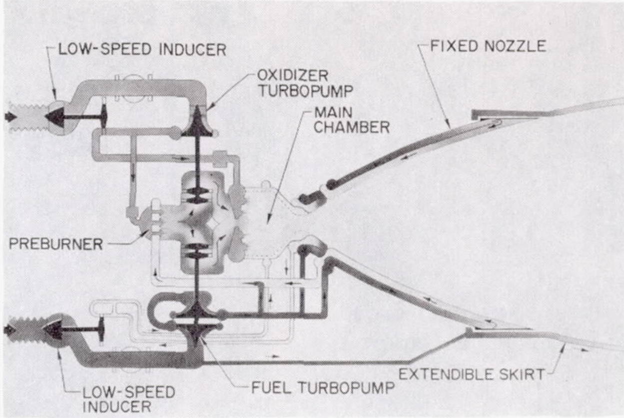

FIGURE 1. SCHEMATIC OF ADVANCED ENGINE, BELL

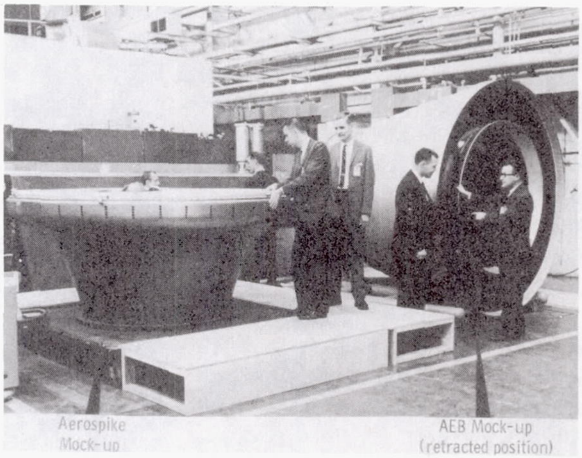

FIGURE 2. ADVANCED ENGINE, BELL MOCK-UP (RETRACTED POSITION)

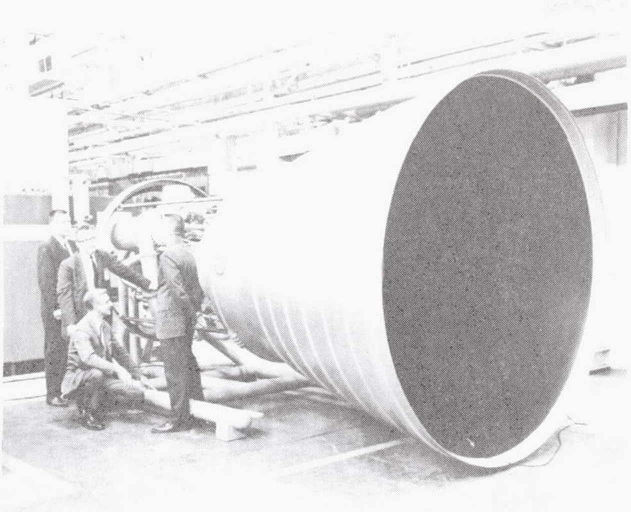

FIGURE 3. ADVANCED ENGINE, BELL MOCK-UP (EXTENDED POSITION)

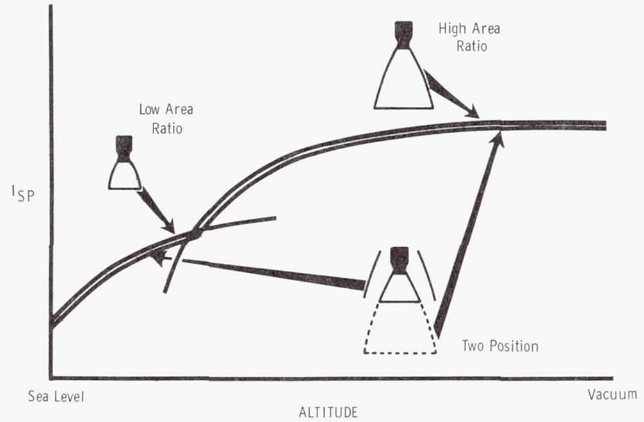

FIGURE 4. INTERCHANGEABLE NOZZLES (I_{sp} VS ALTITUDE)

To yield the desired high performance, the Advanced High-Pressure Bell design must incorporate technological advances in the design of components and systems. Though the engine cycle and the detailed definition of what advanced concepts and components will be included are not yet specific, some general requirements are known, particularly the advantages of higher pressure levels. Timely development of components to fit these requirements will give confidence that the concept is sound and will generate information for arriving at an optimum, component-integration scheme. The design, fabrication, and testing of a breadboard, high pressure, liquid hydrogen pump is in progress to verify performance characteristics desirable for advanced rocket engines [2].

The pump fits a breadboard engine in the 1.56 MN thrust (350,000 lb thrust) class, as outlined previously. Already, some 35 tests have been run on this pump (Fig. 5) and the maximum discharge pressure reached has been slightly more than 3.51×10^7 N/m^2 (5,100 psi), the highest known pressure yet for pumping hydrogen. Initial testing revealed problems in volute strength and the balance piston. These problems were solved by a redesign of the volute tongues and the use of leaded-bronze inserts. Also, the contractor had a problem with non-synchronous, hydro-mechanical oscillations which caused failure of the end bearing. This was corrected by replacing the ball bearing with a roller bearing and increasing the spring rate of the bearing mount. Pump efficiency is about 8 to 10 points lower than the design specified. It is believed that the efficiency can be brought up to the design value by the use of a shrouded impeller, but a change of such magnitude is not within the scope of this investigation.

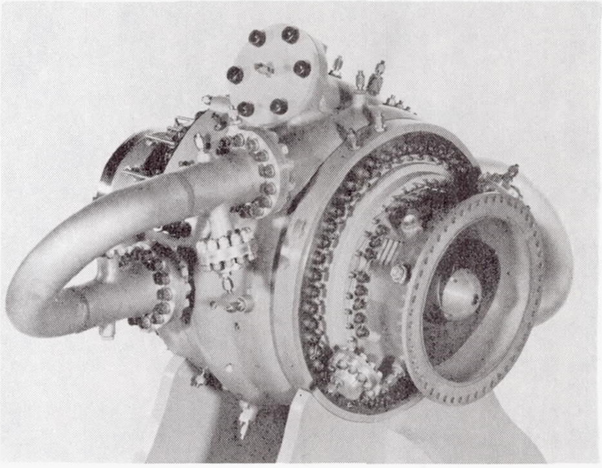

FIGURE 5. HIGH PRESSURE LH_2 PUMP

Although this program has had a number of difficulties and there have been some spectacular failures in testing, the results achieved have been very encouraging. A high probability for the occurrence of failures was allowed in plans for extending the limits of existing technological capability. The information obtained will be very useful if a development program is begun.

A companion task is the design, fabrication, and test of a liquid oxygen, high-pressure pump [3] (Fig. 6) also compatible with the breadboard engine system outlined previously. This program was started approximately one year after the hydrogen pump, and testing has just begun. Early design and testing was very successful. Besides the requirements of thrust, mixture ratio, specific impulse, throttleability and pressure rise, the pump must be stable over the widest possible range of flow and head rise; it must provide pressure-oscillation-free operation; it must be useable in an engine cycle containing either a gas generator or a preburner; and it must operate with minimum before-start temperature conditioning.

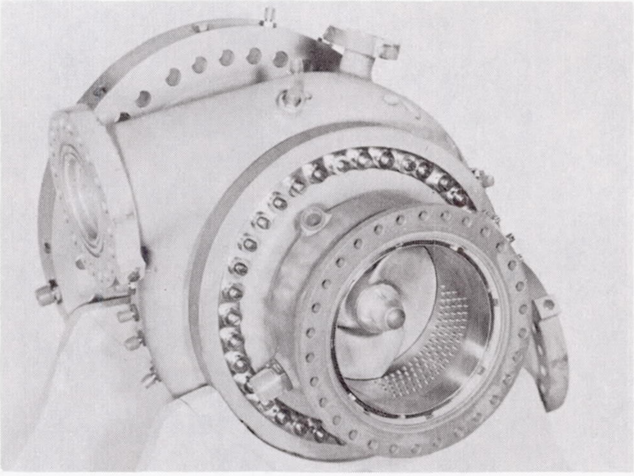

FIGURE 6. HIGH PRESSURE LOX PUMP

Axial and centrifugal designs were considered for both pumps. Designs were evaluated and compared for suitability to alternative engine cycles, vehicle requirements, temperature-conditioning requirements, and development risks. Primarily because of the throttleability requirements (down to 3% of nominal thrust), the centrifugal configuration was selected in both cases.

ADVANCED ENGINE, AEROSPIKE

The other major candidate for the advanced cryogenic rocket engine is the toroidal, aerodynamic-spike thrust-chamber. The upper illustration of Figure 7 is a conventional spike ("plug") nozzle, with a physical plug. In the aerodynamic spike concept, the physical plug is simulated by an aerodynamic flow of warm gas. The primary gas comes from the main combustion chamber, the secondary flow from the gas used to drive the pump turbine(s).

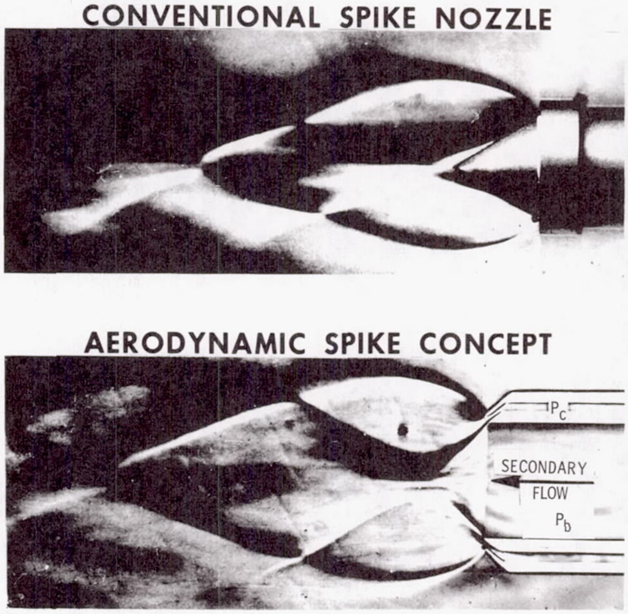

FIGURE 7. CONVENTIONAL SPIKE AND AERODYNAMIC SPIKE COMPARISON

The aerospike has the capability for "altitude compensation" so useful for sea-level-launch applications. Altitude compensation is possible by the decrease in ambient pressure associated with increased altitude; this permits the primary flow to expand (see free jet boundary, Fig. 8). Considerable cold flow data have been gathered to determine the performance of this concept, and these have been verified by hot-firing tests (Fig. 9). A conceptual design of such an engine system is in Figure 10 [4].

An outstanding feature of the Advanced Engine, Aerospike (AEA) concept is the high performance possible from a relatively short nozzle at both sea-level conditions and vacuum conditions. High performance is achieved by efficient combustion and reaction at the largest area ratio permitted by the envelope, augmented by injection of gases into the base of the spike-nozzle to amplify the base pressure, thus providing base thrust augmentation without

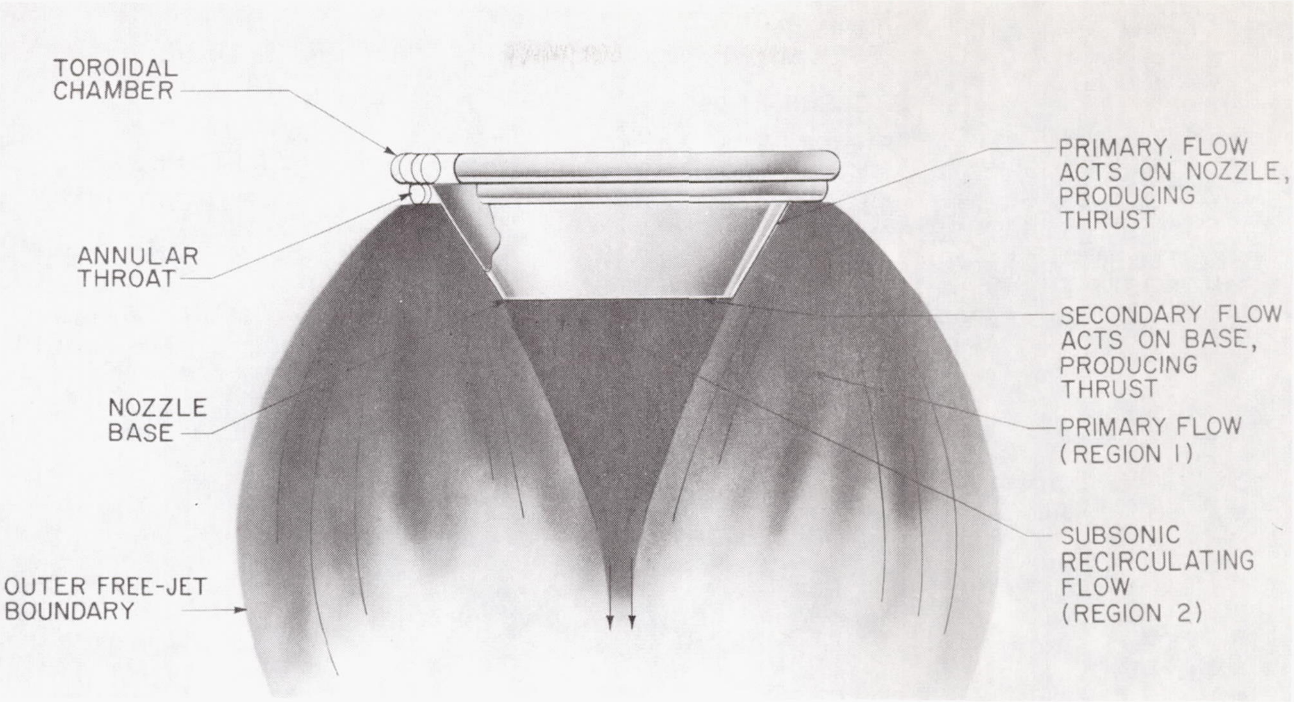

FIGURE 8. AERODYNAMIC SPIKE FLOW FIELD UNDER ALTITUDE CONDITIONS

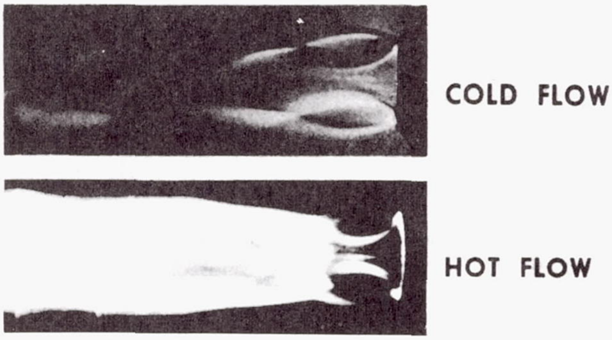

FIGURE 9. AERODYNAMIC SPIKE COLD FLOW AND HOT FLOW COMPARISON

changing the performance of the spike nozzle. Experimental data indicate that for a given nozzle geometry and operating conditions such as chamber pressure and mixture ratio, engine specific impulse is a function of the ratio of secondary-to-primary flow. Propitiously, the optimum secondary flow is nearly equal to that which would normally be provided from the turbine exhaust.

At low altitudes, the base pressure does not drop below ambient, thus removing the characteristic, negative-pressure term of the conventional bell nozzle.

Although the ultimate configuration of the toroidal aerospike engine has not been determined at this time, certain features peculiar to the concept can be and should be investigated, particularly the thrust chamber and the fluid dynamics associated with the starting phase of the operational cycle.

A full-scale, 1.11 MN thrust (250,000 lb thrust) toroidal aerospike chamber is being built and tested (Fig. 11) in a program called "System and Dynamics Investigation" [5]. The objective is to identify the structural and dynamics problems rather than to provide the solution for problems caused by the hardware used. The approach includes analysis, priming, and cold-flow tests, segment and ignition tests, and breadboard thrust-chamber tests. Mainstage and start-transient tests will be made on a pressurized test stand with programmed main valve controls to simulate system dynamics transients. A complete dynamic description of the thrust chamber will be obtained for use in extensive system analysis. The key difference between a hydrogen engine and a hydrocarbon engine is the behavior of the compressible fuel in the thrust chamber cooling jacket. When a chamber is cooled with hydrocarbon fuel such as RP-1 or other nearly incompressible fluids, heat

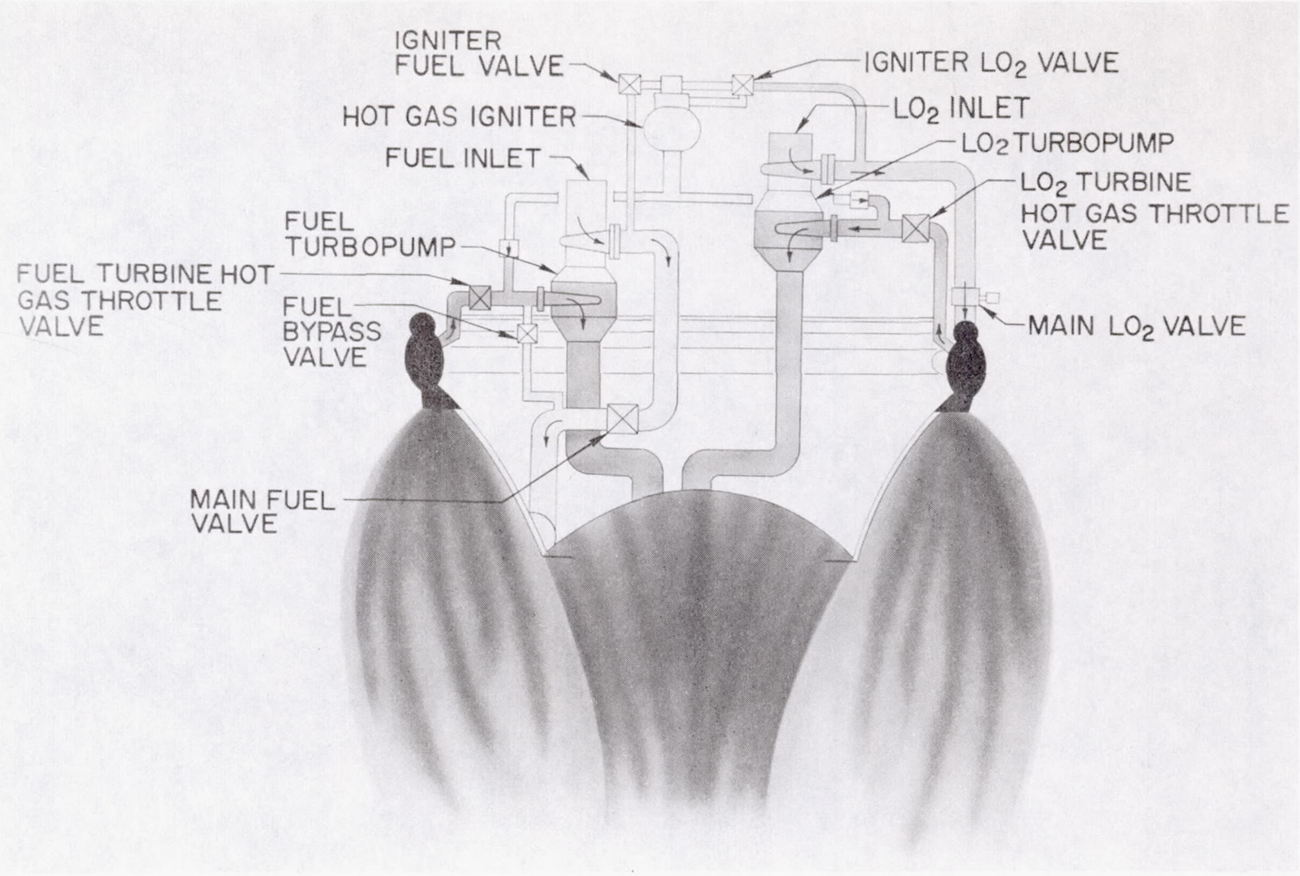

FIGURE 10. SCHEMATIC OF ADVANCED ENGINE, AEROSPIKE

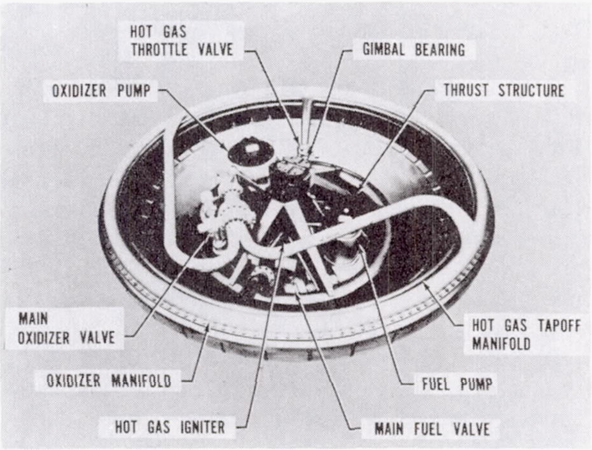

FIGURE 11. AEROSPIKE MOCK-UP

transfer to the liquid has no appreciable effect on the flow process. On the other hand, a hydrogen-cooled thrust chamber behaves in a more complex manner because heat transfer has a direct effect on the flow process and the pressure drop. The hydrogen enters the cooling tubes as a liquid and emerges as a gas. At low operating levels, tube-bundle pressure drop is greater than that for its RP-1 counterpart, and causes the fuel pump to operate at a lower flow coefficient near the stall region. Without external control, there is no way known to avoid this occurrence. Adequate component description and component analysis are required for design of a control to avoid problems such as pump stall.

Because of the toroidal configuration, priming of the propellant manifolds is of major interest. The problems in development of main-propellant manifolds for the toroidal configuration are similar to those for conventional bells, but differ in degree for some areas. Two-phase flow dynamics problems at the start are common to both configurations. The analytical and test program will provide data on steady-state and transient fluid flow phenomena such as (1) manifold and injector priming characteristics and repeatability, (2) system pressure drops, (3) manifold volume influence on system response during throttling and mixture ratio excursions, (4) waterhammer effects or changes of flowrate dictated by start, throttling, or mixture ratio variation, and (5) thrust chamber orientation (vertical and horizontal).

A full-scale transparent model of the LOX manifold has been built, and tests are so scheduled to provide information for design revisions to the breadboard chamber. The tapoff manifold and igniter manifold will be tested for the first time with the breadboard chamber. Although design changes in these systems are not anticipated, they could be made in the full-size hardware after initial tests.

Tests have been made with the LOX manifold installed in both the vertical and horizontal attitude to determine priming characteristics and repeatability, system pressure drops, system response to simulated throttling and mixture ratio excursions, and waterhammer effects. The experimental program was done by photographing (during priming) the jet streams from orifices that simulate the injector around the periphery of the manifold. Time needed between prime of the first and last jets, as determined by analysis of individual frames from the Fastex camera pictures, will be correlated with the data from high-frequency-response pressure measurements for verification of the priming characteristics. It has been determined that (1) uniform priming can be achieved (in less than 30 milliseconds), (2) two tangential inlets function nearly as well as four tangential inlets, (3) radial inlets are probably not desirable, (4) a restriction in one line (as much as 50%) or unequal line lengths cause small effects, (5) centrifugal force separates liquid and vapor during initial priming (this is desirable), (6) torque values are in a tolerable range, and (7) horizontal or vertical position has little effect if inlet pressures are greater than 0.69×10^6 N/m^2 (100 psi).

Two types of full-size toroidal aerospike thrust chambers will be built and tested: a solid-wall workhorse chamber; and two, tube-wall chambers. The relatively inexpensive and rugged, solid-wall workhorse chamber is for early determination of the integrity of the injector and test equipment and igniter testing, all of which would be a moderate risk of damage to the tube-wall chamber. The injector, thrust mount, and structural throat support are identical for both the solid-wall workhorse chamber and the tubular chambers. The breadboard tube-wall chamber is compromised from its flightweight design to favor hot-firing tests. The structure behind the tubes is heavyweight.

ADVANCED LAUNCH VEHICLES

In spite of the fact that the requirement for a new launch vehicle larger than present ones is not urgent, a limited effort consisting of two major and one minor concepts is being considered. One concept is the plug multi chamber, a cluster of modular bell engines mounted on the periphery of the vehicle's base and surrounding a truncated plug (Fig. 12).

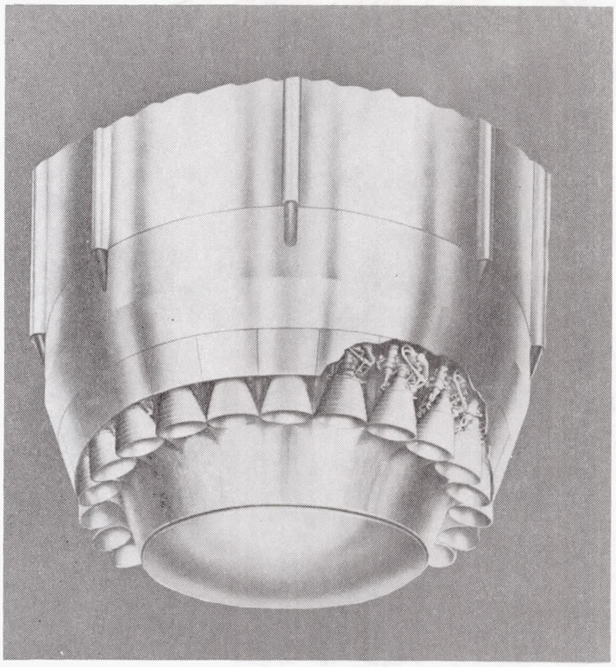

FIGURE 12. PLUG MULTICHAMBER CONCEPT

Another concept is a toroidal chamber around the periphery of the vehicle's base and exhausting onto a truncated plug (aerodynamic spike) in the center (Fig. 13). The other possibility is a group of modular toroidal engines clustered in the conventional manner (Fig. 14).

Analytical studies of the plug multi-chamber concept were made to learn optimum conditions such as the size of the module, the proximity of the adjacent bell chambers, the effect of primary expansion ratio, ways to gain side force, and the effect of plug length.

An experimental program [6] is underway to correlate the data obtained in cold flow testing with those from hot-flow testing. The hot-firing model consists of 18 small rocket engines at 890 N thrust (200 lb thrust) each around a truncated plug (Fig. 15). The individual modules (burning liquid oxygen

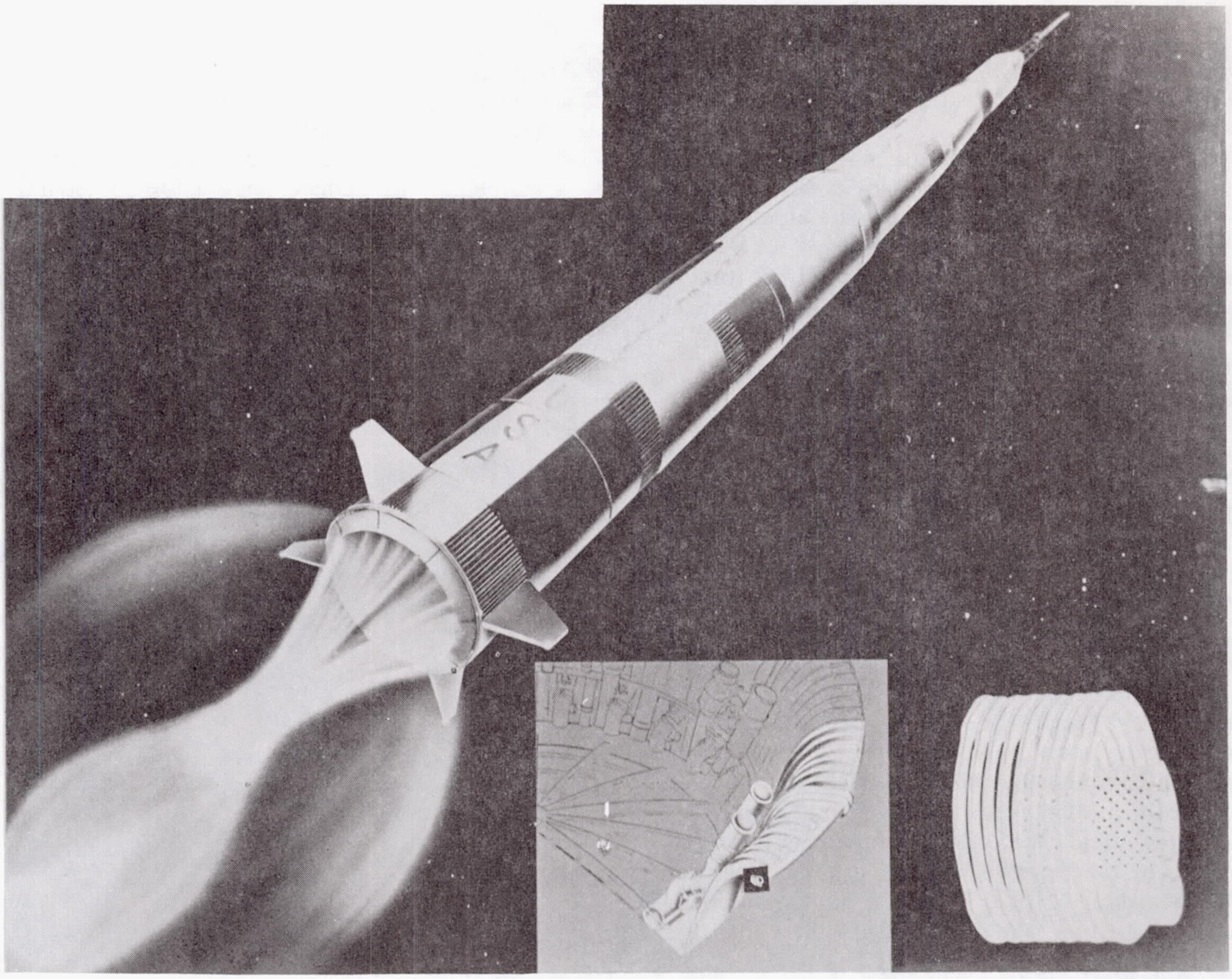

FIGURE 13. TOROIDAL ENGINE APPLICATION

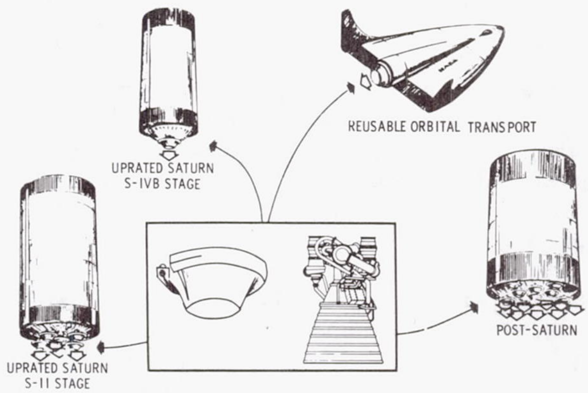

FIGURE 14. CLUSTERED TOROIDAL CHAMBERS

and gaseous hydrogen propellants) are pressure fed from fuel and oxidizer manifolds. The chambers are cooled with high-pressure water. Ignition is by introduction of triethylborane, which is pyrophoric with the oxidizer. There have been some difficulties in igniting the cluster; yet a total of 32 successful tests have been done, with excellent correlation of earlier cold-flow and the hot-flow tests.

Analytical studies were made of the toroidal concept for large boosters [7], as well as a moderate experimental effort [8]. The purpose was to investigate the feasibility of the toroidal hoop combustion chamber for boosters ranging in diameter from 12.2 to 27.4 m (40 to 90 ft), and in thrust from 80 to 134 MN (18 to 30 M lb). The ultimate objective is data from single-tube and multi-tube segment testing applicable to: (1) evaluation of toroid-nozzle attachment criteria and performance, (2) evaluation of inherent and dynamic stability

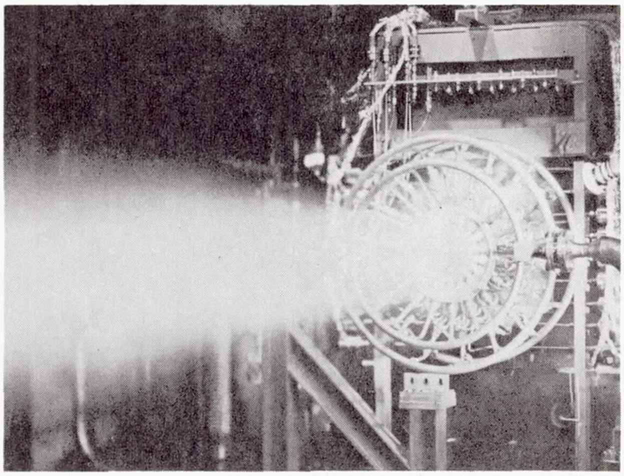

FIGURE 15. HOT-FIRING MODEL OF PLUG MULTICHAMBER CONFIGURATION

characteristics, (3) evaluation of injector design and tube cooling interactions, (4) evaluation of aerodynamically-shaped sonic tubes, and (5) evaluation of performance losses caused by film cooling and subsequent performance recovery in the nozzle resulting from burning of film coolant.

All data will be applicable to the toroidal concept feasibility for engine systems of advanced future booster configurations.

REFERENCES

1. Advanced Engine Design Study (Bell). Pratt & Whitney, Contract NAS8-11427.
2. Design, Fabricate and Test High Pressure LH_2 Pump. Pratt & Whitney, Contract NAS8-11714.
3. High Pressure LOX Pump. Pratt & Whitney, Contract NAS8-20540.
4. Advanced Engine Design Study (Aerospike). Rocketdyne, Contract NAS8-20349.
5. System and Dynamics Investigation (Special Modification of J-2 Engine Development Contract). Rocketdyne, Contract NAS8-19.
6. Experimental Evaluation of the Plug Multichamber Concept. Pratt & Whitney, Contract NAS8-11438.
7. Toroidal System Analysis. Rocketdyne, Contract NAS8-11402.
8. Feasibility Investigation of the Toroidal Chamber. Rocketdyne, Contract NAS8-4013, and NAS8-21038.

J-2 EXPERIMENTAL ENGINEERING PROGRAM (J-2X)

By

James R. Thompson, Jr.

SUMMARY

Recent experimental work sponsored by Marshall Space Flight Center (MSFC) in the area of large LOX/H_2 engines of the J-2 class is summarized. The work reported is divided into near-term and long range product improvement potential for the J-2 engine. No particular mission applications are emphasized, rather discussion is directed toward operating concepts that allow considerable propulsion simplification of today's system, yet still provide new propulsion capabilities for future Saturn V mission growth. The discussions in this paper are necessarily brief; additional information can be obtained from the author or Messrs. R. A. Byron or D. H. Huang of Rocketdyne, North American Aviation, who have been instrumental in assuring a successful engine program.

INTRODUCTION

Engine programs for the Saturn Launch Vehicle historically have been committed to tight development schedules. The engine configurations, specification requirements and design criteria were limited to those concepts proven satisfactory in the past and which were capable of rapid development. An experimental engine effort was desirable to explore new concepts and ideas and bridge the gap between technology and development. Thus an experimental engineering program was established to assure that advances in current technology are considered and experimentally tested for application to the J-2 engine propulsion system as product improvements. In the specific case of the J-2X program, by taking advantage of the J-2 components and experience, a means is available for evaluation of new concepts while leaving the main J-2 engine development and flight support effort relatively undisturbed. In conjunction with mission needs, a low-cost meaningful decision point is thus provided to determine whether a promising concept should be incorporated into a full-scale development program.

For the past several years the Propulsion and Vehicle Engineering Laboratory at Marshall Space Flight Center (MSFC) has directed the J-2 Experimental Engineering Program as a part of the Manned Space Flight (MSF) supporting development effort. The primary goal of the experimental program was the investigation of new and unique concepts which would improve the performance and operational capabilities of the J-2 engine, with the companion goals of reducing engine complexity, improving launch window flexibility and mission capability, reducing servicing costs, and improving the reliability of the over-all engine related propulsion subsystems. During 1966, a number of these experimental concepts advanced to the extent that they could be seriously considered for further development and incorporation into the Saturn Launch Vehicle. These concepts are briefly discussed in the following paragraphs along with their more significant potential contributions to the launch vehicle.

The experimental engine does not have a fixed description or drawing specification, but is rather a test article which constantly changes configuration. The experimental engine basically resembles the J-2 engine, burns liquid hydrogen and liquid oxygen, and is rated at 1.02 MN (230 000 lb) thrust in vacuum. The basic configuration consists of a regeneratively cooled 27.5:1 expansion ratio thrust chamber which has been modified at the forward end to incorporate a hot-gas tapoff system for turbine drive, a liquid hydrogen and a liquid oxygen turbopump with turbines connected in series and driven by hot gases extracted directly from the thrust chamber combustion zone, main and auxiliary valves and sequencing control logic. Thrust and propellant mixture ratio control is obtained by varying the control orifices in the hot gas turbine drive system.

NEAR-TERM SATURN PROPULSION IMPROVEMENTS

Emphasis during the early part of the past year was directed toward establishing a total engine system that would be capable of reliable operation without the extensive thermal conditioning of the engine and propellant feed system hardware prior to an engine firing. As shown in Figure 1, using the

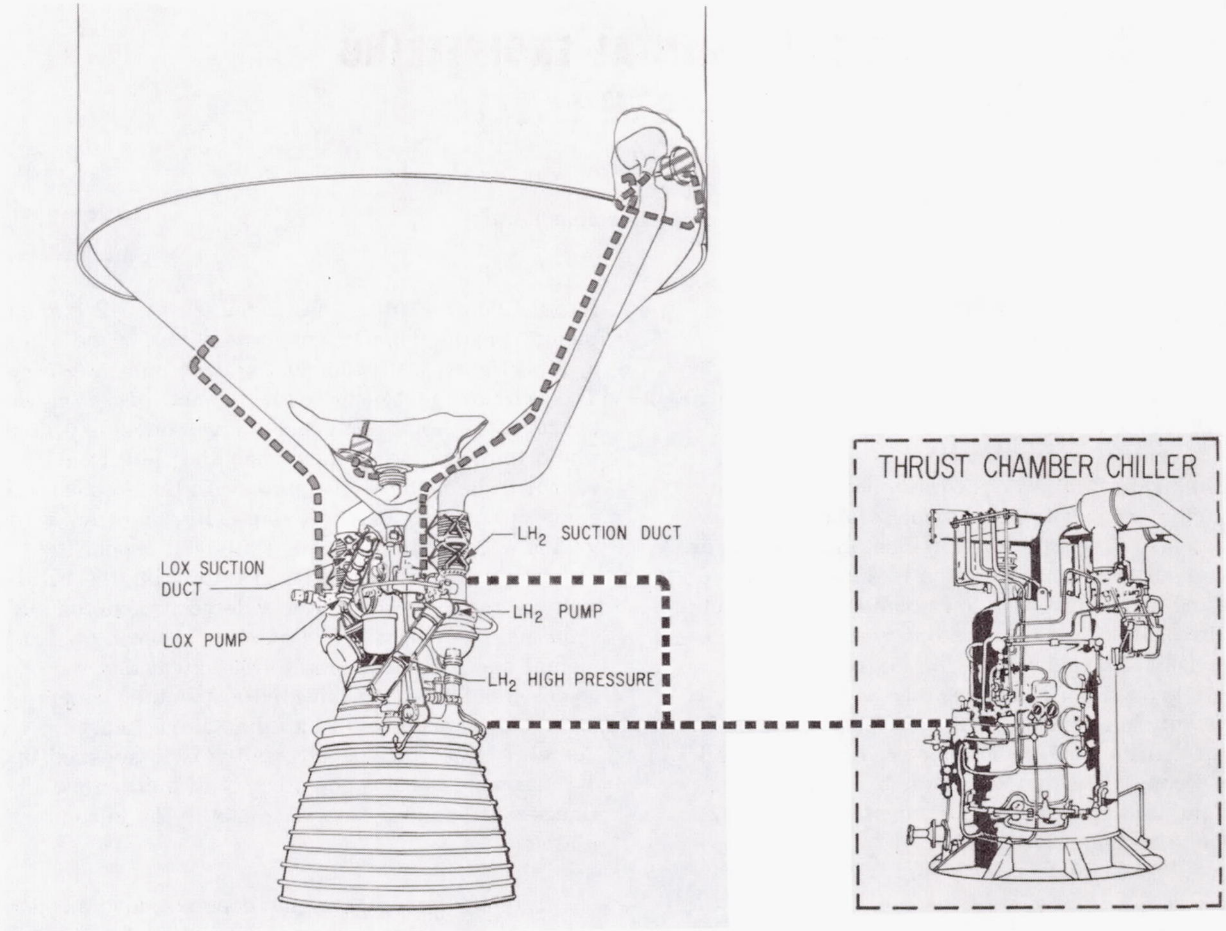

FIGURE 1. J-2 ENGINE PRECONDITIONING FOR START

J-2 engine/S-IVB stage propulsion unit as an example, there are four major areas in today's propulsion system which require hardware conditioning with associated complex operational procedures, costly checkout, and cumbersome ground support equipment (GSE). Briefly, the current propulsion configuration requires both hydrogen and oxygen propellant circulation through the engine/stage feed ducting and engine turbomachinery to assure having adequate liquid propellants and ample net positive suction pressure at initiation of engine start. This is accomplished with small electric driven pumps mounted near the bottom of each propellant tank in ducting joining the main propellant feed lines. Propellants are returned to the stage via separate ducting indicated by heavy dashed lines in the figure. Other areas requiring thermal conditioning are (1) the engine mounted hydrogen bottle used in storing gaseous hydrogen that provides initial starting energy to the engine turbines, and (2) the regenerative thrust chamber tube bundle which must be chilled below 200°K (-100°F) to remove the sensible heat and reduce the hydraulic resistance in the hydrogen flow passages. Both of these subsystems are serviced by ground equipment as indicated in Figure 1. The S-II Stage propulsion system is quite similar, although natural convection of the oxygen through the circulation ducting is used rather than forced pumping.

Eliminating only some of the above described procedures or relaxing operational red line values was not considered as an acceptable program goal, and the experimental effort on the engine was directed toward defining and applying test discipline to a configuration that would completely eliminate all of the above conditioning requirements. To accomplish this, the engine cycle was changed from one employing a gas generator to provide turbine power, to one tapping off combustion gases at approximately 922°K (1200°F) from the thrust chamber to drive the series turbines. Figure 2 provides a cut-away view of the hot-gas tapoff area immediately downstream of the injector face. Early testing indicated that obtaining a consistent tapoff gas temperature would not be a major problem as first

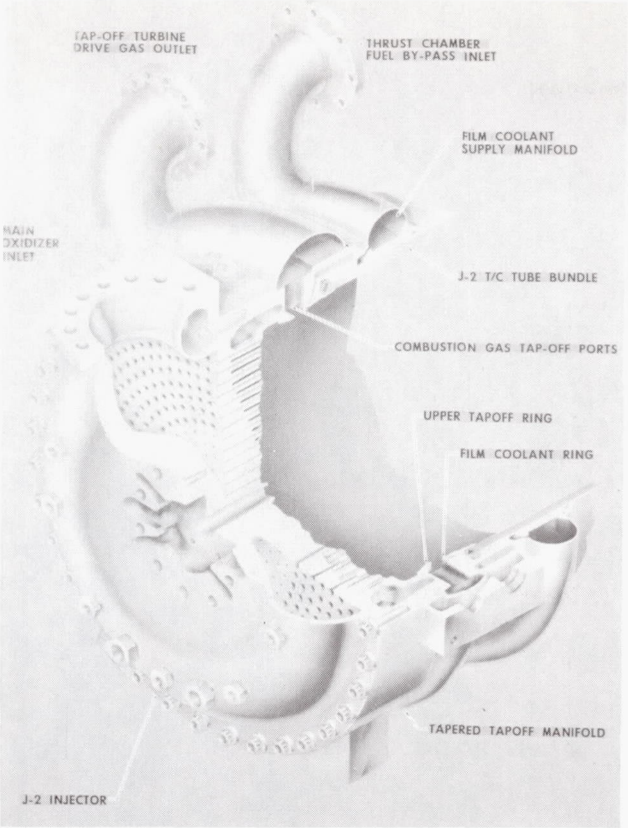

FIGURE 2. J-2X TAPOFF SYSTEM

imagined, but that considerable design effort would be required to obtain a configuration that would provide proper hardware cooling in the immediate tapoff area. The hardware erosion problem primarily centered around the area immediately downstream of the tapoff section illustrated in Figure 3 because the oxidizer was not making the rapid turn to the tapoff manifold as easily as the lighter hydrogen and was thus striking the chamber wall. To date the solution appears to be in film cooling this area with hydrogen supplied by a separate manifold shown in the lower right hand area of the cross-section. Thus far in the program over 300 engine tests on eleven separate configurations have been evaluated using this concept for turbine drive. Over 4000 sec of mainstage operation have been logged with the longest single test lasting 200 sec (the duration limit of the experimental test facility).

Considerable experimental testing has been directed toward integrating the tapoff gas cycle concept into an operational engine starting sequence to achieve the desired simplification. A schematic of the total engine cycle is shown in Figure 4 accompanied by the following description of some of the more unique features. To accomplish propellant and engine hardware conditioning and at the same time provide a settling force to propellant tanks, the engine operates in a low-thrust mode of operation termed "idle mode." During idle mode, the turbomachinery is not rotating and propellants are driven by tank pressures only. The duration of idle mode would be mission dependent to account for the propellant and hardware conditions prior to its initiation. As an example, the duration of idle mode for restart of the S-IVB Stage in the Saturn V LOR mission is estimated to be 50 sec. During this mode of operation, the engine would be capable of producing low impulse bits at thrust levels of approximately 26 700 N (6000 lbs) for additional applications such as stage deorbiting, orbit transfer, staging, gross docking rendevous, attitude control, and other pulse-mode duty cycles. The idle mode engine operating cycle is shown in Figure 5. At this time, it appears maximum idle mode duration should only be limited by the propellant supply. The engine cutoff sequence is designed for a mainstage to idle mode transition; the idle mode thrust provides for propellant slosh control in the vehicle prior to complete shutdown. Three solid-propellant turbine starters (SPTS) mounted on the fuel turbine manifold provide triple-start capability for the S-IVB Stage. The solid propellant turbine start eliminates the need for a gaseous hydrogen start tank with its cumbersome procedures and GSE, and provides the necessary initial turbomachinery power to flush the mixed-phase propellants from the feed ducting and engine during the starting transition to mainstage operation. The burn time of the solid propellant motors is approximately 2 sec in duration and is tailored to provide a gradual but positive buildup in pump speed assuring (1) ample stall margin of the fuel pump, and (2) a consistent starting transition resulting from the relative insensitivity of the solid propellants to the harsh duty cycle environment of the J-2 engine. The requirement to thermally condition the thrust chamber can be eliminated by bypassing most of the hydrogen around the thrust chamber during the starting transient operation and feeding the fuel directly into the injector and tapoff coolant manifolds. During the past year, this technique of simplifying the engine operation has been demonstrated as technically sound and with proper development will provide reliable engine starting with chambers initially at room temperature or warmer. The mechanism which prevents the current engine from ambient chamber starting is the rapid buildup in fuel pump back pressure created by the hydraulic resistance in the regenerative tube bundle. Excessive back pressure will stall the fuel pump. This is alleviated with the bypass feature which unloads the

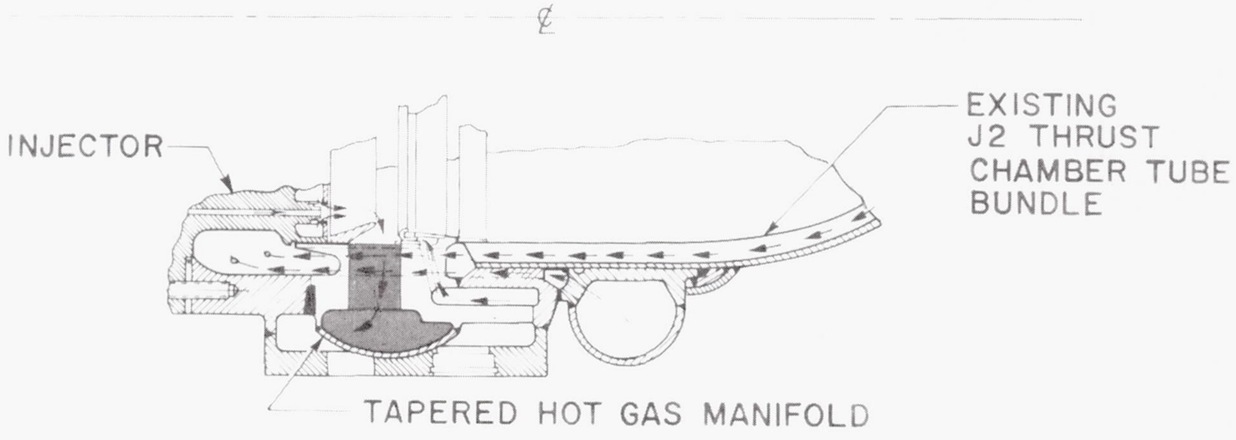

FIGURE 3. J-2X TAPOFF AREA

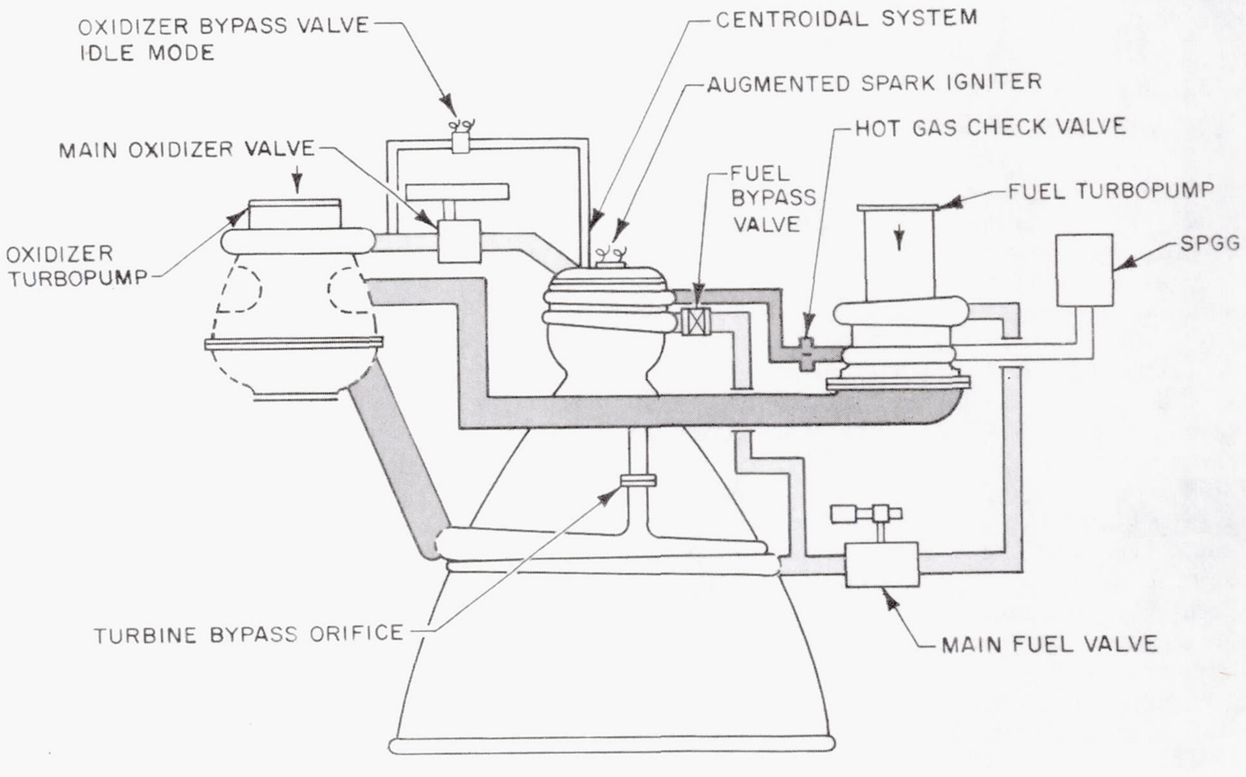

FIGURE 4. SYSTEM OPERATING CONCEPT

pump pressure during the critical early portion of the transient operation. Once propellant flow is well established and the chamber is cooled by hydrogen in the regenerative tubes, the bypass system is

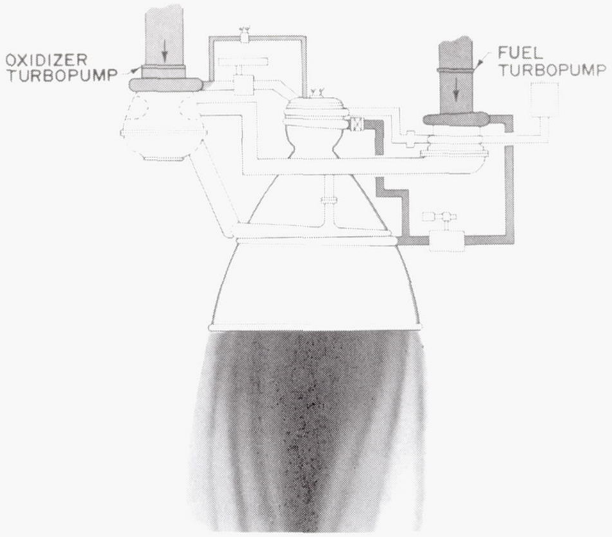

- PROPELLANT ULLAGING
- DEORBITING
- GROSS RENDEZVOUS FOR DOCKING
- PLANE CHANGES

FIGURE 5. EXPLOITING IDLE MODE OPERATION

closed and all the hydrogen is routed through the chamber for mainstage cooling. Thus, another set of pre-start conditioning procedures can be eliminated by functionally accomplishing the same job within the normal sequence of engine starting events.

The significance to the Saturn Launch Vehicle of the engine operational simplification discussed in the preceeding paragraphs can readily be assessed by a comparison of the terminal launch sequence of events that were required on flight AS-201, illustrated in Figure 6, as opposed to that which would have been required with the propulsion system simplifications described above and illustrated in Figure 7. The pre-launch events for the S-II Stage can be reduced by a comparable amount for each engine. In addition to a reduction in operational procedures, considerable hardware and servicing subsystems can be removed from the stages by reducing these engine conditioning requirements as seen in viewing the S-II Stage engine compartment area "before" and "after" illustrations shown in Figure 8.

A considerable number of events associated with thermally conditioning the engine, the propellant feed ducts, and settling the propellants, occur after vehicle launch and can be further reduced by implementing the system concepts discussed above. Figures 9 and 10 graphically identify these events by name and relate them to time after liftoff.

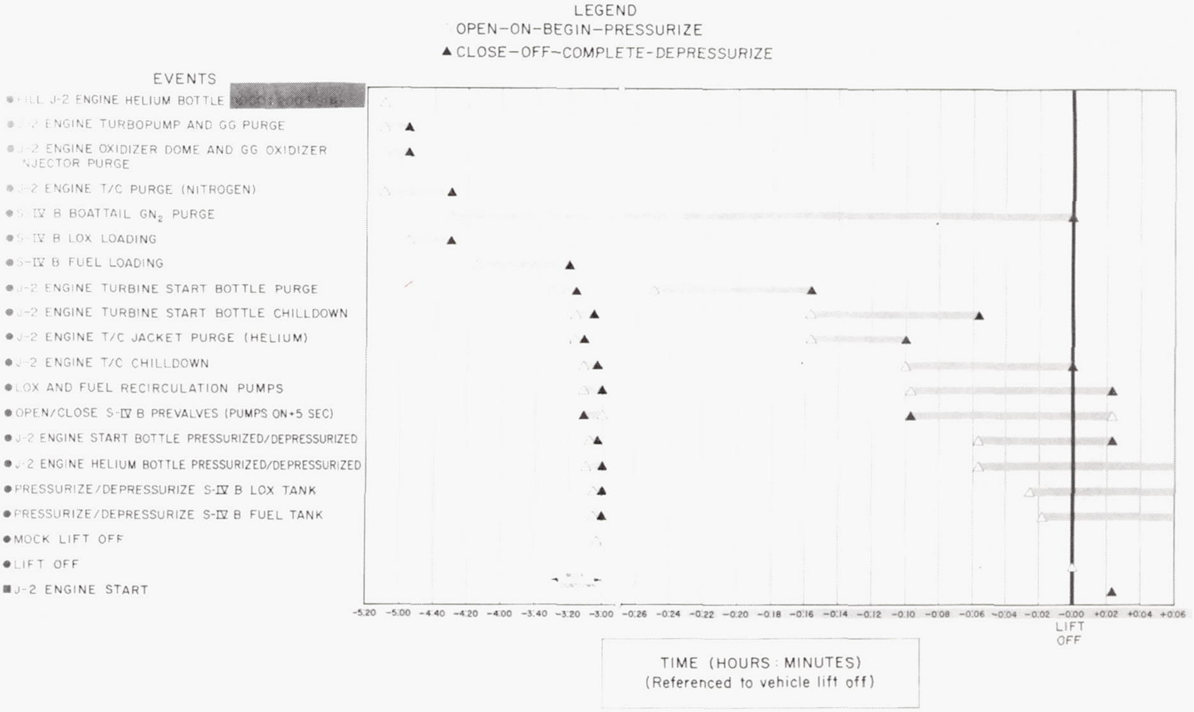

FIGURE 6. FLIGHT 201 S-IVB STAGE PRE-LAUNCH CONDITIONING EVENTS

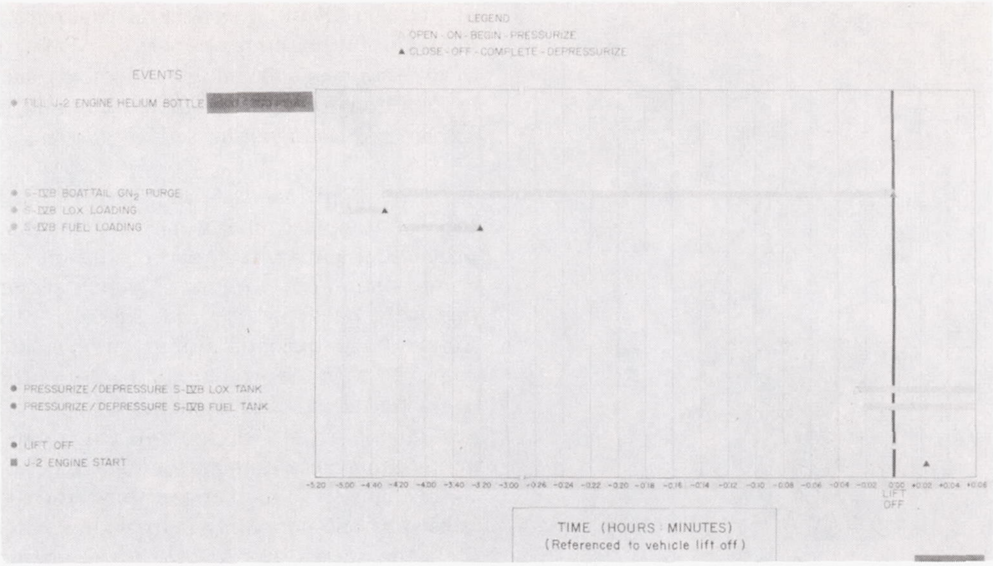

FIGURE 7. POTENTIAL S-IVB STAGE PRE-LAUNCH CONDITIONING EVENTS

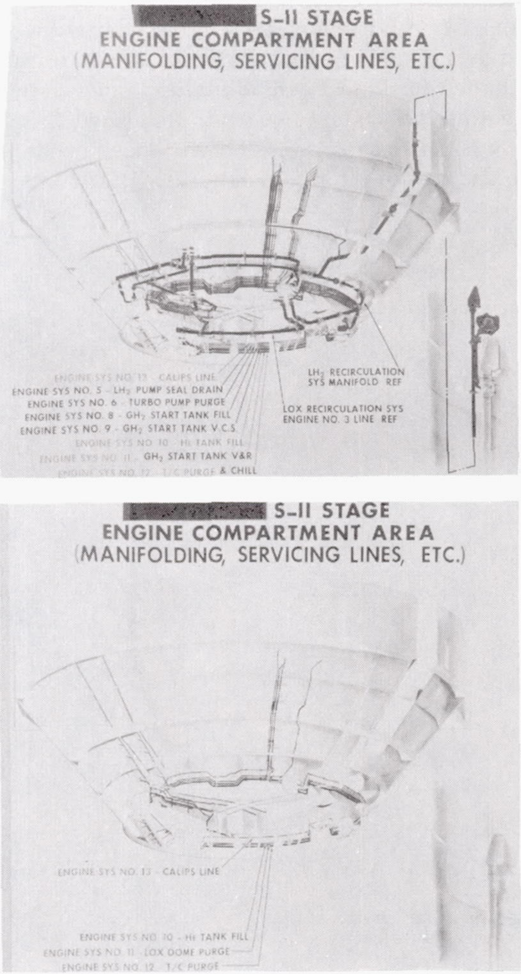

FIGURE 8. S-II STAGE ENGINE COMPARTMENT AREA

During the time that the J-2X program has been under contract with Rocketdyne, MSFC propulsion personnel have continually assessed the impact on the Saturn Launch Vehicle of incorporating into the Saturn Program those specific engine features which have promise of being technically sound. More recently these analyses, in conjunction with the Douglas Aircraft Co. and Space & Information Systems Division of NAA, have concentrated on a detailed investigation of the propulsion features described earlier. In addition to an overall reduction in static firing and launch pre-test procedures and operational simplifications, the S-II Stage analysis has indicated the following elements can be deleted from the stage recirculation and pressurization systems:

1. 176 m (576 ft) of engine and pressurization system manifolds.

2. 26.2 m (86 ft) of vacuum jacketed lines.

3. several batteries.

4. five hydrogen recirculation pumps, motors and inverters.

5. eleven LOX and LH_2 shutoff valves.

6. seven umbilical connections.

7. 79 tubing joints.

8. 58 seals.

9. three helium bottles.

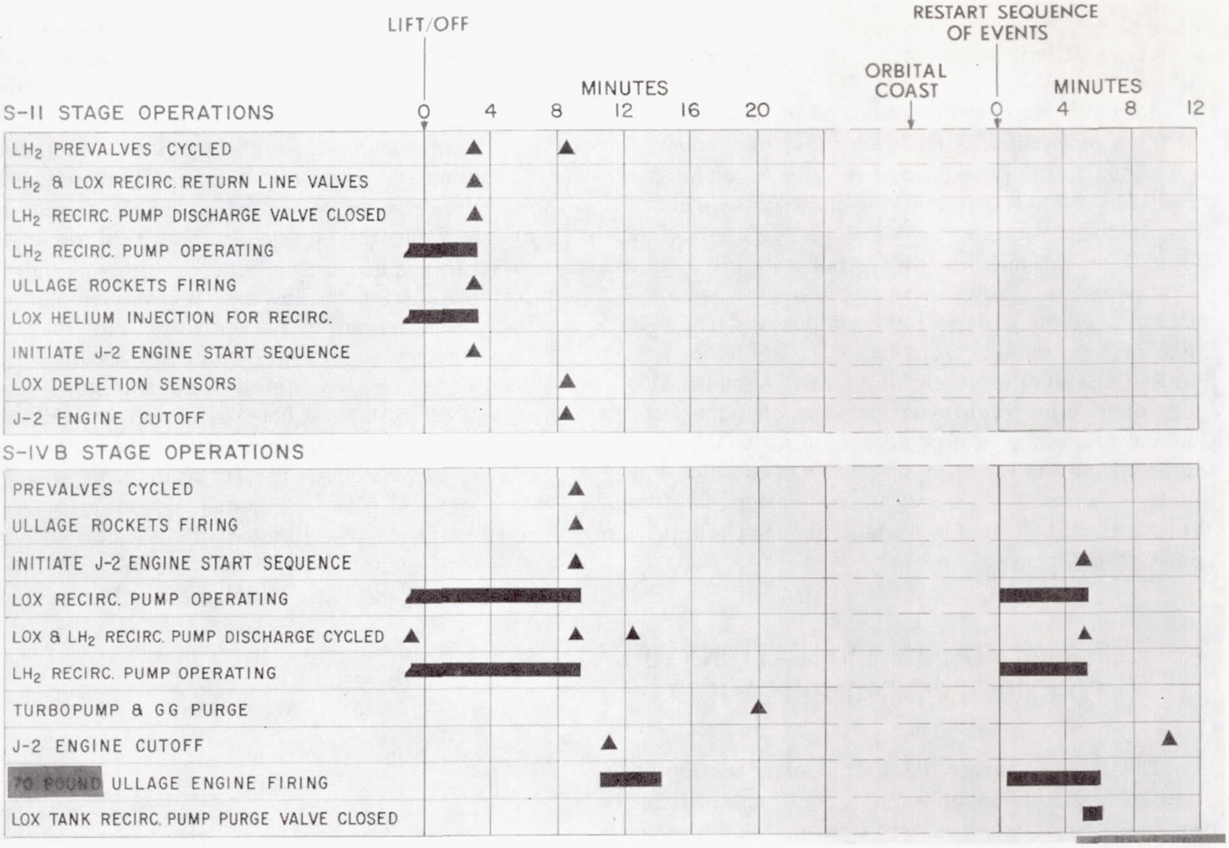

FIGURE 9. CURRENT SATURN V INFLIGHT PROPULSION OPERATIONS (J-2 ENGINE REQUIREMENTS EXCLUDING TANK PRESSURIZATION)

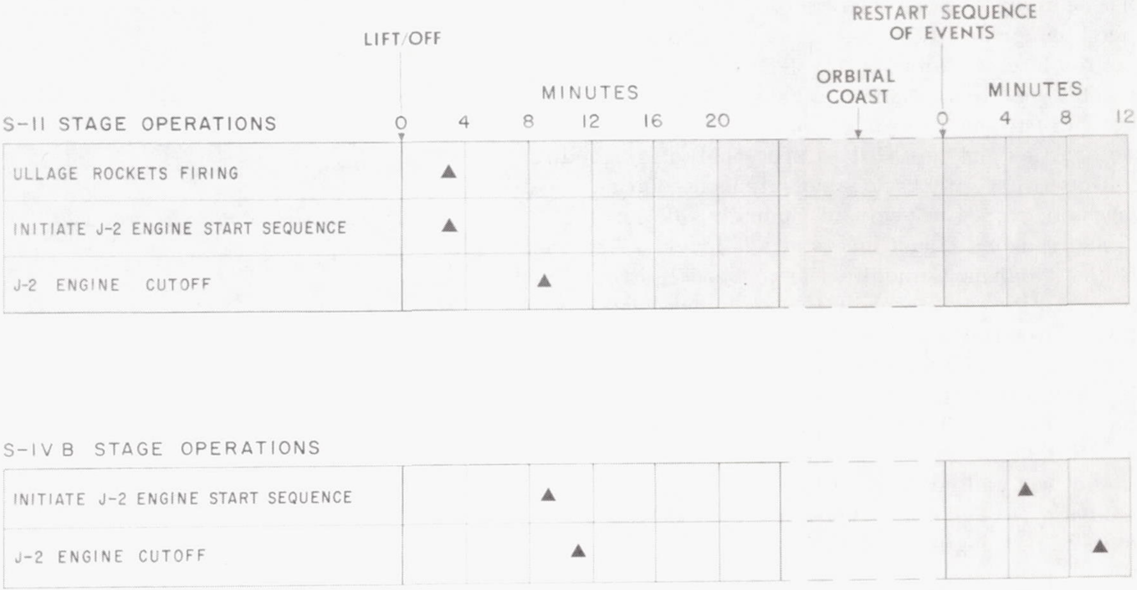

FIGURE 10. POTENTIAL SATURN V INFLIGHT PROPULSION OPERATIONS (J-2 ENGINE REQUIREMENTS EXCLUDING TANK PRESSURIZATION)

10. five check valves.

11. 18 flexible hoses.

Accruing from the elimination of this hardware and from procedural simplifications, checkout operations in the propulsion area alone can be reduced 36%. Study results also indicate existing stage unreliability can be decreased by approximately 30%. Although mass saving is not a major objective of the program, elimination of the system components previously described can result in a S-II Stage mass reduction of over 908 kg (2000 lbs). A detailed analysis of potential benefits to the S-IVB Stage propulsion system are equally encouraging. Current plans are to further demonstrate the technical merits of this type of J-2 propulsion system by functionally integrating a prototype system with the S-IVB ground test stage at MSFC during the coming year.

EXPERIMENTAL INVESTIGATIONS OF LONGER-TERM SIGNIFICANCE

The J-2X program has also been investigating other propulsion concepts that to date are still in the early phases of experimental testing. Some of the initial results are particularly significant and fall into three areas of experimentation: (1) controlled deep throttling, (2) minimizing starting transition chamber side loads, and (3) tank head starting for multi-restarts.

These results should provide technology for any advanced or uprated LOX/H_2 engine configuration as well as for later versions of the J-2 class. To experimentally evaluate these features, J-2X engine 011 was built to incorporate all of the engine characteristics and capabilities previously described, in addition to (1) a thrust chamber truncated at an area ratio of 16.5:1 to evaluate chamber side loading at full and reduced thrust levels at sea level, (2) turbopump clearances modified to reduce required break-away starting torques to enhance tank head starting, (3) a recycle system around the hydrogen pump to provide added pump stall margin at reduced thrust levels, and (4) additional control valves for system throttling. These four engine features are discussed in detail in the following description of test objectives and results. Thirty-five firings for an accumulative test time of 634 sec were conducted on the J-2X 011 engine system.

Engine System Throttling. The specific objectives of the throttling program were to (1) evaluate engine performance at the lower thrust levels with respect to chamber combustion efficiencies and the combustion and system stability characteristics, (2) establish the system gains and engine control requirements to achieve steady state operation at the lower thrust levels, and (3) define chamber heating problems which may be encountered under sea level conditions at the lower thrust levels with a separated nozzle. The ultimate objective of the throttling program would be to achieve continuous and stable transition from the low thrust pressure-fed idle mode to turbine driven engine operation over the entire thrust range at a constant mixture ratio of 5.0:1. The test series consisted of eight tests, accumulating a total of 450 sec of hot-firing with the engine being throttled from mainstage chamber pressure levels of approximately 4.82×10^6 N/m^2 (700 psia) to a low of 0.55×10^6 N/m^2 (80 psia), or near 10:1. Chamber performance, as reflected in characteristic velocity (C*) efficiency, remained high over the throttle range as graphically illustrated in Figure 11. High

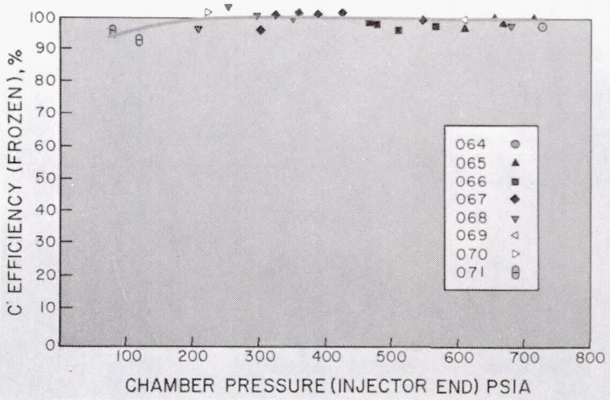

J-2X Throttling Result Summary:

1. Eight tests were conducted for total of 450 sec.
2. Stable engine operation was achieved at a chamber pressure of 0.55 MN/m^2 (80 psia) and engine mixture ratio of 2.37.
3. Combustion instability was encountered during one test.
4. Chamber C* efficiency remained high throughout throttling range.

FIGURE 11. C* EFFICIENCY VS CHAMBER PRESSURE

frequency combustion instability occurred on one test and was analyzed as resulting from a combination of low chamber mixture ratio (hydrogen injection temperatures were near those of liquid hydrogen temperatures) and several tube splits in the regeneratively cooled combustion zone. During this series of engine tests, low frequency or chugging instability in the combustion chamber has never occurred, nor was there any evidence of instability in the hydrogen drive system between the pump and the thrust chamber tube bundle. Control of chamber pressure and mixture ratio was adequate from mainstage chamber pressure levels of 4.82×10^6 N/m^2 (700 psia) to approximately 1.38×10^6 N/m^2 (200 psia). At pressures lower than 1.38×10^6 N/m^2 (200 psia), the experimental control system could not maintain a near constant mixture ratio, resulting in the chamber mixture ratio drifting to about 2.0:1 at the 10% thrust level and thereby considerably reducing the hydrogen injection temperature. With the exception of the combustion instability at the off-design mixture ratio, no problems were encountered over the entire throttle range. The control points used in the engine system to achieve throttling were (1) a control valve in the hot-gas tapoff duct between the chamber and fuel turbine, (2) a control point bypassing the oxidizer turbine, and (3) a fuel recycle path from the pump discharge to inlet. The fuel recycle path was added to avoid the fuel pump stalling at the reduced thrust levels by maintaining pump flow at a relatively high value. Conceptually, the system used is shown in Figure 12. During this test series, approximately 0.0316 m^3/s (500 GPM) were recycled around the fuel pump at the 50% thrust level and provided an additional 0.0316 m^3/s (500 GPM) of stall flow margin. No effort was made to define the effect on pump suction performance, which will be evaluated in subsequent testing. The fuel pump head flow map (Fig. 13) graphically illustrates how the engine was throttled and the control points used at each level. The hot-gas tapoff control throttled the system, at a near constant mixture ratio, to approximately the 60% thrust level, at which time the engine mixture ratio was reduced to approximately 4.0 with the oxidizer turbine bypass control. After opening the fuel pump bypass valve to provide added stall margin, the thrust was further reduced to the 10% level by a combination of the tapoff control and the turbine bypass valve as shown. A sketch of the engine system with control points is shown below the pump map. The lines of constant mixture ratio and constant chamber pressure will assist in identifying the control gains on engine performance.

One mission application for an S-IVB Stage using J-2 class engines capable of throttling is illustrated in Figure 14 and shows the stage used as a shelter on

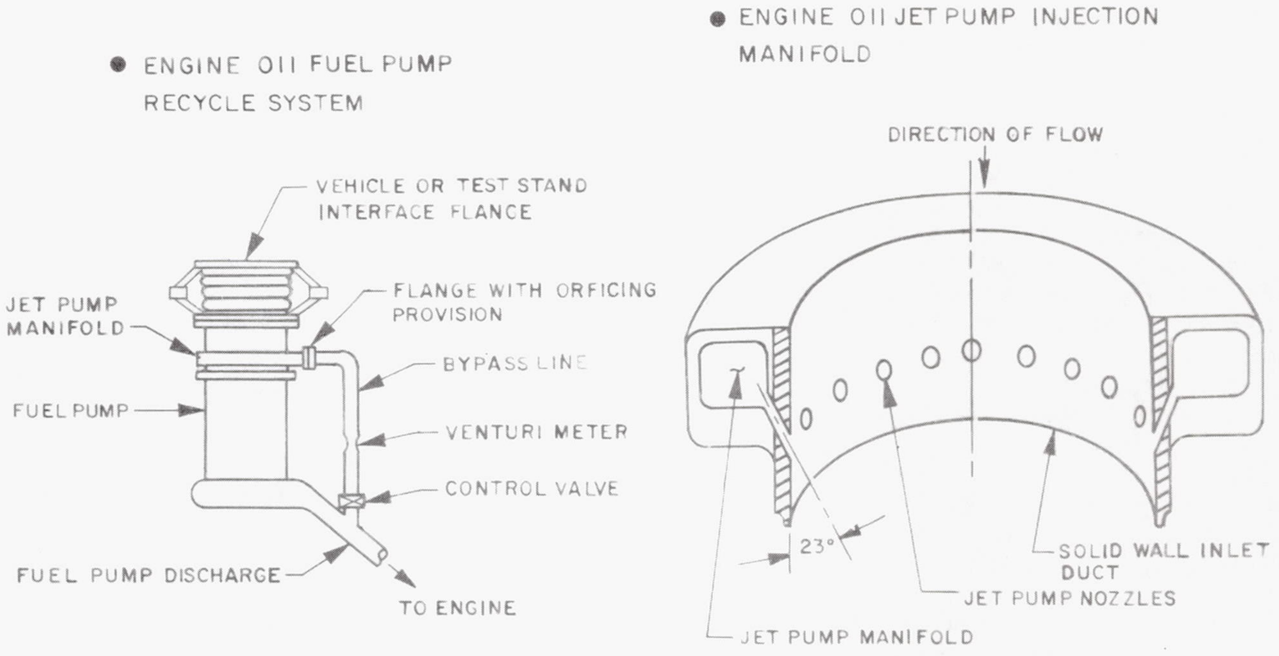

- ENGINE 011 FUEL PUMP RECYCLE SYSTEM
- ENGINE 011 JET PUMP INJECTION MANIFOLD

FIGURE 12. J-2X 011 FUEL PUMP RECYCLE SYSTEM

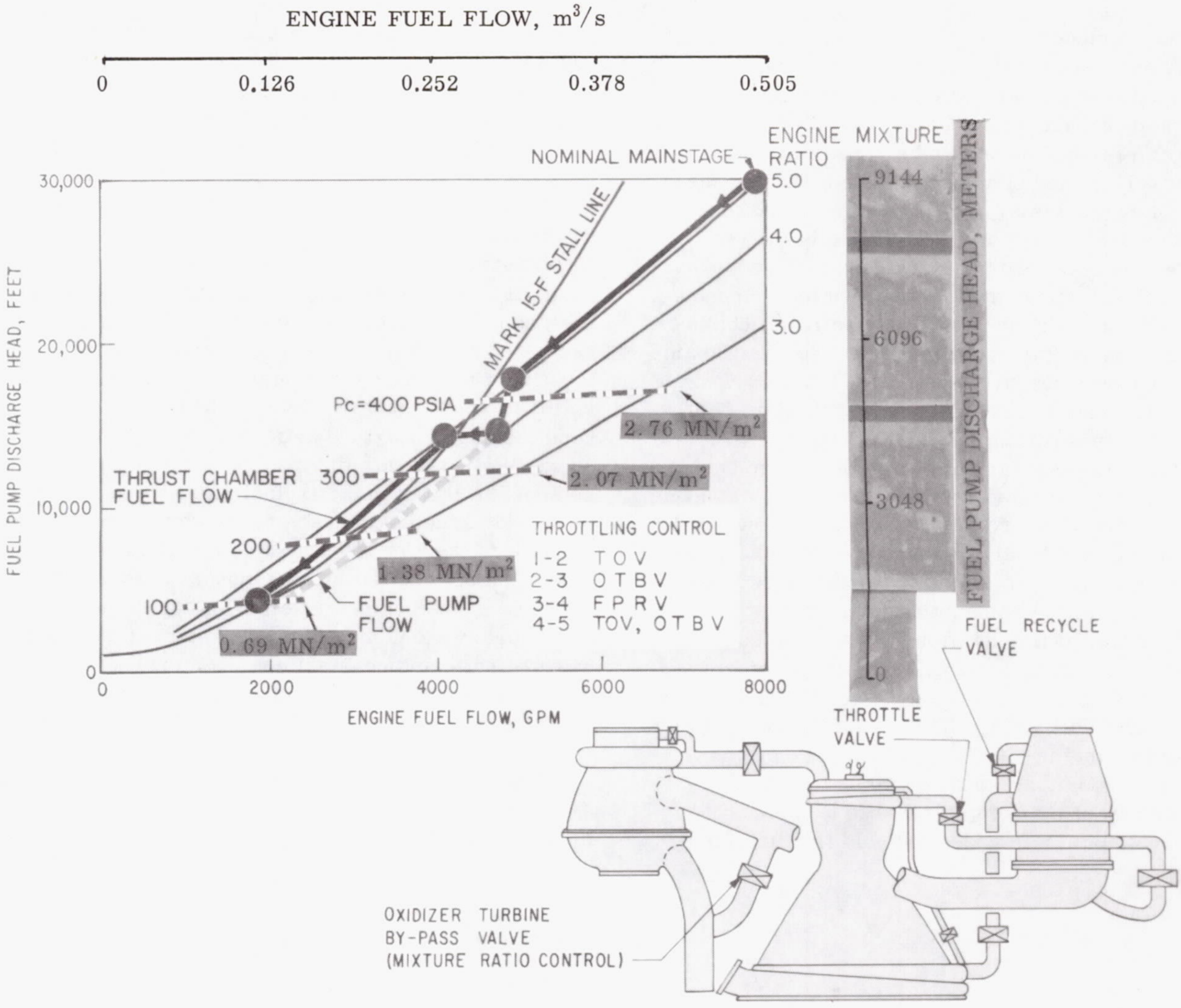

FIGURE 13. J-2X ENGINE 011 FUEL TURBOPUMP THROTTLING MAP

the lunar surface. Missions of this type are used to identify typical performance characteristics for experimental analysis (such as throttling rates, levels, etc.) which may be required for possible future development.

During 1967, Rocketdyne will continue to work on additional engine systems to further define engine throttling capability. Early in 1967, a pressure-fed injector/thrust chamber component throttling program is planned at MSFC to provide additional data and assist in establishing the performance and response characteristics of the injector/chamber from 8900 to 890 000 N thrust (2000 to 200 000 lb thrust) over a mixture ratio range of 3 to 6. The facility to be used at MSFC is currently being prepared (Fig. 15)

Chamber Side Load Reduction. Considerable effort has been expended to minimize or eliminate the starting and cutoff transient thrust chamber side loading that currently exists on all J-2 engine firings at sea level conditions. Under sea level conditions during engine development, production acceptance and stage acceptance testing, the thrust chamber is currently restrained during the starting transition to prevent engine damage. Figure 16 illustrates a typical installation when static firing the J-2 engines installed on the S-II Stage. During the past year, studies were conducted to investigate methods of reducing the chamber transition loading to an acceptable level where restraining mechanisms would not be required, yet still meet the requirements of a full flowing nozzle at mainstage operation. Since the present J-2 chamber contour produces a slowly

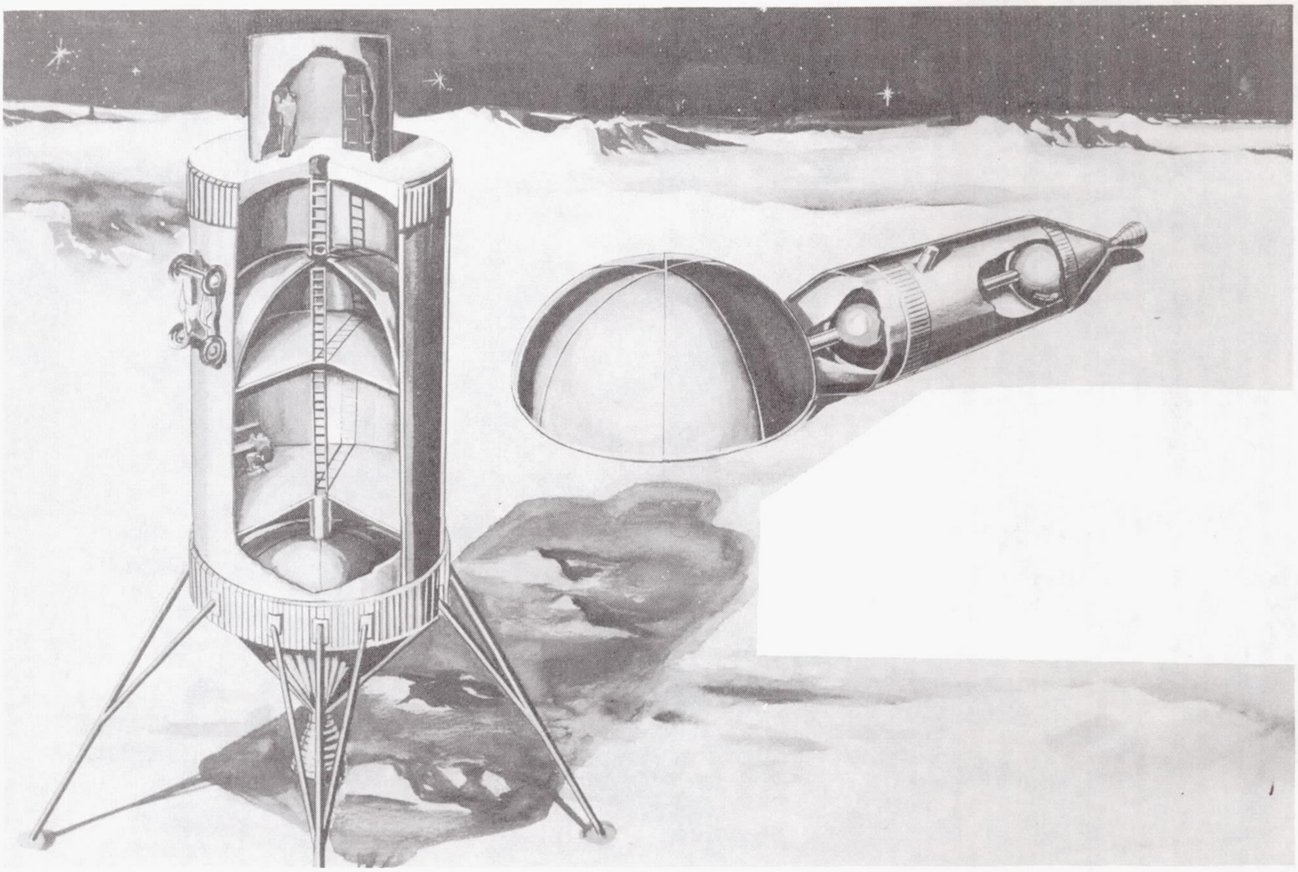

FIGURE 14. S-IVB SPENT STAGE APPLICATION ON LUNAR SURFACE

decreasing pressure profile downstream of the chamber throat and then an increasing pressure gradient from an area ratio of approximately 22:1 to the chamber exit (ϵ = 27.5:1), this has become the prime suspect causing the excessive transition side loads on the current J-2 nozzle. In comparison to other nozzle contours, an early effort was directed toward evaluating the effect of this type of contour on the side loading during transition. Wind tunnel testing indicated that the side loading could be substantially reduced with steeper pressure profiles continuously decreasing from the throat plane to the nozzle exit. To arrive at a nozzle design for full scale fabrication and testing, a series of wind tunnel tests were run with continuously decreasing pressure profiles at several levels of wall pressure at the nozzle exit, and a compromise design was chosen. The contour selected has a 37 degree initial divergence angle downstream of the throat and a 3.5 degree angle at the nozzle exit. The 37/3.5 nozzle was selected because it had the highest exit wall pressure of those tested for a nozzle with a continuously decreasing pressure profile (to assure having a full flowing nozzle at mainstage operation), yet would still produce nozzle performance characteristics at full thrust that were comparable to those of the current J-2 design.

To obtain some early indication as to the validity of the hypothesis that the side loading can be reduced if the pressure profile continuously decreases from the throat to the exit, the J-2X engine 011 nozzle was truncated at approximately an area ratio of 16.5:1 and tested. However, during these tests, the turbine

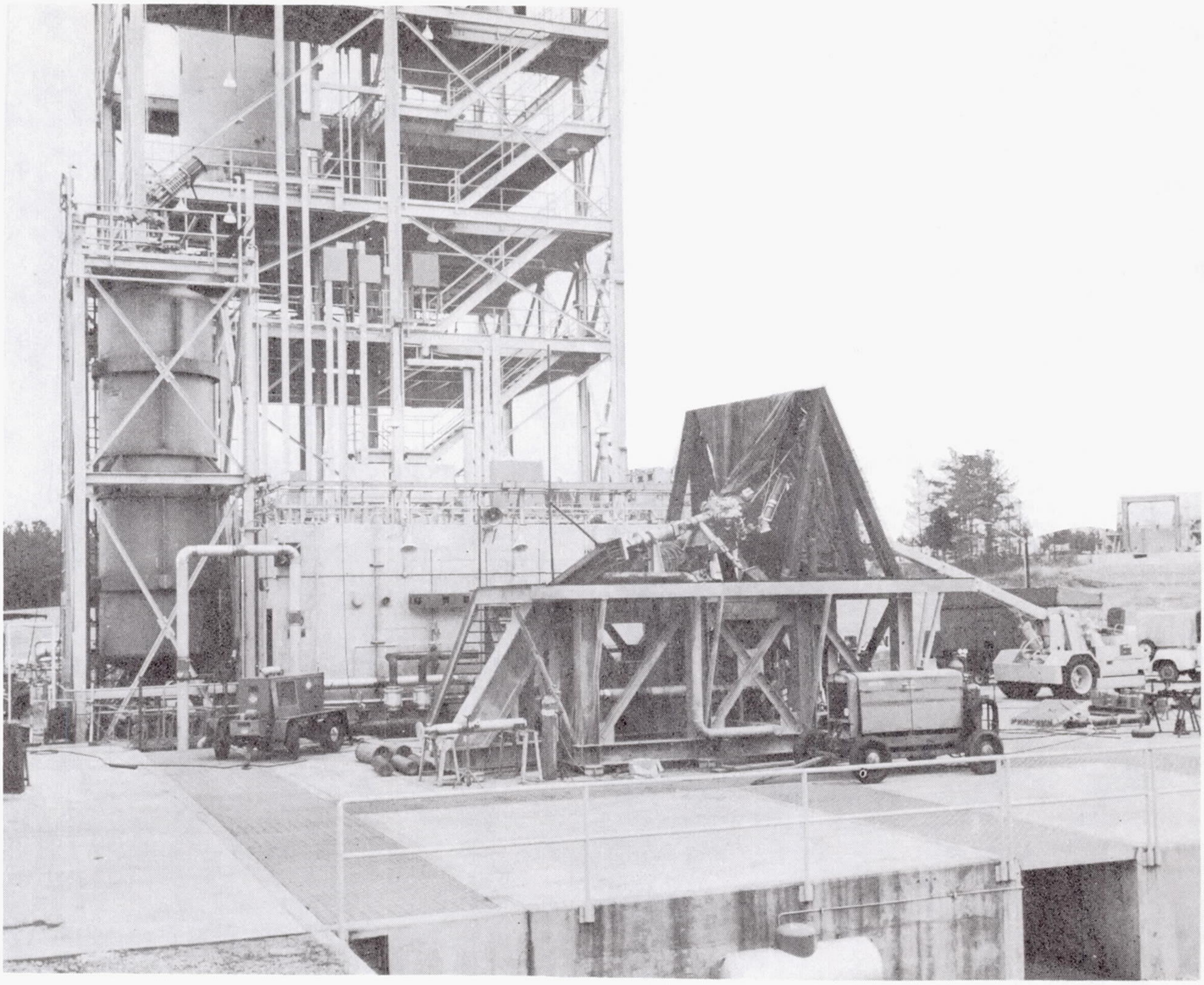

FIGURE 15. MSFC FACILITY FOR PRESSURE-FED THROTTLING TESTING

exhaust gases were ducted overboard rather than being returned to the chamber at an approximate area ratio of 12:1 as is done in the current J-2 design. *(There is some opinion that injection of these gases may in some way assist in triggering the transition side loading by inducing asymmetric separation.)* The results from engine 011's testing were quite encouraging because both starting and cutoff transition loading were substantially reduced as measured by load cells located in outrigger arms attached to the nozzle. Also of interest during the throttling testing (at sea level) discussed earlier, there were no appreciable loads measured that compared to those of the current J-2 transition loads.

These data are summarized below and graphically illustrated in Figure 17.

1. The thrust chamber side load magnitude and duration were significantly reduced from those received with the 27.5:1 chamber.

    a. Maximum loads during start were reduced from 62 200 N thrust (14 000 lbs thrust) (J-2) to 18 700 N thrust (4200 lbs thrust).

    b. Transient duration during start was reduced from 1.0 sec to 0.5 sec.

    c. Maximum loads during cutoff were reduced from 89 000 N thrust (20 000 lbs thrust) (J-2) to 13 330 N thrust (3000 lbs thrust).

    d. Transient duration during cutoff was essentially unchanged.

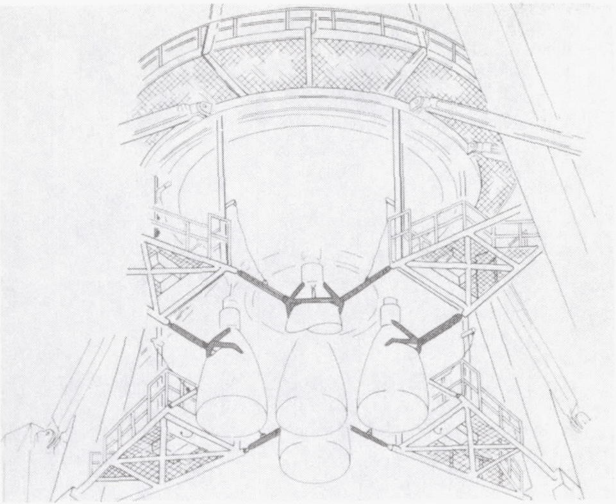

FIGURE 16. SIDE LOAD ARRESTING MECHANISM (SLAM) FOR STATIC TEST - S-II STAGE

2. The throttling side loads reached a maximum of 8450 N thrust (1900 lbs thrust) at 1.62×10^6 N/m^2 (235 psia) chamber pressure.

Fabrication of a full-scale chamber of the 37/3.5 design is scheduled for completion in early 1967 and will be tested shortly thereafter. Successful results from these tests (i.e., indications that restraining mechanisms are not required when starting at sea level) would provide the information to develop this capability into the J-2 engine should this feature become a Saturn Program requirement.

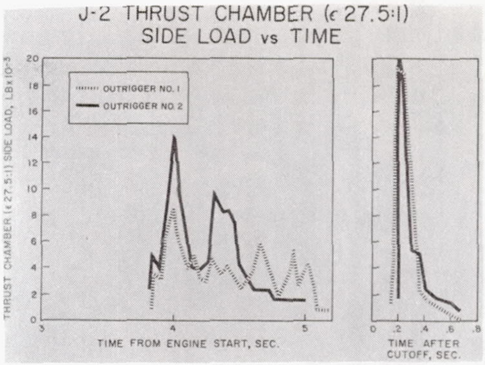

psia

100	200	300	400	500	600	700
0.69	1.38	2.07	2.76	3.42	4.13	4.82

N/m^2 × 10^6

lb thrust × 10^{-3}

2	4	6	8	10	12	14	16	18	20
0.89	1.78	2.67	3.56	4.45	5.34	6.23	7.12	8.00	8.90

N thrust × 10^{-2}

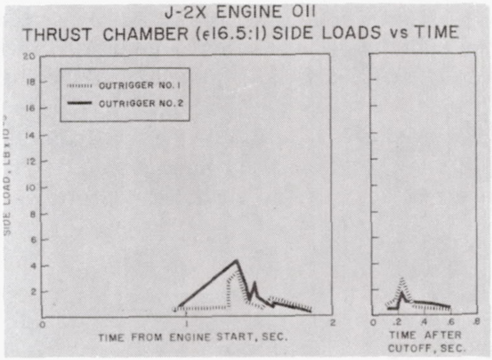

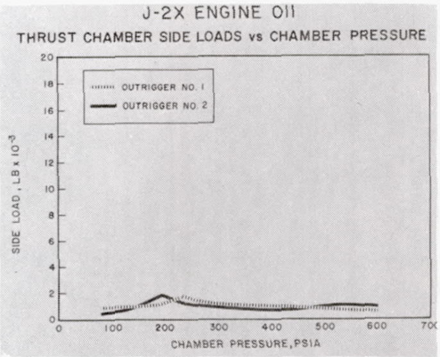

FIGURE 17. THRUST CHAMBER SIDE LOADS DURING ENGINE STATIC FIRING

Tank Head Starting. Although use of the solid propellant turbine starters (SPTS) provides considerable improvement over the current J-2 hydrogen spin bottle in terms of thermal pre-conditioning and servicing, for some of the more advanced missions requiring days in orbit between engine starts, it appears highly desirable to eliminate any need for external initial power to the turbomachinery as provided by the SPTS. This becomes particularly important if the orbital environment at the time engine start is required cannot be predicted, or if the number of starts to mainstage operation prohibits use of the SPTS from strictly a mass standpoint. For these reasons, engine starting by vehicle propellant tank pressures only (tank head starting) has been aggressively pursued in the J-2X Program. Although as of the end of 1966, the number of engine tests (three) conducted without assistance from the SPTS were not impressive, the results from these tests were encouraging enough to warrant spending considerable effort in this direction in 1967. To date, the following results have been obtained:

1. Six tank head start tests were conducted.
    a. Three preliminary tests established sequence control requirements.
    b. Three successful tank head starts were completed to mainstage operation.
2. Significant test results were -
    a. 8.5 sec elapsed from start signal to 90% chamber pressure.
    b. Excellent consistency was obtained.
3. Improved sequence control should result in a starting time of 7.0 sec at sea level.

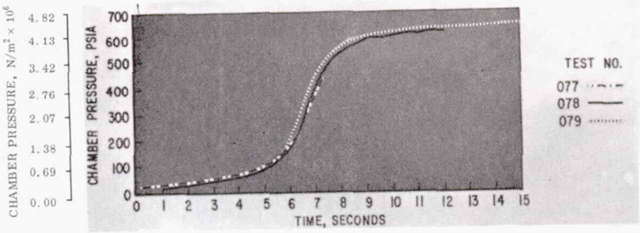

FIGURE 18. TANK HEAD START SUMMARY

Figure 18 illustrates the consistency of transient operation evident on the tests attempted. Based on the engine starting concept discussed earlier, in the opinion of the author, several problems can be expected in the development of a tank head start J-2 engine which is common for all applications. Primarily, it is felt that the function the SPTS serves on the S-II Stage and S-IVB Stage (1st burn) of rapidly purging the propellant feed ducts of warm propellant cannot easily be replaced by a tank head start because for these applications the vehicle has not yet achieved orbital altitude. If the engine starting times (zero thrust to mainstage operation) are excessive, the payload capability will be degraded. This would not appear to be critical for restart applications, typical of the S-IVB Stage, because orbital altitude has been achieved and extended operation in idle mode can be used as the mechanism for purging the warm propellants from the feed systems. This should not substract from the merits of developing tank head starting capability because the use of the SPTS for some missions (long duration between starts) could subject the solid propellant grains to environmental extremes and require thermal conditioning of the SPTS systems, thus rendering them impractical. In 1967, considerable effort will be concentrated on the tank head start capability because of the potential payoff.

Page
Intentionally
Left Blank

CRYOGENIC TECHNOLOGY RESEARCH AT MSFC

March 30, 1967

By

Raymond L. Gause
Douglas A. Gilstad
E. Haschal Hyde
Clyde D. Nevins
James M. Stuckey
Charles C. Wood
Iva C. Yates, Jr.

Page
Intentionally
Left Blank

Page
Intentionally
Left Blank

CONTENTS. . .

PRACTICAL INFLUENCES ON THERMAL DESIGN OF HIGH PERFORMANCE INSULATION

by E. Haschal Hyde

LIST OF TABLES

CONTENTS (Continued) . . .

LIST OF ILLUSTRATIONS

DESIGNING FOR CRYOGENIC INSULATION

by Clyde D. Nevins

LIST OF TABLES

LIST OF ILLUSTRATIONS

CRYOGENIC INSULATION MANUFACTURING TECHNOLOGY

by Iva C. Yates, Jr.

LIST OF ILLUSTRATIONS

DEVELOPMENT OF A COMBINED HIGH PERFORMANCE MULTILAYER INSULATION AND MICROMETEOROID PROTECTION SYSTEM

by James M. Stuckey

CONTENTS (Continued) . . .

LIST OF TABLES

LIST OF ILLUSTRATIONS

CONTENTS (Continued). . .

NUCLEAR GROUND TEST MODULE INSULATION DEVELOPMENT

by Raymond L. Gause

LIST OF TABLES

LIST OF ILLUSTRATIONS

ASSESSMENT OF THE STATUS OF CRYOGENIC INSULATION DEVELOPMENT

LIST OF ILLUSTRATIONS

CONTENTS (Concluded). . .

ADVANCED REQUIREMENTS FOR CRYOGENIC INSULATION

By

Douglas A. Gilstad

Extensive research has been conducted over the past several years directed toward the development of improved insulation systems for space vehicles employing liquid hydrogen. For earth-launch vehicle stages, the storage times are relatively brief and the tanks can be topped off shortly before launch so that nominal thermal performance can be tolerated without significant penalties. Research efforts have provided insulation systems of relative simplicity, reliability, and much greater efficiency than those currently in use on launch vehicles. These insulation system advances were developed extensively in MSFC programs for application to future vehicle development and improvement and have in large measure satisfied the foreseeable needs for booster insulation including the requirements for earth orbital storage of a few hours. Current space flight missions beyond earth orbital and lunar operations involve unmanned systems with no requirements for earth return or recovery. Consequently, these space propulsion needs can be met with available systems of nominal performance.

For manned planetary missions the necessity for high thermal efficiency is imperative for obtaining maximum vehicle thrust and payload. In view of the advantages of systems that use liquid hydrogen as the propellant, substantial research efforts are now devoted to upgrading present insulation systems. Thermal protection required for manned planetary vehicles must be orders of magnitude more effective than that for boost vehicles to minimize boiloff over prolonged storage periods in space. An obvious pacing factor in establishing research goals and approaches is the planning required to define a planetary mission and timetable. Although many studies have been and are continuing to be made of potential future manned planetary missions, the commitment to a manned planetary mission remains somewhat elusive. With a wide variety of system options involving such significant factors as propulsive versus aerobraking modes for planetary capture, nuclear versus storable or cryogenic chemical propulsion for various mission phases, and practical feasibility of large scale orbital assembly operations, to mention only a few, any straightforward direction at this time would require an arbitrary design decision. Even in the absence of such a design decision, research to provide advances in cryogenic storage technology can intelligently proceed.

To provide guidance regarding when adequate technology should be available, it has recently been announced that NASA and AEC intend to proceed with the development of NERVA II, provided that Congressional authorization is forthcoming. The proposed schedule involves initiating preliminary design of a Nuclear Propulsion Module by midcalendar year 1969 with a potential flight test in 1975. Although no allocation of nuclear modules is being made now for any specific future missions, the prototype system should meet the requirements of advanced manned mission applications without requiring a major redesign. During this period, advanced cryogenic as well as space storable chemical rocket systems may also be expected to be candidates for these advanced missions. These expected propulsion system developments will require that cryogenic storage technology achieve a level of maturity by 1970 that will permit a reliable prediction of the thermal protection mass penalty for long-term storage (of at least 12 months) and provide the basis for design of optimum storage systems. This advance in technology should be possible if current and planned research efforts are sustained over this period.

The obvious importance of cryogenic insulation technology to these advanced missions is quite clear. Thermal protection systems to minimize the mass penalties that can result from liquid hydrogen boiloff during prolonged storage periods are readily appreciated. Some concern has been expressed that prolonged storage problems may seriously impede projected system developments. On the other hand, recent predictions indicate that very good thermal performance can be readily achieved. However, to actually fulfill such optimistic predictions will require highly efficient multilayer insulations and the minimization of heat leaks associated with tank supports and piping that must penetrate the basic insulation blanket. Experience to date has indicated that a number of serious problems must be solved to achieve the potential effectiveness of these thermal protection systems. Multilayer insulation is relatively flimsy and must be purged with noncondensible gas or pre-evacuated before launch, be adequately supported during launch, be uniformly expanded in space to provide appropriate evacuated reflective layers, and must also thermally isolate insulation penetrations. Tank supports must have low conductivity and major supports required during launch may need to be retracted during low acceleration phases of space flight. Concepts for dealing with these problems are being developed, but extensive research remains before practical solutions can be made available.

Another potential problem area relates to the protection of insulation systems against damage by meteoroids. Unfortunately, only the near-earth meteoroid environment can be reasonably defined at this time. For planetary missions, particularly to Mars, a knowledge of the interplanetary environment is needed. Since initial statistical measurements cannot be expected for a number of years and a realistic definition of the meteoroid environment for spacecraft design appears to depend upon such measurements, appropriate criteria will not be available to directly influence insulation studies for some time. Perhaps the best approach in the meantime will be to incorporate such features that will aid in meteoroid protection without unduly compromising the performance of thermal protection systems.

Another major difficulty is that of adequately confirming the overall thermal performance of cryogenic storage systems and components prior to construction and launch of the full-scale hardware. The initial conditions of pre-launch purging followed by launch accelerations together with ambient pressure decay are difficult to simulate in ground tests even with small-scale specimens. Long-term vacuum tests can be conducted on systems of reasonable size, but reduced gravity effects can be simulated only for extremely short times. Size-scaling laws can be used to extrapolate certain elements of system thermal performance, but, in general, the overall insulation effectiveness is difficult to predict accurately, particularly in view of the effects of discontinuities associated with insulation penetrations or non-uniformities in system components. Accordingly, it is extremely important that the simulation and scaling techniques be examined with the objective of developing improvements that will enhance the reliability of thermal performance predictions. The pertinent environmental conditions can be provided in flight tests, but the limitations in scaling thermal performance can only be solved by testing large-scale systems. It appears probable that flight testing will be necessary, but the timing, approach, and techniques involved should be very thoroughly evaluated to insure the maximum potential for positive results.

NASA research on thermal protection systems for cryogenic propellants in space propulsion systems is being conducted primarily at two Centers, Lewis Research Center and Marshall Space Flight Center. The primary research emphasis in the Marshall program is the development of large thermal protection systems required to store propellants for long durations, i.e., well beyond 30 days. Research at Lewis is concentrated upon developing smaller thermal protection systems pertinent to unmanned vehicles with relatively short storage times. Many problems involved in these systems are common, and adequate coordination of the research at the two Centers is obviously important.

The current cryogenic insulation research at Lewis consists primarily of contract studies. Development of prefabricated superinsulation panels by Linde is nearing completion; these CO_2-filled panels, self-evacuated by cryopumping, simplify handling and installation problems and would be suitable for relatively short-term storage applications. At McGill University, the effects of meteoroid bumper debris on insulated liquid hydrogen tanks will be determined experimentally in light gas gun facilities during the next year. An evaluation of low heat leak tank support concepts is being initiated under contract, and the practical problems involved in the application of a shadow shielding concept will be the subject of another study. That shadow-shield concept was described during the Cryo-Propellant Storage Conference at MSFC in October, 1966. In past efforts sponsored by Lewis, important contributions have been made in studies of the basic performance of various superinsulation configurations. Also in the Lewis cryogenic storage program, extensive attention is directed toward other factors such as fracture mechanics of tank materials at cryogenic temperatures and the development of advanced tank materials.

In summary, the research program to advance the state of technology for prolonged storage of liquid hydrogen must be considered as extremely important. The following papers describe some of the major efforts at MSFC and how the current and planned program may be expected to provide solutions to the various problems and achieve the critical objectives in a timely manner.

PRACTICAL INFLUENCES ON THERMAL DESIGN OF HIGH PERFORMANCE INSULATION

By

E. Haschal Hyde

SUMMARY

High energy cryogenic propulsion systems offer high specific impulse for space vehicles. The cryogenic propellants for these systems must be protected from excessive boiloff. Multilayer insulation (MLI) offers a lightweight insulation system with excellent thermal qualities. However, development of a high performance insulation (HPI) system requires a balanced combination of (1) material selection, (2) structural design, (3) thermal analysis, (4) unique test equipment, (5) reproducible application procedures and fabrication methods, and (6) accurate test procedures. All environments of flight must be considered, such as prelaunch, ascent, and space conditions.

MSFC's first effort was toward development of a lightweight high performance insulation system for mission durations of 96 hours and up to 30 days. This effort was successful. However, current mission planning requires cryogenic stages for storage times over one year. Although the technology for multilayer insulation on flight-configuration vessels for long-term storage of cryogenics has not been demonstrated, MSFC has gained valuable experience through the inhouse and NASA sponsored HPI programs. From this effort MSFC was able to identify and define the remaining problems and to initiate programs to solve these problems in preparation for the application of multilayer insulation to large size, flight-configuration cryogenic storage tanks (up to and exceeding one year storage capability). This paper will discuss the thermal aspects of the helium-purged 6.35μ (1/4 mil) aluminized mylar insulation system applied to a 2.67-m (105-in.) diameter tank and future requirements and approaches.

INTRODUCTION

Marshall Space Flight Center (MSFC) has been developing high performance insulation (HPI) technology for about five years. Significant inhouse and support contractor effort has been directed toward developing a flight type high performance insulation system for long term storage of cryogenics in space. The initial objective of the HPI program at MSFC was development and application of HPI to flight configuration tanks to store cryogenics for mission durations up to 30 days. Stationary or roadable dewars have used HPI for several years with extremely small propellant losses. The HPI application concepts for insulating these dewars require that the insulations be evacuated to a very low pressure to avoid gas conduction and to reduce the primary mode of heat transfer to radiation and solid conduction. Hard metal shells protect the insulation and withstand the atmospheric pressure that would deteriorate the insulation thermal performance. High performance insulations for flight vehicles are similar; they depend on a vacuum environment for optimum performance.

MSFC has studied both ground and flight type evacuated insulation systems. The Linde insulation system (ground evacuated) is of aluminum foil with low-thermal-conductivity spacers between each reflective layer. Because of severe mass restraints, a flexible jacket replaced the rigid outer metal shell used on ground based storage equipment, permitting evacuation of the material before vehicle launch. The Linde insulation, alternate layers of 6.35-μ (1/4-mil) aluminum foil and 76.2-μ (3-mil) dexiglas paper, is evacuated before filling the tank with a cryogen. The outer jacket is flexible to help maintain a vacuum environment when ground evacuation of the insulation causes the insulation to compress to 25% of its original thickness. Although highly compressed, the insulation provides adequate ground-hold thermal protection. The HPI expands to 50 - 80% of its original thickness during launch and orbital flight; and incomplete physical recovery does not significantly hinder insulation performance (Fig. 1). Ground-hold evacuation of the compressible insulation makes the flexible plastic jacket crinkle and bend. The resulting pin hole leaks that appear will complicate obtaining and maintaining the required vacuum. Therefore, advanced material development has been required to alleviate this major difficulty with the compressible concept. This problem has

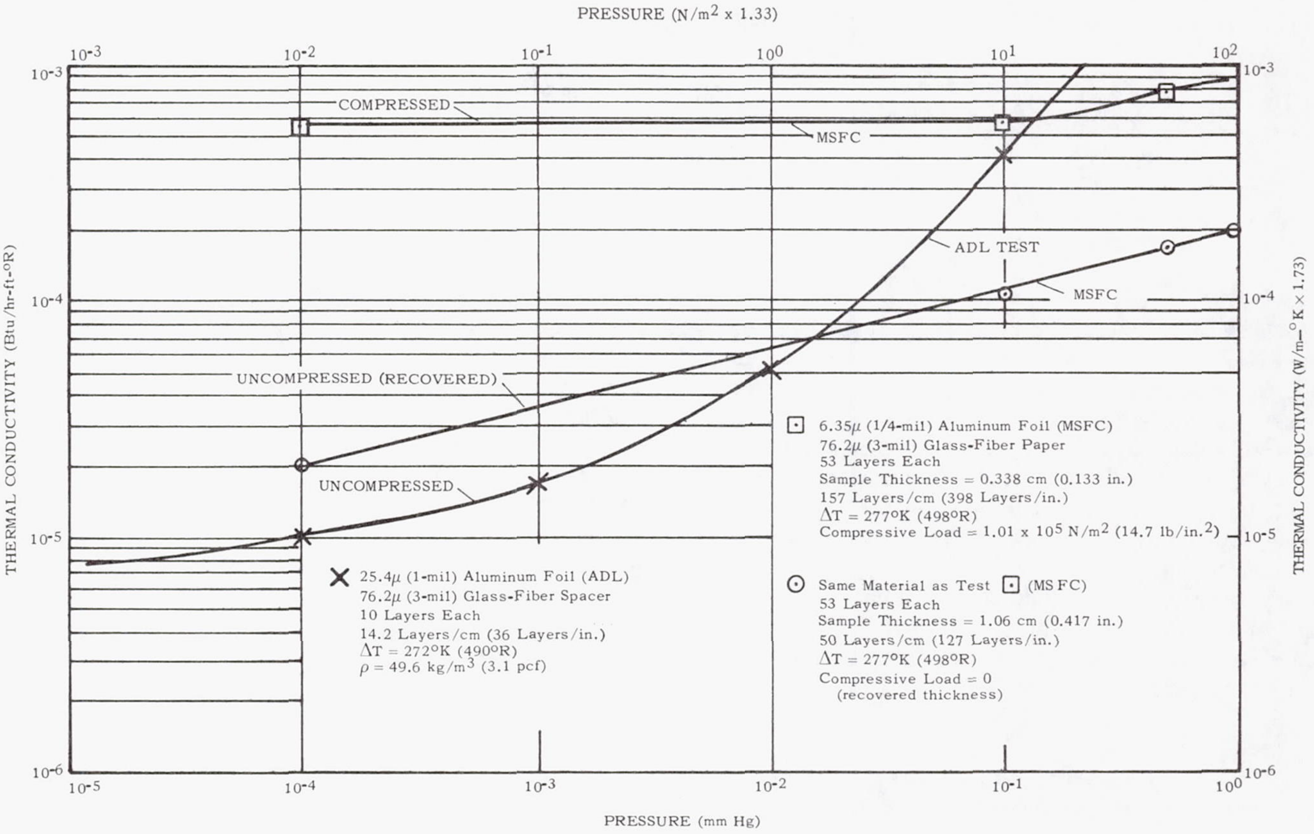

FIGURE 1. THERMAL CONDUCTIVITY OF INSULATION MATERIAL AS A FUNCTION OF HELIUM GAS PRESSURE

been significantly reduced by using a vacuum jacket of lead mylar laminate. A 2.67-m (105-in.) diameter tank has been insulated, evacuated, and is currently ready for testing with liquid hydrogen. This concept will not be discussed in this paper on thermal influences on design, but will be discussed in subsequent papers that deal with structural design and manufacturing procedures.

The other insulation system studied by MSFC was the NRC or crinkled aluminized mylar. This concept is ground purged and evacuation occurs during ascent. The system has layers of 6.35-μ (1/4-mil) aluminized mylar inside a lightweight purge jacket (Fig. 2, NRC). Although the ground-hold heat leak into the tank is much higher with the NRC system than with the Linde system, both systems do equally well if evacuated to less than 0.0133 N/m² (10^{-4} torr). The NRC insulation has an advantage of being about one-fourth the mass of the Linde insulation. The major disadvantages of the NRC system are controlling insulation density, high ground-hold boiloff, and compressibility during and after application to a tank. The NRC system thermal performance is discussed extensively in this paper.

The third system now under study by MSFC has alternate layers of 6.35-μ (1/4-mil) aluminized mylar and thin sliced polyurethane foam (Fig. 2). This concept, too, is helium purged on the ground (to prevent air condensation) and the insulation is allowed to evacuate in flight. A 76.2-cm (30-in.) diameter calorimeter was insulated with this concept; the work will be discussed in a subsequent paper by Dr. J. M. Stuckey.

At the start of the MSFC HPI program, calorimeter thermal performance data existed for most of

	APPROXIMATE DENSITY kg/m^3 (lb/ft^3)	CALORIMETER THERMAL CONDUCTIVITY $289 - 20.6^{0}K$ ($520 - 37^{0}R$) W/m-^{0}K (Btu/hr-ft-^{0}F)	APPROXIMATE LAYERS/cm (LAYERS/in.)	
			RADIATION SHIELDS	SPACERS
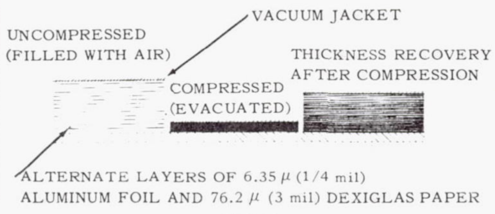 LINDE	88.1 (5.5)	3.46×10^{-5} (2×10^{-5})	27.6 (70)	27.6 (70)
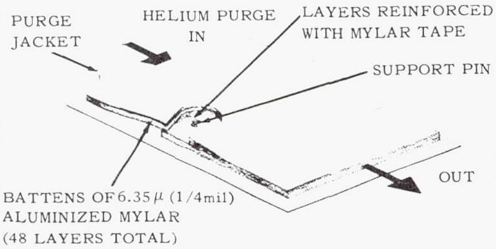 NRC	32.0 (2.0)	5.19×10^{-5} (3×10^{-5})	27.6 (70)	NONE
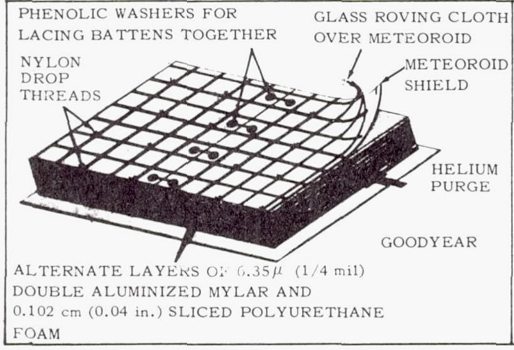 	38.5 (2.4)	6.05×10^{-5} (3.5×10^{-5})	8.66 (22)	8.66 (22)

FIGURE 2. MSFC AND CONTRACTOR BASIC INSULATION SYSTEMS

the commercially available insulations. Since thermal conductivity is only one factor in an insulation system, it was decided to insulate a flight configuration tank to learn all facets of insulation application and performance. It was thought that the insulation thermal performance data from a system applied to a large tank would differ from data from small calorimeter tests for the same insulation application. Experimental results at MSFC and from NASA contractors show this is true. The apparent thermal conductivity of an insulation system compared with data from calorimeters seems to be degraded according to an increase in vessel size and complexity (Fig. 3). This degradation of insulation performance could result from (1) higher gas pressure within the insulation, resulting from longer pumping paths for entrapped residual gases, (2) local compression at penetrations and double contour surfaces, (3) inaccurate prediction of heat transfer rates through ducting and structural support penetrations, and (4) residual gas conduction from leaking gaskets, electrical connectors, and valves.

Simulation of each of the above factors will yield reliable thermal performance data for an insulation system. To simulate the mechanical problems in flight type vessels, a 2.67-m (105-in.) diameter tank was chosen for insulation investigation at MSFC (Fig. 4).

INSULATION PURGING

FLIGHT-CONFIGURATION TANK AND INSULATION SYSTEM DESIGN

A sketch of the 3.18 m (125 in.) long, 2.67-m (105-in.) diameter tank is shown in Figure 4. It has

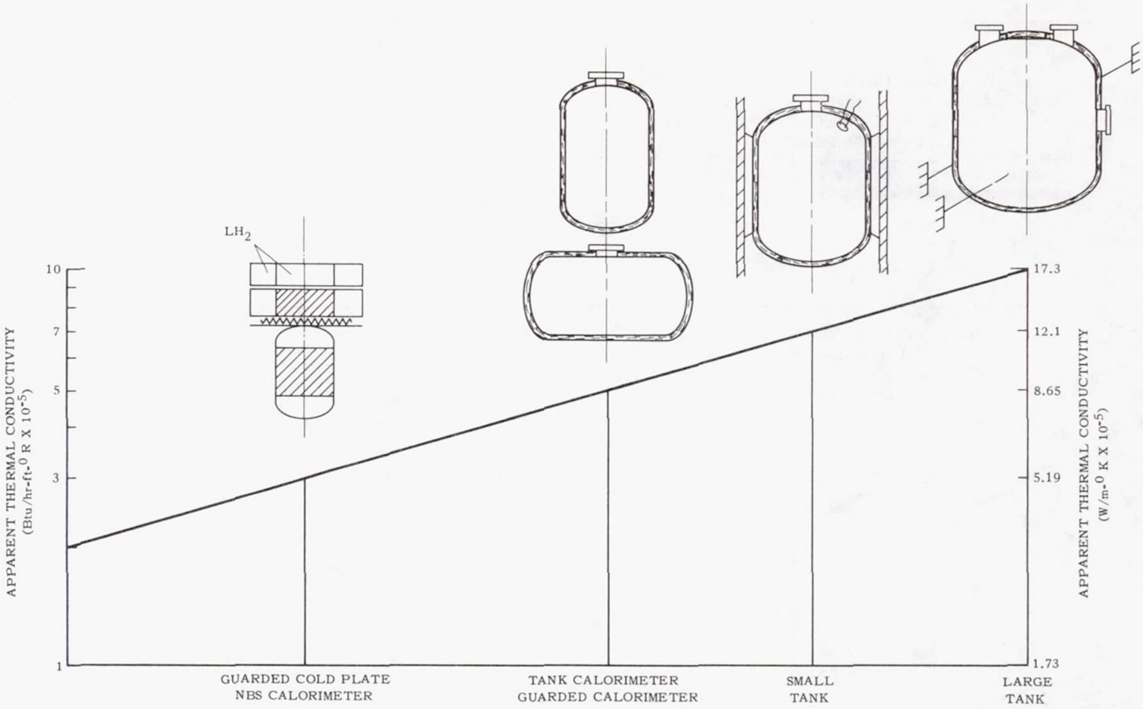

FIGURE 3. APPARENT THERMAL CONDUCTIVITY TREND FOR TESTS ON DIFFERENT TYPE VESSELS

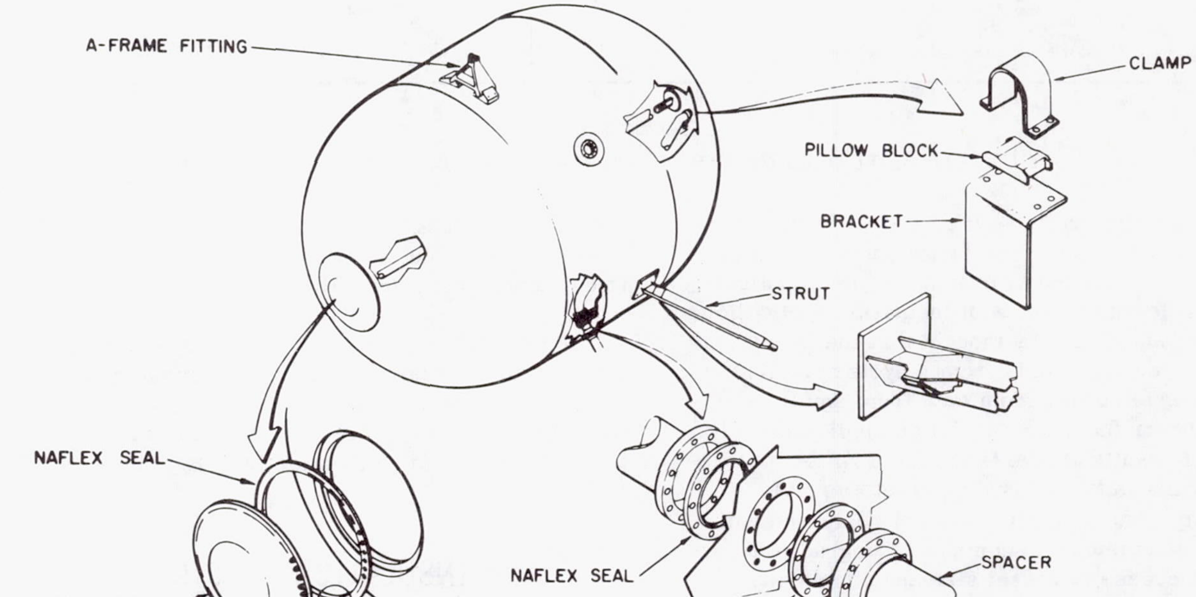

FIGURE 4. 2.67-m (105-in.) CRYOGENIC TEST TANK ASSEMBLY

a surface area of 27.1 m^2 (292 ft^2), and a volume of approximately 12.85 m^3 (454 ft^3). During testing the tank is loaded with approximately 862 kg (1900 lb) of hydrogen. The tank has a three-point support system, four 7.62-cm (3.0-in.) diameter ducting penetrations, an operational manhole cover, and a submersible fill valve. Forty-eight layers of crinkled 6.35-μ (1/4-mil) aluminized mylar were applied to the tank (Fig. 5). The shingle arrangement for applying insulation (Fig. 6) offers a positive attachment of the insulation to the tank sidewall. The shingles are held by 0.635-cm (1/4-in.) diameter aluminum pins. Overlapping shingles are used to help vent the helium purge gas within the layers during rapid ascent of the vehicle.

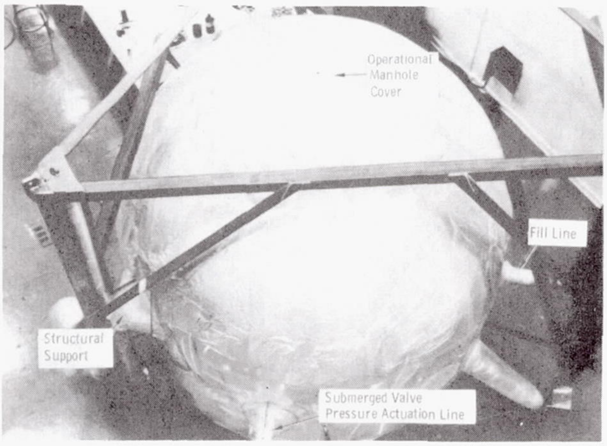

FIGURE 5. 2.67-m (105-in.) DIAMETER TANK WITH He PURGED INSULATION SYSTEM

PURGING REQUIREMENTS

The assembled tank and insulation system are shown in Figure 5. To prevent condensation and solidification of either air or water vapor, a 127-μ (5-mil) mylar purge jacket encloses the insulated tank. The entire insulation system is purged with dry helium gas through a purge collar at each of the support rods and ducting penetrations; purge gas exit ports were at the top and bottom of the purge jacket. A mathematical model of the sidewall insulation applied to the tank is in Figure 6. A one-dimensional gas flow analysis determined if outgassing and sublimation would affect the pressure level within the insulation layers. By ignoring outgassing, calculations showed the insulation system would evacuate rapidly, with the pressure decay of the vacuum chamber. When considering insulation outgassing, the insulation pressure may be two orders of magnitude higher than the vacuum chamber pressure of 0.0048 N/m^2 (3.6×10^{-5} torr). Assumptions in this study were as follows:

1. Insulation outgassing coefficient =

$$1 \times 10^{-2} \frac{\mu \ell}{\text{sec-ft}^2} = 0.1076 \frac{\mu \ell}{\text{sec-m}^2}$$

2. Diffusion coefficient = $0.1785 \frac{m^2}{sec}$ (Helium)

3. Flow length = 54 in. = 1.37 m

Figure 7 shows the study results. Two different cases with the one-dimensional mathematical model are described. In all cases, the vacuum chamber pressure was assumed to be 0.0048 N/m^2 (3.6×10^{-5} mm Hg). The first case assumed the pressure measured under the purge jacket was 0.0133 N/m^2 (1×10^{-4} mm Hg) and was the same as that at the end of the batten. Average gas temperatures for the two cases were selected as 222°K (400°R) and 22.2°K (40°R). As shown in Figure 7, the equilibrium insulation pressure did not vary significantly with temperature. The average gas temperature had even less effect on the pressure at the closed end of the batten when the pressure under the purge jacket was assumed to be 0.133 N/m^2 (1×10^{-3} mm Hg). With the insulation outgassing effect, however, the pressure at the end of the batten degraded approximately one order of magnitude. Another analysis determined if layer density was a significant factor in retarding insulation pressure decay with the insulation outgassing. The resulting pressure was approximately 0.266 N/m^2 (2×10^{-3} torr) for the 15.7 layers/cm (40 layers/in.), 0.40 N/m^2 (3×10^{-3} torr) for the 27.6 layers/cm (70 layers/in.) and 0.80 N/m^2 (6×10^{-3} torr) for the 51.2 layers/cm (130 layers/in.) case. All these studies assumed that the vacuum chamber pressure was 0.0026 N/m^2 (2×10^{-5} torr). Clearly, outgassing causes high equilibrium gas pressures within the insulation layers, and rapid insulation pressure decay is not significantly affected by residual gas temperature or layer density.

FULL-SCALE TEST TANK PURGE RESULTS

Tests were made to establish adequacy of the full-scale tank purge system in reducing the moisture content of the gas to 50 parts per million (ppm), while

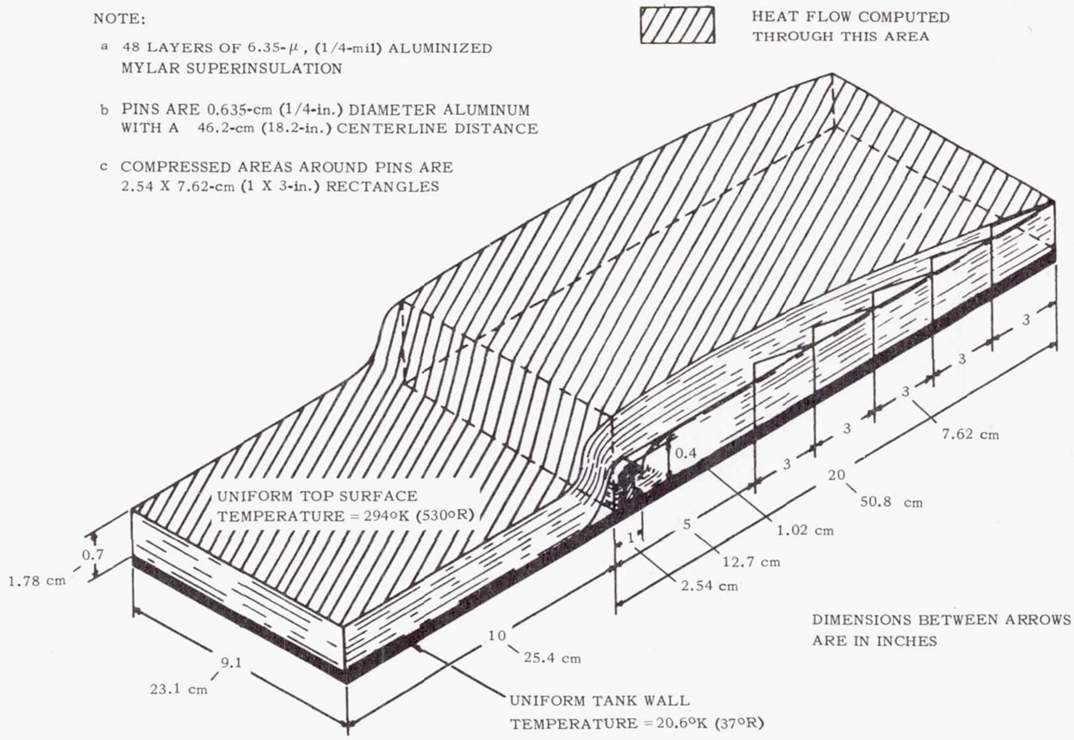

FIGURE 6. SECTION OF INSULATION OVERLAP DESIGN USED FOR COMPUTER THERMAL MODEL

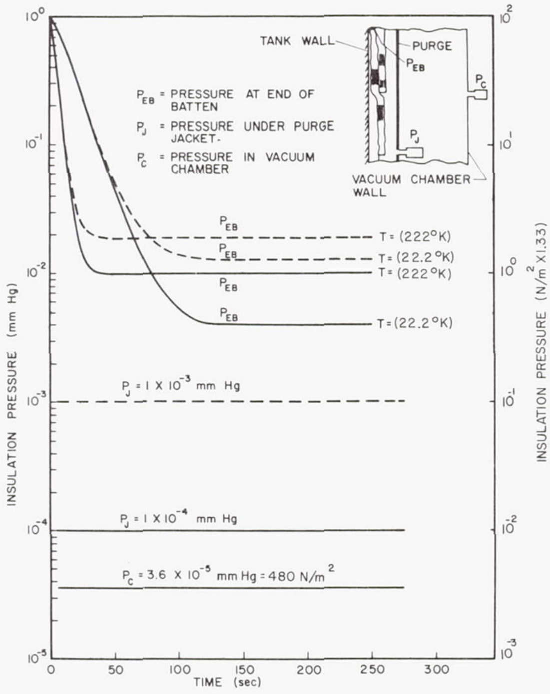

FIGURE 7. ESTIMATED PRESSURE VERSUS TIME AND TEMPERATURE FOR OUTGASSING OF NRC-2 MULTILAYER INSULATION

reducing the air concentration to less than 5%. Residual air content (in the purge gas) within the insulation layers was found before installation of the tank in the vacuum chamber. Equal quantities of helium purge gas (2.5 scfm total) were forced through each of the purge collars of the four piping penetrations, the titanium rod of the A-Frame and the titanium box supports (Fig. 5). Purge gas was vented through the exit ports at the upper and lower bulkheads. The differential pressure across the purge jacket was held at 344 N/m^2 (0.05 psi). A moisture monitor attached to the exit vent ports showed that the moisture content of the gas within the insulation was cut to less than 50 ppm. Calculations indicated that purging the system at a flow-rate of 0.00118 m^3/sec (2.5 scfm) would reduce the air concentration to less than 5%. Purge gas samples during purging operations were taken by a hypodermic needle attached to an evacuated metal bottle. The laboratory gas analysis showed that the original test objectives were reached.

INSULATION PERFORMANCE

CALCULATED INSULATION SYSTEM THERMAL PERFORMANCE - EVACUATED CONDITION

Multilayer insulations are highly anisotropic. That is, the lateral thermal conductivity is much higher than the normal thermal conductivity of the material. For the aluminized mylar system the lateral thermal conductivity is 1 000 times larger than the perpendicular thermal conductivity. Due to its anisotropic nature and irregular configuration after the insulation was applied to the tank sidewall, a computer analysis was made to predict heat transfer rates through the insulated sidewall of the 2.67-m (105-in.) diameter tank. A sketch of the insulation overlap, for the mathematical model to predict the sidewall heat transfer rate, is in Figure 6. For overlap areas, normal and lateral conductivities in both the compressed and uncompressed areas away from the pin, and the compressed areas near the pin, were part of the mathematical model. A thermal conductivity normal to the insulation layers of 8.65×10^{-5} W/m-°K (5×10^{-5} Btu/hr-ft-°R) was used in the computer analysis. Thermal conductivity of 2.08×10^{-2} W/m-°K (1.2×10^{-2} Btu/hr-ft-°R) was assumed parallel to the insulation layers. The parallel thermal conductivity value was calculated for a density of 27.6 layers/cm (70 layers/in.) using the thermal conductivity for solid mylar and aluminum. A normal and parallel conductivity of 0.121 W/m-°K (7×10^{-2} Btu/hr-ft-°R) was used for the compressed areas around the pins [1].

The heat transfer rate of the tank sidewall was calculated by multiplying the heat leak (through a single overlap area) by the 77 overlap areas on the tank. The heat transfer rate through the structural supports and ducting penetrations was found by three-dimensional computer analyses [2]. The simultaneous effects of radiation and conduction down the ducting penetrations were considered. The radiation effect was negligible compared with overall heat transfer rate through the duct connection. Thermal conductivity as a function of temperature was used to calculate heat transfer rates for the titanium structural supports and the stainless steel piping penetrations [3]. Heat transfer rates to the cryogen through the tank sidewall were calculated with and without outgassing of the insulation material. The results are in Table I. With no insulation outgassing, approximately 70% of the total heat input came through the tank sidewall. A boiloff rate of 0.34 kg/hr (0.75 lb/hr) is expected from both sidewall and penetration

TABLE I. ESTIMATED AND CALCULATED HEAT TRANSFER RATES FOR THE 2.67-m (105-in.) DIAMETER TEST TANK

ITEM	GROUNDHOLD HEAT TRANSFER RATES▭ W (Btu/hr)		ESTIMATED VACUUM CHAMBER ENVIRONMENT HEAT TRANSFER RATES▭ W (Btu/hr)		EXPERIMENTAL VACUUM ENVIRONMENT HEAT TRANSFER RATES▭ W (Btu/hr)
	ESTIMATED	EXPERIMENTAL		INCLUDING OUTGASSING EFFECTS	
TANK SIDEWALL*	20 500 (70 000)		29.9 (102)		
BOX SECTION SUPPORT STRUTS (2)	58.6 (200)		3.52 (12)		
FILL LINE	70.3 (240)		0.88 (3)		
INSTRUMENTATION LINES (2)	141 (480)		5.86 (20)		
VENT LINE CONTINUOUS VENTING	0		0		
A-FRAME SUPPORT (TITANIUM ALLOY ROD)	87.9 (300)		0.88 (3)		
TOTAL	20 900 (71 220)	10 140 (34 600)	42.5 (145)	62.1 (212)	141 (480**) 130 (442***)

*LH_2 TEMPERATURE
**C-012-10
***C-012-12

▭ 6.35 μ (¼-mil) crinkled aluminized mylar insulation system heat inputs. With insulation outgassing, approximately 82% of the total heat transfer into the cryogen came through the tank sidewall, resulting in a boiloff rate of 0.499 kg/hr (1.1 lb/hr).

HELIUM PURGE CONDITION

Assuming helium-purged conditions, the rate of heat transfer into the cryogen was calculated as an evacuated condition, with the thermal conductivity of helium gas being substituted for the normal insulation thermal conductivity. The same assumptions were used for the purged case as for the evacuated case, except as noted below, and the equilibrium hydrogen boiloff rate was predicted by hand calculations. An insulation thickness of 1.78 cm (0.7 in.) was used (except in overlap areas where the thickness was doubled). Overlap areas were estimated to cover approximately 30% of the tank surface area. In Table I, nearly all of the total heat was calculated as flowing through the tank sidewall for the purged condition.

PREDICTED VERSUS MEASURED SYSTEM THERMAL PERFORMANCE

Under simulated orbital conditions, a steady-state boiloff of about 1.04 - 1.13 kg/hr (2.3 - 2.5 lb/hr) was measured (Fig. 8). This value represents an insulation performance factor of about 2.77×10^{-4} W/m-°K (1.6×10^{-4} Btu/hr-ft-°R). From Figure 8 and a boiloff rate of about 2% per day, the amount of stored hydrogen lost for a four day mission is about 10%. Therefore, by the addition of more insulation layers, the test tank could be used for mission duration up to 30 days.

The difference between the predicted heat leak and the experimental value obtained from the 2.67-m (105-in.) diameter tank equipped with aluminized mylar insulation (see Table I) was investigated. Indicated reasons for the difference were factors such as (1) inaccurate prediction of penetration heat transfer rates, (2) increased heat conduction from compression of the insulation layers during fabrication and assembly, (3) inaccurate prediction of heat transfer rate through batten overlays, and (4) increased thermal conductivity from gas leakage through the tank wall combined with leakage into the insulation layers from the seals at structural and piping penetrations.

The first and second factors above were eliminated by the following: thermocouples placed at structural heat leak penetrations showed good agreement between measured and predicted values for a steady-state temperature gradient (Fig. 9); calorimeter tests showed that thermal degradation from slight insulation compression did not have a major effect on insulation performance [4].

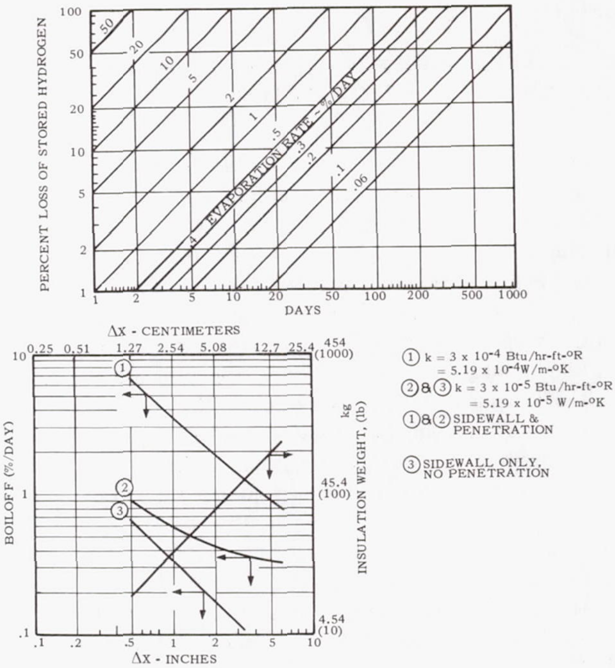

FIGURE 8. BOILOFF RATE VERSUS INSULATION THICKNESS FOR A 2.67-m (105-in.) DIAMETER TANK (INCLUDING HEAT LEAK CAUSED BY PENETRATIONS)

To eliminate the third factor, the accuracy of the computed heat transfer rate through the insulation batten overlap area on the 2.67-m (105-in.) diameter tank was verified. A 24.2 cm (9.5 in.) modified National Bureau of Standards type calorimeter was used to determine the basic insulation configuration thermal performance factor (Fig. 10) [5]. The insulation was applied to the calorimeter with the insulation overlaps in a vertical plane. Equilibrium heat flux value for this test was 0.536 W/m^2 (0.17 Btu/hr-ft^2), verifying that the computed heat transfer rate (Table I) for the insulation overlaps on the 2.67-m (105-in.) diameter tank was correct.

An insulation system similar to that on the 2.67-m (105-in.) diameter tank was put on a 73.6-cm (29-in.) diameter model of the larger tank. The insulation applied to the sub-scale tank had a much

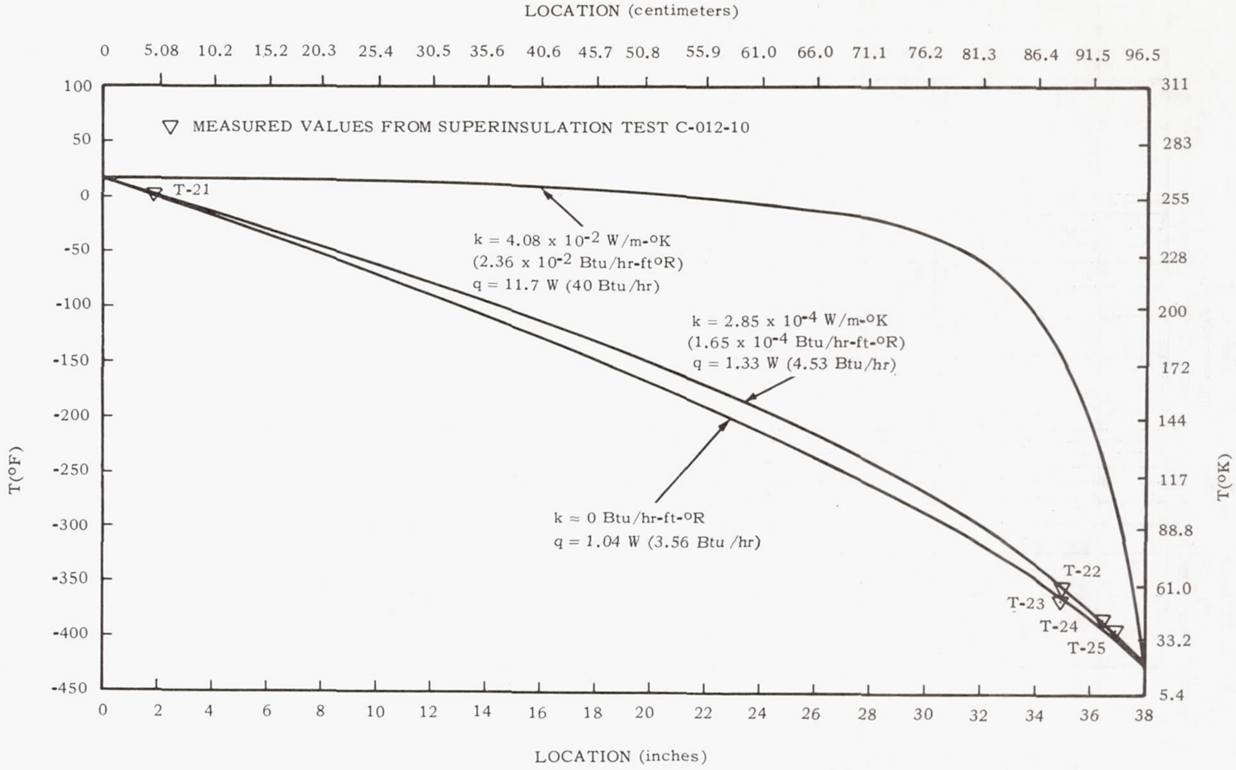

FIGURE 9. TEMPERATURE PROFILE THROUGH A PENETRATION AS A FUNCTION OF INSULATION THERMAL CONDUCTIVITY

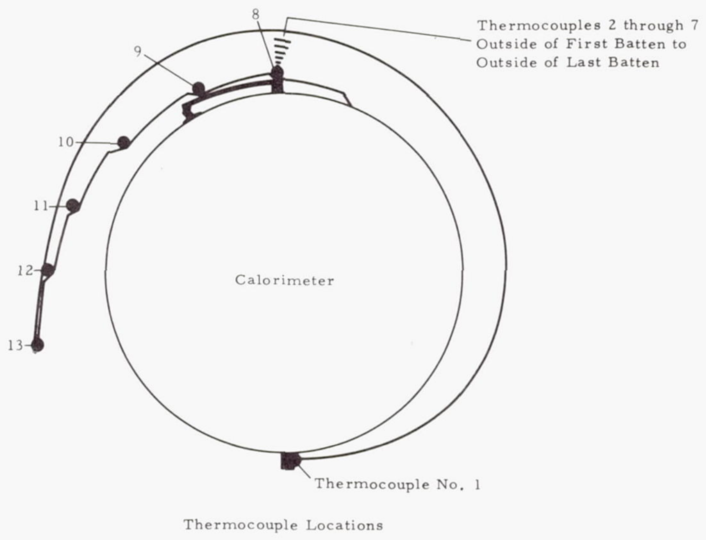

FIGURE 10. THERMOCOUPLE LOCATION FOR CALORIMETER TEST NO. 2 (NASA DESIGN, NCR-2 SHINGLE INSULATION)

higher overall layer density (100 - 125 layers/in.) than the larger tank, and the overlap was reduced to 17.8 cm (7.0 in.) for structural scaling purposes. A thermal test on this sub-scale insulation system gave a heat flux value of 1.17 W/m^2 (0.37 Btu/hr-ft^2) (Fig. 11) [6]. This value was about 25% of that obtained on the 2.67-m (105-in.) diameter test tank during Tests C-012-10 and C-012-12 (Fig. 12) [7]. These two test results proved that the predicted heat transfer rate through the insulation overlaps was accurate. Thus, the difference between the predicted and experimental thermal performance for the 2.67-m (105-in.) diameter tank was obviously due to other causes.

Gas leakage or outgassing seemed to be the major reason for the higher than expected heat transfer rate. Accordingly, calculations were made to find the pressure distribution in the insulation batten as a function of batten length, and the thermal conductivity as a function of average batten pressure. An apparent thermal conductivity of 1.9×10^{-4} W/m-°K (1.1×10^{-4} Btu/hr-ft-°R) was calculated as the average conductivity of the batten with outgassing present (outgassing rates were obtained from Niedorf [8]).

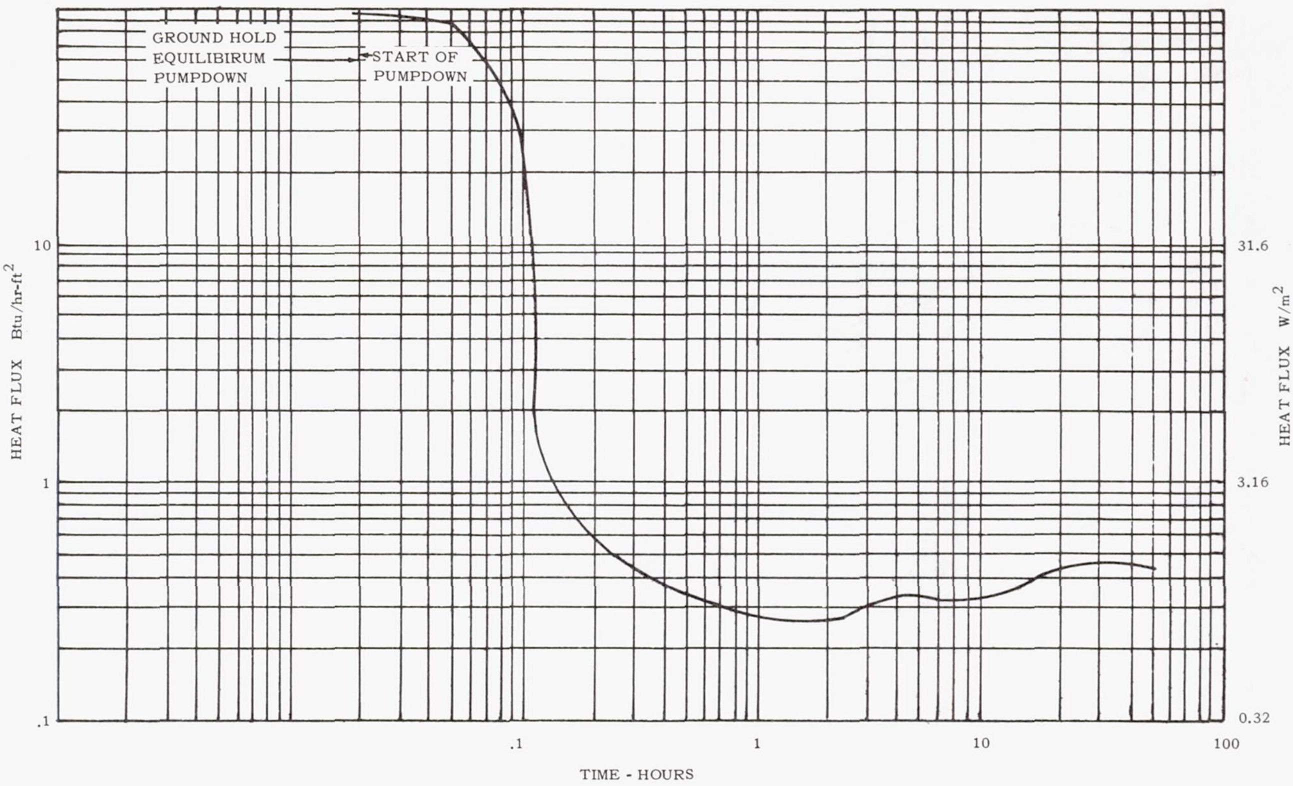

FIGURE 11. HEAT FLUX VERSUS TIME FOR SCALE MODEL TANK, PRELIMINARY THERMAL TEST NO. 1 (NASA DESIGN, NRC-2 SHINGLE INSULATION)

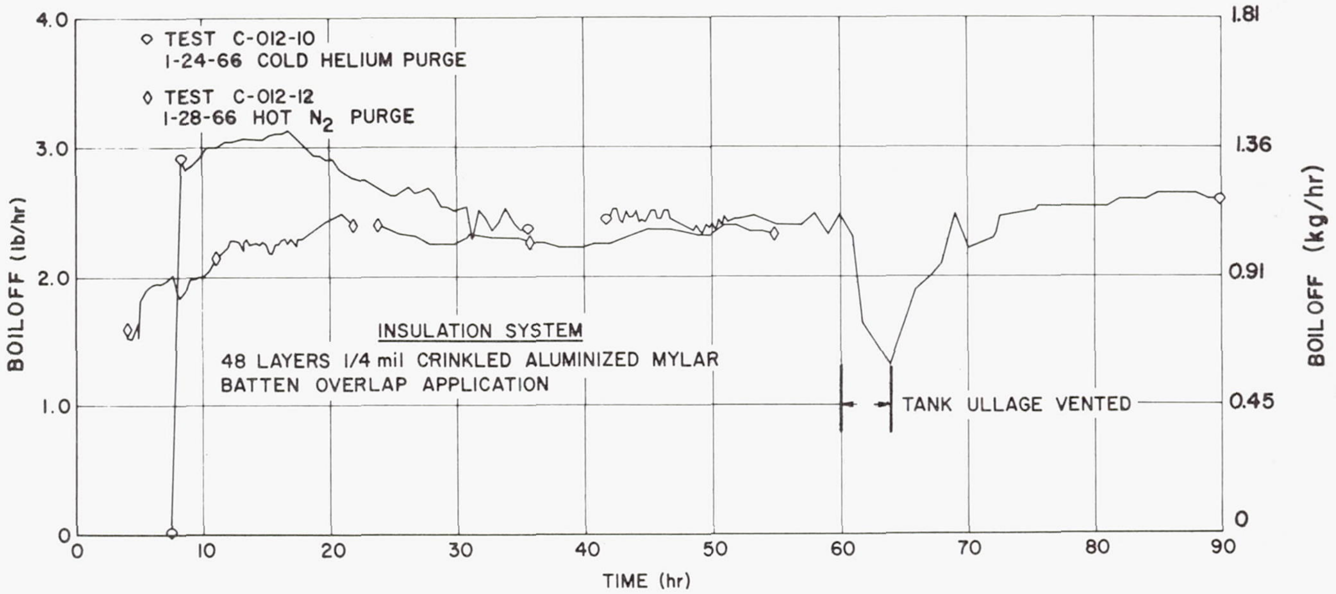

FIGURE 12. BOILOFF RATES FOR THE 2.67-m (105-in.) DIAMETER TEST TANK WITH DIFFERENT INSULATION PRECONDITIONING

The heat transfer rate through the tank sidewall was calculated at 62.1 W (212 Btu/hr) (Table I). This rate was one-half of the total measured heat leak. A gas analysis of the test tank, when filled with LH_2 and located in the vacuum chamber, showed no detectable amounts of GH_2 in the line to the insulation purge jacket. Yet, with the valve open to the purge jacket, the mass spectrometer measured 1.0% hydrogen gas concentration in the insulation system. This indicated a leak of unknown size at either the manhole cover or piping penetration seals. Therefore, with and without outgassing, the difference between computed heat transfer rates and test results on the 2.67-m (105-in.) diameter tank resulted from the increases in apparent thermal conductivity of the insulation caused by hydrogen gas leakage.

As reported by Crawford [9], a lenticular test tank, wrapped with 42 layers of 6.35-μ (1/4-mil) aluminized mylar insulation, was installed in a vacuum chamber. An equilibrium pressure level of 0.40 N/m^2 (3×10^{-3} torr) was measured in the mylar layers when the vacuum chamber pressure was at 1.33×10^{-4} N/m^2 (10^{-6} torr). Because of testing problems and errors, the thermal conductivity of an insulation sample purged with helium gas and located on a lenticular type tank was estimated at 1.95×10^{-3} W/m-°K (1.13×10^{-3} Btu/hr-ft-°F). This value was higher than expected. Even though the estimated thermal conductivity value might have been incorrect, the measured pressure of 0.40 N/m^2 (3×10^{-3} torr) under the insulation layers was thought to be accurate.

Since the higher than expected heat transfer rate through the lenticular tank sidewalls was apparently caused by high interstitial gas pressure, tests were made to find the cause for high pressure in the insulation layers. Water vapor at the 0.133 N/m^2 (10^{-3}mm Hg) level seemed to cause much delay in rapidly evacuating the insulation to the required pressure range of 1.33×10^{-2} to 1.33×10^{-3} N/m^2 (10^{-4} to 10^{-5} mm Hg). But, nitrogen outgassing from the insulation was the delaying factor in the 1.33×10^{-2} N/m^2 (10^{-4} mm Hg) range. However, a 394°K (250° F) helium purge for one hour, before exposing the insulation sample to LH_2, would remove the water vapor and decrease evacuation time significantly. Mass spectrometry work on samples of 6.35-μ (1/4-mil) aluminized mylar indicated no problems with helium sorption or desorption at ambient, LN_2 or LH_2 temperature. Next, a sample of 42 layers of 6.35-μ (1/4-mil) aluminized mylar with 0.5% open area [0.203-cm (0.080-in.) diameter holes on 2.54 cm (1.00 in.) centers] was perforated and applied to a lenticular test tank having a surface area of 2.43 m^2 (26.2 ft^2).

The sample, preconditioned with hot helium gas before testing, yielded a thermal conductivity of 8.21×10^{-5} W/m-°K (4.75×10^{-5} Btu/hr-ft-°R) at a corresponding measured insulation pressure of 2.4×10^{-3} N/m^3 (1.8×10^{-5} torr).

Consequently, optimum thermal performance of the insulation system on the 2.67-m (105-in.) diameter tank was precluded by insulation outgassing and hydrogen gas leakage in the insulation layers.

SYSTEM THERMAL PERFORMANCE

Measuring the boiloff rate of stored propellant is one way of evaluating how well an insulation system functions. For the 2.67-m (105-in.) diameter tank, curves 1, 2, and 3 of Figure 8 were plotted to show how this system would do with different thicknesses of insulation. Curve 1 was generated using a normal thermal conductivity of 5.19×10^{-4} W/m-°K (3×10^{-4} Btu/hr-ft-°R) and a constant penetration heat leak of 11.7 W (40 Btu/hr). Curve 1 shows that use of as much as 15.25 cm (6.0 in.) of insulation can significantly reduce the boiloff rate, even with the penetration heat leak of 11.7 W (40 Btu/hr) included. Curve 2, with normal insulation conductivity of 5.19×10^{-5} W/m-°K (3×10^{-5} Btu/hr-ft-°R) and constant penetration heat leak of 11.7 W (40 Btu/hr), shows that addition of more than 5.08 cm (2.0 in.) of insulation insignificantly lowers the boiloff rate. This results from the penetration heat leak rapidly becoming the principal heat source, so that the sidewall heat transfer rate contributes but a minor portion of the total. Curve 3 shows the importance of minimizing extraneous heat leaks, particularly with high performance insulation. Obviously, the theoretical boiloff rate continues to decrease as additional layers are used. An optimum insulation thickness occurs because the addition of more layers of insulation increases system mass.

Comparison of performance on a percent-per-day basis requires knowledge of tank size and shape, insulation thickness, and thermal conductivity factor. This is illustrated in Figure 13. In generating these curves, a cylindrical tank with hemispherical bulkheads, a length to diameter (L/D) ratio of 2, and no penetration heat leaks were assumed. Figure 13 shows that a propellant loss rate of 2% per day for the 2.67-m (105-in.) diameter tank would decrease to 0.5% boiloff per day for a vessel 10.06 m (33 ft) in diameter. Improving thermal conductivity to 8.65×10^{-5} W/m-°K (5×10^{-5} Btu/hr-ft-°R), would decrease the boiloff to 0.2% per day. An insulation thermal conductivity of 5.19×10^{-5} W/m-°K (3×10^{-5} Btu/hr-ft-°F) and an insulation thickness of 7.62 cm (3.0 in.) would decrease boiloff to 0.025% per day.

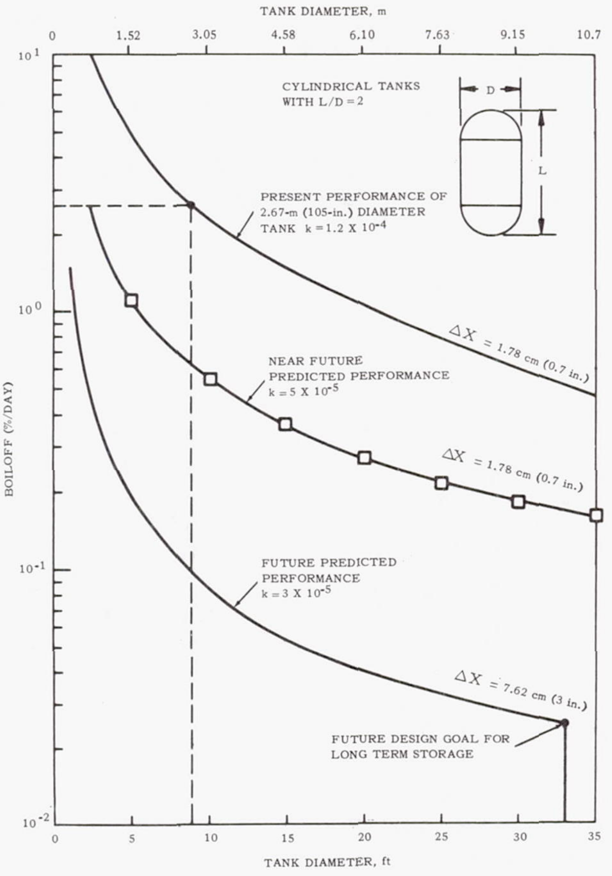

FIGURE 13. BOILOFF RATE AS A FUNCTION OF TANK DIAMETER

Figure 13 is illustrative only because penetration heat leaks have been neglected. To achieve this performance a program for improvement of multilayer insulation must be continued. The following discussion cites some of the parameters to be considered and the effort needed to exploit them.

LONG-TERM CRYOGENIC STORAGE

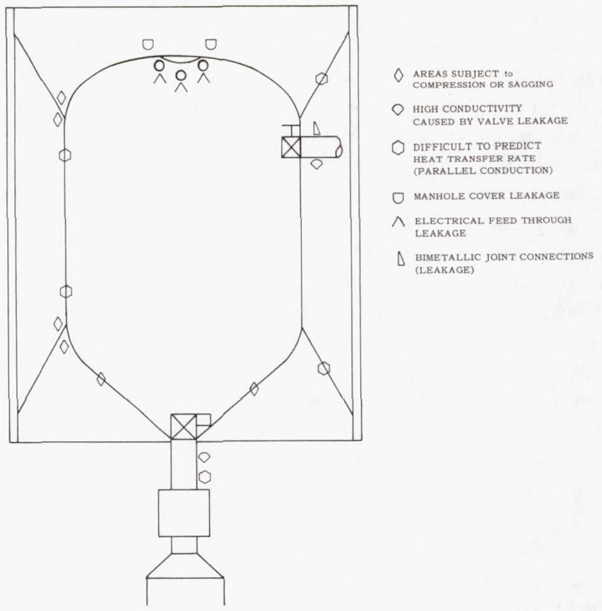

FIGURE 14. TYPICAL VEHICLE INSULATION CONSIDERATIONS

The application of HPI for long-term storage of cryogenics to a flight stage (such as the modular nuclear vehicle) demands careful study and correlation of many factors that are not critical for short-term storage designs. Figure 14 outlines a typical stage showing the basic considerations for applying high performance insulation to a flight-configuration tank. These problems can be combined into five major groups as follows: (1) insulation purging, venting, and evacuation, (2) component leakage and outgassing effects, (3) heat transfer through penetrations, (4) sidewall insulation design and optimization, and (5) accurate insulation system thermal tests. Each of these areas is discussed in the following sections.

INSULATION PURGING, VENTING AND EVACUATION

Rapid evacuation of insulation is necessary to maintain insulation structural integrity and to achieve desired thermal performance. As stated earlier, a purge system is used to remove air and moisture from within the insulation layers. The purge is maintained during ground hold and the insulation is allowed to vent during ascent. A large vent area for this escaping gas is required during ascent for a large flight stage. It is not practical, however, to have a huge exit pipe manifold on a large stage. A solution would be to develop a purge jacket that is gas tight for ground purging and would rupture during ascent. A purge jacket has been designed and fabricated with zipper inserts that will rupture at about 3 400 N/m^2 (0.5 psia) differential pressure and developmental testing will be completed in the immediate future.

Rapid evacuation of the insulation during ascent is important structurally. If the insulation is applied to a tank by a "continuous sheet" method, the purge gases must be vented through seams or holes caused by structural attachments. For thin layer applications, and small tank radii, venting of the purge gases without structural failure is possible. However, with large diameter tanks the insulation system becomes more susceptible to rupture during ascent (Fig. 15). Holes can be placed in the insulation for expediting evacuation and minimizing structural damage, but holes in the radiation shields decrease the insulation thermal performance (Fig. 16). These same perforations can be beneficial for minimizing insulation internal pressure resulting from material outgassing. Additional evacuation data as a function of perforated area and batten thickness are required to prevent overpressurization during ascent and yet provide adequate thermal performance in orbit.

Preliminary experiments using perforated, unperforated, and preconditioned aluminized mylar have been performed to determine the degree by which outgassing could be minimized or eliminated [10]. Results of three different tests are in Figure 17. An unperforated sample of insulation, preconditioned with hot helium gas (about 394°K, or 250°F) and a perforated sample purged with room temperature helium failed to yield pressures below the acceptable level of 0.0133 N/m^2 (10^{-4} torr). An insulation sample perforated with smaller diameter holes 0.318 cm (0.125 in.) on 5.08 cm (2 in.) centers and preconditioned with 394°K (250°F) helium gas yielded an acceptable level of 0.0133 N/m^2 (10^{-4} torr) in a reasonable amount of time. This test data indicated that both perforations and preconditioning will be required for rapid evacuation of insulation. Test fixtures are being designed and evacuation tests are being planned for insulation samples 0.915 m (3.0 ft) square and up to 22.9 cm (9.0 in) thick to further define the effect of outgassing, perforation and preconditioning on equilibrium insulation pressure.

Most insulation materials without spacers evacuate more rapidly than those with spacers. Although the more dense insulations with spacers do not evacuate as quickly as the lighter insulations, they may have uses in spacecraft. For example, if the final equilibrium pressure is at the same level within an

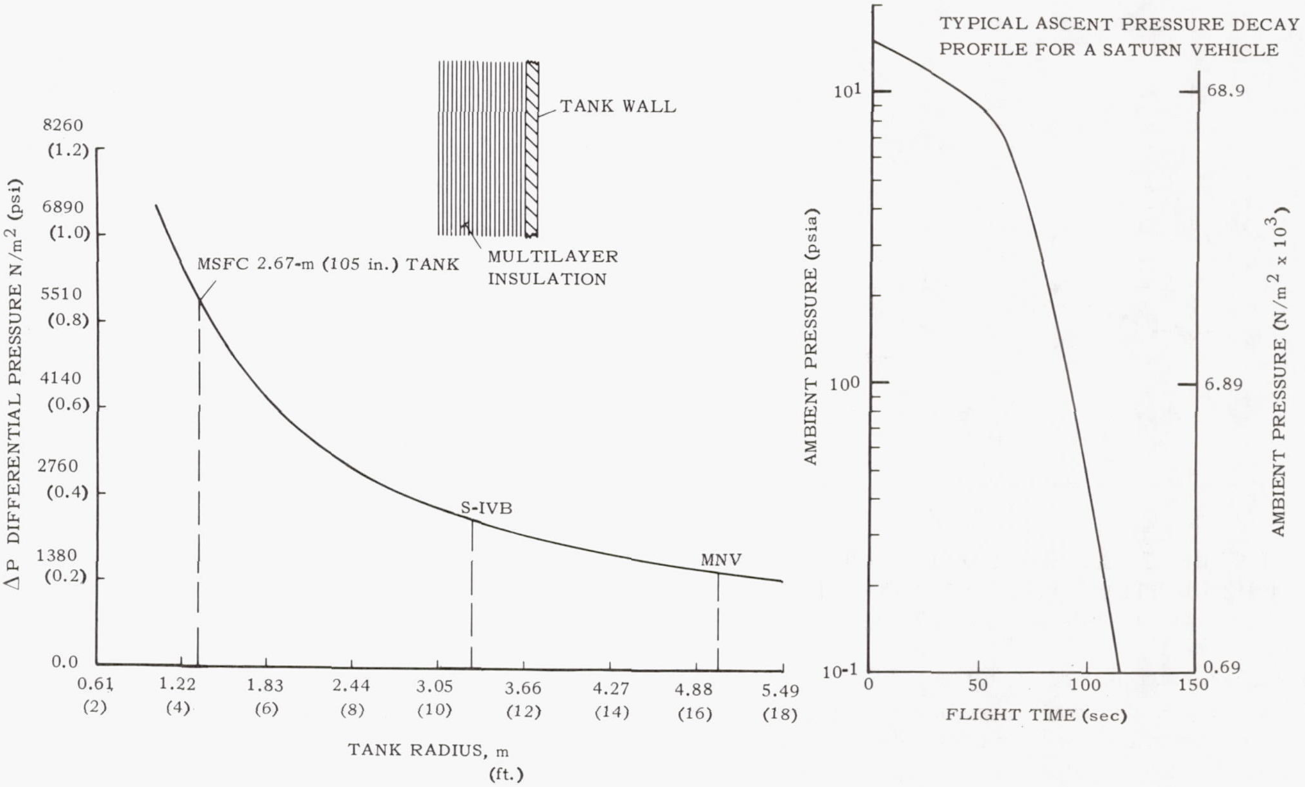

FIGURE 15. ALLOWABLE PRESSURE DROP ACROSS 6.35 μ (1/4 mil) MYLAR DURING BOOST FLIGHT

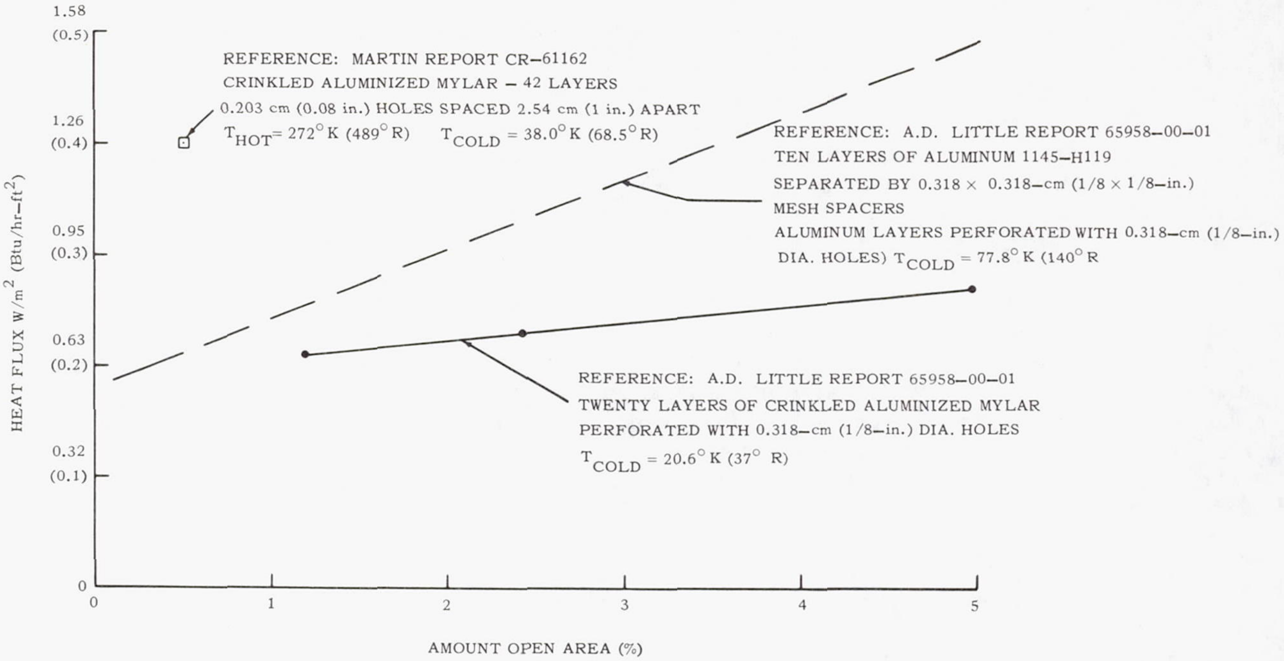

FIGURE 16. EFFECT OF PERFORATIONS ON THE HEAT FLUX THROUGH MULTILAYER INSULATIONS

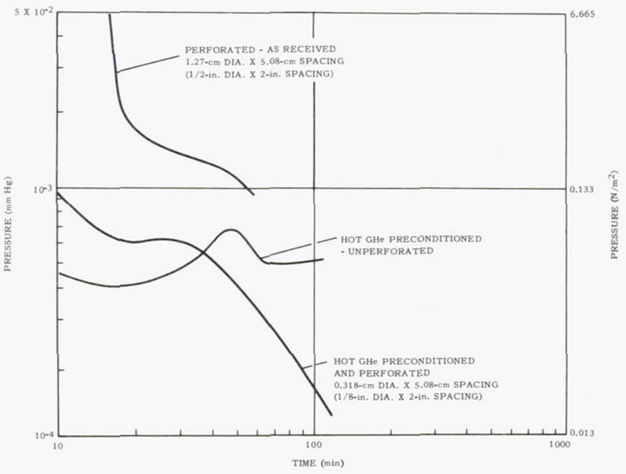

FIGURE 17. EVACUATION OF HOT HELIUM PRECONDITIONED AND PERFORATED NRC-2 AT LH_2 TEMPERATURE

insulation, and the pressure level is inadequate to reduce gas conduction, a significant difference in apparent thermal conductivity is noted for materials with and without spacers (Fig. 18). As shown throughout this paper, low insulation gas pressure is a must for good thermal performance. To accurately assess thermal performance, knowledge of the insulation gas pressure is required. Currently, the apparent thermal conductivity as a function of pressure is found by assuming that the pressures within insulation layers are the same as the local chamber pressure. This is not necessarily an accurate assessment, but, unfortunately, commercial vacuum gauges do not exist which will operate at LH_2 temperatures. Gauges that do exist are also too heavy and cumbersome and impossible to mount within the insulation. A cryogenic vacuum gauge that can be mounted within the insulation layers is being developed. In conclusion, more effort is needed to determine HPI thermal performance as a function of thickness, evacuation rates, and equilibrium pressure level within the layers.

INSULATION PRESSURE DECAY WITH OUTGASSING AND COMPONENT LEAKAGE

Material outgassing and component leakage from hardware such as ducting connections, manhole covers, and electrical connectors have been shown to seriously affect insulation equilibrium pressure, and thus ultimately affect the steady-state thermal performance of the insulation system. A study was

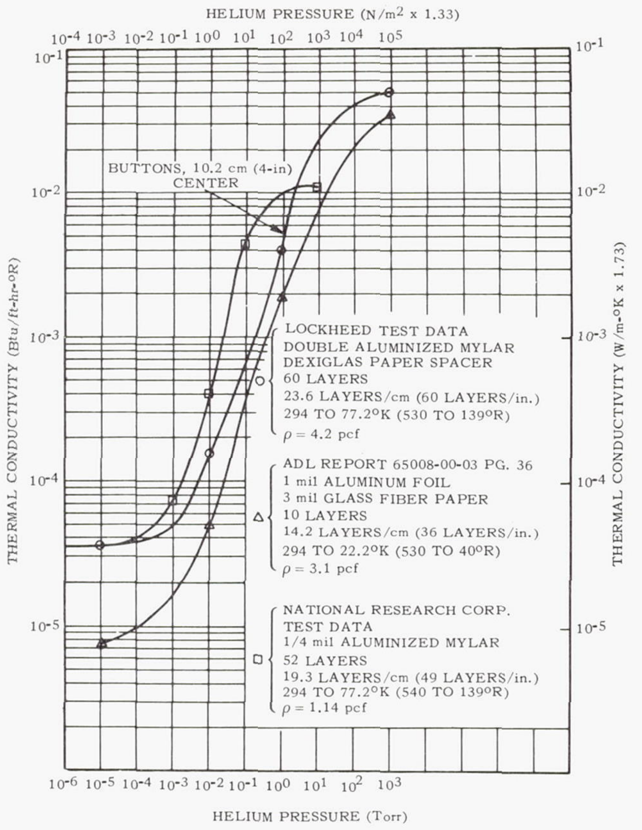

FIGURE 18. THERMAL CONDUCTIVITY OF INSULATION MATERIALS AS A FUNCTION OF HELIUM GAS PRESSURE

made to show the potential equilibrium pressure effect of leaking sources and outgassing within the insulation. Results are shown in Figure 19. The mathematical model chosen was a batten of insulation 137 cm (54 in.) long, 2.54 cm (1.0 in.) thick and infinitely wide. One end of the batten was assumed closed and all leakage or outgassing was assumed to flow through the batten (Fig. 19). Electrical connectors have a combined leakage rate large enough to possibly cause the pressure in the insulation layers to be more than four orders of magnitude higher than the local chamber pressure. Figure 20 shows typical cryogenic electrical connectors and their basic characteristics. The existing cryogenic electrical connector consists of a metal shell with a one piece molded glass insert and fused-in contacts. An important requirement of present electrical feedthrus is that the metal and glass of the feedthru must have matched expansion coefficients to prevent fluid leakage when subjected to required temperature variations. The glass-to-metal seal is also sensitive to mechanical shock and to temperature variations from welding during installation. As a result of these environments, connectors leak worse than when they are tested under less severe static conditions. Cryogenic electrical connector vendors quote a leak rate as low as 1×10^{-8} scc/sec, but connector leak rates of 1×10^{-2} scc/sec, and in some cases 3 scc/sec, have occurred in practical application.

Other parameters, such as electrical insulation resistance and humidity, affect the connector fluid leakage. The optimum glass composition for minimizing the connector leakage has an electrical insulation resistance below the required value. To date, a glass material has not been found with both a low leak rate and a high electrical insulation resistance. A future cryogenic electrical connector required to satisfy both the electrical and low leakage requirements is shown conceptually in Figure 20. Research continues on a search to find an acceptable insert material.

Leakage through the valve seat and valve actuator of fill and drain valves can result in high heat leaks down the penetration because gas will accumulate in the duct. Leakage through the valve actuator can also cause an increase in insulation conductivity if the escaping gas passes through the insulation. The leakage problem through the actuator can be solved by submerging the valves in the cryogen. Valves have been recently developed that will operate while submerged in liquid hydrogen. This advance in valve design results from using bellows instead of dynamic seals in the valve actuator housing. With the bellows, the valve actuator can withstand liquid hydrogen temperatures, but leakage past the ball or the seal have not been eliminated. For short-term missions, this leakage can be tolerated. For longer missions, valve designs with a shear diaphragm of some type will be required and feasibility studies are underway (Fig. 21).

Gas leakage through separable ducting connectors degrades insulation thermal performance. Welding of aluminum ducting to aluminum tanks would eliminate gas leakage, but use of high conductivity aluminum would cause intolerable heat transfer rates. Presently, low thermal conductivity stainless steel ducts cannot be welded directly to aluminum tanks. Thus, a separable flanged type design is required. Likewise, the large manhole cover usually requires a similar type flange design. The recent development of the diffusion bonded joint (Fig. 22) represents a significant technological breakthrough. The leak rate for the diffusion bonded joint is so infinitesimal that it is virtually non-existent. However, the joint can be used only a few times because of a limited amount

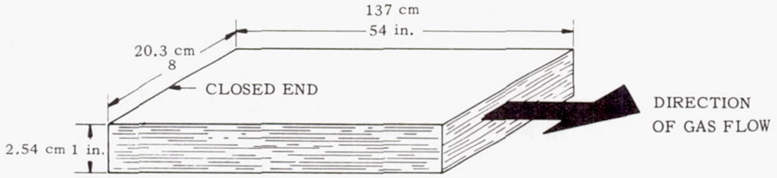

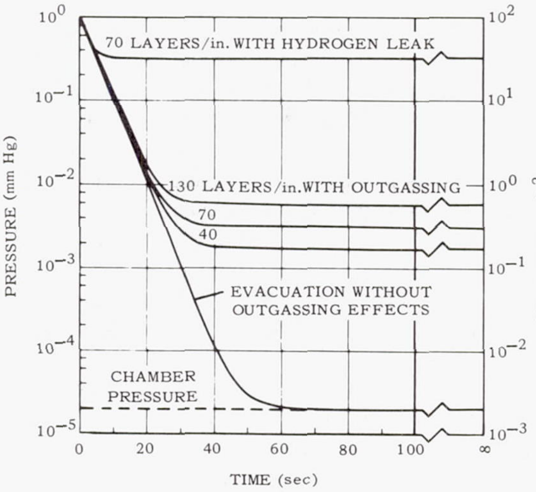

ASSUMPTIONS:

1. HYDROGEN DIFFUSION COEFFICIENT: 0. 253 m^2/sec (2. 72 ft^2/sec)
2. HELIUM DIFFUSION COEFFICIENT: 0. 1785 m^2/sec (1. 92 ft^2/sec)
3. CHAMBER PRESSURE: 2. 67 × 10^{-3} N/m^2 (2 × 10^{-5}mmHg)
4. OUTGASSING COEFFICIENT: 0. 1076 $\mu\ell/m^2$–sec (0. 01 micron liter/ft^2–sec)
5. TEMPERATURE: 55. 5° K (100° R)
6. HYDROGEN LEAK RATE: 0. 0487 kg/m^2–sec (0.01 lb/sec–ft^2)

105 in. TANK LEAK SOURCE	LEAK RATE (STD cc/sec)
1 MANHOLE COVER 3 PIPING PENETRATIONS 3 WIRE CONNECTORS	3 × 10^{-4} 3 × 10^{-4} 3. 00
TOTAL	3. 0006

FIGURE 19. EFFECTS OF LEAKS AND OUTGASSING ON PRESSURE AT CLOSED END OF 6. 35 μ (1/4 mil) ALUMINIZED MYLAR INSULATION BATTEN

CRYOGENIC CONNECTOR	TEMPERATURE RANGE	PINS SUBJECT TO DAMAGE	SUSCEPTIBLE TO PIN CONTACT CHATTER	REUSABLE	APPROXIMATE TOTAL LEAK RATE STD cc/sec
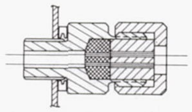 CONAX	WIDE RANGE (DEPENDING ON SEALING MATL.)	NO	YES	YES	10^{-1} - 1.0 1.0 MINIMUM AFTER VIBRATION
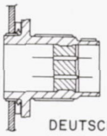 DEUTSCH BOSS TYPE	WIDE RANGE (DEPENDS ON WIRE INSULATION)	YES	YES	YES	10^{-2} - 1.0 DETERIORATES AFTER BEING SUBJECT TO VIBRATION
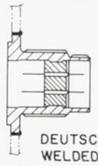 DEUTSCH WELDED TYPE	WIDE RANGE (DEPENDS ON WIRE INSULATION)	YES	YES	NO	10^{-5} - 3.0 DETERIORATES RAPIDLY AFTER BEING SUBJECT TO VIBRATION
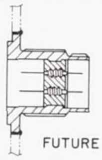 FUTURE	WIDE RANGE (DEPENDS ON WIRE INSULATION)	YES	NO	NO	10^{-7} - LITTLE EFFECT FROM VIBRATION

FIGURE 20. LEAKAGE CHARACTERISTICS OF CRYOGENIC ELECTRICAL FEEDTHRU CONNECTORS

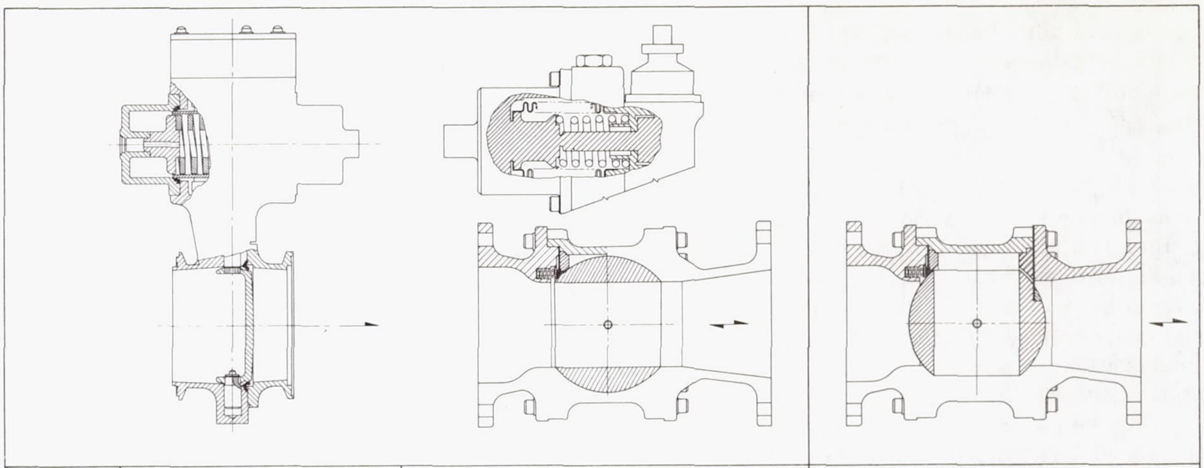

	PAST	PRESENT	FUTURE
• VALVE SEAT LEAKAGE	80 STD cc/sec	9 STD cc/sec	0 STD cc/sec (9 STD cc/sec AFTER SHEAR DIAPHRAGM HAS BEEN BROKEN)
• ACTUATOR LEAKAGE	66 STD cc/sec (DYNAMIC SEALS)	0 STD cc/sec (BELLOWS TYPE)	0 STD cc/sec (BELLOWS TYPE)
• TEMPERATURE RANGE	ACTUATOR TEMPERATURE LIMITED TO 200 to + 366°K (-100 to +200°F) FLOW CHAMBER 20.5 to + 505°K (-423 to + 450°F)	20.5 to + 505°K (-423 to +450°F)	20.5 to + 505°K (-423 to +450°F)

FIGURE 21. VALVES FOR CRYOGENIC TANK APPLICATION

	WEIGHT kg (lb)	FLANGE O.D. / DUCT O.D.	LEAKAGE RATE STD. cc/sec	ASSEMBLY PROBLEMS	SURFACE REQUIREMENTS	REUSABILITY	FLANGE COST	SEAL COST
NAFLEX SEAL 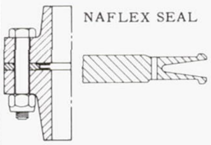	2.50 (5.5)	1.7	10^{-4} PRIMARY, DRAIN OVERBOARD	SEAL HANDLING	FLATNESS 0.051 mm (0.002 in.) SURFACE QUALITY 32	YES	LOW	HIGH
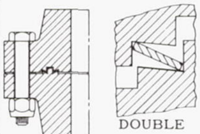 DOUBLE CONO SEAL	3.23 (7.1)	1.8	10^{-6} PRIMARY, DRAIN OVERBOARD	SEAL HANDLING, CAREFUL INSTALLATION	SAME	CHANGE SEALS	HIGH	LOW
 DIFFUSION BOND	1.23 (2.7)	1.2	10^{-12}	PREFABRICATED JOINT, IN-PLACE WELD OF DUCT STUBS	CLEAN	CUT AND WELD	VERY LOW	DIFFUSION BONDING PROCESS (PLATING, BONDING) HIGH

FIGURE 22. DUCT JOINT ATTACHMENT CONCEPTS FOR DISSIMILAR METALLIC JOINTS

of metal available for rewelding. Tests are in progress to flight qualify the diffusion bonded joint as well as other recently developed bimetallic joints using different joining techniques.

Resulting gas leakage at ducting seals or manhole covers can be stopped under any environmental load by simply using a very heavy, rigid non-deforming flange. However, excessive flange mass and materials aspects will not permit such a simple solution for most spacecraft applications. Seals available for consideration for such applications can be separated into five different types (Fig. 23). Only types four and five, the conoseal and weld ring (omega seal) have acceptable leakage characteristics for HPI applications and each of these has disadvantages. The conoseal requires a high bolt loading, does not fit a standard flange, and cannot be reused, yet currently this is the best available gasket connection for use on tanks with multilayer insulation.

The welded ring (omega seal) is the most desirable for reducing leakage; still, it also has some undesirable mechanical features. In place welding of the ring requires two concentric welds of good quality, and a third weld in the center of the ring is required for sealing and must be ground off and rewelded after entry. Limited material for rewelding restricts reusability of this seal. Also, heat generated during the welding process can melt the insulation if it is not removed or thermally protected. In spite of these disadvantages, experimental development of this sealing method is continuing because of a demonstrated low leak rate.

PENETRATION HEAT TRANSFER PREDICTION

Heat transfer through cryogenic tank supports and penetrations is difficult to predict accurately.

CRYOGENIC MANHOLE GASKETS	REUSABLE	FLANGE LOADING REQUIREMENTS	FITS STANDARD FLANGE	GROOVE SURFACE PROTECTED	SENSITIVE TO FLANGE DEFLECTION	SENSITIVE TO RADIAL SCRATCHES	LEAK RATE $\frac{\text{STD cc}}{\text{sec He}}$
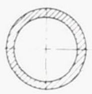 TEFLON COATED "O" RING	YES	HIGH 35.8 – 500 kg/circ. cm (200 – 2800) (lb/circ. in)	YES	YES	YES	YES	1×10^{-2}
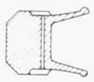 GROOVE TYPE "K" SEALS	YES	LOW 5.36 – 10.7 kg/circ. cm (30 – 60) (lb/circ. in.)	YES	YES	YES	YES	1×10^{-4}
 SPACER NAFLEX SEAL	YES	MEDIUM 12.5 – 17.9 kg/circ. cm (70 – 100) (lb/circ. in.)	YES	NO	YES	YES	1×10^{-4}
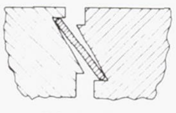 CONO SEAL	NO	HIGH 89.5 – 107 kg/circ. cm (500 – 600) (lb/circ. in.)	NO	YES	NO	NO	1×10^{-6}
 FUTURE OMEGA SEALS	YES	LOW	YES	YES	NO	NO	1×10^{-12}

FIGURE 23. CRYOGENIC SEALS FOR LARGE FLANGES

For irregular tank penetration geometries, a finite difference heat transfer program is essential to predict the heat transfer rate. A mathematical model of the penetration is broken up into nodes of finite length, depth, and width. A thermal resistance factor is then computed for each node, and data must be available on the apparent thermal conductivity of the insulation material as a function of temperature.

However, most thermal conductivity data for multilayer insulation material were obtained using either liquid hydrogen or nitrogen as the cold boundary temperature with the warm side boundary temperature varied between 111 and 333°K (200 and 600°R) (Fig. 24). A few data points were obtained using Freon 12 as a cold sink. The test data indicate that the apparent thermal conductivity of HPI is approximately a factor of three higher at the temperature of Freon 12 than at LH_2 or LN_2 temperatures.

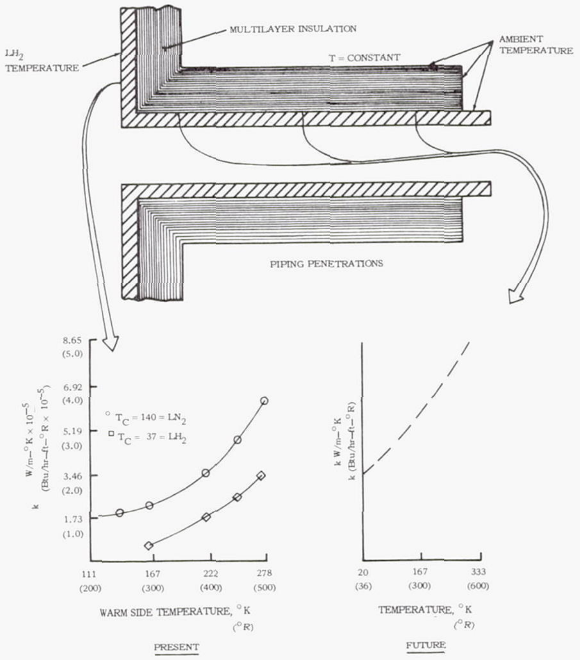

FIGURE 24. POTENTIAL PENETRATION HEAT LEAK ERROR

Unlike tank sidewall heat transfer problems, the penetration hot boundary temperature remains constant and the cold boundary temperature is the variable. Since most data are now input to computer programs as a function of warm side boundary temperature only, a more accurate appraisal of the heat transfer through penetrations demands data input with the warm boundary temperature being a constant and the cold boundary temperature being a variable. Thus, for accuracy, the thermal conductivity data for the computer programs should be independent of the warm and cold boundary temperatures and large temperature differentials (Fig. 25). For the above reasons, a feasibility study has been performed, a calorimeter designed, and preliminary thermal conductivity data are being obtained for different multilayer insulation materials as a function of temperature. Detailed reports of this progress will be available in the near future.

TANK SIDEWALL INSULATION SYSTEM DESIGN

Insulation performance in the applied condition can be significantly affected by attachment methods. Figure 26 shows some different schemes that may be used to attach insulation to the tank sidewall. The results of the study (Fig. 26) were based on a theoretical application to the MSFC 2.67-m (105-in.) diameter tank. Column one in Figure 26 shows the difference in heat transfer rates for different pin materials used for structural attachments. Note the very small difference in computed heat transfer rates when either aluminum or nylon pins were used in concepts A, B, and C. For concept D, however, the uninsulated aluminum pin can cause a 10% increase over the computed heat transfer value for the nylon pin.

The second column, Figure 26, shows the equivalent conductivity of each concept: the product of the total heat flow into the tank and insulation thickness divided by the product of tank surface area and temperature difference through the insulation. This is essentially a systems performance index; in all cases, the equivalent thermal conductivity of the insulation is always greater than the basic thermal conductivity.

The third column in Figure 26 is an estimate of the number of equivalent layers in each concept. A performance-mass comparison can be made for the four concepts. The kN factor in the last column of Figure 26 is the product of the equivalent number of layers and the equivalent thermal conductivity. The lower the kN factor, the better the insulation system. From Figure 26, concept C was predicted to be the best system, with concept D almost as good. Because of manufacturing difficulties and the relatively close kN factors for concepts C and D, concept D would probably be chosen for further study. These concepts were studied for their thermal performance only. This study assumed that each system was fully

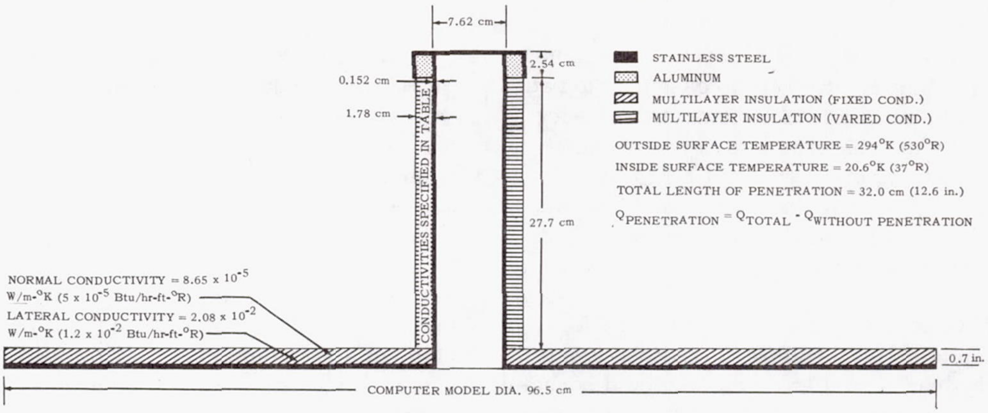

CASE	NORMAL CONDUCTIVITY W/m-°K (Btu/hr-ft-°R)	LATERAL CONDUCTIVITY W/m-°K (Btu/hr-ft-°R)	PENETRATION HEAT LEAK W (Btu/hr)	INCREASE IN HEAT LEAK (PERCENT)
1	8.65×10^{-5} (5×10^{-5})	2.08×10^{-2} (1.2×10^{-2})	3.33 (11.36)	0
2	8.65×10^{-4} (5×10^{-4})	2.08×10^{-2} (1.2×10^{-2})	3.50 (11.93)	5
3	8.65×10^{-3} (5×10^{-3})	2.08×10^{-2} (1.2×10^{-2})	4.70 (16.02)	41
4	8.65×10^{-2} (5×10^{-2})	2.08×10^{-2} (1.2×10^{-2})	7.66 (26.18)	130

FIGURE 25. HEAT TRANSFER THROUGH INSULATED PENETRATION WITH DIFFERENT INSULATION CONDUCTIVITIES

INSULATION SYSTEM DESIGN	Q_{DIST} FOR 2.67–m (105–in.) TANK W (Btu/hr)	k_{EQUIV} W/m–°K (Btu/hr–ft–°R)	AVERAGE NO. OF LAYERS DUE TO STRUCTURAL ATTACHMENTS	Q_{UNDIST} 200 LAYERS W (Btu/hr)	PERCENT INCREASE IN Q DUE TO DISTURBANCE (%)	kN FACTOR W/m–°K (Btu/hr–ft–°R)
A 	ALUMINUM PIN 16.8 (57.2)	11.93×10^{-5} (6.9×10^{-5})	277	10.7 (37.86)	51.1	3.30×10^{-2} (1.91×10^{-2})
	NYLON PIN 16.7 (57.0)	11.91×10^{-5} (6.89×10^{-5})	277	10.7 (37.86)	50.6	3.30×10^{-2} (1.91×10^{-2})
B 	ALUMINUM PIN 18.3 (62.5)	15.32×10^{-5} (8.86×10^{-5})	326	10.7 (37.86)	65.1	4.95×10^{-2} (2.86×10^{-2})
	NYLON PIN 18.2 (62.2)	15.27×10^{-5} (8.82×10^{-5})	326	10.7 (37.86)	64.3	4.95×10^{-2} (2.86×10^{-2})
C 	ALUMINUM PIN 20.7 (70.6)	9.70×10^{-5} (5.61×10^{-5})	190	10.7 (37.86)	86.4	1.85×10^{-2} (1.07×10^{-2})
	NYLON PIN 19.6 (66.9)	9.56×10^{-5} (5.53×10^{-5})	190	10.7 (37.86)	76.8	1.82×10^{-2} (1.05×10^{-2})
D 	ALUMINUM PIN 21.9 (74.8)	11.25×10^{-5} (6.5×10^{-5})	200	10.7 (37.86)	97.5	2.25×10^{-2} (1.30×10^{-2})
	NYLON PIN 19.8 (67.6)	10.13×10^{-5} (5.86×10^{-5})	200	10.7 (37.86)	78.5	2.02×10^{-2} (1.17×10^{-2})

GENERAL ASSUMPTIONS
1. ¼mil SINGLE ALUMINIZED MYLAR
2. 200 LAYERS
3. 235 ANGSTROM ALUMINUM COATING
4. 133 LAYERS/in.
5. SURFACE TEMPERATURE 530°R & 37°R
6. UNCOMPRESSED AREAS
$K_{\perp} = 5 \times 10^{-5}$ Btu/hr-ft-°R
$K_{\parallel} = 2 \times 10^{-2}$ Btu/hr-ft-°R

SPECIFIC ASSUMPTIONS (A, B, C)
1. COMPRESSED AREAS:
$K_{\perp} = 7 \times 10^{-2}$ Btu/hr-ft-°R
$K_{\parallel} = 7.5 \times 10^{-2}$ Btu/hr-ft-°R
2. PIN SIZE:

LENGTH	0.400 in.
O.D.	0.250 in.
I.D.	0.125 in.

SPECIFIC ASSUMPTIONS (D)
1. PIN AREA:
$K_{\perp} = 2 \times 10^{-3}$ Btu/hr-ft-°R
$K_{\parallel} = 4.6 \times 10^{-2}$ Btu/hr-ft-°R
2. PIN SIZE:

LENGTH	1.500 in.
O.D.	0.250 in.
I.D.	0.125 in.

FIGURE 26. COMPARISON OF DIFFERENT INSULATION SYSTEM DESIGNS

evacuated and posed no venting problems during the boost phase of flight. The study showed that the same insulation, when applied in different system configurations, optimizes differently on a thermal conductivity-density basis, and that degrading factors should be used in optimization studies. Programs are now underway to obtain more realistic performance factors for insulation systems.

TESTING OF MULTILAYER INSULATION CONCEPTS

Large vessels at least 2. 44 m (8 ft) in diameter are desirable for studies of thermal systems using high performance insulation. In most cases, this size permits a reasonable simulation of the applied insulation concept to be used for a much larger tank. Application problems, such as structural supports, double contour surfaces, piping penetrations and areas subject to compression or sagging, can be simulated with this type of test tank. Also, sidewall insulation can be simulated because most proposed concepts have been applied in panels. In addition, the larger surface area of a large test tank allows better simulation of gas flow characteristics for all three phases of flight: prelaunch, ascent, and simulated space environments.

Figure 27 is an example of typical errors in thermal conductivity to be expected for vessels the size of the 2. 67-m (105-in.) diameter tank. The

$$\frac{dk}{k}=\frac{d\dot{M}h_{fg}+\dot{M}dh_{fg}+\left[\left(dM_{LI}-d\Delta M_L\right)C_{PL}\Delta T_L+dC_{PL}\Delta T_L\left(M_{LI}-\Delta M_L\right)+d\left(\Delta T_L\right)C_{PL}\left(M_{LI}-\Delta M_L\right)+M_wC_{Pw}d\left(\Delta T_L\right)\right]/\Delta\theta+d\dot{M}C_{Pg}\Delta T_g+\dot{M}C_{Pg}d\left(\Delta T_g\right)+dQ_P}{\dot{M}h_{fg}+\left[\left(M_{LI}-\Delta M_L\right)C_{PL}\Delta T_L+M_wC_{Pw}\Delta T_L\right]/\Delta\theta+\dot{M}C_{Pg}\Delta T_g-Q_P}+\frac{d\Delta x}{\Delta x}$$

ASSUMPTIONS

1.	ULLAGE PRESSURE CONTROL (ΔP)	3440 N/m^2	(0.50 psi)
2.	ERROR IN PRESSURE MEASUREMENT (dP)	826 N/m^2	(0.12 psi)
3.	FLOWMETER ERROR		3.00%
4.	ERROR IN INSULATION THICKNESS MEASUREMENT ($d\Delta x$)	0.254 cm	(0.10 in.)
5.	ULLAGE HEATING (ΔT_g)	19.4° K	(35.00° R)
6.	ERROR IN ULLAGE HEATING ($d\Delta T_g$)	0.167° K	(0.30° R)
7.	LENGTH OF TEST ($\Delta\theta$)		120.00 hr
8.	THERMAL CONDUCTIVITY (k)	8.65×10^{-5} W/m–° K	(5×10^{-5} Btu/hr–ft–° R)

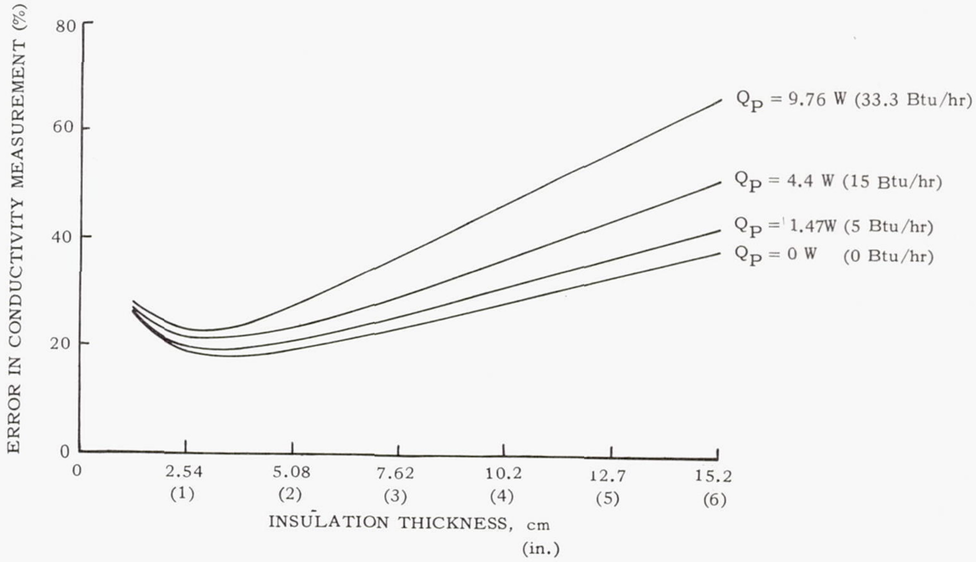

FIGURE 27. ESTIMATED INSULATION THERMAL CONDUCTIVITY ERRORS USING 2. 67-m (105-in.) DIAMETER TEST TANK

error from measuring the performance of HPI concepts can be significant. To determine apparent thermal conductivity of an insulation system applied to a test vessel, the total heat flow must be established and extraneous heat leaks must be calculated and subtracted from the total heat input to the cryogen. To measure total heat flow, measurements such as temperature, pressures, insulation thickness, and boiloff rates are needed. Errors are inherent in each of these measuring instruments as well as in the recording system read-out devices. Many instrumentation measurements and fluid properties are also needed to reduce the boiloff data to an apparent thermal conductivity value as shown in the equation in Figure 27 (see Appendix A). These measured values, such as pressure and temperature, are also used in equations to find fluid properties (enthalpy, specific heat, internal energy, density and latent heat of vaporization). Each of these equations is a curve that has been obtained from experimental data; thus a tolerance is placed on the computed properties that introduces additional measured thermal conductivity error.

An equation for establishing the apparent thermal conductivity error has been programmed for computer solution. Some results from such studies are as follows: (1) control of ullage pressure becomes more important as the penetration heat leak is reduced, (2) for thick insulation applications, it is important to minimize penetration heat leaks, (3) ullage pressure control becomes less critical as insulation thickness is decreased, and (4) accurate computation of penetration heat leaks is important.

An important parameter in the error analysis is the tank diameter. As tank size increases, the sidewall heat transfer rate increases and minimizes the effect of the penetration heat leak error. However, as the volume increases, the error in the computed stored energy of the test fluid increases, resulting in a practical limiting tank diameter. A tank diameter of about 2.44 to 3.05 m (8 to 10 ft) was the optimum size (Fig. 28). The slope of the thermal conductivity error versus tank diameter may take on a new shape, and a new optimum diameter may be found if other parameters (such as insulation thickness, tank shape, penetration heat leak, and instrumentation errors) are varied. Therefore, accuracy of the experimental data of an insulation system must be found after all variables in the equation in Figure 27 have been studied.

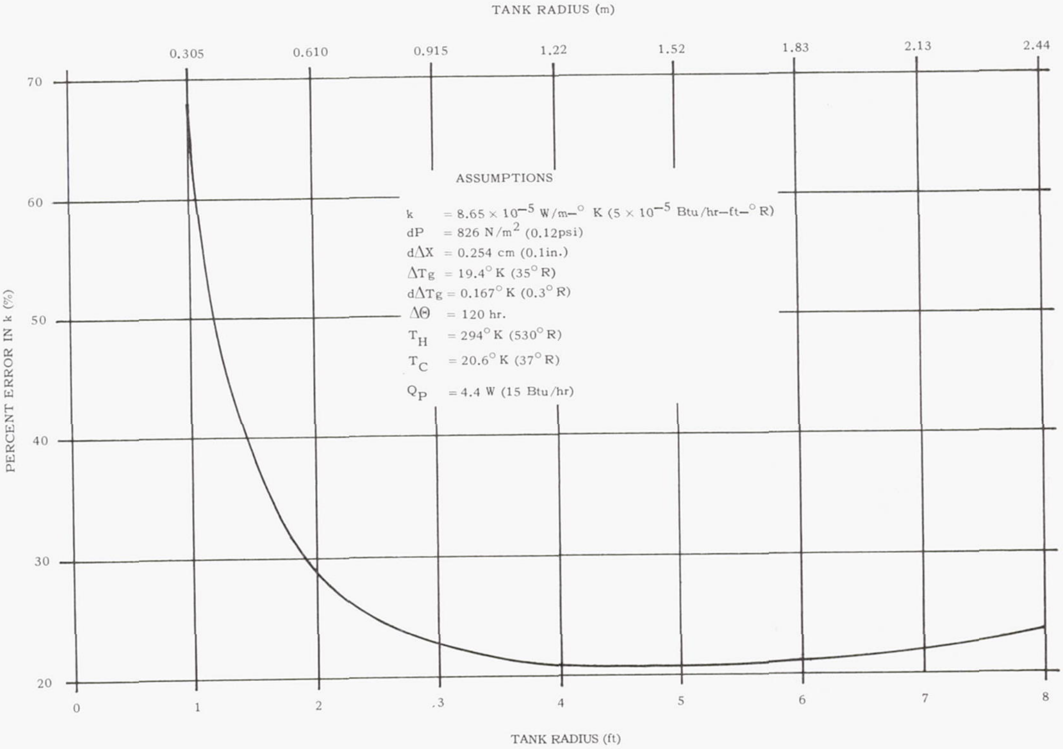

ASSUMPTIONS

$k = 8.65 \times 10^{-5}$ W/m–° K (5×10^{-5} Btu/hr–ft–° R)
$dP = 826$ N/m^2 (0.12psi)
$d\Delta X = 0.254$ cm (0.1in.)
$\Delta Tg = 19.4°$ K (35° R)
$d\Delta Tg = 0.167°$ K (0.3° R)
$\Delta\Theta = 120$ hr.
$T_H = 294°$ K (530° R)
$T_C = 20.6°$ K (37° R)
$Q_P = 4.4$ W (15 Btu/hr)

FIGURE 28. THE ERROR IN SUPERINSULATION THERMAL CONDUCTIVITY VERSUS TANK RADIUS

CONCLUSIONS

Acceptable insulation system performance for short term missions was obtained from the shingle insulation concept applied on the 2.67-m (105-in.) diameter tank. The experience derived from the test tank program helped in identifying additional development problems requiring solutions before multilayer insulation can be used for long term storage.

Insulation evacuation can be improved by the use of preconditioning and perforation. A lightweight purge jacket has been designed to rupture during vehicle ascent to allow the insulation to expand and quickly obtain an equilibrium pressure within the insulation layers. Leakage into the insulation can be reduced by installing diffusion bonded joints at ducting connections, welded omega seals at manhole covers, and submersible fill valves in fill and drain lines. The development of a low leak rate flight type electrical connector is in progress. Thermal conductivity measurements as a function of temperature are currently being generated, and techniques are being improved for computing penetration heat leaks through structural supports, ducting connections and insulation attachments. The development of a low temperature vacuum gage for use with multilayer insulation is in progress.

The design, fabrication, and application of multilayer insulation to flight configuration vessels has been successfully demonstrated. Research is continuing on problems now partially solved, and research programs have been initiated to solve those remaining problems. As a result of the above efforts, application of an insulation system to a large flight stage appears to be practical for long term storage of cryogenics.

REFERENCES

1. Duggan, J. B.: Evacuation of Gases from Batten of Multi-Layer Insulation in a Vacuum Environment. Brown Engineering Co., Inc., Huntsville, Alabama TD-D1-PTE-011 Phase D, August 26, 1966.

2. Shea, D. C., ed.: 3-D Insulation Penetration Model Program Modification. Lockheed Missiles and Space Co., Huntsville, Alabama, Contract NAS8-20438, DCN 1-7-52-20060, Monthly Progress Report LMSC/HREC A784249, 10 May 1967.

3. Powell, R. L.; and Blandied, W. A.: Thermal Conductivity of Metals and Alloys at Low Temperatures. National Bureau of Standards, September 1, 1954.

4. Cody, J. C.; and Hyde, E. H.: Thermal Problems Associated with the Development of a Flight Configured Cryogenic Insulation System. Marshall Space Flight Center, Proceedings of the Conference on Long Term Cryo-Propellant Storage in Space, October 1966.

5. Getty, R. C.: Cryogenic Insulation Development. Monthly Progress Report for November, General Dynamics, Convair, Contract NAS8-18021, 10 December 1966.

6. Getty, R. C.: Cryogenic Insulation Development. Monthly Progress Report for March, General Dynamics, Convair, Contract NAS8-18021, 3 April 1967.

7. Harsh, M. George; and Humphries, William R., ed.: NRC-2 Super Insulation Groundhold and Altitude Tests C-012-4, 5, 7, 10, 11, 12, 13, 15, 16, 17 and 18. George C. Marshall Space Flight Center, Report R-TEST-CT-129-66, 15 December 1966.

8. Niedorf, L. R.: Investigation of a Lightweight Self-Evacuating Prefabricated Multi-Layer Insulation System for Cryogenic Space Propulsion Stages. Quarterly Progress Report Number 1, Linde Company, Contract NAS3-6289, December 16, 1965.

9. Crawford, R. F.; and Hannah, R. G.: Cryogenic Insulation Research, ER 14361, Martin Co., Baltimore Division, Contract NAS8-11397, Sept. 1966.

10. Crawford, R. F.; and Hannah, R. G.: Cryogenic Insulation Research. Final Report, Contract Number NAS8-11397, The Martin Company, CR-61162, January 23, 1967.

BIBLIOGRAPHY

1. Arthur D. Little, Inc.: Basic Investigation of Multi-Layer Insulation Systems. Contract Number NAS3-4181, (ADL 65958-00-01), February 29, 1964.

2. Brogan, J. J.: Design of High Performance Insulation Systems. Summary Report, Lockheed/Sunnyvale, Contract NAS8-11347, August 20, 1965.

3. Cox, J: The Effects of Temperature Dependent Insulation Thermal Conductivity of Penetration Heat Leak. Brown Engineering Co., Inc., Huntsville, Alabama, TE-D1-PTE-011 Phase 23, April 4, 1967.

4. Cox, J.: and Duggan, J. B.: An Analysis of the Errors Involved in Measuring the Thermal Conductivity of Multi-Layer Insulations by Cryogenic Calorimeter Techniques. Brown Engineering Co., Inc., Huntsville, Alabama, TD-D1-PTE-011, Phase 23, May 1, 1967.

5. Design Techniques for Structures - Cryogenic Insulation Integration. Final Report, Contract NAS8-5268, The Martin Company, NASA CR-61038, January 25, 1965.

APPENDIX A

SYMBOLS FOR EQUATION IN FIGURE 27

k	Conductivity of wall insulation, $\frac{W}{m\text{-}^\circ K}\left(\frac{Btu}{hr\text{-}ft\text{-}^\circ R}\right)$
Δx_{ave}	The average tank wall insulation thickness,cm (in.)
Q_P	The heat leak through the penetration, W (Btu/hr)
$\dot{M}$	Mass flow rate of GH_2 out of tank, kg/hr (lb/hr)
M_{L1}	Mass of LH_2 in tank at start of test, kg (lb)
ΔM_L	Mass of H_2 evaporated during the test, kg (lb)
M_W	Mass of tank wall, kg (lb)
C_{PL}	Specific heat of the LH_2, $\frac{J}{kg - ^\circ K}\left(\frac{Btu}{lb - ^\circ R}\right)$
C_{PW}	Specific heat of the tank wall, $\frac{J}{kg - ^\circ K}\left(\frac{Btu}{lb - ^\circ R}\right)$
C_{Pg}	Specific heat of the ullage gas, $\frac{J}{kg - ^\circ K}\left(\frac{Btu}{lb - ^\circ R}\right)$
$\Delta\theta$	The length of time the test is run, hr
ΔT_L	$T_{L2} - T_{L1}$, °K (°R) {difference in LH_2 temperature at start and end of test}
ΔT_g	$T_{gA} - T_{gL}$, °K (°R)
h_{fg}	Latent heat of vaporization for the LH_2, $\frac{J}{kg}\left(\frac{Btu}{lb}\right)$
dQ_P	The estimated error in Q_P, W (Btu/hr)
$d(\Delta x_{ave})$	The instrument error in measuring the thickness of the insulation, cm (in.)
$d\dot{M}$	The error in $\dot{M}$ as a result of measurement error, $\frac{kg}{hr}\left(\frac{lb}{hr}\right)$
dM_{L1}	The error in M_{L1} caused by inaccuracy in calculating the density, kg (lb)
$d\Delta M_L$	The error in ΔM_L caused by inaccuracy in measuring $\dot{M}$, kg (lb)
dC_{PL}	Error in C_{PL} caused by inaccuracy of calculations, $\frac{J}{kg}\left(\frac{Btu}{lb}\right)$
$d(\Delta T_L)$	$dT_{L2} - dT_{L1}$ or to give the maximum error possible, change the - to +, °K (°R)
$d(\Delta T_g)$	$dT_{gA} + dT_{gL}$, °K (°R)
T_{gL}	The temperature of the ullage gas just above the LH_2 surface, °K (°R)
T_{gA}	The average temperature of the ullage gas as it vents over the length of the test, °K (°R)

Page
Intentionally
Left Blank

DESIGNING FOR CRYOGENIC INSULATION

By

Clyde D. Nevins

SUMMARY

Structural design studies at MSFC have shown that the type and means of application of high performance insulation will be a major influence on the design of spacecraft with cryogenic propellants. For long-term missions propellant tankage design requires new approaches, and concurrently, methods must be developed for insulation attachment and protection.

The basic pressure vessel may not require significant change of shape to be adapted for insulation application. However, the concept of an integral pressure vessel that also carries vehicle bending loads suggests a configuration in which the propellant tank is suspended within a load-carrying shroud. Openings into the tank and appendages to the tank use new techniques to minimize heat shorts.

MSFC and several contractors have investigated many insulation systems in thicknesses up to 2.5 cm (1.0 in.) for compatibility with the adverse environments of a rocket vehicle launch. Purged insulation systems now appear much better suited than pre-evacuated systems, both from the ease of attachment and reliability of the insulation covering.

INTRODUCTION

The structural design of propellant tankage for long term cryogenic storage has brought many new and challenging problems to the designer. No longer can a propellant tank be designed solely for the structural loads and then released to the thermal engineers for application of the necessary insulation. Nor can a propellant tank be adapted efficiently to other missions by merely increasing the thickness of insulation. The thermal protection of cryogens now requires consideration by the structural designer from the earliest stages of design.

There are four broad categories which essentially cover the range of considerations of structural engineers in this new technology. These categories are illustrated by the typical cryogenic stage shown in Figure 1 and are: the basic pressure vessel; openings and appendages to the pressure vessel; insulation attachment methods; and the insulation covering, or jacket. The MSFC programs in each of these four categories are the major topics discussed in this paper.

BASIC PRESSURE VESSEL

The general stage design for missions requiring long term storage of cryogens will be considerably altered from the current configuration. Whereas the cryogenic stages of Saturn IB and Saturn V are "integral," i.e., where the propellant tank also forms the external contour of the stage, future stages will most likely be of the nonintegral type. The difference in the two approaches is shown in Figure 2.

The integral stage requires the propellant tank cylindrical walls to carry all the vehicle bending, shear, and axial loads. In this case, the tank skirts would introduce a severe heat short to the cryogenic propellant and excessive propellant boiloff results. In addition, the fragile insulation materials cannot withstand the aerodynamic heating and buffeting to which they would be subjected in this configuration.

The need to minimize the structural heat short and also to protect the insulation results in the nonintegral configuration shown in Figure 2. The tank support structure need be sufficiently strong only to support the pressure vessel and the propellant it contains. The aerodynamic loads on the vehicle and the axial load resulting from an upper stage or payload are carried in the structural shroud surrounding the tank. For long duration missions this configuration also offers excellent protection from meteoroid damage.

Generally the shape of the basic pressure vessel should not be significantly altered by the requirement to store cryogens for long periods of time. In theory, minimizing the surface area to volume ratio, i.e., approaching a spherical shape, is desirable for reducing the total heat flux through the insulation.

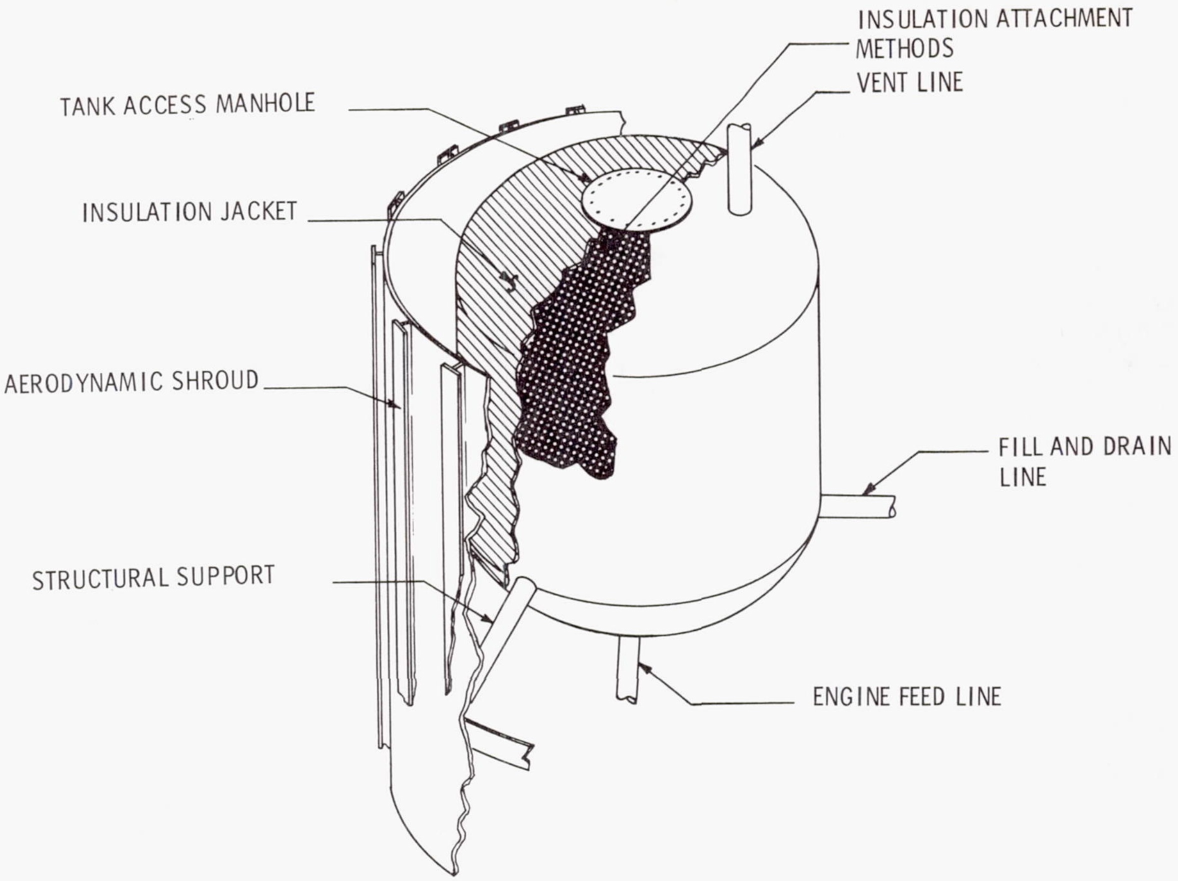

FIGURE 1. A TYPICAL CRYOGENIC STAGE

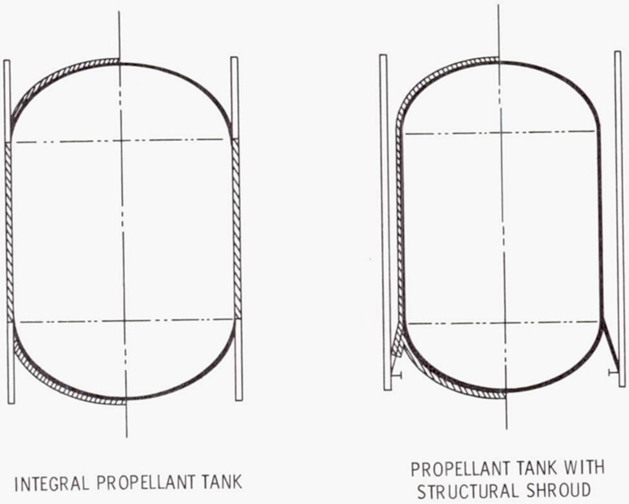
INTEGRAL PROPELLANT TANK

PROPELLANT TANK WITH STRUCTURAL SHROUD

FIGURE 2. INTEGRAL AND NONINTEGRAL TANKS

In actuality, however, spheres are more difficult to insulate because of being composed entirely of a doubly-contoured surface, and insulation performance is degraded compared with that of a corresponding cylinder. Spheres are also very inefficient inhabitants of the cylindrical volume available in the stage contour and seldom look attractive from an overall structural mass standpoint. The conventional cylindrical tanks with elliptical or hemispherical domes that have evolved during a long history of pressure vessel design, strength analysis, and fabrication in the aerospace industry should still be most suitable.

Likewise, materials for tank structures are not significantly affected by the requirement to store cryogens for long periods. The aluminum alloys selected for Saturn I and Saturn V propellant tanks, e. g. , 2219 aluminum alloy, will be quite satisfactory here as well. In some cases, titanium alloys may prove to be superior to aluminum. Titanium can offer a better strength-to-mass ratio for a pure pressure vessel and has the additional advantage of permitting direct welding of low conductivity propellant lines.

OPENINGS AND APPENDAGES

Both openings and appendages present formidable challenges when designing a structure compatible with long term storage requirements.

For large propellant tanks an access opening, or manhole, has proved to be indispensible during launch pad operations on Saturn stages; there is no reason to believe this requirement can be eliminated for stages requiring long term storage of cryogens. Structural supports and propellant lines are mandatory, but their design now becomes a major factor in propellant storage capability.

Measurable leakage (in the order of 10^{-9} cc/sec) of hydrogen into the insulation will seriously degrade the thermal performance of the insulation. Since current flange seal technology does not reliably limit leakage to this extent, this deficiency must be overcome by a design modification to either the sealing method or local insulation application.

One approach to reliably limit the hydrogen leakage is shown in Figure 3. An annular sealing strip is welded to either side of the manhole cover joint, closing off any leakage through the mating surfaces or bolt holes. The disadvantage here is that access to the tank interior would require cutting the sealing strip and then rewelding (and leak checking) as a field operation.

Another approach is to allow for possible leakage through the seal and provide a leak-tight channel through the insulation blanket. By preventing hydrogen leakage into the insulation there will be no degradation other than a small local heat short. Figure 4 shows this latter approach.

Piping penetrations of the insulation can cause a significant heat leak. When aluminum alloys are to be used for construction of the tank, a method must be found to use low-conductivity materials such as corrosion resistant steels or perhaps titanium alloy for the penetrating lines. Until a reliable flange seal is found, the best approach appears to be using a bimetallic transition joint. For this approach the aluminum end of the joint is welded to the tank and the other end is butt welded to a low-conductivity pipe.

Several types of bimetallic transition joints are possible, and three different types have been tested by MSFC: (1) a threaded joint with a silver fusion-welded seal, (2) a commercially available brazed

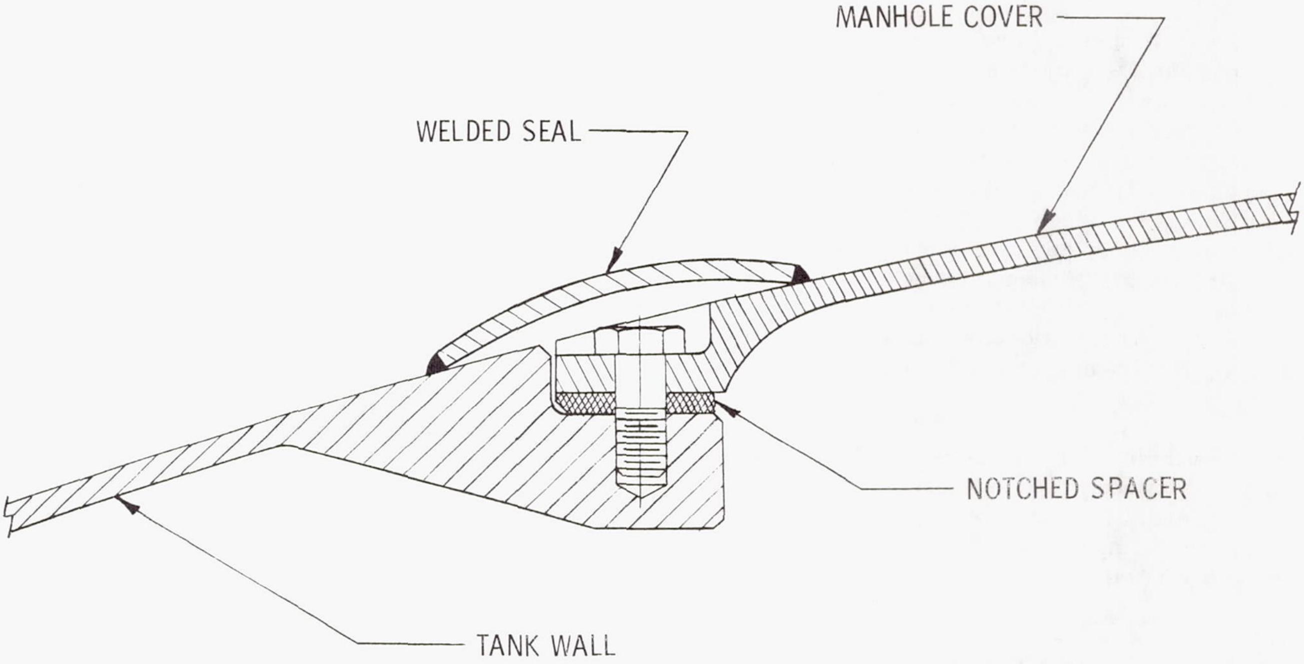

FIGURE 3. A WELDED MANHOLE COVER SEAL

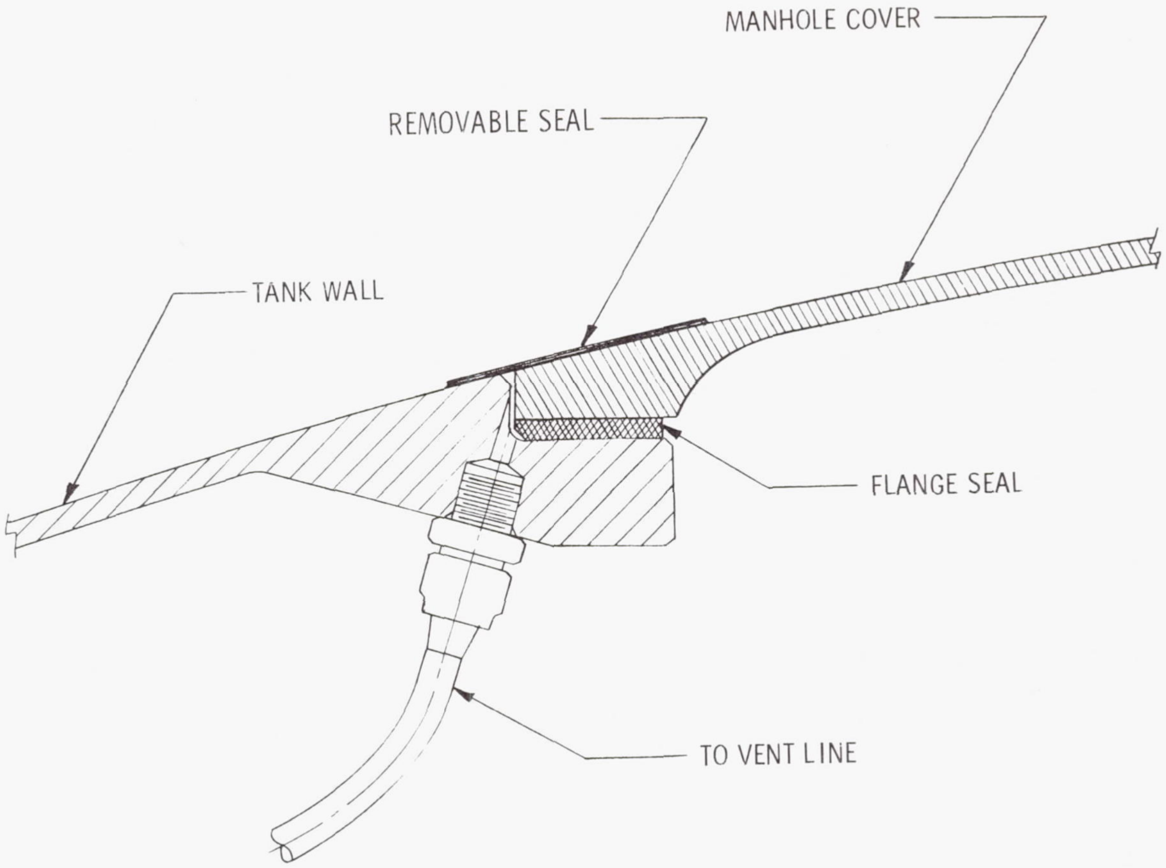

FIGURE 4. A VENTED MANHOLE COVER SEAL

joint, and (3) an explosively swaged joint. Each type of joint was subjected to the following series of tests: (a) preliminary leak check with helium mass spectrometer, (b) cold shock from 353°K (175°F) to LH_2 temperature for 15 cycles, (c) intermediate leak check with helium mass spectrometer, (d) pressurized to 0.38 MN/m^2 (55 psig) and vibrated longitudinally and laterally for 5 minutes each at the major resonant frequency with a 22.7 kg (50 lb) mass. (One of the test specimens is shown mounted in the vibration test fixture in Figure 5.), and (e) final leak check with helium mass spectrometer.

Test results [1] indicated that the commercially available brazed joint was superior to the other types tested. The threaded joint seal failed during vibration testing and one sample of the explosively swaged joint failed to pass the preliminary leak check.

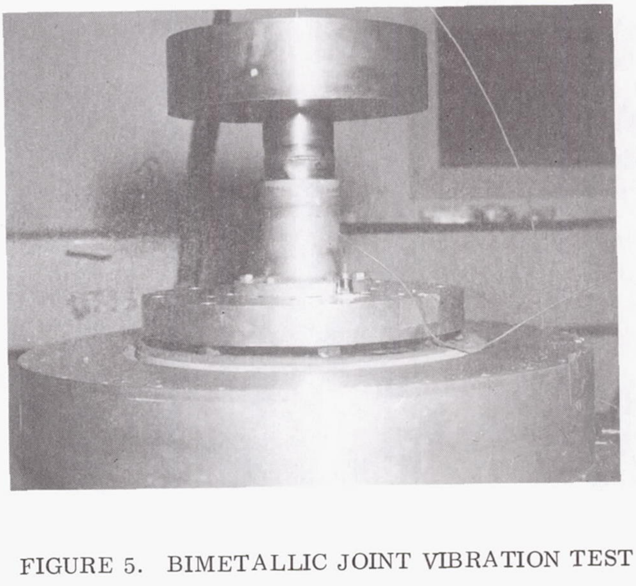

FIGURE 5. BIMETALLIC JOINT VIBRATION TEST

It is more difficult to generalize on the structural support members for cryogenic tankage because of the wide variety of support structures which may be selected. As an illustration of this, the next three figures show the strong dependency of the structural supports on the configuration of the stage. Each of the three structures shown has been carried through preliminary design and analysis, and each yields the lowest system mass penalty for the mission under consideration.

The first support structure was designed for the hydrogen propellant tanks for the S-VI stage (Fig. 6). This stage was studied in some detail by MSFC for use as a "kick" stage and as the basic form of the Multi Mission Module for Lunar logistics missions. The two hydrogen tanks are mounted parallel in the stage. The support structure is comprised of four struts that form two A-frames and pierce the tanks to join at the center. This arrangement allows the two tanks to be supported by only four penetrations of the insulation blanket, the central support being completely insulated and thus offering no heat short into the system. Titanium was used for the penetrating members because high local bending stresses precluded the use of fiberglass.

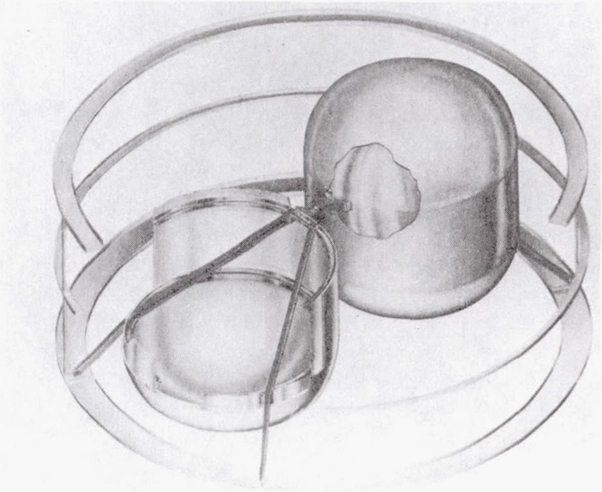

FIGURE 6. SUPPORT STRUCTURE FOR THE LIQUID HYDROGEN TANKS OF THE S-VI STAGE

Figure 7 shows a much different tankage arrangement, and consequently, a much different structural support. The spherical hydrogen tank is supported by a titanium conical frustum attached at the sphere's equator. This particular structural support configuration and material had the lightest overall mass for the eight day mission under consideration. It is interesting to note, however, that had the mission been eleven days or greater (rather than eight), a completely different support system configuration would have been selected. For the longer mission, the preferred system would have been comprised of three discreet attachments to the sphere, and although it would be some 46% heavier than the conical frustum because of the additional structure required within the sphere, only about 1/6 as much boiloff would occur [2].

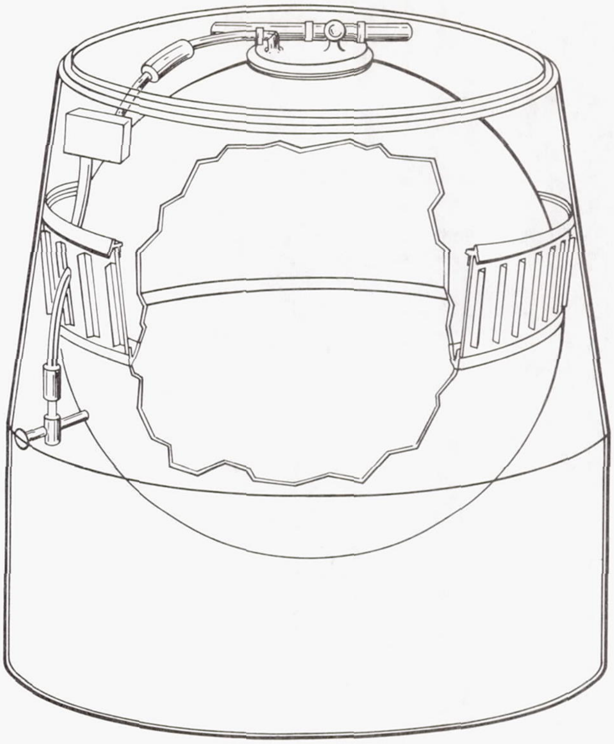

FIGURE 7. STRUCTURAL SUPPORT OF THE SPHERICAL LIQUID HYDROGEN TANK OF A CRYOGENIC SPACECRAFT MODULE

Figure 8 illustrates the support system selected for the experiment tanks of project THERMO, which would include an orbital platform for cryogenic experiments. This system uses six struts which may carry either tension or compression loads. Achieving the objectives of the particular experiment required having not only a minimum heat short, but the minimum number of heat shorts as well. With the additional requirement to mate with a specified Rack structure, the configuration shown provided the minimum heat short with only four penetrations of the insulation. The struts in this case were of fiberglass.

As indicated previously, titanium and fiberglass are the preferred materials for structural supports. In Table I several materials used for aerospace structures are tabulated with their densities, thermal

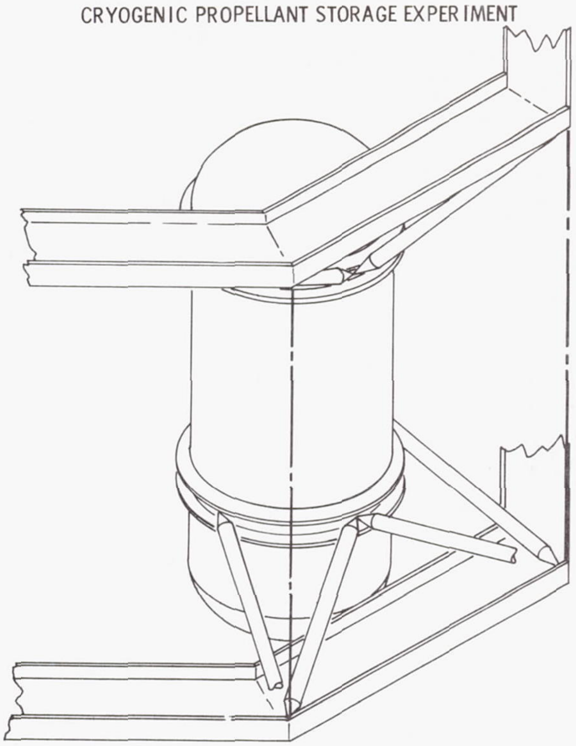

FIGURE 8. STRUCTURAL SUPPORT OF THE CRYOGENIC PROPELLANT STORAGE EXPERIMENT TANK FOR PROJECT THERMO

conductivities, and tensile strengths. At the right is the normalized efficiency index for each material; in this case a low index indicates the higher efficiency. The indices were run for minimizing boiloff for a specified inert mass fraction and assuming pure tension support members [3]. As shown, titanium alloys and filament wound fiberglass are far superior to the other materials. For support structures loaded in both tension and compression, or with superimposed bending loads, titanium supports are more competitive with the fiberglass than indicated by data in Table I.

The advantage of nonmetallic supports for cryogenic tankage is evident, however. Marshall Space Flight Center is now investigating the design problems associated with nonmetallic beams and struts for spacecraft structures [4]. Figure 9 shows a test strut recently completed under this contract and now undergoing structural tests. Figure 10 shows the strut's components and clearly shows the thickness of the nonmetallic cylindrical column. This cylinder is made of five layers of high strength glass filaments, three layers of longitudinal and an inner and outer circumferential wrap, in an epoxy resin. The total wall thickness is 0.084 cm (0.033 in.).

TABLE I. COMPARISON OF STRUCTURAL SUPPORT MATERIALS

	DENSITY kg/m^3 (lb/ft^3)	THERMAL CONDUCTIVITY Joule/m-sec-°K (Btu/ft-hr-°R)	YIELD STRENGTH MN/m^2 (lb/in.^{2} x 10^{-3})	NORMALIZED EFFICIENCY
TITANIUM ALLOY 6 AL 4 VA	4570 (285)	4.8 (2.8)	828 (120)	0.093
ALUMINUM ALLOY 2014-T6	2760 (172)	156 (90.0)	413 (60)	1.000
BERYLLIUM	1780 (111)	151 (87.0)	448 (65)	0.714
STAINLESS STEEL 17-7 PH	7670 (479)	16.9 (9.75)	1034 (150)	0.198
FIBERGLASS S-994 GLASS UFW EPON 826 RESIN	1840 (115)	0.59 (0.34)	758 (110)	0.015

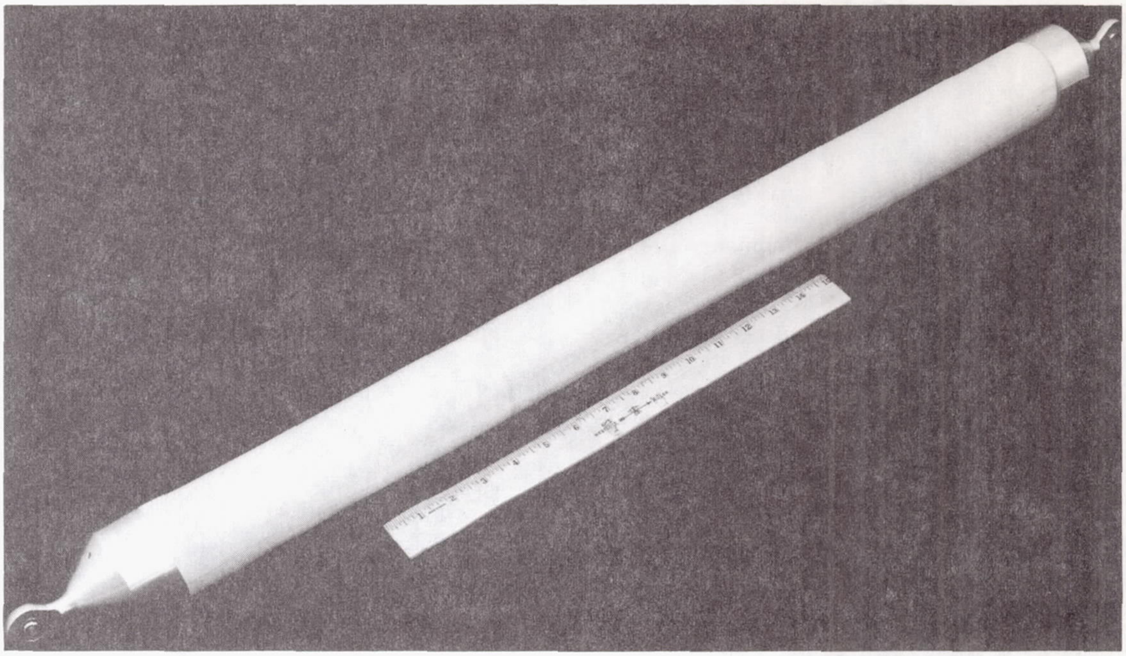

FIGURE 9. A NONMETALLIC STRUCTURAL SUPPORT

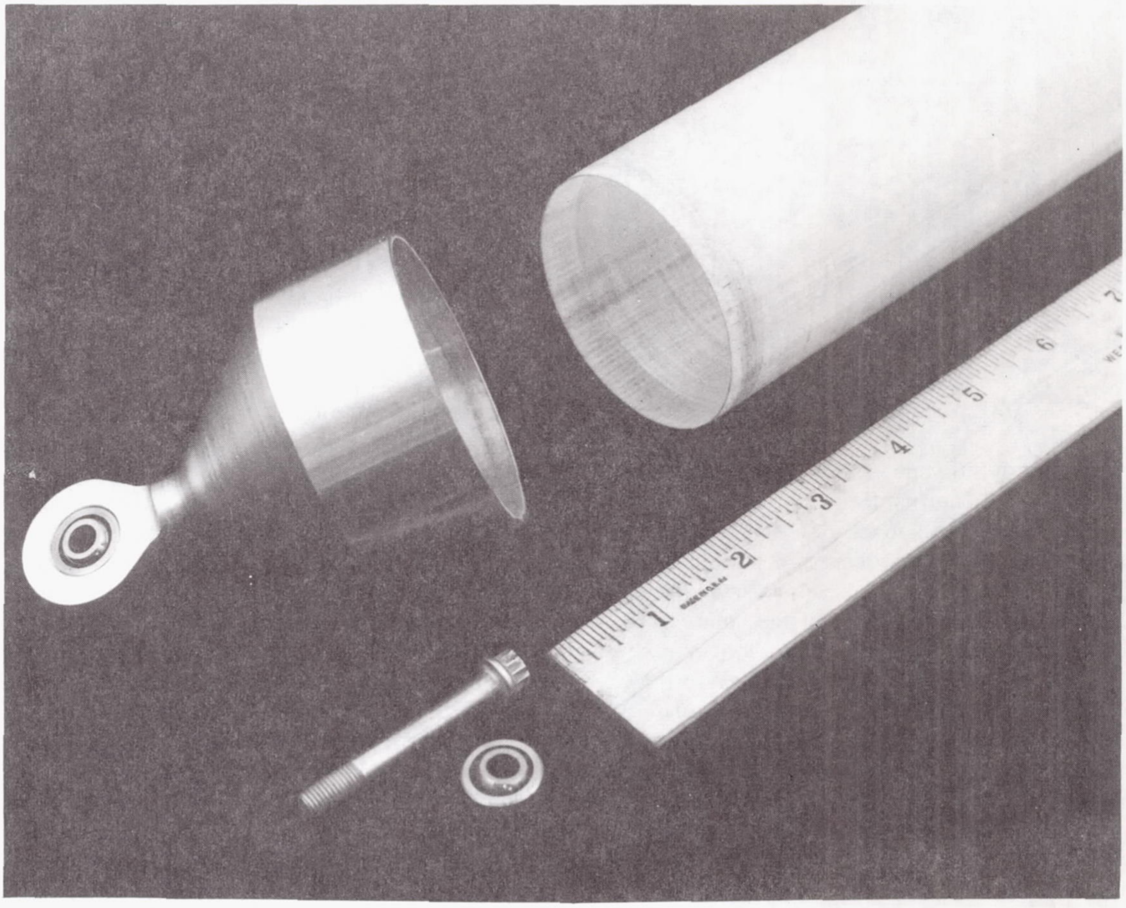

FIGURE 10. DETAIL OF FIBERGLASS STRUT COMPONENTS

INSULATION ATTACHMENT METHODS

The third area of interest to structural engineers is the method of insulation attachment. This is undoubtedly the most challenging of the designer's problems, primarily as a result of the very fragile nature of materials used in high performance insulations. In addition, the insulation must be supported without significant penetration or compaction of the insulation, either of which would degrade the thermal performance of the insulation.

Figure 11 illustrates several types of attachment methods considered for pre-evacuated systems.

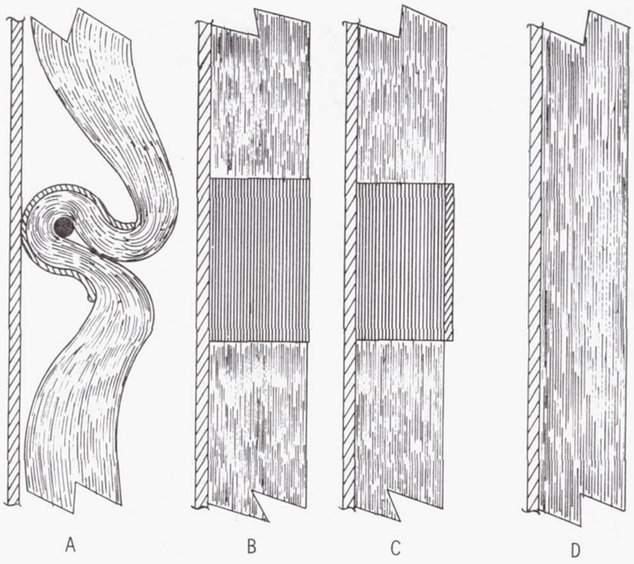

FIGURE 11. ATTACHMENT METHODS FOR PRE-EVACUATED INSULATION SYSTEMS

Method "A" uses nylon ropes placed around the tank and anchored to it. The insulation is clipped at intervals to the ropes as shown. Method "B" uses interwound tension bands. These thin aluminum straps are interwound on the tank along with the insulation. Proper tension control of the bands provides the frictional force necessary to hold the insulation in place. Method "C" is similar to Method "B" in that a tension band is used to provide friction. In this case, however, the band is placed externally and additional spacer material is wound within the insulation to prevent compaction. The band tension is maintained by spring loading. Method "D" is the so-called "envelope" method whereby each layer of insulation is a separate structural shell made by cutting, fitting, and taping each layer individually during installation. Each envelope then supports only its own mass.

Figure 12 illustrates attachment methods suitable for purged insulation systems. Method "E" employs studs bonded to the tank surface, which pierce the insulation at areas where the insulation layers are compacted and bonded together. A hole is then punched through these areas to match the stud locations. This method requires a large overlap of insulation battens to prevent the studs from imposing a serious heat short through the insulation. Method "F" is the tension band method shown in the previous figure which is applicable to a purged system as well. Method "G" uses a pattern of dacron threads piercing the insulation and anchored by buttons at one end and to a Velcro fastener at the tank surface.

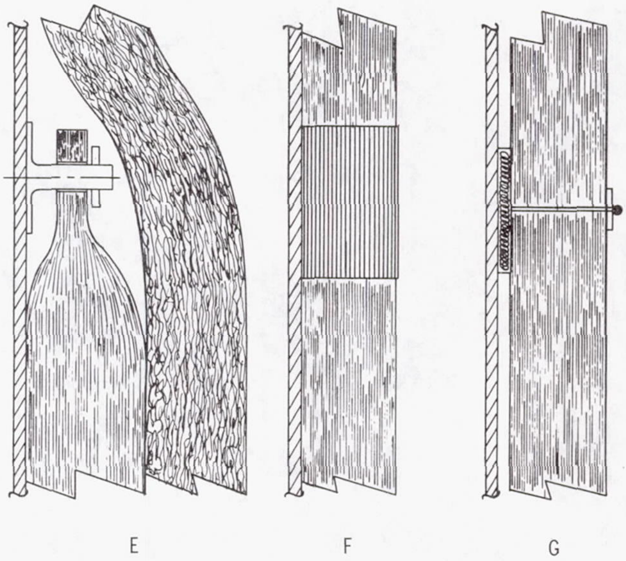

FIGURE 12. ATTACHMENT METHODS FOR PURGED INSULATION SYSTEMS

Each of these attachment methods must withstand the rigors of a rocket vehicle launch without damaging the insulation. In a rocket vehicle trajectory there are four periods that present adverse environments for the insulation and its attachments: first, the high acoustic environment at lift-off, next the rapid ascent and the associated rapid pressure drop (an adverse environment for purged systems only), then the maximum dynamic pressure point where there is the combination of severe vibration and moderately high acceleration, and finally, first stage burnout where the maximum acceleration level occurs.

The capability of each type of insulation attachment method to satisfactorily survive these environments has been assessed in a series of experiments on test tanks such as the one shown in Figure 13.

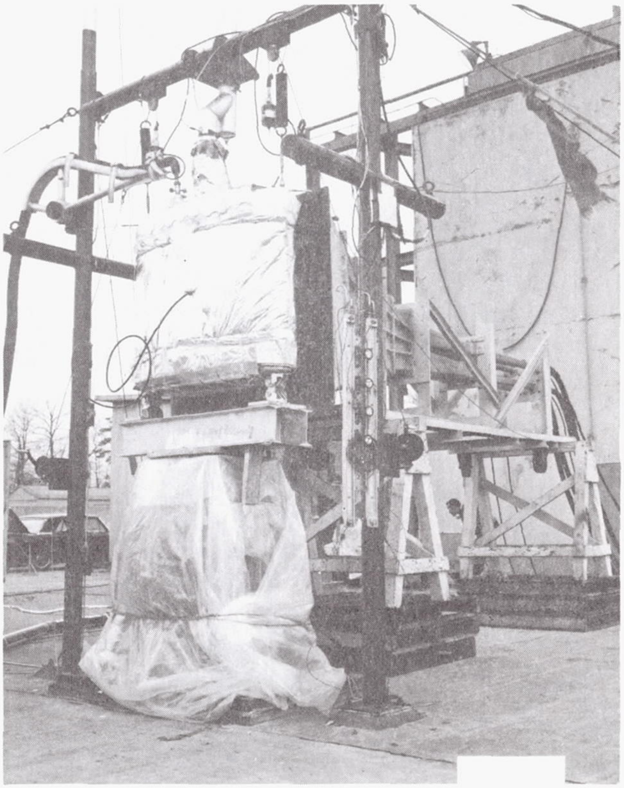

FIGURE 13. VIBRATION AND ACOUSTIC TEST OF AN INSULATED TEST TANK

This tank is a biconvex cylinder with radii of curvature equal to that of the 2.67-m (105-in.) diameter tank. The biconvex shape permits good representation of full scale parameters in a specimen small enough to use readily available test facilities.

In general, the test sequence followed the natural occurrence of environments in an operational mission. A ground-hold thermal performance test was performed initially to evaluate thermal characteristics of the system prior to launch. Next, a combined mechanical and acoustic vibration test was performed at liquid hydrogen temperature (Fig. 13). A steady acceleration test on a centrifuge followed with a 6.6 g acceleration applied in the direction of the tank's longitudinal axis for 5 minutes. Figure 14 shows an insulation system photographed during an acceleration test. After installation in a vacuum chamber (Fig. 15), a rapid evacuation test was performed to simulate the pressure-time history of

FIGURE 14. INSULATED TEST TANK DURING CENTRIFUGE TEST

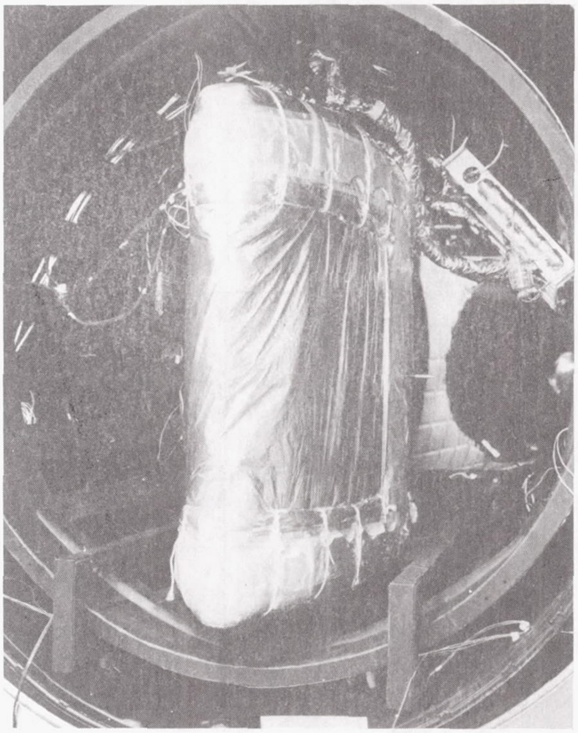

FIGURE 15. INSULATED TEST TANK MOUNTED IN VACUUM CHAMBER

a typical Saturn V boost. Finally, a space thermal performance test was performed to determine the heat transfer characteristics for each system in the space environment.

Results of experiments on test tanks of this general size and shape are summarized in Table II [5, 6]. The rope and clip method failed when metal clips were used, but passed when a nonmetallic clip was used. In the latter case, however, an additional attachment through the insulation had to be incorporated with each clip, thus adding a significant heat short. The tension band method proved to be acceptable if the insulation was not compressed prior to the dynamic environment; i.e., it is acceptable for purged systems but not for a pre-evacuated system. The external tension band satisfactorily solves the shortcoming of the interwound tension band for the pre-evacuated system, but still relies on friction, a somewhat unfaithful servant. The last two methods were developed primarily for purged insulation blankets approximately 2.5-cm (1.0-in.) thick and proved to be very satisfactory for that application. Their application to greater thicknesses has not been established, and is now being evaluated in the MSFC inhouse program.

Although much can be accomplished in small scale tests, it is seldom possible to simulate all the environments adequately in laboratory experiments. To produce the combination of environments coupled with the effects of cryogenic temperature acting on a full-scale insulation system, the rocket sled shown in Figure 16 has been built and is now ready for the first test. The 7260-kg (16 000-lb) sled will be the largest rocket sled ever sent down a track. The insulated 2.67-m (105-in.) diameter tank will be mounted within the shrouded sled and accelerated to about 6 g's, the maximum level expected during a Saturn V launch. Along with the acceleration, there will be vibration induced by the track and a moderate level of acoustic energy.

INSULATION COVERING

Finding a suitable covering for the insulation system is the final task of the structural engineer. The covering must not only protect the insulation system during handling, but also must provide for maintaining proper environmental control within the insulation layers during prelaunch operations.

The covering for a pre-evacuated system presents a particularly difficult set of requirements to meet. This "flexible vacuum jacket" must have low permeability, low moisture absorption, and a low outgassing rate in a vacuum environment. It also has to be flexible over a wide range of temperatures and be durable, i.e., resistant to formation of pinhole leaks at wrinkles. It is desirable that the jacket can be stretch-formed to complex contours, and that it be compatible with LO_2.

Figure 17 shows a jacket sample on a 61-cm (24-in.) diameter test fixture. Materials that

TABLE II. EVALUATION OF INSULATION ATTACHMENT METHODS

ATTACHMENT METHOD	SUITABILITY (INSULATION METHOD)	RESULTS OF DYNAMIC TESTS	REMARKS
ROPES & CLIPS	PURGED PRE-EVACUATED	ONE TYPE PASSED, ANOTHER FAILED	CAREFUL DESIGN REQUIRED
INTERWOUND TENSION BANDS	PURGED	PASSED ACOUSTIC & VIBRATION	FAILED FOR USE WITH PRE-EVACUATED
EXTERNAL TENSION BANDS	PRE-EVACUATED	PASSED ACOUSTIC & VIBRATION	RELIES ON FRICTION
ENVELOPE	PRE-EVACUATED	NOT TESTED	SENSITIVE TO LAY-UP DENSITY
PINS & SHINGLED BATTENS	PURGED	PASSED	FOR THIN INSULATION BLANKET
BUTTONS & STRINGS	PURGED PRE-EVACUATED	PASSED FOR PURGED SYSTEM	NOT TESTED FOR PRE-EVACUATED

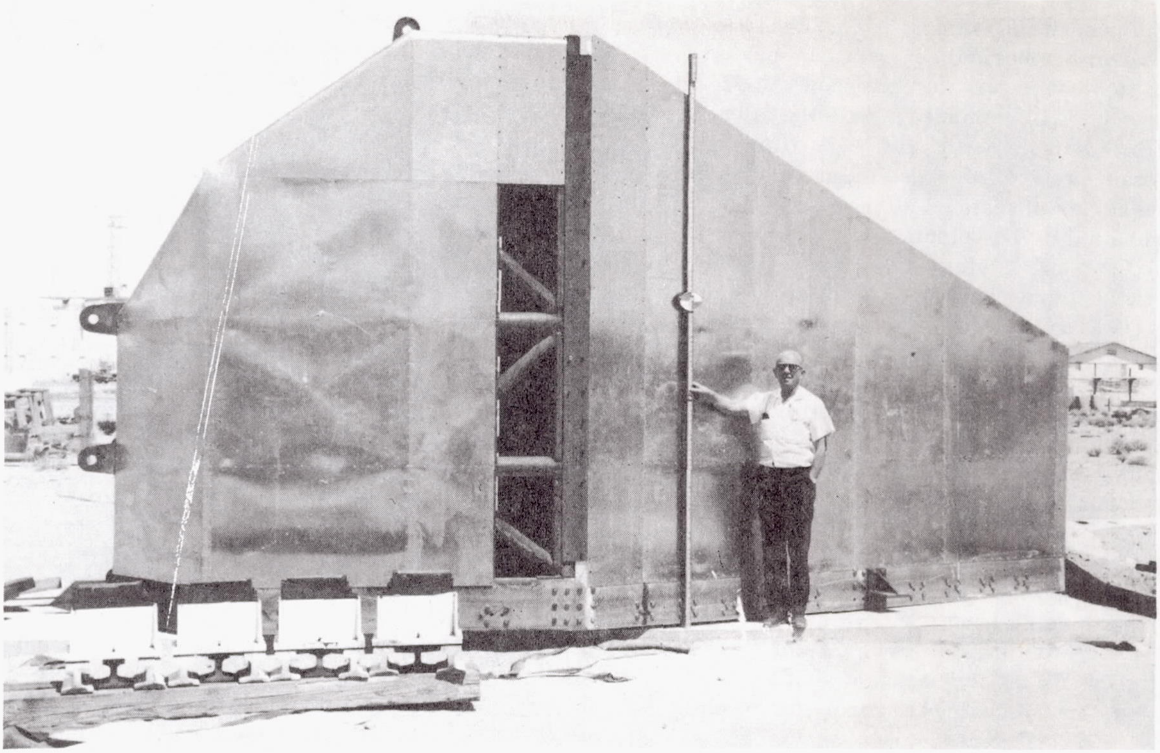

FIGURE 16. ROCKET SLED FOR TESTING FULL-SCALE INSULATION SYSTEMS

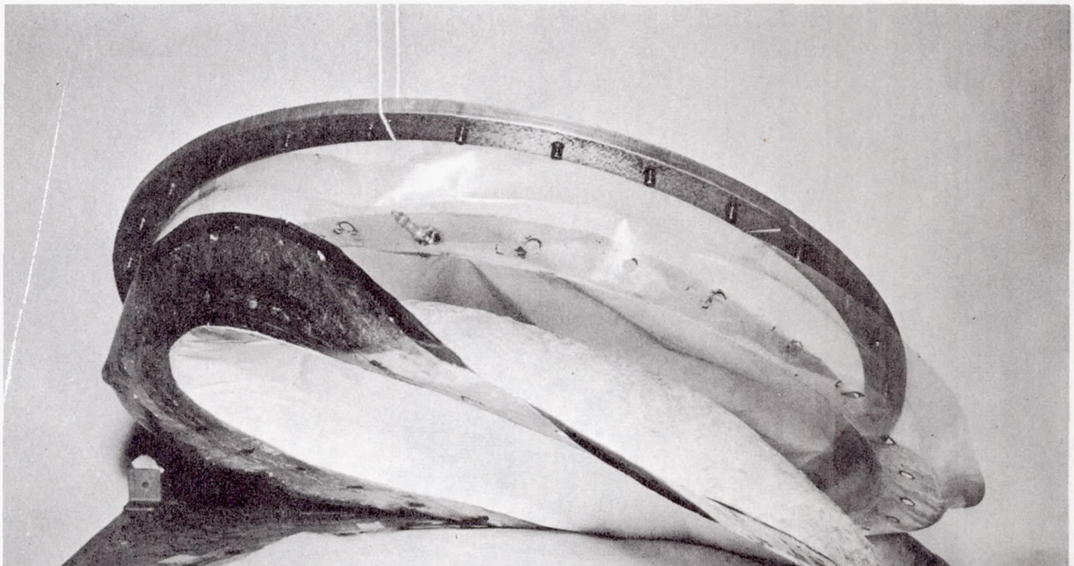

FIGURE 17. TEST SPECIMEN FOR SCREENING MATERIALS FOR FLEXIBLE VACUUM JACKET

satisfactorily passed flat-sample permeability tests were formed into a spherical segment cap and evacuated to the test fixture surface shown in Figure 17. This induced a 10% shrinkage with the attendant wrinkles. Each sample was cycled eight times and the helium leak rate was recorded after each cycle. An extensive series of tests on 30 metal-plastic laminates resulted in the selection of a laminate of 0.0127 mm (0.50 mil) Mylar, 0.0089 mm (0.35 mil) aluminum, 0.0089 mm (0.35 mil) aluminum, and 0.0127 mm (0.50 mil) Mylar as most nearly meeting the requirements of the jacket [7]. Springback data were also recorded on the fixture shown in Figure 17. The final springback test required the specimen to be evacuated for two weeks at which time the vacuum was released. The minimum acceptable springback time was three minutes.

The specimen shown in Figure 17 has two materials supplementing the basic laminated jacket material. Shown on the under side of the specimen is a layer of "two-way stretch" nylon. This layer of material prevents the formation of sharp creases when wrinkled, thus reducing the formation of pinhole leaks and enhancing recovery characteristics. On the outer surface of the jacket is a 5.1-cm (2.0-in.) thick fiberglass mat. This mat has the requisite resiliency to induce acceptable springback characteristics.

Figure 18 shows a nearly completed vacuum jacket for the 2.67-m (105-in.) diameter tank undergoing a pre-installation leak check. When the jacket is in place, the fiberglass mat material will be installed.

Unfortunately, the promise shown by jacket materials during specimen tests has not been realized in applications to test tanks. In general, these tests [5] show a lack of reliability in tank seams and a tendency for the development of tiny leaks that are very difficult to trace. For this reason, flexible vacuum jackets cannot now be considered sufficiently developed for application to a spacecraft.

Purge jackets are somewhat less demanding in their requirements. They must be relatively leak tight, capable of withstanding a small differential pressure, and have some means incorporated to allow the insulation to be evacuated by the vacuum of space. In addition, the jackets should be durable and easily installed.

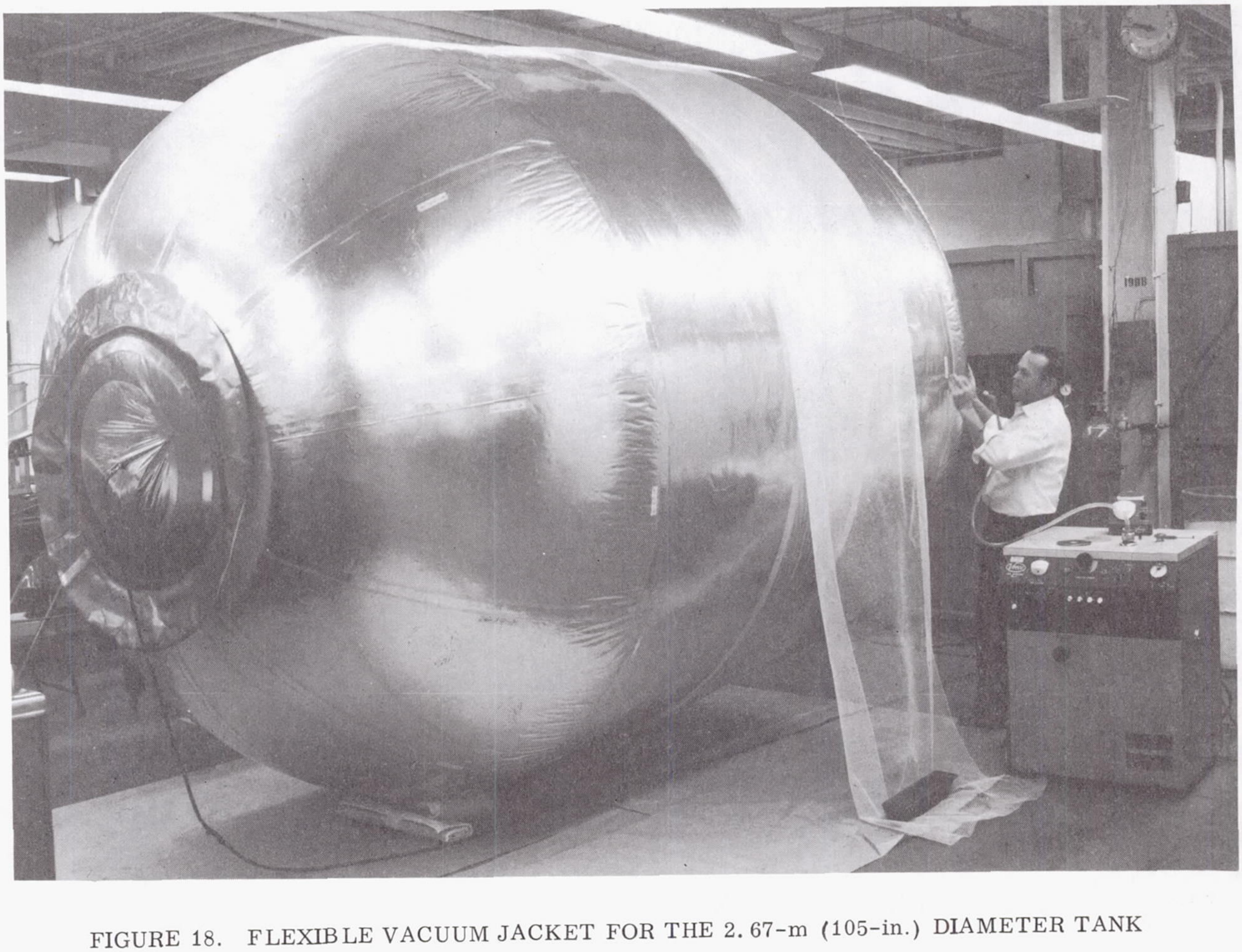

FIGURE 18. FLEXIBLE VACUUM JACKET FOR THE 2.67-m (105-in.) DIAMETER TANK

A purge jacket for the 2.67-m (105-in.) diameter tank is shown in Figure 19. This jacket, developed under contract to MSFC, is made of a polyurethane coated dacron cloth. It is installed by simply zipping it together along the seam shown in Figure 19. Incorporated in the zipper seam is a device which allows the jacket to unzip at a preset pressure differential of about 3450 N/m^2 (0.5 psi).

CONCLUSIONS

The need for high performance insulations on spacecraft cryogenic tanks has not affected the basic shape or materials of the tank to a significant degree. Structural supports for cryogenic tanks, particularly for very long missions, need careful consideration and will use nonmetallic structures or possibly more sophisticated means such as retractable supports. The basic configuration approach for long missions will be the nonintegral tank.

The application of high performance insulation is a challenging but not insurmountable task. In general, purged systems are much easier to support than are comparable pre-evacuated systems; however, thicker insulations have not been investigated sufficiently. Jackets for purged systems are not considered a problem. On the other hand, jackets for pre-evacuated systems have been plagued with the development of leaks during tests and do not appear to have sufficient reliability to be flightworthy.

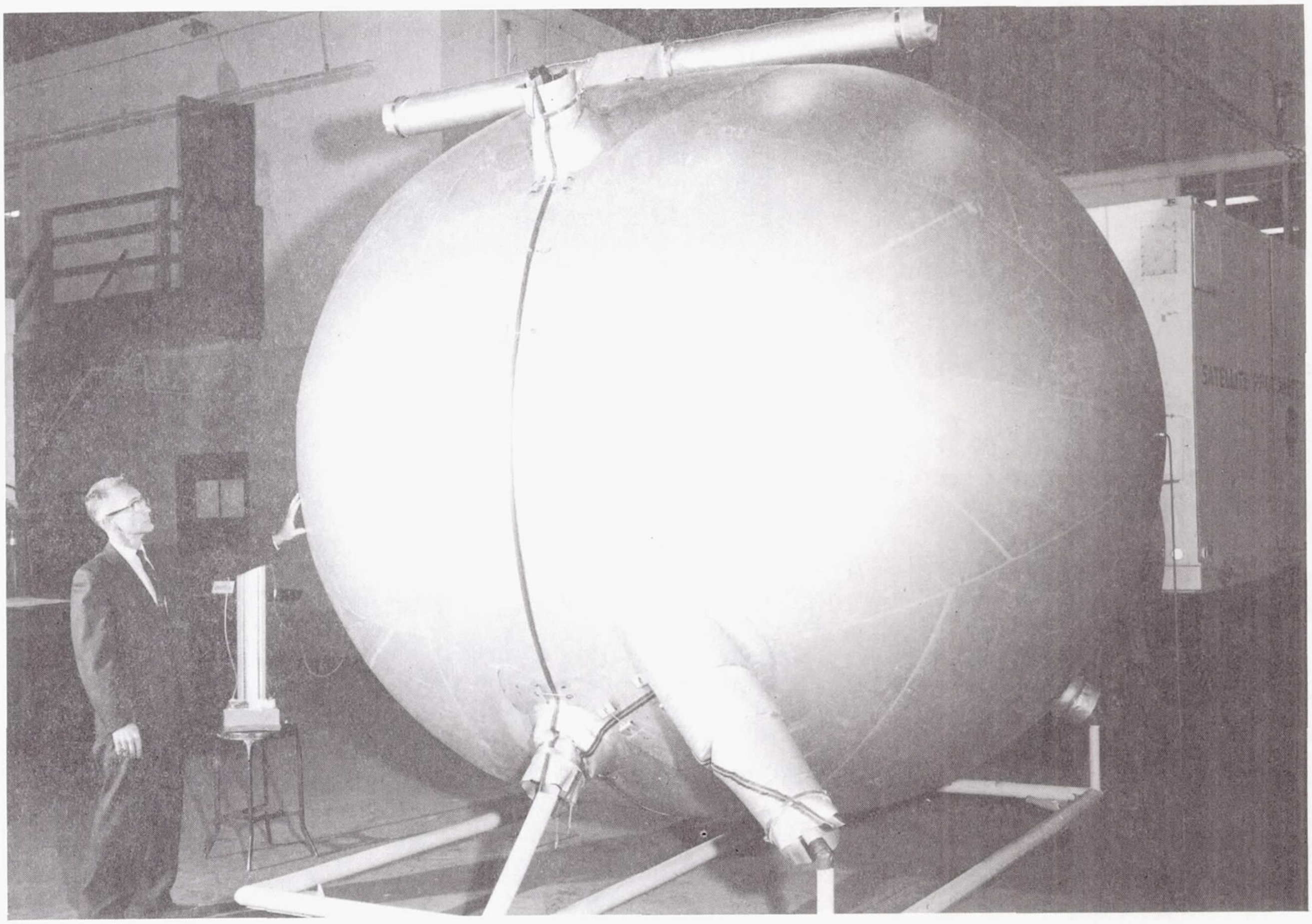

FIGURE 19. PURGE JACKET FOR THE 2.67-m (105-in.) DIAMETER TANK

REFERENCES

1. Sturm, R. G.: Vibration Development Tests of Aluminum-to-Stainless Steel Couplings. Technical Memorandum R-3-65-5, Brown Engineering Company, Inc., March 31, 1965.

2. Sterbentz, W. H.; and Baxter, J. W.: Thermal Protection System for a Cryogenic Spacecraft Propulsion Module. Final Technical Report, Lockheed Missiles and Space Company LMSC-A794993, Volume II, November 15, 1966.

3. Design Techniques for Structure-Cryogenic Insulation Integration. Final Technical Report, Contract NAS8-5268, The Martin Company, ER 13502, October, 1964.

4. Analytical Study of Nonmetallic Parts for Launch Vehicles and Spacecraft Structures. Quarterly Progress Report Number 2, The Boeing Company, February 1967.

5. Crawford, R. F.; and Hannah, R. G.: Cryogenic Insulation Research. Final Report, Contract NAS8-11397, The Martin Company, ER 14361, September 1966.

6. Environmental Tests on Superinsulated Structural Specimens. Test Report, Contract NAS8-11414, Wyle Laboratories, ER 51401-06, October 1, 1964.

7. Shriver, C. B.: Flexible Vacuum Jacket Development. Progress Report No. 10, Contract NAS8-11376, Goodyear Aerospace Corp., GER 11706 S/9, May 5, 1965.

BIBLIOGRAPHY

1. Swalley, F. E.; and Nevins, C. D.: Practical Problems in Design of High-Performance Multilayer Insulation System for Cryogenic Stages. Advances in Cryogenic Engineering, Volume 10, Plenum Press, 1965.

2. Cody, J. C.; and Hyde, E. H.: Thermal Problems Associated with the Development of a Flight Configured Cryogenic Insulation System. Proceedings of the Conference on Long-Term Cryo-Propellant Storage in Space, NASA/MSFC, October 1966.

3. Burge, G. W.: System Effects on Propellant Storability and Vehicle Performance. Final Technical Report AFRPL-TR-66-258, Douglas Aircraft Company, Inc., DAC-59314, October 1966.

4. Program for the Evaluation of Structural Reinforced Plastic Materials at Cryogenic Temperatures. Final Report, Contract NAS8-11070, Goodyear Aerospace Corp., GER 12792, August 31, 1966.

5. Cryogenic Storage System Study (AES Payloads) Program. Technical Final Report, Contract NAS8-20272, The Boeing Company, D2-113345-2, August 1966.

6. Getty, R. C.: Cryogenic Insulation Development. Monthly Progress Reports, Contract NAS8-18021, General Dynamics (Convair).

CRYOGENIC INSULATION MANUFACTURING TECHNOLOGY

By

Iva C. Yates, Jr.

SUMMARY

This paper describes manufacturing techniques and processes used to apply high performance multilayer insulation systems to flight type cryogenic tanks. The methods used in the application of a helium purged concept and a pre-evacuated concept are reported, and the problems associated with each concept are discussed.

It is concluded from these application studies that manufacturing technology is available for the application of high performance insulation systems to cryogenic tanks for short term space storage. Additional studies are needed to more completely assess the effect of manufacturing methods on thermal performance and to develop insulation systems for long term storage of cryogens in space.

INTRODUCTION

The producibility of high performance multilayer insulation systems is of primary concern to designers of advanced space vehicles requiring storage of cryogenic fluids. Even in the preliminary design phase the designer must have an evaluation of the availability and adequacy of manufacturing technology in order to proceed confidently with the design.

The inhouse program for the development of high performance cryogenic insulation was designed to provide a basis for the evaluation of proposed concepts for extended orbital, lunar, and planetary missions. The program has been carried out under the direction of a working group composed of structural, thermal, materials and manufacturing engineers. The procedure generally followed in evaluating a concept consists of a number of screening tests on calorimeters, test fixtures, and small-scale tanks to obtain preliminary data on the thermal and structural performance followed by application to a large-scale tank for complete thermal testing. Application methods and techniques are developed in the process to achieve the most workable solution that will meet the design objectives.

INITIAL PRODUCIBILITY STUDY

At the beginning of the program in 1962, it was decided that a study of the practical problems associated with the application of an high performance insulation system should be carried out inhouse. A simplified cryogenic test tank, 1.78 m (70 in.) in diameter by 4.01 m (161 in.) long, was designed and fabricated to serve as a test article for the application of multilayer insulation systems. The tank shown in Figure 1 has fiberglass support rods, manhole cover, concentric fill, drain, and vent lines, and an instrumentation pole.

FIGURE 1. 1.78-m (70-in.) DIAMETER CRYOGENIC TEST TANK

Contracts were awarded to Linde Division of Union Carbide Corporation and National Research Corporation for the design of insulation systems to be applied to the tank at Marshall Space Flight Center by NASA personnel. The design concepts were synthesized from available technology developed primarily for application to storage vessels and transportable dewars. The insulation systems were designed for typical acceleration, vibration, acoustic, and thermal environments although the tank was not designed for dynamic testing.

The Linde SI-62 insulation system was selected for application to the tank. This insulation system consisted of alternate layers of aluminum foil, 0.006 mm (0.00025 in.) thick, and microglass-fiber paper, 0.05 mm (0.002 in.) thick, encased in a flexible vacuum jacket made of a laminate of mylar-aluminum-mylar. The insulation was applied to the cylindrical part of the tank using a wrapping technique, and the bulkheads, piping and structural supports were insulated by interleaving separate layers of glass-fiber paper and aluminum foil into the cylindrical insulation. The flexible vacuum jacket was partially pre-fabricated and then assembled on the insulated tank using contact adhesives. Major problem areas were: insulation of penetrations, fabrication of the flexible vacuum jacket, and evacuation of the insulation.

A ground hold test of the insulated tank was attempted using liquid hydrogen; however, because of a failure of the vacuum jacket around the vent line, the test was aborted before meaningful data could be obtained. Although the thermal test was a failure, the objective to evaluate available technology and identify areas requiring additional research and development was accomplished. Recommendations were made to do additional work on insulation application, to evaluate materials and adhesives, to develop improved techniques for fabricating flexible vacuum jackets, and to evaluate methods of improving the evacuation of the insulation and leak detection of the vacuum jacket. As a result, the inhouse program was greatly expanded to investigate these areas. Flight type cryogenic tanks, 2.67 m (105 in.) in diameter by 3.18 m (125 in.) long, were designed and fabricated and a program was initiated to develop high performance insulation systems for a 96 hour mission.

APPLICATION OF HELIUM PURGED CONCEPT

The first system selected for application to one of the flight type 2.67-m (105-in.) diameter tanks was a helium purged concept using NRC-2 [6.35-μ (1/4-mil) crinkled aluminized mylar] insulation. Preliminary concepts were applied to models of components such as piping penetrations and structural supports to evaluate attachment techniques and structural integrity when exposed to the acoustic and vibration environments. The final design consisted of battens of NRC-2 insulation wrapped around the tank and mechanically attached to aluminum support pins adhesively bonded to the tank.

The general manufacturing plan for application of the insulation is outlined in Figure 2 and details of the major steps are as follows:

1. Fabricate Major Battens.

Insulation battens were prefabricated from 8 sheets of aluminized mylar bonded together at intervals of about 0.48 m (19 in.) along one edge with a thermo plastic tape adhesive. A complete batten assembly consisted of 6 battens of 8 sheets making a total of 48 layers of insulation. Each of the 6 battens was cut to a different width so that when assembled on the tank, a shingled effect is achieved as shown in Figure 3. The 8 sheets of insulation in each batten were bonded together at the same interval forming a thin, tough area in which holes were punched for attachment to the support pins. The hole spacing was determined by actual measurement of the spacing of the pins bonded on the tank. The hole spacing was increased on successive battens to allow for the build-up in thickness.

2. Install Support Pins.

The location of the support pins was laid out on the tank and each location was etched and cleaned. The pins were bonded to the tank using the room temperature curing NARMCO 7343 adhesive. A vacuum bag was arranged over the pins so that atmospheric pressure provided the clamping force during the curing period.

3. Install Insulation Battens on Tank.

The tank was then installed in the assembly fixture as shown in Figure 4. The driving end was attached to the tank by bolting it to the manhole fitting and a rubber faced ring engaged the lower bulkhead for support. Arc measurements of the distance between pins were taken and transferred to the insulation battens. Holes were punched through the bonded area of the battens with a standard 0.635-cm (1/4-in.) diameter paper punch. The battens were rolled up, transferred to the tank, and installed over the pins. The battens,

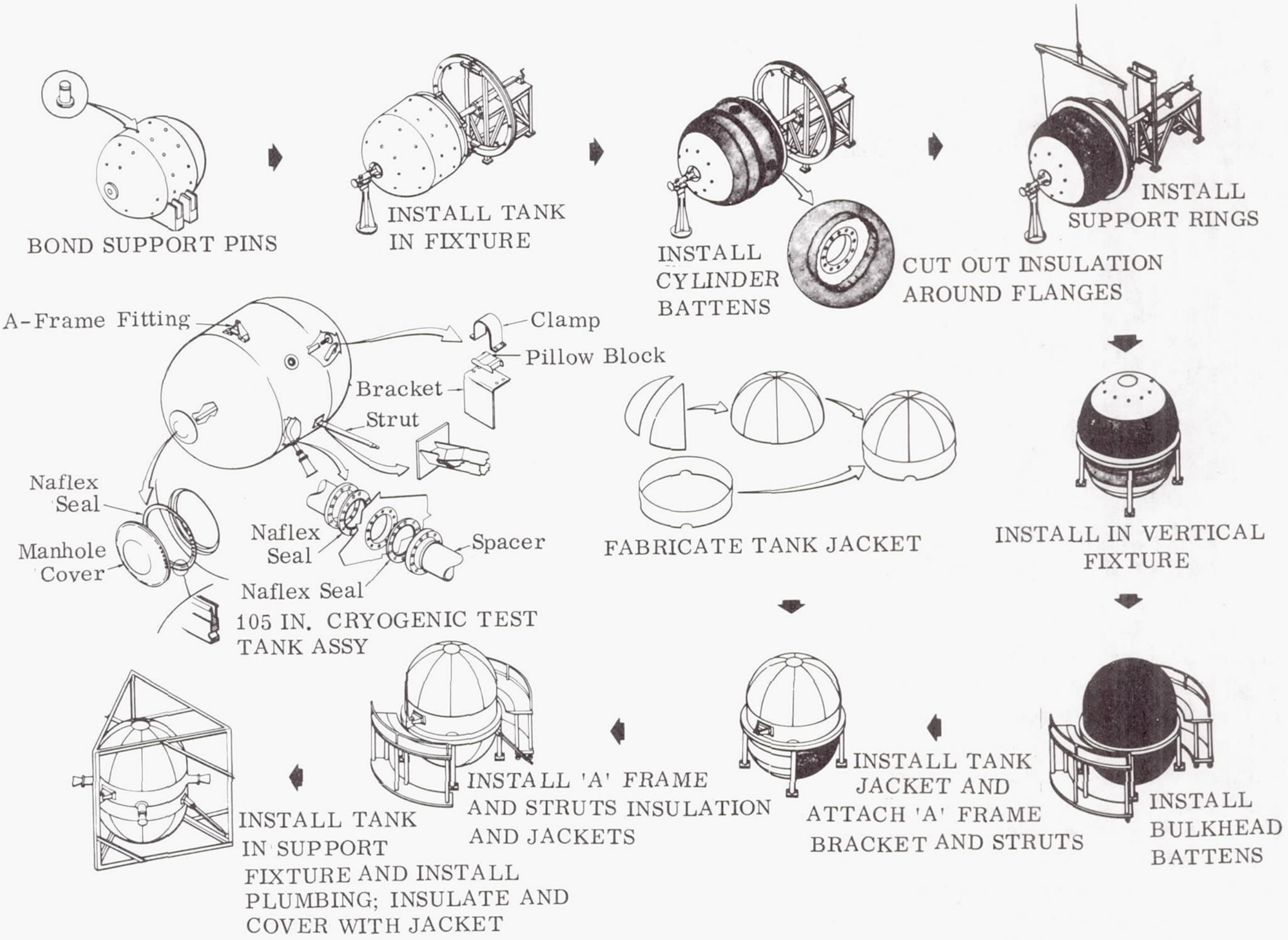

FIGURE 2. MANUFACTURING PLAN, HELIUM PURGED NRC-2 CONCEPT

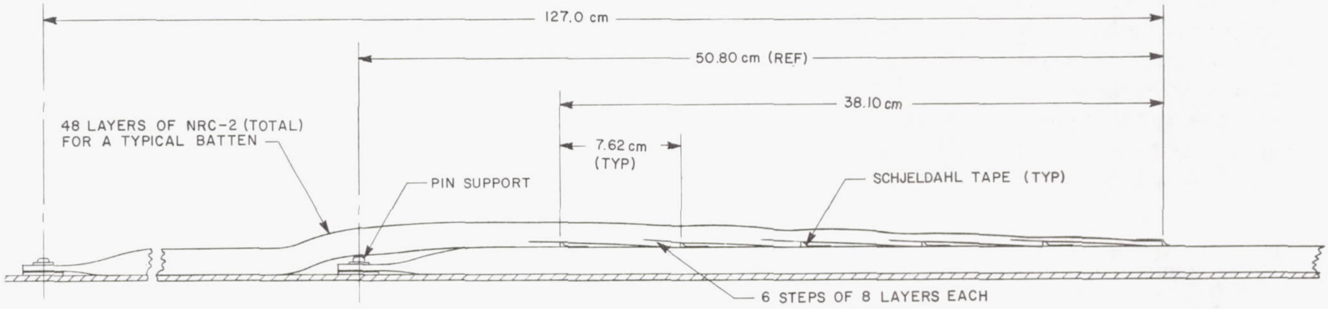

FIGURE 3. TYPICAL BATTEN STEP-DOWN

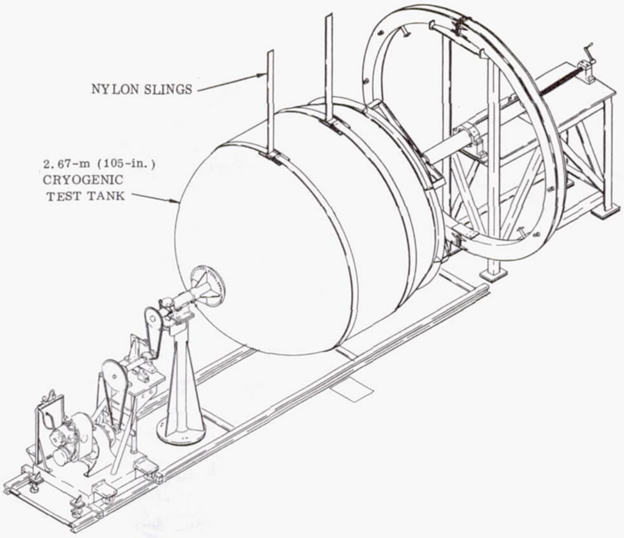

FIGURE 4. INSTALLATION OF CRYOGENIC TEST TANK IN ASSEMBLY FIXTURE

rectangular in shape, had excess material in the areas covering the bulkheads. The excess material was tucked, folded and taped. The location of each of the tucked and folded areas was staggered to control the build up as successive battens were installed. When the last batten was installed over a pin, an E-ring was used as a permanent fastener. Holes 90 degrees apart were cut in the insulation around the center of the cylindrical part of the tank to expose the fittings for the piping penetrations. The handling ring was attached to the tank at these points in order to remove the tank from the assembly fixture (Fig. 5). The tank was then installed in the vertical assembly fixture where the bulkhead insulation was installed.

4. Purge Jacket Fabrication and Installation.

The purge jacket was made of transparent mylar film 127μ (5 mils) thick. The bulkhead portions of the jacket were made of vacuum formed gore sections and assembled with a contact adhesive. A short cylindrical section was bonded to each bulkhead cap forming a complete jacket half. The two jacket halves were then installed on the insulated tank while it was in the vertical assembly fixture (Fig. 6).

5. Installation of Tank in Support Frame.

A lifting lug was attached to the manhole fitting and the tank was supported by an overhead crane while the handling ring was detached. The structural supports were attached to the tank and the tank was installed into its support frame.

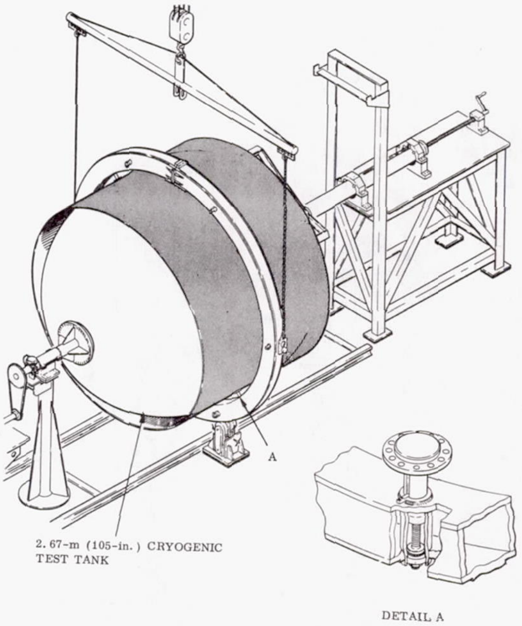

FIGURE 5. REMOVAL OF CRYOGENIC TEST TANK FROM ASSEMBLY FIXTURE

6. Insulation of Piping and Structural Supports and Completion of Purge Jacket.

The insulation was cut back around the four piping penetrations and three structural supports. Precut insulation battens were installed around the piping and structural supports and interleaved into the insulation installed on the tank. Figure 7 shows the insulation cut away from one of the pipes, and Figure 8 shows a completely insulated pipe. After all of the penetrations were insulated, the purge jacket was completed by bonding preformed transition pieces to the purge manifolds and to the main jacket. The completed job is shown in Figure 9.

The installation of NRC-2 insulation was relatively straightforward and easy except for insulation of the penetrations. Interleaving of the insulation is difficult and time consuming, and it is practically impossible to maintain the desired thickness within reasonable tolerances when insulating around discontinuities. One of the main advantages

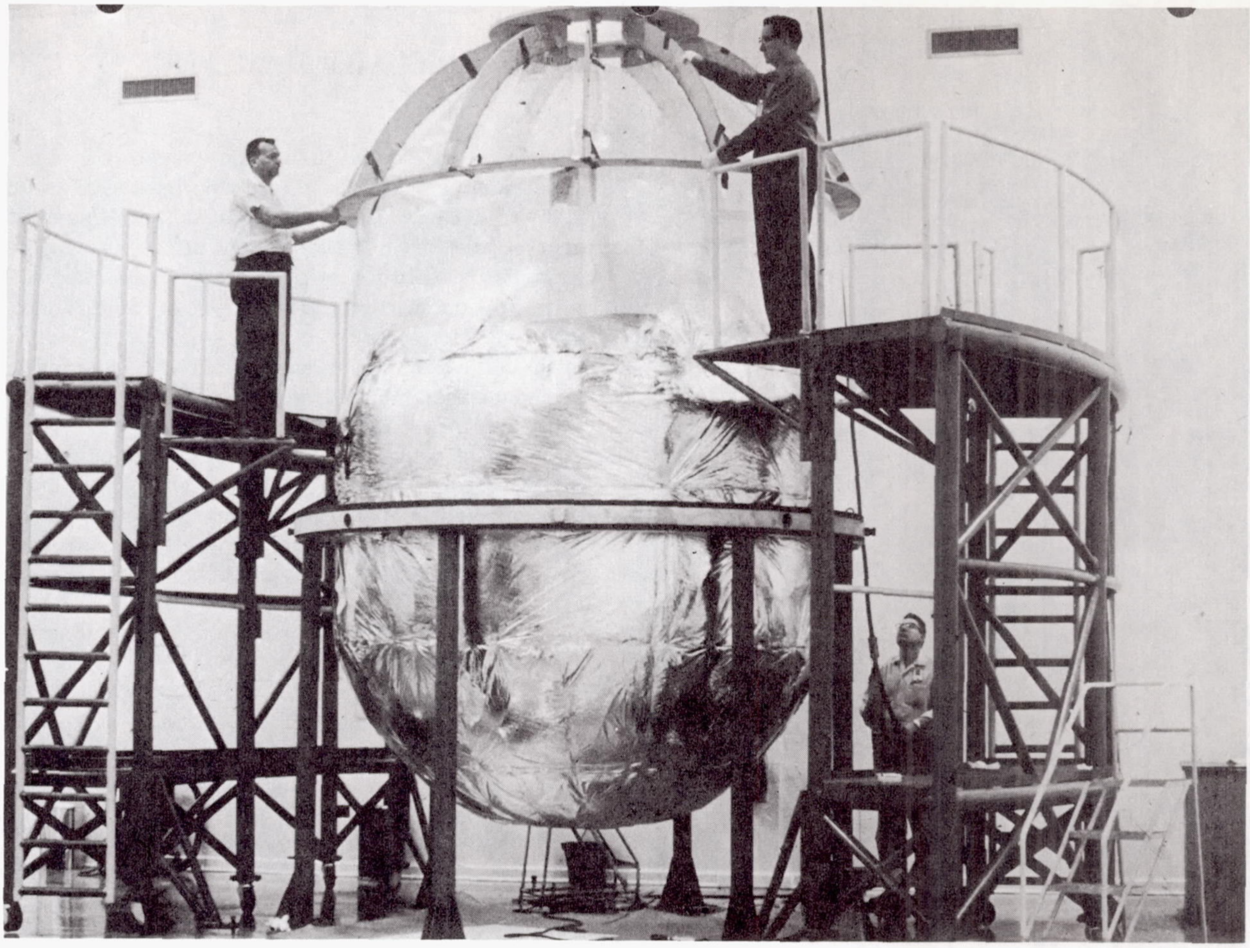

FIGURE 6. INSTALLATION OF PURGE JACKET

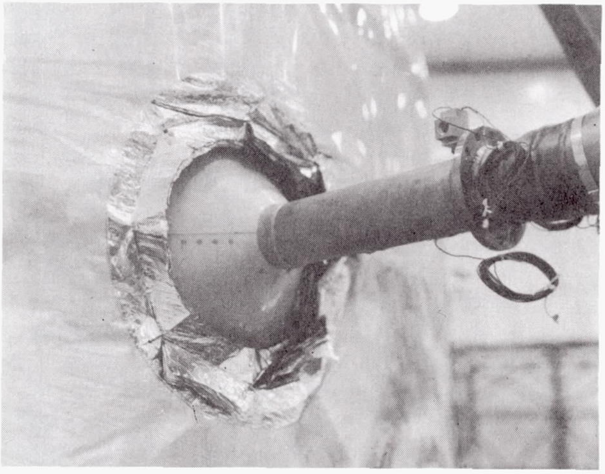

FIGURE 7. PIPING PENETRATION
BEFORE INSULATION

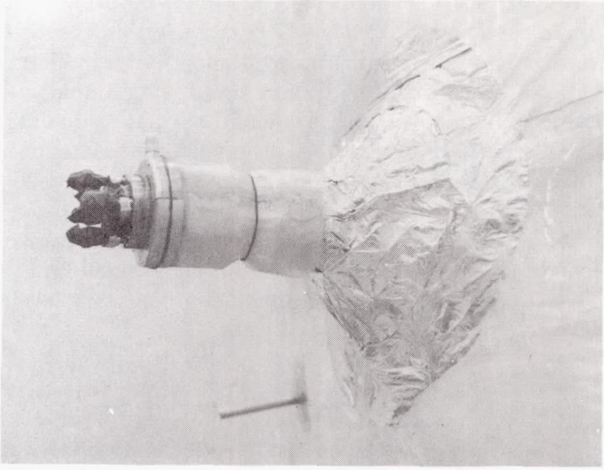

FIGURE 8. PIPING PENETRATION
AFTER INSULATION

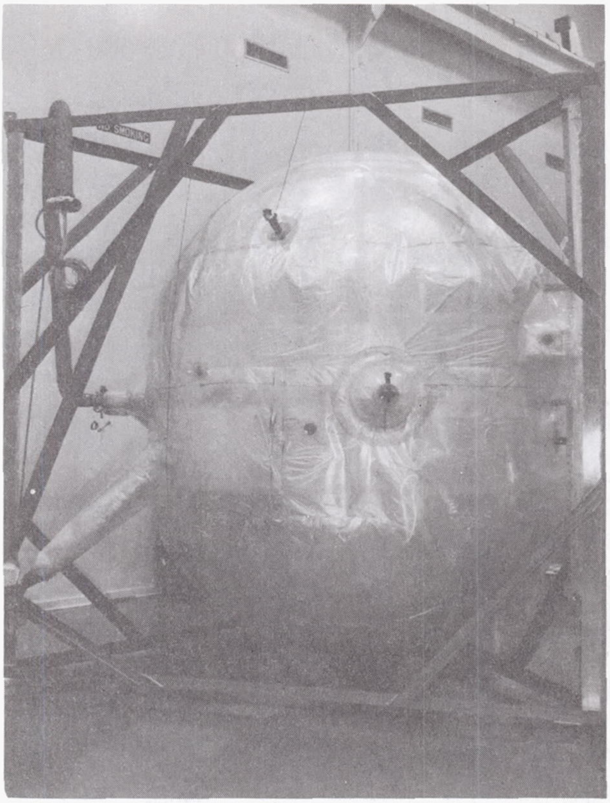

FIGURE 9. COMPLETED HELIUM PURGED INSULATION CONCEPT

of this insulation is its toughness and resistance to handling damage during application. The material should be handled only with clean cotton gloves to prevent degradation of its emissivity by oil secretions from the hands. Cutting of relatively thick layups can be done best with rotary blade electric shears. A few layers may be cut at a time using a sharp knife or scissors. It was found that sharp cutouts should be terminated by a punched hole to prevent tearing. Some problems were experienced in the fabrication and installation of the purge jacket because of the relatively inflexible material. Improved purge jackets were developed on subsequent contracts where zippers and other devices were incorporated to facilitate installation.

The insulated tank was subsequently tested and the hydrogen evaporation loss was less than 2 1/2% per day during the simulated space test. This was satisfactory for the planned mission although the experimental performance was considerably higher than the predicted performance.

PRE-EVACUATED INSULATION CONCEPT

A pre-evacuated insulation concept was designed under contract with Linde for application to one of the 2.67-m (105-in.) diameter test tanks. Under this contract the major development effort was directed towards the solution of problems encountered in the initial producibility study. Flexible vacuum jacket development, effect of compression on the recovery of insulation thickness and its effect on thermal performance, methods of improving evacuation of insulation, and insulation structural support were major tasks in the program. The final design called for SI-62 (aluminum foil and glass-fiber paper) insulation encased in a flexible vacuum jacket made from a laminate of 25.4μ mylar - 20.3μ lead - 25.4μ mylar (1 mil mylar - 0.8 mil lead - 1 mil mylar).

The general procedure used to apply the insulation system was as follows:

1. Apply Cylindrical Insulation.

The tank was set up in the assembly fixture and the rolls of insulation material were placed on either side for simultaneous wrapping onto the tank as shown in Figure 10. Aluminum foil bands were bonded to the tank and two turns were wrapped on the tank while being held in tension by a band tension machine shown in Figure 11. The air actuated brake on the aluminum foil roll can be adjusted to obtain the desired tension in the bands. These tension bands are wrapped onto the tank simultaneously with the insulation and prevent it from telescoping or sagging. After the tension bands were attached and the tension was properly adjusted, the aluminum foil and glass-fiber paper were taped to the tank with pressure sensitive tape, and the wrapping process was started. Periodically, thickness measurements were made, and the band tension was adjusted as needed to control the density. After the required 70 layers of insulation were installed, the insulation was cut off and taped down. An additional two wraps of the tension bands were made and then bonded in place. During the wrapping process holes were cut in the insulation to allow it to pass over the bimetallic joints. The bimetallic joints (aluminum fitting brazed to 7.62-cm (3-in.) stainless steel tubing) were welded into the tank to eliminate the leakage problem caused by bolted joints. The necessity of cutting these holes was a difficult and time consuming operation. The completed cylindrical wrap is shown in Figure 12, with the fittings installed for attachment of the handling ring.

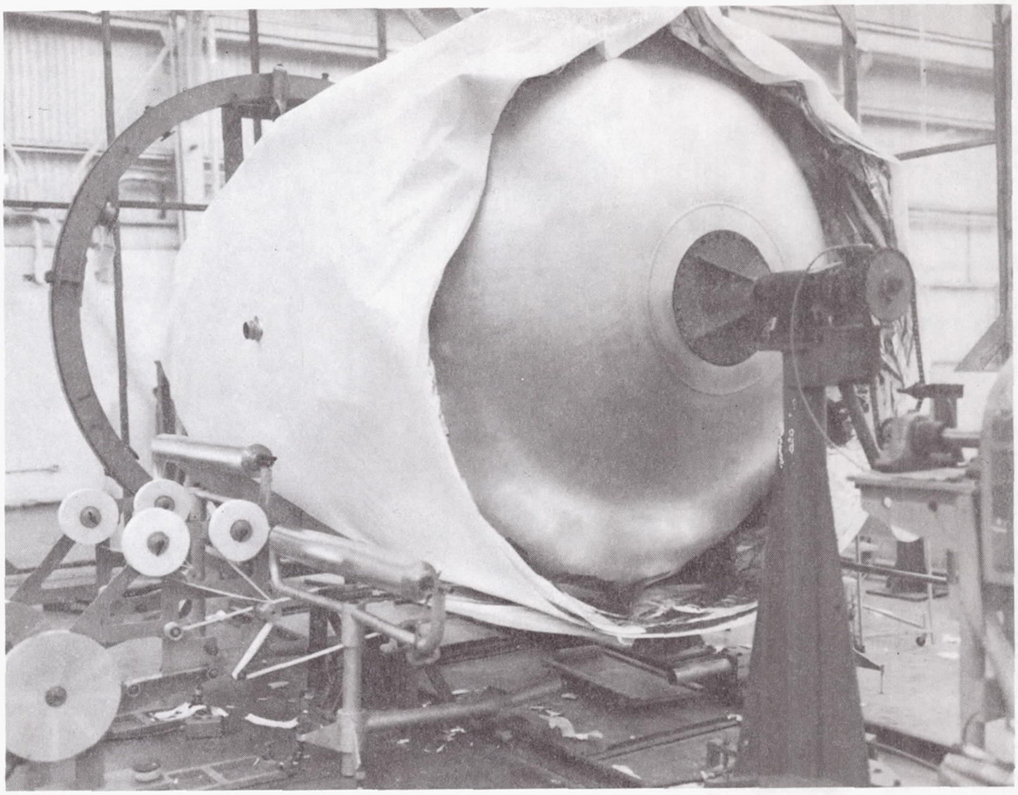

FIGURE 10. WRAPPING OF LINDE SI-62 INSULATION

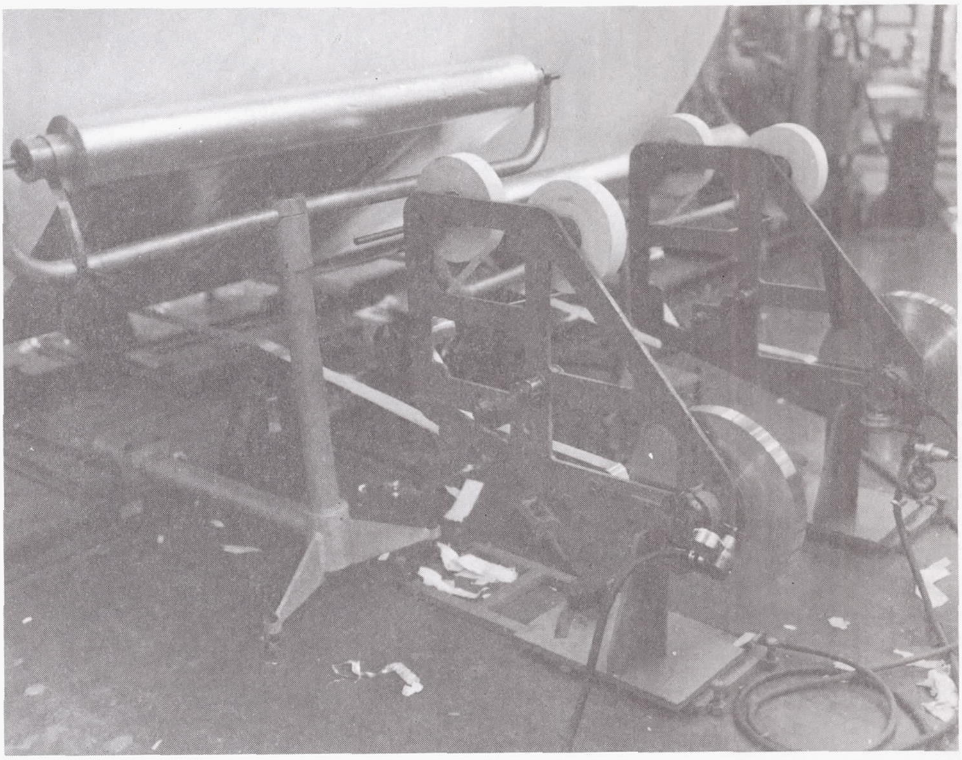

FIGURE 11. BAND TENSION MACHINES

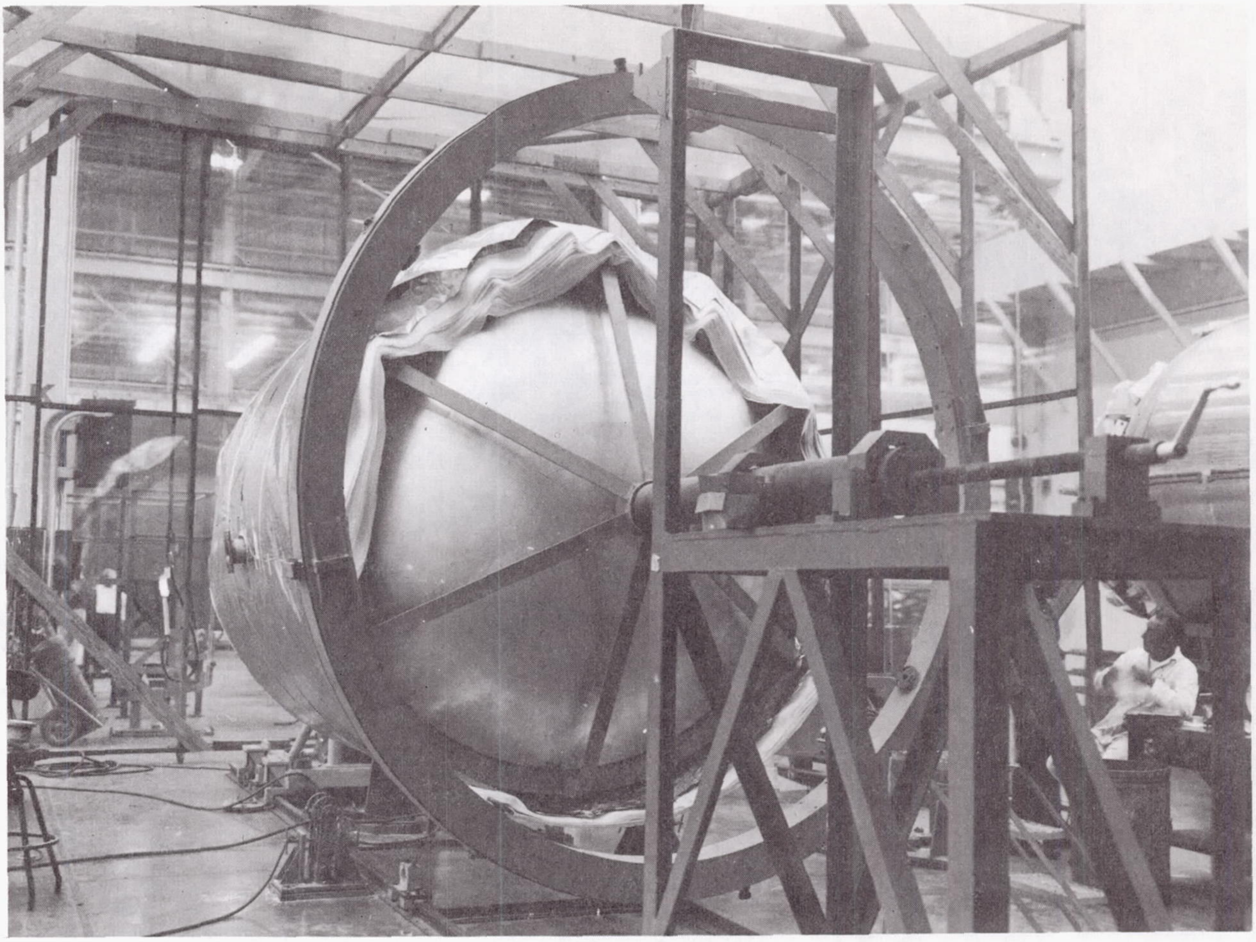

FIGURE 12. COMPLETED CYLINDRICAL WRAP

2. Insulation Bulkheads.

The handling ring was attached to the tank to provide support so that the spider ring supporting the rear bulkhead could be withdrawn. Blankets of insulation were wrapped on an auxiliary fixture to provide the material for insulating the bulkheads. Discs 2.44 m (96 in.) in diameter were cut from these blankets and installed a layer at a time on the bulkheads. The discs of insulation were interleaved into the cylindrical wrap and taped in place. As each disc was installed a layer of foil and a layer of glass-fiber paper from the cylindrical wrap were pulled down over the disc and the excess material folded, tucked and taped. Care was taken so that there was no shorting between layers of aluminum foil. This procedure was followed on each end, the only difference being the treatment around the manhole fitting. The completed insulation on the lower bulkhead is shown in Figure 13.

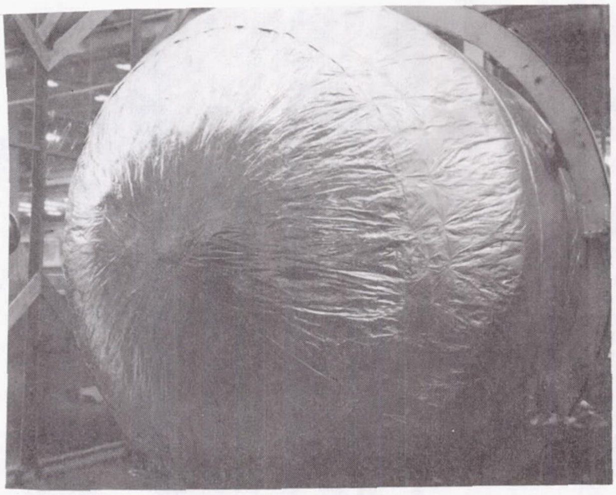

FIGURE 13. COMPLETED INSULATION ON LOWER BULKHEAD

3. Insulate Penetrations.

The tank was removed from the assembly fixture and installed in the support frames. The insulation around each penetration was cut back and layers of opacified paper (glass-fiber and aluminum slurry) interleaved as shown in Figure 14. After the 70 layers were interleaved around the base, the penetration was helically wrapped with aluminum foil and glass-fiber paper as shown in Figure 15.

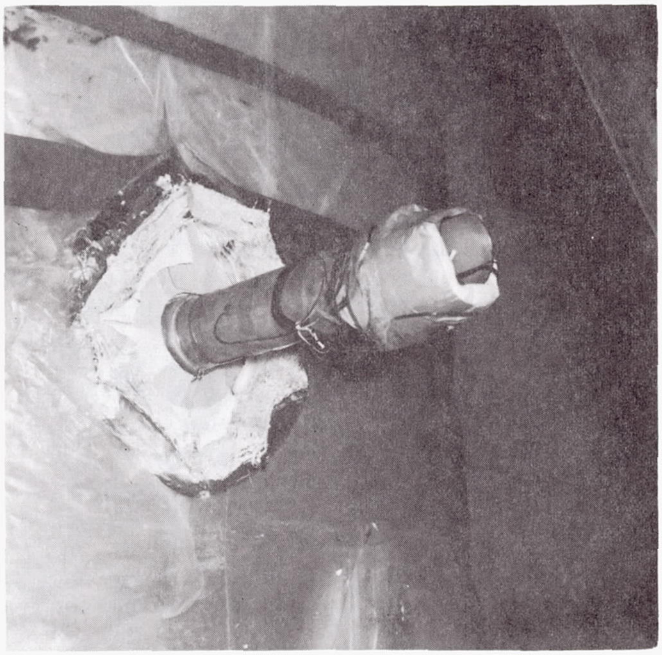

FIGURE 14. INTERLEAVING OPACIFIED PAPER AROUND PIPING PENETRATION

4. Install Flexible Vacuum Jacket.

The vacuum jacket was assembled on the tank using a portable heat sealer. Sheets of the 25.4μ mylar - 20.3μ lead - 25.4μ mylar (1 mil mylar - 0.8 mil lead - 1 mil mylar) laminate were joined to form a cylinder that was in turn joined to vacuum-formed head caps. Sheet metal transition pieces over the penetrations were joined to the flexible jacket by means of a mechanical joint sealed with an 0-ring. The completed vacuum jacket shown in Figure 16 was then evacuated to a pressure of about 66.7 N/m^2 (0.5 torr). During the evacuation process, leak tests were performed with a helium mass spectrometer. Most of the leaks were the result of handling damage. The overall permeability of the material was excellent as was the leak tightness of the heat sealed joints.

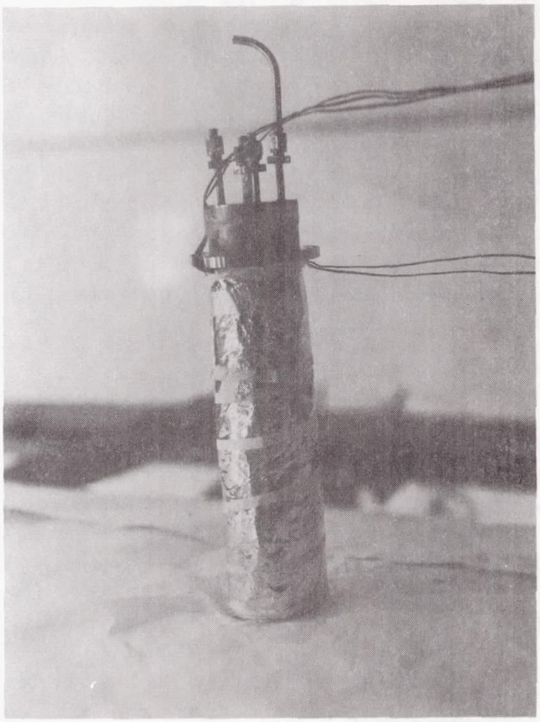

FIGURE 15. HELICALLY WRAPPED INSULATION ON PIPING PENETRATION

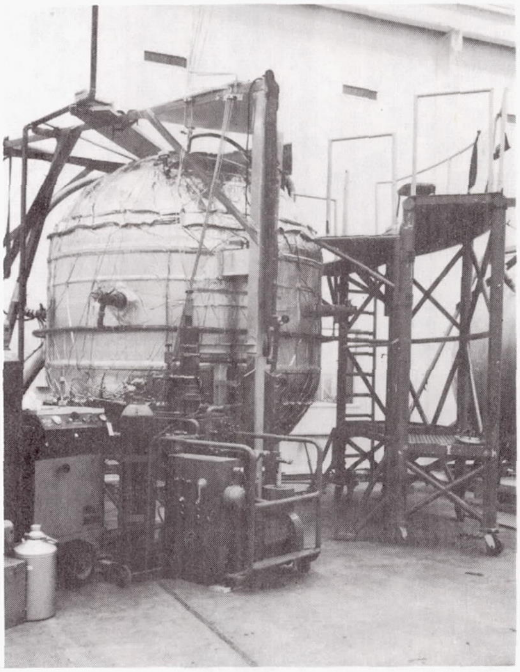

FIGURE 16. COMPLETED PRE-EVACUATED INSULATION CONCEPT

The application techniques employed were effective although improvements are needed in cutting insulation around penetrations. The advantage of fast application by the wrapping technique was nullified by having to cut holes in the insulation during the wrapping process. The requirement for interleaving insulation over bulkheads and around penetrations remained a problem. Flexible vacuum jackets were proven to be within current technology and capable of maintaining a satisfactory vacuum. A satisfactory test of the insulated tank has not been accomplished to date because of problems with a leaking manhole seal and bimetallic joint. These deficiencies have been corrected and the tank was proven to be sound. Plans have been made to test this system within the next few months.

CONCLUSIONS

It was concluded from these application studies that the current technology is adequate for the application of high performance insulation to flight type tanks for short term space storage of cryogenic fluids.

In comparing the pre-evacuated and helium purged concepts from a manufacturing viewpoint, the helium purged concept is favored. The helium purged concept was prefabricated to a large extent and required less time for actual application on the tank. This would result in a shorter flow time for an actual flight vehicle. The purge jacket was much less sensitive to physical damage than the vacuum jacket and was therefore more reliable. The poor conductance of compressed multilayer insulation makes evacuation a slow process. The material used in the helium purged concept was easier to handle and less sensitive to damage during application. The applied density of the pre-evacuated concept was more consistent and predictable than the helium purged concept because a spacer was used. Purged concepts with spacers probably could be applied with the same degree of consistency. Both systems can be repaired in the field although evacuation of a pre-evacuated concept would require considerably more time to repair. Quality control for both concepts would require in-process inspection and is largely dependent upon operator skill and motivation.

Additional development work is necessary to further refine the manufacturing process and to better assess the effects of manufacturing methods on thermal performance. Application of high performance insulation to large vessels as the Nuclear Vehicle for long term storage will require development of panel or modular concepts. Investigations are now underway to develop this advanced technology.

BIBLIOGRAPHY

1. Jones, Robert G.: Purged NRC-2 Super-Insulation Installation on a 105-Inch Diameter Liquid Hydrogen Tank. Manufacturing Development Memorandum, MDM-18-65, November 1965.

2. Aberle, J. L.: Development of Techniques and Hardware for Insulation Wrappings of Cryogenic Containers. Contract NAS8-11041, November 1964.

3. Lindquist, C. R.: Super-Insulation Systems for Cryogenic Test Tank. Contract NAS8-11740, February 1966.

4. Reed, M. E.: The Development of Techniques for Insulation Wrappings of Cryogenic Containers. Contract NAS8-11042.

DEVELOPMENT OF A COMBINED HIGH PERFORMANCE MULTILAYER INSULATION AND MICROMETEOROID PROTECTION SYSTEM

By

James M. Stuckey

SUMMARY

The development of a combined high performance multilayer insulation and micrometeoroid protection system for cryogenic tanks in outer space is discussed. The helium purged system consists of an outer micrometeoroid bumper of polyurethane resin impregnated glass cloth and a multilayer insulation of alternate layers of double aluminized Mylar film reflective shields and thin sliced polyurethane foam spacers. The four combined concepts that have been evaluated include two concepts with and two concepts without a special ground-hold insulation section inserted between the multilayer space insulation and the tank wall. In the combined concepts the aluminized Mylar can be applied in ribbon form using a filament winding technique on tanks not much larger than 3.05 m (120 in.) in diameter. For application to larger tanks the insulation concept was panelized. Excluding the bumper, the density of the basic insulation concepts is slightly more than 32 kg/m^3 (2.0 lb/ft^3). Thermal tests at high vacuum conditions on the filament wound insulation concept installed on a 76.2-cm (30-in.) diameter tank, in thicknesses varying from 3.0 to 5.1 cm (1.18 to 2.0 in.), showed heat leaks of approximately 6.92×10^{-5} W/m-°K (4.0×10^{-5} Btu/hr-ft-°F). The heat leak for the initial panelized concept was somewhat greater, being approximately 1.04×10^{-4} W/m-°K (6.0×10^{-5} Btu/hr-ft-°F). Tests simulating aerodynamic heating have shown that this concept can be applied externally to cryogenic tanks without requiring a protective shroud. Hypervelocity impact tests have shown that the multilayer insulation has energy adsorption capabilities and will tend to dissipate the energy of micrometeoroids that have been shattered by an outer bumper.

INTRODUCTION

The possibilities of incorporating the insulation system needed for cryogenic tanks in outer space with the micrometeoroid protection system required for extended space missions were envisioned at this Center. Assistance was solicited from industrial organizations to develop these possibilities, and in June, 1964, program NAS8-11747 was initiated with the Goodyear Aerospace Corporation to accomplish this objective. The following are the present goals of the program:

1. The average equilibrium heat leak under high vacuum conditions shall not exceed 0.79 W/m^2 (0.25 Btu/ft^2-hr) and should be approximately 0.63 W/m^2 (0.20 Btu/ft^2-hr).

2. The mass of the complete system shall be less than 2.44 kg/m^2 (0.5 lb/ft^2).

3. The composite concept shall be capable of preventing or instantaneously sealing a penetration of a particle in the mass range of 10^{-1} to 10^{-5} g impacting at a velocity of 9150 m/sec (30 000 ft/sec) or greater.

4. When applied externally to a launch or space vehicle, the composite concept shall give reliable service under conditions of prelaunch, launch, and space flight.

5. The composite concept shall be capable of withstanding surface temperature up to 505°K (450°F) for short times during the aerodynamic heating portion of flight.

6. The composite concept shall be capable of being reliably applied to the external surface of launch vehicles that are 10 m (33 ft) in diameter or larger.

7. The composite concept shall allow reliable application to tanks with irregular surface protuberances such as fuel lines, skirt sections, and instrument tunnels.

MULTILAYER INSULATION SYSTEMS

COMBINED SYSTEM DESIGN AND MATERIAL SELECTION

The four insulation concepts developed in this program were derived from the following considerations:

1. From hypervelocity impact test data and information in literature, the bumper wall was displaced approximately 5.1 cm (2 in.) from the tank wall to allow adequate spreading and adsorption of the shattered micrometeoroid particles that penetrate the bumper.

2. Aluminized Mylar was selected for the radiation shields to obtain light mass and have low conductivity along the shield.

3. For a spacer material between the multilayer reflective shields, thin sliced foams are one of the lightest materials that can be used and also possess energy adsorption characteristics.

Flat plate calorimeter screening tests using liquid hydrogen and high vacuum conditions were employed to select the foam spacer material to be used. Variables investigated were types of foam, foam spacer thickness, sample thickness, and surface pressure (compaction). The results of these tests are graphically summarized in Figure 1. The data show that thermal performance was affected by the type of foam, foam thickness, and pressure on the sample. Several of the foams gave essentially the same results. A red polyurethane foam was selected because of its availability commercially in sliced sheets. This material at a density of 27.2 kg/m^3 (1.7 lb/ft^3) is available in nominal 0.762-mm (30-mil) thick, 1.22 by 3.66 m (4 by 12 ft) sheets. The broken cells on the surface afford gas passage through the sheet and minimal contact resistance.

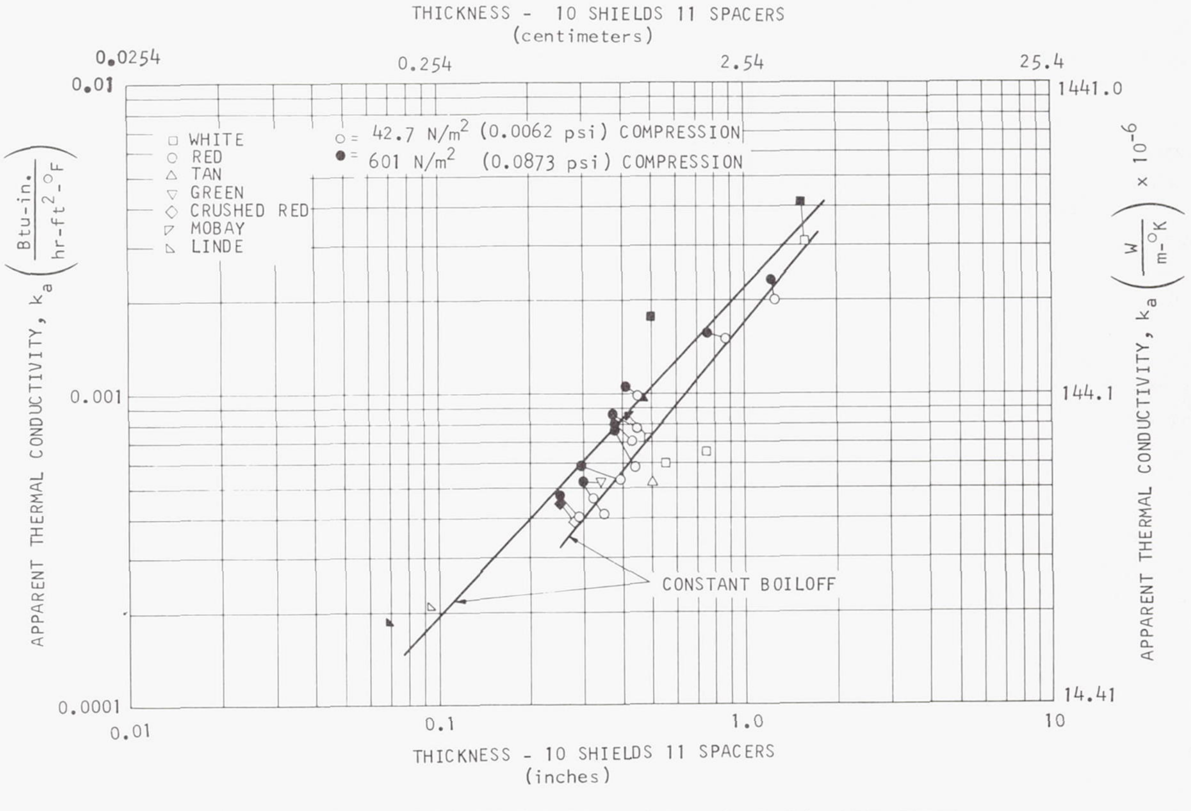

FIGURE 1. FOAM SCREENING ON FLAT PLATE CALORIMETER

INSULATION CONCEPTS INVESTIGATED

The four insulation concepts investigated in this program to date are briefly summarized in Figure 2. For all multilayer systems a dry gas purge is required to protect the aluminized Mylar radiation shields from the degradation effects of moisture. The first concept represents an optimum system for both ground-hold and high vacuum performance. However, there is little or no confidence that a completely leak proof vacuum bag can be consistently fabricated and installed on tanks or that a leak proof vacuum bag will remain in that condition throughout testing until launch. On this basis, sealed-cell Mylar-honeycomb core is bonded directly on the tank for the ground-hold insulation in the second concept. The need for a ground-hold section is based primarily on how close to launch the liquid hydrogen can be replenished. In some cases the liquid hydrogen tanks are topped off shortly before lift-off, thus there is a minimum requirement for a ground-hold section. On this assumption, the ground-hold insulation section was deleted from the third concept. In the fourth concept the third insulation concept was panelized and applied in two approximately 2.54-cm (1.0-in.) thick panels.

INSULATION CONCEPT	GROUND-HOLD SECTION	SPACE SECTION	BUMPER WALL
GAC-1	VACUUM BAG OVER ELEVEN SHIELD-SPACER COMBINATIONS	37 SHIELD-SPACER COMBINATIONS	RESIN IMPREGNATED GLASS CLOTH
GAC-2	SEALED-CELL MYLAR CORE	SAME	SAME
GAC-3	FULL INSULATION THICKNESS IS HELIUM PURGED	48 SHIELD-SPACER COMBINATIONS	SAME
GAC-4	SAME	2 PANELS OF 24 SHIELD-SPACER COMBINATIONS	SAME

FIGURE 2. INSULATION CONCEPTS EVALUATED ON 76.2-cm DIAMETER END-GUARDED CALORIMETER

The first composite insulation concept is described more thoroughly in Figure 3. In this system the lower eleven reflective shield-spacer combinations were encased in a vacuum jacket for the ground-hold insulation. The space insulation is the same as that in the ground-hold section, and consists of alternate layers of double aluminized 6.35-μ (1/4-mil) Mylar and thin foam spacers. The bumper wall consists of 0.375-mm (15-mil) 181 fiberglass cloth impregnated with approximately 17% polyurethane resin. At this low resin concentration, gases readily pass through the bumper wall. The calculated mass for this system is approximately 2.28 kg/m^2 (0.468 lb/ft^2). The third insulation concept is exactly like the first concept except that the vacuum bag has been deleted. On this basis the calculated mass for this system is approximately 1.98 kg/m^2 (0.405 lb/ft^2). The panelization of the third concept was designated as the fourth insulation concept. In insulation concepts 1, 3, and 4, 48 layers of foam spacer-aluminized Mylar were employed.

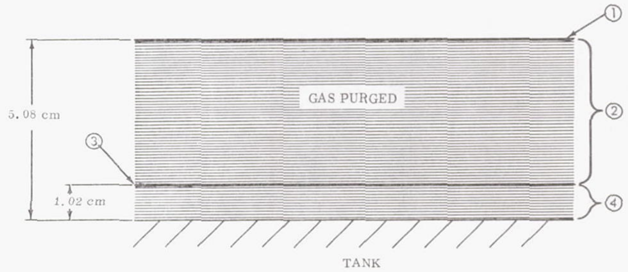

FIGURE 3. COMPOSITE INSULATION SYSTEM GAC-1

Legend for Figure 3:	lb/ft^2	kg/m^2
① Micrometeoroid Bumper [0.0381-cm (0.015-in.) fiberglass cloth impregnated with polyurethane resin]	0.100	0.488
② Micrometeorite Spacer and Multilayer Space Insulation		
37 Radiation Shields [6.35-μ (1/4-mil) aluminized Mylar]	0.067	0.327
37 Insulation Spacers [0.089-cm (0.035-in.) thick polyurethane foam]	0.168	0.820
③ Vacuum Jacket [0.00635-cm (0.0025-in.) MAAM film with nylon backing]	0.063	0.308
④ Sealed Multilayer Insulation		
11 Radiation Shields [6.35-μ (1/4-mil) aluminized Mylar film]	0.020	0.0976
11 Insulation Spacers [0.089-cm (0.35-in.) thick polyurethane foam]	0.050	0.244
Total Mass	0.468 lb	2.28 kg

The second insulation concept, shown in Figure 4, differs from the first concept only in the ground-hold insulation. In the second concept a 1.02-cm (0.4-in.) thick sealed-cell Mylar-honeycomb substrate replaced the 1.02-cm (0.4-in.) vacuum jacketed multilayer section. This system was heavier with a mass of approximately 2.38 kg/m² (0.483 lb/ft²).

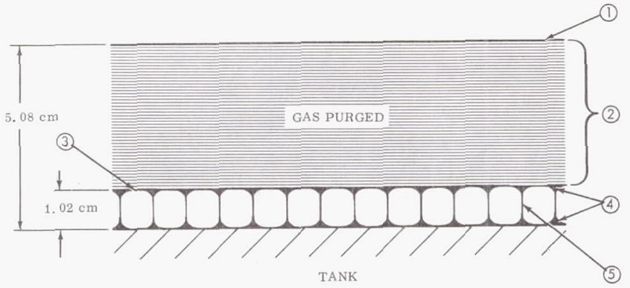

FIGURE 4. COMPOSITE INSULATION SYSTEM GAC-2

Legend for Figure 4:	lb/ft²	kg/m²
① Micrometeorite Bumper [0.0381-cm (0.015-in.) fiberglass cloth impregnated with polyurethane resin]	0.100	0.488
② Micrometeorite Spacer and Multilayer Space Insulation		
37 Radiation Shields [6.35-μ (1/4-mil) aluminized Mylar]	0.067	0.327
37 Insulation Spacers [0.089-cm (0.035-in.) thick polyurethane foam]	0.168	0.820
③ Substrate Seal Layer [0.00635-cm (0.0025-in.) MAAM film]	0.018	0.088
④ Polyurethane Adhesive Bond Lines (2 required)	0.060	0.293
⑤ Core Substrate [1.02-cm (0.40-in.) thick, 0.95-cm (3/8-in.) cell Mylar honeycomb, 34.1 kg/m³ (2.13 lb/ft³) density]	0.070	0.342
Total Mass	0.483 lb	2.36 kg

APPLICATION OF INSULATION CONCEPTS TO TEST TANK

To evaluate the insulation systems, a 76.2-cm (30-in.) diameter stainless steel double-guarded cylindrical tank was designed and fabricated to serve as a subscale tank for application tests and as a space calorimeter. The 2.03-m (80-in.) long calorimeter is shown in Figure 5. Each of the three sections is equipped with liquid hydrogen fill and vent lines. The center measuring section is 1.22-m (4-ft.) long.

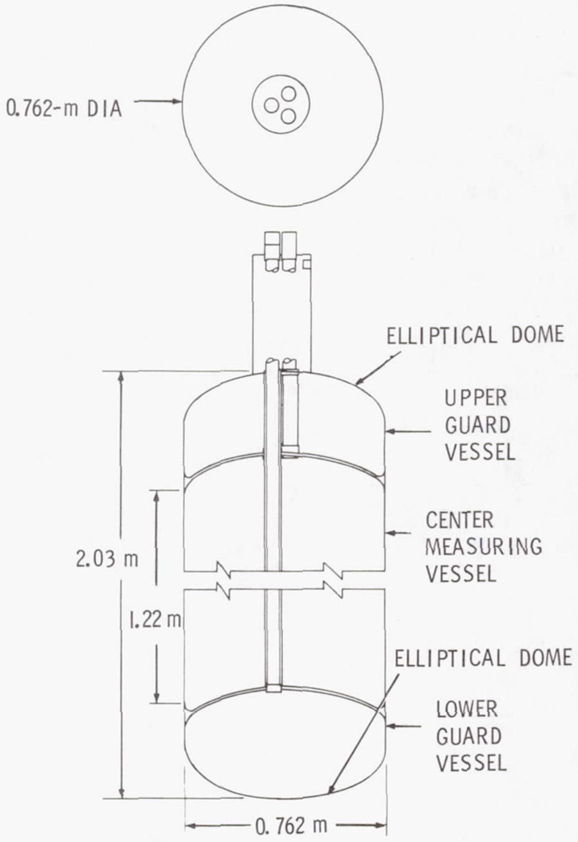

FIGURE 5. 76.2-cm DIAMETER CYLINDRICAL CALORIMETER

To apply the first three insulation concepts, the subscale tank was mounted in a filament winding machine. Installation of the foam spacer is shown in Figure 6. Spot bonding with quick drying adhesive was necessary to hold the foam in place. The foam was gored for application to the domes of the tank. The aluminized Mylar was applied by wrapping with 1.27-cm (1/2-in.) wide tape as shown in Figure 7. In the first insulation concept a vacuum jacket

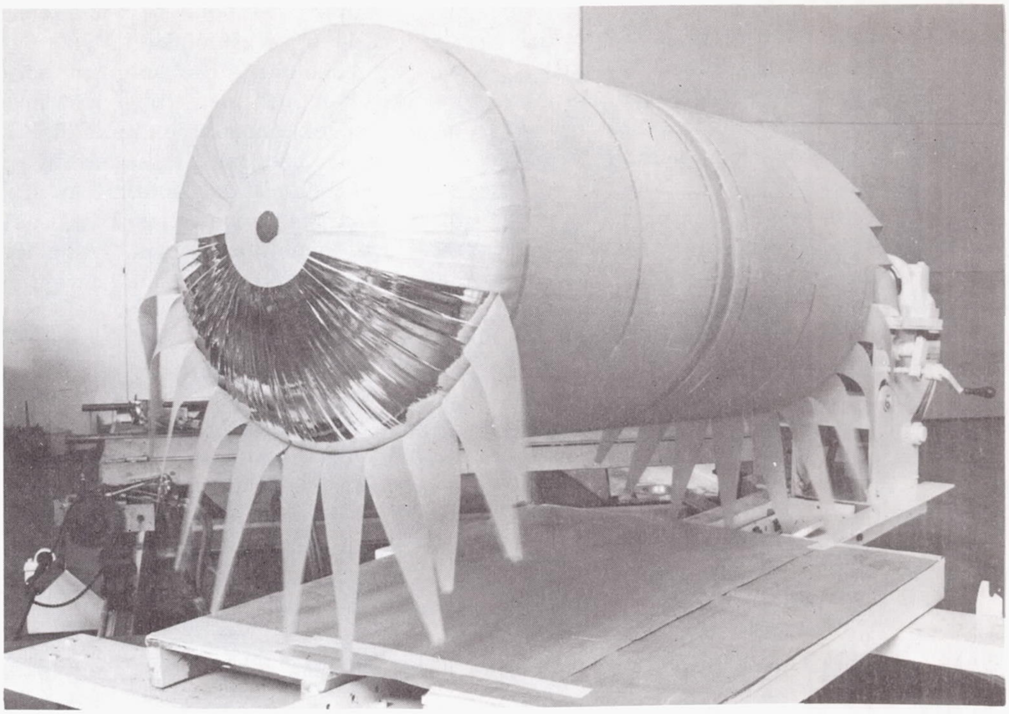

FIGURE 6. INSTALLATION OF FOAM SPACER ON 76.2-cm DIAMETER CALORIMETER

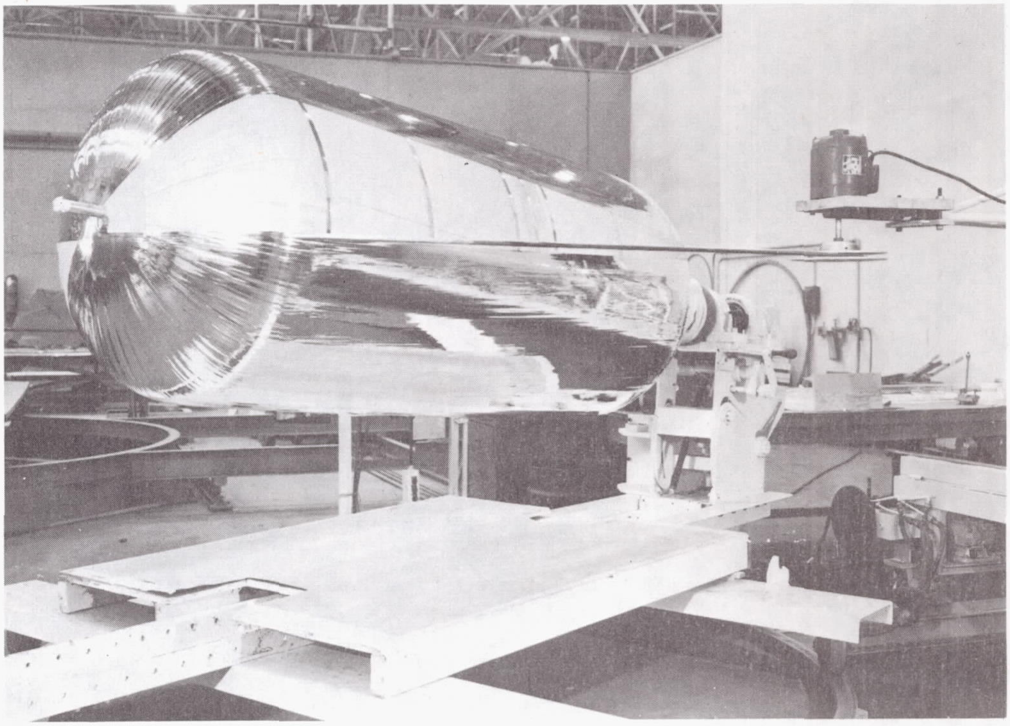

FIGURE 7. WRAP OF ALUMINIZED MYLAR OVER FOAM SPACER ON 76.2-cm DIAMETER CALORIMETER

fabricated with nylon back MAAM was installed over the initial 11 layers of Mylar-foam combinations. MAAM is a composite of 12.7-μ (0.5-mil) Mylar, 8.9-μ (0.35-mil) aluminum, 8.9-μ (0.35-mil) aluminum, 12.7-μ (0.5-mil) Mylar. The evacuation port for the vacuum jacketed section is located on the bottom dome (Fig. 7).

Thirty-seven layers of foam-Mylar combination were applied over the vacuum jacket. The preconstructed bumper wall was installed as two halves over the space insulation using pressure-sensitive tape to facilitate removal.

In the second insulation concept the ground-hold insulation consisted of a 1.02-cm (0.4-in.) thick, 0.95-cm (3/8-in.) cell Mylar-honeycomb core bonded directly to the tank (Fig. 8). Thirty-seven alternate layers of aluminized Mylar and foam spacers were applied over the ground-hold insulation, and a bumper wall was added as previously described. The third insulation concept was fabricated by applying 48 alternate layers of aluminized Mylar and foam spacers and then attaching the bumper wall.

With present equipment and technology the application of the aluminized Mylar by the filament winding technique is probably limited to tanks not much larger in diameter than 3.05 m (120 in.). For large cryogenic tanks similar in size to those used in the Saturn program, this multilayer concept was panelized to facilitate installation. The panelization of the third insulation concept was designated as the fourth insulation concept. A preformed outer panel of the fourth insulation concept as shown in Figure 9 consisted of 24 alternate layers of aluminized Mylar and foam spacers between an inner and outer grid of glass fiber preimpregnated rovings spaced approximately 2.54 cm (1.0 in.) apart with an edge band picture frame of No. 181 glass cloth impregnated with epoxy resin. Load bearing phenolic washers were bonded to the edge band to serve as attachment points for installation. The bumper wall was included within the grid. The panel was held together by Dacron or nylon drop threads through the insulation; the threads were located approximately every 10.2 cm (4.0 in.) and secured to the grids on both sides.

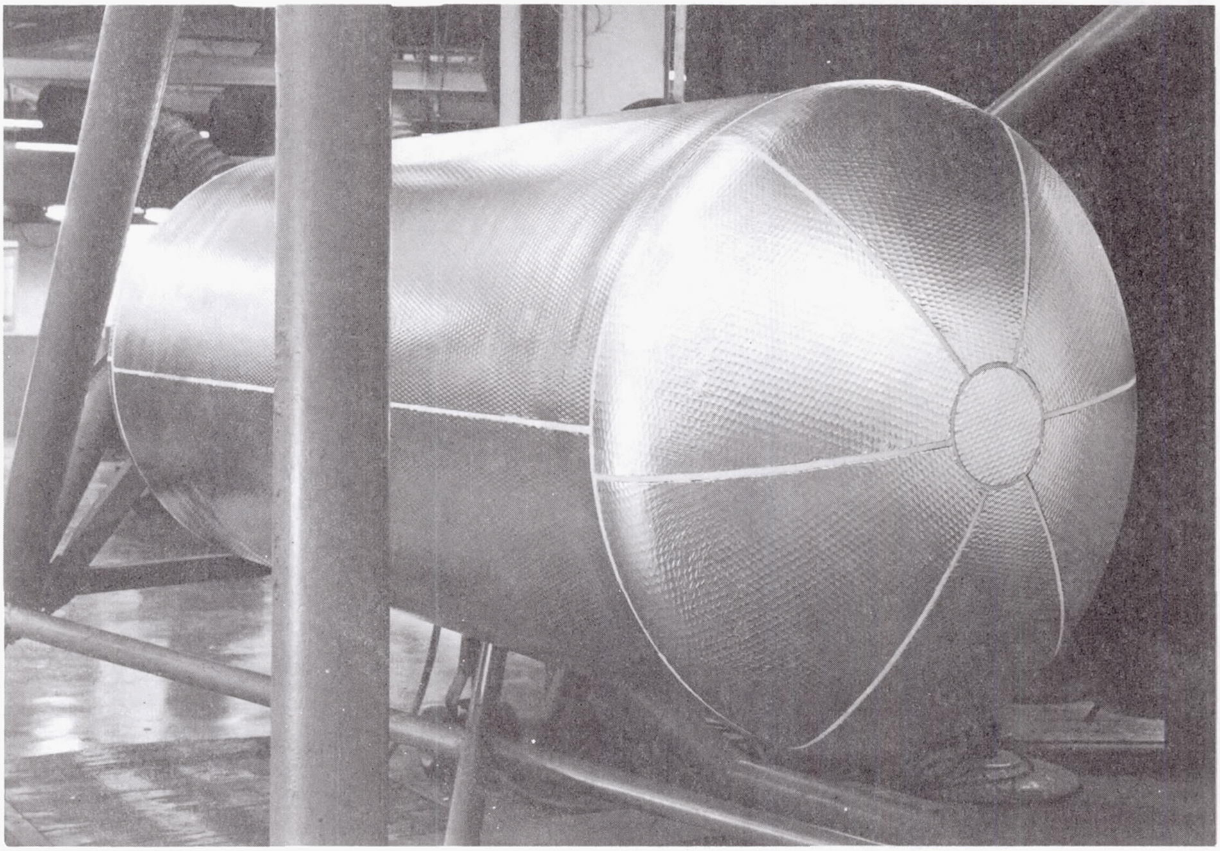

FIGURE 8. SECOND INSULATION CONCEPT: SUBPANEL ON CALORIMETER

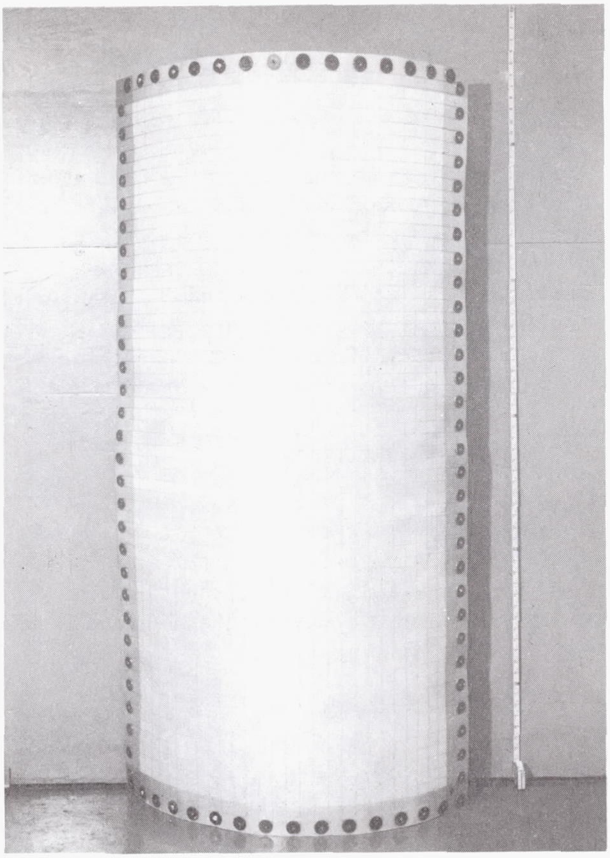

FIGURE 9. PREFORMED OUTER GAC-4 INSULATION PANEL

In the initial attempt at panelization, only the cylindrical section was considered. To save both time and money, the filament wound aluminized Mylar and foam spacers for the third insulation concept were carefully cut so that both dome ends remained intact while removing the cylindrical portion. The cylindrical section was insulated with a set of three inner panels next to the tank, and a set of three outer panels over the inner panels. The outer panels were 10.2 cm (4.0 in.) longer than the inner panels to provide a stepped joint with the domed ends. The insulation panels were supported vertically by a net covering the top dome. The insulation on the bottom dome was held in place by a similar net attached to the panels. The joints of the inner and outer panels were staggered to minimize the heat leaks. The completely insulated tank with the fourth panelized insulation concept is shown in Figure 10. The panels were further supported by lacing them together circumferentially.

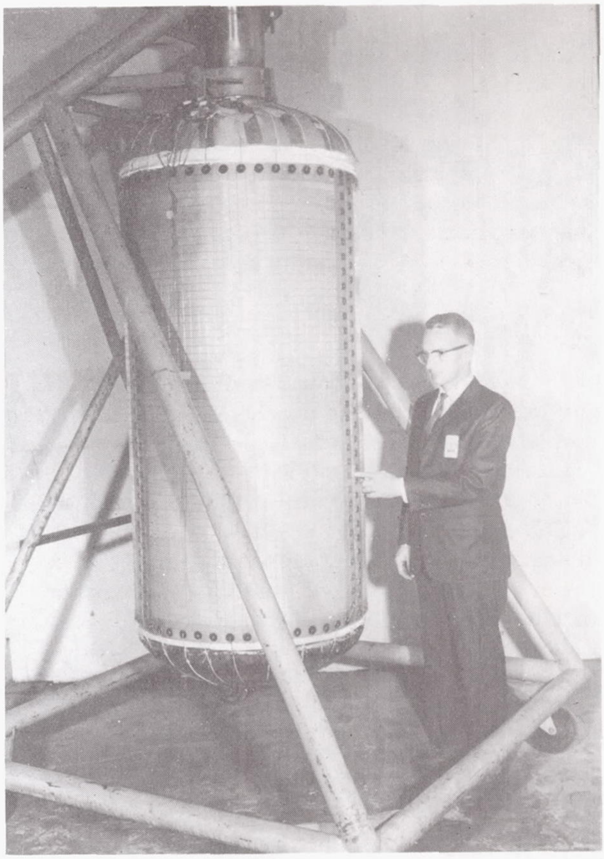

FIGURE 10. INSULATION SYSTEM GAC-4 COMPLETELY INSTALLED ON CALORIMETER

TESTS ON INSULATION SYSTEMS

TEST PROCEDURE AND FACILITIES

Insulation composite systems attached to the 76.2-cm (30-in.) diameter cylindrical test tank were evaluated by subjecting the tank filled with liquid hydrogen to the following sequence and minimum conditions:

1. Boiloff measurements under high vacuum conditions.

2. Five liquid hydrogen fill and drain cycles using a helium purge in the multilayer space insulation to simulate ground testing.

3. Simulated aerodynamic heating cycle combined with atmospheric pressure decay.

4. Boiloff measurements under high vacuum conditions.

The liquid hydrogen test facility used to test the insulation system is shown in Figure 11. The vacuum chamber is equipped with a heater to simulate aerodynamic heating, and can be evacuated to 1.33×10^{-4} N/m^2 (10^{-6} mm Hg).

GROUND-HOLD TESTS

Results of the ground-hold tests for the four insulation concepts are presented in Table I. The data showed that essentially the same thermal performances were obtained with the first, third, and fourth insulation concepts, and approached that of helium. These results together with other data showed that the vacuum jacket used in the first insulation concept leaked, and thus three of the insulation concepts were practically the same.

The second insulation concept differed from the first insulation concept in having a ground-hold insulation section consisting of sealed-cell Mylar-honeycomb core. The performance of this insulation concept with a helium purge reduced the boiloff of hydrogen considerably, and the boiloff was even lower when a dry nitrogen purge was substituted for helium. After the second concept was exposed to 14 ground-hold tests and two simulated aerodynamic heating tests, there was no indication that the sealed-cell Mylar-core ground-hold insulation section had been damaged or adversely affected.

TEMPERATURE, PRESSURE AND BOILOFF DURING SIMULATED ASCENT CYCLE

At the end of a ground-hold test, a simulated aerodynamic heating cycle was performed while evacuating the test chamber. Temperature profiles for simulated ascent cycles for the third and fourth

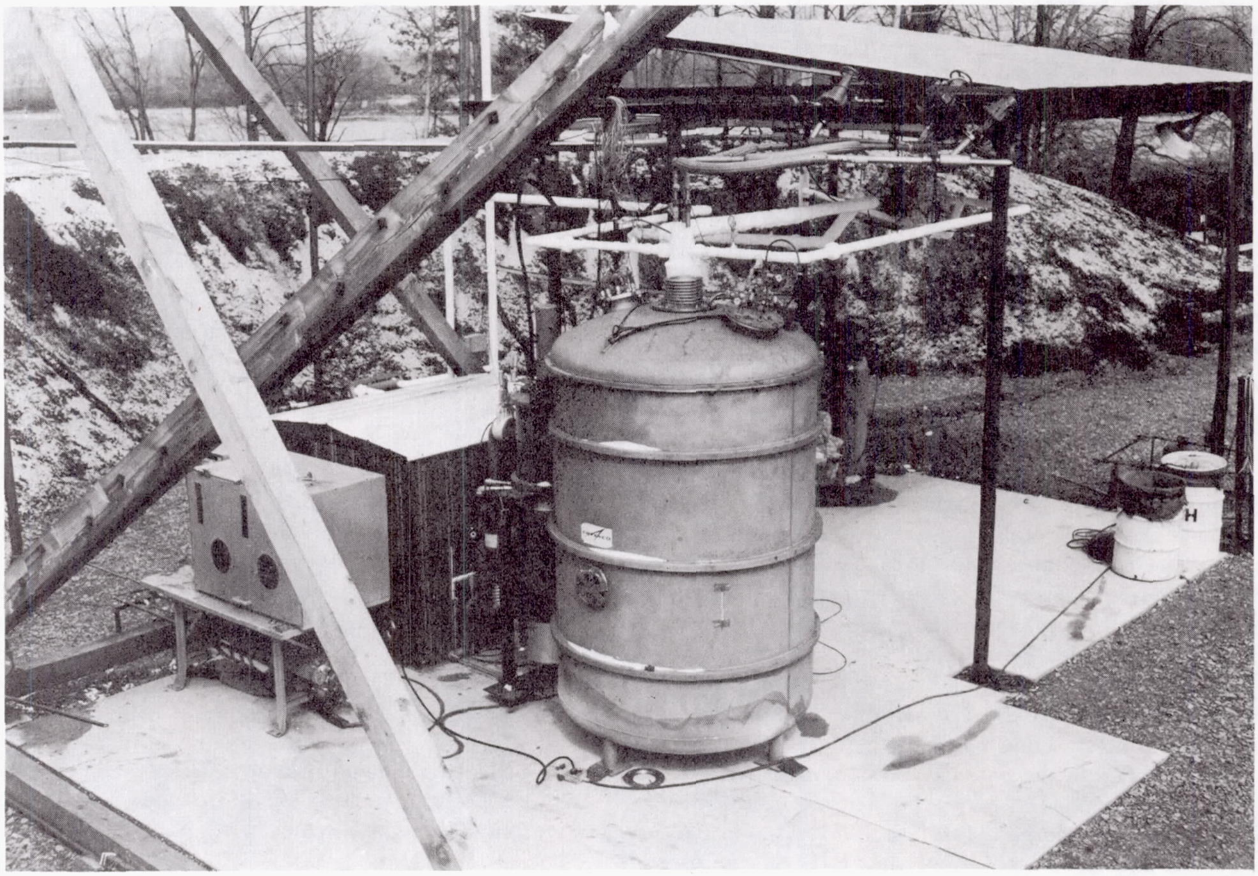

FIGURE 11. LIQUID HYDROGEN TEST FACILITY

TABLE I. THERMAL PERFORMANCE OF HELIUM PURGED INSULATION CONCEPTS

Insulation System	No. of Tests	Purge Gas	Outer Surface Temperature °K (° F)	$\dot{q}$ W/m^2 (Btu/hr-ft^2)	k x 10^{-2} W/m^2-°K (Btu/hr-ft-°R)
GAC-1	5	He	252 to 231 (-6 to -43)	274 - 322 (87 - 102)	6.40 - 7.44 (3.7 - 4.3)
GAC-2	6	He	253 to 244 (-4 to -22)	208 - 252 (66 - 80)	4.50 - 5.71 (2.6 - 3.3)
	4	N_2	272 to 280 (30 to 44)	129 - 148 (41 - 47)	2.60 - 2.94 (1.5 - 1.7)
GAC-3	5	He	244 to 238 (-20 to -32)	318 - 341 (101 - 108)	7.26 - 7.79 (4.2 - 4.5)
GAC-4	5	He	236 to 228 (-35 to -50)	372 - 400 (118 - 127)	9.00 - 9.70 (5.2 - 5.6)
	1	He	214 (-75)	304 (96.5)	7.95 (4.6)

insulation concepts are shown in Figure 12. These results show that the tests reached the desired 505°K (450°F) maximum temperature somewhat later than will be encountered in flight, and that the surface did not cool off as fast as expected in space.

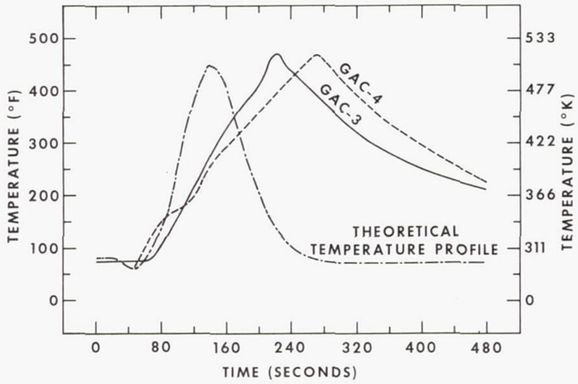

FIGURE 12. TEMPERATURE PROFILES FOR SIMULATED ASCENT CYCLE

Boiloff for the simulated ascent cycles is shown in Figure 13. These tests showed that boiloff of hydrogen decreased markedly within 20 minutes. Pressure profiles during the simulated launch cycle are shown in Figure 14. These results show that a much higher vacuum had been obtained in the test chamber with the third insulation concept than with the fourth insulation concept, indicating that the filament wound concept had better venting characteristics than the panelized concept.

Examination of the insulation systems after the simulated aerodynamic heating cycles to surface temperature of 505°K (450°F) showed that the aluminized Mylar film in the outer 2 or 3 layers had been damaged. This is not considered to be a major problem because aluminized Kapton film can be substituted for the aluminized Mylar film for the outer few layers.

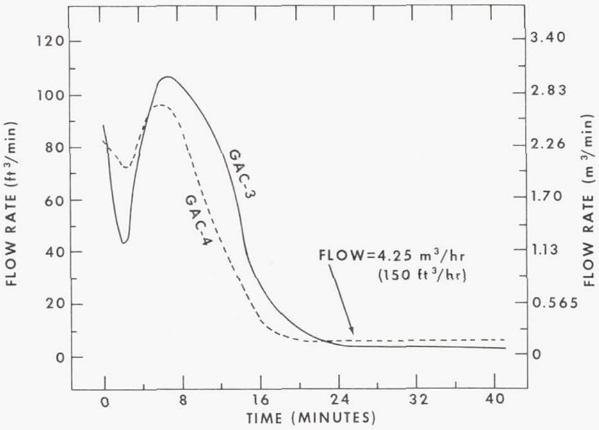

FIGURE 13. BOILOFF PROFILES FOR SIMULATED ASCENT CYCLE

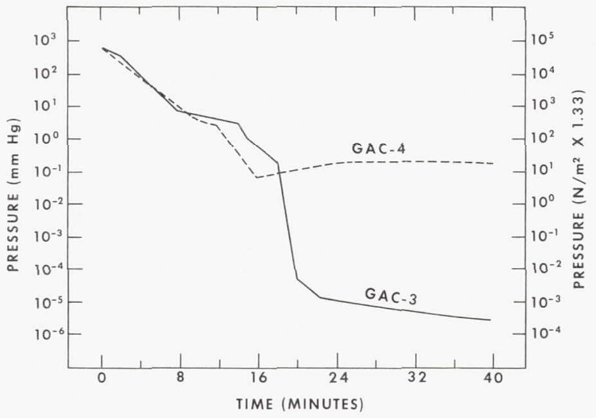

FIGURE 14. VACUUM PUMP-DOWN PROFILES FOR SIMULATED ASCENT CYCLE

INSULATION PERFORMANCE UNDER HIGH VACUUM CONDITIONS

Test results under high vacuum conditions for the first three insulation concepts on the 76.2-cm (30-in.) diameter tank for the center measuring section that is end-guarded are shown in Table II. In all cases the results reported are average values for a 24-hour period. The marked difference in performance between test 1 and 2 on the first insulation concept was attributed to a leak in the vacuum jacket for the ground-hold insulation and the inability to pump out the helium entrapped behind the vacuum jacket in a reasonable period of time.

Since the second insulation concept has a ground-hold insulation section consisting of sealed-cell Mylar core 1.02-cm (0.4-in.) thick, the effective multilayer section was only 4.06-cm (1.6-in.) thick. Under high vacuum conditions, tests have indicated that the Mylar core contributes very little to the thermal effectiveness of the multilayer insulation. Accordingly, only the multilayer section was considered in calculating test results, and on this basis there is general agreement for the results obtained for the first and second insulation concepts. For the fourth test on the second insulation concept, the tank was taken out of the test chamber and the outer 10 layers of the 37 total reflective insulation layers were removed before returning the tank to the test chamber. Space tests on this second insulation concept with only 27 reflective insulation layers showed that again a thermal conductivity value around 6.05 x 10^{-5} W/m-°K (3.5 x 10^{-5} Btu/ft-hr-°F) was obtained. The thermal conductivities determined for the third insulation concept are essentially the same and are in general agreement with the other data on the first and second insulation concepts.

In Table III test results under high vacuum conditions are shown for the panelized fourth insulation concept. Essentially the same thermal performance was obtained during the first three tests on this insulation concept. The first two tests were run for visual observation of the panels during vacuum pump-down, and the third test followed the simulated areodynamic heating cycle. It was expected that thermal performance would be degraded by panelization, but not to the extent encountered.

Several factors probably contributed to this greater heat leak, and the leaks caused by the longitudinal joints were suspected to be one of the major contributors because these joints passed directly across the center measuring section. To eliminate this heat leak, 5.1 to 7.6-cm (2 to 3-in.) wide strips of double aluminized Mylar were interleaved in the joints for all 24 layers in the outer panel. Test No. 4 was run on this configuration, and both the heat leak and thermal conductivity were improved some as shown in Table III. Another possible source of heat leak is the circumferential joints. These were not too good, and their proximity to the junctions of the guard tank and to the center measuring tank probably affected the results, but the extent of this effect has not been adequately determined yet.

TABLE II. THERMAL PERFORMANCE UNDER HIGH VACUUM - INSULATION CONCEPTS GAC-1, GAC-2 AND GAC-3

Insulation System	Test No.	Outer Surface Temperature °K (°F)	Multilayer Thickness Centimeters (Inches)	$\dot{q}$ W/m^2 (Btu/hr-ft^2)	k x 10^{-5} W/m-°K (Btu/hr-ft-°R)
GAC-1	1	286 (55)	5.08 (2.0)	0.306 (0.097)	5.88 (3.4)
	2	285 (53)	5.08 (2.0)	0.678 (0.215)	13.0 (7.5)
GAC-2	1	289 (60)	4.06 (1.6)	0.505 (0.160)	7.61* (4.4)
	2	292 (65)	4.06 (1.6)	0.407 (0.129)	6.05* (3.5)
	4	284 (50)	3.00 (1.18)	0.501 (0.159)	5.88* (3.4)
GAC-3	1	290 (62)	5.08 (2.0)	0.312 (0.099)	5.88 (3.4)
	2	288 (58)	5.08 (2.0)	0.338 (0.107)	6.40 (3.7)

TABLE III. THERMAL PERFORMANCE UNDER HIGH VACUUM - INSULATION CONCEPT GAC-4

Test No.	Outer Surface °K (°F)	Multilayer Thickness Centimeters (Inches)	$\dot{q}$ W/m^2 (Btu/hr-ft^2)	k x 10^{-5} W/m^2-°K (Btu/hr-ft-°R)
1	279 (42)	4.70 (1.85)	0.615 (0.195)	11.24 (6.5)
2	270 (25)	4.70 (1.85)	0.596 (0.189)	11.24 (6.5)
3	270 (26)	4.70 (1.85)	0.609 (0.193)	11.41 (6.6)
4	282 (48)	4.70 (1.85)	0.502 (0.159)	9.00 (5.2)

EFFECT OF COMBINED VIBRATION, ACCELERATION AND RAPID EVACUATION

In contract NAS8-18021 with General Dynamics-Convair, monitored by Mr. Hyde of the Propulsion Division of the Propulsion and Vehicle Engineering Laboratory, insulation concepts are being evaluated under the combined effects of vibration, acceleration, and rapid evacuation while being cooled with helium gas. Later the insulation concepts are tested acoustically. The insulation systems are installed on a scale model of a 2.67- m (105-in.) diameter tank, approximately 73.7 cm (29 in.) in diameter and about 61 cm (24 in.) in length. The panelized insulation concept developed in this program has been included in the evaluation program at General Dynamics and one of the test tanks has been insulated with concept No. 4. The panels used to insulate the tank are shown in Figure 15. The fully insulated tank is shown in Figure 16. The insulated tank has been subjected to all four system tests without causing structural damage to the insulation. Cryogenic tests also showed the same thermal performance both before and after the tests, again indicating that combined environments had little or no adverse effects on the insulation.

FIGURE 15. GAC-4 PANELS EMPLOYED TO INSULATE 73.7-cm DIAMETER TANK

HYPERVELOCITY IMPACT TESTS

To evaluate the potential of these insulation concepts for affording protection to cryogenic tanks from penetration by micrometeoroids, extensive hypervelocity impact tests have been carried out at Illinois Institute of Technology at Chicago. In these tests pyrex balls weighing 5, 17, and 71.4 mg traveling at speeds up to 7160 m/sec (23 500 ft/sec) have been used. A typical sample used in these tests is presented in Figure 17. In Figure 18 is shown the effect of impacting the first and second insulation concepts with 17 mg pyrex balls traveling at 6710 to 7010 m/sec (22 000 to 23 000 ft/sec). In both cases debris penetrated completely through the insulation, but did not damage the 0.762-mm (30-mil) aluminum back-up plate. When 71.4 mg pyrex balls were fired at similar samples at speeds up to 6400 to 6710 m/sec (21 000 to 22 000 ft/sec), no significant depth penetration occurred in the back-up plate. When 5 mg pyrex balls were used at speeds up to 7160 m/sec (23 500 ft/sec), debris did not penetrate the insulation completely. To determine how significant a role the multilayer insulation played in preventing damage to the tank wall from the debris resulting from micrometeoroids striking the bumper wall, hypervelocity impact tests were conducted on samples having only a bumper wall spaced at the same 5.1 cm (2.0 in.) from a 0.476-cm (3/16-in.) aluminum witness plate. The effect of impacting the sample with a 17 mg glass projectile traveling about 6710 m/sec (22 000 ft/sec) is shown in Figure 19. In this test significant penetration of the witness plate occured.

FUTURE PLANS

Future efforts will be concentrated on the optimization of the panelized insulation concept. Panel and joint design, size, thickness, and ultimate methods of panel fabrication will be studied to optimize thermal performance and to enhance reliable installation on large flight vehicles. Purging and venting studies on the insulation will include the design and application of a purge jacket that not only will contain the purge gas but will reliably vent the gas inside the jacket immediately after launch. Improved methods will be developed for applying the insulation around and to protuberances of cryogenic tanks.

Information on the heat leak through the basic panel, panel joints, and joints around protuberances will be developed as feasible.

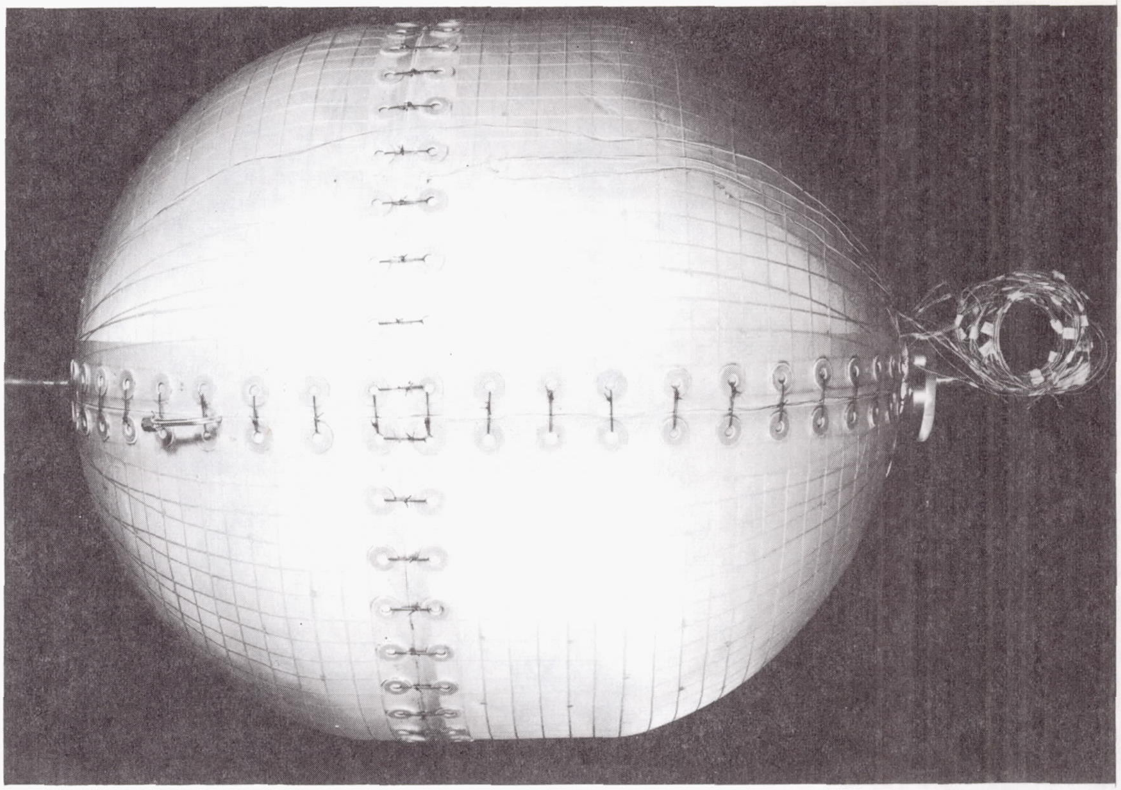

FIGURE 16. GAC-4 INSULATION INSTALLED ON 73.7-cm DIAMETER TANK

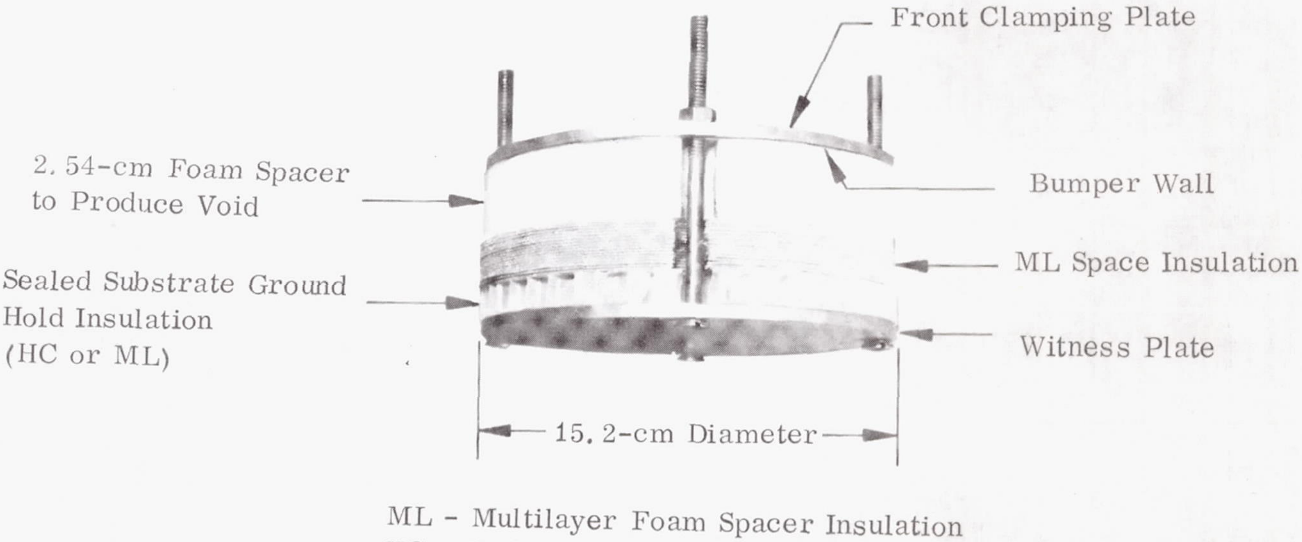

ML - Multilayer Foam Spacer Insulation
HC - Sealed-Cell Mylar Honeycomb

FIGURE 17. SAMPLE FOR HYPERVELOCITY IMPACT TEST

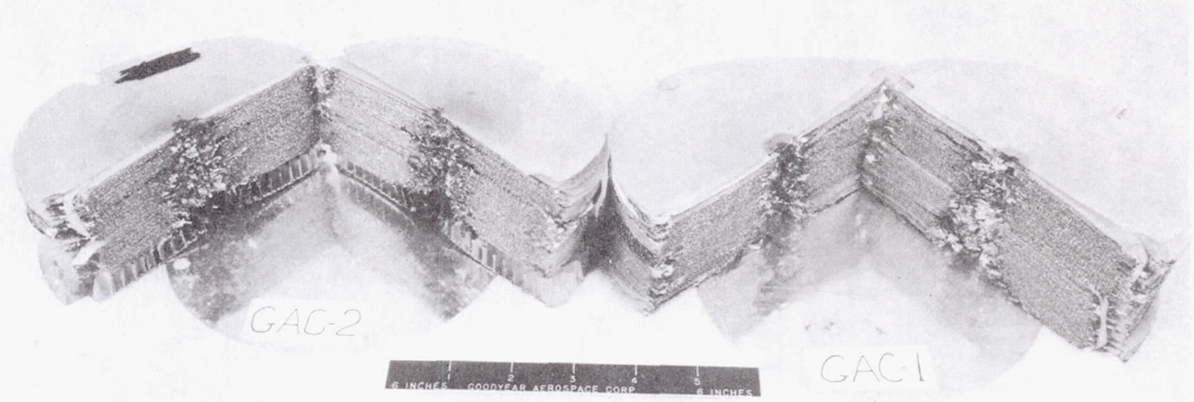

FIGURE 18. HYPERVELOCITY IMPACT TEST ON INSULATION CONCEPTS GAC-1 AND GAC-2

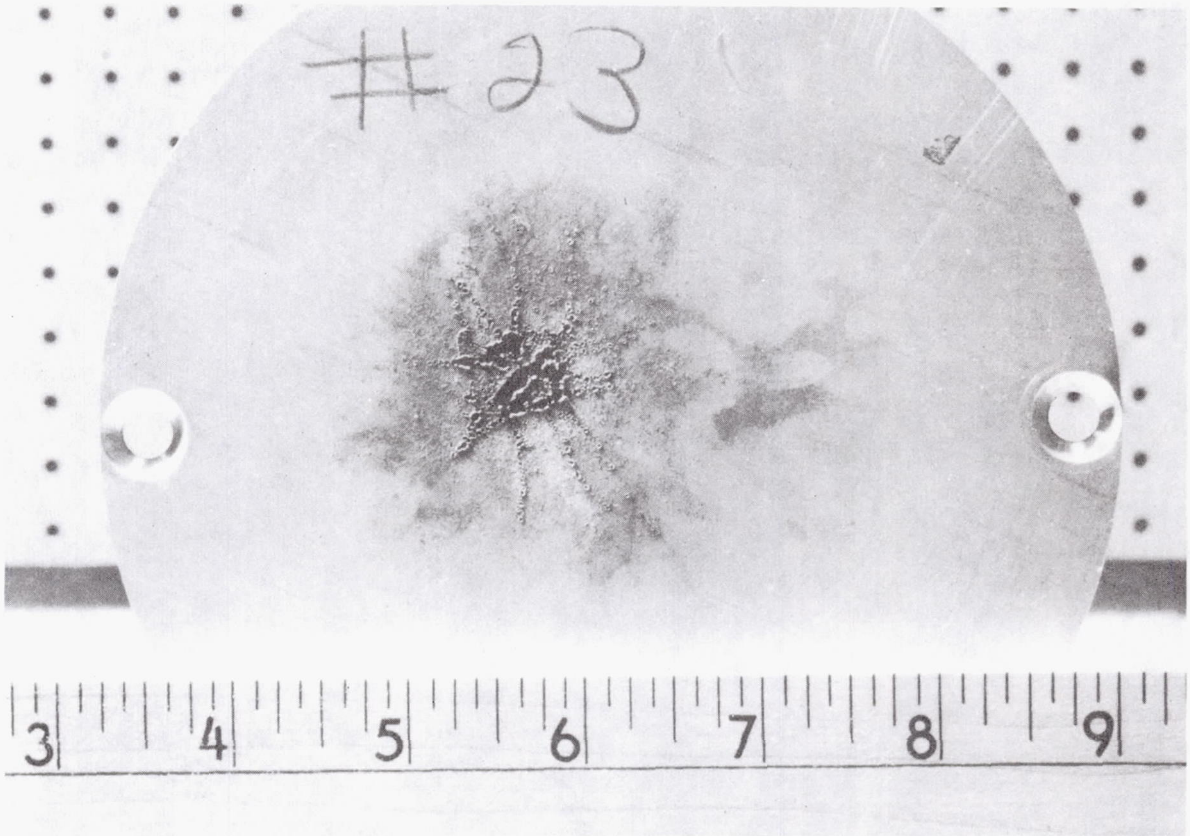

FIGURE 19. HYPERVELOCITY IMPACT TEST ON SAMPLE WITHOUT MULTILAYER INSULATION

Plans are to apply the panelized insulation concept to 2.67-m (105-in.) diameter tanks and perform liquid hydrogen tests under high vacuum conditions to fully evaluate the performance of both the concept and method of application.

The panelized insulation concept is being considered for possible application on the Multiple Docking Adapter (MDA), Orbital Tanker, and other programs.

NUCLEAR GROUND TEST MODULE INSULATION DEVELOPMENT

By

Raymond L. Gause

SUMMARY

A description is given of Project Rover and the Nuclear Engine for Rocket Vehicle Applications (NERVA). The Nuclear Ground Test Module (NGTM) program at MSFC is discussed and the relationship between the NGTM program and the NERVA program is established. The criteria for the design of an insulation system for the NGTM are presented. In addition, the NGTM environment and the impact of this environment on the development of an insulation system with the desired properties are discussed. The selection of the candidate materials for the NGTM insulation system is given and the test program for evaluating their suitability for full-size tanks is outlined.

INTRODUCTION

Ever since their invention by Chinese makers of ceremonial fireworks, rockets have been propelled by the energy liberated by burning chemicals, and this fundamental fact has not been altered by the tremendous strides that have been made in American and Russian rocketry since World War II. Rockets began as fireworks and they are still fireworks. Now, however, after a thousand years this basic truth is about to change as a result of a new breed of rocket engines presently being developed under Project Rover. Project Rover is America's program to develop a nuclear propelled rocket and is jointly sponsored by the Atomic Energy Commission and the National Aeronautics and Space Administration. Currently, nuclear reactors suitable for use as power sources for rocket propulsion are being developed. Larger versions of these reactors will be used in the construction of NERVA (Nuclear Engine for Rocket Vehicle Application), a flight type engine that will be tested at the Nuclear Rocket Development Station (NRDS) at Jackass Flats, Nevada.

To support these NERVA tests at NRDS, the Marshall Space Flight Center presently is involved in an inhouse program to develop the technology required for the design and fabrication of a nuclear ground test module (NGTM). The dual purpose of the NGTM is to provide the propellant tankage and control systems necessary for the hot firing of the NERVA and to serve as a test article for the development of hardware required for future nuclear flight stages. Because the NERVA will use liquid hydrogen (LH_2) as a propellant, the NGTM will require a thermal insulation system to limit propellant boiloff. The unique environments in which this insulation system will have to function, the impact of these environments on the selection of insulation materials, and the test program required to develop an insulation system to meet the necessary design requirements will be described in this paper.

INSULATION SYSTEM DESIGN CRITERIA

In considering the design of an insulation system for the NGTM, the feasibility of developing an insulation which will be suitable for both the ground test module and any future flight vehicle was investigated. To aid in the evaluation of this approach, the design criteria shown in Table I were established.

TABLE I. INSULATION SYSTEM DESIGN CRITERIA

Ground Test Module	Flight Vehicle
Short Term LH_2 Storage	Long Term LH_2 Storage in Space
High Cumulative Radiation Levels	Low Cumulative Radiation Levels
Mass is of Secondary Importance	Minimum Mass Required
Long Term Weathering Protection	Micrometeoroid Protection
High Cumulative Vibration	Short Term Vibration
Considerable Handling	Nominal Handling

An analysis of the criteria in Table I shows that the requirements for the ground test module are completely different from those for an operational flight stage. The operational stage insulation will not be subjected to the mechanical, thermal, and radiation cycling associated with ground stage static testing. The ground test stage probably will be subjected to many full duration hot firings over many months or possibly years, whereas the flight vehicle will be subjected to only one or possibly two short duration firings. In addition, the operational stage will require the long term storage of liquid hydrogen in space by maintaining the rigid control of LH_2 boiloff. For the ground test module, boiloff considerations are less critical. Therefore, based on these considerations, it was concluded that the development of an insulation system that could be used for both the ground test stage and an operational flight vehicle was not feasible at this time. However, studies in this area are continuing. Thus, the approach taken was first to develop an insulation system that would meet all of the requirements for the NGTM and then use the operational NGTM as a test article for the development of a flight type insulation system.

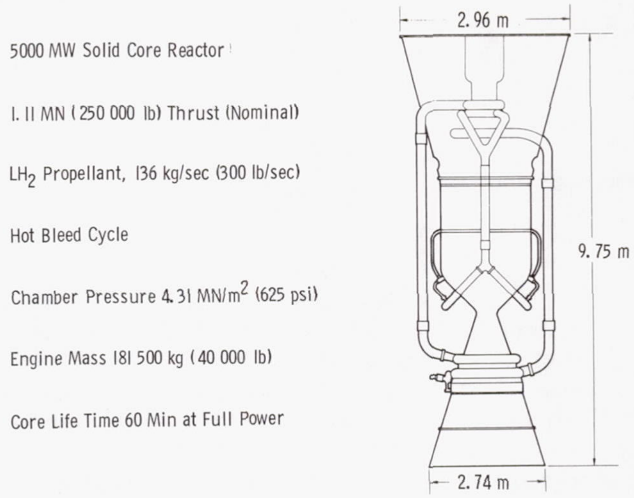

FIGURE 1. THE NERVA ENGINE

THE NGTM ENVIRONMENT

One of the most important considerations in the development of the NGTM insulation system is the environment to which the insulation will be exposed. This environment and the resulting effects on the insulation system must be defined in order to provide a basis for the selection of candidate insulation materials and composites. To arrive at this definition, the operation of the nuclear engine must be examined. Figure 1 shows the configuration of the NERVA, which basically consists of a 5000 MW solid core reactor, a pressure vessel, a liquid hydrogen turbopump assembly, and a nozzle. The engine is designed to produce a nominal thrust of 1.11 MN (250 000 lbf) and a specific impulse in the order of 800 sec for a liquid hydrogen propellant flow rate of 136 kg/sec (300 lb/sec) through the reactor. The NERVA will be larger than any chemical engine presently in use. The reactor core lifetime is expected to be approximately 60 min while operating at 5000 MW. The anticipated neutron flux and gamma dose rates for the engine operating at full power are shown in Figure 2. With the engine located at the test stand and mounted on the GTM, the neutron and gamma radiation levels expected at various points on the GTM are shown in Figure 3. These levels assume no internal engine shield and an operating power level of 5000 MW (a worst case condition). As shown in Figure 3, the maximum neutron and gamma dose rates at the propellant tank bottom (point 2) are expected to be about $1.0 \times 10^9 \dfrac{\text{ergs}}{\text{g(C)} \cdot \text{hr}}$ and $2.0 \times 10^9 \dfrac{\text{ergs}}{\text{g(C)} \cdot \text{hr}}$, respectively. Based on the current requirement that the NGTM be capable of supporting 30 hours of full power engine operation, the materials selected for use in the vicinity of the tank bottom will have to be capable of retaining their functional integrity after a neutron exposure of $3.0 \times 10^{10} \dfrac{\text{ergs}}{\text{g(C)}}$ and a gamma dose of $6 \times 10^{10} \dfrac{\text{ergs}}{\text{g(C)}}$. Because of the uncertainty in these numbers, the radiation effects tests to be described later in this paper will be made to levels greater than these.

The NGTM acoustic level anticipated during an engine firing is about 140 decibels (dB) at a center frequency of 80 Hz. Although it is not expected that this will affect significantly the structural integrity of the insulation, acoustic tests at this level are planned in conjunction with nuclear radiation-cryogenic temperature tests.

Other factors which must be considered as part of the overall NGTM environment include (1) thermal, mechanical, and radiation cycling, (2) the desert weather (sand storms, temperature extremes, etc.), and (3) handling.

It is obvious then that the development of a cryogenic insulation system that will meet the desired performance requirements must include testing in combined environments.

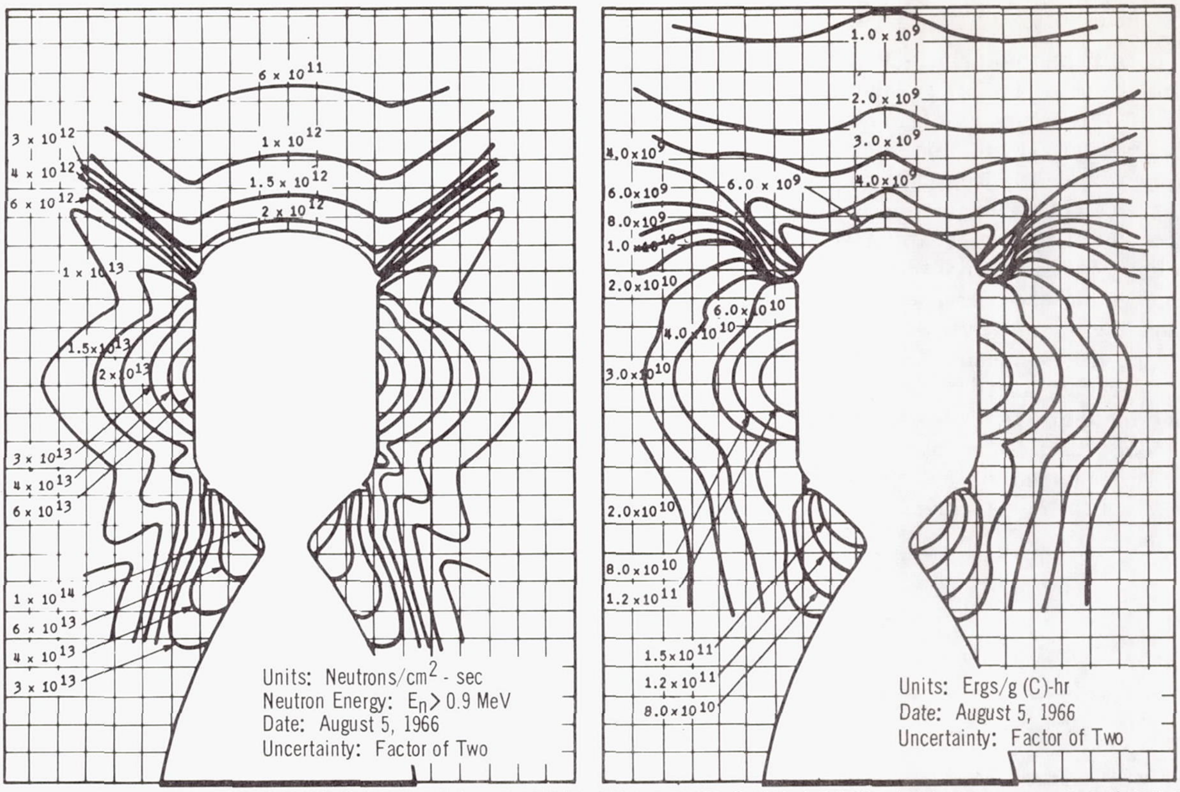

FULL POWER FAST NEUTRON FLUX FOR THE NERVA ENGINE FULL POWER GAMMA DOSE RATES FOR THE NERVA ENGINE

FIGURE 2. RADIATION PROFILES FOR THE 5000 MW NERVA

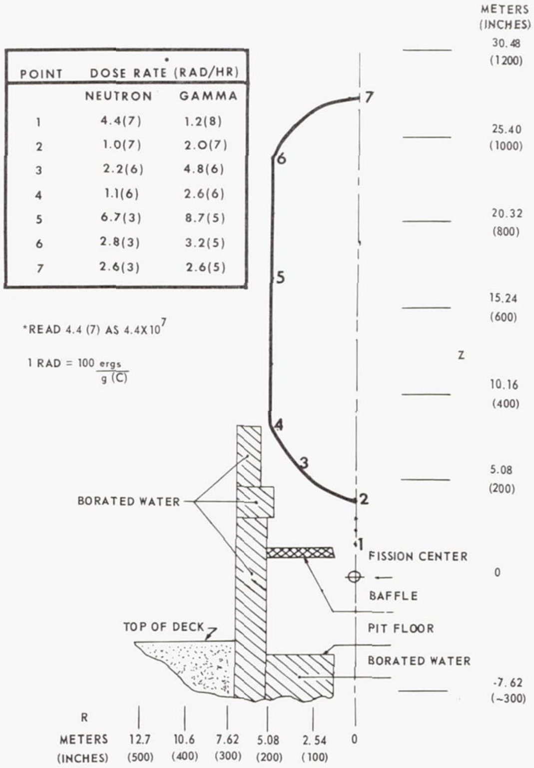

POINT	DOSE RATE* (RAD/HR)	
	NEUTRON	GAMMA
1	4.4(7)	1.2(8)
2	1.0(7)	2.0(7)
3	2.2(6)	4.8(6)
4	1.1(6)	2.6(6)
5	6.7(3)	8.7(5)
6	2.8(3)	3.2(5)
7	2.6(3)	2.6(5)

*READ 4.4 (7) AS 4.4×10^7

1 RAD = 100 $\frac{\text{ergs}}{\text{g (C)}}$

FIGURE 3. NGTM RADIATION ENVIRONMENT

INSULATION DEVELOPMENT CONSIDERATIONS

Several important factors pertaining to performance, maintenance, and cost must be considered during the development of the NGTM insulation system. First, because of the environment just described, materials to be considered for use must have high radiation resistance, good cryogenic properties, and possess some degree of ruggedness. In addition, it is highly desirable from an economic standpoint to have an insulation system which basically is inexpensive, easily applied, uncomplicated, and requires minimum ground support equipment. After the first hot firing of the NGTM, the module will be radioactive and thus limit personnel access for the performance of maintenance and repair tasks. Only insulation systems suitable for external application to the propellant tank are being considered because an internal system would be difficult if not impossible to repair after the tank becomes activated.

The thermal performance of the insulation also has to be considered. Presently, a maximum LH_2 boiloff rate of 454 kg/hr (1000 lb/hr) under cold-flow conditions is being used as one of the criteria for the selection of candidate insulation materials. To limit the boiloff to this value, a thermal conductivity-insulation thickness ratio (K/X) of approximately 0.06 is required as shown in Figure 4. Of course, during hot firing of the engine, the boiloff will be greater than this because of the heating of the propellant by the absorption of nuclear energy and the increased conductance of heat through the metal thrust structure and other bulkhead appendages. Insulation mass, which is of great importance for flight vehicles, is of secondary importance for the NGTM because it will be used only for ground tests. The factors just described, which are summarized in Table II, are the principal ones that affect the development of the NGTM insulation system.

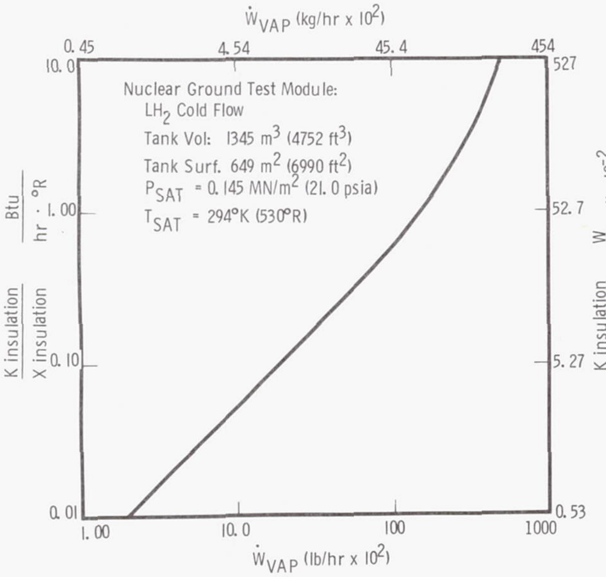

FIGURE 4. NGTM COLD-FLOW LH_2 BOILOFF VS. INSULATION PERFORMANCE

TABLE II. INSULATION DEVELOPMENT CONSIDERATIONS

A.	High Radiation Resistance ($\sim 6 \times 10^{10} \frac{ergs}{g(C)}$ gamma)
B.	Good Cryogenic Properties
C.	Inexpensive
D.	External Application
E.	Uncomplicated
F.	Minimum GSE
G.	Repairable with Minimum Effort
H.	Moderate Thermal Efficiency
I.	Mass Relatively Unimportant

SELECTION OF CANDIDATE INSULATION MATERIALS

With the preceding information as evaluation criteria, several different insulation schemes were reviewed for use in the NGTM program. Included in these systems were the insulations currently used on the various stages of the Saturn V vehicle and the multilayer superinsulations. Many of these were found to have some of the desired properties; however, most of them were not believed to be durable enough to meet the service requirements. The superinsulations, like most of the other insulations considered, are very satisfactory from the standpoint of thermal performance but are not desirable based on installation costs, handling, and repair considerations. One insulation which was proposed by the Boeing Company for this application is corkboard. The thermal properties of cork appear to be adequate, the cost is acceptable, cork should not present any major fabrication problems, and cork is durable. To determine how its properties are affected by radiation, a search of the radiation effects literature was made. Bolt and Carroll [1] have summarized the limited information available on the effects of radiation on cork. In 1951, several types of wood, including cork, were exposed in the Canadian NRX reactor [2]; samples exposed showed only slight darkening after a dosage of $6 \times 10^{11} \frac{ergs}{g(C)}$. In another test, ordinary stopper corks were exposed to a gamma dose of $5 \times 10^{10} \frac{ergs}{g(C)}$; the stoppers showed no discoloration or increased brittleness. In 1958, DeZeih [3] exposed cork to $1 \times 10^{10} \frac{ergs}{g(C)}$, which produced a slight (4%) increase in tensile strength. Flexibility was not impaired and compression and recovery from compression were reduced only about 5%. Another consideration regarding cork insulation is the possible deterioration of the cork binder materials. An evaluation of the binders commonly used showed that they generally are of the thermosetting resin type. Since the phenolic, polyester, and other thermosetting resins usually have high radiation resistance, the binder is not expected to be a source of failure.

After reviewing the information which was available for corkboard and comparing this information with the previously described evaluation criteria, corkboard was selected as one of the candidate insulation materials. The particular corkboard which appeared to be most appropriate for this program was the Insulcork 7326 Cryogenic Insulation, a new lightweight [112-128 kg/m^3 (7-8 lbs/ft^3)] corkboard distributed by the Industry Products Division of the Armstrong Cork Company. A conceptual insulation system design based on this material is shown in Figure 5. It consists of four basic elements: the adhesive bond, the corkboard insulation, the internal vapor barriers, and the protective facing cover. A laminated structure was selected because the layers of insulation can be staggered to preclude the existence of any direct thermal paths through the insulation. Internal vapor barriers are used to provide protection against cryopumping of air in the event the outer cover is ruptured. The system is given a high degree of ruggedness by the protective facing cover which consists of two plies of resin impregnated fiberglass. Presently, other materials are being investigated for this application.

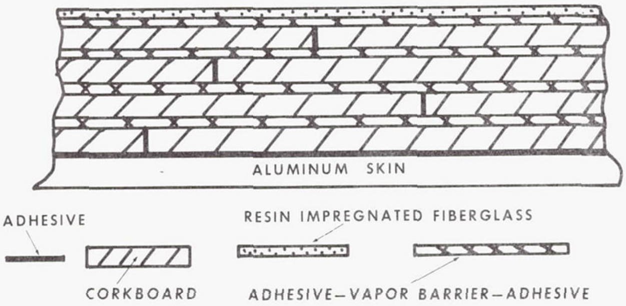

FIGURE 5. LAMINATED CORKBOARD INSULATION SYSTEM

Because of the desire to include more than one basic type of insulation in the development program, an additional insulation material was selected. A type of insulation that has many characteristics desirable for the NGTM insulation is the rigid spray foam insulation. The rigid, small, uniform closed-cell structure of the spray foams gives them an inherently low thermal conductivity. In addition, the foam has extremely low moisture-vapor permeability and a high resistance to water absorption. The structural stability prevents costly heat leaks caused by shrinkage, buckling, or cracking. The application of the foam by spraying provides a convenient method of insulating difficult geometries. Also, repair is simple because the damaged material can be removed easily and replaced by respraying the area. Sealing problems are minimized because the new foam will adhere directly to the undamaged foam. Another major advantage is that the foam can be sprayed directly on the metal, which eliminates the requirement for a separate adhesive bond between the foam and the metal. Foams now are available having low density [nominal 32 kg/m^3 (2.0 lbs/ft^3)] and high strength. The foam that was selected for testing is from a group of isocyanate-polyol resins commonly known as polyurethanes. They are formed by the reactions of compounds containing two or more active hydroxyl, amino, or carboxyl groups, with diisocyanates. The principal polyols used today are either polyesters or polyethers. The highly branched polyesters give rigid polyurethanes. In the spray foam process, the isocynate and polyol reactants are mixed with catalysts chosen to accelerate the reaction sufficiently to bring about foaming within seconds. The reactants are pumped to the spray gun by metering pumps adjusted to provide the proper proportions. In the spray gun, the reactants are mixed and then expelled through a nozzle onto the surface being coated in much the same way as paint is sprayed.

A polyurethane type foam was selected because as a chemical class, the polyurethanes are high on the list of radiation resistant elastomers and plastics. From Harrington's studies [4], it may be stated that polyurethane elastomers are capable of giving satisfactory service to at least $8.7 \times 10^{10} \frac{\text{ergs}}{\text{g(C)}}$. The work by Schollenberger at the B. F. Goodrich Company [5] concluded that limited dynamic application might be practical after an exposure of $1.7 \times 10^{10} \frac{\text{ergs}}{\text{g(C)}}$ and static applications might be feasible after exposure to $4.4 \times 10^{11} \frac{\text{ergs}}{\text{g(C)}}$. Tests made by the General Dynamics Corporation, Fort Worth Division under contract NAS8-2450 on two different polyurethane foams indicated that they were not significantly affected after an exposure of $3 \times 10^{10} \frac{\text{ergs}}{\text{g(C)}}$. Since there are many chemical combinations, temperature cures, and additives, some variation in reported results in radiation effects tests are to be expected. However, a possible service level of $1 \times 10^{11} \frac{\text{ergs}}{\text{g(C)}}$ seems feasible.

The particular spray foam that was chosen as the second candidate insulation material for this program was the CPR 368 rigid urethane foam manufactured by the CPR Division of the Upjohn Company. It is a flame retardent spray foam designed for either airless or air atomized spray equipment for particular use at low ambient temperature conditions. The nominal density is 32-48 kg/m^3 (2-$3 \ lb/ft^3$) and the thermal conductivity is approximately $0.01585 \frac{W}{m \cdot {}^\circ K}$ $\left(0.11 \frac{Btu \cdot in.}{ft^2 \cdot {}^\circ F \cdot hr}\right)$. A conceptual insulation system based on this type of insulation is shown in Figure 6. It consists basically of two elements: the spray foam and the seal coat.

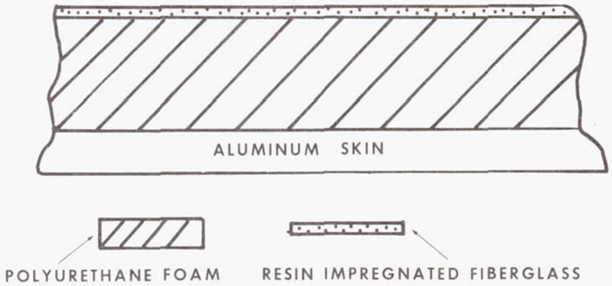

FIGURE 6. POLYURETHANE SPRAY FOAM INSULATION

The foam is sprayed directly on the primed aluminum surface, thereby eliminating the need for adhesive bonding. The desired thickness can be achieved by building successive layers of foam because each layer becomes homogeneous with the previous layers. After the foam is sprayed, it is cured and then the surface is machined to a smooth finish and sealed.

SELECTION OF CANDIDATE ADHESIVE MATERIALS

The adhesives being considered in this program are for bonding the cryogenic insulation to the propellant tank and for bonding the vapor barrier to the insulation. Generally, adhesives which cure at elevated temperatures and high pressures are less attractive because autoclaves and presses are required, which complicate the installation of the insulation system and increase the cost. Thus, the adhesives selected for this program are those which cure at room temperature and require only contact pressure for proper bonding. Since the adhesive in some areas may be subjected simultaneously to both cryogenic temperatures and to nuclear radiation during engine operation, an adhesive material is desired whose functional properties are not seriously affected by this environment.

In reviewing the different chemical classes of adhesives, it is noted that the epoxy and phenolic-base adhesives have a higher radiation tolerance, but most of these are cured at elevated temperatures. The epoxy-nylon types are good cryogenic adhesives, but they also have a high temperature cure. However, the polyurethanes have good radiation resistance and can be cured at room temperature. The epoxy-polyamide adhesives, in general, are better in the radiation environment than many other types. Also, some of these cure at room temperature.

The adhesives that were chosen for inclusion in this program are of the polyurethane and epoxy-polyamide types, and all of them may be used under room temperature and contact pressure conditions. Furthermore, they have been used in previous aerospace programs. These adhesives are listed in Table III.

TABLE III. CANDIDATE ADHESIVE MATERIALS

Adhesive	Chemical Class	Manufacturer
Narmco 7343/7139	Polyurethane	Whittaker Corporation
APCO 1219	Polyurethane	Applied Plastics Company
Lefkoweld 109/LM-52	Epoxy-Polyamide	Leffingwell Chemical Company
Narmco 3135/7111	Epoxy-Polyamide	Whittaker Corporation

SELECTION OF CANDIDATE VAPOR BARRIER MATERIALS

The vapor barrier materials are used to cover cryogenic insulations to prevent moisture or air from penetrating the insulation and increasing the thermal conductivity. Therefore, it is important to have a vapor barrier material which possesses low permeability. Vapor barrier materials may be bare plastic films of various thicknesses, films combined as composites, films laminated with such reinforcements as glass cloth or epoxy-fiberglass, and plastic films vapor deposited, spray coated, or bonded with metal films.

Based on a survey of available information on the effects of radiation and cryogenic temperatures on these films, the following materials were selected as being promising candidate vapor barrier materials for the intended application: a polyimide (Kapton); a polyester (Mylar); a polyvinyl fluoride (Tedlar); and a polyurethane-fiberglass cloth.

THE TEST PROGRAM

The insulation test program for the NGTM is composed of four phases: (I) the environmental testing of candidate materials and composites, (II) the environmental testing of insulations installed on model tanks, (III) the investigation of fabrication and installation techniques for large tankage, and (IV) the evaluation of the selected insulation system on full size tanks available from the Saturn V test program. Currently, the work necessary to accomplish the Phase I objectives is underway and the test plan and schedule for Phase II are being finalized. The radiation effects tests required in these phases will be performed under contract NAS8-18024 with the General Dynamics Corporation, Forth Worth Division. In Phase I, two categories of tests are included for the evaluation of the candidate thermal insulation materials. The first category involves the determination of the physical properties appropriate for each type of material and the various composites. The second is an application test of the two composite insulation systems using a specially fabricated cryogenic insulation test dewar (CITD).

For the physical property tests, various types of specimens fabricated from the different classes of materials will be subjected to the following test conditions: (1) evaluation in air, (2) evaluation in LH$_2$, (3) irradiation in air, and (4) irradiation in LH$_2$. Table IV gives the types of tests, the number of specimens for each test, and the test environments. Some of the 150 specimens irradiated in LH$_2$ will be tested in LH$_2$ immediately after irradiation and without intervening warmup (in situ tests); the others will be tested at room temperature. The configurations of the lap shear (in situ), double lap shear, and composite flatwise tensile specimens are presented in Figures 7, 8, and 9.

To simulate the actual service conditions (radiation, LH$_2$ temperature, and acoustic noise) expected for the cryogenic insulation system, an insulation application test using the specially designed

TABLE IV. MATERIAL EVALUATION TESTS, SPECIMENS, AND ENVIRONMENTS

ASTM Test No.	Test Name	Materials Tested	Number of Specimens				TOTAL
			Control		Irradiated		
			Air	LH$_2$	Air	LH$_2$	
D-1002	Lap Shear	Adhesive	32	32	16	32	112
D-1876	T-peel	Adhesive	16	16	16	16	64
D-882	Thin-Film Tensile	Film Tape	24	24	24	24	96
E96	Thin-Film Permeability	Film Tape	6	6	6	6	24
D-1621	Compression Set	Insulation	8	8	8	8	32
D-1002	Double-Lap Shear	Adhesive Insulation	32	32	32	32	128
C-297	Flatwise Tensile	Adhesive Film Insulation	32	32	32	32	128
TOTAL SPECIMENS			150	150	134	150	584

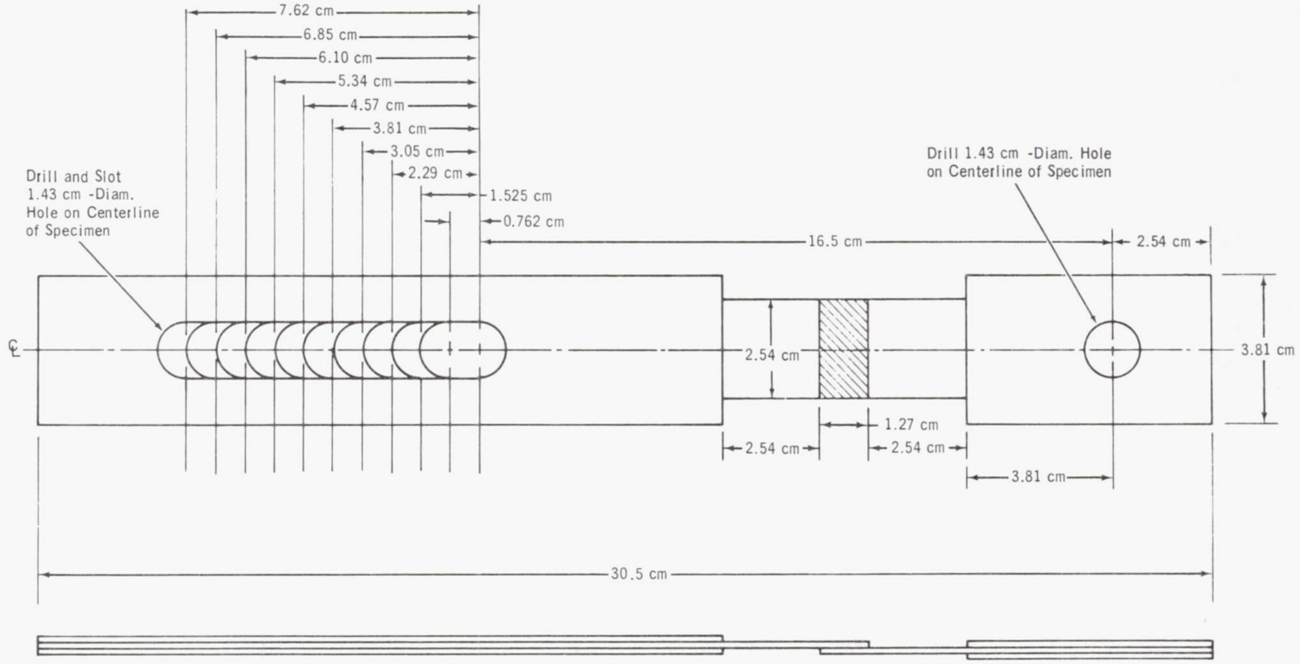

FIGURE 7. TYPICAL LAP SHEAR ADHESIVE SPECIMEN

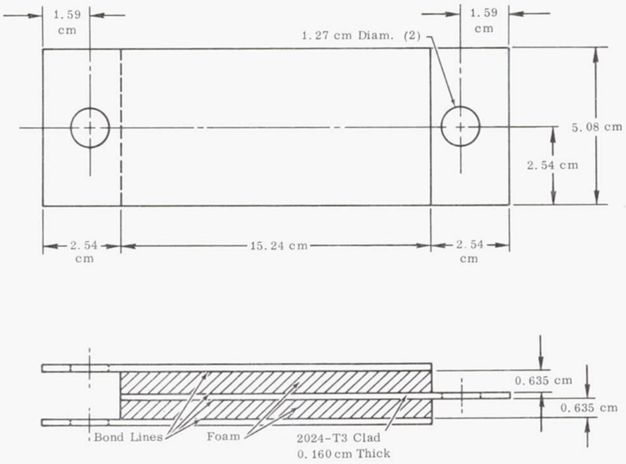

FIGURE 8. COMPOSITE DOUBLE LAP SHEAR TEST SPECIMEN

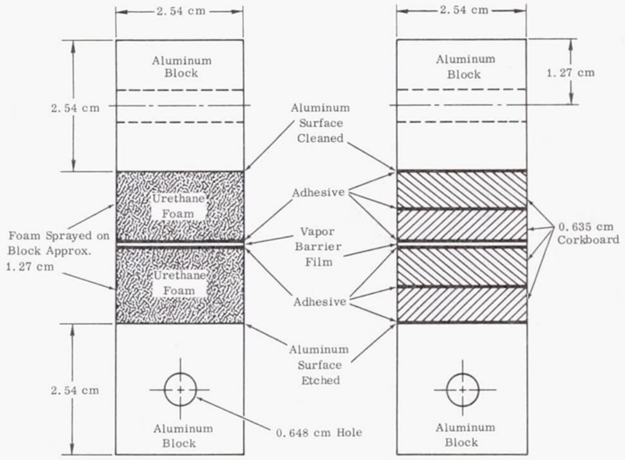

FIGURE 9. TYPICAL COMPOSITE FLATWISE TENSILE SPECIMENS

CITD shown in Figure 10 has been planned. The CITD is a 0.762-m (30-in.) long cubic tank of 1.27-cm (0.50-in.) thick 2219 aluminum with each of the four sides having a 0.635 × 0.635 m (25 × 25 in.) section on the inside surface milled to 0.762 cm (0.30 in.), thus leaving a 6.35-cm (2.5-in.) strip of 1.27 cm (0.50 in.) aluminum around the milled area in each side. The thin center sections correspond to the wall thickness of the NGTM LH_2 tank. This thin section will be used for the evaluation of the mechanical and physical stability of the composite insulation during the environmental tests. Both of the previously described candidate insulation systems are installed on the CITD. Two sides were sprayed to a 5.08-cm (2-in.) thickness with CPR 368 foam. The bottom (except for the legs) and the top of the dewar (except for the shroud cover) were also covered with the foam. The remaining two sides were covered with Insulcork 7326 corkboard. One side has four 1.27-cm (0.50-in.) thick cork panels separated by a 0.0127 cm (0.005 in.) Tedlar vapor barrier bonded with Lefkoweld 109/LM52. An adjacent side has the same configuration except that eight 0.635-cm (0.25-in.) thick cork panels were used. To protect the surface from mechanical damage and to provide an additional vapor seal, the insulation is covered with a layup of two layers of fiberglass cloth impregnated with NARMCO 7343/7139 resin. The cover is painted with a white, epoxy base, thermal control coating. Thermocouples are located in the insulation on two sides to monitor the temperature gradient across the 5.08-cm (2-in.) thickness of each type of insulation.

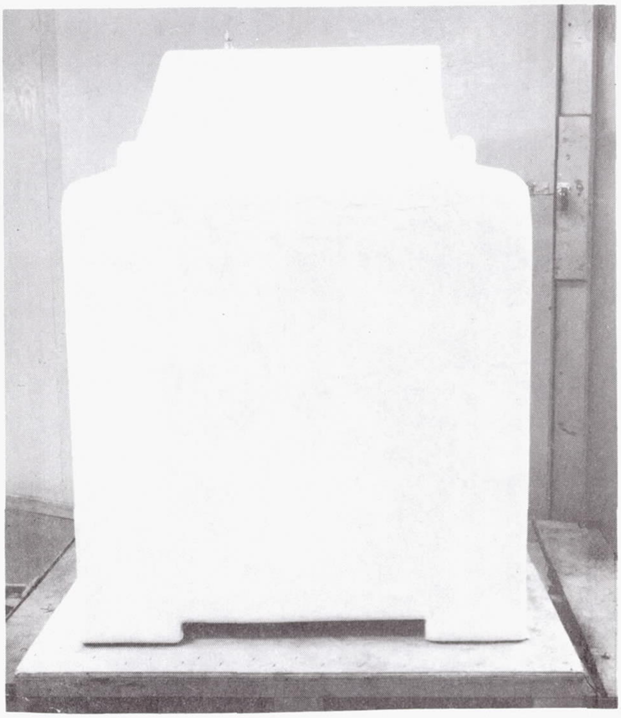

FIGURE 10. CRYOGENIC INSULATION TEST DEWAR

To perform the tests, the dewar will be irradiated to a gamma dose of approximately $1 \times 10^{11} \frac{\text{ergs}}{\text{g(C)}}$ while full of LH_2. During irradiation, the LH_2 level and the temperature profile of the insulation will be continuously monitored. Also, a videotape of the test will be made. After irradiation, the dewar will be drained of LH_2 and moved to an acoustic test facility where the condition of the insulation will be visually inspected before the acoustic exposure is started. If any cracks or other irregularities are visible, they will be photographed before the acoustic exposure. The CITD then will be filled with LN_2 and placed in the acoustic reverberation chamber shown in Figure 11 where it will be exposed to a noise level of 140 dB. After a six-hour exposure, the dewar will be drained of LN_2 and warmed to room temperature for visual inspection of the insulation.

The data obtained from the previously described tests will be used to aid in the selection of insulation materials to be tested in the model tank portion (Phase II) of the overall development program. In Phase II, a 16.65 m^3 (4 400 gal.), 2.74-m (108-in.) diameter tank will be insulated and tested in a radiation, LH_2, and acoustic environment using the test setup shown in Figure 12. In addition to testing the insulation system in a tank configuration, the model tank will also be used as a test article for the evaluation of various NGTM mechanical components.

CONCLUSION

In this paper, a brief description has been given of the program being pursued to develop an insulation system having the thermal protection and lifetime required for the satisfactory operation of the Nuclear Ground Test Module. The environment to which the insulation will be exposed is a severe one, but not an insurmountable one, and the results of the test program should provide an excellent NGTM insulation system as well as providing many answers to the solution for an insulation system for a nuclear stage on a flight vehicle.

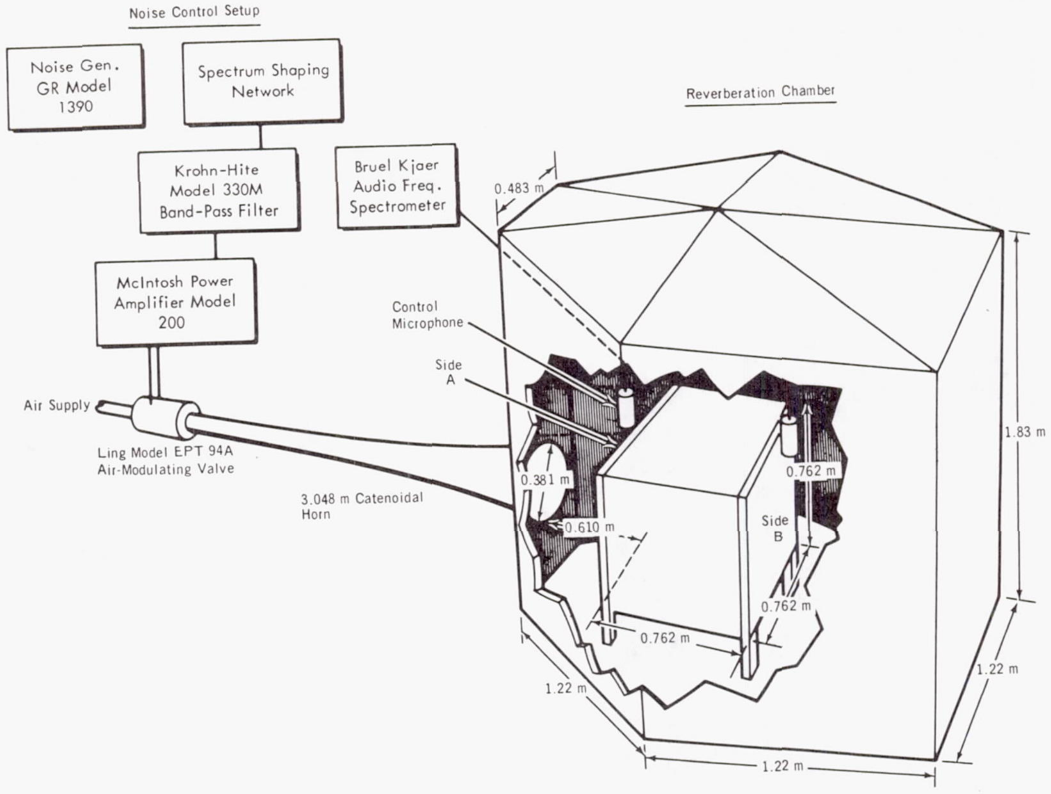

FIGURE 11. ACOUSTIC NOISE SETUP

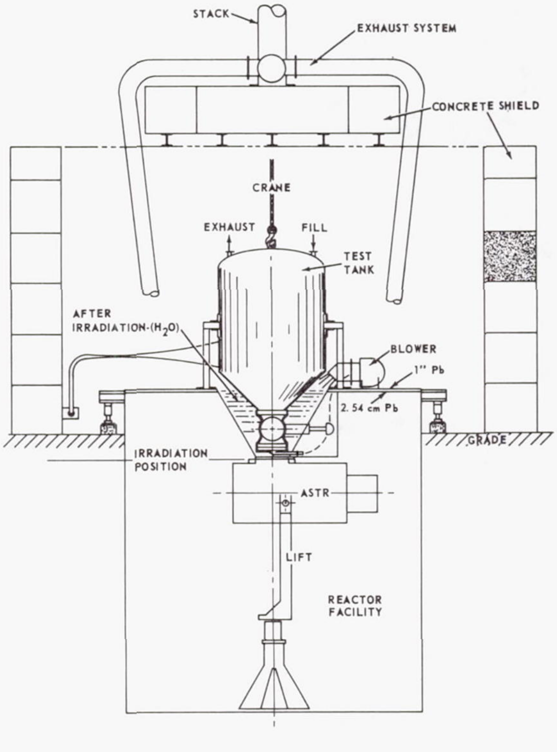

FIGURE 12. SCHEMATIC OF MODEL TANK TEST SETUP (ELEVATION)

REFERENCES

1. Bolt, R. O.; and Carroll, J. G.: Radiation Effects on Organic Materials. Academic Press, New York, 1963.

2. Yoshida, N.; and Horsman, J. C.: Summary of Engineering Materials Irradiated in NRX Reactor. Canadian Report NEI-4, February 1951.

3. DeZeih, C. J.: Effects of Nuclear Radiation on Cork, Leather, and Elastomers. Third Semiannual Radiation Effects Symposium, Paper no. 62, vol. 5, Lockheed - Georgia Company, October 28-30, 1958.

4. Harrington, Robert: Elastomers for Use in Radiation Fields (Part II). Rubber Age, vol. 82, Dec. 1957, pp. 461-470.

5. Schollenberger, C. S., et al,: Polyurethane Gamma Radiation Resistance. Research Center Final Report 6S-72419, B. F. Goodrich Co., June 1, 1959.

Page
Intentionally
Left Blank

ASSESSMENT OF THE STATUS OF CRYOGENIC INSULATION DEVELOPMENT

By

Charles. C. Wood

Marshall Space Flight Center is attempting to develop insulation technology to achieve cryogenic propellant storage for durations from several days to one year or more for future space missions. A portion of this insulation development activity is reported in previous sections of this publication. The insulation concepts for long-duration missions differ significantly from insulation concepts used on the hydrogen tanks of the present generation of launch vehicles that have mission durations varying from a few minutes to several hours.

The vehicle system that requires the storage of large quantities of cryogens for long durations and that is best defined at this time is the Modular Nuclear Vehicle, which is being evaluated for manned interplanetary travel. This vehicle configuration will be used in this paper for comparative purposes and is depicted in Figure 1. It has a hydrogen tank capacity of 104 000 kg (230 000 lb) and a tank diameter of approximately 10.1 m (33 ft). Details of the studies that defined this vehicle are reported by Lockheed [1]. These studies established that the maximum acceptable sum of the hydrogen tank insulation mass and the mass lost by evaporation of propellant was 8% of the mass of propellants at lift-off. The standard used throughout the study to represent insulation performance was the so-called "performance index," the product of insulation density and thermal conductivity. The selected value for the study was $2.77 \times 10^{-3} \frac{\text{W - kg}}{\text{m}^4 \text{ - }^\circ\text{K}}$ $\left(10 \times 10^{-5} \frac{\text{Btu - lbm}}{\text{hr - ft}^4 \text{ - }^\circ\text{R}} \right)$. The lowest known value of this parameter obtained in calorimeter tests under idealized conditions is $1.11 \times 10^{-3} \frac{\text{W - kg}}{\text{m}^4 \text{ - }^\circ\text{K}}$ $\left(4 \times 10^{-5} \frac{\text{Btu - lbm}}{\text{hr - ft}^4 \text{ - }^\circ\text{R}} \right)$. An equivalent value of $5.53 \times 10^{-3} \frac{\text{W - kg}}{\text{m}^4 \text{ - }^\circ\text{K}}$ $\left(2 \times 10^{-4} \frac{\text{Btu - lbm}}{\text{hr - ft}^4 \text{ - }^\circ\text{R}} \right)$, considered typical of thermal performance obtained for similar programs, was obtained on the practical flight-configuration 2.67-m (105-in.) diameter tank that was discussed by Mr. E. H. Hyde. Therefore, for a vehicle configuration represented by the Modular Nuclear Vehicle, an acceptable insulation system requires a factor of two improvement in thermal performance relative to the 2.67-m (105-in.) diameter propellant tank insulation system. Insulation system performance can be improved by two basic means: reduction of insulation density and reduction of thermal conductivity. Minute hydrogen gas leaks within the insulation system and other factors reported by Mr. E. H. Hyde were responsible for major differences between the thermal performance in the applied condition and the thermal performance obtained in calorimeter testing. The major problems that occurred during large-scale testing have been solved on the component level. It is anticipated that the solutions to these problems can be successfully applied to large-scale tanks and that insulation thermal performance in the applied condition will satisfy the requirements for the Modular Nuclear Vehicle missions of interplanetary travel. Other technologies that are essential, or can assist in meeting these requirements, will be discussed in ensuing paragraphs.

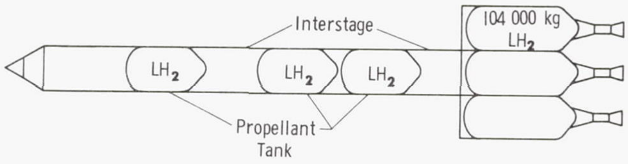

MARS LANDER VEHICLE

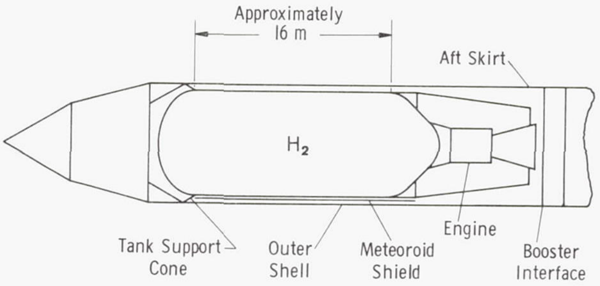

FIGURE 1. MODULAR NUCLEAR VEHICLE CONFIGURATION

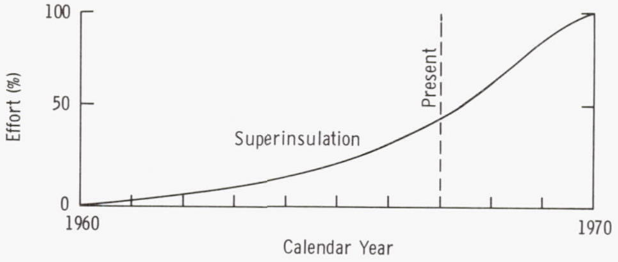

FIGURE 2. ESTIMATION OF EXPENDED AND REQUIRED EFFORT FOR HIGH PERFORMANCE INSULATION DEVELOPMENT FOR SPACE FLIGHT APPLICATION

Figure 2 summarizes insulation technology development efforts for space application occurring between 1960 and 1967, and lists project requirements for the time frame 1967 through 1970. The data are presented in terms of the required total effort to advance insulation technology for space vehicle application from inception to the demonstration of an acceptable system capable of meeting the specified thermal goals. This figure shows that approximately 50% of the required effort for advancing insulation technology has been expended. The increased effort shown to occur between 1967 and 1970 reflects the detailed design and thermal analysis activities required for application of insulation to large flight-configuration containers. Coincident with this accelerated effort is the anticipated rapid improvement in attainable thermal performance of insulation systems because the very latest in available technology will be used in the establishment of new configurations and major efforts will be directed toward unsolved problems.

The storage of cryogens in space for long durations involves technologies other than insulation, such as fluid behavior and propellant tank venting in a reduced or zero gravity environment, determination of the thermal environment, and other modes for reducing propellant loss such as reliquefaction of evaporated propellant, other states of stored propellant (slush or triple point liquid), and improvised methods for shielding the vehicle from solar energy (shadow shields). Figure 3 illustrates the potential for reduction of propellant loss of two such modes: slush propellants and solar shields. These data are for a Mars braking stage of a manned interplanetary vehicle that has been insulated with sufficient high performance insulation so that the mass of the insulation system plus the evaporated propellant loss is 8% of the mass of the lift-off propellant. The combined effect of shadow shields and slush hydrogen theoretically reduced the 8% stage penalty to 2%, greatly enhancing the propellant storage capability. The advancement of technology in the areas of slush hydrogen, shadow shields, propellant tank venting, fluid behavior in reduced and zero gravity, etc., is currently underway at MSFC. Other NASA centers, government agencies, and private industries are also contributing to the advancement of the required technology.

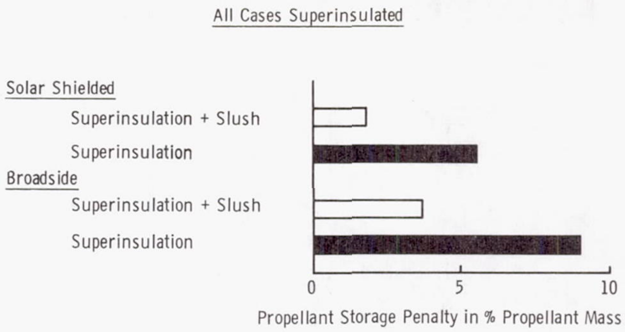

FIGURE 3. SOLAR SHIELD AND PROPELLANT STATE INFLUENCES ON PROPELLANT STORAGE PENALTY FOR A NUCLEAR MANNED MARS BRAKING STAGE

Figure 4 summarizes the future MSFC plans for advancing insulation technology for space vehicles requiring long-term storage of cryogens.

- Develop High Performance Insulation System For Long Term Storage
  - Meet Modular Nuclear Vehicle Performance Goals

    Considering All Practical Flight Vehicle Problems
    - He Purge System
    - Rapid Ascent (Pressure, Acceleration)
    - Outgassing - Preconditioning
    - Low Heat Leak Attachments
    - Piping - Tank Support Penetrations
    - Manufacturing - Reproducibility - Density Control
- Efforts To Develop A Lower Insulation Thermal Conductivity And Density Product For High Performance Insulation

FIGURE 4. FUTURE PLANS FOR HIGH PERFORMANCE INSULATION DEVELOPMENT

The major effort is a combined MSFC and contractor program using the Modular Nuclear Vehicle as a base line vehicle configuration whenever possible. During the next year, insulation concepts will be selected and insulation systems will be designed and evaluated from a thermal and fluid mechanics standpoint. A segment of the insulation system will be manufactured and preliminary tests performed using cryogens only as required to verify the insulation evacuation. Complete thermal testing will be conducted later contingent upon successful completion of the present scheduled program. The goal of a parallel effort is the development of a basic insulation concept having a significantly lower thermal conductivity and density product. The advanced insulation material will be substituted for the materials used initially in the major study. Insulation concepts with the density thermal conductivity product equal to one-half the values of those currently in use appear possible.

REFERENCE

1. Modular Nuclear Vehicle Study, Phase II. Lockheed Missiles and Space Company, Sunnyvale, California, Contract NAS8-20007, 1967.

COMPUTATION RESEARCH AT MSFC

May 25, 1967

8

Page
Intentionally
Left Blank

FOREWORD

Research Achievements Review No. 8, Volume II, was presented May 25, 1967. The paper that follows is a brief discussion of third generation computing at MSFC. This paper was prepared from the material presented at the review, which included the following talks:

1. Introduction to Computing at MSFC — by Helmut Hoelzer
2. History of Computers and Their Use at MSFC — by Charles P. Hubbard
3. The Third Generation Concept in Computing — by William Fortenberry
4. Application of the Third Generation Concept to MSFC Computation Problems — by Carl Prince
5. Technical Description of MSFC's Third Generation Computer System — by John C. Lynn
6. Implementation of Third Generation Computing at MSFC — by James T. Felder, Jr.
7. A Look at the Future in Computing at MSFC — by Helmut Kerner

THIRD GENERATION COMPUTING AT MSFC

LIST OF ILLUSTRATIONS

THIRD GENERATION COMPUTING AT MSFC

INTRODUCTION

The Univac 1108 third generation (3G) computer at MSFC (Fig. 1) will have the capability to handle multiple requests from the equipment shown in Figure 2. This time sharing ability will provide the entire Marshall Center with adequate means to process computer operations from almost any location.

The 55 teletypes that will be provided at remote locations offer rapid response to each individual user.

Letters and numerals can be displayed by the computer on the scope of 28 CRT (Cathode Ray Tube) stations, while 10 other CRT stations can provide computer generated pictures on their screen or allow the user to draw on the screen with a light pen. Thus the pictures can be altered by erasing lines and drawing other lines and picture segments on the screen.

FIGURE 1. 1108 COMPUTER

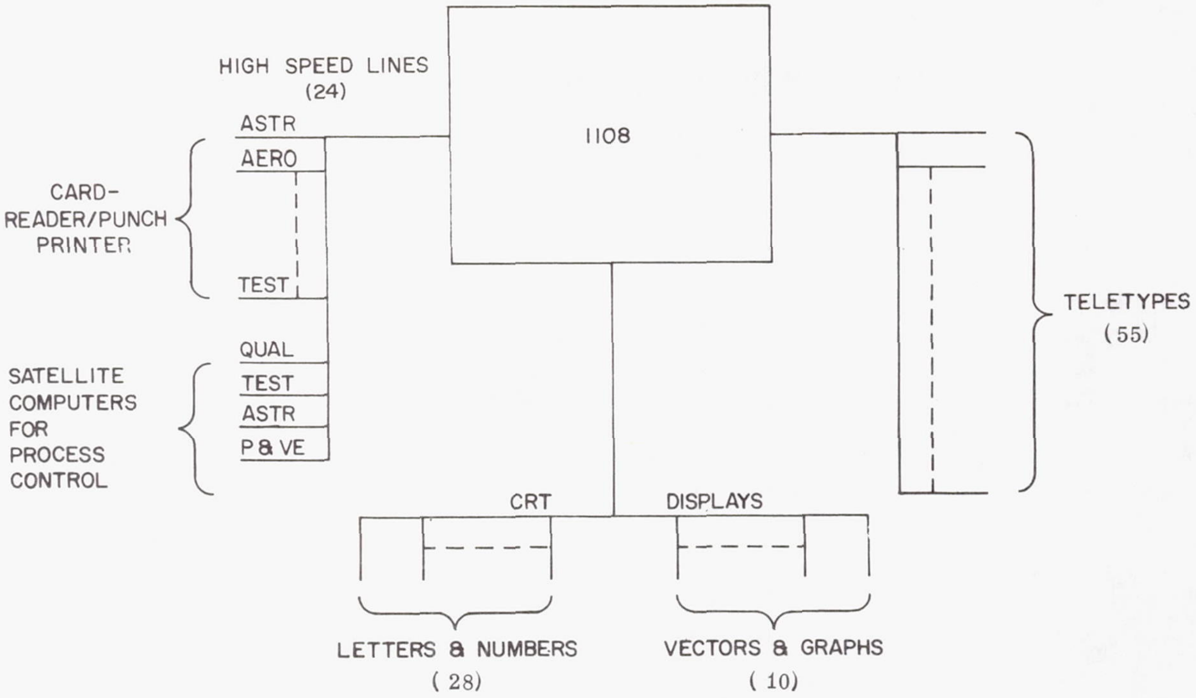

FIGURE 2. 1108 REMOTE STATIONS

A drawing of component or structure can be changed by adding or deleting items to assemble a new design concept.

Most of the 24 high speed lines will connect general purpose remote stations comprised of card readers and printers to the 1108 computer in the Computation Laboratory. A few of the 24 high speed lines will be transmission paths to connect satellite computers to the 1108. The satellite computers in other laboratories may be located up to a distance of one mile from the 1108 in the Computation Laboratory. These satellite computers can possibly be used to control large operations such as the static firing of an engine or the automatic checkout of a complete stage. Each of the 24 high speed lines has the capability to transmit 50,000 bits per second, an ample electronic transmission capability.

COMPUTER OPERATIONS

This operation of the 3G computer is made possible by multiprogramming, multiprocessing, internal and external interrupt capability initiated from either the main 1108 location or the remote sites, and the ability to do all peripheral work (reading cards, printing, storage on tapes) directly from almost any location. The hardware is modular, thus the components, such as memory banks, processors, input-output channels, and peripheral communication devices can be added to the system to increase its power. The engineer's thinking and the machine's computing process can now become one continuous, integrated operation.

Multiprogramming. Multiprogramming is the sharing of a processor when a computer handles several programs in sequential operations. The processor has the ability to address all of the computer's memory through a switching mechanism, and thus can address all of the programs residing there. Many programs can reside in the computer's memory because of its vast size, but are located in different locations; thus the central processor can act upon programs sharing the same memory whenever there is a pause in processing one program. The processor can operate physically on only one program at a time, causing the program to initiate some input or output function during which time a pause in the sequence is required. At this point a switch takes place and the processor moves from the operating program to another program residing in core and initiates some action on the new program. Except for the time needed for switching, the processor is in use 100% of the time.

Multiprocessing. Multiprocessing is the employment of two or more processors that can address the entire computer's memory simultaneously. Several processors provide the capability to independently and simultaneously handle several programs. More programs than the number of processors can be operating, because when some programs are performing input-output functions, the processors have searched memory and found other programs upon which to operate. The 1108 computer at Marshall will have three processors, therefore more than three programs can be operated on by the processors at any given time.

Time Sharing. Time quantums can be allocated to each program when several processors are handling a number of programs. The time quantums are allocated from the total amount of time available in the CPU (Central Processor Unit).

Interrupt System. When an interrupt occurs, the computer allows the program to complete a specific machine function, then moves to a precoded solution to solve the interrupt.

Types of Interrupts:

1. Program dependent types of interrupts (divide by zero in math equation).
2. Nonprogram dependent interrupt
3. Input-Output functions
4. Diagnostic problems (an error occurs in a memory bank and requires the attention of the "EXEC" to mark that memory bank off line automatically).

Storage. The main memory of the second generation computer now in use at MSFC has 32,000 words core storage capability. The 3G computer will have 262,000 words core storage capability. The total of 1 1/2 billion characters of storage can be expanded several orders of magnitude by adding more huge Fastrand drums with the practical limitation being the amount of facility space. The word size for both computers is 36 bits. The validity of results is assured by carrying one extra bit that serves as a check on the information (parity check). There is parity checking on all storage references; and continuous overlapping and interleaving operations are being run. Overlapping means that a reference to main storage is occurring while the processor is decoding the previous instruction. Interleaving is the simultaneous searching of odd and even banks of storage. The total 262,000-word main storage is in banks of 65,000 words that are divided into odd and even sections of 32,000 words each (interleaving on one bank is possible). Since three processors share or compete for memory, the multiprocessor-adapter assures that no processor will be more than one memory cycle behind any other processor in access to a memory bank. The input-output controllers (large multiplexers) will handle 24 high speed data channels that will allow additional input-output devices to join the systems.

Memory Protect Features.

1. Read Protected — Only the author can call up the data.
2. Write Protected (Memory Protect Feature) — A lockout capability prevents the data from being destroyed or overwritten so that several users can share the same data.

Types of Problems.

1. Compute Bound — requires little input and a great deal of manipulating and computation by the processor in the central unit, thus wasting the external communication power of the computer. Typical problems of this unit are (1) to find the Eigenvalues of a large matrix, (2) solving simultaneously a large system of equations, and (3) solving for certain key points along a long trajectory.
2. Input-Output (IO) Bound — requires large amount of IO and little operation by the processor, thus wasting the computing power of the system while the tapes and printers are functioning to receive the data and make a reply. Typical problems of this kind are (1) to furnish personnel reports, (2) to compile contract status reports, (3) to inventory catalogues of data, and (4) to run the payroll.
3. Consolidating Volumes of Data — requires storage capability with up to 1 1/2 billion characters available on Fastran drums for

compiling files of data for engineering requirements. These problems include (1) design and development of a large project, (2) changes to specifications, and (3) data storehouses.

Capabilities. The third generation computer can respond as quickly as the engineer can change the design and data on the CRT screen or review plans and diagrams presented by the computer. To exploit such rapid communications between the engineer and computer requires program-oriented languages that make extensive use of new pictorial and graphical methods for stating the problem and presenting the results. Standard programs on call from memory devices in the computer can be used to solve the problem when the computer has sufficient information, possibly in pictorial form and in equations, and has converted these data to a form to be processed by conventional problem solving programs.

Some computer operations make use of pictorial or graphical means for the statement of the problem and the presentation of the results. They can be separated into two main areas of application (Fig. 3).

1. TOPOLOGICAL
    - A. ELECTRONIC CIRCUIT ANALYSIS
    - B. PERT
2. GEOMETRICAL
    - A. STRUCTURAL AND STRESS ANALYSIS
    - B. VIBRATION STUDIES
    - C. HEAT-TRANSFER STUDIES
    - D. AERODYNAMICS APPLICATIONS
    - E. ENGINEERING DRAWING RETRIEVAL AND/OR MODIFICATION

FIGURE 3. COMPUTER GRAPHICS APPLICATIONS

One group of problems requires providing topological relationships between objects to solve applications involving electronic circuit design and analysis, design of feedback control systems on a block level, PERT systems, and structured data that can be presented in a flow or organizational chart. The other group of problems can be solved by the computer by receiving the data in geometrical form. This type of applications includes structural and stress analyses of space vehicles, vibration studies, heat transfer studies, and aerodynamic applications. In the future, engineering drawings can be modified by drawing on the screen with a light pen and automatically receiving a copy of the revised drawing.

PROBLEM-ORIENTED LANGUAGES

TOPOLOGICAL PROBLEM STATEMENTS

1. Circuits

Circuit analysis problems are stated topologically. The engineer has a choice of block, such as amplifiers or resistors, etc. When the interconnections of the system are defined by the use of the light pen, the computer can evaluate the circuit. Given certain input signals, the response at any point specified by the light pen can be obtained and displayed on the screen.

Likewise, the same process can be followed with feedback control systems of electric or electromechanical systems. In this case the blocks would represent transfer functions. With the light pen the user could interconnect the different blocks and specify the type of block, e.g., a differentiator, adder, and integrator. Then, by using the verbal features of the teletypewriter, functions within the block can be defined by writing the equation. The computer then processes the data and draws and types the results to prepare enough information for the engineer to make decisions.

Figure 4 shows a sample circuit an engineer might design. When needed, the using engineer can change the constants of the transfer function or the equations themselves from the teletypewriter. An iteration of the procedure to find a solution will take only minutes as opposed to at least a day on today's system.

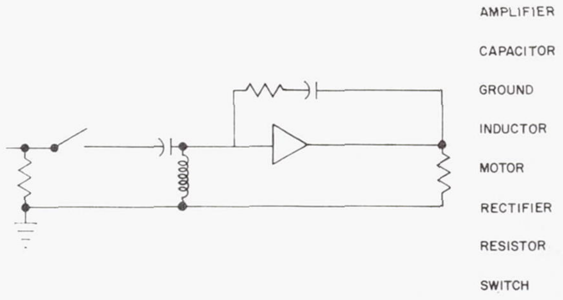

FIGURE 4. ELECTRONIC CIRCUIT DESIGN AND ANALYSIS

2. Marves

Another example of this programming system that was developed at Marshall is MARVES (Marshall

Vehicle Engineering System), a language for computation of trajectories. Each of its 100 modules represents a physical effect or a mathematical method. Most trajectory problems can be constructed with these building blocks. Since the using engineer can not be expected to have a working knowledge of all 100 and more different blocks, some type of retrieval system is needed to assist him in the composition of his program. This service can be requested by typing MARVES on one of the teletypewriters. The computer will respond by offering the first level of options via display on a CRT console (Fig. 5) to the user, who takes his choice by merely pointing with his light pen. Depending on his choice, the computer will offer the next lower level of options and so forth until the problem is completely specified. Whenever the user does not vote for any option, the computer will take a standard route. Finally the computer will list all modules selected, which the user can modify or exchange later.

GEOMETRICAL PROBLEM STATEMENTS

1. Lifting Body

The geometrical form input to the computer could present new techniques for conducting aerodynamic studies of a lifting body. Given a group of basic building blocks consisting of cones, cylinders, spheres, and different two-dimensional features such as triangles, through a movement of the light pen the designer could move the two-dimensional representation of the cone and connect it to the two-dimensional representation of the cylinder and half of a sphere, etc., and a composite picture would appear. Fins for the flight stage can be added later. Thus the designer can define a geometrical body and thereby implicitly define his design problem by using a simple language of pictures supported by numerical parameters.

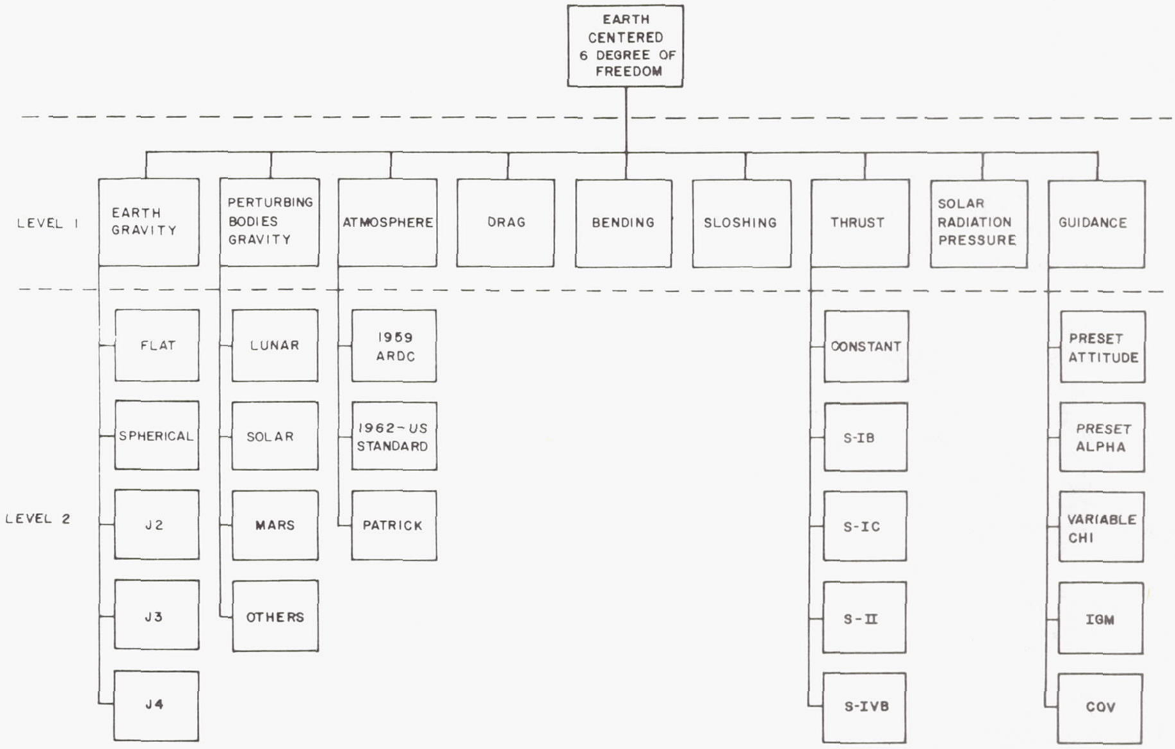

FIGURE 5. EXAMPLE OF LEVEL 1 AND LEVEL 2 OPTIONS AVAILABLE FOR THE 6-DEGREE-OF-FREEDOM EARTH CENTERED TRAJECTORY PROBLEM

To completely define the concept, the engineer stipulates the geometrical aspects of the design to include the thrust required for the vehicle. The computer than makes an evaluation. As a result, drag, lift, and the center of this lifting force can be obtained and displayed on the screen. Whenever the engineer specifies the material property, the center of gravity can be computed (Fig. 6). This is a typical example of a problem-oriented pictorial language.

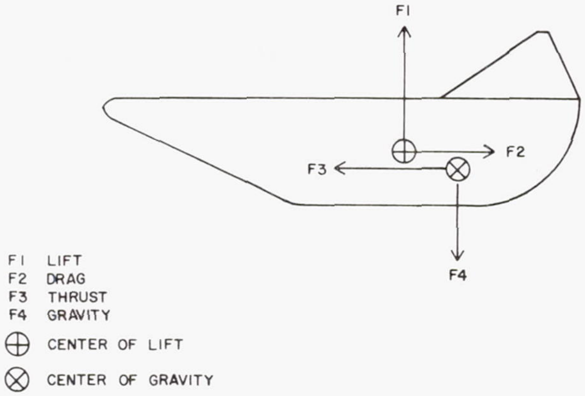

FIGURE 6. AERODYNAMIC STUDIES (LIFTING BODY)

2. Structures

It is quite obvious that a similar procedure can be used for the design of structures. The designer can shape, size, and position any of the basic building blocks, by use of the light pen. At any selected position in space the computer would then produce a three-dimensional (perspective) picture of the composite structure by connecting the basic building blocks (Fig. 7). The computer would also display two-dimensional projections and compute the commands for a numerically controlled manufacturing process.

INFORMATION RETRIEVAL SYSTEMS

A third interesting category of problem-oriented languages is information retrieval systems. A typical example at Marshall Space Flight Center is the technical library. Given a set of key words, the computer will print out a list of all journals or books in the library that deal with the subject matter.

Retrieval systems can be designed for particular organizations and programmed to prevent duplication in data storage and transmission. The design of such systems and access to the data depend upon many factors that are too complex to be discussed in this paper.

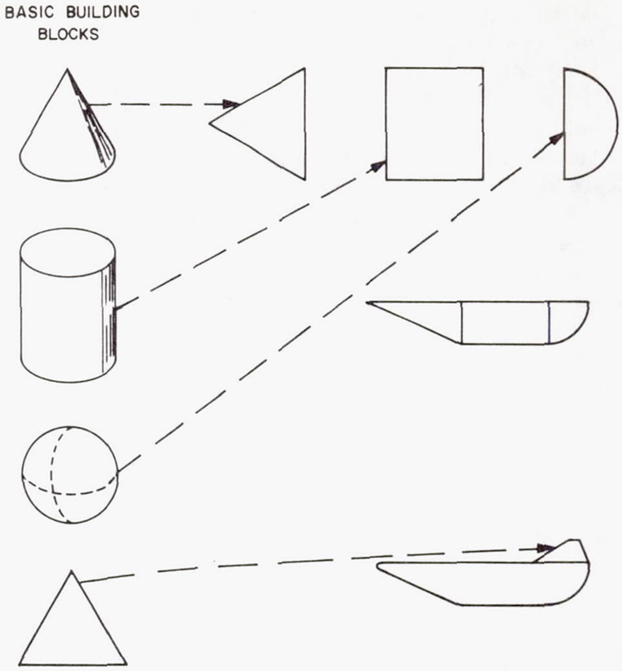

FIGURE 7. STRUCTURAL DESIGN

ONBOARD COMPUTER

A significant evolution is taking place in onboard computers. Previously the onboard computer performed only guidance and control operations. Today's Saturn computer uses only 20 to 30 percent of its time for the classic guidance and control problem. Looking toward Voyager and beyond, it appears that only a small percentage of computer time will be used for the guidance and control function; the main computer function will be data management and data compression. Further, it will be necessary to build a computer that will last at least three to four years for a manned Mars mission. In the case of a failure it should not break down totally (concept of the gracious degradation). Power must be much lower than the present kilowatts; it must be rather in the order of watts only.

It is believed that with the LSI technology that will be available in the early 1970's, it will be possible to build computers to meet such requirements and to find the proper computer organization for these applications. Years of work by mathematicians and computer designers will be necessary. The powerful third generation computer at MSFC will be intensively used for simulations of the onboard machines to obtain knowledge about the reliability of such a predicted new computer concept as to its accuracy and speed. Its executive system will be evaluated toward the features of self-organizing. The Computation Laboratory is presently organizing to begin to work toward these goals.

Page
Intentionally
Left Blank

POWER SYSTEMS RESEARCH AT MSFC

July 27, 1967

By

Richard Acker
Richard J. Boehme
William L. Crabtree
Walter H. Goodhue
Charles B. Graff
Roy Lanier
Jimmy L. Miller
John R. Morgan
Leighton Young

9

Page
Intentionally
Left Blank

Page
Intentionally
Left Blank

INTRODUCTION TO ELECTRICAL POWER SYSTEMS RESEARCH AT MSFC

By Richard J. Boehme

LIST OF ILLUSTRATIONS

ZINC-OXYGEN PRIMARY BATTERY

By Charles B. Graff

LIST OF ILLUSTRATIONS

FUEL CELL SYSTEMS

Page

By Walter H. Goodhue

LIST OF ILLUSTRATIONS

CONTENTS (Continued). . .

FUEL CELL TECHNOLOGY

By John R. Morgan

LIST OF TABLES

LIST OF ILLUSTRATIONS

CONTENTS (Continued). . .

STUDY OF RADIOISOTOPE POWER FOR SATURN APPLICATIONS

By Jimmy L. Miller

LIST OF ILLUSTRATIONS

STUDY OF SOLAR POWER WITH GRAVITY GRADIENT STABILIZATION

By Leighton Young

LIST OF ILLUSTRATIONS

METAL-ARC ILLUMINATOR FOR SOLAR ARRAY TESTING

By William L. Crabtree

LIST OF ILLUSTRATIONS

ELECTRICAL POWER CONVERSION SYSTEM FOR MANNED EARTH ORBITAL VEHICLE

By Richard Acker

LIST OF TABLES

LIST OF ILLUSTRATIONS

CONTENTS (Concluded)...

INVERTERS FOR MOTORS

By Roy Lanier

LIST OF TABLES

LIST OF ILLUSTRATIONS

INTRODUCTION TO ELECTRICAL POWER SYSTEMS RESEARCH AT MSFC

By

Richard J. Boehme

SUMMARY

To successfully complete space vehicle missions, research efforts at the Marshall Space Flight Center (MSFC) have produced significant achievements in developing electrical power systems. Even more stringent mission demands will be imposed on future power systems. This introduction outlines the power systems R&D program, including program effectiveness and organization, and the program planning to assure future success.

PRESENT R&D PROGRAM

The Marshall Center R&D program in electrical power systems has been conducted primarily by the Electrical Systems Division of the Astrionics Laboratory. Emphasis in the past has been on battery systems because they have served as the power workhorse and will see extensive service in the future. Recent efforts have been made to diversify the program without sacrificing effectiveness, and to concentrate on requirements that represent limitations or significant problem areas for future mission systems.

The need for revitalized efforts in developing space power systems was well summarized recently by William Woodward, Acting Director for Nuclear Systems and Space Power, Office of Advanced Research and Technology (OART). In his introductory statement to a Congressional Subcommittee, he said, "Current space power system technology is not yet satisfactory for such future missions as high power communications satellites, science probes and orbiters to distant planets, and for long-duration, manned, earth-orbit, lunar, and planetary missions."

The major part of the MSFC program is sponsored by OART, and R&D work is being performed in support of the MSFC vehicles and study missions. The "Electrolysis Systems" and "Advanced Electrochemical Systems" are new projects in which basic research work has just started.

Previous R&D efforts have been quite successful as shown by the most notable, recent achievement of the technology readiness status reached by the fuel cell system. The remainder of the fuel cell work started in FY 67 will carry the system into a technology utilization and verification phase. This phase of work is being assumed by the Manned Spacecraft Center (MSC) at Houston to adapt the system to their advanced Apollo Applications Program (AAP) missions.

ORGANIZATION

Because of the serious need for advanced technology in power and energy systems, the Power Branch was established under the Electrical Systems Division (Fig. 1) of the Astrionics Laboratory. To emphasize and expand R&D efforts in this critical field, subdivision of the Power Branch has been by

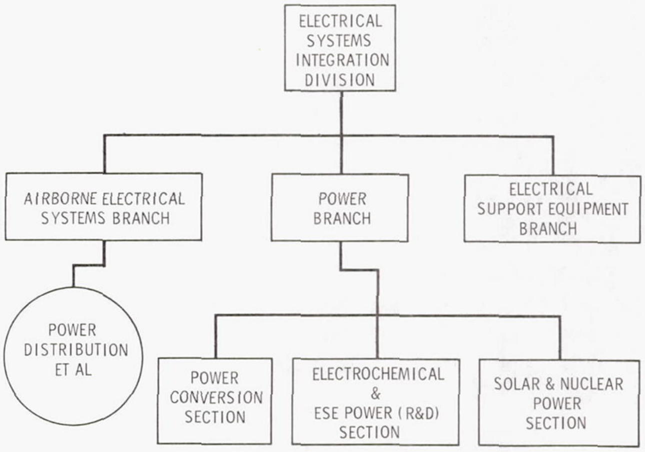

FIGURE 1. ORGANIZATION FOR ELECTRICAL POWER

technical discipline rather than by project. The three sections presently in operation are as follows:

1. The Power Conversion Section

2. The Electrochemical & ESE Power Section

3. The Solar and Nuclear Power Section

Advanced R&D will be performed under the same groups which are responsible for the design and development work for vehicle missions. Program aims are (1) to emphasize R&D in space power, (2) to increase the number of competent persons in the field, and (3) to consolidate efforts and thereby increase the percentage of available resources for advanced R&D.

POWER IN THE FUTURE

Surveys have been made of various future mission requirements for advanced power systems and equipment. Recent technology forecasts by OART and other agencies have also been reviewed. A brief summary of the R&D job to be accomplished for electrical power systems of the future is as follows:

1. Power and energy systems must possess vastly expanded capabilities for successful future space exploration. Large improvements in technology are needed so that the conceptual missions of today will become realities in the next decade. As one example, the requirements in supplying electrical power to electrically propelled vehicles become synonymous with those of generating propulsion power.

2. Improved electrochemical systems will be required for energy storage and short term power. This need extends for several decades.

3. Larger, higher performance solar cell arrays with lighter weight mounting structures are needed. Solar arrays will be used extensively in the next decade for long-duration power. Fifty kilowatt ratings appear quite reasonable for the early 1970 period.

4. Even though technology readiness may be achieved for large nuclear power systems, practical systems will remain in their infancy in the 1970's. Small radioisotope thermoelectric units of several hundred watts will be used extensively. Radioisotope Brayton-Cycle or thermionic systems may find limited application in the later 1970's, but they will be restricted by fuel and installation costs and non-technical factors.

5. The use of large reactor systems in space appears to be reserved for the 1980's. Nuclear systems require better materials, higher conversion efficiencies, and reasonable solutions to thermal dissipation, shielding, and safety constraints.

The MSFC program will be oriented to solving these power systems requirements, especially in the applied research and system integration areas.

PROGRAM ORIENTATION

To support R&D programs coordinated toward one or more common missions, a conceptual mission has been selected as a future baseline toward which most of the power and energy conversion R&D projects will be oriented. Such programing assists in coordinating overall programs and is technically sound, providing that the baseline is properly selected and that a reasonable amount of unconstrained basic research is authorized.

A lunar-surface exploration mission primarily founded on a lunar base concept will serve as the fundamental guide for the power system R&D work. It is assumed that this mission will be established in the mid 1970's for the purpose of conducting extensive lunar surface exploration and scientific investigations. It is further projected that, during the assumed mission, additional programs will be added to evaluate technology, equipment, and capabilities for establishing large, hard bases to support subsequent missions. Thus the lunar surface exploration mission should progressively phase into a hard base mission to provide a permanent lunar installation to sustain continuous operations. As conceived, such missions could (1) permit exploitation of lunar resources, (2) serve as a logistics base for interplanetary exploration, (3) provide expanded, long-term, scientific bases for astronomy, and (4) provide communications relaying and advanced monitoring of space operations. This concept was derived from many studies performed for the government, and the results of these studies will be used extensively in the program. The technology requirements are expected to be quite demanding, and in meeting these demands a capability to fulfill the needs of most any mission expected in the 1970's will be provided.

Figure 2 shows a block diagram of the general system for the selected baseline mission. After a standby mode of up to 6 months, the operation is started upon command through the telemetry station system. A small radioisotope generator (RTG) is used in the secondary power subsystem to provide standby and activation power.

Lunar-surface exploration will begin with the arrival of the base crew and the mobile vehicles. Mobile vehicles powered by H_2/O_2 fuel cells provide the means of exploring vast regions about the base station. These vehicles will carry scientific instruments and geological equipment as well as life support equipment. Initially, the vehicles are furnished with cryogenic reactants, and a means is provided to collect by-product water from the fuel cells during mobile operations. Two week (1 lunar day) sorties have been envisioned and appear feasible. A sortie is completed upon return of the vehicle to the base station for resupply. During resupply, standby electrical power requirements of the vehicles are furnished by the regulation and control subsystem of the base. Reactant loading and unloading of the by-product water from the mobile vehicles are done by base station personnel using the unloading and scavenging equipment in the electrolytic reactants production subsystem. This equipment is also used to receive water from the environmental control system (ECS) and fuel cell systems at the base station. The electrolytic subsystem converts the water to reactants (H_2 and O_2) and delivers gases to liquefaction subsystems or to storage, as required, for reuse. The storage subsystem supplies reactants to reload vehicles and to the base power subsystem to permit fuel cells to operate through the lunar night. The storage subsystem can supply back-up oxygen to the environmental control system of the base or to the vehicles as needed.

Solar arrays sized to 50 kW have been assumed to be available under the lunar equipment primary electrical power system (LEPEPS) to power the base and to operate the electrolysis systems during the lunar day. Later, nuclear reactor power systems could be added to the base complex as a primary power source when expanded operations are desired.

With the requirements for a limited three man base station outlined, investigation continues on the means to expand this station into a complex for a 12 man operation for extended periods.

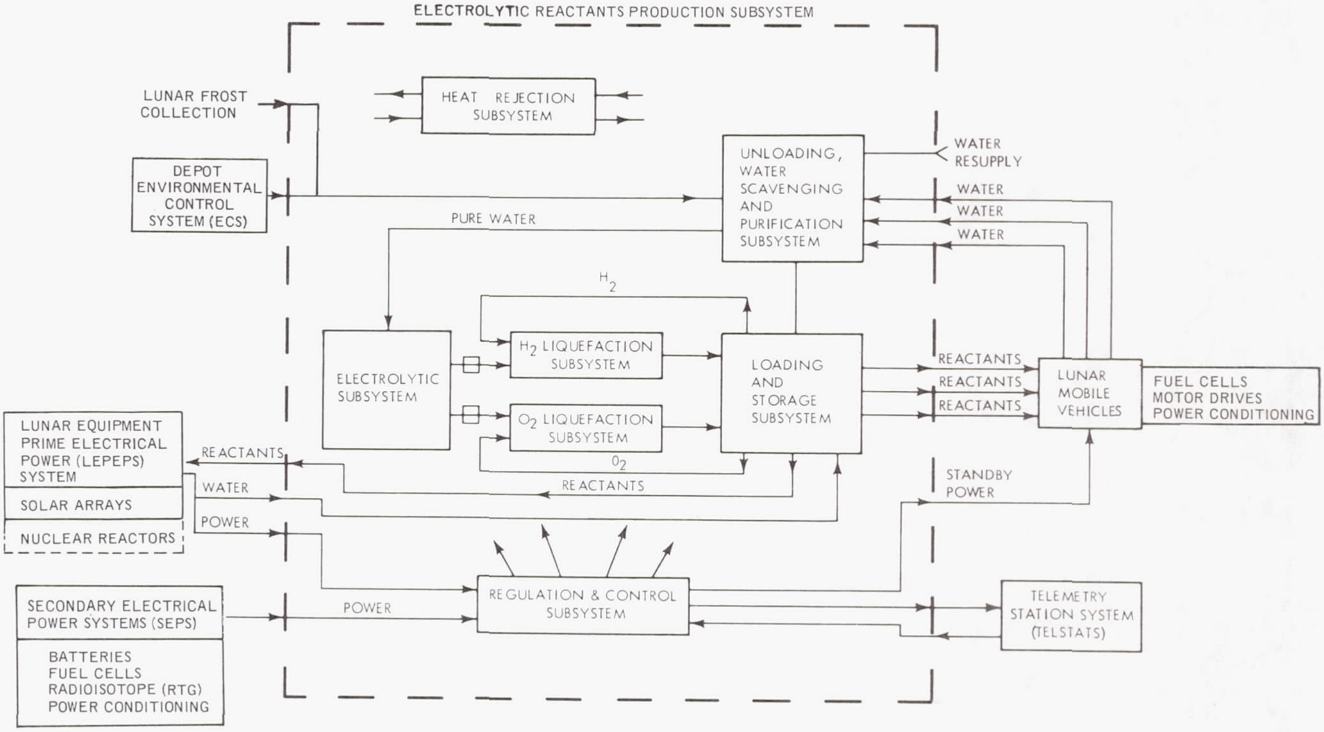

FIGURE 2. SYSTEM FOR R&D BASELINE MISSION

Page
Intentionally
Left Blank

ZINC-OXYGEN PRIMARY BATTERY

By

Charles B. Graff

INTRODUCTION

Development work has been progressing for several years toward a reliable metal-air primary battery system that will be an auxiliary power source in space vehicle applications. One of the most promising systems uses the zinc-oxygen ($Zn - O_2$) battery that yields energy densities far in excess of existing primary batteries. The power source had to meet the following specifications:

Voltage regulation from 20% to full rated load	28 ±2 V
Maximum load	50 A
Minimum load	10 A
Minimum discharge time (full load)	8 hr
Capacity	400 A-hr
Energy density	264 W-hr/kg (120 W-hr/lb) (minimum value)

To meet these goals, Leesona Moos Laboratory (LML) began development of a scale model 6 V, 70 A-hr battery containing cells with the exact electrode configuration and size that will be required for the 28 V, 400 A-hr vehicle power system

DESIGN DATA

The LML zinc-oxygen battery consists of a porous zinc anode, a lightweight, efficient, stable oxygen cathode, an alkaline (KOH) electrolyte, and a supply of oxygen (Fig. 1). The best design of a high-energy density zinc-oxygen battery has a maximum ratio of active or usable zinc weight to total battery weight. An efficient design to obtain the maximum zinc area per unit weight is a bicell construction. The bicell consists of two cathodes connected in parallel and supported by a suitable frame. The zinc anode is wrapped in separator material and inserted into the frame between the two cathodes. Intimate contact between the anode, separator, and cathode is achieved by proper cell support and stacking. Only an amount of electrolyte sufficient to saturate the anode structure and separator material is used. The electrolyte provides a continuous ionic path.

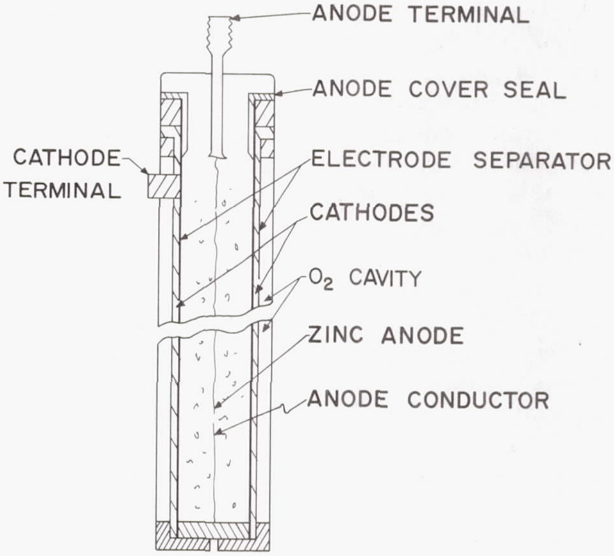

FIGURE 1. $Zn - O_2$ SINGLE CELL CROSS SECTION

The cathode establishes an active medium between the oxygen, catalyst, and electrolyte. The cathode consists of a semi-permeable film which permits oxygen to pass through to the catalyst side to be reduced, and yet retains the electrolyte within the cell. The oxygen cathode does not undergo any physical or chemical change in the course of producing power.

The electrochemical process occurring within the cell is shown below. The cell reactions are:

Anode: $Zn + 4OH^- \rightarrow ZnO_2^= + 2H_2O + 2e^-$

Cathode: $\frac{1}{2}O_2 + H_2O + 2e^- \rightarrow 2OH^-$

Cell: $Zn + \frac{1}{2}O_2 + 2OH^- \rightarrow ZnO_2^= + H_2O$

$Zn + \frac{1}{2}O_2 \rightarrow ZnO$

The zinc is oxidized at the anode, with electrons being released to the external circuit during the process. The electrons are received from the external circuit at the cathode and take part in the reduction of oxygen to hydroxyl ions at this electrode. The total cell reaction then results in oxidation of zinc. The anode reaction proceeds at a potential of + 1.216 V. The cathode potential is - 0.401 V. Overall cell potential is 1.617 V.

The ultimate energy density of a zinc-oxygen system is dependent upon the ratio of usable zinc to total battery weight and operating voltage according to the equation:

$$\text{Energy Density (W-hr/kg)} = \text{Operating Voltage (V)} \times \text{Zn utilization (\%)} \times 818\ \text{A-hr/kg} \times \text{Zn wt(kg)/Battery wt(kg)} \qquad (1)$$

Zinc has an electrochemical equivalent of 818 A-hr/kg zinc (371 A-hr/lb zinc). In a cell operating at 1.25 V, it is theoretically possible to obtain 1020 W-hr/kg (464 W-hr/lb) based upon the weight of zinc alone. Faradic efficiency, cathode weight, electrolyte, and supporting structure limitations reduce this value. Figure 2 is a comparison of the energy density of the zinc-oxygen battery with that of a silver-zinc battery.

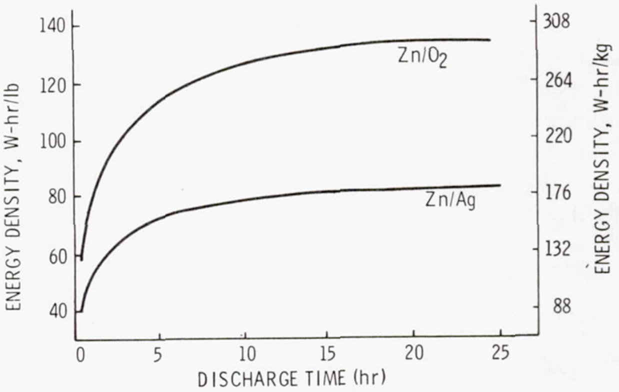

FIGURE 2. Zn - O_2 VS Zn - Ag

The variation of zinc utilization as a function of discharge current density at various anode thicknesses is shown in Figure 3. At low discharge rates, zinc utilization is practically independent of anode thickness. At higher current densities, efficiency

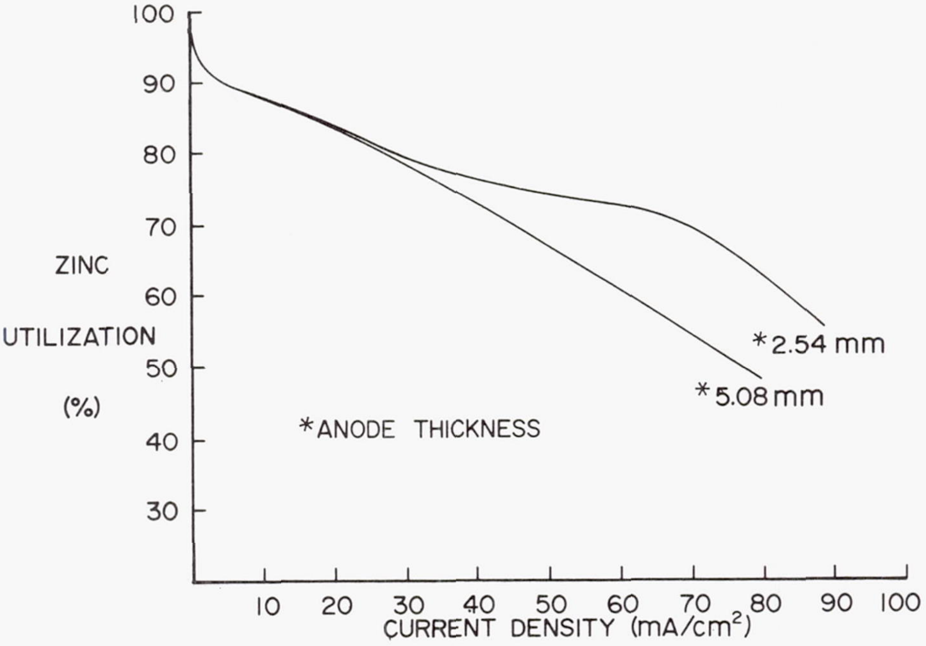

FIGURE 3. ZINC UTILIZATION

decreases with anode thickness. Therefore, low discharge rate batteries can use the thicker anode, and higher discharge rate batteries must incorporate the thinner anodes or the bicell construction.

A typical cathode polarization curve is shown in Figure 4. Current densities up to 350 mA/cm^2 can be supported using oxygen at atmospheric pressure. It can be concluded from the information shown in Figures 3 and 4 that the operating current of the battery is limited by the effect of zinc utilization efficiencies.

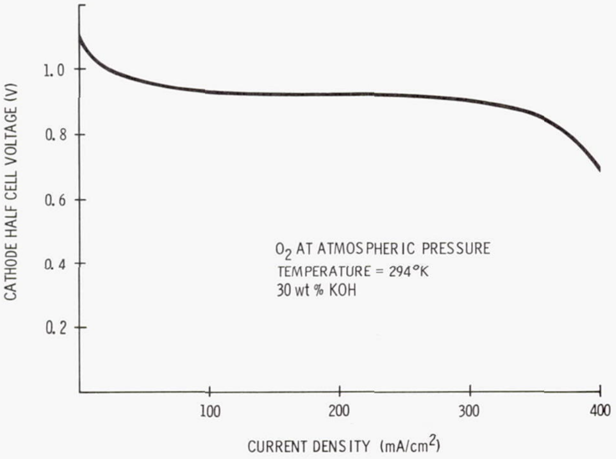

FIGURE 4. ELECTROCHEMICAL PERFORMANCE OF OXYGEN CATHODE

The current-voltage relationship of a fuel cell is flat over a broad region and permits good voltage regulation over a widely varying power profile. Figure 5 illustrates the voltage-time characteristics of a 6 V, 100 A-hr battery at the 8, 16, and 24 hr rates.

ANALYSIS AND DEVELOPMENT

Studies were made of various cell and anode configurations that yielded the maximum ratio of active component weight to frame weight, were easy to manufacture, and were simple to integrate into the battery system. On this basis a square, bicell configuration was selected. A parametric and failure analysis was performed to establish the optimum number of cells and stacking configuration required to yield the maximum energy density and overall system reliability. On the basis of this analysis, maximum energy densities occur when the cells are

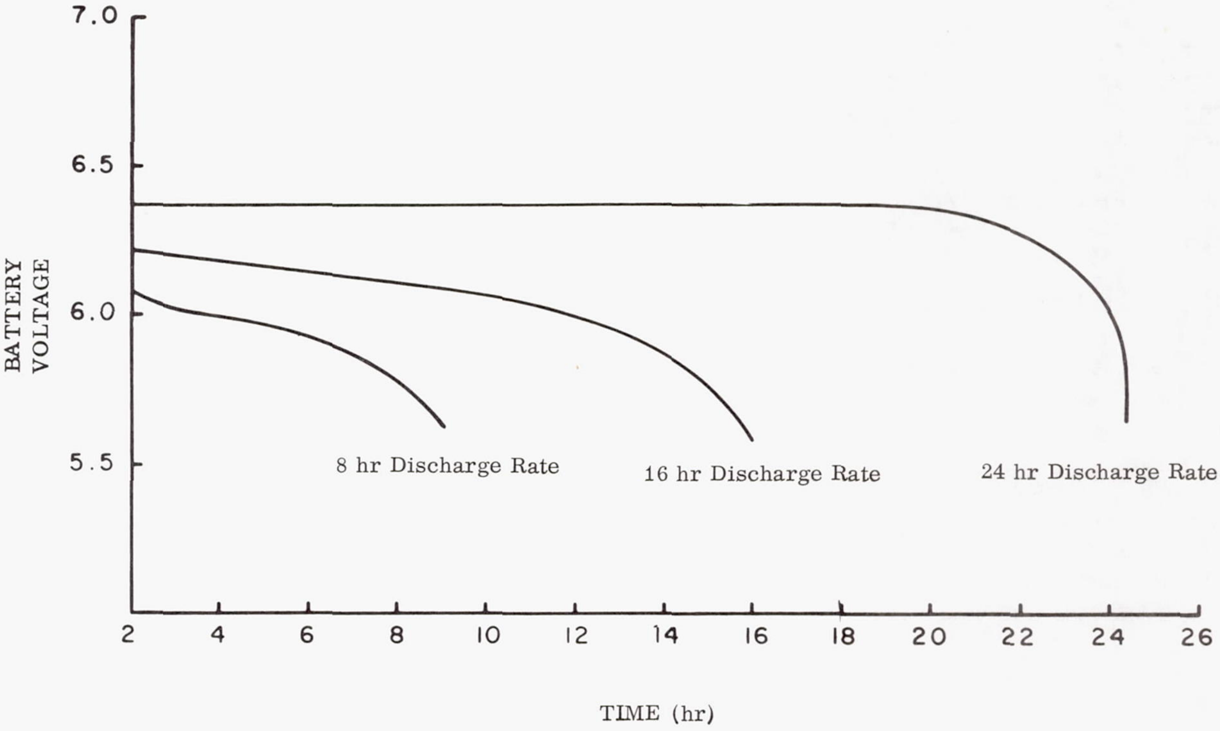

FIGURE 5. BATTERY VOLTAGE VS DISCHARGE TIME

designed to operate at current densities of 30 mA/cm^2. Maximum reliability and minimum system weight are achieved using a stacking configuration of 23 series-connected modules with 6 parallel-connected cells per module. A total of 138 series/parallel connected cells will be required for the final 28 V battery system.

An analysis was made to characterize the degree of heat dissipation. Using the heat of reaction of the zinc-to-zinc oxide process and Faraday's Laws of Electrolysis, the difference between the heat of reaction and useful electrical energy output was calculated as the heat to be rejected to stabilize internal battery temperatures. A new heat removal technique was designed in which the intercell separators are used as the means for heat removal. Figure 6 shows a schematic of the heat removal system. This concept uses corrugated magnesium intercell separators that are positioned between the cells, contacting the cathode surfaces and extending outward to achieve thermal contact with the battery case. The intercell separator actually performs four functions as follows:

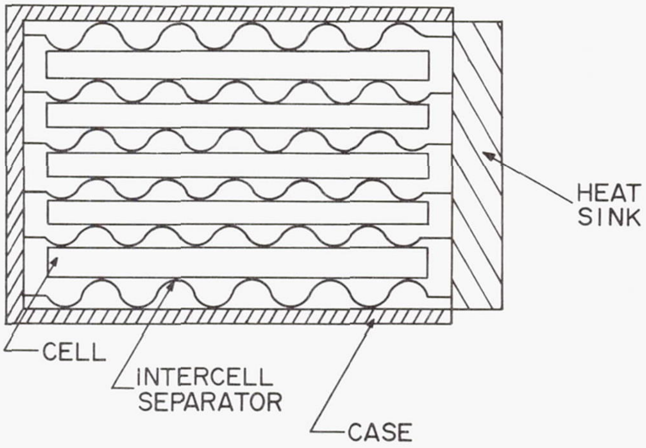

FIGURE 6. HEAT REJECTION SCHEMATIC

1. Allows oxygen to reach the cathode by providing a space between the cells.

2. Maintains intimate contact between the cathode, separator material, and anode.

3. Prevents growth of anodes during discharge.

4. Acts as the means for heat rejection.

Five series-connected cells, intercell separators, stack-support systems, and battery cases have been successfully integrated into a 6 V battery system. Evaluation of this system has demonstrated that its performance exceeds the minimum requirements projected for the 28 V system as shown below:

- Cell voltage regulation from 1.13 V to 1.3 V in excess of 8 hr at 30 mA/cm^2.
- Anode efficiencies in excess of 75%.
- Repeatability of results.
- Stabilization of internal battery temperatures at the 8 hr rate throughout the discharge period.
- Capability of withstanding a 5 to 2000 Hz, 6 to 10 g vibration and acceleration environment.

FUTURE EFFORTS

On the basis of the evaluation of the 6 V battery system, the outlook for successful fabrication of a reliable, constant 28 V, 400 A-hr battery system is excellent. A follow on program was initiated to accomplish this task. The work effort was divided into four phases as follows: (1) systems analysis and design studies, (2) engineering design, (3) fabrication and assembly of hardware, and (4) test and evaluation. The first phase is essentially complete and the second phase is in progress.

Figure 7 summarizes the projected 28 V battery and cell operating characteristics. The cell characteristics are based upon a projected stacking configuration of 6 parallel cells per module and 23 series modules. The first prototype battery to be developed under this program is scheduled for completion in May 1968. An extensive test program is planned to verify design and provide technical data for evaluation.

DISCHARGE TIME (Hr)	CURRENT (A)		CELL CURRENT DENSITY (mA/cm^2)	VOLTAGE			
				SYSTEM		CELL	
	SYSTEM	CELL		MAX.	MIN. (CUT-OFF)	MAX.	MIN. (CUT-OFF)
8	50(RATED)	8.33	30.5	30	26	1.3	1.13
16	25	4.17	15.25				
24	16.7	2.78	10.2				
40	10 (20%RATED)	1.67	6.1				

FIGURE 7. 28 V BATTERY SYSTEM OPERATING CHARACTERISTICS

Page
Intentionally
Left Blank

FUEL CELL SYSTEMS

By

Walter H. Goodhue

SUMMARY

A significant effort has been made by MSFC to develop a capillary matrix closed-loop fuel cell system for space applications. Contracts with Allis-Chalmers Corporation have produced systems that can support a 3 kW continuous load for more than 1500 hr. A 5 kW load was sustained for periods of 1 min. Basic development work resulted in the fabrication of a design verification test (DVT) fuel cell system for qualification on space missions. This effort was performed in conjunction with Manned Spacecraft Center.

INTRODUCTION

Investigation of fuel cell technology and its application to space vehicles began in 1958 at Marshall Space Flight Center (MSFC). In 1964, Manned Spacecraft Center (MSC) became interested in the Allis-Chalmers fuel cell being developed by Marshall as a backup power supply for the Apollo Command Module and Lunar Module. Research Achievement Review Series No. 14, given in November 1965, outlined progress on fuel cell technology up to that time. This report covers the achievements to the present.

A fuel cell is an electrochemical power source that has definite application in space and lunar vehicles. Figure 1 shows the area where fuel cells can make a contribution in the space vehicle power spectrum.

Fuel cells of current technology offer great potential as power modules for 3 to 4 month missions and as energy storage devices for all power systems presently under consideration. Fuel cells are the only power source that produces water as a by-product .

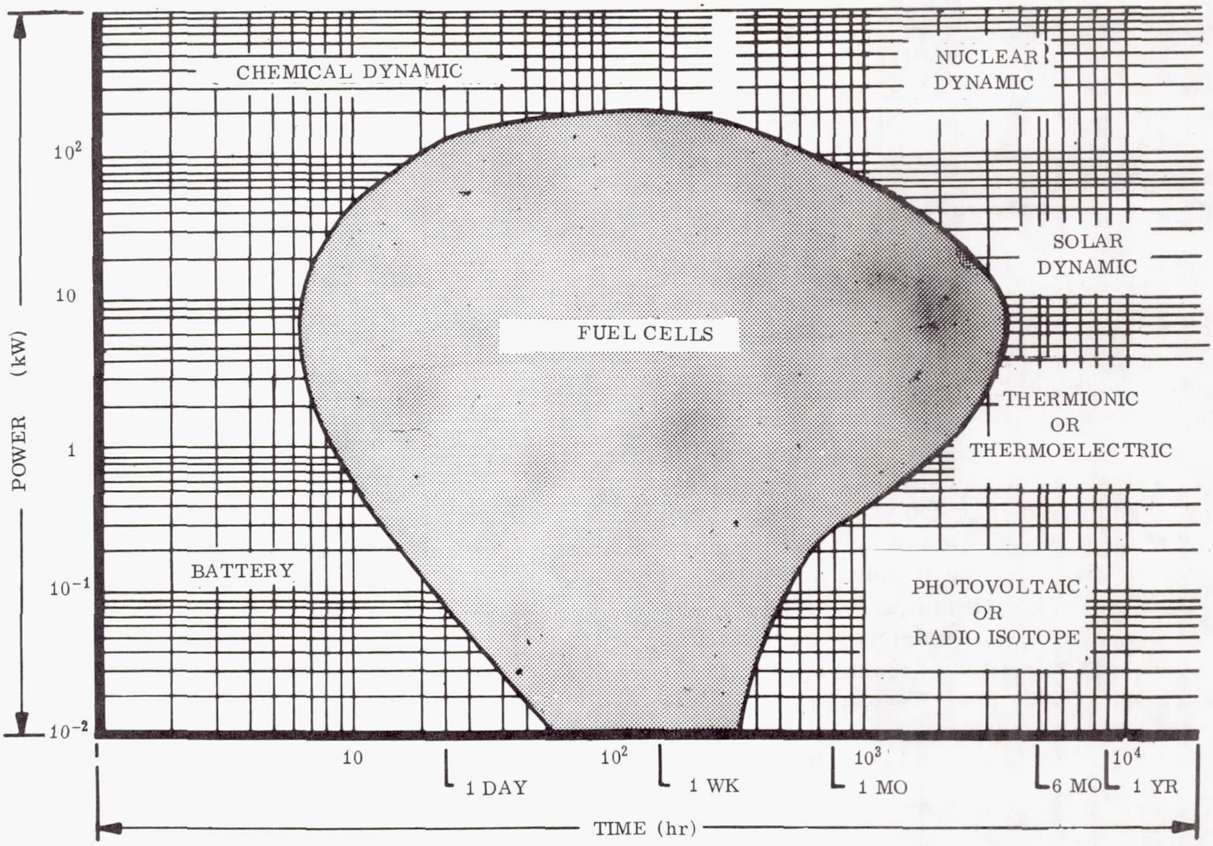

FIGURE 1. ANTICIPATED FUEL CELL RANGE

MSFC FUEL CELL

The fuel cell under development by MSFC is a capillary matrix (alkaline) cell. A fuel cell consumes gaseous hydrogen and oxygen to produce electricity, water, and heat (Fig. 2). The process requires a suitable electrolyte and catalyst. The ionization of hydrogen at the anode produces electrons, and the ionization of oxygen at the cathode consumes electrons. In the electrode reactions, water is produced at the anode and consumed at the cathode. Hydroxyl ions are produced at the cathode and consumed at the anode.

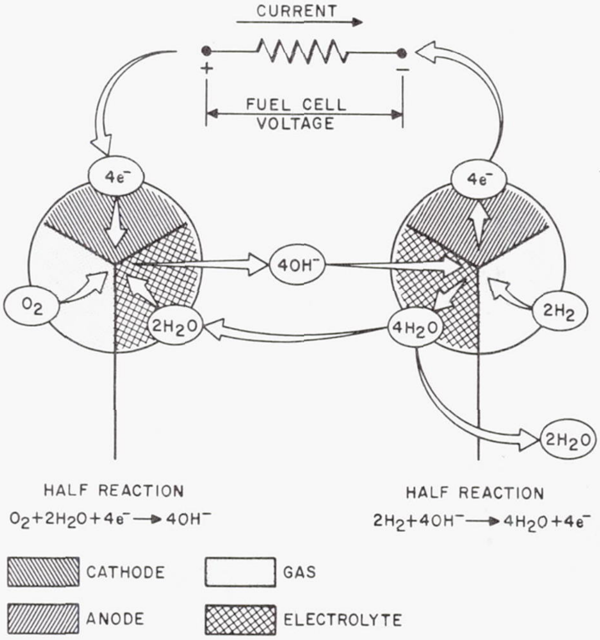

FIGURE 2. SIMPLIFIED FUEL CELL REACTIONS

Figure 3 is an artist's conception of basic fuel cell hardware. Reactants are fed through cavities in the oxygen and hydrogen manifold feed plates. The electrolyte is contained in an asbestos matrix which is sandwiched between the electrodes. Water, which is produced at the hydrogen electrode, is removed from a water removal plate through the water transport matrix. Power pick-off tabs are provided on the reactant plates. This is a completely static system, the only moving parts being the regulating valves. The system readily lends itself to zero gravity conditions because fluid transfer occurs only in the gaseous state, and there are no free liquids or components dependent upon gravity.

The basic fuel cell hardware is shown in Figure 4. The plates are gold plated magnesium with silver and platinum catalysts. Asbestos is used as membrane material. Synthetic gasket material is used to form a seal between plates and cavities.

Figure 5 shows a 2 kW fuel cell stack construction. Each cell has an effective reaction area of 186 cm^2. Stack cooling is accomplished by circulating helium gas through a duct, heat-exchanger subsystem contained within the metal enclosure, or canister.

Figure 6 shows the methods used to electrically interconnect individual cells. Cells are connected in parallel to form sections, and these sections are then connected in series to provide a nominal 29 V output.

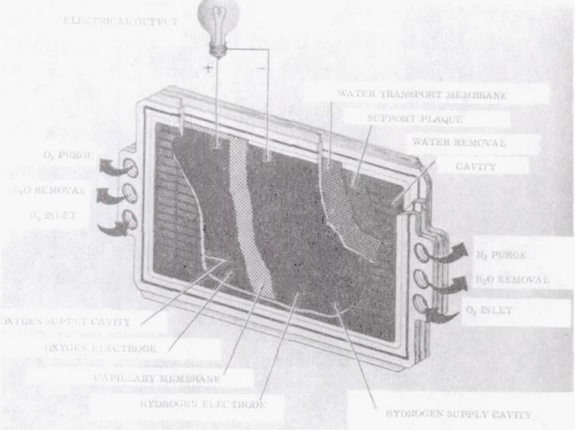

FIGURE 3. FUEL CELL SYSTEM

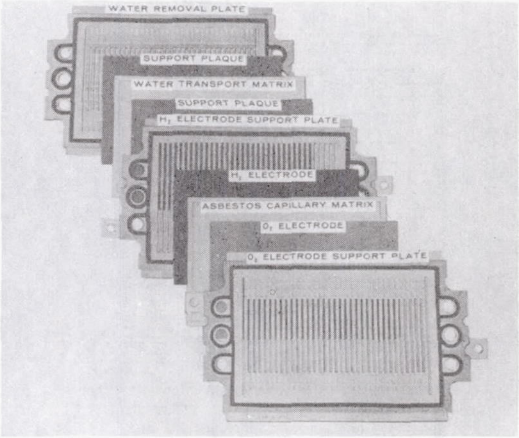

FIGURE 4. BASIC CELL HARDWARE

FUEL CELL DEVELOPMENT

Allis-Chalmers Corporation of Milwaukee, Wisconsin, developed fuel cells under contract NAS8-2696, "Fuel Cell Systems." The original contract had three categories of effort: (1) research and technology tasks, (2) breadboard systems and laboratory support, and (3) engineering model systems. The goal of the program is to develop an efficient, reliable power source to replace batteries and other portable electrical power generating devices in the 2 kW, 28 V range.

The fuel cell module developed for NASA by Allis-Chalmers can be divided into five subsystems (Fig. 7). These subsystems and their functions are as follows:

1. Stack Subsystem
   a. Electrochemically produces power
   b. Produces water
   c. Produces heat
2. Reactant Control and Conditioning Subsystem
   a. Supplies reactant gas to stack
   b. Purges impurities from stack
3. Thermal Control and Conditioning Subsystem
   a. Provides start-up heating
   b. Removes heat from stack, condenser, and inverter
4. Moisture Conditioning Subsystem
   a. Removes product water from stack
   b. Controls KOH concentration of stack
   c. Condenses and transfers product water to storage
   d. Provides open or closed loop operation
5. Electrical Monitoring and Control Assembly
   a. Provides start temperature control
   b. Provides reactant value control
   c. Provides purge control
   d. Provides moisture cavity control
   e. Provides water recovery control

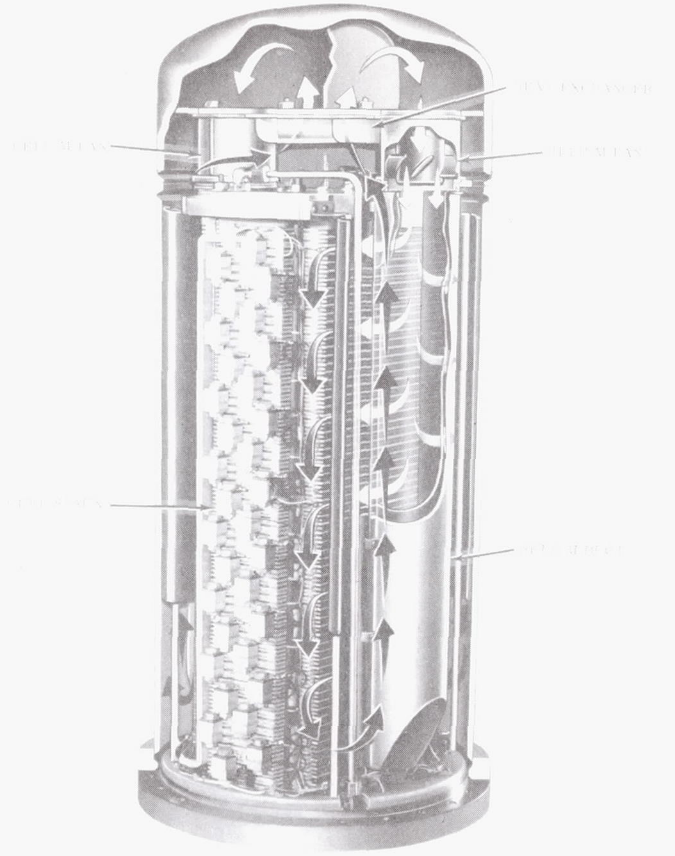

FIGURE 5. FUEL CELL COMPONENTS

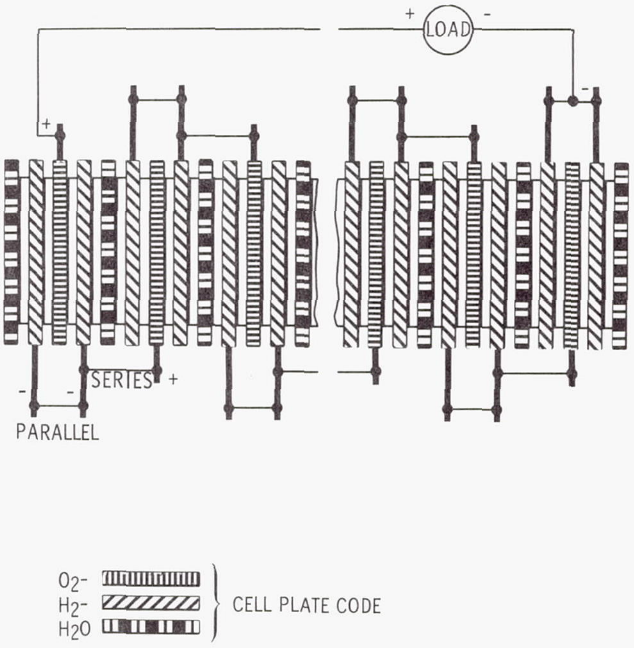

FIGURE 6. SIMPLIFIED SCHEMATIC OF CELL ELECTRICAL CONNECTIONS

NOMINAL POWER RATING	2000 W
OVERLOAD	3300 W FOR 30 S
VOLTAGE REGULATION	29 ± 2 V LOAD RANGE, 800 TO 2000 W
MIN. VOLTAGE AT OVERLOAD	21 V
REACTANT INLET PRESSURE	68.9 to 276 N/cm^2 (100 to 400 psia)
REACTANT INLET TEMPERATURE	255°K to 339°K
REACTANT PURITY (EXPECTED)	99.9%
THERMAL EFFICIENCY	55-65%
ENDURANCE	720 hr UNDER LOAD
COOLANT	60% METHYL ALCOHOL, 40% WATER, BY WEIGHT
COOLANT SUPPLY	113.4 kg/hr (250 lb/hr) AT 15 ± 3°K
COOLANT PRESSURE DROP	3.4 N/cm^2 (5.0 psi)
START-UP AND SHUT-DOWN	1 hr FROM 255°K
ENVIRONMENT (DESIGN CRITERIA ONLY)	MOTION AND THERMAL VACUUM REQUIREMENTS

FIGURE 7. FUEL CELL MODULE SCHEMATIC

Figure 8 shows the initial requirements outlined for the fuel cell system at the beginning of the development. Modifications to the basic contract were made to perform research and development on materials and processes for establishing criteria to design an operational fuel cell power system for space

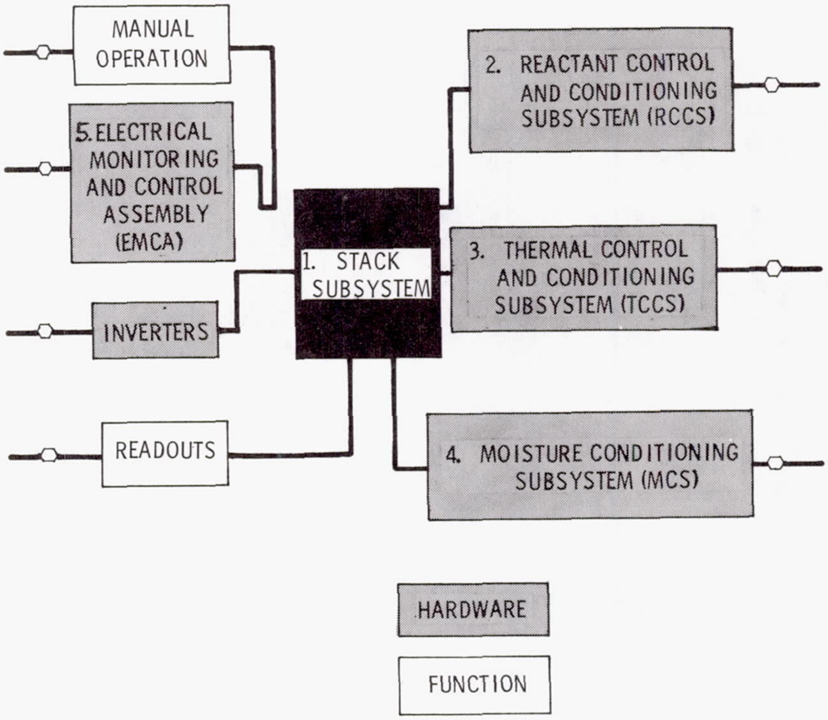

FIGURE 8. FUEL CELL POWER SYSTEM REQUIREMENTS

applications. This program was supplemented by thermal and heat flow studies. Significant progress was made toward development of a 2 kW system with a load life of 720 hr. Upgrading of a manually controlled system to full automatic operation was achieved. Eight test systems were fabricated; four of these were used for verification and endurance testing. Over 3300 hours of integrated system test history were compiled during these tests. Average power produced under the system load profile varied from 1.2 to 1.4 kW. The fuel cell systems have shown exceptional stability under steady state and transient load operation. Responses to load changes between 12 and 90 A were less than 100 ms.

A parallel development program was conducted to achieve the following objectives: (1) develop a closed loop (water recovery) fuel cell system packaged into a flight type configuration to include verification testing of subsystems and components, (2) optimize the system toward 1250 hr flight qualification and 1500 hr life demonstration, and (3) freeze the design and fabricate a flight prototype system and qualify this system for flight. This program produced the fuel cell shown in Figure 9. The DVT fuel cell system contained such design improvements as (1) an integrated reactant control and conditioning subsystem, (2) reactant preheater system, (3) updated moisture conditioning system, (4) water recovery system, and (5) refinements in the electrical monitoring and control system. The DVT fuel cell system also combined results from analyses of a water purification study and a heat exchanger development and study.

MSC increased their support of the Allis-Chalmers fuel cell development and a joint effort was initiated to develop systems that would qualify for AAP applications. Endurance testing of fuel systems to ultimate limits has shown the extreme ruggedness and versatility of the basic system and has defined component limitations. Anticipating their AAP requirements, MSC initiated a contract in October 1966 to develop flight prototype systems, using Contract 2696 model systems as the initial baseline. MSFC efforts were redirected toward providing research support and reliability testing of stacks. The system developed, the Design Verification Test (DVT), is shown in Figure 10. The DVT system may be mounted on any plane. The overall dimensions are 35.6 by 53.4 by 81.3 cm (14 by 21 by 32 in.). The module

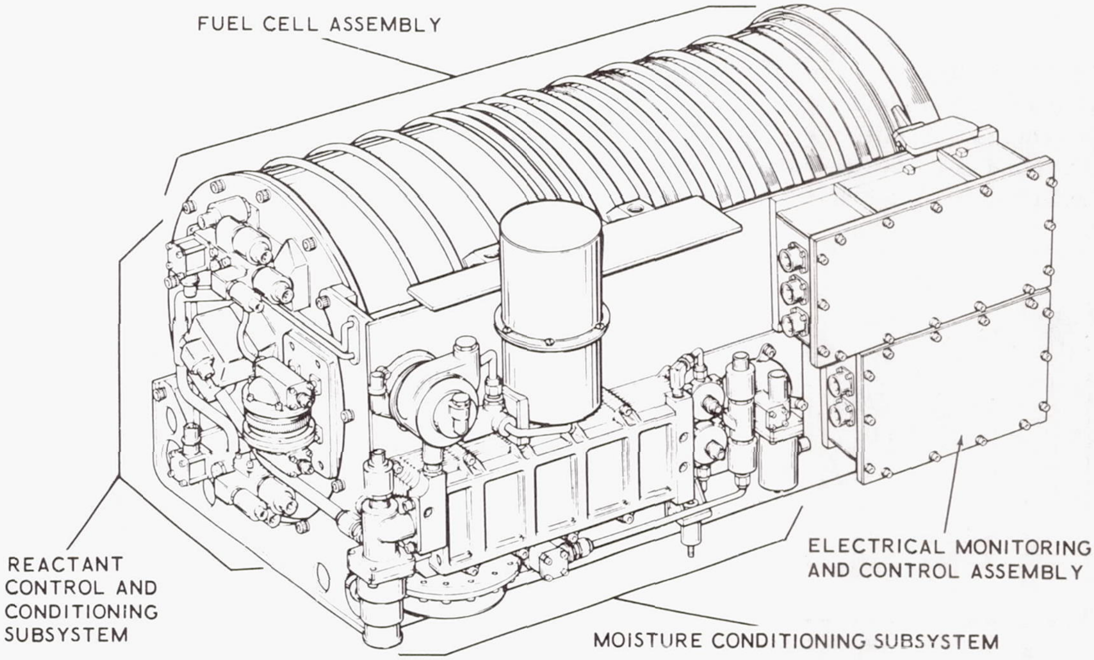

FIGURE 9. ALLIS-CHALMERS DVT FUEL CELL MODULE

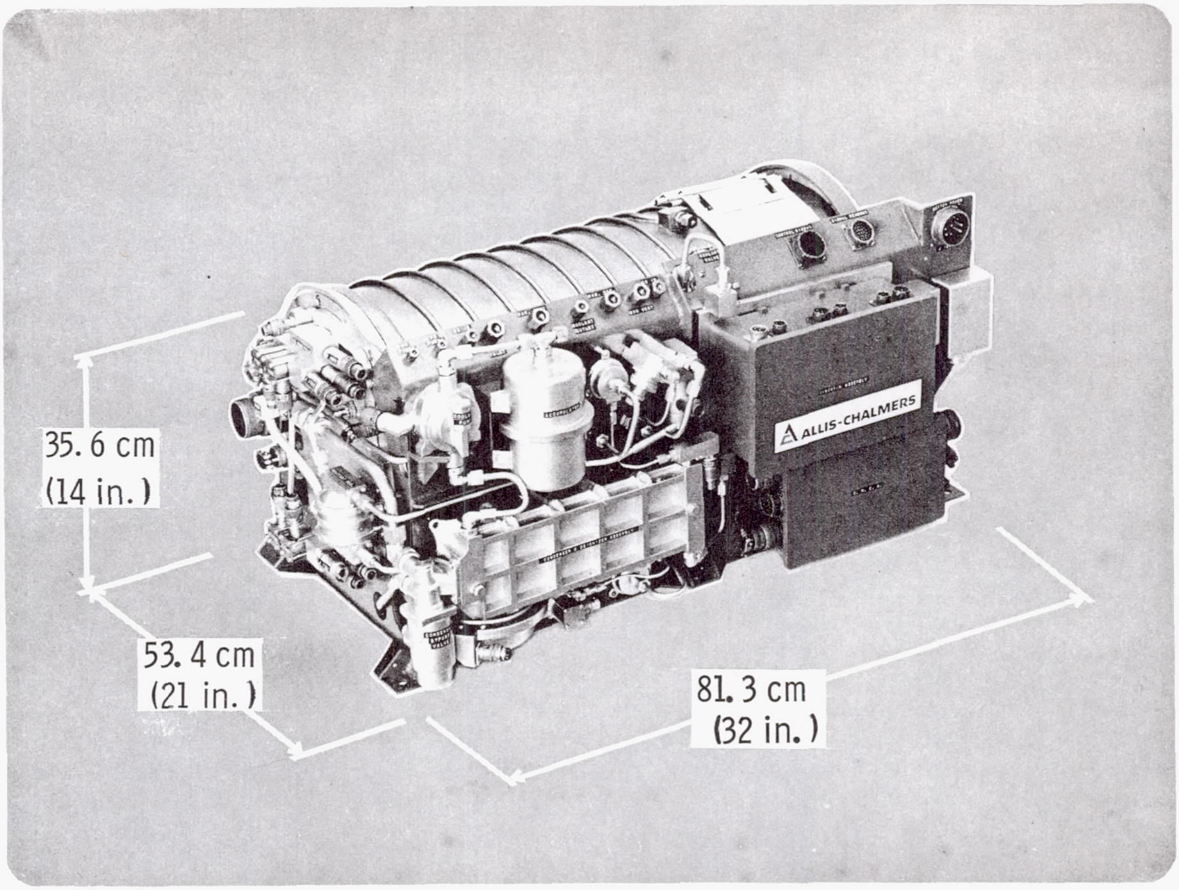

FIGURE 10. NASA 2 kW FUEL CELL MODULE

weight is 76.6 kg (169 lb). Figure 11 shows the voltage-power curves which the DVT unit is expected to meet. An engineering design system has passed 1500 hr testing and is exceeding the performance specified under the DVT contract.

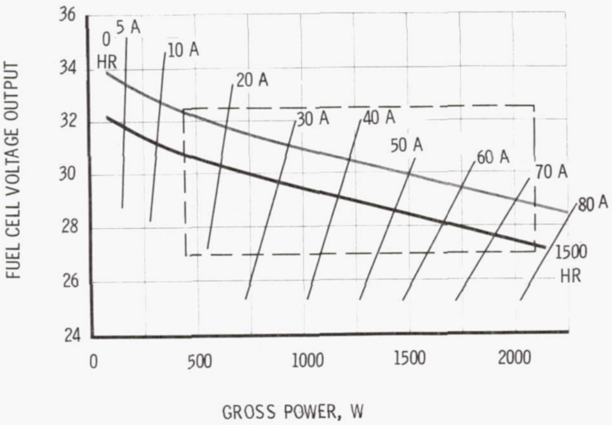

FIGURE 11. MODULE DVT ELECTRICAL PERFORMANCE

FUEL CELL TESTING PROGRAM

A stack testing program, "Fuel Cell Reliability Assessment," was directed toward determining fuel cell stack performance under high stress conditions and toward establishing reliable, operating limitations. The test units were to be eight complete fuel cell stacks of the existing centerline design. The goals were to establish the limits of operating temperature, reactant pressure and pressure differential, and water unbalance. In addition, the performance under continuous overload, high-spiked load, repetitive startup, hot standby, and continuous high power load were studied and evaluated. Figure 12 shows the tests which were to be run on the related fuel cell stacks. At present, testing of the first five stacks has been completed, while testing of the last three stacks is in progress. Total hours of test are as shown.

The construction parameters of the eight stacks were frozen prior to testing to assure uniformity of test data. However, a provision was made for including centerline design changes in the last three stacks.

FUEL CELL STACK NO.	TYPE OF TEST	TOTAL HR TESTED
131	LOAD FAILURE TEST	640.7
132	REACTANT PRESSURE TEST	774.8
133	LOW POWER LIFE TEST	1507.5
134	STARTUP TEST	1535.0
135	LOAD CYCLE TEST	575.1
136	LOW POWER LIFE TEST	
137	THERMAL CYCLE TEST	ON TEST
138	HIGH POWER LIFE TEST	

FIGURE 12. FUEL CELL RELIABILITY ASSESSMENT

Data obtained in operation of the first five stacks were analyzed, and centerline design changes were made in the last three stacks constructed.

Each of the stacks underwent acceptance testing for 40 hr and the optimum KOH concentration was determined during that period. Following the acceptance test, each stack was run at a continuous 40 A load for a 200 hr performance evaluation test. Operating conditions were made as identical as possible during the acceptance and performance evaluation tests. The reliability testing and off-limits testing followed the performance evaluation tests.

The first five stacks (131 through 135) were assembled with the electrolyte being applied individually to the matrices during stacking. This is called the wet stacking method.

The last three stacks (136 through 138) of this program have been loaded with electrolyte by means of a recently developed vacuum loading technique. These stacks have demonstrated a significant improvement in stability over the first five stacks which were filled with electrolyte using the wet stacking method.

The vacuum loading technique eliminates a problem of "crossleaks," which developed when the Cyanamid AB-40 electrodes tended to dry out in spots and perform erratically. The new vacuum loading technique supersaturates the electrode and overcomes an inherent water repellancy. After 750, 1500, and 800 hr of testing, the last three stacks were completely free of crossleaks. Also, a significant improvement in the voltage degradation rate for the vacuum loaded stacks over the wet stacked cells was evident.

Stack 131, which was the Load Failure Test, was operated for a total of 640.7 hr. The stack produced currents in excess of 400 A and 5 kW. Because of heat removal limitations, periods of high power output were limited to 15 s to prevent over-heating the stack. The cooling system was capable of thermal control at a steady state current of 120 A. Figure 13 shows a summary of the high power capability of the stack. Final failure was caused by water transport matrix leakage, resulting from a lack of control in water removal.

TEST RESULTS

LOAD LEVEL Amperes	LOAD LEVEL kW	DURATION min	NO. OF OCCURRENCES
100 - 200	2.5 - 4.5	5.0	21
201 - 250	4.5 - 4.8	2.0	7
251 - 350	4.8 - 5.0	1.0	20
351 - 450	5.0 - 3.0	0.25	10
		TOTAL	58

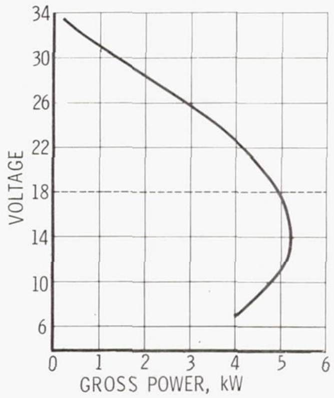

FIGURE 13. MODULE OVERLOAD PERFORMANCE

Stack 132, the Reactant Pressure Test, was operated for a total of 774 hr. Failure resulted indirectly from operation at a pressure of 36.5 N/cm^2 (53 psi). The canister was maintained at a helium pressure several kilograms above the reactants. This caused six of the gaskets to be forced into manifold bores, which resulted in canister to stack leakage.

Stack 133, the Low Power Life Test, was operated at a steady load of 40 A for 1500 hr. Difficulty with purging and cross leakage strongly indicated the need for an increased amount of electrolyte and stabilization of the AB-40 anodes.

Stack 134, used in start-up experiments, was subjected to more than 50 start-stop cycles.

Start-up of the fuel cell stack requires heating the stack to approximately 356° K (180° F). This is done by heaters placed on the stack and obtaining power from an outside source or by "bootstrap" starts (self heating of the stack). Bootstrap starts from 299 to 356° K (78 to 180° F) operating temperature were accomplished in times as short as seven minutes. Figure 14 illustrates the warmup characteristics of the module when terminal voltage was maintained at 27.5 V and shows heatup curves for constant current curves of 100 and 250 A respectively.

TEST RESULTS

ELECTRICAL OUTPUT LIMIT	WARM UP TIME, min
27.5 V	59
100 A	26.5
250 A	6.5

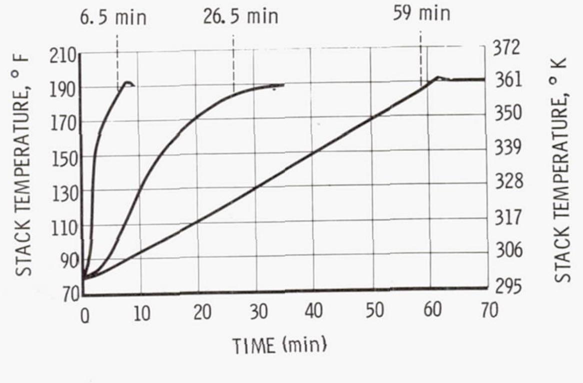

FIGURE 14. BOOTSTRAP CAPABILITY

RESULTS

Stack 135, the Load Cycle Test, was tested under a cyclic load condition for 575 hr. Development of cross leakage resulted in a decision to terminate the testing of the stack. The behavior of this stack was further evidence of the deficiency of electrolyte in the Wet Stacked Group. Figure 15 shows the number of fuel cell stacks tested and gives an indication of hours tested.

From the tests described earlier the following capabilities of the fuel cell system have been demonstrated:

1. Capability of sustaining a continuous load in excess of 3 kW.
2. Brief (1 min) power output capabilities above 5 kW.
3. Brief (15 s) current output capabilities in excess of 400 A.

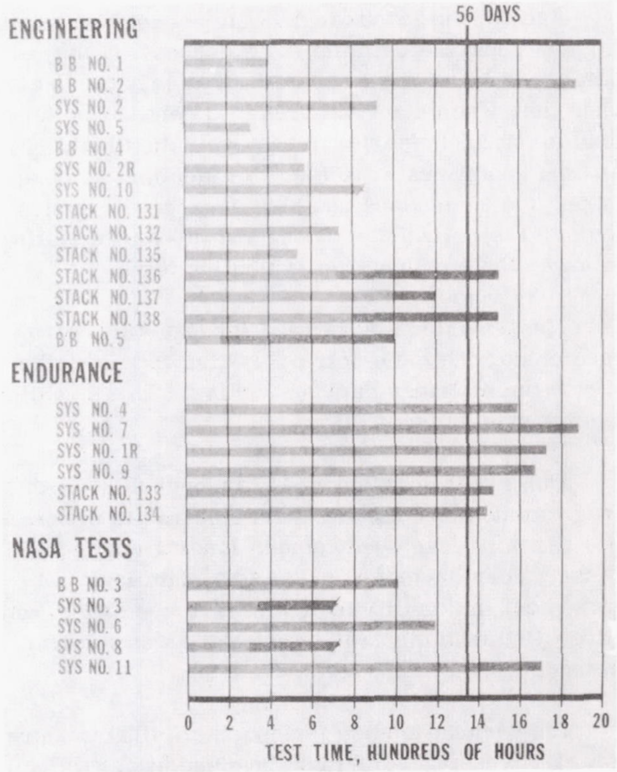

FIGURE 15. NASA HISTORY OF FUEL CELL TESTING

4. Capability of over 1000 hr of continuous on-line power production at a 1200 W level.

5. Capability of over 40 start-up cycles without detrimental effect upon performance.

6. Bootstrap start-up capability from room temperature to operating temperature in less than 7 min.

7. Useful lifetime in excess of 1500 hr.

FUTURE PLANS

Future fuel cell development effort is outlined below and pertains to the general program. This R&D effort extends beyond technology readiness and will demonstrate flightworthiness. It has objectives as follows:

1. Development and Test

   a. Develop a closed cycle 2kW H_2-O_2 fuel cell system for space missions to 90 days.

   b. Complete development of 1500 hr fuel cell system for DVT testing by NASA and Allis-Chalmers. Continue design effort towards a 2500 hr system.

2. Technology

   a. Perform analysis and conduct tests to develop technology for long life, high performance, and reliable fuel cell systems for space applications.

   b. Perform studies and conduct tests on electrodes, matrices, electrolytes, scale-up effects, purging, cooling techniques and operating variables.

3. Reliability Assessment

   a. Evaluation of 2 kW fuel cell performance capability under both normal and overstress conditions, to establish operating limitations for reliable operation.

   b. Perform endurance and off-limits tests to assess reliability.

Page
Intentionally
Left Blank

FUEL CELL TECHNOLOGY

by

John R. Morgan

SUMMARY

The development of fuel cell technology at Marshall Space Flight Center is described. Research was conducted in electrodes and electrolytes at the basic research level and in cooling systems and environmental testing at the systems' analysis level.

INTRODUCTION

NASA research contracts have resulted in a progressive series of fuel cell system research and development efforts. Information obtained from experimental tests performed during 1966 was applied to systems fabricated under the system development contract, NAS 8-2696.

Research contracts are investigating cooling systems that permit a higher radiator temperature, circulating electrolyte, and reduction in size of the radiator, electrodes, catalysts, and electrolytes.

THERMAL ANALYSIS STUDIES

The primary goal of the thermal analysis studies was to develop improved techniques for thermal control of fuel cell systems. The four approaches considered were cold plate cooling, heat pipe cooling, cooling with gases other than helium, and liquid cooling with direct fin contact. The first concept (cold plate cooling) was selected as the approach to be considered for a breadboard fuel cell (Fig. 1).

A cold plate was designed and fabricated for application to a fuel cell stack. After system operation under load in excess of 100 hr, indications are that the cold plate design decreases the temperature differential between the stack and the coolant by a factor of two, thereby increasing the radiator temperature and resulting in a more efficient radiator. A problem area was the selection of an electrically insulating heat transfer material between the fuel cell plate edges and the cold plate. The material finally selected was a silastic adhesive with magnesium oxide added for increased thermal conductivity.

An alternate cold plate configuration, chosen for a second thermal breadboard concept, was to place cold plates between individual cells (Fig. 2). For engineering evaluation, the stack was designed with 9 cells rather than the 32 cells of a full system. The cold plate is fabricated from two separate plates that are stacked to form a sealed cavity containing a separate coolant matrix. The thermal control schematic is given in Figure 3. The coolant is supplied under pressure to one side of the coolant matrix. The coolant is removed in a vapor from the other side of the matrix. The coolant flow rate is controlled by the pressure differential between the inlet and outlet manifolds.

ELECTRODE EVALUATION

To date, 32 single sections have been tested for a total of more than 40,000 hr to evaluate electrodes and catalysts. Twenty-six sections were operated to evaluate the cyanamid AB-40 anode. Six tests were conducted to evaluate a silver-platinum anode. The factors evaluated included construction parameters, operating conditions effects, and electrode conditioning.

Twelve single sections were tested to evaluate variations in assembly procedures. These tests indicated that the AB-40 anode approach was sound and represented a technological improvement over previously used anodes. The construction parameters of a configuration considered acceptable for centerline technology are given in Table I.

Using this centerline technology, 14 modules were fabricated to evaluate operating conditions effects. These tests indicated that voltage degradation rates were higher at higher temperatures and were much lower when the modules were operated at a high current density during the first segment of the test.

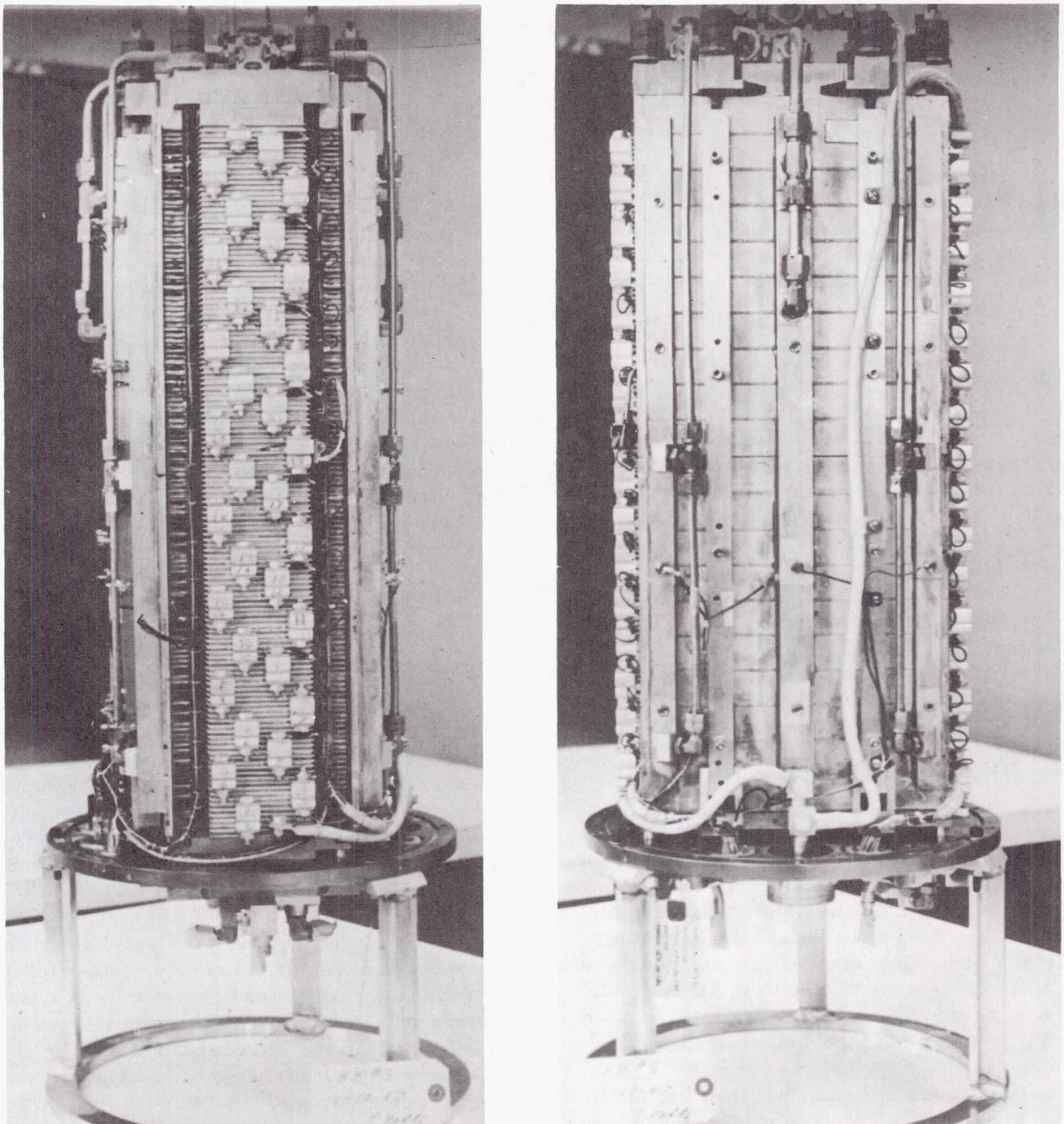

FIGURE 1. COLD PLATE BREADBOARD FUEL CELL SYSTEM

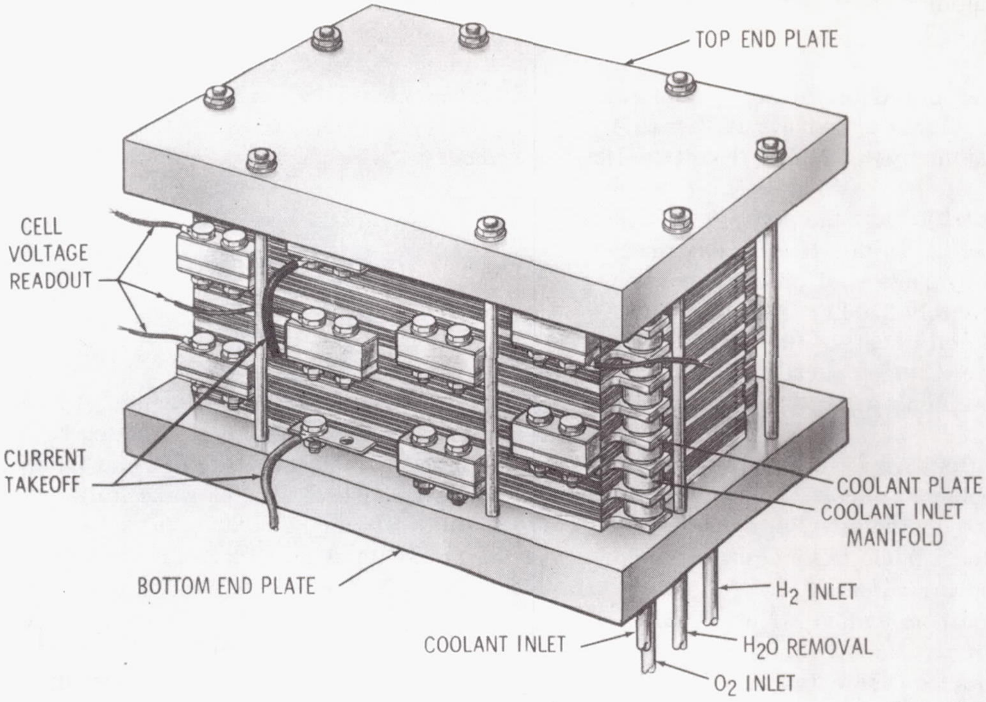

FIGURE 2. ADVANCED COLD PLATE BREADBOARD

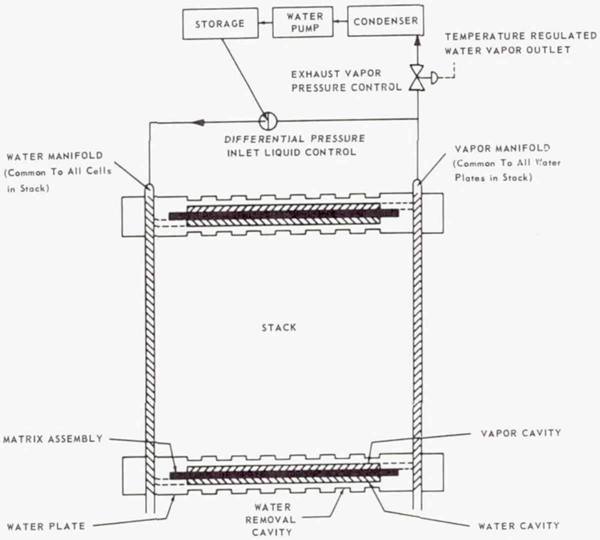

FIGURE 3. INTERNAL COLD PLATE CONTROL

TABLE I. CENTERLINE TECHNOLOGY CONSTRUCTION PARAMETERS

ANODE	CYANAMID AB-40
ELECTRODE	HYSAC - 8
WATER CAVITY MATRIX THICKNESS	1.27 mm (0.050 in.)
REACTANT CAVITY MATRIX THICKNESS	0.75 mm (0.030 in.)
SPACER THICKNESS	1.65 mm (0.065 in.)

An analysis of the operating data for the cells that failed indicated that insufficient electrolyte at the electrodes could have been the direct cause of, or a contributing factor to, failure. As a result, modified methods of loading the electrolyte into the matrix were investigated. The AB-40 anode exhibits limited wettability to the electrolyte and tends to retain trapped gases in the electrode pores, when previous procedures are used. Modules were constructed with this wetting or preconditioning of the electrode being accomplished by vacuum loading the electrode and by flushing a completed module with electrolyte after fabrication. Both methods appear to yield equally favorable results.

Voltage life characteristics of two typical cells with preconditioned anodes are shown in Figure 4. For a 32 cell stack, the system's lower voltage limit of 27 V is equivalent to 845 mV per cell. After an average load time at 1500 hr, the non-preconditioned anode cells degraded below this level. For preconditioned cells, this average load time has been increased to approximately 2500 hr. Compared with non-preconditioned cells, cells with conditioned anodes exhibit lower voltage degradation rates and a more consistent optimum electrolyte concentration.

The wetting difficulties associated with the AB-40 anode make the mechanical properties of the silver-platinum anode more desirable. Six modules were constructed to evaluate performance of these anodes. The catalyst loading varied densities of platinum and a combination of platinum and palladium. All modules were operated under the same conditions. Testing of the silver-platinum anode indicated that the voltage-life characteristics of these cells were inferior to cells fabricated with the AB-40 anodes. Figure 5 is a comparison of voltage envelopes of the silver-platinum anodes with the AB-40 anodes in similarly constructed small modules. With comparable catalyst loadings, the initial cell voltages for the silver-platinum anodes are lower than that of the AB-40 anodes, as is the average voltage degradation rate.

ELECTROLYTE EVALUATION

One degradation mechanism of a fuel cell is the formation of potassium carbonate, K_2CO_3, caused by exposure of the electrolyte to carbon dioxide in the reactant gases. Studies were initiated to investigate the alteration of the vapor pressure-temperature relationship of the electrolyte caused by the presence of K_2CO_3. The studies indicated that the reaction of carbon dioxide with the electrolyte tends to increase the vapor pressure required for constant potassium concentration; however, the effect is not sufficient to induce errors with the existing control methods.

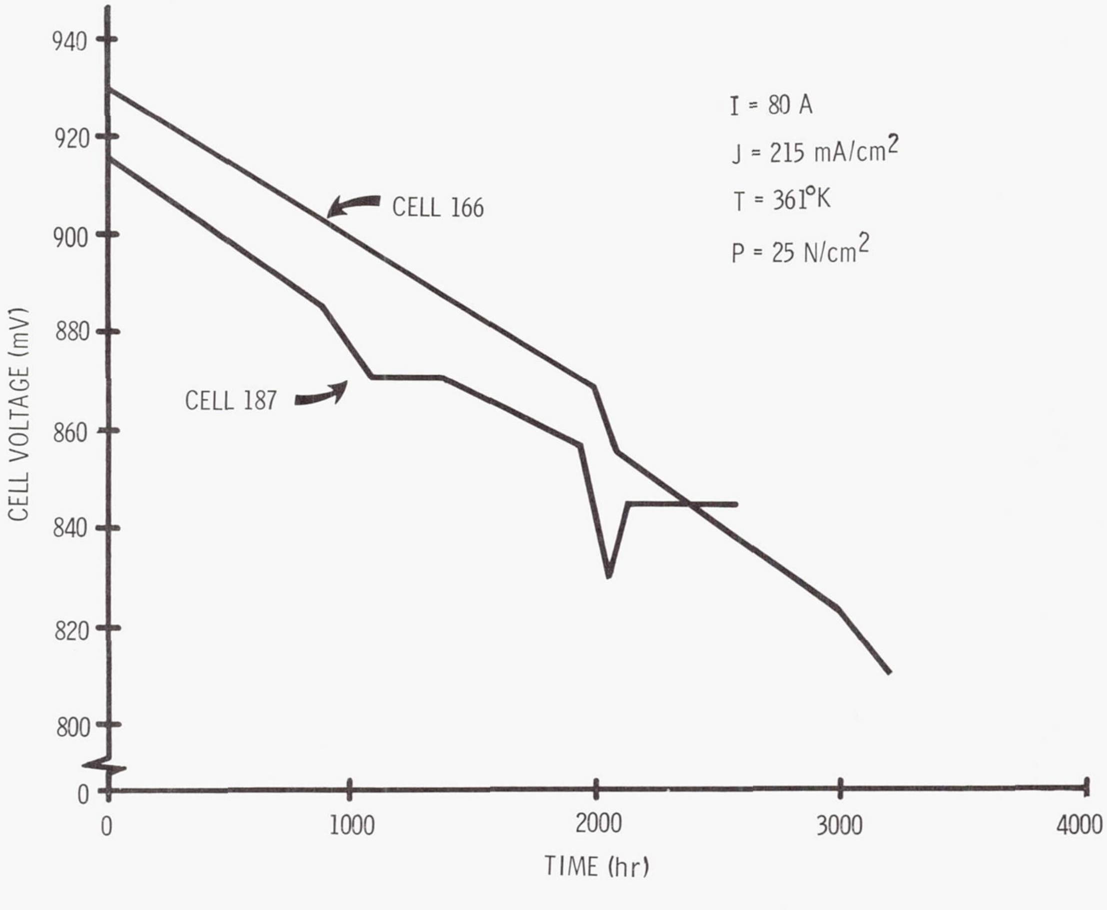

FIGURE 4. TYPICAL PRECONDITIONED ANODE CELL LIFE CHARACTERISTICS

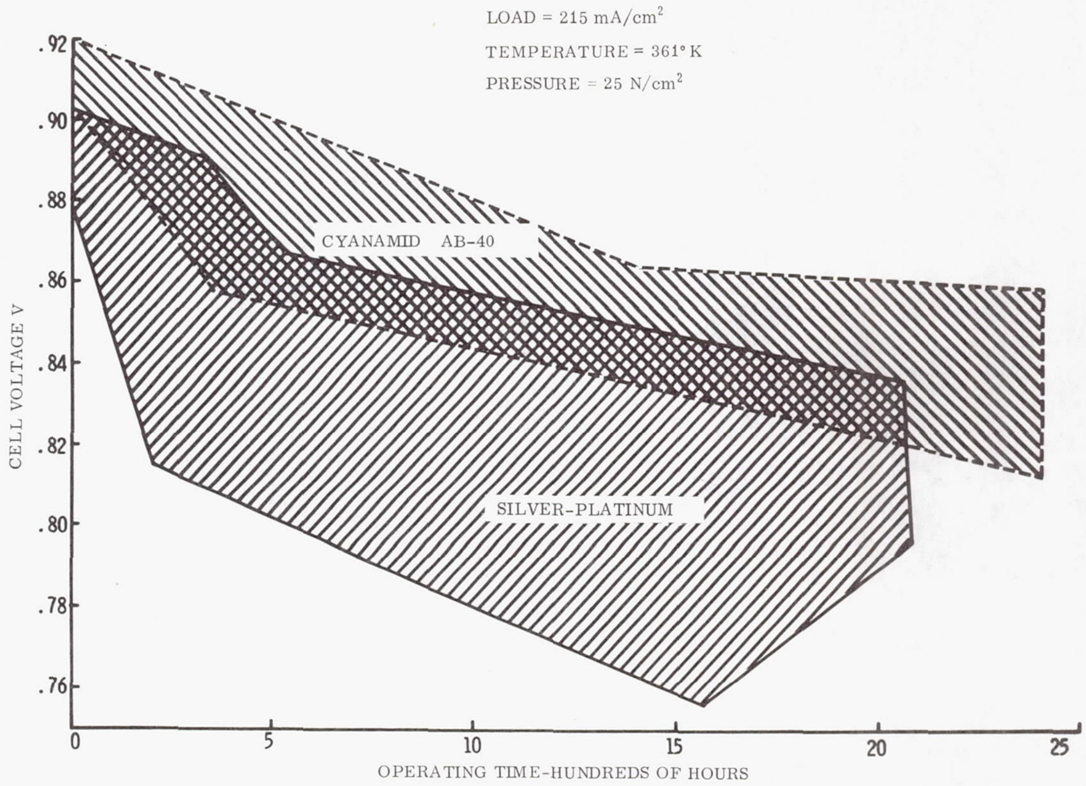

FIGURE 5. CYANAMID AB-40 VS SILVER-PLATINUM ANODE

A test of cesium hydroxide as a fuel cell electrolyte was conducted using two single sections. One section was operated for 2000 hr, the other for 550 hr. As a result of these tests, the following comparisons with potassium hydroxide electrolyte cells have been made: voltage degradation is lower for cells with cesium hydroxide electrolyte, initial voltage at loading is lower, and operating cavity pressure is higher.

INHOUSE TESTING

Inhouse achievements are as follows: completion of a series of environmental tests using Allis-Chalmers system number eight, completion of an electrical monitoring and control system design, initiation of a single cell testing program, and completion of design and construction of a parallel system test console.

The first portion of the environmental test sequence was a thermal-vacuum test. Fuel cell system number eight was mounted in the thermal vacuum chamber with auxiliary test equipment installed nearby (Fig. 6). The fuel cell was operated at a minimum sustaining power level with the chamber wall temperatures down to 188° K, and at a 2 kW power level with the chamber wall temperature up to 358° K.

The fuel cell, installed on a 7.32 m (24 ft) centrifuge for the acceleration testing is shown in Figure 7. The reactant bottles were packaged on the opposite end of the arm, with fluid and gaseous control equipment placed near the center of the centrifuge. The fuel cell was subjected to three, six, and twelve g's acceleration. At each level, the reactant cavities of the system were filled with an inert gas to detect possible leakage. After verification that leaks did not exist, the system was operated at a load of 40A and 80A while under acceleration. This sequence of acceleration testing was performed with the direction of acceleration in each of the three axes of the fuel cell stack.

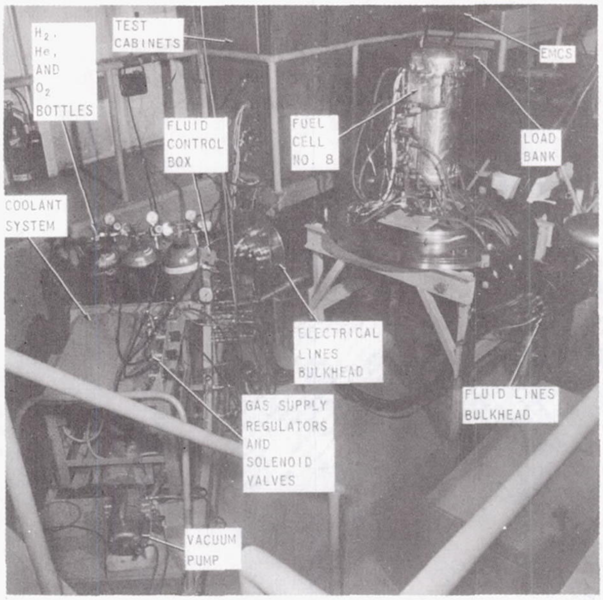

FIGURE 6. THERMAL-VACUUM TEST AREA

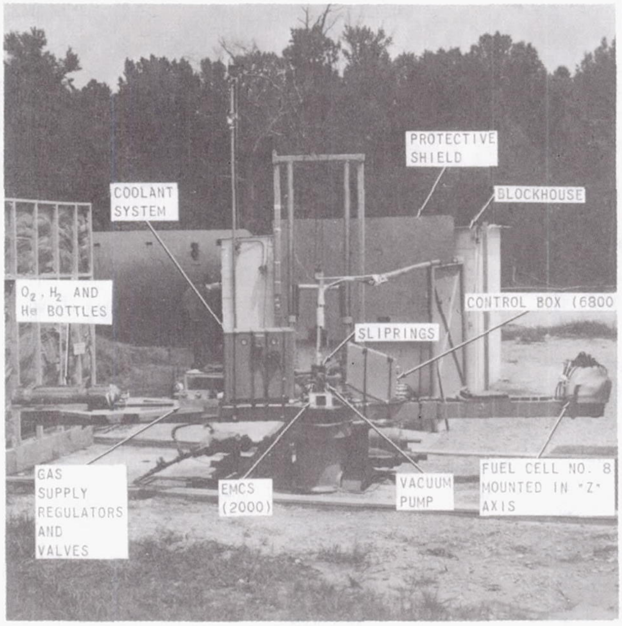

FIGURE 7. CENTRIFUGE TEST AREA

Following the acceleration test, the fuel cell system was mounted on a vibration slip table. The auxiliary control equipment remained on the centrifuge arm. The test set-up is shown in Figure 8. The reactant interface was accomplished by use of flexible hosing. The system was subjected to vibration levels of three and six g's in each axis of the fuel cell stack with the system filled with inert gases and with the system under load.

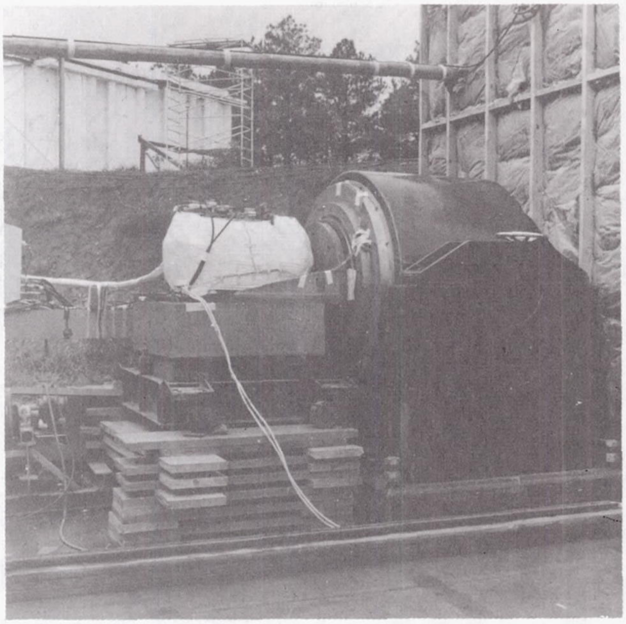

FIGURE 8. VIBRATION TEST AREA

The sequence of environmental tests yielded valuable information concerning instrumentation and control of fuel systems under adverse conditions. The major problem area encountered was auxiliary equipment failure. Several instrumentation wires were broken as illustrated in Figures 9 and 10. These failures did not impair the system operation; secondary instrumentation revealed that the event was an instrumentation failure rather than fuel cell stack failure.

During the vibration sequence, the hydrogen and oxygen pressure transducers and the coolant solenoid on the reactant control and conditioning subsystem (RCCS) plate experienced excessive vibration loads. To reduce these loads, the RCCS plate was modified as shown in Figure 11.

Using the information gained, a new series of acceleration and vibration tests have been initiated to gain more data on fuel cell operation under these conditions. More reliable instrumentation is incorporated in the new set-up. The removal of the RCCS from the canister to prevent component failure during environmental tests is illustrated in Figure 12. Again, the gas bottles are mounted on the centrifuge arm opposite the fuel cell assembly, with all the control equipment located near the center.

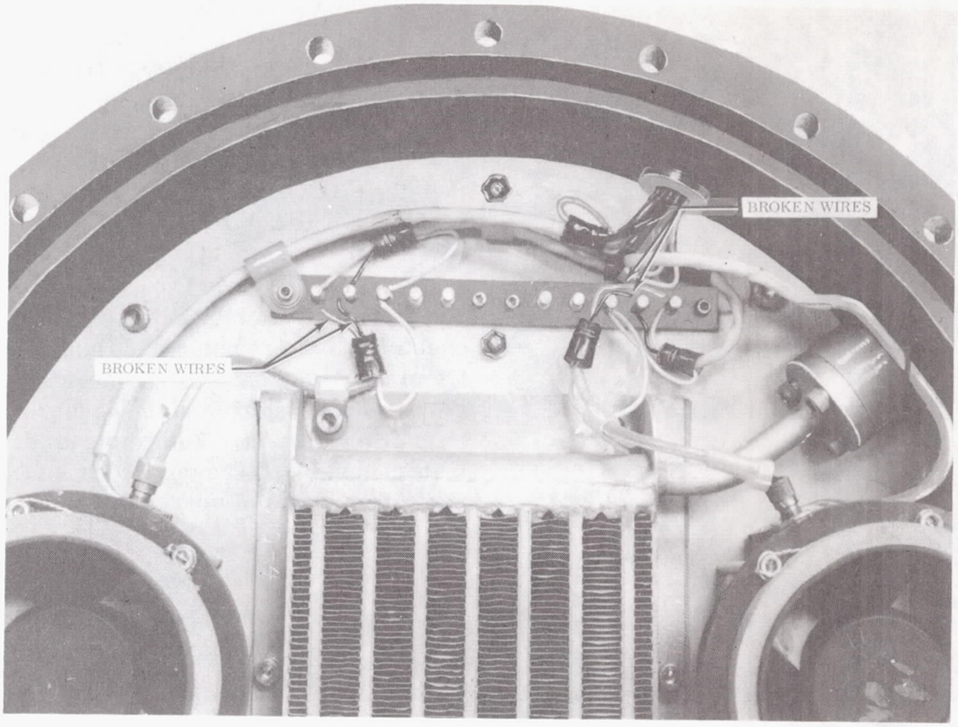

FIGURE 9. FAN RPM READOUT FAILURE

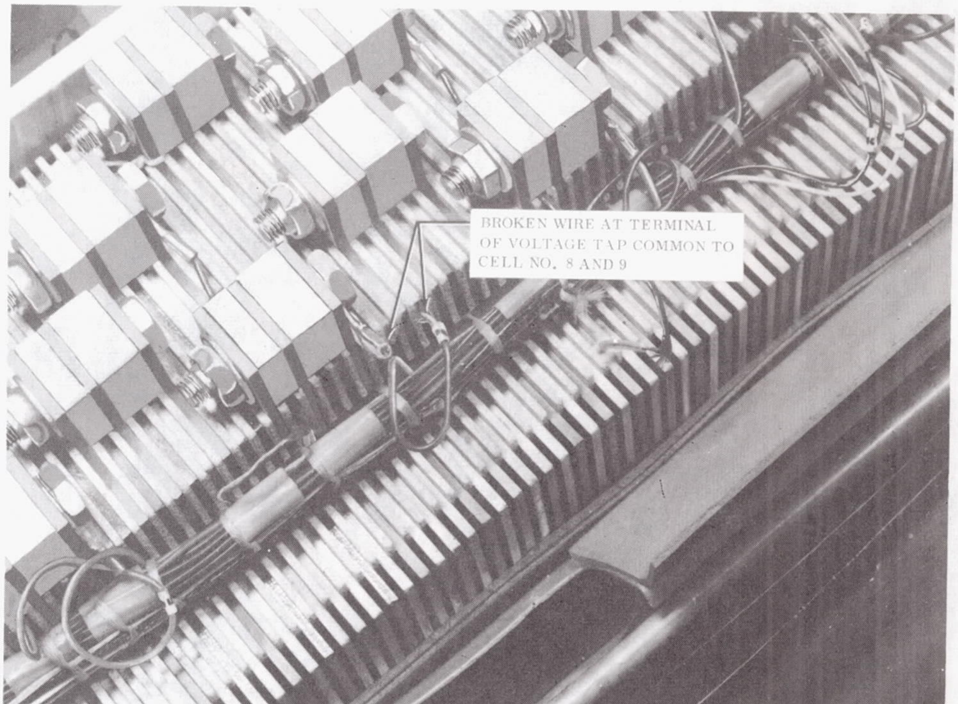

FIGURE 10. CELL VOLTAGE READOUT FAILURE

FIGURE 11. RCCS PLATE AND COMPONENTS MODIFICATION

During the environmental test, the electrical control system proved to be highly sensitive to noise, temperature, and humidity. To eliminate these problems, a new flight-oriented control system was designed and evaluated. Preliminary indications are that this control system will prove to be more rugged than the previous package. Presently, the control system is being constructed in a flight-type package.

A control console for parallel operation of two systems has been fabricated (Fig. 13). This console contains all the reactant and fluid controls, the electrical controls, and the data acquisition system. Strip chart recorders and a data scanner comprise the data acquisition system. Future plans for the parallel tests include load sharing and transient response analysis of parallel operated fuel cells.

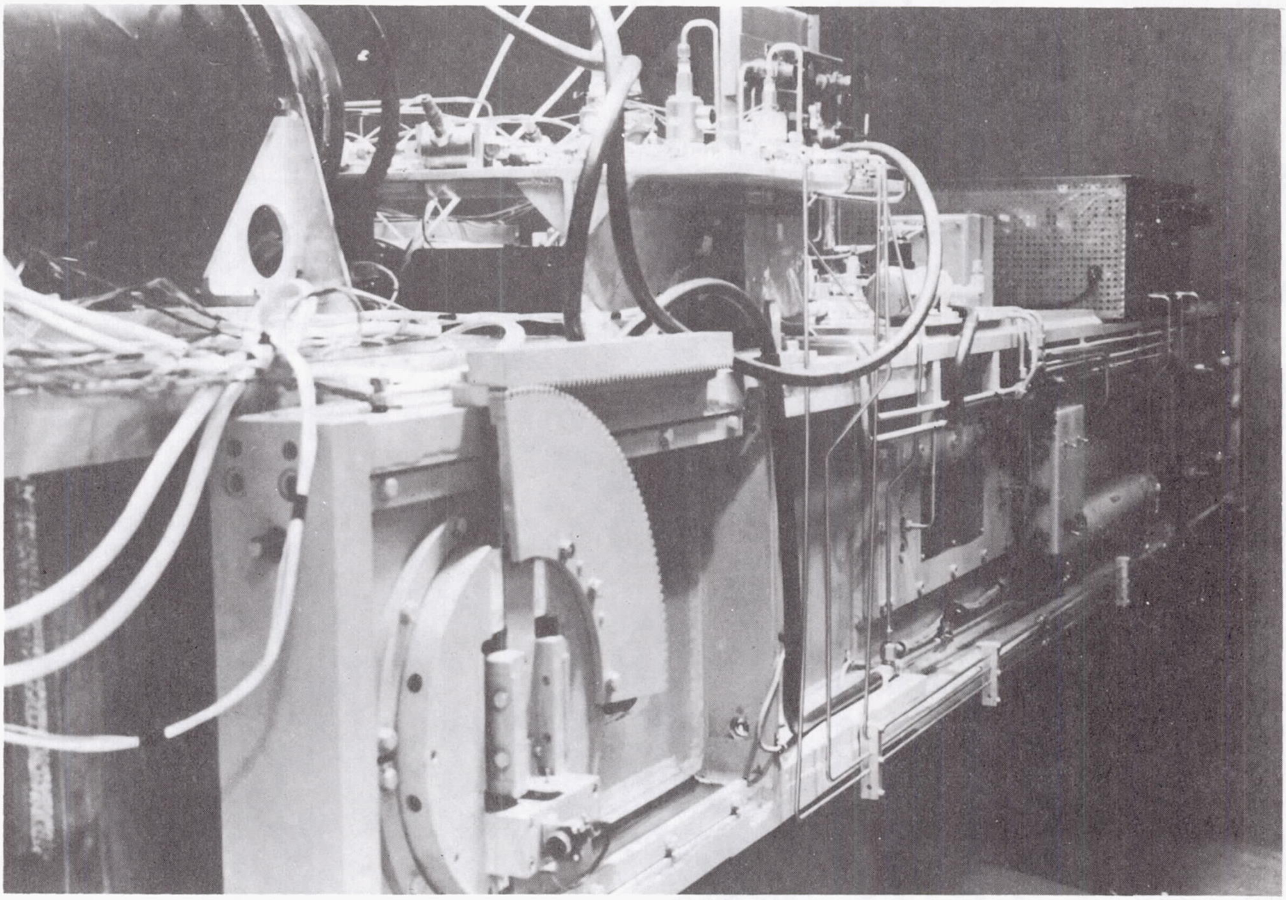

FIGURE 12. IMPROVED CENTRIFUGE TEST AREA

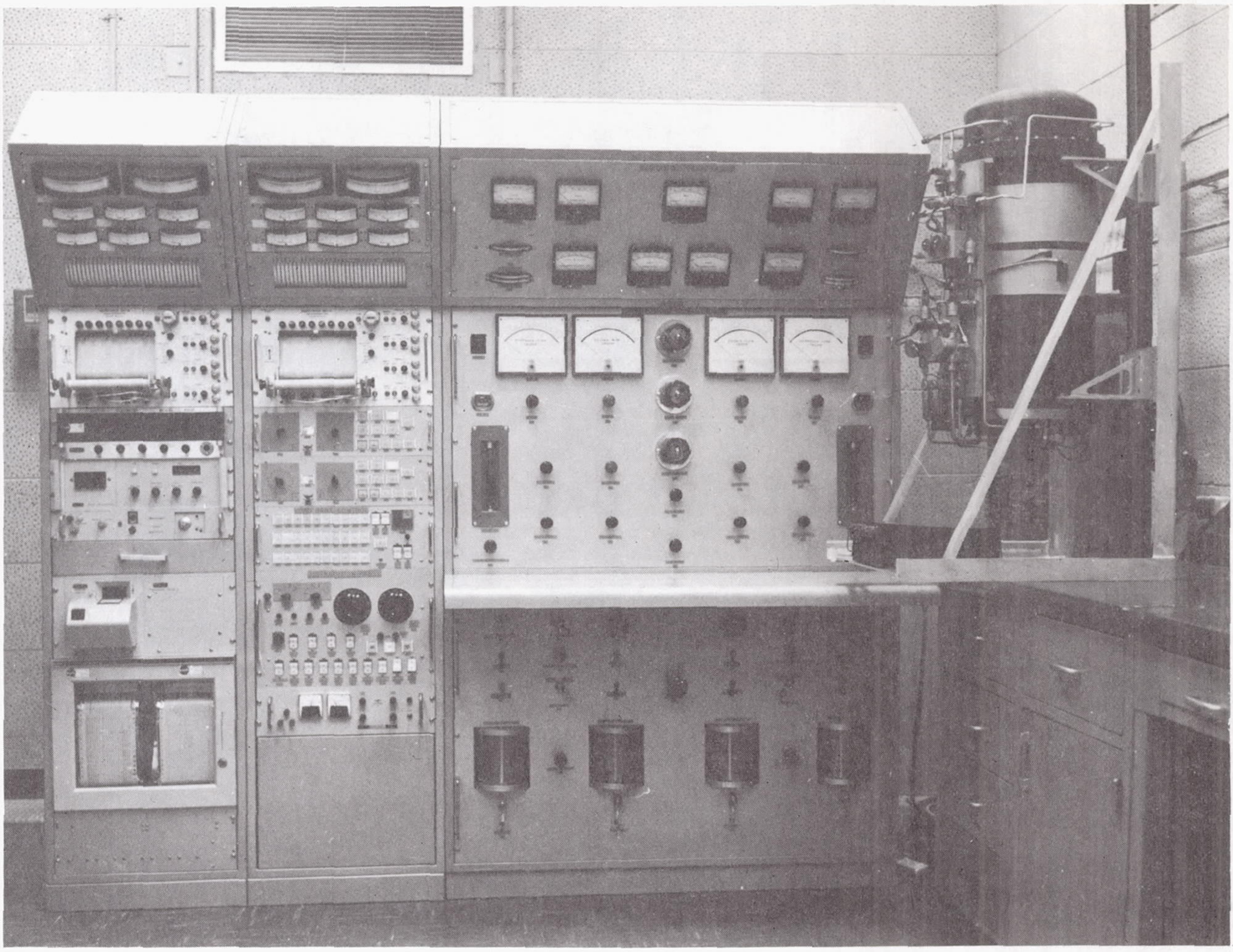

FIGURE 13. PARALLEL TEST CONSOLE

ADVANCED SYSTEM CONCEPT

The single cell optimization study combines several design concepts from different manufacturers. A concept that is basically a modified Allis-Chalmers system is illustrated by Figure 14. This system is compact, self-contained, and requires only coolant and power connections. Presently, this system is in a definition and design phase and has not been implemented into a hardware phase.

The cell is composed of three subassemblies that are stacked in sequence (Fig. 15). The sequence is then reversed and the process is repeated until a unit of the desired rating is constructed. Water removal plate, matrix plate, and coolant plate are the three subassemblies. The control and component subassembly is located at the top of the stack for convenient access. The reactant tanks are mounted around the circumference of the module where rejected heat might be used to supply cryogenic boiloff for reactant pressure. The cell base is provided with access ports, which make a partial interior inspection possible without disassembling the system. All spacer plates are machined with hydrogen, oxygen, water removal, and coolant manifolds to provide a continuous fluid path through the cell.

The matrix spacer, shown in Figure 16, will be fabricated from a filled teflon material to provide insulation and maintain chemical inertness. The electrodes are edge bonded to the matrix. The matrix electrode package is bonded into the spacer. The size of the manifolds and the number of the gas supply ports are intended to prevent any possible plugging of the stack and eliminate a possible variation in gas flow. The hydrogen porting arrangement

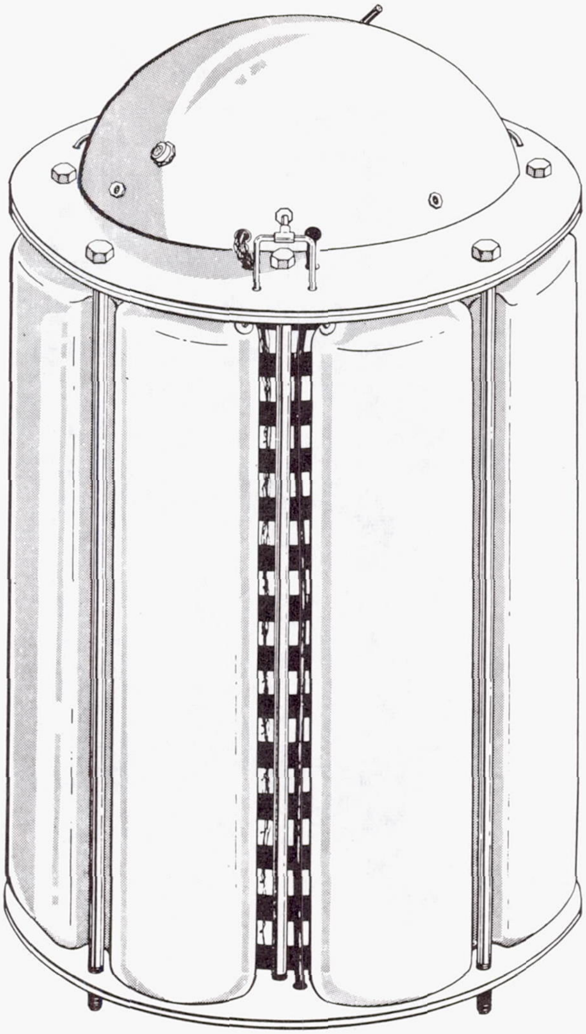

FIGURE 14. ADVANCED SYSTEM CONCEPT

is shown in Figure 16. The oxygen porting is on the underside of the plate edges, perpendicular to the hydrogen porting and identical to it in construction.

The system is intended to employ the static water removal mechanism developed by Allis-Chalmers. In this system a vapor pressure is maintained in the plate cavity, which corresponds to the equilibrium vapor pressure for the electrolyte concentration in the cell. By-product water is removed in this manner, thereby maintaining the desired electrolyte concentration. The water removal spacer will be fabricated from magnesium to save weight (Fig. 17). The matrix is covered by the back-up plate and supported by a corrugated or honeycomb configuration. The back-up plate is dimpled sheet metal with perforations.

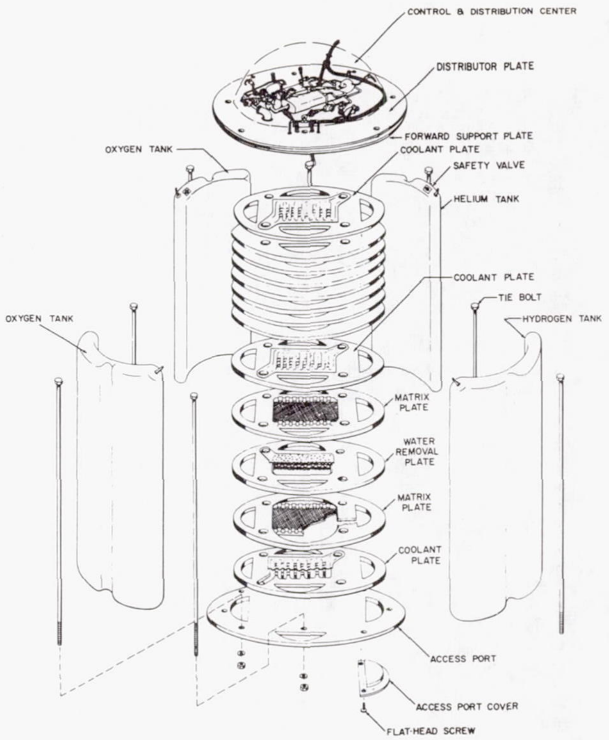

FIGURE 15. EXPLODED VIEW OF ADVANCED SYSTEM CONCEPT

The dimples insure good electrical contact with the electrode. The perforations provide channels between the water vapor in the reactant cavity and water removal cavity. The cavity is vented to the water removal manifold through two opposed corner ports under the welded arm of the back-up plates.

The cell will be cooled by internal cold plates mounted between each set of opposed matrix spacers on the oxygen side. The simplicity of the cold plates is shown in Figure 18. Coolant is circulated through the coolant passage and allowed to evaporate in this space. This spacer is also magnesium, but it is gold plated to protect against corrosion because the environment of the oxygen cavity is more corrosive than that of the hydrogen cavity. The oxygen back-up plate is sheet metal, which is welded around the edges and along the ribs of the coolant plate.

The overall schematic of the system given in Figure 19 illustrates the simplicity of the system. The system as shown must use either reactant gases or helium, precluding the possibility of air or impurities entering during a changeover of gas supplies. All external connections are made through quick

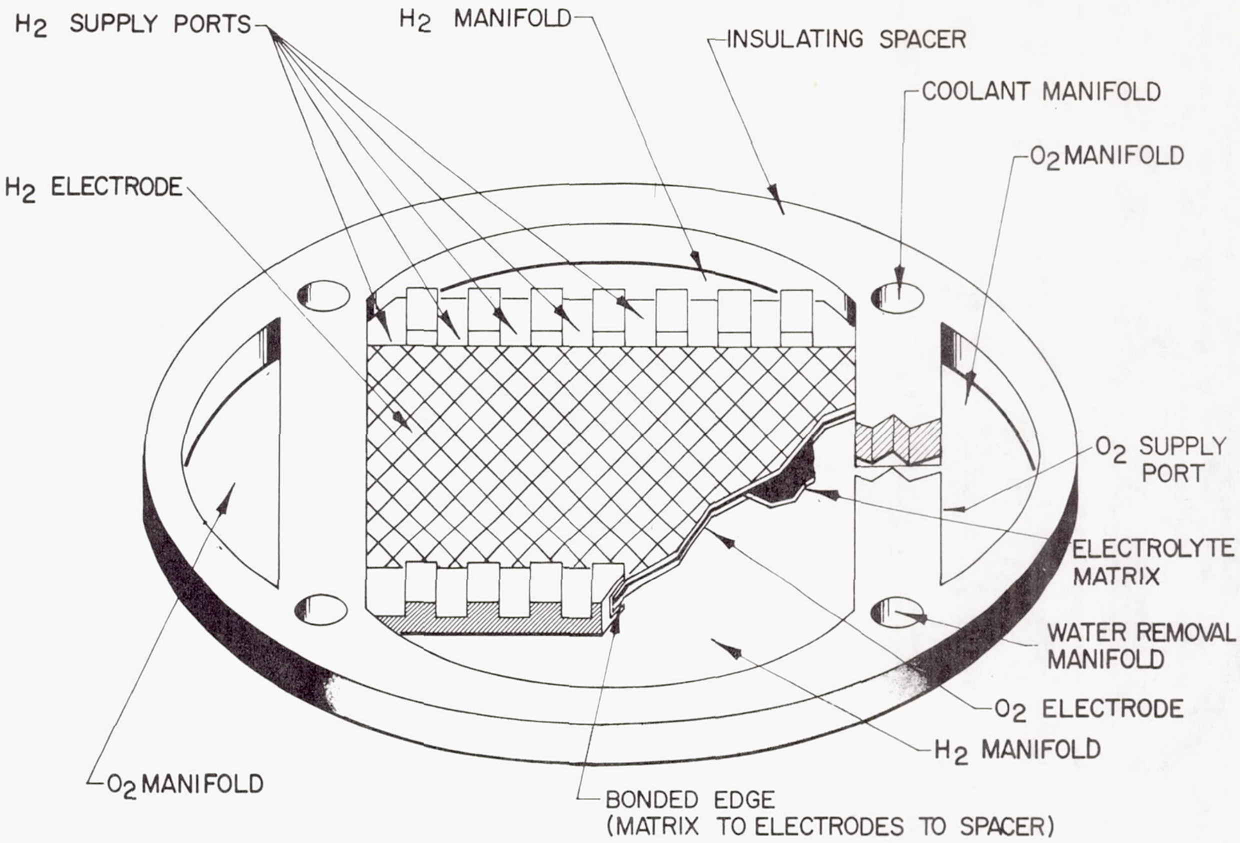

FIGURE 16. MATRIX SPACER

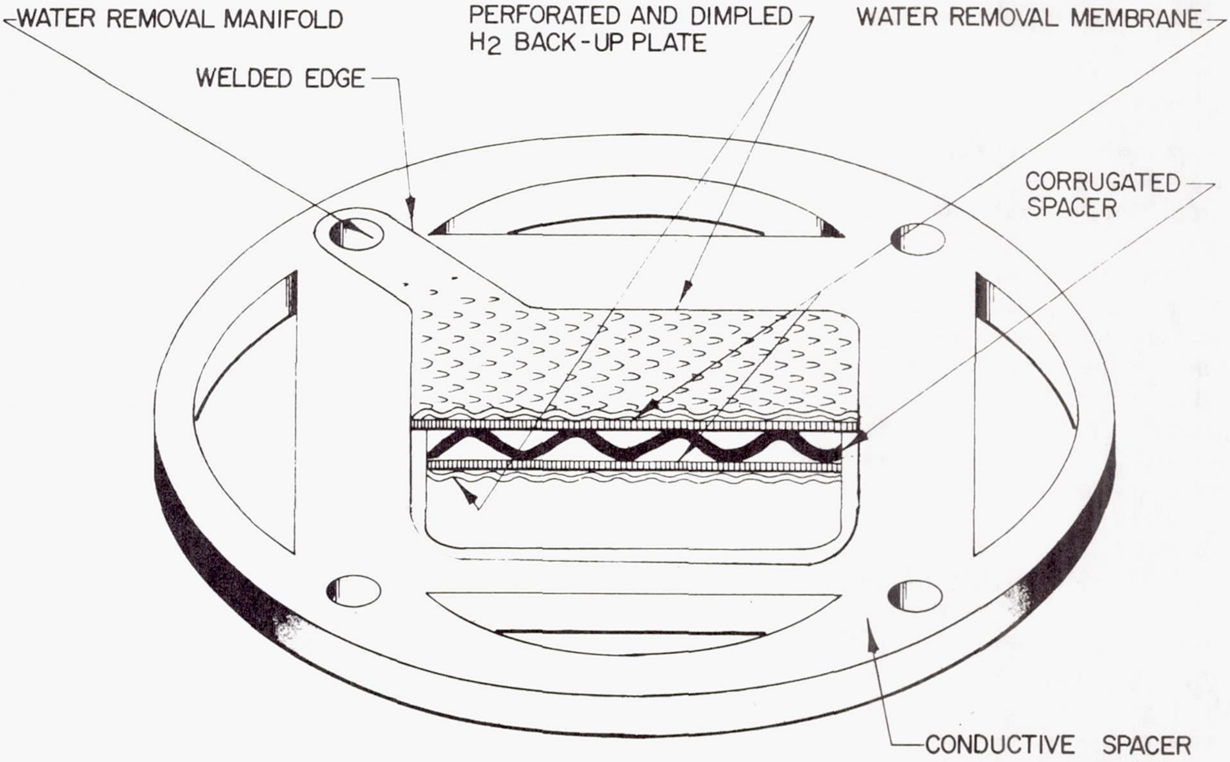

FIGURE 17. WATER REMOVAL SPACER

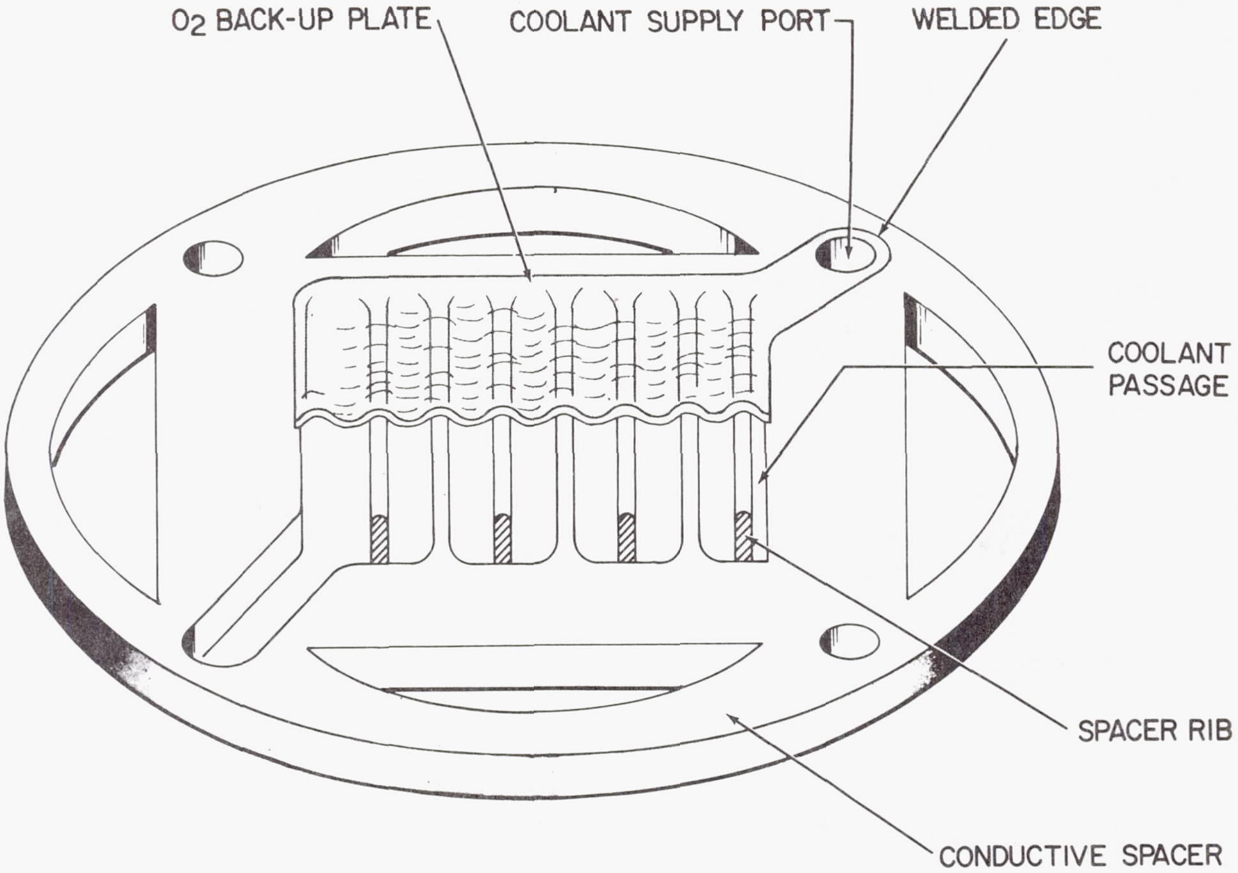

FIGURE 18. COOLANT SPACER

disconnect bulkhead fittings. The hydrogen and oxygen pressure regulators are referenced to the helium pressure regulator, as is the coolant system, and the helium regulator is referenced to the water cavity vacuum. This prevents over-pressurization of any cavity with respect to any other system cavity. The reactant cavities can both be purged with helium through a three-way solenoid on the vent side of the cell. One side of the supply line is opened to ambient pressure for purging. A similar device flushes the water removal cavity. The system warm-up is by means of an electrical in-line heater on the coolant system.

FUTURE PLANS

Future plans in the cell optimization study are to examine any possible improvements in performance obtained by changes in operational concepts. A cell operating on the cycle shown in Figure 20 uses product water to saturate the incoming oxygen. This should eliminate a shortage of water at the oxygen reaction zone, which appears to be a current limiting phenomenon. A single cell test stand has been designed and fabricated to evaluate this operational concept. The goal of the first test sequence is to evaluate the changes in polarization losses caused by saturation of the reactants with water. If water saturation of the inlet oxygen proves to be advantageous, a feasibility study will be initiated to investigate applying this operational concept to a full system.

A continuation of the environmental test program, initiating the load sharing analysis of the parallel test, and configuration of the single cell optimization study are future plans for inhouse testing. A continuation of the cold plate design evaluation, final design and fabrication of a fuel cell stack using a recirculating electrolyte, further analysis of electrode preconditioning techniques, and investigation of new concepts are future plans for contract research.

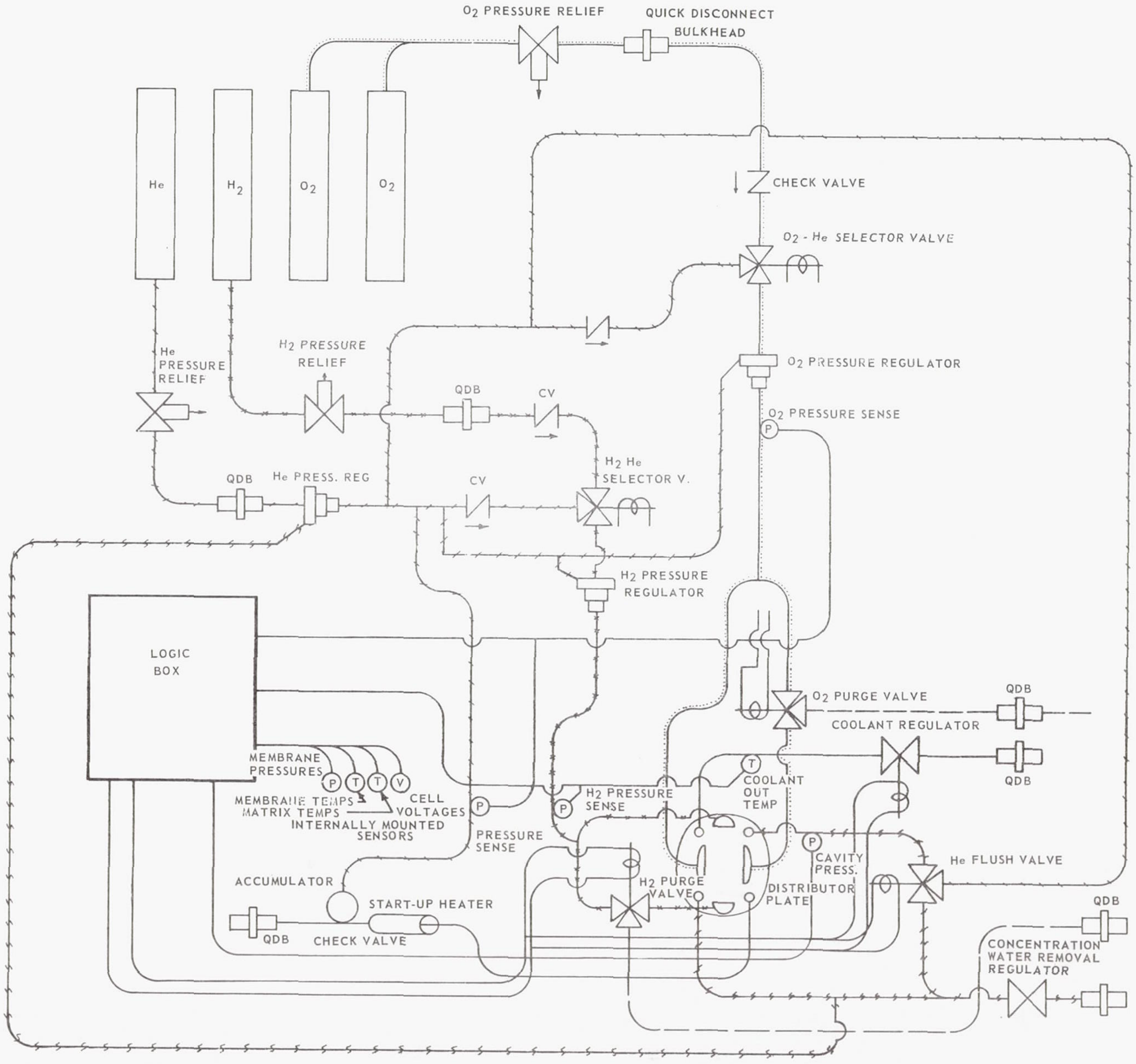

O_2 PRESSURE RELIEF
QUICK DISCONNECT BULKHEAD
He
H_2
O_2
O_2
CHECK VALVE
O_2 - He SELECTOR VALVE
He PRESSURE RELIEF
H_2 PRESSURE RELIEF
QDB
CV
O_2 PRESSURE REGULATOR
O_2 PRESSURE SENSE
P
H_2 He SELECTOR V.
QDB
He PRESS. REG
CV
H_2 PRESSURE REGULATOR
LOGIC BOX
O_2 PURGE VALVE
QDB
COOLANT REGULATOR
QDB
MEMBRANE PRESSURES
P
T
T
V
MEMBRANE TEMPS
MATRIX TEMPS
CELL VOLTAGES
INTERNALLY MOUNTED SENSORS
P
PRESSURE SENSE
P
H_2 PRESSURE SENSE
T
COOLANT OUT TEMP
P
CAVITY PRESS.
He FLUSH VALVE
ACCUMULATOR
START-UP HEATER
H_2 PURGE VALVE
DISTRIBUTOR PLATE
QDB
QDB
CHECK VALVE
QDB
CONCENTRATION WATER REMOVAL REGULATOR

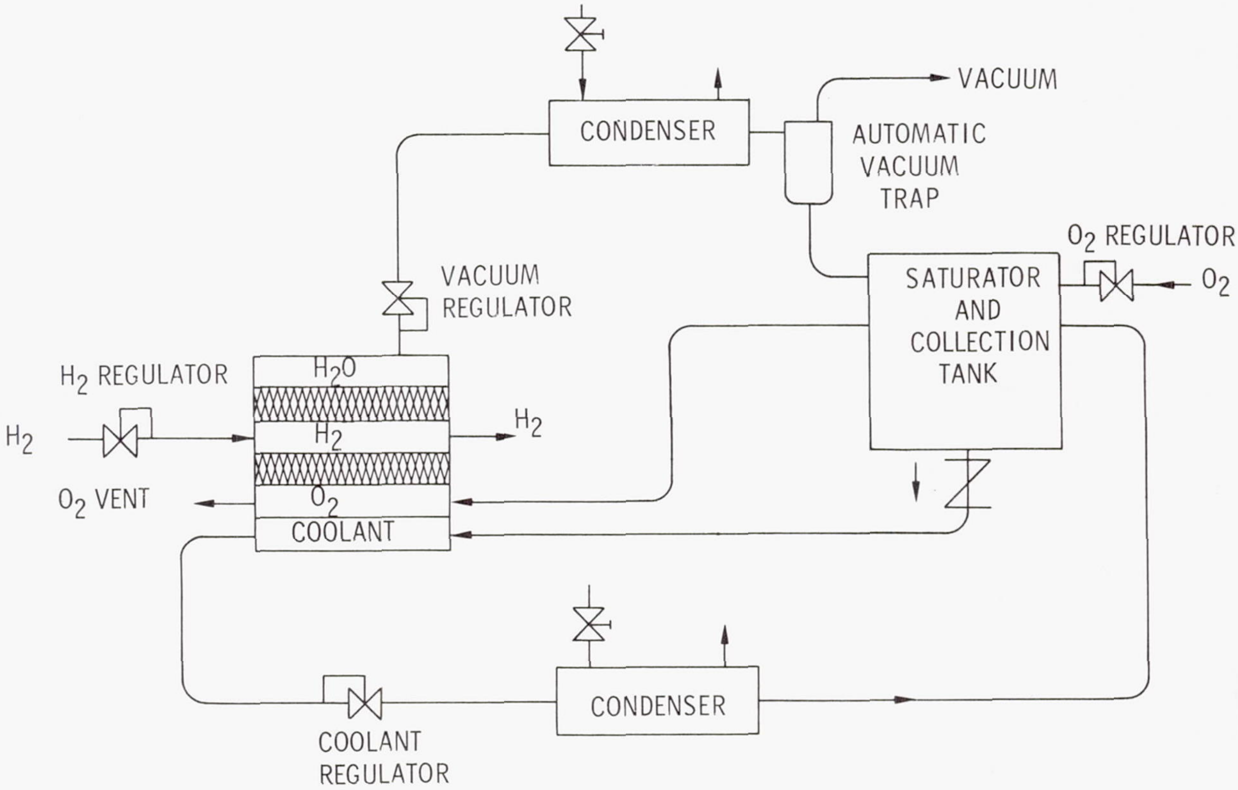

FIGURE 20. ADVANCED OPERATIONAL CONCEPT SCHEMATIC

STUDY OF RADIOISOTOPE POWER FOR SATURN APPLICATIONS

By

Jimmy L. Miller

INTRODUCTION

The operating capability of the present Saturn Instrument Unit (IU) is limited by the 6-1/2 hr lifetime of the primary battery power source. This powered interval for the IU is adequate for Apollo lunar missions as they are presently defined. However, considering the vast amount of guidance and communication gear contained within the IU and carried into orbit, the flexibility offered by a longer life power system such as a radioisotope power system would permit significant upgrading of mission concepts.

Radioisotope thermoelectric power systems ranging from a few tens of watts to a few hundred watts are under development in AEC sponsored programs and will become flight qualified in the next 3 to 5 years. Depending upon progress in fuel form technology, radioisotope thermionics may or may not ever become available in any size. Reactor thermionics in larger sizes (100 kW or larger) will undoubtedly become available in the late 1970's.

POWER REQUIREMENTS

A feasibility study was conducted in 1965 to determine if radioisotopically generated electrical power would be suitable for space vehicle applications. The present peak IU electrical load during launch is slightly in excess of 3 kW, and peak load for the orbital workshop is approximately 2 kW. Based on these criteria, the requirement for a radioisotope power source of 2 kW was established. This would essentially provide the total power requirement for missions like the 56-day workshop, with the possible advantage of direct radioisotope thermal energy for heating. The 2 kW power level would increase Apollo mission flexibility by extending the IU operational lifetime in earth orbit. The primary battery would only be used when supplying the peak loads (above 2 kW required during the launch phase).

In choosing a location on the Saturn vehicle for the radioisotope system, there were three primary considerations: (1) space available for radiators, (2) allowable heat loss to the Saturn vehicle, and (3) ease of nuclear shielding. Tradeoff studies quickly revealed that the aft Saturn Lem Adapter (SLA) was the most feasible location for the radioisotope system. There was sufficient area at this point to support large radiators, and the heat loss into the Saturn systems may be maintained within allowable limits. The SLA location minimizes the major hazards that would exist if the heat source were located adjacent to the S-IVB LOX or liquid hydrogen tanks. In addition, the SLA is adjacent to the IU and may logically remain attached to it in any mission which uses the radioisotope power system.

In terms of converter system selection, the 2 kW power level required large system technology. The SNAP 29 system was chosen as the basis for the study because of its desirable geometry, high power, and advanced state of development.

SNAP 29 GENERATOR

The SNAP 29, shown in Figure 1, is a 500 W generator using Po^{210} fuel and is under development by the Martin Company. It is designed to have an operational life of 104 days. This life span will provide a 90-day space life after operation at the launch pad for up to 14 days.

There are essentially five subsystems composing the SNAP 29.

1. Heat source fuel block contains the Po^{210} and measures approximately 83. 9 by 94. 0 by 2. 54 cm (33 by 37 by 1 in.). The fuel block is designed for intact reentry and containment of the fuel under normal atmospheric reentry or for any abort situation. It will also withstand impact against any substance and burial in any location without loss of radioactive material.

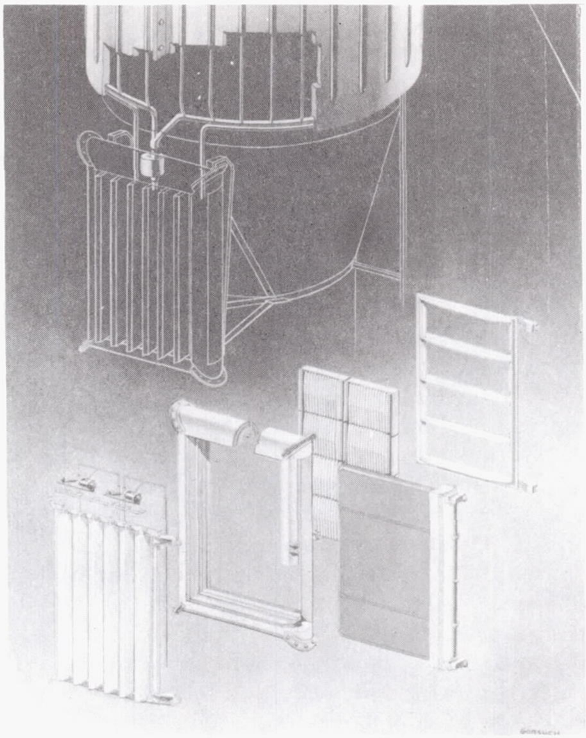

FIGURE 1. SNAP 29 COMPONENTS

2. Thermoelectric conversion subsystem consists of eight modules, each of which produces 62.5 W of electrical power. Each module contains 82 Pb Te conversion elements and has dimensions 38.1 by 20.3 by 6.35 cm (15 by 8 by 2.5 in.).

3. Thermal control subsystem consists of six thermal shutters with mechanical linkage to an actuating device. This temperature sensing actuation device is driven by NaK fluid coupled to the hot plate of the module. Contraction and expansion of the NaK through a bellows-piston mechanism operates the shutters. As the fuel ages and produces less heat, the shutters are gradually closed to maintain a constant electrical output.

4. Heat rejection subsystem consists of about 7.9 m^2 (85 ft^2) of radiator surface and a NaK coolant loop driven by electromagnetic (EM) pumps. The radiator geometry may be tailored to fit the spacecraft configuration.

5. Structural subsystem consists primarily of a frame that will break apart during reentry to allow the fuel block to reenter separately.

Four SNAP 29 systems mounted on the aft SLA almost fill the entire SLA area with radiator (Fig. 2). Each system will be located in the center of its radiator quadrant with one half of the NaK flow going through each side of the radiator. The net electrical power will be 2 kW.

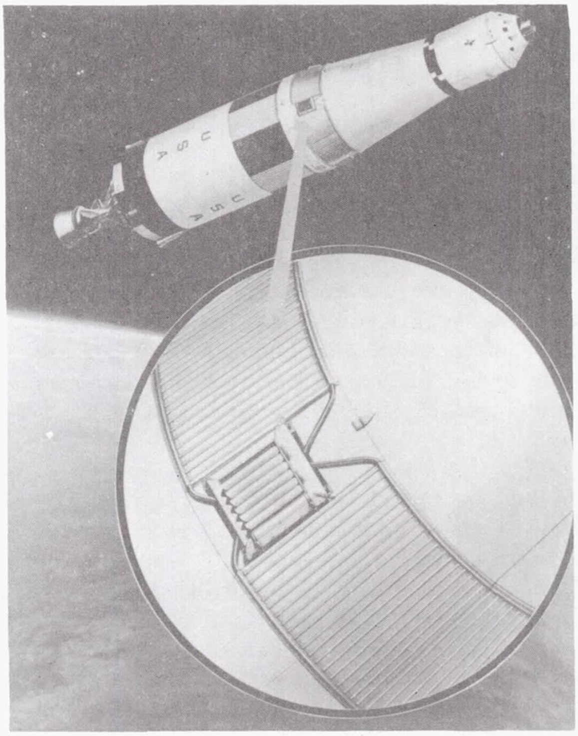

FIGURE 2. RADIOISOTOPE POWER SUPPLY ON SATURN VEHICLE

SYSTEM ANALYSIS AND DESCRIPTION

Valid analytical data are obtained when engineering analysis and computer results are verified by detailed design, fabrication, and testing. The objectives of the present program are to (1) complete a design of the selected approach, (2) fabricate a simulation test article, (3) demonstrate the feasibility of the approach by testing , and (4) define criteria unique to RTG applications which directly influence their use.

Certain basic assumptions that reflected directly upon the design study were made. To assure the utility of the system, little or no modifications to the existing and flight qualified SLA structure should be needed. The design analysis should not decrease the load carrying capability or change the structural integrity of the system. The allowable thermal loss into the SLA honeycomb would be a maximum of 250 W per SNAP 29 system, or a maximum of 1000 W additional heat into the IU compartment. This insures that the SLA honeycomb will remain at a relatively low temperature. The system must withstand the prelaunch environment and launching stresses. The radiator must be operating for some period of time inside the service structure on the launch pad. This phase of operational considerations has not been extensively investigated to date, but will be the subject of a later study.

A requirement of the SNAP 29 system is that the fuel block must separate from the SLA during reentry. The SNAP 29 system will be mounted on the outside of the SLA to have the generator frame in the airstream so that it may break away and fall free of other hardware when aerodynamic heating begins. The aerodynamic design of the fuel block assures that it will reenter intact after it separates from the SLA. The only necessary SLA modifications are some mounting holes at the attachment points. The external location does require an aerodynamic shroud for vehicle launch, and this shroud must be jettisoned in orbit or in the event of launch abort.

Present mission definitions call for the forward SLA shrouds to be opened back 45 degrees. This position was assumed in the study to calculate the effective radiator view factor. Obviously the forward shrouds could not be folded back all the way because of their interference with the radiator. The most desirable situation is for the forward SLA panels to be jettisoned. Using these basic assumptions, a preliminary design has been worked out which locates the SNAP 29 and associated radiator on a quadrant of the aft SLA.

Figure 3 shows the split radiator sections with the generator system located between the radiator segments. The NaK loop flows into and returns from the radiator sections through 2.54 cm (1.0 in.) outside diameter, 2.44 cm ID (0.96 in. ID) header tubes. The vertical radiator tubes are 0.7938 cm (0.3125 in.) outside diameter, 0.6922 cm (0.2725 in.) ID and are

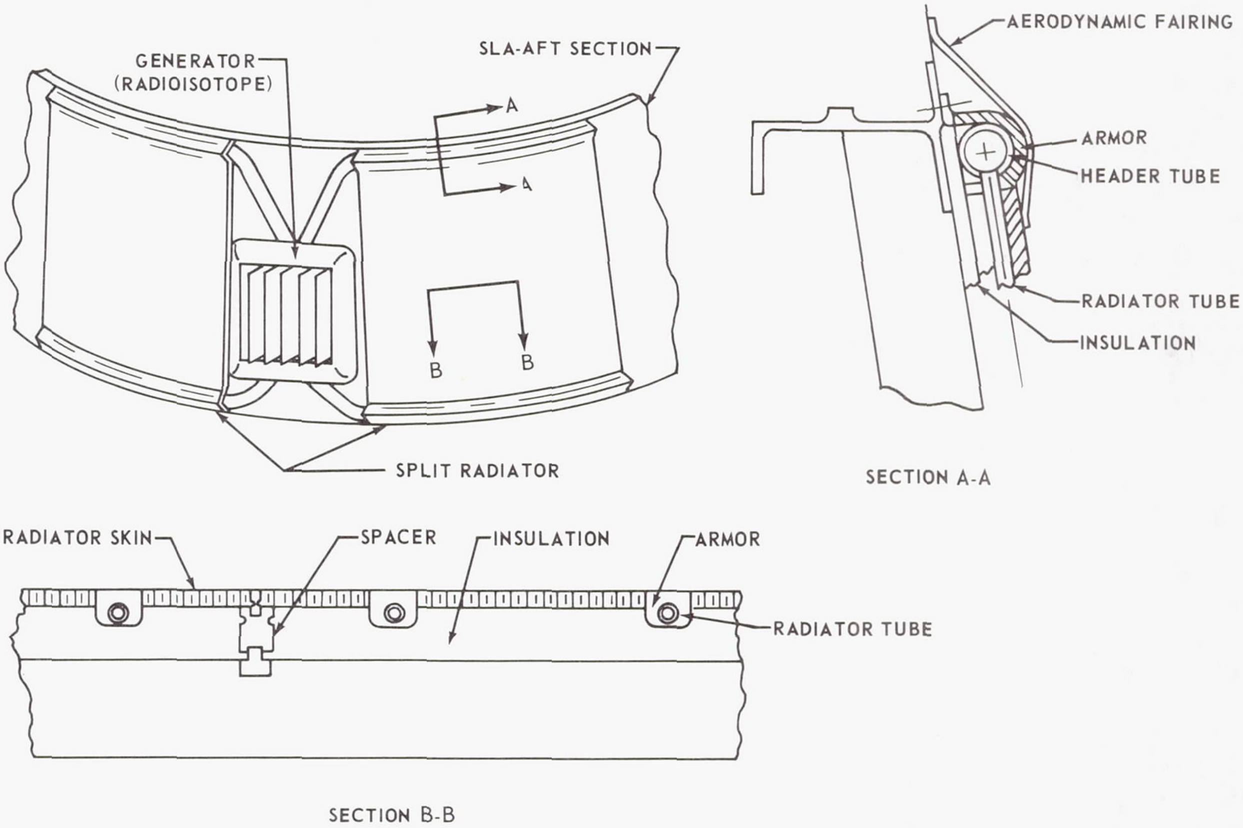

FIGURE 3. RADIATOR FLIGHT CONFIGURATION

spaced 11.8 cm (4.63 in.) between centers out of the top header. Because of the conical geometry of the radiator, the tube spacing increases down their 2.13 m (7 ft) length and enters the bottom header on 13.0 cm (5.11 in.) spacing between centers. The primary structural support for the radiator is through the bolting of the header armor brackets into the top and bottom SLA rings. The radiator skin is spaced away from the SLA skin by 40 insulated standoff fasteners. The total radiator thermal dissipation is approximately 10 kW, and the NaK flow rate required to accomplish this energy transfer is 2100 kg/hr (4620 lb/hr). The flow maldistribution down the radiator tubes is calculated to be ± 3.5%, which is within a tolerable limit.

To meet the objective of 250 or less thermal watts lost to the SLA, an insulating material will be required between the radiator and SLA honeycomb.

A number of insulating materials were studied. Figure 4 shows a comparison among dimpled H-film, eccofoam, and thermoflex, which were three of the more promising materials. The insulating material needs to be lightweight and have a low coefficient of thermal conduction. Therefore, as a comparison basis, the product of thermal conductivity and density was used. Dimpled H-film appeared to be considerably superior.

MATERIAL	k $\frac{W}{m^2 \cdot {}^\circ K}$ 366° K $\left[k \left(\frac{Btu}{hr \cdot ft^2 \cdot {}^\circ F} \right) (200^\circ F) \right]$	ρ $\frac{kg}{m^3}$ 366° K $\left[\rho \left(\frac{lb}{ft^3} \right) (200^\circ F) \right]$	kρ
DIMPLED H-FILM	0.00284 (0.0005)	43.3 (2.7)	0.123 (0.00135)
ECCOFOAM	0.068 (0.012)	32.0 (2.0)	2.18 (0.024)
THERMOFLEX	0.159 (0.028)	48.0 (3.0)	7.64 (0.0785)

FIGURE 4. RADIATOR INSULATION SELECTION

To maintain the SLA temperature at around 366° K (200° F) with the radiator at 450° K (350° F), the insulation must consist of 6 layers of dimpled H-film. This number of layers can be compressed into a blanket about 0.254 cm (0.1 in.) thick and placed between the radiator backside and the SLA skin as shown in Figure 5.

Two problems remain to be investigated. One is the method for removing heat on the launch pad where the dimpled H-film is filled with air and does not perform at its peak efficiency as an insulating blanket. The other is a potential problem of shifting or tearing of the H-film during launch when the insulating blanket is being evacuated. To investigate the second problem, a rapid pull-down vacuum test on a specimen is planned for some time in the future.

During the thermal cycle of the radiator, a differential expansion will take place between the radiator and SLA. Assuming a difference in temperature of 366° K (200° F) on the SLA to 450° K (350° F) on the radiator, the differential expansion could be as high as 0.726 cm (0.286 in.). To allow for this expansion, slotted mounting points were provided at the four corners at an angle with the horizontal that would allow proportional expansion in the vertical and horizontal directions. During launch, this mounting permits the aerodynamic loads to be transmitted to the SLA structure.

A loose fit between the top header and the header armor permits the differential expansion motion without strain. The problem in this design is that sheer stresses act on the weld between the header and radiator tubes.

The NaK radiator tubes must be stainless steel to contain the NaK, and the radiator and armor are aluminum. Therefore, a stainless steel to aluminum bond is required for the 2.13 m (7 ft) long radiator tubes. This is accomplished by nickel plating the stainless steel and then casting in aluminum. The casting is then machined into the cross-section, shown in Figure 6, and welded to the inside of the radiator plate.

For the thermal test model, a number of temperature channels as well as flow distribution channels will be provided. With the thermocouples placed in line (Fig. 6) effective thermal conductivities across the entire structure may be obtained.

Recent studies on the SNAP 29 heat rejection subsystem have resulted in direction by the AEC to switch the design from a circulating NaK loop to a multiple "water heat pipe" system. The radiator

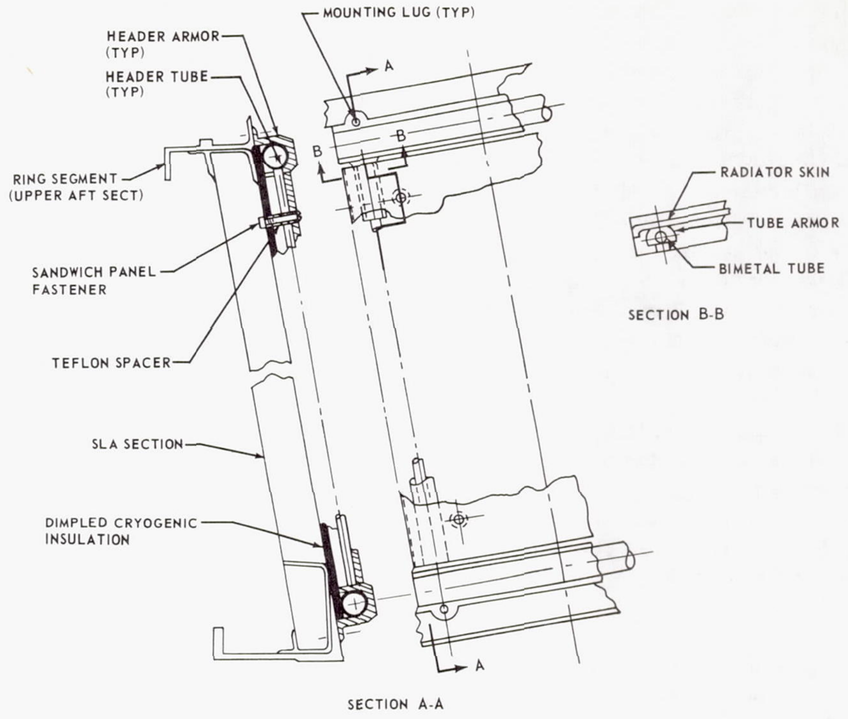

FIGURE 5. SATURN RADIATOR

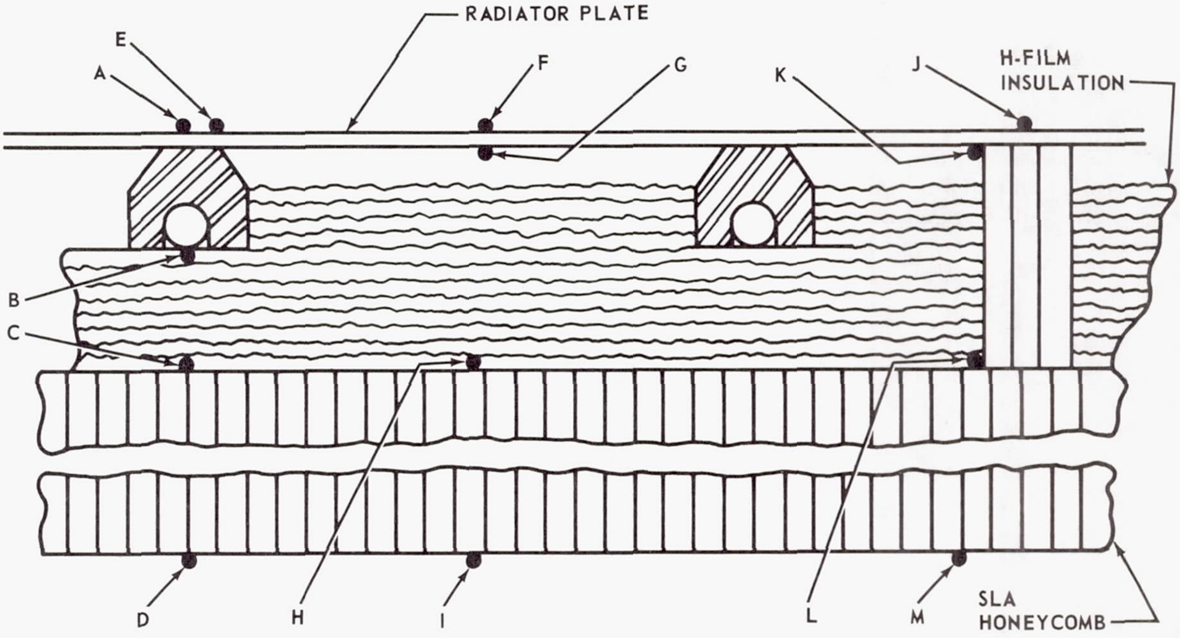

FIGURE 6. THERMOCOUPLE LOCATIONS ON RADIOISOTOPE POWER SUPPLY

area requirements will remain essentially unchanged, but the simple approach of using heat pipes will result in the elimination of header tubes. As a result, the problem of shear stresses between the header and radiator tubes is eliminated. The heat pipes will be essentially the same diameter as the radiator tubes, but instead of running vertically they will extend horizontally around the circumference of the radiator. Since each heat pipe functions independently of the others in the system, a high reliability factor may be achieved by adding redundant pipes and permitting a greater probability of puncture by meteoroids. This eliminates the requirement for meteoroid armor and will result in a much lighter system.

As the heat pipe design tradeoffs are completed, the results will be fed into the Saturn system study and the test article design will be modified. After all tradeoff decisions have been finalized, the radiator simulator will be fabricated. The unit will then be tested under ambient conditions and later under environmental conditions.

When a mission requirement for a radioisotope power system on Saturn vehicles is defined, the problem of vehicle launch operations will be investigated. Figure 7 shows one concept of a shielded fueling device. This device will weigh about 2720 kg (6,000 lb) and will consist of a tool for extracting the electrical checkout heaters from the SNAP 29 and inserting the Po^{210} fuel block. This operation is performed just prior to launch for obvious reasons of nuclear safety.

FUTURE PLANS

Future plans include the investigation of radioisotope handling and safety. The safety program will be extensive and will be performed for six event phases as follows: (1) handling, storage, and transportation, (2) launch pad, (3) launch and ascent, (4) orbit, (5) reentry, and (6) impact. Future plans will require investigating launch pad support equipment and operational problems. It is conceivable that a mission readiness date as early as fall of 1971 could be realized for a radioisotope electrical power system for Saturn vehicles.

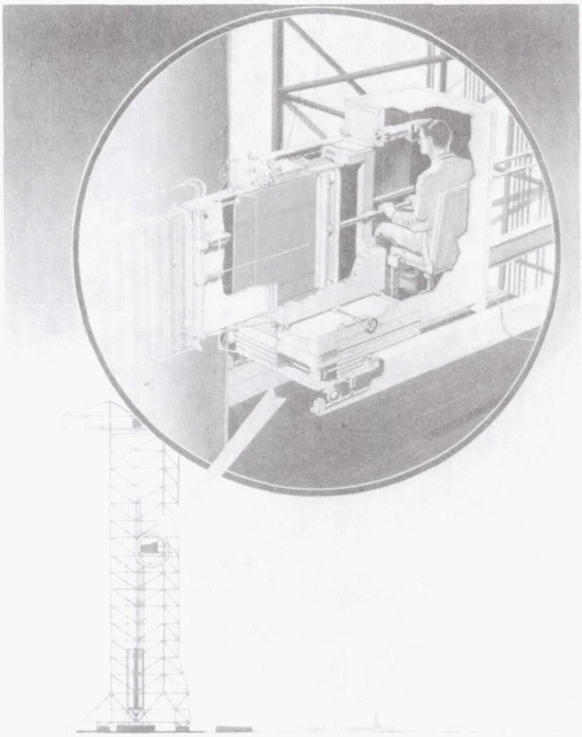

FIGURE 7. SNAP 29 FUELING DEVICE

STUDY OF SOLAR POWER WITH GRAVITY GRADIENT STABILIZATION

By

Leighton Young

SUMMARY

A method for predicting the amount of power available from a solar array in circular orbit and under gravity gradient stabilization is presented. Six possible solar array orientations are discussed. Equations derived can be modified to fit an infinite number of orientations. Oscillatory conditions are not investigated, but the equations derived can be helpful in determining useful solutions for such situations.

INTRODUCTION

Power from a solar array in "Air Mass 0" sunlight depends upon the electrical power rating of the array, array temperature, and the angle of incident sunlight, as summarized in the following equation:

$$P_0 = P_r \tau A \qquad (1)$$

where P_0 = output power (to be determined)

P_r = power rating of the array

τ = normalized temperature power coefficient

A = normalized effective array area

The array power rating is determined from design parameters. Three factors remain to be resolved before output power can be determined.

1. Temperature Effects - Array temperature variations must be known before τ (normalized temperature power coefficient) can be determined.

2. Angle of Incident Sunlight - The cosine of this angle is the normalized effective array area (A in eq. (1)).

3. Entrance and Exit Points into the Earth's Shadow - The period of orbit when the satellite is in the earth's shadow must be known so that solar array power can be equated to zero.

A detailed discussion of each of these controlling factors follows.

TEMPERATURE EFFECTS

Temperature variations experienced by a solar array in near earth orbit will be similar to those shown in Figure 1. For this range of temperatures, array power varies with temperature in an approximately linear fashion (0.5% per degree Kelvin) as shown in Figure 2. Here τ is normalized at 343°K and is read from the right ordinate of the curve. By taking temperatures from Figure 1, and obtaining the corresponding τ from Figure 2, a curve can be plotted for τ over the range of temperature experienced by the solar array.

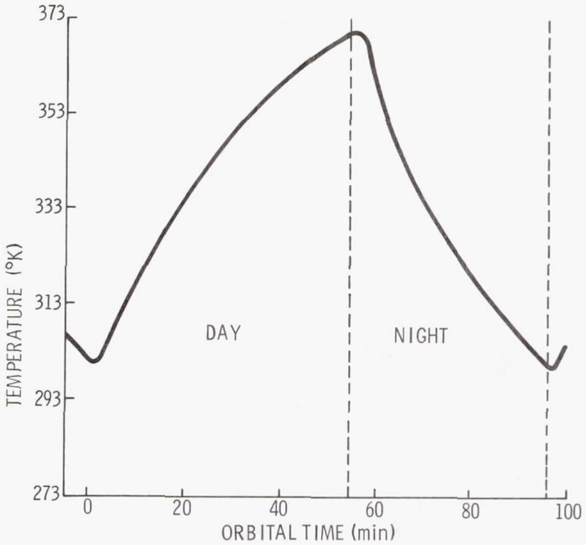

FIGURE 1. TEMPERATURE VS. ORBITAL TIME FOR A NOMINAL ORBIT

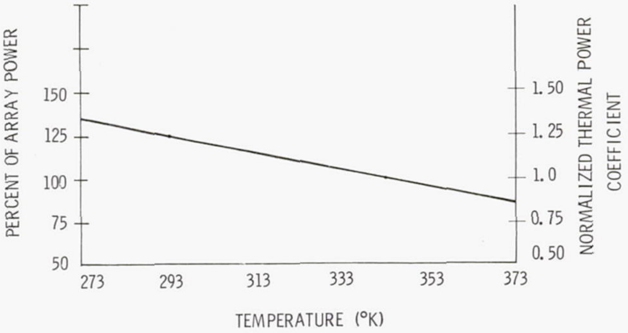

FIGURE 2. NORMALIZED THERMAL POWER COEFFICIENT

If τ is equated to zero during the time the array is in the earth's shadow, the curve will appear as shown in Figure 3. If average power is desired rather than instantaneous power, an average value for τ may be used in the formula $P_0 = P_r \tau A$.

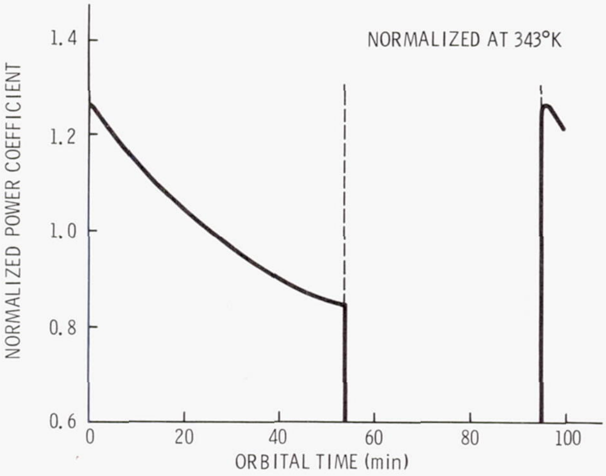

FIGURE 3. THERMAL POWER COEFFICIENT (τ)

DETERMINATION OF ANGLE OF INCIDENT SUNLIGHT

This method for determination of the angle of incident sunlight considers the satellite as being a cube in orbit with the possibility of the solar array being mounted on either of the cube's six surfaces as shown in Figure 4. The array could be pointed in either of six directions as described by vectors $\vec{N}_1$ through $\vec{N}_6$. The location of the satellite in relation to earth is defined by angles i, Ω, and Θ, which are referenced to the equatorial plane. The angle of inclination of the orbital plane is i, Ω is the angle between the X axis and the line of nodes (the line of nodes being the line drawn through the points where the satellite intersects the equatorial plane), and Θ is the angle between the line of nodes and the earth-satellite vector. To locate the satellite in reference to the sun, another angle must be used. This angle is called α and is measured from the vernal equinox as shown in Figure 5. Power available from a solar

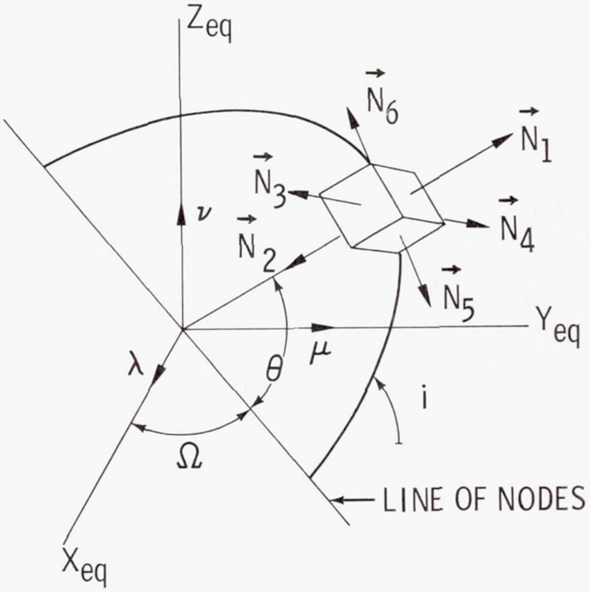

FIGURE 4. REFERENCE COORDINATES FOR CUBE IN EARTH ORBIT

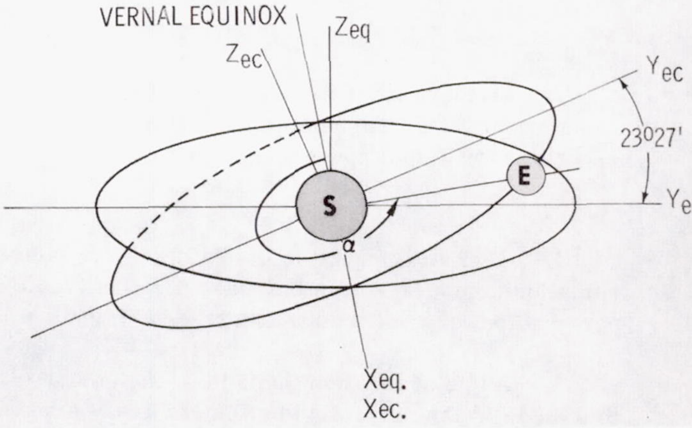

FIGURE 5. EQUATORIAL AND ECLIPTIC PLANES

array under gravity gradient stabilization in circular orbit of the earth is a function of α .

NORMALIZED EFFECTIVE ARRAY AREA

In the equation $P_0 = P_r \tau A$, P_r is the array power rating under the following conditions:

- "Air Mass 0."
- Temperature corresponding to the value 1.0 for τ (normalized temperature power coefficient).
- Direct incident sunlight - Sun vector normal to the surface of the solar array.

The normalized effective array area, A, is the cosine of the angle of incident sunlight. A method of solving for A is given by the dot product:

$$A_m = \vec{N}_m \cdot \vec{S}$$

$$\vec{N}_m \cdot \vec{S} = N_m S \cos\left(\angle \vec{N}_m \vec{S}\right) \tag{2}$$

The value 1.0 is assigned to $N_m S$ since, by definition, A_m equals the cosine of the angle between the two vectors.

The steps necessary to arrive at A are as follows.

1. Mathematically define the relation between equatorial coordinates and ecliptic coordinates. From Figure 6 the following equations are obtained:

$$X_{eq} = X_{ec}$$

$$Y_{eq} = Y_{ec} \cos 23° 27' - Z_{ec} \sin 23° 27' \tag{3}$$

$$Z_{eq} = Y_{ec} \sin 23° 27' + Z_{ec} \cos 23° 27'$$

$$\sin 23° 27' = 0.39795$$

$$\cos 23° 27' = 0.91741$$

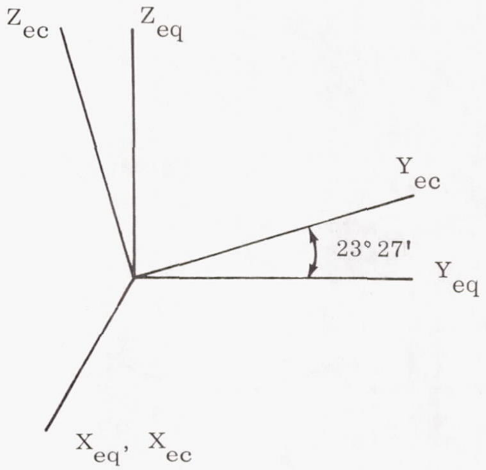

FIGURE 6. EQUATORIAL AND ECLIPTIC COORDINATES

In matrix form the relation becomes:

$$\left|\begin{matrix} X_{eq} \\ Y_{eq} \\ Z_{eq} \end{matrix}\right| = \left|\begin{matrix} 1 & 0 & 0 \\ 0 & 0.9174 & -0.3979 \\ 0 & 0.3979 & 0.9174 \end{matrix}\right| \left|\begin{matrix} X_{ec} \\ Y_{ec} \\ Z_{ec} \end{matrix}\right| \tag{4}$$

2. Define the sun vector in terms of rectangular component vectors using equatorial coordinates. The following equations, obtained from Figure 7, define the sun vector in terms of its rectangular component in the ecliptic plane.

$$S_{X_{ec}} = S \cos \alpha$$

$$S_{Y_{ec}} = S \sin \alpha \tag{5}$$

$$S_{Z_{ec}} = 0$$

The transformation to equatorial coordinates is shown by the following relations:

$$\left|\begin{matrix} S_{X_{eq}} \\ S_{Y_{eq}} \\ S_{Z_{eq}} \end{matrix}\right| = \left|\begin{matrix} 1 & 0 & 0 \\ 0 & 0.9174 & -0.3979 \\ 0 & 0.3979 & 0.9174 \end{matrix}\right| \left|\begin{matrix} S_{X_{ec}} \\ S_{Y_{ec}} \\ S_{Z_{ec}} \end{matrix}\right| \tag{6}$$

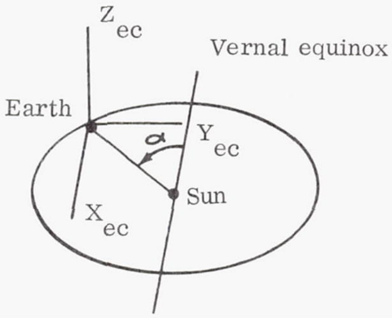

FIGURE 7. ECLIPTIC COORDINATE SYSTEM

Substituting for $S_{X_{ec}}$, $S_{Y_{ec}}$, and $S_{Z_{ec}}$:

$$\begin{vmatrix} S_{X_{eq}} \\ S_{Y_{eq}} \\ S_{Z_{eq}} \end{vmatrix} = \begin{vmatrix} 1 & 0 & 0 \\ 0 & 0.9174 & -0.3979 \\ 0 & 0.3979 & 0.9174 \end{vmatrix} \begin{vmatrix} S\cos\alpha \\ S\sin\alpha \\ 0 \end{vmatrix} \qquad (7)$$

$$\begin{aligned} S_{X_{eq}} &= S\cos\alpha \\ S_{Y_{eq}} &= 0.9174\left(S\sin\alpha\right) \\ S_{Z_{eq}} &= 0.3979\left(S\sin\alpha\right) \end{aligned} \qquad (8)$$

The sun vector described in the equatorial coordinate system is

$$\vec{S} = S_{X_{eq}}\vec{i} + S_{Y_{eq}}\vec{j} + S_{Z_{eq}}\vec{k} \qquad (9)$$

3. Define the vector normal to the solar array in terms of rectangular components using equatorial coordinates. Using λ_m, μ_m, and ν_m to represent the X, Y, and Z components respectively of $\vec{N}_m$ (Fig. 4), the following equations are obtained. The method used to obtain these equations is treated by Escobal [1].

For $\vec{N}_1$ and $\vec{N}_2$

$$\begin{aligned} \lambda_1 &= (\cos\Theta\cos\Omega - \sin\Theta\cos i\sin\Omega)\ N_1 \\ \mu_1 &= (\cos\Theta\sin\Omega + \sin\Theta\cos i\cos\Omega)\ N_1 \\ \nu_1 &= N_1\sin\Theta\sin i \end{aligned} \qquad (10)$$

and since $\vec{N}_2 = -\vec{N}_1$

$$\begin{aligned} \lambda_2 &= (-\cos\Theta\cos\Omega + \sin\Theta\cos i\sin\Omega)\ N_1 \\ \mu_2 &= (-\cos\Theta\sin\Omega - \sin\Theta\cos i\cos\Omega)\ N_1 \\ \nu_2 &= -N_1\sin\Theta\sin i. \end{aligned} \qquad (11)$$

For $\vec{N}_3$ and $\vec{N}_4$

$$\begin{aligned} \lambda_3 &= N_3\sin i\sin\Omega \\ \mu_3 &= -N_3\sin i\cos\Omega \\ \nu_3 &= N_3\cos i \end{aligned} \qquad (12)$$

and since $\vec{N}_4 = -\vec{N}_3$

$$\begin{aligned} \lambda_4 &= -N_3\sin i\sin\Omega \\ \mu_4 &= N_3\sin i\cos\Omega \\ \nu_4 &= -N_3\cos i. \end{aligned} \qquad (13)$$

For $\vec{N}_5$ and $\vec{N}_6$

$$\begin{aligned} \lambda_5 &= (\sin\Theta\cos\Omega + \cos\Theta\cos i\sin\Omega)\ N_5 \\ \mu_5 &= (\sin\Theta\sin\Omega - \cos\Theta\cos i\cos\Omega)\ N_5 \\ \nu_5 &= -N_5\cos\Theta\sin i \end{aligned} \qquad (14)$$

and since $\vec{N}_6 = -\vec{N}_5$

$$\begin{aligned} \lambda_6 &= (-\sin\Theta\cos\Omega - \cos\Theta\cos i\sin\Omega)\ N_5 \\ \mu_6 &= (-\sin\Theta\sin\Omega + \cos\Theta\cos i\cos\Omega)\ N_5 \\ \nu_6 &= \ N_5\cos\Theta\sin i. \end{aligned} \qquad (15)$$

4. Obtain the dot product of the sun vector and the vector normal to the solar array.

$$A_m = \vec{N}_m \cdot \vec{S} \qquad m = 1, 2, 3, 4, 5, 6 \qquad (2)$$

where $N_m = \lambda_m\vec{i} + \mu_m\vec{j} + \nu_m\vec{k}$

$$\vec{S} = S_X\vec{i} + S_Y\vec{j} + S_Z\vec{k}$$

$$A_m = \lambda_m S_X + \mu_m S_Y + \nu_m S_Z \qquad (16)$$

Example: Find the equation for the normalized effective area for a solar array mounted on surface five of the orbiting cube under consideration. Given that $A_5 = \vec{N}_5 \cdot \vec{S}$, where $\vec{N}_5 = \lambda_5 \vec{i} + \mu_5 \vec{j} + \nu_5 \vec{k}$, and the equations for λ_5, μ_5, and ν_5 are as given under 3 above, take

$$\begin{aligned} S_X &= S \cos \alpha \\ S_Y &= 0.9174 \left(S \sin \alpha \right) \\ S_Z &= 0.3979 \left(S \sin \alpha \right) \end{aligned} \tag{17}$$

so that

$$\begin{aligned} \lambda_5 S_X &= \left[\left(\sin \Theta \cos \Omega + \cos \Theta \cos i \sin \Omega \right) N_5 \right] S \cos \alpha \\ \mu_5 S_Y &= \left[\left(\sin \Theta \sin \Omega - \cos \Theta \cos i \cos \Omega \right) N_5 \right] 0.9174 S \sin \alpha \\ \nu_5 S_Z &= \left(- N_5 \cos \Theta \sin i \right) \; 0.3979 \; S \sin \alpha \end{aligned} \tag{18}$$

and $N_5 S = 1.0$ by definition,

then

$$A_5 = \lambda_5 S_X + \mu_5 S_Y + \nu_5 S_Z \tag{19}$$

where

$$\begin{aligned} \lambda_5 S_X &= \left(\sin \Theta \cos \Omega + \cos \Theta \cos i \sin \Omega \right) \cos \alpha \\ \mu_5 S_Y &= \left(\sin \Theta \sin \Omega - \cos \Theta \cos i \cos \Omega \right) 0.9174 \sin \alpha \\ \nu_5 S_Z &= \left(- \cos \Theta \sin i \right) \; 0.3979 \sin \alpha . \end{aligned} \tag{20}$$

Equation (19) yields the normalized effective area for a solar array mounted on surface five of the cube at a specific point in orbit. If the normalized effective area is desired as a function of time, the following substitutions may be made:

$$\begin{aligned} \Theta &= \Theta_0 + \dot{\Theta} t \\ \Omega &= \Omega_0 + \dot{\Omega} t \\ \alpha &= \alpha_0 + \dot{\alpha} t \end{aligned} \tag{21}$$

where

Θ_0, Ω_0, α_0 = initial space coordinates

$\dot{\Theta}$ = satellite's angular velocity around earth

$\dot{\Omega}$ = rate of orbit precession

$\dot{\alpha}$ = earth's angular velocity around sun

t = time in orbit.

DETERMINATION OF PERIOD OF EARTH'S SHADOWING

Figure 8 illustrates a satellite in circular orbit around the earth. An extension to the line drawn from the center of the earth to the entrance or exit point has the same direction and position in space as $\vec{N}_1$. Therefore when A_1, the dot product of $\vec{N}_1$ and $\vec{S}$, equals cosine ψ, the satellite is at either the entrance or exit point. When $A_1 <$ cosine ψ, the satellite is in the shadow of the earth and the normalized effective array area (A_m) is set equal to zero. All negative values of A_m are also set equal to zero since this indicates that sunlight would be shining on the rear of the solar array.

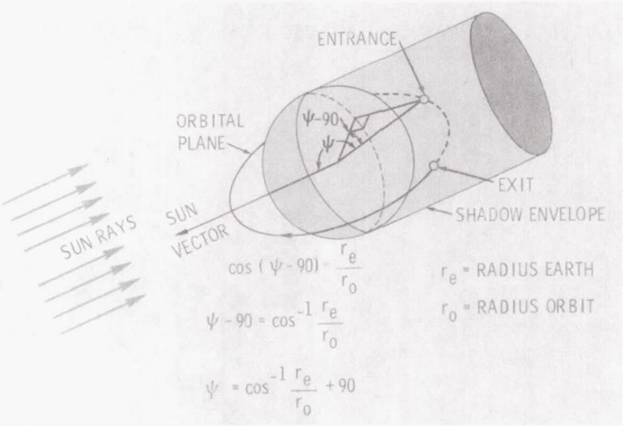

FIGURE 8. SATELLITE IN CIRCULAR ORBIT AROUND THE EARTH

Application to the Apollo Telescope Mount (ATM) of the method described in this paper over the period of one orbit gives results as shown in Figure 9. Sunlight shines on the rear of the solar array until t = 24 min and hence electrical power is not produced. At t = approximately 54 min the satellite reenters the shadow of the earth.

CONCLUSIONS

The equations that have been derived adapt well to a computer program. If the array orientation is at some attitude other than as defined by the faces of

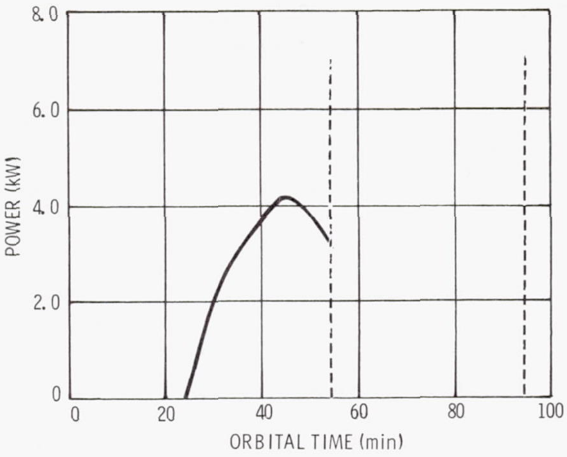

- POWER AVAILABLE FOR A MINIMUM EFFECTIVE SUNLIGHT ORBIT (Ω = 180 degrees, α = 270 degrees)
- GRAVITY GRADIENT ATTITUDE CONTROL
- BASED ON 8400 W ARRAY RATING

FIGURE 9. POWER CURVE FOR NOMINAL ORBIT

the cube, slight modifications to the equations must be made. Computer runs using ATM orbital parameters indicate that a solar array looking perpendicular to the plane of orbit could go for long periods of time without supplying any power. If the ATM should become gravity gradient stabilized with its solar array facing the earth, the solar array would be eclipsed by the earth during most of the time that it would normally be producing power. As different attitudes for ATM are given consideration, the method described in this paper is used to accurately determine the amount of solar array power available.

REFERENCE

1. Escobal, P. R.: Methods of Orbit Determination. John Wiley and Sons, Inc., New York, 1956.

METAL-ARC ILLUMINATOR FOR SOLAR ARRAY TESTING

By

William L. Crabtree

INTRODUCTION

Large area solar cell arrays are being designed to be an integral part of manned space vehicles. Solar arrays coupled with battery systems offer a reliable power supply for space vehicle applications.

Finding a method to obtain reliable test results to accurately predict solar cell array power outputs in space has long been a difficult problem for solar array design engineers. There are basically two approaches to the solution of this problem. The first approach makes use of a light source that accurately simulates the sun's spectrum and intensity at "Air Mass 0," which would be the condition at one astronomical unit in space. This type of source would actually cause the array to produce the same power that it would produce in space if it were located at one astronomical unit. Of the various types of sources that are used to accomplish this, probably the most successful is the mercury xenon lamp. Although mercury xenon does not provide the closest spectral match of any source, it does provide a reasonably good spectrum with a constant illumination, and this is difficult to obtain with light sources that more closely match the sun's spectrum.

The second approach makes use of a light source which simulates "Air Mass 1" conditions in the solar cell response region. This type of light source provides a simple, inexpensive means of determining the power output of the solar array without the need for the more expensive and usually more elaborate solar simulator. The power output of an array under this light source must be scaled up to determine the array's power output in space; this is usually done by relating the output of a primary standard cell (one which has flown in space) under this source to its output in space. The initial investigation of a light source of this type is the subject of this paper.

TUNGSTEN FILAMENT LAMP SOURCE

At present, the most widely accepted light source is the tungsten filament lamp. The problems associated with the use of the tungsten lamp are as follows:

1. Rapid Degradation - Normally, tungsten bulbs suited for solar array testing have a short lifetime, some as short as six hours; therefore, the bulbs must be replaced after only a few hours of operation.

2. Excessive Infrared Radiation - Tungsten lights have excessive emission near the infrared region, thus requiring a water filter to decrease this infrared before it reaches the test plane area.

3. High-Heat Generation - The excessive infrared generated by the tungsten lamp heats the simulator and requires that the water in the water filter be circulated to keep it cool.

Figure 1 shows the lamp that is presently being investigated as a potential light source for use in solar array testing. It is an arc discharge type of lamp containing the rare metal halide scandium iodide, which is contained in the quartz arc tube shown in the figure. These lamps are available in wattages of 175, 400, and 1000; those used in these initial investigations were the Sylvania 400 W type.

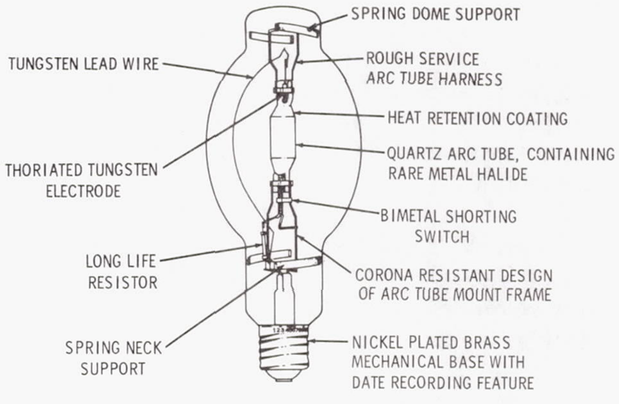

FIGURE 1. METAL-ARC LAMP

Figure 2 shows a comparison of spectral responses. The curve that begins at zero relative intensity and rises most rapidly is the sun's spectrum at "Air Mass 1," the curve with highest relative intensity is the tungsten spectrum unfiltered, and the curve under the filtered area shows the result of filtering

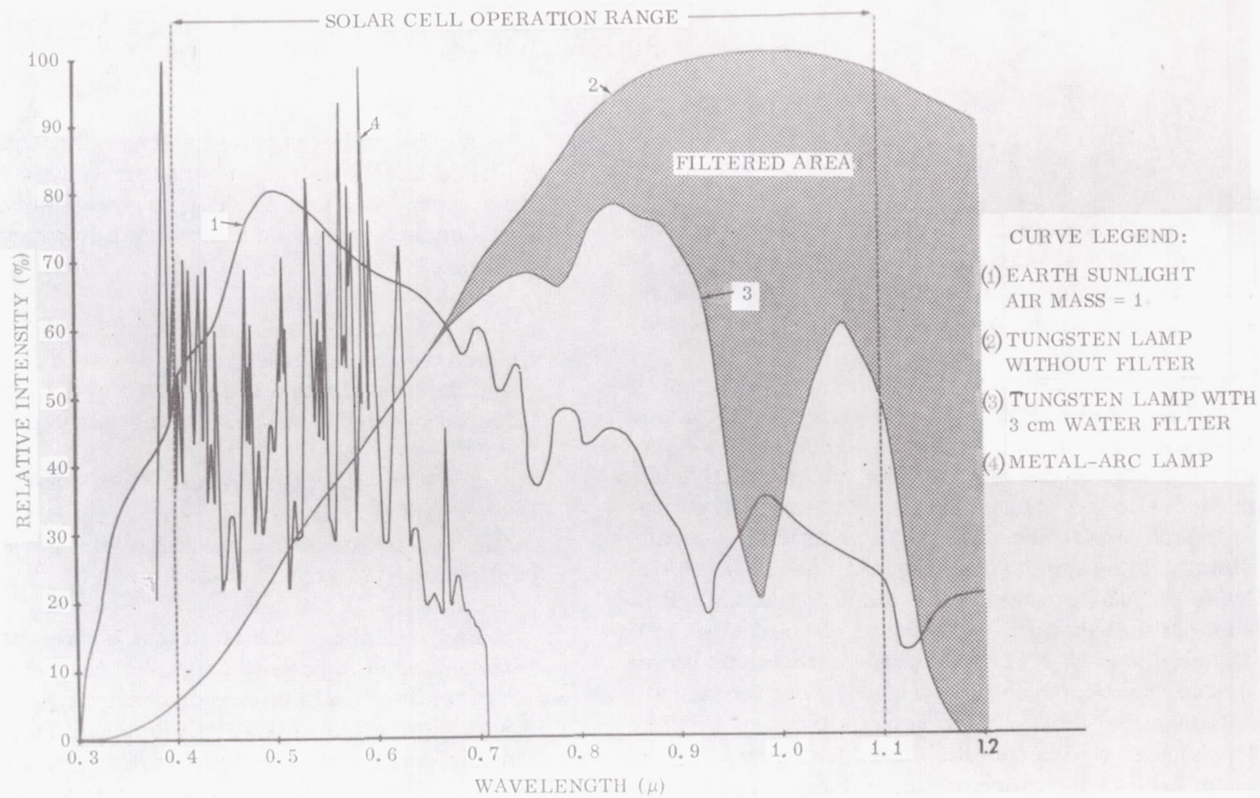

FIGURE 2. NORMALIZED SPECTRAL INTENSITY CURVES

the tungsten spectrum through 3 cm of distilled water. The spiked curve is the spectrum of the rare metal halide; the spikes represent the characteristics of the rare metal halide in its ionized state and are distinctive to the elements contained in the inner quartz envelope. The object is to simulate the "Air Mass 1" curve in the solar cell response region, which is also outlined in Figure 2.

Figures 3 and 4 show the lamps mounted for initial testing and are indicative of the early stages of development underway. Figure 3 shows a close-up of the five lamps used in the tests.

A secondary standard solar cell (Fig. 4), calibrated to a primary standard cell, is used to determine the magnitude and uniformity of intensity over the test plane area. Figure 5 shows the overall test set-up with the simulator in operation. This is done by using a digital voltmeter to measure the voltage drop across a one-ohm resistor to determine the short circuit current of the solar cell. The use of a one-ohm resistor enables the current to be read directly from the digital voltmeter. Since the short-circuit current of the cell is directly proportional to the intensity of the light impinging on its surface, it is only necessary to know the relationship between the short-circuit currents of the primary and secondary standards to determine the intensity of the light source. By moving the cell to various points on the test plane while observing the reading on the voltmeter, the uniformity of the intensity over the test plane area can also be determined.

An iron-constantan thermocouple temperature read-out device was used to determine the temperature of the secondary standard. Relatively constant temperature was maintained by circulating water through its base with a systaltic pump.

The ballasts required for each of the lights to establish the initial high arc and limit the current once it has been established are shown mounted on the sides of the simulator near the bottom (Fig. 5).

Although no specific attempt was made in these early tests to duplicate "Air Mass 1" intensities, or to establish uniform intensity over large areas, the five lamps shown produced 50% of the "Air Mass 1" intensity over an area 0.635 m × 0.635 m (25 in. ×

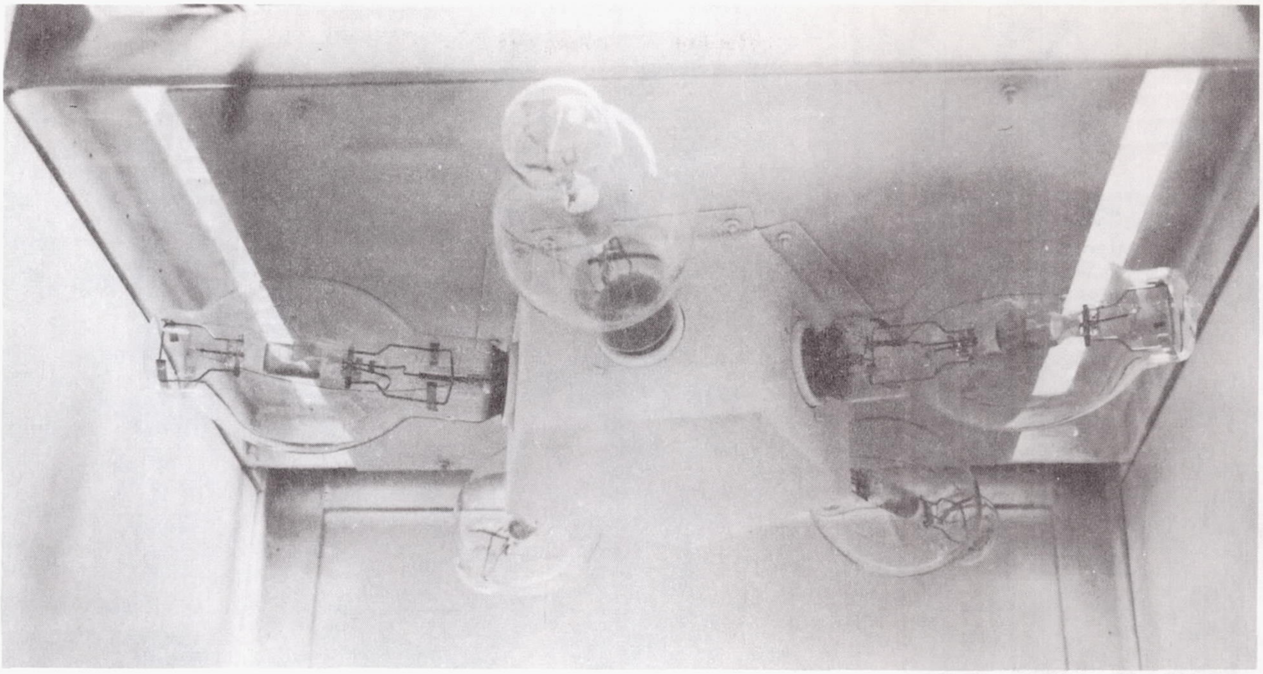

FIGURE 3. TUNGSTEN FILAMENT LAMPS

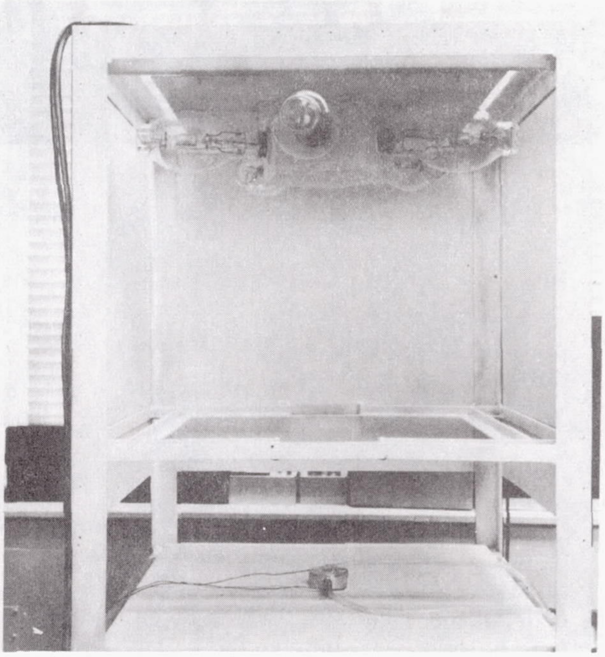

FIGURE 4. ILLUMINATION CHAMBER WITH SOLAR CELL

25 in.), with intensity gradients of ± 10%. No attempt was made to collimate the light during initial tests.

METAL-ARC LAMP SOURCE

Results of the present exploratory investigations indicate the following potential advantages of metal-arc:

1. Low heat generation at the lamp.

2. Reduced infrared radiation - eliminating the need for a water filter and the accompanying water cooling apparatus.

3. Increased radiation at shorter wave-lengths.

4. Long lifetime - The 7500 hr rated average lifetime of this source makes it particularly attractive for use in solar simulation.

5. Economy - The price of these lamps compares very favorably with that of tungsten lights because of their longer lifetime.

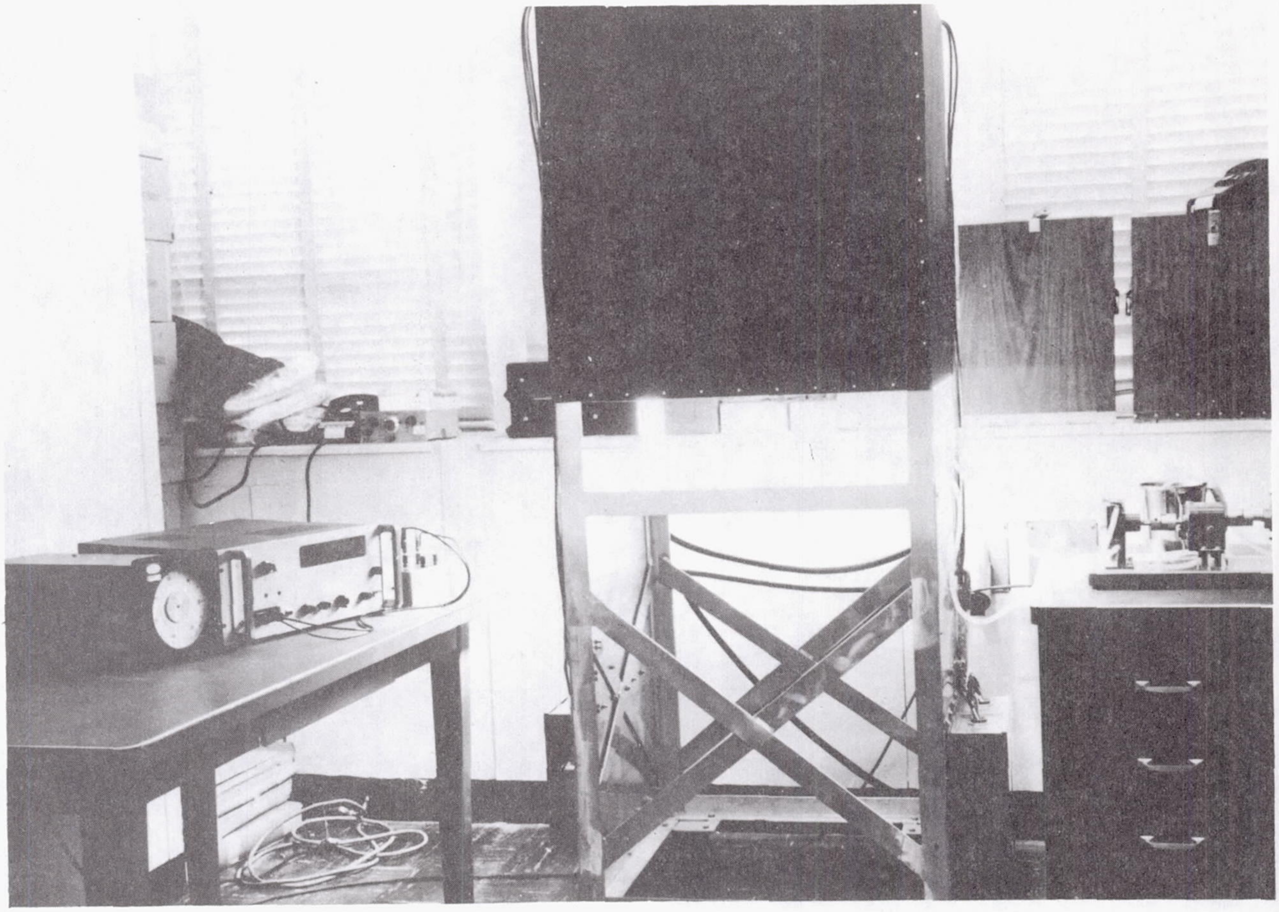

FIGURE 5. SOLAR ARRAY TEST METHOD USING ILLUMINATION SOURCE AND SOLAR CELLS

FUTURE PLANS

Future plans are as follows:

1. Obtain output in the 0.7 μ to 1.1 μ wavelength band to closer simulate the "Air Mass 1" curve in the solar cell response region. Sylvania, whose lamps were used for these tests, indicates that this is possible.

2. Illuminate an area 0.635 m × 0.635 m (25 in. × 25 in.) to "Air Mass 1" illumination level.

3. Reduce the intensity gradients at the test plane.

4. Investigate the stability of emission with time.

5. Investigate collimation.

Investigations have not yet proceeded to such a point that a metal-arc lamp can definitely be shown to be a feasible source for solar array testing. However, if the results of further investigations prove its feasibility, the metal-arc lamp could provide solar cell array design engineers with a source for array testing which is economical, has a long lifetime, and requires a minimum of auxiliary equipment for operation.

ELECTRICAL POWER CONVERSION SYSTEM FOR MANNED EARTH ORBITAL VEHICLE

By

Richard Acker

SUMMARY

An electrical power conversion system designed for a manned earth orbital vehicle is described. The mission considered is typical of future manned spacecraft flights.

INTRODUCTION

The design constraints established for the mission are listed in Table I. The spacecraft would be placed in a 481-km (260-nm) orbit oriented to the sun during the 18-month mission. The orbit period is 94 min (58 min of solar illumination and 36 min of earth occultation).

TABLE I. DESIGN CONSTRAINTS

- Solar Cell Array
  - Oriented to Sun
  - Temperature Range ~ 255 to 351°K
- Mission Length ~ 1 1/2 Years Maximum
- Orbital Period ~ 94 min
  - Night ~ 36 min
  - Daylight ~ 58 min
- Passive Cooling
- Electrical Loads ~ 3600 W Average
- No Single Point Failures
- Central Converters
- High Efficiency
- Minimum Weight
- Minimum Volume

The major spacecraft constraint is the requirement for passive cooling of the power system components. This constraint requires the electronic packages' view of space to be optimized as most of the heat must be dissipated by radiation. The resulting temperature is dependent upon the available radiating area. High power conversion and energy efficiencies are necessary to reduce the amount of heat generated.

Other constraints imposed on the power conversion system include minimum weight and volume, central converters, and no single point failure that will result in a system failure.

For the electrical load requirement of 3600 W average power, three types of power sources were considered: fuel cell, radioisotope thermoelectric generator (RTG), and solar cell array.

Fuel cell operation is limited by reactant storage and heat removal problems and by mission duration. Power systems of 2 to 4 kW capacity require an active coolant loop to remove the waste heat, and fuel cell systems with proven life capability of greater than 2000 hr are not yet available.

The RTG system has the limitations that fuel is not available for a large system and radiation danger to personnel could exist. The present RTG's are being developed with maximum power output capabilities of 500 W. Conversion efficiencies of approximately 5% demand active cooling.

A solar cell array sized electrically to 2-1/2 times the spacecraft load would be required to allow for charging secondary energy storage devices to supply power during earth occultation periods. Solar cells with proven performance and reliability are readily available, and the low earth orbit decreases degradation caused by energetic particle bombardment. Solar cells are particularly attractive on sun oriented missions because of the availability of 90 degree incident solar radiation without ancillary array pointing systems.

SELECTED POWER SYSTEM

The selected power system is depicted in Figure 1. The solar cell array is modular in design and, aside from cabling and bussing philosophy, each source is capable of operating independently of all others.

The charger/battery/regulator modules (CBRM) of the electrical power conversion system provide building block capability to make a flexible system that can be readily modified to accommodate changing power demands. The CBRM's are connected in parallel. Failure of a single module will cause the loss of only 1/N of the power conversion system and will not result in a system failure, thus satisfying the no single point failure requirement. Each CBRM will have individual overload protection in the form of current limited output. A droop characteristic in the CBRM output voltage will force all modules to share the load equally. Power available for charging the batteries will be shared by all batteries depending on individual charge requirements, and the battery chargers will provide power management by forcing the solar cell array to operate at or above a nominal 40 V. Protection, monitoring, and control circuits will be self-contained in each CBRM.

SOLAR CELL ARRAY OUTPUT CHARACTERISTICS

The solar cell array (Fig. 2) is required to supply 9 kW average power during daylight periods to maintain the electrical power conversion system output of 3.6 kW average power over the entire orbit. The array is divided into forty 225 W sources that are individually diode coupled to the solar cell bus. The loss of any one source (from micrometeoroid damage, cable damage, etc.) will cause a total power loss of 2-1/2%.

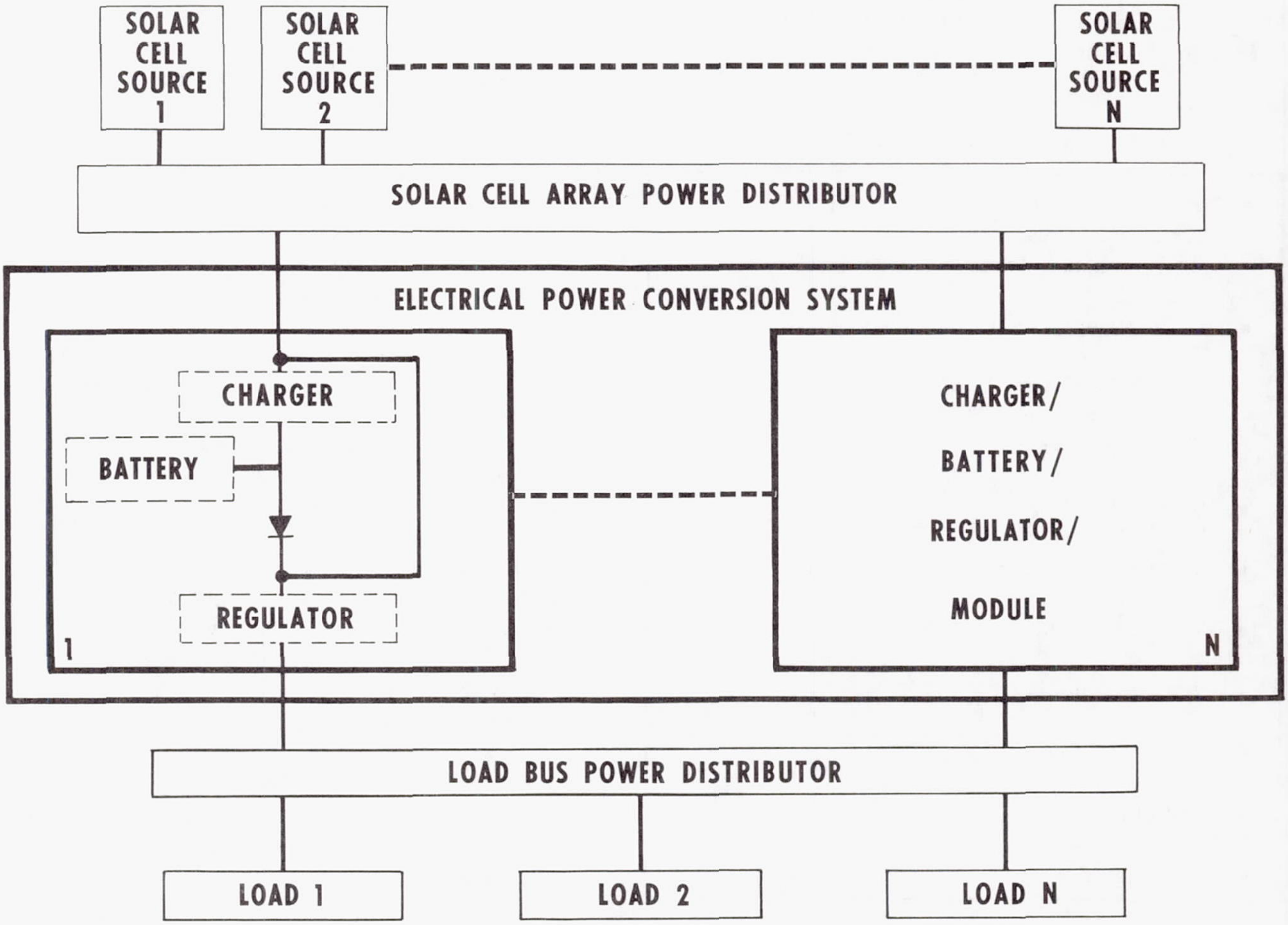

- **VOLTAGE**
  MAXIMUM ~ DEPENDENT ON ARRAY TEMPERATURE AND LIMITED BY AVAILABLE COMPONENT VOLTAGE RATINGS

  OPERATING RANGE ~ DEPENDENT ON TEMPERATURE AND LOAD

- **POWER ~ DEPENDENT ON POWER CONVERSION SYSTEM EFFICIENCY**

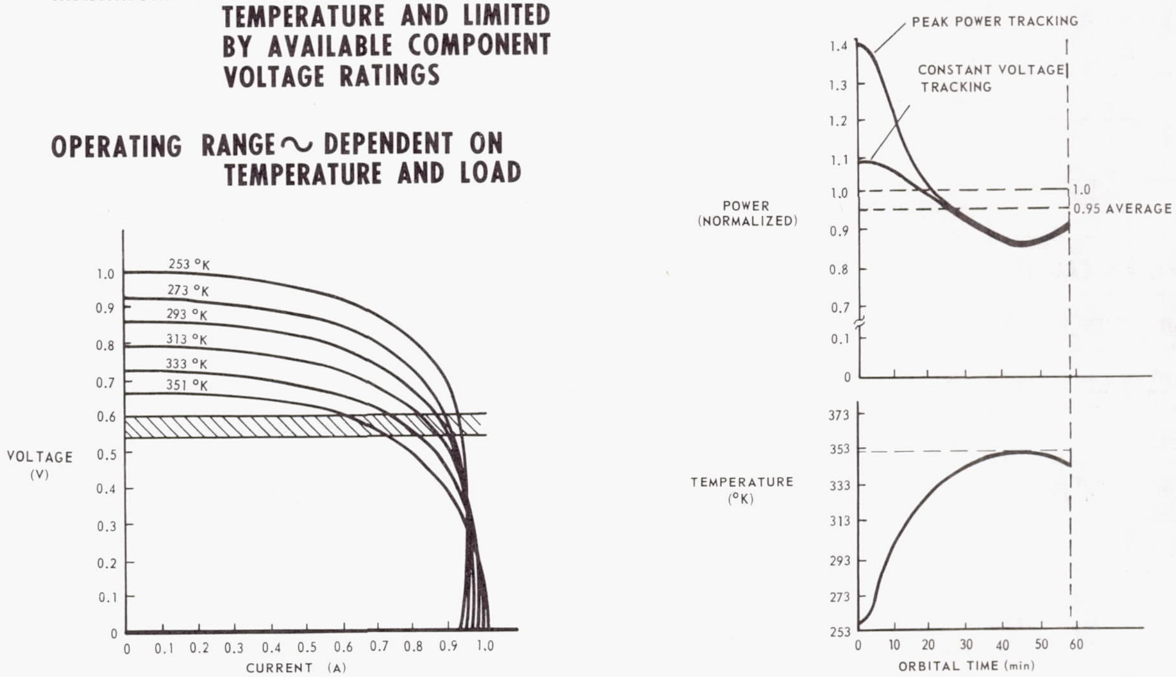

V-I CURVE NORMALIZED

POWER vs. TEMPERATURE NOMOGRAPH

FIGURE 2. SOLAR CELL ARRAY OUTPUT CHARACTERISTICS

The maximum output voltage for the solar cell array is dependent upon array temperature, and the array must be designed to limit this voltage to component voltage ratings. The operating voltage range is dependent upon temperature and electrical load.

The electrical power available for battery charging and spacecraft loads is dependent upon the power conversion system efficiency. The large area of the array precludes the use of peak-power point tracking because of temperature gradients across the array at any point in time. The battery charge rate is automatically controlled to force the array to operate at or above a constant voltage, which approximately coincides with the peak-power point at a chosen temperature. Constant voltage tracking utilizes 95% of the available solar cell array power as shown in Figure 2.

LOAD REGULATOR CIRCUIT COMPARISON

Three basic types of switching regulators and their comparative characteristics are shown in Figure 3. The step-up or -down type was chosen because it possessed inherent characteristics of (1) being able to operate with an input voltage below or above the output voltage, (2) source-load isolation, (3) absence of single point system failure (a single failure will not damage load or remaining regulators), (4) load current limiting, and (5) a respectable conversion efficiency.

The step-down regulator was chosen for the battery charger because high efficiency was the primary consideration. A shorted switching transistor, which would apply the normally high input

	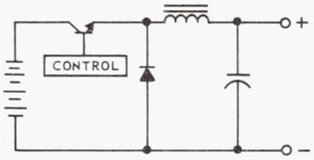	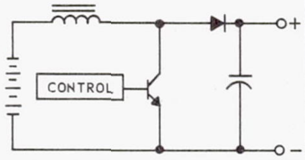	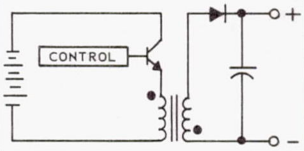
TYPE	**STEP-DOWN**	**STEP-UP**	**STEP-UP OR-DOWN**
SINGLE POINT FAILURE	**YES**	**NO**	**NO**
OVERLOAD PROTECTION	**YES**	**NO**	**YES**
INPUT VOLTAGE	**HIGH**	**LOW**	**HIGH OR LOW**
ISOLATION	**NO**	**NO**	**YES**
POWER (PER UNIT)	**1**	**1**	**0.5**
EFFICIENCY	**95**	**93**	**88**

FIGURE 3. LOAD REGULATOR CIRCUIT COMPARISON

voltage to the load, is effectively decoupled by the battery and the load regulator; therefore, the single point failure that would exist if the circuit were used for the load regulator would not apply to the battery charger.

SECONDARY BATTERY

The only proven secondary battery available with cycle life and capacity necessary for an 18-month mission is the nickel cadmium unit (Fig. 4). This battery is capable of operating for the required 8,400 cycles with its twenty-four, 20 A-hr cells connected in series.

- Battery Cycle Life Requirements $\sim$ 8,400 Cycles
  Nickel Cadmium Selected $\sim$ Twenty-Four,
  20 A-hr Cells per Battery
  At 298°K Battery Center Temperature and 10 A Charge Rate

- Energy Efficiency
  With Third Electrode $\sim$ 80%
  Without Third Electrode $\sim$ 64%

- Ampere-Hour Charge/Discharge Ratio
  With Third Electrode $\sim$ 1.14
  Without Third Electrode $\sim$ 1.41

FIGURE 4. SECONDARY BATTERY

Individual cell third electrodes are used to indicate the battery recharge state. The voltage potential at the third electrode rises sharply as the battery reaches a state of full charge, thus giving an accurate indication of the battery having reached its full capacity. This allows the charge to be terminated before the overcharge region is reached where a large portion of the electrical charging energy would be transformed into heat energy. With third electrode control, the energy efficiency is approximately 80% and the ampere-hour charge to discharge ratio is approximately 1.14, as opposed to control without third electrode with an energy efficiency of 64% and a charge to discharge ratio of 1.41.

CHARGER / BATTERY / REGULATOR MODULE

Figure 5 is a functional schematic of the CBRM showing the battery charger and load regulator characteristics. The battery charger performs a power management function by using only that power for battery charging that is not demanded by the load.

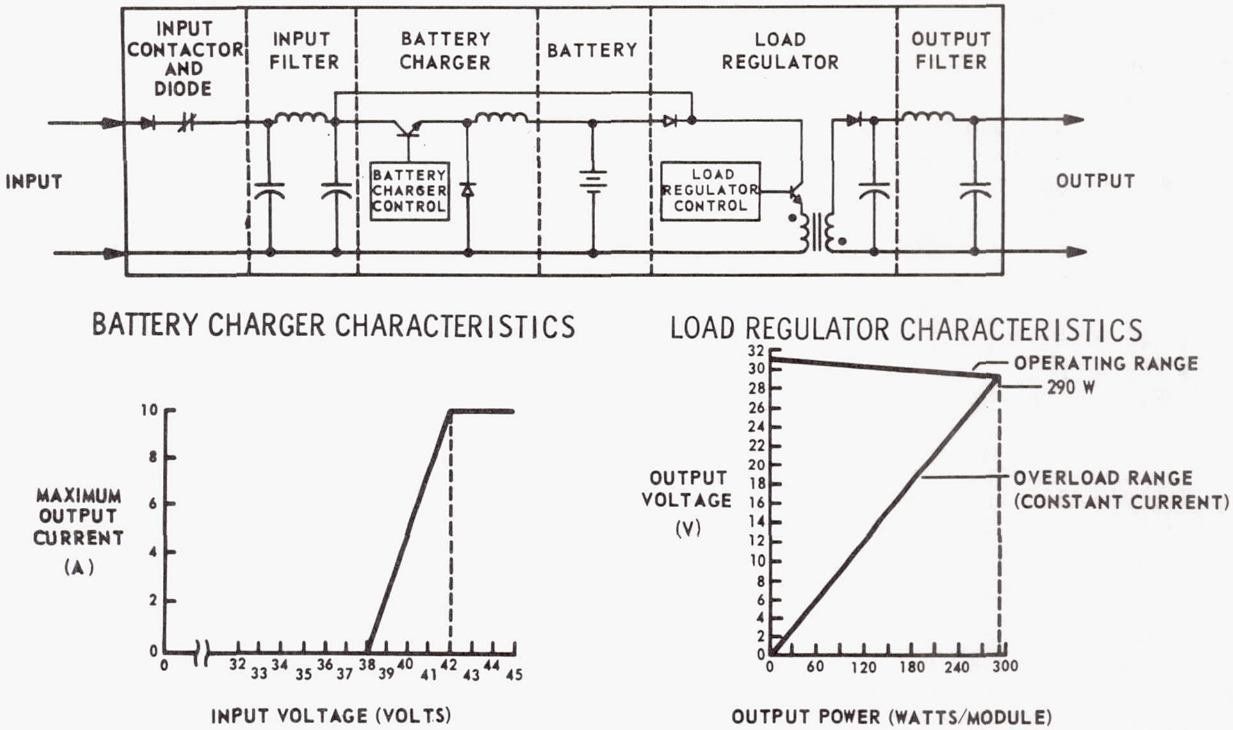

FIGURE 5. CHARGER/BATTERY/REGULATOR MODULE

The battery charger will be a step-down switching regulator, selected because of its high efficiency. The four signals used to control the battery charger are the module input voltage (solar cell array voltage), battery current, battery voltage as a function of temperature, and third electrode signal as a function of battery charge state.

The charger will charge the battery at a constant current until the battery terminal voltage reaches a predetermined level which is a function of battery temperature. The constant current level is 10 A when the solar cell array input voltage is greater than 42 V. At or above this voltage, enough power is available to charge the battery at 10 A and also supply the load. If the load increases substantially, the solar cell array voltage will drop below 42 V and the battery charger will limit the charge current to less than 10 A. At 38 V the battery charger will turn off, thus allowing the load regulator to supply all available power to the load. This sloping battery charger characteristic insures adequate power to the spacecraft's electrical loads. At the constant current charger cut-off point, the charger will commence charging the battery at a constant voltage, modified by battery temperature, until the third electrode signal level reaches a preselected level. When the selected third electrode potential is reached, the charger will cut off and remain off until reset. During the battery discharge period (earth occultation), the solar cell array voltage will drop below 38 V, resetting the charger for the next charge cycle.

The load regulator will be a step-up or -down switching regulator with an isolation transformer to isolate input from output. This configuration combines high efficiency with overload protection and maximum overvoltage protection to the output. Because of possible damage to the loads, a primary design goal is to hold the output voltage below 32 Vdc. The regulator will control the output voltage from 31 Vdc at no load to 29 Vdc at a full load of 10 A. The output voltage is controlled by feedback signals from the output voltage and current. The output voltage slope from 31 to 29 Vdc forces all CBRM's to share in supplying the spacecraft's electrical loads. In the event one regulator would attempt to supply a relatively larger amount of current than the others, its output voltage to the load bus would decrease and the other regulators would assume a proportionate share of the load.

POWER CONVERSION EFFICIENCY

The electrical parameters used to calculate the efficiency of the electrical power conversion system are given in Figure 6. Assuming 200 W per CBRM, 18 modules will be required to supply the spacecraft's electrical load of 3600 W. Using conversion efficiencies of 95% for the battery charger and 88% for the load regulator and an energy efficiency of 79.8% for the battery, the CBRM energy conversion efficiency is 70.2%. Allowing for distribution and decoupling losses, this conversion efficiency is 64.8% for the complete electrical power system. A solar cell array to spacecraft electrical load power ratio of 2.5 is achieved.

ELECTRICAL POWER CONVERSION SYSTEM SUMMARY

A summary of the electrical power conversion system characteristics and load handling capabilities is given in Figure 7. Eighteen CBRM's operating from a solar cell array of 9 kW average (58 min of a 94 min orbit) will supply a continuous spacecraft electrical load of 3600 W. A peak average daylight load of 5.22 kW (limited by load regulator maximum power output) can be supplied. For the batteries to be completely recharged within one orbit, this day load must be accompanied by a night load not exceeding 1.93 kW average power usage. The maximum discharge the battery receives is 26%, thus enhancing long battery life. For a mission of shorter duration requiring an average load of 3600 W, the number of CBR modules could be reduced by increasing the power output capability of each regulator and allowing for greater drain on the battery.

- NUMBER OF CBR MODULES REQUIRED . . . 18
- INPUT:
  SOLAR ARRAY VOLTAGE . . . . 40-75 Vdc
  SOLAR ARRAY POWER (P_{SA}) . . . . 9 kW AVERAGE (58 min/94 min ORBIT)
- BATTERY: MAXIMUM DISCHARGE 26%
- OUTPUT:
  VOLTAGE
  STEADY STATE . . . . 29-31 Vdc
  RIPPLE . . . . $0.1V_{PK-PK}$ MAX. @5-10 kHz
  POWER
  PEAK . . . . 5.22 kW

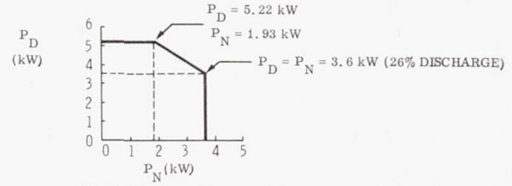

AVERAGE LOAD/ORBIT NOMOGRAPH

FIGURE 7. ELECTRICAL POWER CONVERSION SYSTEM SUMMARY

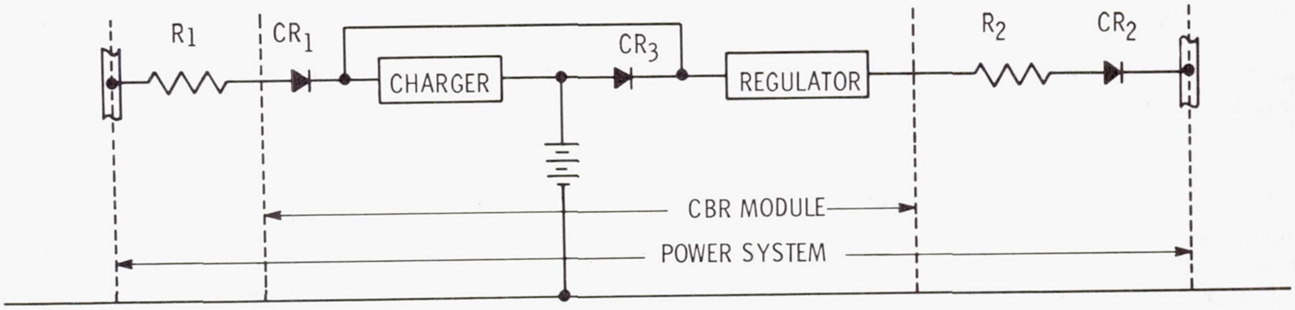

SYSTEM PARAMETERS

- 200 W/MODULE
- POWER CONVERSION EFFICIENCY - CHARGER ~ 95%, REGULATOR ~ 88%
- 24 CELL BATTERY
- $R_1 = 0.1\ \Omega$
- $R_2 = 0.05\ \Omega$
- $V_{CR1} = V_{CR2} = V_{CR3} = 1$ V DROP

SYSTEM ENERGY CONVERSION EFFICIENCY

- POWER SYSTEM ~ 64.8%
- CBR MODULE ~ 70.2%

POWER RATIO P_{SA}/P_O

- POWER SYSTEM ~ 2.5
- CBR MODULE ~ 2.3

FIGURE 6. POWER CONVERSION EFFICIENCY

INVERTERS FOR MOTORS

By

Roy Lanier

SUMMARY

Electric motors are used in many space vehicle systems. A comparison is made of several typical motors used to power auxiliary equipment up to 1.5 kW, and the advantages and disadvantages of each type motor are mentioned. The inherent simplicity and reliability of the ac induction motor are recognized and methods of overcoming its disadvantages are discussed. The development of inverters to drive ac induction motors, and techniques used to provide desired performance are described. Incorporation of these techniques makes the reliable ac induction motor ideal for most motor applications.

INTRODUCTION

A demand exists for reliable, long life motors to power the auxiliary equipment used in launch vehicles and spacecraft. Several types of electric motors are available for use in pumps, blowers, positioners, traction drives, tracking drives, and general drives. The requirements for motors for these applications vary with the specific load characteristic, but some general requirements are listed in Table I.

TABLE I. ELECTRIC MOTOR REQUIREMENTS

Supply Voltage	28 to 56 Vdc
Power Output	1 to 1500 W
Operating Life	Up to 10,000 hr
Speed	Constant or variable
Efficiency	High over wide speed range
Starting Torque	High
Surge Current	Limited
Motor Rotation	Reversal required
Environmental Operation	Vacuum, high temperature, low temperature, vibration

Generally an electric motor is selected based on the system requirements. Quite often this results in compromises in one or more areas. These compromises can be largely overcome by selecting a 3-phase ac squirrel cage induction motor with the proper power supply inverter as described in this paper.

COMPARISON OF MOTORS

Three types of electric motors widely used in the drive applications are the conventional (brush type) dc motor, the brushless (permanent magnet, electronically commutated) dc motor, and the inverter supplied squirrel cage ac induction motor. The commutator and brushes of a conventional dc motor severely limit its use since most of the applications require operation in a vacuum and/or in a severe vibration environment. The permanent magnet brushless dc motor can be designed to overcome these disadvantages. However, it has the disadvantages of being more complex and of having a permanent magnet rotor that may be demagnetized. The squirrel cage ac induction motor is the most rugged and reliable motor of the three, having neither the brushes and commutator nor the permanent magnet rotor. In the past, the induction motor, although more rugged, has been limited to the relatively low starting torque, constant speed applications when high efficiency was required. However, by using an inverter capable of sensing and controlling various motor parameters such as drive frequency, voltage, and current, the induction motor may be preferred for most applications. Sensing and control of the various parameters and the expected results are discussed in the following section.

INVERTER DRIVEN AC INDUCTION MOTOR

Even though the starting current is high, a basic ac induction motor designed for high efficiency has characteristics of relatively low starting torque and relatively constant operating speed. This is shown later in the speed-torque curve for a conventional ac induction motor. An inverter design capable of driving the motor in such a manner as to overcome these deficiencies plus provide the capability of motor reversal is the goal of this effort as described in the following.

A 3-phase inverter output stage with its transistor switching sequence is shown in Figure 1. The circuit shows a method of connecting a motor directly across

TRANSISTOR SEQUENCING

Q1	ON	ON	OFF	OFF	OFF	OFF
*Q2	OFF	OFF	OFF	ON	ON	OFF
Q3	OFF	OFF	ON	ON	OFF	OFF
*Q4	ON	OFF	OFF	OFF	OFF	ON
Q5	OFF	OFF	OFF	OFF	ON	ON
*Q6	OFF	ON	ON	OFF	OFF	OFF

0 60 120 180 240 300 360
PORTION OF CYCLE-DEGREES

*TRANSISTORS SWITCHED OFF AND ON DURING CONDUCTION TIME TO PROVIDE MODULATION

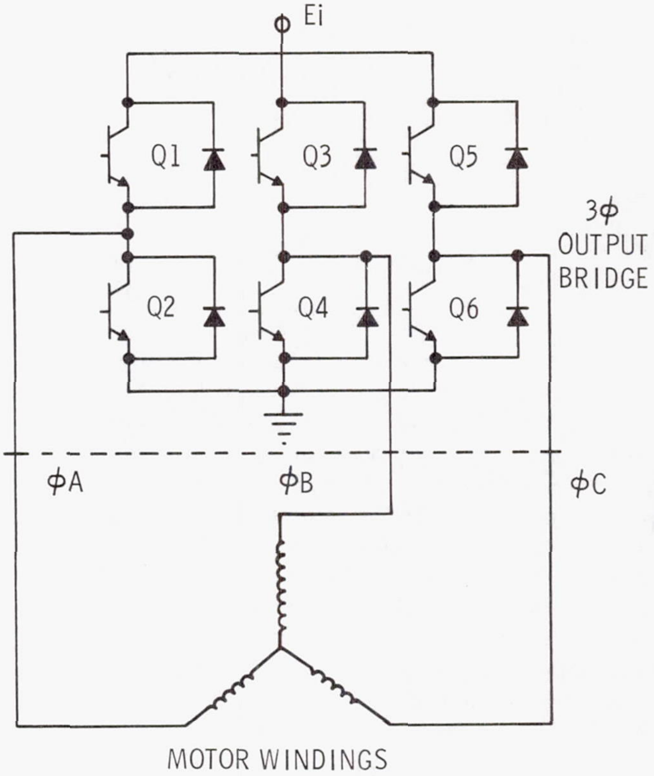

FIGURE 1. TYPICAL 3-PHASE OUTPUT BRIDGE AND MOTOR WINDINGS WITH TRANSISTOR SEQUENCING

a low voltage dc supply (28-56 V) without using a transformer, thus saving weight and improving efficiency and reliability. Transistors Q_2, Q_4, and Q_6 may be rapidly switched off and on during their conduction phases to provide efficient voltage control.

Figure 2 shows the control parameters used and the resulting voltage waveforms. The average voltage across the motor windings will be raised or lowered as the commutation off-time is decreased or increased, respectively. Thus with the necessary inputs to

CONTROL PARAMETERS

CONDUCTION TIME THUS ADJUSTING EFFECTIVE VOLTAGE

WAVEFORM PERIOD THUS ADJUSTING FREQUENCY

SWITCHING SEQUENCE THUS CHANGING DIRECTION OF MOTOR ROTATION

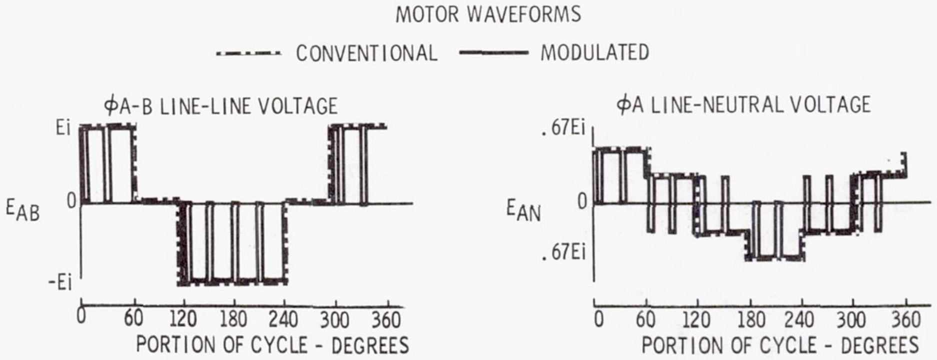

FIGURE 2. TYPICAL CONTROL PARAMETERS AND MOTOR WAVEFORMS

the 3-phase inverter bridge transistors, the effective voltage to the motor may be varied efficiently, the drive frequency to the motor may be changed by varying the cycle period, and the direction of rotation may be altered by varying the phase sequence. Proper use of this flexibility will result in the desired characteristics.

Figure 3 is a block diagram of an inverter driven ac induction motor with a current limiting feature. The curves show a typical transistor current peak with and without this feature. The oscillator, 3-phase logic, power source, and 3-phase power amplifier are typical for any inverter application. The current detector senses the input current from the power source and controls the voltage applied to the motor by modulating the 3-phase power amplifier and inverter bridge transistors as previously discussed. The result of the operation through the 3-phase logic is to reduce the voltage to prevent a peak current from being exceeded. The peak current is limited to protect the power transistors or the power supply.

Figure 4 is a block diagram of an inverter driven ac induction motor with a high starting torque. The torque speed curve of a conventional, single frequency driven motor and that of a slip frequency controlled motor are shown. In an efficient conventional motor the relative torque is low at zero speed (slip frequency equals operating frequency).

The starting torque per phase of a polyphase ac induction motor is:

$$T_{st} = \frac{K_1 p\, I_2^2\, r_2}{4\pi\, f_1} \qquad (1)$$

where T_{st} = starting torque per phase

p = number of poles

I_2 = rotor current per phase

r_2 = effective rotor resistance per phase

f_1 = applied frequency

K_1 = a constant.

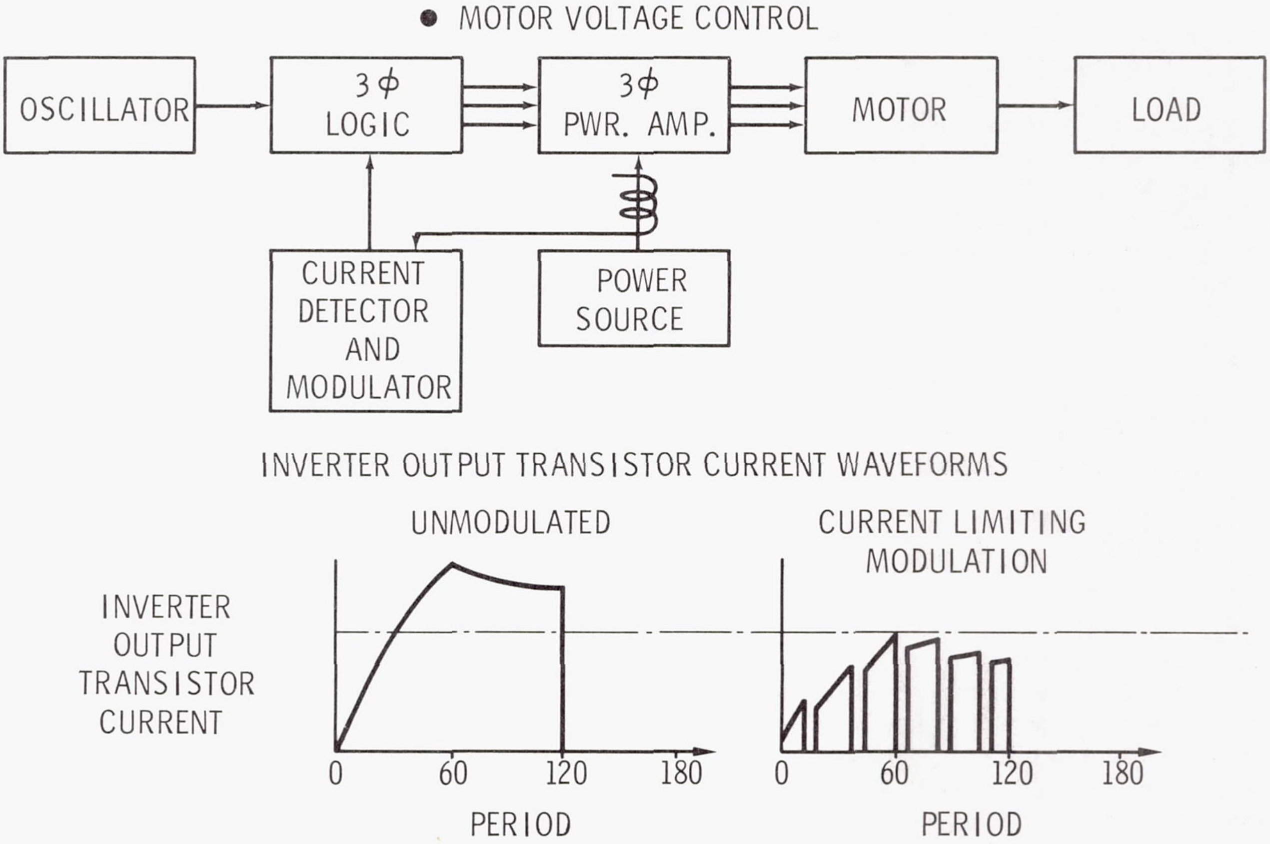

FIGURE 3. MOTOR - INVERTER SYSTEM FOR OBTAINING CURRENT LIMITING

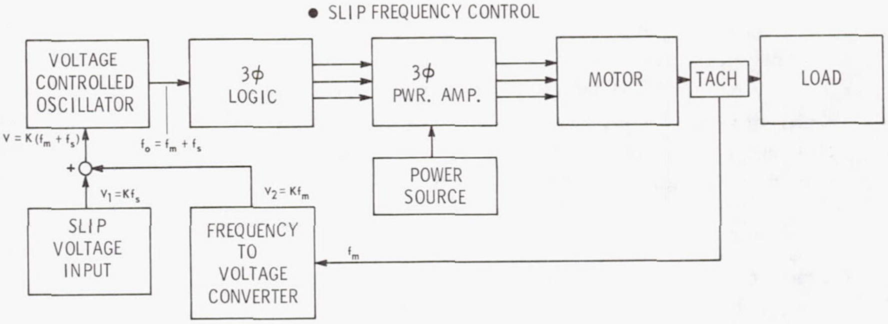

SPEED-TORQUE CURVES OF CONVENTIONAL AND SLIP FREQUENCY CONTROLLED AC INDUCTION MOTORS

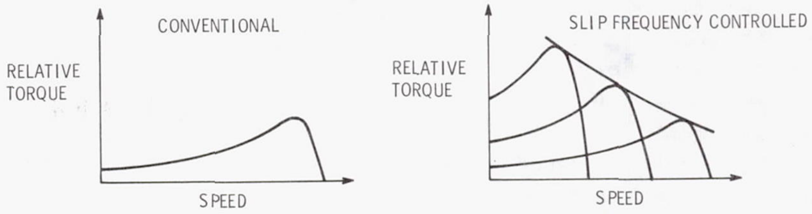

FIGURE 4. MOTOR-INVERTER SYSTEM FOR OBTAINING HIGH STARTING TORQUE

Equation 1 will reduce to

$$T_{st} = K_2 \, I_2^2/f_1 \qquad (2)$$

where K_2 = a constant for a given motor because the number of poles and rotor resistance are fixed.

Equation 2 shows that the starting torque of a motor may be controlled by controlling either of two parameters, rotor current or applied frequency. However, from an approximately equivalent circuit of an induction motor (neglecting the exciting current), the rotor current in terms of applied voltage at start is

$$I_2 = \frac{V_1}{\sqrt{(r_1 + r_2)^2 + 4\pi^2 f_1^2 (\chi_1 + \chi_2)^2}} \qquad (3)$$

where V_1 = applied voltage
r_1 = stator resistance
r_2 = rotor resistance reflected to the stator
χ_1 = stator reactance
χ_2 = rotor reactance reflected to the stator

The rotor current is then a function of both the applied voltage and the frequency, increasing with increasing voltage and decreasing frequency. Some practical lower frequency limit must be recognized because of magnetic circuit considerations. In addition, a maximum current limit must be recognized based on winding size and thermal considerations and/or inverter power transistors. This maximum current is observed by reducing the voltage as previously discussed or by reducing the source voltage which is normally constant. By decreasing the applied frequency, the motor will be forced to start at a lower slip frequency. As previously shown, frequency, although constant in many systems, is a parameter that may be conveniently controlled in an inverter. The circuit shown in Figure 4 provides the capability of obtaining a voltage proportional to the motor rotational frequency, f_m, and adding it to a voltage proportional to the desired slip frequency, f_s, selected on the basis of motor characteristics and load requirements. The sum of these voltages is proportional to the frequency required to drive the motor at f_m with the desired slip frequency at that instant. By using this voltage sum as the input to the voltage controlled oscillator, an output frequency, f_o, is obtained to drive the motor after proper logic operation. This forces the motor to operate at a frequency only slightly above its running frequency, even at start, thus assuring a high relative starting torque. Typically the frequency may be decreased to as little as one tenth the normal operating frequency, giving a starting torque of approximately ten times normal starting torque and up to five times rated load torque for a typical conventional motor. Equation 3 gives the relationship of applied voltage, frequency, and rotor current, and shows that there is an integral relationship among the three. Thus the feedback control of frequency and voltage are interrelated and require careful consideration for each case. However, with proper consideration, a torque-speed characteristic to match any practical load may be obtained, as may be deduced from this discussion and the curve shown in Figure 4. Work is continuing in this area.

- SLIP FREQUENCY CONTROL
- MOTOR VOLTAGE CONTROL
- HIGH EFFICIENCY OVER WIDE SPEED RANGE

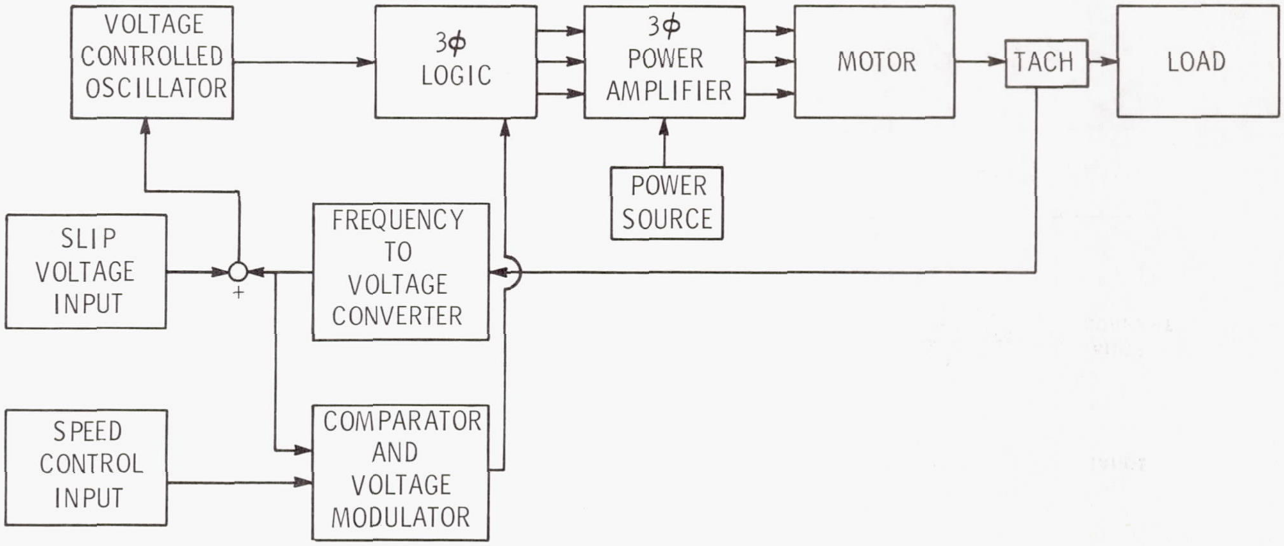

FIGURE 5. MOTOR - INVERTER SYSTEM FOR OBTAINING SPEED CONTROL

Figure 5 is a block diagram of an inverter driven ac induction motor capable of efficient operation over a wide range of speed. The operation is similar to that of the slip frequency controlled circuit in Figure 4, except an additional input to the 3-phase logic to provide voltage modulation is provided. This method may be used to provide a constant or multi-speed characteristic by furnishing one or more reference inputs to the comparator and voltage modulator, which in turn will generate the necessary digital signal input to the 3-phase logic to vary the voltage at any time an error between the actual and desired frequencies or speeds exists. However, its chief advantage would be the capability of operating at high efficiencies over a wide range of speed, thus making it desirable for traction drive applications.

A block diagram of an inverter driven ac induction motor with motor reversal capabilities is shown in Figure 6. The logic diagram shows a method of changing the phase sequence from A-B-C to B-A-C, thus reversing the motor rotation. The most important feature of this straightforward method is that the reversal is accomplished at a very low power level by operating on the low-level logic.

Figure 7 is a block diagram of a typical inverter driven ac induction motor system incorporating all of the features discussed. The system is capable of developing a high starting torque to current ratio, possesses a high efficiency over a wide range of speed, and has remote control of rotation direction and speed, torque or power.

FUTURE EFFORTS

Although all of the techniques discussed have been shown to be technically feasible, much work remains to be done to produce operational systems. Proper frequencies, modulation methods, materials, etc., must be determined to obtain optimum use of available capabilities. Most work to date has been with small (100 W) motors. Future efforts will develop capabilities in systems using motors with ratings up to 1.5 kW. In addition, the following efforts are planned for the future:

1. Continue investigation of inverter and control techniques.

2. Define detailed inverter configuration for various load requirements.

3. Define desired motor characteristics for various load requirements.

4. Design inverters for higher power applications.
5. Determine design criteria for various environmental considerations.
6. Investigate electronic components to determine proper characteristics for motor drive applications.
7. Design inverter control elements using integrated circuits for compactness and reliability.

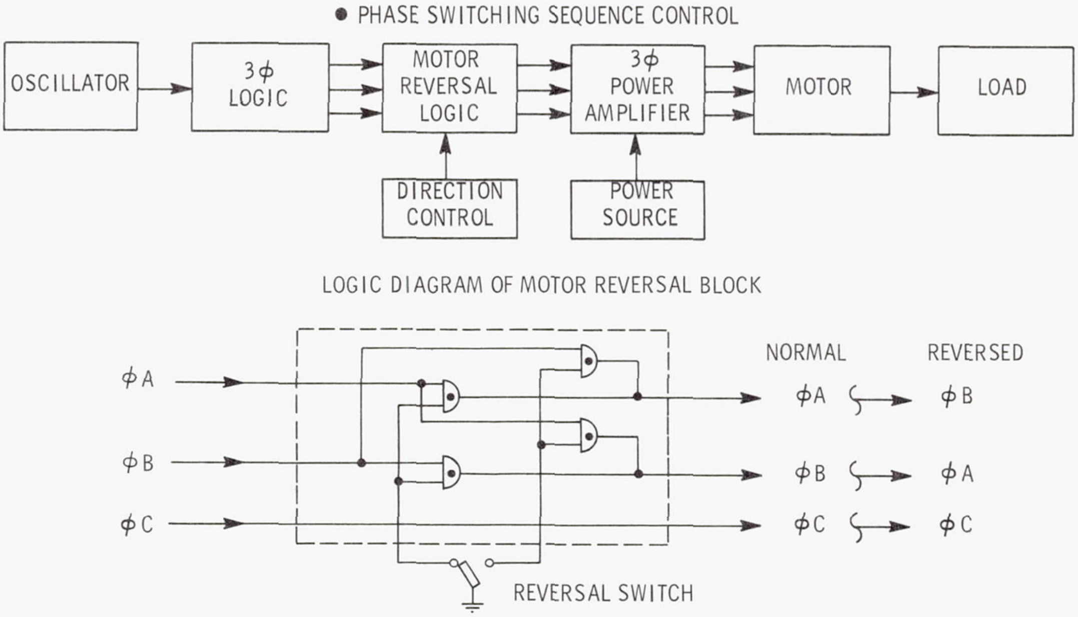

FIGURE 6. MOTOR - INVERTER SYSTEM FOR OBTAINING MOTOR REVERSAL

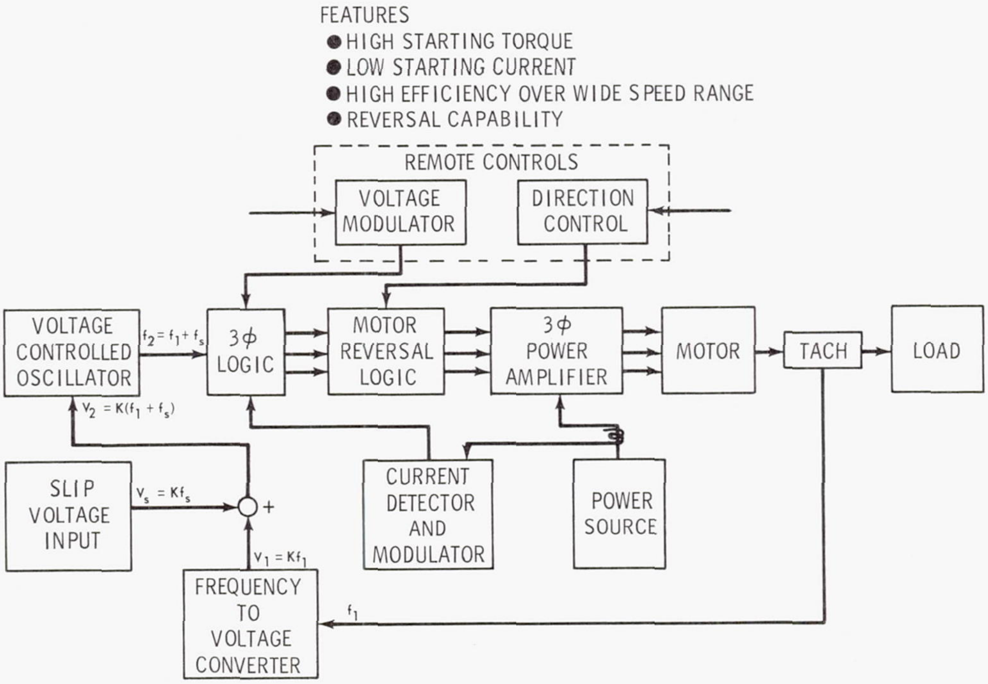

FIGURE 7. TYPICAL MOTOR - INVERTER SYSTEM

Page
Intentionally
Left Blank

TERRESTRIAL AND SPACE ENVIRONMENT RESEARCH AT MSFC

September 28, 1967

By

Margaret Alexander
S. Clark Brown
Dennis W. Camp
Charles C. Dalton
Lee W. Falls
George H. Fichtl
Ernst D. Geissler
C. Kelly Hill
J. W. Kaufman
William T. Roberts
O. E. Smith
Robert E. Smith
George S. West, Jr.

CONTENTS . . .

CONTENTS (Continued) . . .

LIST OF ILLUSTRATIONS

A STATISTICAL ANALYSIS OF WINDS FOR AEROSPACE VEHICLE DESIGN, MISSION PLANNING, AND OPERATIONS

by O. E. Smith, Lee W. Falls, and S. Clark Brown

LIST OF TABLES

CONTENTS (Continued). . .

LIST OF ILLUSTRATIONS

CONTENTS (Continued). . .

DIURNAL VARIATION OF DENSITY AND TEMPERATURE IN THE UPPER ATMOSPHERE

by Robert E. Smith

CONTENTS (Continued). . .

LIST OF ILLUSTRATIONS

IONOSPHERIC DISTURBANCES CAUSED BY GROUND BASED ACOUSTIC ENERGY SOURCES

by William T. Roberts

LIST OF ILLUSTRATIONS

THE MASSES OF METEORS AND THE SELECTION OF A REPRESENTATIVE DATA SAMPLE

Page

by Charles C. Dalton

LIST OF ILLUSTRATIONS

CONTENTS (Continued) . . .

Page

MARTIAN ATMOSPHERIC VARIABILITY

by George S. West, Jr.

LIST OF ILLUSTRATIONS

INTRODUCTION TO RESEARCH ACHIEVEMENTS REVIEW ON AEROSPACE ENVIRONMENT RESEARCH AT MSFC

By

Ernst D. Geissler

This review is concerned with problems of terrestrial and space environment and is the second of this kind on this subject. The first review was held in September 1965 and covered four topics. The present review covers seven items on terrestrial and space environment research.

The seven papers in this review are only samples of related activities in the Aerospace Environment Division of the Aero-Astrodynamics Laboratory. Several important topics are not included in this review, for example, investigation of fine structure of winds at altitudes around maximum dynamic pressure (jet stream level) and the broad problems of analysis and prediction of the atmosphere at orbital altitudes which are so important for orbital lifetime predictions.

The first topic was discussed in the previously mentioned research review, but many high resolution measurements of wind profiles have been obtained since then and valuable insights have been gained.

The second topic has been given coverage in a recent seminar program under the title "Environment Induced Orbital Dynamics" June 6&7, 1967 at MSFC [1].

Also, environmental research activities are carried out in the Space Sciences Laboratory, in particular in the areas of space radiation and micrometeoroids. Discussions of these activities will be given in another meeting.

The responsibility within MSFC for formulating aerospace environment criteria is part of the Aero-Astrodynamics Laboratory's function and is directly related to the laboratory's work in the area of systems engineering and mission analysis. The Aerospace Environment Division is the responsible organizational element within the laboratory for conducting studies and research directed toward establishment of design and operational aerospace environment criteria.

The significance of having an integral group within the organization responsible for the study of atmospheric and space environment relations to engineering program requirements was recognized many years ago. Whereas earlier the concern was primarily with the atmosphere, in recent years increasing interest has also been directed towards aeronomy, planetary atmospheres and general space environment.

The development of an adequate set of space vehicle design and operational criteria is a job which requires a close relation between the scientific community and the engineers. The Aero-Astrodynamics Laboratory is striving to do enough research and to monitor enough outside research to provide the necessary input into various vehicle design and operational studies. Development of proper conceptual statistical tools is an important aspect of this endeavor.

While it may appear that there is only one set of terrestrial and space environment data, which would apply to all vehicles and increase in scope only with extension of the sphere of operations, actual experience shows a constant widening of the type of questions asked and data needed.

Even today, after many years of research and several generations of space vehicles, the major portion of the laboratory's effort is still devoted to the area of atmospheric dynamics for that early portion of the flight, where the vehicle is exposed to the largest external forces.

The significance of ground wind effects has increased with increasing size of the vehicles, and the sensitivity of the large Saturn V vehicle to ground wind effects required introducing a mechanical damping system for the vehicle on the ground as a fairly late design modification. In addition to this, a program was initiated to measure and interpret atmospheric turbulence phenomena close to the ground because the atmospheric turbulence is a vehicle load producing factor during its stand on the launch pad and immediately after take-off. Also, the vulnerability to high ground winds required a thorough knowledge of exposure probabilities and related statistical techniques. The first three papers in this review will be devoted to this subject area.

The remaining papers will be concerned with more exotic items. The discussions of diurnal variation of density and temperature in the upper atmosphere [120 - 330 km] is just one sample of recent experimental results out of a very broad effort directed to gain understanding of high altitude atmospheric properties. They are subject to strong statistical and periodic variations and are of immediate interest for lifetime predictions, altitude control and station keeping studies connected with the AAP program.

The next discussion about ionosphere disturbances represents a modest attempt to make a contribution towards the understanding of the dynamics of the upper atmosphere, the flow fields and interaction of the electrically charged particles with general pressure disturbances of the neutral component of the upper atmosphere.

The presentation about masses of meteors and sample selections is considered a valuable contribution towards the proper interpretation of optical meteor sightings which contains about the most critical particle size from the designers point of view and where some question exists about interpretation of observational data.

Finally, there will be some discussion of models available for the Martian Atmosphere. These models have been studied recently as a contribution for the planning of a planetary exploration program. The obvious message here is the lack of precise information and the indication of many gaps to be filled.

Much of the Aero-Astrodynamics Laboratory's design and operational criteria work is formulated into environmental criteria guideline reports. One report considers the terrestrial atmosphere up to an altitude of 100 km. The other covers altitudes above 100 km, including the space environment, lunar, and planetary environments. These documents have been widely used in MSFC's programs, by other NASA organizations and by the DOD.

REFERENCE

1. Environment Induced Orbital Dynamics, Volumes I and II. Seminar Program, June 6-7, 1967, Marshall Space Flight Center, prepared by the Aero-Astrodynamics Laboratory, Volume I 31 July 1967, Volume II 31 October 1967.

STRUCTURE OF ATMOSPHERIC TURBULENCE

By

George H. Fichtl

SUMMARY

The properties of the longitudinal component of turbulence are examined. It is found that the ratio of the variance of turbulence to the surface friction velocity is an increasing function of z/L' for unstable conditions and a constant for stable conditions. For neutral conditions, this ratio is 3.1. Tentative design values for the variance of turbulence are based upon this ratio for neutral conditions and KSC design ground wind envelopes. A theory of the variation of the gust factor with height based upon Rice's theory of exceedance probabilities is presented.

Finally the spectrum of turbulence is analyzed. An examination of the spectra of Dryden, von Kármán, and Lappe revealed that the turbulence data fit the three spectra equally.

INTRODUCTION

Within the atmospheric boundary layer, defined in this paper to be the first 150 m of the atmosphere, a thermally stratified shear flow exists. Energy is transferred from the mean shear flow to the turbulent portion of the total flow field via the gradients of mean velocity and entropy which produce Reynolds stresses and cause heat transfer to occur, respectively. Accordingly, the structure and intensity of turbulence in the atmospheric boundary layer are directly dependent upon the mean flow conditions. In principle, once the boundary conditions and the distributions of mean velocity and temperature are specified, the statistics, such as second and higher order velocity moments, of the turbulent portion of the total flow can be determined through the hierarchy of the turbulence moment equations. In general, a closure hypothesis is required since the moment of equations constitute an infinite set of equations. The above comments imply that, associated with each mean (steady state) wind profile, i.e., 95.0, 99.0, and 99.9 percentile profiles, there is a unique set of design statistics that characterize the turbulence structure of steady state design wind profiles. This means that the steady state design wind profiles and turbulence design statistics, in the form of spectral inputs or in the form of discrete gust inputs, should be prescribed so that they consistently reflect the coupling implied by the equations of motion. This may be accomplished experimentally, in part, by relating the longitudinal variance of turbulence to the mean flow since the square of the variance of turbulence is the net energy contained within the longitudinal spectrum. Accordingly, the first purpose of this paper is to relate the variance of the longitudinal component of turbulence and the gust factor to existing steady state design wind profiles for Kennedy Space Center. Based upon experimental observations, the longitudinal spectrum can be prescribed and related to the mean flow by allowing adjustable parameters like the integral scale of turbulence, for example, to appear in the analytical representation of the spectrum. Once the mean flow is related to the variance of turbulence and the scale of turbulence, the turbulence design input associated with a given steady state wind profile may be prescribed consistently.

Therefore, the second purpose of this paper is to test the analytical expressions of the longitudinal spectrum of turbulence derived by Dryden, von Kármán, and Lappe as to the adequacy of these expressions being reasonable representations of turbulence at KSC.

If, on the other hand, a gust factor is desired rather than a spectral wind input to describe turbulence, the variance of turbulence may still be used to couple the steady state wind profile to the turbulent portion of the flow field by introducing a suitable assumption about the statistical process of the turbulence. In particular, the assumption that turbulence is a Gaussian process is employed in this paper, and an expression is obtained that relates the gust factor to the variance of turbulence.

To relate the mean flow properties to the turbulence existing in the atmospheric boundary layer even on an experimental basis, as in this paper, a closure hypothesis must be introduced to effect a dimensional analysis that will imply the universal functions needed. In this paper the closure hypothesis of Monin and Obukhov [1] has been employed to imply relationships between the variance of turbulence and the mean flow.

VARIANCE OF TURBULENCE

The similarity hypothesis of Monin and Obukhov [1] predicts that within the steady mean-flow surface-boundary layer, characterized by constant tangential eddy stress and constant vertical heat flux,

$$\frac{\sigma}{u^*} = f\left(\frac{z}{L'}\right), \qquad (1)$$

where σ and u^* denote the variance of the longitudinal wind fluctuations and the surface friction velocity, respectively, and $f(z/L')$ is a universal function of z/L' where z is the height and L' is given by

$$L' = \frac{u^* \frac{d\bar{u}}{dz} T}{kg \frac{d\theta}{dz}} . \qquad (2)$$

In eq. (2), $\bar{u}$ is the mean wind speed, T and θ denote the mean Kelvin temperature and potential temperature, respectively, k and g denote the von Kármán constant with numerical value equal to 0.4 and the acceleration of gravity, respectively, and u^* plays the role of a scaling velocity that is related to the surface stress τ through the relationship

$$u^* = \left(\frac{\tau}{\rho}\right)^{1/2} ,$$

where ρ is the mean density of air. Formally,

$$\tau = -\rho \overline{u'w'}$$

where u' and w' denote the longitudinal and vertical components of the turbulence portion of the velocity vector and the overbar denotes the time-averaging operator. In the absence of w' data, which is the situation at Kennedy Space Center at the present time, it is necessary to estimate u^* through a knowledge of the mean wind and temperature profiles.

Upon employing the Boussinesq approximation as discussed by Dutton and Fichtl [2] and invoking the conditions of Reynolds number similarity [3], steady state and horizontally homogeneous flow with negligible mean horizontal pressure gradient and hypothesizing that the ratio of the eddy heat conduction coefficient to the eddy momentum coefficient is a unique function of the gradient Richardson number, the similarity hypothesis of Monin and Obukhov predicts that

$$\frac{kz}{u^*}\frac{d\bar{u}}{dz} = \phi\left(\frac{z}{L'}\right), \qquad (3)$$

where $\phi(z/L')$ is a universal function of z/L'. Upon integrating the above expression, subject to the boundary condition that the mean wind must vanish at z_0 (the mean height of the roughness elements at the surface of the earth), it is easily shown that

$$\bar{u} = \frac{u^*}{k}\left(\ln\frac{z}{z_0} - \psi\left(\frac{z}{L'}\right)\right), \qquad (4)$$

where

$$\psi\left(\frac{z}{L'}\right) = \int_0^{-z/L'} \frac{1-\phi(\xi)}{\xi}\, d\xi. \qquad (5)$$

The definitions of L' and ϕ permit one to write

$$\frac{z}{L'} = \phi\left(\frac{z}{L'}\right) \mathrm{Ri}, \qquad (6)$$

where Ri is the gradient Richardson number defined to be

$$\mathrm{Ri} = \frac{\frac{g}{\theta}\frac{d\theta}{dz}}{\left(\frac{d\bar{u}}{dz}\right)^2} . \qquad (7)$$

It follows from eq. (6) that

$$\frac{z}{L'} = h(\mathrm{Ri}), \qquad (8)$$

where $h(\mathrm{Ri})$ is a universal function of Ri. Ri is a parameter that characterizes the stability in a gravitational stratified shear flow [2] so that eq. (8) implies that z/L' is an equally valid parameter for specifying stability provided that z/L' is a single-valued function of Ri. This requirement is satisfied in general. The functions $h(\mathrm{Ri})$, $\psi(z/L')$ and $\phi(z/L')$ are given by Lumley and Panofsky [4].

For the sake of conciseness, these functions will not be presented in this paper, but they are known and are determined from data that consist of simultaneous measurements of heat flux, surface stress, and the mean wind and temperature profiles. The procedure for determining u* based upon measurements of the mean wind and temperature profiles, with a known value of the surface roughness length, is as follows: (a) determine Ri and evaluate z/L' with eq.(8), (b) determine $\phi(z/L')$ from eq.(6) and thus $\psi(z/L')$ with eq (5), and (c) calculate u* with the aid of eq.(4).

The scaling velocity u* has been determined for seven cases of turbulence at KSC, and the ratio σ/u^* for these cases as a function of z/L' is shown in Figure 1. It appears that, for fixed L' and u*, that σ is a decreasing function of height for unstable conditions ($z/L' < 0$), while σ is invariant with height for stable conditions ($z/L' > 0$). In addition, it appears in the case of neutral conditions ($z/L' = 0$), that σ/u^* has a wide spread of values; however, this spread may be false as a result of trends that existed in the data and which could perhaps cause unusually high values of σ. In the case of neutral stability, the Monin-Obukhov similarity hypothesis predicts σ/u^* to be a constant, f(0). Based upon a mean value of σ/u^* for neutral conditions, f(0) = 3.1. Values of f(0) reported by other authors are 2.45 by Davenport [5], 2.3 by Monin [6], 2.9 (O'Neill, Nebraska), 2.5 (Australia), 2.1 (Brookhaven), and 2.2 (pipe flow) by Lumley and Panofsky [4], and 2.7 by Prasad [7]. This wide range of values of f(0) can be attributed to differences in the horizontal

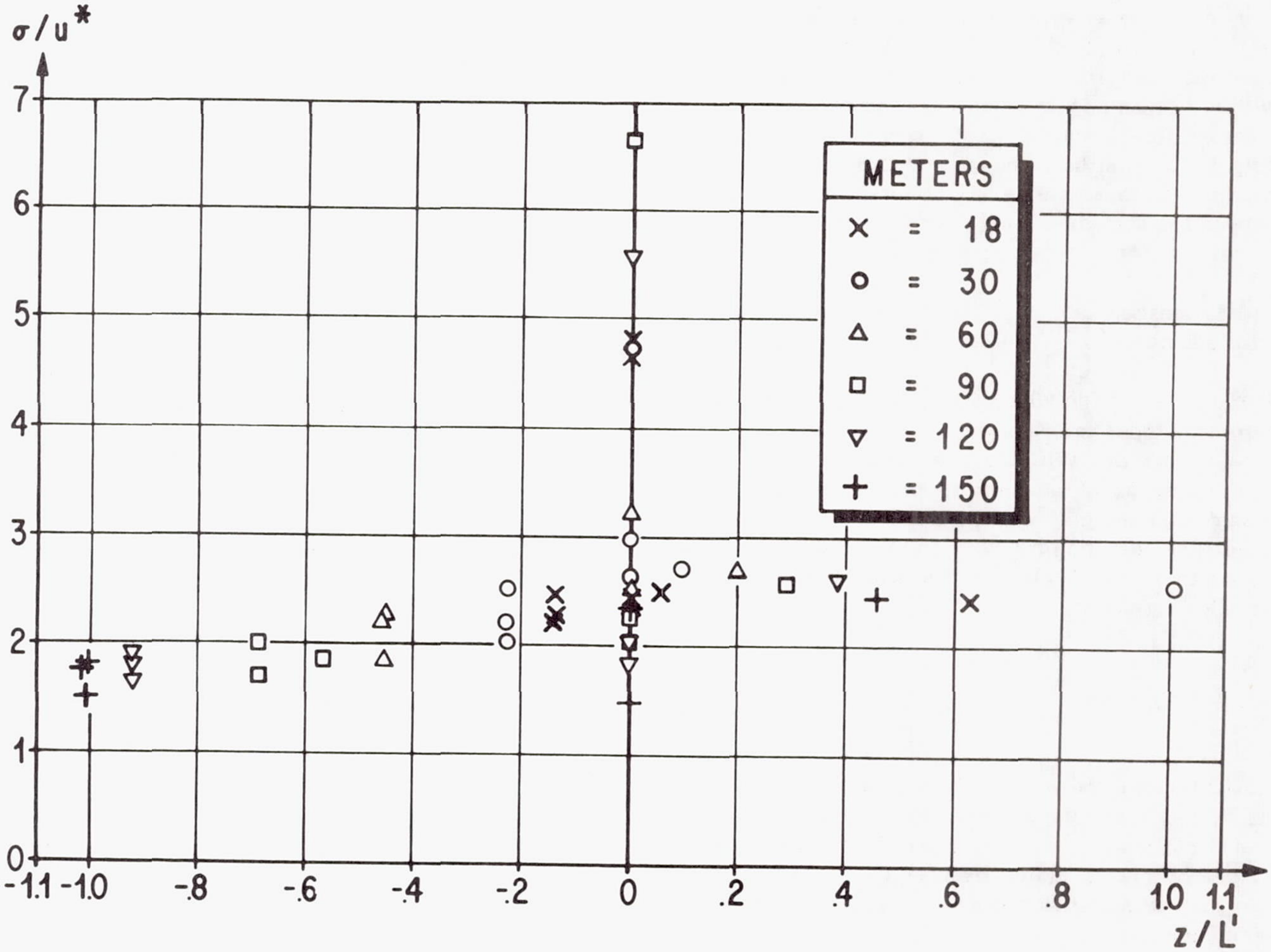

FIGURE 1. σ/u^* VERSUS z/L'

distribution of obstacles (houses, trees, hills, etc.). Gurvitch (Panofsky [8]) has found that σ/u^* is essentially constant for unstable conditions (z/L'). However, in his analysis, he used local values of u^* and L', while in this study u^* and z/L' were determined with the wind and temperature data at 18 and 60 m. In general, the horizontal tangential eddy stress should decrease with height above the boundary layer so that the results of Gurvitch imply that σ decreases with height in the same proportion as the local friction velocity. The results in this study show that σ/u^* decreases with decreasing z/L' for unstable conditions. This appears to be in agreement with Gurvitch since u^* in this study is the surface friction velocity, thus requiring σ/u^* (surface u^*) to decrease with height.

The relationship between σ and u^* can play a useful role in the development of wind inputs for launch vehicle response calculations. In particular, it could aid in (1) the problem of developing a spectral input since σ^2 is the net energy contained within a given spectrum and (2) the development of a theory for the variation of the gust factor with height. It must be remembered that spectral inputs and gust factors are merely different ways of representing the same thing, namely, the wind fluctuations about a steady state profile.

In most instances strong winds are associated with a neutral $\left(\frac{z}{L'} = 0\right)$ atmospheric boundary layer. In the cases of the 95.0, 99.0, and 99.9 percentile wind envelopes for Kennedy Space Center [9], the wind speeds are sufficiently strong so that neutral conditions can be assumed to exist if and when they occur, and one may interpret these design wind envelopes as wind profiles. In the case of the neutral boundary layer, $\psi(0)$ vanishes and the neutral wind profile is given by

$$\bar{u} = \frac{u^*}{k} \ln \frac{z}{z_0} \quad . \qquad (9)$$

Table I shows the values of σ associated with the 95.0, 99.0, and 99.9 percentile levels of occurrence wind profiles for Kennedy Space Center based on values of u^* calculated from eq. (9) with the aid of the 18.3 m design winds and a surface roughness equal to 0.05 m.

It was pointed out previously that according to the similarity hypothesis of Monin and Obukhov, σ/u^* is an invariant with height for neutral conditions. This is strictly true within only the lowest portion of the atmospheric boundary layer where the tangential eddy stress and vertical heat flux are constants. The upper limit of this layer is in the order of 60 m at most. Above the constant stress and vertical heat flux layer, σ decreases so that above 60 m the values of σ in Table I are probably slightly conservative.

Table I. Values of σ

Percentile level of occurrence	Wind speed (m sec^{-1})	σ (m sec^{-1})
95.0	10.3	2.2
99.0	13.5	2.8
99.9	16.9	3.6

GUST FACTORS

If we assume that low level atmospheric turbulence is a stationary and random Gaussian process, then the theory of Rice [10] and the experimental results presented above provide a means for constructing a meaningful theory of the variation with height of the gust factor. Rice's theory predicts that the expected number of horizontal wind fluctuations per unit time that exceed the horizontal fluctuation velocity u' is given by

$$N(u') = N_0 e^{-u'^2/2\sigma^2} \quad , \qquad (10)$$

where N_0 is the total number of positive crossings of the turbulence trace about the steady state wind per unit time. Combining eqs. (1), (4), and (10),

$$u' = \left(-2 \ln \frac{N}{N_0}\right)^{1/2} kf\left(\frac{z}{L'}\right)\left(\ln \frac{z}{z_0} - \psi\left(\frac{z}{L'}\right)\right)^{-1} \bar{u} \quad . \qquad (11)$$

By definition the instantaneous wind u is merely the sum of the mean wind and the departure from that mean, so that upon using eq. (11), the result is

$$u(z) = G\left(z, \frac{N}{N_0}\right) \bar{u}(z), \tag{12}$$

where

$$G\left(z, \frac{N}{N_0}\right) = 1 + \left(-2 \ln \frac{N}{N_0}\right)^{1/2} k f\left(\frac{z}{L'}\right) \left(\ln \frac{z}{z_0} - \psi\left(\frac{z}{L'}\right)\right)^{-1} \tag{13}$$

G may be interpreted as the gust factor. For the case of strong winds (neutral wind conditions, $z/L' = 0$), $f(0) = 3.1$, and $\psi(0) = 0$, so that eq. (13) reduces to

$$G\left(z, \frac{N}{N_0}\right) = 1 + \left(-2 \ln \frac{N}{N_0}\right)^{1/2} \frac{k\, 3.1}{\ln z/z_0} \tag{14}$$

Figure 2 shows G as a function of z for $1 - N/N_0 = 0.5, 0.95, 0.99, 0.999$, and $z_0 = 0.05$ (tentative value of surface roughness for the NASA 150 m meteorological tower site at KSC). G may be interpreted as that gust factor which, when applied to the mean wind, will yield a peak wind that accounts for an expected fraction of gusts equal to $1 - N/N_0$. The results for $z > 60$ m are probably conservative since

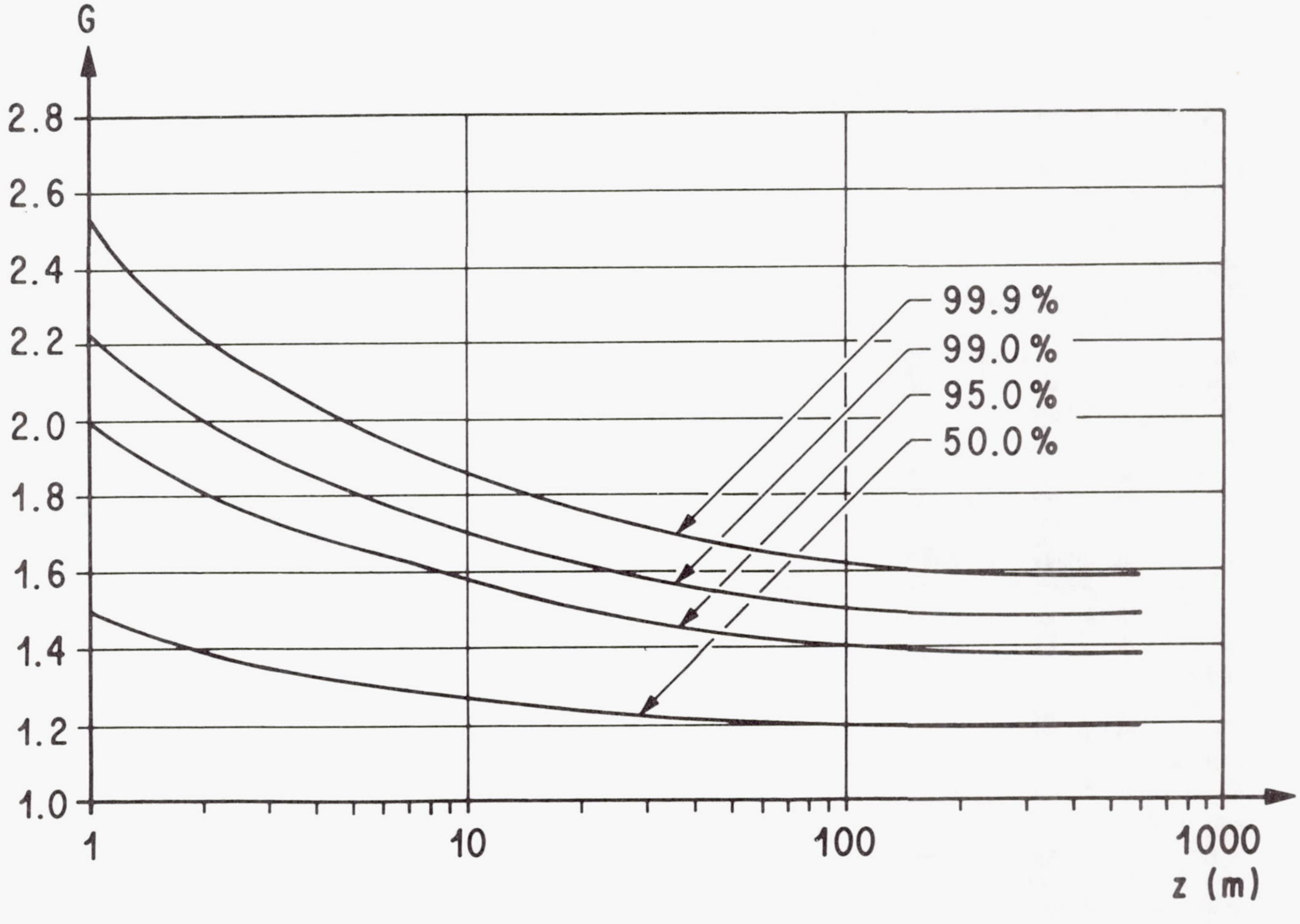

FIGURE 2. G VERSUS z

σ is overestimated as a result of breakdown of the Monin-Obukhov similarity hypothesis above 60 m. The curves for $z < 60$ m appear to be in agreement with the recent experimental results for KSC by Alexander [11].

WIND SPECTRA

In many instances it is useful to provide spectral wind inputs in the form of an analytical expression. For this purpose the analytical expressions of the longitudinal component of turbulence derived by Dryden and von Kármán [12] and Lappe [13] were selected to be tested against data from the NASA 150 m meteorological tower at Kennedy Space Center. These expressions are given by

$$\text{Dryden} \quad \Phi(\nu) = \sigma^2 \frac{4L}{1 + (2\pi L\nu)^2} \tag{15}$$

$$\text{von Kármán} \quad \Phi(\nu) = \sigma^2 \frac{4L}{(1 + 70.78\,(L\nu)^2)^{5/6}} \tag{16}$$

$$\text{Lappe} \quad \Phi(\nu) = \sigma^2 \frac{2\pi L}{(1 + 2\pi L\nu)^2}\,, \tag{17}$$

where $\Phi(\nu)$ is the spectral energy per unit wave number, L is the scale of turbulence, ν $(=\omega/\bar{u})$ is the wave number in units of cycles per meter, and ω is the frequency in units of cycles per second. The most obvious difference between these spectra is the asymptotic behavior at large values of wave number. The spectra of Dryden and Lappe both behave like ν^{-2} for large wave number, while the von Kármán spectrum behaves like $\nu^{-5/3}$, in accordance with the concept of the inertial subrange by Kolmogorov (MacCready, 1962) [14]. Although the von Kármán spectrum behaves correctly for large wave numbers, both the Dryden and Lappe spectra facilitate analytical computations because of their rational form.

To compare the above mentioned representations with observations, time spectra obtained at 18, 30, 60, 90, 120 and 150 m were averaged in the vertical and converted to space spectra with the aid of Taylor's hypothesis [15] employing the 60 m level mean wind. These spectra were fitted to the analytical expressions given by eqs. (15) through (17) by the method of least squares and yielded a value for the scale of turbulence for each type of spectrum under consideration. Experimental values of the horizontal integral scales of turbulence were obtained by vertically averaging the associated time correlation functions and then employing Taylor's hypothesis to convert time correlations to space correlations with the aid of the 60 m level wind speed and finally producing the integral

$$L = \int_0^\infty R(\xi)\,d\xi\,, \tag{18}$$

where ξ denotes lag distance. To account for trends that produce a constant value for the correlation function, R^*, greater than zero for large ξ, the observed correlation function $R_0(\xi)$ was corrected by the relationship

$$R(\xi) = \frac{R_0(\xi) - R^*}{1 - R^*} \tag{19}$$

derived by Webb [16]. Figure 3 shows a plot of the scale of turbulence obtained from the analytical expressions of von Kármán against the values of L calculated with the aid of eq. (18). Similar results were obtained for the Dryden and Lappe spectra.

The results appear to show a one to one correspondence between the two scales of turbulence in each case, and it appears that each spectrum may fit the data equally well. The results of the von Kármán spectrum appear to be in agreement with recent observations from Project Lo-Locat [17]. However, the results with regard to the Dryden and Lappe spectra appear to disagree in that the project Lo-Locat data revealed a poor fit to these analytical expressions. This may be attributed to the fact that the comparison in Project Lo-Locat was primarily in the inertial subrange, while the comparison in this paper was concerned with a wider range of wavelengths which included the inertial subrange as well as the knee of the spectrum.

CONCLUDING COMMENTS

The variance of turbulence has been shown to be related to the mean wind profile through the surface friction velocity and the Monin-Obukhov similarity hypothesis. This permits a prediction to be made of the energy associated with the horizontal wind fluctuations that would be consistent with a design wind envelope, assuming that a design wind envelope may be interpreted as a wind profile. The technique presented in this paper is valid up to the 60 m level. However, above this level, an allowance should be made for the effects of the variation with height of the horizontal Reynolds stress, the Coriolis forces, and the pressure gradient forces upon the mean flow. Blackadar's [18] recent theory of the wind profile above the surface layer appears to account for these factors. In addition to these problems, it is necessary to be sufficiently judicious in the selection of parameters so that all the pertinent parameters are included in a dimensional analysis that would predict the dimensionless groupings of these parameters upon which σ/u^* is dependent. The wind profile law could aid in the solution of this problem. For example, the surface Rossby number

$$R_0 = \frac{u_g}{2\,\Omega z_0 \sin\phi} \quad ,$$

appears in the wind law of Blackadar [18], and it is reasonable to assume that σ/u^* also depends upon this parameter since the mean flow drives the turbulent portion of the flow. In defining R_0, u_g Ω, and ϕ denote the geostropic wind at the top of the boundary layer, the angular velocity associated with the rotation of the earth on its axis, and the latitude, respectively. Finally, the variance of turbulence is dependent upon the surface roughness length. This means that a design value for σ derived from the NASA 150 m tower data may not be applicable at a given launch site because this σ was obtained for roughness conditions different from those on the launch pad. However, this effect may be taken into account by assuming that σ/u^* for neutral wind conditions (strong winds) is a true constant and evaluating u^* with the neutral wind profile using the launch site roughness. In this calculation it is implicitly assumed that the turbulence over the launch pad would be in equilibrium; this assumption is open to question.

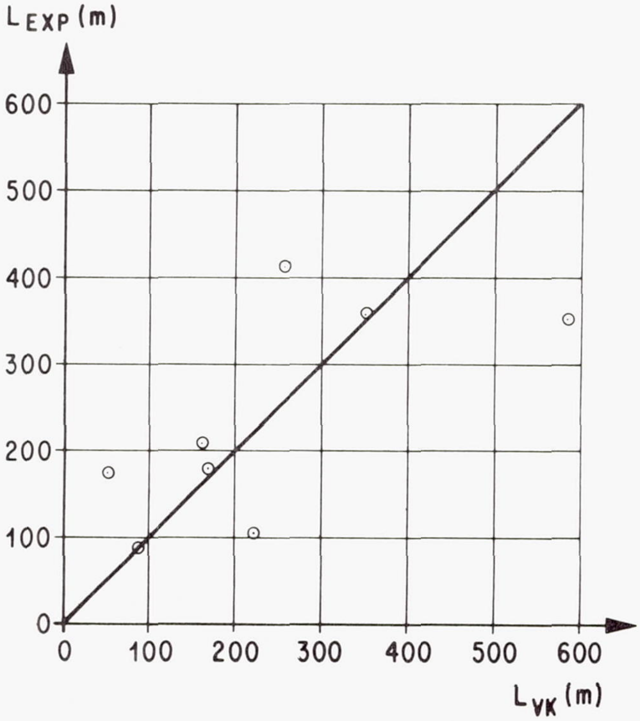

FIGURE 3. EXPERIMENTAL VALUES OF TURBULENCE VERSUS VON KÁRMÁN VALUES OF TURBULENCE

It was noted earlier that the gust factor prediction in this paper is in agreement with the recent experimental results of Alexander [11] for the case of the neutral boundary layer. This agreement is best in the region below 60 m. The prediction above the 60 m level could be improved by accounting for the variation of the variance with height. In addition, the prediction of the gust factor at all levels could be improved by a better definition of the probability density function of the longitudinal wind fluctuations. Experimental and theoretical evidence now exists suggesting that the wind fluctuations at a point do not constitute a Gaussian process as assumed in this paper. It would perhaps be worthwhile to examine the statistical distribution of wind fluctuations. This information would also be useful in problems related to the diffusion of toxic fuels.

The results concerning the analysis of the horizontal scales of turbulence are most applicable at the 60 m level. The spectra used in this study appear to show a variation with height for both unstable and stable conditions, implying that the scale of turbulence is a function of height. However, for the neutral cases (strong winds), the spectra appeared to have no variation with height, thus implying that the horizontal scale of turbulence is independent of height for the strong wind situation. These results appear to agree with those of Davenport [5].

REFERENCES

1. Monin, A. S.; and Obukhov, A. M.: Basic Regularity Inturbulent Mixing in the Surface Layer of the Atmosphere. Trudy Geophysical Institute, ANSSSR, 24, 1954, p. 163.

2. Dutton, J. A.; and Fichtl, G. H.: Approximate Equations of Motion for Gases and Fluids. Unpublished manuscript.

3. Townsend, A. A.: The Structure of Turbulent Shear Flow. Cambridge at the University Press, Cambridge, Maryland, 1956.

4. Lumley, J. L.; and Panofsky, H. A.: The Structure of Atmospheric Turbulence. Interscience Publishers, New York, 1964.

5. Davenport, A. G.: The Spectrum of Horizontal Gustiness Near the Ground in High Winds. Quarterly Journal Ray Meteorological Soc., vol. 87, 1961, p. 194.

6. Monin, A. S.: Empirical Data on Turbulence in the Surface Layer of the Atmosphere. Journal of Geophysical Research, vol. 67, 1962, p. 3103.

7. Prasad, V.: Private communication, 1967.

8. Panofsky, H. A.: Private communication, 1967.

9. Daniels, G. E.; Scoggins, J. R.; and Smith, O. E.: Terrestrial Environment (Climatic) Criteria Guidelines for Use in Space Vehicle Development, 1966 Revision. NASA TM X-53328, NASA-Marshall Space Flight Center, Huntsville, Alabama, May 1, 1966.

10. Rice, S. O.: Mathematical Analysis of Random Noise. Bell System Technical Journal, vol. 23, 1944, p. 46.

11. Alexander, M.: Private communication, 1967.

12. Pritchard, F. E.; Casterbrook, C. G.; and McVehil, G. E.: Spectral and Exceedance Probability Models of Atmospheric Turbulence for Use in Aircraft Design. TR AFFDL-TR-65-122, Air Force Flight Dynamics Laboratory, Research and Technology Division, Air Force Systems Command, Wright-Patterson Air Force Base, Ohio, 1965.

13. Lappe, U. O.: Design of a Low Altitude Turbulence Model for Estimating Gust Loads on Aircraft. Technical Report AFFDL-TR-64-170, Air Force Flight Dynamics Laboratory, Research and Technology Division, Air Force Systems Command, Wright-Patterson Air Force Base, Ohio, 1965.

14. MacCready, P. B., Jr.: The Inertial Subrange of Atmospheric Turbulence," Journal of Geophysical Research, vol. 67, 1962, p. 1051.

15. Taylor, G. I.: The Spectrum of Turbulence. Proc. Ray. Soc., A164, 1938, p. 476.

16. Webb, F. K.: Autocorrelations and Energy Spectra of Atmospheric Turbulence. Technical Paper No. 5, Melbourne, C. S. I. R. O., Div. Met. Physics, 1955.

17. Gault, J. D.: Low Altitude Atmospheric Turbulence, Lo-Locat Mid-term Technical Data Analysis. Systems Engineering Group, Research and Technology Division, Air Force Systems Command, Wright-Patterson Air Force Base, Ohio, 1967.

18. Blackadar, A. K.: The Vertical Distribution of Wind and Turbulent Exchange in a Neutral Atmosphere. Journal of Geophysical Research, vol. 67, 1962, pp. 3095-3102.

WIND AND GUST CHARACTERISTICS IN THE LOWER 150 m OF THE ATMOSPHERE AT KSC, FLORIDA

By

Margaret Alexander,
Dennis W. Camp,
C. Kelly Hill, and
John W. Kaufman

SUMMARY

The results of recent research studies for improving our knowledge of the lower atmosphere at KSC, Florida, are presented. These studies involve data measurements obtained from NASA's 150-m meteorological tower located at KSC, Florida, close to Launch Complex 39A, the launch site for the Saturn vehicle. This proximity to the Saturn launch site makes the tower facility especially useful for obtaining ground wind information for input to Saturn design and launch criteria.

A gust factor is defined as the maximum wind speed during some finite period divided by the mean wind speed for the same period. Mean and maximum gust factors are plotted as a function of mean wind speeds for several different time-averaging periods and for six levels on the tower.

Relationships are shown between mean wind speeds and the standard deviations of wind speed and direction. Statistics of the frequency of occurrence of gusts versus their duration, obtained from data measurements on the tower, have been computed using large samples of gusts with periods of 4 to 6 sec.

Studies using these tower data provide new and pertinent information on peak wind speed profiles, gusts, and gust factors.

INTRODUCTION

Earlier measurements of lower atmospheric wind data for the KSC, Florida area were obtained from wind sensors installed at a single height above the ground. Such observations have been made at Patrick Air Force Base and at the Cape Kennedy Weather Station for several years. The lack of descriptive wind profile data, however, has severely limited the amount of research that could be undertaken to investigate lower atmospheric turbulence and its effects on Saturn vehicles during exposure to such winds while on the launch pad. Consequently, a 150-m meteorological tower was erected at KSC, Florida in the vicinity of Launch Complex 39 (Fig. 1) and has been in operation since December 1965. It has thus far been an excellent source of wind and temperature profile data and measurements of atmospheric pressure, humidity and radiation data. The capability of this facility to obtain measurements of both high resolution magnetic tape recorded wind profile data and paper strip chart data makes it extremely valuable for studying Saturn response characteristics to winds.

There are numerous acceptable ways to analyze NASA's 150-m meteorological tower data. Some of the more effective analytical approaches are discussed in this report. Although the results from these analyses of wind profile data are not final, they do give some valuable insight into the solution of problems dealing with ground winds for the design and launch of Saturn vehicles.

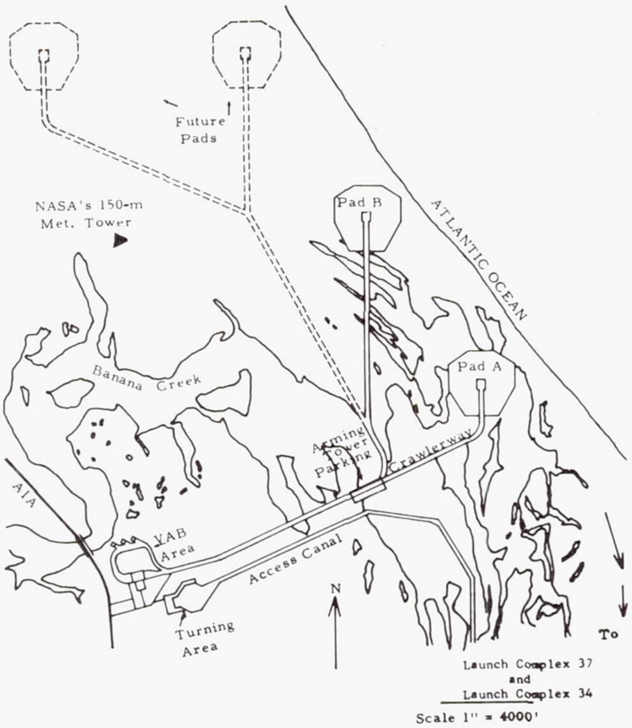

FIGURE 1. NASA LAUNCH COMPLEX 39, KSC, FLORIDA

NASA'S 150-m METEOROLOGICAL TOWER FACILITY

This important new source of lower atmospheric data [1] from KSC, Florida, now being used to develop wind and turbulence criteria for MSFC vehicle programs, is situated about 3 1/2 miles northwest of Launch Complex 39A and approximately 3 miles north of the Vehicle Assembly Building. Prominent topographical features in the vicinity of the tower include a creek about 150 m southwest and a line of palmetto trees oriented in a north-south position about 300 m west of the facility. Otherwise, the terrain around the tower is relatively flat with no large man-made structures nearby, other than the tower itself, which would cause significant changes in the local wind environment. The total facility consists of the 150-m tower, a smaller 18-m tower located 18 m northeast of the large tower, and a small building in which the wind, temperature, humidity, pressure and solar radiation data are recorded.

Wind data are measured by sensors on dual-mounted booms (3.66 m) positioned on the northeast and southwest sides of the large tower and on the northeast corner of the small tower. Figure 2 depicts the six positions of the wind sensors on the large tower (18, 30, 60, 90, 120, and 150 m) and two positions on the small tower (3, 18 m). The small tower is necessary to obtain a representative wind profile near the ground because the large tower significantly disturbs the flow and causes unrepresentative measurements below the 18-m level. Other meteorological measurements at this facility, including six levels of temperature (3, 18, 30, 60, 120, 150 m) and three levels of dewpoint (3, 60, 150 m), surface pressure and pyranometric measurements (direct and diffused solar radiation), are recorded inside the small building near the base of the tower. A 14-channel magnetic tape recorder also located in this building is used to record high resolution wind data either hourly or during special short selected periods for gust and turbulence studies. An automatic wind direction switching device that chooses the best exposed bank of wind instruments is incorporated into the tower facility.

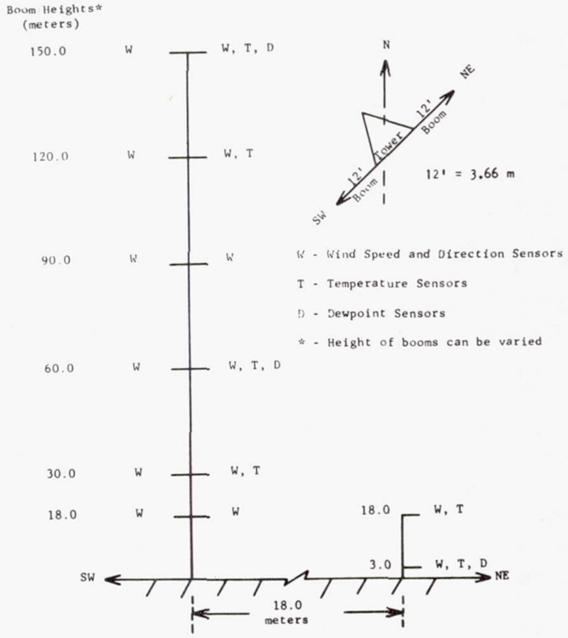

FIGURE 2. SCHEME FOR PLACEMENT OF METEOROLOGICAL SENSORS ON NASA'S 150-m METEOROLOGICAL TOWER, KSC, FLORIDA

This tower facility was purposely built near Launch Complex 39 for effective use of the wind statistics and related gust and turbulence information developed from the tower data in Saturn vehicle design and launch criteria.

CHARACTERISTICS OF WIND VELOCITY PROFILE DATA

VARIABILITY OF WIND SPEED AND DIRECTION

The variability of lower atmospheric wind speed and direction is often presented in the form of standard deviations (S. D. or sigma values). Figure 3 shows how the standard deviations of wind speed and direction behave as a function of wind speed. These mean sigma curves were "smoothed in" using approximately 80 S.D. values computed for each height represented (i.e., 18, 30, 60, 90, 120, and 150 m). The standard deviations were calculated from 5-min samples of data, which were recorded simultaneously during the afternoon when the thermal lapse rates were neutral to unstable. The mean wind speeds for these data samples fell within ranges of 2.0 to 15.0 m/sec for the lower level (18 m) and from 2.0 to about 25.0 m/sec for the higher levels (i.e., 90, 120, and 150 m).

As expected, the variability of wind speed increases with increasing wind speed and decreases as a function of height. Wind direction variability, however, decreases with increasing wind speed and decreases with height.

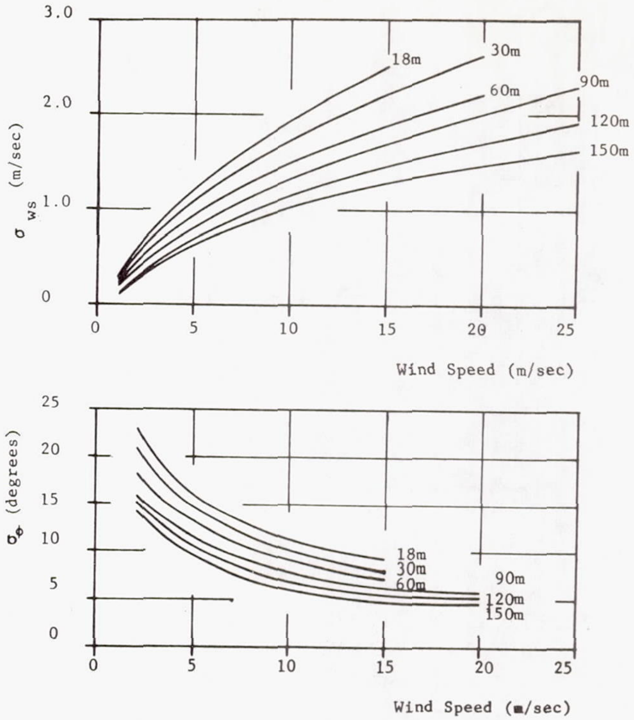

FIGURE 3. SIGMA (S.D.) CURVES OF WIND SPEED AND WIND DIRECTION VERSUS WIND SPEED COMPUTED FROM WIND VELOCITY DATA RECORDED AT NASA'S 150-m METEOROLOGICAL TOWER, KSC, FLORIDA

RATIO OF MAXIMUM WIND SPEEDS TO PEAK WIND SPEEDS

The question is often asked, "Can peak wind speeds for each individual height occur simultaneously in a given time interval over the entire length of the Saturn vehicle?" To gain some insight into this question, a direct approach was taken to determine if the simultaneously measured maximum wind speeds did closely approximate or equal the peak wind speeds. As an example, a 5-min sample of wind speed data was simultaneously recorded from anemometers located at the 18, 30, 60, 90, 120, and 150 m levels on NASA's 150-m meteorological tower. (Such data are actually digitized from analog magnetic tape recorded data at the rate of 10 samples/sec.) The arithmetic mean wind speed was then computed for these 5-min samples for each level. These mean values were then plotted, and a mean wind speed profile was drawn (Fig. 4). After the peak wind speed for the 5-min sample for each height was determined and plotted, a peak wind speed profile was established. It must be realized that the peak wind speeds over a finite time period seldom, if ever, occur simultaneously at all levels. The maximum integrated value of simulatenously measured wind speeds for this 5-min sample was determined by calculating an average wind speed ($\overline{ws}$) using digitized 0.1-sec wind speeds measured at the six levels. This 5-min sample, digitized at a rate of 10 samples/sec, provides 3,000 simultaneous wind profiles. The ratio of the average maximum wind speed profile ($\overline{ws}_m$) to the average of the peak wind speeds ($\overline{ws}_p$) was then determined; i.e., $\overline{ws}_m/\overline{ws}_p = 0.95$ for the sample shown in Figure 4.

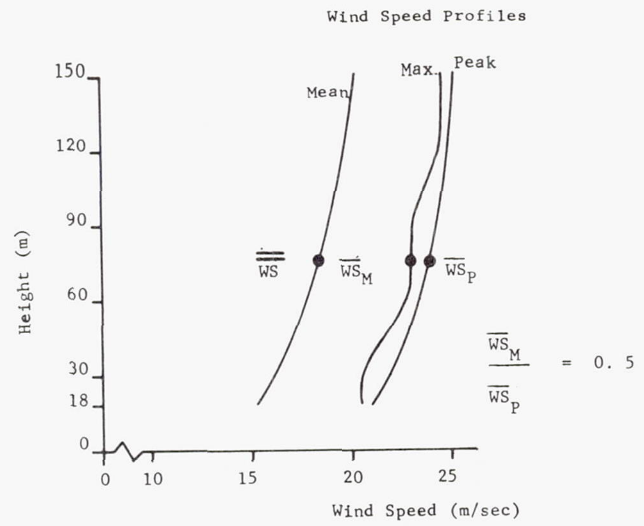

FIGURE 4. RATIO OF MAXIMUM WIND SPEEDS TO PEAK WIND SPEEDS COMPUTED FROM ONE 5-min SAMPLE OF DATA

Figure 5 shows 74 ratios of $\overline{ws}_m/\overline{ws}_p$ plotted as a function of the mean of mean wind speed profiles ($\overline{\overline{ws}}$); i.e., the mean wind speeds computed for each of the six levels were simply averaged. From the relationship of the ratios of average maximum wind speeds ($\overline{ws}_m$) to average peak wind speeds, as shown in Figure 4, it can be seen that, although the maximum wind speeds did not equal the peak wind speeds, the maximum instantaneously measured winds can very closely approximate the peak wind. Ratios up to 0.97 were computed for the mean of mean wind speeds ($\overline{\overline{ws}}$) beginning at approximately 7.0 m/sec speed and above (Fig. 5). Consequently, it is justifiable to design vehicles to withstand peak wind speed conditions; this has been the policy followed by MSFC/NASA space vehicle engineers in the past [2].

WINDS ASSOCIATED WITH A THUNDERSTORM

During a thunderstorm in the vicinity of NASA's 150-m meteorological tower at KSC, Florida, on May 9, 1967, at approximately 1418 Z wind profile data were recorded from 7 anemometer levels (i.e., 3, 18, 30, 60, 90, 120, and 150 m). Wind speed data recorded and digitized from analog magnetic tape recordings were plotted for every 15 sec and for each of the 7 levels. From this, a height-time cross section of a 10-min period which included these thunderstorm winds (Fig. 6) showed that (1) the wind speeds increased (decreased) to their maximum (minimum) values in about a 15- to 30-sec time period, (2) wind speed increases and decreases were in the order of 6 to 9 m/sec, (3) two maximum wind speed regimes were characterized (one between the 120- and 150-m level and the other between the heights of 18 and 60 m), (4) generally, the maximum winds occurred at the top levels first, then worked down to the lower levels, and (5) the maximum winds did not occur simultaneously (see the time of occurrence of maximum wind speeds at different levels as shown on Figure 6). Two other sets of wind profile data similarly measured during the passage of thunderstorms at the tower site, but are not shown here, strongly support comments (4) and (5) above.

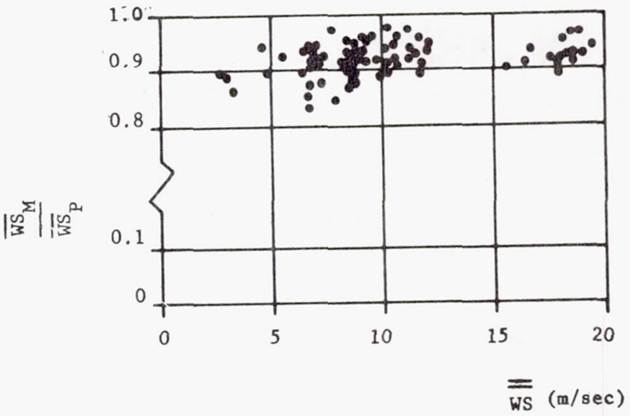

FIGURE 5. RATIO OF MAXIMUM WIND SPEEDS TO PEAK WIND SPEEDS AS A FUNCTION OF MEAN WIND SPEED BASED ON 74 5-min SAMPLES OF WIND SPEED PROFILE DATA

The variability of wind velocity profile data is, indeed, fascinating both from its relationship to vehicle structural design and from a purely academic viewpoint. This section has discussed the measurement and analysis of conditions in the lower 150 m of the atmosphere, and an anomaly of winds associated with a thunderstorm. Several research projects are in progress which hopefully will provide a better understanding of the winds in the lower atmosphere. Lower atmospheric data are being continuously recorded at the KSC, Florida launch area for use in these studies.

* HEIGHT (m)	TIME (zulu)	WS PEAK (m/sec)
150	14:18:10.5	17.9
120	14:18:10.2	17.5
90	14:18:0.8	13.5
60	14:17:52.3	16.3
30	14:18:14.4	16.5
18	14:18:14.7	16.8
3	Missing	Missing

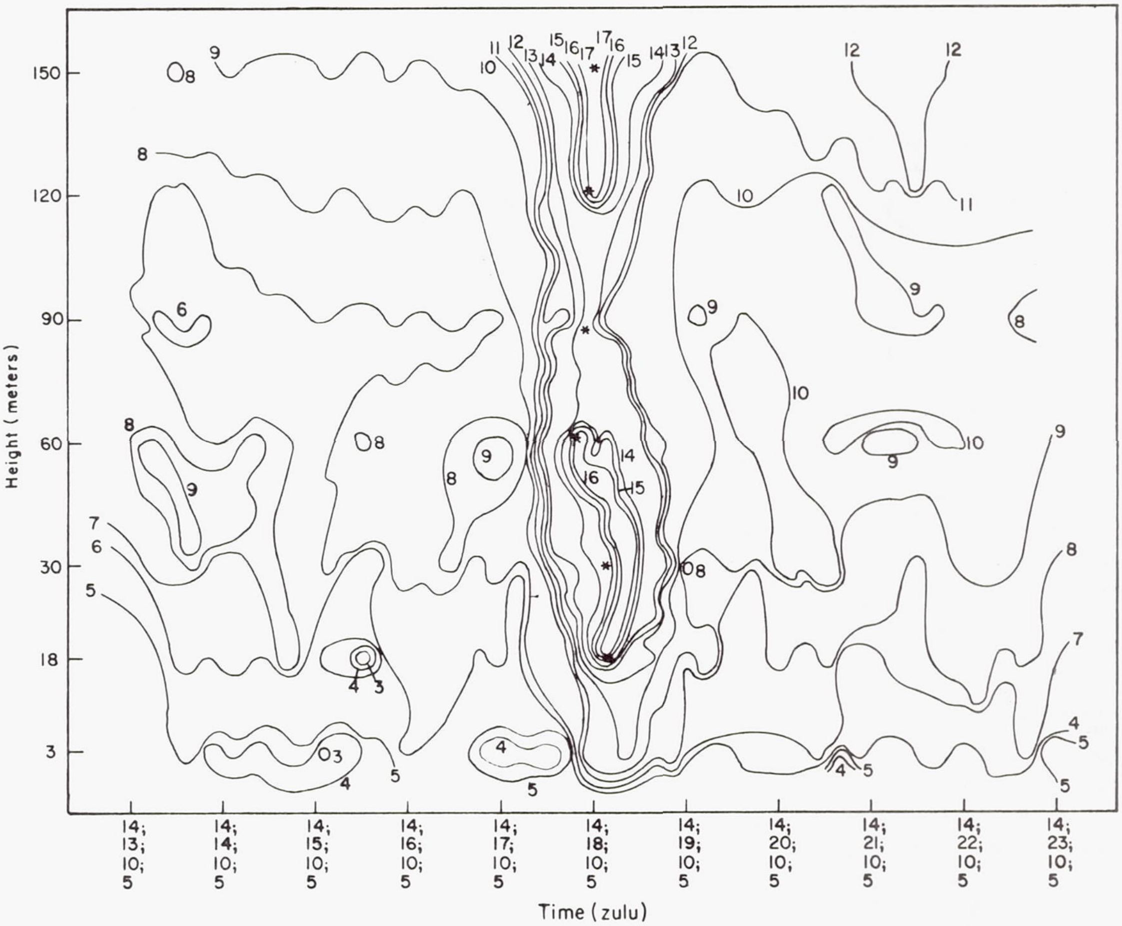

FIGURE 6. HEIGHT-TIME CROSS SECTION OF WIND ASSOCIATED WITH A THUNDERSTORM AS OBSERVED AT 150-m METEOROLOGICAL TOWER, KSC, FLORIDA, ON MAY 9, 1967 (14:13:10.5 - 14:23:10.5 ZULU) TEST NUMBER 150094; ws-m/sec

GUST FACTOR ANALYSIS

Marshall Space Flight Center has adopted a gust factor of 1.4 [2] for Saturn vehicle design and operational problems at KSC, Florida. The general practice has been to treat the gust as acting over the entire length of the vehicle. However, numerous questions regarding vehicle response calculations for drag and lateral lifting forces resulted in initiating a more detailed gust factor analysis. The gust factor represents a maximum wind speed fluctuation about a steady state speed and is a function of steady state or mean wind speed, the length of time used to obtain the mean wind, the prevailing stability conditions, terrain features, and height.

To more precisely determine the gust factor to a height of 150 m, analyses have been made relating gust factor to height, mean wind speed, and various time averaging periods to define the mean wind speed. Data used in these studies were recorded during September 1966 through August 1967 at NASA's 150-m meteorological tower facility located in the vicinity of Launch Complex 39 at KSC, Florida. Florida.

A gust factor is computed by dividing the peak wind speed which occurs over a finite period by the mean wind speed for the same time period. Figure 7 shows how the gust factor is computed using wind data recorded on paper strip charts during September 1966 at the 3- and 150-m heights. The 3-m sample occurred on the third of September about noon; the 150-m sample occurred on September 19 about 10 pm EST. In both cases, a mean wind speed averaging period of five minutes was used. At 3 m, a peak wind speed of 5.5 m/sec and a mean wind speed of 2.8 m/sec give a gust factor of 2.0, while a 25 m/sec peak wind speed at the 150-m height and a 20 m/sec mean wind speed give a gust factor of 1.2. In other words, a large gust factor is not necessarily the result of a high peak gust.

Results of the analysis of 63 one-hour samples of data recorded on magnetic tape during hours when the atmosphere is generally unstable (daytime data) are presented in Figures 8 and 9. How the mean gust factors vary as a function of height (18, 30, 60, 90, 120, and 150 m), mean wind speed (2 through 24 m/sec), and mean wind speed averaging period (0.5, 1, 2, 5, and 10 min) is illustrated in Figure 8. A similar illustration for maximum gust factors is presented in Figure 9. Between 4570 and 7028 gust factors were computed for each mean gust factor curve in Figure 8 for mean wind speeds ranging from 2 to 24 m/sec. Figure 9 shows the maximum gust factor curves obtained by enveloping the extreme gust factors associated with the mean gust factors of Figure 8. Both figures illustrate that the mean and maximum gust factors decrease with height, increasing wind speeds, and shorter averaging periods for mean wind speed.

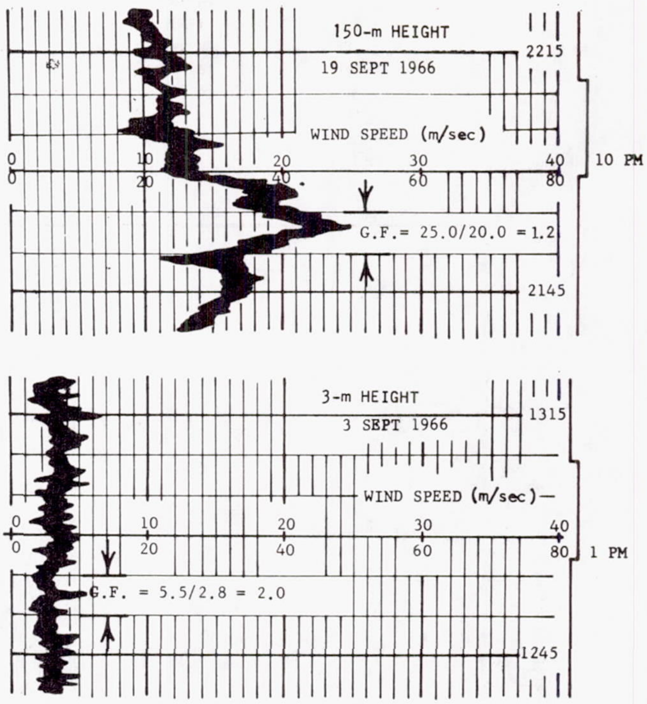

$G.\ F. = WS_{max} / \overline{WS}.$

where

G. F. is gust factor

WS_{max} is maximum wind speed during a 5 minute period

$\overline{WS}$ is mean wind speed for the 5 minute period

FIGURE 7. EQUATION FOR COMPUTING GUST FACTOR WITH TWO EXAMPLES

The MSFC environmental criteria value of 1.4 for gust factor over an averaging period for mean wind speed of two minutes appears to be a representative one. This fact is indicated by comparing this 1.4 value to the two-minute averaged curves for the 18-through 150-m heights. The analysis of gust factor, however, is continuing with emphasis on deriving a general equation (most likely an exponential one) for gust factor with variables of time, height and mean wind speed. Results will be documented in the near future.

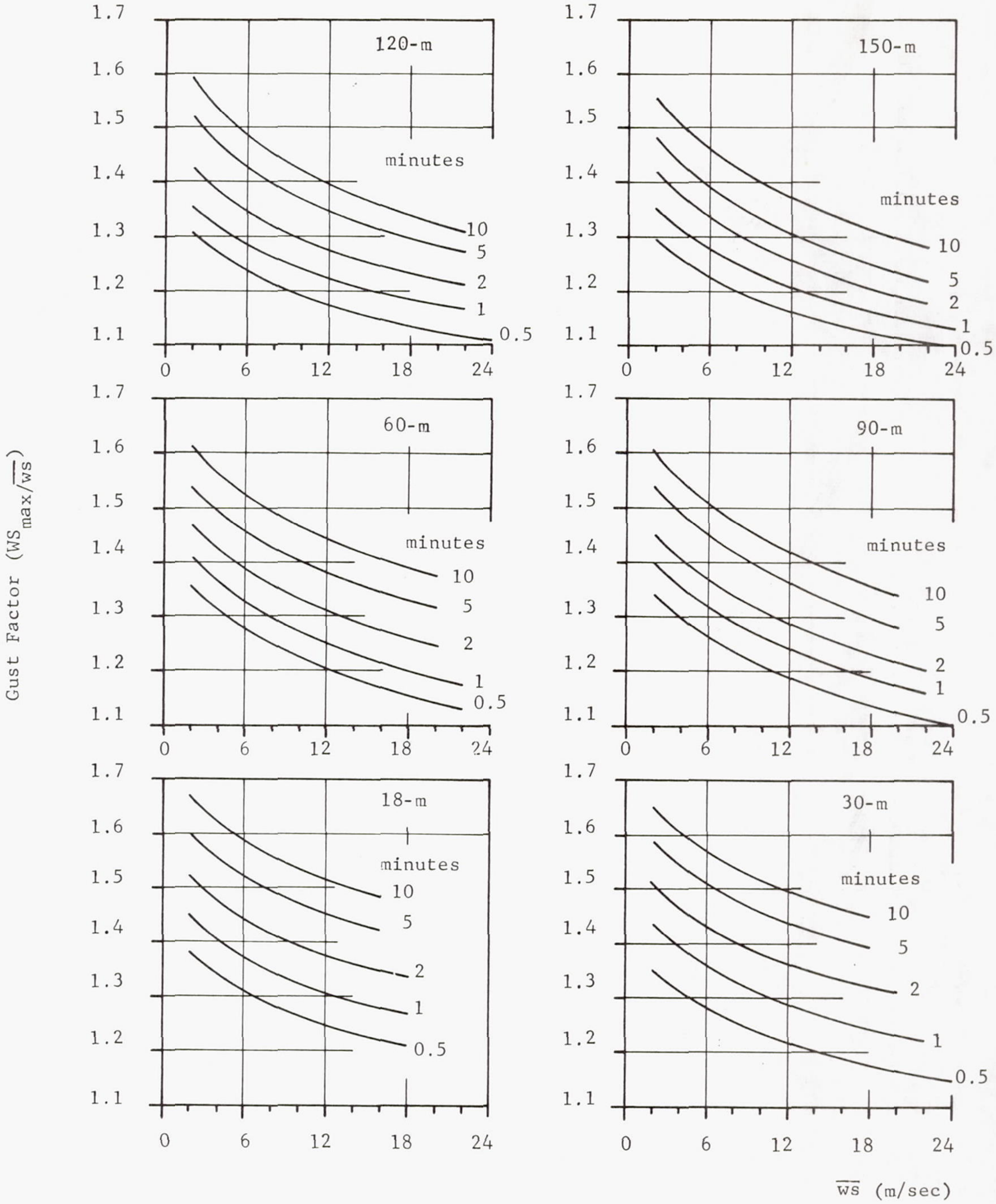

FIGURE 8. MEAN GUST FACTOR FOR SIX HEIGHTS AS A FUNCTION OF MEAN WIND SPEED AND FIVE MEAN WIND SPEED AVERAGING PERIODS FROM DATA RECORDED AT NASA'S 150-m METEOROLOGICAL TOWER, KSC, FLORIDA

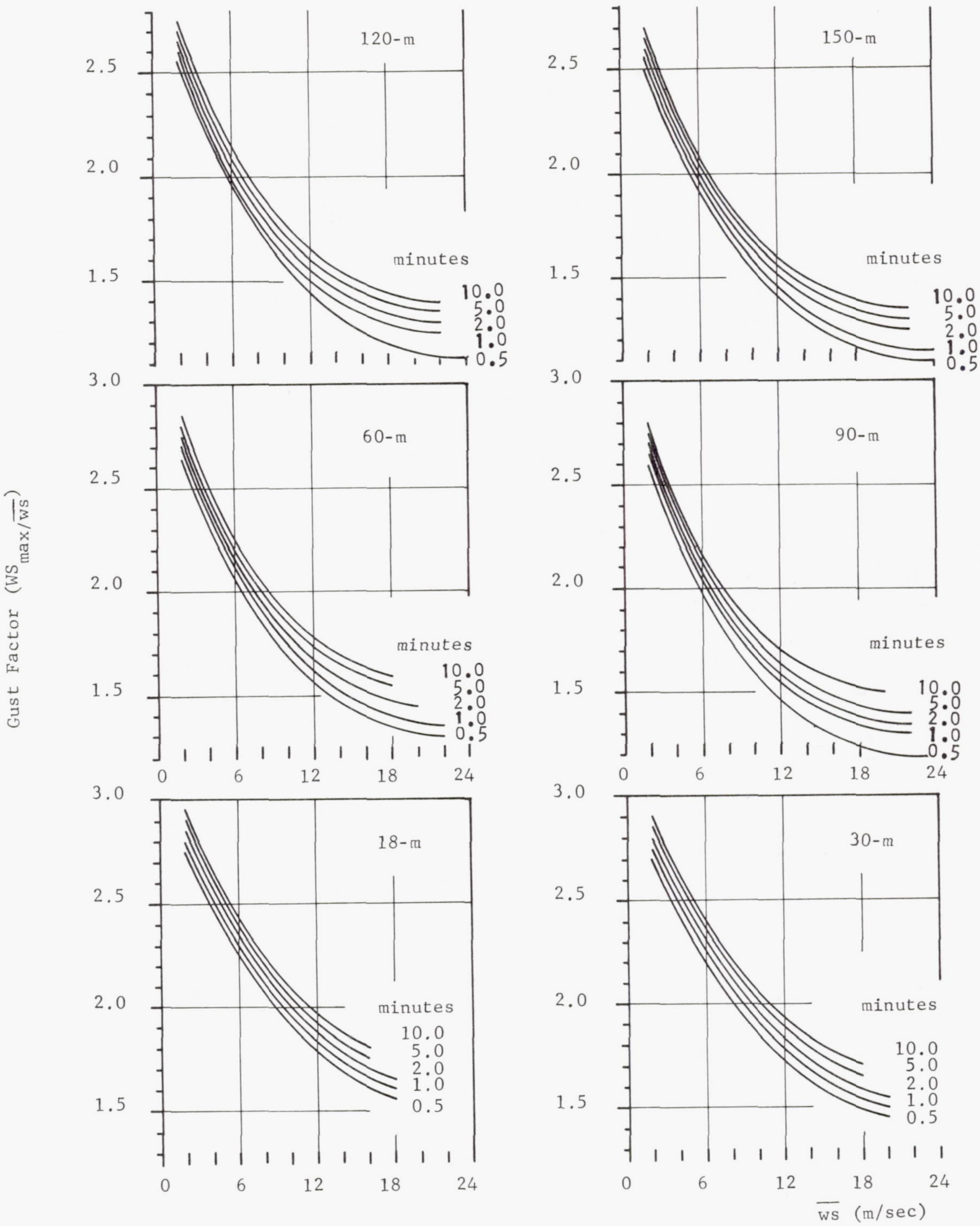

FIGURE 9. MAXIMUM GUST FACTOR FOR SIX HEIGHTS AS A FUNCTION OF MEAN WIND SPEED AND FIVE MEAN WIND SPEED AVERAGING PERIODS FROM DATA RECORDED AT NASA'S 150-m METEOROLOGICAL TOWER, KSC, FLORIDA

GUST CHARACTERISTICS

Before discussing the characteristics of a gust, it is necessary to define the wind gust as used in this analysis. A wind gust is defined as a build-up in the measured instantaneous wind speed above a two-minute arithmetic mean wind speed to an amplitude equal to or greater than 0.5 m/sec and a decay back to the mean wind speed (Fig. 7). With this definition of a wind gust, two characteristics of the gust were considered: (1) percentage of occurrence of gusts for various gust period durations and (2) a statistical gust for various gust duration periods.

Figure 10 illustrates the percentage of occurrence of gusts for various gust duration periods based on 1400 gusts recorded at the 18-m level on NASA's 150-m meteorological tower. As expected, gusts having the shorter duration periods occur more frequently. Almost identical percentage-of-occurrence distributions were obtained for the other tower levels. A more detailed presentation of the percentage of occurrence of various gusts will be published soon. A statistical gust is illustrated in Figure 11, where the 50, 90, 95, and 99 percentile values, determined from a cumulative frequency distribution of 583 measured wind gusts having a period of 4.0 to 6.0 sec, are plotted. Superimposed on the statistical curves is an actually measured wind gust. This observed gust has been plotted for every 0.2 sec. Statistical gusts for the levels above 18 m were similar to the ones shown in Figure 11, but the magnitudes of the gusts were smaller.

CONCLUSIONS

The tower data from NASA's 150-m facility at KSC, Florida are now contributing significantly to MSFC's Saturn vehicle research efforts through the application of results from studies of lower atmospheric wind profiles and turbulence. As additional tower data become available, improvements are expected in the relationships of the shape of wind profiles and their characteristic fluctuations in speed and direction. The conclusions pertaining to wind gusts and gust factors are vitally important in the establishment of vehicle design and launch guidelines for Saturn vehicles. Deriving a general equation for the gust factor and determining the function which most nearly defines the gust shape will be emphasized in future studies.

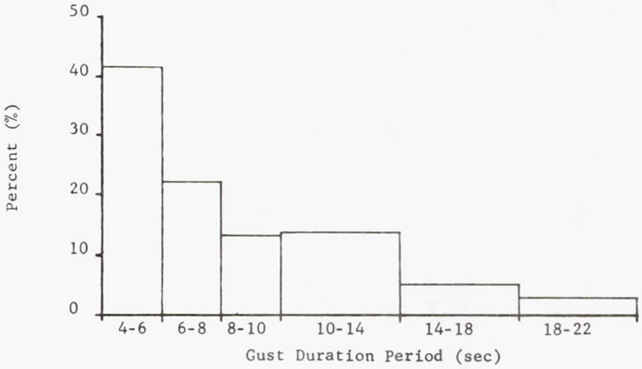

FIGURE 10. PERCENTAGE OF OCCURRENCE OF GUSTS HAVING VARIOUS DURATIONS BASED ON 1400 GUSTS RECORDED AT THE 18-m LEVEL ON NASA'S 150-m METEOROLOGICAL TOWER, KSC, FLORIDA

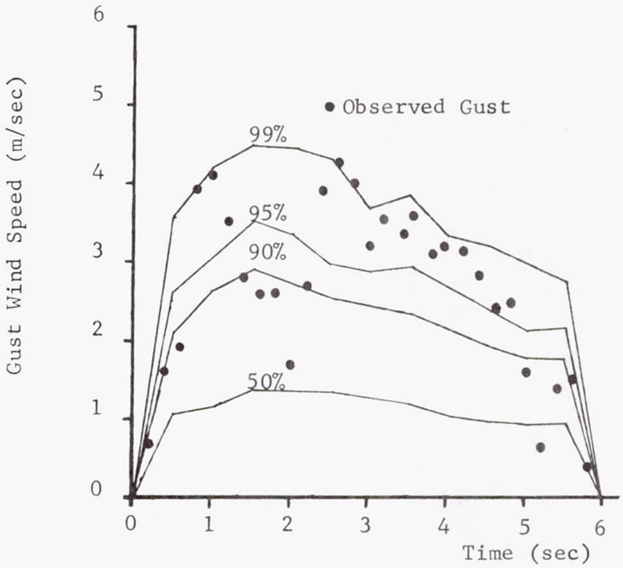

FIGURE 11. PERCENTILE GUST SHAPES BASED ON 583 GUSTS OF TIME DURATION OF 4 TO 6 sec OCCURRING AT THE 18-m LEVEL

REFERENCES

1. Kaufman, John W.; and Keene, Lester, F.: NASA's 150-m Meteorological Tower Located at Cape Kennedy, Florida. TM X-53259, Marshall Space Flight Center, May 12, 1965.

2. Daniels, Glenn E.; Scoggins, James R.; and Smith, Orvel E.: Terrestrial Environment (Climatic) Criteria Guidelines for Use in Space Vehicle Development, 1966 Revision. TM X-53328, Marshall Space Flight Center, May 1, 1966.

A STATISTICAL ANALYSIS OF WINDS FOR AEROSPACE VEHICLE DESIGN , MISSION PLANNING, AND OPERATIONS

By

Orvel E. Smith, Lee W. Falls, and S. Clark Brown

SUMMARY

Several statistical concepts in the analysis of a time ordered data sample are presented in terms of wind statistics applicable to aerospace vehicle design and operational problems. These concepts include extreme values, calculated risk, exposure period probabilities, exceedance probabilities, persistence, runs, and conditional probabilities. Examples of the resulting wind statistics for these probabilities, using a sample of hourly peak winds and eight years of serially complete winds aloft records for Cape Kennedy, Florida, are presented.

INTRODUCTION

The statistical analysis of a variable such as wind speed is difficult because of the extreme variability of this atmospheric element in time and space. Statistical methods of analysis may be divided into two general categories, descriptive and analytical, both of which depend primarily on the basic laws of probability. Descriptive methods reduce large amounts of data to a few meaningful "statistics" such as measures of location (mean, mode) and measures of variation (variance, standard deviation). A theoretical statistical model is assumed for the observations, and analytical methods are used to determine how well the empirical data fit this model. Thus, the analytical procedures determine the "goodness-of-fit" between theory and observation.

The many estimates of peak wind speed probabilities derived from empirical statistics in the past have not been completely satisfactory. Classical statistical methods are not adequate when the variable of interest is the largest in a set of observations. The theory of extreme values developed by the late E. J. Gumbel [1] was found to be an efficient and adequate statistical model for the analysis of extreme surface winds for vehicle launch and mission planning purposes.

After considering the range of the winds aloft and the rather high time correlation between observations, it was decided to develop empirical statistics from this data sample. Consequently, all probability statements concerning the winds aloft are empirical statistics.

EXTREME VALUE THEORY

In a set of N independent extremes, x_1, x_2, . . . , x_n, each being the extreme of one of N sets of n observations (where the N extremes are unlimited, exponentially distributed variables), as both N and n grow large the cumulative probability that any of these N extremes will be less than any chosen quantity, x, approaches

$$\Phi(x) = \exp\left[-e^{-y}\right] , \qquad (1)$$

where

$$y = \alpha(x - \mu) , \text{ or } x = \mu + \frac{y}{\alpha} \qquad (2)$$

for largest extremes. In eq.(2), α is a measure of concentration about the mode μ; i.e., α is a scale parameter and μ is a location parameter.

By the theory of least squares, α and μ can be estimated from the sample by

$$\alpha = \frac{\pi}{S_x\sqrt{6}} \quad \text{and} \quad \mu = \bar{x} - \frac{\gamma}{\alpha} \tag{3}$$

where γ = Euler's constant = 0.57722, and $\bar{x}$ and S_x are the mean and standard deviation of the set of N observed extremes.

We define return period, T_x, as

$$T_x = \frac{1}{1 - \Phi(x)}, \tag{4}$$

which may be interpreted as the average interval between recurrences of an event in a particular series of trials.

From eqs. (2) and (3), we obtain an expression for x:

$$x = \bar{x} + \frac{S_x\sqrt{6}}{\pi}(y - \gamma). \tag{5}$$

Figure 1 is an extreme probability graph on which y is one of the scales on the abscissa. There is also a scale of $\Phi(x)$ from eq. (1) and of return period, T_x, from eq. (4). The ordinate is a linear scale of the random variable, x, in our case, wind speed.

Equation (5) produces a straight line on this graph paper. This represents a best fit curve to the data sample by the least-squares method. The set of the N observed extremes furnishes values for the calculation of S_x and $\bar{x}$ in eq. (5).

In some cases, the scatter of the observations about the least-squares line of eq. (5) is so fine that the theory can be accepted on the basis of a visual inspection. In other cases, the deviations about the theoretical line may be such that the question arises whether the observations are compatible with the theory. To decide the question of how far the observations can deviate without invalidating the theory, control curves are constructed showing upper and lower limits within which the values can vary with a prescribed probability of, say, 0.68. This level is chosen because it corresponds to the one standard deviation limit for the normal distribution. This gives a graphical criterion for the "goodness-of-fit" between theory and observations. For example, Figure 1 shows the probability of a maximum peak wind associated with a thunderstorm on any day in July being less than or equal to 22 m/sec (42 knots) (10-m reference level) is approximately 0.99. Also, the average interval of recurrence (T_x) of this 22 m/sec (42 knot) peak wind in July is approximately 100 days.

Now, let P = probability of an event not occurring in any of N trials, and P_1 = probability of an event occurring at least one time in N trials. We now introduce the concept of calculated risk, U, which is the probability of encountering a peak wind speed (referenced to 10-m level) at least one time in N trials (days, hours, etc.). Thus, our event of interest in P_1 above is peak wind speed, and from the definition of multiple event probability,

$$U = P_1 = 1 - [\Phi(x)]^N,$$

or from eqs. (1) and (2),

$$U = 1 - \exp[-Ne^{-\alpha(x - \mu)}], \tag{6}$$

where x = wind speed, and N = the number of trials or the exposure time of a vehicle on the launch pad. The parameters α and μ are defined by eq. (3).

The function $\Phi(x)$ given by eq. (1) is a member of a class of statistical functions called extreme value distributions and is the appropriate type of statistical model for investigation in the analysis of a variable such as extreme wind speed. Fisher and Tippett [2] discovered that the limiting extreme value distribution can take only three forms, Types I, II, and III, which are illustrated in Figures 2, 3, and 4, respectively. The Fisher-Tippett Type I, the distribution defined by eq. (1), is the one used by Gumbel [1]. Also, Type I is the limiting form of Types II and III. Type I is unbounded at both ends, Type II is bounded below at zero, and Type III is bounded above at zero. Since wind speed has a physical lower bound at zero, it may be desirable to investigate distribution Type II for our statistical model. Thom [3] uses the Fisher-Tippett Type II distribution for ground wind distributions.

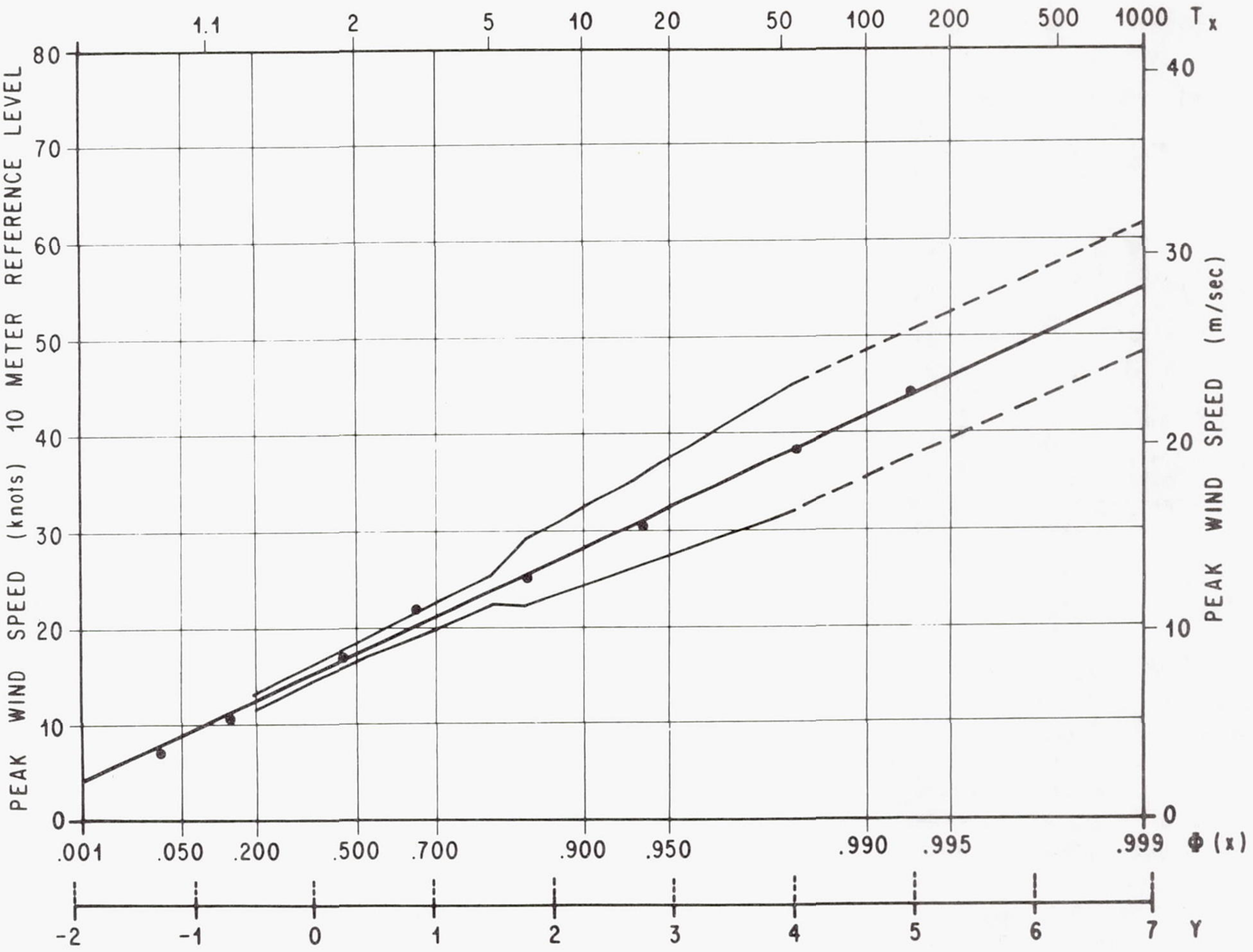

FIGURE 1. PROBABILITY OF MAXIMUM DAILY PEAK THUNDERSTORM WINDS AT CAPE KENNEDY, FLORIDA

$$\Phi(x) = \exp\left[-\exp\left[-a(x-\mu)\right]\right], \quad -\infty < x > \infty$$

TRANSFORMATION: $x = \mu + y/a$

DENSITY: $\phi(x) = a \exp\left[-a(x-\mu)\right] \Phi(x)$

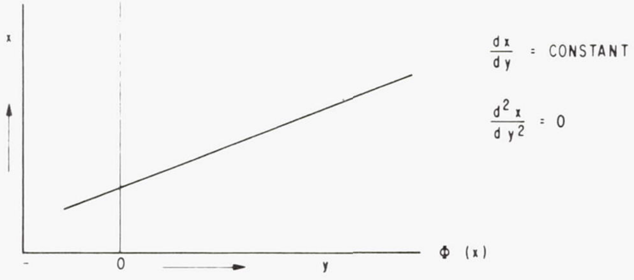

FIGURE 2. FISHER-TIPPETT TYPE I DISTRIBUTION (GUMBEL DISTRIBUTION)

$$\Phi(x) = \exp\left[-\left(\frac{x-\epsilon}{\mu-\epsilon}\right)^{-k}\right], \quad x \geq \epsilon, \quad \mu > \epsilon, \quad k > 0$$

TRANSFORMATION: $x = \epsilon + (\mu - \epsilon) \exp\left[y/k\right]$

DENSITY: $\phi(x) = \left(\frac{k}{\mu-\epsilon}\right)\left(\frac{x-\epsilon}{\mu-\epsilon}\right)^{-k-1} \Phi(x)$

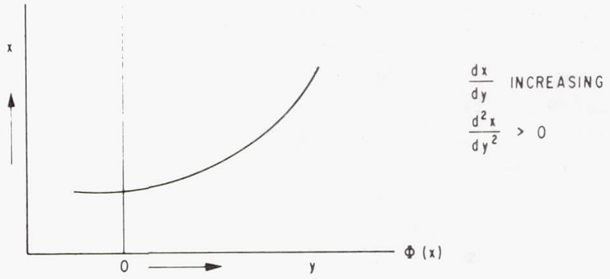

FIGURE 3. FISHER-TIPPETT TYPE II DISTRIBUTION

$$\Phi(x) = \exp\left[-\left(\frac{\omega - x}{\omega - \mu}\right)^{k}\right], \quad x \le \omega, \quad \mu < \omega, \quad k > 0$$

$$\text{TRANSFORMATION: } x = \omega - (\omega - \mu)\exp\left[-y/k\right]$$

$$\text{DENSITY: } \phi(x) = \left(\frac{k}{\omega - \mu}\right)\left(\frac{\omega - x}{\omega - \mu}\right)^{k-1}\Phi(x)$$

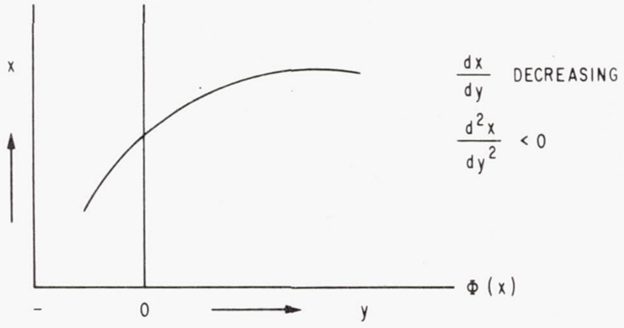

FIGURE 4. FISHER-TIPPETT TYPE III DISTRIBUTION

The concept of calculated risk has been proposed by Court [4] as wind design criteria for facilities. Gumbel [1] uses Court's term "calculated risk" in this connection. In other terms and applications, the fundamental principles have a long history stemming from early statisticians who were interested in the probability theory of games. In this paper, the calculated risk concept is extended to analyze time ordered data which vary systematically with time and which may be highly correlated with respect to time. This extension to calculated risk is called exposure period probability when used in reference to the probability that the vehicle will experience ground winds while exposed to the natural elements; e.g., while being readied for launch on the pad.

An exposure period probability is an empirical statistic of ground winds derived from a time-ordered sample of winds and involves counting the occurrences of wind speeds equal to or greater than specified magnitudes in all possible combinations. Thus, an exposure period statistic expresses the probability that an event will occur one or more times in k-consecutive time intervals. The probability of the event may vary with respect to time (from trial to trial) without invalidating any fundamental principle. Calculated risk requires that the probability of the event remain constant with respect to time (from trial to trial). With special attention given to the effects of uncompleted runs at the ends of a finite sample series, exceedance probabilities can be derived from the probability of runs and therefore from exposure period probabilities.

WIND DATA SAMPLES FOR CAPE KENNEDY

HOURLY PEAK WIND SAMPLE

The surface (~ 10-m level) wind data normally available for statistical analysis from the Environmental Science Services Administration, National Weather Records Center, Asheville, North Carolina. are in the form of card deck 144 taken from Standard Form WBAN-10. These records contain, among other measurements and observations, wind measurements averaged over one minute taken at hourly intervals. In general, these records are referred to as hourly observations. After several attempts at adjusting these hourly wind data failed to yield consistent statistical results between hourly peak winds and daily peak winds, it was considered necessary to read the original anemometer chart records (continuous recorder traces) to produce a data sample of hourly peak winds. This tedious task of reading the original chart records was performed by the National Weather Records Center, supported by the NASA-MSFC Aero-Astrodynamics Laboratory, Aerospace Environment Division with funds both from Program and Supporting Research. (The serially-complete winds-aloft records to be described subsequently were also produced and sponsored by the same organizations.)

From the continuously recording charts, the highest instantaneous indicated wind speed (and associated direction) that occurred during each hour was selected for the data sample. If more than one maximum (peak) wind speed of equal magnitude occurred during a given hour, only the first occurrence was selected. The resulting data sample of hourly peak wind speeds (and associated directions) exist only for Cape Kennedy, Florida. The reference height for these data is 10 m above natural grade. The period of record is from September 1958 to December 1966 with missing data from March 1961 to November 1961, and from November 29, 1962, to March 31, 1963.

This is the first report on the analysis of hourly peak winds for Cape Kennedy. The analysis is incomplete only in that all statistics of interest for the aerospace vehicle programs have not been derived to date. The validity and adequacy of conclusions made from numerical data depend upon the accuracy and reliability of the data sample. In this case, statistical conclusions and interpretations based upon this hourly peak sample will be valid and reasonable.

DAILY PEAK WIND SAMPLE

From an hourly peak wind sample, a daily peak wind sample, a monthly peak wind sample, and a yearly peak wind sample can be derived, provided that records exist for all hours. The sample size becomes proportionately smaller for each larger reference period; e.g., a sample size of daily peak winds would be 1/24 that of an hourly peak wind sample. Statistical analysis of samples derived from hourly peak winds have not been completed to date.

For this report, a daily peak wind sample was derived from records previously used in NASA TM X-53116 [5] which consists of fifteen years of daily peak wind speeds for Cape Kennedy. The original sample consists of three types of measurements: Type I, peak gust; Type II, observed gust; and Type III, hourly wind. The daily peak wind for each day of the fifteen years of record is from one of these three types. To obtain an unbiased representative sample of the population of daily peak surface wind speeds for Cape Kennedy, the available fifteen-year sample was reduced by choosing the latter part of the record in which all wind measurements were significantly Type I, peak gust. These measurements were obtained from continuously recording charts, and thus provide a true daily peak wind value. This revised daily peak sample consists of 2,525 measurements, and the period of record is from February 1, 1959, through June 30, 1966.

WINDS ALOFT SAMPLE

The winds aloft sample is composed of radiosonde observations made twice daily (at 0000Z and 1200Z) at Cape Kennedy covering the period from January 1, 1956, through December 31, 1963. The observations are serially complete with wind direction and speed recorded at 1 km intervals from 0 to 27 km altitude. The total number of observations is 5,844. This data sample is described in References 6 and 7, and is available from the National Weather Records Center as Card Deck 600. This data sample, which has been generally accepted by the aerospace industries for certain space vehicle applications, is being used extensively for the Saturn program. Extension of several statistical techniques using this data sample promises to yield even broader applications to advanced NASA programs such as AAP (Apollo Applications Program) and Voyager.

ANALYSIS

PEAK WIND SPEEDS AT 10-m REFERENCE HEIGHT ABOVE NATURAL GRADE

Peak Ground Winds. It has been estimated that only a few seconds are required for the wind to produce steady drag loads on the vehicle while it is on the pad. Because of vortex shedding, a steady wind as low as 9 m/sec for 15 or more seconds may introduce dynamic loads on the Saturn V vehicle in some configurations. To overcome dynamic wind loads, dynamic dampers supported by the launch umbilical tower and the mobile service structure are attached to the Saturn V vehicle. When the damper is attached to the vehicle, the total wind loading capability of the vehicle system is increased, thus decreasing the risk of structurally compromising the vehicle. However, during certain operations, the dampers must be retracted, making the vehicle more susceptible to structural damage from ground winds. The Saturn V ground wind criteria for vehicle launch have been defined in terms of the peak wind at the 18.3-m (60-ft) reference level above natural grade. Therefore, it is the occurrence of peak wind that becomes the important and meaningful statistic to be used in systems design and operational considerations. If an operation requires, say, one hour to complete, and if the critical wind loads on the vehicle can be defined in terms of the peak wind, then it is the probability of occurrence of the peak wind during one hour that gives a measure of the probable risk of structurally damaging the vehicle.

To serve as a convenient reference in the following discussion, the NASA-MSFC design ground wind profile for Cape Kennedy is reproduced from NASA TM X-53328 [8] as Table I. This study is restricted to determining statistics of peak wind speeds taken at one height, namely, at the 10-m reference height above natural grade at Cape Kennedy. There is still the problem of relating these wind statistics of peak winds at a specific height to the wind profile. The two previous articles in this review are devoted to the problem of defining the wind profile structure near the ground.

Empirical Statistics. A first step in making a statistical summary from a sample is to arrange the data into homogeneous groups. From the hourly peak wind sample, the smallest possible groupings are by hour of day. Winds associated with the hurricanes

TABLE I. PEAK DESIGN WIND PROFILES

Height Above Natural Grade m	ft	95 Percentile m/sec	knots	99 Percentile m/sec	knots	99.9 Percentile m/sec	knots
3.0	10	10.1	19.6	13.3	25.8	16.6	32.2
9.1	30	12.6	24.4	16.5	32.1	20.7	40.2
18.3	60	14.4	28.0	18.9	36.8	23.7	46.1
30.5	100	16.0	31.1	21.0	40.9	26.3	51.1
61.0	200	18.4	35.7	24.1	46.9	30.2	58.7
91.4	300	19.9	38.6	26.1	50.8	32.7	63.6
121.9	400	21.1	41.0	27.7	53.9	34.6	67.3
152.4	500	22.0	42.8	29.0	56.3	36.2	70.4

have been eliminated from this sample to further assure a homogeneous sample. It is assumed that such winds belong to a separate and distinct population. Winds associated with thunderstorms are, however, included in the sample. If the means and variances of two or more groupings (or subsamples) are not significantly different, then the subsamples may be further grouped into a larger sample. Cumulative percentage frequencies of hourly peak winds, grouped by like hour and all hours combined, were computed for monthly reference periods. Examples of the empirical cumulative percentage frequencies for January and July are shown on normal probability graph paper in Figures 5 and 6, respectively.

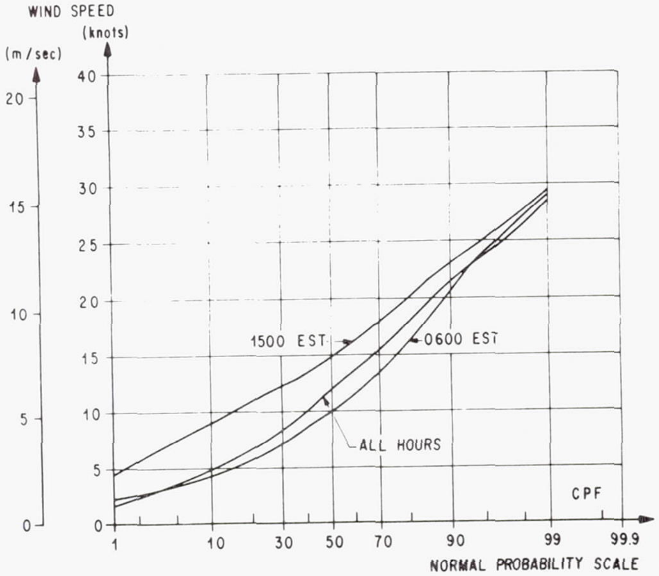

FIGURE 5. JANUARY HOURLY PEAK WIND SPEED CUMULATIVE PERCENTAGE FREQUENCY (10-m LEVEL) AT CAPE KENNEDY, FLORIDA

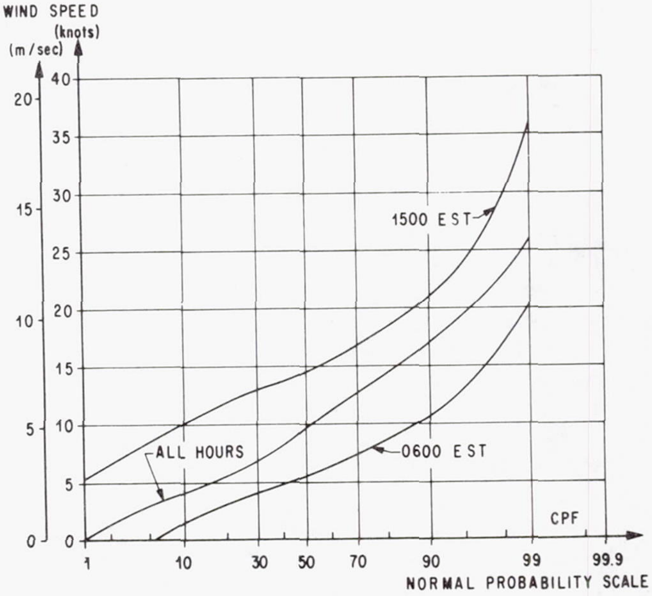

FIGURE 6. JULY HOURLY PEAK WIND SPEED CUMULATIVE PERCENTAGE FREQUENCY (10 m LEVEL) AT CAPE KENNEDY, FLORIDA

From the empirical cumulative percentage frequencies, any desired percentile value can be interpolated. The resulting percentiles for hourly groupings of hourly peak winds are illustrated in Figures 7 and 8 for January and July. From these figures, it is seen that the time of day to conduct an operation to avoid the probability of encountering high wind speeds is after 2100 EST and before 0700 EST, provided that it takes one or less hours to complete the operation. Furthermore the diurnal amplitude of all percentiles for July is greater than the corresponding percentiles for January. The

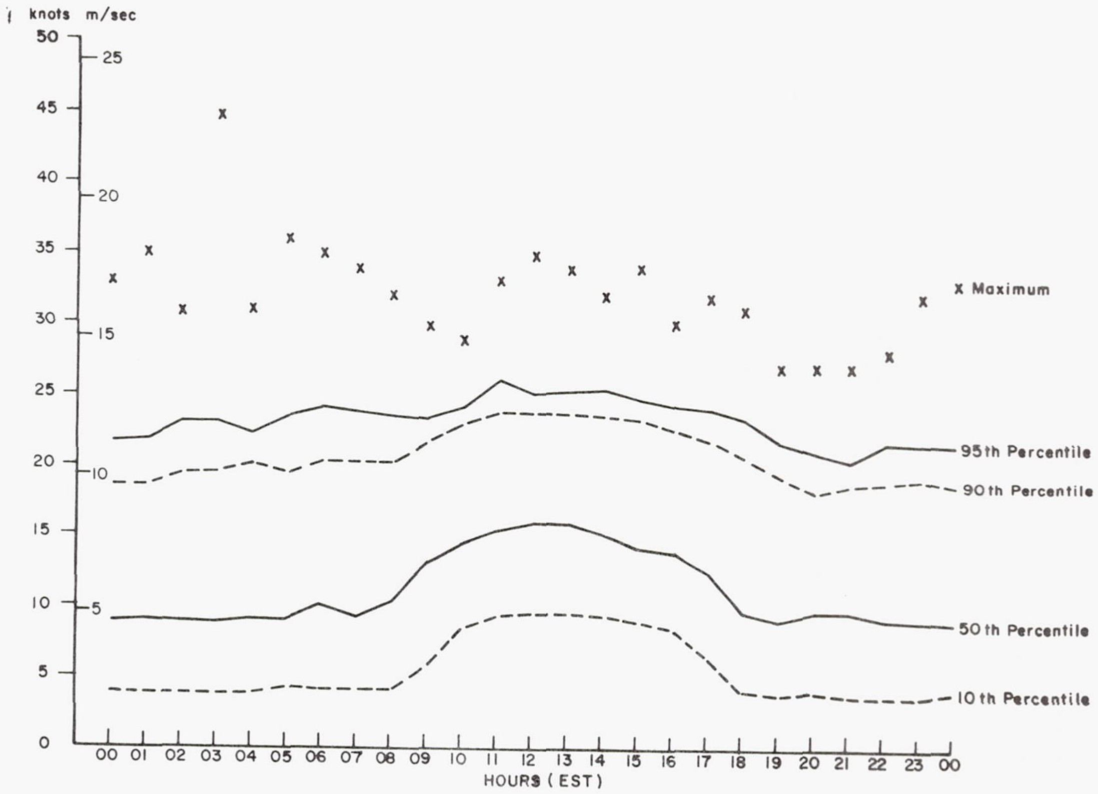

FIGURE 7. JANUARY HOURLY PEAK WIND SPEED PERCENTILES VERSUS TIME OF DAY (10-m LEVEL) AT CAPE KENNEDY, FLORIDA

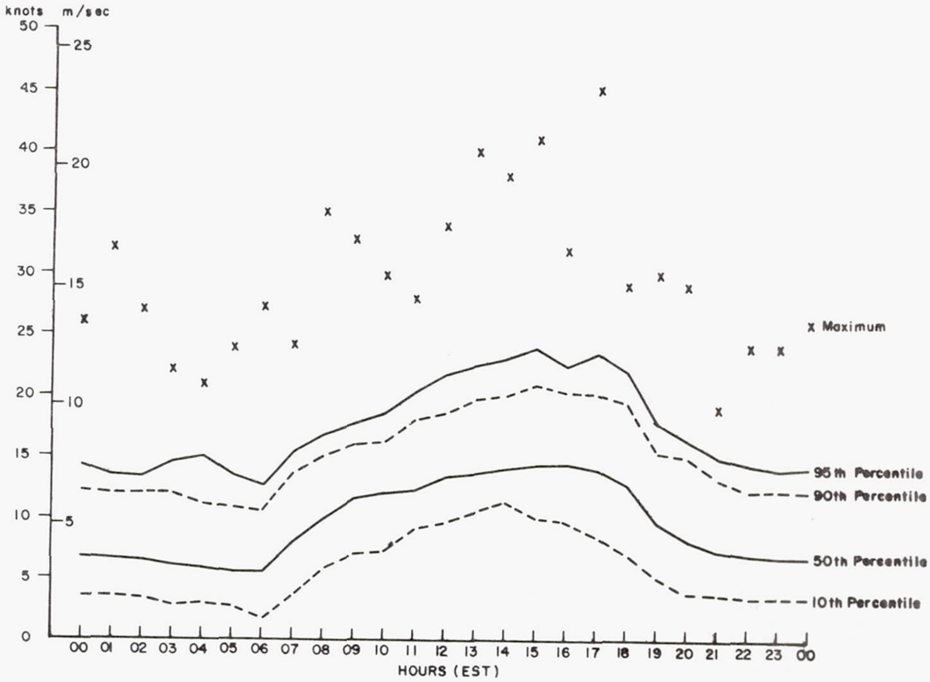

FIGURE 8. JULY HOURLY PEAK WIND SPEED PERCENTILES VERSUS TIME OF DAY (10-m LEVEL) AT CAPE KENNEDY, FLORIDA

diurnal amplitude also increases with higher percentiles during July, whereas the amplitude decreases with increasing percentiles during January. This feature is attributed to the high frequency of air mass (afternoon) thunderstorms during July (or in general, during the summer months) in contrast to the occurrence of frontal thunderstorms during January (or in general, during winter and spring) which may produce high winds at any time of the day.

If it is not known what time of day an operation is to take place, the statistics for all hours combined for monthly reference periods may be used. A comparison of the monthly and annual percentiles of hourly peak winds for all hours is presented in Figure 9. It must be recognized that this grouping is a very inhomogeneous sample. There are some hours of the day (primarily the afternoon hours) during which there is a higher probability of the wind exceeding these percentiles, and other hours (primarily early morning hours) for which there is a lower probability for the indicated percentiles. The principal conclusion to be drawn by a comparison of Figures 7 and 8 with Figure 9 is that the amplitude of the median (50th percentile) wind over a 24-hr period is greater than the seasonal amplitude at this percentile.

Thunderstorm Winds. Thunderstorms are a recognized special weather phenomenon, and the high frequency of thunderstorms during the summer months is the cause of much concern relative to vehicle operations at Cape Kennedy. Standard weather observing practice is to report the occurrence of a thunderstorm for the observing station if thunder is heard. Thus, the occurrence of a thunderstorm is determined by an observational method. An observer can hear thunder over a radius of approximately 25 km. The frequency at which thunderstorms were observed on the hour (at standard reporting times) for each hour versus

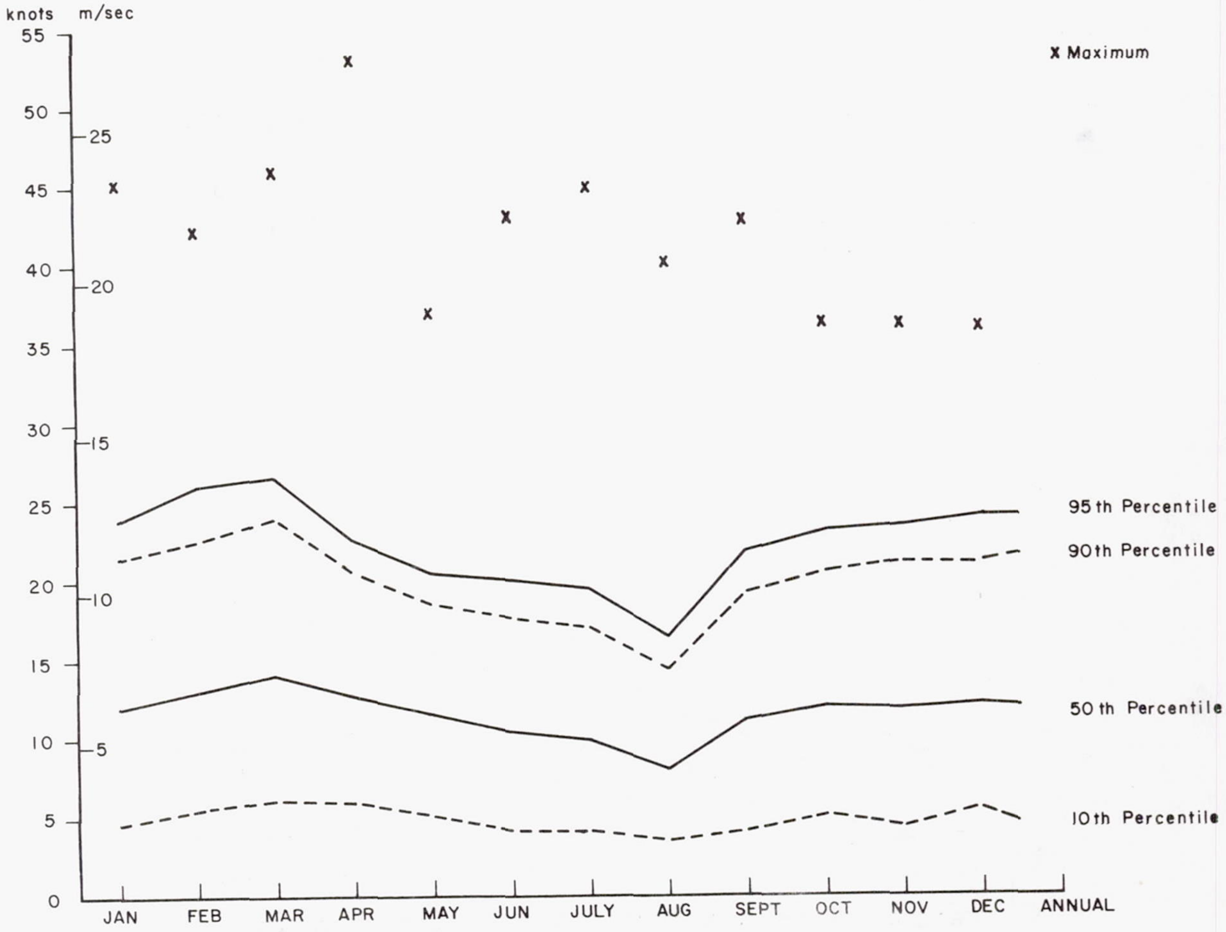

FIGURE 9. MONTHLY PERCENTILES (ALL HOURS) HOURLY PEAK WIND SPEED (10-m LEVEL) AT CAPE KENNEDY, FLORIDA

month is given in Figure 10. For example, there is a 24 percent chance that thunder will be heard at 1600 EST during July from a single observing point at Cape Kennedy. One or more thunderstorms may occur within the observing range at a given time and during some time interval. From NASA TM X-53635 [9], there is a 44.1 percent chance that one or more thunderstorms will occur during any arbitrary afternoon (1200 - 1959 EST) in July. There is a 45.2 percent chance that one or more thunderstorms will occur on any arbitrary day in July. To determine the probability of thunderstorm winds striking the vehicle, a sample of daily peak thunderstorm winds was obtained. For July, this sample as fitted to the Fisher-Tippett Type I (or Gumbel [1]) distribution function is shown in Figure 1.

The theoretical distribution of Figure 1 is reproduced in Figure 11 to compare with the distribution of daily peak winds. It is concluded from Figure 11 that there is only a 1 percent chance that a daily peak thunderstorm wind greater than 22 m/sec (42 knots) will occur at a specific point over Cape Kennedy; i.e., strike the vehicle at the 10-m reference height during any day in July even though there is a high probability, 0.452 [9], that one or more thunderstorms will occur during any day in July over the Cape Kennedy area (over a radius of approximately 25 km).

Now compare the distribution of daily peak thunderstorm winds with daily peak winds for July (Fig. 11). Notice that the slopes of these curves are not the same; this indicates that on some days the peak wind for the day was greater than the maximum observed peak wind during a thunderstorm observation.

Because of the excellent fit of the daily peak thunderstorm winds to the theoretical distribution function, and recalling from Section II that the theory of extreme values requires independence in the data sample, it may be assumed that the occurrence of peak thunderstorm winds at a specific location on Cape Kennedy is a random phenomenon. It certainly cannot be assumed that the daily occurrence of thunderstorms is random. In fact, given that a thunderstorm occurred on a specific date, there is a 70 percent chance that a thunderstorm will occur on the next day. A study on thunderstorm persistence at Cape Kennedy, NASA TM X-53635 [9], concludes that "a first order Markov model may be used to approximate the distribution of sequences of summer afternoons with thunderstorms. The second order Markov model may be used to approximate the distribution of sequences of summer afternoons without thunderstorms."

Theoretical Probabilities. The extreme value theory has been applied to these surface wind samples to provide probability statements of a critical wind speed striking the launch vehicle during a specified exposure period.

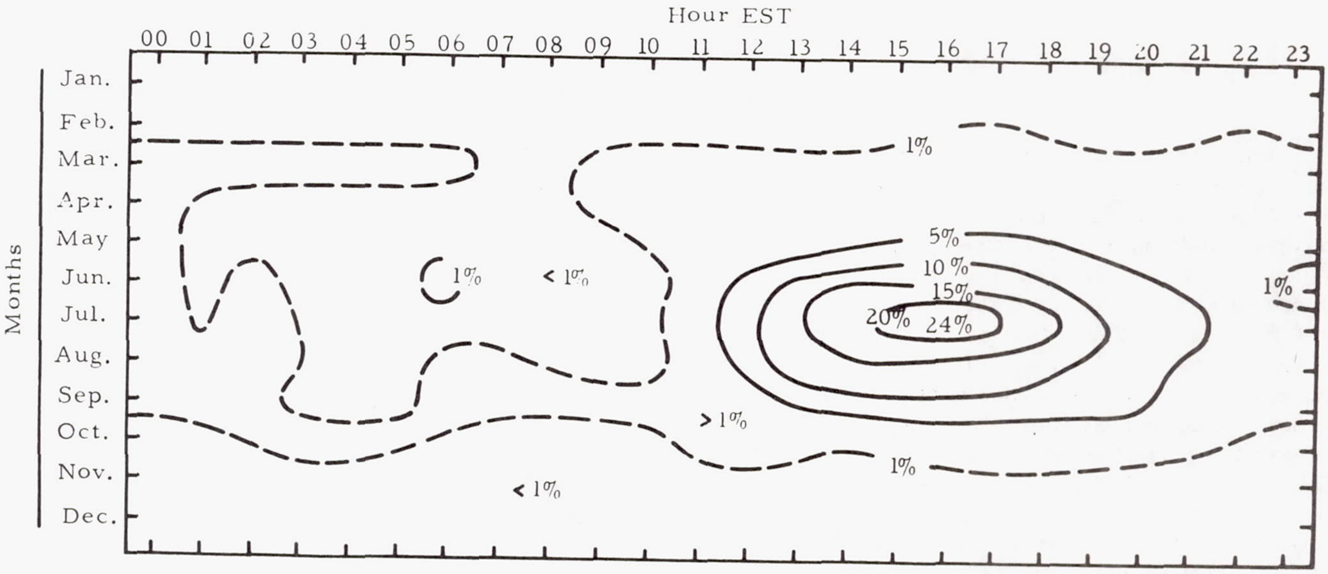

FIGURE 10. PROBABILITY (%) OF OCCURRENCE OF THUNDERSTORMS BY MONTHS VERSUS TIME OF DAY IN THE CAPE KENNEDY AREA FOR THE PERIOD JANUARY 1957 - DECEMBER 1962

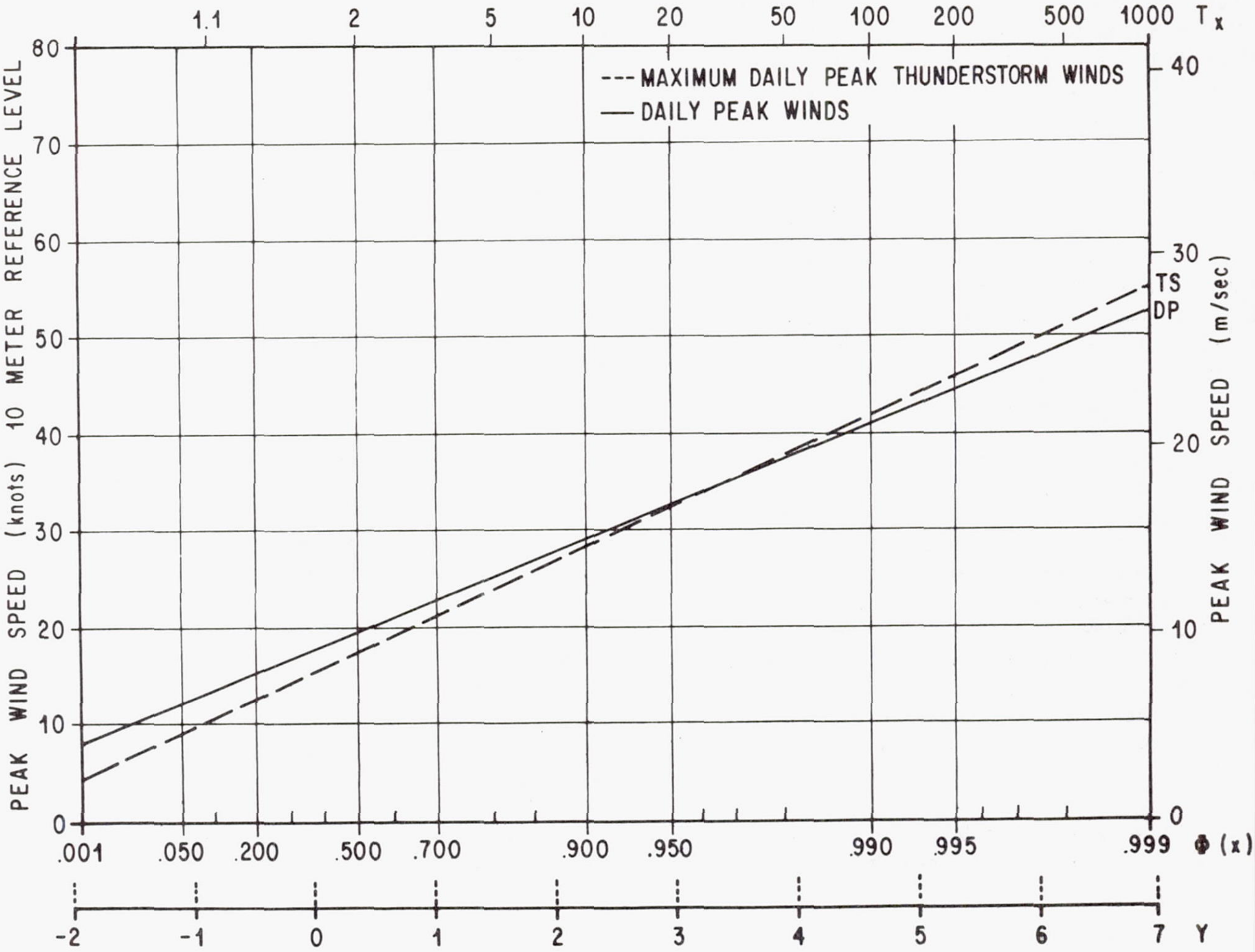

FIGURE 11. COMPARISON OF DAILY PEAK WINDS WITH MAXIMUM DAILY PEAK THUNDERSTORM WINDS IN JULY

The calculated risk probabilities answer probabilistic statements such as the probability of the event (peak wind) occurring at least one time during a continuous time interval, N, which begins at any time in a continuous time interval, k. For convenience, we make probability statements in reference to monthly periods; i.e., k is approximately 30 days, and N ranges from 1 day to 90 days. Since N is defined in this wide range of continuous time, it would not be proper to group our data sample by monthly periods alone. For example, consider the question: "What is the probability of encountering a certain peak wind at least one time beginning on any day in January for an exposure period of 90 days?" Obviously, since there are only 31 days in January, if we begin a 90-day exposure of a vehicle on the last day of January, the exposure time will extend into February, March, and April.

For this reason, the probabilities presented in Figures 12 (July) and 13 (October) were computed from eq. (6) by grouping the revised daily peak wind speed sample for Cape Kennedy into monthly, bimonthly, trimonthly, and quadmonthly reference periods; i.e., monthly reference periods are (January), (February), . . . , (December); bimonthly reference periods are (January, February), (February, March), (March, April), . . . , (December, January); trimonthly reference periods are (January, February, March), (February, March, April), (March, April, May), . . . , (December, January, February); quadmonthly reference periods are (January, February, March, April), (February, March, April, May), (March, April, May, June), . . . , (December, January, February, March).

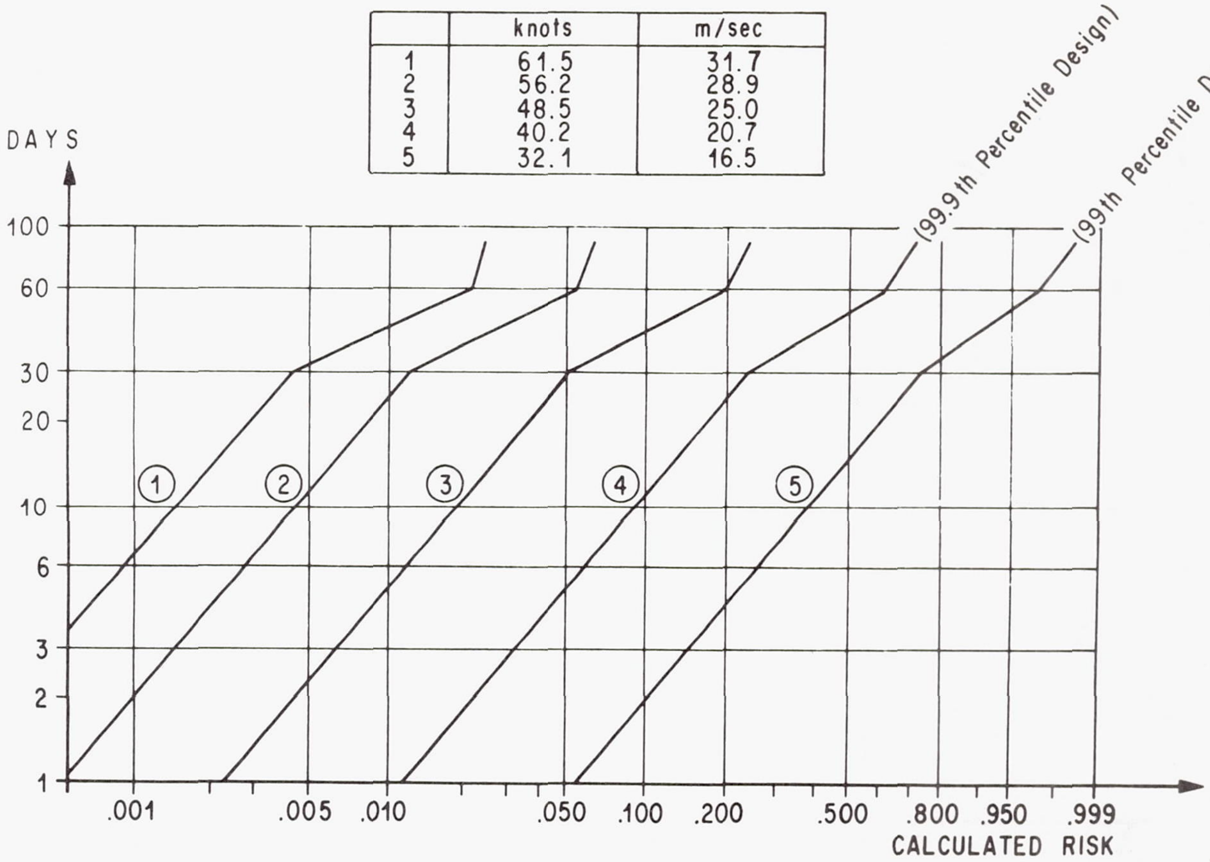

FIGURE 12. CALCULATED RISK VERSUS EXPOSURE TIME WITH PEAK WIND SPEED REFERENCED TO 10-m (30 ft) LEVEL AT CAPE KENNEDY, FLORIDA IN JULY

In Figures 12 and 13, exposure times of one day (N = 1) were computed from the monthly reference periods; exposure times of 30 days (N = 30) were computed from the bimonthly reference periods; exposure times of 60 days (N = 60) were computed from the trimonthly reference periods; and exposure times of 90 days (N = 90) were computed from the quadmonthly reference periods. For each month of the year and a given wind speed, these points were connected by a straight line on ln versus ln ln graph paper. Since ln N versus ln[-ln (1 - U)] is a linear function, computer programs were written and used to generate all calculated risks U_i for all N_i based upon eq. (6). The method described imparts the proper connotation to our probabilistic statements in regard to convenient monthly time periods.

For example, Figure 12 shows that the calculated risk of encountering a 25.0 m/sec (48.5 knot) peak wind speed (referenced to 10-m height) at least one time in 30 days beginning on any day during the month of July at Cape Kennedy, Florida, is 0.050. Figure 13 shows that the calculated risk of encountering a 16.5 m/sec (32.1 knot) peak wind speed (referenced to 10-m height) at least one time in 20 days beginning on any day during the month of October at Cape Kennedy is 0.550.

Figure 14 illustrates the distributions for October peak winds taken for different reference periods. From this graph, the probability of the peak winds for the indicated reference periods can be read. For example, the probability that the peak wind for the hour indicated as 0600 EST will be > 16.5 m/sec (32 knots) is 0.003 (i.e., 1 - 0.997 = 0.003). In symbols, this statement is expressed as $P\{W \leq 16.5 \text{ m/sec}\}$ for hourly peak wind during the period from 0530 to 0630 EST is 0.997. Therefore, the

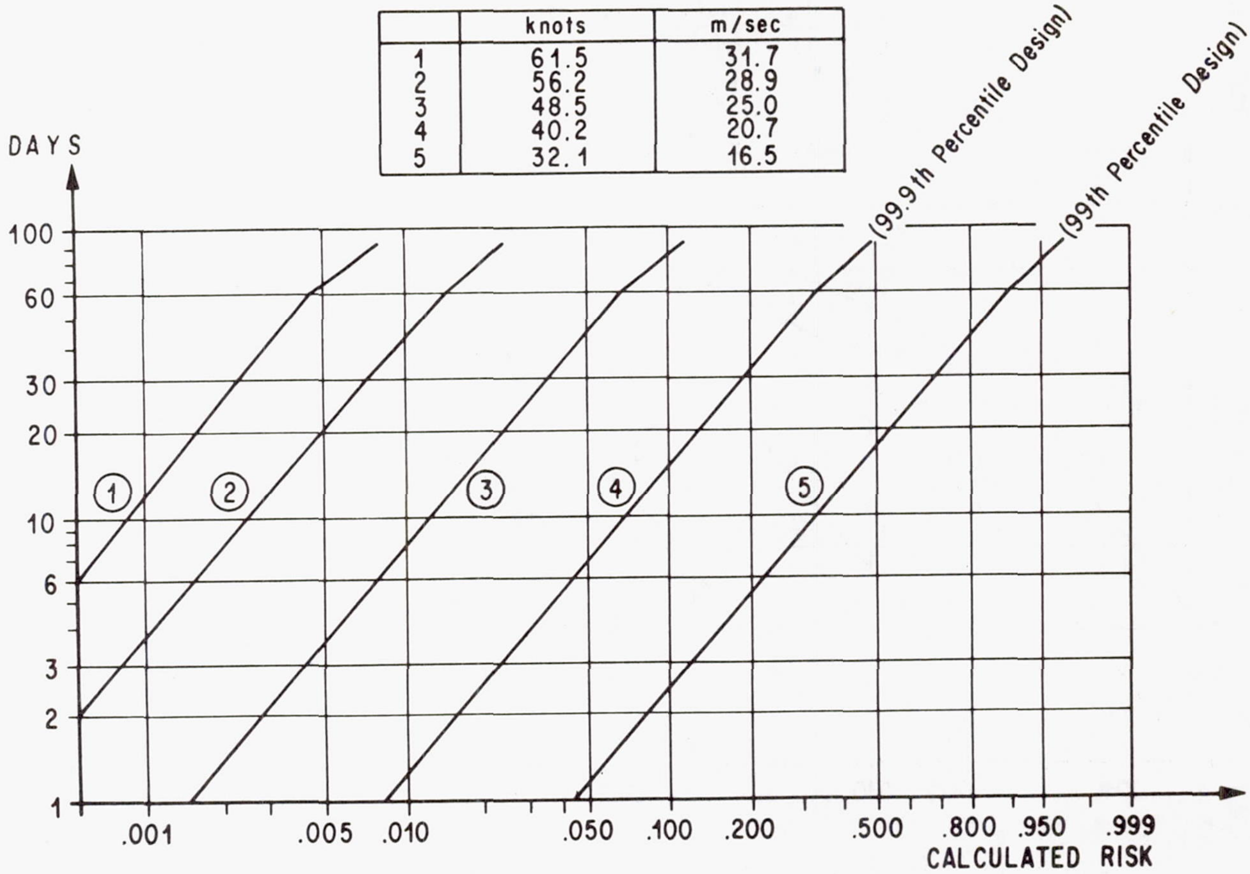

	knots	m/sec
1	61.5	31.7
2	56.2	28.9
3	48.5	25.0
4	40.2	20.7
5	32.1	16.5

FIGURE 13. CALCULATED RISK VERSUS EXPOSURE TIME WITH PEAK WIND SPEED REFERENCED TO 10-m (30 ft) LEVEL AT CAPE KENNEDY, FLORIDA IN OCTOBER

$P\{W > 16.5 \text{ m/sec}\}$ is 0.003. Similar probability statements can be made for other reference periods and wind speeds.

Figure 15 represents the calculated risk of encountering peak ground wind speeds for hourly exposure periods for the month of October at Cape Kennedy. This is a cross-plot taken from the probabilities illustrated in Figure 14. The dashed line (0600 EST) and the solid line (1500 EST) graphically illustrate the diurnal change of the probability of encountering a given wind speed of 16.5 m/sec (32 knots at the 10-m level) if the exposure time begins on specified hours over the twenty-four hour day. The heavy dashed lines (calculated risk) indicate the unrealistic change of probability with exposure time where the probability in eq. (6) for each successive hour in the exposure period is assumed constant. Also included on Figure 15 is the calculated risk for exposure periods from 1 to 3 days.

Exposure Period Probabilities. The term "exposure period probability" is used to express the risk the vehicle would have in encountering a critical wind speed when exposed on the launch pad for k-consecutive hours, days, or even months. A computer counting procedure is used to determine the probability that the wind speed will equal or exceed specified values (critical wind magnitudes to the vehicle or any value of interest) at least one time in k-consecutive time increments. This empirical statistic is thus seen to fall into the general class of probabilities referred to as exceedance probabilities. To derive exposure period probabilities requires serially complete data records. The advantage of exposure period probabilities over calculated risk probabilities is that the probability from trial to trial may change without invalidating any fundamental principle. The resulting statistics are more realistic for a variate that changes systematically or which is highly correlated with respect to time, such as winds near the ground taken on an hourly basis. The

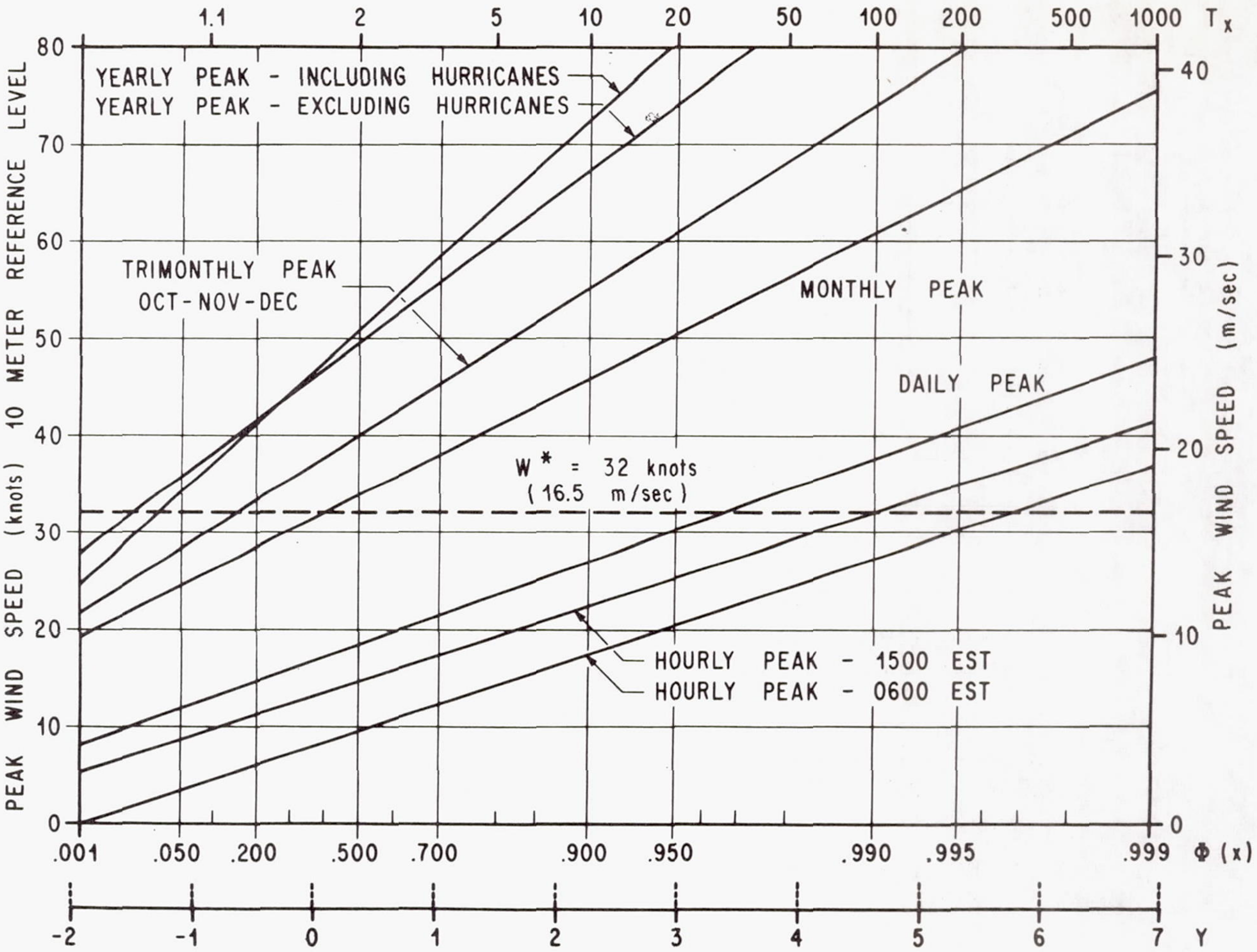

FIGURE 14. FISHER-TIPPETT TYPE I DISTRIBUTION COLLATED TO PEAK WIND SPEED SAMPLES AT CAPE KENNEDY, FLORIDA IN OCTOBER

single disadvantage of exposure period probabilities is that statistics are empirical. Estimates outside the observed range of the variate cannot be obtained.

To emphasize the importance of extreme value statistics, Gumbel [1] quips, "Some day the improbable will happen . . ." In our terms, the longer the vehicle is exposed to the natural elements, the higher the probability is that the vehicle will experience a high wind.

WINDS ALOFT ANALYSIS

Selection of the Maximum Wind Speed in the 10-15 km Layer. The following discussion is devoted to the statistical analysis of winds aloft taken from the data sample described previously under "Winds Aloft Sample." A unique presentation of the probability that winds aloft will equal or exceed a given magnitude versus altitude and month is presented for wind speeds $\geq$ 50 m/sec and $\geq$ 75 m/sec in Figures 16 and 17, respectively. Figure 16 shows a 5 percent chance and greater that winds will be $\geq$ 50 m/sec over the altitude region from 7 km to 16 km from the latter part of October to the first part of May. Figure 17 shows that wind speeds $\geq$ 75 m/sec occur between 11 and 14 km altitude during February to the first part of March with a frequency of 5 percent or greater. This is in excellent agreement with the MSFC winds aloft design criteria [8] which were based on a much earlier and less complete wind sample.

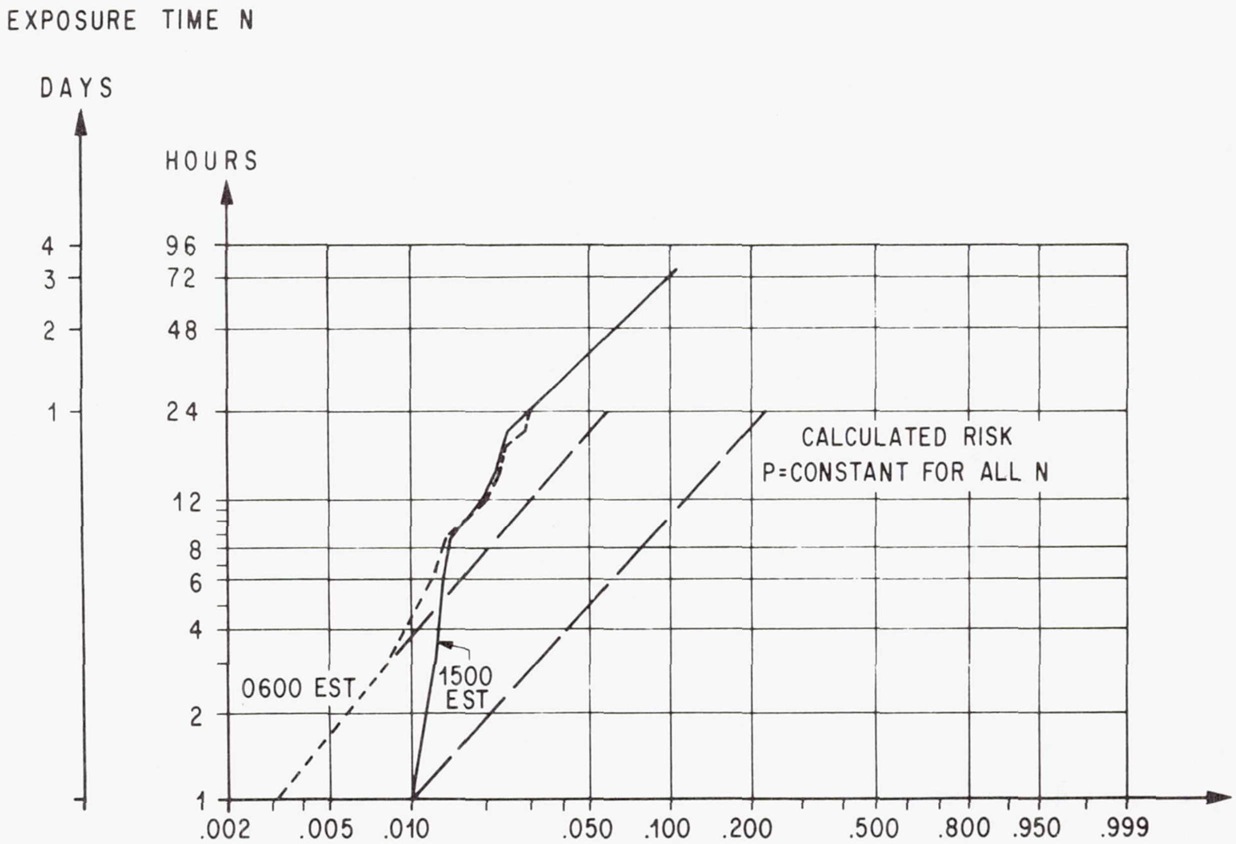

FIGURE 15. HOURLY EXPOSURE PERIOD PROBABILITY FOR PEAK WIND SPEED BEING > 32 KNOTS (10-m LEVEL) AT CAPE KENNEDY, FLORIDA IN OCTOBER

To depict the data sample from which a number of useful statistics for aerospace mission analysis are derived, a serial plot of the twice daily maximum wind speeds that occurred in each profile at 10 km through 15 km altitude for eight years of serially complete rawinsonde records is presented in Figure 18. This graph makes for an interesting subjective analysis, and many words could be written to describe these data. This plot (Fig. 18) represents the complete data sample from which all of the following statistics are derived. After giving some justification for the use of this sample of maximum wind speeds in the 10-15 km layer, some representative statistics will be presented.

The arguments for using the maximum wind speed within the 10-15 km layer rather than the winds at a discrete altitude are as follows:

(1) The most critical altitude for wind loads are not always known during early design phases of a vehicle development program. It is reasonable to assume that the critical altitude will be near that of maximum dynamic pressure; and for large boosters, this altitude is, in general, within 10-15 km altitude.

(2) The maximum winds, particularly during the winter, occur in the 10-15 km layer.

(3) The individual wind measurements are considered representative of quasi-steady state wind values averaged over approximately 600-m altitude. These are winds determined from rawinsonde using standard data reduction methods.

(4) The standard MSFC flight performance and structural load procedures require the use of an embedded gust superimposed on the synthetic design wind profiles [8].

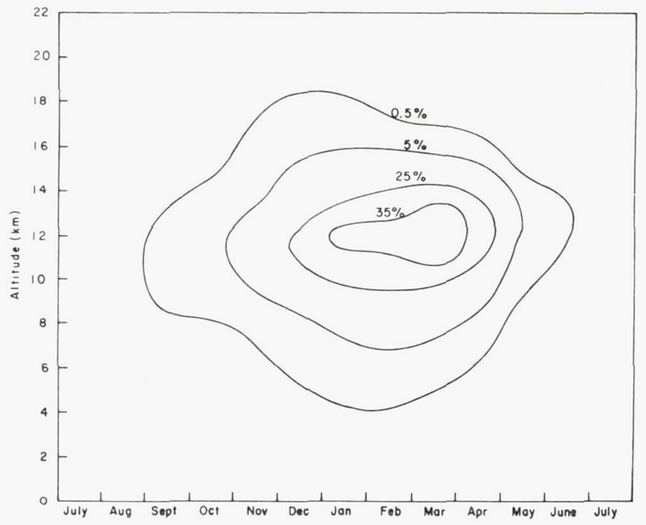

FIGURE 16. FREQUENCY OF SCALAR WIND SPEED EXCEEDING 50 m/sec AS A FUNCTION OF ALTITUDE AND MONTHS FOR THE YEARS 1956-1963 AT CAPE KENNEDY, FLORIDA

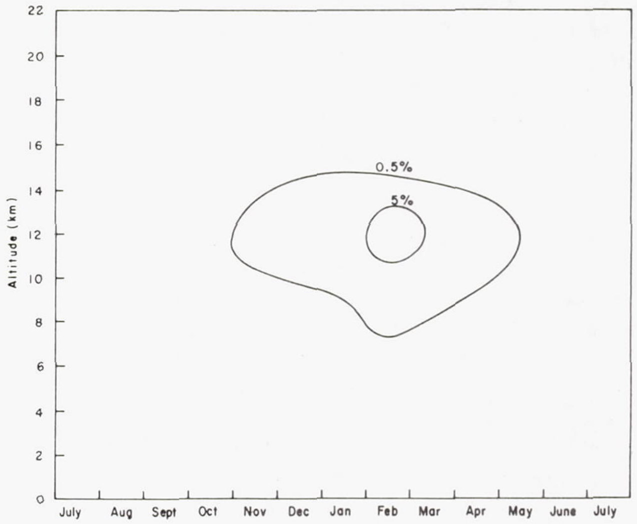

FIGURE 17. FREQUENCY OF SCALAR WIND SPEED EXCEEDING 75 m/sec AS A FUNCTION OF ALTITUDE AND MONTHS FOR THE YEARS 1956-1963 AT CAPE KENNEDY, FLORIDA

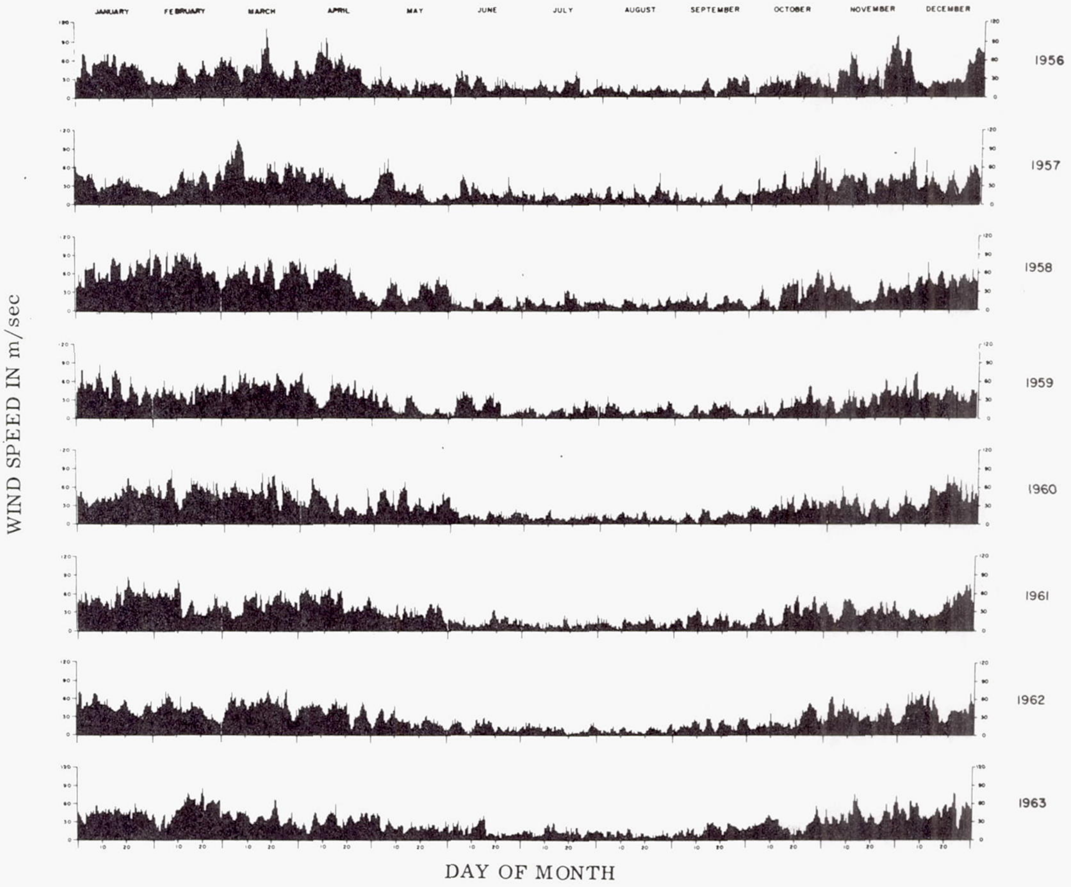

FIGURE 18. TWICE DAILY MAXIMUM WIND SPEED IN THE 10-15 km LAYER AT CAPE KENNEDY, FLORIDA

(5) The resulting statistics from a sample of the maximum wind in the 10-15 km layer yield higher percentile values than the corresponding percentile values of the wind at discrete altitudes or the envelope of the percentiles determined at discrete altitudes. A comparison is presented as Table II.

(6) It is considered that predictions of the maximum wind speed within the 10-15 km layer can be made more reliable than predictions at discrete altitudes. The use of the maximum wind for the 10-15 km layer as the data sample for mission analysis and the envelope of percentile values taken at discrete altitudes for design studies and design criteria introduces a double standard: one data sample for design and another for mission analysis. This double standard is not unreasonable when viewed from the standpoint that the critical wind loads may be considered to occur anywhere within the 10-15 km altitude region. On the other hand, the maximum wind in the 10-15 km layer data sample cannot be used to construct synthetic wind profiles because the sample is selective; i.e., extremes for the layer are used and this would introduce a fictitious discontinuity in the profile.

Serial Correlation Coefficients. That many meteorological parameters are persistent is certainly well known, in fact, many forecast schemes are based on persistence. As a measure of the persistence of the Cape Kennedy winds aloft, serial correlation coefficients were computed for each month of each year by Kendall's formulation

TABLE II. COMPARISON OF THE 90TH AND 95TH PERCENTILE DESIGN WIND SPEED AT 10-14 km ALTITUDE WITH MAXIMUM WIND SPEED FOR THE 10-15 km LAYER AT CAPE KENNEDY, FLORIDA

	From Design Envelopes 10-14 km		From Maximum wind 10-15 km layer	
	90th- m/sec	95th-Percentiles m/sec	90th- m/sec	95th-Percentiles m/sec
Jan	66.0	72.0	71.0	76.8
Feb	68.0	75.0	72.8	84.9
Mar	68.0	75.0	73.2	80.0
Apr	61.0	66.0	65.3	71.0
May	44.0	50.0	45.9	52.2
June	28.0	34.0	32.8	37.8
July	19.0	23.0	23.0	26.9
Aug	19.0	22.0	21.2	24.3
Sept	23.0	26.0	27.8	30.3
Oct	41.0	47.0	45.5	52.2
Nov	47.0	53.0	52.5	62.0
Dec	57.0	63.0	65.0	70.9

$$r_k = \frac{\frac{1}{N-k}\sum_{j=1}^{N-k}(X_jX_{j+k}) - \frac{1}{(N-k)^2}\left(\sum_{j=1}^{N-k}X_j\right)\left(\sum_{j=1}^{N-k}X_{j+k}\right)}{\left[\frac{1}{N-k}\sum_{j=1}^{N-k}X_j^2 - \frac{1}{(N-k)^2}\left(\sum_{j=1}^{N-k}X_j\right)^2\right]^{\frac{1}{2}}\left[\frac{1}{N-k}\sum_{j=1}^{N-k}X_{j+k}^2 - \frac{1}{(N-k)^2}\left(\sum_{j=1}^{N-k}X_{j+k}\right)^2\right]^{\frac{1}{2}}} .$$

$$X_j = X_1, X_2, \ldots . X_{n-1} \qquad X_{j+1} = X_2, X_3, \ldots X_n$$

The mean monthly correlation coefficient was obtained by first performing the Z' transformation

$$Z' = \tfrac{1}{2}\ln\frac{1+r_k}{1-r_k}$$

for each r_k, then computing $\bar{Z}'$ from

$$\overline{Z'} \; \frac{\sum_{k=1}^{k=N/2} Z'_k\,(N-k-3)}{\sum_{k=1}^{k=N/2}(N-k-3)}$$

and finally determining $\bar{r}_k$ from

$$\bar{r}_k = \tanh \bar{Z}'_k \; .$$

Although the correlation coefficients vary widely from year to year (Fig. 19) in the mean, the January wind speeds show a significant positive correlation for approximately 6 twelve-hour periods (3 days).

Empirical Exceedance Probabilities. By considering the wind speeds as a step-wise continuous (over 12-hr intervals) time series, a number of useful statistics have been derived which have very important applications to the design, mission planning, and ultimately launch operations of aerospace vehicles. The assumption of constant wind over 12-hr intervals is imposed because rawinsonde wind measurements were not made routinely at closer intervals for the eight years of record. Therefore, the basic wind records were serially completed only for wind profiles twice daily for Cape Kennedy. For most purposes, this assumption does not greatly handicap the statistical analysis, but in the case of time-dependent statistics, inferences for the initial time period less than 12 hr are precluded. For time periods after the initial 12-hr increment, the time-dependent probabilities may be considered continuous and interpolations would be valid.

The probability of the maximum wind speed (W) in the 10-15 km layer exceeding (and not exceeding) specified values of wind speed (W^*) one or more times in k-consecutive 12-hr periods is presented in Table III (parts A and B). The computational method used in deriving these statistics was a combinational counting procedure. Identical results can also be derived from an analysis of runs (a run is a succession of like events). Furthermore, the probability of a run of length k can be derived from Table III.

The probability of runs and conditional probabilities can be derived from the exceedance probabilities (Table III). An example is presented below, and the following definitions are helpful.

Let $P\{B\} = P[W \geq W^*]$ denote the probability that $W \geq W^*$ one or more times in k-consecutive 12-hr periods (these statistics are given in Table IIIB); then $[1-P\{B\}] = P\{B'\}$ is the probability that $W < W^*$ for k-consecutive 12-hr periods. The probability $P\{B'\}$ is also the probability of a run <u>below</u> W^* of length k in units of 12-hr periods.

TABLE III. PROBABILITY (%) THAT THE MAXIMUM WIND SPEED, W, IN THE 10-15 km LAYER WILL OCCUR ONE OR MORE TIMES LESS THAN (EQUAL TO OR GREATER THAN) SPECIFIED VALUES, W*, FOR K-CONSECUTIVE 12-HR PERIODS AT CAPE, KENNEDY, FLORIDA

MONTH---JANUARY
Number of Observations---496

[A] SPEED ---less than---05, 10, . . . 110---m/sec

W*	05	10	15	20	25	30	35	40	45	50	55	60	65	70	75	80	85	90	100	110	Min. Speed	No. Occ.
K 1	.0	.0	.0	.0	2.0	6.3	12.5	21.0	34.3	49.6	64.9	76.4	84.1	88.9	94.0	96.6	98.4	99.8	99.8	100.0	21	1
K 2	.0	.0	.0	.0	3.0	8.9	16.3	27.0	42.7	58.5	73.6	83.5	88.5	93.1	96.4	98.6	99.4	100.0	100.0	100.0	21	1
K 3	.0	.0	.0	.0	4.0	10.7	19.4	31.9	49.0	65.3	79.0	87.9	91.5	95.8	98.0	99.4	99.8	100.0	100.0	100.0	21	1
K 4	.0	.0	.0	.0	5.0	12.5	22.2	36.1	54.2	69.8	83.1	91.1	93.8	96.8	99.8	99.8	100.0	100.0	100.0	100.0	21	2
K 5	.0	.0	.0	.0	6.0	14.1	24.4	39.9	58.3	73.6	86.3	93.5	95.2	97.4	99.4	100.0	100.0	100.0	100.0	100.0	21	3
K 6	.0	.0	.0	.2	7.1	15.7	26.6	43.1	61.5	76.4	88.5	95.4	96.4	97.8	99.8	100.0	100.0	100.0	100.0	100.0	15	1
K 7	.0	.0	.0	.6	8.3	17.1	28.8	46.4	64.3	79.0	90.1	96.6	97.2	98.2	100.0	100.0	100.0	100.0	100.0	100.0	15	1
K 8	.0	.0	.0	1.0	9.3	18.5	30.8	49.0	66.5	81.3	91.3	97.6	98.0	98.6	100.0	100.0	100.0	100.0	100.0	100.0	15	1
K 9	.0	.0	.2	1.4	10.3	20.0	32.9	51.4	68.5	83.3	92.3	98.4	98.6	99.0	100.0	100.0	100.0	100.0	100.0	100.0	13	1
K 10	.0	.0	.4	1.8	11.3	21.4	34.5	53.2	70.4	84.7	93.1	99.2	99.2	99.4	100.0	100.0	100.0	100.0	100.0	100.0	13	1

[B] SPEED ---equal to or greater than---m/sec

W*	05	10	15	20	25	30	35	40	45	50	55	60	65	70	75	80	85	90	100	110	Max. Speed	No. Occ.
K 1	100.0	100.0	100.0	100.0	98.0	93.8	87.5	79.0	65.7	50.4	35.1	23.6	15.9	11.1	6.0	3.4	1.6	.2	.2	.0	101	1
K 2	100.0	100.0	100.0	100.0	98.8	96.4	91.3	84.5	73.8	59.5	44.2	30.8	20.6	15.5	8.5	5.4	2.6	.4	.4	.0	101	1
K 3	100.0	100.0	100.0	100.0	99.4	97.6	94.0	87.3	78.2	65.3	50.8	35.9	24.4	19.0	10.9	7.7	3.8	.6	.6	.0	101	1
K 4	100.0	100.0	100.0	100.0	99.6	97.8	95.6	89.1	80.8	69.4	55.4	39.7	28.0	22.4	12.9	9.5	4.8	1.0	.8	.0	101	1
K 5	100.0	100.0	100.0	100.0	99.6	98.0	96.4	90.7	83.5	72.2	58.9	42.9	31.3	25.2	14.9	11.3	5.8	1.2	1.0	.0	101	1
K 6	100.0	100.0	100.0	100.0	99.6	98.2	97.2	92.1	85.7	74.4	61.5	45.8	34.7	27.8	16.5	12.9	6.9	1.4	1.2	.0	101	1
K 7	100.0	100.0	100.0	100.0	99.6	98.2	97.6	93.1	87.3	76.6	63.7	48.4	37.9	30.6	18.1	14.5	7.9	1.6	1.4	.0	101	1
K 8	100.0	100.0	100.0	100.0	99.6	98.2	97.8	93.8	88.7	78.2	65.7	50.4	40.3	33.1	19.8	16.1	8.9	1.8	1.6	.0	101	1
K 9	100.0	100.0	100.0	100.0	99.6	98.2	98.0	94.4	89.7	79.8	67.5	52.0	42.5	35.3	21.2	17.5	9.9	2.0	1.8	.0	101	1
K 10	100.0	100.0	100.0	100.0	99.6	98.2	98.0	95.0	90.7	80.8	69.2	53.2	44.2	37.3	22.6	18.8	10.7	2.2	2.0	.0	101	1

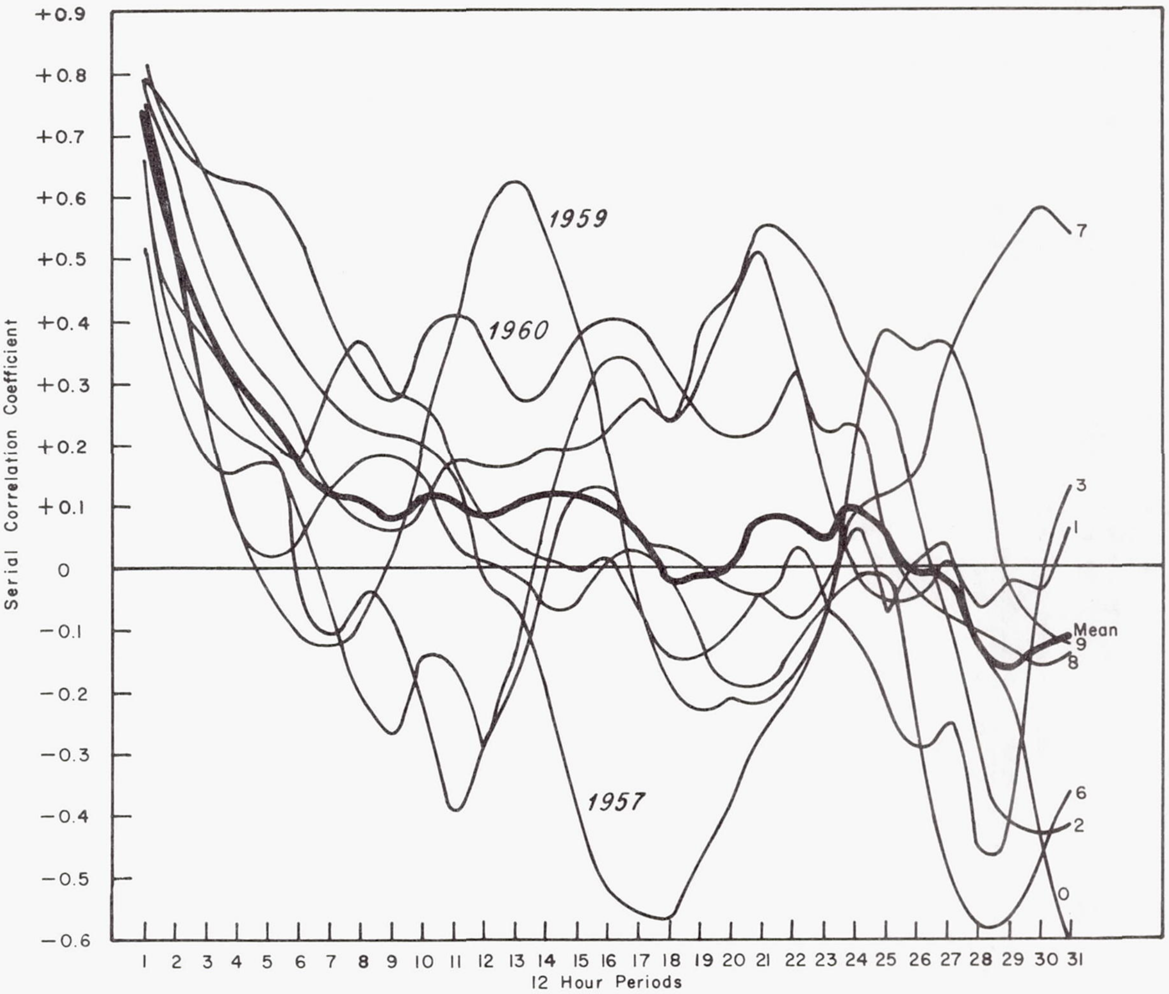

FIGURE 19. PLOT OF MAXIMUM WIND SPEED IN THE 10-15 km LAYER FOR THE YEARS 1956-1963 DURING JANUARY AT CAPE KENNEDY, FLORIDA

Let $P\{A\} = P[W < W^*]$ denote the probability that $W < W^*$ one or more times in k-consecutive 12-hr periods (these statistics are given in Table IIIA); then $[1 - P\{A\}] = P\{A'\}$ is the probability that $W \geq W^*$ for k-consecutive 12-hr periods. The probability $P\{A'\}$ is also the probability of a run above W^* of length k in units of 12-hr periods.

Using 50 m/sec for W^* from Table III, the January statistics, and the above definitions, the probability of a run <u>above</u> 50 m/sec and a run <u>below</u> 50 m/sec of length k in units of 12-hr periods is illustrated in Table IV. The computational procedure to derive conditional probabilities from $P\{B'\}$ is also illustrated in Table IV. The conditional probabilities from $P\{A'\}$ can also be computed in like fashion.

When W^* is defined as the critical wind speed prohibiting the launch of a vehicle, several statistical inferences in terms of vehicle operations can be made.

1. The probability of $P\{B\} = P[W \geq W^*]$ as previously defined is the probability of no-launch at least one time in k-consecutive 12-hr periods. From Table IIIB for $W^* = 50$ m/sec, the probability is 0.504 for k=1. Stated in another way, there is a 50.4 percent chance of no-launch during any arbitrary 12-hr period during January under the assumption that when the wind is critical, it is critical for 12 hr. There is an 80.8 percent chance of no-launch at least one time in 10 consecutive 12-hr periods (or 5 days). This probability is also read from Table III.

TABLE IV. AN EXAMPLE FOR JANUARY IN THE COMPUTATION OF PROBABILITIES OF RUNS AND CONDITIONAL PROBABILITIES FOR MAXIMUM WIND IN THE 10-15 km LAYER AT CAPE KENNEDY, FLORIDA

k-12 hr periods (k)	$P\{B\}$ $P[W \geq 50^*]$ (%)	$P\{A\}$ $P[W < 50^*]$ (%)	$P\{B'\}$ $[1-P\{B\}]$ (%)	$P\{A'\}$ $[1-P\{A\}]$ (%)	Comparison with a random variable	Conditional Probabilities (%), from $P\{B'\}$ P_k/P_i, $i \leq k$.			
						i= 1	i= 2	i= 3	i= 4
1	50.4	49.6	49.6	50.4	50.0	100			
2	59.5	58.5	40.5	41.5	25.0	82	100		
3	65.3	65.3	34.7	34.7	12.5	70	86	100	
4	69.4	69.8	30.6	30.2	6.25	62	76	88	100
5	72.2	73.6	27.8	26.4	3.12	56	69	80	91
6	74.4	76.4	25.6	23.6	1.56	52	63	74	84
7	76.6	79.0	23.4	21.0	0.78	47	58	67	76
8	78.2	81.3	21.8	18.8	0.39	44	54	63	71
9	79.8	83.3	20.2	16.7	0.20	41	50	58	66
10	80.8	84.7	19.2	15.3	0.10	39	47	55	63
	From Table III. B	From Table III. A	runs below	runs above					

* Units, m/sec

2. The probability $P\{A\} = P[W < W^*]$ as previously defined is the probability of launch at least one time in k-consecutive 12-hr periods. From Table IIIA for $W^* = 50$ m/sec, this probability for k = 10 consecutive 12-hr periods in 0.847.

3. The probability $P\{B'\} = [1-P\{B\}]$, which can be computed from Table IIIB or taken directly from Tables V and VI, is the probability of launch for k-consecutive 12-hr periods. From Table IV for January for $W^* = 50$ m/sec, there is a 19.2 percent chance that the wind will not be critical for launch for 10 consecutive 12-hr periods or for a 5-day period.

4. The probability $P\{A'\} = [1-P\{A\}]$, which can be computed from Table IIIA or taken directly from Tables VI and VII, is the probability of no-launch for k-consecutive 12-hr periods. From Table IV for January for $W^* = 50$ m/sec, there is a 15.3 percent chance that the wind will be critical for launch for 10 consecutive 12-hr periods or for a 5-day period.

5. Conditional probabilities can be readily computed from the run statistics ($P\{B'\}$ and $P\{A'\}$, as illustrated in Table IV or taken directly from Tables V-VIII). The January statistics for wind speed $\geq$ 50, < 50, $\geq$ 75, and < 75 m/sec for the

probabilities of runs above and runs below these specified wind speed values and the resulting conditional probabilities are presented in Tables V, VI, VII, and VIII, respectively. The explanation for the columns for these tables is as follows:

Column 1 is the length of a run in increments of 12-hr periods; i.e., k - 12-hr periods.

Column 2 is the number of runs of length k (denote this column as N_{rk}). (This is the absolute frequency of a run of length k.)

Column 3 is the number of observations of length k or greater. (This is the cumulative absolute frequency of runs of length k; denote this column by N_k.)

Column 4 is the number of observations in the sample. This is a fixed value for each month corresponding to the number of observations for the given month in the eight-year data dample.

Column 5 is the probability of having a run of length k or greater. Denote this column by P_k, where

$$P_k = \frac{N_k}{N} .$$

Column 6 and all other columns are the conditional probabilities:

$$P_{c(k,i)} = \frac{N_k}{N_i} , \qquad \begin{array}{l} i \leq k \\ i = 1, 2, 3 \ldots \end{array}$$

where column 6 is for i = 1, column 7 is for i = 2, etc.

For vehicle mission analysis and launch planning, conditional probabilities give answers to such questions as, "What is the probability that the winds will remain critical for launch, given that they are critical at 24 or 12 hr prior to the scheduled launch?" Conversely, given that the winds are not critical at 24 or 12 hr before launch, "what is the probability that they will remain not critical up to the scheduled launch?"

From Table IV at 24 hr before launch, suppose that the wind is below critical limits (< 50 m/sec) for the first time in a series of wind measurements, then there is a 70 percent chance that the wind will remain below critical limits at launch time. Suppose wind measurements at 12 hr before launch revealed that the magnitudes are still below the critical limits; now the conditional probability for launch time is 0.86, or there is an 86 percent chance that the winds will be below critical limits at launch time. This conditional probability is read from Table IV at k = 3 and i = 2.

Clearly, if the wind is observed to be less than 50 m/sec, the probability of this event occurring at a given time is 1.00, or as indicated in Table IV, 100 percent. Based on this information, the predicted occurrence of the event two days hence is 56 percent (read from Table IV at i = 1 and k = 5); whereas, there was only a 49.6 percent chance of the wind being less than 50 m/sec on any arbitrary observation during the month. To continue the example, suppose the wind is observed 12 hr later (corresponding to i = 2) and it is still below 50 m/sec; then, the probability that the wind will be below 50 m/sec 24 hr in the future is 76 percent. This value is read from the table at i = 2, k = 4. Now, compare the probabilities at k_2i_1, k_3i_2, etc. (or the values above the diagonal); these probabilities increase but will later decrease and even fluctuate as the computations are carried out further. In a similar manner, the conditional probabilities can be carried out for $P\{A'\}$ and corresponding interpretations can be made. The meteorologist terms this behavior of an atmospheric variable with respect to time as "persistence." In principle, the conditional probabilities could be used in conjunction with other meteorological information to make a deterministic wind prediction. Another possible application of the conditional probabilities would be to serve as base-line values for wind forecast verifications.

By comparing $P\{B'\}$ and $P\{A'\}$ with the statistics of a random variable (see Table IV), it is concluded that the wind sample is not stochastically independent. What happens to the conditional probabilities for the random series? The conditional probabilities remain 0.50.

Probability of Runs and Conditional Probabilities. From an analysis independent of that for exceedance probabilities, the run probabilities and conditional probabilities for the same data sample (the maximum wind speed 10-15 km over Cape Kennedy) were computed for specified wind speeds. Since these statistics were determined at different times and using different techniques, the notation is slightly different. The most satisfying feature is that the resulting statistics are identical, thus giving rise to confidence in the correctness of the computation processes, as well as providing an independent approach to the same problem. Figure 20 is a useful graphical form to display the probabilities of runs.

TABLE V. RUNS AND CONDITIONAL PROBABILITIES FOR THE MAXIMUM WIND IN THE 10-15 km LAYER BEING < 50 m/sec (JANUARY, CAPE KENNEDY, FLORIDA)

k	N_{rk}	N_k	N	P_k	P_{c1}	P_{c2}	P_{c3}	P_{c4}	P_{c5}	P_{c6}	P_{c7}	P_{c8}	P_{c9}	P_{c10}	P_{c11}	P_{c12}	P_{c13}	P_{c14}	P_{c15}	P_{c16}
1	16	246	496	.496	1.0															
2	9	201	496	.405	.82	1.0														
3	7	172	496	.347	.70	.86	1.0													
4	3	152	496	.306	.62	.76	.88	1.0												
5	0	138	496	.278	.56	.69	.80	.91	1.0											
6	3	127	496	.256	.52	.63	.74	.84	.92	1.0										
7	1	116	496	.234	.47	.58	.67	.76	.84	.91	1.0									
8	3	108	496	.218	.44	.54	.63	.71	.78	.85	.93	1.0								
9	1	100	496	.202	.41	.50	.58	.66	.72	.79	.86	.93	1.0							
10	0	95	496	.192	.39	.47	.55	.63	.69	.75	.82	.88	.95	1.0						
11	0	91	496	.183	.37	.45	.53	.60	.66	.72	.78	.84	.91	.96	1.0					
12	1	87	496	.175	.35	.43	.51	.57	.63	.69	.75	.81	.87	.92	.96	1.0				
13	0	83	496	.167	.34	.41	.48	.55	.60	.65	.72	.77	.83	.87	.91	.95	1.0			
14	1	80	496	.161	.33	.40	.47	.53	.58	.63	.69	.74	.80	.84	.88	.92	.96	1.0		
15	1	77	496	.155	.31	.38	.45	.51	.56	.61	.66	.71	.77	.81	.85	.89	.93	.96	1.0	
16	0	75	496	.151	.30	.37	.44	.49	.54	.59	.65	.69	.75	.79	.82	.86	.90	.94	.97	1.0

k = Number of 12-hr periods (run).

N_{rk} = Number of runs of exact length k.

P_k = The probability that run of length k or greater will occur.

N_k = Number of occurrences of runs equal to or greater than i.

N = Number of possible outcomes.

P_c = Conditional probability

TABLE VI. RUNS AND CONDITIONAL PROBABILITIES FOR THE MAXIMUM WIND IN THE 10-15 km LAYER BEING < 75 m/sec (JANUARY, CAPE KENNEDY, FLORIDA)

k	N_{rk}	N_k	N	P_k	P_{c1}	P_{c2}	P_{c3}	P_{c4}	P_{c5}	P_{c6}	P_{c7}	P_{c8}	P_{c9}	P_{c10}	P_{c11}	P_{c12}	P_{c13}	P_{c14}	P_{c15}	P_{c16}
1	1	466	496	.940	1.0															
2	2	454	496	.915	.97	1.0														
3	0	442	496	.891	.95	.97	1.0													
4	2	432	496	.871	.93	.95	.98	1.0												
5	0	422	496	.851	.91	.93	.95	.98	1.0											
6	0	414	496	.835	.89	.91	.94	.96	.98	1.0										
7	1	406	496	.819	.87	.89	.92	.94	.96	.98	1.0									
8	0	398	496	.802	.85	.88	.90	.92	.94	.96	.98	1.0								
9	0	391	496	.788	.84	.86	.88	.91	.93	.94	.96	.98	1.0							
10	0	384	496	.774	.82	.85	.87	.89	.91	.93	.95	.96	.98	1.0						
11	2	377	496	.760	.81	.83	.85	.87	.89	.91	.93	.95	.96	.98	1.0					
12	1	370	396	.746	.79	.81	.84	.86	.88	.89	.91	.93	.95	.96	.98	1.0				
13	1	365	496	.736	.78	.80	.83	.84	.86	.88	.90	.92	.93	.95	.97	.99	1.0			
14	1	361	496	.728	.77	.80	.82	.84	.86	.87	.89	.91	.92	.94	.96	.98	.99	1.0		
15	0	358	496	.722	.77	.79	.81	.83	.85	.86	.88	.90	.92	.93	.95	.97	.98	.99	1.0	
16	0	355	496	.716	.76	.78	.80	.82	.84	.86	.87	.89	.91	.92	.94	.96	.97	.98	.99	1.0

k = Number of 12-hr periods (run).
N_{rk} = Number of runs of exact length k.
P_k = The probability that run of length i or greater will occur.
N_k = Number of occurrences of runs equal to or greater than k.
N = Number of possible outcomes.
P_c = Conditional probability.

TABLE VII. RUNS AND CONDITIONAL PROBABILITIES FOR THE MAXIMUM WIND IN THE 10-15 km LAYER BEING ≥ 50 m/sec (JANUARY, CAPE KENNEDY, FLORIDA)

k	N_{rk}	N_k	N	P_k	P_{c1}	P_{c2}	P_{c3}	P_{c4}	P_{c5}	P_{c6}	P_{c7}	P_{c8}	P_{c9}	P_{c10}	P_{c11}	P_{c12}	P_{c13}	P_{c14}	P_{c15}	P_{c16}
1	11	250	496	.504	1.0															
2	12	206	496	.415	.82	1.0														
3	3	172	496	.347	.69	.83	1.0													
4	5	150	496	.302	.60	.73	.87	1.0												
5	1	131	496	.264	.52	.64	.76	.87	1.0											
6	2	117	496	.236	.47	.57	.68	.78	.89	1.0										
7	1	104	496	.210	.42	.50	.60	.69	.79	.89	1.0									
8	3	93	496	.188	.37	.45	.54	.62	.71	.79	.89	1.0								
9	1	83	496	.167	.33	.40	.48	.55	.63	.71	.80	.89	1.0							
10	2	76	496	.153	.30	.37	.44	.51	.58	.65	.73	.82	.92	1.0						
11	0	70	496	.141	.28	.34	.41	.47	.53	.60	.67	.75	.84	.92	1.0					
12	0	66	496	.133	.26	.32	.38	.44	.50	.56	.63	.71	.80	.87	.94	1.0				
13	1	62	496	.125	.25	.30	.36	.41	.47	.53	.60	.67	.75	.82	.89	.94	1.0			
14	2	58	496	.117	.23	.28	.34	.39	.44	.50	.56	.62	.70	.76	.83	.88	.94	1.0		
15	0	55	496	.111	.22	.27	.32	.37	.42	.47	.53	.59	.66	.72	.79	.83	.89	.95	1.0	
16	0	54	496	.109	.22	.26	.31	.36	.41	.46	.52	.58	.65	.71	.77	.82	.87	.93	.98	1.0

k = Number of 12-hr periods (run).

N_{rk} = Number of runs of exact length k.

P_k = The probability that run of length k or greater will occur.

N_k = Number of occurrences of runs equal to or greater than i.

N = Number of possible outcomes.

P_c = Conditional probability.

TABLE VIII. RUNS AND CONDITIONAL PROBABILITIES FOR THE MAXIMUM WIND IN THE 10-15 km LAYER BEING ≥ 75 m/sec (JANUARY, CAPE KENNEDY, FLORIDA)

k	N_{rk}	N_k	N	P_k	P_{c1}	P_{c2}	P_{c3}	P_{c4}	P_{c5}	P_{c6}
1	4	30	496	.060	1.0					
2	4	18	496	.036	.60	1.0				
3	1	10	496	.020	.33	.56	1.0			
4	1	6	496	.012	.20	.33	.60	1.0		
5	1	3	496	.006	.10	.17	.30	.50	1.0	
6	1	1	496	.002	.03	.06	.10	.17	.33	1.0

k = Number of 12-hr periods (run).

N_{rk} = Number of runs of exact length k.

P_k = The probability that run of length i or greater will occur.

N_k = Number of occurrences of runs equal to or greater than k.

N = Number of possible outcomes.

P_c = Conditional probability.

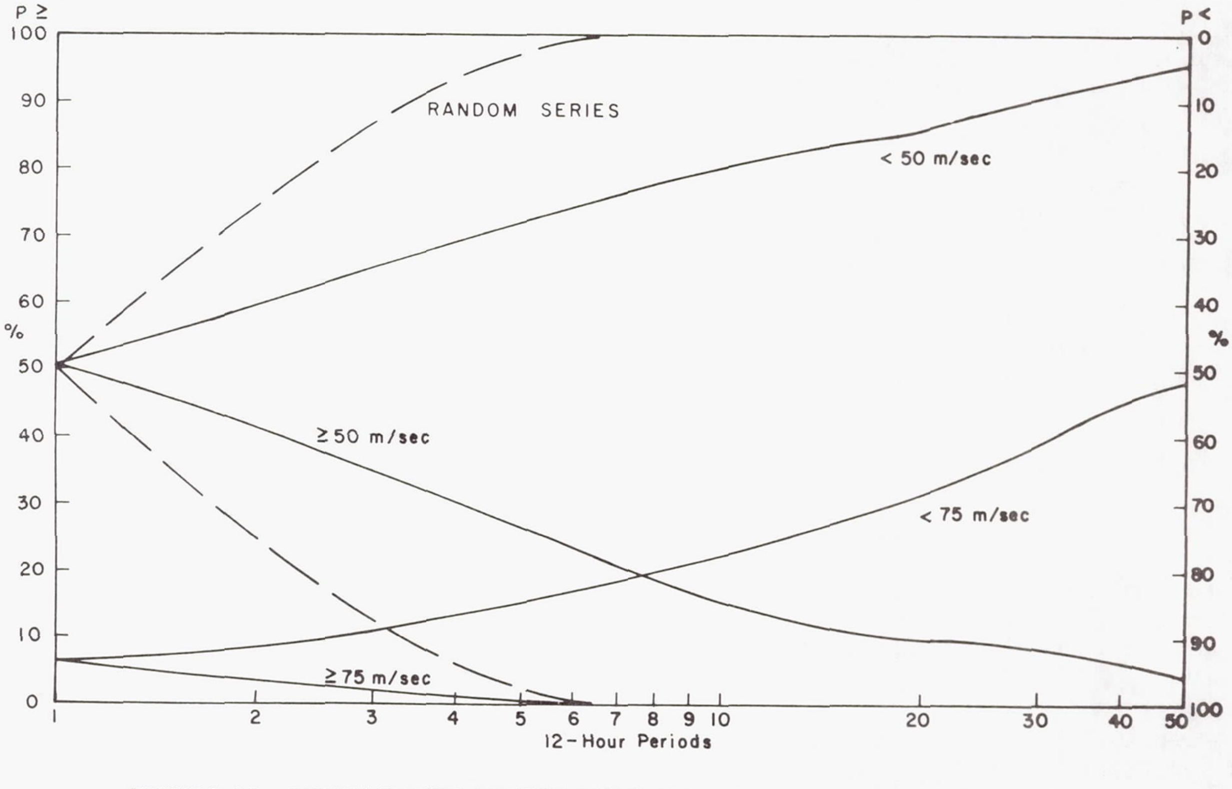

FIGURE 20. PROBABILITY OF THE MAXIMUM WIND SPEED IN THE 10-15 km LAYER BEING ≥ AND < SPECIFIED VALUES FOR k 12-HR PERIODS DURING JANUARY AT CAPE KENNEDY, FLORIDA

From the definitions presented in the section "Empirical Exceedance Probabilities," an inverse operation can be performed to calculate the exceedance probabilities from the probabilities of runs given in Tables V-VIII. For example, the probability that the maximum wind speed in the 10-15 km layer will exist for 10 consecutive 12-hr periods at a magnitude ≥ 50 m/sec in January (Table VII, column 5, corresponding to $k = 10$) is 0.153. In symbols, this statement is expressed as $P\{W \geq 50 \text{ m/sec}\}$ for 10 consecutive 12-hr periods is 0.153.

The probability that the wind speed will not exceed 50 m/sec at least one time in 10 consecutive 12-hr periods is 0.847 ($1 - 0.153 = 0.847$). The probability that the wind speed will exceed 50 m/sec at least one time in 10 consecutive 12-hr periods in January is obtained from Table V, $1 - 0.192 = 0.808$.

Empirical Multiple Exceedance Probabilities. *The longest succession of maximum wind speed in* the 10-15 km layer with wind speeds ≥ 75 m/sec occurred during the winter of 1958. This year would be referred to as a high wind year. In terms of runs, the longest runs ≥ 75 m/sec by months are as following:

Max. Length of Run in 12-hr Periods	Year/Month	Dates and Times Inclusive
6	1958/Jan.	25, 12Z - 27, 12Z
14	1958/Feb.	10, 00Z - 16, 12Z
7	1958/Mar.	28, 12Z - 31, 12Z
3	1958/Apr.	15, 12Z - 16, 12Z
(There were no values ≥ 75 m/sec for May - October)		
6	1956/Nov.	25, 03Z - 27, 15Z
4	1956/Dec.	29, 03Z - 30, 15Z

The counting rule for runs is as follows: If a run begins in one month and extends into a following month, it is counted as a run for the month in which it begins.

Beginning at 12Z on January 25, 1958, the wind blew at a speed ≥ 75 m/sec for fifty-three 12-hr periods (26 1/2 days) with only 6 exceptions: There were two single breaks, i.e., twice that the wind dropped below 75 m/sec; twice the wind dropped below 75 m/sec for two 12-hr periods; and twice the wind dropped below 75 m/sec for three 12-hr periods. For this particular sample period of 53, there was a 77 percent chance that the wind was equal to or greater than 75 m/sec. Yet, for the entire sample of eight Januaries, there was a 6 percent chance that the wind speed was equal to or greater than 75 m/sec in the 10-15 km layer.

Now return to the discussion on the probabilities $P\{B\}$ and $P\{A\}$; i.e., the probability that $W \geq W^*$ and $W < W^*$ one or more times in k-consecutive 12-hr periods. To base an entire mission on the probability of having at least one opportunity to launch because of a winds-aloft constraint in k-consecutive 12-hr periods, even though this probability can be well above a 95 percent chance of launch within the launch opportunity period, may be a rather high risk to the project in view of the consequences: loss of the mission. For this reason, the computations have been extended to derive the probability of 2, 3, 4, . . . i, ($i = 20$) launch opportunities (because of arbitrary winds-aloft constraints) in k-consecutive 12-hr periods. These latter statistics are referred to as the probability of i successes in j periods: $P\{i \text{ successes in } j \text{ periods}\}$. The extreme approach would be to base the probability of mission success on the probability that the winds aloft would be below the launch constraint value continuously for k-consecutive 12-hr periods. These statistics will find immediate application to multiple vehicle launches such as will be required for AAP in the concept of "cluster vehicles." Where the mission successes depend upon getting two or more vehicles launched at intervals from 1 to 3 days separation.

The probable number of launch opportunities (wind speed < critical) in a given number of periods expressed in terms of i successes (where success is the occurrence of wind speed < critical) in j periods is shown in Table IX. For example, suppose a mission has a 4-day launch window in January, and the vehicle is constrained to wind speeds less than 50 m/sec. Of concern to the mission planner is the probability that at least one observation of wind speeds < 50 m/sec (one launch opportunity) will occur during the launch window (eight 12-hr periods). This probability, 0.813, is read from Table IX, line 8, column 1. If, however, after considering other factors, it is decided that 4 successes in the 8 periods are required, that probability, 0.550, is read from line 8, column 4. Table X contains similar probability statements except here it is required that the successes be consecutive. With this additional restriction, the probability of success will naturally be lower. Using the example above, one obtains 0.431 from Table X versus 0.550 from Table IX.

TABLE IX. P{I SUCCESSES IN J PERIODS} MAXIMUM WIND BEING < 50 m/sec IN THE 10-15 km LAYER (JANUARY, CAPE KENNEDY, FLORIDA)

J 12-hr periods	1	2	3	4	5	6	7	8	9	10	11	12	13	14	15	16
1	.496			-												
2	.585	.405		-												
3	.653	.488	.347	-												
4	.698	.560	.427	.306												
5	.736	.599	.504	.379	.278											
6	.764	.631	.540	.464	.341	.256										
7	.790	.649	.577	.506	.423	.313	.234									
8	.813	.669	.591	.550	.468	.399	.280	.218								
9	.833	.690	.605	.565	.516	.450	.369	.258	.202							
10	.847	.714	.619	.583	.530	.498	.425	.343	.236	.192						
11	.859	.732	.641	.593	.548	.510	.480	.403	.315	.220	.183					
12	.867	.754	.655	.611	.558	.524	.492	.468	.379	.288	.208	.175				
13	.875	.774	.671	.621	.577	.534	.506	.482	.454	.351	.268	.198	.167			
14	.883	.790	.692	.631	.589	.548	.520	.494	.470	.431	.325	.254	.188	.161		
15	.889	.806	.702	.653	.599	.560	.532	.510	.482	.458	.399	.308	.240	.181	.155	
16	.891	.825	.712	.667	.617	.569	.546	.520	.500	.472	.429	.383	.288	.232	.175	.151

TABLE X. P {I CONSECUTIVE SUCCESSES IN J PERIODS} MAXIMUM WIND BEING < 50 m/sec
IN THE 10-15 km LAYER (JANUARY, CAPE KENNEDY, FLORIDA)

J 12-hr periods	1	2	3	4	5	6	7	8	9	10	11	12	13	14	15	16
1	.496															
2	.585	.405														
3	.653	.466	.347													
4	.698	.528	.393	.306												
5	.736	.577	.440	.399	.278											
6	.764	.611	.484	.371	.304	.256										
7	.790	.637	.518	.401	.331	.282	.234									
8	.813	.653	.540	.431	.355	.308	.256	.218								
9	.833	.667	.563	.460	.379	.333	.278	.238	.202							
10	.847	.681	.575	.482	.401	.357	.298	.258	.216	.192						
11	.859	.696	.585	.504	.423	.379	.319	.276	.230	.204	.183					
12	.867	.706	.595	.518	.442	.401	.337	.294	.244	.216	.196	.175				
13	.875	.716	.605	.530	.460	.423	.355	.310	.258	.228	.208	.188	.167			
14	.883	.726	.615	.542	.472	.442	.373	.327	.270	.240	.220	.200	.177	.161		
15	.889	.736	.625	.554	.482	.460	.391	.343	.282	.250	.232	.212	.188	.171	.155	
16	.891	.746	.635	.567	.494	.472	.407	.359	.294	.260	.242	.224	.198	.181	.165	.151

The data shown here were extracted from tables covering all months for wind speeds ≥ and < 5, 10, 15, . . . 90 m/sec, where $i = 1, 2, 3, \ldots 20$, and $j = 1, 2, 3, \ldots 40$.

Since a large number of statistics can be derived from the statistics like those presented in Tables III and V-VIII, these tables can serve as basic inputs to computer simulation programs for mission analysis purposes. However, transitional conditional probabilities cannot be derived from these tables. The winds can change with time from critical for launch to noncritical several times during a mission opportunity or during a long countdown. For example, there are 20 possible combinations for conditional probabilities of critical and noncritical winds in only five consecutive periods. Because of the large volume of resulting statistics, the presentation of all possible conditional probabilities must take the form of mathematical statistical models. The most suggestive forms are to be found in order statistics involving Markov processes.

The message in these winds aloft launch probability statements is: "If you don't first succeed, try and try again, but beware that the longer you try and don't succeed, the probability becomes greater that something else will cause a problem." The application of this thought is inherent in such areas as trade-off studies, mission analysis, systems engineering analysis, etc.

Wind Bias Profiles. Two alternatives are, in principle, feasible to lower the probability of launch delays caused by winds aloft, particularly during the winter months. One is to use wind bias profiles, and the other is to develop an advance guidance system for wind load relief. Based on monthly median pitch plane wind component profiles, the vehicle tilt program is biased to yield a small angle of attack and thus reduce structural loads. This procedure could also be applied to the yaw plane, but it has not been used to date. When properly applied, the wind bias technique lowers the probability of launch delay from winds aloft. Wind bias profiles have been used for a number of Saturn flights; e.g., SA-4 launched March 28, 1963; SA-5 launched January 29, 1964; SA-9 launched February 16, 1965; AS-201 launched February 22, 1966; and Saturn 501 launched November 9, 1967. The SA-6, launched May 28, 1964, was wind biased to intentionally introduce a larger angle of attack and thus greater structural loads than would otherwise be likely from the natural occurrence of the wind profile during that time of year. Because of the nature of some missions, it is expected that the use of wind-biased techniques would be operationally more complicated than for these flights. If the launch azimuths have large range during a launch window, a system to update the wind bias would be required. The merits of the wind-biased technique must be analyzed for each mission. The information needed for the analysis includes:

1. Launch opportunities - dates.
2. Launch windows - hours within the launch opportunities.
3. Launch azimuth versus launch windows.

CONCLUSIONS

Through the use of examples, the importance of ground winds and winds aloft statistics to the aerospace vehicle programs has been presented. There is still much work to be done to extend this study to improve the theoretical probability models and to present the resulting statistics in a form amenable for use in management decisions involving systems engineering. A number of statistical concepts have been advanced relative to the application of wind statistics to aerospace vehicle design, operational, and mission problems. The determination of the probability of launch as a function of several atmospheric launch constraints (e.g., ground winds, winds aloft, and clouds) taken simultaneously and in combination is the subject of a separate study. The proper balance in supporting research funds and program funds to continue these efforts will serve to the mutual benefit of several interests within all NASA Centers. The realization of the importance of these and similar studies will become more apparent with the changing role of the MSFC space program from that of research and development of large boosters to that of space exploration and application.

REFERENCES

1. Gumbel, E. J.: Statistics of Extremes, Columbia University Press, New York, 1958.

2. Fisher, R. A.: Contributions to Mathematical Statistics, John Wiley and Sons, Inc., New York, 1950.

3. Thom, H. C. S.: Distribution of Extreme Winds in the United States. Journal of the Structural Division Proceedings of the American Society of Civil Engineers, April, 1960.

4. Court, Arnold: Some New Statistical Techniques in Geophysics. Advances in Geophysics, New York, Academic Press, 1952, pp. 45-85.

5. Lifsey, J. David: An Empirical Analysis of Daily Peak Surface Wind at Cape Kennedy, Florida for Project Apollo. NASA TM X-53116, August 27, 1964.

6. Canfield, N. L.; Smith, O. E.; and Vaughan, W. W.: Progress in Circumventing Limitations of Upper Wind Records. Journal of Applied Meteorology, vol. 5, no. 3, June 1966, pp. 301-303.

7. Canfield, N. L.; Smith, O. E.; and Vaughan, W. W.: Serial Completion of Upper Wind Records. Journal of Geophysical Research, vol. 72, no. 4, pp. 1389-1392.

8. Daniels, G. E.; Scoggins, J. R.; and Smith, O. E.: Terrestrial Environment (Climatic) Criteria Guidelines for Use in Space Vehicle Development, 1966 Revision. NASA TM X-53328

9. Lee, R. F.; Ownbey, J. W.; and Quinlan, F. T.: Thunderstorm Persistence at Cape Kennedy, Florida. To be published as NASA TM X-53635.

DIURNAL VARIATION OF DENSITY AND TEMPERATURE IN THE UPPER ATMOSPHERE

By

Robert E. Smith

SUMMARY

Results of six rocket-launched probes instrumented to measure neutral molecular nitrogen densities and electron densities and temperature between 140 and 325 km are presented and compared with current atmospheric models. Measured N_2 number densities are substantially lower than model value predictions.

DIURNAL VARIATIONS IN ATMOSPHERIC DENSITIES

Since atmospheric drag is the largest force acting on a vehicle in low-earth orbit, the selection of the model most representative of the upper atmosphere of the earth is very important to MSFC program activities. Current models of the earth's upper atmosphere are based solely upon:

1. Density values deduced from analyses of satellite orbital decay. Analyses of satellite orbital decay show that the upper atmosphere expands outward in response to heating from the sun. This outward expansion, referred to as the diurnal bulge, results in a maximum density at all satellite altitudes at about 2 p.m. with a minimum density at about 4 a.m.

2. Time invariant single values for all model parameters at an altitude of 120 km.

Our investigations of the various atmospheric models combined with the orbital dynamics and lifetime studies in which they were to be used at MSFC pointed out that the shape of this diurnal bulge of the atmosphere was just as important as the absolute magnitudes of the density values.

Our investigations also showed that (1) density measurements made by satellite or rocket-borne probes differ from orbital decay analyses values by a factor of 2 to 3 and (2) no attempt had been made to define the shape of this diurnal curve in the 100-200 km altitude region where rocket-launched probes are required. To correct this omission, on January 24, 1967, personnel of the MSFC and the University of Michigan launched six payloads from Cape Kennedy, Florida (Fig. 1).

The payloads were instrumented to measure the neutral molecular nitrogen density with an omegatron mass analyzer located in one end of the cylinder and the electron temperature and density with a Langmuir probe located in the central part of the cylinder. The payloads were ejected at about 70 km with a coast up to an apogee of about 325 km. Measurements were made on both up- and down-legs of the flight.

Figure 2 shows the six vertical N_2 density profiles compared with the Community on Space Research International Reference Atmosphere (CIRA) 1965 Model No. 4 values [1]. The measured values are substantially lower than the corresponding model values.

Figure 3 is a plot of the N_2 number densities versus time at four specific altitudes. The crosses are the measured data points that are connected here by the solid lines. The dashed line connects N_2 values predicted by Jacchia's [2] 1964 static diffusion model for the same geophysical conditions, while the circles are values predicted by the CIRA 1965 Model No. 4. It is readily apparent that the measured values are substantially lower than the model values at all altitudes and all times of the day. At 300 km, the afternoon maximum is about 3.3 times

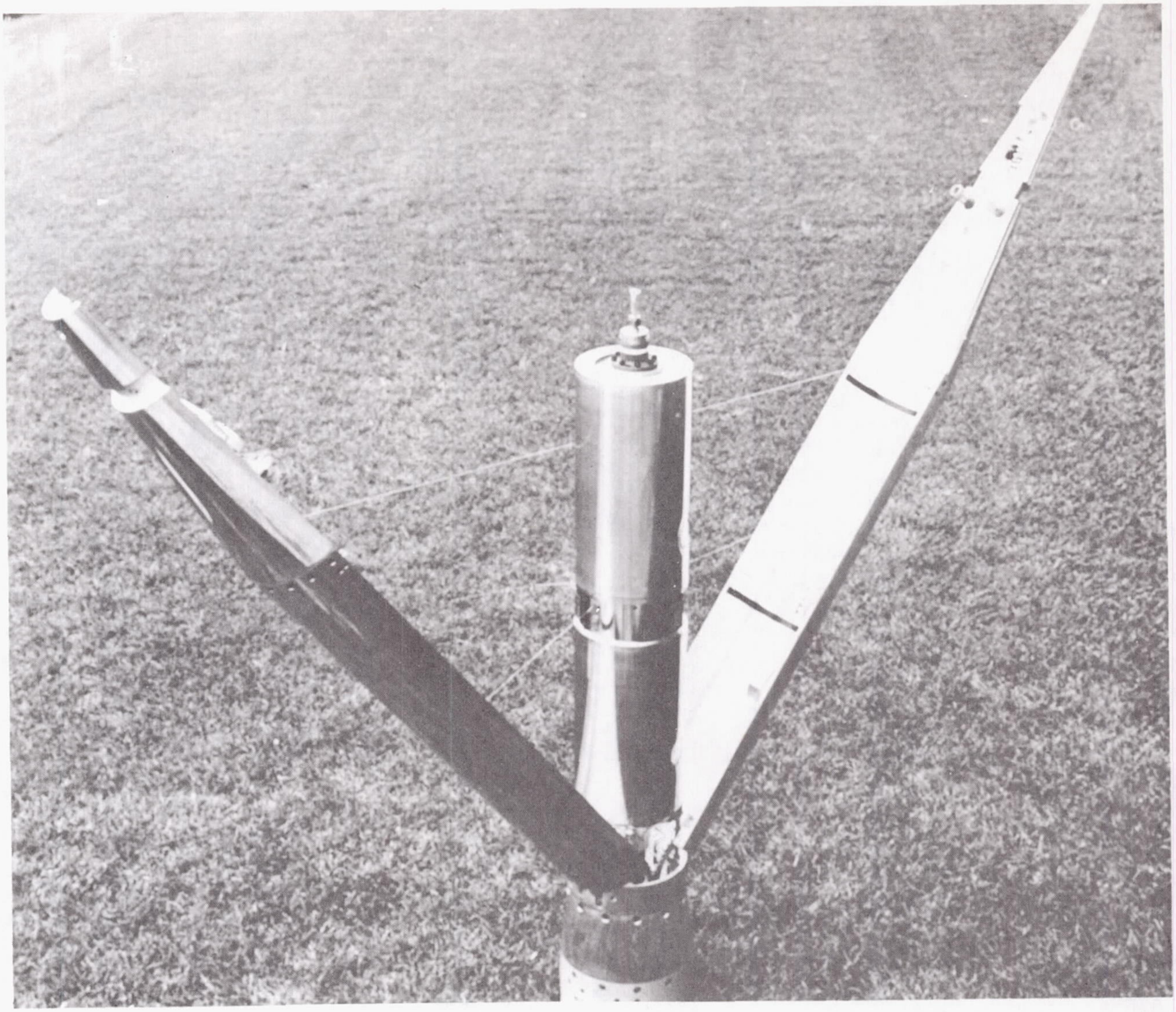

FIGURE 1. THERMOSPHERE PROBE

the morning minimum. At 150 km, this ratio decreases to 1.25. The data clearly show a greater diurnal variation at the lower altitudes than predicted by either model since both models assume single fixed boundary conditions at 120 km. The gauges used in this survey were cross calibrated four at a time on the same system, and special care was taken to insure that all had identical post-calibration histories. For this reason, it is believed that the total uncertainty in the relative values are ±7 percent.

Figure 4 shows the six vertical profiles of N_2 temperature obtained through a downward integration of the density profiles according to the hydrostatic equation. The maximum temperature occurred at 2 p. m. at all altitudes above 145 km; however, the minimum temperature above 240 km occurred at 6:30 a. m. (just after sunrise). Between 170 and 240 km the minimum temperature occurred at 9:30 p. m.; while below 170 km, the minimum temperature occurred at 3:30 a. m.

Figure 5 shows N_2 temperature versus time at selected altitudes compared once again with the Jacchia 1964 static diffusion model for the appropriate geophysical conditions. Gauge sensitivity does not affect the temperature derivation; thus the ±5 percent error bars are conservative, assuming diffusive equilibrium. Agreement between model and derived temperature values is very good with the most notable

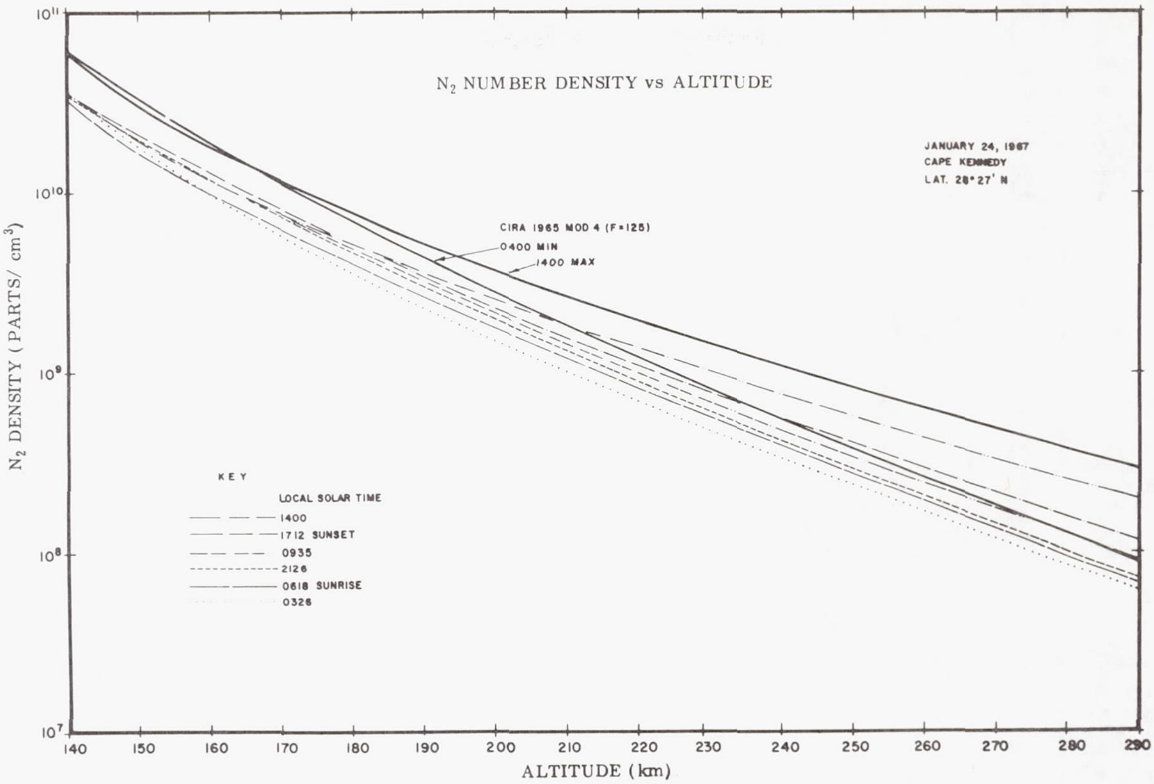

FIGURE 2. DIURNAL SURVEY OF THE THERMOSPHERE

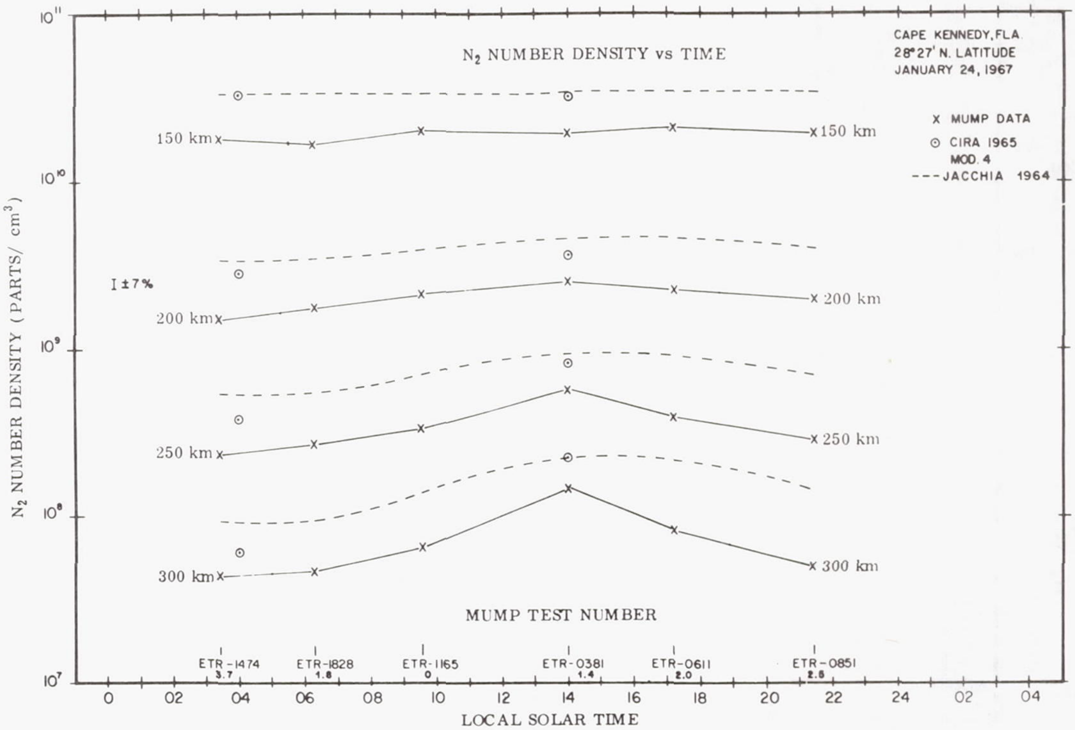

FIGURE 3. MARSHALL - UNIVERSITY OF MICHIGAN PROBE (MUMP) DIURNAL SURVEY OF THE THERMOSPHERE

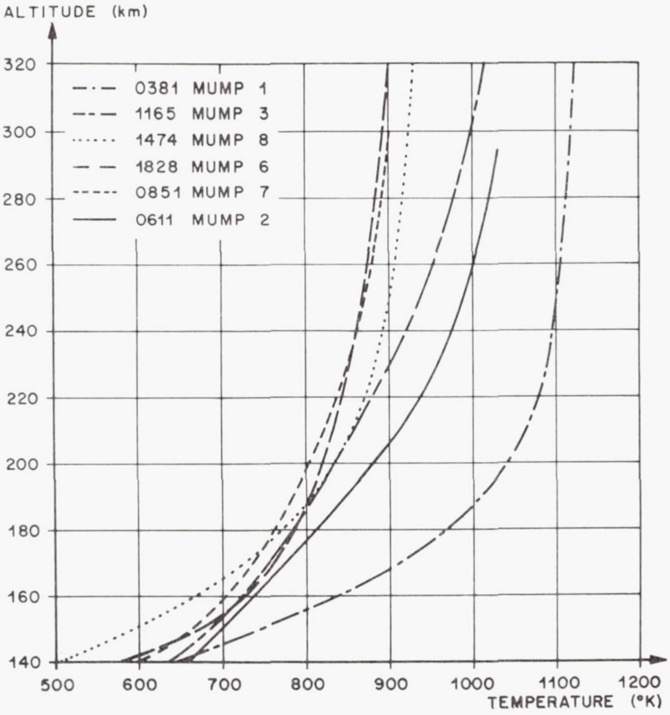

FIGURE 4. TEMPERATURE - HEIGHT PROFILES

difference being the steeper slope of the afternoon-derived temperature decrease. There is a very interesting agreement between this model and the derived temperature in regard to the decrease in the exospheric temperature between 3:30 a. m. and sunrise. According to the model, this is caused by a decrease in the geomagnetic index, a_p, from 3.7 to 1. 8. The disagreement at the lower altitudes during the corresponding time period is unexplained so far.

CONCLUSIONS

The six atmospheric probes produced results that:

1. Reaffirmed the discrepancy of a factor of 2 to 3 between gauge measured densities and densities deduced from orbital decay analyses.

2. While confirming that the models provide a fair representation of the general behavior of

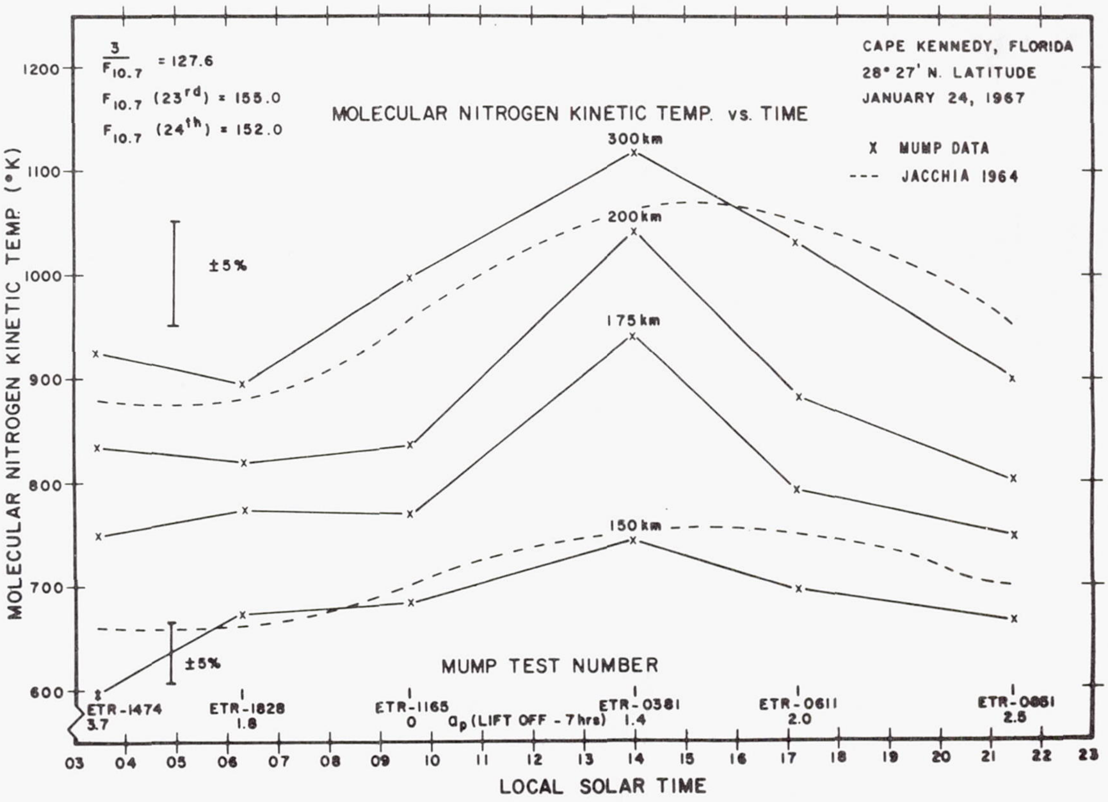

FIGURE 5. MUMP DIURNAL SURVEY OF THE THERMOSPHERE

the upper atmosphere, also pointed out that (1) the upper atmosphere is much more variable than the models predict, (2) the lower boundary condition cannot be time invariant, (3) much additional information is required concerning atmospheric reaction times, and (4) there is still a possibility that the diurnal maximum atmospheric temperature occurs later in the afternoon, as recent Thomson [3] backscatter results have indicated.

FUTURE ACTIVITIES

Future efforts in the program will be directed toward making (1) measurements between 80-140 km, the altitude region containing the postulated lower boundary, and (2) a series of probe launches at approximately one-hour intervals during the late afternoon to more exactly determine the time of occurrence of the afternoon maximum atmospheric density and temperature.

REFERENCES

1. Harris, I.; and Priester, W.: The Upper Atmosphere in the Range from 120 to 800 km. Institute for Space Studies, Goddard Space Flight Center, New York, New York, August 25, 1964.

2. Jacchia, L. G.: Static Diffusion Models of the Upper Atmosphere with Empirical Temperature Profiles. Smithsonian *Contribution to Astrophysics*, vol. 8, no. 9, 1965, pp. 215-257.

3. Nisbet, J. S.: Neutral Atmospheric Temperatures from Incoherent Scatter Observations. Ionospheric Research Laboratory, The Pennsylvania State University, University Park, Pennsylvania, February 16, 1967.

Page
Intentionally
Left Blank

IONOSPHERIC DISTURBANCES CAUSED BY GROUND BASED ACOUSTIC ENERGY SOURCES

By

William T. Roberts

SUMMARY

Traveling ionospheric disturbances (TID) have long been observed through ionospheric measurements. Ionospheric radio measurements have revealed that these ionospheric movements occur at all geophysical locations and at virtually all heights. These upper atmospheric motions were formerly thought to result solely from solar-terrestrial interactions, but in recent years there has been increasing evidence to indicate that many of the sources for these traveling waves may be ground based. Traveling ionospheric disturbances have definitely been observed to result from atmospheric nuclear blasts and large earthquakes. Recently, the suggestion has been made that atmospheric gravity waves may be generated as a matter of course in such natural events as thunderstorms [1]. There is also some reason to believe that static test firings of large rocket engines and boosters generate sufficient acoustic energy in the low frequency bandwidths to propagate to ionospheric heights and create large disturbances. An analogy has often been made of the similarity between ionospheric traveling disturbances and ripples generated in a smooth pond when a rock is thrown into the water.

IONOSPHERIC DISTURBANCES

The Space Environment Branch is currently engaged in a study of these traveling ionospheric disturbances caused by ground-based acoustic energy sources such as static test firings of large rocket boosters and high energy meteorological phenomena such as thunderstorms. Since the Space Environment Branch is the Marshall Space Flight Center group responsible for the development of atmospheric models, it has a responsibility as well as a deep interest in the dynamics of the upper atmosphere. The three primary purposes of the program are (1) to collect data to show that ground-based acoustic energy sources do generate pressure waves which can and do propagate to ionospheric heights, (2) to study the propagation of these waves, taking into account winds, temperature profiles, acoustic frequency cutoff regions caused by atmospheric density stratification, absorption, defocusing caused by large temperature gradients such as those that exist at the base of the thermosphere, etc., and (3) to formulate the theoretical mechanisms through which neutral motions in the upper atmosphere are coupled to the ionospheric electrons.

The third purpose has extremely interesting implications. If the coupling relationship can be established with consideration to the magnetic field and the production and loss rates, it may then be possible to determine the neutral motions of the upper atmosphere from the motions of the ionospheric electrons. The electron dynamics may be derived by a relatively simple array of ground-based transmitters and receivers. The main method presently used to measure upper atmospheric winds is to observe the motions of chemiluminescent clouds produced through the release of vapor trails by rockets launched to high altitudes. A second method used to investigate upper atmospheric winds is to observe the decay in satellite inclinations. This method, however, is useful only for altitudes over 200 km and relies heavily on estimated values for the drag coefficient and average cross-sectional area of the satellite.

Funding for this program was provided by the Office of Space Science and Applications following a similar inhouse study on the effects of vehicle launches on the ionosphere [2].

The current site arrangement is shown in Figure 1. Each transmitter site is equipped with three transmitters broadcasting on different frequencies. The frequencies are regulated by crystal-controlled oscillators stable to within one part in 10^8 per day. Any Doppler shift of the received signal thus results from changes in the ionospheric reflection point and not transmitter drifting. The frequencies were selected so that the frequency separation from one site to another would be on the order of 6 Hz. The received signals are recorded on magnetic tape and processed by a Rayspan analog spectrum analyzer. All signals which fall outside ± 10 Hz of the center frequency are filtered from the data.

The signals are assumed to reflect at the midpoint of the lines joining the transmitter to the receiver, and the distances d_1, d_2, and d_3 are the distances from the static test stand to these three midpoints. Since $d_1 < d_2 < d_3$, the horizontal velocities of traveling waves may be measured by determining the time at which the wavefront passes each point. Discrepancies in wave passage caused by the intervening winds and temperature profiles are considered in the data reduction.

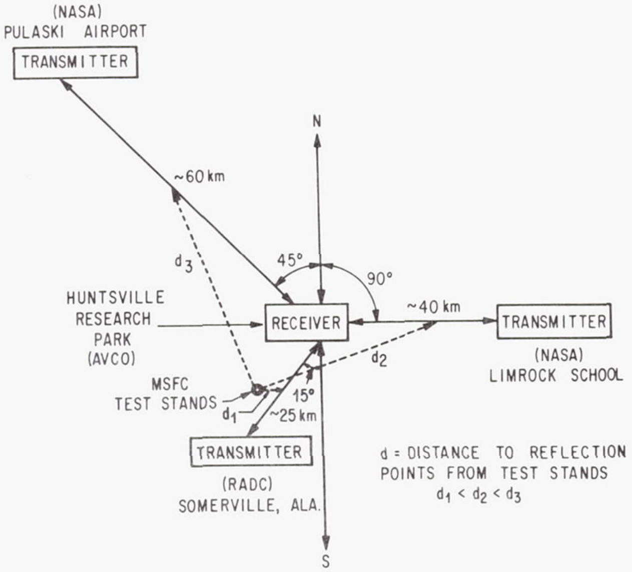

FIGURE 1. PHASE-PATH SOUNDER SITE ARRANGEMENT

The transmitter sites are equipped with Heathkit DX-60 A's modified with crystal-controlled oscillators, which provide ultra-stable frequency references to drive the transmitters. The six oscillators were purchased from Bliley Mfg. Co. and cut to the following frequencies: 1998482 Hz, 2731992 Hz, 4080992 Hz, 5734992 Hz, 4759992 Hz, and 6184992 Hz. The site is also equipped with a microbarograph to measure pressure changes as low as 0.6 N/m^2 (6 μbars) with periods in the order of 0.1 min to 6.0 min. The microbarograph is composed mainly of a Sanborn differential gas pressure transducer and transducer converter insulated from the atmosphere except for the testing values [3].

Figure 2 shows the antenna array at the Pulaski site. The towers are Rohn Mfg. Co. 22.9-m (75-ft) crank-up towers which support three inverted vee antennas. The guys for the antennas are polypropylene ropes to avoid interference with the antenna pattern. At one site, nylon rope was used by mistake and after the first large storm the towers were found lying on the ground with the guy ropes still tied.

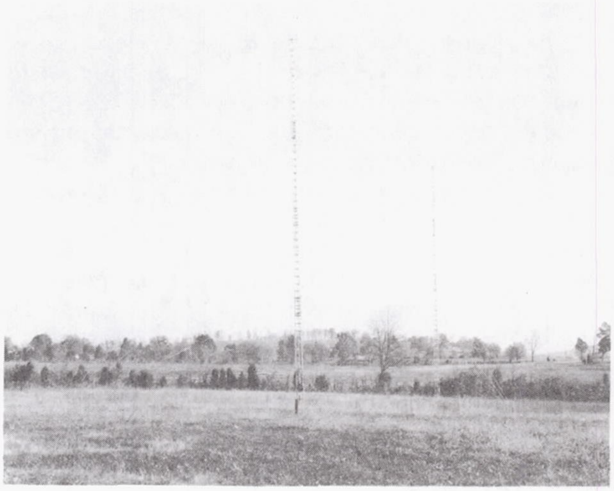

FIGURE 2. PULASKI, TENNESSEE SITE ANTENNA TOWERS

Figure 3 is a photo of the receiver site equipment. There are three SP-600JX receivers operating from a common 455 kHz local oscillator. Each receiver has its own crystal-controlled first-conversion oscillator at a frequency which places the received output at a nominal second IF center frequency of 90 Hz. Each receiver signal is recorded on a separate channel as are the 90 Hz reference output and a WWV timing signal. The tape recorder

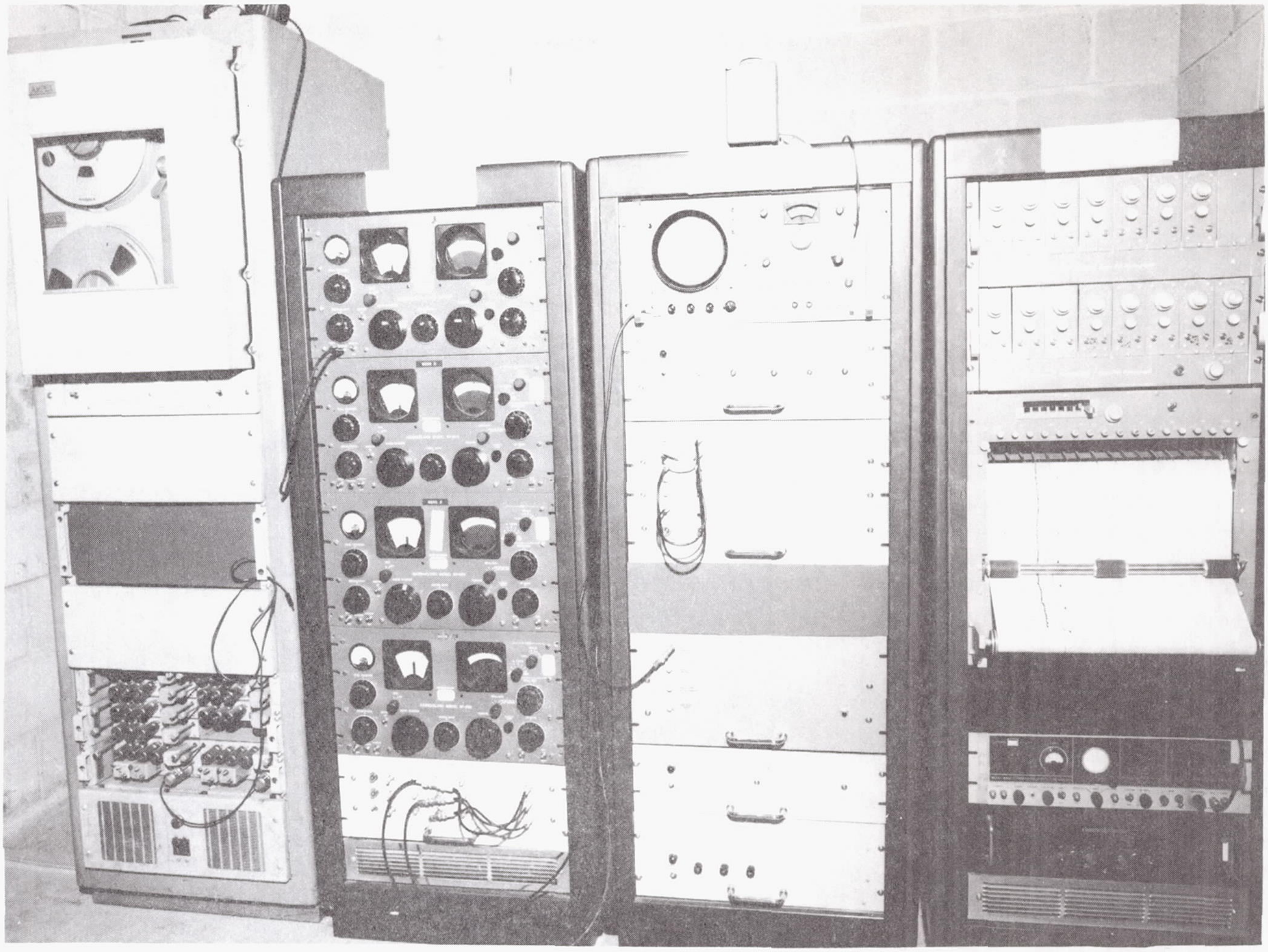

FIGURE 3. HUNTSVILLE RECEIVER SITE

is an Ampex FR-1107 operating at a speed of 2.38 cm/sec (15/16 in./sec). The later playback of the tape at 152 cm/sec (60 in./sec) when coupled with the 90 Hz output will place the recorded data in the frequency range of the Rayspan spectral analysis equipment. The 90 Hz reference signal will provide compensation for tape speed fluctuations or power source variations so that the phase variations observed may be assumed to be caused solely by ionospheric motions. The Rayspan spectral processing will filter any signal outside of ± 10 Hz of the center frequency. The center frequency for each oscillator is the frequency of the Somerville, Alabama, site and the other oscillators are cut to frequencies offset from ± 6 Hz to ± 8 Hz from this center frequency. As a result, one frequency from each site will fall within the ± 10 Hz bandwidth of the processed data.

Figure 4 is a diagram of a transmitter-receiver combination of the phase path sounder technique. Each site transmits three separate frequencies which reflect in the ionosphere at a point where

$$f = 9 \times 10^3 N^{1/2} . \tag{1}$$

In this equation, f is the transmitted frequency in Hertz and N is the electron density in electrons per cubic centimeter. Since three frequencies are being broadcast from each site, three points in the ionosphere are being monitored simultaneously, and if the reflection heights are known, the vertical velocity of wave passage may be determined.

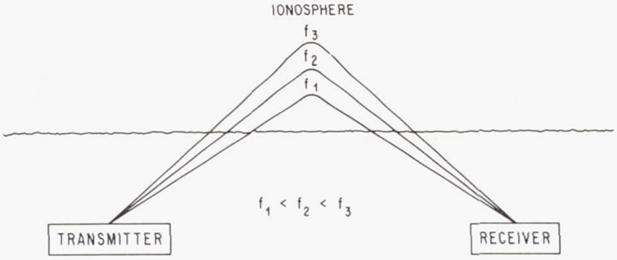

$f = 9 \times 10^3 \ N^{1/2}$

N = ELECTRON DENSITY (electrons/cm^3)

FIGURE 4. IONOSPHERIC REFLECTION OF TRANSMITTED WAVES

Figure 5 is a photograph of the MSFC model C-4 swept-frequency ionosonde. This equipment is operated in conjunction with the program to provide information on the height of signal reflections and for the detection of slow but large vertical ionospheric motions that might be beyond the resolution of the phase path sounders.

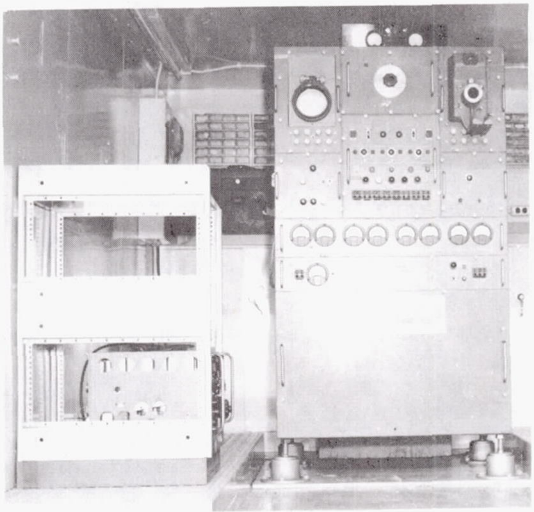

FIGURE 5. MSFC SWEPT-FREQUENCY IONOSONDE

The inclusion of the term "gravity" in acoustic gravity wave is somewhat unfortunate. An acoustic wave is simply a pressure wave which propagates outward when some resonant source becomes activated, and is normally damped out by the effects of atmospheric density. An acoustic gravity wave is this same type of wave traveling upward so that gravity acts as a restoring force on the atmospheric particles in the pressure wave.

Figure 6 shows a record obtained following the S-IVB static test firing made on April 20, 1967. During this test only one site was operational so that only one frequency, 6.185 MHz, was recorded. The static test firing began at 1300 Central Standard Time and was 40 sec in duration. The slow, smooth, Doppler gradient observed from about 1300 to 1308 indicates the background motion of the ionosphere.

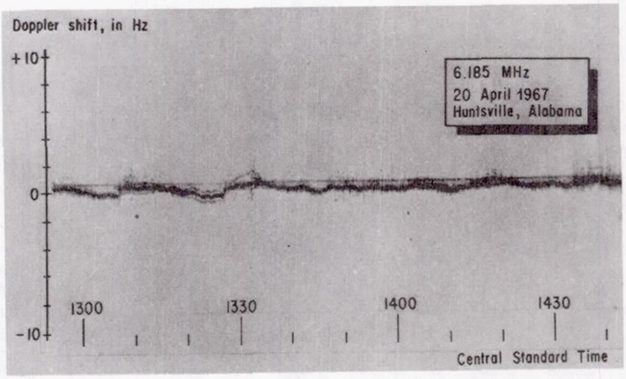

FIGURE 6. RECORD OF PASSAGE OF ACOUSTIC-GRAVITY WAVE

(Interestingly enough, this same motion has been subsequently observed at the time that ignition took place, and in one instance about 30 sec before.) Theoretically, the propagation time to the ionosphere should be on the order of 8 min, and at 1308 CST, a decisive change occurred in the record trend. There was a shift in the positive direction of about 1/2 cycle and a subsequent wave dispersion that may have been the reflection of the transmitted signal from the wavefront. The signal then stabilized, and subsequently, the ionosphere resumed a gradient similar to that observed before the wavefront passage. At about 22 min after the first wavefront passage, there was another rather large shift very similar to the first. It appeared that some resonant effect was taking place, although no satisfactory explanation for this currently exists, and the result is thus considered to be coincidental. This was the first recorded measurement in which the effects of static test firings on the ionosphere are shown.

Work is now underway on the theoretical mechanisms of propagation and coupling. To theoretically predict the magnitude of the wave at ionospheric height, its velocity, frequency range, etc., the effects of winds, temperature profiles and gradients, viscosity, and collision frequency must be considered.

Figure 7 depicts two effects that limit the frequency ranges that may propagate to ionospheric heights. The lower frequency range is limited by the acoustic cutoff frequency, w_a, where

$$w_a = \frac{a}{2H} = \frac{\gamma g}{2a} . \qquad (2)$$

Here a is the sound speed, H is the scale height, g is the acceleration due to gravity, and γ is the ratio of specific heats. The acoustic cutoff frequency results from atmospheric density stratification.

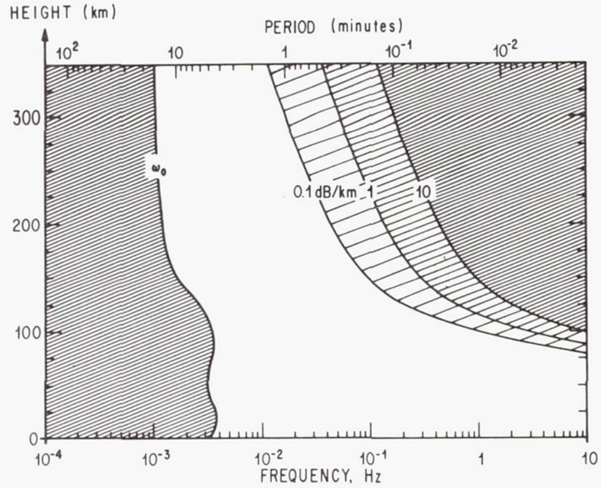

FIGURE 7. THE FREQUENCY RANGE OF ACOUSTIC WAVES THAT CAN EXIST IN THE ATMOSPHERE (LIGHT AREA) CONSIDERING THE LIMITATIONS IMPOSED BY ABSORPTION AND ACOUSTIC CUTOFF [6]

Based on the formulas used in atmospheric attenuation, and by calculating the "time constant" for the elasticity of air, the frequency can be calculated for which a given attenuation occurs.

By using the classical analogy of elasticity and inertia in the mass-spring system, a characteristic time constant, τ, may be calculated by

$$\tau = \frac{\mu}{\rho_o a^2} \qquad (3)$$

where μ is the coefficient of viscosity, ρ_o is the gas density, and a is the speed of sound. According to Lord Rayleigh [4], the amplitude attenuation coefficient, α, for sound waves is

$$\alpha = \frac{8 \pi^2 N}{3 \lambda^2 a} , \qquad (4)$$

where N is the kinematic viscosity, $N = \mu/\rho_o$, and λ is the wavelength of the sound wave. Sears [5] put this in a more usable form,

$$\alpha = \frac{8 \pi^2 f^2}{3 a \gamma V} , \qquad (5)$$

where f is the sound wave frequency, γ is the ratio of specific heats (assumed to be constant at 1.4), and V is the molecular collision frequency. Thus,

$$f = 2.5 \times 10^{-3} (Va)^{1/2} \qquad (6)$$

and since V and a may be derived from atmospheric models, f may likewise be determined as a function of altitude.

Figure 7 shows the rates of attenuation of 0.1 dB/km, 1 dB/km, and 10 dB/km. According to this graph, a wave whose period lies between 1.4 min and 4 min may freely propagate to a height of 350 km. Although they are neglected here, the effects of defocusing and reflection of the wave must be considered in the construction of a realistic model.

FUTURE PLANS

Data are now being taken to further identify ionospheric effects of ground-based acoustic energy sources. The problem of deriving a ray-tracing program for the propagation of these waves considering realistic model atmospheres is now being studied.

The coupling mechanisms are also being developed so that the experimental data may be thoroughly analyzed.

REFERENCES

1. Pierce, A. D.; and Coroniti, S. C.: A Suggested Mechanism for the Generation of Acoustic-Gravity Waves During Thunderstorm Formation. Nature, vol. 210, June 18, 1966, p. 1209.

2. Felker, J. K.; and Roberts, W. T.: Ionospheric Rarefaction Following Rocket Transit. Journal of Geophysical Research, vol. 71, no. 19, October 1, 1966, p. 4692.

3. Claerhart, J. F.; and Madden, T. R.: Initial Observations of 2-20 Minute Period Atmospheric Pressure Variations. 47th Annual Meeting of the AGU, Transactions, vol. 47, no. 1, March 1966.

4. Reyleigh, Lord (J. W. Strutt): Theory of Sound. McMillan and Co. Ltd., London, 1894.

5. Sears, F. W.: Thermodynamics. Addison-Wesley, Reading, Massachusetts, 1950.

6. Georges, T. M.: Private Communication, 1967.

THE MASSES OF METEORS AND THE SELECTION OF A REPRESENTATIVE DATA SAMPLE

By

Charles C. Dalton

SUMMARY

The mass of the particle of design interest for protection against meteoroid puncture of large vehicles with long missions in space is relatively nearly equal to that of a typical photographic meteor particle. But the usefulness of the photographic meteor data for this design interest has been beclouded by markedly different physical theory for the determination of the mass of the particle from the photographic data. A method is presented by which it is expected that a choice can be made when considering the relative plausibility of the alternative statistical results from an analysis of two samples of photographic meteor data selected according to the respective extrapolations of absolute photographic magnitude to low velocity.

LIST OF SYMBOLS

A	total square meters of surface area of a space vehicle exposed to meteoroids
C_t	target en-mass longitudinal sonic velocity, km/sec
e	base of natural logarithms
I_{pm}	maximum photographic luminous intensity
k_t	target material parameter
log	common logarithm, base ten
m	meteoroid mass in grams
m_∞	"Harvard mass" elevation for m
M	"Öpik mass" evaluation for meteoroid mass m
M_{pg}	maximum absolute photographic magnitude
M_{pgo}	value of M_{pg} extrapolated to correspond with 11 km/sec for V_∞
p	target sheet thickness in centimeters
R	probability of vehicle not encountering a meteoroid larger than m grams
t	exposure duration in seconds
V_∞	meteor air-entry velocity in km/sec
Z_R	zenith-to-radiant angular displacement
β	meteor luminous efficiency; ratio of $\int_0^T I_{pm}\, dT$ and $\frac{1}{2}\, m\, V_\infty^2$
β_{11}	value of β extrapolated to correspond with 11 km/sec for V_∞
Δ	meteor magnitude-above-plate limit
Δ_o	value of Δ extrapolated for $(V_\infty, Z_R) = (11$ km/sec, 60 degrees$)$

ϵ_t	target ductility, relative elongation
ζ	relative effective exposability of total surface area
ρ_t	target specific gravity

INTRODUCTION

Here at the NASA-Marshall Space Flight Center (MSFC) the interest in photographic meteors relates primarily to the puncture hazard of large vehicles exposed for long missions in space. An example of such interest is illustrated in Figure 1, which shows mission duration contours for the probability, R, that the S-IVB Orbital Workshop will not encounter a meteoroid with mass larger than m grams. Thus, when the probability of no meteoroid puncture during a 1-year mission of the Orbital Workshop must be as high as 0.995, then the vehicle must be protected against the impact of particles as large as about $10^{-1.6}$ grams. The formula (for the mission duration contours) in Figure 1, showing log log (1/R) as a polynomial function of the independent variable [0.24 + (19/54) log m], is based on a model which was first constructed by Dalton [1] in 1966 by extrapolation both of laboratory hypervelocity impact data from the NASA-Ames Research Center and of satellite puncture and photographic meteor data. Some refinements in the model were also presented by Dalton [2] in 1967. By this model, the independent variable [0.24 + (19/54) log m], mentioned above, is equal to the abscissa $(k_t + \log_p)$ of Figure 2. Thus, in Figure 2, the photographic meteor and thickest Pegasus target tie points correspond to just-sufficient-mass meteoroids of $10^{-0.68}$ and 10^{-6} grams, respectively. The particle mass of interest in the example from Figure 1, $10^{-1.6}$ grams, is then relatively closer to the mass of a typical photographic meteor particle. This example illustrates the primary practical basis for the interests in photographic meteors at MSFC.

DATA SAMPLES OF METEORS

In the puncture hazard model illustrated in Figures 1 and 2, the thickness of a sheet of a given material which can be punctured by a meteoroid is proportional to the product of the cube root of the

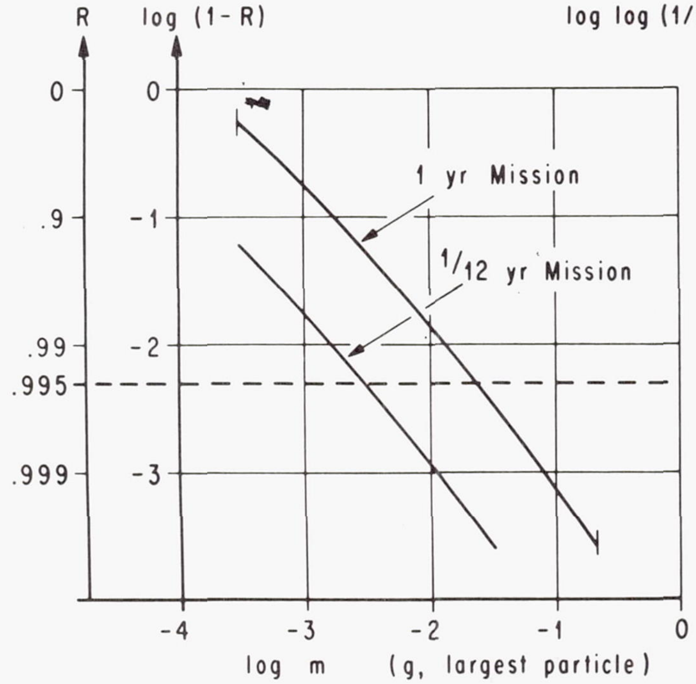

$$\log\log(1/R) = \log(\zeta A t \log e) - 13.03 - 3.81\left[.24 + (19/54)\log m\right] - .384\left[.24 + (19/54)\log m\right]^2 - .017\left[.24 + (19/54)\log m\right]^3$$

ζ = Effective Exposability of Total Surface Area = .663 at 482 km (260 n mi) Altitude

A = Total Surface Area (m^2) = 141.5 m^2 for Orbital Workshop

t = Exposure time (sec) = 3.15×10^7 sec for 1 year

FIGURE 1. PROBABILITY OF NOT ENCOUNTERING LARGER METEOROIDS

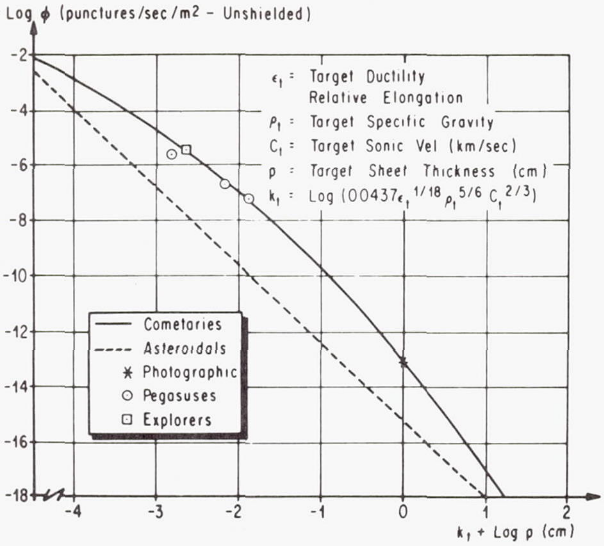

FIGURE 2. MEAN PUNCTURE FLUX FROM METEOROID INFLUX

kinetic energy and the (1/54)-power of the mass of the particle. The velocities of the photographic meteor particles are known sufficiently accuractly so that the uncertainty in the mass values is caused primarily by the uncertainty in the kinetic energy values. The kinetic energy is not directly ascertainable, but must be inferred from the integrated meteor trail intensity in consideration of a physical theory of meteors functionally relating the meteor luminous efficiency with initial mass and velocity. The luminous efficiency is the mean relative part of the rate of loss of kinetic energy of the particle which is accountable in the luminous intensity of the meteor.

To abbreviate notation in this discussion, one can refer to the "small sample" as the 285 sporadic meteors of known maximum absolute photographic magnitude in the random sample published by Hawkins and Southworth [3] in 1958. Some of the results which will be used for these meteors were published also by Hawkins and Southworth [4] in 1961. Also, let the "large sample" be the 2040 sporadic meteors of known maximum absolute photographic magnitude in the sample of 2529 meteors published by McCrosky and Posen [5] in 1961. In calculating the meteor mass values, which they published for the "large sample," McCrosky and Posen [5] used Whipple's [6] formulation for luminous efficiency as $10^{-4.07}$ times the air-entry velocity in kilometers per second, independently of mass, similarly as Hawkins and Southworth [4] did for the "small sample," and stated that "the masses are therefore on the same scale as others published by the Harvard Meteor Project." This formulation or the corresponding mass values will be represented here by "Harvard luminous efficiency" or "Harvard mass" values. Although some of the earlier papers of E. J. Öpik, some of them dating as far back as 1922, were referenced by Whipple [6], who said that his luminous efficiency "has been taken from the calculations by Öpik," the "Öpik luminous efficiency" and "Öpik mass" will refer here to the more recent physical theory as given by Öpik [7] in 1958 and as further illustrated numerically by Öpik [8] in 1963. The "Öpik luminous efficiency," unlike the "Harvard luminous efficiency," is a nonlinear function of velocity and is not independent of mass.

Figure 3 shows, for the "small sample," the distribution of the most obvious parameters; i.e., velocity and absolute photographic magnitude, M_{pg}, which is a linear function of the logarithm of the maximum luminous flux adjusted for a 100-km height overhead. Actually the time integral of luminous intensity is of more interest in the determination of the mass because it is relative to the product of luminous efficiency and mass. Although it is considered a random sample of sporadic (i.e., non-stream) meteors, neither the "large sample" nor the "small sample" illustrated in Figure 3 constitutes a random sample of the sporadic meteoroids which enter the earth's atmosphere, because some of the entering particles with mass considerably above some lower value are not detected as meteors at low velocity and high zenith angle, whereas particles of intermediate mass may be detected as meteors if they have higher velocity or if their radiants are nearer the zenith. Thus, the sample of particles in a random sample of sporadic meteors is biased by physical selectivity. This bias can be counteracted in either the "large sample" or the "small sample" if an appropriate statistical weighting function can be found, but the choice is not obvious and may be difficult to justify.

The authors of the reports from which both the "small sample" and the "large sample" were taken tabulated values for Whipple's [9] statistical "cosmic weight" inversely proportional to the product of Öpik's [10] earth-encounter probability and the square of the air-entry velocity. In 1965 Dalton [11] reported an analysis of the "small sample" with statistical weighting inversely proportional to the product of the 1.5-power of the velocity and the square of the height at maximum brilliance, with some

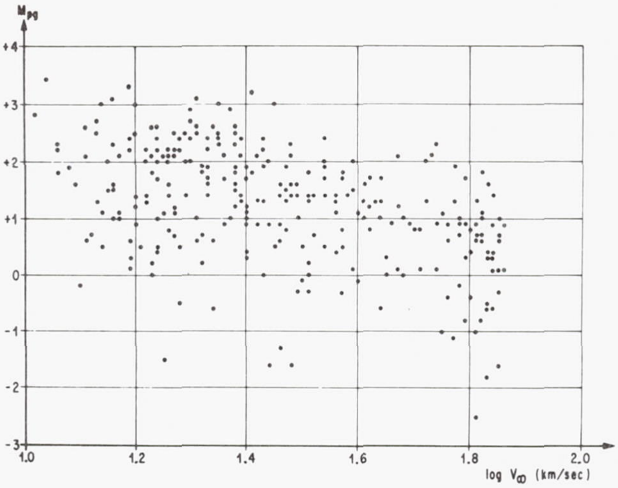

FIGURE 3. METEOR VELOCITY VERSUS ABSOLUTE PHOTOGRAPHIC MAGNITUDE

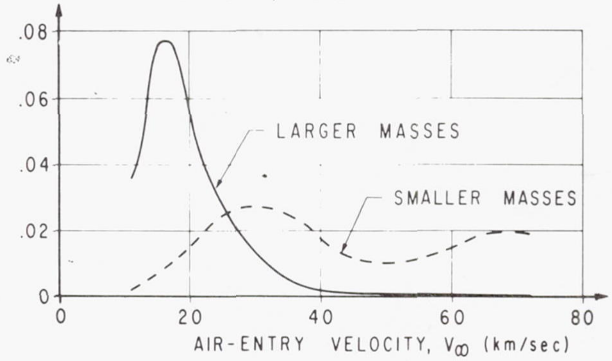

FIGURE 4. WEIGHTED DISTRIBUTION OF VELOCITY FOR HARVARD-MASS REGIMES

further weighting to restore symmetry with respect to the ecliptic plane. Whipple [9] had considered that weighting inversely with the square of the height should be nearly equivalent to weighting inversely with the 0.5-power of the velocity, which was the justification for Dalton's weighting [11]. But the weighted correlation between the logarithms of the air-entry velocity and the "Harvard mass" was computed as -0.69, which is arithmetically much higher than one would expect. Suspecting the statistical weighting as a function of velocity, Dalton [12] later replaced it with Upton's and Hawkins' [13] weighting as a function of the meteor magnitude above the limit of the photographic plate [this function was intended to represent the relative detectability of the meteor]. The weighted correlation between the logarithms of velocity and "Harvard mass" was computed as -0.83, which was arithmetically higher and less plausible than the corresponding result with the weighting as a function of velocity. These results are illustrated in Figure 4 by partitioning the sample with respect to "Harvard mass" into two subsamples of equal statistical weight and showing the velocity distribution for each superimposed. Suspecting the velocity dependence of the "Harvard luminous efficiency," Dalton [14] improvised a formula, involving velocity and maximum absolute photographic magnitude, for roughly approximating mass values proportional to "Öpik mass" values. Here this formula was applied to the "small sample," the correlation between the logarithms of mass and velocity was computed as 0.024 with uniform weighting [14], and as 0.010 [14] and -0.11 [12] with the two respective weighting functions mentioned above. Either of these correlations is arithmetically small enough for physical plausibility, but they are accompanied by a complication. Dalton [11] showed that the slope of the logarithm of the weighted cumulative distribution plotted versus the logarithm of the parameter of interest should be invariant with respect to any parameter which is the product of mass and any power of velocity, provided that mass and velocity are statistically independent. But, with either of the weighting functions, Dalton [15] found that the recomputed mass values gave slopes of -1.34, -1.09, and -0.92 for mass, momentum, and kinetic energy, respectively. On the other hand, the "Harvard mass" values satisfy a -1.34 slope invariantly even though, with such a strong inverse correlation, it would not be expected.

It must be concluded, then, (1) that the "small sample" is too small for analysis with statistical weighting to remove the bias between mass and velocity resulting from physical selectivity, (2) that "Öpik mass" should be computed from the integrated meteor intensity instead of from the maximum absolute photographic magnitude, and (3) that the statistical weighting effort must be minimized by selecting a subsample of meteors from the "large sample" bright enough to have been detected even if they would have had only the 11 km/sec "escape" velocity. Some further analysis with the "small sample," shown in Figures 5 and 6, has been helpful in establishing criteria for selecting subsamples from the "large sample" which are compatible with the respective formulations for luminous efficiency presupposed.

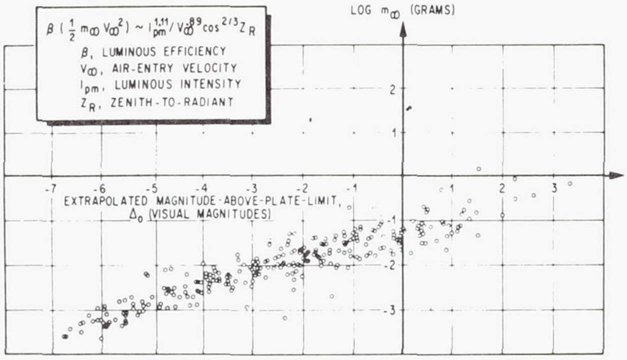

FIGURE 5. RELATION BETWEEN HARVARD METEOR MASS AND MAGNITUDE-ABOVE-PLATE-LIMIT EXTRAPOLATED FOR 60 DEGREES ZENITH-TO-RADIANT AND 11 km/sec PRESUPPOSING HARVARD LUMINOUS EFFICIENCY

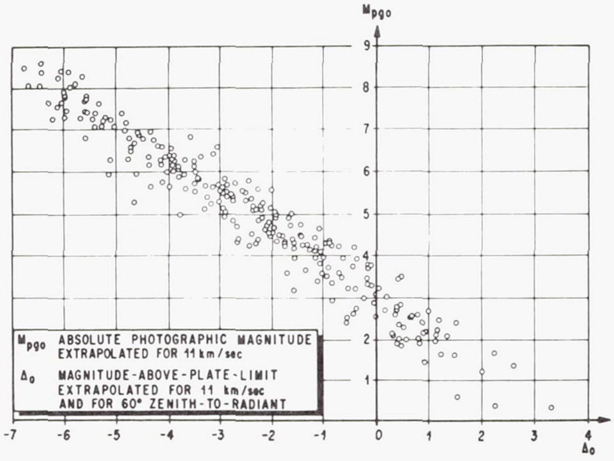

FIGURE 6. EXTRAPOLATED RELATIONS BETWEEN METEOR ABSOLUTE PHOTOGRAPHIC MAGNITUDE AND MAGNITUDE-ABOVE-PLATE-LIMIT PRESUPPOSING HARVARD LUMINOUS EFFICIENCY

An empirical relation for meteors by Jacchia, Verniani, and Briggs [16] indicates that the integrated photographic intensity, and therefore also the product of luminous efficiency and kinetic energy, should be proportional to

$$I_{pm}^{1.11}/V_\infty^{0.89} \cos^{2/3} Z_R,$$

where I_{pm} is the maximum photographic luminous intensity and Z_R is the zenith-to-radiant deviation. If the same particle had entered at 11 km/sec and a 60 degree zenith-to-radiant, then the absolute photographic magnitude and magnitude-above-plate limit would have been, by designation, M_{pgo} instead of M_{pg}, and Δ_o instead of Δ, respectively. Then

$$M_{pgo} = M_{pg} + \frac{(5/2)}{1.11} \log (\beta/\beta_{11}) \, (V_\infty/11)^{2.89} \qquad (1)$$

$$\Delta_o = \Delta - \frac{(5/2)}{1.11} \log (\beta/\beta_{11}) \, (V_\infty/11)^{2.89} \left(\frac{\cos Z_R}{\cos 60°} \right)^{2/3}, \qquad (2)$$

where the luminous efficiency, β, would have the value β_{11} at 11 km/sec.

Values for the magnitude-above-plate limit, Δ, are not available for the "large sample"; but the values of Δ_o computed for the "small sample" by eq. (2) are shown in Figures 5 and 6 versus "Harvard mass", m_∞, in Figure 5 and the corresponding values of M_{pgo} in Figure 6, extrapolated for M_{pg} by substituting the "Harvard luminous efficiency" for β in eq. (1). The mean resultant linear fit for Figure 6 is not so shallow as in Figure 5 and gives a somewhat sharper relation (because mass values are computed from the time integral of intensity rather than from the maximum value); i.e.,

$$M_{pgo} = 3.0 - \Delta_o \quad . \qquad (3)$$

Then by eqs. (1) and (3), the criterion for selecting the subsamples from the "large sample" is

$$M_{pg} + \Delta_o \leqq 3.0 - (2.5/1.11) \log (\beta/\beta_{11}) \, (V_\infty/11)^{2.89}, \qquad (4)$$

where the ratio of the luminous intensity values, β/β_{11}, depends upon the physical theory which is presupposed. This criterion, giving $V_\infty/11$ for β/β_{11} with the "Harvard luminous efficiency" for β, is illustrated in Figure 7.

In order to select a subsample as large as 333, from the "large sample" of 2040 sporadic meteors, it was necessary to choose Δ_o as low as 0.7 when

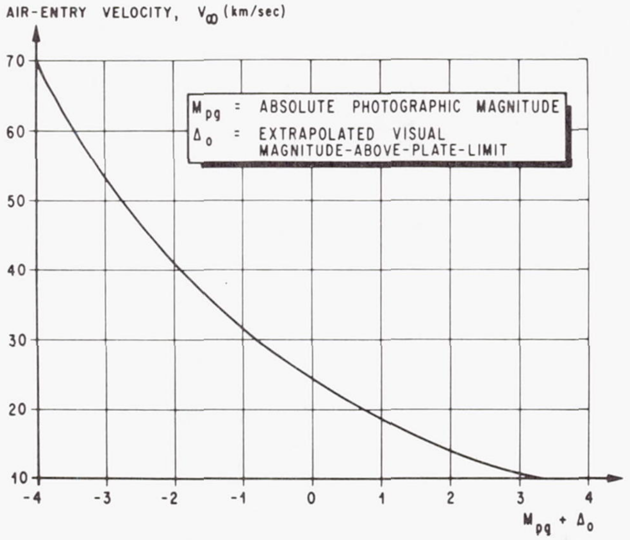

FIGURE 7. MEAN RELATION BETWEEN METEOR VELOCITY, ABSOLUTE PHOTOGRAPHIC MAGNITUDE, AND MAGNITUDE-ABOVE-PLATE-LIMIT EXTRAPOLATED FOR 60 DEGREES ZENITH-TO-RADIANT AND 11 km/sec PRESUPPOSING HARVARD LUMINOUS EFFICIENCY

the "Harvard luminous efficiency" was substituted for β in eq. (4). By Upton and Hawkin's [13] graphical relation for meteor relative visibility as a function of the magnitude-above-plate limit, Δ, meteors barely satisfying this criterion would have a probability of detection on the photographic plates increasing from about 0.20 at a 60 degree zenith-to-radiant, to about 0.60 at the zenith. It may be of some interest to note that only one of these 333 meteors, which could be selected with "Harvard luminous efficiency," β, had a velocity $V_\infty \geqq 32$ km/sec; whereas the (uniformly weighted) average velocity for the (random) "small sample" is 34 km/sec (Dalton [2]). The median value of the "Harvard mass," m_∞, for this subsample is 0.110 gram.

The physical theory of meteors given by Öpik [7] in 1958 seems most suitable for calculating the mean luminous efficiency, β, and consequent integrated intensity for a particle of given structure and mass entering the atmosphere at a given angle and velocity. The integrated intensity, which is equal to the product of the kinetic energy and mean luminous efficiency, was used in the computation for the "large sample" tabulated values for "Harvard mass," m_∞, for dividing by the "Harvard luminous efficiency" $10^{-4.07}$ V_∞. Therefore, the problem at hand is to compute the mean "Öpik luminous efficiency," β, for a known integrated intensity and unknown mass, instead of for a known mass and unknown integrated intensity. The air-entry "Öpik mass," M, is found subsequently by dividing the known product $M\beta$, by the mean "Öpik luminous efficiency" β. In 1963 Öpik [8] gave three tables of values for the application of his physical theory [7] to stone dustballs, compact iron meteoroids, and compact stony meteoroids. Some of these values are illustrated in Figure 8 to show fixed "Öpik mass" contours for the velocity dependence of the mean "Öpik luminous efficiency," β, for dustball meteors. It may be of interest to note that although at above average velocity, the "Öpik luminous efficiency," β, in Figure 8 is a decreasing function of velocity, V_∞, the product of luminous efficiency and kinetic energy, $\beta\left(\frac{1}{2} M V_\infty^2\right)$, and therefore also the integrated intensity, is an increasing function of velocity.

Concerning the structure of meteoroids, the current practice for design criteria purposes at MSFC is to consider that the distribution of compact meteoroids within the photographic meteor range corresponds to Parkinson's [17] extrapolation of Hawkins' [18] results for air-entry mass cumulative influx adjusted from stone and iron meteorite statistics. The results, as can be seen in Figure 2, are that about one percent of the photographic meteors may be compact particles of asteroidal origin, and the remaining 99 percent are stone dustballs with a mean body density only about ten percent as high as that for compact meteoritic stone. Jacchia, Verniani, and Briggs' [16] results are of interest on this point too. The 413 photographic meteors which they selected for study gave an average specific gravity of only 0.26, and only one of them was found to possess all the requisites to qualify as being of asteroidal origin. Therefore, in the absence of specific information which might suggest which of the meteors in the "large sample" belong to the three structural types in Öpik's [8] tables, they will all be presupposed as dustballs. Also the "Öpik luminous efficiency" will be approximated from a mathematical model which will now be constructed in consideration of Öpik's [8] 24 values for dustball meteoroids illustrated as specific points in Figure 9.

The mathematical model illustrated in Figure 9 has linear relations between the repeated logarithms of the reciprocals of β and $M\beta$ for the dependent and independent variables, respectively, with slope, intercept, and break-point depending on velocity, V_∞, as an auxiliary independent variable as illustrated in Figures 10 through 12, respectively. The model

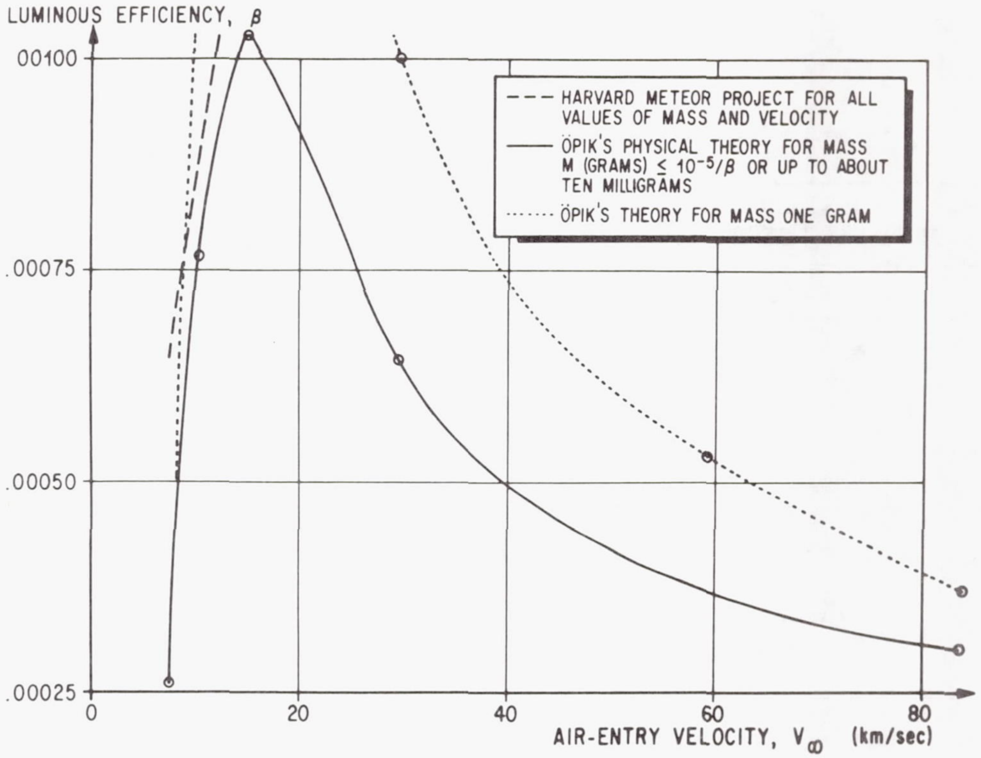

FIGURE 8. LUMINOUS EFFICIENCY VERSUS VELOCITY FOR DUSTBALL METEORS

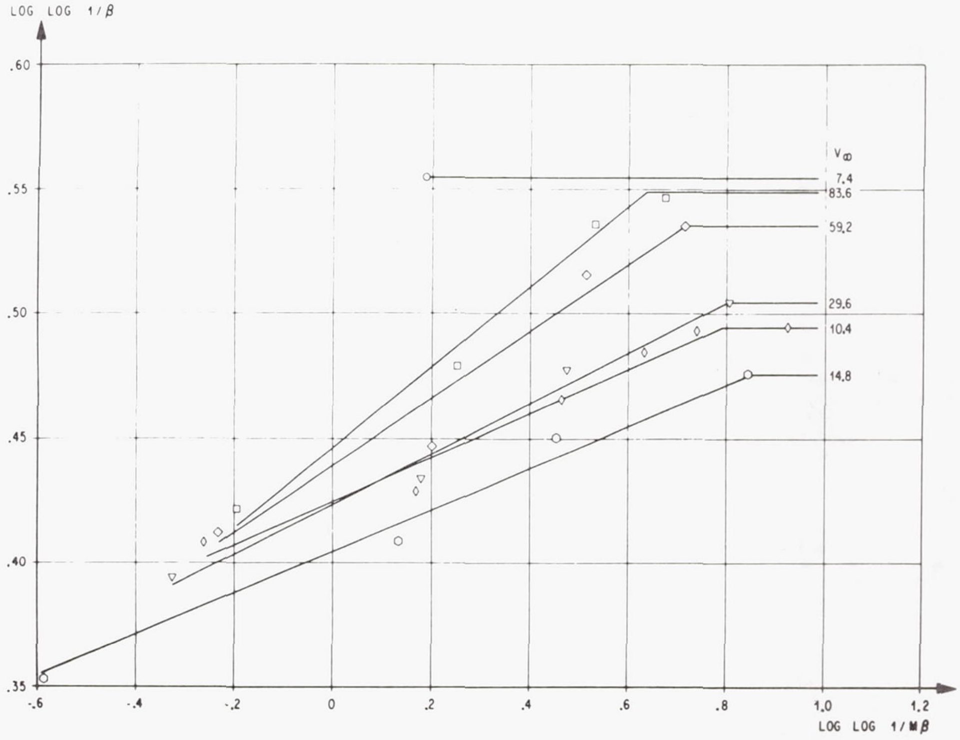

FIGURE 9. MODEL APPROXIMATING ÖPIK'S LUMINOUS EFFICIENCY FOR DUSTBALL METEOROIDS SMALLER THAN ONE HUNDRED GRAMS

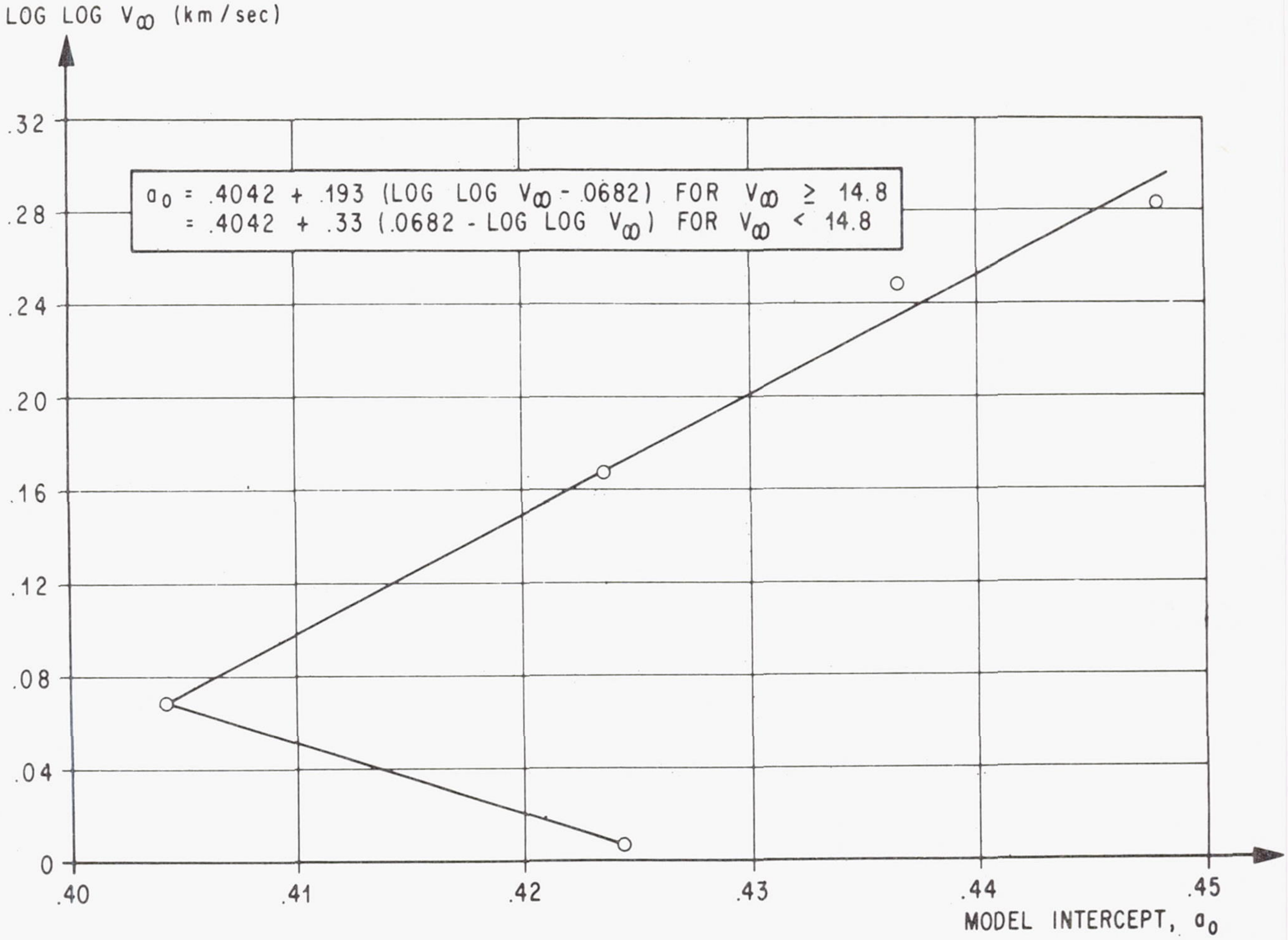

FIGURE 10. VELOCITY-DEPENDENCE OF THE INTERCEPT FOR THE MODEL IN FIGURE 9

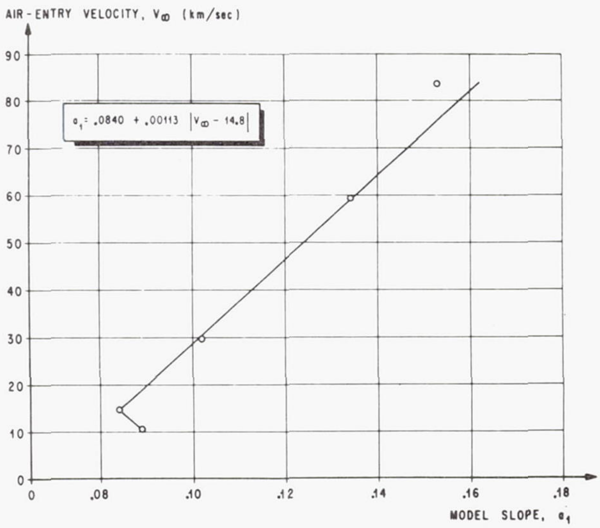

FIGURE 11. VELOCITY-DEPENDENCE OF THE SLOPE FOR THE MODEL IN FIGURE 9

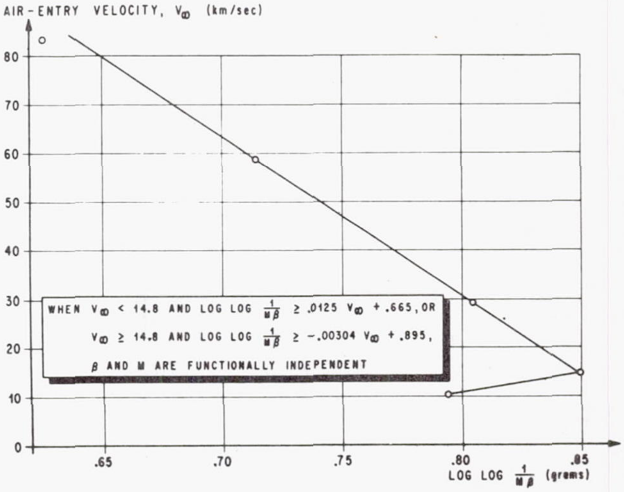

FIGURE 12. CRITERION FOR THE RIGHT-HAND DISCONTINUITY IN FIGURE 9: LUMINOUS EFFICIENCY INDEPENDENT OF MASS FOR SMALLER METEOROIDS

was constructed independently of the values given for velocity 7.4 km/sec. The highest specific points on each of the other five velocity contours were given as limiting values in the sense as indicated. Those limiting points were ignored in the least squares preliminary velocity contour fittings. The intercepts, slopes, and break-points for the respective least squares preliminary velocity contour fittings are shown as specific points in Figures 10 through 12, respectively. The plotted specific points in Figures 10 through 12 were used as visual aids for the construction of the indicated linear segments, the equations for which constitute the model represented by the line segments in Figure 9.

For computational purposes the model illustrated in Figure 9 is described as follows: β and M are functionally independent when either

$$V_\infty < 14.8 \text{ and } \log\log 1/M\beta \geqq 0.0125\, V_\infty + 0.665$$

or

$$V_\infty \geqq 14.8 \text{ and } \log\log 1/M\beta \geqq -0.00304\, V_\infty + 0.895;$$

otherwise,

$$\log\log 1/\beta = a_o + a_1 \log\log 1/M\beta$$

where

$$a_o = 0.4042 + 0.193\,(\log\log V_\infty - 0.0682) \text{ for } V_\infty \geqq 14.8$$

$$= 0.4042 + 0.33\,(0.0682 - \log\log V_\infty) \text{ for } V_\infty < 14.8$$

and

$$a_1 = 0.0840 + 0.00113\, |V_\infty - 14.8|.$$

This model has a maximum deviation from the "Öpik values," as shown by the next to the lowest point for the 59.2 km/sec contour in Figure 9, of 33 percent too high for β or too low for M, which would result in a value of 12 instead of 16 grams for the value of M for that particular point.

The model approximation for the "Öpik mass" M is found by dividing Mβ by the model approximation for the "Öpik luminous efficiency," β. The role of the product Mβ in the model follows from the fact that the product of luminous efficiency and kinetic energy, and therefore also the product of luminous efficiency and mass, is invariant between different physical theories; i.e.,

$$M\beta = 10^{-4.07}\, m_\infty V_\infty, \qquad (5)$$

where m_∞ is the "Harvard mass" tabulated for the "large sample" and V_∞ is the known velocity.

By eqs. (1) and (3) with the values for the "Öpik luminous efficiency," β, approximated by the model in the preceding paragraph, the values for the extrapolated magnitude-above-plate limit, Δ_o, corresponding to 11 km/sec and 60 degree zenith-to-radiant, were calculated for the "large sample" of 2040 sporadic meteors and ranked. In order to select a subsample the same size as was selected with the "Harvard luminous efficiency," 333 meteors with the largest values of Δ_o, the limiting criterion for Δ_o was 1.04. By Upton and Hawkins' [13] relative detectability function, this minimum value of Δ_o would correspond nominally at 11 km/sec to a probability of detection on the photographic plates varying from about 0.44 for 60 degree zenith-to-radiant to about 0.83 at the zenith. Of the 59 meteors in this subsample which were not selected by the other criterion, there were 25 meteors with velocity $V_\infty \geqq 32$ km/sec; whereas, of the 274 meteors common to both subsets only one of them is that fast. The median value of the model-approximated "Öpik mass," M, for this subsample is 0.138 gram.

Statistical analysis and comparison of the results for the two subsamples, each of 333 meteors selected from the "large sample," are being pursued currently here at MSFC. No more significant results are available at this time (28 September 1967); and one does not presume to know which of the alternative physical theories may be more nearly correct. But the distributions of and correlations between various dynamic and orbital parameters should be of most important interest for comparison of results correspondingly developed with the alternative subsamples. It is not yet possible to anticipate whether or not the results might be such that one could discount one of the alternative formulations of luminous efficiency on grounds of obvious physical implausibility.

CONCLUSIONS

Two alternative formulations for meteor luminous efficiency, the model used by the Harvard Meteor Project since 1943 (see Whipple [6] and McCrosky and Posen [5]) independent of mass but proportional to velocity, and the 1958 formulation by Öpik [7] depending nonlinearly on both mass and velocity, are used as bases for selecting corresponding subsamples for statistical analysis. Each subsample consists of the 333 meteors, from McCrosky and Posen's [5] 2040 sporadic meteors of known magnitude, which would have been most easily detected if both velocity had been as low as 11 km/sec and zenith-to-radiant had been as high as 60 degrees. With the various known parameters, and with the mass values consequent to each of the two formulations for luminous efficiency, the subsamples are thought to constitute a pertinent basis for comparative statistical analysis which might facilitate a resolution of alternatives on grounds of physical plausibility.

REFERENCES

1. Dalton, C. C.: Effects of Recent NASA-ARC Hypervelocity Impact Results on Meteoroid Flux and Puncture Models. NASA TM X-53512, September 7, 1966.

2. Dalton, C. C.: Near Earth and Interplanetary Meteoroid Flux and Puncture Models. Paper NO. EN-14, American Astronautical Society 1967 National Symposium "Saturn V/Apollo and Beyond," Huntsville, Alabama, 11-14 June, 1967, vol. I, pp. AAS 67-334 (EN-14-1) through AAS 67-334 (EN-14-21).

3. Hawkins, G. S.; and Southworth, R. B.: The Statistics of Meteors in the Earth's Atmosphere. Smithsonian Contributions to Astrophysics, vol. 2, no. 11, Smithsonian Institution, Washington, D. C., 1958, pp. 349-364.

4. Hawkins, G. S.; and Southworth, R. B.: Orbital Elements of Meteors. Smithsonian Contributions to Astrophysics, vol. 4, no. 3, Smithsonian Institution, Washington, D. C., 1961, pp. 85-95.

5. McCrosky, R. E.; and Posen, A.: Orbital Elements of Photographic Meteors. Smithsonian Contributions to Astrophysics, vol. 4, no. 2, Smithsonian Institution, Washington, D. C., 1961, pp. 15-84.

6. Whipple, F. L.: Meteors and the Earth's Upper Atmosphere. Reviews of Modern Physics, vol. 15, no. 4, October 1943, pp. 246-264.

7. Öpik, E. J.: Physics of Meteor Flight in the Atmosphere. Interscience Publishers, Inc., New York, 1958.

8. Öpik, E. J.: Tables of Meteor Luminosities. The Irish Astronomical Journal, vol. 6, no. 1, March 1963, pp. 3-11.

9. Whipple, F. L.: Photographic Meteor Orbits and their Distribution in Space. Astronomical Journal, vol. 59, number 6, No. 1218, July 1954, pp. 201-217.

10. Öpik, E. J.: Collision Probabilities with the Planets and the Distribution of Interplanetary Matter. Proceedings, Royal Irish Academy, vol. 54, Sec. A, 1951, pp. 165-199.

11. Dalton, C. C.: Statistical Analysis of Photographic Meteor Data, Part II; Verniani's Luminous Efficiency and Supplemented Whipple Weighting. NASA TM X-53360, November 18, 1965.

12. Dalton, C. C.: Velocity Dependence of Meteor Luminous Efficiency and Consequent Statistical Results. Appendix in "Effects of Recent NASA-ARC Hypervelocity Impact Results on Meteoroid Flux and Puncture Models." NASA TM X-53512, September 7, 1966, pp. 23-31.

13. Upton, E, K. L.; and Hawkins, G. S.: The Influx Rate of Meteors in the Earth's Atmosphere. Interim Report 24, Contract AF 19(122)-458, Sub-contract No. 57, October 1957.

14. Dalton, C. C.: Statistical Analysis of Photographic Meteor Data, Part I: "Öpik's Luminous Efficiency and Supplemented Whipple Weighting." NASA TM X-53325, September 2, 1965.

15. Dalton, C. C.: Inferences from Photographic Meteors. Proceedings of the Symposium "Meteor Orbits and Dust," Cambridge, 9-13 August 1965, Smithsonian Contributions to Astrophysics, vol. 11, pp. 81-90 (NASA Special Publication SP-135, SCA Vol. 11, 1967.)

16. Jacchia, L. G.; Verniani, F.; and Briggs, R. E.: An Analysis of the Atmospheric Trajectories of 413 Precisely Reduced Photographic Meteors. Special Report No. 175, Smithsonian Astrophysical Observatory, Cambridge, Mass., April 23, 1965.

17. Parkinson, J.: Space Environment Criteria. MSFC Contract NAS8-11285, Aerojet-General, presented 26 May 1965.

18. Hawkins, G. S.: Impacts on the Earth and Moon. Nature Magazine, vol. 197, no. 4869, 23 February 1963, pp. 781.

Page
Intentionally
Left Blank

MARTIAN ATMOSPHERIC VARIABILITY

By

George S. West, Jr.

SUMMARY

This paper traces the background of Martian atmospheric model development and indicates why present MSFC models have been developed to overcome difficulties experienced with previous models and interpretations of available data. It also indicates future plans for acquiring observational data for improvement of the present models.

INTRODUCTION

Natural environmental criteria are essential to the design and mission planning of spacecraft used for planetary exploration, for example, the successful Mariner IV mission to Mars, and the planned Voyager missions to Mars in the 1970's [1].

Only the thermal aspects of the upper and lower atmosphere that affect orbital entry heating and orbital lifetime for vehicle design are discussed in this paper. These thermal aspects are determined from kinetic temperature, molecular temperature, atmospheric pressure, atmospheric density, molecular weight, density scale height, pressure scale height, number density, speed of sound, columnar mass, mean free path, and coefficient of viscosity. Surface and atmospheric winds are not treated in this paper.

For any planet, the establishment of environmental information must be considered an iterative process; the environmental parameters logically planned for measurement by a planetary probe are those required for the design and planning of a planetary mission in the first place. Mariner IV yielded a wealth of new information on surface conditions, the atmosphere, the planetary magnetic field, and the planetary mass. From the data acquired, more realistic evaluations of the planetary environment of Mars have been extracted, thereby making possible the derivation of engineering and design parameters of a higher confidence level for use, for example, in orbital entry heating and orbital lifetime analyses for the Voyager missions to Mars contemplated for the 1970's.

In planning the Voyager program, for example, a very detailed estimate of the Martian atmosphere is required for the selection of an optimum orbit altitude for the science package that does not violate planetary quarantine restraints. In turn, each Voyager mission will provide data for more sophisticated and realistic criteria as each successive iteration narrows the range of values.

BASIS FOR DEVELOPMENT OF THE MSFC MODELS

In the initial development of the required environmental information, it was first necessary to consider what information was available. Prior to the Mariner IV occultation experiment in 1965, polarimetric and spectrophotometric observations of Mars were used to derive surface pressure and atmospheric composition; i.e., radiometric observations were used to obtain surface temperatures, while atmospheric temperature profiles were based primarily upon earth analogies. Figure 1 shows that the temperature profiles and surface pressure values derived by these techniques differed considerably. This was caused, in part, by differences in the observations, but was primarily caused by differing opinions and interpretations of the investigators.

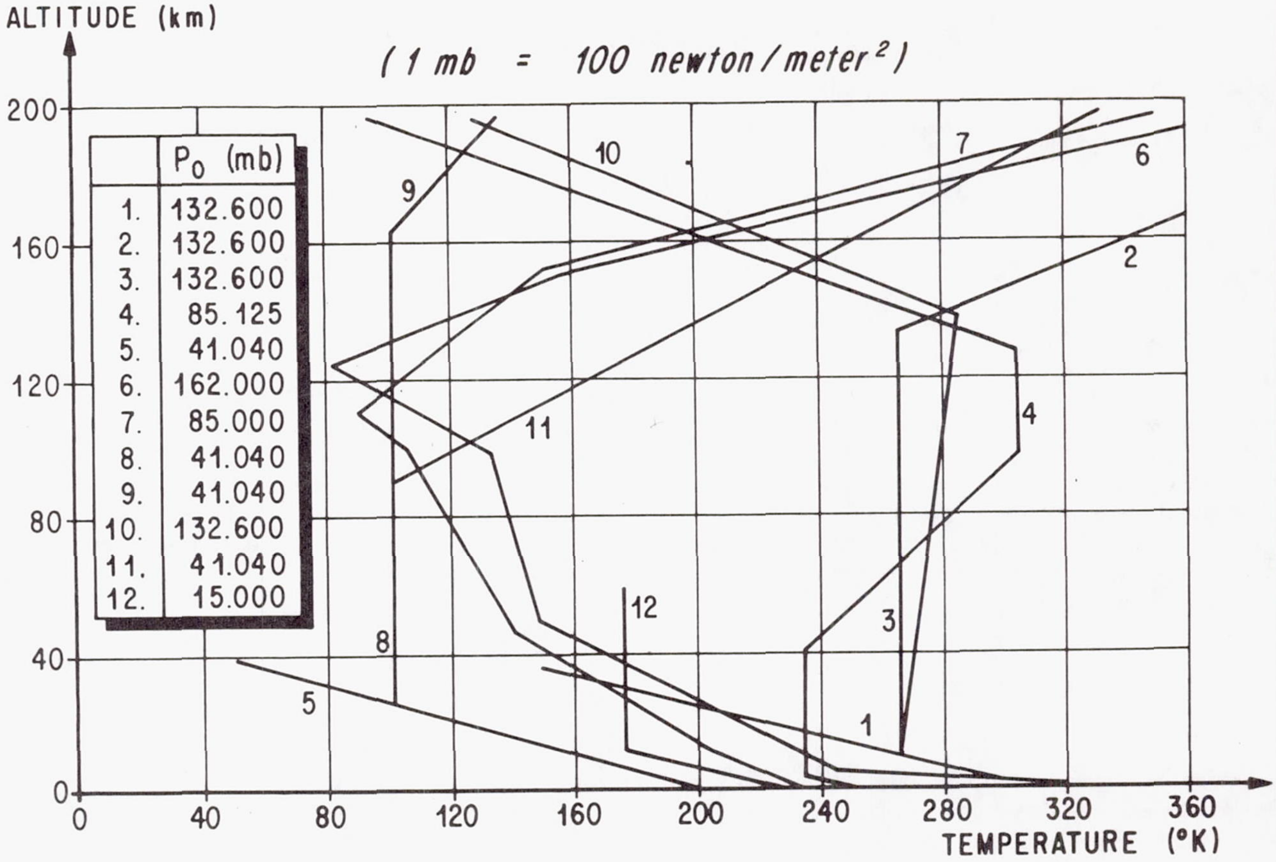

FIGURE 1. PREVIOUS MODELS OF THE MARS ATMOSPHERE

The Mariner IV occultation experiment was designed to measure two profiles of the electron density of the Martian atmosphere. From these two electron density profiles, parameters of interest such as pressure, temperature, and density may be derived. However, in transforming the electron density profiles to the desired parameters, it is necessary to establish the atmospheric constituent distribution at the ionospheric base and employ a theoretical concept of the Martian atmospheric chemical processes and related reaction rates, time constants, etc. This technique, of necessity, leads to many differing interpretations of the Mariner IV data. Some of the temperature profiles derived from these data are illustrated in Figure 2. Some investigators have taken the envelope formed by the different interpretations of data as representative of the variability of the Martian atmosphere. This is not a valid assumption. The differences in these profiles are caused solely by the different techniques, applications, and opinions of the various investigators. Dr. F. S. Johnson [2] of the Graduate Research Center of the Southwest has postulated that the Martian ionosphere is similar to the F_2 layer of the earth's ionosphere, which implies that the main ion is O^+. Chamberlain and McElroy [3] of Jet Propulsion Laboratory (JPL) have theorized that the Martian ionosphere is an E-type layer where the main ion is NO^+ or O_2^+. In studying the various interpretations of the Mariner IV data, the F-type layer interpretation was chosen for use in formulating the Mars atmospheric studies and models [4]. This choice was made because of the reasonable agreement of the temperature of F-type ionospheric models with temperature of theoretical heat budget computations, and from what appears to be unreasonable effective recombination coefficients and average ion mass assumptions in order to make an E-layer compatible with the ionization profile measured by Mariner IV [5].

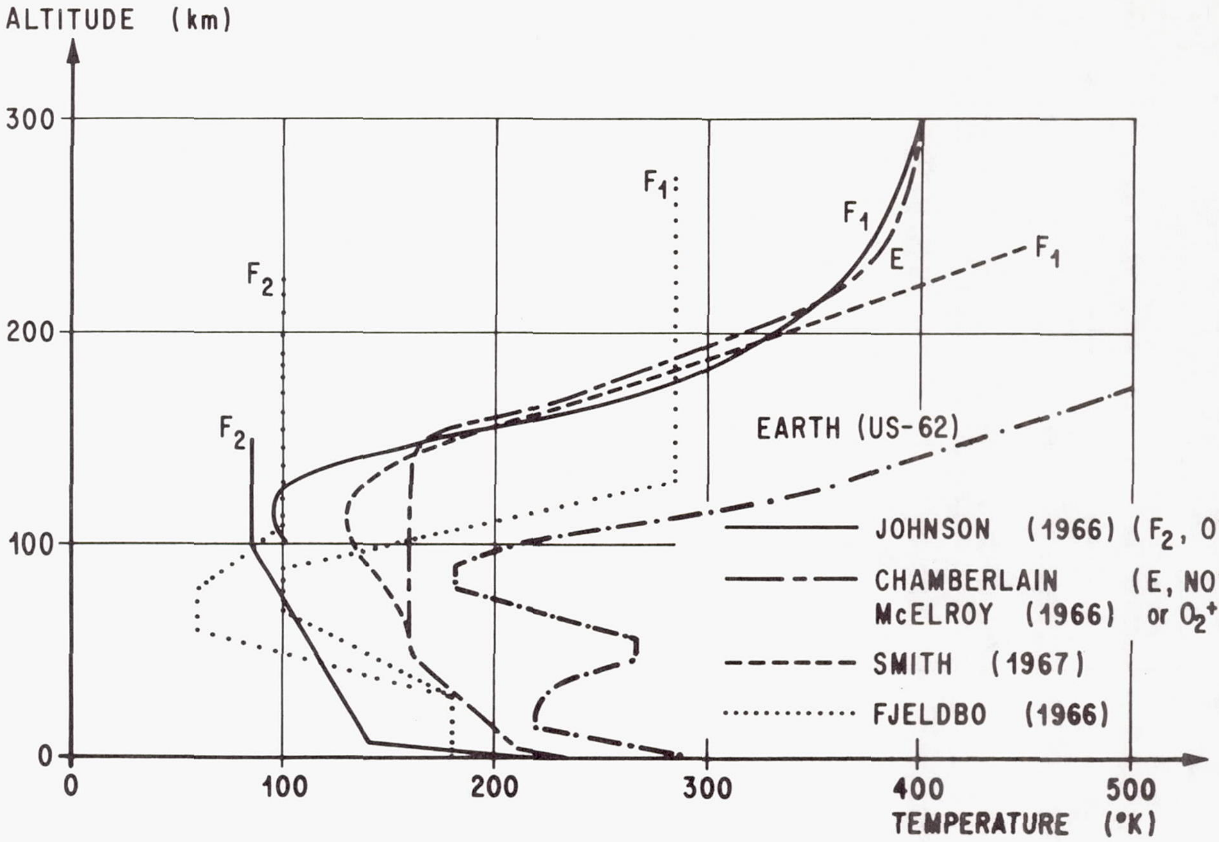

FIGURE 2. COMPARISON OF MARTIAN TEMPERATURE PROFILES DERIVED FROM MARINER IV

One other point that should be stressed is that the Mariner IV data do not represent the mean atmosphere as some investigators have indicated. These data represent two profiles for two points in space at the time of orbital entry and exit. The entry data, for example, concern the main ionization layer over electris ~ (50 degrees S, 177 degrees E) at 1300 hrs., local Martian time in late winter.

In developing the natural environmental criteria for Voyager, we have conducted detailed studies in these areas:

1. The various radiative models.
2. Various interpretations of Mariner IV data.
3. The diffusion and possible escape of Martian exospheric constituents.
4. The relationship of temperature and exospheric constituent distribution.
5. The probability of space plasma and Martian exospheric mixing.
6. The dependence of exospheric temperature on solar flux and sunspot cycle.

Temperature profiles generated by these studies are illustrated in Figure 3. The lower portion of these profiles is based upon the Mariner IV data. In establishing the upper portions, consideration was given to the relationships between temperature and atmospheric constituent distribution. These temperature profiles, in conjunction with derived molecular weight profiles and surface pressure values of 400, 800, and 1000 N/m^2 (4, 8, and 10 mb) that are based upon improved spectrophotometric observations and the Mariner IV data, were used to derive the density profiles illustrated in Figure 4. The extreme density envelopes pictured here, which include five orders of magnitude, represent our best estimate of the total variation to be expected in the Martian atmosphere. However, this five orders of magnitude variation might be reduced if more observational data were available.

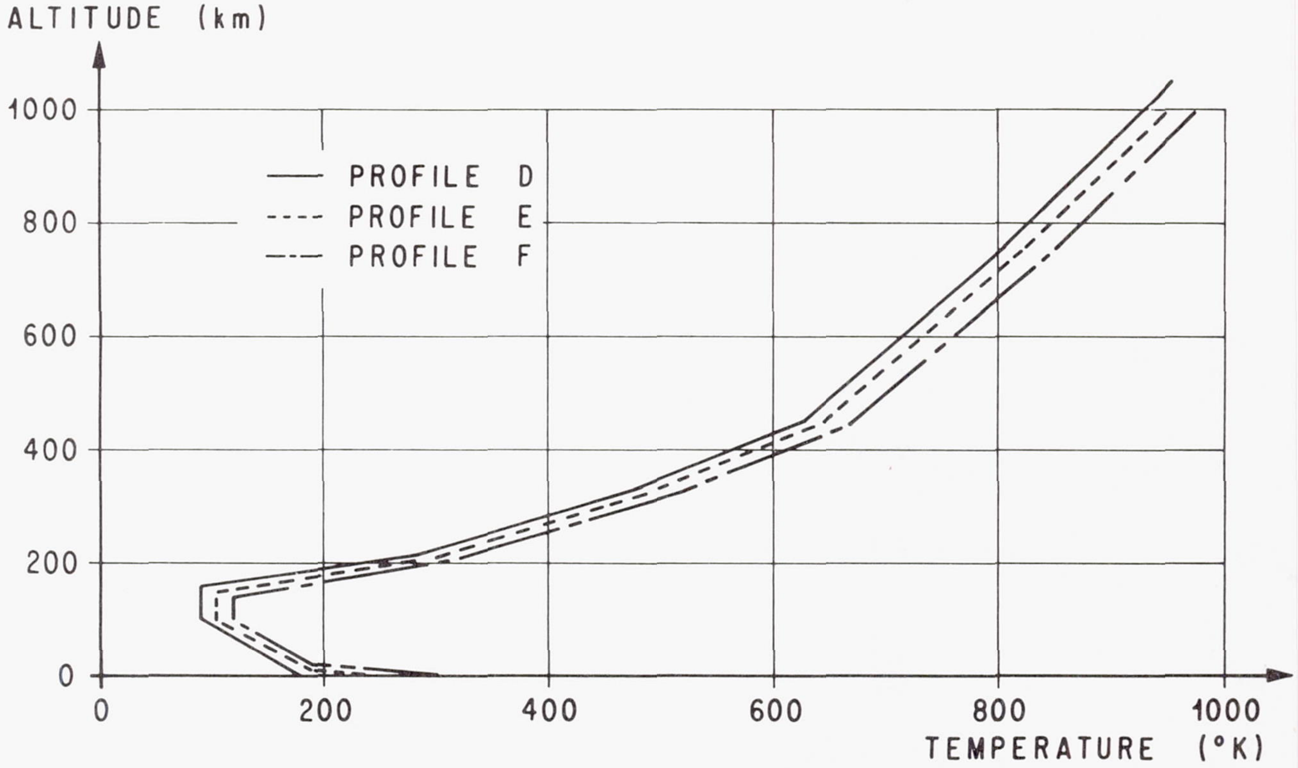

FIGURE 3. IDEALIZED MARTIAN TEMPERATURE PROFILES ASSUMING F_2 OR F_1 IONIZATION LAYER

PLANS FOR OBTAINING FUTURE DATA

In attempting to obtain required observational data, an electromagnetic probing experiment has been proposed for the Mars atmosphere, and studies have been conducted concerning the feasibility of obtaining Martian atmospheric information through vacuum simulation experiments. In the area of "on-the-spot" data acquisition (Fig. 5) a method of great promise for obtaining large amounts of data from occultating absorption and radiometric techniques for actual measurements of a planetary atmosphere are inherent in the orbiting satellite pair. Briefly, the orbiting pair would accomplish electromagnetic measurements of a planetary atmosphere and ionosphere, such as Mars, by essentially an occultation approach in which the source of radiation and the detector are both relatively near the planet to be probed. If two satellites are placed in similar orbits about the planet, refractivity measurements may be made along the line of sight by methods derived from the Mariner IV radio occultation technique. Absorption spectroscopy measurements may be made by methods tested on the NRL-1965-16-D satellite at two points on each orbit where there is a direct line of sight relationship between the two satellites and the sun. Radiometric techniques for planetary surface temperature measurement are derived from standard techniques. The occultation measurements yield electron density, species, pressure, and temperatures, and from these data the atmospheric refractivity profile and scale height may be directly derived. The spectroscopic data yield identification of the species and determination of the mean molecular weight and number density. The radiometric measurements provide the surface temperature. Surface temperature and mean molecular weight allow an independent derivation of the atmospheric scale height, which can be cross checked with the atmospheric scale height obtained directly from the refractivity measurements.

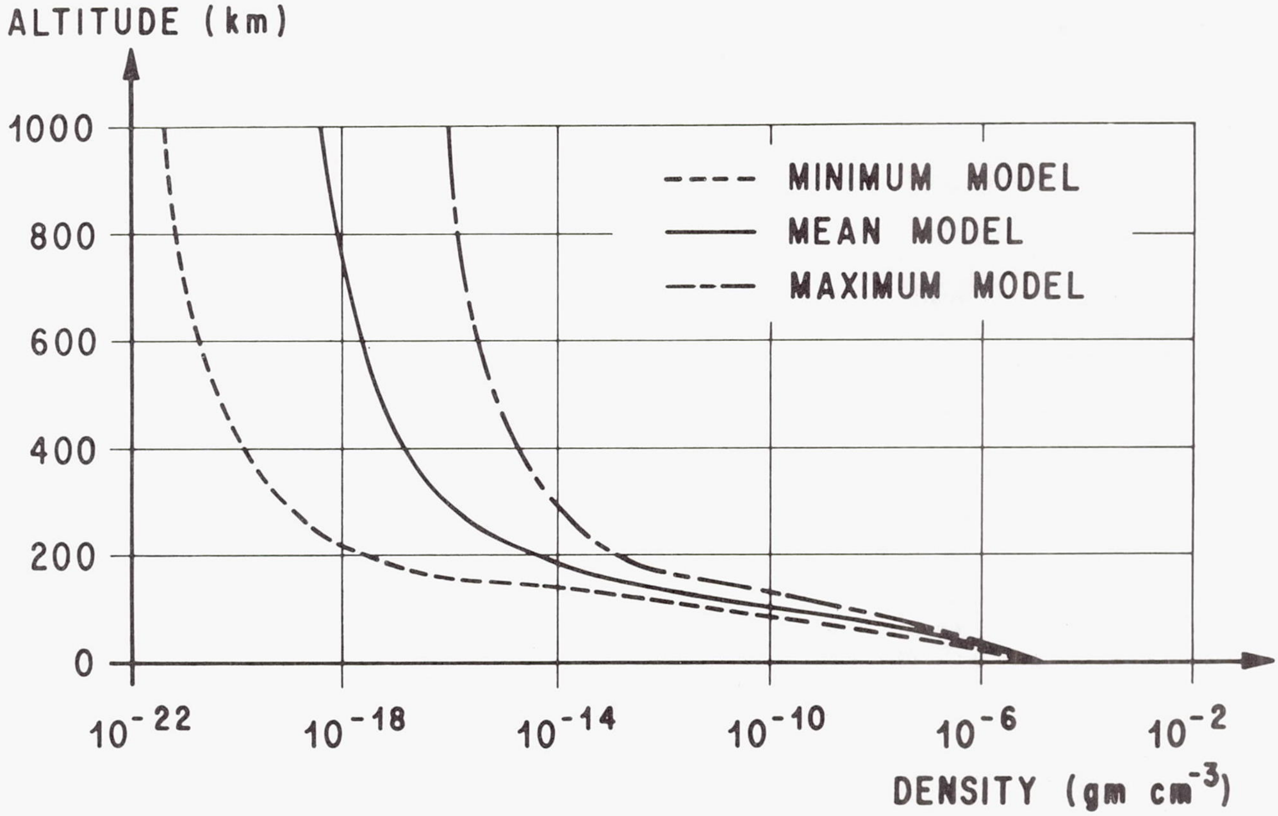

FIGURE 4. ATMOSPHERIC DENSITY

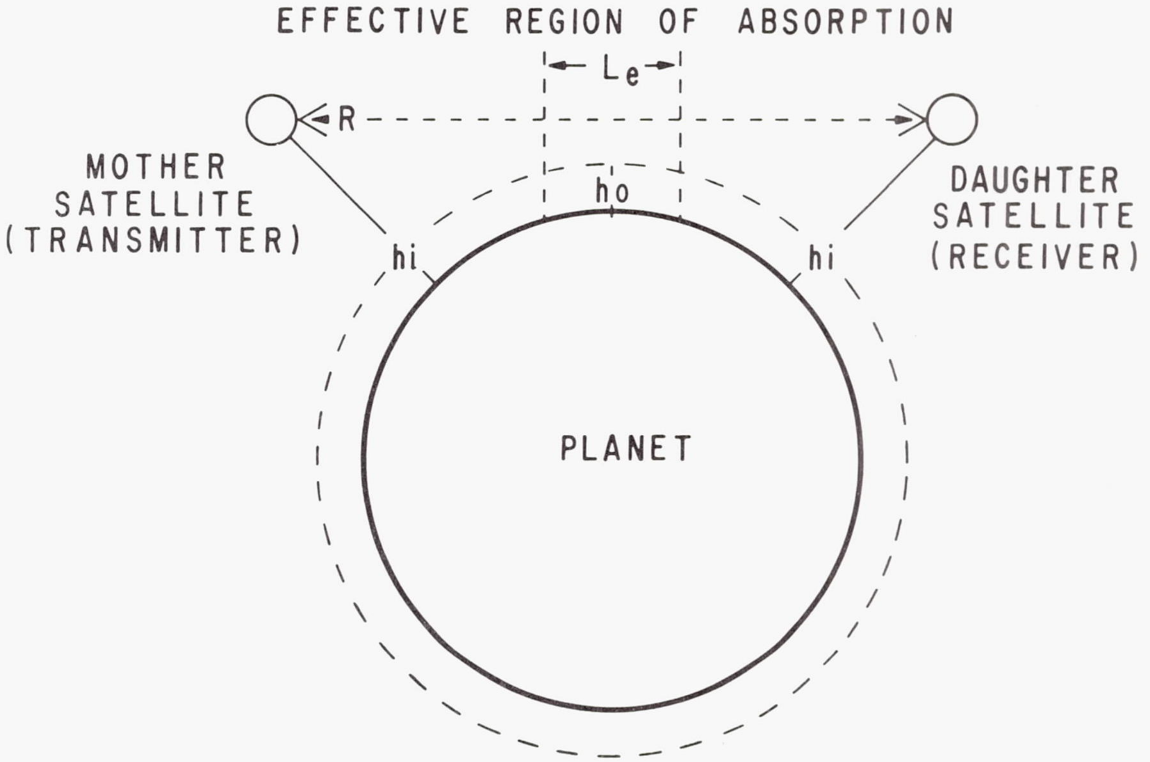

FIGURE 5. MICROWAVE SPECTROSCOPY EXPERIMENT CONFIGURATION

Current results are listed in Reference 1, and future studies and programs are as follows:

1. Mars atmospheric simulation.
2. Orbiting satellite pair.
3. Theoretical studies.
    a. Seasonal-latitudinal studies.
    b. Solar cycle.
    c. Martian atmospheric processes.

REFERENCES

1. Weidner, D. K.; and Hasseltine, C. L.: Natural Environment Design Criteria Guidelines for MSFC Voyager Spacecraft for Mars 1973 Mission. TM X-53616, MSFC, Huntsville, Alabama, June 8, 1967.
2. Johnson, F. S.: The Atmosphere of Mars. Science, vol. 150, 1965, p. 1445.
3. Chamberlain, J. W.; and McElroy, M. B.: Martian Atmosphere: The Mariner Occultation Experiment. Science, vol. 152, no. 2718, April 1, 1966, p. 21.
4. Smith, Newburn; and Beutler, Abigail E.: A Model Martian Atmosphere and Ionosphere. Space Physics Research Laboratory, The University of Michigan, Ann Arbor, Michigan.
5. Gross, S. H.; McGovern, W. E.; and Rasool, S. I.: Mars: Upper Atmosphere. Science vol. 1515, March 1966.

BIBLIOGRAPHY

1. Smith, R.: Space Environment Criteria Guidelines for Use in Space Vehicle Development (1967 Revision). NASA TM X-53521, MSFC, Huntsville, Alabama, February 1, 1967.
2. Weidner, D. K.: A Preliminary Summary of the MSFC Planetary Atmosphere Computer Program. NASA R-AERO-IN-5-67, (Internal Note), MSFC, Huntsville, Alabama, June 30, 1967.
3. DeVaucoulers, G.: Physics of the Planet Mars. Faber and Faber Limited, 24 Russell Square, London, England.

Page
Intentionally
Left Blank

MANUFACTURING ENGINEERING RESEARCH AT MSFC

November 30, 1967

By

Robert T. van Aller
Frederick J. Beyerle
Charles R. Cooper
Robert V. Hoppes
Ronald L. Nichols
P. Gordon Parks
John R. Rasquin
Paul H. Schuerer
Douglas L. Stephens
William A. Wall, Jr.
Vaughn H. Yost

11

Page
Intentionally
Left Blank

Page
Intentionally
Left Blank

CONTENTS. . .

CONTAMINATION CONTROL

by Robert T. van Aller and Frederick J. Beyerle

LIST OF TABLES

LIST OF ILLUSTRATIONS

CLOSED CIRCUIT TV ARC GUIDANCE DEVELOPMENT FOR WELDING

by William A. Wall, Jr. and Douglas L. Stephens

CONTENTS (Continued) . . .

LIST OF TABLES

LIST OF ILLUSTRATIONS

CONTENTS (Continued) . . .

MECHANICAL DEVICES FOR ZERO GRAVITY SIMULATION

by Vaughn H. Yost

LIST OF TABLES

CONTENTS (Continued). . .

LIST OF ILLUSTRATIONS

CONTENTS (Continued). . .

LIST OF ILLUSTRATIONS

LASERS USED IN MANUFACTURING

by John R. Rasquin

LIST OF ILLUSTRATIONS

NEUTRAL BUOYANCY SIMULATION

by Charles R. Cooper, Paul H. Schuerer, and Ronald L. Nichols

LIST OF ILLUSTRATIONS

ALUMINUM WELDING DEVELOPMENT COMPLEX

by Robert V. Hoppes

LIST OF TABLES

LIST OF ILLUSTRATIONS

EXPERIMENTAL ELECTRON BEAM WELDING IN SPACE

by P. Gordon Parks

CONTENTS (Concluded)

LIST OF ILLUSTRATIONS

CONTAMINATION CONTROL

By

Robert T. van Aller and Frederick J. Beyerle

THE CONTAMINATION CONTROL PROGRAM

Contamination control cannot be effectively applied without an understanding of what constitutes contaminants and an analysis of their detrimental effects on environments in which they are found. Contamination comes in many forms: the metal chip in a pneumatic valve; the fiber which clogs a filter; and the loose nut, bolt, or washer in a fuel tank or in a spacecraft.

Many factors need to be considered in the evolution of a comprehensive contamination control program to make it as effective and as economical as possible. Consideration must first be given to the various types and levels of contamination that can be tolerated without adversely affecting the reliability of the product. Factors that must be carefully considered are (1) the processes and tools, (2) the facilities and their monitoring equipment, (3) the cleanliness verification methods, and (4) personnel training. Briefly the considerations for a contamination control program can be summarized as follows:

1. The need for contamination control.
2. Tolerance levels in contamination controlled products.
3. Relationship of processes, the product, contamination sources, and facilities.
4. The product cleaning.
5. Personnel factors.

SPECIFICATIONS AND PROCEDURES

To bridge the gap between theory and practice in the field of contamination control, MSFC embarked upon a program to develop the best methods to clean both intricate and large spacecraft parts to the levels required by NASA specifications. This program began in the Redstone days when there was only one specification, and it called out cleanliness levels to a degree that was quite difficult to meet and almost impossible to verify because of the lack of tools and knowledge in testing parts for contamination.

The R&D effort on space vehicles was accomplished on a priority basis with tight schedules. However, most, if not all, of the schedules were met, and although many problems occurred during the cleaning programs, the complex spacecraft parts cleaned inhouse met the specified requirements. Accomplishments in contamination control programs for the Redstone, Jupiter, Saturn I, and Saturn V vehicles will be summarized in this paper.

For the Saturn vehicles a method was developed for internal spray cleaning of large LOX and fuel tanks and lines to MSFC cleaning levels. This method is now being used by prime contractors such as Boeing, Douglas, Chrysler, and North American Rockwell to clean their launch vehicle tanks.

Figure 1 shows the fuel exclusion riser that was developed and successfully tested for use in the Saturn V S-IC fuel tank sump. Its purpose is to replace the heavier JP fuel in the sump area with urethane foam blocks for a large weight savings to the vehicle and to eliminate the need for excess fuel removal after static firing tests.

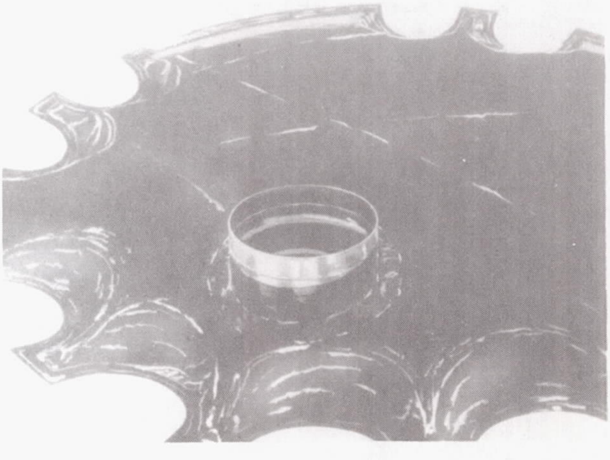

FIGURE 1. FUEL EXCLUSION RISER

About 100 procedures were written for use in MSFC contamination control programs during the development of the Redstone, Jupiter, Saturn I, and Saturn V vehicles. These procedures specified cleanliness levels for hardware such as (1) vehicle tanks, (2) valves and regulators, (3) stainless steel bellows and lines, (4) liquid oxygen gaskets (5) flared tubing, and (6) honeycomb parts. Specific cleaning procedures were developed for crucial or intricate items that included (1) gas-bearing parts in gyroscopes, (2) high pressure spherical tanks in the S-IB stage (3) heat exchangers on F-1 engines, (4) electrical connectors, (5) nonmetallic gaskets for LOX service, and (6) various hydraulic parts.

Some methods in corrosion protection specified (1) electropolishing small parts, (2) deoxidation and conversion coating of aluminum alloys, and (3) electroless nickel plating. A spray anodizing technique and equipment (Fig. 2) were developed under contract to Reynolds Metals Company, Richmond, Virginia. The technique involves applying an anodized coating to an aluminum seam, such as a weld area, after a space vehicle tank has been welded together. The present vehicle tanks are protected from atmospheric corrosion with a conversion coat during their manufacture and assembly operations. These coatings are easily and cheaply applied (compared to other coatings), but these coatings also are the least resistant to corrosion attack. The conversion coating was chosen because it was the only coating that could be applied feasibly to a weld area on large surfaces such as space vehicle tank surfaces. Now, however, with the development of the spray flush anodizing technique, it is possible to apply a coating with an electric current in a matter of seconds rather than the 30 to 60 min it formerly took. The anodized coating offers maximum protection to the areas most susceptible to corrosion.

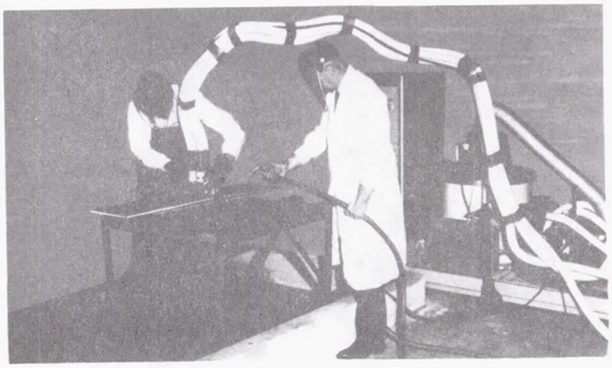

FIGURE 2. SPRAY ANODIZING EQUIPMENT

A contract was awarded to the Sandia Corporation, a prime contractor of AEC, to develop a handbook in contamination control to be used by designers and engineers working on contamination control programs. One document presently being released by the Office of Technology Utilization (OTU) of NASA Headquarters is entitled <u>Principles of Contamination Control,</u> which is the forerunner to the main document entitled <u>Handbook for Designers and Engineers in Contamination Control</u>. This last document will be available for release in August, 1968.

Table I shows a NASA contamination control panel initiated at Marshall Space Flight Center. One of the functions of the panel is to standardize documentation such as specifications, standards, and procedures in contamination control work. The Manned Spacecraft Center at Houston, the center at Cape Kennedy, and Marshall Space Flight Center are all jointly involved.

TABLE I. NASA CONTAMINATION CONTROL PANEL

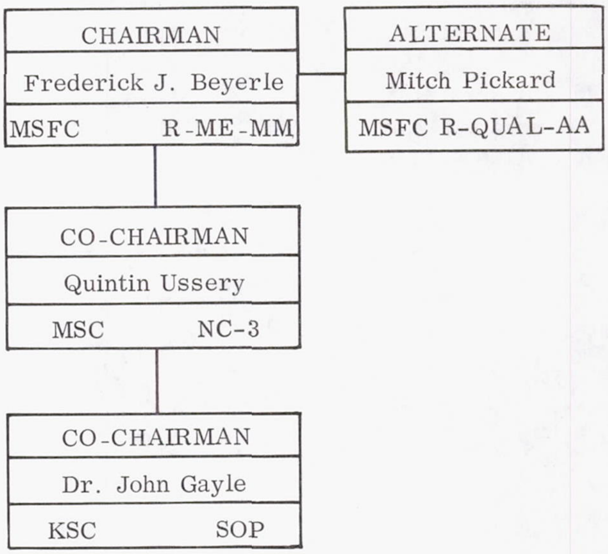

FORMAT:

1. Sponsorship: NASA Headquarters
2. Meets once a month alternately at each center.
3. Each center visited chairs the panel.

SPACECRAFT STERILIZATION

Spacecraft sterilization is an important area in contamination control programs. One of the major goals of planetary exploration is to provide information about the existence of extraterrestrial life. Forerunners to manned exploration are automated biological laboratories designed to detect life on planetary surfaces with very sophisticated instruments. To assure the validity of information from these craft, it is absolutely essential that there be no life on the device when it lands. This is in itself justification for a spacecraft sterilization program, and is totally aside from any possible moral implications of infecting a planet with earth-type microbes that may be lethal to indigenous life. Present NASA policy stipulates three fundamental requirements that unmanned planetary landers must fulfill. They are as follows:

1. The lander will be assembled in clean rooms at specified levels of assembly. This is interpreted to mean biologically clean rooms in which the number of living organisms in the air is maintained at or below one organism/cu ft.

2. The landing assembly will be subjected to an approved sterilization procedure. Dry heat is currently the only approved method of sterilization; however, it is recognized that certain items not compatible with the dry heat sterilization cycle may require sterilization by other methods. Also, chemical decontamination may be used for biological load reduction prior to dry heat terminal sterilization.

3. The landing assembly will be enclosed in a bacteriological barrier.

Present NASA procedures call for 24.5 hr at 125°C for terminal dry heat sterilization. The conditions necessary for the decontamination of surfaces by using ethylene oxide (ETO) gas require not less than 300 mg of ethylene oxide per liter of space in the enclosure, a minimum exposure time of 4 hr, and an exposure temperature of not less than 21°C. Prior to ETO treatment, surfaces must be exposed to more than 35% relative humidity (RH) for 72 hr or longer. Proof that decontamination has been achieved may be obtained in each case by pre- and post-treatment culturing of representative parts from the group treated. ETO cannot be used for internal decontamination but might conceivably be used for terminal sterilization.

Design and manufacturing procedures must allow for these considerations and is the subject of a study conducted by the General Electric Company for the Manufacturing Engineering Laboratory. The information has been compiled in three volumes. Volume I considers Design Guidelines, Volume II deals with Manufacturing Procedures, and Volume III is a Biological Handbook for Engineers.

In Volume I, Design Guidelines, it is established that as a general rule the design for sterilizability does not invalidate established practices for good design. Particular attention must be paid, however, to a number of critical details. Very early in this study, it was determined that moist heat could not be used for spacecraft sterilization. At the temperatures required, air saturated with water vapor has a deleterious effect on most spacecraft components. On the basis of information gained from the study, the decision was made to use dry heat.

It was also found that parachutes present unique sterilization problems. Table II shows tensile strength variations of 3 parachute materials as a result of thermal sterilization. These types of nylon are degraded to a large extent and therefore should be excluded from this application.

TABLE II. TENSILE STRENGTHS OF SEVERAL PARACHUTE MATERIALS RESULTING FROM HEAT STERILIZATION

MATERIAL	CONTROL	COVERAGE STRENGTH AFTER EXPOSURE
Dacron		
Types 52 & 56	1	0.90
Nomex	1	0.99
Nylon		
Types 300 & 380	1	0.20

Most planetary spacecraft contain a number of explosively actuated devices. The Mariner flyby has approximately 30 explosive squibs. Heat sterilization creates a severe environment for these devices, and it must be recognized that the requirement for sterilization must be considered during the squib design and not as an afterthought. Table III shows special problems associated with some representative devices. Squib manufacturers are generally of the opinion that explosive mixtures capable of withstanding sterilization temperatures can be found for most applications.

TABLE III. TYPICAL EXPLOSIVELY ACTUATED DEVICES FOR PLANETARY SPACECRAFT

DEVICE	DESCRIPTION – TYPICAL USES	SPECIAL PROBLEMS
Valves	Valve closed or opened using explosive actuator. Used for disconnecting cooling loops, attitude control loops, propulsion lines.	Leaks – Increased pressure during sterilization may aggravate.
Pin Pullers	Gas pressure drives piston which retracts. Used for separating structural systems, jettison of stores, release of science experiments.	May utilize heat labile "O" rings.
Bolts	Frangible section of bolt is cut by charge. Used for separation of structural systems, band clamps, etc.	Fragmentation – Material properties may be changed by heat.
Cable Cutters	Explosively actuated piston and cutter impacts on anvil. One shot device used for cutting cables, electrical harness, chute lines.	
Nuts	Frangible nut enclosed in jacket which contains pieces after fracture. Used to release structural systems.	Fragmentation
Shaped Charges	Shaped charge uses "Monroe effect" to sever. Used for separation, jettison, or deployment release.	Fragmentation
Thrusters	Explosively actuated piston works like pin-puller in reverse. Used for separation, deployment, or jettison.	May utilize heat labile "O" rings.
Gas Generators	Provide sustained gas pressure. Used to inflate impact limiters. Deploy scientific payload devices.	

An initial study was made of the effect of ETO gas and heat on electronic components. Briefly, some transistors suffer a slight decrease in beta after exposure to ETO. Some resistors, such as carbon composite, metal film, and oxide film, show marked resistance drift and life loss after exposure to dry heat. Failure occurs in some transistors such as the 2N 559 GE Mesa transistor, and in polymeric wire insulations after the dry heat exposure. In general, the effects that may occur from dry heat and ETO gas sterilization treatment are shown in Table IV. The Design Guidelines manual also included a detailed discussion of structural and thermal analysis, materials selection, and canister design.

Volume II, Manufacturing Procedures, deals with the problems which arise from manufacturing and assembling a planetary lander which is to be sterilized. The currently preferred procedure for achieving a sterile planetary lander is assembly under closely controlled environmental conditions to achieve a low biological population, enclosure in a biological barrier, and dry heat sterilization. To avoid excessively long sterilization times which may adversely affect the reliability of critical lander systems, assembly of the lander with a low biological population is necessary. This requirement fundamentally affects all manufacturing and assembly operations. The maintenance of particulate and

TABLE IV. EFFECTS OF STERILIZATION TREATMENT

EFFECTS	TREATMENT	
	GASEOUS DECONTAMINATION	DRY HEAT STERILIZATION
Physical	Absorption or adsorption of the decontaminant or its constituent gasses.	Expansion, weakening, stress generation, stress relief, sublimation, outgassing, fractional distillation of volatiles. Rupture or fracture due to increased stress and loss of permanent magnetism.
Chemical	Reaction with decontaminant, polymerization of ETO on surfaces.	Decomposition, exo- or endothermic reaction within part, and reaction of part with contiguous materials.

biological cleanliness becomes as important as functional reliability. This manual gives detailed procedures for the manufacture and assembly of major components, subsystems, systems, and the complete spacecraft. It is recommended that piece parts be manufactured by conventional or non-bioclean methods, and that they be decontaminated or sterilized prior to their use in subassemblies. Subassemblies that should be manufactured by special procedures are listed in Table V. Final spacecraft assembly is to be performed in a clean room with bioclean controls.

TABLE V. SPACECRAFT SUBASSEMBLIES

ELECTRICAL SYSTEMS

- Electronic Cordwood Modules
- Printed Circuits
- Black Boxes
- Electrical Relays
- Electrical Harnesses
- Photosensitive Tubes
- Magnetometers
- Batteries

ELECTROMECHANICAL SYSTEMS

- Tape Recorders
- Gyroscopes
- Solar Arrays
- Antennas

THERMAL SYSTEMS

- Thermal Insulation
- Thermal Coatings
- Heat Shield

MECHANICAL SYSTEMS

- Structure
- Honeycomb
- Parachutes
- Pyrotechnic Devices
- Solid Rocket Motors

Volume II also contains sections on cleaning and decontamination, as well as parts packaging and special facilities such as laminar flow clean rooms and assembly/sterilizer rooms. A view of an assembly/sterilizer room is shown in Figure 3. This type of facility is proposed for use in final assembly after sterilization so that components sterilized by techniques other than heat can be introduced into the lander. The room is protected from microbial contamination from humans by enclosing the personnel in sealed, extendable suits.

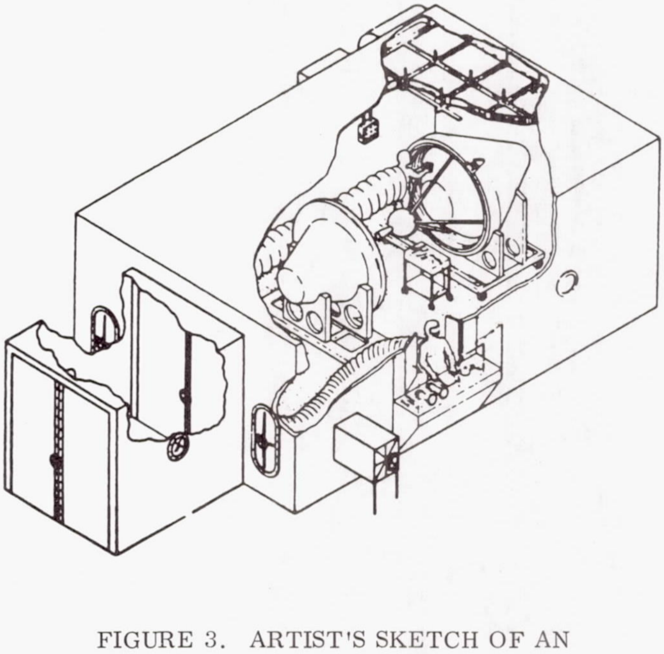

FIGURE 3. ARTIST'S SKETCH OF AN ASSEMBLY-STERILIZER

Volume III, the Biological Handbook for Engineers, provides microbiological background information useful to personnel who have had training and experience in the physical sciences but none in the life sciences. Subjects covered in Volume III are as follows:

1. Characteristics of microorganisms
2. Decontamination and sterilization procedures
3. Contamination control
4. Facilities
5. Bioassay
6. Effects of decontamination on materials

The first subject discussed, characteristics of microorganisms, provides basic information on microbiology required for a better understanding of the later sections of the handbook. The decontamination and sterilization section describes the techniques that may be employed in the manufacture and assembly of spacecraft that are to be sterilized. The section on contamination control describes sources of contamination, and the discussion of facilities describes clean rooms and personnel selection, motivation, and training. Bioassay describes the current approved methods of measuring bioloading on spacecraft and their components.

A serious problem in sterilization procedures is the need to remedy functional problems discovered after terminal sterilization (during prelaunch checkout). One approach is to use a heat sealable plastic envelope, which allows previously sterilized components to be inserted into a sealed spacecraft without breach of sterile integrity. This concept is shown in Figure 4. In each step shown, the sterile spacecraft is on the right and the sterile replacement item is contained in a plastic bag on the left. After the plastic bag is sealed to the plastic covered entry port on the spacecraft, the center is removed by cutting around the port through the middle of the 0.8 cm (5/16 in.) wide band of heat sealed plastic. Heat sealing and cutting are accomplished with tools included in the bag with the replacement item. After work on the spacecraft is completed, heat sealing a piece of replacement plastic to the entry port returns

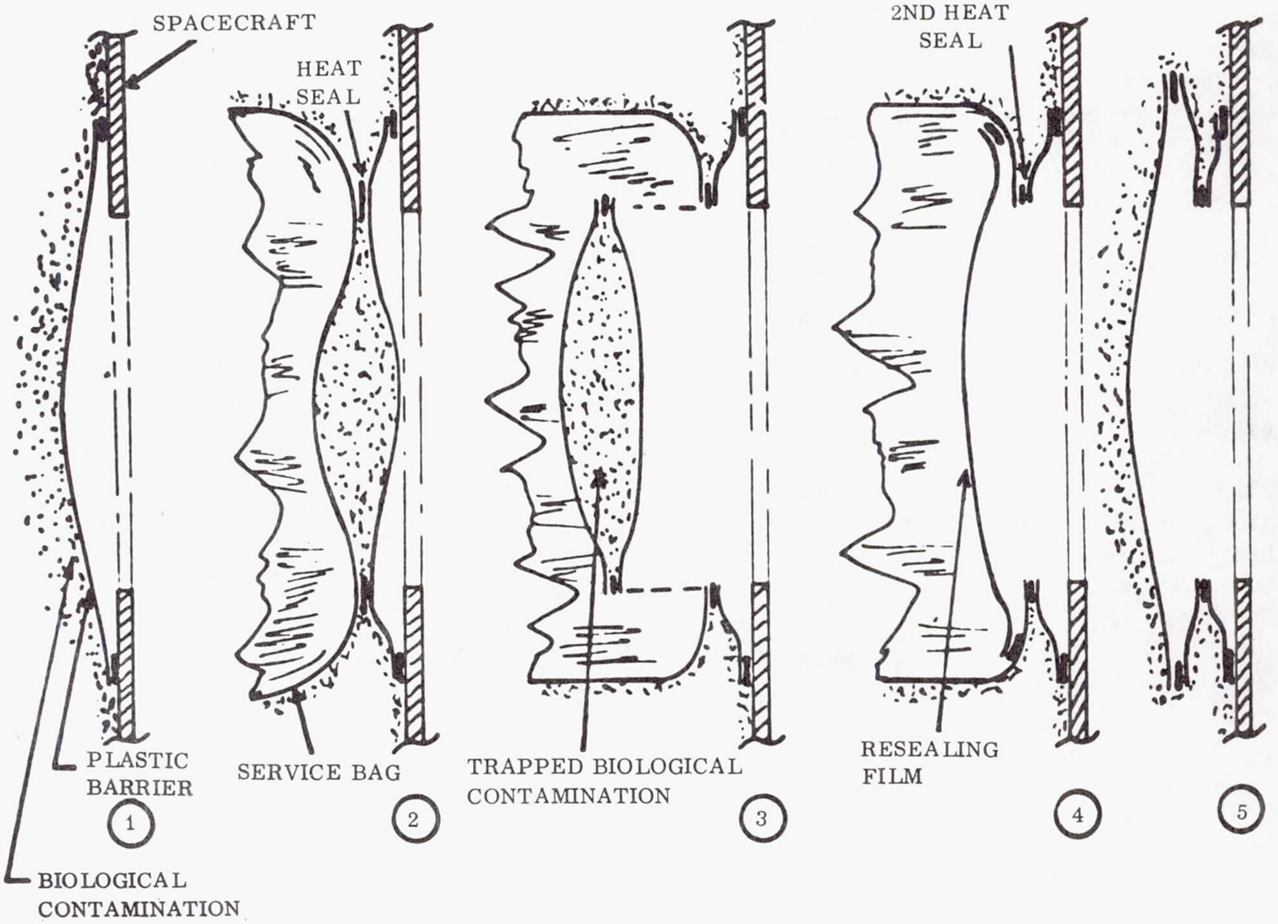

FIGURE 4. GENERAL CONCEPT FOR STERILE INSERTION

the craft to a flight readiness condition. The Manufacturing Engineering Laboratory has a contract with the Martin Company of Denver, Colorado, to investigate an initial phase of this plan. Any heat sealing and seam cutting processes used must not allow microorganisms trapped during heat sealing to be released from the cut seam into the sterile bag. It is essential to have perfect seals with no air pockets, and no live microorganisms should be exposed during cutting. The conditions of time, temperature, and pressure of sealing have been developed, which ensures strong seals and almost complete bacterial kill in the seam area. It has also been shown that the probability of release of organisms remaining viable after the heat sealing process is very remote.

Challenge System. It has been recognized that there will be certain components that probably cannot be heat sterilized in an assembled condition: that the parts will have to be sterilized before assembly and the component assembled in a sterile enclosure (Fig. 5). In a study conducted for the Manufacturing Engineering Laboratory by the McDonnell-Douglas Company, a particulate challenge system was developed and tested. This facility is shown in operation in Figure 6. The system consists of a double wall glove box with an aerosolized fluorescent dye contained between the double wall. The dye particles simulate bacteria. Within the inner wall is a very sensitive instrument for detecting any fluorescent dye particles which may be released through an accidental puncture in the inner wall. In this

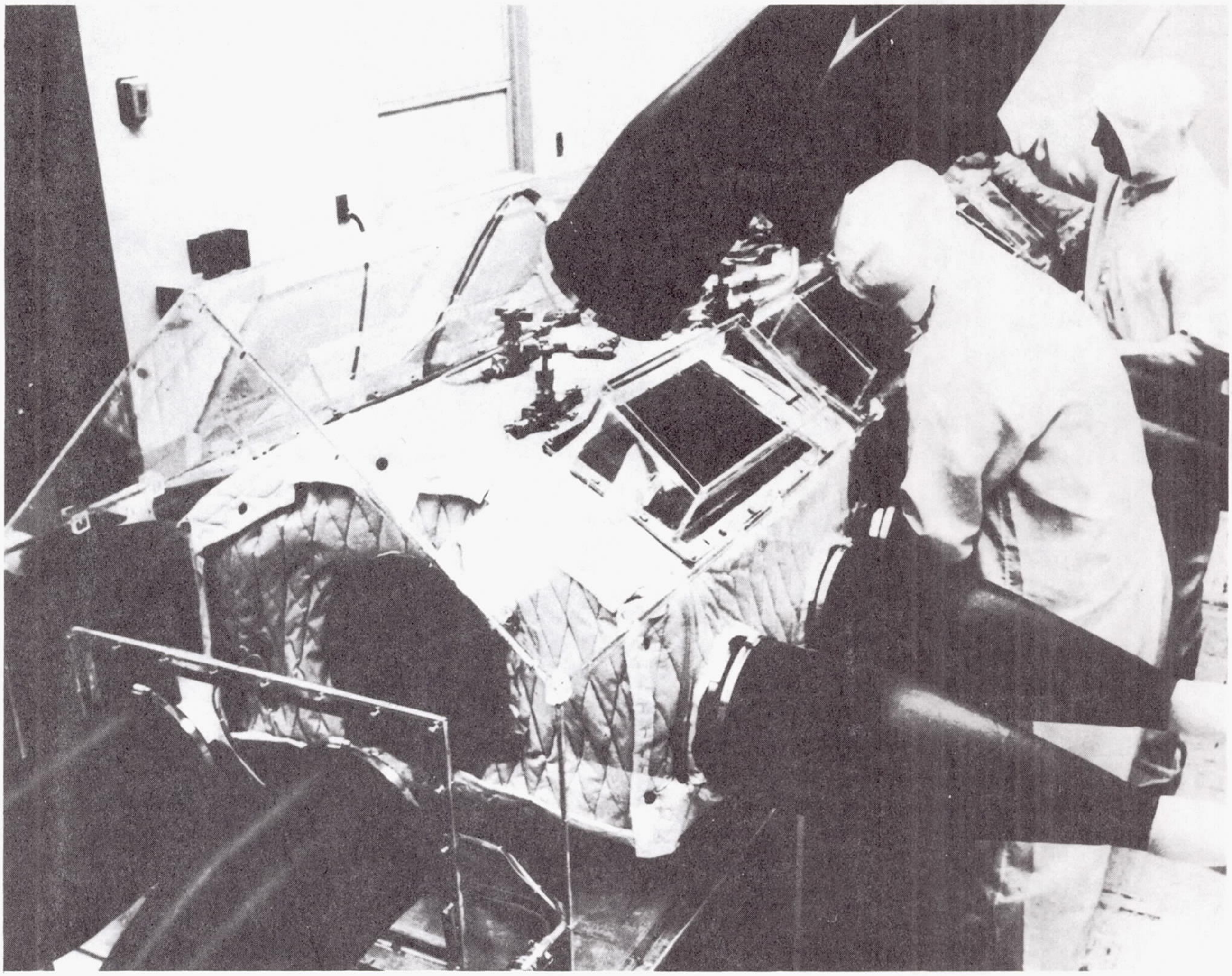

FIGURE 5. BIOLOGICAL CHALLENGE SYSTEM

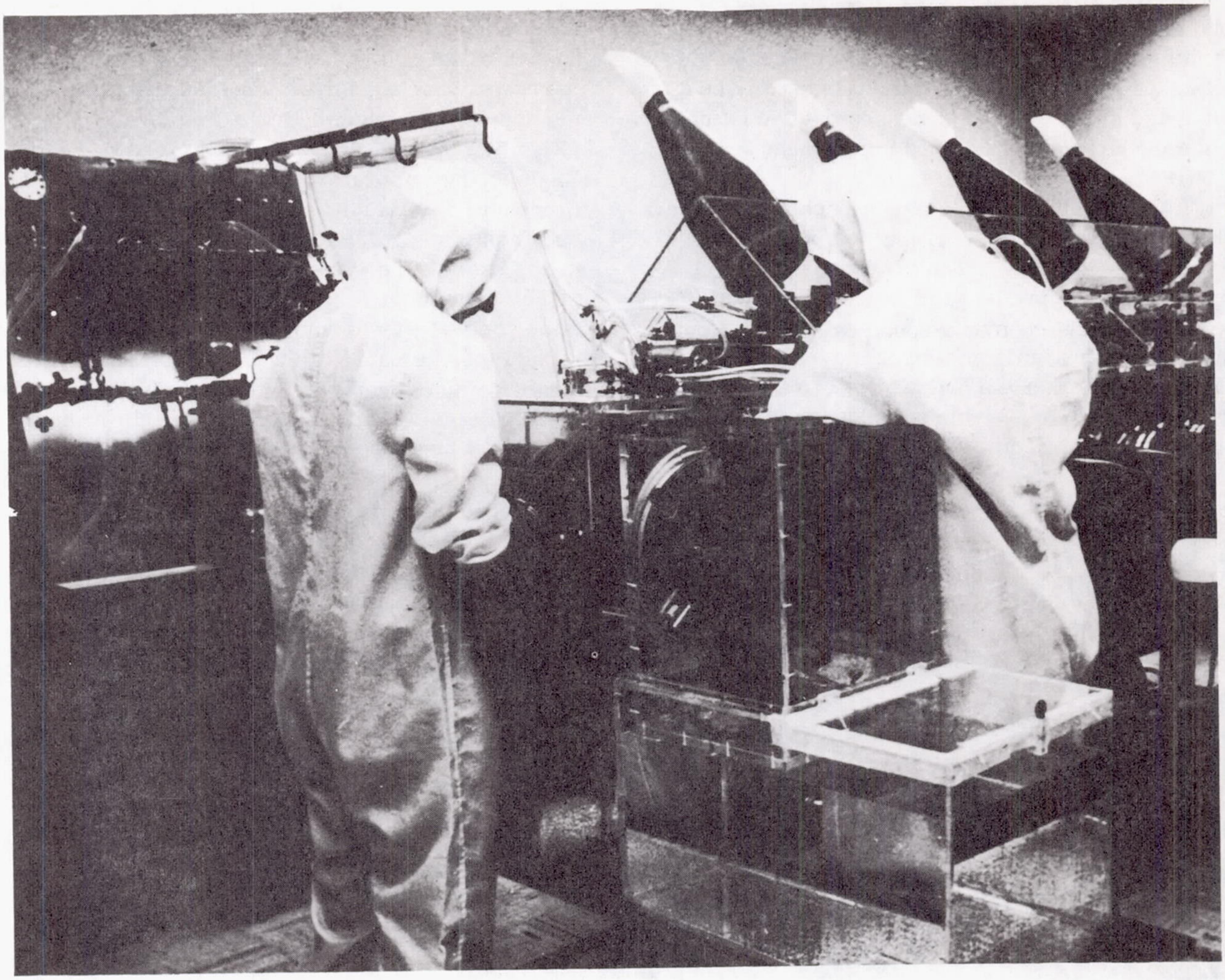

FIGURE 6. VIEW OF BIOLOGICAL CHALLENGE SYSTEM SHOWING DUNK BATH

manner, assurance of sterility is maintained during assembly

Information was also obtained concerning handling difficulties caused by the loss of tactile sensitivity when using the double rubber gloves. For example, it was found that assembly of tape recorders and pressure bottles in this sterile facility required approximately 12 times as many man hours as the same assembly on a conventional clean bench.

CLOSED CIRCUIT TV ARC GUIDANCE DEVELOPMENT FOR WELDING

By

William A. Wall, Jr. and Douglas L. Stephens

SUMMARY

Manufacturing engineers have long sought a reliable automatic arc guidance system for welding to simplify tooling and to perform remote welding. Several welding systems using automatic guidance techniques have been developed, but so far the results have been too limited for widespread industrial application. None of the systems were designed to track tack-welded joints. Tack welding aligns the weld components. Many complex parts are now tack welded prior to automatic welding, and this is when an automatic arc guidance system is really needed.

As a result, a program was initiated at MSFC to develop an automatic arc guidance system for welding. It was found that a closed circuit television (CCTV) signal furnished the data to permit the development of an automatic guidance system for the welding torch. This paper discusses the new CCTV system, its basic principles, and its scope of application. For system reliability, digital counting and logic techniques are used throughout the control circuitry.

The automatic video technique has shown considerable promise. Moreover, the creation of a new family of instrumentation can be achieved by using the same basic techniques developed for arc guidance control.

INTRODUCTION

Arc guidance may be defined as the means to accurately guide a welding torch along a weld joint. This function can be accomplished manually, mechanically, or automatically, with each mode having its unique application. The vast majority of space vehicle automatic welding uses mechanical tooling to maintain the required tracking accuracy of ±0.75 mm (±0.031 in.). Precision tooling is expensive, especially as parts increase in size and/or complexity. Automatic arc guidance could bring about a significant decrease in welding costs by minimizing the time required to assure that the torch and the joint are in perfect alignment. Moreover, there are some applications where the operator must, by necessity, be remote from the welding torch. Examples of this condition are the electron beam welding process and repair of radioactive parts. However, automatic guidance has not been widely used because there is no known commercially available sensing transducer that is sufficiently versatile.

PRIOR TECHNOLOGY

At least four general types of arc guidance sensors were evaluated, or considered for Saturn welding. These systems fall into the following major categories:

1. Electro-inductive.
2. Optical with photocell detectors.
3. Resistance of material.
4. Mechanical probes.

ELECTRO-INDUCTIVE TRANSDUCERS

The electro-inductive sensor [1] of Figure 1 operates on the principle of inducing eddy currents into the workpiece. Any shift in the weld joint will cause an unbalance in the reflected signal. The major advantages of this sensor are its compactness and ability to home in on the weld joint from a distance of at least 2.5 cm. Its major disadvantages are its susceptibility to stray electrical signals and other inherent problems listed in Table I.

TABLE I. RELATIVE MERIT RATING

AUTOMATIC ARC GUIDANCE MAJOR PROBLEM AREAS	RELATIVE TRACKING SYSTEM CHARACTERISTIC RATING*				
	ELECTRO-INDUCTIVE	OPTICAL WITH PHOTO CELL DETECTORS	RESISTIVE PROBE	MECHANICAL PROBE	CCTV ARC GUIDANCE
1. Type of material to be welded	Poor	Good	Poor	Excellent	Good to Excellent
2. Thickness of material to be welded	Poor to Good	Good to Excellent	Good to Excellent	Poor to Excellent	Good to Excellent
3. Symmetry of holddown tooling	Poor to Good	Excellent	Poor	Excellent	Excellent
4. Ferrous tooling metals	Poor	Excellent	Poor	Excellent	Excellent
5. Weld joint offset	Good	Good to Excellent	Good	Poor to Good	Poor to Good
6. Weld joint fitup	Excellent	Good to Excellent	Poor	Excellent	Good to Excellent
7. Distance changes from work to transducer (Proximity changes)	Poor to Good	Poor	Good	Good	Good to Excellent
8. Work surface finish	Excellent	Poor to Good	Poor	Excellent	Excellent
9. Welding arc light	Excellent	Good to Excellent	Excellent	Excellent	Good to Excellent
10. Welding arc heat	Poor	Excellent	Excellent	Good to Excellent	Excellent
11. Welding arc smoke	Excellent	Good	Excellent	Excellent	Good
12. Welding arc electromagnetic radiation	Poor	Good	Excellent	Excellent	Excellent
13. Stray electrical pickup interference	Poor	Poor	Good	Good to Excellent	Excellent
14. Electrical resistance of work material	Poor	Excellent	Poor	Excellent	Excellent
15. Weld joint special preparation required	Excellent	Poor	Good	Poor	Poor
16. Probe does not touch work	Excellent	Excellent	Poor	Poor	Excellent
17. Transducer field of view	Excellent	Poor	Excellent	Good	Excellent
18. System resolution of the field of view	Good	Excellent	Poor	Excellent	Excellent
19. Linearity of transducer signal over field of view	Poor	Poor	Good	Good	Excellent
20. Ability to track a tack-welded joint	Very Poor	Poor	Poor	Poor	Good to Excellent
21. Cost of system (Relative)	Good	Poor to Good	Excellent	Excellent	Good

* Excellent — Excellent system characteristic
Good — Had moderate bearing on performance
Poor — Had critical bearing on performance

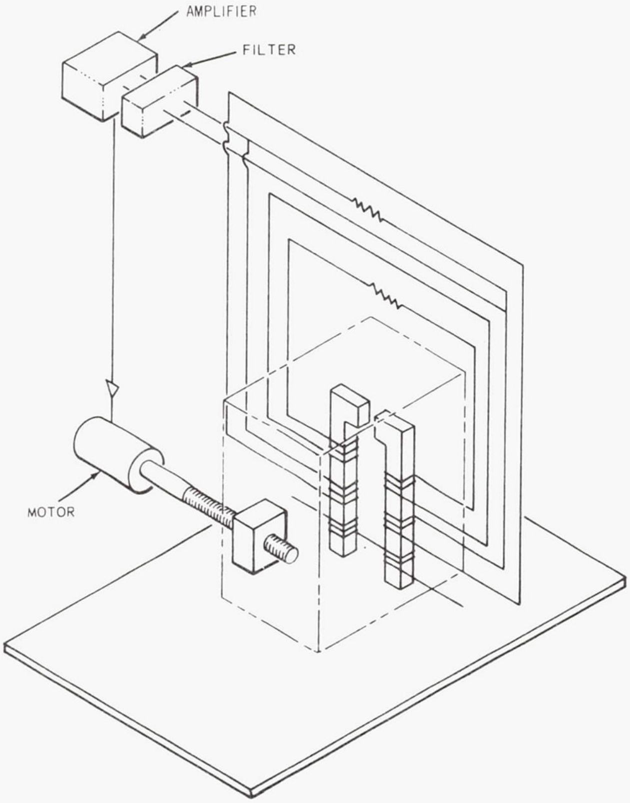

FIGURE 1. BASIC EDDY CURRENT ARC GUIDANCE

OPTICAL TRACKERS

Optical arc guidance trackers (Fig. 2) obtain their signal by focusing an intense light beam on a chamfered weld joint and sensing the reflected light amplitude on a photocell array. Setup of this equipment over the weld joint is very delicate; also, the sensor becomes completely lost if the light beam ever strays from the weld joint for any reason. This blindness is mainly a result of its very small field of view.

RESISTANCE OF MATERIAL TRACKERS

The resistance of material technique is implemented by two probes, one on either side of the weld joint. These two probes ride on the work surface and are take-off points for measuring the electrical resistance of the material for guidance purposes. Any resistive deviation from the initial setup condition would indicate a shift in the weld joint. This method was never successful on aluminum material because of the material's low electrical resistance.

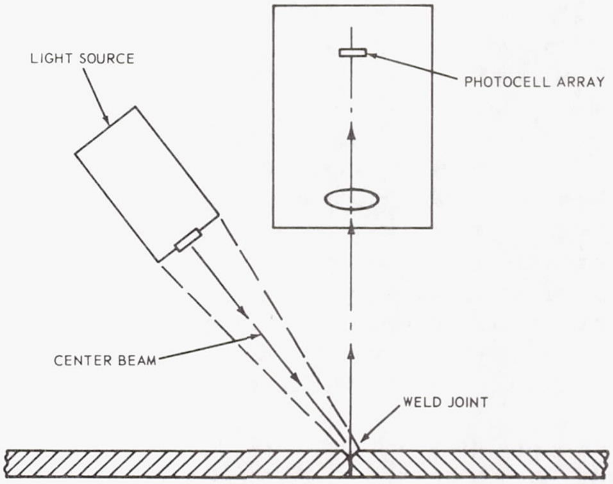

FIGURE 2. BASIC LIGHT BEAM ARC GUIDANCE

MECHANICAL PROBES

The fourth method, or mechanical probe, is basically very simple. A mechanical probe attached to a delicate electromechanical transducer is dragged along a groove in the weld joint. In theory, any seam deviation is reflected as an electrical signal from the electromechanical sensor. For several reasons, this technique may not always be desirable. Weld joint offset can cause considerable error; in addition, a dragging probe can distribute minute particles of contaminates along the weld seam. This is serious because contamination has been established as the major cause of weld porosity. For this reason it has long been a welding requirement at MSFC that nothing touches the welding area after it has been cleaned.

SUMMARY

It is not the intent of this report to thoroughly discuss the merits and limitations of prior technology

Rather, these welding techniques are briefly mentioned to stress the fact that there is good reason to pursue a more reliable system. Arc guidance was needed on the Saturn V S-IC bulkhead weld fixture, but early in the welding program it was determined that the weld joints must be tack welded [1] to maintain alignment of the large parts. Since none of the above mentioned systems would work on tack-welded joints, manual cross seam control was the only resort. Fortunately, this mode of operation was successful primarily because the welding process travel speed was very slow (7.5 - 30 cm/min). Following some promising preliminary feasibility tests, a project was initiated to take advantage of the visual aspects of closed circuit television (CCTV) to solve the problem of tracking tack-welded joints. As a result of this effort, such a system is fast emerging as a workable model (Figs. 3 and 4). Table I gives a relative rating of prior tracking systems and the CCTV guidance system when judged in light of the 21 major problem areas. A rating of excellent in all 21 categories would indeed indicate an ideal arc guidance

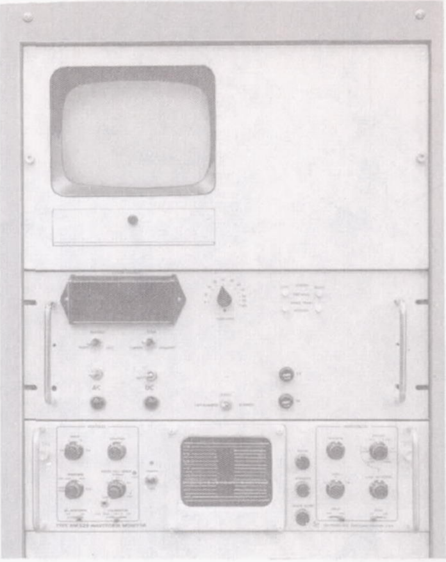

FIGURE 3. CCTV TRACKING ELECTRONIC CONTROL CABINET

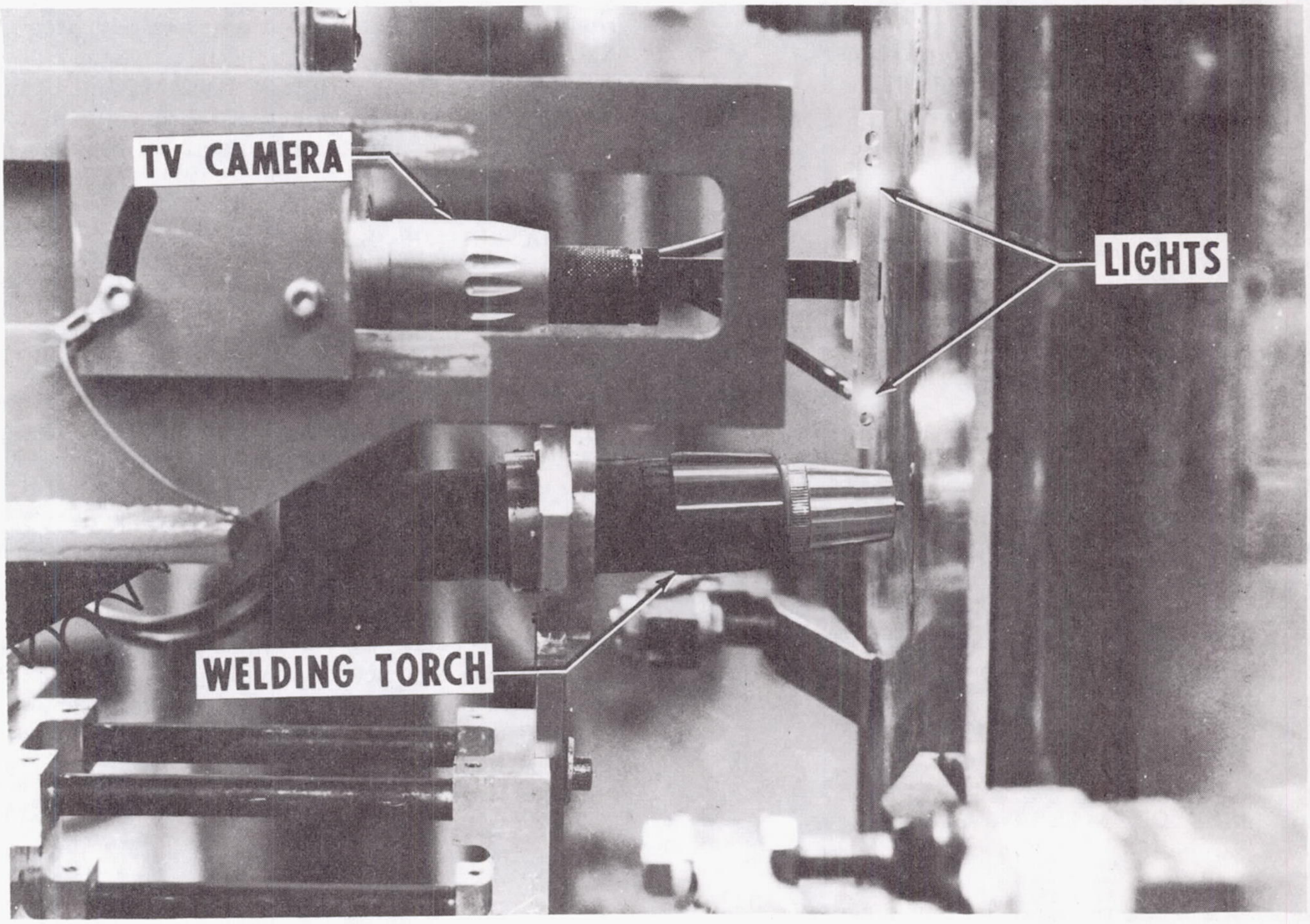

FIGURE 4. CCTV TRACKING WELDING HEAD

technique. A rating of poor in any category indicates that either special design or application precautions must be taken or that the system is inherently below par when compared with the ideal criteria.

CCTV ARC GUIDANCE

To better grasp how the CCTV arc guidance system functions, it may be helpful to review some of the basic principles of standard television equipment. The electronic equipment in a television camera systematically scans the scene that is to be reproduced and, by a photo-electronic means, produces a voltage proportional to the light intensity of the particular portion of the scene being scanned. Scanning has a certain pattern sequence and rate. As a scene is scanned by the electronics of the TV camera, it is simultaneously reproduced in the receiver. The rate of scan is rapid enough to give the appearance of motion as another scene appears. Figure 5 is a diagram of the pattern and sequence of scanning, which is termed the raster.

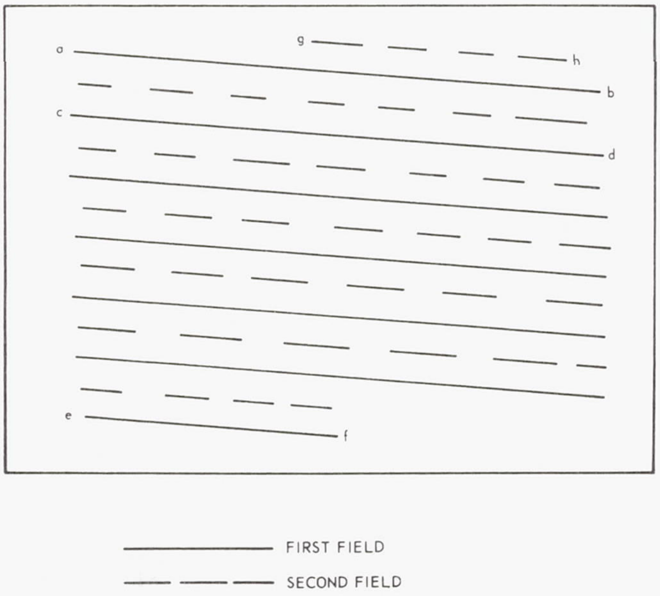

FIGURE 5. TV RASTER SCAN

TELEVISION RASTER SCAN

The scanning spot starts at point a and travels at a uniform rate to point b. When point b is reached, the scanning spot quickly returns to point c to start the second line cd. During return intervals, the spot is blanked out and is not shown in the figure. The standard television field is scanned from top to bottom and returned to the top in 1/60 sec. When the scan of the first field is completed, a second field is scanned and then interlaced between the lines scanned in the first field. The two fields make up one television picture frame. There are 525 scan lines in a frame, or 262.5 lines in each field.

The scan beginning at the top of each field and the start of each horizontal line must have a precise timing control. A voltage pulse is generated 60 times a second, which is recognized by the television circuitry as the beginning of a field scan. This is termed the vertical synchronization pulse. Another form of pulse is generated at a rate so that there are 525 pulses during the period of 2 fields, or 1 frame (1/30 sec). These pulses control the beginning of horizontal scan movement, which results in 262.5 lines per field. They are termed horizontal synchronization pulses.

One method of reproducing the video information in electrical form is to optically focus the scene on a photo sensitive surface in an electronic tube. The tube has an electron gun that emits a beam of electrons to strike the photo sensitive surface. The vertical and horizontal sync pulses control the electronic focusing circuits that guide the electron beam to strike the photo sensitive surface in the scanning pattern at a given instant of time; therefore, the beam will be striking the surface at a particular point. Because of the characteristics of the photo surface, the magnitude of the electron beam current will be proportional to the light level at any particular spot on the surface. Since the beam position is scanning or varying with time, the beam current will also vary with time. This current produces a voltage signal representative of the light variations along the scan path.

The varying voltage or video information from the camera is then formed into a composite signal, along with the vertical and horizontal timing pulses, before being transmitted to the receiver. A basic composite signal is shown in Figure 6. The video information is the upper portion of the composite signal, and its height is above the 0.5 V line. Amplitudes of the video information are proportional to the relative whiteness of the scan position on the screen. The part below the 0.5 V line on the composite signal is the timing information for use in the receiver that must reproduce the picture on its screen.

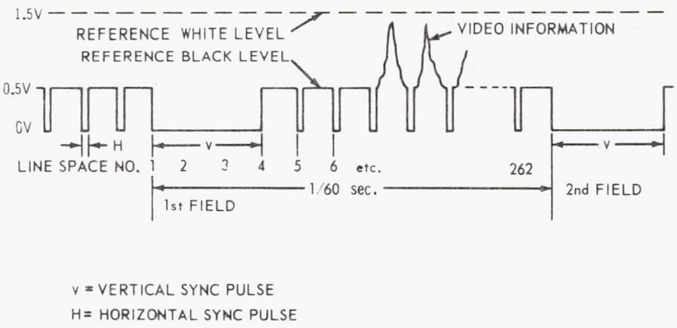

FIGURE 6. COMPOSITE VIDEO SIGNAL

The receiver screen is the face of a tube treated so that its area will glow in proportion to the electron density striking its surface. The receiver separates the video information from the timing pulses. Tube scanning is controlled by the signal pulses, and the receiver beam current is controlled by the video information level to reproduce the picture on the screen.

BASIC SYSTEM OPERATION

Figure 7 is a symbolic diagram of the operation of the basic video welding arc guidance system. The purpose of welding arc guidance is to maintain the welding arc on the weld seam as the area to be welded moves past the torch in the Y direction. A closed circuit television camera is assumed to be mounted in-line with the torch, and the camera is positioned so that the weld centerline runs horizontally, left to right, as viewed on a television monitor. Since the weld joint centerline is parallel to the horizontal lines of the television scan, the centerline image will mainly occupy only one scan line as viewed on a television monitor. Proper arrangement of lighting on the weld joint by two bright light sources will cause this video scan line to be much brighter than the remainder of the lines. This extra bright line in the video signal is easily separated from the composite video signal and is used for guidance purposes.

In operation, the composite video signal from the TV camera is first routed to video viewing and waveform monitors and then to a blanking circuit to remove unwanted portions of the signal. Next, the signal is amplified to raise its voltage and power to a level that can be used by the logic section. Logic circuits then separate the video information from the synchronizing pulses to control a binary counter. Because of the control in the logic circuit, the counter will begin counting at the top of the television field and will count each successive horizontal line (1, 2, 3, 4, 5. .) until the bright line caused by

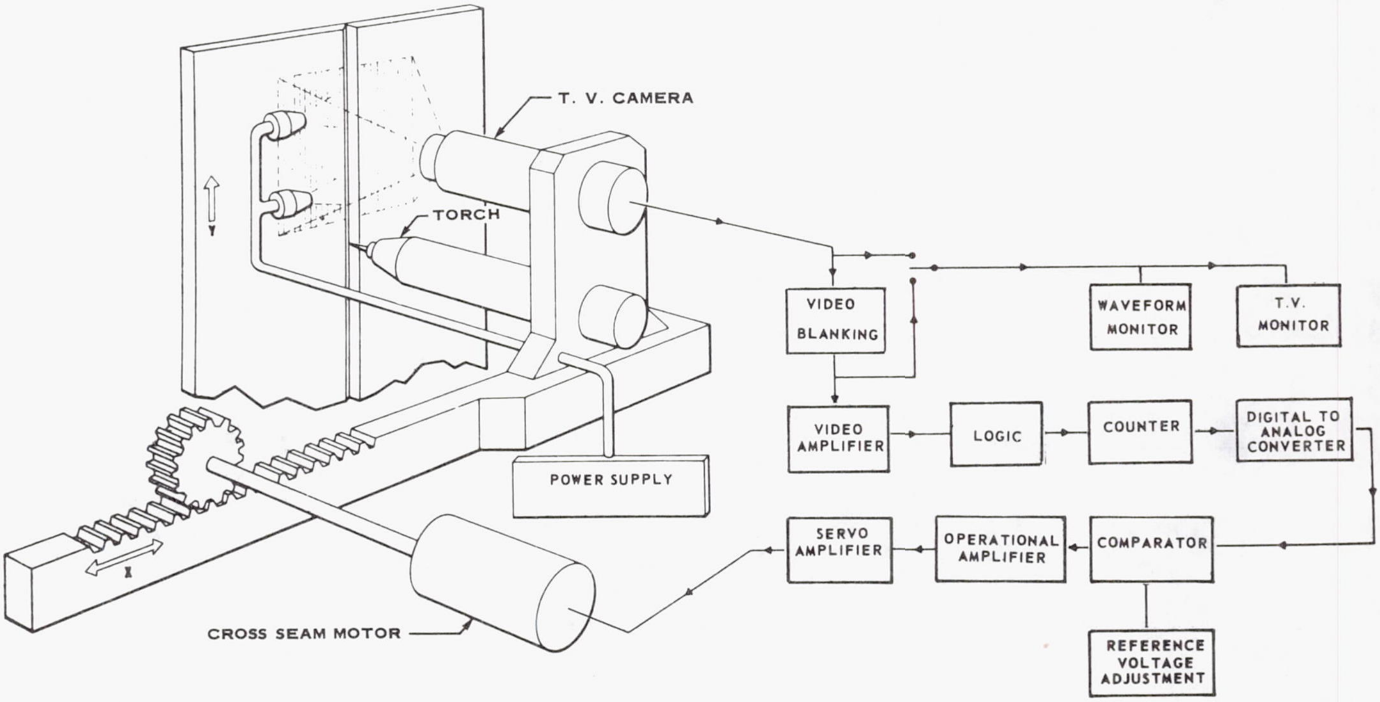

FIGURE 7. BASIC CCTV ARC GUIDANCE SYSTEM BLOCK DIAGRAM

the weld joint illumination is sensed. Appearance of the bright line stops the counter on that horizontal line number. This number is then stored in a flip-flop register and the counter is reset for operation during the next television field.

The stored horizontal line number in the register is next fed to a digital-to-analog (D-A) converter which converts the number to a proportional dc voltage. This dc voltage representation of the stored number is then algebraically summed with a reference voltage. The reference voltage can be set to a level corresponding to any scan line position desired, but it is usually set to a level near the center of the field of view. If the (D-A) output dc voltage level is either less than or greater than the reference dc voltage level, the difference between the two voltages will be a plus or minus dc error signal to the torch positioning servo amplifier.

An error signal to the servo amplifier causes it to drive the motor in a direction that will move the camera-torch carriage along the X axis. Polarity of the error signal to the servo amplifier determines the direction of the X axis movement until the error difference is nulled. New error information is received much more rapidly than the carriage can move because the counter is counting and supplying new tracking data each time a television field is scanned. Since the television field is scanned sixty times per second, the counter will supply new tracking data each 1/60th of a second. A continuous and rapid supply of position information allows the servo system to guide the welding arc on the weld centerline.

CAMERA AND LIGHT SOURCE POSITIONS

Figure 8 shows a typical arrangement of light projections and the relationship of the weld subject and camera for butt welding tack-welded joints. Two illumination devices containing projection lamps focus their intense light on the receiving end of two fiber-optic tubes. The emission ends of the fiber-optic tubes serve as illumination sources to project light as shown in Figure 8. In Figure 8-A, the path of light from the fiber-optic tube is shown reflecting from the chamfer of the weld joint into the camera. The angle of incidence, A, is equal to the angle of reflection, B, so that the light reflected from the chamfered surface is much brighter at the lens position than is any of the light received from other surfaces of the metal. This capability to obtain an extra bright image at the chamfered surface makes it useful as a reference of the true weld centerline position. The light beam sources and the camera may be mechanically attached so that they have a fixed physical relationship. When the weld joint appears near the top or bottom of the field of view, rather than the center of the field of view, the angle of reflection will change and cause the brightness of the chamfer image to diminish slightly. However, there is not sufficient loss of brightness to affect the tracking capability.

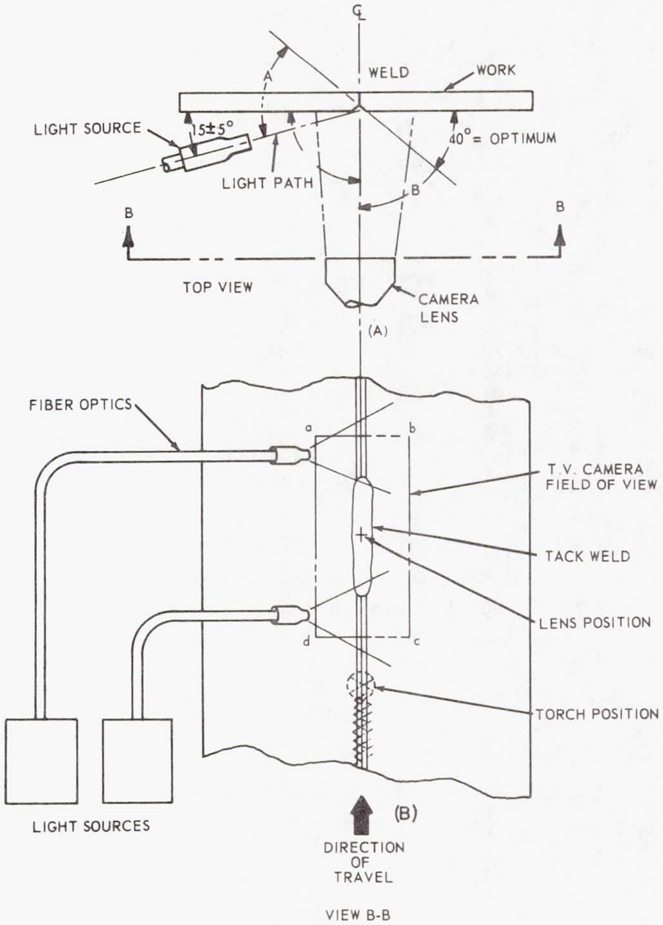

FIGURE 8. JOINT ILLUMINATION SCHEME

In Figure 8-B, area abcd will be the field of view displayed by the television monitor screen of Figure 9. The two light sources shown in Figure 8-B serve to provide the necessary illumination of the chamfered surface when a tack weld appears in any portion of the field of view. Tack welds must

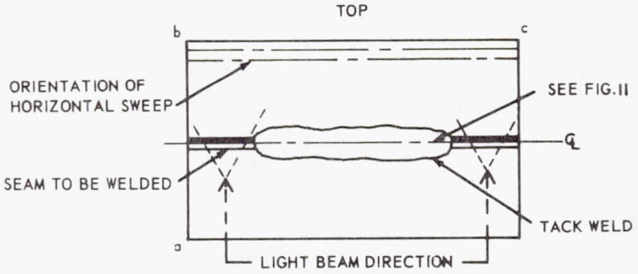

HEAVY BLACK LINE
DENOTES BRIGHTEST AREA

FIGURE 9. MONITOR SCREEN

be limited to less than the length (bc) of the field of view so that some part of the chamfered surface will always be visible to the camera.

VIDEO WAVEFORM

The shape of the TV waveform is important to the electronic tracking circuitry. Figure 10 is an example of the necessary waveshape of the vertical sweep of the closed circuit television system. The high positive peak of this waveshape is caused by the bright reflection from the above described chamfered surface. This high peak is made up of the few horizontal television lines that are the brightest area of the monitor screen shown in Figure 9. The 0 to 0.5 V pulses of the waveshape are standard vertical and horizontal synchronization pulses of a composite television signal. Figure 11 shows the waveform of the brightest horizontal line sweep of the monitor screen.

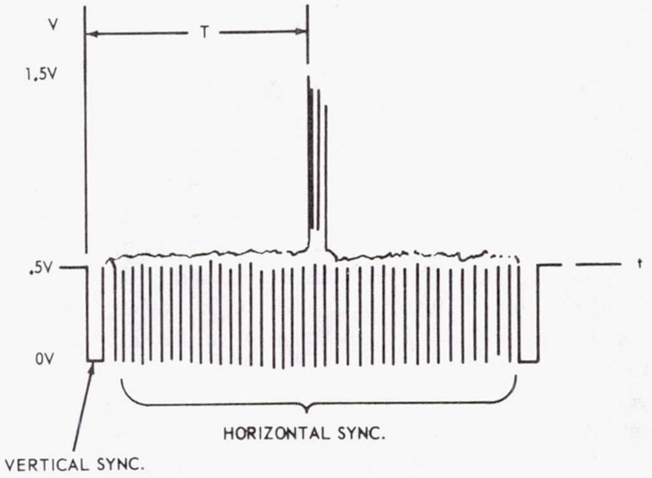

FIGURE 10. WAVEFORM OF VERTICAL FIELD

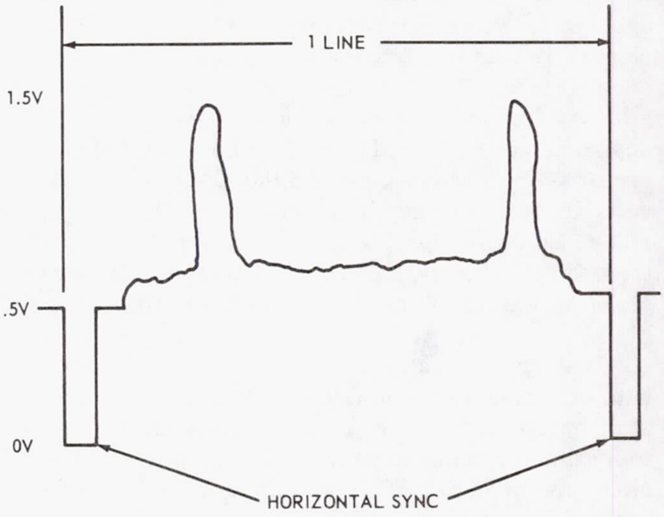

FIGURE 11. WAVEFORM OF HORIZONTAL LINE CONTAINING BRIGHTEST REFLECTIONS

VIDEO BLANKING

In most automatic tracking situations the horizontal line waveform of Figure 11 is the most desired form of tracking information. The high peaks on the left and right side of this waveshape are the only desired information; high peak information between these two peaks would only be caused by some unwanted reflection from a surface scratch or tack-weld edge. The video blanking circuit may be switched on to eliminate the effect of such reflections and is one of the video systems' means of discriminating true information from error information.

The video blanking circuit is timed by the horizontal synchronizing pulses. The blanking circuit operates by chopping out all video information in each horizontal line except at the left and right ends of the line or screen. The resulting video monitor appearance is shown by Figure 12. The effect is

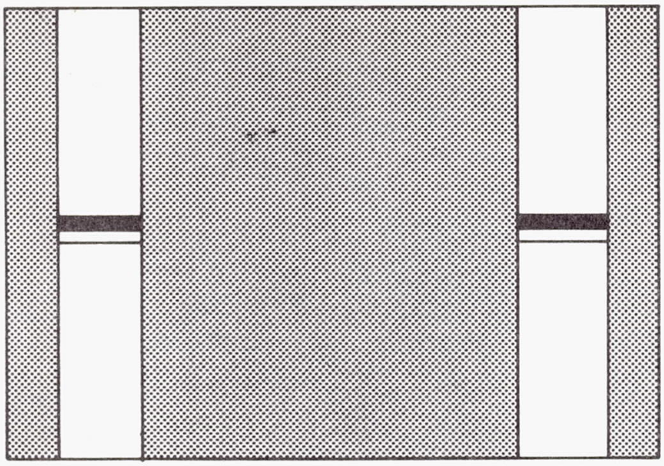

FIGURE 12. MONITOR SCREEN VIEW WITH BLANKED SIGNAL

that of masking off all except two strips of the viewing area of the subject, and any light reflections in the dark area of the picture will have no effect on the tracking. Of course, width and position of blanking are fully adjustable in the actual hardware.

In practice, use is made of the two light sources to track tack-welded joints. If the weld joint is not tack welded, only one light source is required. Although the one-light system is fairly straightforward, the technique used to track tack-welded joints warrants further explanation.

TRACKING TACK-WELDED WELD JOINTS

Two modes of tracking, "straight" and "curved," are available in the CCTV guidance system.

In the "straight" tracking mode, the seam to be followed must not deviate from a straight line more than the prescribed tolerance of ±0.75 mm (±1/32 in.) in 7.5 cm (3 in.). Although the seam must be straight, the angle of the seam with respect to direction of travel is not critical and the guidance can easily follow the constant offset. This mode is the simplest to set up and operate.

In the "curved" mode of operation, initial camera alignment is such that the seam can be followed when the seam varies from a straight line at a rate exceeding 75 mm in 2.5 cm. Analog computing and memory circuits are used in this mode and are not used in the "straight" tracking mode; therefore, the "straight" tracking mode should be used whenever possible to avoid tolerance buildup.

Straight Mode. Figure 13 points out the relation between the direction of travel, the arbitrary seam angle, and the camera orientation. In Figure 13 the camera has been rotated so that the horizontal scan lines of the camera are parallel to the straight weld seam. This causes bright spots X_1 and X_2 to appear in the same scan line. Now, when the tack weld moves to blank out the X_1 bright spot, bright spot X_2 will still provide the information to indicate which scan line the weld seam occupies. A distinct advantage of this mode is that the tack weld does not have to be sensed in order to switch computing circuits.

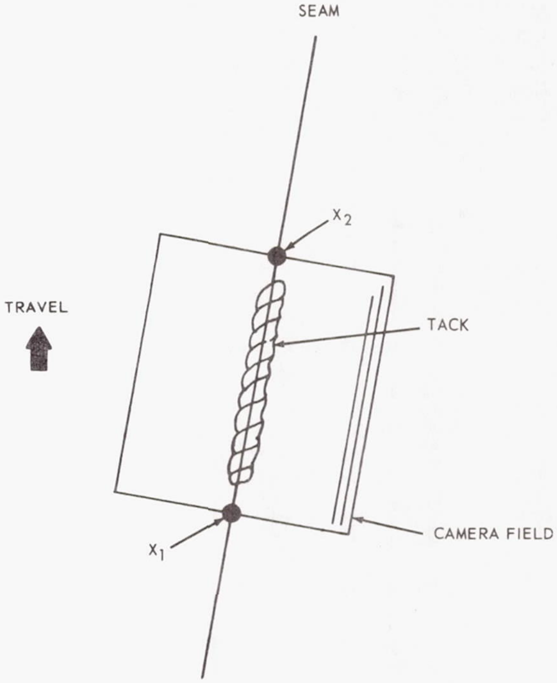

FIGURE 13. STRAIGHT SEAM OPERATION

Curved Mode. Figure 14 describes a possible curve tracking situation and points out the relation between the direction of travel, and the camera orientation and the variable seam. In Figure 14 the camera has been rotated so that the horizontal scan lines of the camera are parallel to the plane of travel. Bright spots X_1 and X_2 each have a video field line position dependent on the seam's angular relation to the planes of travel. As the tack weld moves to block out X_1, the circuits sense the tack weld and hold in memory the last true information giving the scan line positions of X_1 and X_2. The analog circuits are then switched into the circuit to use (1) the ΔS information supplied by the memory of X_1 and X_2 and (2) the known time Δt. This information is necessary to provide a computed path from X_1 to X_2 for the welding torch to follow during the loss of video information caused by the tack weld. At the end of the tack-weld period, the system switches back to X_1 to follow the seam.

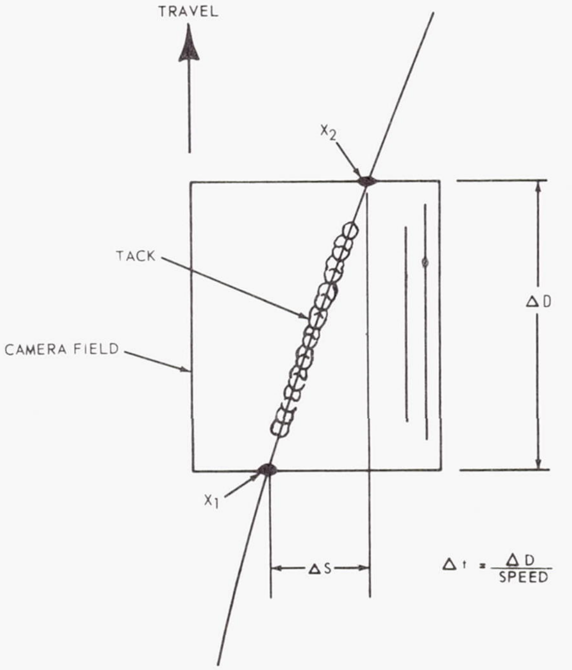

FIGURE 14. CURVED SEAM OPERATION

Since the camera normally follows a straight line from X_1 to X_2 over tack welds, it is desirable to place tack welds over a relatively straight portion of the weld joint. Error caused by following a straight line through a curved tack will depend on the degree of curvature. A higher order of computing could be added, if necessary, to produce a curved path from X_1 to X_2.

APPLICATION NOTES

The present equipment is being developed to track the following general types of weld joints:

1. Highly irregular weld joints without tack welds.

2. Moderately irregular weld joints with tack welds.

3. Butt joints, overlap joints, or tee joints.

In addition, the guidance equipment should operate equally well on a wide variety of metals including, but not restricted to, (1) aluminum, (2) steel, (3) stainless steel, (4) copper, (5) titanium, and (6) alloys of these metals. The surface condition of the work (bright, dull, painted, rusty, etc.) generally has no effect on the operation; however, some joint preparation is necessary to assure success. Examples of the typical joint preparation are shown in Figure 15. It should be pointed out that the required joint preparation is a relative consideration. The amount and type of chamfer is only that necessary to get a good reflection. On a dull material, such as steel, simply breaking the edge with a file or router would probably suffice. As a general rule, the more precise the tracking requirement, the more precise the joint preparation.

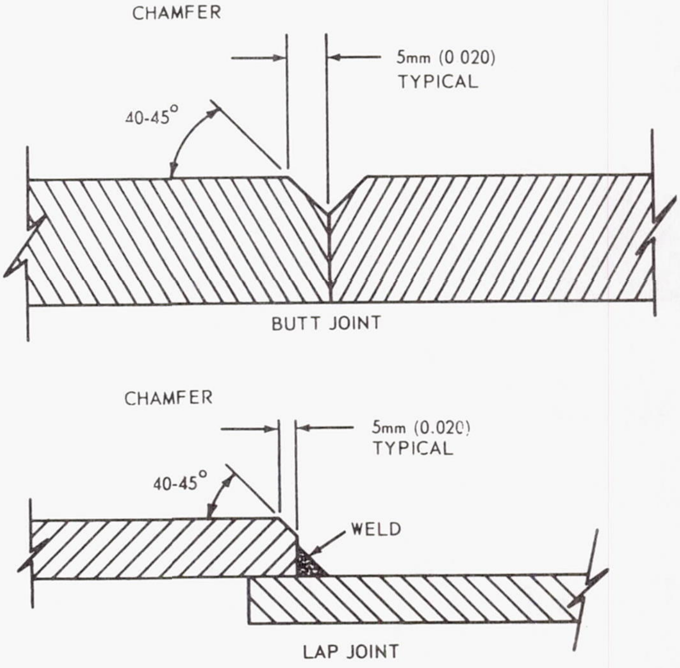

FIGURE 15. TYPICAL JOINT PREPARATION

As for camera location, one major advantage is that the CCTV system can operate almost equally well whether the camera is stationary mounted (Fig. 16) or integrally mounted with the welding torch cross seam positioning mechanism (Fig. 17). If necessary, generous use can be made of coherent fiber optics to pipe the light signals into the camera.

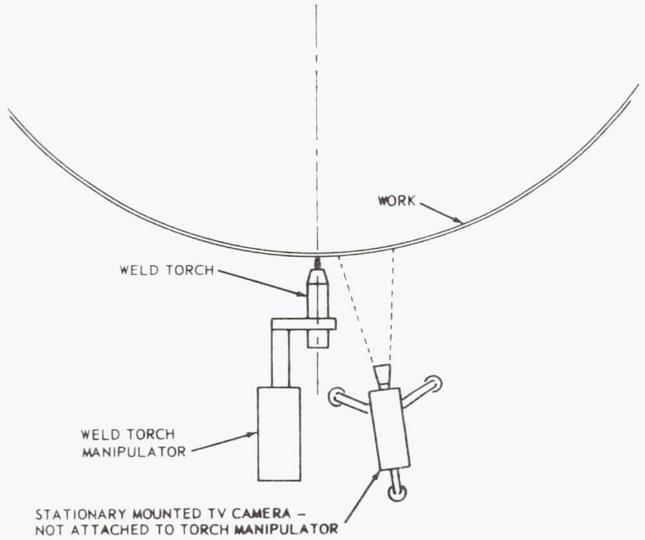

FIGURE 16. CCTV CAMERA MOUNTED REMOTE FROM TORCH

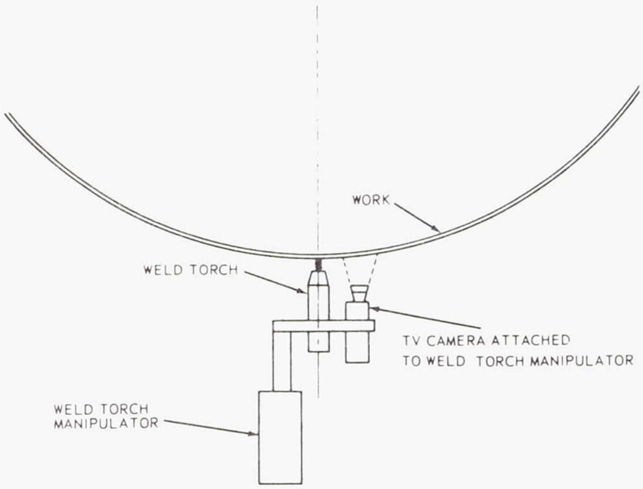

FIGURE 17. CCTV CAMERA MOUNTED WITH TORCH

Also included as an option is a dc signal time-delay unit. This module accepts the dc signal from the digital-to-analog converter and delays it for torch positioning a few seconds later. A delayed signal is needed when the joint varies at a rate exceeding ±0.75 mm (±0.031 in.) per every 5 cm (2 in.) of weld. If this delay were not used, the torch would not necessarily be located over the joint although the guidance intelligence is correct. Of course, this is because the intelligence is being sensed ahead of the torch. The closed circuit video equipment which may be used to view the joint is standard broadcast quality Vidicon apparatus. Generally, this means that the horizontal and vertical sync pulse generator outputs a signal meeting broadcast standards. This requirement assures steady, accurate tracking. CCTV equipment of this type is not necessarily expensive, and has been developed to a high degree of economy and reliability. Except for the blanking, the power amplifier, and the logic sections of the system block diagram, the equipment is, or could be, standard vendor's items. Packaging of all the electronic control equipment on the prototype model, Figure 3, is within a 48.26 x 137 cm (19 in. x 54 in.) rack space. This includes the time-delay module that was mentioned earlier.

UNIQUE ADVANTAGES OF CCTV ARC GUIDANCE

In brief, some of the major highlights of this welding arc guidance technique are as follows:

1. The sensor has the capability, like the eye, to look at a relatively large welding area. Yet the accuracy, or resolution, is as fine as the physical distance between two TV lines projected on the image plane. This resolution is a result of the video-digital technique used to extract the joint location. Accuracy, therefore, is a function of the vertical field of view, in centimeters (inches), at the image plane, divided by the number of TV lines of the system. For a 525 line system, the resolution is ±0.2 percent of the field of view.

2. The video system takes advantage of a digital technique to yield a go or no-go signal. Use of the sweep, or scan, technique of video allows the engineer unparalleled latitude in designing circuits to derive tracking information, time information, and electronic logic control.

3. One sensor, the TV camera, is all that is required to gather the welding arc guidance information even when tack welds are present on the work piece. This camera may be located reasonably remote from the joint.

4. The signal from the tracking circuit digital-to-analog converter is essentially linear; hence, the camera could be mounted stationary, if required, and the torch could be accurately guided. This feature would eliminate the need to keep the TV camera close to the welding torch if conditions were adverse in that area.

5. The tracking signal from the standard video camera is relatively large, usually 1 V or greater. This amount of signal is almost immune to most electrical noise problems when standard precautions are taken.

6. This system is engineered to track tack-welded joints as well as nontack-welded joints, and hence exceeds the capability of all known welding arc guidance equipment.

7. This system can track thin or thick metals with equal capability. Generally, weld tooling is no problem and stray light does not normally present a problem. The blanking circuit in this system can be adjusted prior to welding to electronically block all but the wanted signals from entering the tracking logic electronics. At the same time, the entire composite picture can be viewed by the weld operator on a conventional video monitor.

8. The mounting distance from the work to the TV camera (transducer) can vary from a few centimeters to meters. Variation of proximity distance, within the depth-of-field of the lens, does not affect tracking accuracy.

9. Offset of the welding joint edges (one side higher than the other) for square butt joints need not affect tracking accuracy since this trouble spot can be eliminated by proper design of the joint lighting system.

CONCLUSIONS

The CCTV arc guidance development is not a panacea, but it could well turn out to be the most versatile welding arc guidance system yet developed. Use of the scanning method, the vertical and horizontal sync timing pulses, and the digital electronic go or no-go logic circuits literally opens the door for the imaginative engineer. As a result, engineers have only begun to take advantage of the visual information available. Not only are major improvements to the CCTV guidance system possible, but also a completely new class of instrumentation could be created for alignment and recording purposes. Much work still remains to be done to qualify the necessary optical and mechanical hardware for practical application in the field. However, progress has been rapid, and there is every reason to believe that this technique will prove to be highly effective.

REFERENCE

1. Selected Welding Technique, NASA SP-501, Washington, D. C., April 1963.

MECHANICAL DEVICES FOR ZERO GRAVITY SIMULATION

By

Vaughn H. Yost

SUMMARY

Mechanical simulator development conducted in support of the Apollo Applications Program and in anticipation of future programs is summarized in this review. Mechanical simulators that have been developed are illustrated and their characteristics described. Results are reported on investigations of air bearing systems, air bearing cart thrust systems, and devices for supporting hand tools and the serpentuator. Applications of mechanical simulators are also illustrated.

INTRODUCTION

The Manufacturing Engineering Laboratory divides earth orbital weightless and lunar gravity simulation devices into two categories: mechanical and neutral buoyancy. Mechanical simulators include all those devices that do not use a liquid such as water to support the subject, workpiece, or tool.

Some of the objectives of mechanical simulation are evaluation of design concepts, evaluation of hardware, and determining the subject's capability for performing tasks.

Mechanical simulation offers certain advantages over neutral buoyancy simulation in that much less preparation time is required. It can be performed by a minimum of two people (a test subject and technician to balance him and operate the suit), and the simulators can be moved to the work site. The advantages of neutral buoyancy simulation over mechanical simulation are that complete tasks requiring vertical clearance or large changes in vertical elevation can be performed in one operation as opposed to breaking the task up into several part tasks so that it can be performed in a mechanical simulator.

The research and development efforts in the mechanical simulation category are discussed in this review under the divisions of mechanical simulators, air bearing systems, air bearing cart thrust system development, devices for supporting hand tools and serpentuator, and the use of mechanical simulators.

MECHANICAL SIMULATORS

FIVE-DEGREES-OF-FREEDOM SIMULATOR

1. General Information

The five-degrees-of-freedom simulator is an aluminum framework mounted on air-bearing pads. Yaw and horizontal translation in two directions are obtained by moving the entire simulator on its air-bearing pads. Pitch and roll motions are obtained through gimbals mounted with anti-friction bearings. Pitch is the only motion that is limited. This simulator was designed to be used with the Lunar Gravity and Earth Orbital Simulator that is described in this paper.

2. Technical Information

The five-degrees-of-freedom simulator consists of three major assemblies: a cradle or seat, roll yoke, and base (Fig. 1). The cradle, or seat, supports the subject in an erect position and contains provisions for adjusting the position of the subject relative to the roll and pitch axes of the simulator. The roll yoke supports the cradle at the pitch axis and permits 108 degrees of rotation in pitch between the cradle and the yoke. The yoke also contains a system for supplying ventilation, breathing, and pressurization gases to a subject in a space suit.

The "U"-shaped yoke is supported at the base of the "U" roll bearings that permit unlimited rotation around the roll axis. The base structure supports the roll bearings and distributes the total load of the simulator and subject to three air-bearing pads equally spaced around the nominal yaw axis.

The simulator has an onboard air supply which requires a 115 Vac, 5 A, 60 Hz (60 cps) power input.

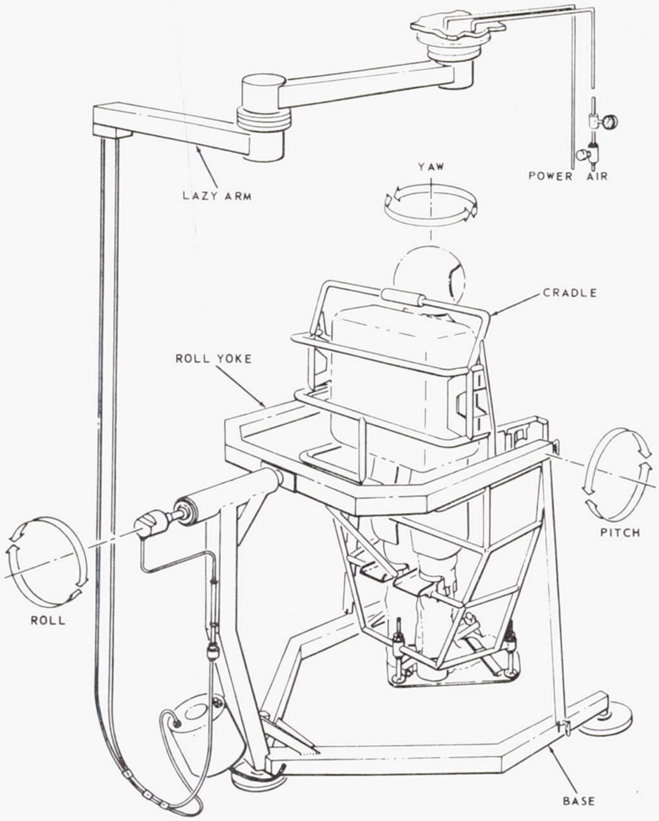

FIGURE 1. FIVE-DEGREES-OF-FREEDOM SIMULATOR

In addition, there are provisions for supplying 0.283 m^3/min (10 scfm) of breathing and suit pressurization air at 0.31 MN/m^2 (45 psig) through a hose to the subject.

A lazy arm may be used to minimize the hose and power cable drag by positioning the hose in an essentially constant vertical position. Air is fed through rotating unions so that each of the two sections of the lazy arm is capable of unlimited rotation.

Cradle Assembly. The cradle assembly consists of the supporting structure for subject and back pack; the subject's restraint system, consisting of the torso corset, leg supports, and restraining straps; and the vertical and fore and aft balancing adjustments and pitch axis ball bearings (Fig. 2).

The supporting structure is welded tubular aluminum with an aluminum foot plate supported by three adjustment screws. The adjustment screws permit raising or lowering of the subject's center of gravity (c.g.) over a 0.152 m (6 in.) range to place the c.g. within the range of the vertical balancing adjustment. The back pack supports are attached with machine screws fitted in slotted holes to permit vertical adjustment of the back pack position over a range of 0.076 m (3 in.). Right and left adjustment of the back pack position is accomplished by selective tightening or loosening of the back pack attachment screws. An angle on each side of the cradle is provided for attachment of the torso corset. These angles are located in the plane of the subject's back, and they establish the fore and aft positioning of the subject. The torso corset is attached to each angle at 4 points with 8 machine screws. Threaded screw holes are provided on 0.013 m (0.50 in.) centers over a range of 0.229 m (9 in.) and slotted holes in the corset attachment fitting permit locating the corset at any point within the extreme limits. A 0.203 m (8 in.)

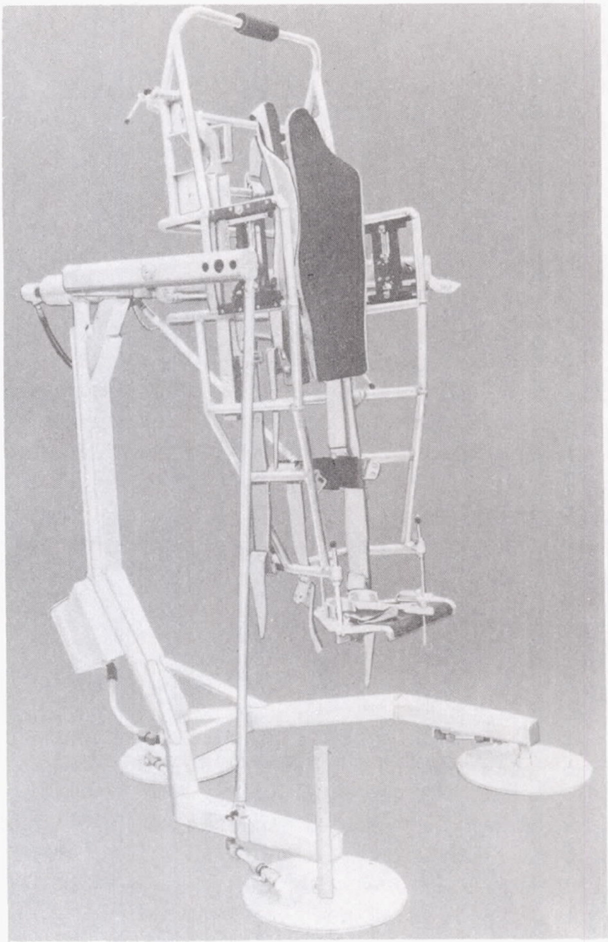

FIGURE 2. FIVE-DEGREES-OF-FREEDOM SIMULATOR WITH CRADLE ASSEMBLY ATTACHED

section of tube is welded to the back of the structure, perpendicular to the vertical axis of this cradle. It is used for attachment of counterweights, if required, to bring the cradle and subject's c. g. within the range of the balancing mechanism.

The subject's restraint system confines his torso and legs while his head and arms remain free. The torso restraint consists of a two-piece fiberglass corset. The two pieces of the corset are supported by two 0. 025 m (1 in.) diameter aluminum tubes bolted to the angles described above. The two pieces of the corset can be adjusted horizontally to move the subject right or left and to accommodate different torso widths. The sections are clamped into place on the tubes by the integral split ring clamps and bolts accessible from the front. Supplementing the corset are restraining straps located at the following positions: shoulders, pelvis, knees, and feet. The two shoulder straps are fastened to the corset at the approximate location of the shoulder blades. Each strap is brought over the shoulder, across the upper chest, and back under the opposite arm to attach to the cradle structure at waist level. These straps consist of two parts that are connected together with aircraft-type, quick-release, adjustable buckles located in the upper chest area. The pelvic strap is a one piece strap around the corset and subject at his hips. It is attached to one side of the corset to prevent slipping and has the same type buckle as the shoulder straps.

The legs are restrained at the knees by individual, sponge-rubber padded, contoured supports attached to the cradle structure. The supports may be adjusted side to side and fore and aft. Each support has a continuous strap held in place to prevent slipping and fastened on the outside of the knee with the adjustable quick-release buckle.

The foot plate is covered with corrugated rubber tread and is provided with semi-circular heel retainers and a foot strap. The heel retainers prevent the heels from slipping backward and the strap restrains the feet from forward or vertical movement. The strap is attached at both ends with adjustable strap restrainers and, normally, enough slack is left to permit insertion of both feet under the strap. After both feet are in place, a locking bar, pivoted at the back between the heels, is dropped into place between the feet and is secured by engaging a "J" hook with front edge of the foot plate. A screw handle permits tightening the "J" hook to apply tension to the foot strap.

The balancing adjustments (Fig. 3) are built into the right and left sides of the cradle to permit movement of the subject's c. g. 0. 038 m (1. 5 in.) vertically and fore or aft from the nominal c. g. position with respect to the pitch axis ball bearings. Each adjustment consists of a crosshead and adjustment screw that provides fore and aft motion of the cradle. The adjustment screw slides through a bushing and is locked in place by two adjusting nuts, one on each side of the bushing. The crosshead carries the pitch axle support and vertical adjusting screw. The pitch axle support slides on the crosshead, the adjusting screw passing through it. Two adjusting nuts, one on the top and one on the bottom, permit vertical adjustment and locking. The crosshead has two reference scales, one for vertical adjustment and one for horizontal. The cradle has a pointer for the horizontal scale and there is an index mark on the pitch axle support for vertical reference. The scales permit equal adjustment of both right and left sides. When a subject has been balanced previously, the balancing adjustments can be preset, thereby reducing the time required to accomplish this task.

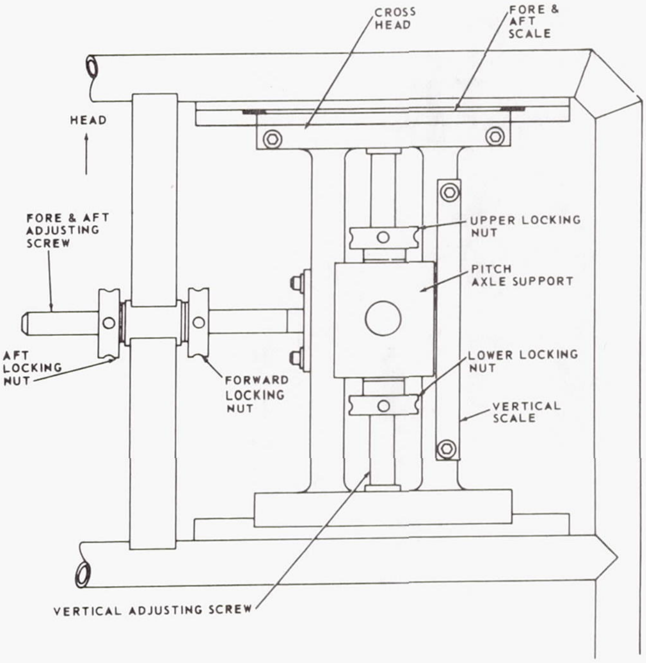

FIGURE 3. BALANCING ADJUSTMENT

The pitch axle fits into the bore of a self-aligning ball bearing mounted by two bolts to the roll yoke.

The axle has a threaded hole accessible from the outer edge. This can be used for attachment of instrumentation to obtain a readout on the pitch movement.

Seat Assembly. The seat assembly consists of the supporting structure for the subject; the subject restraint system consisting of the bicycle seat, back support, and restraint straps; and the cradle vertical and fore and aft balancing adjustments with pitch axis ball bearings (Fig. 4).

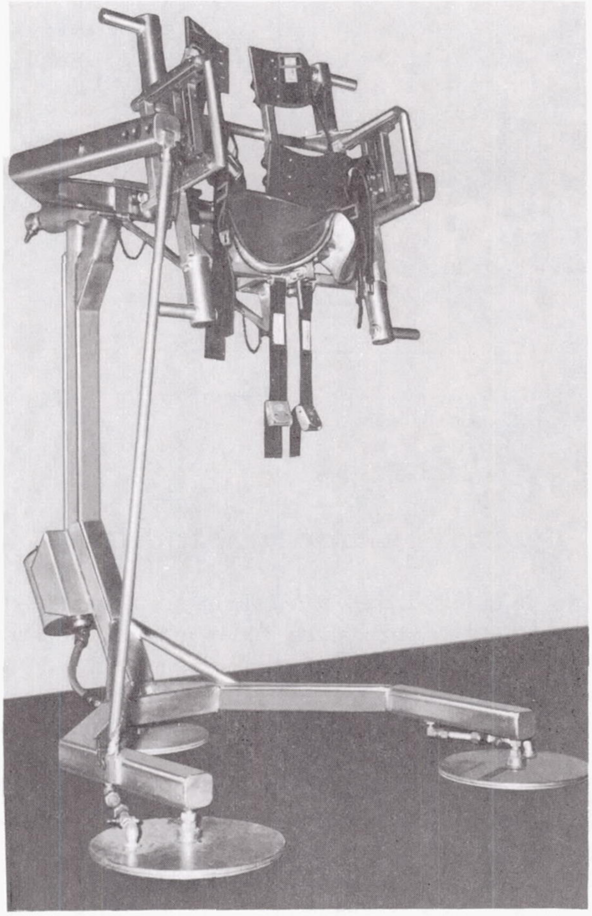

FIGURE 4. FIVE-DEGREES-OF-FREEDOM SIMULATOR WITH BICYCLE SEAT ASSEMBLY ATTACHED

The supporting structure is made of aluminum tubes welded together and a bicycle seat that is fastened in place with a set screw. The adjustment of the seat height permits raising and lowering the subject's c. g. over a 0. 152 m (6 in.) range to place the c. g. within the range of the vertical balancing adjustment. The back supports are attached with machine screws fitted in slotted holes to permit horizontal adjustment. A 0. 203 m (8 in.) section of tube is welded to the back of the structure, perpendicular to the vertical axis of seat. It is used for attachment of counterweights, if required, to bring the seat and subject's c. g. within the range of the balancing mechanism.

The subject's restraint system confines his torso while his head, arms, and legs remain free. The torso restraint consists of four curved-aluminum, sponge-rubber lined, back supports. The four back supports are supported by two 0.0254 m (1 in.) square aluminum tubes welded to the structure. The four back supports can be adjusted horizontally to move the subject right or left and to accommodate different torso widths. Supplementing the back supports are restraining straps for the torso and pelvis. The two straps are fastened to the upper back supports at the approximate location of the shoulder blades. Each strap is brought over the shoulder, across the upper chest and back under the opposite arm to another strap attached to the lower back support at waist level. These straps consist of two parts which are connected together with an aircraft-type quick-release adjustable buckle located in the upper chest area. The two parts of the pelvic strap are attached to the lower back supports. It has the same type of adjustable buckle as the shoulder straps.

The subject is held on the bicycle seat by two strap assemblies, one of which goes over each leg. The ends of each strap are attached to the frame below and behind the crotch and the lower back supports.

The seat uses the same balancing adjustment mechanism as the cradle.

Roll Yoke. The roll yoke supports the pitch bearings in a "U" shaped structure of welded 0. 076 m (3 in.) square aluminum tubing attached to a hardened steel shaft. The yoke permits a pitch movement of 108 degrees with approximately equal pitch-up and pitch-down motion. The cradle has adjustable stops that strike rubber pads on the yoke to limit the cradle motion so that the subject does not strike the base during extreme motion in both pitch and roll.

The yoke also has two small tabs, one welded to the front of the right arm of the yoke and the other to the bottom at the rear center. These tabs are attachment points for locking bars. Locking the pitch movement is accomplished by attaching a 0. 025 m (1 in.) diameter aluminum tube to the back tab and to the rear of the cradle at about the knees. A notch in each end of the bar slips over the tabs on the cradle and the yoke, and each end is held secure to the tab by a ball lock pin. Locking the roll movement is accomplished by attaching the roll locking bar between a tab on the base and the tab on the yoke arm. Locking of one axis does not restrict the motion of the other axis.

The roll axle fits through the roll yoke and the bearings. It is attached to the roll yoke from the front (inside the U) by two machine screws. The axle has a 0.013 m (0.50 in.) diameter passage which connects through standard pipe fittings to a Hansen 5000 series quick-disconnect fitting at the front end of the left arm. This is used to provide breathing and pressurization air to the subject in a space suit. The aft end of the axle has a Deublin model 20-8 rotating union to provide rotating freedom and a continuous air supply. The shaft of the rotating union extends completely through the union and may be drilled and tapped to provide a mounting for instrumenting the roll axis, if desired.

The vernier roll balance adjustment is located between the arms of the yoke to the rear of the cradle. It has a 1.36 kg (0.0933 slugs) lead mass mounted to slide freely on a threaded rod. Nuts on each side provide locking for the lead mass. The hole in the lead is positioned slightly off center so that it will hang at about a 50 degree angle from the vertical to clear the cradle in the extreme pitch-up position. The upper corner of the lead has been beveled and padded with rubber to minimize damage to the back pack in the event that contact does occur.

Base Assembly. The base is an aluminum square tube structure that provides support for the roll axle and the three air bearing pads. The vertical member of the base supports the roll axis approximately 1.59 m (62.5 in.) off the floor. It is designed to provide clearance for the cradle to permit unrestricted roll in any pitch attitude with the cradle foot plate in the lowest position.

The bottom tubular structure provides support for the air bearing pads that are equally spaced on a 0.635 m (25 in.) radius circle about the nominal yaw axis. One pad is directly under the vertical base member and the other two are forward and to the side to give stability.

The air bearing pads on 0.019 m (0.75 in.) threaded rods are screwed into fittings welded to the base.

The tubular base structure serves as a plenum chamber to equalize air flow to the pads and minimize line surges. The input to the base plenum is located on the right rear side.

Lazy Arm Assembly. The lazy arm provides for positioning the upper end of both the power cable and breathing and suit pressurization air hose at any point within a 3.66 m (12 ft) diameter circle (Fig. 1). The lazy arm consists of two 0.915 m (3 ft) sections that rotate on thrust bearings to provide minimal friction forces. The lazy arm mounting plate is bolted to the supporting structure and leveled. Suspended from the mounting plate is the inner arm, which rotates about the center on thrust bearings that are concentrically mounted around the rotating unions. The two unions are tandem-mounted on the rotating axis and are capable of unlimited rotation. There's a similar rotating joint between the inner and outer arms. The outer arm terminates in fittings for the attachment of the power cable and flexible hose leading to the simulator. Although the nominal restriction in the rotating union is 0.0063 m (0.25 in.) ID, larger diameter hoses have been provided to minimize functional losses in supply lines. Air is provided through a 0.0095 m (0.375 in.) ID hose.

A force of approximately 0.556 N (0.125 lbf) applied at the hose fittings is required to move the lazy arm when it is fully extended.

Basic Data. Figures 5 and 6 show detailed dimensions and operating clearances for the five-degrees-of-freedom simulator. The total mass of the

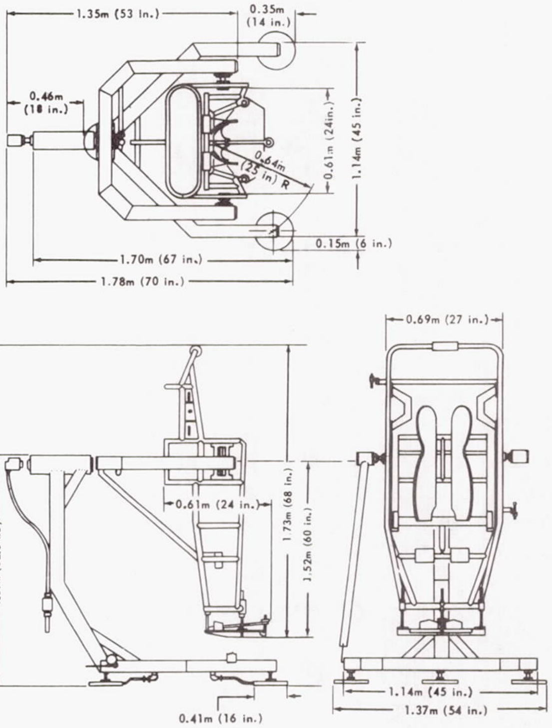

FIGURE 5. BASIC DATA

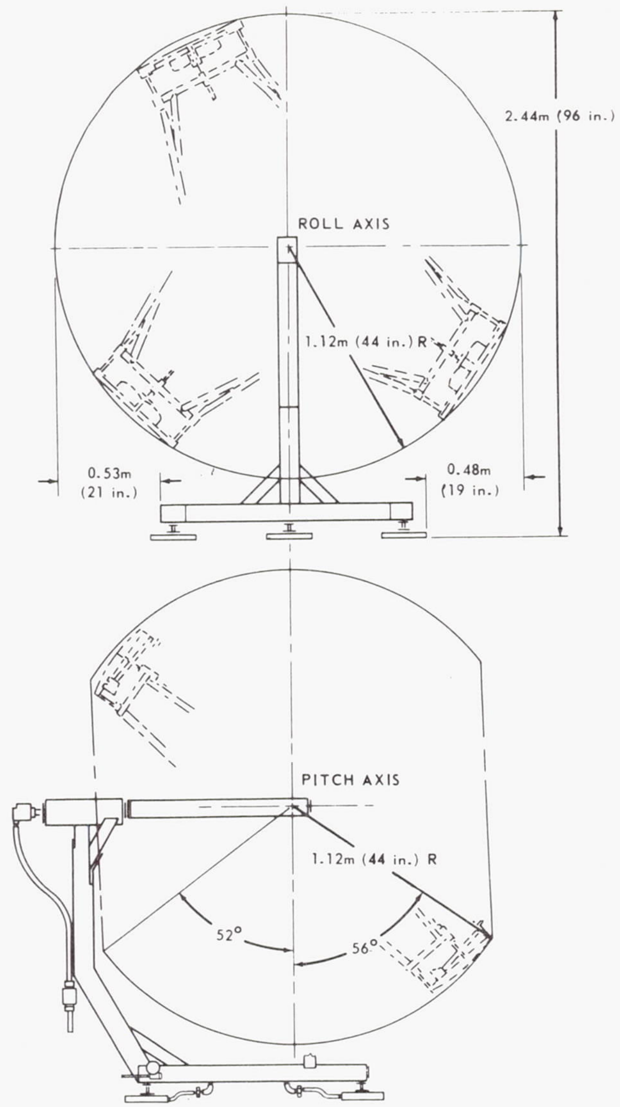

FIGURE 6. CLEARANCES REQUIRED FOR OPERATIONS

simulator with the cradle is 90 kg (6.15 slugs). The cradle has a mass of 28.6 kg (1.96 slugs) and the base and yoke 61.4 kg (4.20 slugs).

The torques required to overcome the static friction of the simulator are the following: pitch, 0.284 J (40 in. oz); roll, 0.494 J (70 in. oz); and yaw, 0.007 J (1 in. oz).

ACTION-REACTION FREE-FALL SIMULATOR

1. General Information

The action-reaction free-fall simulator or six-degrees-of-freedom simulator is a mechanical apparatus that allows the subject to react to any force as he would in space, except where the subject is required to translate over great distances (Fig. 7). This is accomplished by designing the experiment so that the desired test data are obtained.

Assume the following for the purpose of demonstrating that the subject can produce a translation acceleration just as he would in space by properly designing the experiment:

F_a = force applied to the object by the subject, assume 13.3 N (3 lbf)

F_s = force required to bend the pressure suit, given as 44.4 N (10 lbf) for 2.41×10^4 N/m^2 (3.5 psia) pressurization.

$F_c = F_a + F_s$

F_μ = force required to produce translation of the moving parts of the simulator, given as 0.58 N (0.13 lbf)

$F_T = F_a + F_s + F_\mu$

m_m = mass of the moving parts of the simulator, 114 kg (7.78 slugs) [a weight of 1110 N (250 lbf) at 1 g]

m_s = mass of subject and space suit, 91 kg (6.21 slugs) [a weight of 889.6 N (250 lbf) at 1 g]

g = acceleration, standard free fall, 9.80 m/sec^2 (32.16 ft/sec^2)

From Newton's Second Law of Motion, "The change of motion is proportional to the motive force impressed; and is made in the direction of the straight line in which force is impressed," we can determine the subject's acceleration in space.

$$F_c - F_s = ma$$

$$a = \frac{F_c - F_s}{m}$$

$$a = \frac{57.7 - 44.4}{91} = 0.146 \text{ m/sec}^2 \ (0.51 \text{ ft/sec}^2)$$

To produce the same acceleration in the simulator, it is necessary to change a parameter(s) that will produce the correct applied force, F_a, and not degrade the test data. Solving for the total force, F_T, we obtain

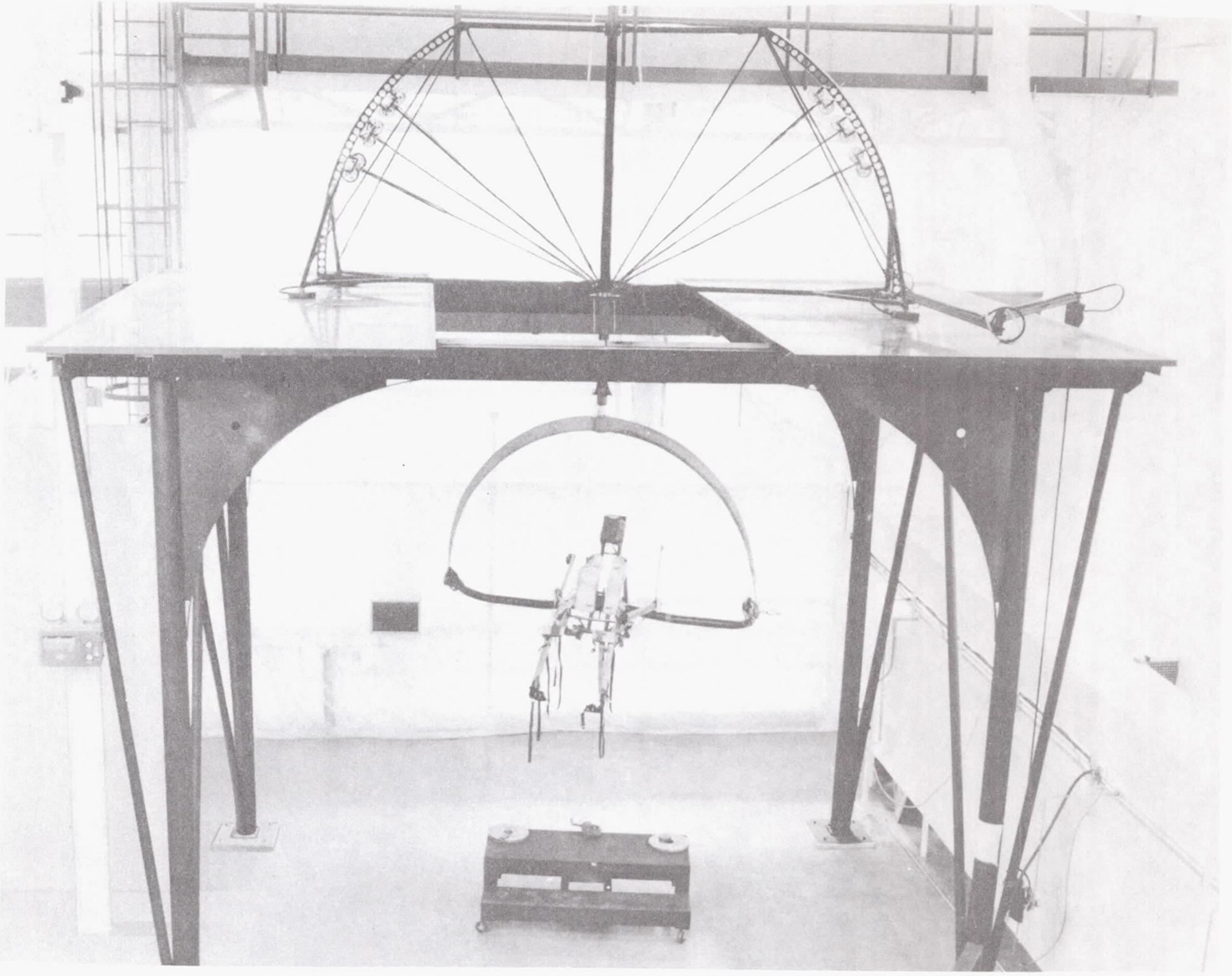

FIGURE 7. ACTION-REACTION FREE-FALL SIMULATOR

$$F_T = ma = (m_m + m_s) a$$

$$F_T = (114 + 91) \times 0.146 = 30 \text{ N } (6.75 \text{ lbf})$$

$$F_T = F_a + F_s + F_\mu$$

Since F_μ is an inherent characteristic of the simulator, it cannot be changed. Assume that the F_a is to be the same as it would be in space. This leaves only F_s which can be altered.

$$F_s = F_T - F_a - F_\mu$$

$$F_s = 30 - 13.3 - 0.58 = 16.12 \text{ N } (3.63 \text{ lbf})$$

A force of 16.12 N (3.63 lbf) to bend the suit can be obtained by reducing the suit pressure to 1.19×10^4 N/m^2 (1.74 psig).

The same analysis can be done for the other degrees-of-freedom for the action-reaction free-fall simulator.

2. Technical Information

The subject is strapped into a fiberglass harness that both positions him properly in the gimbal axis and adjusts to fit anyone between 1.65 and 1.86 m (65 and 73 in.) tall. The test subject is supported in such a way that he can rotate freely about any axis. He is capable of moving to either his left or right side, forward and backward, or up and down. (Fig. 8.) In other words this is a six-degrees-of-freedom simulator.

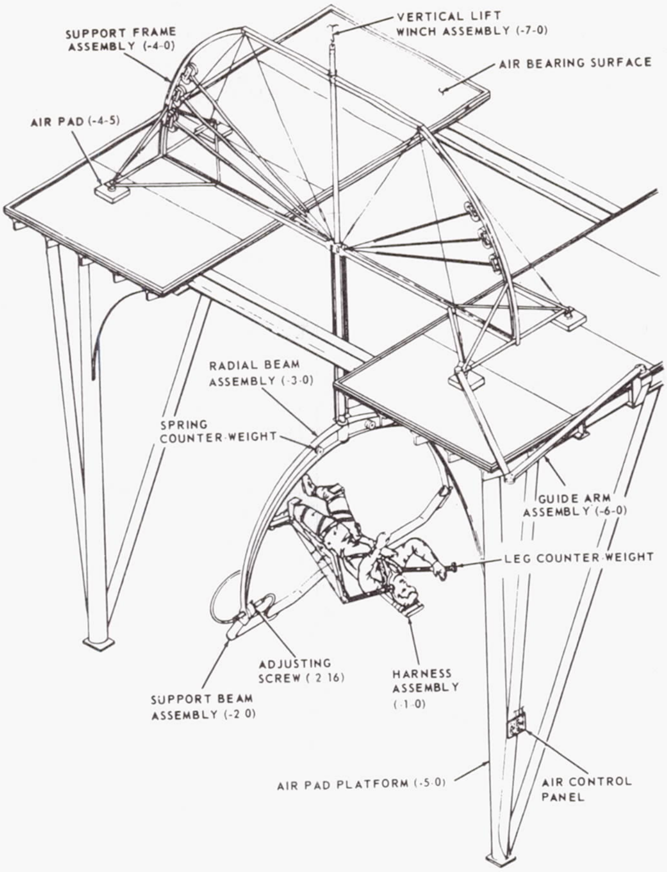

FIGURE 8. ACTION-REACTION, FREE-FALL SIMULATOR

The harness allows the astronaut free leg movements (Fig. 9), while counter-weighting them in any position, and keeping his center of gravity in the same place.(Fig. 10). The gimbal axis and harness have a built-in air line for breathing and space suit pressurization and cooling. This allows the subject to train for weightlessness either with or without his suit.

To allow the astronaut to move freely horizontally, the simulator is mounted on four almost frictionless air bearings. This, combined with the small mass of the simulator, less than 114 kg (9.33 slugs) gives almost no resistance to movement through its 1.83 × 3.66 m (6 × 12 ft) horizontal working envelope. Negator springs, which resemble a belt wound on a spool, are attached to the gimbal axis. By mounting sets of springs as shown in Figure 11, the springs can exert any constant force over their six feet of vertical travel.

Adjustments of the simulator can also be made to lift five-sixths or two-thirds of the test subject's mass. In this way, Lunar, Mars, and Venus gravity can be simulated.

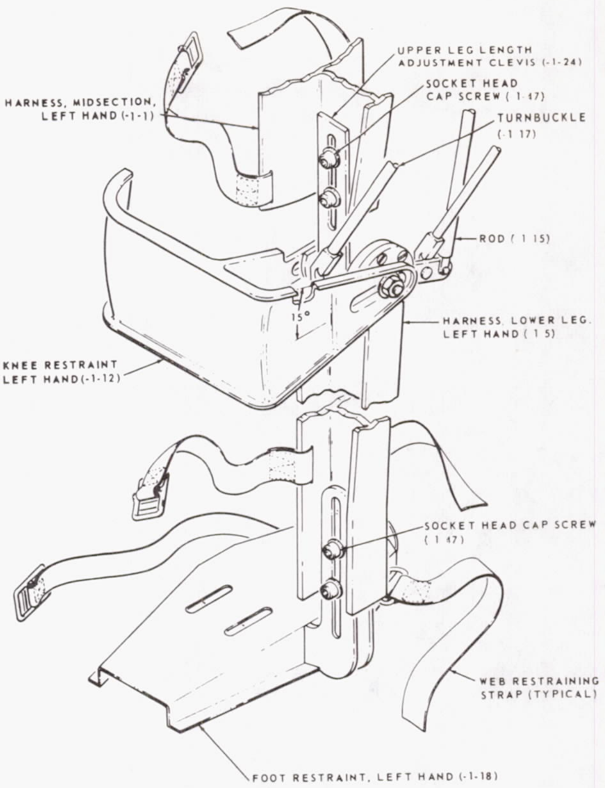

FIGURE 9. ADJUSTING HARNESS ASSEMBLY

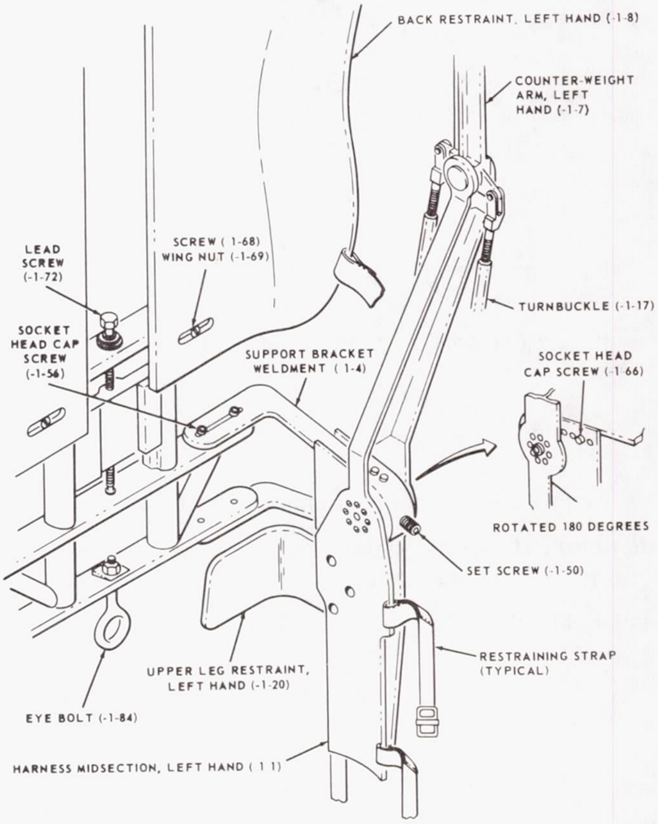

FIGURE 10. ADJUSTING HARNESS ASSEMBLY

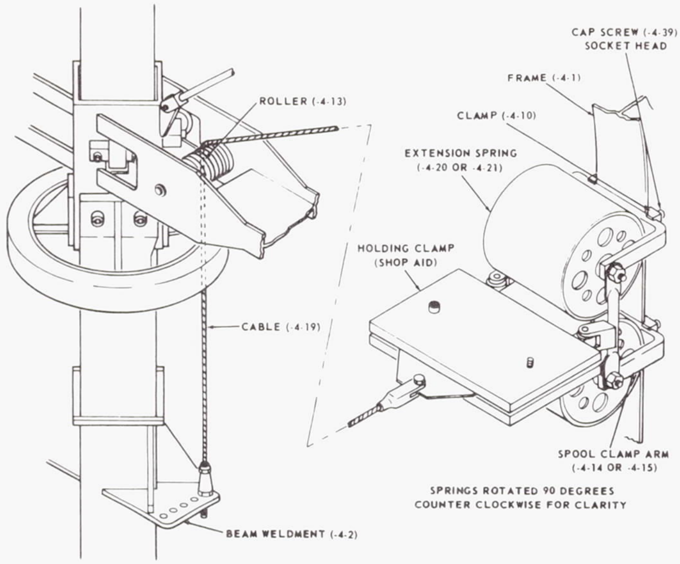

FIGURE 11. INSTALLATION OF EXTENSION SPRINGS

LUNAR GRAVITY AND EARTH ORBITAL SIMULATOR

1. General Information

This simulator was designed to be used with the five-degrees-of-freedom simulator (Fig. 12). The purpose of this simulator is to support the object the subject is working on. It provides four degrees-of-freedom for the workpiece. Vertical translation is produced by moving the work panel up and down. The remaining three degrees-of-freedom are in the horizontal plane. The simulator is supported by three air bearing pads which offer a minimum of resistance to horizontal translation.

For simulating lunar gravity, the subject stands on the semicircular platform (Fig. 12). A mass equal to one-sixth of the subject's mass is placed in the counterweight box. This added mass produces an upward force on the subject's feet which gives him the sensation of walking on the lunar surface.

In the earth orbital (zero gravity) mode, the semicircular platform is removed and sufficient mass is added to the weight box to bring it and the work panel into equilibrium.

2. Technical Information

The lunar gravity and earth orbital simulator consists of the following components: base and support structure, parallelogram arms, work panel assembly, platform assembly, counterweight assembly, and air bearing system (Fig. 13).

Base and Support Structure. The base structure consists of a welded triangular, tubular aluminum base that holds the air bearing pads and serves as a plenum for air supply. The support structure is a rectangular frame made of aluminum channel and welded to the base structure. The support structure supports the parallelogram and transmits all loads to the base.

Parallelogram Arms. The parallelogram arms are two welded aluminum channel assemblies that are supported near their centers on the support structure. Each arm is a lever connecting the work panel and platform assembly to the counterweight assembly. Each arm contains six self-aligning ball-bearing joints for vertical motion.

Work Panel Assembly. The work panel assembly, attached to the front of the parallelogram arms, provides a vertical mounting surface for work objects.

Platform Assembly. The detachable platform is provided for a walking or foot placement surface for experiments other than those performed in zero gravity. An aluminum lip around the edge of the platform is provided to permit gravel or simulated "moon dust" to be placed on the platform for more realistic testing. Folding legs on the platform can be extended for stability when setting up the experiments. These are folded out of the way during operation.

Air Bearing System. The air bearing system consists of a blower and variable transformer control, an air distribution system, and three air bearing pads. The base structure serves as a plenum chamber to prevent air pulses and consequent bearing instability. The front two air bearing lines are provided with bleed-off air valves. The rear pad uses a restriction type valve. The three valves and the variable transformer can be adjusted to provide an even lifting force to elevate the entire structure.

AIR BEARING CAPTURE AND TRANSFER SIMULATOR

1. General Information

This simulator was designed to provide the capability to investigate the following: docking, grappling mechanisms for capture and attachment to work surfaces, manipulators for handling and maneuvering of masses, and boom dynamics associated with mechanisms for capture, despin, respin, and insertion of cooperative and noncooperative objects in earth orbit.

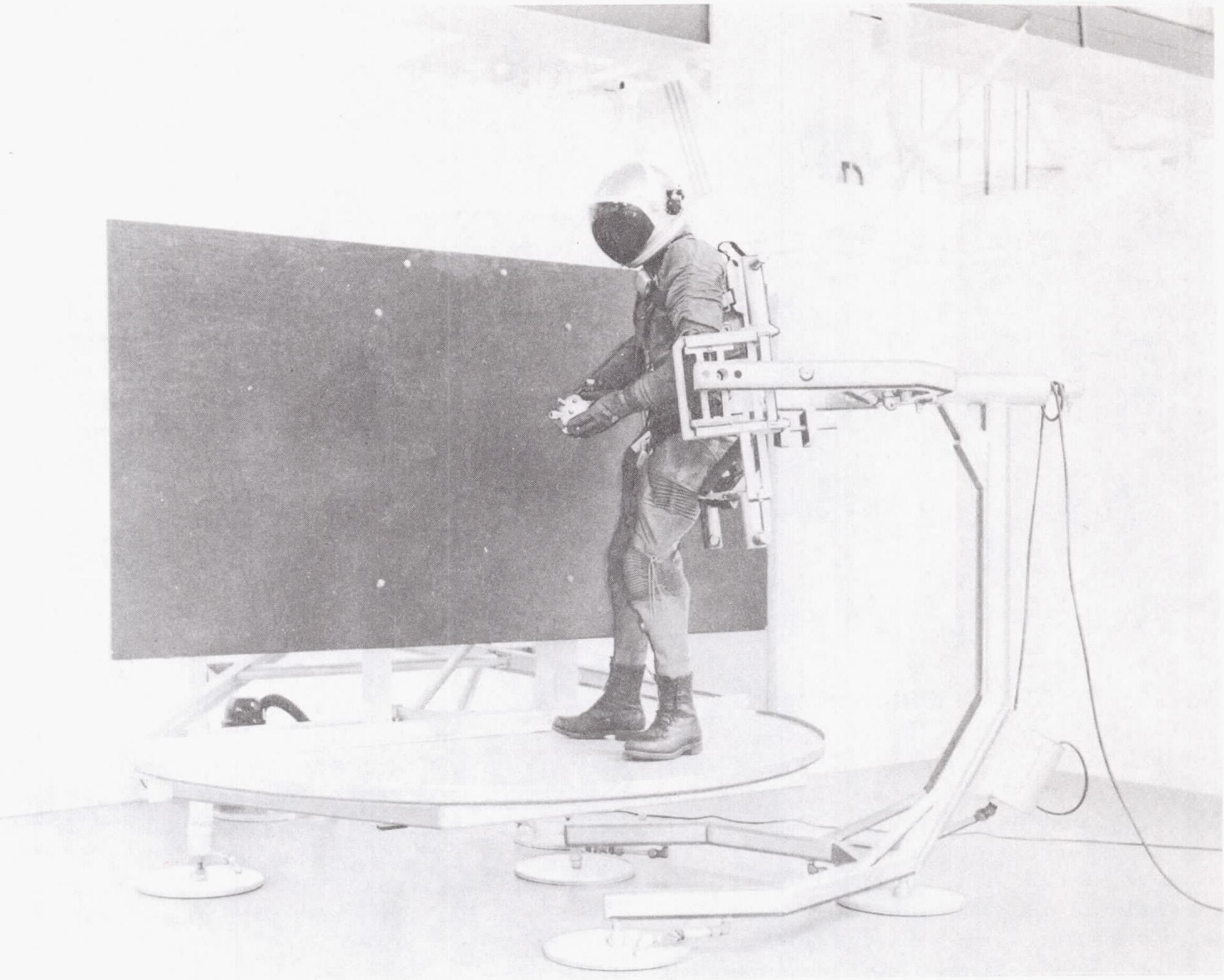

FIGURE 12. LUNAR GRAVITY AND EARTH ORBITAL SIMULATOR AND FIVE-DEGREES-OF-FREEDOM SIMULATOR BEING USED FOR LUNAR GRAVITY SIMULATION WORK

2. Technical Information

The air bearing capture and transfer simulator (Fig. 14) consists of the following major components: frame assembly, walking beam assembly, air bearing pads, air supply system for pads, thruster system (Fig. 15), thruster control electronics package and control stick assembly, transportation casters, and personnel seat assembly.

Frame Assembly. The frame 10 is rectangular in shape, made of square aluminum tubes welded together, and serves as a plenum for the pad air. The front air bearing pads are attached to it.

Walking Beam Assembly. The beam 35 is free to pivot in a plane perpendicular to the frame. This provides the simulator with the same leveling effect on an uneven floor as three air pads but with the load carrying capacity of four pads.

Air Bearing Pads. The pads like the one shown in Figure 16 are used on this simulator.

Air Supply System for Pads. A Black & Decker Manufacturing Company Model 820 EDA heavy-duty central cleaning system unit 12 is used on this simulator.

Thruster System. Six thrusters 60 are used with this system. A high pressure storage sphere 11, fill valve 44, regulator 46, ball valve 50, manifold 56, solenoid valves 57, and tubes 53 and 55 make up the other major components of the system (Fig. 15).

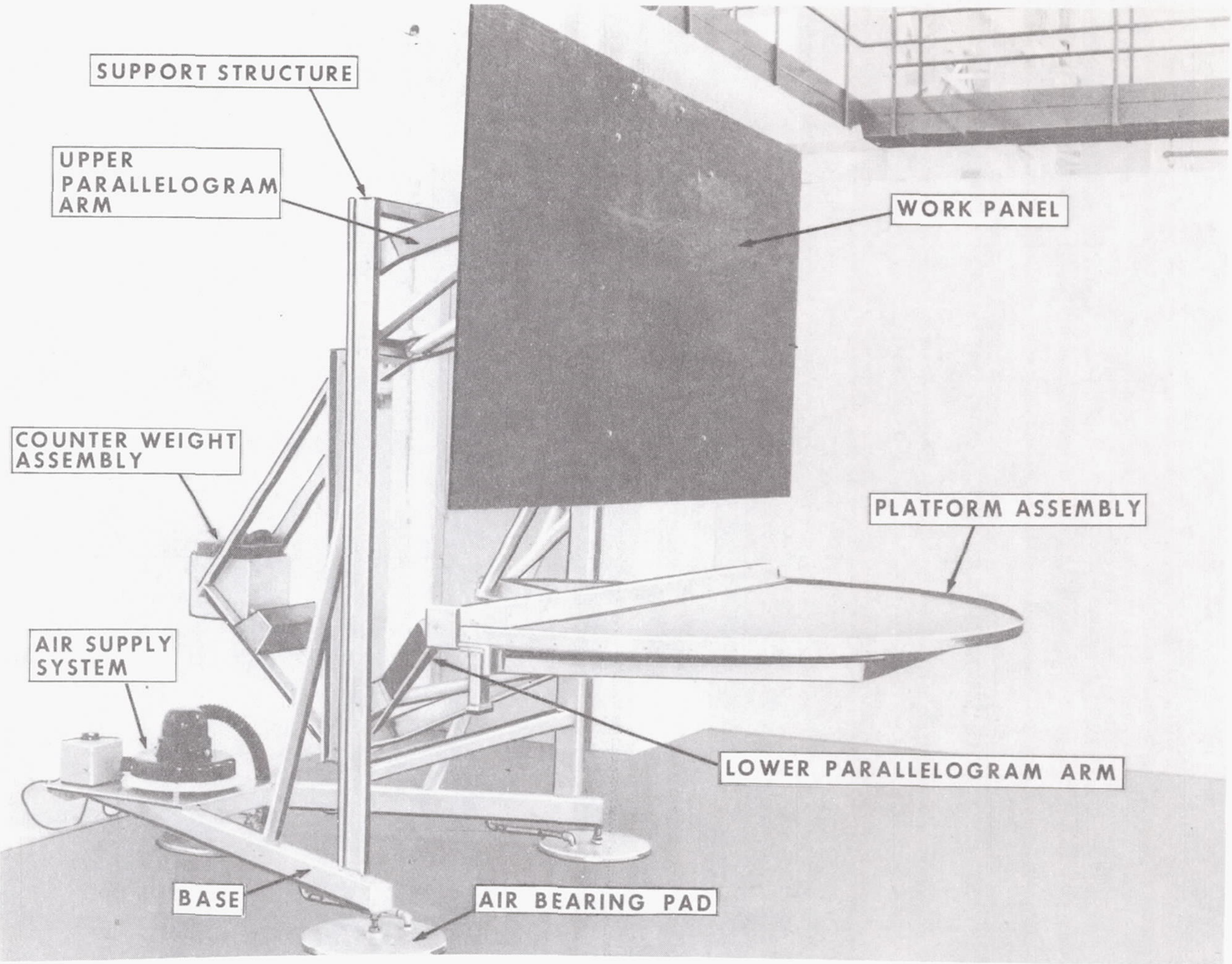

FIGURE 13. LUNAR GRAVITY AND EARTH ORBITAL SIMULATOR

Thruster Control Electronics Package and Control Stick. A military aircraft control stick SA/2-0 electrically actuates relays in the control electronics package, which in turn electrically actuates the solenoid valves 57.

Transportation Casters. These casters 1 provide a means of moving the simulator other than on its air bearing pads. When in use the pads do not touch the floor.

Personnel Seat. The seat support 28 provides a place to attach the air supply 12 as well as support the personnel seat 29.

3. Application.

A grappler developed for use as a means of attaching spacecraft to work surfaces is shown mounted on the simulator. When tests have been completed it can be removed and so the simulator can be used for other tests.

AIR BEARING SYSTEM DEVELOPMENT

MEDIUM INLET PRESSURE AIR BEARING SYSTEM

Air Bearing Pads. A Hovair air bearing pad made by the Inland Division of General Motors Corporation is shown in Figure 17. This pad will support various loads with the pressures and volumes of air described by the load map shown in Figure 18. Inlet pressures of approximately 0.62 MN/m^2 (90 psig) are used with this pad. For the purpose of this review, this is a medium inlet pressure.

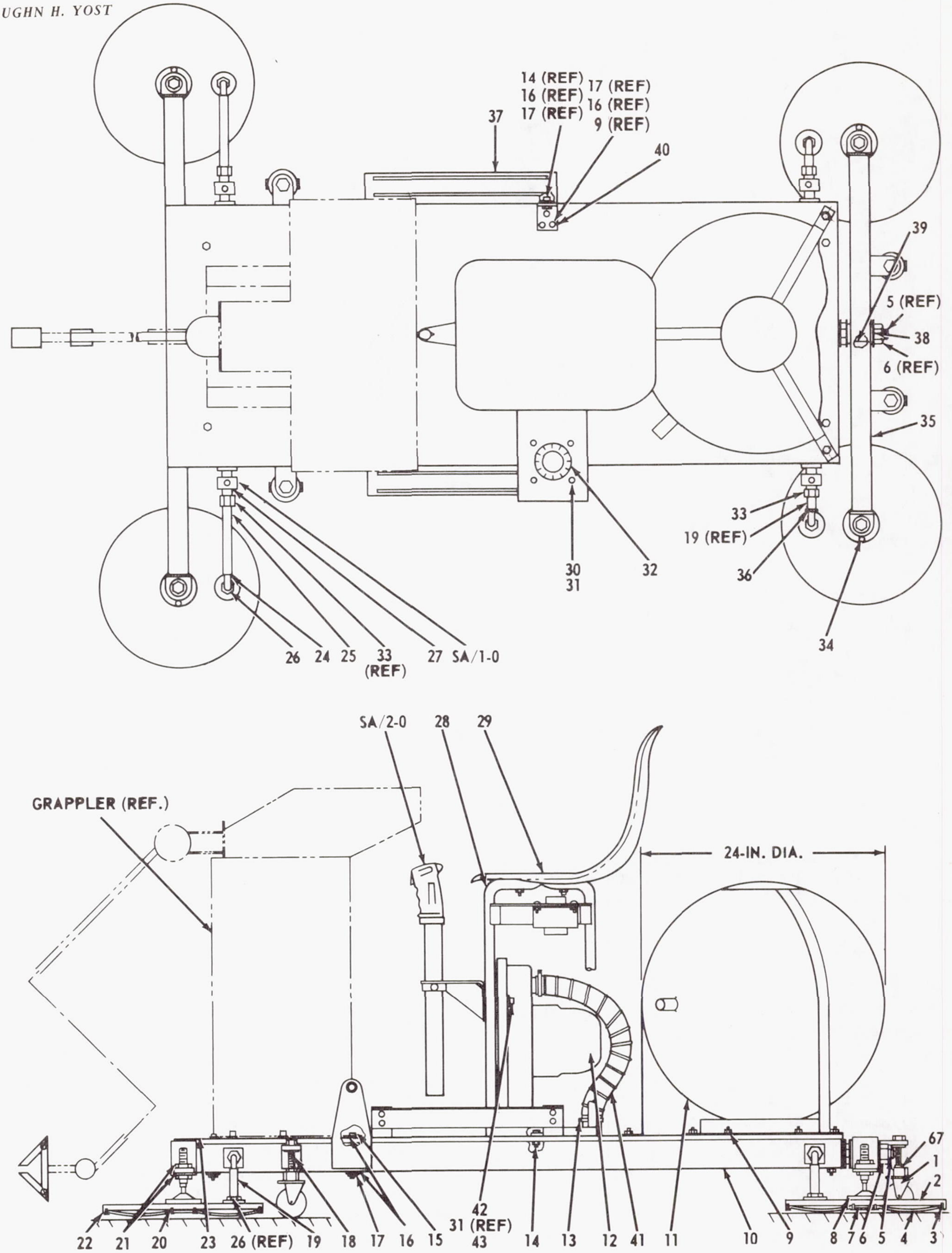

FIGURE 14. AIR BEARING CAPTURE AND TRANSFER SIMULATOR — TOP AND SIDE VIEW

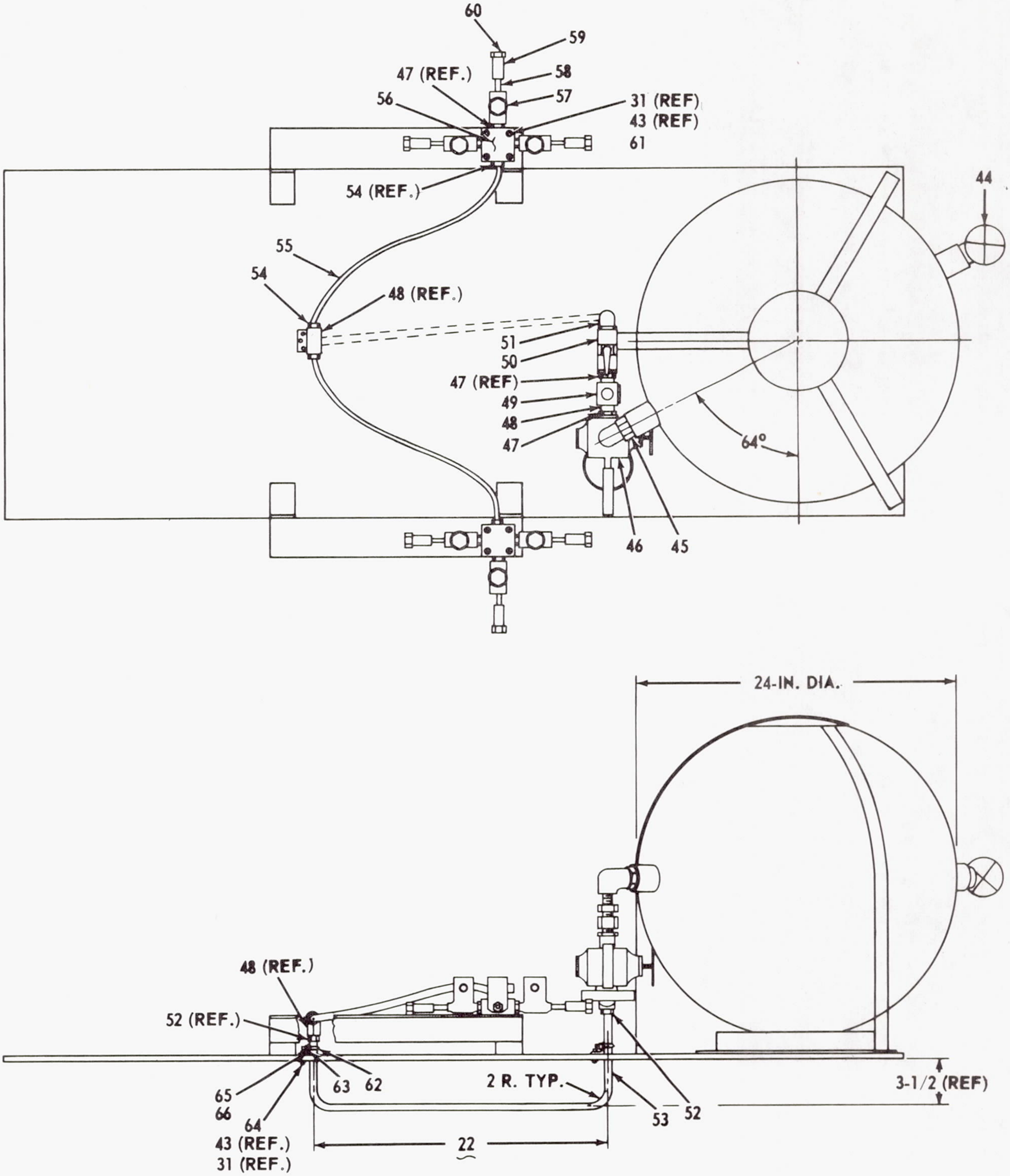

FIGURE 15. THRUSTER SYSTEM FOR AIR BEARING CAPTURE AND TRANSFER SIMULATOR

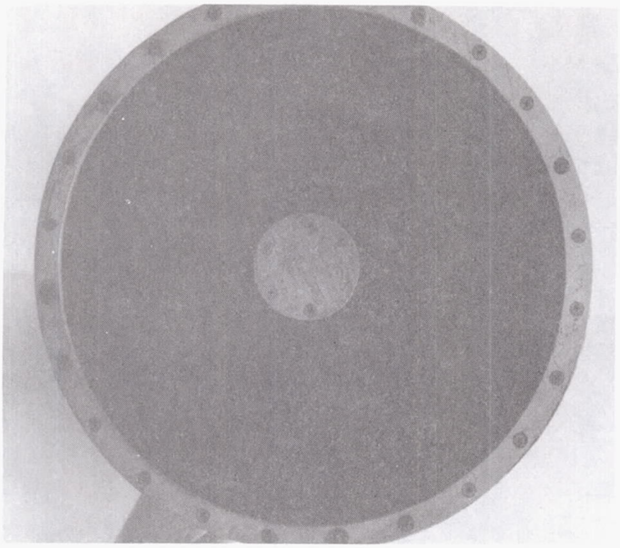

FIGURE 16. LOW INLET PRESSURE AIR BEARING PAD MADE BY MARTIN-MARIETTA CORPORATION

Air Supplies. There are at least three ways of supplying air at medium pressures. They are the following: mounting a high pressure {2063 N/cm^2 (3000 psig)} sphere and regulating equipment on the device, mounting an air compressor on the device, or attaching a medium pressure air line to the device.

LOW INLET PRESSURE AIR BEARING SYSTEM

Air Bearing Pads. A low inlet pressure pad designed by the Martin-Marietta Company, Baltimore Division, is shown in Figure 16. This cushion operates on inlet pressures and volumes of air obtainable with vacuum cleaner motors described in subsequent paragraphs.

Air Supplies. The two types of air supplies that have been used are described below.

Lamb Electric Model 115250. This is a two-stage direct air flow vacuum motor for domestic canister and tank type vacuum cleaners (Fig. 19). Since the motor is cooled by discharge of the vacuum air from the blower section, this type of unit is not suitable for use in applications where the air flow could be sealed

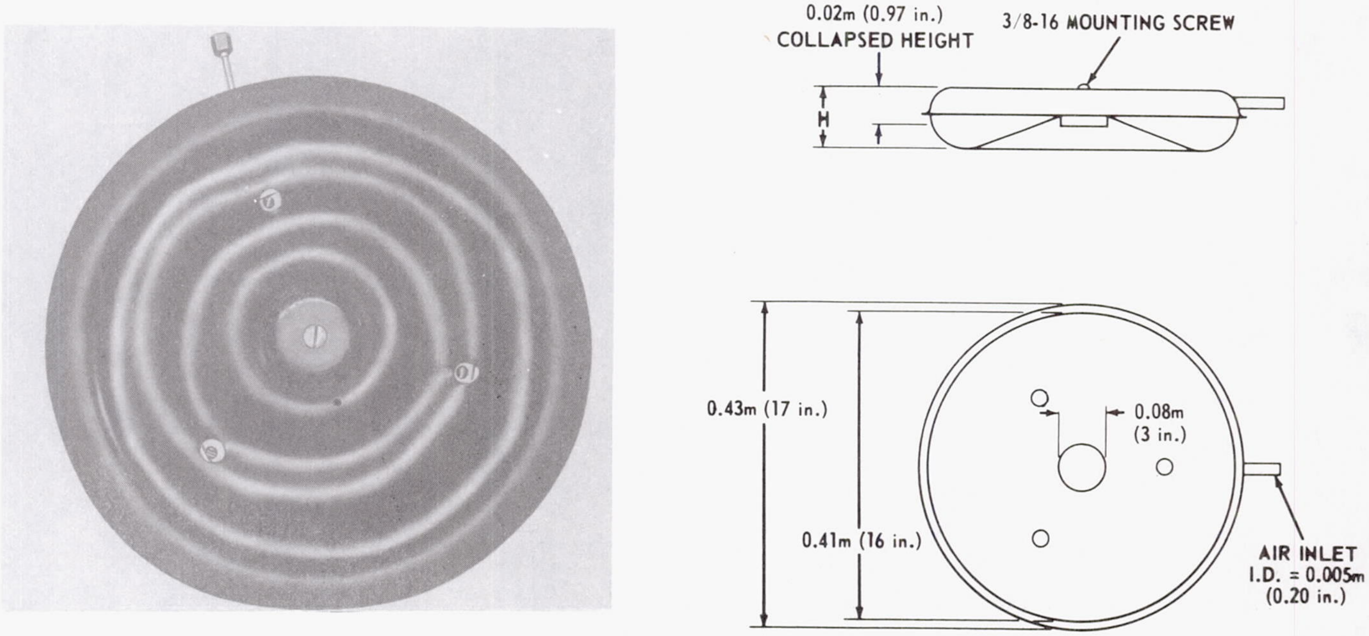

Specifications

Diaphragm Material	3032-50 Urethane	Support Area @ 5.2 psig	192 in.^{2}
Diaphragm Thickness	0.050 in. Nominal	Seal Perimeter @ 5.2 psig	4.10 ft
Top Plate Material	Steel	Air Inlet	1/4 in. Tubing
Top Plate Thickness	0.060 in.		

FIGURE 17. HOVAIR MEDIUM INLET PRESSURE AIR BEARING PAD MADE BY THE INLAND DIVISION OF GENERAL MOTORS CORPORATION

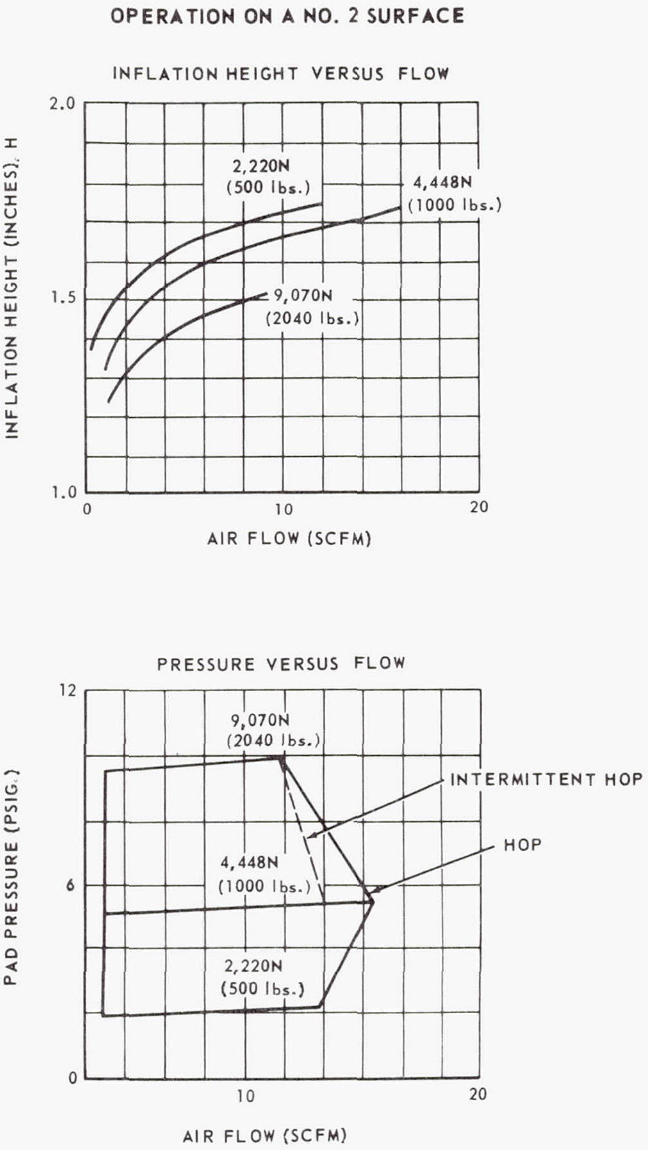

FIGURE 18. LOAD MAP FOR HOVAIR XD 16009 AIR BEARING PAD

off for an appreciable length of time. The motor performance curves are shown in Figure 20. Curve "A" shows the characteristics of a vacuum cleaner which was designed for Lamb's older Model 1S-14750 but has been replaced with Model 115250. Vacuum cleaners having the performance specified in Curve "B" draw the maximum amount of power allowable for #18 SV line cord when using Model 115250.

Black & Decker Manufacturing Company Model 820EDA. This is a heavy-duty central cleaning system 1680 W (2-1/4 h.p. maximum) unit, for medium size homes and apartments (Fig. 21). Since the motor is cooled separately, this type of unit is suitable for use in applications where the air flow could be sealed off.

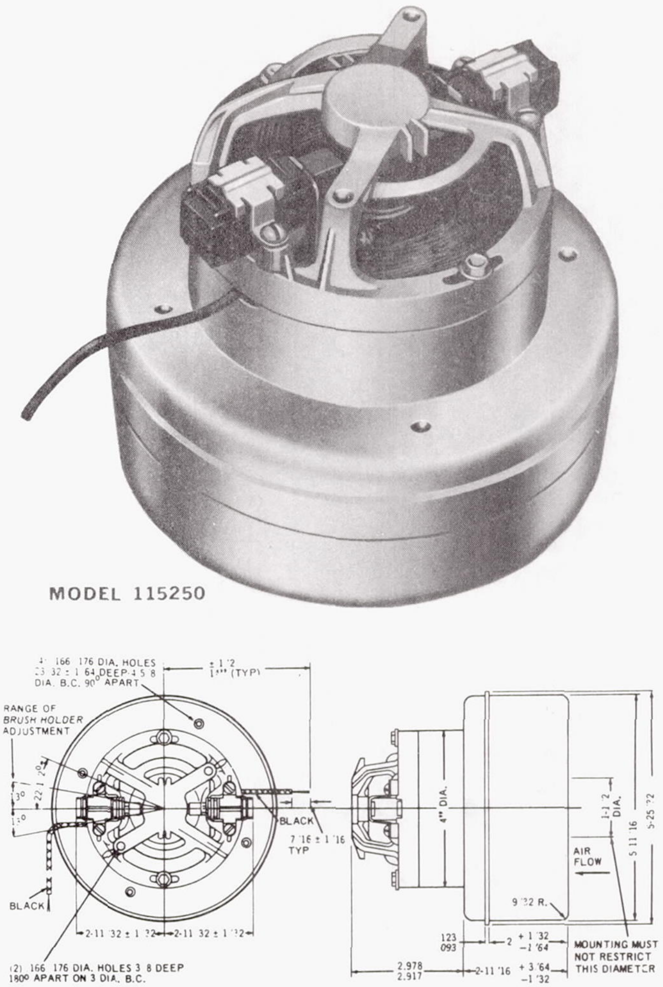

FIGURE 19. LAMB ELECTRIC MODEL 115250 TWO-STAGE DIRECT AIR FLOW VACUUM MOTOR FOR DOMESTIC CANISTER AND TANK TYPE VACUUM CLEANERS

COMPARISON OF MEDIUM AND LOW INLET PRESSURE AIR BEARING SYSTEMS

Mass. Assuming the air supply is mounted on the device, the mass of the low pressure system is lesser of the two. The lower the mass of simulator supporting the subject or work piece, the more accurate the simulation data will be.

Force. When medium pressure shop air lines are attached to the device, the forces required to produce translation are increased, thereby degrading it for simulation purposes.

Floor Finish. A smoother floor is required for medium inlet pressure pads (Fig. 17) than for low inlet pressure pads (Fig. 16).

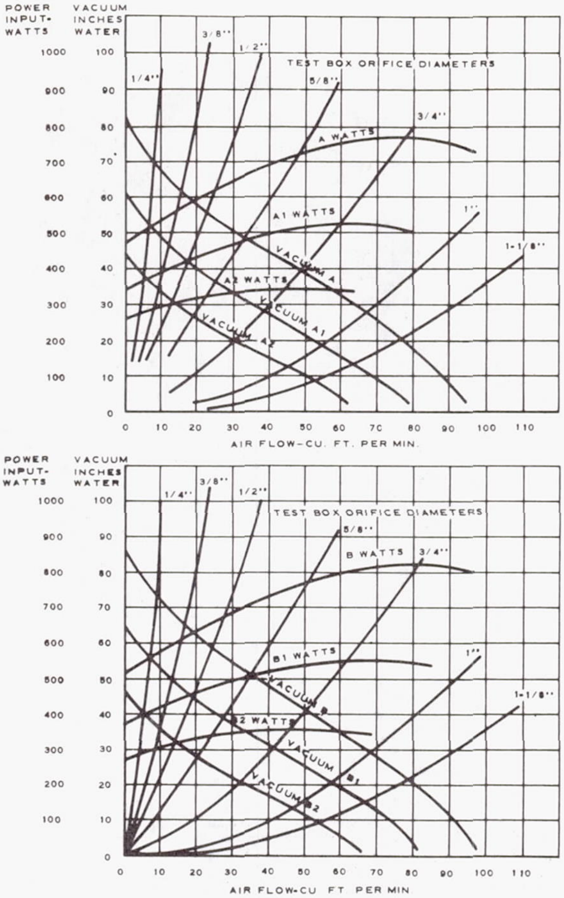

AVERAGE TEST DATA CORRECTED TO STANDARD BAROMETER OF 29.92 IN. HG. AND 68°F.

NOTE: CURVES MARKED WITH FRACTIONAL INCH DESIGNATIONS INDICATE AIR FLOW AND VACUUM THROUGH SHARP-EDGED THIN PLATE TEST ORIFICES OF DIAMETER INDICATED.

FIGURE 20. LAMB ELECTRIC MODEL 115250 VACUUM MOTOR PERFORMANCE CURVES

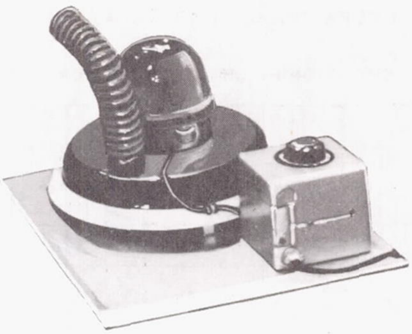

CENTRAL CLEANING SYSTEM UNIT

Horsepower Rating Max.	2 1/4
R.P.M. Rated	12,000
Amperage	10
Voltage	115
Current	AC
Cycles	50-60
Inches sealed water lift	72
Inches Mercury	5.32
C.F.M.	118
Fans	2 stage
Cooling System	by-pass

FIGURE 21. BLACK & DECKER MODEL 820 EDA HEAVY DUTY CENTRAL CLEANING SYSTEM VACUUM MOTOR AND VARIAC SPEED CONTROL

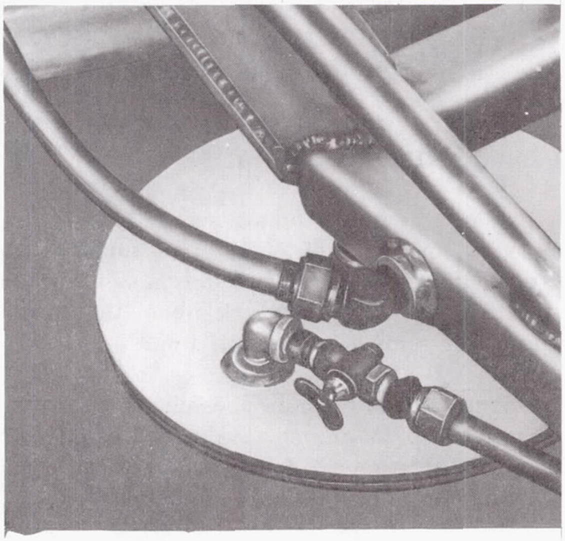

FIGURE 22. METAL TUBING AND FITTINGS USED WITH LOW OR MEDIUM INLET PRESSURE AIR SUPPLY (NOTE BALL VALVE)

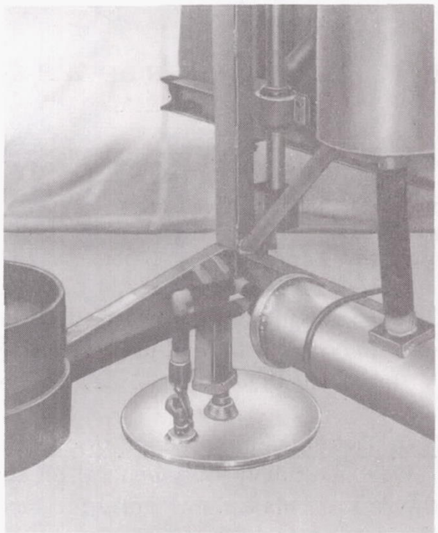

FIGURE 23. NONMETALLIC TUBING AND FITTINGS USED WITH LOW INLET PRESSURE AIR SUPPLY

Plumbing. The plumbing required for a medium inlet pressure system costs more than for a low inlet pressure system. Nonmetallic water pipe and fittings can be used with the latter system (compare Figs. 22 and 23).

MANIFOLD AND AIR SUPPLY RESERVOIRS

The frame of the device may be used for both medium and low pressure systems. This produces a significant weight savings.

REGULATION OF THE VOLUME OF AIR SUPPLIED TO EACH AIR BEARING PAD FOR MEDIUM AND LOW PRESSURE SYSTEMS

Ball Valves. Metallic and nonmetallic ball valves can be used with either system (Figs. 22 and 23).

Bleed Off Valve. See Figure 24.

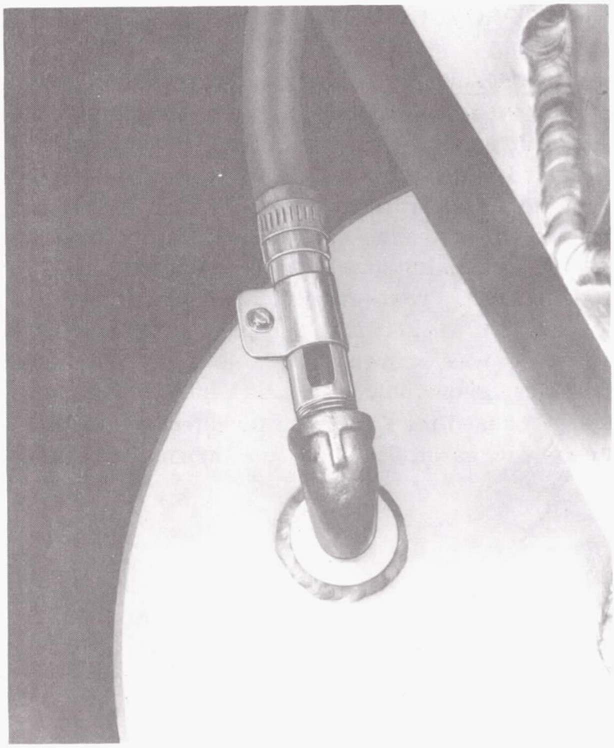

FIGURE 24. BLEED-OFF VALVE USED WITH AIR SUPPLY MOTORS THAT ARE COOLED BY DISCHARGE OF THE VACUUM AIR FROM THE BLOWER SECTION

Comparison of Ball and Bleed Off Valves. Commercially available ball valves generally cost less than the labor and materials required to make bleed off valves. Bleed off valves (Fig. 24) should be used with vacuum cleaner motors that are cooled by the air discharge from the blower section.

AIR BEARING CART THRUST SYSTEM DEVELOPMENT

1. General Information

The design criteria for this system were the following:

Cart Mass. The total mass of the cart less operator and item to be tested was estimated to be 168 kg (11.5 slugs). The masses of the operator and item to be tested were estimated to be 81.3 and 68.2 kg (5.60 and 4.66 slugs) respectively. A total mass of 318 kg (21.8 slugs) for the cart, operator and item to be tested was used for design purposes.

Velocity. The cart is to reach a velocity of at least 1.52 m/sec (5 ft/sec) in less than 6.1 m (20 ft).

Propellant. Select a propellant that has the best specific impulse for the following characteristics: easy to handle, readily available, inexpensive, requires no protective equipment for handling or use, and the exhaust products must not be toxic or nauseating.

Utilities. No propellant lines were to be attached to the cart during operation. One 120 Vac power cable could be attached to the cart during operation to run the vacuum cleaner motor, thruster control system, and item being tested.

Miscellaneous. Select inexpensive, lightweight, commercially available hardware and use it in such a manner as to produce a reliable minimum-maintenance system.

2. Technical Information

Test Setup. The apparatus shown in Figure 25 was designed to test different propellants. Its major components are a high pressure sphere 2, regulator 8, relief valve 23, ball valve 11, solenoid valve 17, and the candidate thruster 18. This apparatus was attached to a platform scale to determine thrust levels for different propellants and thruster designs. The

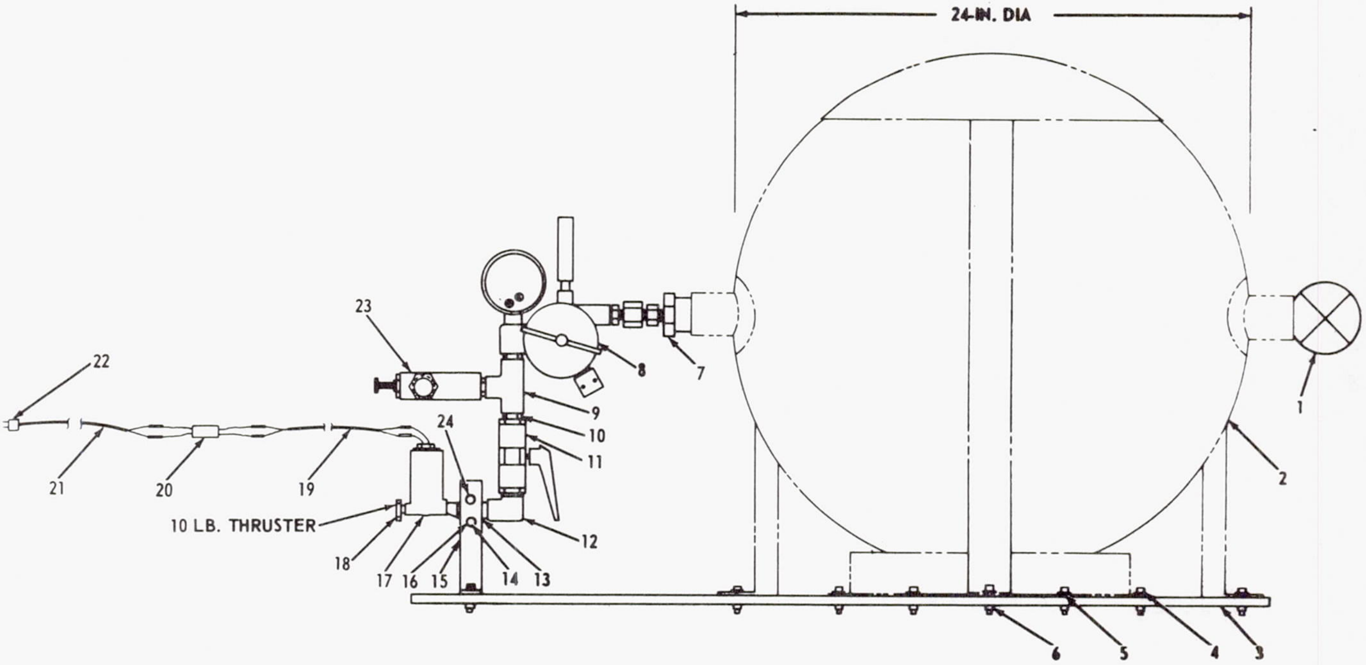

FIGURE 25. TEST SETUP USED FOR SELECTION OF PROPELLANT AND THRUSTER

center line of the thruster was perpendicular to the platform with the exit nozzle pointing upward. For determining the velocity and acceleration obtainable with each propellant, the apparatus was attached to a test cart (Fig. 26).

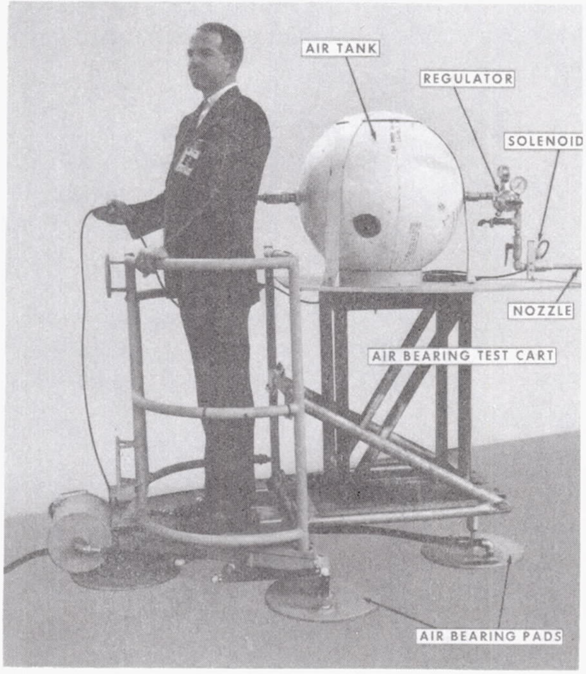

FIGURE 26. TEST SETUP USED TO DETERMINE VELOCITY AND ACCELERATION OBTAINABLE WITH EACH PROPELLANT AND THRUSTER

Test Results. Air was the first and only propellant tested. It produced the desired results after several thruster designs and tubing configurations were tried. The thruster shown in Figure 27 produced the maximum thrust once the flow into the inlet nozzle was changed to laminar. This thruster has inlet and outlet nozzle areas equal to 4 and 2 times the throat area, respectively. The throat area is 3.38×10^{-5} m^2 (0.0523 in.^{2}). In the earlier tests the thruster 18 was screwed into the outlet of the solenoid valve 17 as shown in Figure 25. The solenoid valve passage caused the flow to be turbulent. This turbulence decreased the maximum thrust of the thruster.

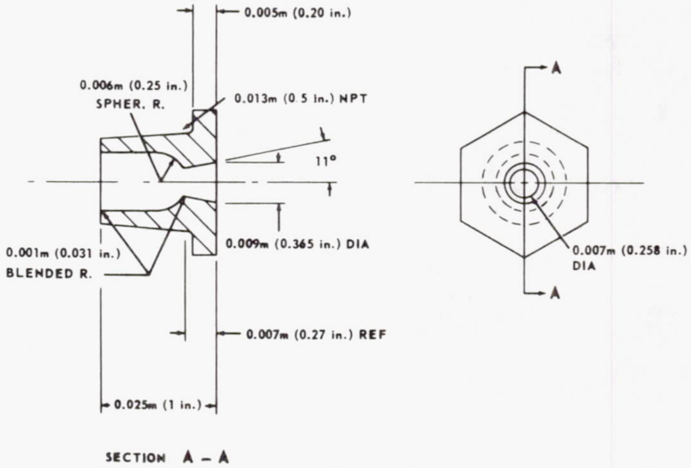

FIGURE 27. THRUSTER SELECTED FOR AIR PROPULSION SYSTEM

The flow into the inlet nozzle of the thruster was changed from turbulent to laminar by putting a pipe nipple 10 times the pipe diameter between the solenoid valve and thruster as shown in Figure 26. Table I data were obtained with the apparatus shown in Figure 25 mounted on the platform scale and a 0.127 m (5 in.) pipe nipple between the solenoid and thruster.

DEVICES TO SUPPORT EQUIPMENT FOR MECHANICAL SIMULATION

1. General Information

The weight of equipment, e.g., hand tools, which a subject uses to perform tasks, cannot be effectively balanced with a simulator balancing system because as soon as equipment is moved, the subject is out of balance. If the subject is balanced without the equipment and then handed the equipment he is out of balance too. To remedy this situation the equipment may be supported with a helium filled balloon. The balloon can be filled to produce a force equal to the weight of the equipment for earth orbital gravity simulation, or 5/6 its weight for lunar gravity simulation.

Equipment designed for earth orbital or lunar gravity work will not necessarily function in an earth gravity, one "g", environment because of its mass, deflections caused by cantilevered members, etc. One way of solving this problem is to support the equipment with a pedestal attached to the platform supported by air bearing pads. These devices are called Air Bearing Platforms.

2. Technical Information

Balloons. In Figure 28 an impact wrench is supported by a 1.83 m (6 ft) diameter weather balloon filled with sufficient helium to provide an upward force equal to the weight of the wrench.

The balloons presently used were made especially for simulation work by the G. T. Schjildahl Company, Northfield, Massachusetts. These balloons are 2.54 m (8 ft) in diameter consisting of 12 gores of two layers of 25.4 μm (0.001 in.) thick polyester bilaminate with 2 plastic inflation valves 180 degrees apart. These balloons will lift a mass up to 8.2 kg (0.56 slugs).

Air Bearing Platform. These platforms are designed to provide a stable base for simulating a near-frictionless environment by means of air bearing pads operating on a smooth level floor. Two configurations of the platform are presently being used: the manned version including a man-seat pedestal and serpentuator attach bracket (Fig. 29), and the unmanned version that includes the serpentuator support bracket (Fig. 30). The components that make up these configurations have the following masses: platform air bearing, 25 kg (1.71 slugs); serpentuator attach post and

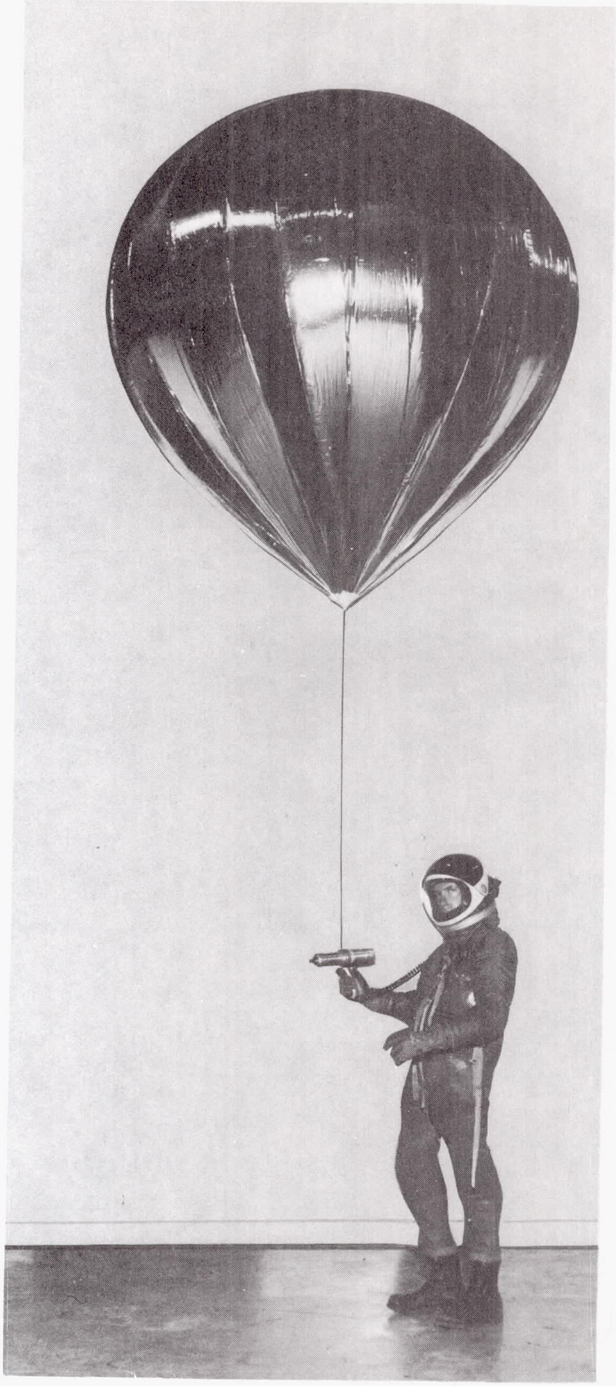

FIGURE 28. HELIUM FILLED WEATHER BALLOON SUPPORTING THE IMPACT WRENCH

TABLE I. AIR BEARING CART TEST THRUSTER ASSEMBLY THRUST TESTS

OCTOBER 13, 1967

TEST NUMBER	TIME CYCLE (sec)	SET REGULATOR AT 215 psi	DYNAMIC PRESSURE 150 psi TIMED	SPHERE PRESSURE PRIOR TO TEST	SPHERE PRESSURE AFTER TEST	INITIAL WEIGHT OF SPHERE PRIOR TO TEST (AT 1 g)	TOP READING OF BLAST TEST	BOTTOM READING OF BLAST TEST	THRUST AT TOP READING	THRUST AT BOTTOM READING	WEIGHT OF SPHERE AFTER TEST (AT 1 g)	ROOM TEMPERATURE
	sec	psi	psi	psi-N_2	psi-N_2	lbf	lbf	lbf	lbf	lbf	lbf	° F
1	7	215	150	2500	2400	179.50	188.00	187.50	8.50	8.00	178.50	68
2	10	215	150	2500	2375	179.50	188.00	186.75	8.50	6.75	178.00	69
3	12	215	150	2500	2350	179.25	188.00	186.50	8.75	7.25	177.75	70
4	15	215	150	2500	2325	179.50	188.00	186.00	8.50	6.50	177.25	73
5	5	215	150	2500	2450	178.50	188.00	187.50	8.75	8.25	178.50	72

OCTOBER 20, 1967

TIME START: 10:00 a.m. TIME END: 11:30 a.m.

TEST NUMBER	TIME CYCLE	SET REGULATOR AT 215 psi	DYNAMIC PRESSURE TIMED	SPHERE PRESSURE PRIOR TO TEST	SPHERE PRESSURE AFTER TEST	TOP READING OF BLAST TEST	BOTTOM OF BLAST TEST	THRUST AT TOP READING	THRUST AT BOTTOM READING	WEIGHT OF SPHERE BEFORE TEST (AT 1 g)	WEIGHT OF SPHERE AFTER TEST (AT 1 g)	ROOM TEMPERATURE	SPHERE TEMPERATURE	DATA RECORDING TIME
	sec	psi	psi	psi-N_2	psi-N_2	lbf	lbf	lbf	lbf	lbf	lbf	° F	° F	min
1	5	215	150	2500	2425	189.75	187.50	11.25	9.00	178.50	178.00	72.0	78.0	6
2	5	215	150	2425	2360	188.75	186.50	10.75	8.50	178.00	177.00	71.0	76.0	3
3	5	215	150	2360	2300	187.75	185.25	10.75	8.25	177.00	176.25	71.5	76.0	2
4	5	215	150	2300	2225	187.00	184.50	10.75	8.25	176.25	175.25	72.0	75.0	1
5	5	215	150	2225	2175	186.50	183.50	11.25	8.25	175.25	174.50	72.0	75.0	1
6	5	215	150	2175	2100	185.25	182.75	10.75	8.25	174.50	173.50	71.5	75.0	1
7	5	215	150	2100	2050	184.50	181.75	11.00	8.25	173.50	172.75	71.5	74.0	1
8	5	215	150	2050	2000	183.25	181.00	10.50	8.50	172.75	171.75	71.5	73.5	1
9	5	215	150	2000	1950	182.25	181.00	10.50	9.25	171.75	170.75	71.0	73.0	1
10	5	215	150	1950	1875	181.50	179.00	10.75	8.25	170.75	170.00	71.0	72.0	1
11	5	215	150	1875	1825	180.75	178.00	10.75	8.00	170.00	169.00	71.0	71.5	1
12	5	215	150	1825	1775	179.75	177.00	10.75	8.00	169.00	168.25	71.5	70.5	1
13	5	215	150	1775	1710	178.75	176.50	10.50	8.25	168.25	167.25	72.0	70.0	1
14	5	215	150	1710	1650	177.75	175.00	10.50	7.75	167.25	166.25	72.0	69.0	1
15	5	215	150	1650	1600	176.50	174.00	10.25	7.75	166.25	165.25	72.0	69.0	1
16	5	215	150	1600	1550	175.75	173.25	10.50	8.00	165.25	164.50	71.0	68.0	1
17	5	215	150	1550	1510	174.75	172.50	10.25	8.00	164.50	163.75	72.0	67.0	1
18	5	215	150	1510	1470	173.75	171.50	10.00	7.75	163.75	162.75	72.0	67.0	1
19	5	215	150	1470	1400	173.00	170.50	10.25	8.75	162.75	162.00	72.0	67.0	1

TABLE I. AIR BEARING CART TEST THRUSTER ASSEMBLY THRUST TESTS (Concluded)

TEST NUMBER	TIME CYCLE	SET REGULATOR AT 215 psi	DYNAMIC PRESSURE TIMED	SPHERE PRESSURE PRIOR TO TEST	SPHERE PRESSURE AFTER TEST	TOP READING OF BLAST TEST	BOTTOM OF BLAST TEST	THRUST AT TOP READING	THRUST AT BOTTOM READING	WEIGHT OF SPHERE BEFORE TEST (AT 1 g)	WEIGHT OF SPHERE AFTER TEST (AT 1 g)	ROOM TEMPERATURE	SPHERE TEMPERATURE	DATA RECORDING TIME
	sec	psi	psi	psi-N_2	psi-N_2	lbf	lbf	lbf	lbf	lbf	lbf	°F	°F	min
20*	5	215	149	1400	1375	172.25	169.75	10.25	7.75	162.00	161.00	72.0	65.0	1
21	5	215	149	1375	1310	171.25	169.00	10.25	8.00	161.00	160.00	72.0	75.0	1
22	5	215	148	1310	1280	170.50	168.00	10.50	8.00	160.00	159.25	72.0	64.0	1
23	5	215	148	1280	1210	169.50	167.00	10.25	7.75	159.25	158.25	72.0	64.0	1
24	5	215	147	1210	1200	168.50	166.00	10.25	7.75	158.25	157.50	72.0	63.0	1
25	5	215	147	1200	1150	167.75	165.25	10.25	7.75	157.50	156.50	72.0	73.0	1
26	5	215	146	1150	1100	167.00	164.50	10.50	8.00	156.50	155.75	72.0	62.0	1
27	5	215	145	1100	1050	165.75	163.50	10.00	7.75	155.75	155.00	72.0	61.0	1
28	5	215	144	1050	1010	165.00	162.50	10.00	7.25	155.00	154.00	72.0	60.0	1
29	5	215	144	1010	1000	164.00	161.75	10.00	7.75	154.00	153.25	72.0	59.0	2
30	5	215	143	1000	960	163.00	160.75	9.75	7.50	153.25	152.25	72.0	59.0	1
31	5	215	142	960	910	162.00	160.00	9.75	7.75	152.25	151.50	72.0	58.0	1
32	5	215	142	910	890	161.25	159.00	9.75	7.50	151.50	150.75	71.5	58.0	1
33	5	215	141	890	850	160.25	158.00	9.50	7.25	150.75	150.00	71.5	58.0	1
34	5	215	135	850	800	159.50	156.75	9.50	6.75	150.00	149.25	72.0	57.0	1
35	5	215	135	800	770	158.25	155.75	9.00	6.50	149.25	148.50	72.0	57.0	1
36	5	215	130	770	750	157.50	155.00	9.00	6.50	148.50	147.75	72.0	57.0	1
37	5	215	130	750	700	156.50	154.25	8.75	6.50	147.75	147.00	72.0	57.0	1
38	5	215	125	700	680	155.75	153.25	8.75	6.23	147.00	146.25	72.5	57.0	1
39	5	215	120	680	650	155.00	152.50	8.75	6.25	146.25	145.50	72.5	57.0	1
40	5	215	115	650	600	154.00	151.50	8.50	6.00	145.50	144.75	72.5	56.5	1
41	5	215	115	600	580	153.00	150.75	8.25	6.00	144.75	144.00	70.0	56.0	1
42	5	215	115	580	525	152.25	150.00	8.25	6.00	144.00	143.25	69.0	55.0	1
43	5	215	110	525	510	151.50	149.00	8.25	5.75	143.25	142.75	68.0	55.0	1
44	5	215	110	510	500	150.50	148.25	7.75	5.50	142.75	142.00	68.0	54.0	1
45	5	215	110	500	480	149.75	147.50	7.75	5.50	142.00	141.25	68.0	54.0	1
46	5	215	105	480	425	149.00	146.75	7.75	5.50	141.25	140.75	69.0	54.0	1
47	5	215	100	425	400	147.75	145.50	7.00	4.75	140.75	140.00	70.0	54.0	1
48	5	215	95	400	390	147.25	145.00	7.25	5.00	140.00	139.50	70.0	54.0	1
49	5	215	85	390	350	146.25	144.25	6.75	4.75	139.50	138.75	71.0	54.0	1
50	5	215	80	350	310	145.50	143.25	6.75	4.50	138.75	138.25	72.0	54.0	1
51	5	215	80	310	300	144.50	142.50	6.25	4.25	138.25	137.75	72.0	54.0	1
52	5	215	80	300	290	143.75	141.75	6.00	4.00	137.75	137.25	72.0	54.0	1
53	5	-	75	290	250	142.75	141.00	5.50	3.75	137.25	136.75	72.0	54.0	1
54	5	-	70	250	220	142.00	140.25	5.25	3.50	136.75	136.25	72.0	54.0	1
55	5	-	65	220	210	141.00	139.25	4.75	3.00	136.25	135.75	72.0	54.0	1
56	5	-	60	210	200	140.25	138.50	4.50	2.75	135.75	135.50	72.0	54.0	1

*Sphere started to frost up.

1 g weight of sphere was measured at AEC Oak Ridge Tenn. facility

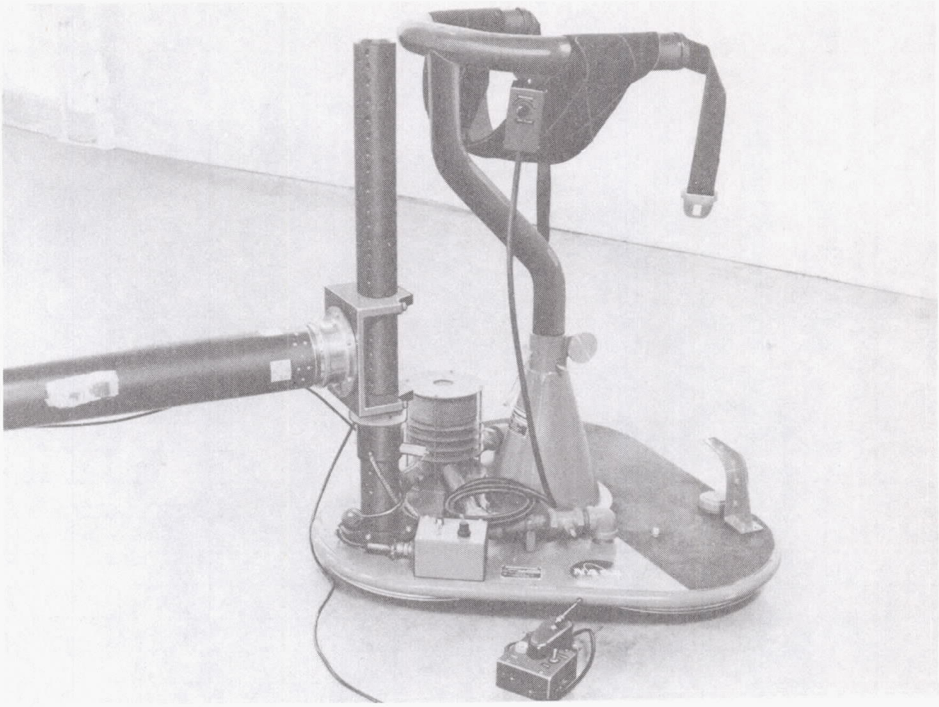

FIGURE 29. MANNED VERSION OF THE AIR BEARING PLATFORM

FIGURE 30. UNMANNED VERSION OF THE AIR BEARING PLATFORM

bracket, 4.45 kg (0.373 slugs); serpentuator support, post and bracket, 4.45 kg (0.373 slugs); and the operator's mast and safety yoke, 8.18 kg (0.56 slugs). Each platform will support a nominal load of 273 kg (18.7 slugs). The platform flotation lifting height can be adjusted by controlling the speed of the air supply motor. When unbalanced loads are supported by the platform, it can be leveled by manually adjusting valves which restrict the air flow delivered to each pad. The air supply motor is protected by a 10 A combination circuit breaker/toggle switch mounted in the electrical control box. The unmanned speed control is also contained in the electrical control box. On the manned version the air supply motor runs as long as the foot-treadle is depressed, and the air supply speed control is mounted on the operator's seat yoke. The air supply is capable of maintaining a plenum pressure of 17 220 N/m^2 (2.5 psig) for flows up to 0.438 standard m^3/min (15.5 scfm). The only power requirement is single phase 115 Vac 60 Hz (60 Cps) with maximum current of 10 A.

Application. In Figure 31 the serpentuator and operator are supported by the air bearing platforms described above.

FIGURE 31. AIR BEARING PLATFORMS SUPPORTING SERPENTUATOR AND OPERATOR

BIBLIOGRAPHY

1. Air Bearing Platform, T50-2, Final Report. Contract NAS8-20855, North American Rockwell Corporation, Space Division, Downey, California, October 31, 1967.

2. Bread-Boarded Thruster Assembly, TR SE-33-67, Contract NAS8-20083, Hayes International Corporation, Huntsville, Alabama, December 12, 1967; and Evaluation Test Plan for the Air Bearing Thrusted Scooter Assembly and LTV Grappler Module, December 21, 1967.

3. Design, Fabrication and Proof Testing of a Low Pressure, Air Bearingized Frictionless Parallelogram, Technical and Program Plan, and Progress Reports 1, 2 and 3; Operation and Maintenance Instruction Manual for Lunar Gravity and Earth Orbital Simulator. Contract NAS8-20821, Martin-Marietta Corporation, Baltimore Division, Baltimore, Maryland, May through October, 1967.

4. Evaluation of Six-Degree-of-Freedom Mechanical Simulator, TR SE-1-67. Contract NAS8-20083, Hayes International Corporation, Huntsville, Alabama, February 9, 1967.

5. Lunar Gravity and Earth Orbital Simulator (Parallelogram), TR SE-19-67. Contract NAS8-20083, Hayes International Corporation, Huntsville, Alabama, October 9, 1967.

6. Operation and Maintenance Instructions for the Frictionless Simulator. Contract NAS8-17264; Martin-Marietta Corporation, Baltimore Division, Middle River, Maryland, November 20, 1963.

7. Operation Plan for Action-Reaction Free-Fall Simulator, MIT-375-14529. Manufacturing Engineering Laboratory, MSFC, Huntsville, Alabama.

8. Upgraded Lunar Gravity Simulator, TR SE-26-67. Contract NAS8-20083, Hayes International Corporation, Huntsville, Alabama, November 6, 1967.

Page
Intentionally
Left Blank

LASERS USED IN MANUFACTURING

By

John R. Rasquin

SUMMARY

The chief manufacturing uses for the laser are in the areas of welding, cutting, and hole punching. These uses are now leading to new manufacturing methods. The lasers used for these tasks can be classified into two types: the continuous wave laser and the pulsed laser. It has been the experience of this laboratory that the continuous wave (CW) laser is better for welding and that the pulsed laser is better for cutting and hole punching.

PULSED LASER

The use of a pulsed laser for welding, when the pulse repetition rate is slow enough so that the weld nugget does not remain molten, results in a series of spot welds, one on top of the other. This method usually does not produce a good weld because the odds of producing oxide inclusions, incomplete fusion, etc., are greatly increased. If the pulse repetition rate is high enough to keep the weld nugget molten, then there are the problems of crystal cooling and having a power supply large enough to charge this energy storage system rapidly enough.

The large capacitor bank used in the Manufacturing Engineering Laboratory has a capacity of 240, 000 J and takes 15 sec to charge fully. A pulse repetition rate of four times a minute is relatively fast for an electrical apparatus of this size. Yet it is evident that even this rate will not suffice to maintain a weld crater. It is estimated that a repetition rate of at least four times a second is needed to maintain a molten crater. This makes the size of the power supply ridiculously large.

Figure 1 shows the interior of the 240 kJ ruby laser gun which has been used for welding, cutting, and hole punching. Figure 2 shows that a 0.635-cm (0.25-in.) thick aluminum sheet can be pierced quite easily using this laser. The ruby laser gun was developed and built in the Manufacturing Engineering Laboratory. Energy outputs as high as 2800 J have been measured.

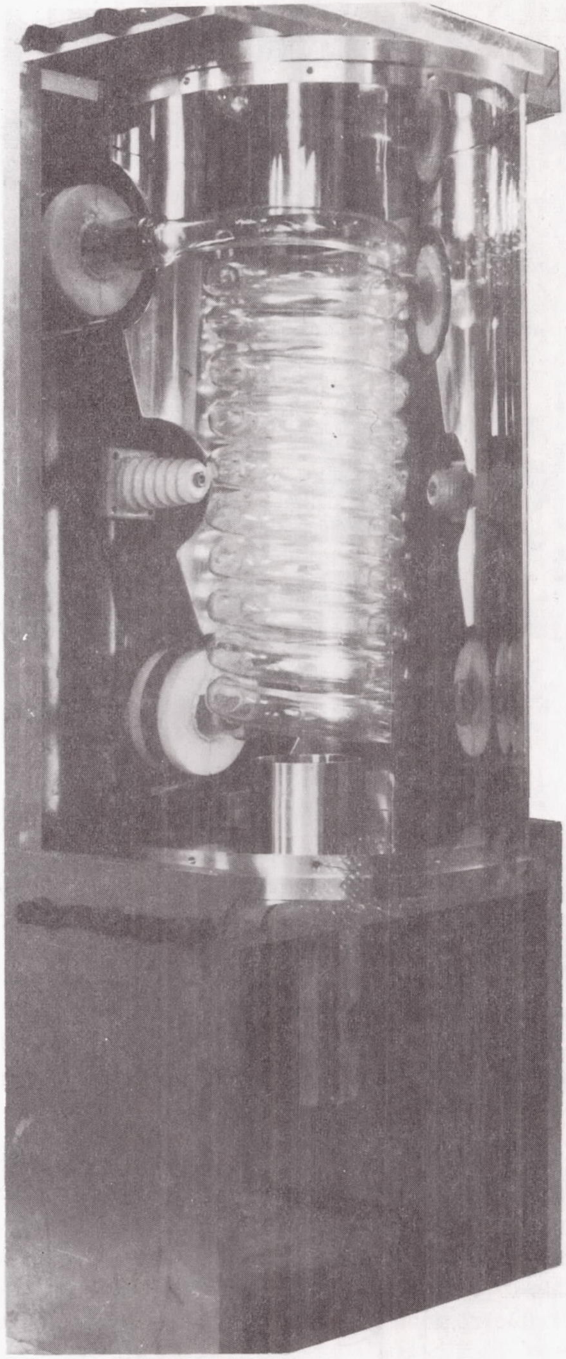

FIGURE 1. INTERIOR VIEW OF 240 kJ RUBY LASER GUN

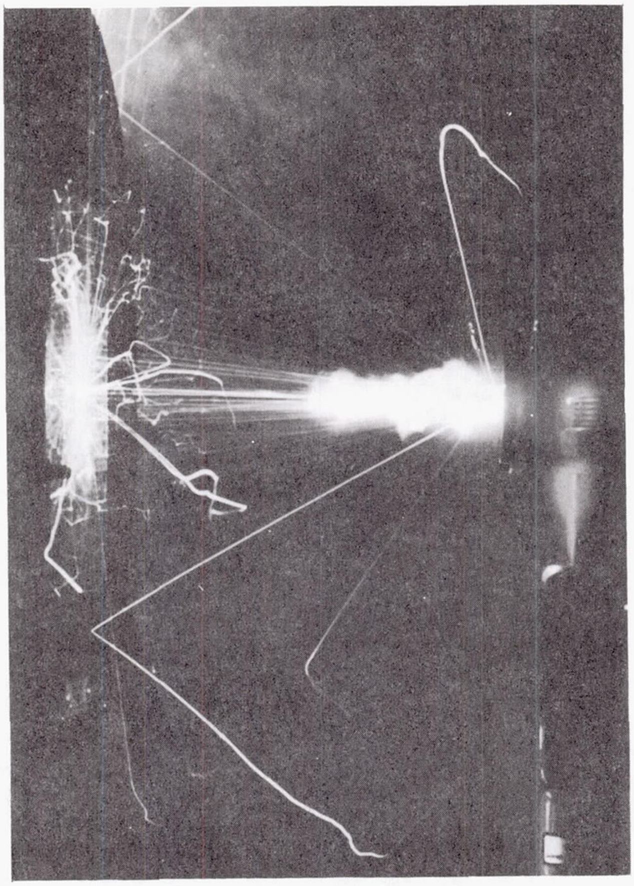

FIGURE 2. LASER PENETRATION OF 0.635-cm (0.25-in.) THICK ALUMINUM SHEET

Two problems that are annoying with rapid-pulse repetition rates are (1) radiation damage to the crystal by the intense ultraviolet (uv) output from the lamp, and (2) keeping the crystal cool enough so that the threshold for lasing remains reasonable. New Pyrex filters will stop almost all the uv radiation from reaching the crystal, but at high lamp intensities the Pyrex will solarize badly. Liquid nitrogen is used to cool the crystal, but it is relatively difficult to use and is somewhat hazardous.

Figure 3 shows the light output from our flash tube. When the radiation gets this high in the visible light region, it can be easily seen that the uv radiation is tremendous because when flash tubes are run at this level the uv output is greater than the light in the visible region.

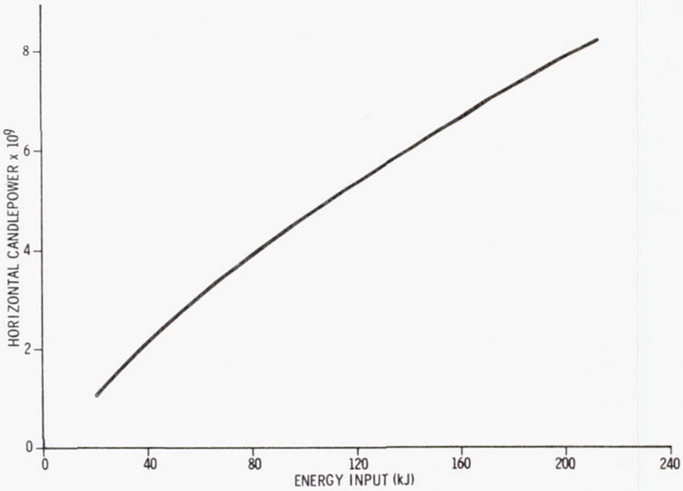

FIGURE 3. FLASH TUBE LIGHT OUTPUT

It is this laboratory's opinion that a liquid coolant is needed for the laser. This liquid coolant should have the following properties, listed in the order of their relative importance.

1. Excellent ultraviolet absorber.
2. Transparent in the pumping bands for ruby lasers.
3. Extremely low freezing point.
4. Liquid at ambient temperatures.
5. Large specific heat.
6. Inexpensive and readily available.
7. Nontoxic.

A contract was negotiated with Auburn University to investigate possible liquid coolants. This contract has not yet been concluded, but so far it has been found that a mixture of substances will probably be the best solution. The result will probably be a silicone oil because of its stability as a coolant when mixed with a uv absorber material.

Elements on the periodic chart that have unfilled inner electron orbits exhibit intense absorption bands. If it is possible to find an element with this property that absorbs at the proper wavelengths for the laser crystal, then this element will make a much better solute than any compound that absorbs energy between a bond of two atoms, because the absorption of tremendous amounts of radiation will destroy the bond and decompose the solute.

There are three primary groups of elements that have unfilled inner electron shells: the transition metals, the lanthanide series, and the actinide series. Absorption spectra have been run on a majority of the transition metals including manganese, iron, cobalt, nickel, and copper, chosen because of their low cost and availability. Of all these, copper is the only element that absorbs at the proper wavelengths to be an effective laser coolant solute.

The most suitable coolant will probably be a suspension of copper sulfate in a silicone oil. Since the silicone oils have an affinity for glass, the copper sulfate will probably be mixed in glass in the molten state. After cooling, the glass will be powdered and mixed in the oil.

Another contract has been awarded to the Linde Crystal Division of Union Carbide Corporation to investigate the damage done to ruby crystal by uv radiation. It is possible that the Cr^{+++} ion becomes Cr^{4+} or even Cr^{6+} from the radiation. Of course, Cr^{4+} and Cr^{6+} will not lase.

A sample of the original boules from 5 crystals was subjected to spectroscopic analysis. These 5 crystals were used by this laboratory until badly damaged by radiation and were then shipped to Linde Crystal Division where another sample was cut from the rod. Preliminary spectroscopic analysis of these samples shows that the crystal becomes absorbent at 6934 Å. It is hoped that with a better understanding of how degradation occurs in the crystal when it is exposed to radiation, it may be possible to make rods more radiation resistant.

When cutting and hole punching are done with a pulsed laser, the best cuts are made when the material is completely vaporized. This produces clean cuts and the absence of tears on the back of the material. The pulsed laser does a good job of vaporizing material, and is superior to the CW laser when used for this task.

CONTINUOUS WAVE LASER

An important consideration in the application of lasers in the welding field is efficiency. Generally the laser is simply not efficient. The most efficient laser with respect to power requirements is the CO_2 laser. This CW laser will operate at an efficiency as high as 15%. To weld metals of practical thickness, at least a 500 W input into the weld zone is needed. When considering 95% reflection at this wavelength in aluminum, the power requirement is increased to about 72 kW. In spite of this, the CO_2 laser is the most efficient laser for welding. The main drawback is the huge size of the laser; one meter of discharge tube is required for every 50 W of output. This means that a 500 W CO_2 laser would be roughly 10 m (30+ ft) long. Obviously any welding job done with this laser would have to be brought to the laser, instead of the laser being transported to the job. Otherwise a very expensive optical system would have to be made to guide the laser beam. Therefore this laboratory took the next best choice and decided upon the YAG laser. Here the lasing element is a small YAG crystal, and the welding head for this laser would not be so large as to be impractical. The acronym YAG means Ytterbium Aluminum Garnet.

Accordingly, a 100 kW argon vortex arc light pump (Fig. 4) was made for this laboratory on a contract with the Korad Division of Union Carbide. This equipment has been received and will be tested as soon as it can be hooked up. The output of this welding head should exceed 300 W at a wavelength of 1.06 μ.

Figure 5 shows a close-up view of the pressure control panel. These argon arc lamps are potentially explosive. The higher the gas pressure the more intense the light. Pressures of 7 MN (1000 psi) are not uncommon, although this lamp uses 2.1 MN (300 psi) gas pressure. A closeup of the electrical control panel is shown in Figure 6; and Figure 7 shows a close-up of the lamp assembly. This unit is small enough to fit on a Linde side-beam carriage so that no special fixture will have to be made to use it for welding. Also this unit was designed to operate from two standard electric welding machines for power supplies. This is a great saving of money in building this apparatus. If this machine is successful, it can weld sheet metal up to 0.635-cm (0.25-in.) thickness as easily as a tig (tungsten inert gas) or mig (metallic inert gas) welder can do the job. This ought to make the laser a practical tool for the shop.

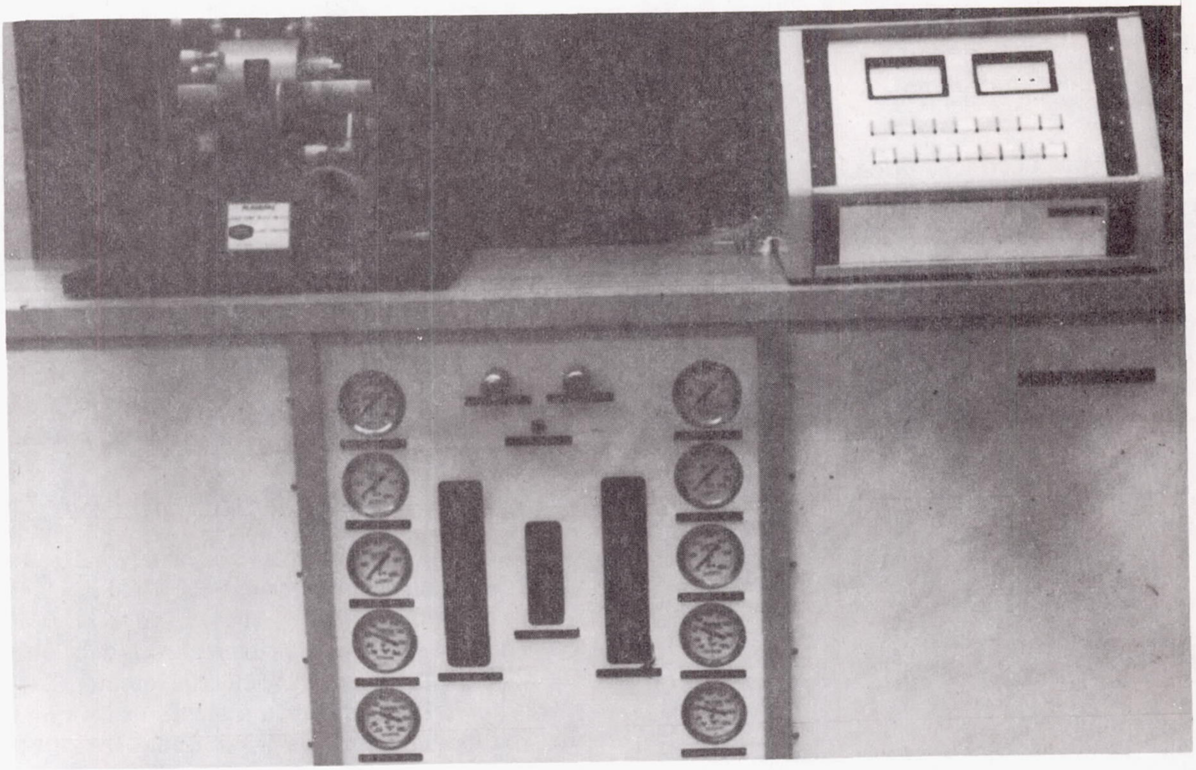

FIGURE 4. VIEW OF 100 kW VORTEX ARC PUMP

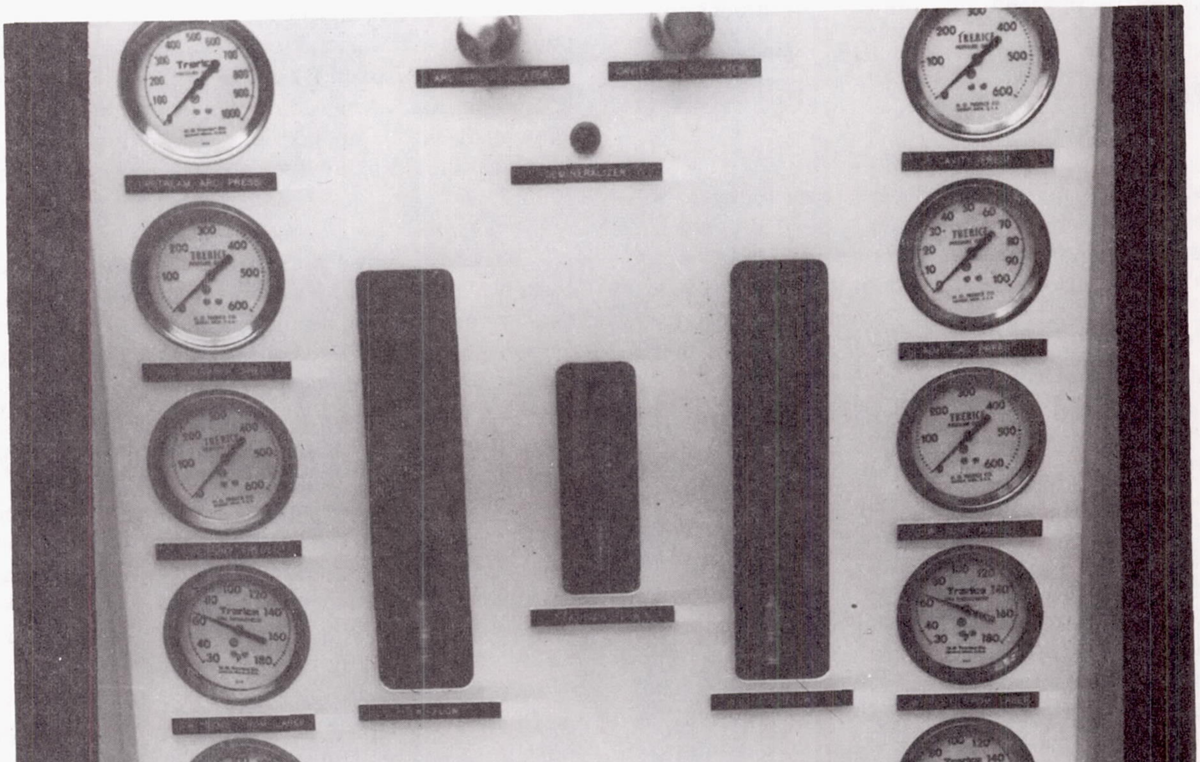

FIGURE 5. PRESSURE CONTROL PANEL

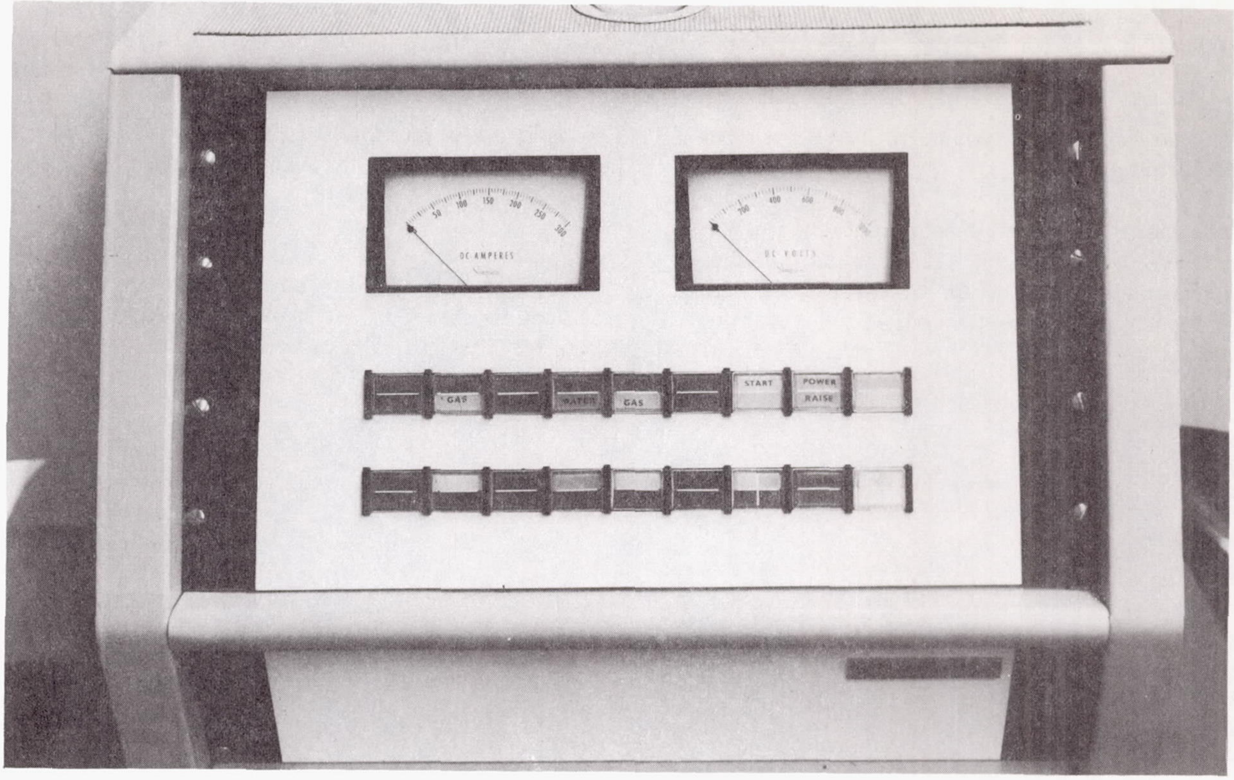

FIGURE 6. ELECTRICAL CONTROL PANEL

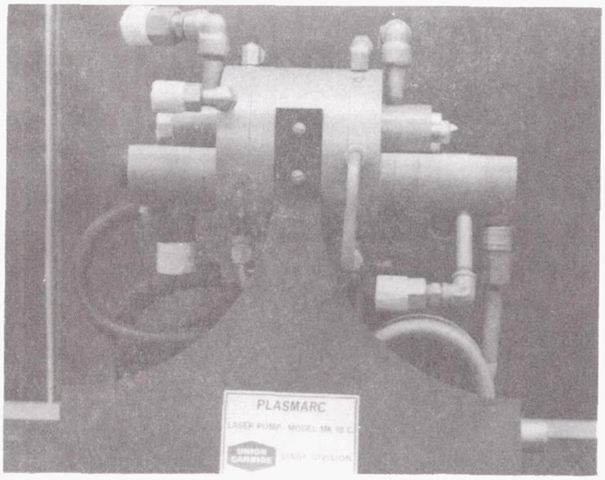

FIGURE 7. LAMP ASSEMBLY

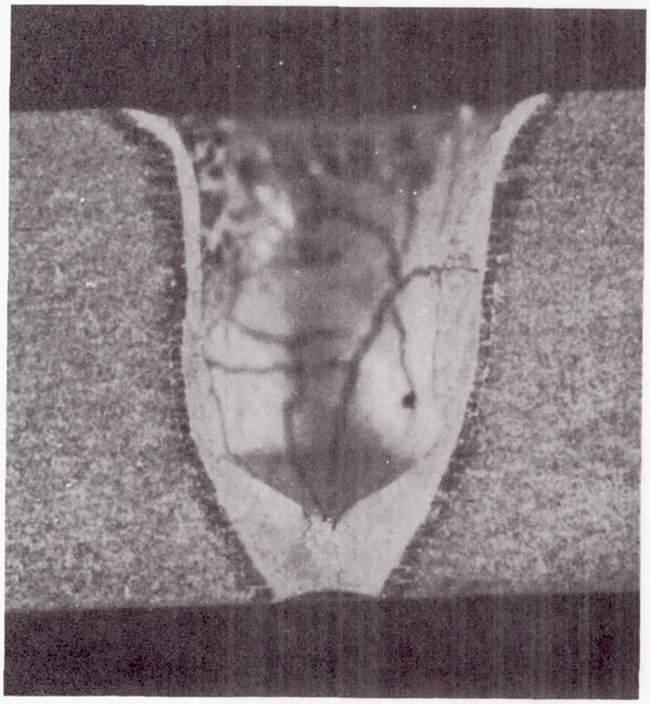

FIGURE 8. WELD CRACKING IN THICK MATERIALS (PULSED-LASER WELD)

Figure 8 shows the cracking and porosity that result when trying to weld with a pulsed laser in thick material. This laboratory favors the continuous wave laser approach to welding seams. The weld nugget shown is in 0.635-cm (0.25-in.) thick aluminum.

The laser has several unique properties that can be exploited when used for welding. These are as follows:

1. The source of heat will not in itself contaminate the weld in any way.

2. The laser will weld at relatively great distances from the welding head. This means that the weld could be made inside a pipe or valve where the opening is too small to insert a conventional welding head or torch.

3. The laser beam can be projected through glass without harm to the glass. If a toxic material such as beryllium needs to be welded, a box vented to a safe location could be fitted with a glass top. The weld material could be placed in the box and the laser beam projected through the glass and a weld made with perfect safety.

4. If it is desired to bore extremely hard material such as diamond, or if extremely small holes are to be bored, a high powered pulsed laser is ideal.

NEUTRAL BUOYANCY SIMULATION

By

Charles R. Cooper, Paul H. Schuerer,
and Ronald L. Nichols

SUMMARY

With the advent of the Apollo Applications (AAP) Program, it became apparent that Marshall Space Flight Center (MSFC) would be called upon to develop hardware that would be man operated in a zero gravity environment. A capability for evaluating the hardware to be produced was urgently needed.

In 1966 a small electrohydraulic forming tank was converted for use as the first neutral buoyancy facility. This tank was 1.8 m (6 ft) in diameter and 2.4 m (8 ft) deep. The first task assignment was to evaluate a Marshall concept for the S-IVB Orbital Workshop hatch cover; and the tests were made with the diver wearing scuba gear.

In 1967 Marshall converted its explosive forming tanks into a neutral buoyancy facility; this facility and associated equipment will be described in this paper.

INTRODUCTION

MSFC is engaged in two types of zero gravity simulation testing: mechanical simulation and neutral buoyancy. Two distinct advantages of mechanical simulation are that (1) preparation times are short, and (2) the test environment is relatively free of hazards. However, mechanical simulation testing has limited application because of handicaps created by the equipment when conducting task studies. This limitation is one of the major reasons why MSFC decided to develop a capability in neutral buoyancy testing.

The three major objectives to be achieved through zero gravity simulation testing are as follows:

1. To provide information on spacecraft and component design concepts prior to freezing the design for production of test items.

2. To provide statistical data to the design engineers on the capabilities of men working under zero gravity conditions.

3. To be a method of evaluating hardware by testing under conditions that simulate zero gravity of the space environment in which the components will eventually function.

NEUTRAL BUOYANCY FACILITIES AND EQUIPMENT

The operational structure from which neutral buoyancy tests are conducted is shown in Figure 1. This structure possesses the highest degree of safety devices for conducting these tests. The entire operation is controlled by the Test Conductor who has overall responsibility during any test being performed.

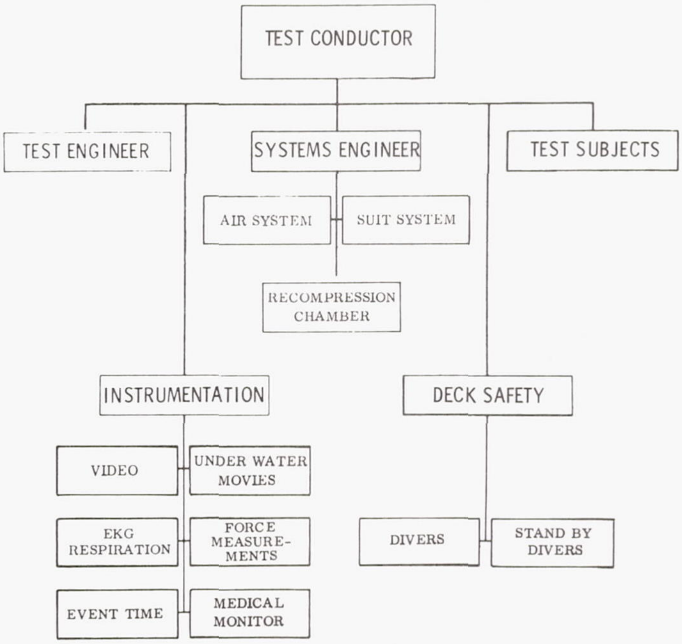

FIGURE 1. OPERATIONAL STRUCTURE

The Test Engineer's primary function is to explain to the diver the sequence of events to be accomplished in the tank. The Systems Engineer is responsible for the air system, suit system, and recompression chamber. Hopefully, the recompression chamber will never have to be used, but when working with underwater activities at depths and pressures being planned for future tests, it is a necessary piece of equipment. Skilled divers perform the underwater tests. The Deck Safety is also the above-water observer for the test. The Instrumentation Engineer is responsible to record all the data and to monitor the instruments while the test is being performed.

Figure 2 shows a schematic of the present facility. There are two tanks in the area: a small 4.6 m (15 ft) diameter, 3.1 m (10 ft) deep tank that is used in good weather, and a larger tank, 7.6 m (25 ft) in diameter and 4.6 m (15 ft) deep, in which most of the tests are currently performed. This larger tank is covered with an air structure containing the control panels (Fig. 3). The tank has one air lock for personnel and another air lock through which large mock-ups and equipment are transported (Fig. 4). The instrumentation (Fig. 5) and recompression chamber (Fig. 6) are housed in the structural area near the tank.

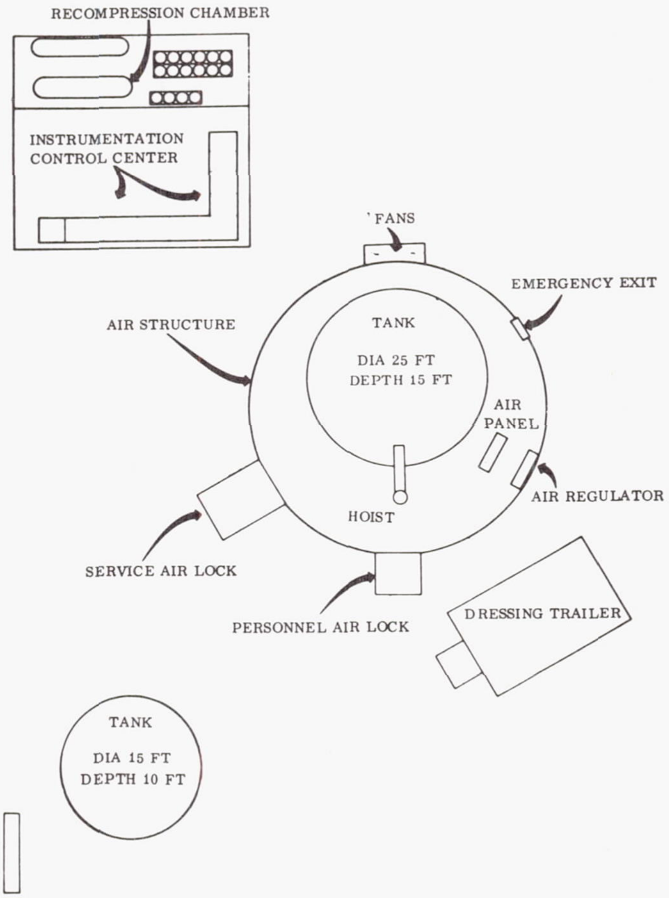

FIGURE 2. SCHEMATIC OF NEUTRAL BUOYANCY FACILITY

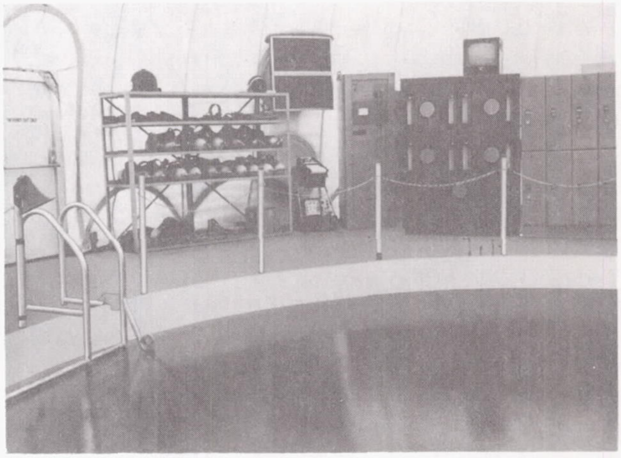

FIGURE 3. TANK WITH SUIT AND HELMET PRESSURE MONITORING EQUIPMENT

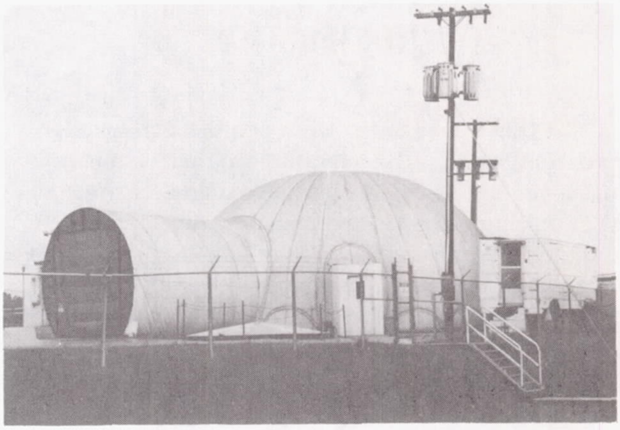

FIGURE 4. AIR STRUCTURE FOR NEUTRAL BUOYANCY FACILITY

When neutral buoyancy testing was initiated, divers had to use scuba gear instead of pressurized suits. One of the most significant advances since then is the introduction of pressure suit testing.

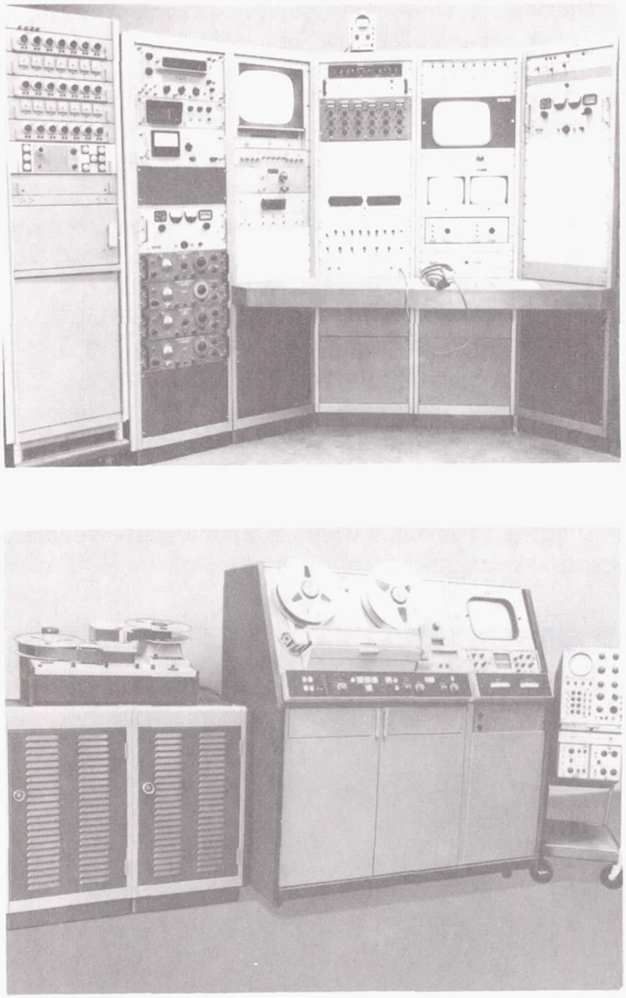

FIGURE 5. MONITORING AND RECORDING EQUIPMENT

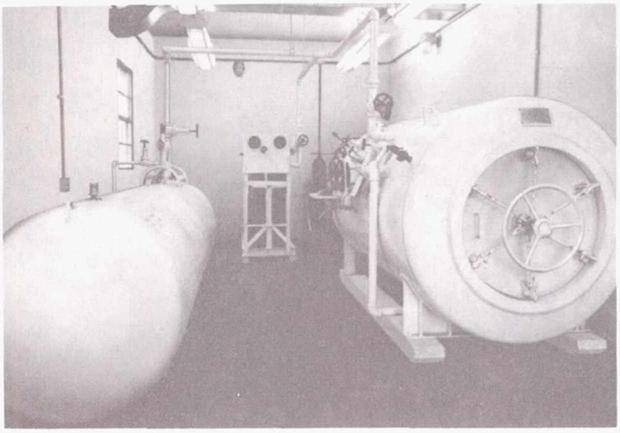

FIGURE 6. RECOMPRESSION CHAMBER

Figure 7 shows some of the types of instruments to record measurements. A continuation of these programs will allow expanding and improving the data acquired from these devices.

BIOMEDICAL, METABOLIC AND ENVIRONMENTAL

A. Six Channel Telemetry (Low Level)

1. EKG
2. Respiration
3. Internal Body Temperature
4. Skin Temperature
5. Differential Pressure
6. Absolute Pressure

B. Carbon Dioxide Monitor (2 Channels)

EXPERIMENT INSTRUMENTATION

A. Magnetic Tape Recorder (14 Channels)

B. Strip Chart Recorder (8 Channels)

C. Signal Conditioning and Amplifiers

D. Transducers

VIDEO EQUIPMENT

A. Ampex VR 2000 and VR 1500 Recorders

B. Underwater Cameras (3)

C. Above-Water Cameras

PHOTOGRAPHY

A. Underwater Movie Cameras (2) 16 mm

B. Underwater Still Cameras (2) 35 mm

C. Above-Water Movie and Still Cameras

FIGURE 7. INSTRUMENTATION

Telemetry equipment is used to measure EKG, respiration, internal body temperature, differential pressures, absolute pressure, and carbon dioxide concentration. Instruments to record the data include magnetic tape recorders, strip chart recorders, signal conditioning devices, amplifiers, and transducers for measuring forces in force measurement studies. Video equipment consists of Ampex VR 2000 and VR 1500 recorders, and underwater and above-water cameras.

NEUTRAL BUOYANCY TESTING

The Human Engineering Maintenance and Repair Study was a program to gather statistical data on the amount of force that could be applied by a diver wearing a pressure suit and working against various types of restraint systems. Variables in the program included (1) test subject, (2) type of suit pressurization, (3) restraint systems, and (4) orientation of the force measuring apparatus.

In Figure 8, the diver is performing activities in the Human Engineering Maintenance and Repair Study. He is wearing an Apollo State-of-the-Art pressure suit with a modified helmet having pressurization modes of water or air. This suit is air pressurized to 24 000 N/m^2 (3.5 psi). The diver is operating a force receiver that transmits data to a digital tape recorder.

The cue panel that the driver reads to obtain instructions is shown in Figure 9. The test engineer in the instrumentation control center has a cue panel that matches this one to instruct the diver orally and visually to perform an operation.

The translation study on the Apollo Telescope Mount (ATM) included developing a handrail that could be used by the astronaut to maneuver from the Lunar Excursion Module (LEM) work station of the ATM to the Sun work station on the opposite end. Figure 10 shows the evaluation of this translation device when attached to the exterior of the ATM. The diver is translating from the Lunar Module (LM) work station to the Sun work station with the assistance of this mobility aid, and is performing this test in a Mark IV full pressure suit.

Figure 11 shows a diver in scuba attire performing a mass transfer study of moving packages through

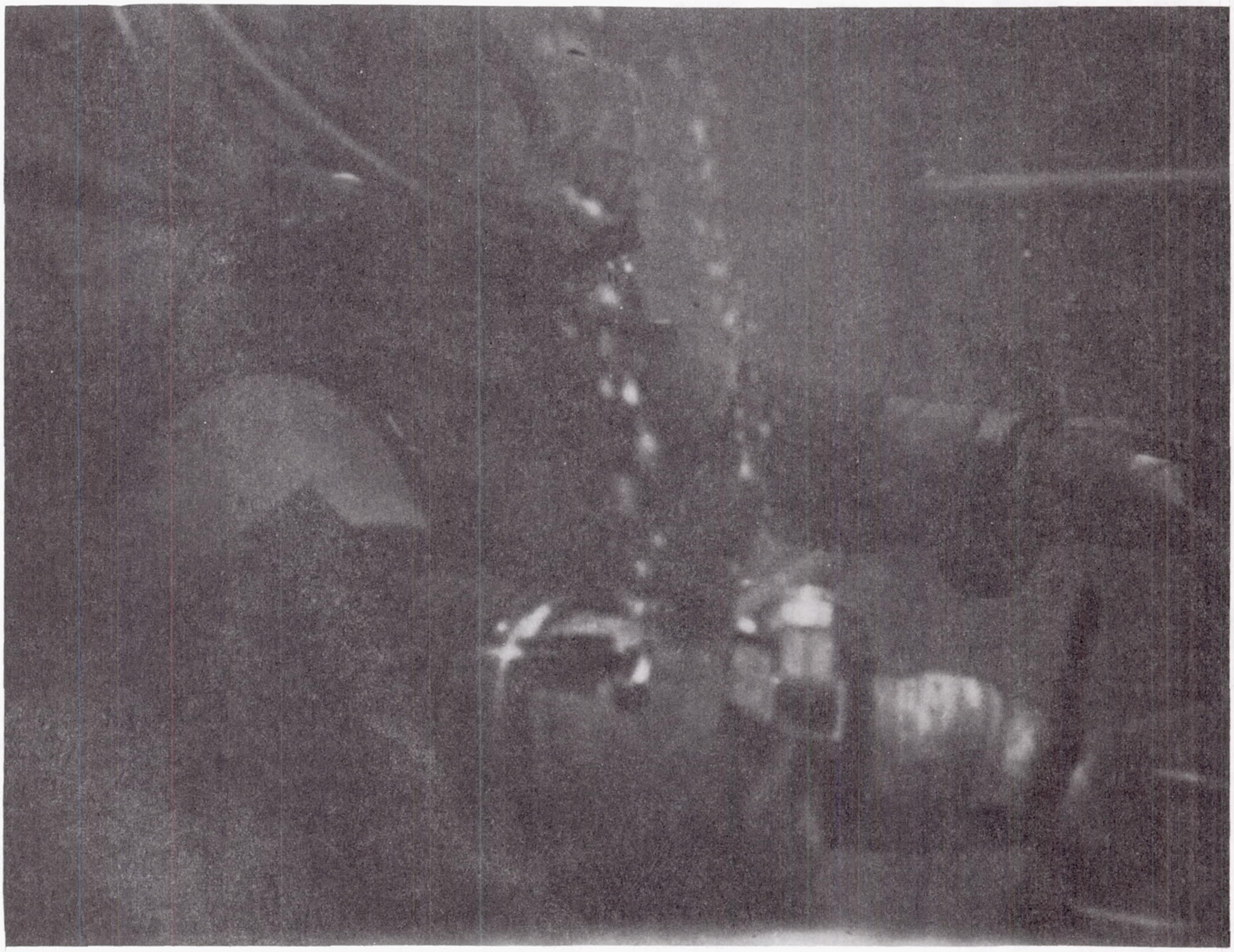

FIGURE 8. TEST BEING PERFORMED IN APOLLO PRESSURE SUIT

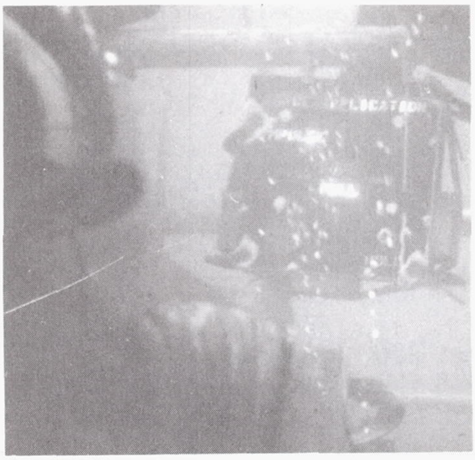

FIGURE 9. CUE PANEL ISSUING INSTRUCTIONS TO DIVER

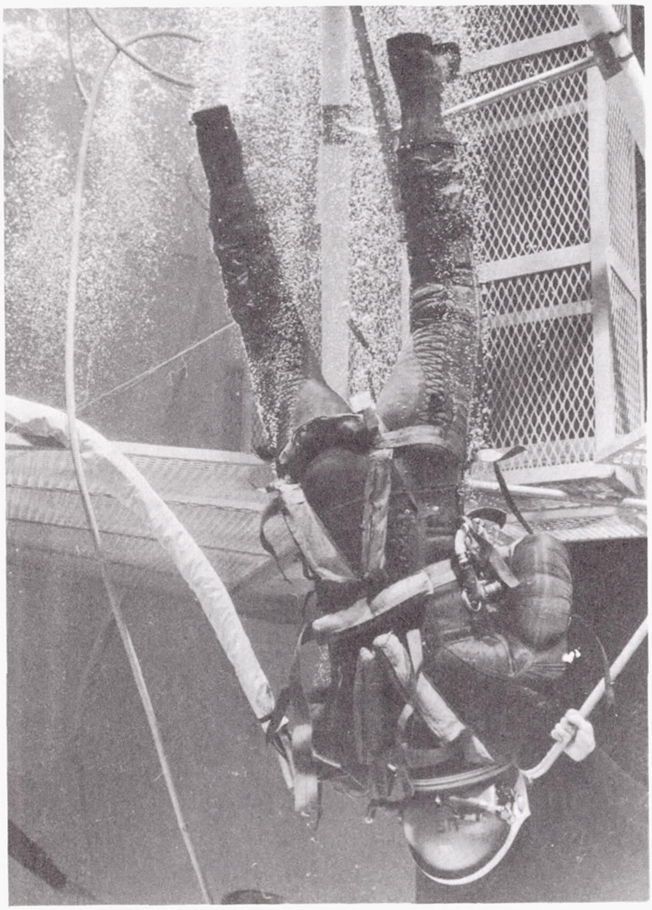

FIGURE 10. TRANSLATION DEVICE TEST IN MARK IV PRESSURE SUIT

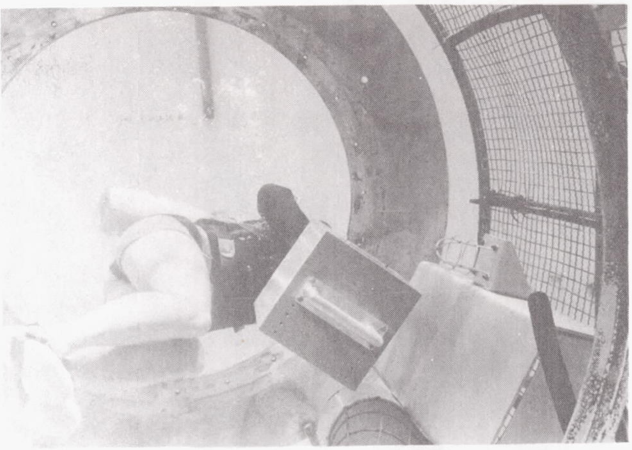

FIGURE 11. MOVEMENT OF EQUIPMENT INTO THE ORBITAL WORKSHOP

the airlock module into the Orbital Workshop. One of the preliminary Orbital Workshop evaluations was to determine if the floor grid would be useful as an aid in maneuvering throughout the Orbital Workshop crew quarters (Fig. 12). The diver was pressurized to 24 000 N/m^2 (3.5 psi) in the Mark IV suit and was wearing Apollo thermal gloves. The test program established that the floor grid was a mobility aid.

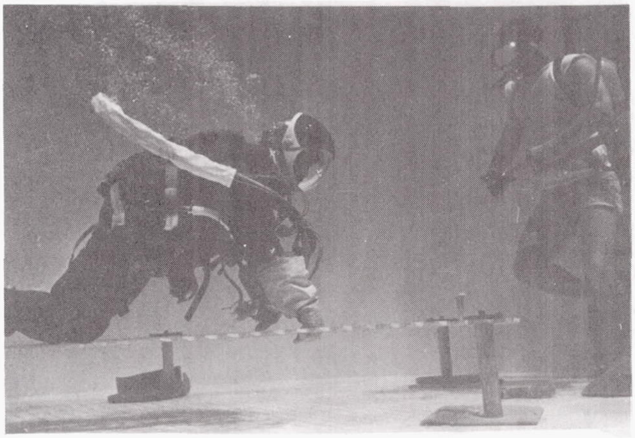

FIGURE 12. MOVEMENT OF EQUIPMENT ACROSS THE FLOOR GRID OF THE ORBITAL WORKSHOP

Prior to activating the S-IVB Workshop, it is necessary to double seal all penetrations through the tank wall. Under normal conditions, this would be accomplished in an unpressurized suit. Under Contingency Mode Conditions, however, it would be necessary to accomplish this task in a pressurized suit.

In Figure 13 the diver is performing one of the tasks required to seal all the penetrations in the aft

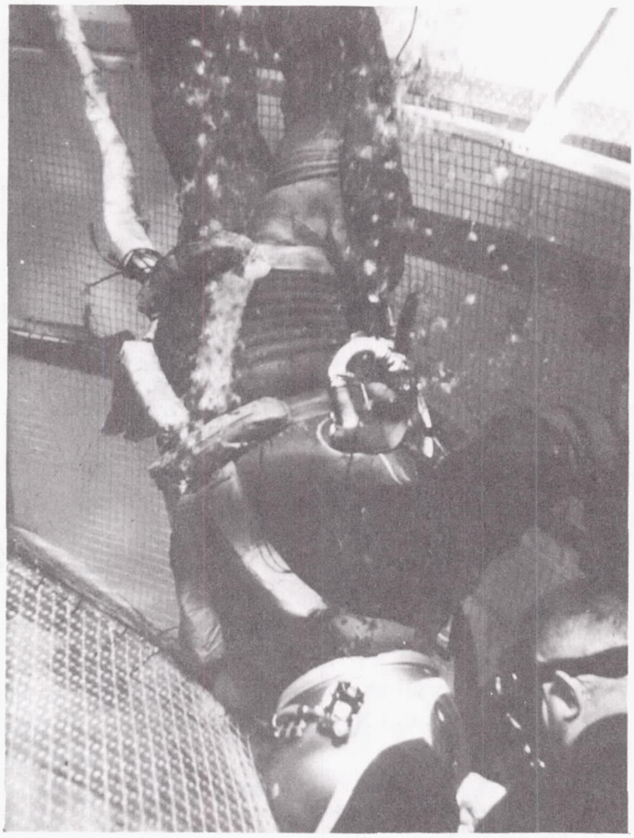

FIGURE 13. SEALING THE AFT DOME PENETRATION OF THE ORBITAL WORKSHOP

dome section of the Orbital Workshop. Although these penetrations are sealed by valves, mechanical seals will be installed as an additional safety measure to ensure that the module remains pressurized. Four sealing devices are required: the LH_2 chill pump seal, the LH_2 feed line plug, chill system return line seal, and the fill and drain line plug.

CONCLUSIONS

1. Neutral buoyancy provides the most realistic long time simulation of zero gravity conditions. Other simulation techniques are limited to either short test times of a maximum of 30 sec in the parabolic flight of the KC-135, or to localized work areas, as is the case with mechanical simulators. Zero gravity testing under neutrally buoyant conditions can be conducted over several hours and is restricted only by the physical capabilities of the man performing the test and the confines of the pool in which the test is being conducted.

2. Primary benefits are obtained when tests are conducted with the diver in a pressure suit. Most individuals possess an inherent knowledge of man's capability to perform work under zero gravity conditions if he is not restricted by a pressure suit. This may be related somewhat to experiences connected with swimming. This knowledge is not available, however, when a man must work in zero gravity while constrained by a pressure suit.

3. Probability of mission success can be significantly improved by both evaluating hardware and training personnel in its use under zero gravity conditions. Hardware must be tested in the environment in which it will be used to determine the best design and the amount of personnel training required.

4. Instrumentation and equipment must be improved and/or developed to more closely equate the water and space environments. Work to date indicates many areas in which further development is required. Medical monitoring systems need to be improved and expanded. Hopefully, hard wires can be eliminated between the test subject and surface mounted instruments so that eventually the diver will be completely free of outside attachments. This will require providing the diver with a miniaturized breathing apparatus, and alternate methods of data transmission must be found. Perhaps the use of liquid air would be another solution to this problem.

Improved systems for making the divers neutrally buoyant are required. The present system of weights is time consuming to employ, although it is effective.

New, neutrally buoyant, high-strength materials, from which more realistic mockup components can be produced, must also be found.

These are but a few of the many equipment and hardware developments needed. In the coming months improved mockups should be available of all AAP hardware for which MSFC has design or fabrication responsibility. Experience to date from MSFC and other personnel who have used the neutral buoyancy facility indicates the value of this type of zero gravity simulation testing and is an encouragement for its continued use in the AAP and follow-on programs.

ALUMINUM WELDING DEVELOPMENT COMPLEX

By

Robert V. Hoppes

SUMMARY

First, a description of the past welding situation and identification of the first group of studies are presented. Second, a review of technical data and how an analysis of such data have led to new studies are discussed. Finally, a summary of welding contributions to the Saturn V vehicle and to technology in general is described.

INTRODUCTION

In 1963 a survey of the aerospace industry was made to determine common aluminum welding problems, what was being done about these problems, and what areas still needed investigation. It was expected that the survey would find duplication of effort and redundancy, but this was not the case. Each company was either concentrating on a unique problem, or was employing a distinct approach. On the other hand, none of the companies was attempting to survey the whole area of fusion welding. It was decided that MSFC could most effectively function by compiling and analyzing the results from the many studies about fusion welding, and thus determine which future studies were needed to solve complex welding requirements.

In 1964 a symposium was held in which Marshall and industry representatives discussed common welding problems and postulated solutions. A general outline for a comprehensive welding development program was then formulated, and the first group of studies in this program included the following aspects of welding:

1. Defects (in particular, porosity)
2. Mechanical strength of weld joints
3. Transferability of welding parameters (process control)
4. Process and equipment improvement

During 1964 and 1965 several studies were initiated (Fig. 1). The area of porosity was broken into the subareas of (1) the source of porosity, in which shielding gas, material composition, and material surface were studied, (2) porosity formation, in which the mechanism of formation and porosity inhibitors were investigated, and (3) the effect of weld defects on joint performance.

Mechanical strength and processes and equipment were covered by studies of (1) welding energy effect on Al alloy strength, (2) new power sources with different wave shape combinations, (3) magnetic shaping of the Gas Tungsten Arc to increase its power density, (4) data transfer, that is, how to confidently transfer welding techniques and procedures from the laboratory to production, or from facility to facility, (5) development of plasma and nonvacuum electron beam systems, and (6) development of a solid state brazing generator.

TECHNOLOGICAL DEVELOPMENTS

Analysis of this generation of studies has made it possible to further define welding development needs and to concentrate on more significant areas. A summary of data from the 1964 through 1966 studies is discussed with respect to meeting these developments. From a quantitative study of contaminants in helium shielding gas, a tentative guide has been constructed for space vehicle fabrication (Fig. 2). The guide shows contamination levels where significant changes occur. Weld density begins to increase with 250 ppm of oxygen and to decrease with the same amount of hydrogen; porosity begins to occur with 350 ppm contamination; the welding arc begins to

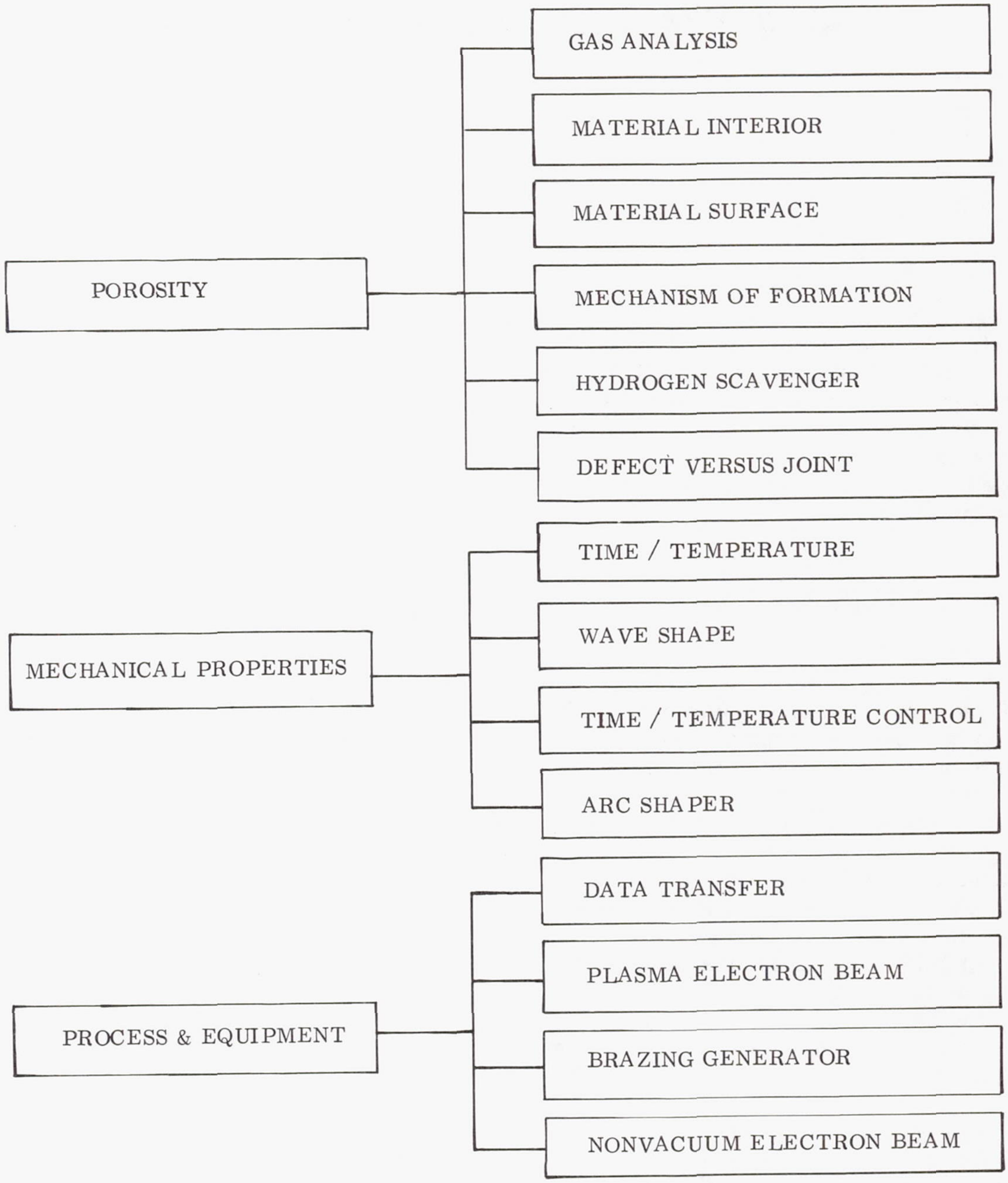

FIGURE 1. WELDING DEVELOPMENT COMPLEX (1964 - 1966)

waver at 800 ppm contamination, etc. More importantly, it is now known that the shielding gas purchased to the present MSFC specification is a minor source of weld porosity.

In a like manner, the weld defect potential of Al plate was examined with regard to the effect of chemical content, internal impurities, and hydrogen content (Table I). Although statistically there are

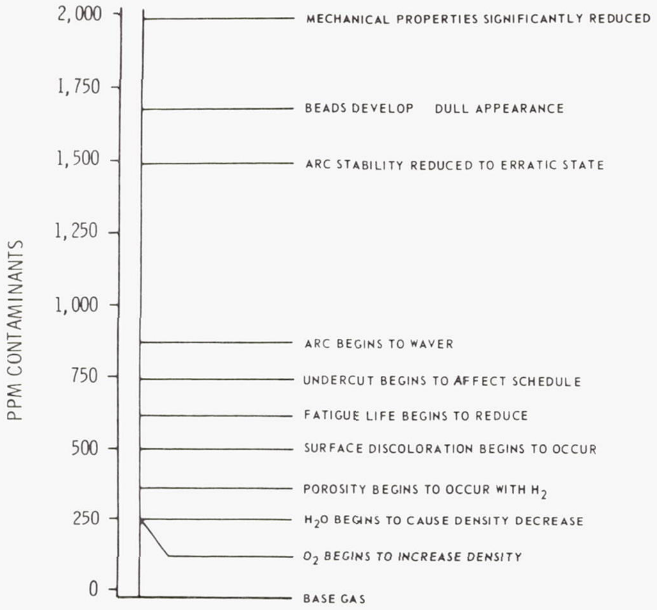

FIGURE 2. CONTAMINATION CONCENTRATION LEVELS AT WHICH SIGNIFICANT CHANGES OCCUR IN WELD QUALITY

TABLE I. VARIABLES VERSUS POROSITY
(In Order of Importance)

1. Arc Shielding - Gas and Water Content
2. Alloying Content
3. Internal Impurities
4. Internal Hydrogen Content

significant differences in the effect of these variables, it was again concluded that material composition is a secondary source of porosity. If materials were fabricated to the upper limits of current specifications, an increase in weld defects could be expected. However, this is not the case; aluminum companies control material fabrication to a remarkable degree of accuracy on the lower limits of specifications.

In the preceding studies there was convincing evidence that contaminants on the surface of the material might be the greatest source of porosity. The investigators calculated that an influx of 0.6% of air saturated with water vapor would result in 250 ppm of hydrogen in the shielding gas. Less than 0.16 mg/cm (1 mg/in) of hydrogen on the surface could generate 250 ppm of hydrogen, and a single fingerprint could cause a 750 ppm increase in hydrogen contaminants.

Laboratory analysis has now confirmed the conclusion that surface contaminants are a major source of porosity. The investigators have made a list of common cleaning procedures and their relative potential for producing defects in welds (Fig. 3). "As-machined surfaces result in defect-free welds. All other treatments induce some degree of weld impairment," the investigators stated. Surface treatments are listed as follows in increasing potential to produce defects in welds: chemically cleaned, chemically cleaned plus stored in water, degreased in benzene, anodized (according to time), and coated with silicon.

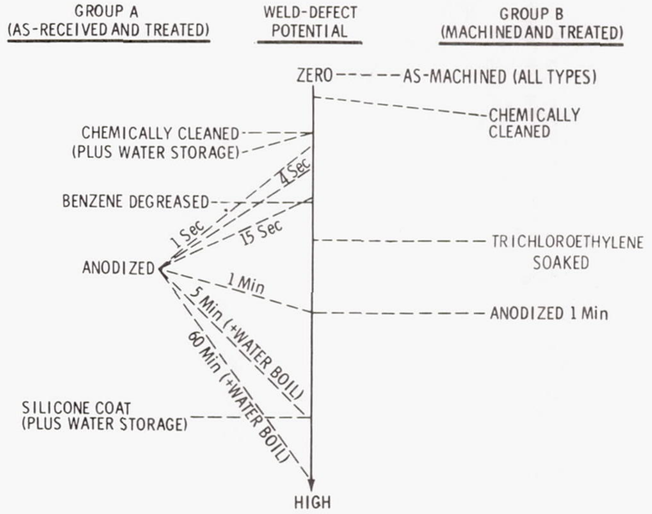

FIGURE 3. CLEANING PROCEDURES

The areas of mechanical properties were covered by an inhouse time-temperature study: a study of the effect of welding energy on the material's strength (Fig. 4). It was concluded that the use of low-energy produces welds with greater strength than those from high-energy welding. Welding energy is expressed as energy in joules of heat per unit length of travel divided by material thickness, or joules/cm^2. As the welding energy in joules decreased, the weld strength increased in 2219 Al weld joints and the peak weld strength of 393 MN/m^2 (57,000 psi) occurred at 1,550 J/cm^2 (10,000 J/in^2), made possible by the highly efficient electron beam welding process. The 2219-T87 Al base metal had a strength of 475 MN/m^2 (69,000 psi) of which about 69 MN/m^2 (10,000 psi) was a result of strain hardening. This metal in the unstrained condition, T6, is listed at 407 MN/m^2 (59,000 psi) weld strength, nearly reached in electron beam welds at 1,550 J/cm^2 (10,000 J/in^2).

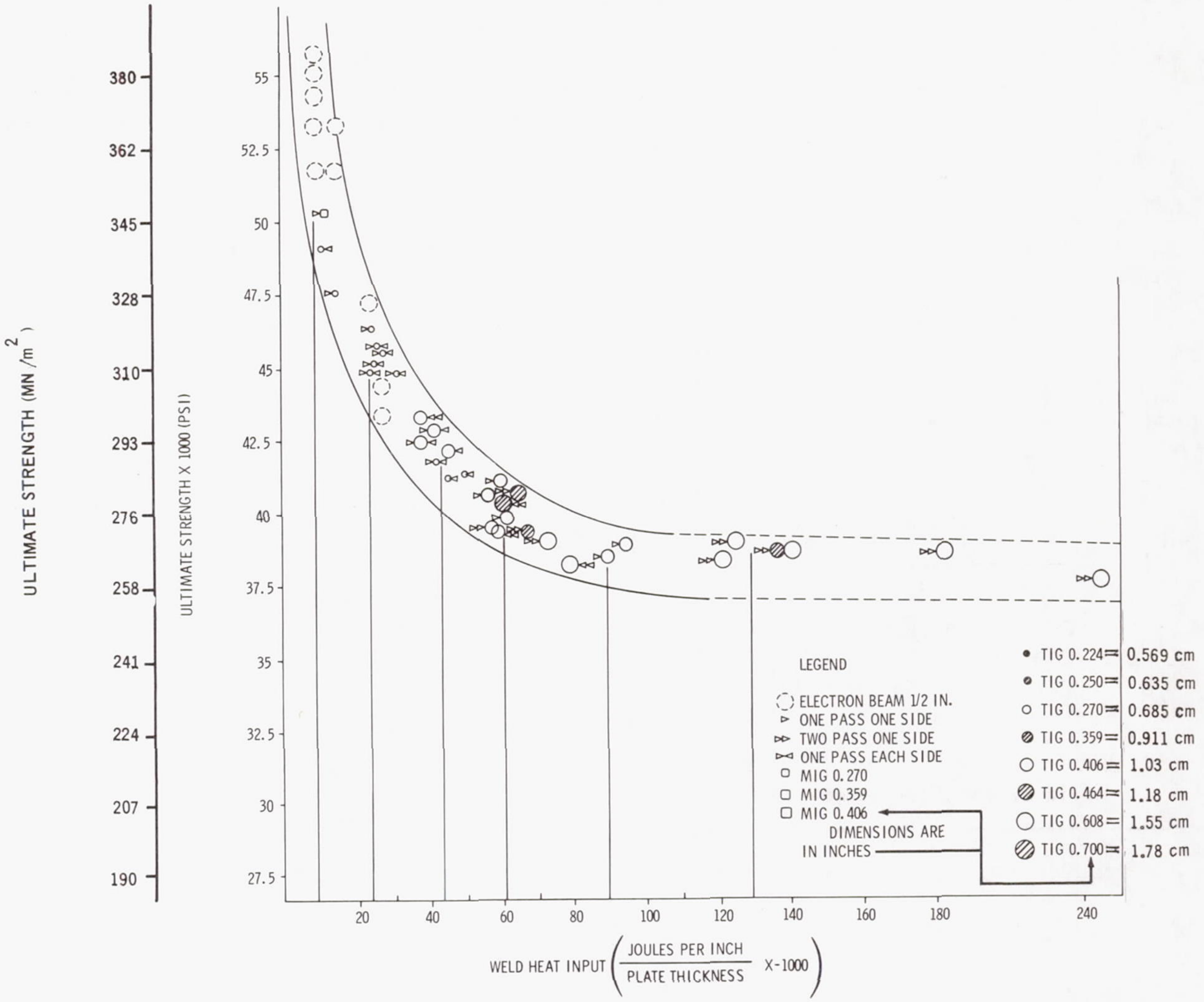

FIGURE 4. HEAT INPUT VERSUS ULTIMATE STRENGTH IN 2219-T87 AND T81 Al ALLOY

Growth of pores (porosity) also is affected by time-at-temperature ratios (Fig. 5). Heating for a long time-at-temperature allows gas to escape from the molten weld puddles; heating the weld area for a short time inhibits pore growth. Unfortunately, most welding is done at a travel speed and temperature that allows gas to expand but not to escape, thus forfeiting the significant increase in weld joint strength obtained in low-energy welding. Porosity frequency plotted against porosity size at different welding travel speeds also shows the effects of thermal gradients or solidification time on porosity formation (Fig. 6). At some level of decreased time-temperature, the formation of porosity should be almost entirely stopped, or at least so finely dispersed that it would not be discernible. Other responses, such as elongation, may require greater energy. In any case, knowledge of the thermal characteristics necessary for any given response allows for purposive, planned uses of welding processes.

Process Control. Some significant progress has been made in the area of process control. Process control is nearly impossible without an efficient system of measurements and records. In addition, records are static in that they represent events that have occurred, and are not influenced by events that are occurring. Keeping records should be preceded by a knowledge of what to measure and to what accuracy. In the past, miles of recording paper have been used, but the variations in the ink lines on the paper were

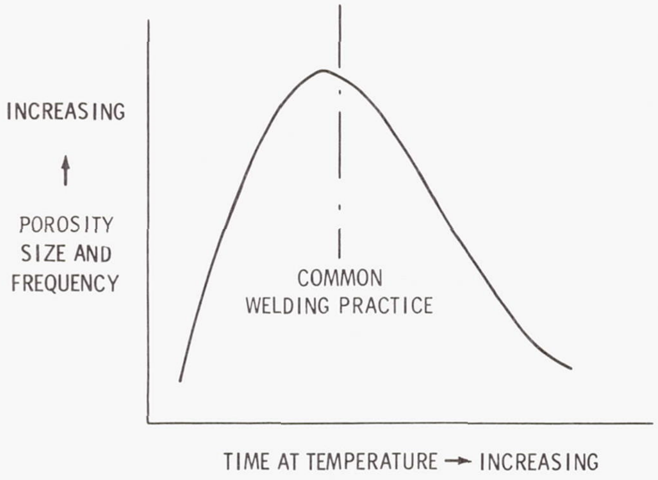

FIGURE 5. TIME-AT-TEMPERATURE RATIOS

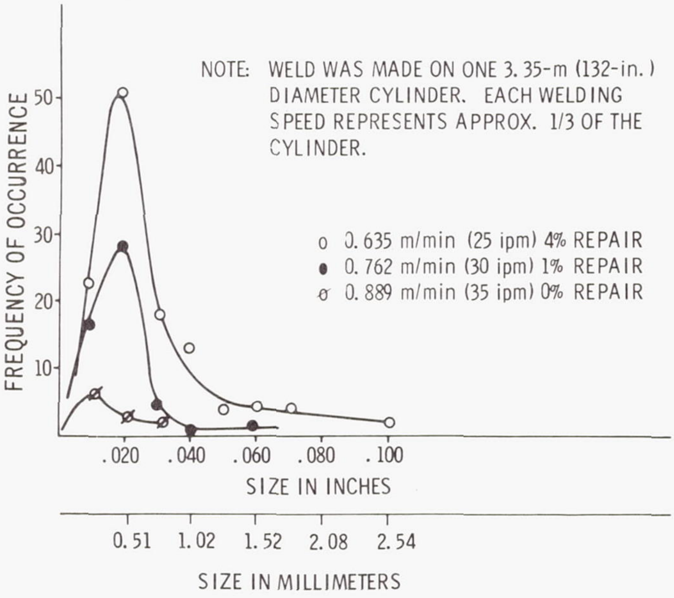

FIGURE 6. DEFECT SIZE VERSUS FREQUENCY IN 0.224-in. THICK 2219 Al MIG SINGLE WELD PASS

seldom used as a mode of inspection; the significance of deviations was not understood. Since 1964, emphasis has been placed on putting meaning into measurements. A welding study at Lockheed was made in two phases. First, an analysis was made of the interaction of several welding variables and combinations to determine their relative importance. Second, a practical measurement and recording system was formulated. Some results of these studies are described in the following paragraphs.

The tungsten electrode position was the most significant variable for controlling yield strength in two side 1.9 cm (3/4 in.) plate welds; it accounted for 41% of the variation measured in yield strength. This tungsten electrode position also appeared in six other regression equations as the second or third important variable.

To review the order of significance of the independent variables as they affect the dependent variables of the weld, it appears that the travel speed (T) is the most important; the electrode position (EP) is second, with the current (C) and voltage (V) being third and fourth, respectively (Fig. 7).

Dependent Variable	Independent Variable	% of Total Variation Explained
Ultimate Strength	T, EP	62.5%
Yield Strength	EP, T	54%
Elongation	T, EP	55.5%
Penetration	T, EP	64%
Area of Melt Zone	T, C, EP	76%

FIGURE 7. ORDER OF SIGNIFICANCE OF INDEPENDENT VARIABLES FOR EACH DEPENDENT VARIABLE

Computer data from the Lockheed program were quite voluminous. The Lockheed program manager proposed the following example of how such data might be applied as a potential process control. Assume that in two side tungsten welding of 1.9 cm (3/4 in.) 2219 aluminum plate it is desirable to control ultimate strength to 6.9 MN/m^2 (1,000 psi), and penetration depth to ±0.0813 cm (±0.032 in.) variation. If any one of the variables changes from an established welding program, the expected result will change as shown in Table II. Here then is the start of a welding process specification (a set of limits that will enable an inspector to put meaning into ink lines on recorder paper). With this information a decision can be made on the acceptability of a weld, and if and where repairs are necessary.

TABLE II. VARIABLES - CHANGES AND RESULTS

If Any Set-Up Parameter is Changed By:	We Can Expect a Change of:
T[0.561 cm/min (0.221 in./min)] EP[0.032 cm (0.0126 in.)] V [0.119 volt] GP[0.458 ppm x 100]	-6.9 MN/m^2 in Ultimate Strength (-1000 psi in Ultimate Strength)
T[2.64 cm/min (1.04 in./min)] EP[0.0675 cm (0.0266 in.)] C [0.2377 amp x 100] D[0.0546 cm (0.0215 in.) dia.] GP[2.8318 ppm x 100] GP = Gas Purity	+0.0813 cm in Penetration (+0.032 in. in Penetration)

The 1967 and 1968 development plan reflects the preceding negative and positive conclusions (Fig. 8). These studies are concentrated in the areas of porosity, metallurgy, power density; and later some problems related to stress were added.

With the assumption that removing metal is the most effective cleaning procedure, plans are being made to clean by machining and to develop instruments for obtaining a quantitative measure of cleanliness.

The inhouse time-temperature studies have shown that low-energy welding produces superior weld joints, but more basic data are needed on what happens to the material structure during the heating-cooling cycle of welding. Thus, engineers at MSFC are currently studying the microscopic disorganization and reorganization of material as affected by the welding energy.

Also involved in low-energy welding is the effort to develop the efficient nonvacuum and plasma electron beam systems; and proposals have been evaluated for a study to increase the power density of the tungsten electrode arc.

Three studies are in process in the area of stress analysis. One study is an empirical and mathematical look at metal movement during welding. Such movement often results in permanent mismatch and angular distortion of vehicle components. To date, computer programs have been developed for (1) prediction of welding isotherms based on energy input and welding speed and (2) prediction of dynamic stress patterns based on isotherms and changing yield strength of the material. From such data, designers may determine the critical rigidity of a component (that point at which buckling or metal movement will occur).

A second study is the reduction of dynamic stress by cryogenic cooling. An area of expanding metal caused by the heat from welding would be bordered by areas of shrinking metal, thus theoretically causing zero stress and consequently zero distortion (Fig. 9).

The third study is concerned with the ultrasonic measurement of residual stresses in weldments. This is particularly important in repair welding. Repeated local heating of the material creates unidentified complex stress patterns that can be detrimental to the performance of mechanical joints. This unknown residual stress lowers confidence in the reliability of the mechanical joint.

CONTRIBUTIONS TO SATURN V PROGRAM

Some principal contributions to the Saturn V program have come from this weld development survey.

First, the importance of material preparation has been established. A welding technique that includes metal removal as the optimum cleaning procedure was demonstrated. Second, data that stresses the benefits of discriminate use of energy (low-energy welding) was distributed.

Third, it was shown that (1) shielding gas and material composition are minor sources of porosity, (2) welds are not improved by arc shaping and exotic power sources, and (3) expensive humidity-controlled clean rooms will not in themselves ensure quality welds, but have limited use in preventing recontamination of carefully cleaned aluminum surfaces.

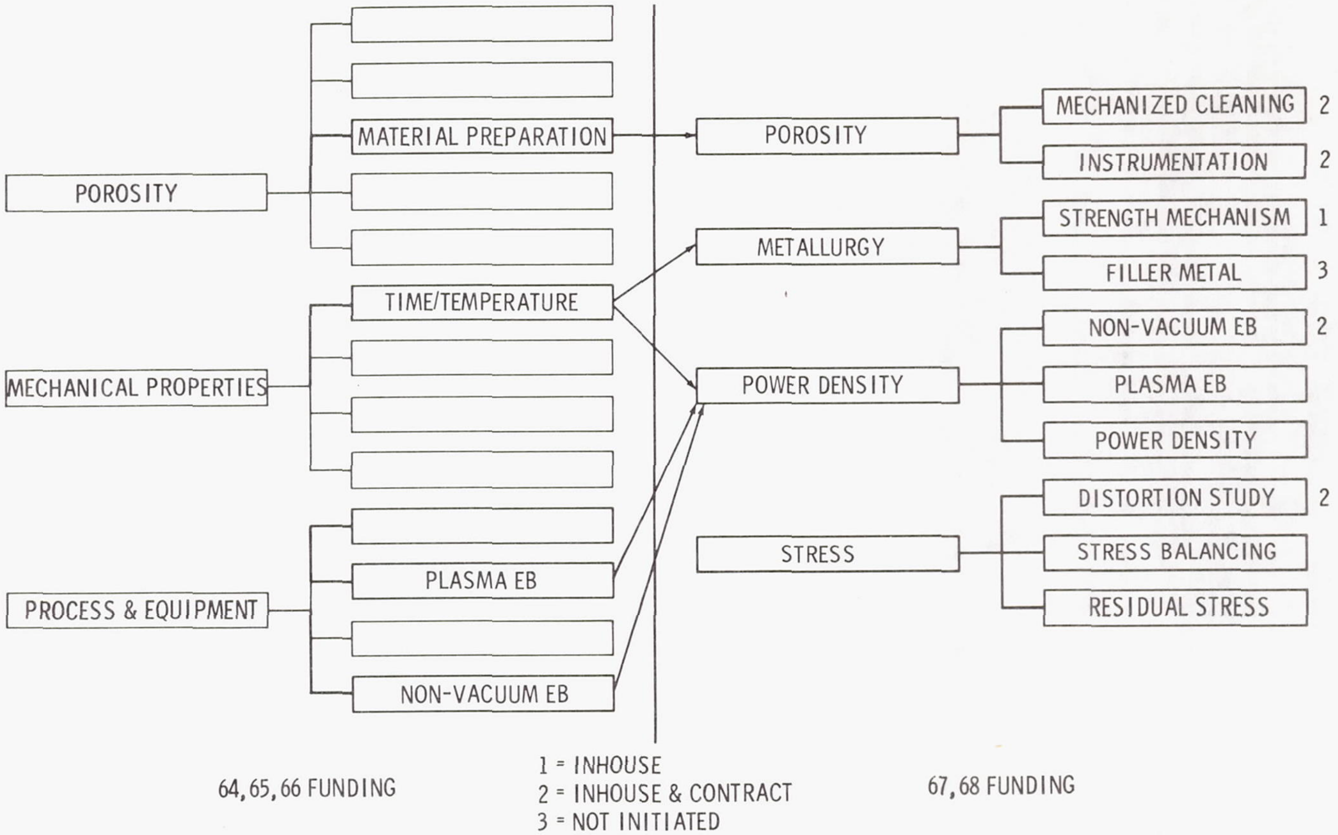

FIGURE 8. WELDING DEVELOPMENT COMPLEX (1967 - 1968)

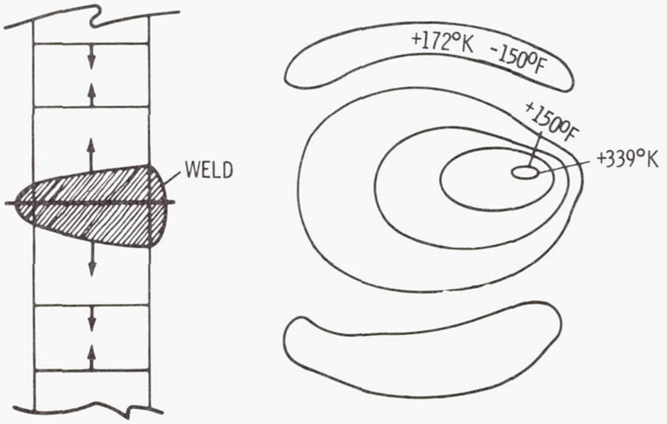

FIGURE 9. STRESS BALANCING

Fourth, the importance of a quantitative data analysis has been emphasized as a methodology in welding studies. The Lockheed-Marietta Corporation has now become so proficient and enthusiastic about quantitative analysis that it is a mandatory part of their welding development program, and has been applied to their Air Force contracts. Many welding engineers and management are pursuing weld development in a more systematic, engineering manner. The consequences, not immediately spectacular, will be solid, enduring advances in all areas of welding.

Finally, the welding process has been analyzed and identified as a dynamic whole, an entirety. It is a series of interrelated, interdependent events. Engineers are not yet able to analyze minutely the dynamic whole, but must arbitrarily select restricted areas for study, which might be considered fragments of the map of welding.

The time has come, however, when the fragments must be integrated and the whole map constructed before we can understand welding, achieve process control, and make full use of the data. The first nine studies on welding were compiled into a single report, now available through the Redstone Scientific Information Center and as announced in the NASA STAR. Each year all completed pertinent studies will be added to the report and it will be redistributed.

Engineers at MSFC intend to so analyze welding problems and avenues of solution that the welding development effort will be a logical, coherent system of meaningful studies.

Page
Intentionally
Left Blank

EXPERIMENTAL ELECTRON BEAM WELDING IN SPACE

By

P. Gordon Parks

INTRODUCTION

During the Research Achievement Review, May 1965, it was announced that a lightweight, self-contained, electron beam (EB) welding system was being developed under contract with the Westinghouse Electric Corporation; if successful, the system could probably be used to weld objects located in the vacuum of space. This Saturn application unit, designed for limited weld fabrication, or weld repair within a portable vacuum chamber, was to be built to these six general specifications:

1. The mass of the complete unit — gun, power supply, and controls — would be no more than 34 kg (75 lb).
2. The unit would be capable of operating continuously for 2 min.
3. The maximum operating potential would be no more than 20 kV.
4. The unit must be operable in a pressure range of 1.3×10^{-2} N/m^2 (10^{-4} torr), or lower, down to 1.3×10^{-7} N/m (10^{-9} torr).
5. The unit would have a gun-to-work range from 0.64 to 3.8 cm (0.25 to 1.5 in.).
6. The beam diameter at the work piece would be no greater than 0.051 cm (0.020 in.).

THE SATURN APPLICATION UNIT

The Saturn application unit shown in Figure 1 more than met the six specifications. The Saturn application unit has a mass of 27.7 kg (61 lb), is 53.4 cm (21 in.) long, and 30.5 cm (12 in.) in diameter. The small end of the focus coil protrudes 25.4 cm (10 in.) below the body of the unit. It can be operated at 98 mA and 20 kV for as long as 5 min without battery drain. In addition, it can be operated independently of the battery power supply. This feature eliminates the dependency on batteries and increases its potential usefulness. A schematic of the unit is shown in Figure 2. This gun has welded aluminum and stainless steel 0.64 cm (0.25 in.) thick at speeds up to 1.0 m/min (40 in./min). The technical significance of this achievement is recognized by comparing the Saturn application unit with the conventional EB system shown in Figure 3. The conventional system, including the vacuum chamber, controls, and power supply, has a mass of approximately 6800 kg (15 000 lb) and requires 5.66 m^3 (200 ft^3) of space. Needless to say, it is not portable. Items to be welded must be brought to it. Physical capacity for welding is limited by the work chamber size.

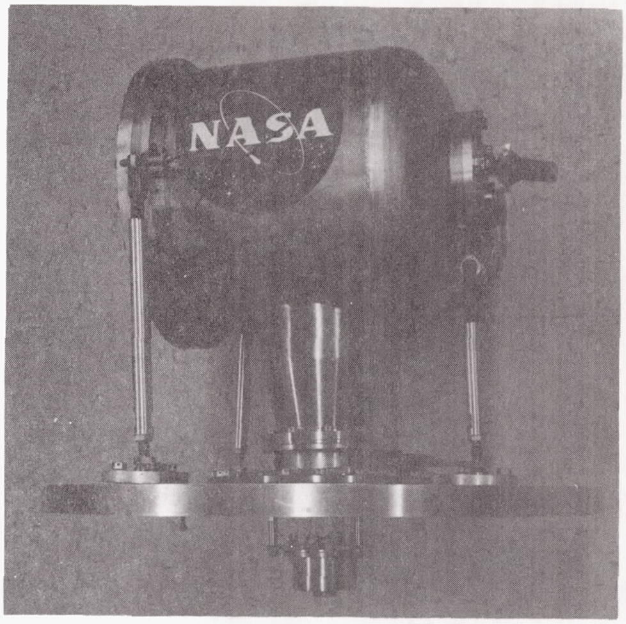

FIGURE 1. SATURN APPLICATION UNIT

With the successful development and functional use of the Saturn application unit (considering that the problems of bulk and mass of the power handling equipment have been overcome) it was proposed that the system be adapted for welding in the S-IVB orbital workshop.

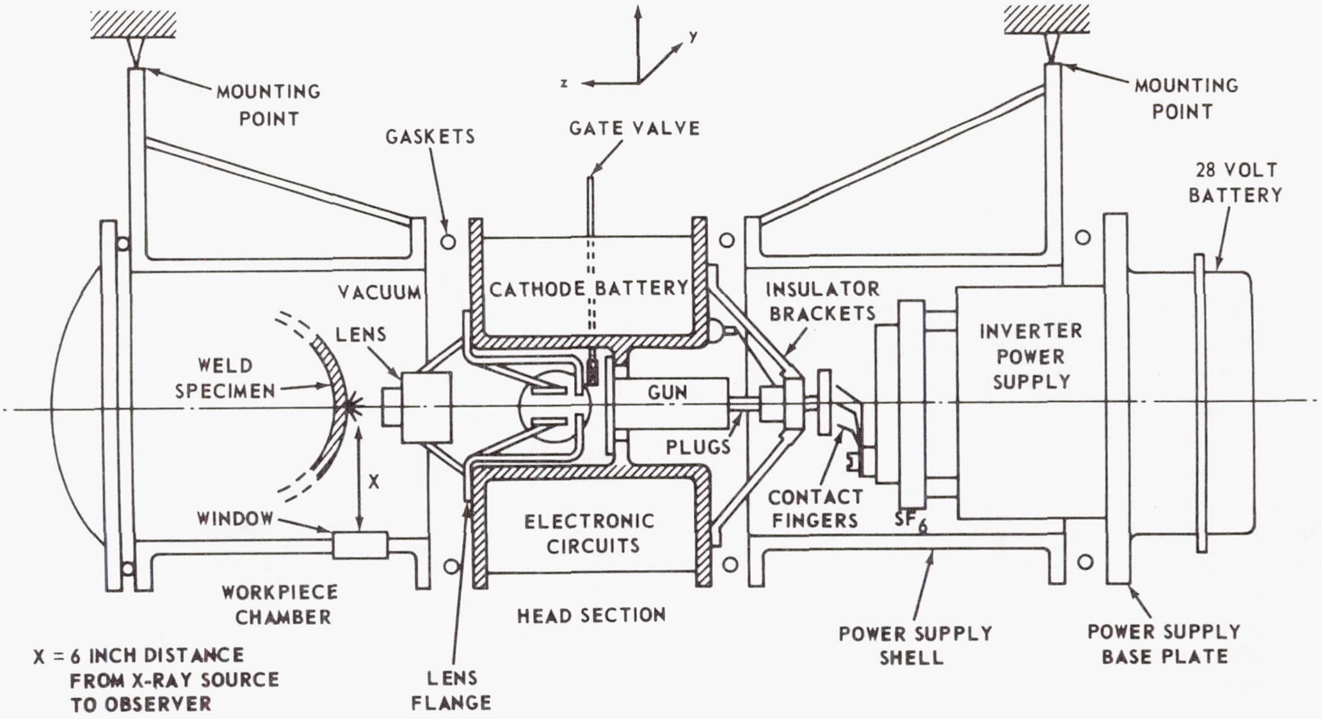

FIGURE 2. SCHEMATIC OF THE STRUCTURAL DESIGN OF THE BATTERY POWERED ELECTRON BEAM WELDER

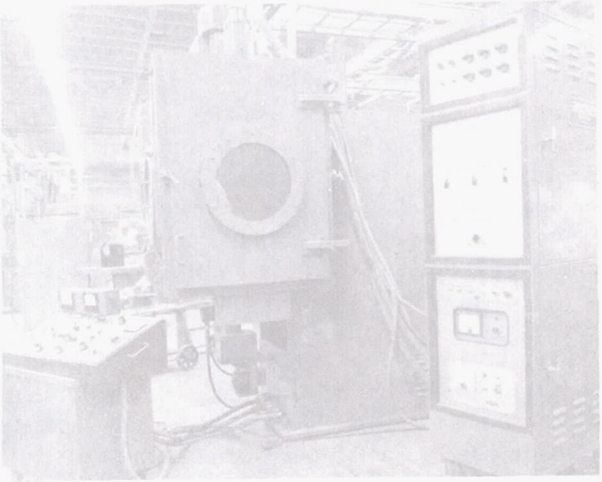

FIGURE 3. CONVENTIONAL ELECTRON BEAM WELDING UNIT

ELECTRON BEAM WELDING IN SPACE

The electron beam welding experiment under zero-gravity conditions in the S-IVB Orbital Workshop is described in the following paragraph. A battery-powered 2 kW, 20 kV electron beam system with a mass of approximately 45.4 kg (100 lb) has been built for this experiment. The weight increase was the result of integrating the control and the use of space-rated components. Battery, power conditioning circuits, electron gun and lens (Fig. 4) are mounted in a cylinder 76.2 cm (30 in.) long by 30.5 cm (12 in.) in diameter. The inverter in the center section of the case is insulated with sulfur hexafluoride (SF_6) at a pressure of 2.1×10^5 N/m^2 (30 psi) gauge. Design concepts used for the application unit and the advanced space welding electron beam unit, the work plan, and the experiment objectives are described.

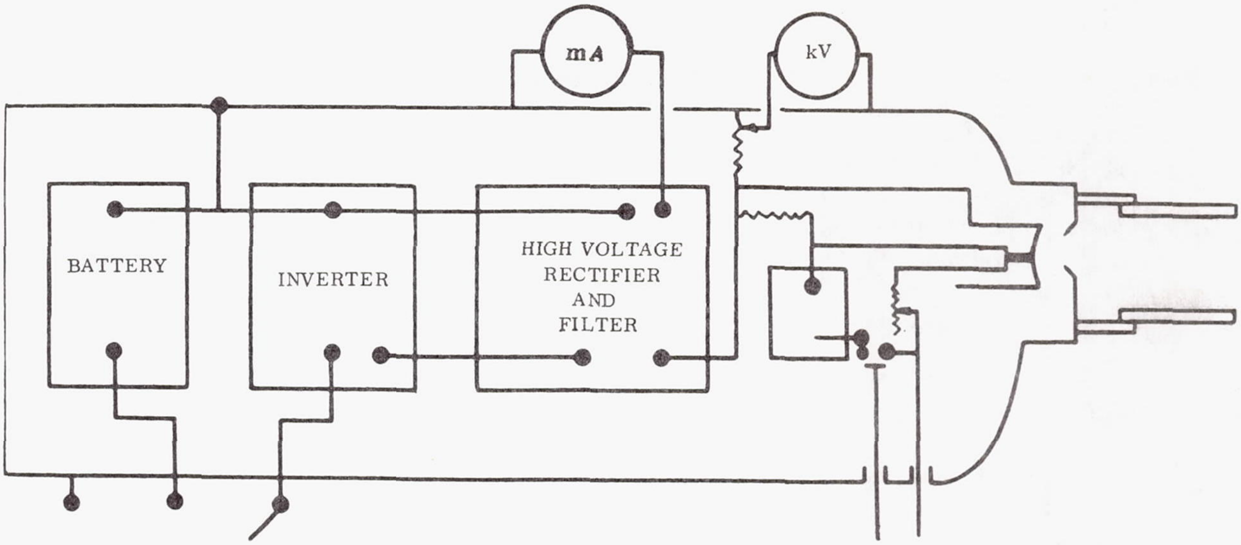

FIGURE 4. SCHEMATIC OF CONVENTIONAL ELECTRON BEAM WELDING UNIT

SPACE EB UNIT

Figure 5 shows the completely self-contained space electron beam unit that has been built and is undergoing advanced testing at the Westinghouse Research Laboratories. An identical unit will be used for the flight experiment in the S-IVB Orbital Workshop. The most obvious difference between the flight model and the laboratory model is the position of the gun relative to the power supply and battery pack. This in-line configuration is designed to be mechanically sturdier during launch and will be positioned so that the long axis is parallel to the direction of maximum acceleration.

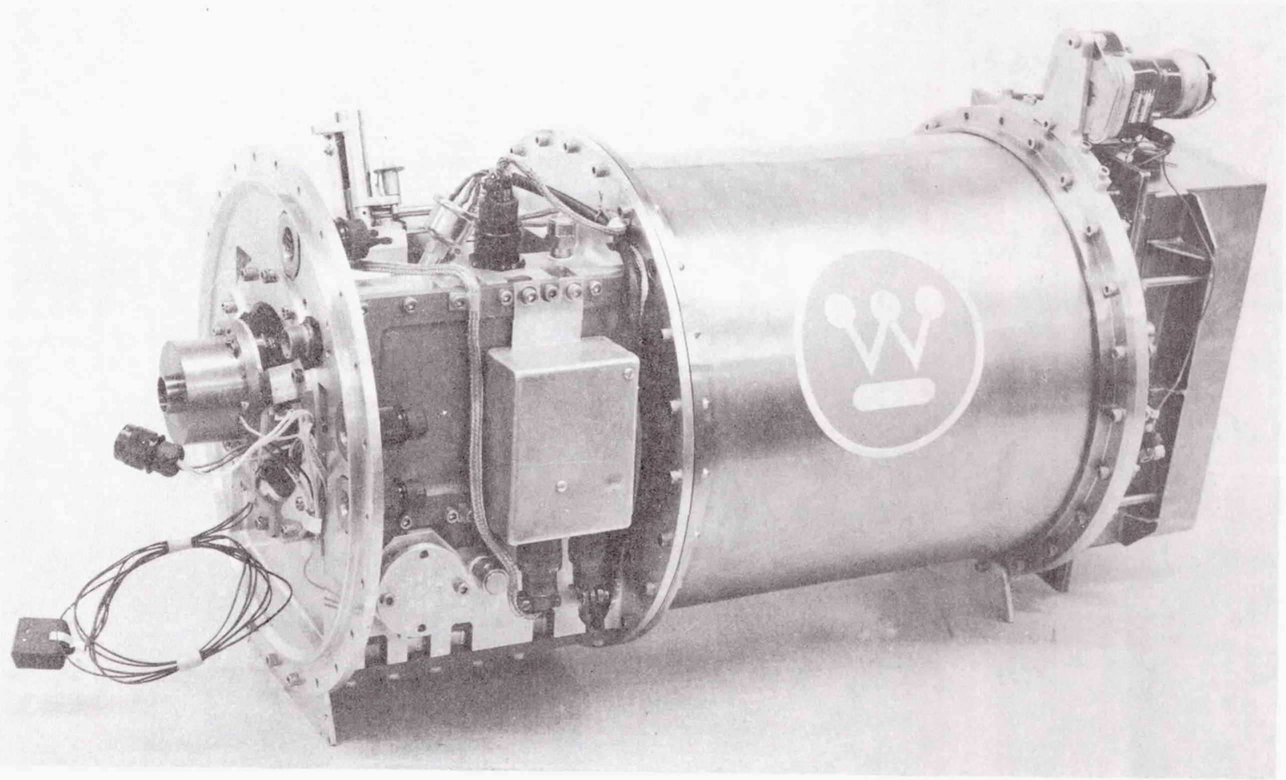

FIGURE 5. SELF-CONTAINED ELECTRON BEAM WELDING UNIT

Control Panel. Another obvious change is the integral control panel (Fig. 6). This panel contains all controls and meters required for the welding experiments. The astronaut will have direct control of beam current; he can also control lens current to optimize beam focus on the work pieces. The high voltage output of the inverter power supply is maintained at 20 kV, regulated to ± 400 V with no adjustments required. Meters monitor the beam voltage and current. Switches are provided for the high voltage power supply, the magnetic lens, the weld specimen drive motor, and the lights that are required for the two recording cameras.

Battery Package. For increased reliability, over that of the Saturn application gun, the original battery pack has been replaced with a Gemini-rated Yardney missile battery pack, which provides up to 100 **A** at a nominal 28 V for approximately 10 min, or two times the life of the original unit's batteries. Included in the battery capacity are the power requirements for lights, fixture drive, and camera operation.

Inverter Power Supply. The inverter power supply employs two stages: A saturable-inductor power oscillator and a 2 kW inverter consisting of two banks of silicon transistors. Each power transistor is separately fused so that failure of any one transistor will not cause additional failures.

Gun System. The gun consists of an anode, grid, and filament (Fig. 7). The anode is at ground potential; the filament and grid operate at a high negative voltage relative to the anode and are insulated from the anode by a glass envelope. The glass envelope also acts as a seal between the SF_6 pressurized power

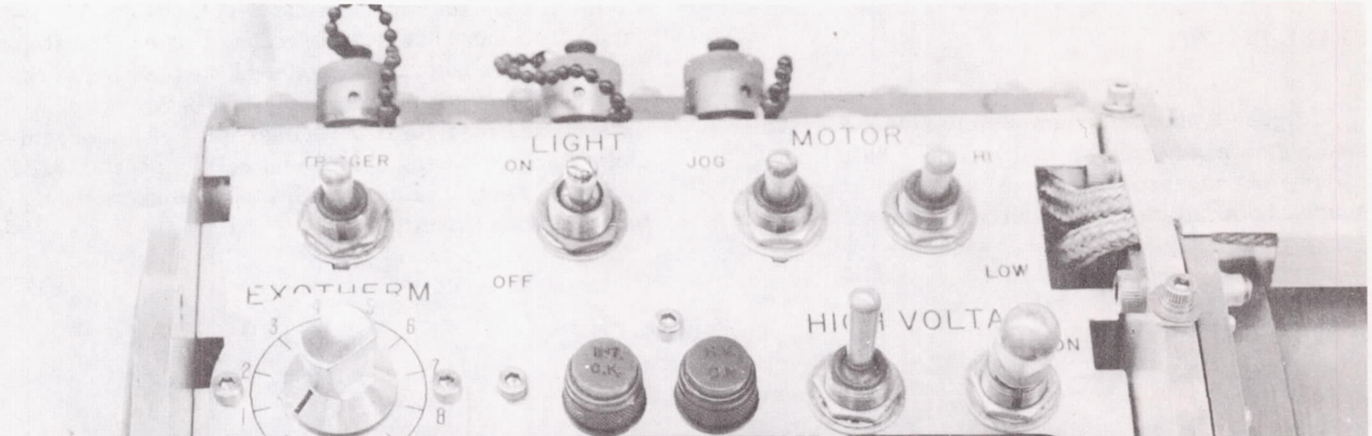

FIGURE 6. CONTROL PANEL FOR THE SATURN ELECTRON BEAM WELDING UNIT

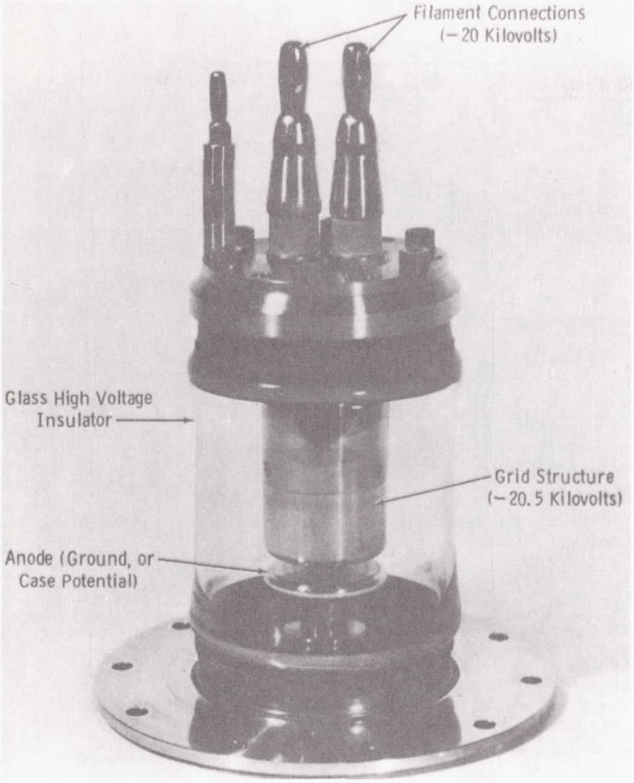

FIGURE 7. ELECTRON BEAM GUN FOR BATTERY POWERED WELDER

supply section and the hard vacuum required for the gun. The gun filament is a pure tungsten ribbon. The last section of the gun is the magnetic lens that is used to refocus the beam at the work piece. The beam is refocused approximately 5.1 cm (2 in.) from the center of the lens, or about 1.9 cm (0.75 in.) below the end shield. The axis of the lens has been moved about 1.9 cm (0.75 in.) from the axis of the electron beam gun and two electromagnetic deflection coils added to steer the beam from the former axis to the latter. This is required to reduce the possibility of damage by droplets of metal being ejected from the molten weld pool and floating into the gun elements.

DEVELOPMENT SCHEDULE

Figure 8 illustrates the work plan and the time schedule. As can be seen, there are five major work phases. The total effort involves four laboratories: Manufacturing Engineering, Astrionics, Propulsion and Vehicle Engineering, and Quality and Reliability Assurance, as well as the supporting effort of the Westinghouse Corporation. The MSFC effort involves approximately 80 people. The work phases are illustrated and explained as follows:

PHASE I — Application Model. This is the welding fixture in the bell jar (Fig. 9) where preliminary EB welding tests leading to a statistically designed experiment are conducted.

PHASE II — Dynamic Test Unit. This phase will cover the evaluation of the test package, which consists of the chamber, the valve, the EB unit, and the welding fixture, and will permit the study of simulated dynamic loads on the entire test package. Dynamic testing will include vibration tests, acceleration tests, and acoustical tests (Fig. 10). Later this unit will be sent to MSC at Houston for involved space simulation evaluation.

PHASE III — Mock-Up Unit. By the use of the mock-up unit (Fig. 11) in the neutral buoyancy tank, the astronaut will become familiar with the operation of the experiment. Involved will be the human engineering analysis of handling equipment and the motions required to conduct all operations.

PHASE IV — Qualification Model. The qualification model will be used to perform the statistically designed one-gravity reference experiment with the astronauts participating. In addition, it will be thoroughly retested and finally put into a "stand-by" position. Figure 12 is a model of the complete space package: the vacuum chamber, the welding fixture at the open end of the chamber, the controls, and the gun, as attached to the workshop wall. Not visible is the valve for exhausting the chamber and the gun system. The test weldment, a ring consisting of three alloys — stainless steel, aluminum, and titanium — is visible at the open end.

PHASE V — Flight Unit. The flight model which will be identical to the qualification unit, will receive limited preflight functional testing. It will be considered flightworthy on the detailed testing accomplished with the qualification model. However, it will receive astronaut performance checks, and finally, after installation in the flight vehicle, it will have fresh batteries installed and be subjected to final checkout.

Additional experiment requirements include spare parts (batteries, specimens, lights, etc.), GSE — electronics and vacuum test equipment, vacuum pump, and insulating gas. Documentation includes experiment plan, operating manuals, flight qualifications,

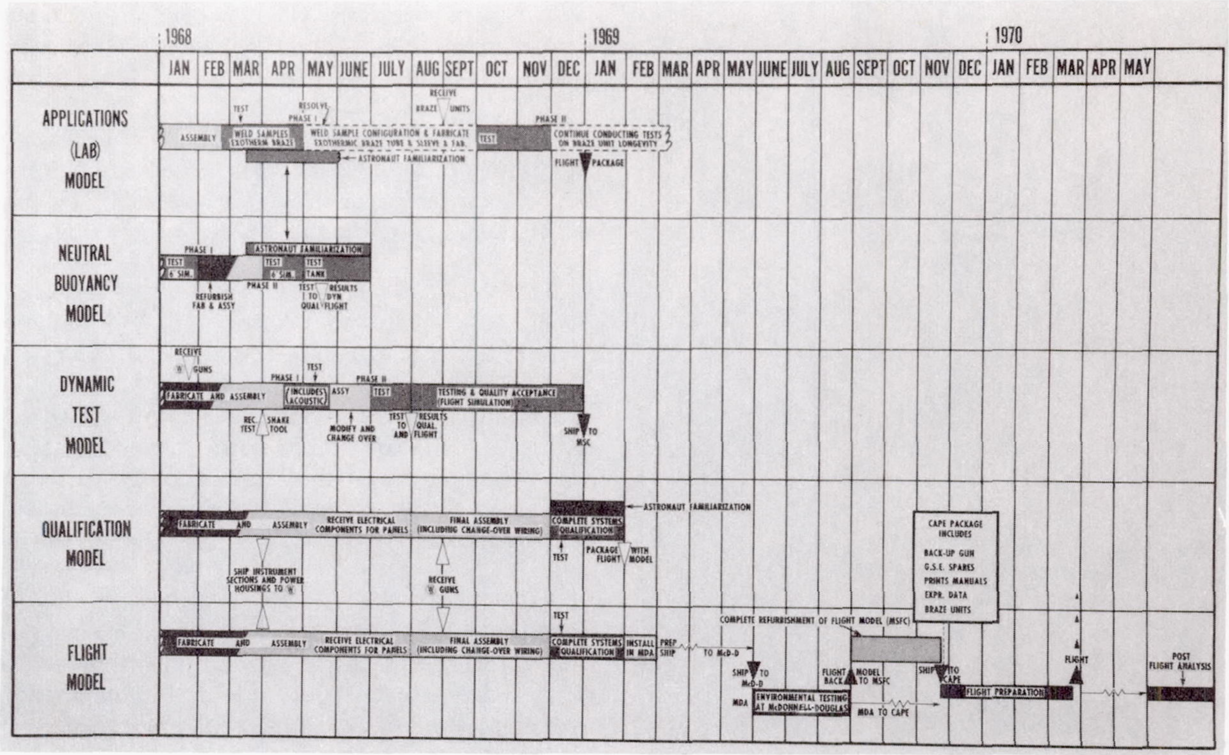

FIGURE 8. PRODUCTION AND APPLICATION SCHEDULES FOR EB UNITS

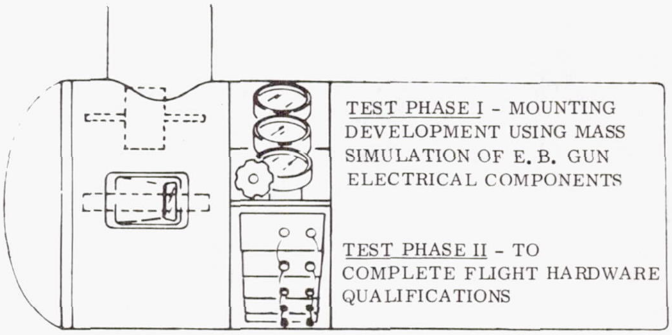

FIGURE 10. DYNAMIC TEST MODEL

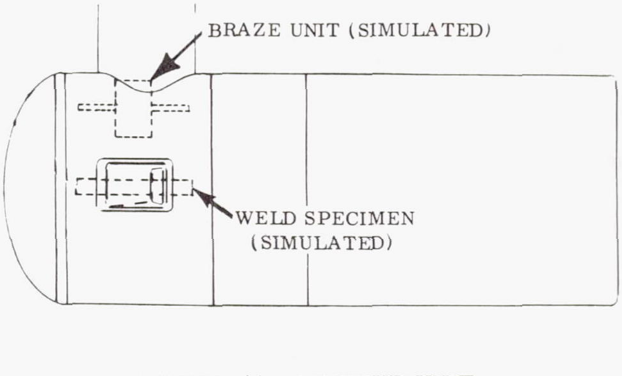

FIGURE 9. NEUTRAL BUOYANCY MOCKUP

FIGURE 11. MOCKUP UNIT

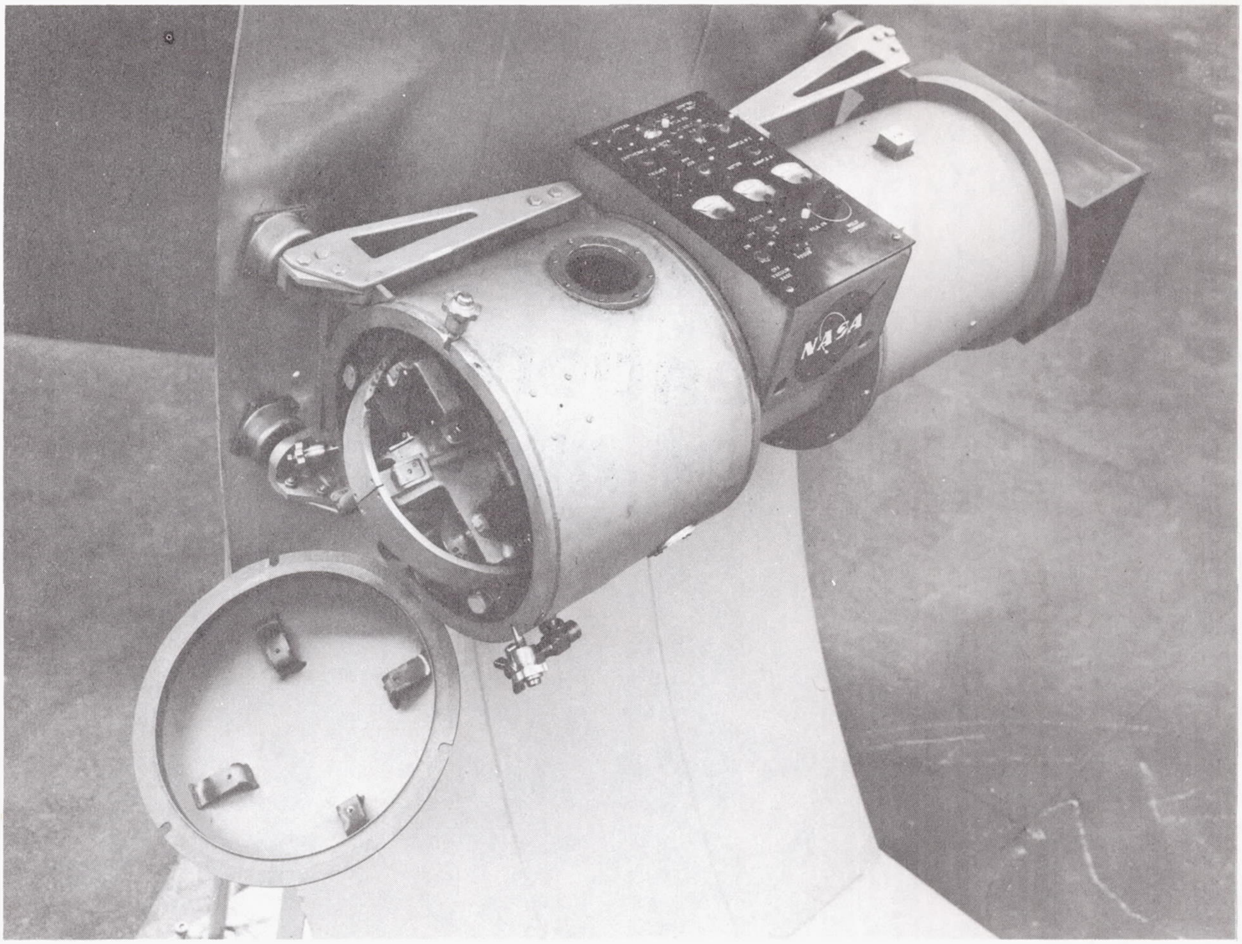

FIGURE 12. QUALIFICATION MODEL

experiment debriefing, and engineering drawings. Astronaut familiarization includes neutral buoyancy tank and functional welding using qualification model.

This is an outline of supporting equipment, documents, and the astronauts' part in attaining flight status and conducting the experiment in space.

EXPERIMENT OBJECTIVES

The experiment is designed to obtain as much useful information and data as is practical. All performance parameters (such as beam power and welding speed) and environmental conditions (such as temperature, vacuum, and radiation) will be established in preflight tests. The general objective of the experiment is to determine and to attempt to understand the effects of weightlessness on molten metal.

In conclusion, the experiment will accomplish these specific objectives:

1. Determine that the development of equipment, processes, and data at one gravity can be utilized at zero gravity.

2. Observe and record molten metal behavior considering:

   A. Metal surface tension

   B. Vaporization and sublimation

   C. Weld spatter and "floating"

3. Waste heat dissipation characteristics of gun system and weld specimen.

4. Retrieve space-made welds and photographic records of each weld for laboratory study and evaluation for comparison to the one-gravity weld data.

Page
Intentionally
Left Blank

INSTRUMENTATION RESEARCH FOR GROUND TESTING AT MSFC

January 25, 1968

By

Thomas L. Greenwood
Harlan S. Harman
Helmut G. Lackner
Alvin M. Payne
Albert E. Schuler

12

Page
Intentionally
Left Blank

Page
Intentionally
Left Blank

CONTENTS . . .

INTRODUCTION TO INSTRUMENTATION RESEARCH FOR GROUND TESTING AT MSFC

HYDROGEN SLUSH DENSITY INSTRUMENTATION

by Alvin M. Payne

LIST OF ILLUSTRATIONS

PRESSURE TRANSDUCERS FOR ENVIRONMENTAL EXTREMES

by Harlan S. Harman

CONTENTS (Continued) ...

LIST OF ILLUSTRATIONS

THE USE OF THE MÖSSBAUER EFFECT AND LASER INTERFEROMETRY TO DETERMINE EXTREMELY SMALL AMPLITUDES FOR VIBRATION MEASUREMENTS AND CALIBRATIONS

by Helmut G. Lackner

CONTENTS (Continued) ...

LIST OF ILLUSTRATIONS

LIST OF ILLUSTRATIONS

INTRODUCTION TO INSTRUMENTATION RESEARCH FOR GROUND TESTING AT MSFC

By

Albert E. Schuler

The research and development activities of the Instrument Development Branch in the Test Instrumentation and Control Division comprise inhouse and contracted basic and applied research to provide instruments and measuring or calibration systems required for the various activities of the Test Laboratory. In addition to the four papers selected for this review, total success in some programs and partial progress in a few other programs will be discussed very briefly in the following paragraphs.

A hydrogen gas detector was developed under a completed research contract with Beckman Instruments. In this electrochemical or polarographic instrument the hydrogen diffuses through a polystyrene diaphragm into a catalytic cell where hydrogen molecules ionize and generate a current proportional to the partial pressure of hydrogen in the gas mixture. This hydrogen detector was used successfully at the S-II stand of the Mississippi Test Facility.

Spacecraft, Inc., developed an analytical system to determine how much liquid nitrogen mixes with the liquid oxygen when the LO_2 tank is pressurized with gaseous nitrogen. This instrument utilizes the electric susceptibility difference between the two liquids. Calibration and test stand applications demonstrated the accuracy and reliability of this instrument. Later a dielectric circuit was developed for optional plug-in to determine the water vapor content of the gas.

In an inhouse research program an instrument was developed for measurement of pulse flow on attitude motors. Studies and research measurements led to a contract for modification of a flowmeter prover system originally developed by the Flow Technology Corporation under the sponsorship of Edwards Air Force Base. The main purpose of this positive displacement meter was to provide in-line spot checks of turbine flowmeter calibration factors. The meter uses a precision piston-cylinder assembly within a fluid bypass chamber. To make a measurement, the piston is released to obstruct the entrance to the bypass chamber; this forces the liquid and piston through the cylinder. The piston passes two or more Hall-effect switches that are used to determine the time for displacing an accurately known volume. In our modified version the motion of the piston is measured by an optical encoder that transmits 52.8 pulses/cm^3 (200,000 pulses/gal or about 900 pulses/$in.^3$). After successful laboratory tests the instrumentation is now being prepared for use on the test stand. This prover system is very accurate and provides an entirely new concept of flowmeter calibration for measuring moderate quantities, which could be desirable in many applications that include the S-IVB Orbital Workshop and other long range missions.

In another successfully completed project a 25.4-cm (10-in.) diameter liquid hydrogen densitometer for the S-IVB suction line was developed and delivered to MSFC by Industrial Nucleonics Corporation. This meter uses nuclear radiation attenuation, and the tests so far indicate very good results.

A completed study contract with Industrial Nucleonics Corporation was requested to determine the feasibility of using nuclear methods for hydrogen mass flow measurement. As a result, Industrial Nucleonics Corporation proposed to develop a nuclear mass flowmeter, but their study did not indicate sufficient evidence for success of their proposal. Therefore a contract was not awarded. Instead, a nuclear mass flowmeter was designed to operate by injecting beta particles at one end of the flow tube and using capacitive detection of their velocity and density at the other end of the flow tube. Presently, Oak Ridge National Laboratory will build this meter for $10,000 for delivery in June 1968.

In another research project, Trans-Sonics, Inc., used the nuclear resonance technique to develop a digital thermometer for measuring cryogenic temperatures in the range of 3 to 100°K with an accuracy of ±5 millidegrees. In this technique, a material such as chromium tribromide or potassium chloride is placed in the field of a high frequency oscillator. The nuclei of the material will start to resonate, reorient themselves, and absorb energy from the oscillator when the frequency of the oscillator reaches the nuclear resonance frequency of the material. This frequency is a function of temperature, and thus the calibration factor depends only on the chemical structure of the sample and not on its dimensions, which is a great advantage. A laboratory model of this nuclear resonance thermometer has been built and tested. The soundness of the principle has been established, and an extension of the contract is planned to build a workable field instrument, including a servo system for regulating the oscillator frequency to the nuclear resonance frequency at the respective temperature.

A contract with Engineering Physics Corporation is for the development of a mass flowmeter with a separate density or quality indication needed for slush hydrogen research and testing. This instrument uses the electromagnetic induction principle with a high frequency electromagnet to measure the velocity of the nonconductive liquid, and the Clausius-Masotti relation between density and dielectric constant is used for density measurement. There was a problem to join the dielectric nonmagnetic spool piece for the electromagnet with the stainless steel flow line. This problem seems to be solved by using a stainless steel adapter to press the fiber glass against the stainless steel. The breadboard setup of the electronics for the flowmeter is in working condition, and the design of the meter will soon be completed for manufacturing the flowmeter.

For test and calibration of this and other mass flow and quality meters for weighing volumes of liquid and slush hydrogen, a flow stand with advanced features was designed in an inhouse research project. A stand pipe is used for draining LH_2 without affecting the weighing. A triple tank arrangement permits having a very light tank for weighing the hydrogen, since the open tank for weighing liquids has the same pressure inside and outside. A weighing system with calibration weights and remotely programmed weight application permits calibration checks at any time. In another version the weighing system might be used only as a comparator. During the test, weights are added that have the same mass as the mass of liquid hydrogen taken out of the tank. The tank and the weight system are being manufactured by Inca Corporation and are due at MSFC in June 1968.

HYDROGEN SLUSH DENSITY INSTRUMENTATION

By

Alvin M. Payne

SUMMARY

The transition of liquid hydrogen to slush hydrogen, which is the reducing of a mass of hydrogen to a more compact form, will help to achieve the prolonged space storage of fuel that is essential for long-term missions. Thus slush hydrogen will increase the cryogenic storage capabilities of hydrogen fueled space vehicles. Meaningful testing and analysis of test results to determine the mass of the slush hydrogen can only be accomplished when accurate and reliable measurements of slush quality or density are available. This paper describes the development of an accurate slush density reference system and two different transfer standards for making reliable field measurements of the mass of slush hydrogen after calibration with the reference system.

HYDROGEN SLUSH DENSITY REFERENCE SYSTEM

Figures 1 and 2 illustrate the principle of the slush hydrogen reference system. A cryostat is nearly full of triple-point liquid hydrogen and a lightweight container is completely submerged in this liquid hydrogen, while hanging on a weighing system on top of the cryostat. First the weight container is filled with triple-point liquid hydrogen (Fig. 1) and the scale of the weight-system is made to read zero. Then solid hydrogen is introduced into the weight tank and the weight system indicates the weight of the solid introduced minus the weight of the triple-point liquid displaced (Fig. 2). The quantity, now measured by the weighing system, is the apparent or buoyed weight of the solid, and it can be used in the following equation to compute the solid mass fraction (quality) of the hydrogen slush contained in the weight container:

$$\rho Vg - \rho_\ell Vg = M_b g$$

$$\rho = \frac{M_b}{V} + \rho_\ell \qquad (1)$$

where

ρ = density of the hydrogen slush

ρ_ℓ = density of triple point hydrogen

V = Volume of the weight container

M_b = Apparent mass of the buoyed solid

g = local acceleration of gravity

One of the most accurate methods of determining density is the application of Archimedes' principle. The density of a solid is determined by weighing it while it is submerged in liquids with known densities. The density of a liquid is determined by submerging and weighing a solid body with a known mass and volume. Slush hydrogen, a mixture of solid and liquid, can be weighed in a lightweight container that is suspended by a weighing system and submerged in triple-point liquid hydrogen.

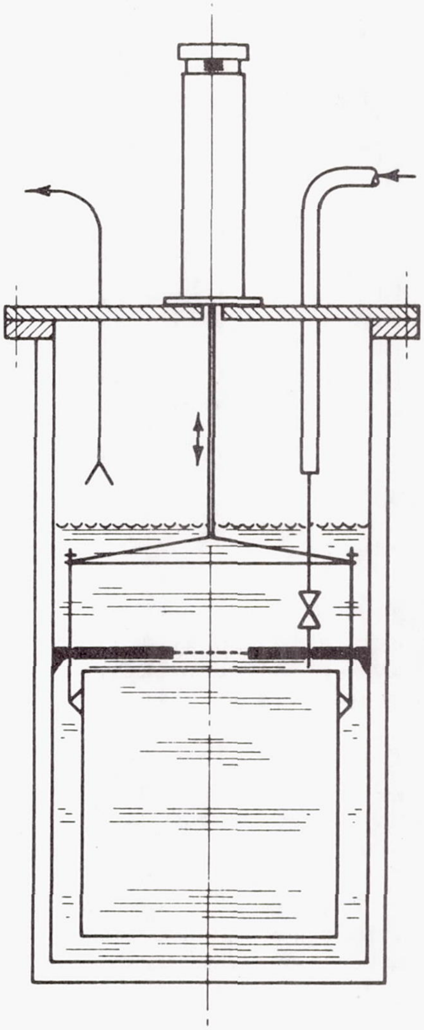

FIGURE 1. CRYOSTAT AND CONTAINER FILLED WITH TRIPLE-POINT LIQUID HYDROGEN

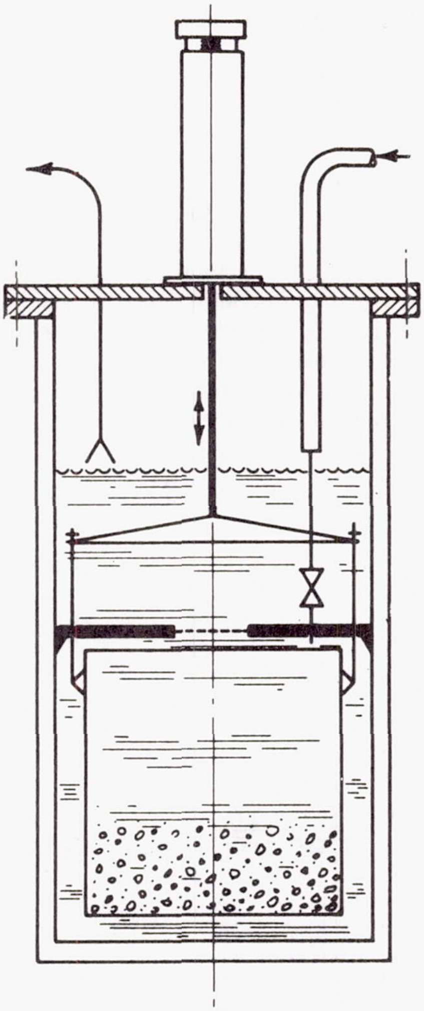

FIGURE 2. HYDROGEN SLUSH IN CONTAINER; CRYOSTAT FILLED WITH TRIPLE-POINT LIQUID

The Volume, V, is determined with water at ambient temperature, before assembling the reference system. Buoyancy and shrinkage corrections are applied to this value. As a double check the volume, V, is also determined by the difference in weight of the container, filled with triple-point liquid hydrogen, and the weight of the empty container. Hydrogen gas at constant low temperature surrounds the container at both weighings and a buoyancy correction, based on the density of this gas, is applied to the results. The difference in the weight of the hydrogen filled container and the empty container is used to compute the volume of the container as follows:

$$\text{Weight full} - \text{Weight empty} = M_\ell g = \rho_\ell Vg$$

$$V = \frac{M_\ell}{\rho_\ell}$$

where

M_ℓ = mass of triple point liquid hydrogen

ρ_ℓ = density of triple point liquid hydrogen

Substituting the above quantity for V in equation (1) gives the slush density

$$\rho = \rho_\ell \left(\frac{M_b}{M_\ell} + 1 \right) \tag{2}$$

The density of triple-point liquid hydrogen is a physical constant and known from literature [1] to be 77.017 g/l with an uncertainty of ±0.1%. M_b and M_ℓ must be determined by weighing. M_ℓ is a constant for the particular reference system and is about 2000 g for the container with a diameter of 28 cm and a depth of 37 cm. The value of M_b will vary from a few grams for a low solid fraction to about 137 g for 60% solid fraction.

An error analysis for the reference system requires some reasonable assumptions of the weight determination. If calibration masses and a suitable method for their application and removal during the experiment are provided, it should be quite easy to determine both M_b and M_ℓ to within ± 0.5% of their true values. However, to determine a safe value of the accuracy limits, it is assumed that the inaccuracy in the weighing can be as much as ± 2.0%.

A general expression for compounding of errors in y, where $y = f(x_1, x_2 \ldots\ldots x_n)$ is

$$(dy)^2 = \sum_{i=1}^{n} \left(\frac{\partial f}{\partial x_i} \right)^2 (dx_i)^2$$

if the components of error, dx, are independently distributed and symmetrical with respect to positive and negative values [2]. Using this rule for equation (2),

$$(d\rho)^2 = \left(\frac{\partial\rho}{\partial\rho_\ell}\right)^2 (d\rho_\ell)^2 + \left(\frac{\partial\rho}{\partial M_b}\right)^2 (dM_b)^2 + \left(\frac{\partial\rho}{\partial M_\ell}\right)^2 (dM_\ell)^2 \tag{3}$$

typical values for the variables are as follows:

M_b = 117 g (the value for a solid fraction of 0.50)

M_ℓ = 2000 g

ρ_ℓ = 77.017 g/l .

From these values and the assumed fractional errors in weighing, together with the ± 0.1 uncertainty in ρ_ℓ, the following relationship can be made:

$$\frac{dM_b}{M_b} = 0.02, \text{ or } dM_b = 2.34 \text{ g}$$

$$\frac{dM_\ell}{M_\ell} = 0.02, \text{ or } dM_\ell = 40.0 \text{ g}$$

$$\frac{d\rho_\ell}{\rho_\ell} = 0.001, \text{ or } d\rho_\ell = 0.077 \text{ g/l.}$$

The partial derivatives are

$$\frac{\partial\rho}{\partial\rho_\ell} = \left(\frac{M_b}{M_\ell} + 1\right) = 1.05856$$

$$\frac{\partial\rho}{\partial M_b} = \frac{\rho_\ell}{M_\ell} = 0.03854$$

$$\frac{\partial\rho}{M_\ell} = \frac{-\rho_\ell M_b}{M_\ell^2} = -0.002256 .$$

From equation (3),

$(d\rho)^2 = 0.00665 + 0.00814 + 0.00818$, or

$(d\rho)^2 = 0.0230$, and

$d\rho = \pm 0.15$ g/l .

Note that the three terms which add together to get $(d\rho)^2$ are approximately equal in magnitude even though the uncertainty in the triple-point liquid density (which gives the first term) is ±0.1%, whereas the uncertainty in each of the two weighings is ± 2.0% or 20 times as great. This comes about because of the functional relationship expressed in equation (2). By making use of Archimedes' Principle, it is possible to capitalize heavily on the high degree of accuracy with which the triple-point liquid density ρ_ℓ is known.

As an example, equation (2) and the typical values mentioned before are used to find the mean for a solid fraction of 0.50. Thus

$$\rho = \rho_\ell\left(\frac{M_b}{M_\ell} + 1\right) = 77.017\left(\frac{117}{2000} + 1\right) = 81.53 \text{ g/l .}$$

The fractional error in ρ is

$$\frac{d\rho}{\rho} = \pm\frac{0.15}{81.53} \text{ or } \pm 0.18\% \text{ .}$$

From these considerations it may be concluded that the density of hydrogen slush at 0.50 solid fraction can be determined with an uncertainty of less than ± 0.2% if a weighing system which is accurate to ± 2.0% is used. Figure 3 shows how the uncertainty in slush density will vary for the assumed system as the density itself is varied. A scale of mass fraction solid (sometimes called "quality") is shown for comparison with density. The uncertainty is shown in grams per liter as well as percent of measured mean density.

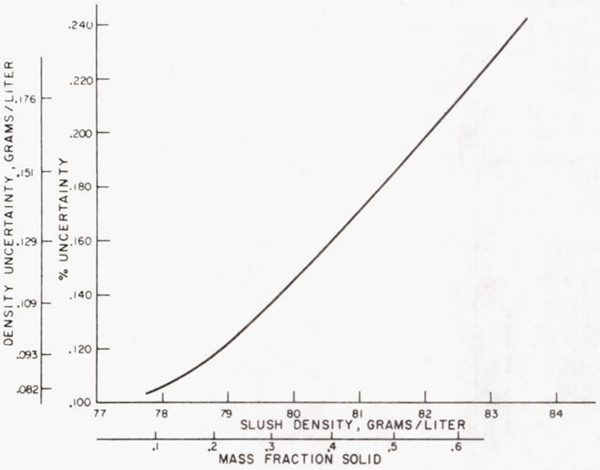

FIGURE 3. GRAPH SHOWING RESULTS OF ERROR ANALYSIS

Figure 4 is a detailed diagram of the slush density cryostat. The container is suspended from a load cell which is located on top of a cylinder above the top plate of the cryostat. The cylinder houses a series of calibration masses. Two windows provide observation and access to the dead weight calibration system. The container can easily be lifted from the suspension system by raising it against the cover plate, and one or more of the calibration masses can be substituted. Slush is transfered from the slush generator while the container is in the raised position. The solids are retained while the excess liquid is pumped off. When a convenient solid fraction has been added to the liquid, the final weighing is made.

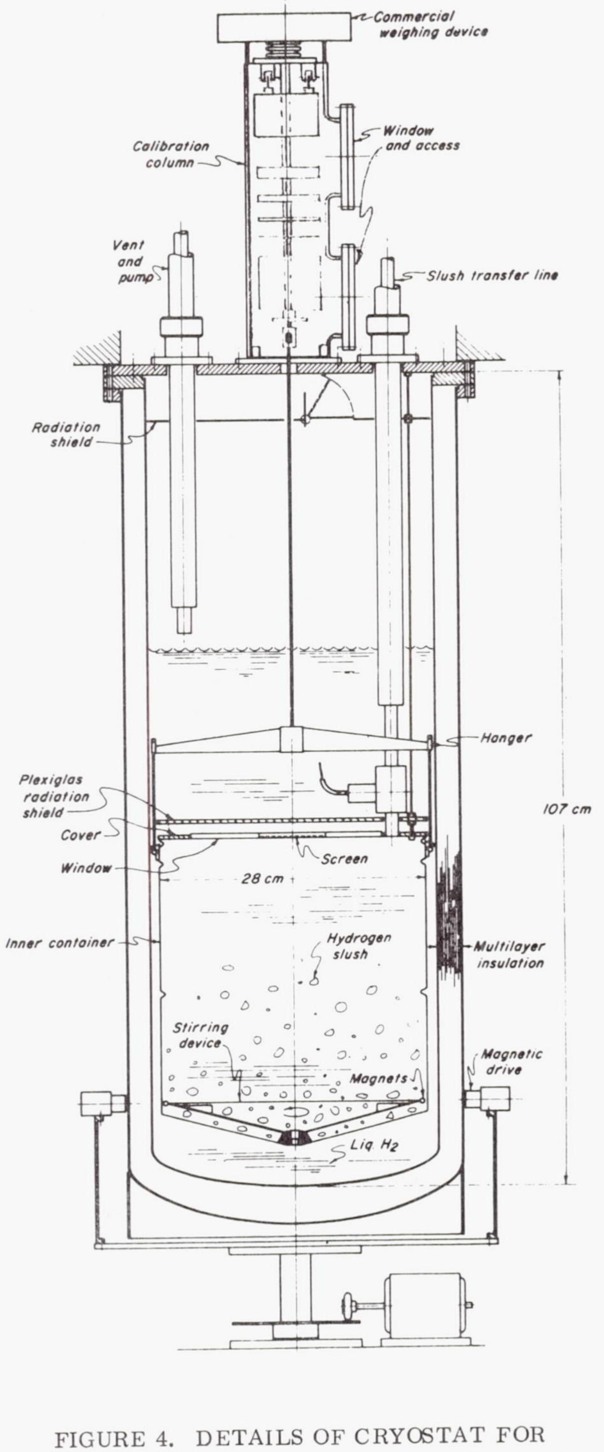

FIGURE 4. DETAILS OF CRYOSTAT FOR DETERMINATION OF HYDROGEN SLUSH DENSITY

After a determination of average slush density in the container has been made, it must be correlated with a reading or series of readings from the transfer standard that is being calibrated. There are presently two types of transfer standards available: the Nuclear Radiation Attenuation (NRA) Transfer Standard and the Internal Point Densitometer, both described in this paper. The Internal Point Densitometer is located inside the slush container and is supported from the cover, which serves as a lid when in the raised position. When the container is lowered for weighing, it no longer contacts the cover, so that the cover and attachments to it are not weighed.

The Nuclear Radiation Attenuation Transfer Standard is mounted outside the dewar. This arrangement has many advantages for both calibration and field use.

To maintain a favorable attenuation ratio between hydrogen slush and metal, the cryostat and container walls have been made as thin as possible. Type 316 stainless steel is used for the container and both shells. The outer shell is 0.13 cm thick, the inner shell is 0.08 cm, and the inner container walls are 0.06 cm thick. The attenuation of gamma rays by the total of 0.54 cm of steel will be about the same as the attenuation by the 28 cm of hydrogen slush having an average density of 80 g/l.

Access ports offering less gamma ray attenuation can be provided where the beam passes through the 0.13 cm thick outer walls, but the attenuation ratio without access ports is sufficiently favorable to justify avoiding this complication in the initial fabrication. Easy modification of the outer shell is made possible by providing separate removable vacuum seals for both inner and outer shells at the top plate.

The cryostat is insulated with evacuated multilayer aluminized Mylar sheets alternating with porous glass paper. The annular space is 2.5 cm, about 3/4 of which will be filled with the laminae. The resulting 3.8 cm of loosely layered Mylar sheets and glass paper is not a significant barrier for energetic gamma radiation, but does provide an efficient thermal barrier. Total heat flux through the multilayer insulation will be approximately 2 W out of a total expected heat leak of 15 W. Solid conduction will account for about 6 W, radiation from the top plate about 4 W, and gas conduction about 3 W.

Practically all of this heat will be intercepted by the triple-point liquid surrounding the slush container. This is important since it is impractical to simultaneously weigh and take readings from the transfer standard because the mixture will not be homogeneous unless it is stirred, and accurate weighings cannot be made while stirring.

The small amount of heat which reaches the contents of the container will melt some of the solid hydrogen and continuously change the average slush density. The density thus becomes a function of time, and it will be necessary to determine this time dependence when experimental measurements begin. A preliminary task is to analyze the accuracy with which this can be done. Since there will always be some elapse of time between a density determination and a readout from a transfer standard which is in place and being calibrated, it is apparent that the time dependence of ρ must be known with a high degree of accuracy.

This analysis, which is part of the error analysis for the system, has been carried out and shows that even if generous assumptions are made about the heat leak to the inner container and time elapse between load cell and transfer standard readings, the heat leak correction can be incorporated without addition of any significant new uncertainty.

Most density sensitive transducers (including a beam of gamma rays) will normally sample a relatively small fraction of the slush in the container, and therefore this reading will not indicate the true average density unless the mixture is kept homogeneous during the reading interval. To keep the central part of the container clear of protrusions, a method for stirring magnetically from outside the cryostat was devised. A low-mass rotor inside the container carries slender bar magnets which link flux with heavy permanent magnets carried on a wheel surrounding the cryostat. This magnetic driving wheel can be spun by hand or turned by a small motor operating against a friction disc. Stirring will always be done with the container in its raised and closed position to prevent loss of solids. When the container is lowered for a weighing, the magnetic driving wheel will be dropped away by means of a simple elevator and lever arrangement so that there will be no magnetic force exerted on the rotor.

Thus the sequence of operations, starting with slush in the container, is as follows:

1. With the container raised, calibrate the weighing system.

2. Lower the container and weigh it.

3. Raise the container and stirring driver.

4. Stir and read the transfer standard.

A check on homogeneity can be obtained by taking several readings of the transfer standard while stirring at slightly different rates for each reading. If the readings are constant, the mixture should be homogeneous. The slush density reference system is now operational, and calibration of transfer standards will be started in the near future.

NUCLEAR RADIATION ATTENUATION TRANSFER STANDARD

A 450 liter slush generator has been in use for the past year. A commercial densitometer based on gamma ray attenuation has recently been installed on the slush generator. Initial results obtained with this device have been very encouraging.

The densitometer consists of a 4 Ci, 0.663 MeV, cesium 137 source; an ion chamber detector; an impedance matching unit; and an instrument console. The signal from the densitometer is measured with a digital volt meter and recorded on a strip recorder. Figure 5 shows the position of the source and the detector with respect to the slush generator. The beam must penetrate 1.12 cm of stainless steel, 1.27 cm of aluminum, and 76 cm of liquid or slush hydrogen. About one-half of the attenuation of the beam takes place in the hydrogen.

Figure 6 shows the experimental results obtained with the densitometer. The millivolt output of the densitometer is in each case the mean value of at least 10 digital voltmeter readings. The density was determined by three different methods, depending on the state of the hydrogen.

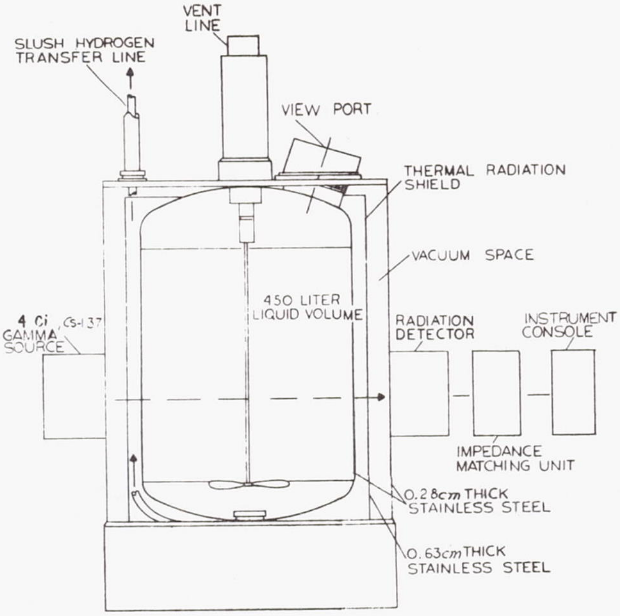

FIGURE 5. 450-LITER HYDROGEN SLUSH GENERATOR WITH NRA DENSITOMETER

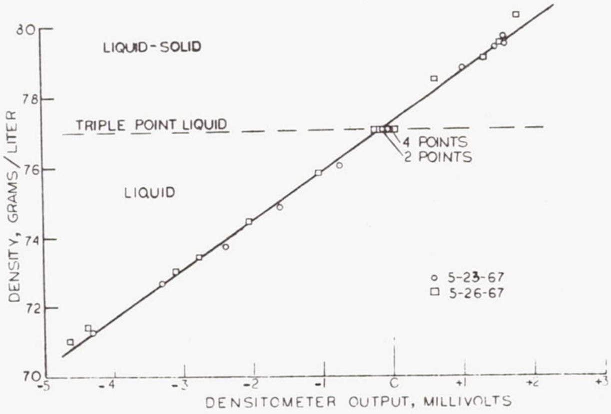

FIGURE 6. NRA DENSITOMETER RESULTS

In the liquid region at pressures above the triple point, the density was determined by measurement of the vapor pressure over the liquid. The triple-point liquid condition was determined by making a small amount of solid in the slush generator, mixing the solid particles thoroughly by stirring, and then taking the densitometer reading as the last of the solid particles settled past the region penetrated by the beam.

The density in the liquid-solid region was determined calorimetrically. After a densitometer reading was taken on stirred slush formed by the freeze-thaw production process [3], a heater in the bottom of the generator was energized until the triple-point liquid condition was achieved. The solid fraction, and hence the density, was then determined from the sum of the heater energy and heat leak.

The densities used in the liquid region are those reported by Roder [1], and the triple-point solid density is given by Dwyer, et al., [4].

The standard deviation of the measured densities about the least squares straight line in Figure 6 is 0.17 g/l. The slope of the curve does not change in passing from the liquid to the liquid-solid region, so it is possible to predict densities in the liquid-solid region by linear extrapolation of a liquid region calibration.

The uncertainty of the measured density values is estimated as a few parts in 1000. Since this uncertainty is of the same order as the scatter in the results, further evaluation of the NRA densitometer awaits completion of the density reference system.

INTERNAL POINT DENSITOMETER

A hydrogen slush densitometer based on previous research contracts, developed first for liquid oxygen and later modified for liquid hydrogen, has been further modified for slush hydrogen. The ORTEC slush hydrogen densitometer consists of three encapsulated surface barrier radiation detectors and sealed strontium-90 sources, and three channels of modular electronics instrumentation for processing detector signals.

Each detector probe assembly is composed of a 50 mm^2 active area 500-μ thick totally depleted surface barrier detector housed in a stainless steel capsule having a 0.051 mm (0.002 in.) thick stainless steel window. The source housing, also fabricated of stainless steel, contains a sealed 15 mCi strontium-90 beta source. For additional safety, a 0.025 mm (0.001 in.) thick stainless steel window has been fabricated into the source housing. The detector probe-source housing assembly is designed so that axial and lateral geometry alignment is constant, thus requiring only source-to-detector distance adjustments.

Beta particles from the source are absorbed by the detector, thereby producing minute electrical pulses or charges. These pulses, in the form of electrical current, are fed through the preamplifier to the linear amplifier. The linear amplifier shapes and further amplifies the pulse, which is then fed to the discriminator where it is determined to be either above or below a given energy threshold. The discriminated pulses are converted to a dc signal corresponding to the pulse rate, and finally re-converted to a dc output that is to be calibrated to indicate the percent solid fraction in the liquid hydrogen slush. A block diagram of a channel is shown installed in the reference system in Figure 7.

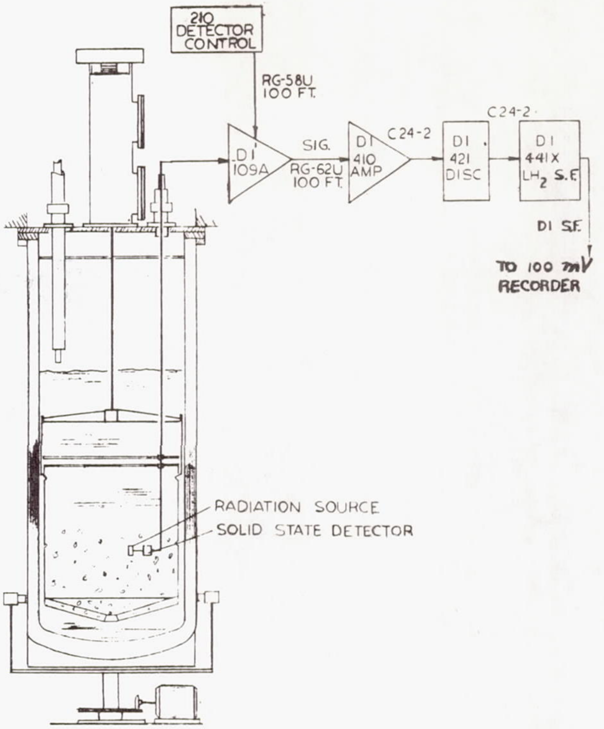

FIGURE 7. ORTEC SLUSH HYDROGEN DENSITOMETER

REFERENCES

1. Roder, H. M.; Weber, L A.; and Goodwin, R. D.: Thermodynamic and Related Properties of Parahydrogen, from the Triple Point to 100° K at Pressures to 340 Atmospheres. NBS Monography 94, 1965.

2. Wilson, E. B., Jr.: An Introduction to Scientific Research. McGraw-Hill Book Co., Inc., 1952.

3. Mann, B. D.; Ludtak, P. R.; Sinat, C. F.; and Chelton, D. B.: Liquid-Solid Mixtures of Hydrogen Near the Triple Point. Advances in Cryogenic Engineering, Plenum Press, New York, N. Y., vol. 11, 1966, pp. 207-217.

4. Dwyer, R. F.; Cook, G. A.; Berwaldt, O. E.; and Nevins, H. E.: Molar Volume of Solid Parahydrogen Along the Melting Line. J. Chem. Phys., vol. 43, 1965, p. 801.

PRESSURE TRANSDUCERS FOR ENVIRONMENTAL EXTREMES

By

Harlan S. Harman

SUMMARY

This review covers two research programs. One of them discusses design development and fabrication of an experimental high temperature, high frequency response pressure transducer for combustion instability studies requiring frequency response of 20 kHz in an environment where temperature reaches 4144°K (7000°F) and the heat flux can be as high as 8200 W/cm^2 (50 Btu/in.^{2}-sec). The second program covers the design, development and fabrication of a cryogenic pressure transducer for static and dynamic measurements at liquid helium temperatures of 4°K.

HIGH TEMPERATURE, HIGH FREQUENCY RESPONSE PRESSURE TRANSDUCER

The accurate measurement of the amplitude and frequency of dynamic pressures in a rocket combustion chamber during unstable combustion has been a problem for several years. The required temperature and frequency response capabilities of a pressure transducer operating in an unstable combustion environment were such that they could not be met with existing transducers. Commercially acceptable transducers would be destroyed by the high heat flux of up to 8200 W/cm^2 (50 Btu/in.^{2}-sec) generated in the chamber during unstable combustion.

Past techniques used to cool the pressure sensing portion of pressure transducers have been unsatisfactory. These techniques were as follows:

1. Water-cooled flush-mounted diaphragm. This approach used a nucleate boiling technique of storing water on a flush-mounted diaphragm to act as a flame shield for a strain gage type sensing element. The proper frequency response was achieved, but the transducer diaphragm burned through during unstable combustion.

2. Small gas passage technique. In this technique the pressure sensing element is mounted a short distance away from the high temperature region in a small opening in the combustion chamber. Satisfactory cooling of the sensing element is achieved with this technique; however, a considerable reduction in frequency response does result.

3. Spray cooling technique. Cooling is accomplished by flowing water or other fluid past a sensing element and injecting the flow into the combustion chamber. To adequately protect the sensing element from the high heat flux environment required an excessive amount of fluid to be injected into the combustion chamber.

To achieve high frequency response, the transducer must be flush mounted in the combustion chamber. Past experience with the above cooling methods showed that a new cooling technique would have to be developed to satisfactorily meet this requirement.

A concept of using mass transfer or transpirational cooling of a dense porous plug appeared to be the most promising technique of adequately protecting a flush mounted pressure transducer from the high temperature environment. Transpirational cooling is accomplished by flowing a gas through a porous material. A theoretical analysis of this cooling technique shows that the temperature difference between the plug material and the coolant gas is very small, and the heat conducted through the plug material is carried away by the coolant.

The research effort centered around the development of the transpirational cooling technique that is necessary for having a reliable high temperature, high frequency response pressure transducer capable of continuous operation in unstable combustion environments. Figure 1 is a sectional view of the pressure transducer developed from this research effort. This view shows the important components in the transducer. The porous plug at the upper end of the transducer is flush-mounted in the rocket chamber at the point desired. Pressure (both static and dynamic) in the rocket chamber acts upon the porous plug, and the force is transmitted down the inner column to the strain gage sensing bridge at the lower end of the transducer. Semiconductor gages were used rather than resistance gages to achieve the high output required with the low strains.

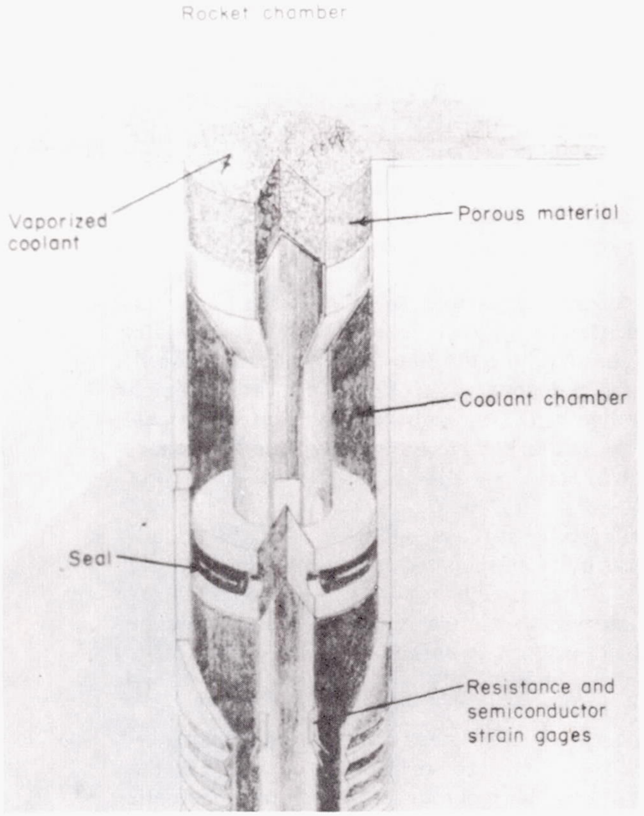

FIGURE 1. CONCEPTUAL DESIGN

The steady or transient heat fluxes are kept from the sensing element by bleeding a coolant, compatible with the combustion process, through the porous material. Because of the very small passages in the porous material, essentially the transient pressures will "see" the plug as a solid material. Thus, imposed strains in the lower portion of the column are the same as if the plug were solid. The coolant, either gaseous helium or hydrogen, is introduced through the center of the inner column at a point below the porous material and at a steady pressure higher than that encountered in the combustion instability regions. Figure 2 shows a sectional view of the transducer. A No. 29 hypodermic needle 0.0178 cm i.d. (0.007 in. i.d.) is used to meter the flow and to act as a critical flow passage to maintain the flow at a constant mass flow rate. Although in this design some changes in output occur with changes in coolant pressure, this error is small and may be eliminated by taking a zero reading after full coolant pressure is established. The coolant supply pressure must be sufficiently high that critical flow through the orifice is maintained at the highest rocket chamber pressures.

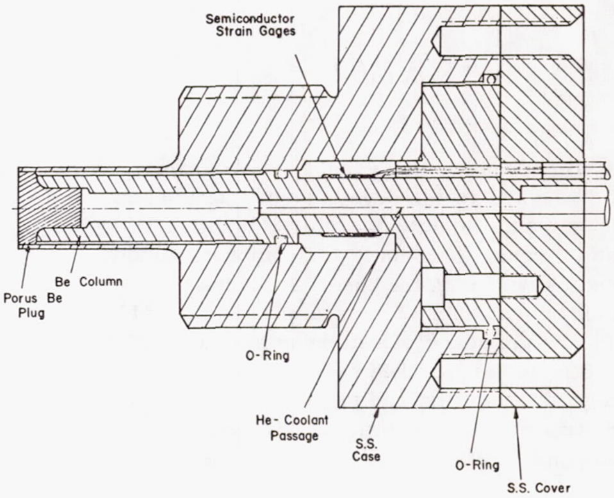

FIGURE 2. SECTIONAL VIEW OF TRANSPIRATIONALLY COOLED PRESSURE TRANSDUCER

Using a small column in compression and maintaining low strains for the maximum design pressure allows for attaining a very high natural frequency for this system. In addition, beryllium, which has an exceptionally high stiffness-to-weight ratio, was selected so that both the porous plug and inner column would have a high natural frequency.

TYPICAL SPECIFICATIONS

Minor variations in material properties, tolerances, strain gage characteristics, etc., require that calibration and response characteristics of each transducer must be determined experimentally. However, in general, typical specifications for this transpirational-cooled pressure transducer are as follows:

Range	0 - 1379 N/cm^2 (0 to 2000 psig)
Output-sensitivity at least	0.0046 mV/V-psi
External Vibration Sensitivity	
Axial	less than 0.012% full scale per peak g
Transverse	less than 0.007% full scale per peak g

Thermal Shift from 299.8° to 327.5°K (80° to 130° F)	less than 0.14% full scale

Although the thermal shift was determined for the ranges 299.8 to 327.5°K (80° to 130°F), the temperature at the sensing bridges is not expected to vary more than 11.0°K (20°F).

Combined error caused by thermal shift nonlinearity, hysteresis, and repeatability, is ± 3% full scale. Most of this error is hysteresis and is attributed to the O-ring seals. With a modified O-ring groove that has been incorporated into the design, this error is expected to vary by less than ± 2% full scale.

Resonant Frequency (axial)	74 kHz
Frequency Response	Flat or 1% to 7.5 kHz

These specifications reflect the values determined for the two prototype transducers fabricated at the end of this program and supplied to NASA.

The development of this concept into a useable transducer involved three parallel efforts, each in a different technical field. These efforts are (1) thermal studies, (2) porous material development, and (3) mechanical design and evaluation of transducers. These subjects will be discussed only briefly, but full details are available to those having further interest.

The work in the thermal phase was directed toward evaluating the cooling concept and determining the relation between the particle size and porosity of the porous plug and the coolant flow rate required to provide adequate cooling for the transducer. The plugs are fabricated by compaction of nearly spherical beryllium or tungsten particles into a body. The principal variables affecting the flow are average particle size, particle size distribution, and degree of compaction. This last variable is correlated in practice with percent of theoretical density of the metal being used. An effort was made early in the program to develop a correlation from flow tests with regards to the effect on flow of the particle sizes and densities of the porous material. Thus, tungsten plugs of only two particle sizes and of various densities were fabricated and flow tested.

For the transducer development, two kinds of plugs were selected from those available for thermal evaluation on the basis of gas permeability. This choice proved to be correct from evidence revealed during the thermal tests. The two kinds of porous plugs were the 115 μ, 83.5% dense tungsten plug and the 50 μ, 77.4% dense beryllium plug.

SIGNAL TRANSMISSION

The transducer senses the rocket chamber pressure through the elastic response of the beryllium parts. The gaseous coolant is used for the sole purpose of thermal protection. Any signal transmission in the gas passage within the plug only tends to complicate the phenomenon and might distort the signal being measured. In the state of the art, it is not clear whether there is any interaction between the signals transmitted through the solid and the signal transmitted through the gas within the passages in the solid, and what is the effect on the transducer accuracy, if any. Under this circumstance it was believed reasonable to attempt to minimize the signal transmitted through the gaseous medium. An attempt was made to analyze the signal transmitted in a gas passing through a porous material. The details of this analysis and its application to the transducer are available in the final report of the contractor [1]. The same applies to many other details in the following sections of this paper [1, 2]. The analysis showed that the signal transmitted through the gas within the porous plug is not significant in practical plug materials as are being used in the transducer.

Thermal tests of both plugs and complete transducers were carried out to determine the amount of coolant required for safe operation; to estimate the temperature distribution in the porous materials; to study the coolant system so that an adequate amount of gas is supplied; and also to determine peak temperature at the sensors. One third or more of the total development effort in this contract was used in the development of a suitable porous plug. Tungsten and beryllium plugs were successfully manufactured.

ROCKET MOTOR TEST ARRANGEMENT

A brief description of rocket motor test arrangement is shown in Figure 3. The rocket motor used in the transducer testing part of this program consists of a 3.81 × 15.2 cm ($1\frac{1}{2} \times 6$ in.) cylindrical combustion chamber, an injector with six oxidizer jets impinging onto a central fuel jet, a convergency nozzle which provides a rectangular throat, and a transducer test section mounted downstream of the nozzle. Gaseous hydrogen and oxygen propellants were used in a 5 to 1 weight ratio.

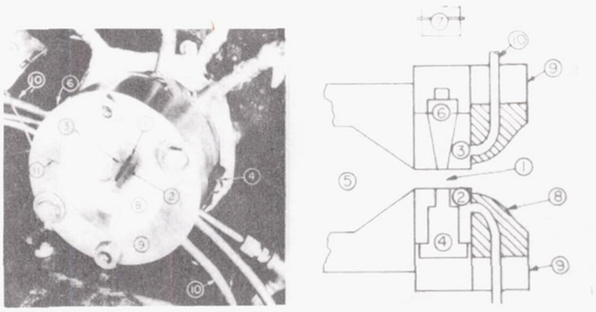

1. Rectangular nozzle throat extension
2. Water-cooled transducer nozzle block
3. Water-cooled window block, also a calorimeter
4. Pressure transducer
5. Combustion chamber
6. Quartz window
7. Radiation pyrometer, "Rayotube"
8. Refractory ceramic potting material
9. Brass retaining body
10. Cooling water lines to nozzle blocks
11. Ignition wire for rocket combustion

FIGURE 3. ROCKET MOTOR TEST ARRANGEMENT

INNER COLUMN OF TRANSDUCER

The inner column element (Fig. 4) is the most important component in the transducer. The response of this element to the pressure in the rocket chamber is measured and interpreted as pressure. The strains created in this column by the pressure must be high enough to produce the required output while at the same time be low enough to maintain the high axial response frequency of the element. The geometry of this element is such that it responds only to axial loads. Lateral motions are minimized because the column is guided by the porous plug and seals. In addition, bending strains can be completely cancelled out in the sensing bridge by proper location of the strain gages.

a) Inner column

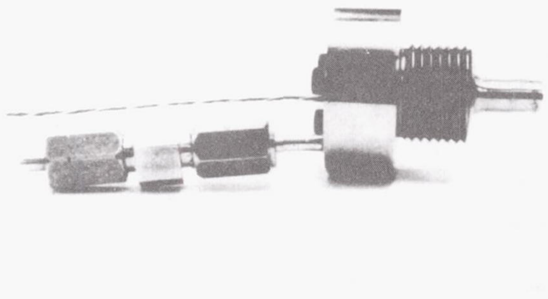

FIGURE 4. INNER COLUMN AND ASSEMBLED TRANSDUCER

FREQUENCY RESPONSE

Pressure pulses impinging on the surface of the porous plug cause compressive strains in the inner column. These strains are imparted to the strain gages, and resulting changes in resistance are monitored and interpreted as pressure amplitude. Errors in the output signal occur as the frequency of the pressure signal approaches the resonant frequency of the column. In these units the damping is very small (damping ratio less than 0.05), and the output amplitude is larger by 1% when the frequency of the pressure signal reaches 1/10 of the column resonant frequency. When output errors of less than 1% are desired, and the maximum frequency of the pressure signal is 20 kHz, it is necessary to have a column resonant frequency in excess of 200 kHz.

In general, three choices are available for increasing the resonant frequency of a column element. These choices are:

1. Use a material with a higher stiffness-to-weight ratio.

2. Shorten the length of the column.

3. Increase the stiffness by increasing the lower column area.

Beryllium was selected initially for the inner column because of its high stiffness-to-weight ratio, and later it was also selected as the best choice based on the stiffness-to-weight ratio of the applicable materials.

Shorter length columns were investigated but it was found that if the column is shortened appreciably, fabrication and assembly problems are more severe and larger temperature excursions at the strain gage bridge are possible. Therefore, it was decided not to reduce the length of the inner column.

The only route left open to increase the resonant frequency of these units was to increase the column cross-sectional area at the base. A column area of 0.175 cm^2 (0.0272 $in.^2$) was selected (increase of 75%) to insure a minimum output of 30 mV at maximum rated pressure. With a 75% increase in the column stiffness the resonant frequency should increase 32% to approximately 100 kHz.

INSTALLATION AND COMPENSATION OF THE STRAIN GAGE BRIDGE

Because of small size and output sensitivity desired for the transducer, semiconductor strain gages of small gage length and moderate resistance were selected as the most desirable sensing element. The resistance of all gages was measured before installation to allow selection of sets of four gages nearly equal in resistance. The selection of matched sets was considered important to avoid the need of excessive compensation.

The gages were installed in a Poisson bridge arrangement to measure axial strain and provide temperature compensation. The first fully instrumented prototype transducer with a 77.4% dense porous beryllium plug and a 127-μ (5-mil) coolant flow orifice was thermally tested in the rocket motor at the conditions as follows: chamber pressure: 276 N/cm^2 (400 psig); heat flux 4140 W/cm^2 (25.3 $Btu/in.^2$-sec); duration of test: 30 sec; plug surface temperature: 888.7° to 949.8°K (1140° to 1250°F); coolant supply pressure: 1411 N/cm^2 (2050 psig). In addition, a thermocouple was inserted in the vent hole in the lower chamber until it contacted the lower flange of the O-ring seal. The temperature of this point, monitored during each test, did not change. That is, it remained at room temperature, thus indicating that there was sufficient coolant flow for these conditions. Inspection of the transducer after the tests revealed only minor erosion of the surface of the porous plug.

CRYOGENIC PRESSURE TRANSDUCER

The testing of rocket engines that use cryogens requires accurate measurements of static and dynamic pressures at temperatures down to that of the liquid helium (4°K). The transducer should be small, lightweight and capable of being inserted in a standard boss; it should be capable of reaching thermal equilibrium quickly, be insensitive to dynamic temperature changes, and should be capable of responding to high frequency pressure oscillations. Accurate measurement of pressure parameters is important because it permits design verification of hardware, auxiliary equipment, pumps, flow, plumbing systems, etc., and it permits design modification of the engine, fuel, oxidizer, thrust chamber conditions and control systems. It permits detection and analysis of malfunctions of subsystems.

Two approaches were considered to meet these criteria during this program. One approach was the use of gallium antimonide as a hydrostatic pressure sensitive material, and the other approach was the use of silicon gages bonded to metallic pressure sensitive diaphragms.

Initially it was proposed to fabricate elements of the gallium antimonide from bulk crystal material. This proved impractical for two reasons. First, in order to obtain a bridge resistance of 100 Ω or greater, a length-to-area ratio of 20,000 to 1 was required. Second, assuming these high resistivity crystals could be grown, elements fabricated from them would have extremely nonlinear "resistance-to-temperature characteristics," and temperature compensation over a wide range, therefore, would not be practical. As an alternative, high resistance elements were produced by diffusion techniques. Surface diffusion results in a very thin (approximately 1 μ) surface layer of selected gallium antimonide material electrically isolated from a thicker, mechanically strong substrate through P - N junction action. This shallow depth permits fabrication of sensor elements having practical length, width, and resistances values, while at the same time allowing for the use of impurity levels that are high enough to insure linear resistance to temperature relationships. A satisfactory process for making N and P type gallium antimonide surface layers was developed. The resistance of the N-type gallium antimonide increases by roughly 1% per 689 N/cm^2 (1000 psi) hydrostatic pressure.

The P-type exhibited no appreciable hydrostatic pressure sensitivity. A working transducer using the P and N type GaSb was never successful because of the difference in the temperature resistance characteristics of the P and N type elements. This problem is not insurmountable, but requires more time for the development of technique in fabrication. During the course of the development it was noted that balco nickel wire had a resistance — temperature characteristic corresponding to that of N-type GaSb (Fig. 5). This material was substituted for the P-type GaSb for completing the bridge. Three transducers were then fabricated (Fig. 6). They were just recently received and therefore have not been evaluated.

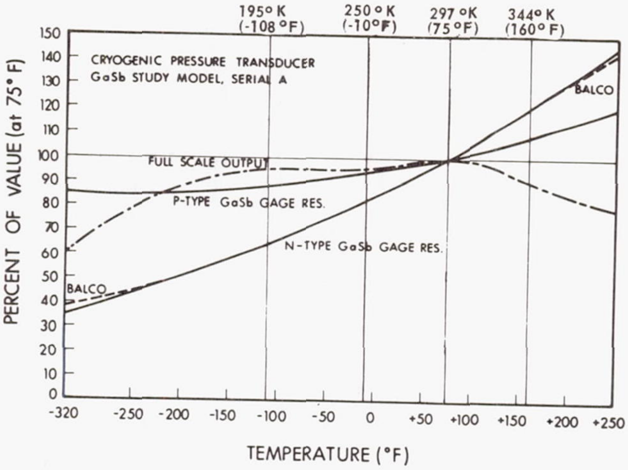

FIGURE 5. BALCO WIRE COMPARED WITH N-TYPE GaSb GAGE RESISTANCE

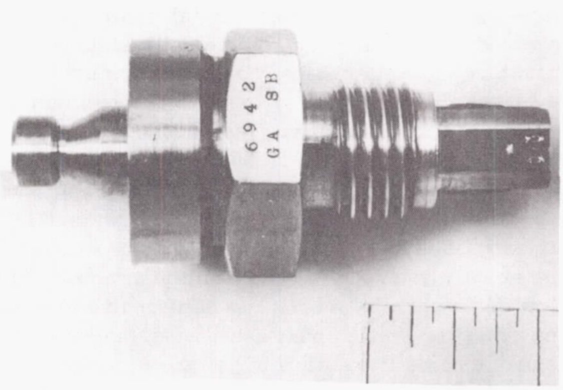

FIGURE 6. GaSb TRANSDUCER

The second approach, the use of silicon strain gages, required careful consideration of not only the mechanical and electrical properties of the silicon elements, but also the mechanical properties and geometry of the sensing diaphragm. A number of approaches using single chip silicon gages bonded to diaphragms were unsuccessful as a result of large changes in compression stresses sensed by the compression gages at low temperature. These changes were caused by diaphragm structural and dimensional changes with temperature and from the increased strength of bonding agents between gage and diaphragm at low temperatures.

The next approach was to use heavily doped diffused silicon strain gages bonded to nispan c diaphragms in a four active arm bridge configurations. Diffused silicon gages with surface impurity concentrations of 1.4, 3, and 5 × 10^{20} boron atoms/cm^3 were produced (Fig. 7). These gages bonded to the nispan c diaphragm and excited with a constant current power supply were capable of stable operations over a range of 3.70° to 394°K (-453° to +250° F) (Fig. 8). Sensitivity shifts of 2 to 3% per 55.6°K (100° F) from 3.70° to 394°K (-453° to +250°F) were proven feasible with a minimum of compensation circuitry. Sensitivity of less than 1% per 55.6°K (100° F) was achieved over narrow temperature spans. A zero shift of 1 to 2% per 55.6°K (100° F) was attained from 3.70° to 394°K (-453° to +250° F). Figure 9 shows typical transducer elements. Figure 10 shows a disassembled transducer. Three prototype transducers were furnished for further evaluation (Fig. 11). Figure 12 shows a typical performance curve when transducers are subjected to liquid nitrogen.

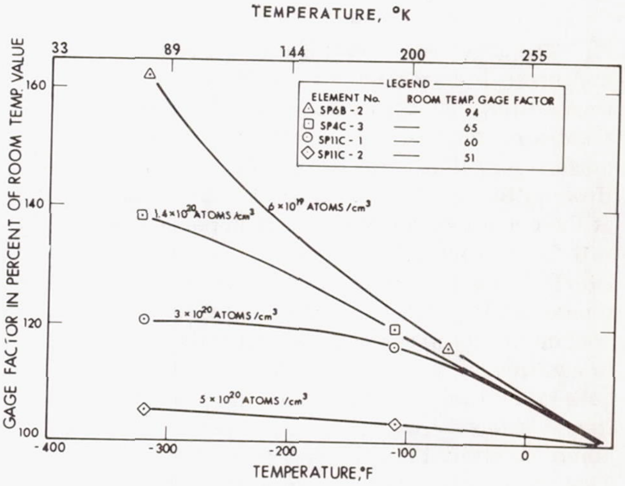

FIGURE 7. GAGE FACTOR CHANGE vs TEMPERATURE

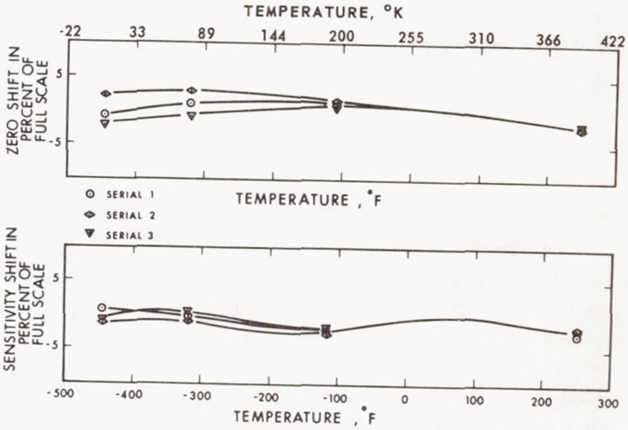

FIGURE 8. CRYOGENIC PRESSURE TRANSDUCER — ZERO AND SENSITIVITY SHIFT WITH TEMPERATURE

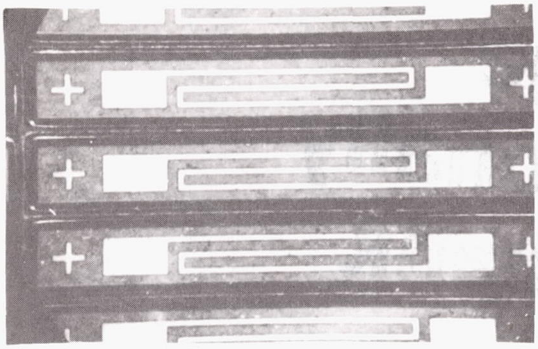

FIGURE 9. TYPICAL TRANSDUCER ELEMENTS

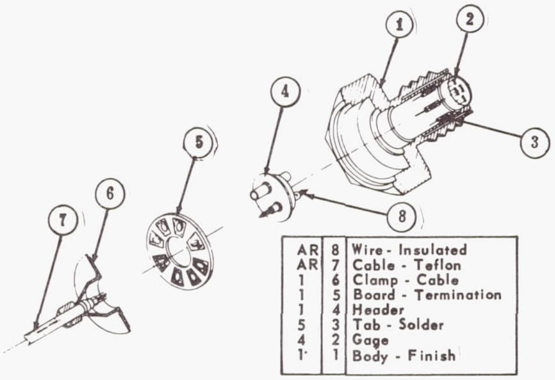

AR	8	Wire - Insulated
AR	7	Cable - Teflon
1	6	Clamp - Cable
1	5	Board - Termination
1	4	Header
5	3	Tab - Solder
4	2	Gage
1	1	Body - Finish

FIGURE 10. DISASSEMBLED CRYOGENIC PRESSURE TRANSDUCER

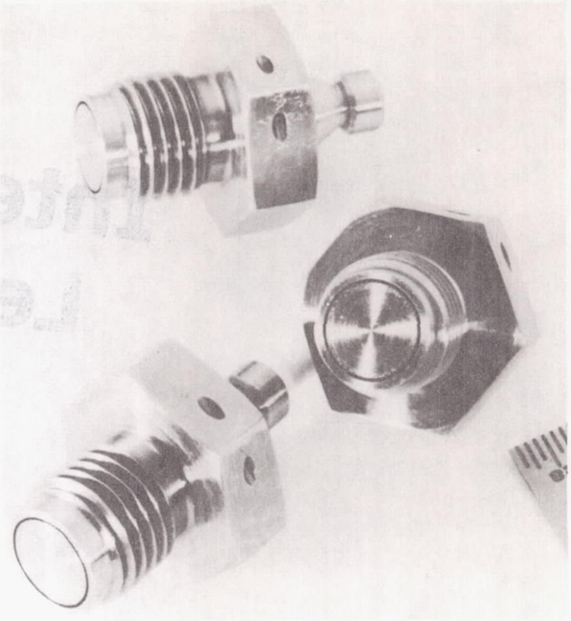

FIGURE 11. COMPLETED TRANSDUCERS

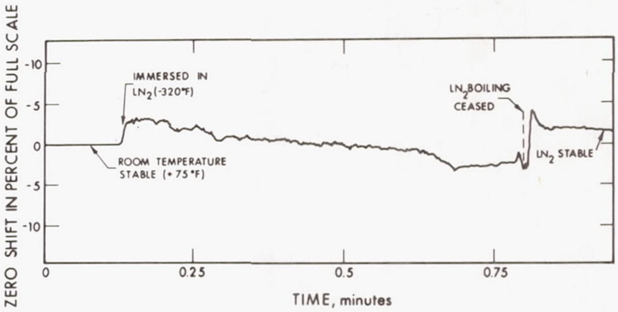

FIGURE 12. TYPICAL PERFORMANCE CURVE (RESPONSE OF TRANSDUCER ZERO OUTPUT TO STEP CHANGE IN TEMPERATURE)

REFERENCES

1. Design, Development and Fabrication of an Experimental High Temperature High Frequency Response Pressure Transducer. Final Report, NASA (MSFC) Contract No. NAS8-11933, Battelle Memorial Institute, Columbus, Ohio.

2. Study and Investigation Design, Development and Fabrication of A Cryogenic Pressure Transducer. Final Report, NASA (MSFC) Contract No. NAS8-11934, Electrical-Optical Systems, Inc., Pasadena, California.

Page
Intentionally
Left Blank

THE USE OF THE MÖSSBAUER EFFECT AND LASER INTERFEROMETRY TO DETERMINE EXTREMELY SMALL AMPLITUDES FOR VIBRATION MEASUREMENTS AND CALIBRATIONS

By
Helmut G. Lackner

SUMMARY

Two methods for making an improvement of the state of the art in obtaining precise vibration measurements and calibrations are presented in this paper. The discussion concentrates on vibration tests on scale models, and each test often requires making measurements and calibrations of amplitudes that are much smaller than an optical wavelength. The two independent methods described in this paper allow for collecting data well beyond the results obtained by conventional techniques of measuring extremely small amplitudes. One method makes use of the Mössbauer Effect (recoil-free emission and absorption of gamma rays): the extremely sharp resonance lines are dissolved by Doppler shift and can be used for measuring velocities of a fraction of a millimeter per second. This method is used to obtain vibration measurements by measuring and comparing velocities. Since the peak of a Mössbauer line or the peaks of its hyperfine structure are fundamental constants expressed in velocity, a simple calibration technique for electromechanical oscillators has been developed where the instantaneous velocity of the oscillating object is compared with a Mössbauer line. With this method, vibration measurements and calibrations can be performed both in the optical and the suboptical range. The other method makes use of refined laser interferometry where monochromaticity, coherence and intensity of laser light are used to produce a stable photocurrent in which the ratio of its frequency components depends on the vibration amplitude. Both methods will allow reaching minimum amplitudes of a few angstrom units with an estimated uncertainty of 2%.

INTRODUCTION

Vibration measurements and calibrations frequently need to be performed in an amplitude range that is too small to be covered by conventional methods, especially if one has to investigate the behavior of scale models that are excited with alternating forces of much higher frequency than those to which the original object would be exposed. The amplitudes of the responding oscillations have to be decreased accordingly to maintain a realistic simulation, for example, to obtain information about the g-load to be expected. Obtaining data is sometimes difficult because commercial instruments to measure vibration amplitudes below one tenth of a wavelength of light do not exist, or are experimental setups for the laboratory only. However, vibration measurements in the amplitude range below one tenth of an optical wavelength are of great importance for vibrational investigations of scale models.

Our research, therefore, concentrated on methods with which vibration amplitudes from the optical range down to the order of angstrom units could be measured, and methods with which calibrations could be performed. Two completely independent methods which supplement each other were considered: one applies the Mössbauer effect, the other makes use of refined laser interferometry.

MÖSSBAUER EFFECT

The Mössbauer effect is the phenomenon of recoilless resonance fluorescence of gamma rays from nuclei bound in solids. It is characterized by the fact that under certain temperature limitations a nucleus that is embedded in a lattice and is emitting or absorbing a gamma quantum does not recoil because the crystal as a total represents the recoiling mass.

Since the mass of the crystal is infinitely larger than the mass of the nucleus, the recoil energy for the nucleus vanishes. Under this condition the emitted or absorbed gamma line keeps its natural frequency because it is not shifted by the recoil of the nucleus, and furthermore, this gamma line maintains its natural linewidth because it is not broadened by the thermal Doppler effect (Fig. 1). (The thermal Doppler effect is necessarily connected with a transfer of an impulse to an individual nucleus, and this cannot happen for a Mössbauer Line.) However, the movement of the whole crystal causes a Doppler shift (Fig. 2). Because of the extremely sharp resonance lines, a relative movement of emitter and absorber of only a fraction of a millimeter per second will introduce a Doppler shift from which a perfect resolution of the natural line profile can be obtained.

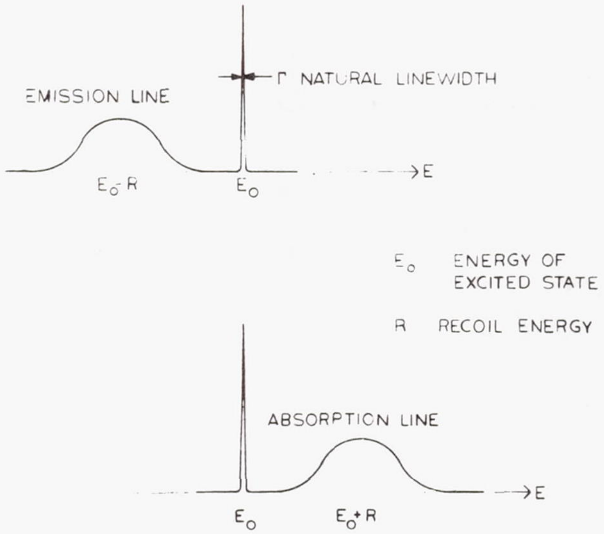

FIGURE 1. MÖSSBAUER LINE AND EMISSION AND ABSORPTION LINE

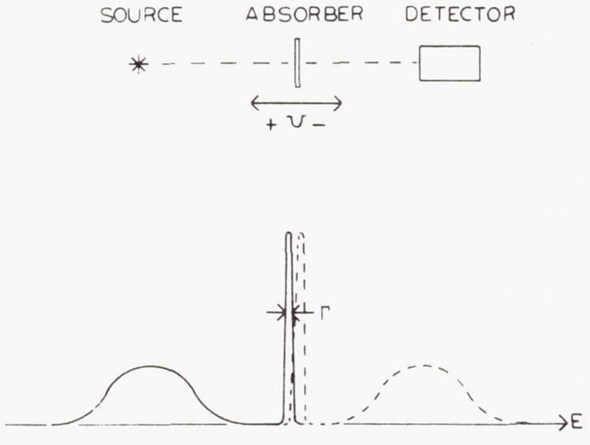

FIGURE 2. PRINCIPLE OF MÖSSBAUER APPARATUS AND DOPPLER-SHIFTED GAMMA LINE

This method does not provide a direct measure of the absolute energy of a line, but it is extremely sensitive in detecting line shifts. In the case of Fe^{57}, for example, the energy of the gamma ray is known to be 14.36 keV with an uncertainty of ± 10 eV, but differences in the energy as small as 10^{-10} eV can be readily measured. Relative changes in energy can be measured with the extreme accuracy of $\frac{\Delta E}{E} = 10^{-13}$. That means that the energy of the gamma ray is defined to within 1 part in 10^{13}, and thus it is the most accurately defined electromagnetic radiation available for physical experiments.

This extremely sensitive energy resolution makes the method ideally suited to measure the interactions of the surrounding electrons and the external fields with the nuclei, whereby three important phenomena associated with the nuclear hyperfine structure have to be considered: the isomer shift, the quadrupole splitting, and the nuclear Zeeman effect.

Emission and absorption lines are only centered at the same energy if the corresponding nuclei are in similar environments. If this is not the case, for example, by a change in the electrostatic interaction between the nucleus and its electron shell that might arise from a change in valence, a shift of the nuclear levels will result and manifest itself in a zero velocity shift of the resonance curve, which is called isomer shift. If both source and absorber are at rest, little or no resonance will be observed. To reestablish resonance, the absorber or the source is moved with a certain velocity. In this special case of Co^{57} diffused into palladium as source, and stainless steel as absorber, it is -0.26 mm/sec (Fig. 3). (By definition a positive sign stands for approaching, a negative sign for departing source and absorber). The velocity between source and absorber is a measure of energy shift. Therefore, it is usual to express the small energies in Mössbauer experiments in terms of velocity.

Quadrupole splitting is a split in the nuclear levels as a result of the interaction of the nuclear quadrupole moment with the gradient of the electric field arising from other charges in the crystal (Fig. 4). It reflects the deviation of the nucleus from spherical symmetry. Quadrupole splitting is exhibited by different compounds of Mössbauer isotopes. In this example the source is again Co^{57}; the absorber is crystalline ferrous sulfate.

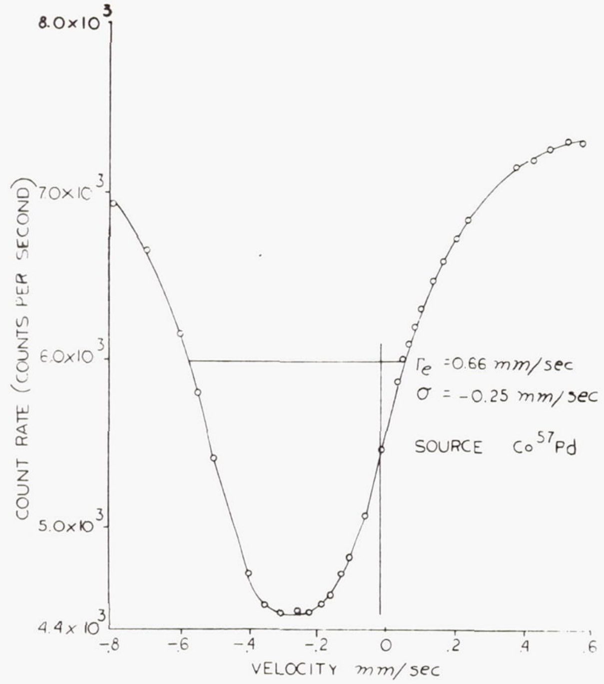

FIGURE 3. CALIBRATION SPECTRUM FOR STAINLESS STEEL ALLOY 310 ENRICHED

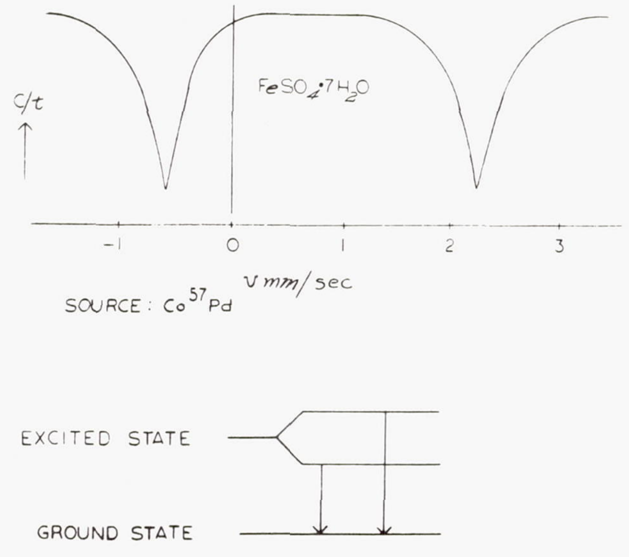

FIGURE 4. QUADRUPOLE SPLITTING

In the case of the Nuclear Zeeman Effect, gamma ray transitions are observed between two nuclear levels that both exhibit magnetic hyperfine splitting (Fig. 5). The gamma lines correspond to transitions from a particular magnetic sublevel of an excited nuclear state to a sublevel of a ground state. This magnetic hyperfine splitting is caused by the interaction of the nuclear magnetic dipole moment with the magnetic field of the electrons of the atom. The material used in this experiment was Co^{57} diffused into Pd as source, and metallic iron enriched with Fe^{57} as absorber. Since the peak of a Mössbauer line or the peaks of its hyperfine structure are fundamental constants expressed in velocity, they are ideally suited to measure velocities.

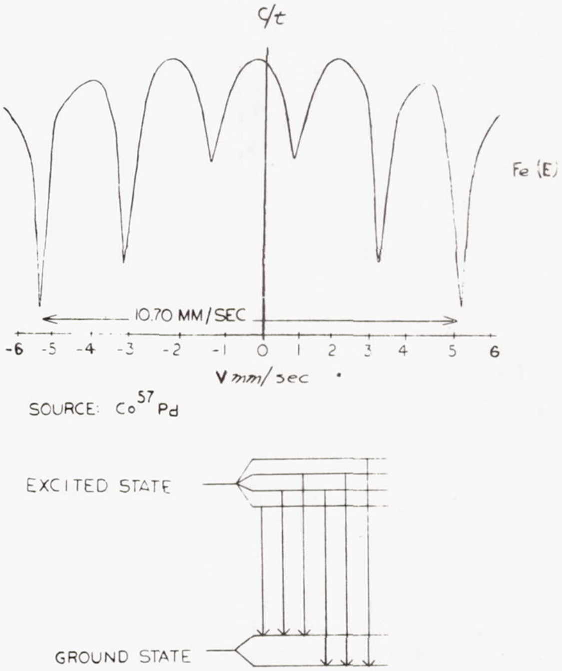

FIGURE 5. NUCLEAR ZEEMAN EFFECT

When using earlier methods to obtain vibration measurements, usually the amplitude or the acceleration was determined. Velocity variations were seldom considered. In utilizing the Mössbauer effect, however, velocity is measured. By restricting the vibrations examined in this investigation to steady state sinusoidal oscillations, it is possible to calculate with certainty (1) the displacement amplitude and acceleration from measuring the frequency, and (2) the velocity variations. However, it is also possible to measure nonharmonic oscillations.

Vibration investigations were conducted by using a loudspeaker and different piezoelectric transducers. The source is mounted on the vibrating object and the absorber is at rest. With this arrangement different cases can be investigated by using partial resonance, off resonance, and resonance conditions.

The partial resonance case makes use of the isomer shift in such a way that zero velocity corresponds to a certain count rate in the middle of the linear portion of the absorption curve (Fig. 6). Any positive or negative velocity will increase or decrease this count rate. Thus the velocity-time function will be transferred into a countrate-time function.

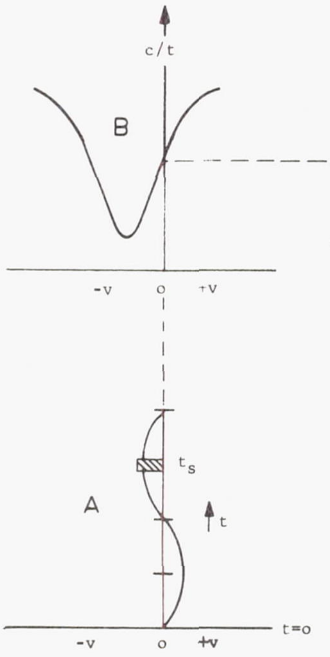

FIGURE 6. DIAGRAM OF THE PARTIAL RESONANCE CASE TRANSFER FUNCTION

An electronic device triggers the counter for an adjustable fraction of an oscillation period to permit repeated sampling within a small increment (Fig. 7). After enough counts have been collected for statistical accuracy, the gate is shifted by delaying the trigger pulse which opens the gate, and the next portion of the curve is counted. Finally point for point samples of a period have been collected. Corrections for the influence of gate length and nonlinearity of the characteristics are provided.

Figure 8 depicts amplitude measurements of a piezoelectric shaker. The upper portion shows the sinusoidal fluctuations of the countrate as collected point for point for one period, and by knowing the countrate-velocity relationship, the velocity curve on the bottom has been found. The peak amplitude is derived by the relation: velocity = amplitude times angular frequency, which in this special case is 125 Å for 2 kHz at 35 V driving voltage. At higher frequencies even lower amplitudes can be measured, for example down to 3.5 Å at 10 kHz (Fig. 9).

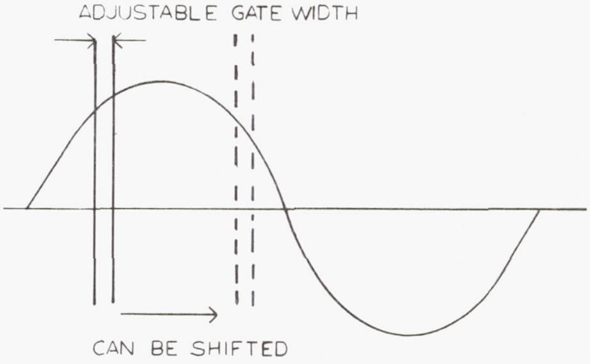

FIGURE 7. ELECTRONIC SAMPLING

The useful range of the partial resonance case is shown in Figure 10. This is a double logarithmic plot of velocity versus frequency for various values of acceleration and peak displacement. The lower frequency limit is arbitrarily set at the lower limit of the audio spectrum, the upper frequency limit is imposed by the experimental apparatus used. However, with an improved apparatus that is to be delivered soon, the limit of the technique will exceed 100 kHz.

Another method which is particularly of interest to vibration calibrations is the off resonance case. It deals with source and absorber combinations that are essentially out of resonance at zero velocity, but are tuned to resonance by an introduced relative velocity. These conditions can be obtained with material displaying quadrupole splitting or the nuclear Zeeman effect.

The basic idea of this method is that the calibration relies only on the position of the absorption lines of the hyperfine structure of various Mössbauer absorbers. The gating and sampling technique is similar to that of the off resonance case. Figure 11 illustrates the transfer function of this technique. The sinusoidal oscillation has a larger amplitude and exceeds the line of continuity in the spectral curve, which in this case represents the inner lines of metallic Fe^{57}. The remaining lines of this Zeeman splitted display were omitted to simplify the illustration. The outcome does not resemble the original sinewave,

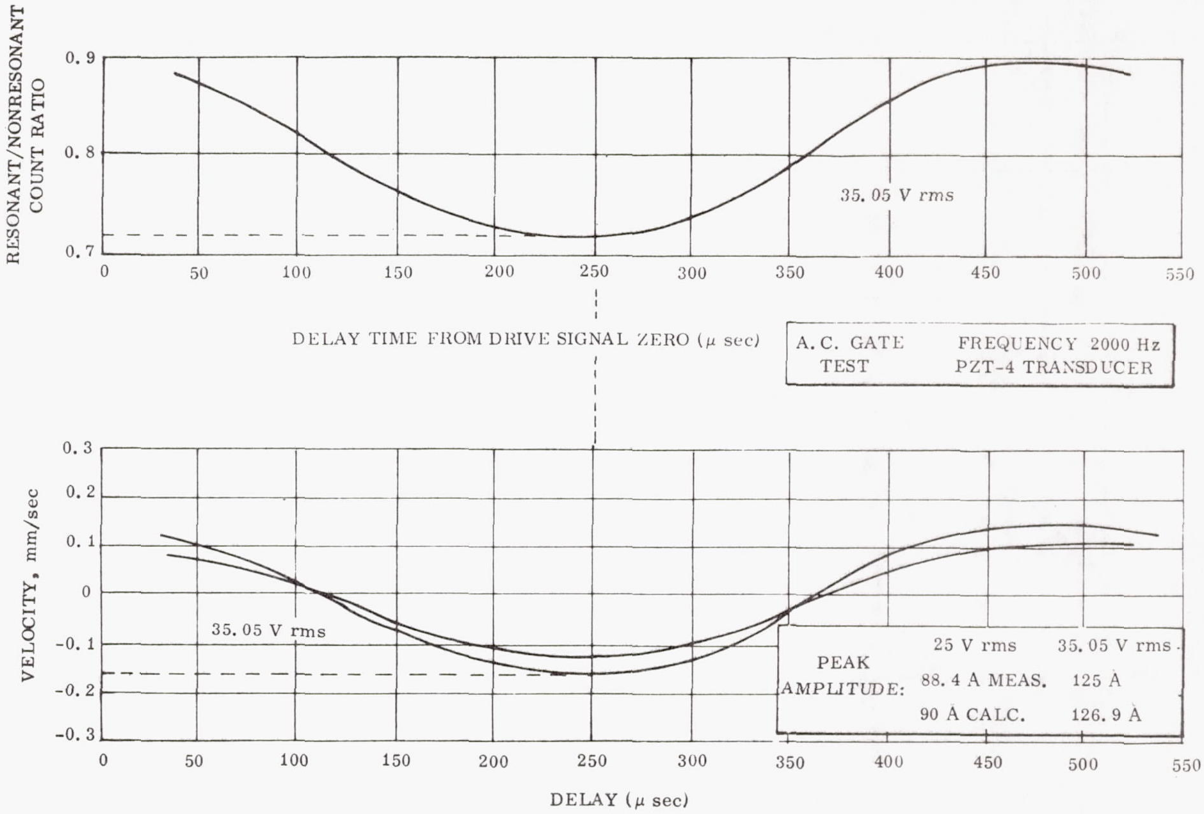

FIGURE 8. AMPLITUDE MEASUREMENTS OF A PIEZOELECTRIC SHAKER

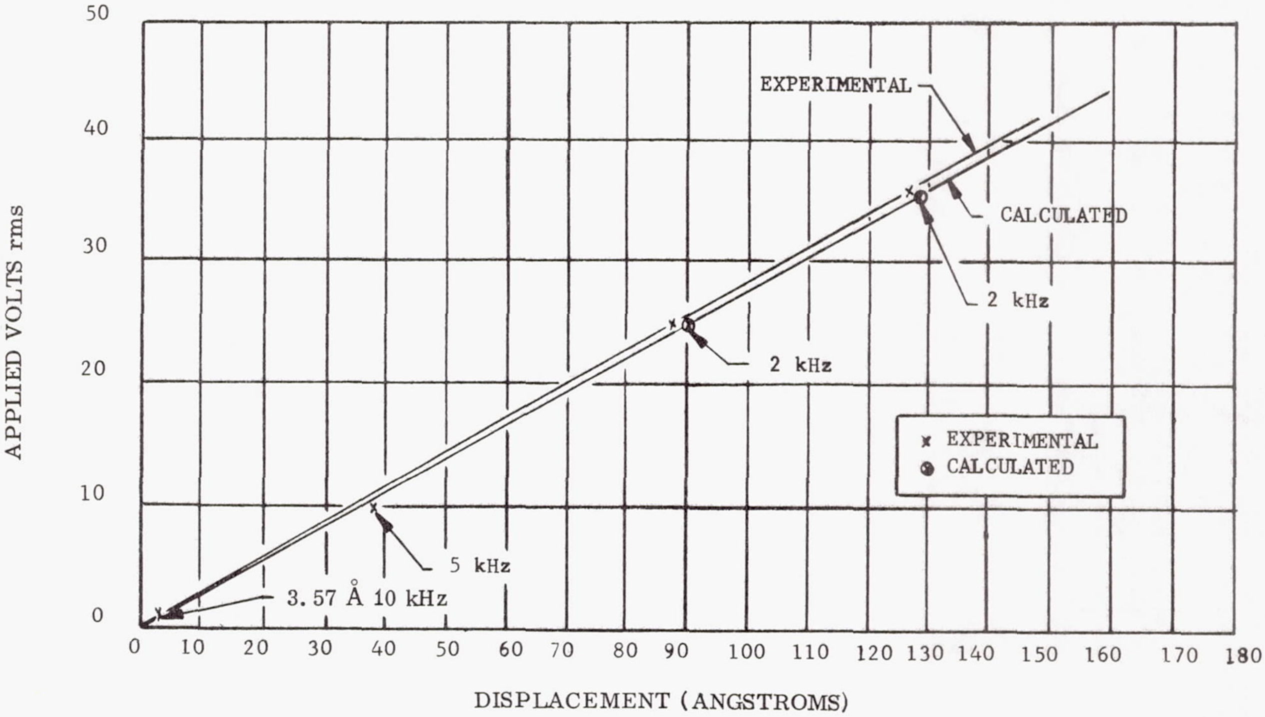

FIGURE 9. COMPARISON OF EXPERIMENTAL AND CALCULATED PEAK DISPLACEMENTS OF A PIEZOELECTRIC TRANSDUCER

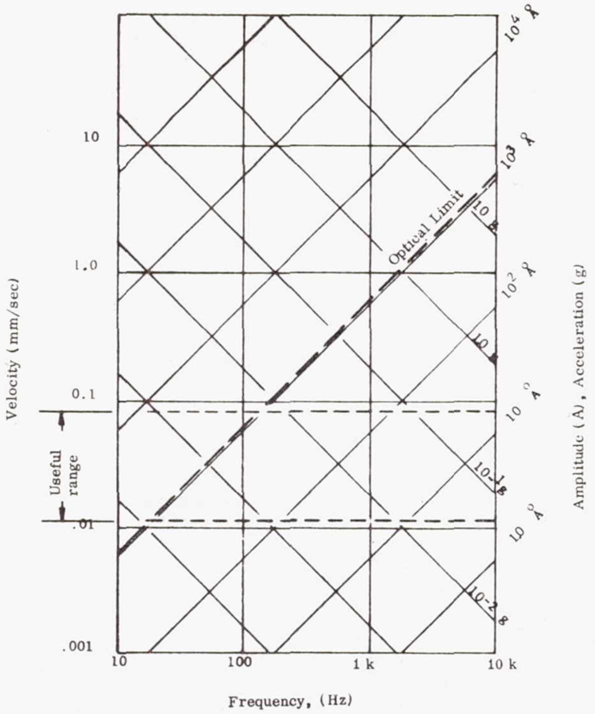

FIGURE 10. USEFUL RANGE OF PARTIAL RESONANCE CASE

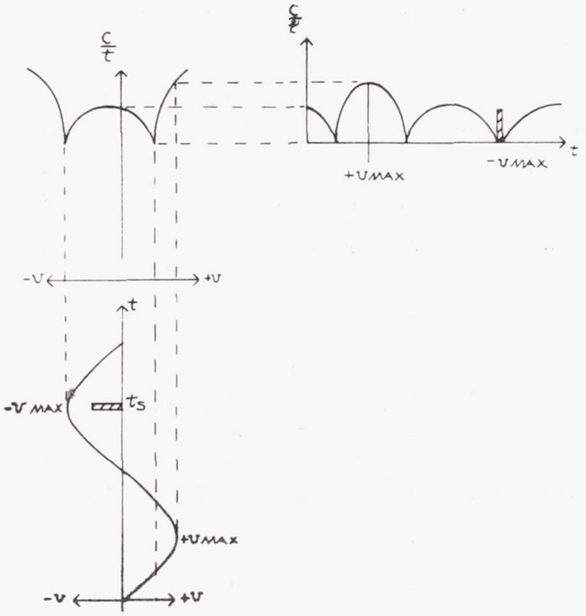

FIGURE 11. MULTIPLE POINT CALIBRATION TECHNIQUE TRANSFER FUNCTION

but the extrema correspond to the extrema in the original curve, and furthermore, the discontinuities correspond to the spectral lines in the absorber spectrum. This permits a calibration based on fundamental constants as they are displayed in the Mössbauer spectrum. All one has to do is to set the electronic gating device to a positive or negative velocity maximum, which is determined by wave tracing as in the partial resonance case, and regulate the driving voltage of the oscillator until a minimum in the counting rate is reached. At this point the maximum velocity of the transducer is equal to the velocity associated with the spectral line of the absorber. If the frequency of the harmonic motion is known, the displacement amplitude can be calculated. Using different spectral lines of the hyperfine structure, or different absorbers, a variety of calibration points can be obtained.

Figure 12 shows the calibration curve of a small loudspeaker with unknown characteristics. The points delivered by isomer shift, quadrupole split, and Zeeman effect are marked. The peak amplitude was calculated from the frequency and the peak velocity. For 8 kHz the calibration factor is 56.4 Å per volt rms. This is just to demonstrate the simple calibration technique for small amplitude electromagnetic, ferroelectric, and piezoelectric transducers.

The useful range of this multiple point calibration technique is shown in Figure 13. This plot of velocity versus frequency is in the same scale as the similar graph describing the partial resonance case; however, here the useful range is broader and shifted to higher velocities. The frequency range of the new apparatus will exceed 100 kHz.

A third method that makes use of the Mössbauer technology for vibration measurements and calibration is the resonance case, which pertains to source-absorber combinations having unsplit lines and being resonant at zero velocity. The perfect resonance is disturbed if the source is allowed to vibrate, and the measured count rate will increase with increasing velocity.

While the resonance curves used in the previous cases were based on constant velocities, the resonance curve discussed now is derived by using sinusoidal velocities and has a different shape. Mathematically it is a function of the counts per unit time on average count rate c/t, depending on the off resonance count rate N_0, the peak velocity δ_1, the full line width at half maximum Γ, and the absorption

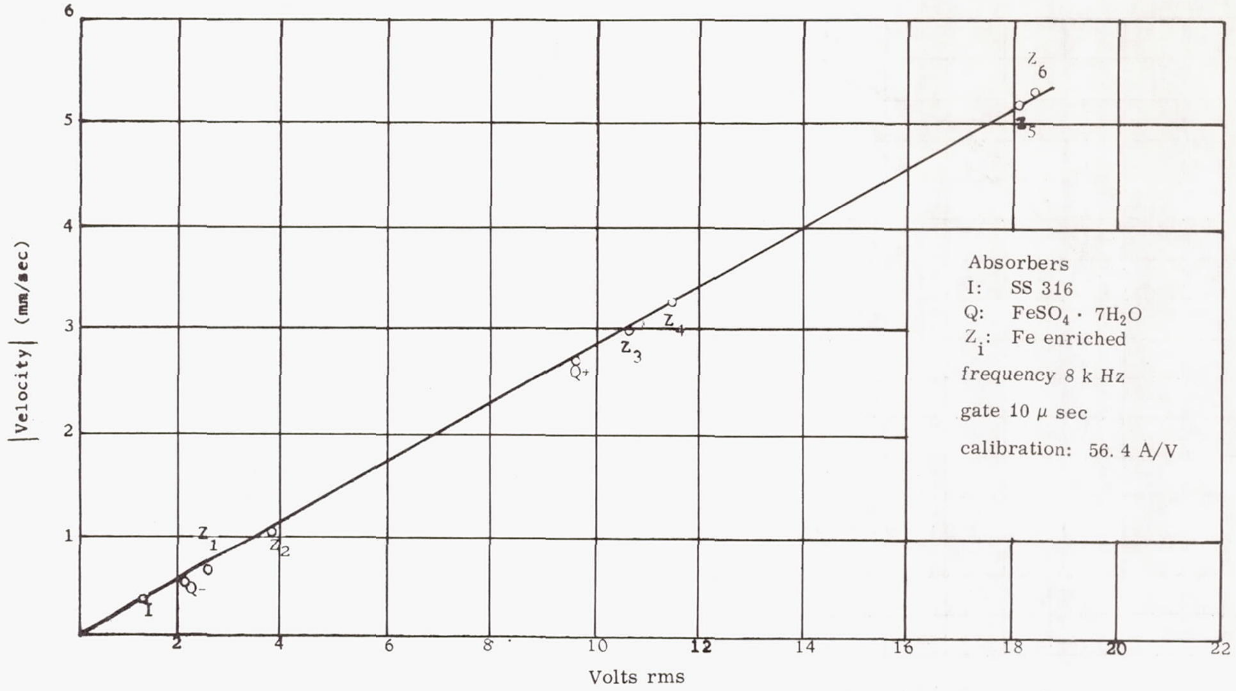

FIGURE 12. LOUDSPEAKER CALIBRATION BY RESONANCE ABSORPTION LINE POSITION

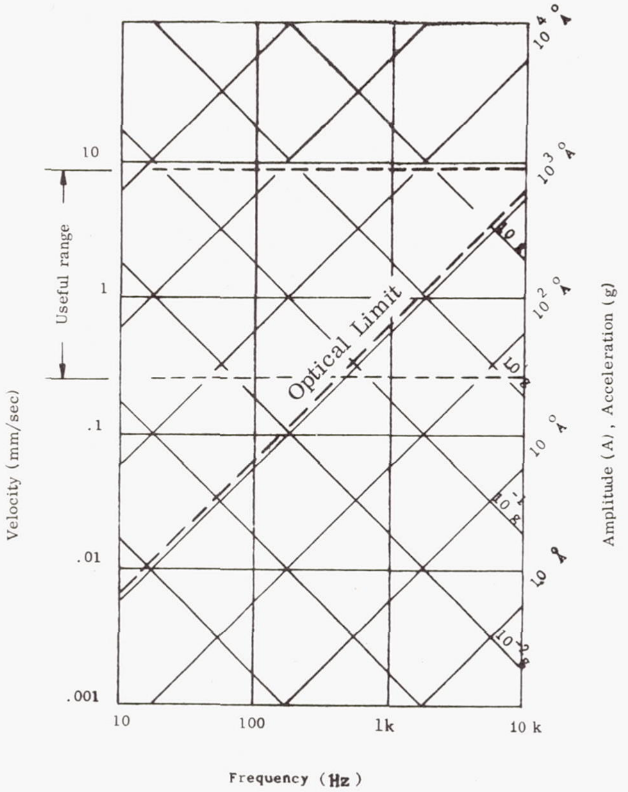

FIGURE 13. USEFUL RANGE OF THE MULTIPLE POINT CALIBRATION TECHNIQUE

fraction A, as given by

$$\frac{c}{t} = N_0 \frac{\delta_1^2 + 2\Gamma^2 A}{\delta_1^2 + 2\Gamma^2} \quad . \qquad (1)$$

Figure 14 represents such an absorption curve. The difference at high velocities between the theoretical and the experimental values is caused by some simplified assumptions in the derivation of the equation. The lower curve was derived by introducing experimentally determined values for the constants Γ and A.

Both curves agree perfectly up to 0. 4 mm/sec velocity. The lower curve is very well suited to calibrate piezoelectric transducers at low velocities. Two transducers were calibrated with this resonance technique. Data in Figure 15 were obtained with the source mounted on a loudspeaker. The driving frequency was 8 kHz. Displacements in the range of 10 to 100 Å could be measured. Figure 16 shows the calibration curve of a piezoelectric transducer excited by a 40 kHz signal. It was possible to measure displacements of a few angstroms.

Figure 17 shows the useful range of the resonance case calibration method. It can be seen that at high frequencies even fractions of an angstrom can be measured and respectively calibrated.

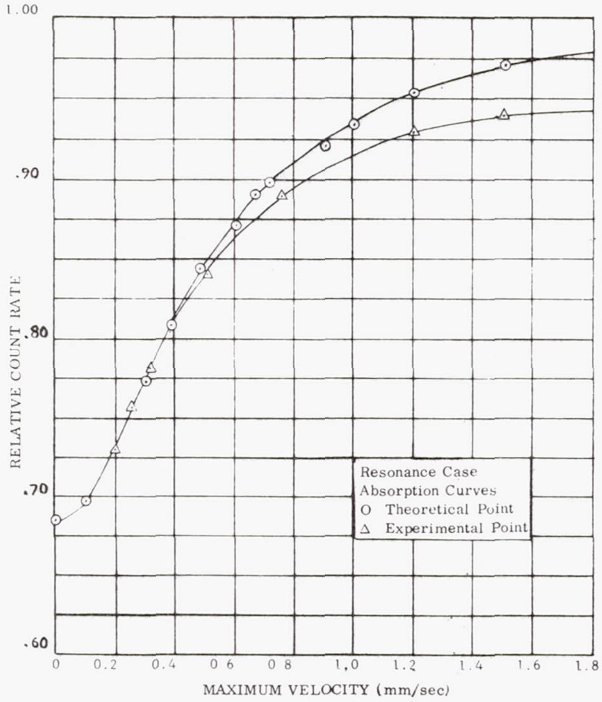

FIGURE 14. RESONANCE CASE ABSORPTION CURVES

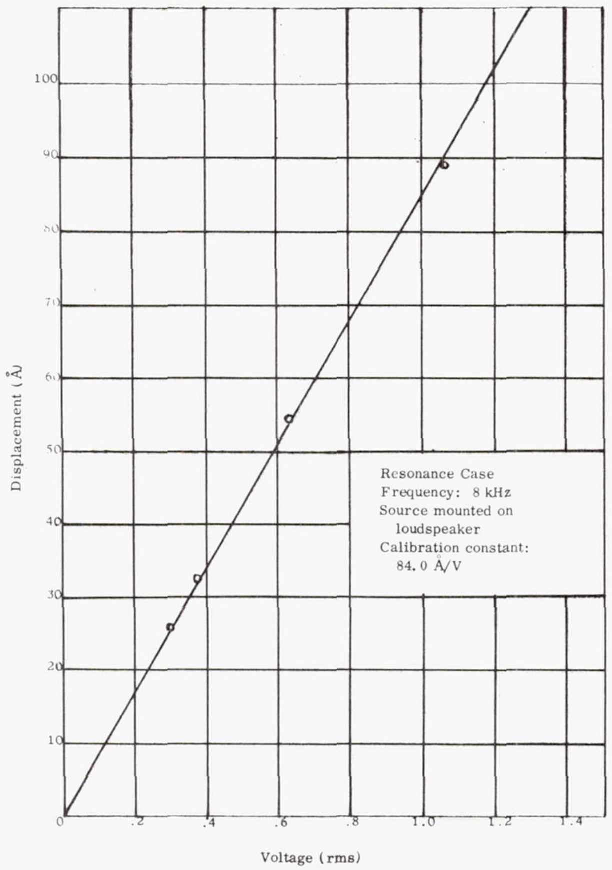

Resonance Case
Frequency: 8 kHz
Source mounted on
loudspeaker
Calibration constant:
84.0 Å/V

FIGURE 15. SOURCE MOUNTED ON LOUDSPEAKER

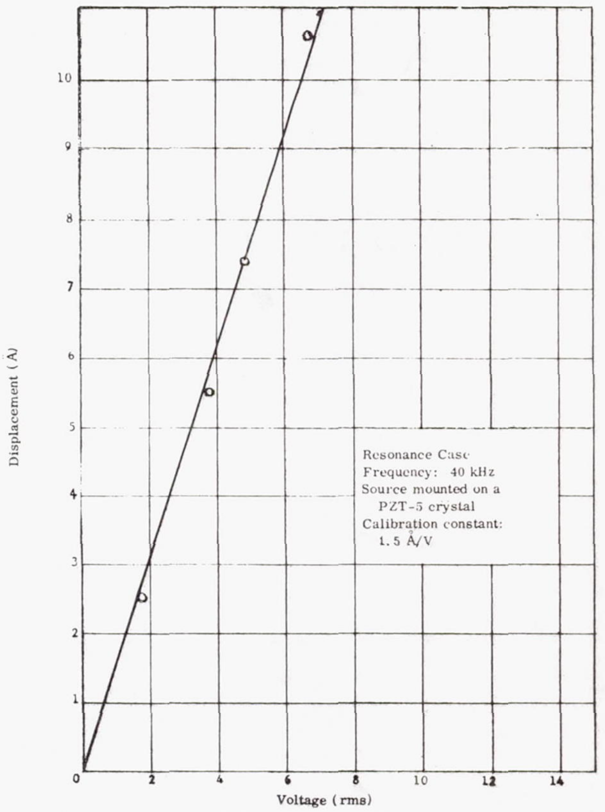

Resonance Case
Frequency: 40 kHz
Source mounted on a
PZT-5 crystal
Calibration constant:
1.5 Å/V

FIGURE 16. SOURCE MOUNTED ON PZT-5 CRYSTAL

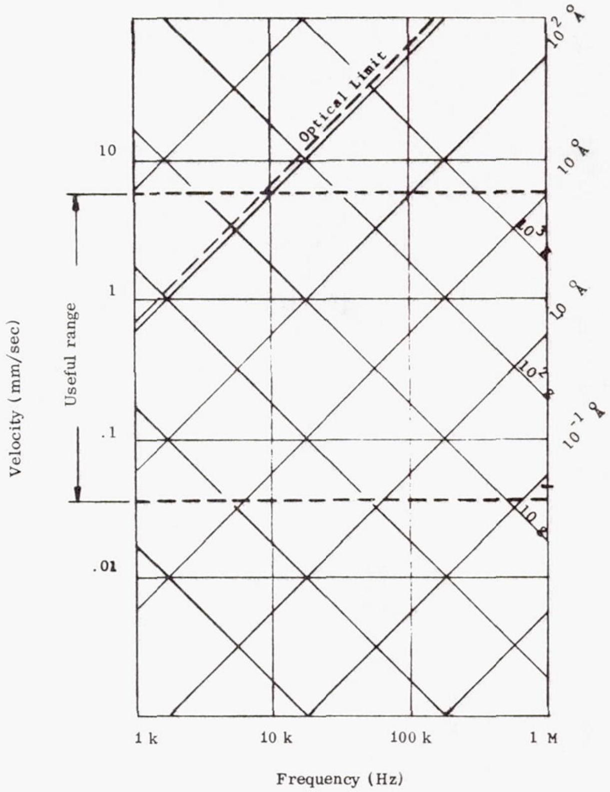

FIGURE 17. USEFUL RANGE OF THE RESONANCE CASE

This method has virtually no frequency limitation as long as the waveform is perfectly sinusoidal and the velocity falls within the useable range.

In the overall range the counting time required per point will be about three minutes and it will still be possible to keep the errors in peak velocity at 2% or less.

The development of these measuring and calibration methods was done at Rocketdyne. The contract requires the delivery of a laboratory calibrator (Fig. 18) and a transfer standard.

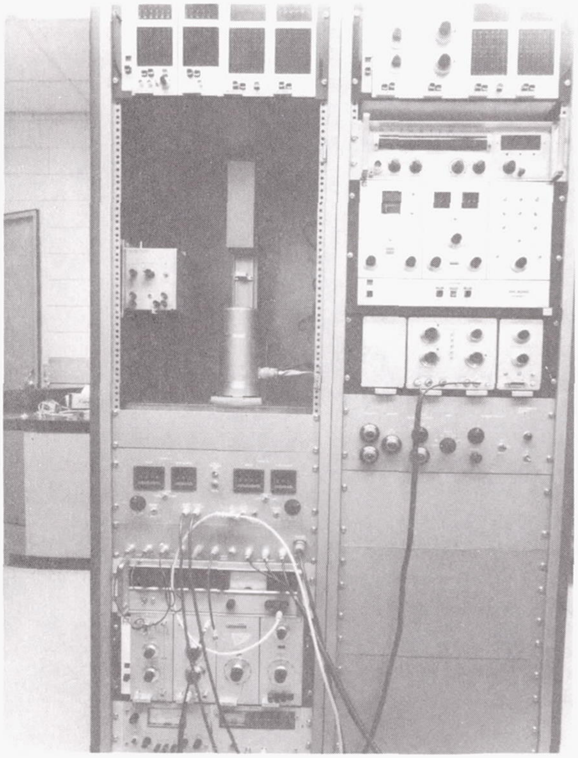

FIGURE 18. MÖSSBAUER EFFECT VIBRATION CALIBRATOR

The great advantage of the Mössbauer-type vibration calibrator is that it is based directly on an absolute standard, namely a Mössbauer line, which is a natural constant. However, the calibrations with these methods have a general disadvantage: they are very time consuming and therefore are not likely to be used for routine calibrations where multiple data points in a short time are required. For this purpose optical methods are faster. In recent years optical methods have become known, and with these methods it will become possible to sense vibration amplitudes in the order of a few angstroms. However, although these methods are based on reasonable assumptions, they should be cross checked with an absolute method. This can be done with the absolute Mössbauer method.

LASER INTERFEROMETRY

Conventional interferometric methods are used to measure minimum vibration amplitudes in the order of one tenth of a wavelength only, which is not sufficient for our needs. Therefore, we initiated a contract with the National Bureau of Standards (NBS) to extend the optical measuring range at least two orders of magnitude below the conventional interferometric range. The method used to accomplish this measurement is especially suitable for calibration because it makes use of the monochromaticity, coherence, and intensity of laser light in an optical interferometer.

In the following, a short sketch will be given of the application of the laser interferometer in conducting vibration measurements and calibrations. If an interference pattern is formed by combination of two coherent beams of light in an interferometer, the current from the photocell receiving light from a small area is given by

$$I = A + B \cos k\delta, \quad k = \frac{2\pi}{\lambda} \qquad (2)$$

where

A, b ... constants related to the intensity of the two light beams

δ ... optical path difference between the two interfering rays

λ ... wavelength of the incident light.

This cos function of the photocurrent has nothing to do with an oscillating motion; it is obtained with stationary mirrors and represents the influence of the wavelength of the light and its phase as a result of differences in the optical pathlength.

Now, if one mirror vibrates sinusoidally, the difference in the optical pathlength δ changes sinusoidally and the current from the photodetector is given by

$$I = A + B \cos (k\delta + 2\xi \cos \omega t) \tag{3}$$

where

ξ ... amplitude of vibration

ω ... $2\pi f$, the angular frequency of the vibration.

The optical path difference δ may drift with changes in the dimension of the structure supporting the reflectors and can be adjusted by a dc bias applied to the shaker.

This expression for the photocurrent can be expanded in a Fourier series. The coefficients are expressed as Bessel functions with the argument $(2k\xi)$.

$$\begin{aligned} I = A &+ B \cos k\delta \Big[J_0(2k\xi) - 2J_2(2k\xi) \cos 2\omega t \\ &+ 2J_4(2k\xi) \cos 4\,\omega t \ldots \Big] \\ &- B \sin k\delta \Big[2J_1(2k\xi) \cos \omega t - 2J_3(2k\xi) \cos 3\omega t \\ &+ 2J_5(2k\xi) \cos 5\,\omega t \ldots \Big] \end{aligned} \tag{4}$$

where J_n is the Bessel function of the first kind and nth order. The separate terms of the Fourier series can be isolated by band pass filters. A filter set for the vibration frequency gives $C_1 \sin k\delta \cdot J_1(2k\xi)$, and a filter set for the second harmonic of the vibration gives $C_2 \cos k\delta \cdot J_2(2k\xi)$.

The constants C_1 and C_2 contain the insertion loss of a filter and also the constant B from the equations for the photocurrent.

The distance, δ, can be adjusted so that the ratio of the sin and cos factors is a known value, in particular, unity. Then the ratio of the output voltages of the second harmonic to the fundamental is

$$R_{21} = \frac{C_2}{C_1} \cdot \frac{J_2(2k\xi)}{J_1(2k\xi)} \, . \tag{5}$$

If the series expansion of the Bessel functions is used, the ratio is

$$R_{21} = \frac{C_2}{C_1} \, \frac{\pi\xi}{\lambda} \left(1 + \frac{2\pi^2\xi}{3\lambda^2} + \frac{2\pi^4\xi^4}{3\lambda^4} + \frac{32\pi^6\xi^6}{45\lambda^6} + \ldots \right) \cdot \tag{6}$$

This series converges for amplitudes less than the first zero of J_1 which is about 1920 Å. The convergence for larger values has not been investigated, but this is of no concern because larger values of amplitude can be covered by conventional optical methods.

If the 6328 Å line of a He-Ne laser is used, the error in dropping all terms of the series after the first is less than 1% for vibration amplitudes less than 240 Å. If the first two terms are used, a cubic equation has to be solved and the error is less than 1% for amplitudes less than 700 Å. Similarly, when using three terms and a slightly more complicated computer program, one can solve the fifth degree equation and find that the measuring range goes up to 1900 Å within an accuracy of 1%. This provides a considerable overlap with presently used methods. However, for the experiments done to investigate the usefulness of the theory, only the first order equation

$$\xi = \frac{\lambda}{\pi} \, \frac{C_1}{C_2} \, R_{21} \tag{7}$$

was used. The experimental setup is sketched in Figure 19. An oscillator drives a shaker whose vibrations are sensed by the laser-type interferometer and transformed into current by the photomultiplier. The photocurrent is analyzed by tracking filters that are synchronized from the oscillator, and the amplitude ratio of the second harmonic to the fundamental is obtained. To overcome difficulties in the zero drift of the shaker, an automatic feed-back mechanism is considered, the principle of which has been proved to work in manual operation.

It is felt that the uncertainties in vibration calibrations using this method would be about 2%.

Some preliminary results are given in Figure 20. This is a double logarithmic plot taken over four decades of amplitudes at 2 kHz. The abscissa is the shaker voltage, which can be assumed to be linear with displacement. The ordinates of the lines with the slope of one are the accelerometer output and the fundamental component of the photocurrent $E_1(x)$. The ordinate of the line with the slope of two is the component of the photomultiplier current with the

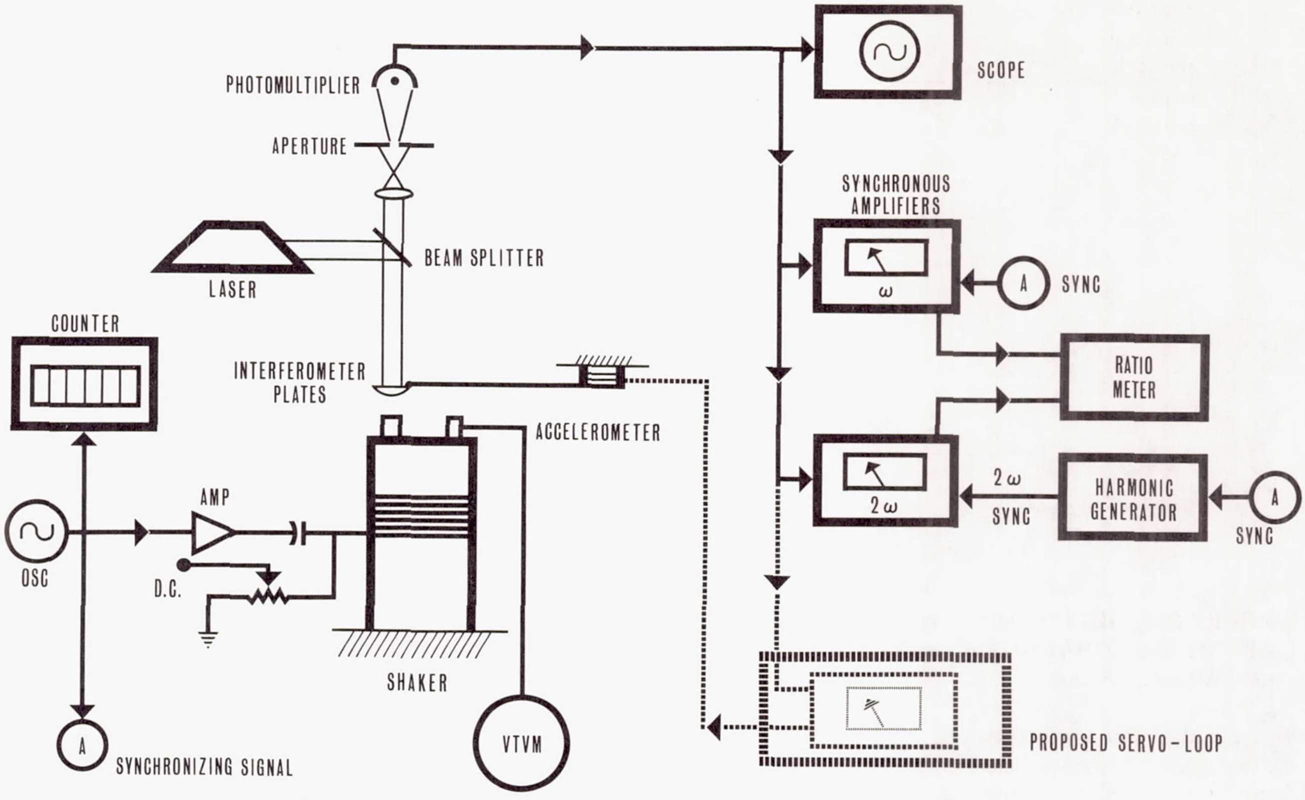

FIGURE 19. BLOCK DIAGRAM OF THE LASER INTERFEROMETRY SYSTEM

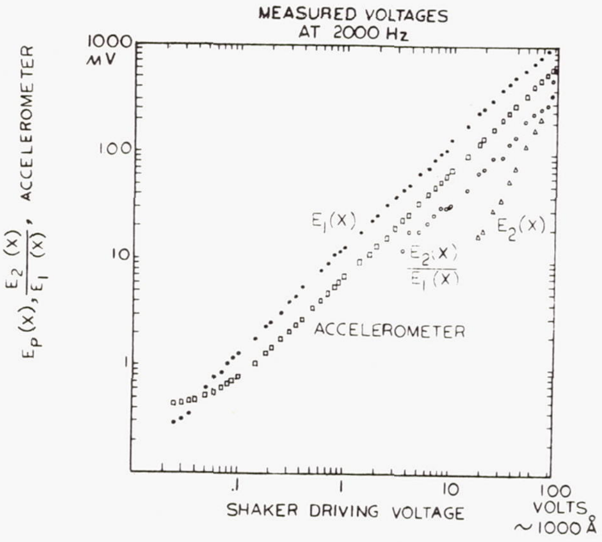

FIGURE 20. OUTPUT OF THE FUNDAMENTAL, OF THE FIRST HARMONIC, THEIR RATIO, AND OF THE MONITORING ACCELEROMETER VERSUS SHAKER DRIVING VOLTAGE

second harmonic $E_2(x)$. The ratio of the component of the photomultiplier signal at the second harmonic of the vibration frequency to the component at the fundamental vibration frequency $\frac{E_2(x)}{E_1(x)}$ is also shown with a slope of one. Figure 21 shows the result of similar measurements at 1 kHz. These data show linear relationship, which confirms that the experiment is in excellent agreement with the theory.

The signal of the second harmonic could be received to an amplitude of 10 Å. Below 10 Å it was lost in the noise in the photomultiplier and airborne sound in the room. Cooling with dry ice and a good sound insulation improved the measurements. Under favorable laboratory conditions 5 Å vibrations could be measured. The present main problem is the noise caused from improper electronics and hardware. Specifications for tracking filters have been written and two manufacturers responded positively. We expect that with improved filters the objective of the project, measurement and calibration of vibrations to within 1 Å amplitude at 100 kHz, can be reached.

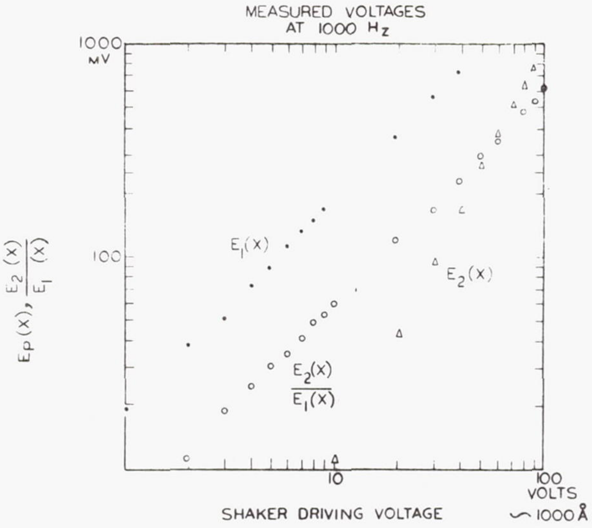

FIGURE 21. OUTPUT OF THE FUNDAMENTAL, OF THE FIRST HARMONIC, AND THEIR RATIO VERSUS SHAKER DRIVING VOLTAGE

Whether this method can be used for absolute calibrations depends on the linearity of the calibration factor for all lower amplitudes, once the system had been calibrated with a conventional method at 800 Å (in the first maximum of the first order Bessel Function). It is reasonable to assume that the calibration factor holds to 1 Å amplitude or even below because this method has the advantage that it requires only the ratio of two calibration factors to be linear over the range of amplitudes rather than the absolute value of either, and this linearity has been demonstrated in Figures 20 and 21.

On the other hand, the availability of the calibration method using the Mōssbauer Effect gives for the first time an independent, nonoptical way of verifying the accuracy of the optical calibration method. The two methods provide cross-checks that guard against systematic errors in either calibration method. In fact, several organizations from government as well as from private industry requested information about this unique possibility of cross-checking the interferometer with an independent, nonoptical method.

The National Bureau of Standards is working on a method that provides vibration calibrations below 800 Å. This is accomplished with an interferometer in which one light path is extended by multiple reflections between a stationary and an oscillating mirror, thus increasing the sensitivity by the number of reflections. As depicted in Figure 22, light from a He-Ne gas laser is divided by a beam splitter. The transmitted beam is reflected from a mirror on the shake table to an auxiliary, stationary mirror and back to the vibrating mirror a number of times, and then to a second beam splitter where part of it is combined with the reflected beam from the first beam splitter to form an interference pattern. The convenience of the method results from the intensity and collimation of the laser light. Each reflection produces a small red spot on the mirror so that the system can be aligned easily, and the number of reflections can be counted easily without ambiguity. The focusing lens is used to insure that the laser beam is as narrow as possible in the region of multiple reflections. It expands beyond that region. The optical attenuator is used to adjust the intensity of the light reflected from the first beam splitter to match the intensity of the light from the vibrating surface. The expander lens is used to set the fringe pattern to an optimum size and intensity for visual observation.

The folded beam interferometer is used to set the amplitude of vibration to a known value by the techniques of interference fringe disappearance. If the 6328 Å line of the He-Ne laser is used, the usual fringe disappearance would occur at 1211 Å. In the folded beam interferometer, disappearance occurs at 1211 Å divided by the number of reflections.

This method works fine, provided all surface elements are oscillating in phase. This has been checked by placing three accelerometers on the shaker surface and comparing their output voltages on the x and y plates of an oscilloscope. If all transducers are oscillating in phase, the display on the scope is a straight slant line. If they are out-of-phase, the scope shows an ellipse.

It has been found that up to 30 kHz the shaker is oscillating in phase all over its surface. At higher frequencies this is not guaranteed any more; however, for calibration purposes, certain frequencies where there is no uniformity in phase have to be avoided.

In a laboratory setup ten reflections could be achieved, which means that with the He-Ne laser vibration amplitudes down to 120 Å could be detected.

The contract with the NBS contains provisions for the development of shakers covering a frequency range up to 100 kHz, but this is not a subject of this paper.

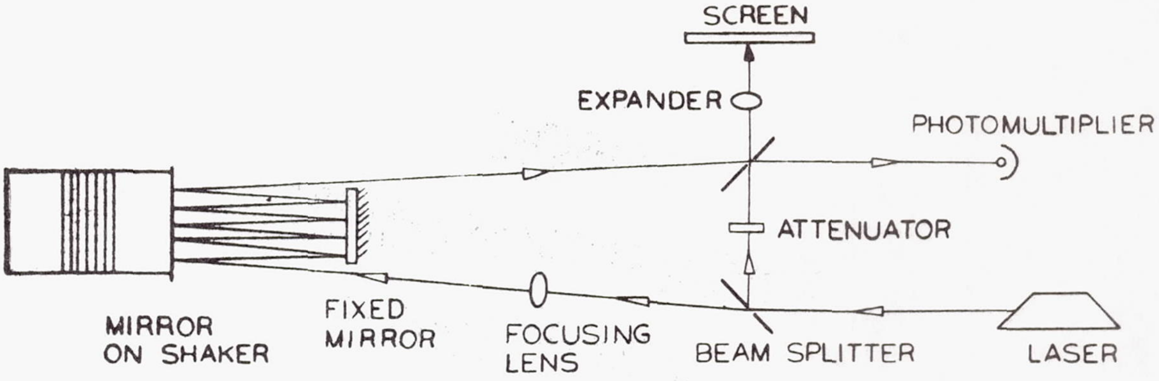

FIGURE 22. MULTIPLE BEAM REFLECTION INTERFEROMETER

Page
Intentionally
Left Blank

PARACTOR, A NEW TOOL FOR ACCURATE DC AMPLIFICATION AND DIGITAL DATA TRANSMISSION

By

Thomas L. Greenwood

INTRODUCTION

Several years ago the Test Laboratory became interested in the development of an improved digital data acquisition system in which the analog transducer output would be converted to digital form in the vicinity of the transducer. Transmitting the data in digital form will reduce the probability of error caused when long cable circuits carry analog signals. Contract NAS8-5439 was awarded to Trans-Sonics, Inc., to develop such a system using magnetic amplifier techniques in the comparison circuit of a successive-approximation analog-to-digital converter.

The Parametron, invented by Goto of Tokyo University and used extensively in Japanese computers as a logic element, seemed suited to this application. It has the property of producing oscillations with the phase depending on polarity of magnetic flux in the input coil, and can be produced in small physical dimensions approximating the size of a cable connector.

PARACTOR RESEARCH AND DEVELOPMENT

Investigation of the Parametron device by Trans-Sonics, Inc., engineers showed that significant improvements could be made in its operation. The improved Parametron, a form of second harmonic modulator, was called the Paractor, for "parametric reactor." It was driven by a continuous wave ac, and developed a large ac output in the form of a self-oscillation, the phase of which was under the control of the dc input signal. Only two phases could be generated, 0 and π radians, and these signals could be used as commands to control the logic steps in the successive-approximation technique for analog-to-digital conversion. The circuit was the super-regenerative type in that the phase of the output signal could not be changed without first stopping the oscillations.

Further improvement indicated that this Paractor, while exhibiting very high gain, had one property that was extremely undesirable in the case of the planned application. This property was that the Paractor "remembered" large input signals. Any overload of the control winding caused a zero shift in the Paractor, which was equivalent to a direct current in the input winding.

The Paractor circuit was modified to provide pulse excitation instead of sine wave excitation, and is now known as the Pulsed Paractor. Its operation may be described as follows: The coil that carries the control or input signal as well as the output pulses is referred to as the flux coil (Figs. 1 and 2).

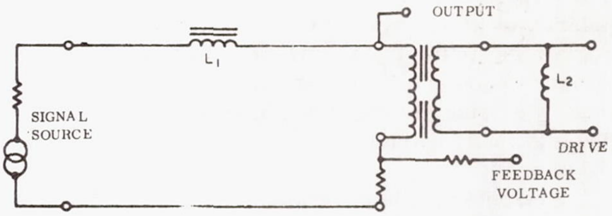

FIGURE 1. PULSED PARACTOR

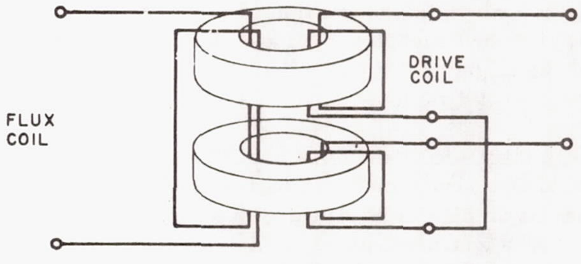

FIGURE 2. PARACTOR MAGNETIC CIRCUIT

The two coils through which the drive pulse is applied are called drive coils, and the circuit that includes the drive coils and the apparatus driving the coils is referred to as the drive circuit. The function of the drive coils is merely to establish the permeability of the cores around which the flux coil is wound. To prevent drive currents from being induced in the flux coil, the magnetic material is divided into two cores, each of which carries a drive coil. The drive coils are connected so that the drive flux induced in each of the two cores is in opposite directions. For example the upper core might have flux induced in the clockwise direction while the lower core might have flux induced in the counterclockwise direction. If these fluxes are identical, no voltage would be induced in the flux coil that threads both cores (Fig. 2).

Immediately before the drive pulse is applied, the cores are in a state of high permeability. Any signal current flowing in the flux coil will result in a relatively high flux being induced in the two cores inside the flux coil. This flux is caused by the control signal operating on the high permeability of the cores. The drive pulses are of sufficient amplitude to drive the cores into saturation. As the cores saturate, the instantaneous permeability of the iron decreases and approaches zero as a limit. As the permeability approaches zero the flux induced by the control signal must disappear since the permeability is too low to support the flux. As the flux disappears, a voltage is induced in the flux coil as a result of the rate of change of flux. This voltage is the output signal, the phase or polarity of which depends on the polarity of the direct current in the input coil. Rapid saturation is necessary to obtain a large output. This is accomplished by driving the cores with a large current pulse having a low duty cycle.

The output pulse is prevented from flowing back into the dc source circuit by the inductor L_1. Resetting the cores to a zero magnetic condition is accomplished by the "kickback" from the inductor L_2 after the drive pulse has decayed to zero. The inductance value is chosen so that the "kickback" is strong enough to reduce the magnetism of the saturated cores to zero between each drive pulse. This eliminates the undesirable "memory" effect that was encountered in the early prototype models.

The magnetic modulators, or Pulse Paractors, designed and constructed on Contract NAS8-5439, have gains as high as 60 dB, and production quality control may guarantee gains as high as 55 dB. Signals in the order of 10-15 W in the input circuit have been amplified to a useful level.

MULTICHANNEL DIGITAL DATA ACQUISITION SYSTEM

DESIGN OF 120 CHANNEL SYSTEM

The goal of the development contract was a multichannel digital data acquisition system, and after the Pulsed Paractor was developed to a point where its usefulness was demonstrated, specifications were written for a 120 channel system with magnetic tape recording.

The original concept of an improved system was to accomplish the analog-to-digital conversion as near to the transducer output as possible. The digital data could then be transmitted to any distance without degradation. Present analog-to-digital conversion systems, which include several hundred feet of wire conducting the analog signals to the conversion equipment, suffer degradation of the analog signal as a result of noise and other disturbances in the wire. The system concept provided for the conversion function to be accomplished in a circuit that has the comparator within a few inches of the transducer output terminals. The comparator-logic loop could be as much as a few hundred feet long without affecting the operation, as the logic signals are in digital form and would not be degraded by the wire link circuit. Thus, the comparator could be a small size suitable for mounting in the same environment as the transducer, and the logic circuit could be some distance away in a sheltered location.

DEVELOPMENT OF COMPARATOR CIRCUIT

Development of the system proceeded along these lines, and a prototype with a signal channel was successfully operated. However, it was realized that serious problems in the transmission of logic signals to the comparator would have to be solved if a system for a large number of channels could be designed. This circuit is shown in Figure 3. The bandwidths required might be in the order of 1 MHz. It was decided to try another approach. Figure 4 shows a circuit in which the feedback "balancing" voltage from the logic circuits is transmitted as a narrow band signal. However, this still required that the Paractor pulse output be transmitted over a wide band circuit. Further improvement in operation was obtained by using the circuit in Figure 5. The Paractor pulse output is integrated and sent to the logic equipment as a narrow band signal. This signal controls the decision-making function in the logic circuits, and the logic output signals are sent as narrow band voltage steps to the comparator input circuit to provide a potentiometric measurement of the input signal.

This comparator circuit provides all the functions and advantages as the original circuit concept. It transfers a high level replica of the input signal, through a tight feedback loop, to a convenient point for analog-to-digital conversion.

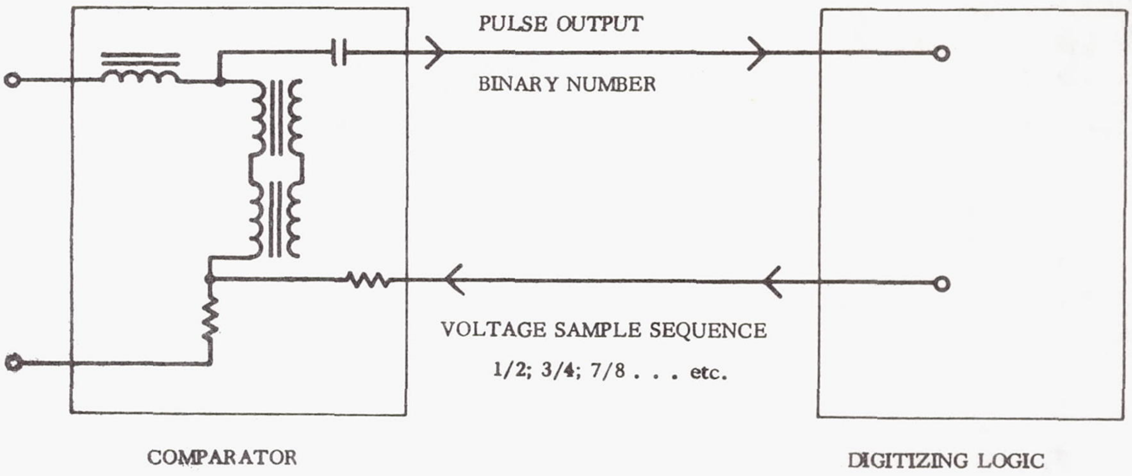

FIGURE 3. INITIAL INPUT CONFIGURATION

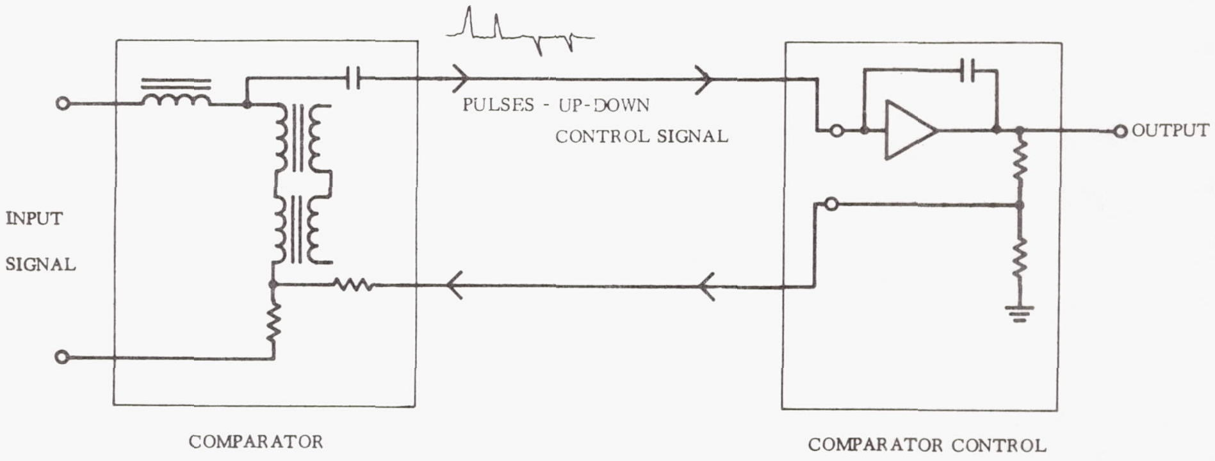

FIGURE 4. IMPROVED CIRCUIT

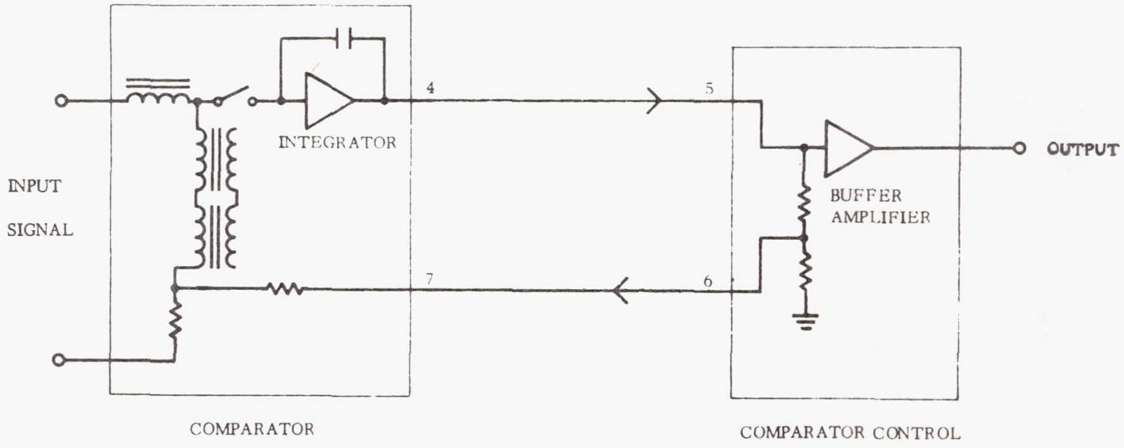

FIGURE 5. FINAL CONFIGURATION

DESCRIPTION OF THE SYSTEM

A system was designed and constructed for 120 channels, using the comparator circuit described above, each channel being sampled 20 times per second with a resolution of 1 part in 2000. Input signals are ±5 V fixed fullscale range, and a variable fullscale range from 10 to 50 mV. The equipment arrangement is shown in Figure 6 together with relative distances between the components of the system. Figure 7 shows a block diagram of the system.

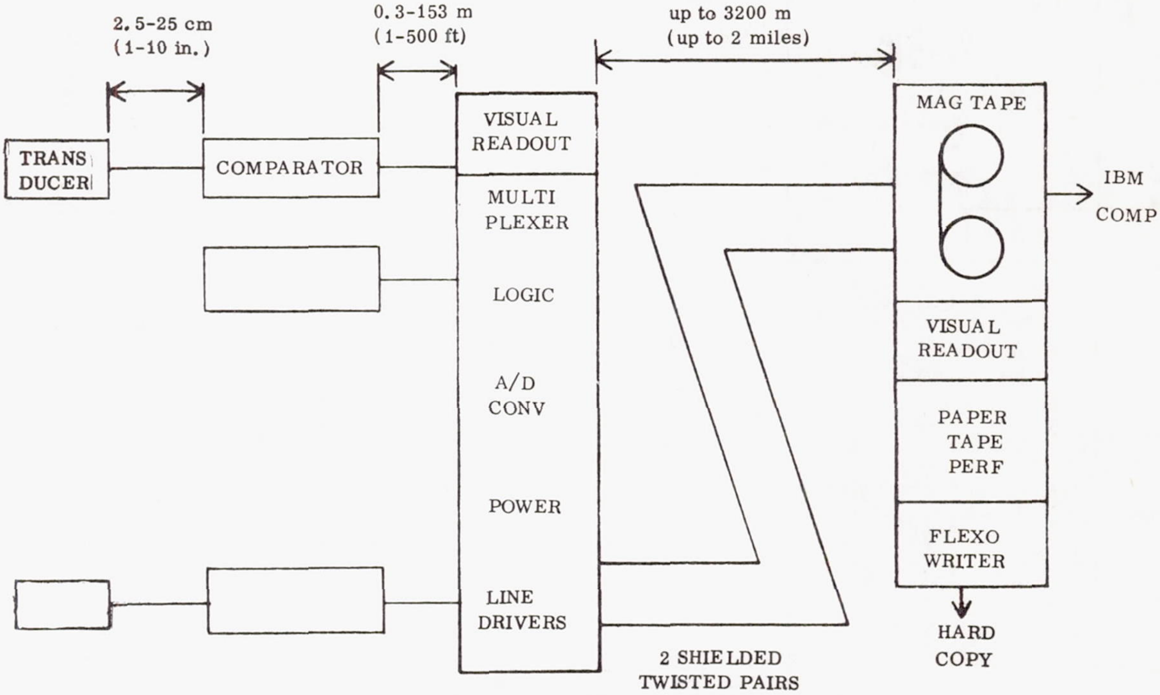

FIGURE 6. ARRANGEMENT OF COMPONENTS

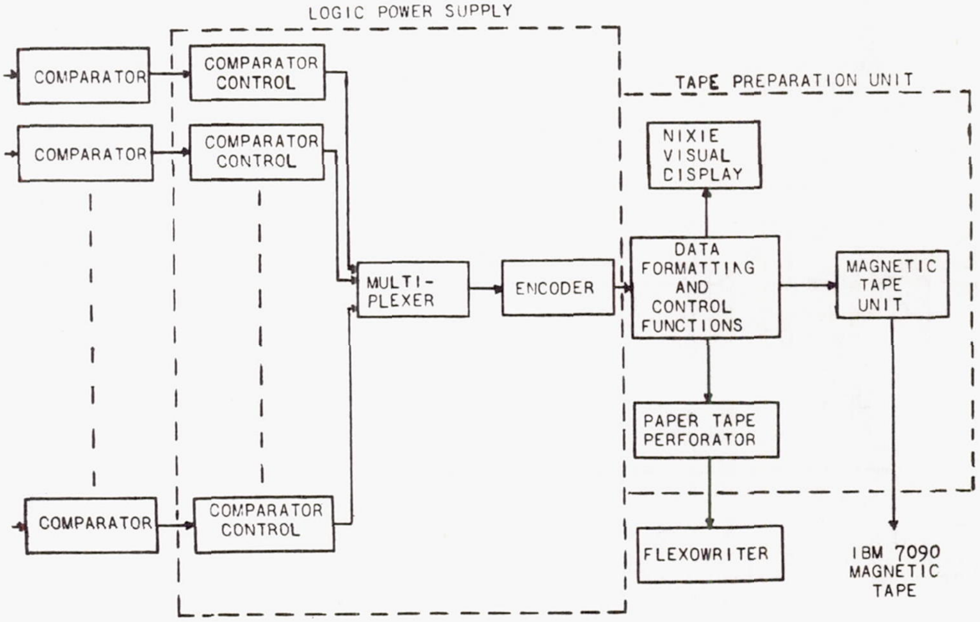

FIGURE 7. SYSTEM BLOCK DIAGRAM

The comparator unit includes a Pulsed Paractor, a pulse oscillator for driving the Paractor coils, an integrating amplifier, and resistance network for the feedback voltage providing the potentiometric measurement. This is encased in an environment-proof cylindrical enclosure of 3. 3 cm (1. 3 in.) diameter and 20. 3 cm (8 in.) length. Cable connectors are provided at each end.

Logic control, power supplies, and visual digital monitors are provided in equipment racks suitable for mounting in the instrument room of a test stand, or other sheltered place. The digital signals are transmitted over two shielded twisted pairs to the recorder, which may be as far away as 2 miles. At the recording location, which could be a blockhouse, is the magnetic tape recorder, visual digital monitor, paper tape perforator and Flexowriter for printout. The magnetic tape recorder is the incremental digital type, which uses tape only when recording digital pulses, and produces IBM compatible tape recordings. The system has been checked out at Marshall Space Flight Center and has been put to use gathering data in Test Laboratory operations.

ADDITIONAL APPLICATIONS

Besides attaining the goal of the contract, the development of the precision comparator circuit gave promise of other applications in the instrumentation field. Trans-Sonics, Inc. , packaged the new comparator circuit in a single enclosure as a "Precision dc Amplifier" using the circuit shown in Figure 8. This is essentially an electronic-servo-balanced potentiometric measuring system, similar in technique to a servo-balance strip-chart recorder. The amplifier is designed for input signals in the millivolt ranges. The output is an optional 5 or 10 V. The bandwidth extends from 0 to 1 kHz. Provisions are made for use with various transducers, including resistance thermometers, strain gages, and thermocouples. A regulated power supply and bridge completion networks are provided for transducer bridge circuit requirements. Primary power supply requirement is 28 Vdc. Figure 9 shows the packaged amplifier.

The Paractor input coil, being usually a low resistance, lends itself to various low impedance circuits. For example, for strain measurement without strain gages on the metal skin of a structure like a missile, electrical connections would be attached at the corners of a square, with excitation current being supplied to opposite corners, and the output reading would be taken from the other diagonal connections. This is essentially a low resistance bridge circuit.

Any change in resistance of a portion of the skin, caused by strain, would change the resistance balance of the bridge circuit, and the output would be amplified by the Paractor amplifier. The advantage is that the Paractor provides its best amplification when the input circuit is a low resistance.

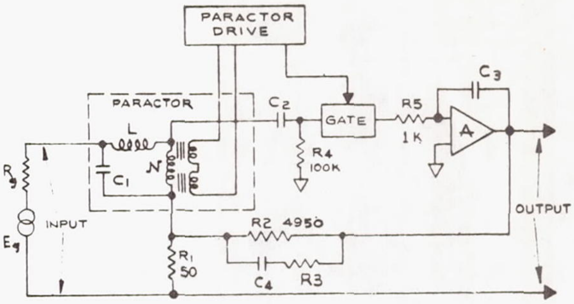

SIMPLIFIED CIRCUIT

FIGURE 8. PRECISION AMPLIFIER USING PARACTOR

FIGURE 9. PRECISION DC AMPLIFIER

CONCLUSIONS

The goal of the development contract NAS8-5439 has been attained. A 120 channel digital data acquisition system has been developed and checked out satisfactorily, and is now used in Test Laboratory operations. A precision dc amplifier with improved characteristics has also been obtained by using techniques developed for the digital system. Its features of good stability under unfavorable environmental conditions, such as temperature extremes and vibration, have been demonstrated. This amplifier should prove useful in many instrumentation applications.

APPROVAL NASA TMX-53793

RESEARCH ACHIEVEMENTS REVIEWS
Volume II, Series 1 through 12

The information in these reports has been reviewed for security classification. Review of any information concerning Department of Defense or Atomic Energy Commission programs has been made by the MSFC Security Classification Officer. These reports, in their entirety, have been determined to be unclassified.

William G Johnson

William G. Johnson
Director, Experiments Office

UNITS OF MEASURE

In a prepared statement presented on August 5, 1965, to the U. S. House of Representatives Science and Astronautics Committee (chaired by George P. Miller of California), the position of the National Aeronautics and Space Administration on Units of Measure was stated by Dr. Alfred J. Eggers, Deputy Associate Administrator, Office of Advanced Research and Technology:

"In January of this year NASA directed that the international system of units should be considered the preferred system of units, and should be employed by the research centers as the primary system in all reports and publications of a technical nature, except where such use would reduce the usefulness of the report to the primary recipients. During the conversion period the use of customary units in parentheses following the SI units is permissible, but the parenthetical usage of conventional units will be discontinued as soon as it is judged that the normal users of the reports would not be particularly inconvenienced by the exclusive use of SI units."

The International System of Units (SI Units) has been adopted by the U. S. National Bureau of Standards (see NBS Technical News Bulletin, Vol. 48, No. 4, April 1964).

The International System of Units is defined in NASA SP-7012, "The International System of Units, Physical Constants, and Conversion Factors," which is available from the U. S. Government Printing Office, Washington, D. C. 20402.

SI Units are used preferentially in this series of research reports in accordance with NASA policy and following the practice of the National Bureau of Standards.